Chemical Engineering Methods and Technology

PEROVSKITES

Structure, Properties and Uses

Maxim Borowski
Editor

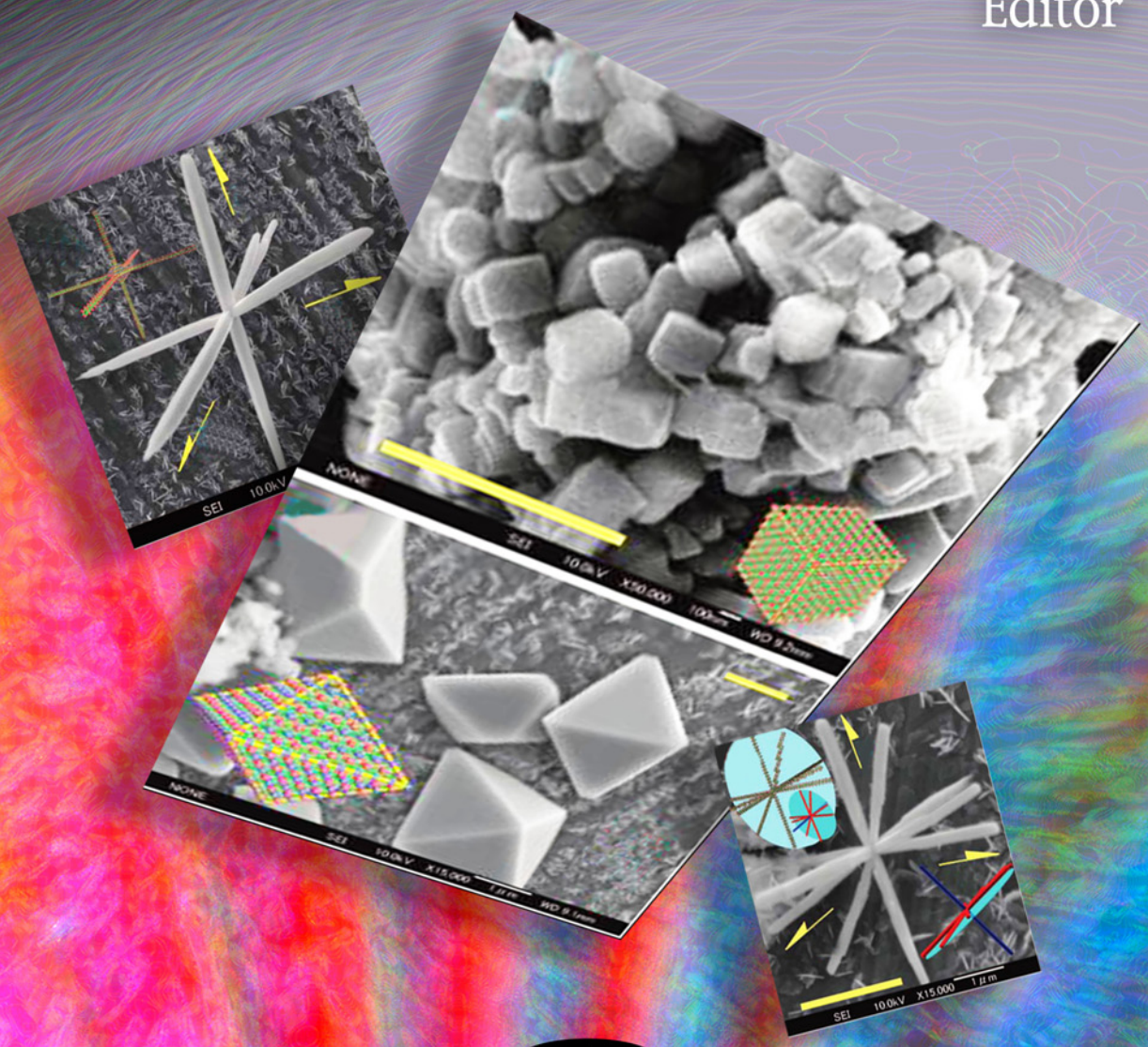

NOVA

CHEMICAL ENGINEERING METHODS AND TECHNOLOGY

PEROVSKITES: STRUCTURE, PROPERTIES AND USES

CHEMICAL ENGINEERING METHODS AND TECHNOLOGY

Additional books in this series can be found on Nova's website under the Series tab.

Additional E-books in this series can be found on Nova's website under the E-books tab.

CHEMICAL ENGINEERING METHODS AND TECHNOLOGY

PEROVSKITES: STRUCTURE, PROPERTIES AND USES

MAXIM BOROWSKI
EDITOR

Nova Science Publishers, Inc.
New York

LIBRARY OF CONGRESS CATALOGING-IN-PUBLICATION DATA

Perovskites : structure, properties, and uses / editor, Maxim Borowski.
> p. cm.
> Includes index.
> ISBN 978-1-61668-870-7 (eBook)
> 1. Perovskite. I. Borowski, Maxim.
> QE391.P47P474 2010
> 549'.528--dc22
> 2010007616

Published by Nova Science Publishers, Inc. + New York

CONTENTS

PREFACE

Perovskite is a calcium titanium oxide mineral species composed of calcium titanate. This new book discusses perovskite thin films, which are widely employed in today's advanced technology. The broad range of physical properties in such category of materials has offered various functionalities in devices ranging from dynamic random access memories and ferroelectric nonvolatile memories to piezoelectric and optical devices. The structural, magnetic and electron transport properties of ordered-disordered perskovite cobaltites is discussed as is perovskite-type oxides, ferroelectric PbTiO3 from a single-domain state to composite components.

Chapter 1-Perovskite-type oxides and perovskite-like oxides can tolerate substantial substitutions in one or both cationic sites while maintaining their original crystal structures. Such a feature renders the chemical tailoring of the materials via partial replacement of the cationic site(s) with foreign metal ions, hence modifying their physicochemical properties. Perovskite-type oxides and perovskite-like oxides have been found many applications in physics and chemistry. The physicochemical properties of these materials are dependent on the crystal structure, lattice defect, exposed lattice plane, surface morphology, particle size, and specific surface area as well as the pore structure. Up to now, a large number of perovskite-type oxides and perovskite-like oxides have been generated and investigated for clarifying their physicochemical properties. In the past years, although several books and reviews relevant to such a kind of materials appeared in the literature, a systematic summarization on the newly published works related to the fabrication, characterization, and catalytic applications of perovskite-type oxides and perovskite-like oxides with the particles being nanosized, specifically morphological or porous has not been available. Due to the unique properties of these nano- and/or porous materials with low dimensionality, author shall summarize the results of such functional solid materials recently reported in the literature, and aim to gain insights into the relationship between structure and property and the potential applications in catalysis. Therefore, author shall focus the author attention in Section 2 on the controlled fabrication of perovskite-type oxides and perovskite-like oxides with specific morphologies, such as nano/microwires, nano/microrods, nano/microtubes, nano/microfibers, nano/microcubes, nano/microspheres, nano/microflowers, and etc. Due to the superiority in physicochemical property of porous materials to their bulk counterparts, author shall also include the synthesis of macro- and/or mesoporous perovskite-type oxides and perovskite-like oxides (although limited works have been done in the aspect) in this section. In Section 3,

author shall highlight the physicochemical properties of perovskite-type oxides and perovskite-like oxides fabricated by the researchers mentioned in Section 2, so that one can generalize some clear correlations between the fabrication strategy and the crystal or porous structure or morphology. In Section 4, author shall concentrate on the applications of these addressed materials in catalysis, such as NO_x elimination, CH_4 complete oxidation, and volatile organic compounds removal, and etc. Finally, author shall propose the perspectives and concluding remarks of the research in the future in Section 5.

Chapter 2- This paper presents results of research aimed at elucidating factors controlling mobility and reactivity of the surface and bulk oxygen of complex perovskite-like $A_nB_mO_z$ oxides (manganites, ferrites, cobaltites, nickelates of La/Sr) and their nanocomposites with fluorite-like oxides (doped ceria or zirconia) as related to their performance in the intermediate temperature solid oxide fuel cells (IT SOFC) cathodes and oxygen separation membranes. Real/defect structure and surface properties of these materials as a function of both composition, preparation route and sintering temperature were studied by combination of TEM with EDX, XRD, EXAFS, UV-Vis and XPS methods. Lattice oxygen mobility, strength of oxygen species bonding with the surface sites and their reactivity for both dispersed and dense materials were estimated by oxygen isotope exchange, temperature-programmed desorption and reduction by H_2 and CH_4. Coefficients of oxygen diffusion in dense materials were estimated by analysis of dynamics of the oxygen loss monitored by measurements of the weight loss or conductivity relaxations. For analysis of atomic-scale factors controlling oxygen bonding strength and mobility, quantum-chemical approaches including the Density Functional Theory (DFT) in spin-polarized SLDA approximation and semiempirical Interacting Bonds Method were applied.

For simple perovskites, along with well-known effects of anion vacancies/interstitial oxygen atoms and high- charge transition metal cations generated due to the oxygen non-toichiometry, pronounced effects of the surface faces termination, ordering of oxygen vacancies and appearance of extended defects were found to affect the oxygen mobility and reactivity as well. From the microscopic point of view, decreasing the Me-O bonding strength and increasing the distance between A and B cations due to the lattice parameter increase helps to decrease the activation barriers for the oxygen diffusion in the perovskite-like lattice.

For perovskite-fluorite nanocomposites, interfaces were shown to be paths for fast oxygen diffusion due to redistribution of cations between contacting phases.

The most promising combinations of perovskites and perovskite-fluorite nanocomposites possessing a high lattice oxygen mobility and conductivity were used for synthesis of functionally graded cathodes of IT SOFC with thin layers of doped zirconia electrolytes as well as for manufacturing asymmetric Ni-Al compressed foam supported membranes for oxygen separation and syngas generation. High and stable performance of these materials promising for the practical application was demonstrated.

Chapter 3- Strong interplay between electronic behavior, structure and magnetism in doped perovskite manganites gives rise to the enhanced sensitivity of transport properties to magnetic and structural peculiarities. The optimally doped manganite compounds are metallic and ferromagnetic at low temperatures, while their conductivity displays activated behavior at high temperatures. The metal-insulator transition between these two states is strongly associated with the magnetic ordering one, and this manifests itself in the formation of a resistivity peak in the vicinity of Curie temperature T_C. However, in some peculiar cases, manganite samples exhibit an additional low-temperature resistivity peak (LT-peak) (or a

tendency to its emergence in a form of a plateau), which is not associated with any magnetic or structural transition and nature of which remains unclear hitherto. In this chapter, based on a simple phenomenological model, author demonstrate that the formation of the LT-peak may be a result of a strong broadening of the ferromagnetic transition. The approach developed examines the electrical properties of a system consisting of paramagnetic and ferromagnetic phases which exhibit opposite trends in the temperature dependences of resistivity and coexist over a wide temperature range. It is shown that, as the region of the phase coexistence increases, the resistive transition first broadens, then, in addition to the resistive peak near T_C, the LT-peak emerges and begins to grow, later on it becomes dominant and, eventually, only a weak shoulder-like feature remains at T_C. Such an approach is shown to be applicable to the description of the magnetic and electric properties of a number of inhomogeneous and phase-separated manganite systems, including micro- and nanocrystalline samples, ultrathin epitaxial films, etc.

Chapter 4- Rare earth perovskite cobaltites are increasingly recognized as materials of importance due to rich physics and chemistry in their ordered-disordered structure for the same composition. Apart from colossal magnetoresistance effect, like manganites, the different forms of cobaltites exhibit interesting phenomena including spin, charge and orbital ordering, electronic phase separation, insulator-metal transition, large thermoelectric power at low temperature. Moreover, the cobaltites which display colossal magnetoresistance effect could be used as read heads in magnetic data storage and also in other applications depending upon their particular properties. The A-site ordered-disordered cobaltites exhibit ferromagnetism and metal-insulator transitions as well as other properties depending on the composition, size of *A*-site cations and various external factors such as pressure, temperature, magnetic field etc. Ordered cobaltites, having a *112*-type layered structure, are also reported to have an effectively stronger electron coupling due to layered *A*-site cationic ordering. Most importantly for the present article author focus on *La-Ba-Co-O* based ordered-disordered perovskite phases, which exhibit interesting magnetic and electron transport properties with ferromagnetic transition, $T_C \sim 177K$, and it being the first member of lanthanide series. *Zener* double exchange mechanism considered to be crucial for understanding basic physics of the ferromagnetic-metallic phase, yet does not explain clearly the insulating-type phase. In terms of electron transport the ferromagnetic-metallic or insulating/semiconducting states have been discussed in the present article with different types of hopping model.

Chapter 5- Perovskite thin films are widely employed in today's advanced technology. The broad range of physical properties in such category of materials has offered various functionalities in devices ranging from dynamic random access memories and ferroelectric nonvolatile memories to piezoelectric and optical devices. In addition to the aforementioned applications, perovskites have been revealed to be promising candidate materials in many novel applications including electrically tunable microwave devices and resistive switching memories. Thin films of the perovskite ferroelectrics are being used to develop the tunable microwave devices owing to their strong electric field dependent dielectric constant in the paraelectric state. Reversible switching between high- and low- resistance states induced by electric field makes perovskite thin films suitable for the applications in resistive switching memories. This chapter focuses on the author recent progress on these two kinds of electrically tunable properties in perovskite thin films. Based on the origin of dielectric tunability that is defined as the variation of dielectric constant in a certain electric field range, approaches to improve the tunable dielectric properties will be introduced. On the other hand,

although resistive switching behaviors have been discovered in many perovskites during the last decade, the origin of such switching is not well understood yet. In this chapter, some proposed mechanisms responsible for the resistive switching will be discussed.

Chapter6- The perovskite family of materials is of considerable technological importance for its excellent temperature stable microwave properties for dielectric resonator based filters, oscillators and antenna applications. In this chapter author review the preparation, characterization and the microwave dielectric properties of $Ca[(Li_{1/3}A_{2/3})_{1-x}M_x]O_{3-\delta}$ [A=Nb, Ta and M=Ti, Zr, Sn] dielectric ceramics. This family of perovskite materials shows relative permittivity in the range 20 to 56 with a quality factor up to 45000 GHz and temperature coefficient of resonant frequency (τ_f) in the range from −21 to +83 ppm/°C. The τ_f can be tailored by adjusting the titanium content. The sintering temperature can be lowered below 950 ^oC to suit LTCC by the addition of low melting glasses.

Chapter 7- Two topics of perovskite-type oxides were browed and discussed in this chapter: one is the synthesis method and the other is its application in catalysis. Because of the diverse applications of perovskite-type oxides, special properties are usually required depending on the ultimate use, while the desired properties could be achieved by choosing a proper synthesis method. For example, using coprecipitation method could lead to a well crystallized structure, while by a nanocasting method perovskite with high surface area could be achieved. Thus, an overview of synthesis method for perovskite-type oxides reported in the publications was made for better understanding the advantage of each method.

Efforts on the application of perovskite-type oxides were made exclusively in catalysis in this part. Attentions on using these oxides as catalyst are increasing year by year not only because of their low manufacturing cost but also due to the unique properties, such as high thermal stability, exchangeability of cations and of course, considerable activity. Many catalytic reactions using perovskite-type oxides as catalyst has been attempted, and although for a given reaction catalyst with different ions, either at A- or B-site, show different catalytic activities, a common point is that the presence of oxygen vacancy is necessary for the reaction to proceed. From the nature of catalytic reaction, that is the difficulty of electron transferring between reactant and catalyst, it was proposed, exampled by the reactions of NO decomposition and NO+CO reduction, that the crucial pre-requisite for a catalytic reaction to occur is that the full redox cycle of catalyst can proceed easily. Thus only when this requirement is fulfilled, other parameters, such as the amount of active sites, could come into the focus of catalyst design.

Chapter 8- The chapter presents general analysis and results of experimental data on the structure-chemical investigation of process of formation of perovskite type structures in different groups of layered oxides, which exhibit a number of practically important properties. In many cases the layered perovskite-like phases are formed in a multistage way. The composition and stability of the intermediates can strongly affect both reaction rate and the structure of the final compound. Examples of such impact for several Ruddlesden-Popper and Aurivillius phases are considered. Formation of the double-perovskite layered phases for the series of high temperature aluminates $Ln_2SrAl_2O_7$ (Ln=La, Nd, Sm, Eu, Gd, Ho) is discussed in terms of the dependence of mechanism of reaction on the nature of rare earth elements. For the double-layered manganites $LnSr_2Mn_2O_7$ (Ln=La, Nd, Gd) the structure and stability of the intermediate perovskite phase affects both the reaction speed and the microstructure of the resulting Ruddlesden-Popper phase, including phase separation in the CMR manganites. The double-layered ferrites $Ln_2SrFe_2O_7$ (Ln=La, Nd, Gd) exhibit the evolution of oxidation state

of iron along the process of synthesis. Mechanism of formation of the ferroelectric Aurivillius phase Bi_3TiNbO_9 demonstrates the limitations on the Bi→Ln and Ti→Mn substitution in this structure. The stability of the intermediate phase results in the substitution limitations. Investigations of the processes occurring in the reaction mixture during synthesis of the perspective ionic conductors and catalyst $(Na,Nd)_{n+1}Ti_nO_{3n+1}$ allow to explain the necessity of the excess of alkali metal containing starting compound, optimize the conditions of synthesis and significantly decrease the size of particles.

Chapter 9- The behavior of the system $La_{1-x}Ca_xMnO_3$ is considered theoretically at the absolute zero temperature (magnetic configurations), at the low temperatures (spin waves) and at the high temperatures (magnetization).

The appearance of the different magnetic configurations in the row $0 \le x \le 1$ is studied. Superexchange, double exchange and anisotropy energy are taken into account. The spin operator of double exchange interaction in crystal between ions with different valence Mn^{3+} and Mn^{4+} is the straight generalization of two - spin operator problem of Anderson – Hasegawa molecule. Ground state energy minimization gives 11 types of magnetic configurations: two ferromagnetic, three collinear antiferromagnetic and six non-collinear. When the concentration of Ca ions changes, then the spin configurations replace one another as the ground state. As a whole the sequence of configurations when x changes from 0 to 1 can be brought in correspondence to those observed at the experiment. The appearance of the angle configurations in the systems may occur if the Heisenberg and non – Heisenberg exchange exist simultaneously. The comparison with experiment was made by means of mixed procedure: part of the numerical values of interaction parameters and transition concentrations x were taken from the experiment while the missing values of these parameters were calculated with the help of the corresponding theoretical relations. The proposed dynamical alloy model of different spins can be used for description of real perovskite-like systems behavior.

The elementary spin excitations were studied in ferromagnets and antiferromagnets for the compounds with the special contents and theoretical dispersion curves were compared with experimental ones obtained by neutron inelastic scattering method for different directions in the first full Brillouin zone. Theoretical expressions are obtained for the spin-wave spectrum in a ferromagnetic cubic crystal with variable-valence ions. Interactions up to the fourth coordination shell are taken into account. Two kinds of exchange are assumed to occur in the system. As a result, the numerical values of total exchange parameters for each of the coordination shells can be found. These studies are made for ferromagnets at $x = 0.17, 0.25, 0.30$. Theoretical expressions are obtained for energy of spin waves in layered antiferromagnetic structure of the perovskite-like compound $LaMnO_3$. The quadratic exchange interactions of the central spin moment of the trivalent manganese ion with its eighteen neighbors from five coordination shells and single-ion magnetic anisotropy energy are taken into account. For the three principal crystallographic directions, the theoretical results are compared with the experimental data. It is shown that the in-plane ferromagnetic interaction can be more than sixteen times as great as the interplanar antiferromagnetic interaction.

The high temperature dependence of spontaneous magnetization at a separate site in the compounds with $0 \le x \le 1$ is investigated in the molecular field approximation using a homogeneous model for the magnetic sub-lattice with allowance for the Heisenberg and double exchange between nearest neighbors. Unlike with the usual magnets having one type of magnetic ions, in this case there appears a system of equations with two unknowns mean spins of manganese ions. In the vicinity of the ordering temperature, this system can be solved analytically and the expression for the ordering temperature can be obtained as well. To find the temperature dependence of magnetization in the whole temperature range the exact expression for the double exchange operator containing spin operators under square root was used. The numerical solutions were found in this case.

Chapter 10- In the chapter two approaches to the crystals ordered states description are used. The first is basing on the group theoretical considerations incorporated in theory with the help of Landau potential. The second way of ordering description consist of accounting different models of interatomic interactions. The author goal is to elucidate correlations between these two approaches. Complex oxides with composition $AB_c^{/}B_{1-c}^{//}O_3$ and perovskite like structure are considered as an example. Six supercells which may be realized as stable states in these solid solutions in accord with Landau theory are analyzed in the framework of both approaches. The potential of interatomic coupling includes van der Waals energy and terms following from pseudopotential model. The sum of interatomic energy in twelve coordination spheres was accounted to get correlation between the parameters of Landau potential and coefficients of interatomic energy and to define the domain of different ordering state stability in the space of phenomenological parameters. In particular it is shown that under certain conditions the type of ordering in a surface area may differ from the type of ordering in a bulk of crystal. Using a new approach to X-ray diffraction pattern interpretation there was established definite correlations between the parameters of pair interactions potential and the peculiarities of ordered states which may be defined from the experiment.

Chapter 11- The term `perovskite` is used to denote a category of inorganic crystalline solids with the general formula ABX_3, where A and B are cations and X (oxides or halides) is an anion. The perovskite structure occupies a prominent place under all the known ternary systems of composition ABX_3. This is due not only to its wide occurrence, but also to a series of interesting and useful properties associated with this structural type. Crystallographic behaviour of perovskites is of great interest because most structures are close to an ideal cubic structure, however, frequently they are slightly distorted resulting in structures with lower symmetry such as orthorhombic, tetragonal, rhombohedral, trigonal systems and so on. These lattice distortions and structure changes are governed by temperature, pressure, chemical composition, and in some cases, electric field. As a rule, with rising temperature, perovskites tend to undergo a series of transitions to progressively higher symmetry, culminating in the cubic structure where experimentally accessible. They are widely investigated, not only because of interest in their crystal structural behaviour, but perovskites also exhibit a variety of interesting electronic, electromechanical and conductive properties, which are the basis for many existing and potential applications. Such properties are often symmetry dependent. In this chapter, a summary of the scientific work performed on the ABX_3 (X = Oxides and Halides) system during the last few years is presented.

Chapter 12- Regular ferroelectric lead titanate ($PbTiO_3$) is one of the well-known perovskite-type compounds with physical properties studied intensively in the last decades.

Of specific interest is $PbTiO_3$ as an element of a hierarchical chain 'single-domain single crystal – polydomain single crystal – poled ceramic – composite', and the last element, composite, can be based on other elements of the aforementioned chain. In this chapter examples of modern piezo-active composites based on either $PbTiO_3$ or $PbTiO_3$-type solid solutions are considered. These composites are regarded as matrix ones with 0–3 and 1–3 connectivity patterns and with a regular distribution of inclusions. To characterize the effective electromechanical properties of the composite, two methods are applied. The effective properties of the 0–3 composite with spheroidal inclusions and of the 1–3 composite with circular cylindric inclusions are predicted by means of the effective field method. The effective properties of the 1–3 composite with inclusions in the form of rectangular parallelepiped are determined within the framework of the matrix method. In both the methods, an electromechanical interaction between components is taken into account. The role of the $PbTiO_3$-containing component is emphasized in connection with the large piezoelectric anisotropy and considerable piezoelectric sensitivity of the composite in certain volume-fraction ranges.

Chapter 13- Materials with high proton or oxide ion conductivity are widely studied for their potential application as electrolytes in fuel cells, electrolysers, batteries, sensors, etc. [1-5]. *Acceptor doped* perovskite-type oxides $ABO_{3-\delta}$ where A is Sr, Ba and B is Ce, Zr are well-known high temperature proton conductors in wet atmosphere. It was found that the main factor responsible for the appearance of protons in the structure was the presence of oxygen vacancies. Upon hydration by equilibration with water vapor the oxygen vacancies may be filled by oxygen from water and, in accordance with dissociative mechanism of water dissolution, the hydroxide ions are formed.

Chapter 14- Author have studied the influence of Pb-doping on critical behavior of polycrystalline manganites of $La_{1-x}Pb_xMnO_3$ (x = 0.1, 0.2 and 0.3) around their ferromagnetic-paramagnetic phase transition temperature (T_C) by means of analyzing isothermal magnetization data *M-H*. According to the critical criterion proposed by Banerjee, it was found that all three samples undergo the second-order phase transition as showing a positive slope of isotherm plots of H/M versus M^2. The critical parameters were determined by the modified Arrott method, used the Arrott-Noakes equation of state $M^{1/\beta}$ versus $(H/M)^{1/\gamma}$ and the asymptotic relations in the critical region. The obtained results reveal that with increasing the Pb-doping concentration in $La_{1-x}Pb_xMnO_3$, the T_C value increases from 162.0 K (for x = 0.1) to about 346.3 K (for x = 0.3). Concurrently, there is a remarkable variation in their critical exponents: β = 0.498, γ = 1.456 and δ = 3.92 for x = 0.1; β = 0.499, γ = 1.241 and δ = 3.49 for x = 0.2; and β = 0.502, γ = 1.063 and δ = 3.12 for x = 0.3. Having compared to the critical parameters expected from the theoretical models of mean-field theory, 3D-Ising model, and 3D-Heisenberg model, author have found an existence of the short-range ferromagnetic order in the samples with x = 0.1 and 0.2, and the long-range ferromagnetic order in the x = 0.3 sample. Under such circumstances, magnetic interaction mechanisms between Mn^{3+}-Mn^{4+} in the samples would be changed, particularly in the paramagnetic region.

Chapter 15 - In the past (1980), the ceramic pigments, 51 pigments in all, were classified into 14 structures of industrial interest and these were classified into black, white and colored pigments. These structures are oxides, materials used in ceramic as pigments because of their greater stability in oxygen-containing ceramic systems. However, thanks to modern and more

refined methods of scientific investigation, new structures, new pigments, new synthetic methods and new applications were also included. Among these author have the development of new red ceramic pigments as perovskite structure of formula A3+B3+O3 as ferrites LnFeO3 and chromium aluminates LnAl1-xCrxO3 (Ln, lanthanide). These lanthanides aluminates ceramic pigments have been synthesized by different methods and characterization studies were realized by X ray diffraction, SEM, UV-VIS spectra, etc. The properties and uses of these lanthanides are appropriate as ceramic pigments; nevertheless, new possibilities for these pigments are its use for luminescent coatings in a diversity of devices or lasers.

In: Perovskites: Structure, Properties and Uses
Editor: Maxim Borowski, pp. 1-66
ISBN 978-1-61668-525-6

Chapter 1

CONTROLLED FABRICATION AND CATALYTIC APPLICATIONS OF SPECIFICALLY MORPHOLOGICAL AND POROUS PEROVSKITE-TYPE OXIDES

Jiguang Deng, Lei Zhang, Yuxi Liu and Hongxing Dai*
Laboratory of Catalysis Chemistry and Nanoscience, Department of Chemistry and Chemical Engineering, College of Environmental and Energy Engineering, Beijing University of Technology, Beijing 100124, China

ABSTRACT

Perovskite-type oxides and perovskite-like oxides can tolerate substantial substitutions in one or both cationic sites while maintaining their original crystal structures. Such a feature renders the chemical tailoring of the materials via partial replacement of the cationic site(s) with foreign metal ions, hence modifying their physicochemical properties. Perovskite-type oxides and perovskite-like oxides have been found many applications in physics and chemistry. The physicochemical properties of these materials are dependent on the crystal structure, lattice defect, exposed lattice plane, surface morphology, particle size, and specific surface area as well as the pore structure. Up to now, a large number of perovskite-type oxides and perovskite-like oxides have been generated and investigated for clarifying their physicochemical properties. In the past years, although several books and reviews relevant to such a kind of materials appeared in the literature, a systematic summarization on the newly published works related to the fabrication, characterization, and catalytic applications of perovskite-type oxides and perovskite-like oxides with the particles being nanosized, specifically morphological or porous has not been available. Due to the unique properties of these nano- and/or porous materials with low dimensionality, we shall summarize the results of such functional solid materials recently reported in the literature, and aim to gain insights into the relationship between structure and property and the potential applications in catalysis. Therefore, we shall focus our attention in Section 2 on the controlled

* Corresponding author: Tel.: +86-10-6739-6588, fax: +86-10-6739-1983; E-mail address: hxdai@bjut.edu.cn

fabrication of perovskite-type oxides and perovskite-like oxides with specific morphologies, such as nano/microwires, nano/microrods, nano/microtubes, nano/microfibers, nano/microcubes, nano/microspheres, nano/microflowers, and etc. Due to the superiority in physicochemical property of porous materials to their bulk counterparts, we shall also include the synthesis of macro- and/or mesoporous perovskite-type oxides and perovskite-like oxides (although limited works have been done in the aspect) in this section. In Section 3, we shall highlight the physicochemical properties of perovskite-type oxides and perovskite-like oxides fabricated by the researchers mentioned in Section 2, so that one can generalize some clear correlations between the fabrication strategy and the crystal or porous structure or morphology. In Section 4, we shall concentrate on the applications of these addressed materials in catalysis, such as NO_x elimination, CH_4 complete oxidation, and volatile organic compounds removal, and etc. Finally, we shall propose the perspectives and concluding remarks of the research in the future in Section 5.

1. INTRODUCTION

Catalysts play an important role in modern chemical industry and environmental protection [1]. The majority of the catalysts are based on single metal and/or metal oxides. Among the mixed metal oxides, perovskite-type oxides and perovskite-like oxides occupy a prominent status. They can tolerate substantial substitutions in one or both cationic sites while maintaining the original crystal structures [2–4]. Such a feature renders the chemical tailoring of the materials via partial replacement of the cationic site(s) with foreign metal ions, hence modifying the physicochemical properties. Perovskite-type oxides and perovskite-related oxides have been found many applications in physics and chemistry. The physicochemical properties of these materials are dependent on the crystal structure, lattice defect, exposed lattice plane, surface morphology, particle size, and specific surface area as well as the pore structure. Up to now, a large number of perovskites have been generated and investigated for clarifying their physicochemical properties. In the past years, although several books and reviews relevant to such a kind of materials appeared in the literature [2,3,5,6], a systematic summarization on the newly published works related to the fabrication, characterization, and catalytic applications of perovskite materials with the particles being nanosized, specifically morphological or porous has not been available. Due to the unique properties of these nano- and/or porous materials with low dimensionality, we summarize the results of such functional solids recently reported in the literature, and aim to gain insights into the relationship between structure and property and the potential applications in catalysis. Therefore, we shall focus our attention in Section 2 on the controlled fabrication of perovskite-type oxides and perovskite-like oxides with specific morphologies, such as nano/microwires, nano/microrods, nano/microtubes, nano/microfibers, nano/microcubes, nano/microspheres, nano/microflowers, and etc. Owing to the superiority in physicochemical property of porous materials to their bulk counterparts, we shall also include the synthesis of macro and/or mesoporous perovskites (although fewer works have been done in the aspect) in this section. In Section 3, we shall highlight the physicochemical properties of perovskites fabricated by the researchers mentioned in Section 2, so that one can generalize some clear correlations between the fabrication strategy and crystal or porous structure or morphology. In Section 4, we shall

concentrate on the applications of these addressed materials in catalysis, such as NO_x elimination, CH_4 combustion, and volatile organic compounds removal. Finally, we shall propose the perspectives and concluding remarks of the research in the future in Section 5.

2. PREPARATION OF NANO/MICROSCALE PEROVSKITES

2.1. Nanoparticle

Nanocrystals exhibit physical and chemical properties that are distinct from their bulk counterparts [7,8]. Controllable fabrication of nanometer perovskites is critical for fundamental studies as well as for potential applications. In the past decade, a lot of methods, such as novel solid-state method [8,9], sol-gel [10−18], hydrothermal synthesis [19], co-precipitation [20,21], reactive grinding method [22,23], microemulsion method [24−26], and nanocasting method [27], have been used to synthesize nanometer perovskites.

In the synthesis of titanate and zirconate nanomaterials, several groups have obtained interesting results. By using barium titanium ethyl hexano-isopropoxide ($BaTi(O_2CC_7H_{15})[OCH(CH_3)_2]_5$) as precursor and oleic acid as stabilizing agent, O'Brien and co-workers fabricated monodispersed cubic $BaTiO_3$ nanoparticles with diameters ranging from 6 to 12 nm (Figure 1) through a sol-gel process at 100−140 ^oC in an argon or nitrogen atmosphere [7]. Morse and co-workers reported a novel vapor-diffusion sol-gel method without the use of a structure-directing template to generate well-defined cubic $BaTiO_3$ nanocrystals (6 nm in size) at low temperatures [28]. The nanocrystals are readily generated by the kinetically controlled vapor diffusion of $H_2O_{(g)}/HCl_{(g)}$ into a non-aqueous solution of the bimetallic alkoxide $BaTi[OCH_2CH(CH_3)OCH_3]_6$ at 16 ^oC. Via the interaction of alkaline earth metals dissolved in benzyl alcohol with transition metal alkoxides at lower temperatures (200−220 ^oC), Niederberger et al. obtained well-grown cubic or tetragonal $BaTiO_3$ and $BaZrO_3$ nanoperovskites [29]. The average size of $BaTiO_3$ nanoparticles is about 6 nm, whereas the primary $BaZrO_3$ particles are not isolated but form worm-like agglomerates with a diameter of 2−3 nm and a length of up to 50 nm. With the aid of hydrothermal treatment at 140−200 ^oC under strong alkaline conditions, Wang et al. generated $BaTiO_3$ nanoparticles (17−20 nm in diameter) [19]. Through a simple solid-state reaction between metal oxalates and anatase TiO_2 in a molten NaCl medium at 820 ^oC in the presence of a nonionic surfactant NP-9 (nonylphenyl ether), Mao and Wong produced the $Ca_{1-x}Sr_xTiO_3$ (x = 0−1) nanomaterials with a mean size of < 100 nm [8]. The substitution of smaller Ca^{2+} (radium = 0.134 nm) with larger Sr^{2+} (radium = 0.144 nm) induces a reduction in symmetry from cubic to orthorhombic.

As we know, among the perovskites used as catalyst, $LaMO_3$ (M = Co, Mn, Fe, Cr, Ni)-based compounds have been received much attention due to their satisfactory catalytic performance [2]. In the past years, our group have developed a novel strategy, citric acid complexing-hydrothermal coupled method, to prepare nanoscale perovskites [30,31].

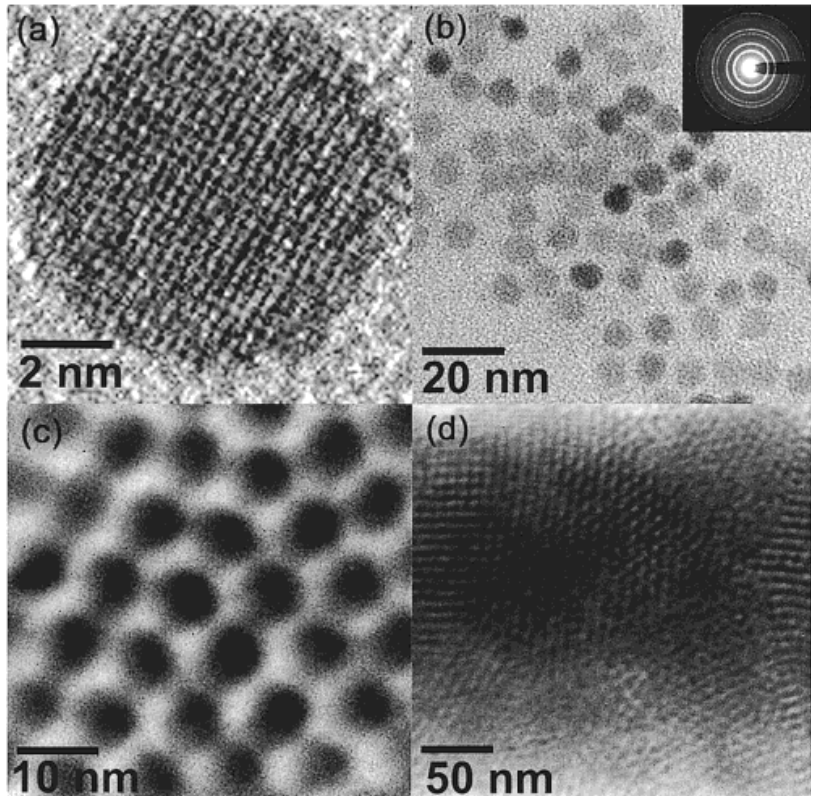

Figure 1. TEM micrographs and the SAED pattern (inset) of (a) a high-resolution lattice image of an individual 8 nm diameter nanoparticle, (b) an ensemble of discrete $BaTiO_3$ 8 nm nanoparticles, (c) self-organization of $BaTiO_3$ nanoparticles, and (d) superlattice of 8 nm diameter $BaTiO_3$ nanoparticles[7].

Using this method, we have obtained a number of highly active nanoperovskite catalysts, including rhombohedral or orthorhombic $La_{1-x}Sr_xMO_3$ (M = Co, Mn, Fe) and $La_{1-x}Sr_xM_{1-y}Fe_yO_3$ (M = Co, Fe). The typical preparation procedure of $LaCoO_3$ is as follows: lanthanum nitrate (0.01 mol), cobalt nitrate (0.01 mol), and a certain amount of citric acid (metal/citric acid molar ratio = 2/1) are mixed in deionized water under constant stirring for complete complexing of the metal ions. Then a certain amount of ammonia (28 wt%) solution is added dropwise to adjust the pH value of the solution to 9.5 at which a sol is formed. The sol is transferred to a 50-mL Teflon-lined stainless steel autoclave with a packed volume of 40 mL, and the autoclave is placed in an oven (for hydrothermal treatment) at 180 ^oC for 20 h. Without filtering and washing, the obtained precursors are dried at 120 ^oC for 5 h. The dried materials are well ground and calcined in air at a ramp of 1 ^oC/min in a muffle furnace to 400 ^oC and kept at this temperature for 2 h, and then heated to 650 ^oC and remained at this temperature for 2 h [32]. Shown in Figure 2 is the HRSEM image of the as-fabricated $LaCoO_3$ sample. The particles are relatively uniform in size with the typical diameter ranging from 30 to 140 nm.

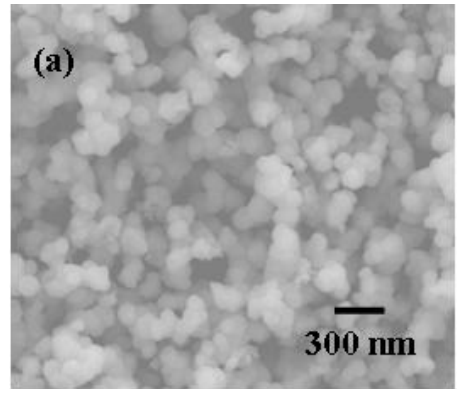

Figure 2. SEM image of $LaCoO_3$ nanoparticles [32].

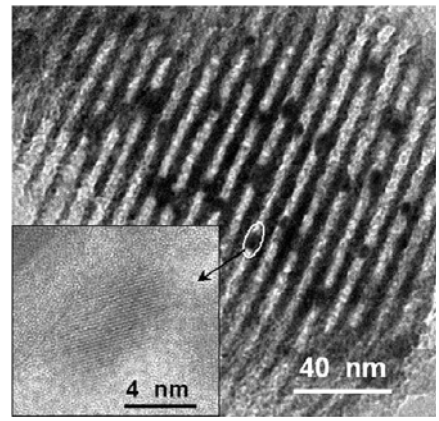

Figure 3. TEM image of the $LaCoO_3$/SBA15 sample[39].

In order to overcome the drawback of lower surface areas of perovskite-type oxides, a solid framework with a large surface area can be used to support them. For example, supported $LaCoO_3$ perovskites with 10 and 20 wt% loadings are fabricated by incipient wetness impregnation of $Ce_{1-x}Zr_xO_2$ (x = 0−0.3; 23−38 m^2/g) in a "citrate" solution [33−35]. Recently, mesoporous silica materials (e.g., MCM-41 and SBA-15) with high surface area, large pore volume, and narrow pore size distribution have been widely investigated as support. Using an impregnation method with mixed LaCo citrate complex precursors, Nguyen et al. loaded $LaCoO_3$ on mesoporous silica [36], and Makshina et al. deposited $LaCoO_x$ into the mesopores of MCM-41 [37,38]. Compared to MCM-41, SBA-15 with a well-ordered mesopore structure is larger in pore size and higher in hydrothermal stability. Via a novel microwave-assisted process with La-Co citrate complex as precursor, Cao and co-workers embedded crystalline $LaCoO_3$ nanoparticles in the mesopores of SBA-15 [39], as shown in Figure 3. It is clearly seen that the $LaCoO_3$ particles with an average size of 5−8.5 nm are uniformly dispersed within the nanotubular channels of SBA-15. Recently, our group have generated the $y$$LaCoO_3$/SBA-15 ($y$ = 10−50 wt%) catalysts by an *in-situ* hydrothermal method [40]. At a loading of less than 35 wt%, the $LaCoO_3$ species can be highly dispersed on SBA-15. Compared to the impregnation method, the *in-situ* hydrothermal strategy is more suitable for the fabrication of well-dispersed $LaCoO_3$ on SBA-15.

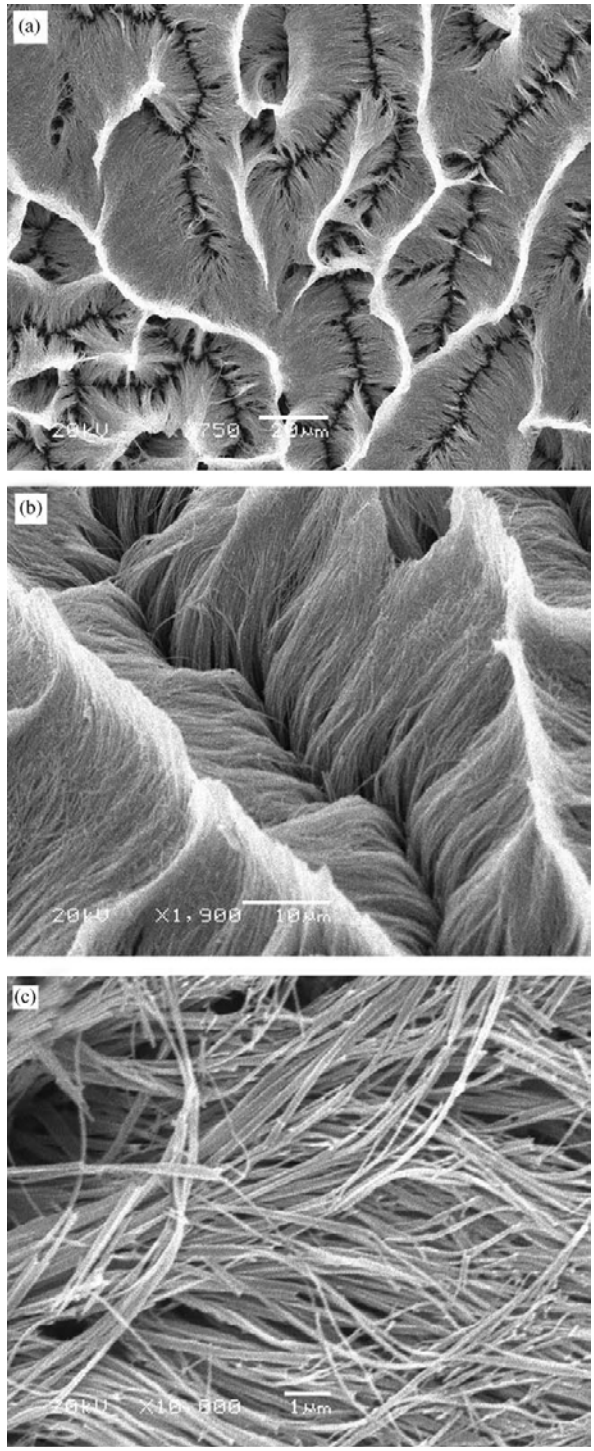

Figure 4. SEM images of $LaNiO_3$ nanowires with the AAO template partly dissolved: (a, b) top view in low magnification and (c) cross-section in high magnification[57].

2.2. One-Dimensional Nano/Microstructure

Owning to their unique physicochemical properties and potential applications in various fields, one-dimensional (1D) nanostructured materials have been received great attention [41−44]. Considering the material diversity, cost, throughput, and large-scale production potential, we here summarize the chemical fabrication of perovskite-type oxides with morphologies of nano/microsized wires, rods, fibers, and tubes [45].

2.2.1. Hard-Templating Synthesis

Among the various methods, hard-templating synthesis is one of the straightforward routes to obtain 1D nanostructural materials [41−44,46]. The hard template adopted serves as a scaffold, within or around which a different material is generated *in-situ* and shaped into a nanostructure with its morphology complementary to that of the template. The advantage of hard-templating strategy is that the shape and size of the product can be controlled by those of the template. Considering the factors that (i) the pores of the hard template can be filled with a variety of materials [47,48], (ii) the pores of the hard template are uniform and dense (offering an opportunity to prepare monodisperse nanomaterials in high yield), and (iii) the shape and size of the product can be controlled [41], one can employ the micro/nanoporous hard templates (e.g., anodic aluminum oxide (AAO) , carbon nanotubes (CNTs), and porous polycarbonate (PC) films [41,42,49−53]) to fabricate 1D nanomaterials.

For the process using AAO as hard template, it is often combined with the sol-gel method. The general procedure includes the following steps: (i) preparation of porous AAO templates; (ii) fabrication of an appropriate concentration sol; (iii) filling the pores with the precursor solution by dipping; (iv) calcination at a desired temperature; and (v) removing the AAO template with a NaOH solution. Following the procedure, one can generate highly ordered and densely packed polycrystalline rhombohedral $LaCoO_3$ [54], orthorhombic $LaFeO_3$ [55,56], cubic $LaNiO_3$ [57], $BiFeO_3$ [58], monoclinic $La_{1-x}Ca_xMnO_3$ [59], and $Pb(Zr_{0.53}Ti_{0.47})O_3$ [60] nanowires. Shown in Figure 4 are the typical SEM images of the as-prepared perovskite nanowires [57]. It can be seen that $LaNiO_3$ nanowires are abundant, uniform, and highly ordered in a large area. The length of $LaNiO_3$ nanowires is about 50 μm, corresponding to the thickness of the AAO template adopted; the external diameter of the nanowires is about 100 nm, equivalent to the pore diameter of the template employed. Similarly, a series of perovskite nanotubes, such as $LaNiO_3$ [61], $BiFeO_3$ [62,63], monolithic $La_{0.6}Sr_{0.4}CoO_3$ [64], $ATiO_3$ (A = Pb, Ba) [65−68], $Pb(Zr_{0.52}Ti_{0.48})O_3$ [69], cubic $Ba_{0.6}Sr_{0.4}TiO_3$ [70], and $(Pb_{0.25}Ba_{0.15}Sr_{0.6})TiO_3$ [71] nanotubes, have also been fabricated. As shown in Figure 5, tetragonal $PbTiO_3$ nanotubes synthesized using the 200-nm AAO membrane as hard template display a diameter of 200−400 nm and length of 2−10 μm [67]. Due to the heterogeneity of the membrane used, the produced nanotube array is also inhomogeneous, as can be seen from a side view (Figure 5b). Although the nanotubes are bundled together during the drying process after the membrane removal, they can detach from each other easily by sonication (Figure 5c and d). Nevertheless, because the only driving force in the process is the capillary action, it is hard to pour the viscous sol in the nanochannels with a small pore diameter [72−74]. Although a rise in concentration of the sol has a promotional effect, too high a concentration will result in either a viscous sol (causing the filling of the pores to be difficult) or destabilization of the sol [75]. In order to overcome this drawback, several

strategies, such as spin-coating technique [76], electrophoretic deposition [77,78], and liquid-phase deposition [79], have been developed to facilitate the sols to enter the pores. Hu et al. fabricated pseudocubic $LaMnO_3$ nanowires by means of a novel technique, i.e., through the converse diffusion or convection process, metal ions and precipitation agents were first transported in the nanochannels of the AAO template, and then reacted *in-situ* to generate a 1D nanostructure of the $LaMnO_3$ perovskite [72].

Similar to AAO, CNTs with at least one open end can also be filled with liquids (molten salts or solutions) with the aid of capillary action [80–82]. However, it is hard to achieve complete filling of CNTs with a high yield of the desired product due to its small diameter. Moreover, CNTs in water or even in an organic solvent is apt to aggregate, hindering their further manipulation. Recently, Gao et al. found that the addition of the surfactant P123 (poly(ethylene glycol)-*block*-poly(propylene glycol)-*block*-poly(ethylene glycol), EO_{20}-$PO_{70}EO_{20}$) and H_2O_2 could disperse the CNTs thoroughly and homogeneously in the hydrothermal fabrication of La_2CuO_4 nanofibers with single-walled carbon nanotubes (SWNTs) as the template [83–85]. The formation of a perovskite structure often requires high-temperature (> 650 ^oC) calcination [31], but CNTs can be completely oxidized to CO_2 in air at about 650 ^oC [86]. In order to obtain 1D perovskite nanomaterials by CNTs-templating methods, it is necessary to add some reagents (such as citrate) to reduce the crystallization temperature of the catalyst. For example, Zhu and co-workers generated single-phase polycrystalline rhomhohedral $LaCoO_3$ and $LaSrCuO_4$ nanowires with CNTs as template in the presence of citrate at 600 ^oC [87,88].

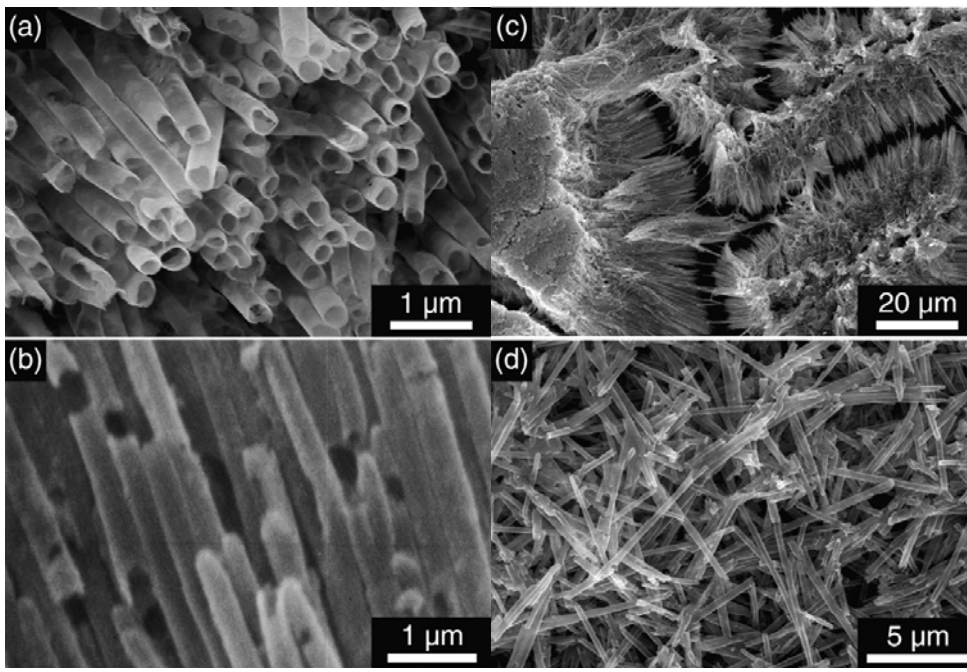

Figure 5. SEM images of nanotubes synthesized in 200 nm membranes: (a) nanotube ends, (b) side view revealing growth inhomogeneties, (c) the nanotubes bundled during drying after dissolving the membrane, and (d) Free-standing nanotubes after sonication[67].

In addition to AAO and CNTs, porous PC films have also been adopted to fabricate 1D perovskite-type oxides. Leyva and co-workers prepared $La_{0.67}Ca_{0.33}MnO_3$ [89], $La_{0.325}Pr_{0.300}Ca_{0.375}MnO_3$ [90,91], and $La_{1-x}Sr_xCo_{1-y}Fe_yO_3$ [92] nanotubes via a porous PC film-templating route in an adequate precursor system for syringe filtration. The typical SEM image of $La_{0.6}Sr_{0.4}CoO_3$ nanotubes obtained with porous PC (diameter = 800 nm) as template [92] is shown in Figure 6. Clearly, the shape and size of the perovskite tubes are determined by the characteristics of the template pores. The typical dimensions of the tubes are 770 nm in diameter, 80 nm in wall thickness, and 3−4 μm in length. As mentioned above, electrophoretic deposition is one of effective approaches to overcome the problems encountered in the direct sol-filling method. In the former method, an applied electric field can induce electrophoretic motion of the nanoclusters in the sol, and pull charged nanoclusters into the template pores, favoring the formation of a dense nanostructure (Figure 7) [75,93]. By means of a combination of sol-gel processing and electrophoretic deposition, Cao and co-workers obtained $Pb(Zr_{0.52}Ti_{0.48})O_3$ nanorods with the PC membranes as template [75,93]. However, since the force from the electric field is determined by the zeta-potential magnitude of the nanoclusters, acidic or alkaline sols are usually required for the generation of a good nanostructure. Moreover, a small absolute value of the zeta potential may result in the formation of a poorly-structured product. Hence this method is unfavorable for the fabrication of biologically active materials that are sensitive to acidic or alkaline environments. In view of this consideration, the same group has developed a novel strategy, i.e. sol-gel processing coupled with centrifugation. With the assistance of adjustable centrifugation force, sol nanoclusters can be effectively pulled into the template pores. The so-obtained $Pb(Zr_{0.52}Ti_{0.48})O_3$ nanorods show a dense and uniform structure (Figure 8). Furthermore, such a method is suitable for a variety of sol systems, including proteins or enzymes that may be sensitive to highly acidic or alkaline environments [74].

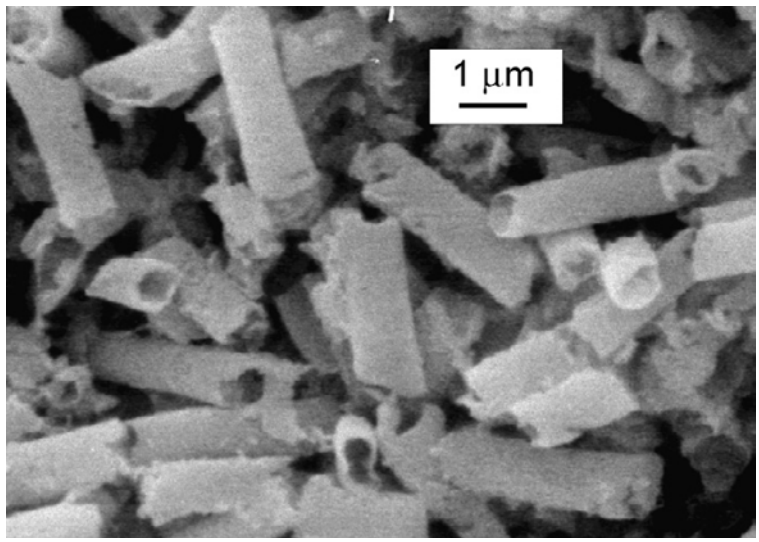

Figure 6. SEM image of the $La_{0.6}Sr_{0.4}CoO_3$ nanotubes[92].

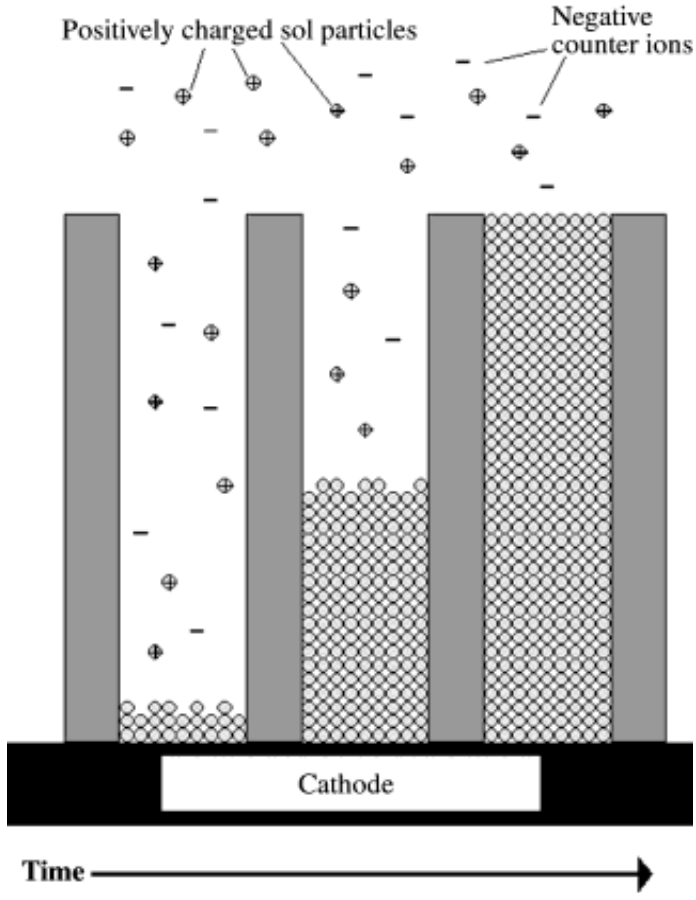

Figure 7. Schematic illustration of the progression of the growth process. Positively charged sol particles are moving electrophoretically towards the negative electrode, depositing at the bottom of the pore, while the negatively charged counter ions are moving in the opposite direction[75].

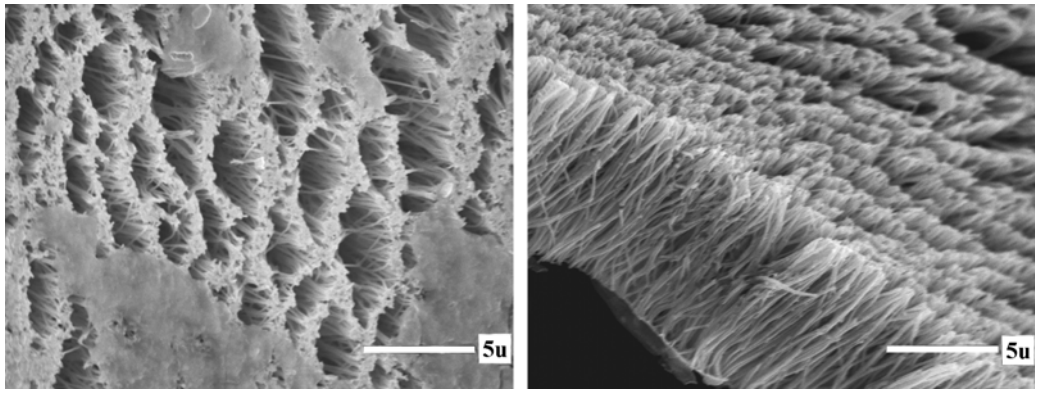

Figure 8. SEM images of the top view (a) and side view (b) of $Pb(Zr_{0.52}Ti_{0.48})O_3$ nanorods grown from the precursor sol by centrifugation at 1400 rpm for 1 h[74].

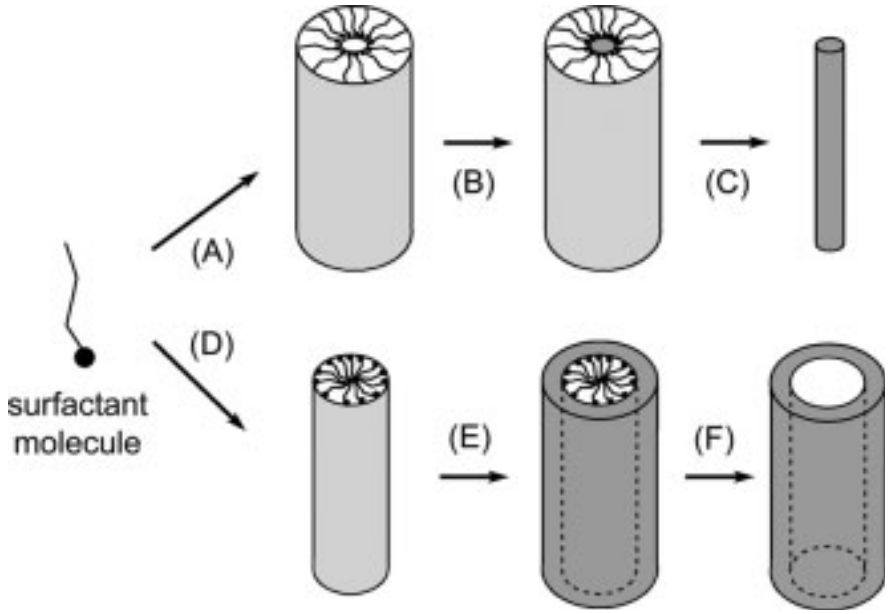

Figure 9. Schematic illustrations showing the formation of nanowires by templating against mesostructures self-assembled from surfactant molecules: (A) formation of a cylindrical micelle; (B) formation of the desired material in the aqueous phase encapsulated by the cylindrical micelle; (C) removal of the surfactant molecules with an appropriate solvent (or by calcination) to obtain an individual nanowire; and (D−F) similar to the process illustrated in (A−C), except that the exterior surface of an inverted micelle serves as the physical template[42].

As we know, carbon nanofibers have been widely used in various areas, such as in electronic components, as polymer additives, for gas storage, and as catalyst support [94]. Via the decomposition of hydrocarbons or carbon monoxide over Ni, Co or Fe catalysts, a large quantity of carbon fibers can be produced. Moreover, these carbon fibers with different sizes and shapes, such as straight, bent, thin and helical, etc., could be synthesized by controlling the reaction conditions [95–99]. With carbon nanofibers as template, Ueda and co-workers prepared a number of single and binary transition metal oxide nanofibers and/or nanotubes, including $LaMnO_3$ and $LaFeO_3$ nanofibers and nanotubes [99–102].

Although hard-templating synthesis provides a simple and versatile pathway to fabricate 1D perovskite nanomaterials, the quantity produced in each run is relatively small. Removal of the template through a post-synthesis process may also cause damage to the product. Furthermore, the so-obtained samples are often polycrystalline, which may limit their use in device fabrication and fundamental studies [42]. Therefore, it is highly demanded to develop alterative methods that are effective to synthesize 1D perovskite nanomaterials.

2.2.2. Surfactant-Templating Synthesis

Surfactant-templating method has been widely used to synthesize nanoscale materials. Up to now, most of the 1D nanomaterials prepared by surfactant-templating method are single metal and metal oxides, and only a few works deal with the fabrication of 1D mixed metal oxides via this pathway [103−105]. The principle of surfactant-templating synthesis is that when the concentration of the surfactant molecules reaches a critical value, they will

spontaneously organize into rod-shaped or inverse micelles (Figure 9), which can be immediately used as a soft template to promote the formation of 1D nanomaterials [42]. Based on this principle, Xu et al. [106] synthesized tetragonal $PbZr_{0.52}Ti_{0.48}O_3$ nanorods hydrothermally at 200 ^oC for 12 h by using tetrabutyl titanate, zirconium oxychloride, and lead nitrate as starting materials, potassium hydroxide as mineralizer, and poly(vinyl alcohol) (PVA) as surfactant. The surfactant plays an important role in the preferential nucleation and growth of the final product. Without PVA addition, the as-prepared particles are cubic in shape [107]. As indicated by the arrows in Figure 10, there are much more transparent films of amorphous PVA gel attached to the sides than to the head of the $PbZr_{0.52}Ti_{0.48}O_3$ nanorods. It provides a direct evidence for the templating role of a surfactant. In addition, the coupling of sol-gel process with surfactant-templating method can give rise to single-crystalline $BaTiO_3$ nanorods [103].

Compared to the preparation of 1D single metal or metal oxides with a surfactant as template, there are much more difficulties in coordinating the interaction between the surfactant molecules and the A-/B-site metal ions for the generation of the stoichiometric product ABO_3. Moreover, the preparation and removal of the micellar phase is often difficult and tedious. All of the problems encountered in the surfactant-templating process limit its wide applications in fabricating 1D perovskites.

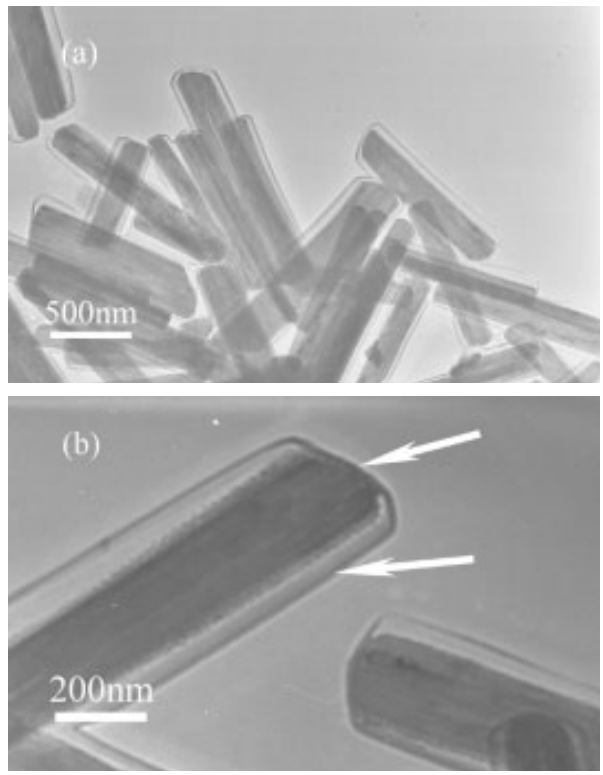

Figure 10. (a) TEM image of the $PbZr_{0.52}Ti_{0.48}O_3$ nanorods prepared by the hydrothermal method at 200 ^oC for 12 h assisted only by PVA; and (b) magnification of (a) [106].

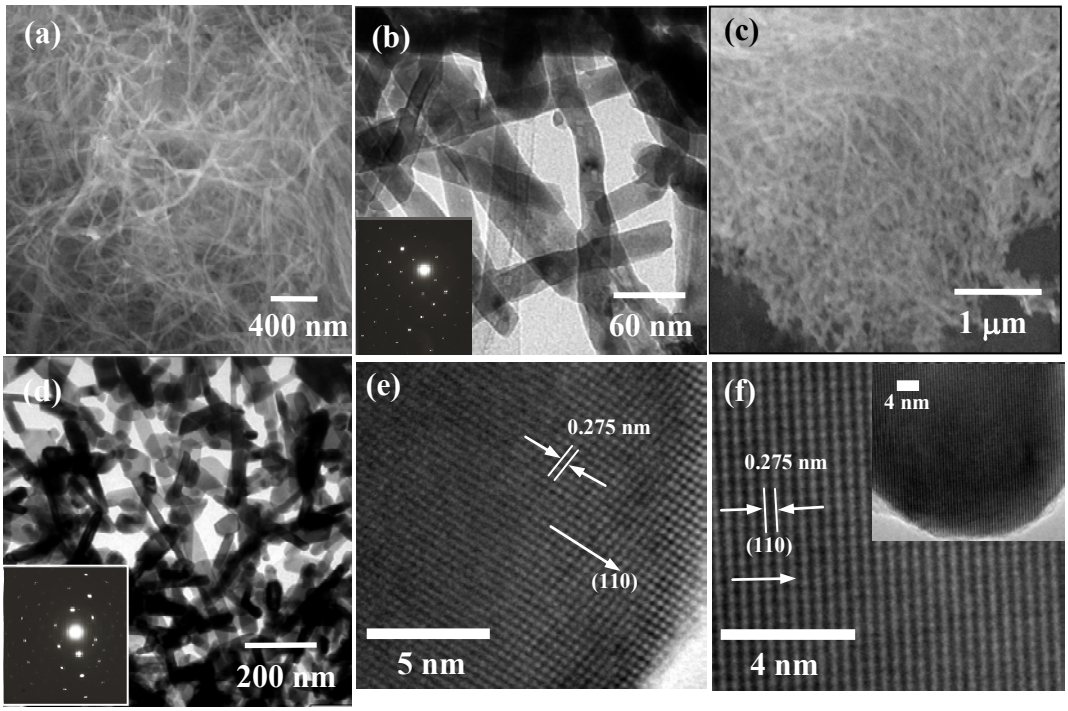

Figure 11. HRSEM (a, c), HRTEM (b, d, e, f) images and SAED patterns (insets) of the $La_{0.6}Sr_{0.4}CoO_{3-\delta}$ sample calcined (a, b, e) at 650 °C and (c, d, f) at 650 °C[116].

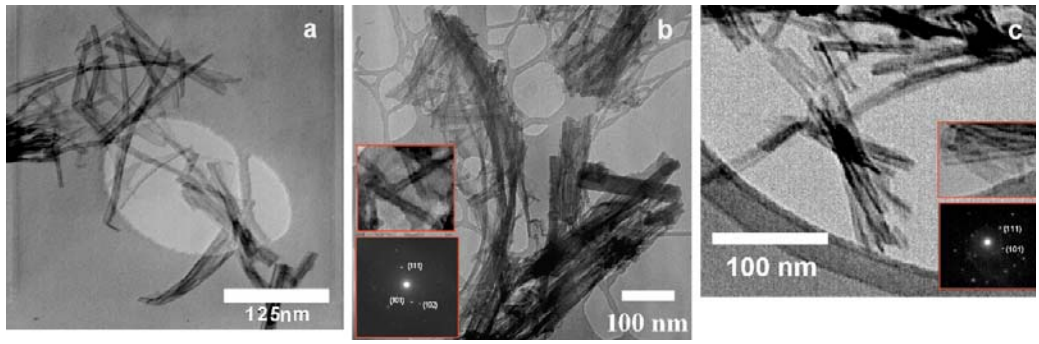

Figure 12. TEM images of (a) TiO_2, (b) $BaTiO_3$, and (c) $SrTiO_3$ nanotubes. Inset in (b) and (c) show higher magnification images (50 nm × 50 nm in (b) and 40 nm × 60 nm in (c)) of single tubes and electron diffraction patterns, respectively[132].

2.2.3. Hydrothermal Synthesis

In the past several years, an important advancement has been achieved in the synthesis of 1D nanomaterials via hydrothermal treatments [19,42,44,108]. The typical procedure is that precursors and proper agents capable of regulating or templating the crystal growth are added to distilled water with appropriate ratios, and then the mixture is placed in an autoclave for the crystallization at an elevated temperature, time, and pressure. The major advantage of this technique is that lots of materials can be made soluble in water by heating and pressurizing the system close to the critical points [42]. As a result, a number of raw materials are usable

to synthesize the desired products by means of this approach. It has been reported that, after hydrothermal treatment at a temperature (120−275 ^{o}C) for a desired time (3 h−7 day) and without the assistance of a soft template (surfactant), one can directly generate a series of 1D single-crystalline perovskite nanomaterials, including cubic $MTiO_3$ (M = Ba, Sr, Pb) [109−112], $MNbO_3$ (M = Na, K) [113−115], cubic $La_{0.6}Sr_{0.4}CoO_3$ [116], and Ag_2MO_4 (M = Cr, Mo, W) [117] nanowires, and Zn_2SnO_4 [118] nanorods. Representative HRSEM and HRTEM images as well as SAED patterns of the hydrothermally derived cubic $La_{0.6}Sr_{0.4}CoO_{3-\delta}$ nanowires/nanorods are shown in Figure 11 [116]. It is observed that the sample calcined at 650 ^{o}C consists of a large quantity of uniform nanowires (typical diameter = 15–30 nm) (Figure 11a and b). A mixture of nanorods and nanowires (Figure 11c and d) is obtained after calcination at 800 ^{o}C, and the typical diameter of the nanorods and nanowires fall into the range of 15–35 and 20–85 nm, respectively. The corresponding SAED patterns (insets) show regularly aligned lines of bright spots, disclosing that the $La_{0.6}Sr_{0.4}CoO_{3-\delta}$ nanowires and nanorods are well-grown single crystallites. According to the HRTEM photographs (Figure 11e and f), the *d* spacing of the (110) plane is estimated to be 0.275 nm, not far away from the corresponding value (0.271 nm) of polycrystalline $LaCoO_3$ (JCPDS No.: 75-0279). It should be pointed out that all of the 1D single-crystalline perovskite nanomaterials (except for Ag_2MO_4 (M = Cr, Mo, W)) mentioned above are hydrothermally fabricated in the alkaline environment with NaOH, KOH, $NH_3{\cdot}H_2O$ or $N_2H_4{\cdot}H_2O$ as mineralizer. The pH value of the reactant solution plays an important role in formatting the 1D nanostructure, which will be discussed later. Based on the results of O'Brien's group [119], Park and co-workers reported the synthesis of single-crystalline cubic $BaTiO_3$ and $SrTiO_3$ nanorods through the hydrothermal decomposition of bimetallic alkoxide precursors ($BaTi(OCH(CH_3)_2)_6$ and $SrTi(OCH(CH_3)_2)_6$) at 280 ^{o}C for 6 h [120−122]. However, the preparation of such bimetallic alkoxide precursors is rather difficult and expensive. Therefore, a wide application of this approach is greatly limited. Other groups have also claimed to successfully fabricate single-crystal perovskite $La_{0.5}A_{0.5}MnO_3$ (A = Sr, Ba, Ca) "nanowires" hydrothermally [123−126], however, the very recently reported results reveal that these "nanowires" are actually wire-like $La(OH)_3$ nanocrystals, rather than the perovskite nanocrystals [127−131].

It is interesting that there are works on the hydrothermal generation of 1D titanate perovskites with 1D TiO_2 and $Na_2Ti_3O_7$ nanoparticles as sacrificial template. For example, cubic $ATiO_3$ (A = Ba, Sr, Pb) nanotubes (Figure 12) are hydrothermally synthesized using the TiO_2 nanotubes as precursor [132,133], in which the $BaTiO_3$ and $SrTiO_3$ nanotubes are 8–15 nm in outer diameter, 4–7 nm in inner diameter, and 50–500 nm in length (Figure 12). By utilizing the highly active TiO_2 nanofibers as raw material, orthorhombic $CaTiO_3$ microtubes, cubic $SrTiO_3$ and $BaTiO_3$ microfibers can be generated hydrothermally in basic solutions at 150 ^{o}C for 24 h. The formation of microtubular $CaTiO_3$ involves the initial dissolution of the TiO_2 nanofibers and the conversion to microsized fiber-bundles after an Ostwald ripening process, while the fabrication of $SrTiO_3$ and $BaTiO_3$ microfibers is associated with the ion exchange reaction and *in-situ* growth process at the TiO_2 nanofiber framework (Figure 13) [134]. A variety of single-crystalline nanostructured $BaTiO_3$ with morphologies of nanowire-, nanosheet-, nanocube-, coral-, starfish-, and sword-like shapes as well as hexagonal nanoparticles (Figure 14) have been produced hydrothermally employing the $Na_2Ti_3O_7$ nanotubes and nanowires as precursor via the control of reaction temperature and

concentration of $Ba(OH)_2$ [135]. Kang et al. observed the formation of single-crystalline $BaTiO_3$ nanorods from the $K_2Ti_4O_9$ nanorod/wire precursor, the former aggregated into nanoparticles with a rise in hydrothermal time from 42 to 72 h [136]. Although only 1D titanates mentioned above have so far been successfully obtained through a hydrothermal route, this strategy could be applied to fabricate other 1D perovskites in the future. Moreover, taking into account the fact that the controllable synthesis techniques of 1D single metal oxides have gained a great progress in the last decade [19,41,42,44,137,138], it is possible to generate 1D or other specifically morphological perovskites (other than titanates) by templating against 1D oxide of the A- and/or B-site metal(s). Furthermore, it is even likely to obtain 1D multiphase-paragenous compounds with a template-cored and perovskite-shelled structure. Such symbiotic materials may show interesting physicochemical properties as compared to the single phase of template or perovskite.

In addition, hydrothermal method coupled with other techniques has been received great attention in preparing 1D perovskites [139−142]. For example, by adopting sol-gel and hydrothermal coupled method, Hou and co-workers successfully synthesized single-crystalline $K_{0.5}Bi_{0.5}TiO_3$ and $(Na_{0.8}K_{0.2})_{0.5}Bi_{0.5}TiO_3$ nanowires [140,143]. Compared to the conventional hydrothermal method, the microwave-hydrothermal combined process allows the internal heat generated from the microwave irradiation to heat the reactants very rapidly for crystallization, thus saving time and energy. By using this coupled strategy, single-crystalline $PbTiO_3$ nanowires can be readily produced [142].

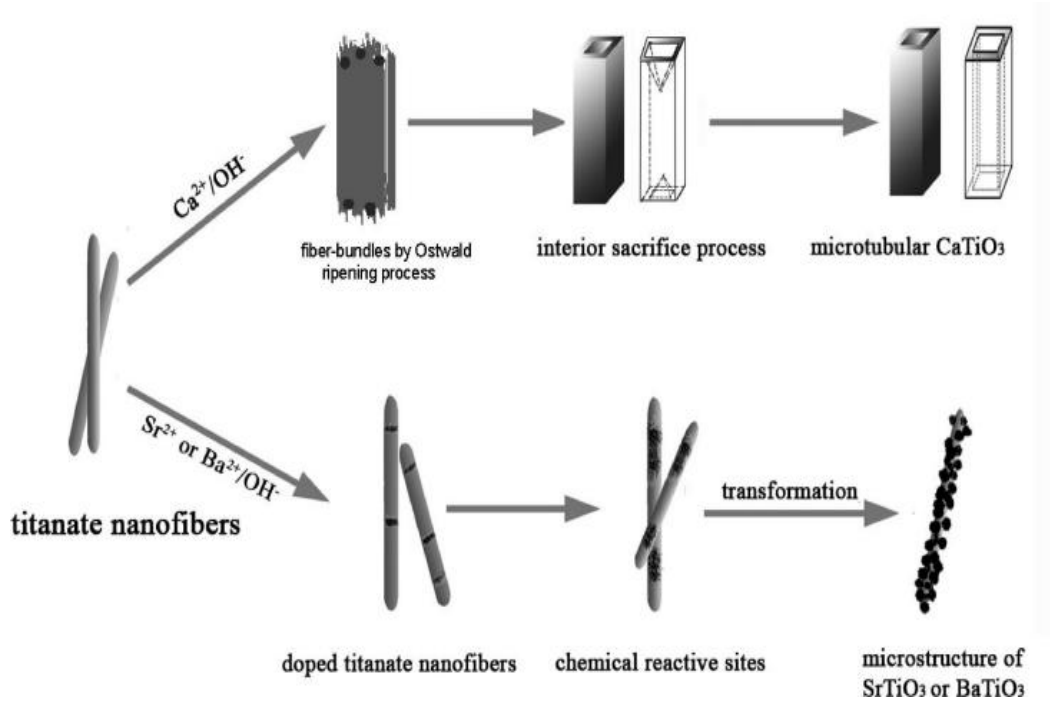

Figure 13. Schematic illustration of the possible formation mechanism of $MTiO_3$ (M = Ca, Sr and Ba) perovskites with various morphologies[134].

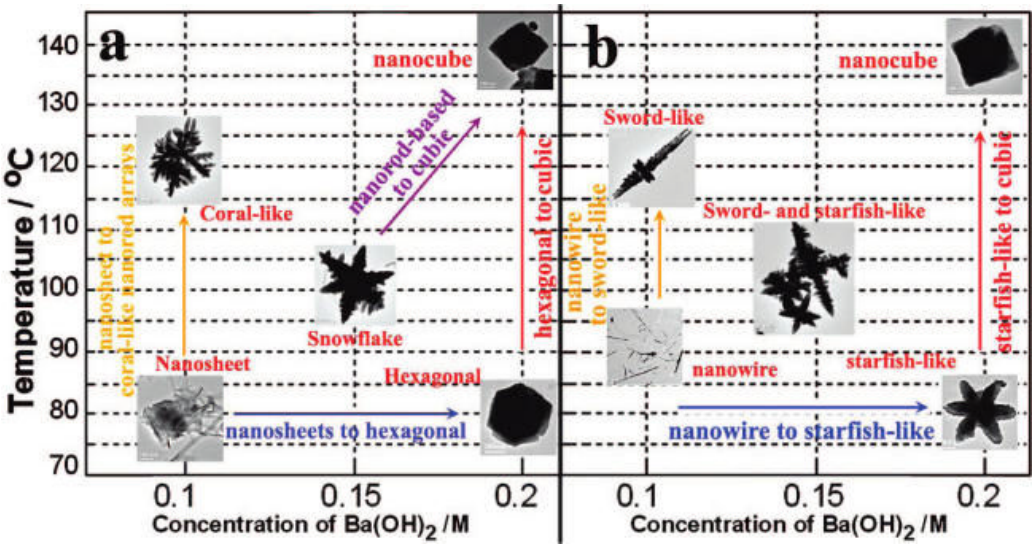

Figure 14. Influence of the concentration of $Ba(OH)_2$ and the hydrothermal temperature on the morphology and structure of $BaTiO_3$ products prepared from (a) $Na_2Ti_3O_7$ nanotubes and (b) $Na_2Ti_3O_7$ nanowires[135].

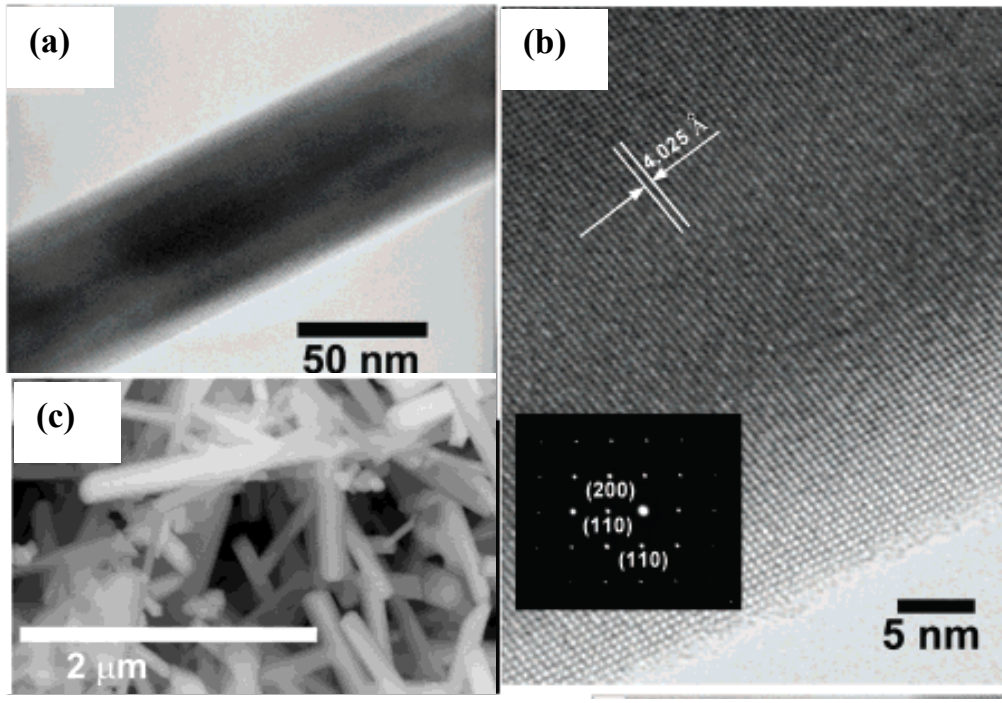

Figure 15. (a) TEM, (b) HRTEM, and (c) SEM images of the $BaTiO_3$ nanowires. Inset of (b) is the SAED pattern of a $BaTiO_3$ nanowire[145].

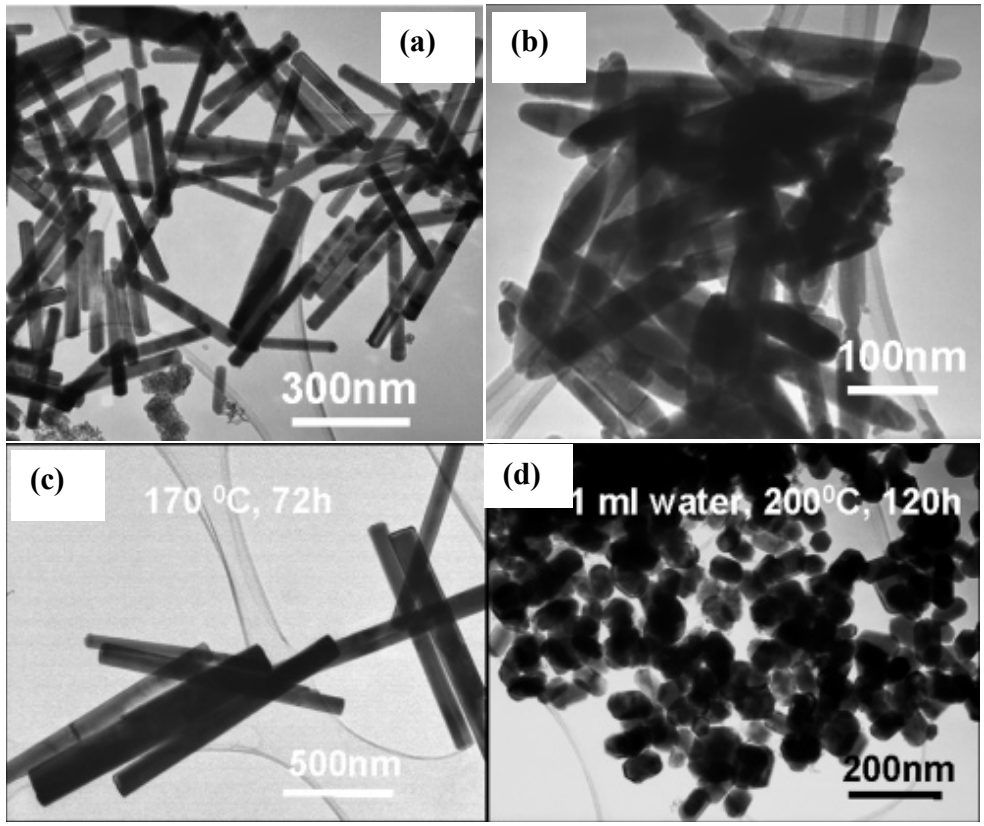

Figure 16. TEM images of (a) $BaMnO_3$ at 200 °C for 120 h, (b) $BaTi_{0.5}Mn_{0.5}O_3$ at 200 °C for 48 h, (c) $BaMnO_3$ at 170 °C for 72 h, and (d) $BaMnO_3$ at 200 °C for 120 h, adding 1 mL of water[151].

Although a number of perovskite nanowires and nanorods can be generated via the hydrothermal route, there are still no reports on the fabrication of micro/nanotubular perovskites (except for titanites) by means of this method. Moreover, since a lot of parameters, such as hydrothermal temperature and time, pressure, precursor nature, base strength, and solvent, etc., can influence the physicochemical properties (including the morphology) of the final product, further work on optimizing this preparation strategy is highly needed to achieve controlled fabrication of 1D perovskites in the future.

2.2.4. Novel Solid-State Method

In recent years, a great progress in solution synthesis of 1D perovskites has been achieved. To extend the method for 1D perovskite preparation, the solid-state process has been developed. In 1986, Hayashi et al. reported the generation of rod-shaped $BaTiO_3$ from rod-like $TiO_2 \cdot nH_2O$ and $BaCO_3$ in molten chloride [144]. With barium oxalate and TiO_2 (anatase) as precursor and in the presence of NaCl and nonionic surfactant NP-9, Mao et al. obtained single-crystalline cubic $BaTiO_3$ after calcination of the well-grounded reactant intermediate mixture at 820 °C for 3.5 h [145]. The $BaTiO_3$ particles mainly possess straight, smooth, and crystalline wire-like morphologies (Figure 15), in which the nanowires are 50−80 nm in diameter and 1.5−10 μm in length. Very recently, by employing the mixed chlorides (NaCl/KCl molar ratio = 1:1) instead of NaCl as reaction medium, 1D $MTiO_3$ (M =

Ba, Sr, Pb) nanostrips were generated at 950 ^{o}C for 5 h without the assistance of any surfactants [146]. With La_2O_3, $Sr(NO_3)_2$, and a $Mn(NO_3)_2$ solution (50 wt%) as starting materials, Feng and co-workers prepared $La_{0.7}Sr_{0.3}MnO_3$ nanorods by means of a combined strategy of sol-gel and molten salt synthesis in the NaCl-KCl (mass ratio = 1:4) flux molten salts [147]. The sol-gel treatment step can guarantee the formation of homogeneous precursor mixture. In addition, the authors also synthesized $La_{0.7}Sr_{0.3}MnO_3$ nanorods by adopting the two steps: (i) $KMnO_4$ and $MnCl_2$ (molar ratio = 2:3) are well mixed and grounded to prepare a precursor of MnO_2 fibers, and (ii) stoichiometric amounts of La_2O_3, $SrCl_2$, and the fibrous MnO_2 precursor are well mixed and grounded with 1 mL of ethanol, then dried at 70 ^{o}C, and finally calcined at 950 ^{o}C for 5 h [148,149]. It is believed that the MnO_2 fibers function as the crystal seed in the growth of $La_{0.7}Sr_{0.3}MnO_3$ nanorods.

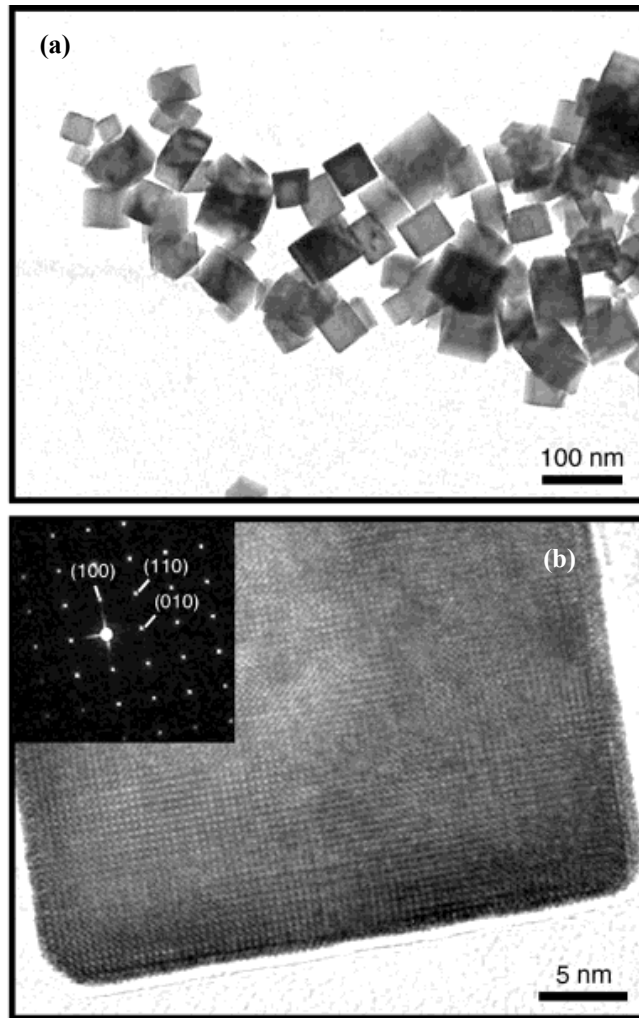

Figure 17. (a) TEM and (b) HRTEM images as well as the SAED pattern (inset) of $La_{0.5}Ba_{0.5}MnO_3$ nanocubes prepared at 300 ^{o}C for 24 h[127].

An approach, called the composite-hydroxide-mediated method, was developed by Wang and co-workers. It has been employed to synthesize single-crystalline hexagonal $BaMnO_3$ nanorods, $BaTiO_3$, $Ba_{1-x}Sr_xTiO_3$, and Fe_3O_4 nanocubes, $BaTi_{0.5}Mn_{0.5}O_3$, $CoFe_2O_4$, and $Pb_2V_2O_7$ nanobelts, and $BaCeO_3$ nanoflowers [150−152]. This method is based on the reaction between a metallic salt and a metal oxide in a molten mixed solution of NaOH and KOH (molar ratio = 51.5:48.5) at 200 ^oC. One of the key factors for the successful synthesis of the above morphological materials at 200 ^oC or lower temperatures is that an eutectic point as low as 165 ^oC can be achieved in the alkali molten solution at a NaOH/KOH molar ratio of 51.5:48.5 [150], although the melting points of pure KOH and NaOH are much higher (360 and 323 ^oC, respectively). The possible mechanism involving in the formation of perovskite phase (take $BaTi_xMn_{1-x}O_3$ as an example) can be described as the following:

$$BaCl_2 + NaOH \rightarrow Ba(OH)_2 + NaCl$$
$$xTiO_2 + (1-x)MnO_2 + 2NaOH \rightarrow Na_2Ti_xMn_{1-x}O_3 + H_2O$$
$$Ba(OH)_2 + Na_2Ti_xMn_{1-x}O_3 \rightarrow BaTi_xMn_{1-x}O_3 + 2NaOH$$

Due to the big viscosity of hydroxide, formation of a perovskite nanostructure is slow, thus minimizing the extent of particle agglomeration. It is the reason why dispersive single-crystalline nanostructured perovskites could be obtained during the reaction without the use of a surface capping agent, as shown in Figure 16. The $BaMnO_3$ nanorods obtained at 170−200 ^oC for 72−120 h display a width of 50−100 nm and a length of 200−1000 nm (Figure 16a and c). The morphology of $BaTi_{0.5}Mn_{0.5}O_3$ is different from that of $BaMnO_3$. The particles of the former material show an architecture of elliptical nanobelts with about 40 nm in width, 20 nm in thickness, and 500 nm in length (Figure 16b). It should be noted that such a fabrication approach is carried out in the absence of water. The addition of little (1 mL) water to the reaction system would change the morphology of the product from nanorods to nanoparticles (Figure 16d) [151].

2.2.5. Other Methods

In addition to the above fabrication strategies, there are other methods to produce 1D perovskites. For example, single-crystalline tetragonal $Ba_{1-x}Sr_xTiO_3$ nanorods can be obtained via a simple ultrasonic radiation and sol-gel combined approach [153]. The electrospinning technique has been used to generate single-crystalline tetragonal $PbTiO_3$ nanowires [154], polycrystalline $Pb(Zr_{0.52}Ti_{0.48})O_3$ [155], cubic $Ba_{0.6}Sr_{0.4}TiO_3$ [156], and $BaTiO_3$ [157] nanofibers. Zhou and co-workers developed a pulsed laser deposition strategy to produce novel transition metal oxide core-shell nanowires, including $MgO/La_{0.67}Ca_{0.33}MnO_3$, $MgO/La_{0.67}Sr_{0.33}MnO_3$, $MgO/YBa_2Cu_3O_{6.66}$, $MgO/PbZr_{0.58}Ti_{0.42}O_3$, and MgO/Fe_3O_4 [158−160]. With the ion-exchangeable titanate nanotubes as starting material, thin films of single-crystalline $SrTiO_3$ nanorod arrays can be formed by annealing the Sr^{2+}-introduced titanate nanotubes [161]. Alkalides are crystalline ionic salts consisting of crown ether or cryptand complexed alkaki metal cations. When being dissolved in nonreducible solvents, the alkalides can give alkaki metal cations, which are nearly as a thermodynamically powerful reducer as a solvated electron, the most powerful reducer possible in any given solvent, and are capable of transferring two electrons simultaneously. Alkalide reduction of metal salts leads to the generation of a nanoscale colloid (2−15 nm in diameter). Through such an alkalide reduction,

Wagner and co-workers generated single-crystalline orthorhombic $NaTaO_3$ nanorods [162]. Highly anisotropic pseudo-cubic $KNbO_3$ nanocrystallites with morphologies of nanoneedles and nanoplatelets can be obtained after the crystallization of the precursor gel derived from a polymerized complex process, which is based on the Pechini-type reaction route that starts from a precursor solution of the respective metal-citrate complexes [163].

2.3. Nano/Microcube

It is well known that optical, magnetic, electronic, and catalytic properties of a material are dependent on its particle size and shape [164–166]. Owning to the unique properties arising from the exposing well-defined crystal planes and the advantages in serving as a building block for further construction of multifunctional devices [167], cube-shaped nano/microcrystals have received great interests. Up to now, a number of works have been devoted to synthesizing the perovskites with a cube-like morphology, among which mixed valence manganites have been paid considerable attention due to their colossal magnetoresistivity (CMR) [168,169]. In the past years, our group [130,131,170] and several other groups [124,127,128,170–175] have developed a facile hydrothermal strategy to prepare the single-crystalline manganite $A_{1-x}A'_xMnO_3$ (A = La, Pr, Nd; A' = Ca, Sr, Ba; x = 0.3−0.6) micro/nanocubes without calcination at high temperatures. The hydrothermal synthesis, which involves the reaction between MnO_4^- and Mn^{2+} in the presence of lanthanum and alkaline earth metal salts to give the desired manganese oxidation state, is carried out at a temperature of 220−300 ^oC for 24−72 h in a concentrated KOH solution. Shown in Figure 17 are the representative TEM images and the SAED pattern of the pseudocubic $La_{0.5}Ba_{0.5}MnO_3$ sample obtained hydrothermally at 300 ^oC for 24 h [127]. Obviously, the products are single crystalline and exhibit a nanocube-like (50−100 nm in edge length) morphology. As mentioned above, reaction parameters, such as solution pH value, hydrothermal temperature and time as well as pressure, have great influence on the particle size and morphology of the final product. In other words, it is possible to controllably grow a crystal with the desired particle size and shape by carefully adjusting the above experimental parameters. A typical example is from the work done by Chai et al. [173]. They successfully synthesized single-crystalline $La_{0.5}Ba_{0.5}MnO_3$ with flower- and micro/nanocube-like shapes by controlling the reaction conditions, especially the concentration of KOH (Table 1 and Figure 18). During the preparation process of the $A_{1-x}A'_xMnO_3$ micro/nanocubes, KOH actually took part in the reaction leading to perovskite structure formation. Hence, KOH concentration may influence or even change the growth mechanism [173,176], and further alter the shape and size of the final product.

Table 1. The influence of fabrication parameter on the morphology of $La_{0.5}Ba_{0.5}MnO_3$ [173]

Sample no.	KOH concentration (mol/L)	Filling fraction (vol%)	Hydrothermal temperature (^oC)	Hydrothermal time (h)	Morphology
1	6	60	270	25	Layered flower
2	10	60	270	25	Microcube
3	14	60	270	25	Nanocube
4	6	40	270	25	Nonlayered flower
5	6	80	270	25	Irregular
6	6	60	250	25	Nonlayered flower
7	6	60	230	25	Amorphous

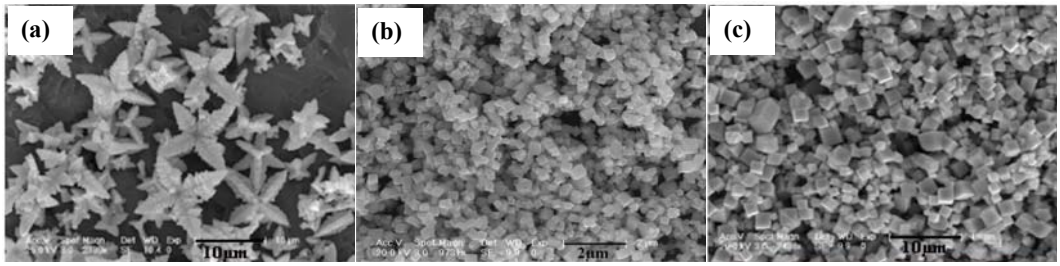

Figure 18. SEM images of $La_{0.5}Ba_{0.5}MnO_3$ prepared at 270 ^oC for 50 h under (a) 6 mol/L, (b) 10 mol/L, and (c) 14 mol/L KOH conditions[173].

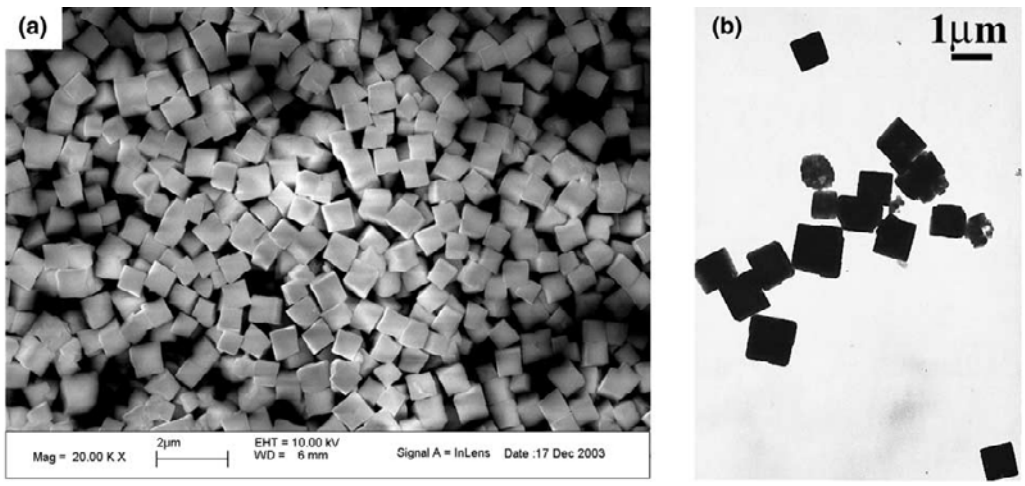

Figure 19. (a) Typical SEM image of the $CaSn(OH)_6$ precursor prepared by using 2 mL PVP; (b) typical TEM image of the $CaSnO_3$ product after heat treatment of the precursor as shown in (a) at 500 ^oC for 5 h[181].

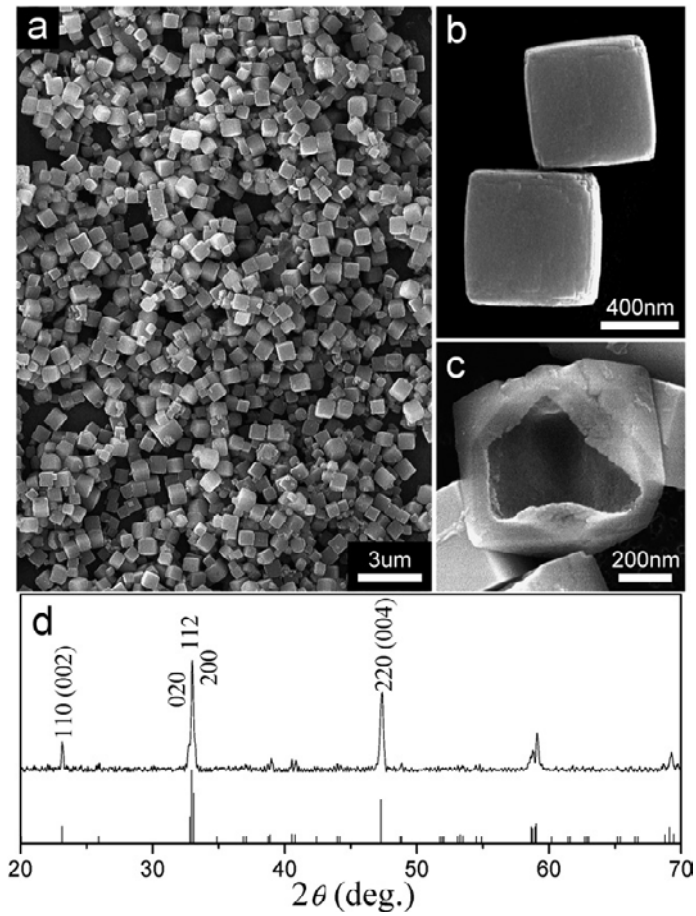

Figure 20. SEM images of (a) $CaTiO_3$ microcubes prepared at 180 °C for 15 h, (b) two individual $CaTiO_3$ cubes, (c) a broken cube showing hollowed interior, (d) powder XRD patter of the product compared with reference to $CaTiO_3$ JCPDS card no. 82-0229[182].

In addition to $A_{1-x}A'_xMnO_3$, $LaFeO_3$ [177] and $K_{1-x}Na_xNbO_3$ (x = 0−1) [114,178] micro/nanocubes can also be fabricated hydrothermally in the absence of a surfactant. Although many single metal and metal oxide nanoparticles with a cube-like morphology have been prepared with the adding of a surfactant to control the growth process [167,179], only a few cube-like perovskites were generated with the aid of a surfactant [180,181]. For example, in the presence of ployvinylpyrrolidone (PVP), Li and co-workers obtained orthorhombic $CaSnO_3$ micro/nanocubes after hydrothermal tretament at 140 °C for 10 h [181]. The PVP acts as a shape-directing agent. It is preferentially adsorbed on different crystal faces of the precursor, thus favoring formation of the cube-like morphological product. The SEM image of the $CaSn(OH)_6$ precursor obtained using 2 mL of PVP is shown in Figure 19. Apparently, all of the particles are uniform both in shape (cube) and size (~1 μm in edge length). The uniform $CaSnO_3$ micro/nanocubes can be readily generated after calcination of the $CaSn(OH)_6$ precursor at 500 °C for 5 h. The challenge of such a surfactant-assisted hydrothermal strategy is to properly regulate the interaction between the surfactant molecules and the A- and B-site metal ions in ABO_3, and hence to control the composition, stoichiometry, and crystal structure of the ABO_3 material. It deserves further investigations.

Interestingly, by adopting a solvothermal process coupled with the surfactant-directing technique in a poly(ethylene glycol) solvent, Yang et al. fabricated single-crystalline orthorhombic $CaTiO_3$ hollow microcubes (Figure 20) [182]. Furthermore, the authors also observed that the morphology of the as-prepared product is highly sensitive to the crystal growth condition. With an increase in water amount used, the morphology of the product changes from hollow microcube to prismatic rectangular rod, and from butterfly-shaped crystal to irregularly shaped crystal.

Compared to the conventional solid-state reaction, molten salt synthesis is believed to be one of the simplest, most versatile, and highly cost-effective approaches available for producing functional materials at lower temperatures [145,147–149,183,184]. Wong and co-workers have made many efforts in preparing perovskites with various morphologies via the molten salt synthesis route [8,145,183,185]. They have shown that parameters, such as nature and amount of salt, surfactant, reaction temperature and duration, precursor type and molar ratio, heating/cooling rate, exert influence on the purity, particle size and shape, and morphology of the product. Moreover, due to the effects of solubility and reactivity associated with the salt, which may greatly alter the synthesis process and the resultant particle size and shape, selection of the salt is a key issue. Through adjusting the preparation parameters properly, one can generate cubic $SrTiO_3$ [145] and cubic $BaZrO_3$ [183,185] nanocubes and nanospheres, $BaTiO_3$ nanowires [145], and $Ca_{1-x}Sr_xTiO_3$ nanoparticles [8]. As mentioned in Section 2.2.4, single-crystalline $BaTiO_3$ and $Ba_xSr_{1-x}TiO_3$ nanocubes (Figure 21) can be obtained via the composite-hydroxide-mediated approach [150]. Very recently, by using the titanium foils and $BaCO_3$ instead of TiO_2 and $BaCl_2$ as precursor, He et al. [186] synthesized single-crystalline cubic $BaTiO_3$ nanocubes using the same method. As compared with the comprehensive investigations on shape control in liquid-phase reactions [179,187], however, fewer works have been done on particle shape control by means of the mentioned novel solid-state process. Therefore, more efforts are needed to put on achieving the rational synthesis of desired products by this technique.

2.4. Other Specific Morphologies

Perovskites with other morphologies, such as octahedral and dodecahedral, solid and hollow spherical, dendritic, bur-, multipod-, and star-like shapes have also been fabricated. By regulating the reaction conditions (e.g., hydrothermal temperature and time, reactant concentration, and solvent constitution), single-phase perovskite $BaZrO_3$ microcrystals with controllable shapes of truncated rhombic dodecahedron and spheres (Figure 22) can be synthesized [188]. It is found that the solvent polarity, which is governed by the solvent composition, plays an important role in determining the geometric structure of the product. A rise in the volume ratio of ethanol to water from 0 to 3 can bring about the evolution of morphology from truncated dodecahedral to spherical (Figure 22d). Based on the inherent properties of the templates, many methods have been proposed for the synthesis of hollow spherical materials. For example, by templating against amorphous TiO_2 spheres, Zhang and co-workers have prepared monodispersed porous cubic $SrTiO_3$ and $BaTiO_3$ spheres after hydrothermal treatment at 180 ^oC for 12 h [189]. Since the adopted template is amorphous, a relatively high-temperature treatment is required to transform the amorphous oxide shells into crystallites. However, such a processing step might result in deterioration of the shell and

tendency for perforation and fragmentation. In view of this, Yang and co-workers tried to prepare hollow spherical $BaTiO_3$ and $SrTiO_3$ by employing the sulfonated polystyrene (PS) spherical gel as template [190]. The typical procedure includes (i) the preparation of sulfonated PS gel spheres, (ii) the adsorption of tetrabutyl titanate (TBT) by dispersing the as-prepared template into a mixture of absolute ethanol and TBT (1:1 v/v, 2 mL) for 24 h, and (iii) the treatment with $Ba(OH)_2$ or $Sr(OH)_2$ (0.3 mol/L, 4 mL) at 70 ^oC for 12 h under stirring. Because the preparation is carried out under mild conditions, intact shells are guaranteed, as shown in Figure 23. Using sodium dodecylbenzene sulfonate (SDBS) or poly(sodium 4-styrenesulfonate) (PSS) as surfactant, bur-like three-dimensionally hierarchical $PbTiO_3$ nanostructures consisting of a microsphere core with an outer shell of nanorods (Figure 24) are obtained by *in-situ* self-assemblying of nanoparticles under hydrothermal conditions [191]. As can be observed from the SEM images (Figure 24), the microspheres are 1−5 μm in diameter and the nanorods are 50−100 nm in diameter with a length in the range from hundreds of nanometers to 2 μm. The possible mechanism for formation of the tetragonal bur-like $PbTiO_3$ nanoparticles is illustrated in Figure 25. It can be seen that only part of the generated $PbTiO_3$ nanoparticles directly aggregate into microsphere, whereas some of them become nonspherical building blocks on the microspheres and then ripen to nanorods.

As mentioned in Section 2.2.3, the microwave-hydrothermal method is one of the versatile and cost-effective approaches to fabricate crystalline and pure micro/nanoscale materials in shorter reaction time at lower temperatures. By means of the microwave-hydrothermal method, microsized decaoctahedral cubic $BaZrO_3$ powders (Figure 26) are firstly synthesized at 140 ^oC for 40 min [192]. By using a molten K_2CO_3 flux, Loye and co-workers synthesized single crystals of $RERhO_3$ (RE = La, Pr, Nd, Sm, Eu, Tb) for the first time [193]. All of the compounds are found to crystallize in orthorhombic space group *Pbnm*, which is confirmed by the truncated octahedral geometry of the $LaRhO_3$ single crystal. Since the multipod-shaped crystals are only synthesized under non-equilibrium conditions, it is hard to fabricate perovskites with a multipod shape by conventional methods. In order to overcome these problems, Toshima et al. developed a novel strategy, i.e., the self-propagating high-temperature synthesis method, for the production of multipod cubic $SrTiO_3$ crystals by using titanium powder, $NaClO_4$, and $SrCO_3$ as the raw materials [194]. The key step for successful fabrication is the choosing of irregularly shaped titanium powders. Using spherical powders with smooth surface as the Ti source, cube- and octahedron-shaped $SrTiO_3$ crystals are obtained (Figure 27). However, hexapod- and decapod-shaped $SrTiO_3$ crystals (Figure 28) are generated by employing irregularly shaped Ti powders. Very recently, the preparation of dendritic $BaTiO_3$ cubic single crystallites has been reported first by Wang et al. [195]. Shown in Figure 29 are the SEM images of the hydrothermally derived $BaTiO_3$ products that consist of homogeneous dendritic structures. It is found that the KOH concentration plays a key role in the formation of $BaTiO_3$ dendrites. With a decrease in KOH concentration from 1.0 to 0.7 mol/L, and then to 0.1 mol/L, the particle morphology changes from spherical to star-shaped, and then to dendritic, accordingly. In addition, periodic arrays of nanorings of morphotropic phase boundary lead zirconium titanate can be fabricated using a complicated physical technique [196].

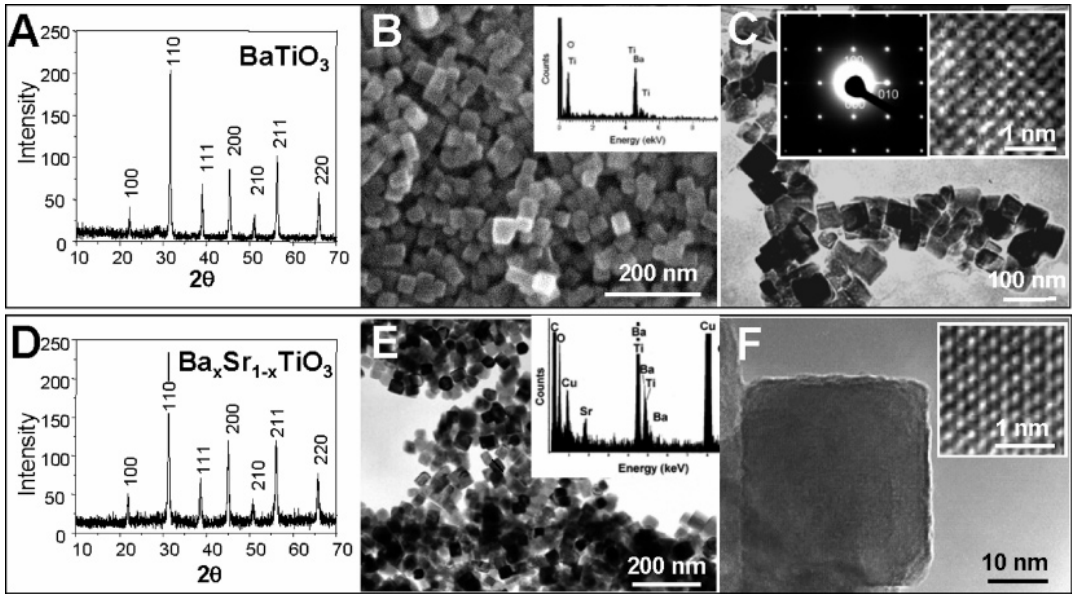

Figure 21. (A−C) $BaTiO_3$ and (D−F) $Ba_xSr_{1-x}TiO_3$ nanocubes synthesized by the composite-hydroxide-mediated approach. (A, D) XRD patterns of $BaTiO_3$ and $Ba_xSr_{1-x}TiO_3$ nanopowder. (B, E) SEM images of $BaTiO_3$ and $Ba_xSr_{1-x}TiO_3$ nanocubes; the inset is the EDS pattern. (C,F) TEM images of $BaTiO_3$ and $Ba_xSr_{1-x}TiO_3$ nanocubes; the insets are the SAED pattern and HRTEM images of a nanocube, showing its single-crystal structure[150].

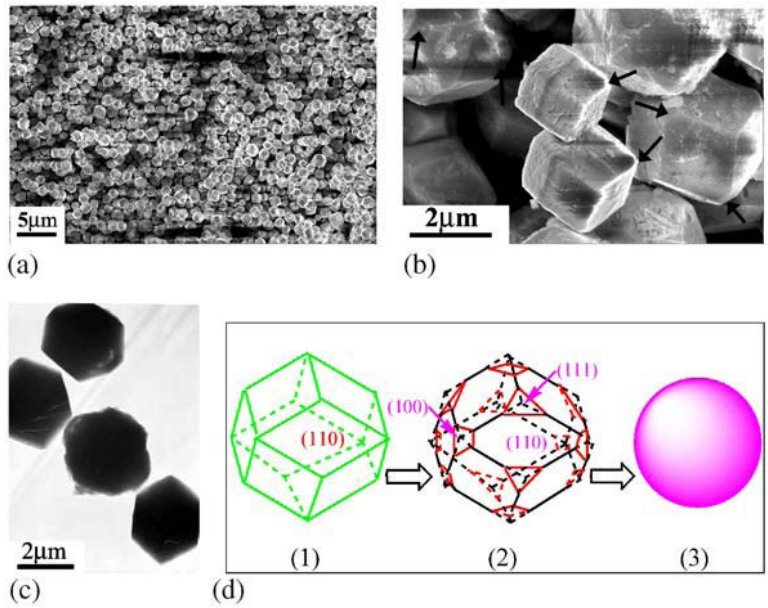

Figure 22. (a, b) SEM and (c) TEM images of slightly truncated rhombic dodecahedral $BaZrO_3$ microcrystals. The arrow shown in (b) is indication of truncated corners. (d) Simulated morphology evolution process of the three states of regular rhombic dodecahedron, truncated dodecahedron and sphere[188].

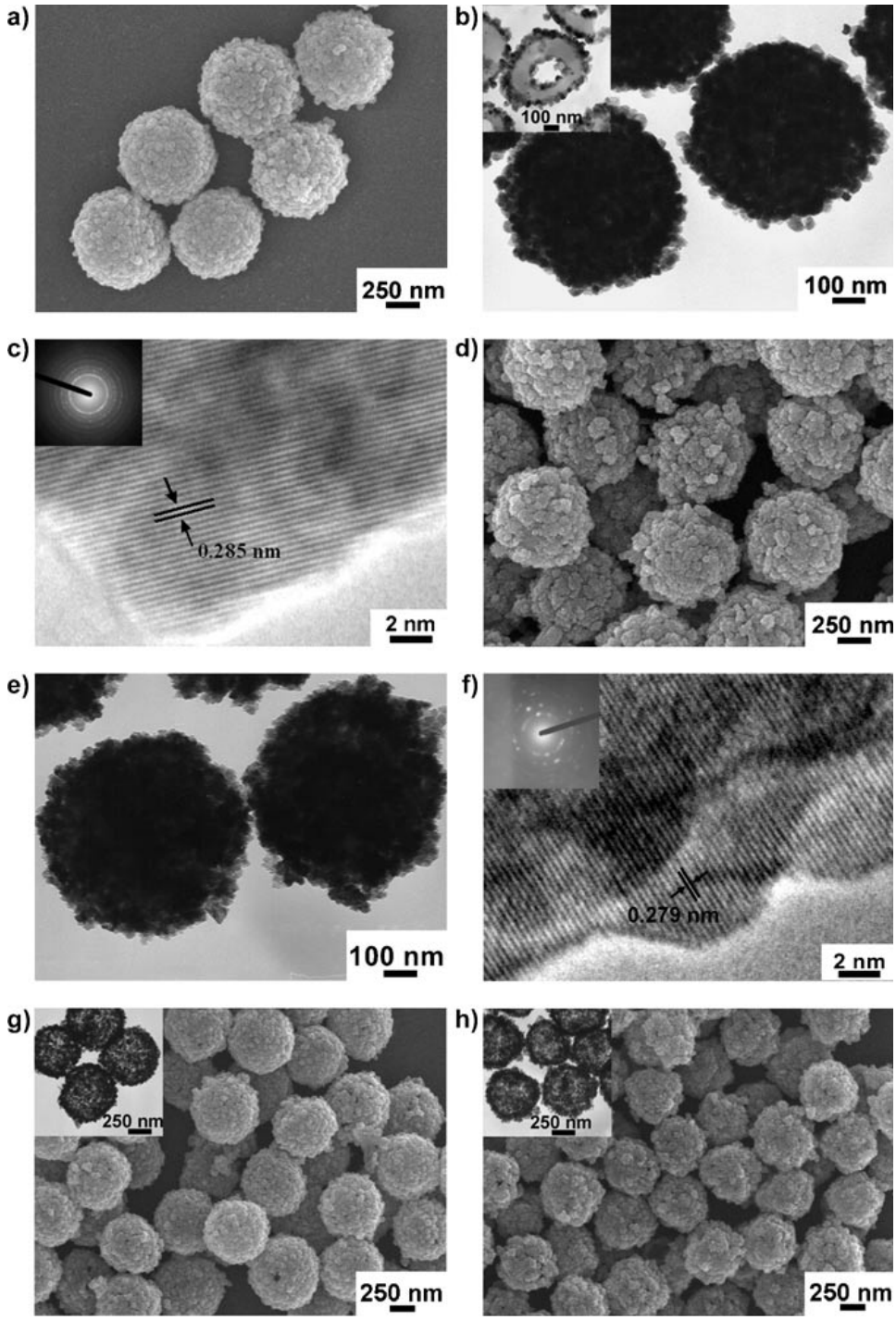

Figure 23. (a, d) SEM and (b, e) TEM images of (a, b) $BaTiO_3$/PS and (d, e) $SrTiO_3$/PS composite hollow spheres; inset of (b): microtome image. (c, f) HRTEM images of a typical particle on the shell of (c) $BaTiO_3$/PS and (f) $SrTiO_3$/PS composite hollow spheres; inset of (c, f): SAED patterns. (g, h) SEM and TEM (inset) images of (g) $BaTiO_3$ and (h) $SrTiO_3$ hollow spheres obtained after $BaTiO_3$/PS and $SrTiO_3$/PS composite hollow spheres were calcined in air at 450 ^oC[190].

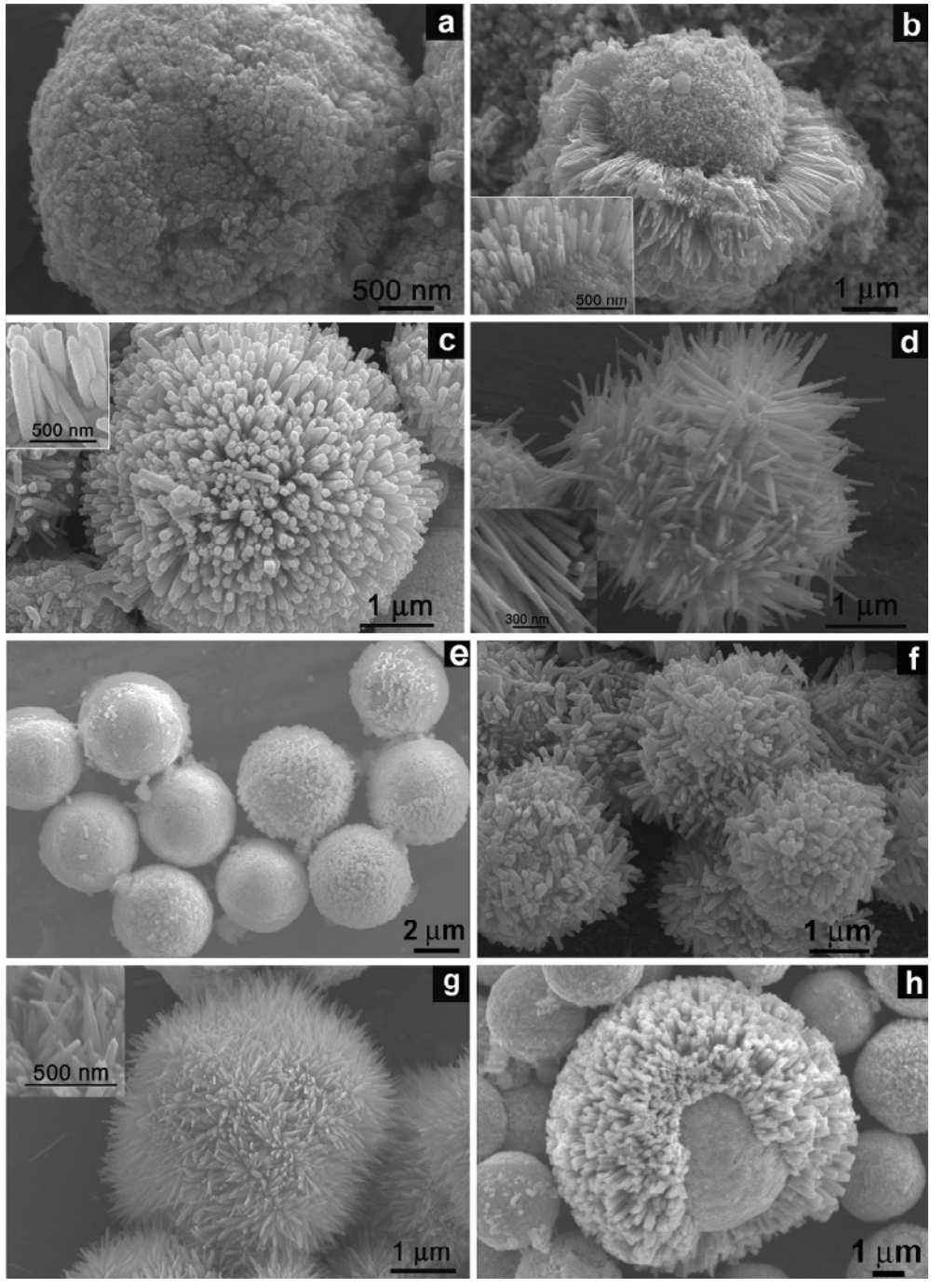

Figure 24. SEM images of $PbTiO_3$ nanostructures prepared by the hydrothermal method from Pb-Ti-citrate sol for 48 h. (a−d) With different SDBS concentration at 180 ^oC: (a, b) 0.1 mol/L, (c) 0.2 mol/L, and (d) 0.3 mol/L. (e) Without surfactant at 180 ^oC. (f, g) With 0.2 mol/L SDBS concentration at different temperatures, (f) 150 ^oC and (g) 200 ^oC. (h) 0.2 mol/L PSS concentration at 180 ^oC. Insets in images are the selected parts imaged at higher magnification[191].

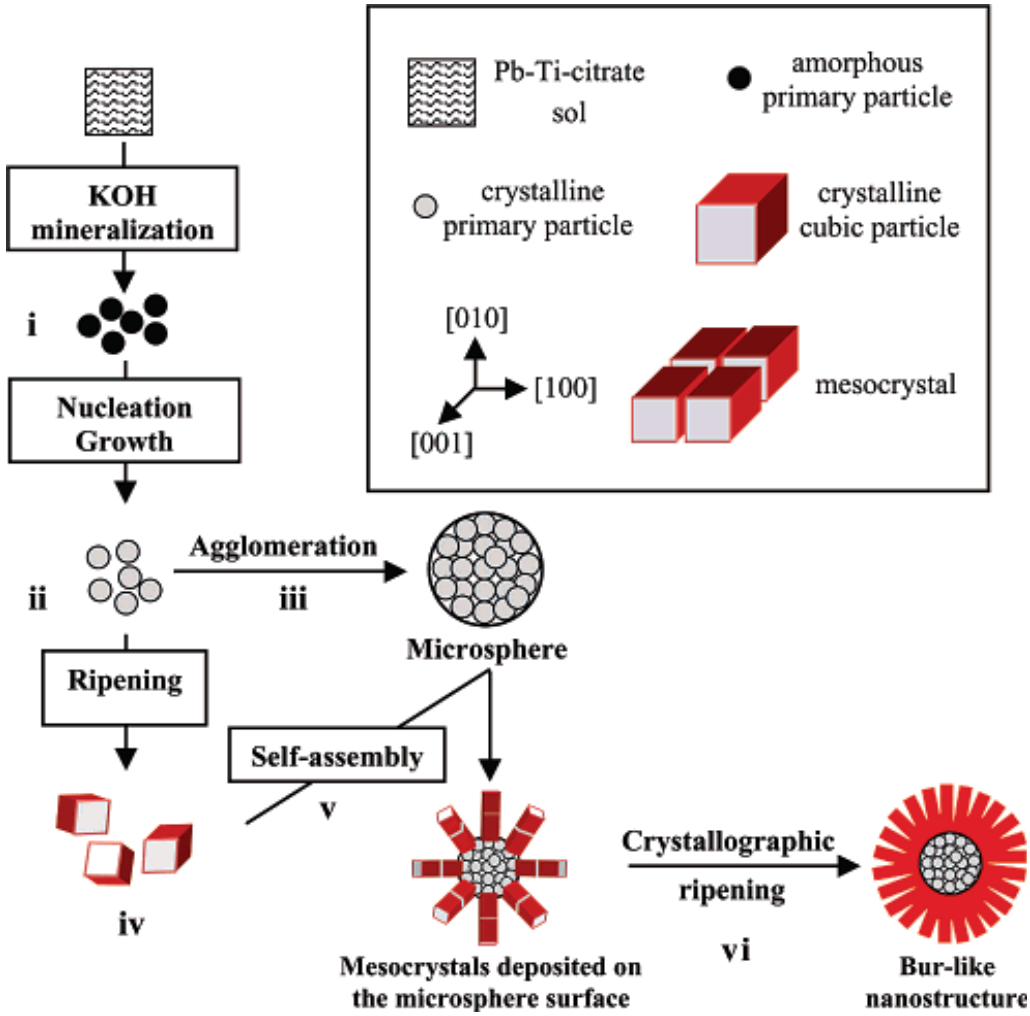

Figure 25. Schematic mechanism for the formation of bur-like nanostructure[191].

Generally speaking, adopting the above-mentioned hard/soft-templating method, hydrothermal method, novel solid state method, sol-gel method, and their coupled technique can give rise to a number of single-crystalline or polycrystalline perovskites with various morphologies. Even so, however, a lot of works needs to be done. For example, catalysts with the same chemical composition derived from various methods may exhibit greatly different catalytic activities for the same reaction due to the presence of difference in exposed crystal planes [197,198]. Therefore, the development of a strategy to control crystal growth (maximizing the exposed ratios of more reactive crystal planes, minimizing those of less reactive ones, and thus optimizing the desired structure of active sites) should be paid enough attention.

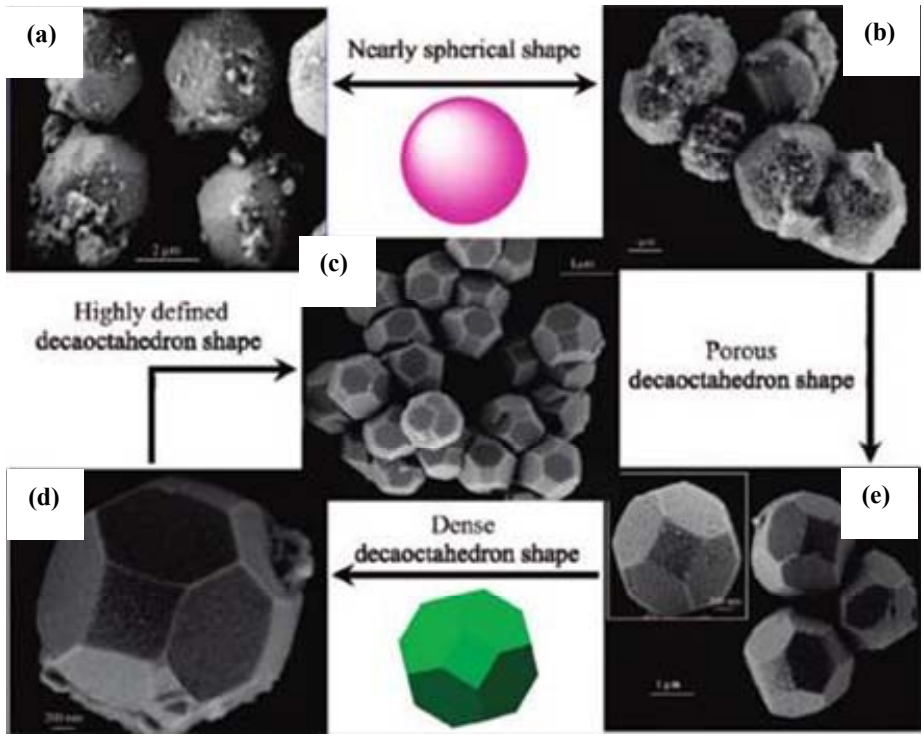

Figure 26. SEM images of nearly spherical $BaZrO_3$ powders obtained for (a) 10 and (b) 20 min, and of decaoctahedral $BaZrO_3$ powders obtained for (c) 40, (d) 80, and (e) 160 min at 140 ^oC[192].

2.5. Macro/Mesoporous Perovskite Synthesis

Because of the attractive physicochemical properties and potential applications in catalysis, biotechnology, adsorption, and separation, fabrication of hierarchically porous (macro/mesoporous) materials, especially for the three-dimensional ordered macro/ mesoporous (3DOM) materials, has been a focus in the research on materials science and engineering in recent years [99,199,200]. By using close-packed arrays of monodisperse spheres, such as polystyrene (PS), poly(methyl methacrylate) (PMMA), and silica as template, metals [201,202], metal oxides [203–208], metal chalcogenides [209], silica [204,210,211], carbon [212,213], polymers [214,215], and hydroxyapatite [216] with 3DOM structures have been generated.

Most of 3DOM metal oxides are fabricated by an alkoxide-based sol-gel process. The typical procedures include: (i) preparation of a colloidal crystal template by ordering monodispersive microspheres (e.g., PS, PMMA or silica) into a face-centered close-packed array; (ii) infiltration of a metal alkoxide solution into voids in the colloidal crystals, and *in-situ* solidification of the precursor via a sol-gel process; and (iii) template removal via a calcination or extraction pathway [99,217–219]. Using the alkoxide-based sol-gel method, 3DOM oxides of Si, Ti, Zr, Al, Sb, W, Fe, and 3DOM mixed oxides of some of them can synthesized due to the moderate reactivity of their alkoxide precursors [99]. However, most of the other metal alkoxides exhibit high reactivity and their reactions are too quick to be

controlled. Moreover, it is usually difficult and expensive to obtain the alkoxides of transition metals and lanthanide metals. Due to the low melting points, commercially available salts of these metals are usually not suitable for the use as starting material. At a temperature where the polymer template decomposes, these metal alkoxide salts melt, and hence causing a destruction of the 3DOM structure. Therefore, it is very important to solidify the transition or lanthanide metal elements before decomposition of the polymer template. To resolve these problems, it is a good strategy to add oxalic acid [220], ammonia [221] or EDTA [222] to the preparation system because they can first react with the metal salts (acetates or nitrates) in the voids of the colloidal crystals and then solidify the metal components. By means of these techniques, a number of 3DOM metal oxides (e.g., MgO, Cr_2O_3, Mn_2O_3, Fe_2O_3, Co_3O_4, NiO, and ZnO) have been successfully synthesized [220]. Unfortunately, since metal species show different reactivity towards oxalic acid, ammonia or EDTA, and the generated oxalate salts or metal hydroxides have different solubility in the reacting media, controllably fabricating a mixed metal oxide with a desired metal ratio using the above methods is still difficult.

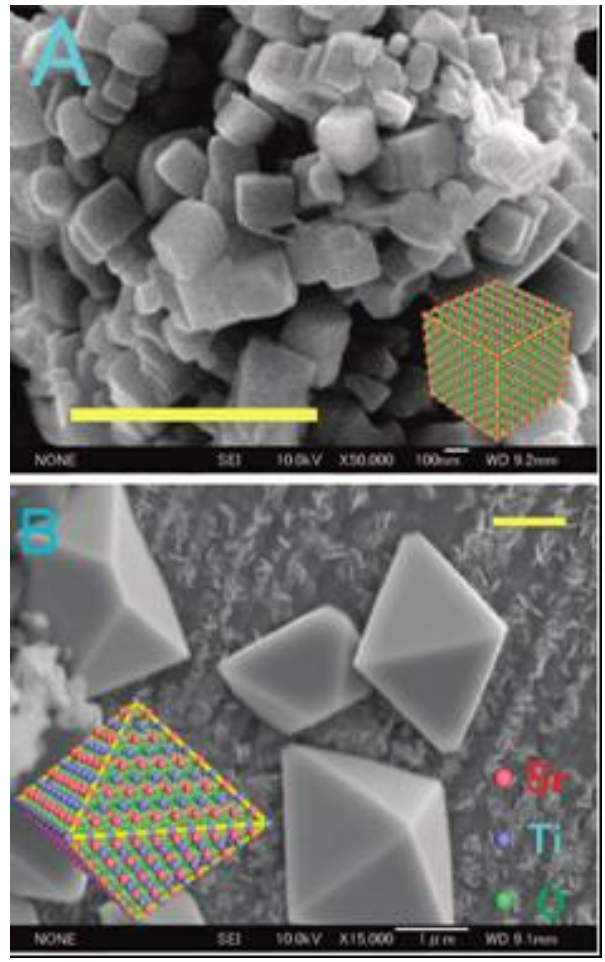

Figure 27. SEM images of $SrTiO_3$ crystal with (A) cubic shape and (B) octahedral shape. Scale bar is 1 μm[194].

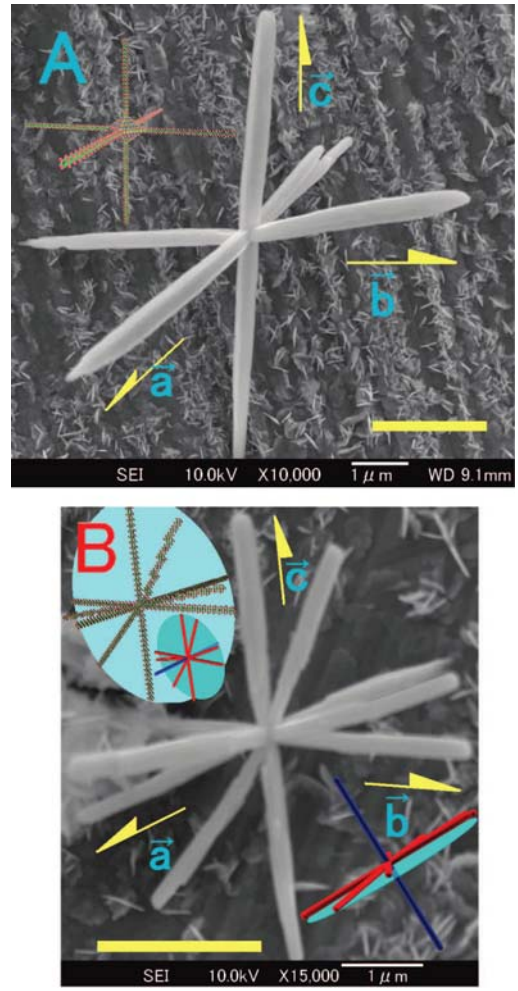

Figure 28. SEM images of $SrTiO_3$ crystals with (A) hexapod and (B) decapod shape. Insets are models of configuration of the $SrTiO_3$ legs. All of the red-colored legs in panel b lie on the cyan-colored disk (b−c plate). Scale bar is 2 μm[194].

To obtain 3DOM perovskites, several groups have developed the synthesis procedures, which ensure chemical homogeneity of the product. The only example without a solidification process is the fabrication of 3DOM $Sm_{0.5}Sr_{0.5}CoO_3$ from mixed metal nitrates [223]. Using a mixed metal alkoxide precursor derived from a stoichiometric mixture of lanthanum acetate, calcium acetate, strontium acetylacetonate, and manganese acetate in acidified 2-methoxyethanol, Hur and co-workers generated 3DOM $La_{0.7}Ca_{0.3-x}Sr_xMnO_3$ with PMMA as a colloidal template [224,225]. As shown in Figure 30, the as-prepared perovskite displays a very smooth surface and a long-range ordered porous structure over large areas. The size of the spherical voids is almost the same as that of the PMMA microspheres used, indicating that little shrinkage of the overall structure occurs during the sintering process. Using PS beads (diameter = 3 μm) as template, a crystallized 3DOM $Li_{0.35}La_{0.55}TiO_3$ membrane can be obtained by annealing the intermediate containing mixed Li-La-Ti-O and PS gel at 1000 ^oC. The Li-La-Ti-O sol is derived from the mixed solution of CH_3COOLi, $La(CH_3COO)_3{\cdot}1.5H_2O$, $Ti(OCH(CH_3)_2)_4$, CH_3COOH, *i*-C_3H_7OH, and H_2O with a molar ratio

of 0.35:0.55:1:10:20:140 [226−228]. The 3DOM $La_{0.75}Sr_{0.25}Cr_{0.5}Mn_{0.5}O_{3-\delta}$−YSZ (yttria-stabilized zirconia) and $Ba_{0.5}Sr_{0.5}Co_{0.8}Fe_{0.2}O_{3-\delta}$−YSZ composites are fabricated via a novel route, which comprises (i) the preparation of a mixture consisting of solid powders of the targeted phase and PMMA microspheres in an appropriate ratio, and (ii) the addition of polyvinyl alcohol to the mixture as a binder to increase the cohesion between the particles and secure the stability of the structure at high temperatures [229].

It is worth pointing out that Ueda and co-workers generated a number of 3DOM single or mixed metal oxides, such as Al_2O_3, Mn_2O_3/Mn_3O_4, Fe_2O_3, Cr_2O_3, $ZnAl_2O_4$, $LaAlO_3$, $LaCrO_4$, $ZnCr_2O_4$, MFe_2O_4 (M = Co, Ni, Zn, Zn_xNi_{1-x} (x = 0.2−0.8)), $La_{1-x}Sr_xFeO_3$ (x = 0−0.4), and $LaMnO_3$, by a facile one-pot synthesis route without the need of any alkoxide precursors [99,217−219]. Such an interesting and relatively versatile strategy is to use an ethylene glycol (EG)-methanol solution of metal nitrates, which can be converted to a mixed metal glyoxylate salt during *in-situ* nitrate oxidation at a lower temperature before the template PMMA or PS is removed. Further calcination at higher temperatures causes the glyoxylate salt to decompose to the desired 3DOM metal oxides, in the meanwhile removes the polymer template. A typical procedure for the fabrication of $La_{1-x}Sr_xFeO_3$ perovskites [218] is as follows: desired amounts of mixed metal nitrates (total metal concentration = 1−2 mol/L) is dissolved with about 5 mL of EG in a 100-mL beaker at room temperature for 2 h under stirring, and the produced EG solution is poured to a 25-mL volumetric flask. Methanol (40 vol%) and EG are added in the amount necessary to achieve the desired concentration. Then about 1.0 g of the PS colloidal crystals (161 ± 10 nm in size) is soaked in the produced dark brown solution for 5 h. The excess solution is removed from the impregnated PS template by filtration. The obtained sample is allowed to dry in air at room temperature overnight. 0.5 g of the desired sample is mixed with 2.5 g of quartz sands (10−15 mesh) and calcined in an air flow of 50 mL/min at a rate of 1 ^oC/min from room temperature to 600 ^oC and kept at this temperature for 5 h in a tube furnace. Shown in Figure 31 are the typical SEM images of the as-prepared perovskites. Clearly, well-ordered air spheres and interconnected walls create a three-dimensional “inverse-opal” macroporous architecture with a pore size of 72−94 nm, which corresponds to a shrinkage of 45−58% (with respect to the initial PS size) due to the melting of PS microspheres and sintering of the formed perovskite. Addition of methanol to the EG solution is a key step for successful fabrication of the desired 3DOM material. With a rise in methanol content from 0 to 40 vol%, the complete penetration time shortens from 10 to 5 h, thus resulting in an increase in the fraction of the 3DOM structured particles from 60−70% to 80−90%. The possible formation mechanism of the 3DOM structure derived by this method is illustrated in Figure 32 [99,217]. At first, the reaction taking place between the mixed metal nitrates and EG gives birth to the mixed metal glyoxylate or oxalate salts in the voids of the template microspheres at a low temperature. Then during the thermal treatment process, the pore size is reduced due to the melting of the template and the air space in void (shell structure) is generated after evaporation of methanol and remaining EG. Further calcination results in a total removal of the template and formation of the desired crystal phase. The subsequent crystallite growth causes the 3DOM materials to transform from the “shell structure” to the “skeleton structure”.

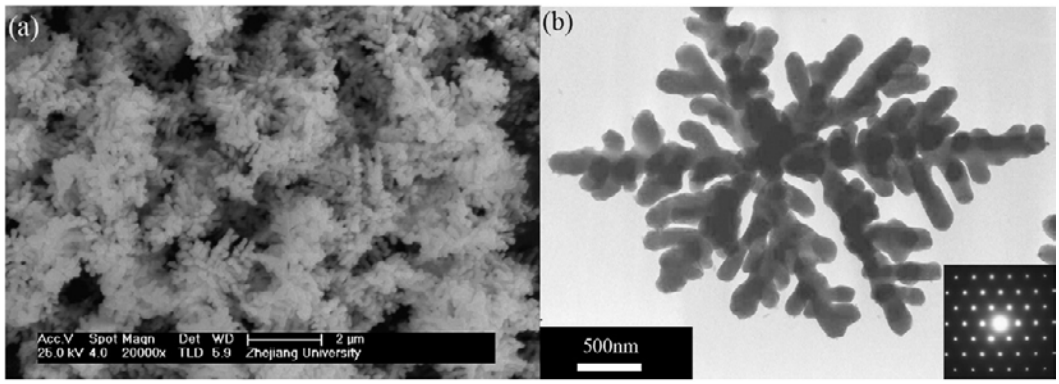

Figure 29. SEM images of single-crystal $BaTiO_3$ synthesized at 200 ^oC for 6 h with 0.1 mol/L KOH. Inset is the SAED pattern[195].

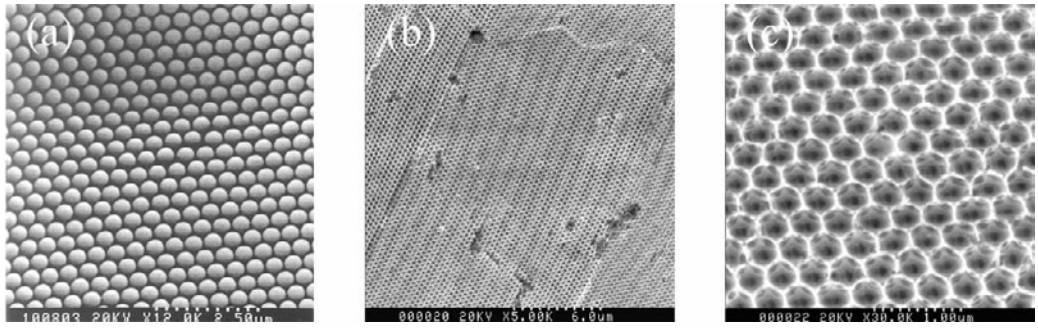

Figure 30. (a) A typical SEM image of the PMMA template. (b) A low-magnification SEM image of the macroporous $La_{0.7}Ca_{0.2}Sr_{0.1}MnO_3$ film showing the presence of cracks and defects produced after removal of template. (c) A higher magnification SEM image of the same porous sample[224].

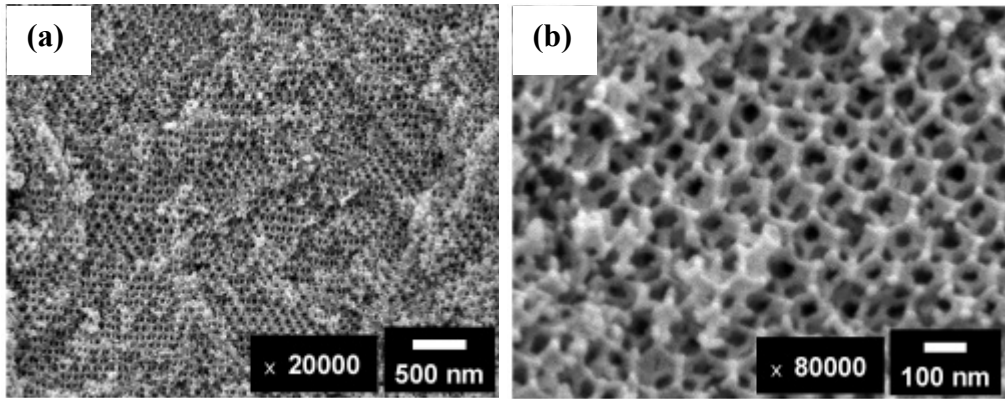

Figure 31. SEM images of $LaFeO_3$ obtained with PS infiltrated by EG-methanol (40 vol%) mixed solution of $Fe(NO_3)_3$ and $La(NO_3)_3$ (total metal concentration = 2 mol/L) and calcined at 600 ^oC for 5 h[218].

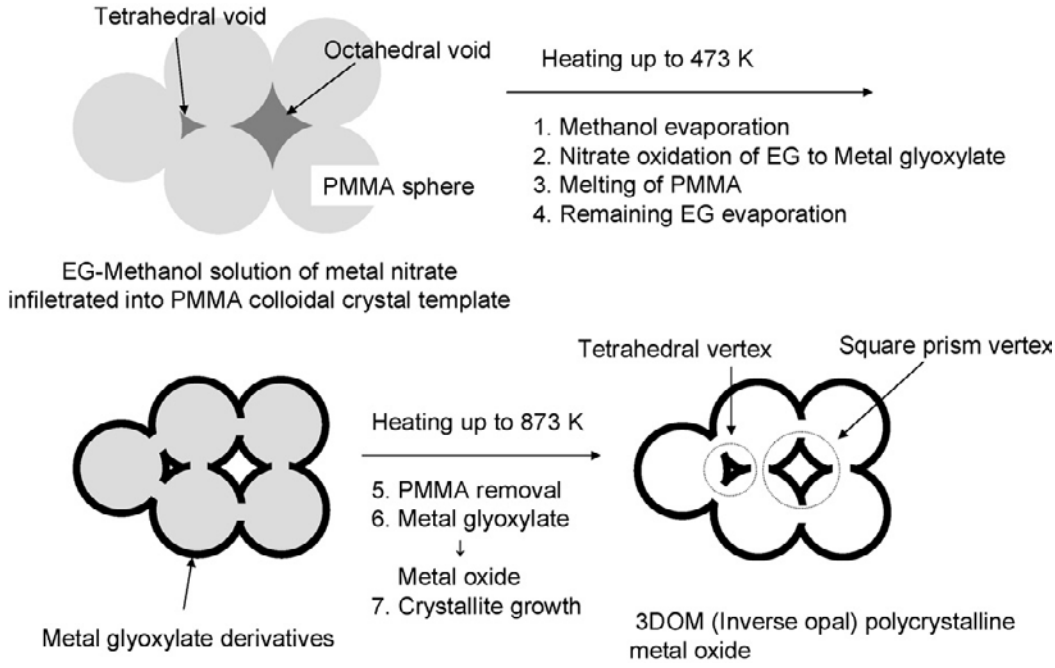

Figure 32. Formation mechanism of 3DOM metal oxide[99].

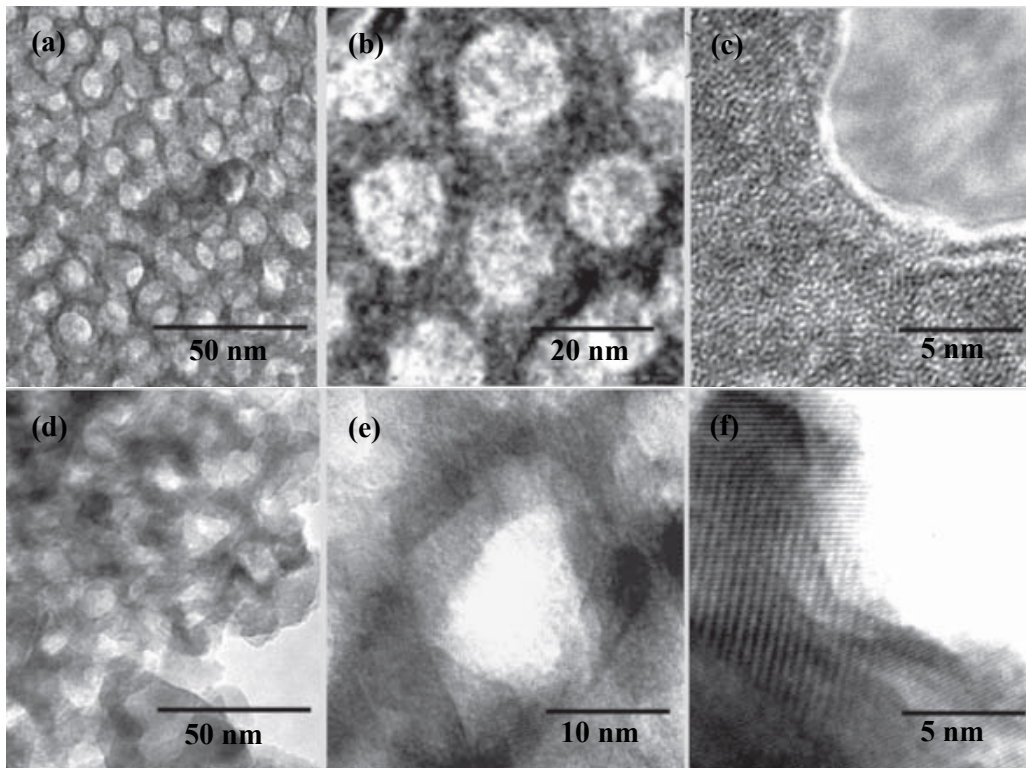

Figure 33. HRTEM images of a $SrTiO_3$ mesoporous ordered network (a−c) before crystallization, obtained at 590 ^oC, and (d−e) after crystallization, obtained at 630 ^oC[233].

Although 3DOM metal oxides can be synthesized following the above mentioned methods, their surface areas are still relatively low (< 100 m^2/g) and the pores are only macropores without mesopore formation on the walls. These drawbacks inevitably inhibit wide applications of such porous materials. Therefore, high-surface-area 3DOM metal oxides with mesoporous walls are highly desirable. Recently, our group used P123 as soft template, regularly packed PMMA microspheres as hard template, and tetraethyl orthosilicate as Si source to successfully make 3DOM silica with 2D ordered mesoporous walls and unusually large pore volume (2.1 cm^3/g) [230]. Following this idea, we introduced P123 or F127 ($EO_{106}PO_{70}EO_{106}$) to the mixed alcoholic solution containing PMMA-metal nitrates, and generated a number of high-surface-area 3DOM MgO (243 m^2/g), γ-Al_2O_3 (145 m^2/g), and $Ce_{1-x}Zr_xO_2$ (x = 0.3, 0.4) (100 m^2/g) with mesoporous crystalline walls [231]. This strategy is promising in the fabrication of 3DOM perovskites with mesoporous walls.

Based on the evaporation-induced self-assembly (EISA) method reported by Yang et al. [232], a number of mesoporous single and mixed metal oxides have been produced. However, only one pervoskite-type oxide, i.e. $SrTiO_3$ with mesoporous structure was prepared using the EISA method with a specially formulated non-ionic block-copolymer KLE3739 (PBH_{79}-*block*-PEO_{89}, PBH = hydrogenated poly(butadiene)) template [233]. As shown in Figure 33, the walls are composed of nanoparticles (10−20 nm in size). If the annealing treatment at the crystallization temperature is stopped, amorphous mesoporous networks can be crystallized without extensive degradation of the meso-organization. The porosity of $SrTiO_3$ is about 31 vol% (estimated using the Bruggeman effective medium approximation model applied to ellipsometric data). Unfortunately, utilization of such a methodology is greatly hindered due to the use of extremely expensive and noncommercial template. Very recently, an alternative method to prepare perovskites with a mesoporous structure has been reported by Vilarionho and co-workers [234,235]. They adopted cetyltrimethylammonium chloride (C_{16}TMAC, 25 wt% sol in water) as the cationic surfactant to generate cubic $BaTiO_3$ single crystallites with wormhole-like mesopores via the sol-precipitation route [235]. Further investigations made by the same group reveal that nanoporous cubic $BaTiO_3$ single crystallites can be obtained with the assistance of nonionic block-polymer Pluronic PE 10300 ($EO_{15}PO_{70}EO_{15}$) but without subsequent thermal treatments [234]. Disordered nanoporous structures (Figure 34) are formed in the sample calcined at 300 or 400 ^oC. These materials show a BET surface area of about 70 m^2/g and a nanopore volume fraction of 44.7%, larger than those of porous $BaTiO_3$ derived with a cationic surfactant C_{16}TMAC [235]. Because of the closure and collapse of partial pores, calcination at a higher temperature (e.g., 600 ^oC) results in an obvious decrease in surface area from 70 to 44 m^2/g. Therefore, this method seems to be not suitable for the generation of mesoporous perovskites because a high-temperature (> 650 ^oC) treatment is needed for perovskite phase formation. Nevertheless, it provides a thinking line to directly synthesize mesoporous perovskites with the aid of a surfactant.

It is well known that the nanocasting strategy with mesoporous silica or carbon as hard template is an effective technique to fabricate mesoporous metal and metal oxides [236–238].

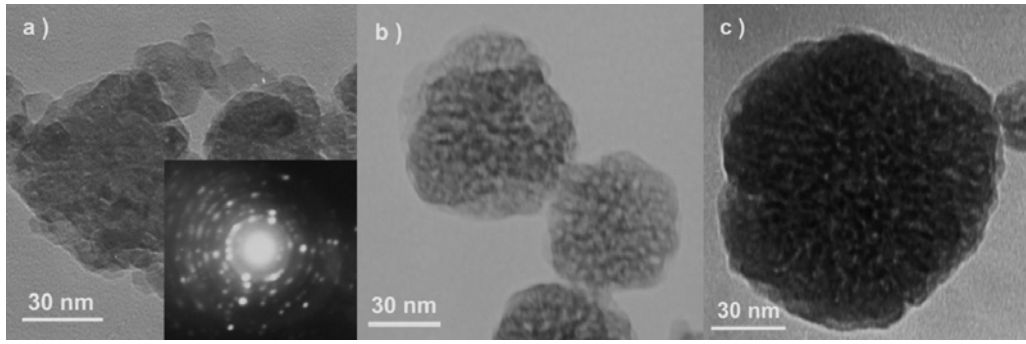

Figure 34. TEM images of (a) as-prepared $BaTiO_3$ crystallites and the SAED pattern (inset), nanoporous $BaTiO_3$ calcined (b) at 300 ^oC and (c) at 400 ^oC[234].

Compared to mesoporous single metal oxides, reports on the synthesis of mesoporous binary or mixed oxides via a nanocasting route are few [237–240]. To the best of our knowledge, there is no report claiming the successful preparation of mesoporous perovskites following such a nanocasting route. By carefully controlling the calcination temperature for perovskite structure formation and fully filling the mesopores of the hard template with a homogenous precursor solution, however, it is possible to make mesoporous perovskites through the nanocasting process.

3. PHYSICOCHEMICAL PROPERTIES

3.1. Magnetic Property

In an ideal cubic perovskite (ABO_3) structure, each oxygen atom is shared by two B-site ions (B-O-B angle = 180^o), which is favorable for the super-exchange interactions between magnetic B cations. Such an exchange usually leads to antiparallel coupling of nearest-neighbor magnetic moments. Because the alignment of Fe moments is not strictly antiparallel but slightly canted on $LnFeO_3$ (Ln = lanthanide), a small net magnetization is generated. Among the orthorhombic $LnFeO_3$ (Ln = La, Pr, Nd, Sm, Eu, Gd) nanocrystallites prepared by a general nanosized heterobimetallic precursor approach at 500 ^oC, $SmFeO_3$ is paramagnetic rather than superparamagnetic, ascribable to the paramagnetic susceptibility of Sm ions and a minor ferrimagnetic contribution from the canting of the Fe sublattice, whereas the other ferrites are weak ferromagnets. Moreover, the $EuFeO_3$ and $GdFeO_3$ nanocrystallites exhibit better weak ferromagnetic behavior with the corresponding saturation magnetization intensity being 3.99 and 3.89 emu/g, much higher than those (0.325−1.335 emu/g) of the $EuFeO_3$ and $GdFeO_3$ materials prepared via the sol-gel and solution-based chemical routes [9]. Below the magnetic ordering temperature, compared to the $CaMn_{1-x}Nb_xO_3$ ($x \leq 0.08$) samples obtained through a conventional solid-state reaction at 1400 ^oC for 6 h, the ultrafine manganite nanoparticles derived from ultrasonic spray combustion display a pronounced ferromagnetic suppression coupled to an abrupt increase of the absolute thermopower value. This might be associated with the different compositions on grain boundaries and/or a weakening of the double exchange ferromagnetism phenomena due to the small size of the nanoparticles [241].

On the basis of the experimental results, Feng and co-workers deduced that the disorder in the grain boundary region of the rod-shaped $La_{0.7}Sr_{0.3}MnO_3$ sample is larger than that of the particle in the same size range, which leads to a decrease in the Curie temperature (T_c) and effective magnetization (χ_m) [147,148]. The T_c of $La_{0.7}Sr_{0.3}MnO_3$ nanorods fabricated by the molten-salt method is −11 °C, much lower than those (−87~−93 °C) of $La_{0.7}Sr_{0.3}MnO_3$ synthesized via a solid-state reaction route. The χ_m of $La_{0.7}Sr_{0.3}MnO_3$ nanorods is 2.075 μ_B, about half of the ideal effective moment (4.17 μ_B). At room temperature, $BiFeO_3$ nanoparticles (80−120 nm in size) and $BiFeO_3$ nanotubes (20 nm in wall thickness) exhibit a weak ferromagnetic order, quite different from the linear relationship of magnetization *vs* magnetic field in the bulk $BiFeO_3$. The weak ferromagnetic order in the $BiFeO_3$ nanoparticles and nanotubes is attributable to the grain size confinement effect [11,62]. By comparing the magnetic behaviors of $La_{0.325}Pr_{0.300}Ca_{0.375}MnO_3$ nanotubes and powders with the same average particle size, Curiale et al. pointed out that the nanostructure plays an important role in the magnetic properties [91]. The tube-like structure favors the orientation of the moments by the action of magnetic field, which should be directly related to the presence of magnetic interactions between the grains. Although the general feature of magnetization *vs* temperature has been reproduced, the $La_{1-x}Ba_xMnO_3$ (x = 0.3, 0.5, 0.6) nanocubes, compared to those of the bulk counterparts, show a slight reduction in saturation magnetization as well as a suppression of the phase transition temperature. It may originate from the enhanced surface-to-volume ratio or the presence of a superparamagnetic phase in these nanocrystalline samples [127]. Based on the results mentioned above, one can find that both the particle size [127,241] and crystal morphology [91,147,148] have important effects on the magnetic property. Recently, Chai et al. pointed out that the product particle size exerts a bigger impact than its morphology on the magnetic properties of the flower-, microcube-, and nanocube-like $La_{0.5}Ba_{0.5}MnO_3$ perovskites [173]. In other cases, however, it is hard to say which one (crystal particle size or morphology) plays a more important role in influencing the magnetic performance.

In addition, remarkable metal-insulator phase transitions and pronounced colossal magnetoresistance have been observed in the core-shell $MgO/La_{0.67}Ca_{0.33}MnO_3$ and $MgO/La_{0.67}Ca_{0.33}MnO_3$ nanowires [158−160]. The results are likely related to the relaxation of the stress in the radial direction unique in core-shell nanowires. Interestingly, the magnetic moment of porous $La_{0.7}Ca_{0.3}MnO_3$ perovskite is smaller than that of its single crystalline counterpart [225]. The reduced moment in the porous perovskite can be attributed to the presence of a superparamagnetic phase resulting from nanocrystalline domains in the ferromagnetic matrix. On the other hand, porous $La_{0.7}Ca_{0.3}MnO_3$ shows a much higher T_c value than its single-crystalline counterpart. The possible reason for T_c enhancement is the occurrence of composition fluctuation and/or an oxygen annealing effect. The porous material can adsorb much more oxygen than the bulk one. Thus, oxygen saturation may result in an enhancement of T_c. Although the T_c value of macroporous $La_{0.7}Ca_{0.2}Sr_{0.1}MnO_3$ is close to that of its corresponding bulk polycrystallite, the resistivity of the porous perovskite throughout the temperature region (−248~102 °C) is about two orders of magnitude higher than that of its polycrystalline counterpart due to the connectivity between the porous grains and nanosized grains [224]. The magnitude of magnetoresistance observed in the porous perovskite is about twice as much as that observed in the polycrystalline one, a result due to the spin-polarized tunneling at the nanosized grain boundaries.

3.2. Electrical Property

Electrical properties of perovskites have been received special attention due to their superconductivity [242]. The electrical behaviors in perovskites depend on the outermost electrons, which may be localized at specific atomic sites or collective. Because localized electrons can carry a spontaneous moment, there is a strong correlation between the electrical and magnetic property of the perovskite material [2]. It is found that the ferroelectric properties (e.g., T_c, mean polarization, area of hysteresis loop, coercive electric field, and remnant polarization) of $BaTiO_3$ nanowires alter linearly with the diameter of nanowires only when the diameter is less than 20 nm [243]. Due to the nanosize effect in the $BaTiO_3$ nanowires, the dielectric constant measurement shows a shift in the transition temperature (105 ^oC) compared to the bulk transition temperature (132 ^oC) [110]. As for an individual $NaNbO_3$ nanowire with a width of 200 nm and a length of 80 nm, the piezoelectric coefficient (d_{zz}) along the vertical direction is 0.95 pm/V, whereas it is 4.26 pm/V for the one with 100 nm in width and 120 nm in length, suggesting that a nanowire with a larger length-to-width ratio vibrates more easily under an applied electric field [114]. Polycrystalline $PbTiO_3$ [66] and $Pb_{0.25}Ba_{0.15}Sr_{0.6}TiO_3$ nanotubes [71], $PbZr_{0.53}Ti_{0.47}O_3$ nanowires [60], and $BiFeO_3$ nanowires [58] or nanotubes [63] display highly ordered ferroelectric behaviors. In the coercive field in the amplitude and phase loops of a single $PbZr_{0.53}Ti_{0.47}O_3$ nanowire piezoresponse, a positive shift is observed. This result may be caused by the surface change at the electrode and $PbZr_{0.53}Ti_{0.47}O_3$ interface or the space change stored in the alumina template walls [60]. The remnant polarization (11 $\mu C/cm^2$) of the $BiFeO_3$ nanowires is much higher than that (6 $\mu C/cm^2$) of the bulk $BiFeO_3$. The hysteresis phenomenon is associated with the polarization switching and ferroelectric properties of the $BiFeO_3$ sample [58]. Due to a high surface area of nanotubes, there is an enhancement in ferroelectric polarization of $Pb_{0.25}Ba_{0.15}Sr_{0.6}TiO_3$ nanotubes compared to that of the nanofilm counterpart [71]. Very interestingly, the dielectric constant of $BaTiO_3$ greatly decreases after nanoporosity introduction, which can be modified by varying the initial block copolymer type and/or content and by changing the post thermal treatment conditions. As the frequency increases from 10 kHz to 1 MHz, the dielectric constant of nanoporous $BaTiO_3$ decreases from 375 to 110 whereas that of nonporous $BaTiO_3$ decreases from 2530 to 700. That is to say, it provides an effective way to manipulate the dielectric constant in a wide range, especially where low dielectric constant is desired to achieve high figures of merit in pyroelectric and piezoelectric applications [234].

3.3. Optical Property

Perovskites are a good candidate of optical materials for the generation of new optoelectronic devices with high performance. Recently, photoluminescence (PL) of perovskites arising from the imperfection and defect has attracted increasing attention [182,185]. It is observed from the room-temperature PL spectra of single-crystalline $PbTiO_3$ nanowires that there is a blue light emission band at a wavelength of about 471 nm (2.63 eV), and the signal intensity increases with a rise in excitation wavelength [111,112]. At an excitation wavelength of 488 nm, the room-temperature PL spectra of $PbTiO_3$ nanotubes show a strong green emission band at 550 nm (2.25 eV) [133]. Since the excitation energy

used is lower than the band gap energy (about 4.15 eV) of $PbTiO_3$ nanowires, the light emissions observed from 420 to 560 nm are not related to a direction electron transition from the valence band to conduction band. Actually, oxygen vacancies of $PbTiO_3$ nanowires, which can produce a heterogeneous band gap structure with a tail of localized states and possible mobile edges, might be responsible for the light emission [111,112]. A similar explanation can be used in the case of $PbTiO_3$ nanotubes. Due to the high surface area, numerous local defects (e.g., oxygen vacancies and dangling bonds) inevitably exist in a highly ordered nanotubular structure. Such defects are an emission source, resulting in a unique PL behavior of $PbTiO_3$ nanotubes [133]. As for the $BaZrO_3$ perovskite with a decaoctahedral morphology, the structural feature associated with distorted octahedral (ZrO_6) and dodecahedral (BaO_{12}) clusters plays an important role in determining the PL property [192]. It is known that $BaTi_{0.5}Mn_{0.5}O_3$ is a high dielectric material and $BaMnO_3$ is not a luminescent material. Nevertheless, Wang and co-workers found that $BaTi_{0.5}Mn_{0.5}O_3$ nanorods exhibit an excellent PL performance, showing blue and green fluorescence with the corresponding emission bands at λ = 465 and 593 nm in the PL spectrum of this nanorod-like perovskite [151].

In addition, perovskites are interesting when they are used as a host material for rare earth photoluminescence. The room-temperature PL spectra of Eu^{3+}-doped spherical, cubic or dodecahedral, and agglomerated $BaZrO_3$ are shown in Figure 35 [185,188]. The PL spectral feature in the range of 570–660 nm can be ascribed to emissions from the excited $^5D_0$ state level to lower lying ^7F_J (J = 0, 1, 2, 3, 4) levels of the $4f^6$ configuration of Eu^{3+}. The most prominent band at 612 nm is due to the $^5D_0 \rightarrow {}^7F_2$ transition, as expected from the Judd-Ofelt selection rule. Although similar in spectral shape, their intensities differ in the Eu^{3+}-doped $BaZrO_3$ perovskites with various morphologies. Since the intrinsic geometry of spherical $BaZrO_3$ particles minimizes the scattering of light from the sample surface, as compared with cubic, polyhedral, and agglomerated $BaZrO_3$ particles, it is understandable that the spherical particles show the highest emission intensity. On the other hand, the aggregated particles possess more bulk defects, surface cracks, and intraparticle residual elastic strains, hence giving rise to a reduced luminescence yield. Such a morphology-dependent PL property has also been observed in the case of $CaTiO_3:Pr^{3+}$ [182]. Under the same conditions, the $CaTiO_3:Pr^{3+}$ mesocubes exhibit considerably stronger red emission at about 612 nm than the prismatic rectangular $CaTiO_3:Pr^{3+}$ rods.

Very recently, the photoelectrochemical performance of microtubular $CaTiO_3$ and fibrous $SrTiO_3$ and $BaTiO_3$ has been reported. $CaTiO_3$ microtubes show better photoelectrochemical responsing ability relative to $SrTiO_3$ and $BaTiO_3$ microstructures. Beside the smaller diameter, the 1D structure can effectively reduce the contact resistance at grain boundaries to improve electron transport, leading to an enhancement in photocurrent and conversion efficiency [134]. The current *vs* voltage characteristics of 1D Ag_2MO_4 (M = Cr, Mo, W) nanowires exhibit a unique rectifying behavior with the fast and reversible photo-switching response under on/off light exposure conditions [117]. Oxygen ions play an important role in the photoconductivity. The light-to-dark conductivity ratios of these 1D compounds are correlated with the ionic potential of the metal. This result suggests the possible application in photosensitive devices in the future.

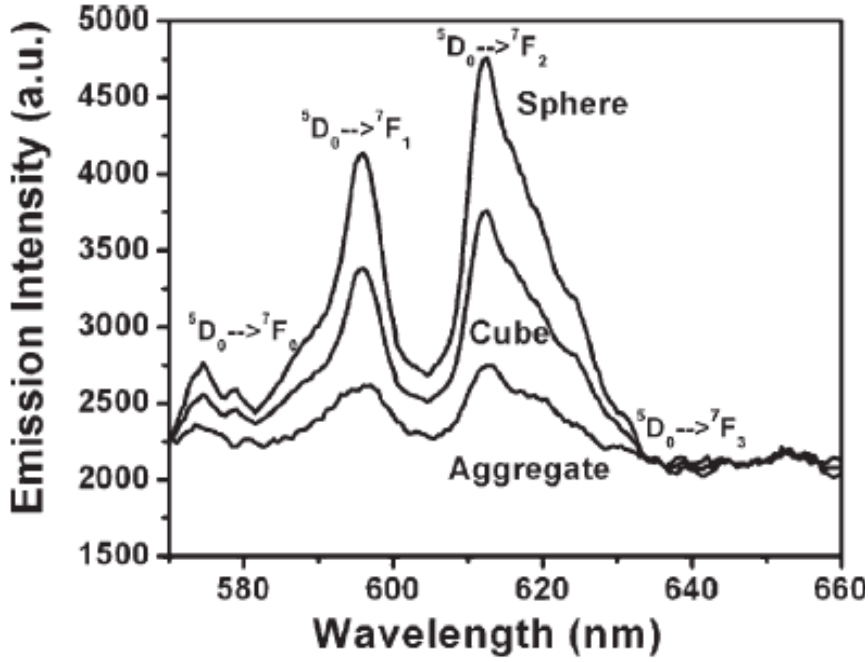

Figure 35. Room temperature PL emission (λ_{ex} = 256 nm) spectra of the 2% Eu^{3+}-doped $BaZrO_3$ samples with different morphologies[185].

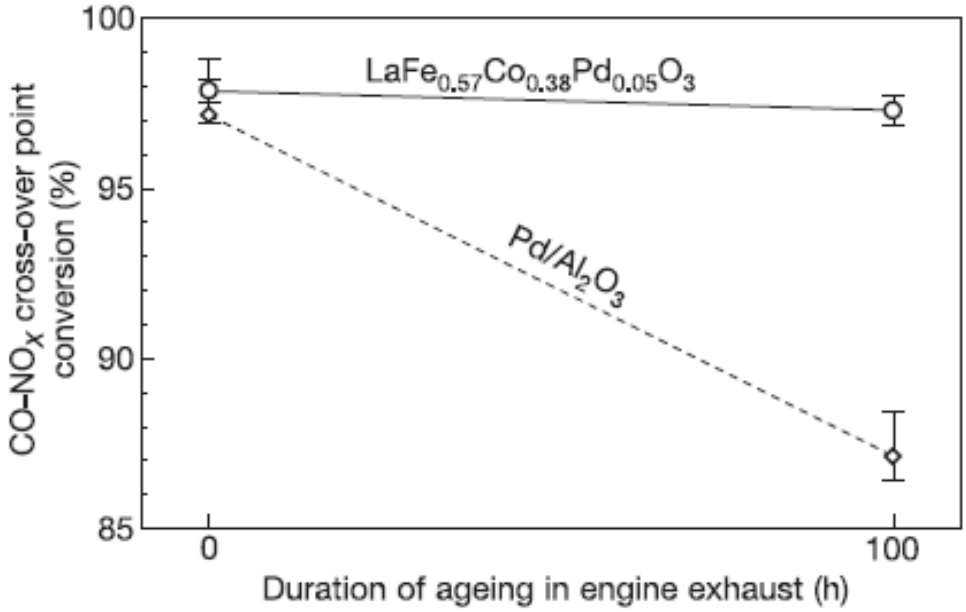

Figure 36. The ageing dependence of the CO−NO_x cross-over point conversion over the $LaFe_{0.57}Co_{0.38}Pd_{0.05}O_3$ and Pd/γ-Al_2O_3 catalysts[257].

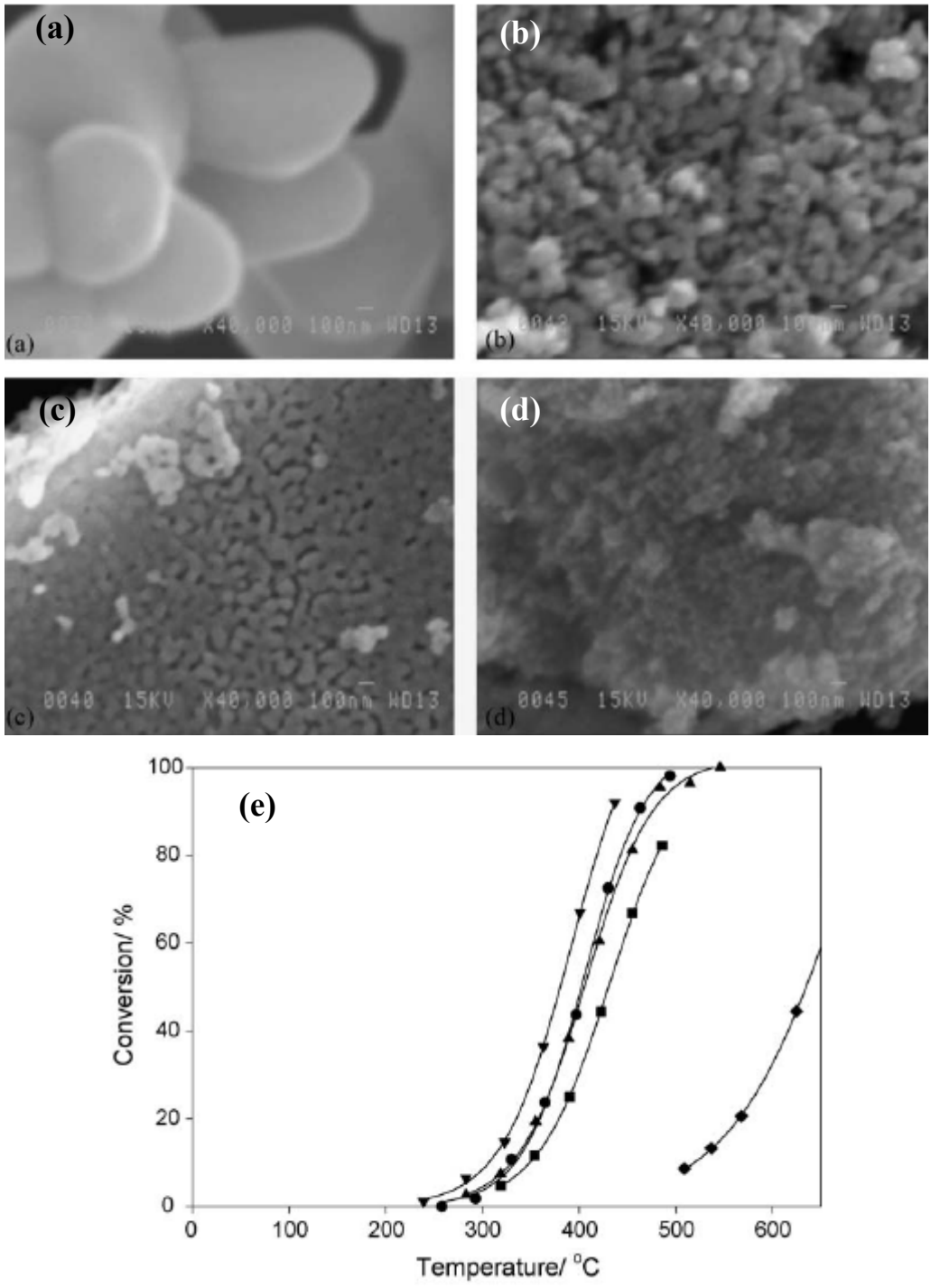

Figure 37. SEM photographs of the $LaCoO_3$ catalysts obtained after calcination: (a) SS; (b) COP; (c) CIT; and (d) COPRG. (e) Steady-state conversions obtained for the oxidation reaction of 0.25% CH_4 as a function of the reaction temperature over $LaCoO_3$: (▼) COPRG, (●) RG, (▲) CIT, (■) COP, and (◆) SS[258].

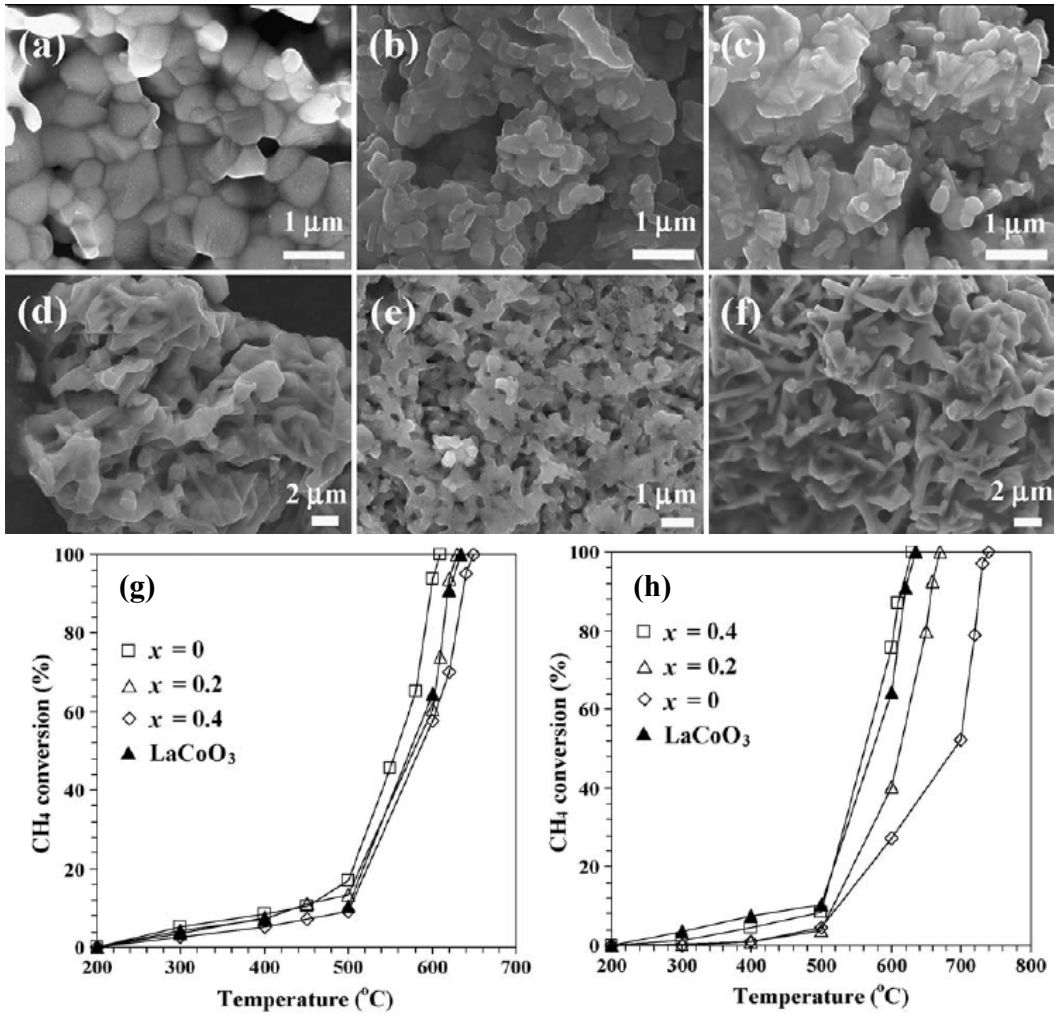

Figure 38. SEM images of (a–c) $NdSrCu_{1-x}Co_xO_{4-\delta}$ and (d–f) $Sm_{1.8}Ce_{0.2}Cu_{1-x}Co_xO_{4+\delta}$ at $x = 0$ (a, d), 0.2 (b, e), and 0.4 (c, f). CH_4 conversion as a function of reaction temperature over (A) $NdSrCu_{1-x}Co_xO_{4-\delta}$ and (B) $Sm_{1.8}Ce_{0.2}Cu_{1-x}Co_xO_{4+\delta}$ as well as over $LaCoO_3$ under the conditions of CH_4/O_2 molar ratio = 1/20 and space velocity = 10000 h^{-1}[263].

4. APPLICATIONS IN CATALYSIS

4.1. Nitrogen Oxide Elimination

Nitrogen oxides (NO_x) emitted from vehicles and industrial activities are one of severe pollutants to the environment. Direct decomposition of NO_x and reduction of NO_x with H_2, CO, NH_3, and hydrocarbons are the good ways to eliminate such a kind of pollutant. Several reviews relevant to this topic can be seen in the literature [244–246]. However, a summarization on catalytic performance of the specifically morphological perovskites for NO_x removal is still unavailable.

As a "green" process, NO_x decomposition has been received much attention. By using CNTs as template under hydrothermal conditions, Gao et al. [83] fabricated La_2CuO_4 (i.e., $La_2Cu_{0.88}^{2+}Cu_{0.12}^{+}O_{3.94}$) nanofibers with a surface area of 105 m^2/g. Below 300 °C, NO can be totally decomposed to N_2 and O_2 over the cuprate nanofibers. Over the bulk La_2CuO_4 catalyst (i.e., $La_2Cu_{0.92}^{2+}Cu_{0.08}^{3+}O_{4.04}$) with a surface area of 2.7 m^2/g prepared by a solid-state reaction method, only 78% NO can be decomposed even at 800 °C and the products are N_2, O_2, and NO_2. The authors attributed the good catalytic performance of the nanofibrous cuprate material to the co-presence of nanofibrous morphology, high surface area, appropriate Cu^+/Cu^{2+} molar ratio, and uncompetitive O_2 and NO adsorptions [83]. Via a highly exothermic and self-sustaining reaction route, the $LaBO_3$ (B = Cr, Mn, Fe, Co) nanoparticles with a typical size of 55−75 nm can be prepared [247]. The performance of these perovskites for the decomposition of N_2O to N_2 and O_2 depends on the nature of the B-site ions, with the $LaCoO_3$ catalyst showing the best activity. By adopting the sol-gel route, colloidal crystal templating, and reactive grinding methods, Granger and co-workers prepared nanosized rhombohedral $LaCoO_3$ catalysts. The morphology of the product has a great impact on the catalytic activity for N_2O decomposition. The $LaCoO_3$ catalyst fabricated by the reactive grinding method exhibits the best performance, which may be related to a higher surface area and a higher oxygen vacancy density as well as the presence of trace amounts of Fe and Zn impurities introduced during the preparation process [248].

The improvement in physicochemical properties (including surface area) of perovskites can enhance their efficiency of NO_x removal. By using the reverse microemulsion method, $LaMO_3$ (M = Mn, Fe) [24], $La_{1-x}A_xFeO_3$ (A = Sr, Ce) [25], and $La_{0.8}Ce_{0.2}B_{0.4}Mn_{0.6}O_3$ (B = Cu, Ag) [26] nanoparticles with a diameter of 50−150 and 40−50 nm can be prepared, respectively. Such high-surface-area (14−61 m^2/g) nanocatalysts showed better catalytic activity for (NO + CO) reaction than the catalysts derived from the common ceramic and sol-gel methods. In the case of $LaMnO_3$, besides the high surface area, the presence of Mn^{3+}−O−Mn^{4+} pairs (favorable for adsorption-desorption flip-flops) is a factor contributing to the excellent performance [24]. The sequence in catalytic activity is $La_{0.8}Ce_{0.2}FeO_3$ > $La_{0.8}Sr_{0.1}Ce_{0.1}FeO_3$ > $La_{0.85}Sr_{0.15}FeO_3$ > $LaFeO_3$, in accordance with the order in increment of their surface areas [25]. It is reported that $La_{0.8}Ce_{0.2}Cu_{0.4}Mn_{0.6}O_3$ outperforms $La_{0.8}Ce_{0.2}Ag_{0.4}Mn_{0.6}O_3$ for the selective reduction of NO with CO [26]. This result is understandable because the dominant Cu^+ ions and their redox reaction $Cu^+ \Leftrightarrow Cu^{2+}$ favor the NO adsorption and reduction by CO. Nanosized $LaFe_{1-x}Co_xO_3$ catalysts can be obtained using a porous carbon as hard template [27]. The surface area of $LaFeO_3$ and $LaFe_{0.6}Co_{0.4}O_3$ is 30.5 and 49.3 m^2/g, much higher than that (5.6 and 3.6 m^2/g) of the citrate-complexing derived counterparts, respectively. The larger surface area allows the exposure of a higher number of accessible active sites in the nanocasting-derived perovskites, resulting in a better catalytic activity for the reduction of NO with CO.

In the last years, Kaliaguine and co-workers fabricated a series of nanoscale perovskites $LaCo_{1-x}Cu_xO_3$, $LaMn_{1-x}Cu_xO_3$, $LaFe_{1-x}(Cu, Pd)_xO_3$, and $La_{0.88}Ag_{0.12}FeO_3$ (surface area = 23−48 m^2/g) via a reactive grinding route, and investigated their catalytic behaviors for the (NO + CO) and (NO + C_3H_6 + O_2) reactions [249–256]. The catalytic mechanism of NO reduction with CO or C_3H_6 is different. The NO reduction with C_3H_6 as a reducer and in the presence of O_2 gives rise to the NO_3^- species over the catalyst surface, which can be reduced by C_3H_6 to form organo nitrogen compounds; in the reduction of NO by CO, however,

nitrosyl species (NO^-) is the main adsorbed species [249]. The partial substitution with Cu ions can increase the anion vacancy density (facilitating the adsorption and dissociation of NO) and the lattice oxygen mobility (favoring the regeneration of the anion vacancies). Such a substitution brings about a significant improvement in catalytic performance of the perovskite for the (NO + CO) reaction [249,250]. In the selective catalytic reduction of NO by C_3H_6, a marked enhancement in N_2 yield can be achieved after Cu incorporation to the perovskite lattice since the doping of copper ions promotes the formation of NO_3^- and subsequent generation of organo nitrogen compounds (the rate-determining step) [250,251,256]. Owning to the outstanding redox property of $LaFe_{0.97}Pd_{0.03}O_3$, 96% NO and 86% CO conversions at 300 ^oC for the (NO + CO) reaction and 67% N_2 yield and 68% C_3H_6 conversion at 350 ^oC for the (NO + C_3H_6 + O_2) reaction can be achieved [249,251]. In addition, this research group also examined the sensitivity to water vapor and poisoning to SO_2 of nanosized $La(Co, Mn, Fe)_{1-x}(Cu, Pd)_xO_3$ materials for the reduction of NO by C_3H_6 [254,255]. A moderate deactivation at 300−500 ^oC and a slighter deactivation at 700 ^oC over these catalysts are observed in the presence of 10% H_2O in the feed gas mixture. Due to the abundant anion vacancies, $LaCoO_3$ shows a lower sensitivity to water vapor compared to $LaFeO_3$ and $LaMnO_3$. Further improvement in resistance to H_2O deactivation of $LaCoO_3$ can be achieved by Cu-doping. The introduction of palladium to the $LaFeO_3$ lattice enhances the ability of resistance to H_2O deactivation. It should be pointed out that the deactivation of the above perovskite catalysts induced by water vapor is reversible and can be well recovered after removal of H_2O from the feed [255]. The effect of SO_2 on NO reduction by C_3H_6 over $LaFe_{0.8}Cu_{0.2}O_3$ is somewhat complicated. At SO_2 concentration ≤ 20 ppm, most of the SO_2 are chemisorbed at anion vacancies of the perovskite, and a minor amount of gaseous SO_2 is oxidized to generate sulfite and sulfate on the perovskite surface. The competitive adsorption between SO_2 and reactant molecules results in a slight modification on the physicochemical property of the perovskite. After removal of SO_2 from the feed, the induced deactivation is reversible. With a rise in SO_2 concentration up to 80 ppm, however, a partial destruction takes place due to the formation of significant amount of sulfate, causing a great decrease in catalytic activity. After being treated first in a 5% H_2/He flow and then in an oxidized atmosphere, the deactivated perovskite catalyst can be partially regenerated [254].

It is worth mentioning that the doping of noble metal ions to a perovskite framework has a promotional effect on catalytic performance. As mentioned above, $LaFe_{0.97}Pd_{0.03}O_3$ shows excellent catalytic activity for NO_x removal [249,251]. The incorporation of Pd to the perovskite lattice can also circumvent the aggregation problem encountered in supported noble metal catalysts. Nishihata et al. reported a $LaFe_{0.57}Co_{0.38}Pd_{0.05}O_3$ catalyst that possesses a self-regeneration character [257]. The authors believed that Pd can move into and out of the perovskite lattice via the process $Pd^{2+} \Leftrightarrow PdO$ when the perovskite is exposed to a fluctuation atmosphere of the emission exhaust. A stable catalytic activity (Figure 36) of $LaFe_{0.57}Co_{0.38}Pd_{0.05}O_3$ confirms the above viewpoint.

4.2. Methane Oxidation

Taking into consideration the serious concerns on environmental pollution and energy shortage, most people think that natural gas (methane content 80–90%) is a relatively clean

and rich energy resource owing to its abundant storage, low price, convenient utilization, high thermal efficiency, and minor pollution. The direct combustion of methane usually takes place at high temperatures (> 1200 ^{o}C), giving rise to a significant amount of NO_x that is harmful to the atmosphere. Catalytic combustion of methane, however, can avoid the formation of NO_x since its oxidation undergoes at low temperatures (< 900 ^{o}C) over a catalyst. Therefore, such a catalytic strategy represents one of the best ways for methane combustion.

Traditional catalysts employed for methane combustion are supported noble metals (Pd, Pt, Rh) [5], which show excellent light-off activity and anti-sulfur poisoning ability but the shortcomings (such as rather high cost and easy sintering at high temperatures) limit their wide applications. Perovskite-type or perovskite-like oxides are cheap and exhibit good catalytic performance for methane combustion. The partial substitution in one or both cationic sites by heterovalent ions can stabilize the B-site ions with unusual oxidation states and generate structural defects (such as cationic or anionic vacancies), thus bringing about a significant enhancement in catalytic performance. The catalytic activities of some perovskite-type oxides and perovskite-like oxides for methane combustion are summarized in Table 2.

Table 2. Surface morphologies, BET surface areas, preparation and reaction parameters, and catalytic performance of some perovskite-type oxide catalysts

Catalyst	Morphology	Surface area/ calcination temperature (m^2/g / ^{o}C)	$CH_4/O_2/BG$[a] molar ratio; space velocity	$T_{10\%}$ (^{o}C)	$T_{50\%}$ (^{o}C)	$T_{90\%}$ (^{o}C)	Ref.
60 wt% $LaCoO_3$/SBA-15	Mesoporous structure	510 / 700	1/4/95; 20000 h^{-1}	406	510	550	39
$LaCoO_3$	Nanoparticle	6.0 / 700	1/4/95; 20000 h^{-1}	521	596	640	39
$La_{0.5}Sr_{0.5}MnO_3$	Nanocube	3.73 /–	1/10/39; 100000 mL g^{-1} h^{-1}	360	492	570	128
$La_{0.5}Sr_{0.5}MnO_3$	Nanoparticle	7.57 / 700	1/10/39; 100000 mL g^{-1} h^{-1}	440	541	620	128
$La_{0.5}Sr_{0.5}MnO_3$	Nanoparticle	9.28 / 700	1/21/78; 60000 mL g^{-1} h^{-1}	365	478	558	267
$La_{0.5}Sr_{0.5}MnO_3$	Nanocube	4.50 / –	1/21/78; 60000 mL g^{-1} h^{-1}	453	522	572	267
$LaCoO_3$-SS[b]	Nanoparticle	0.4 / 1000	0.25/1.0/98.75; 5625 h^{-1}	510	615	–	258
$LaCoO_3$-COPRG[c]	Nanoparticle	18.7 / 500	0.25/1.0/98.75; 5625 h^{-1}	305	370	418	258
$LaMnO_3$	Nanoparticle	11.5 / 700	1/4/95; 60000 h^{-1}	460	565	655	260
$LaSrCuO_4$	Spindle-like	11.9 / 850	1/10/39; 50000 mL g^{-1} h^{-1}	485	618	668	268
$YBa_2Cu_3O_7$	Nanorod	6.1 / 850	1/10/39; 50000 mL g^{-1} h^{-1}	468	640	711	269
$YBa_2Cu_3O_7$	Nanosphere	4.5 / 850	1/10/39; 50000 mL g^{-1} h^{-1}	500	660	722	269

[a] BG represents the balance gas; [b] the catalyst was obtained by the solid-state reaction of the metal oxides; and [c] the catalyst was fabricated via the reactive grinding of amorphous La-Co precursor.

It is generally accepted that preparation strategy has a strong influence on the performance of a catalyst. Royer et al. [258] adopted various methods, such as the solid-state reaction of the metal oxides (SS), coprecipitation of the metal nitrates (COP), citrate complexation (CIT), reactive grinding of the metal oxides (RG) and of amorphous La-Co precursor (COPRG), to fabricate $LaCo_{1-x}Fe_xO_3$ with the particle size of 100 nm–10 μm (Figure 37). The authors observed that, among the five catalysts, the COPRG one shows the highest activity ($T_{50\%}$ (the temperature required for 50% conversion of methane) = 375 °C at 5625 h^{-1}) for methane oxidation, and the specific reaction rate is intimately related to the preparation procedure adopted. By adopting an annealing method with metal oxides as the precursor, Petrović et al. fabricated $LaMO_3$ (M = Mg, Ti, Fe) and $LaMg_{0.5}Ti_yFe_xO_3$ catalysts, and found that the $LaMg_{0.5}Ti_yFe_xO_3$ ($0.13 \le x \le 0.53$, $0.1 \le y \le 0.4$) materials show good catalytic performance, with the $LaMg_{0.5}Ti_{0.2}Fe_{0.4}O_3$ one performing the best ($T_{50\%}$ = 660 °C at 100000 h^{-1}) for methane combustion [259]. Through a citric acid gel process and after calcination at 600 °C, Hammami et al. [260] obtained lanthanum manganite (surface area = 13 m^2/g) that gives a $T_{50\%}$ of 565 °C at 60000 h^{-1} for methane oxidation. Via the malic acid-complexing and dry-wet impregnation pathways, $LaMn_{0.4}Fe_{0.6}O_3$-loaded Pd (diameter = 5–15 nm) catalysts can be prepared. It is observed that the 5 wt% Pd/$LaMn_{0.6}Fe_{0.4}O_3$ catalyst ($T_{100\%}$ (the temperature required for 100% conversion of methane) = 500 °C at 120000 mL/(g h)) outperforms the catalysts with other Pd loadings [261]. Over the $LaMn_{1-x}Mg_xO_3$ (x = 0–0.5) nanocatalysts (size = 25–80 nm) synthesized by means of a citrate-complexing method [262], 50% methane conversion can be achieved at 435 °C and 4320 h^{-1} over $LaMn_{0.8}Mg_{0.2}O_3$ obtained after 800 °C-calcination for the complete oxidation of methane. Such a good catalytic performance is due to the rich oxygen adspecies. Recently, our group have prepared $NdSrCu_{1-x}Co_xO_{4-\delta}$ (containing Cu^{3+}/Cu^{2+} ions and oxygen vacancies) and $Sm_{1.8}Ce_{0.2}Cu_{1-x}Co_xO_{4+\delta}$ (x = 0–0.4) (containing Cu^{2+}/Cu^{+} and excess oxygen) using citric acid complexing method [263]. It is found that there is a morphological evolution from macroporous woven-like to adobe-like architecture in $NdSrCu_{1-x}Co_xO_{4-\delta}$ at elevated Co doping, whereas petal-like or porous morphologies are formed in $Sm_{1.8}Ce_{0.2}Cu_{1-x}Co_xO_{4+\delta}$. Among the two series of catalysts, the $NdSrCuO_{3.70}$ and $Sm_{1.8}Ce_{0.2}Cu_{0.6}Co_{0.4}O_{4.19}$ ones show the best catalytic performance, with the $T_{50\%}$ value being 550 and 560 °C at a space velocity of 10000 h^{-1} for methane combustion (Figure 38), respectively. The high-oxygen nonstoichiometry and strong Cu^{3+}/Cu^{2+} or Cu^{2+}/Cu^{+} redox ability account for the good activity. By adopting the citrate-complexing sol-gel, flame-hydrolysis or flame-spray pyrolysis approach, Forni and co-workers prepared $SrTiO_{3\pm\delta}$ and $Sr_{1-x}M_xTiO_3$ (M = Ag, K, Gd; x = 0, 0.1) [264–266], among which the $Sr_{0.9}K_{0.1}TiO_3$ (particle size = 100–250 nm) catalyst derived from the flame-hydrolysis route and the $Sr_{0.9}Ag_{0.1}TiO_3$ catalyst fabricated by the citrate-complexing sol-gel method (particle size = 30–100 nm and surface area = 24 m^2/g) exhibit the best catalytic performance ($T_{50\%}$ = 560 and 400 °C at 6000 mL/(g h), respectively) for methane oxidation. The good catalytic activity is associated with the formation of suprafacial O_3^- species and O^-/Ti^{4+}, O_2^-/Ti^{4+}, O_3^-/Ti^{4+}, O^-/Sr^{2+}, and O_x^-/Ag^{2+} or O_x^-/Ag ion pairs induced by the doping of potassium or silver ions.

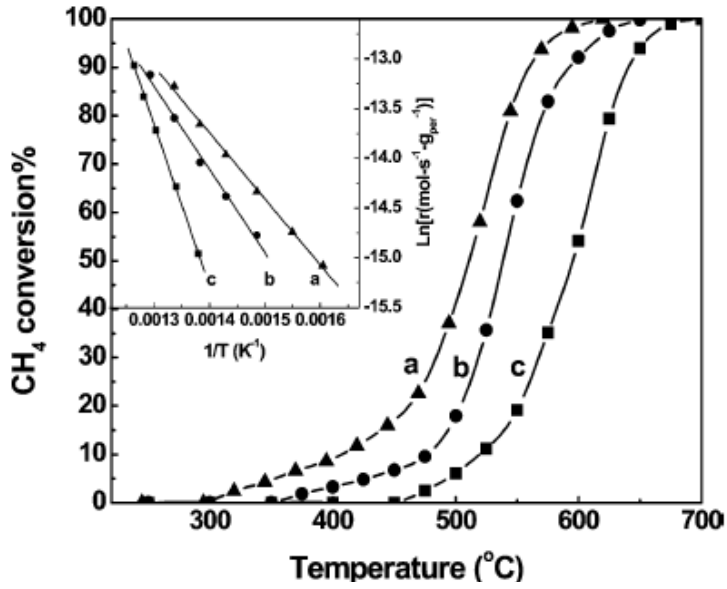

Figure 39. Light-off curves of methane conversion as a function of temperature measured with (a) MLC-60 (microwave-assisted method), (b) CLC-60 (conventional method), and (c) bulk $LaCoO_3$ perovskites. The inset shows the corresponding Arrhenius plot[39].

It is well known that a catalyst with high surface area usually exhibits a good catalytic activity for the total oxidation of an organic compound. Perovskite-type or perovskite-like oxides prepared by means of conventional methods are low in surface area (< 20 m^2/g), which is not favorable for the improvement in catalytic performance. One of good ways to solve this problem is to disperse the low-surface-area and active perovskite-type or perovskite-like oxide on a high-surface-area support. For example, introducing $LaCoO_3$ nanocrystals (5.0–8.5 nm) to the mesopores of high-surface-area SBA-15 via the microwave-assisted route can enhance its catalytic performance for methane combustion, with the $T_{50\%}$ value being 510 ^oC over $LaCoO_3$/SBA-15 and 596 ^oC over $LaCoO_3$ [39] (Figure 39). Using a citric acid-complexing-assisted impregnation method, Nguyen et al. [36] prepared mesoporous silica supported $LaCoO_3$ catalysts, in which the $LaCoO_3$ nanoparticles are highly dispersed in the mesopores of silica. The authors observed that the 38.5 wt% $LaCoO_3$/silica catalyst displays the highest activity ($T_{50\%}$ = 390 ^oC at SV = 4500 h^{-1}) for the oxidation of methane, which is better than that ($T_{50\%}$ = 416 ^oC) over the bulk $LaCoO_3$ catalyst under similar conditions.

It is known that particle surface morphology of a material has a great impact on the catalytic performance. Zhu et al. [128,267] fabricated $La_{0.5}Sr_{0.5}MnO_3$ microcubes (edge length = 1.5 μm) and nanoparticles (diameter = 30–50 nm) using hydrothermal treatment (at 240 ^oC for 24 h) and citrate-complexing methods, respectively. A high conversion of CH_4 can be achieved over microcube-like perovskite ($T_{90\%}$ (the temperature required for 90% conversion of methane) = 572 ^oC) and the nanosized perovskite ($T_{90\%}$ = 558 ^oC) at 12000 h^{-1} (Figure 40). Recently, we adopted a hydrothermal method to generate nano/mircosized single-crystalline perovskite-like oxides $La_{2-x}Sr_xCuO_4$ (x = 0, 1) with spindle-, rod-, and short chain-like morphologies (Figure 41) [268]. It is shown that at a space velocity of 50000 mL/(g h), the rod-like $LaSrCuO_4$ (particle size = 150–300 nm and length = 1–3 μm) exhibits the highest catalytic activity ($T_{100\%}$ = 675 ^oC and the corresponding reaction rate = 40.9

mmol/(g h)). The good catalytic performance of $LaSrCuO_4$ nano/microrods is associated with the higher surface oxygen vacancy concentration, unique single-crystalline structure, and specific surface morphology. Nano/microsized $YBa_2Cu_3O_7$ single crystallites with spherical and rod-like (0.5–1.0 μm in diameter and 5–20 μm in length, respectively) morphologies can be fabricated hydrothermally at 260 °C [269] (Figure 42). The $YBa_2Cu_3O_7$ catalyst (derived hydrothermally with the nanoplatelet Y_2O_3 as yttrium source and $Cu(NO_3)_2$ and $Ba(OH)_2$ as the copper and barium sources, respectively) shows a 90% methane conversion at 711 °C and SV = 50000 mL/(g h). Factors such as more oxygen adspecies, better reducibility, single crystallinity, and unique morphology are responsible for the good catalytic performance of the hydrothermally derived $YBa_2Cu_3O_7$ single crystallite.

4.3. Volatile Organic Compounds Removal

Volatile organic compounds (VOCs), such as aldehydes, ketones, alcohols, esters, carboxylic acids, aromatics, and aliphatic hydrocarbons, emitted from industrial and transportation activities are major pollutants to the atmosphere. Most of them are malodorous, toxic, and contribute to the formation of photochemical smog [270]. A large number of technologies, including adsorption, absorption, condensation, pyrolysis, and catalytic oxidation, have been developed to remove VOCs. Catalytic oxidation is capable of completely destroying VOCs with a wide range of concentrations at relatively low temperatures. Thus, such a strategy is considered as one of the most effective pathways to eliminate VOCs. The removal efficiency is determined by the activity, selectivity, and stability of the catalyst employed. Among the catalysts investigated so far, perovskites are promising materials for the catalytic combustion of VOCs.

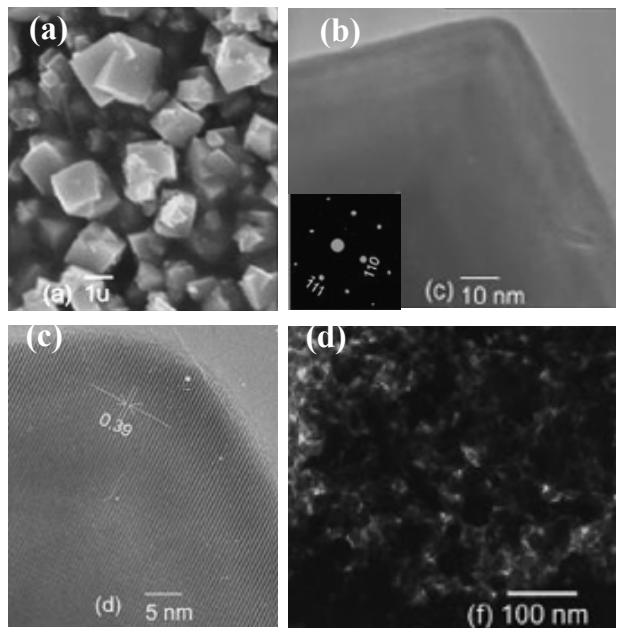

Figure 40 (Continued)

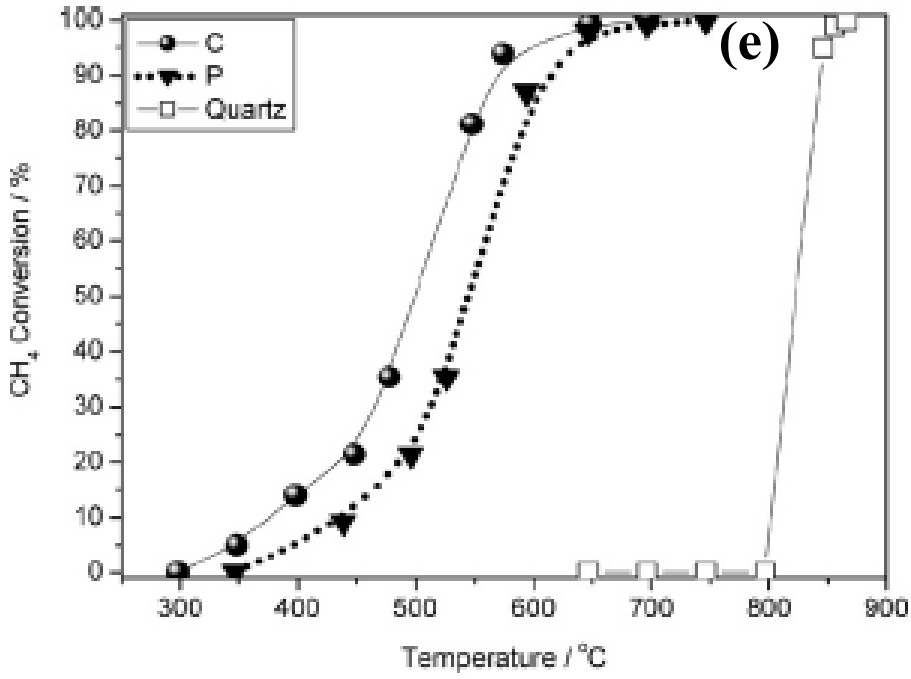

Figure 40. SEM, TEM, and HRTEM images as well as the SAED pattern (inset) of (a–c) single-crystal $La_{0.5}Sr_{0.5}MnO_3$ cubes and (d) $La_{0.5}Sr_{0.5}MnO_3$ nanoparticles. (e) Light-off curves of CH_4 oxidation over the $La_{0.5}Sr_{0.5}MnO_3$ catalysts (C: cube; P: nanoparticle)[128]

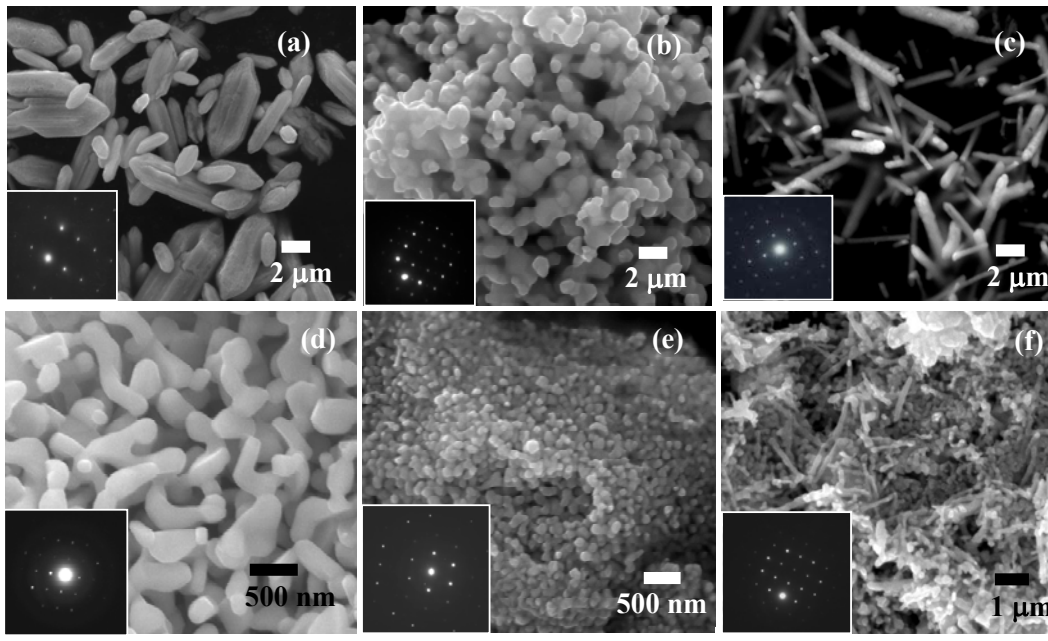

Figure 41. (Continued)

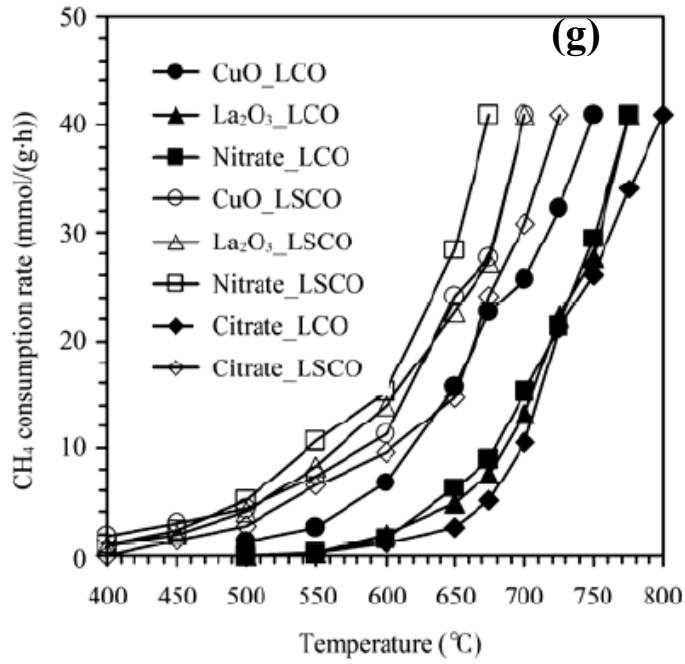

Figure 41. SEM and TEM images as well as SAED patterns (insets) of (a) CuO_LCO, (b) La_2O_3_LCO, (c) Nitrate_LCO, (d) CuO_LSCO, (e) La_2O_3_LSCO, and (f) Nitrate_LSCO. (g) CH_4 consumption rate as a function of reaction temperature over the $La_{2-x}Sr_xCuO_4$ catalysts. LSO: La_2CuO_4; LSCO: $LaSrCuO_4$. The CuO, La_2O_3, and Nitrate in front of the "_" symbol represents the precursor for the perovskite LCO or LSCO preparation, respectively[268].

Most of researchers believe that the B-site cations play an important role in governing the catalytic performance of perovskite-type oxides (ABO_3) for the complete oxidation of organic compounds [2,3]. The effect of the B-site cations on the physicochemical and catalytic properties of lanthanum-based perovskites has been intensively studied, and the perovskite-type oxides with Mn, Co, Fe or Cr as the B-site element are found to be the most active in hydrocarbon combustion [2,12,18,20,271]. The catalytic activity of a perovskite is associated with the chemical composition, lattice defect, redox ability, surface area, and particle morphology, among which the latter four factors are usually influenced by the preparation method. For example, Agarwal and Goswami studied the catalytic oxidation of toluene over $LaMO_3$ (M = Co, Fe, and Cr) prepared by a decomposition method, and observed a catalytic activity order of $LaCoO_3$ > $LaFeO_3$ > $LaCrO_3$ [272]; Levasseur and Kaliaguine prepared a series of $LaBO_3$ (B = Co, Mn, Fe) catalysts by adopting an approach called as "the reactive grinding method", and found that the catalytic performance for methanol oxidation follows the sequence of $LaMnO_3$ > $LaCoO_3$ > $LaFeO_3$ [23]. Working on the catalytic removal of hexane over $LaMO_3$ (M = Co, Mn, Fe) fabricated via calcination of the metal citrate precursors at 800 ^oC for 5 h, however, Spinicci et al. reported a catalytic activity order of $LaFeO_3$ > $LaCoO_3$ > $LaMnO_3$ [273]. Very recently, we have demonstrated that the catalytic performance for toluene oxidation follows the sequence of $LaFeO_3$ > $LaCoO_3$ > $LaMnO_3$ [274]. The above discrepancy could be due to the differences in preparation method and the nature of VOCs.

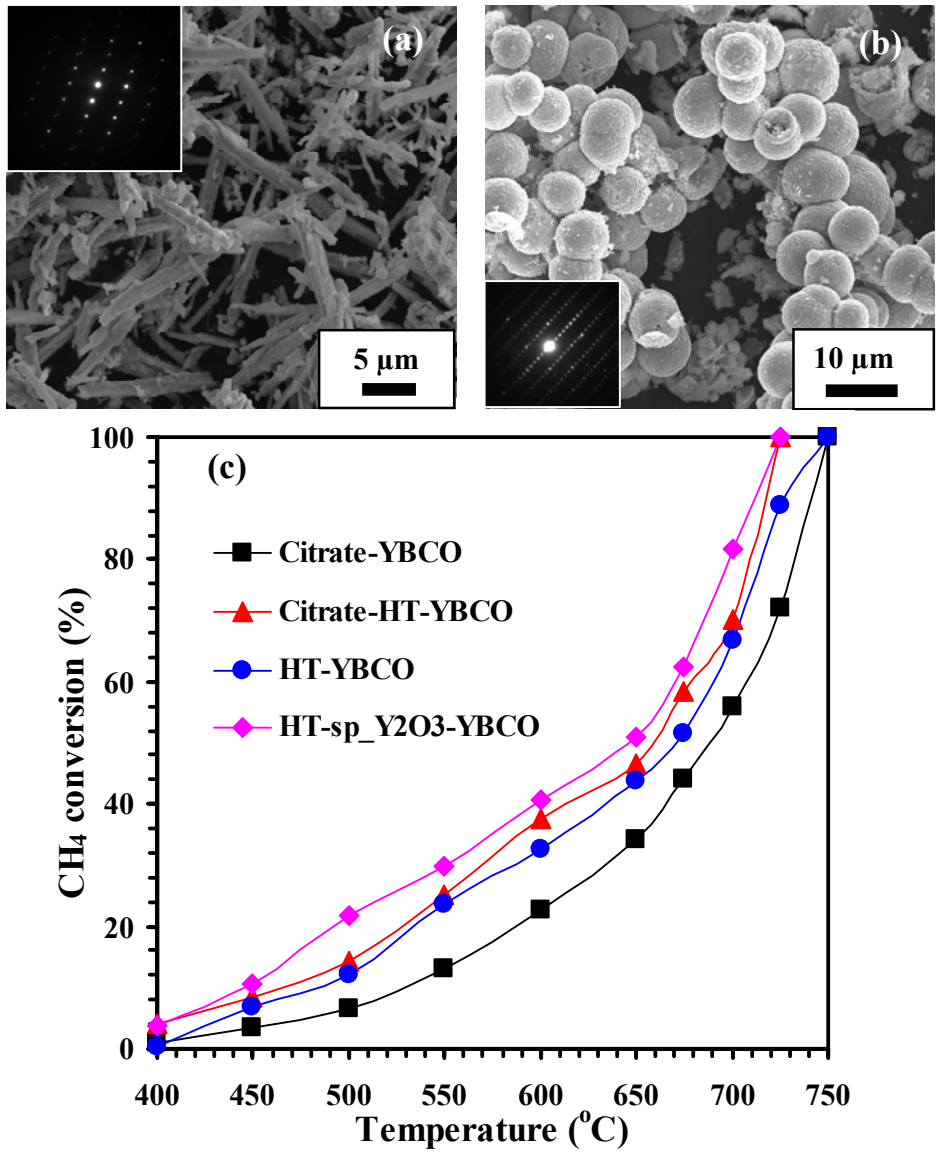

Figure 42. SEM images and SAED patterns (insets) of (a) $YBa_2Cu_3O_7$ fabricated hydrothermally at 260 °C with Y_2O_3 as yttrium source (HT-sp_Y_2O_3-YBCO) and (b) $YBa_2Cu_3O_7$ synthesized by citric-acid-complexing-assisted hydrothermal treatment at 180 °C (Citrate-HT-YBCO). (c) CH_4 conversion versus reaction temperature over the as-fabricated YBCO catalysts. Citrate-YBCO: $YBa_2Cu_3O_7$ fabricated by citric-acid-complexing method; HT-YBCO: $YBa_2Cu_3O_7$ fabricated hydrothermally at 260 °C with metal nitrates as precursor [269].

The partial substitution of the A- and/or B-site cations can modify the catalytic behavior of a perovskite. Up to now, various metal ions, including alkali metal ions (e.g., Na^+, K^+), alkaline earth metal ions (e.g., Ba^{2+}, Sr^{2+}, Ca^{2+}), and noble metal ions (e.g., Ag^+, Pt^{4+}, Pd^{2+}), have been used to substitute the A-site cations [17,20,275]. The impact of such a substitution on catalytic performance may be positive or negative. For example, the partial substitution of Sr^{2+} for La^{3+} can improve the redox process of $M^{n+} \Leftrightarrow M^{(n+1)+}$ (M = Fe, Co, Mn; n = 2, 3), and

then enhance the catalytic activities of $La_{1-x}Sr_xMO_3$ nanoparticles for the combustion of toluene, ethyl acetate, cyclohexane, and propanol [21,30–32]. The incorporation of a noble metal ion to the perovskite lattice not only improves the performance of the catalyst but also stabilizes the highly active component (noble metal) against sintering and volatilization. For instance, Ag-doped $LaMnO_3$ perovskite catalysts show higher activities than the $LaMnO_3$ catalyst in the oxidation of ethanol, n-heptane, and toluene [20]. A dual substitution at the B-site can give rise to the changes in the B-site redox ion couples and crystal structure stability. Such conclusions have been confirmed by the results obtained over $LaFe_{1-x}Ni_xO_3$ [276], $LaMn_{1-x}Co_xO_3$ [277], $LaFe_{1-x}Co_xO_3$ [13,278,279], and $LaNi_{1-x}Co_xO_3$ [280] for the catalytic oxidation of VOCs. Similarly, dual substitutions at both cationic sites can also regulate the catalytic performance of a perovskite material. For example, Rousseau et al. adopted a sol-gel method to prepare $La_{1-x}Sr_xCo_{1-y}Fe_yO_3$ nanomaterials, and observed that a significant improvement is achieved by substituting 30% of La^{3+} by Sr^{2+} in $LaCoO_3$ and a slight increase in catalytic performance for toluene combustion is observed by substituting 20% of cobalt by iron in $La_{0.7}Sr_{0.3}CoO_3$ [14]. Similar results have been obtained by our group. Due to the presence of Fe^{3+}–O–Fe^{4+} couples and a transition of electronic structure, the doping of a small amount of iron to the $La_{0.6}Sr_{0.4}MO_3$ (M = Co, Mn) lattice (i.e., $La_{0.6}Sr_{0.4}M_{0.9}Fe_{0.1}O_3$) can greatly improve its catalytic activity [274]. In the case of $La_{1-x}Ce_xCo_{1-y}Fe_yO_3$, however, the Fe-doped catalysts are inferior to the Fe-free counterparts in performance for VOCs catalytic oxidation. It is likely to be a result due to the deterioration in oxygen mobility and B-site cation reducibility induced by Fe doping [22].

The major drawback of traditional perovskites is low in surface area. As mentioned in Section 2, there are various methods to fabricate high-surface-area perovskites. For example, via a novel strategy of citric acid complexing coupled with a hydrothermal process, high-surface-area (16–33 m^2/g) nanosized $La_{1-x}Sr_xMO_3$ (M = Co, Mn, Fe; x = 0, 0.4) and $La_{0.6}Sr_{0.4}M'_{0.9}Fe_{0.1}O_3$ (M' = Co, Mn) catalysts have been generated by our group [30–32,274]. All of these nanocatalysts show excellent catalytic performance for the complete oxidation of typical VOCs (e.g., toluene and ethyl acetate). Under the reactions of toluene/O_2 (ethyl acetate/O_2) = 1/400–1/100, space velocity (SV) = 5000–80000 h^{-1}, toluene or ethyl acetate can be totally converted to CO_2 and H_2O below 400 ^oC without generation of any by-products over the $La_{1-x}Sr_xMO_3$ (M = Co, Mn, Fe) and $La_{0.6}Sr_{0.4}M'_{0.9}Fe_{0.1}O_3$ (M' = Co, Mn) nanoperovskites. Moreover, these nanoperovskite catalysts perform better than the low-surface-area (7.2–9.8 m^2/g) counterparts synthesized by the conventional citrate-complexing method [31]. Usually, a nanoperovskite highly dispersed on a high-surface-area support is desired for catalytic performance improvement. For example, Alifanti et al. observed improved catalytic performance over $Ce_{1-x}Zr_xO_2$ (23–38 m^2/g) supported $LaCoO_3$ nanomaterials for benzene, toluene or methane removal [33–35]. Makshina et al. demonstrated the specific activity over MCM-41-supported $LaCoO_x$ catalyst superior to that over the bulk $LaCoO_x$ catalyst [37,38]. Recently, we have examined the effects of SBA-15 mesoporous structure and $LaCoO_3$ loading on catalytic performance for the combustion of toluene and ethyl acetate. It is observed that in terms of specific activity, the 35–40 wt% $LaCoO_3$/SBA-15 catalysts fabricated *in-situ* by the hydrothermal method outperform the 35 wt% $LaCoO_3$/SBA-15 catalyst generated by the incipient wetness impregnation method and the bulk $LaCoO_3$ catalyst derived from the sol-gel method. The excellent performance is

attributed to the good dispersion of highly reducible $LaCoO_3$ species in the $LaCoO_3$/SBA-15 catalyst [40].

Most of the $La_{1-x}Sr_xMO_3$ (M = Fe, Co, Mn, Cr, Ni) catalysts reported in the literature are polycrystalline, and it is rare to come across single-crystalline $La_{1-x}Sr_xMO_3$ in catalytic applications. Recently, single-crystalline $La_{1-x}Sr_xMnO_{3+\delta}$ microcubes and $La_{0.6}Sr_{0.4}CoO_3$ nanowires/nanorods fabricated hydrothermally have been reported by Teng et al [128] and our group [116,129−131]. Such single-crystalline $La_{1-x}Sr_xMnO_{3+\delta}$ and $La_{0.6}Sr_{0.4}CoO_3$ materials show excellent catalytic performance for the complete oxidation of methane and VOCs (toluene and ethyl acetate), and their catalytic behaviors are related to the unique crystalline structure and surface morphology. Under similar reaction conditions, the single-crystalline $La_{0.5}Sr_{0.5}MnO_{3+\delta}$ microcubes fabricated by the hydrothermal method exhibit the $T_{50\%}$ and $T_{100\%}$ values of 252 and 280 ^oC, much lower than those (296 and 368 ^oC, respectively) over the polycrystalline counterpart prepared by the citric acid-complexing method [129]. Similarly, the single-crystalline $La_{0.6}Sr_{0.4}CoO_3$ nanorods are also much superior in catalytic activity ($T_{50\%}$ = 235 and $T_{100\%}$ = 245 ^oC) to the polycrystalline $La_{0.6}Sr_{0.4}CoO_3$ catalyst ($T_{50\%}$ = 306 and $T_{100\%}$ = 339 ^oC) for toluene combustion [116]. Obviously, the single-crystalline catalyst outperforms its corresponding polycrystalline one. Furthermore, the hydrothermal temperature and time as well as the base strength also have a remarkable effect on the surface composition, Mn oxidation state distribution, oxygen nonstoichiometry, and surface area of the manganite, and hence modifying the catalytic performance of single-crystalline $La_{0.5}Sr_{0.5}MnO_{3+\delta}$ and $La_{0.6}Sr_{0.4}MnO_{3+\delta}$ [129,131]. A higher hydrothermal temperature, a shorter hydrothermal time, and a proper amount of KOH favor the generation of a $La_{0.6}Sr_{0.4}MnO_{3+\delta}$ material with more amounts of nonstoichiometric oxygen, surface Mn^{4+}, and better low-temperature reducibility. These factors are responsible for the improvement in catalytic activity for the removal of VOCs [131].

4.4. Other Applications

Perovskites with specifically morphologies also exhibit other excellent properties in gas sensoring, adsorption, photocatalysis, CO oxidation, and methanol reforming.

Because of the stability in thermal and chemical atmospheres, a number of perovskite-type oxides, including $LnMO_3$ (Ln = La, Sm, Nd; M = Co, Mn, Cr, Ni, Fe, Ti, V) have been used as gas-sensing materials [2]. Owning to the presence of oxygen vacancies in single-crystalline $BaMnO_3$ nanorods, the conductance peak of the sample in O_2 atmosphere shows an *n*-type semiconductive behavior. The ultrasensitivity towards O_2 of $BaMnO_3$ nanorods can be attributed to the smaller size and higher specific surface area, especially the clean surface on the nanorods synthesized without using capping reagents [152]. The sensors based on the cube-like $CaSnO_3$ show much stronger responsing ability to ethanol, ammonia, and acetone than the sensor based on the irregularly morphological bulk $CaSnO_3$ particles, with the sensitivity of about 1.45, 1.3, and 1.15, respectively [180]. The gas-sensing performance is mainly mediated by the surface properties. On the one hand, there are more active centers for trapping the target gas in microcube-like $CaSnO_3$ (due to their higher surface area) than those in bulk $CaSnO_3$. On the other hand, the cube-like morphology provides a high fraction of well-defined (100) crystal planes that are more sensitive to ethanol. Therefore, $CaSnO_3$

microcubes exhibit sensitivity towards ethanol higher than those towards ammonia and acetone. Due to a smaller size, the sensor based on $BaTiO_3$ nanocubes shows a high sensitivity towards a trace amount of hydrogen peroxide [186].

So far, the adsorption of NO_x on superconducting compounds, such as Y-Ba-Cu-O [281] and Mn-Zr-Y [282], has been reported. A large amount of NO_x can be removed by these active adsorbents. However, in the presence of CO_2, the formation of stable carbonate leads to a deactivation of these adsorptive materials. Interestingly, incorporation of alkali metal ions to the perovskite lattice is capable of inhibiting carbonation. Perovskites like $BaSnO_3$ [283], $La_{0.8}Cs_{0.2}MnO_3$ [284], and $La_{0.8}Cs_{0.2}Mn_{0.8}Ga_{0.2}O_3$ [284] display excellent performance for NO_x adsorption even in the presence of 5% CO_2. The discrepancy in carbonation behavior of bulk alkali metal oxide and alkali metal-doped perovskite can be reasonably explained by the fact that strongly held carbonates are formed on the former, whereas this is not the case on the latter. Actually, nitrate adspecies rather than carbonate adspecies tend to be formed over the alkali metal-doped perovskite material [283]. In addition, owing to its higher surface area and cotton-like powders, the $La_{0.8}Cs_{0.2}Mn_{0.8}Ga_{0.2}O_3$ sample containing nanorods show a higher NO_x adsorption capacity than the nanrod-free $La_{0.8}Cs_{0.2}MnO_3$ sample [284].

Over the $BiFeO_3$ nanosized photocatalyst, more than 90% methyl orange (MO) can be decolorized after 8 h under UV-visible irradiation. Nevertheless, the MO degradation is maintained at about 70% over the bulk $BiFeO_3$ photocatalyst after 16 h of UV-visible illumination. The better degradation efficiency of the nanoperovskite catalyst is attributed to its higher surface area. Moreover, compared to the conventional TiO_2 material, nanosized $BiFeO_3$ shows visible-light photocatalytic activity [11]. It is reported that single-crystalline $KNbO_3$ nanowires perform much better than the $KNbO_3$ nanoparticles and nanocubes in the photocatalytic water splitting reaction, giving a highest H_2 evolution rate of 5.17 mmol/(g_{cat} h) from a CH_3OH aqueous solution. The excellent performance of nanowire-like photocatalyst is associated with its high surface area and good crystallinity [115]. Although $SrTiO_3$ is known to be inactive in photoinduced hydrophilic reactions, the surface of single-crystalline $SrTiO_3$ nanorods can become superhydrophilic by the oxidation of the surface organic contaminants under UV illumination because their initial water contact angles are less than 3^o [161]. Therefore, the superhydrophilicity of the $SrTiO_3$ nanorod arrays originates from the presence of surface nanostructure.

As mentioned in Section 2.1, the sol-gel method with citric acid as the complexing agent is a simple pathway to prepare polycrystalline nanoparticles showing good catalytic activities. Unfortunately, such a nanocatalyst tends to sinter upon calcination at high temperatures and in a long-duration run. Hence, fabricating a catalyst with good thermal stability is still a challenge. Recently, Zhu and co-workers claimed that polycrystalline nanowire-like catalyst shows much better thermal stability than the polycrystalline irregularly morphological nanosized counterpart fabricated by citrate-complexing method [87,88]. A complete conversion of CO over polycrystalline $LaCoO_3$ nanowires and nanoparticles calcined at 600 ^oC for 5 h can be achieved at 190 and 170 ^oC, respectively. Obviously, the nanoparticles outperform the nanowires, a result due to a higher surface area (20.5 m^2/g) of the latter than that (14.6 m^2/g) of the former. Calcination at 750 ^oC for 48 h causes the surface area of $LaCoO_3$ nanowires and nanoparticles to drop to 13.9 and 12.1 m^2/g, respectively, resulting in a catalytic performance ($T_{100\%}$ = 220 ^oC) over the former much better than that ($T_{100\%}$ = 310 ^oC) over the latter [87]. Similar results are also observed over the polycrystalline $LaSrCuO_4$ nanowires and nanoparticles [88]. For the steam reforming of methanol to CO_2 and H_2, the

nanofibrous La_2CuO_4 catalyst shows a much better activity than the bulk one synthesized by citrate-complexing method [84]. At 150 ^oC and steam/methanol molar ratio = 1.3, methanol can be completely converted to H_2 and CO_2 without CO generation. The excellent catalytic performance is associated with the higher surface area, the co-presence of Cu^{2+}/Cu^+, and oxygen vacancies in La_2CuO_4 nanofibers.

5. PERSPECTIVES AND CONCLUDING REMARKS

It is known that perovskite-type oxides and related materials with various morphologies, such as tubular, spherical, wire-, rod-, and cube-like micro/nanoarchitectures, can be fabricated successfully using the hard-templating, hydrothermal, and molten salt synthesis routes. However, no reports are seen in the literature on the synthesis of micro/nanotubular perovskites (except for titanates) by means of the hydrothermal and molten salt approaches. With close-packed PMMA, PS or silica microspheres as hard template in an EG-methanol solution of the metal nitrates, one can generate three-dimensionally ordered macroporous perovskites. Nevertheless, such a method is not suitable for the preparation of mesoporous perovskites. It has been demonstrated that the perovskites and related materials with specific morphologies or porous structures possess unique physicochemical (e.g., magnetic, electrical, optical, adsorption, and gas sensing) properties, and show outstanding catalytic activity for the removal of nitrogen oxides, methane, and VOCs. The unusual performance is associated with the factors, such as particle size, morphology, nonstoichiometric oxygen, exposed crystal plane, crystallinity, surface area, and pore structure.

Since catalytic reaction usually takes place on the surface of a catalyst, a more amount of exposed active crystal planes of the catalyst favors the heterogeneous catalysis process and hence results in an improvement in catalytic performance. The traditional preparation methods usually give rise to catalysts with most of the exposed crystal planes being low in surface energy. Such stable crystal planes do not favor the enhancement in catalytic activity. The 1D perovskites derived from hard-templating methods mentioned above are predominantly polycrystalline. It has been observed that the single-crystalline perovskites exhibit better catalytic activity than the polycrystalline counterparts, although the inherent reasons are not fully clarified. As we know, the quantity of crystal planes (especially active crystal planes) exposed on the surface of a single-crystalline material with specific morphology is fewer than that of the corresponding polycrystalline one with irregular morphology. To optimize the construction of active sites of a single crystallite by maximizing the exposure ratio of more reactive crystal planes and minimizing the exposure ratio of less reactive crystal planes, it is highly needed to develop a fabrication strategy to accurately control the growth of such a single-crystalline material with the desired architecture.

As pointed out in the previous sections, the hydrothermal (or solvothermal) and molten salt routes are promising in specifically morphological perovskite fabrication. Due to the variety of influencing factors (precursor nature, solvent, base strength, temperature and time, molten salt nature, etc.), controlled morphofabrication of perovskites is still a big challenge even by adopting the two synthesis techniques. Although the surfactant-templating method is difficult in generating stoichiometric perovskites, the surfactant employed may play a morphology-oriented role. An appropriate modification on the synthesis parameters might

lead to the successful production of desired perovskites. Therefore, it is possible to fabricate single-crystalline perovskites and related compounds with specific morphologies via a surfactant-directing solvothermal or molten salt process. Further work is needed on the sophisticated control of high percentage of exposed active crystal planes. It could be achieved through the adjusting of crystal morphology. In addition, extensive and intensive researches are also required to clarify the relationship between the morphology, crystal plane exposure ratio or single crystallinity and catalytic performance.

It has been reported that, compared to the bulk transition metal oxides, their mesoporous counterparts exhibit much better catalytic performance due to the mesopore structure and high surface area. Based on this viewpoint, one can envisage that macro- or mesoporous perovskite materials would show higher catalytic activity than the bulk ones. Therefore, it is greatly desirable to establish an effective strategy to fabricate porous perovskites. The polymer or silica microsphere-templating method with a surfactant (e.g., P123 or F127) as soft template is promising in the fabrication of three-dimensionally ordered macroporous perovskites with mesoporous walls. The rise in glassy temperature of the polymer microbeads is beneficial for the generation of macro- or mesoporous perovskites because formation of a perovskite structure needs a high-temperature calcination process. The successful generation of mesoporous $SrTiO_3$ due to the use of the KLE3739 [233] might be useful in fabricating other mesoporous perovskites. Of course, if the mesopores of a hard template could be fully filled by the homogenous precursor solutions, one would be able to obtain mesoporous perovskites and related materials through the nanocasting pathway.

REFERENCES

[1] Bell, A. T. *Science* 2003, *299*, 1688-1691.
[2] Peña, M. A.; Fierro, J. L. G. *Chem. Rev.* 2001, *101*, 1981-2017.
[3] Tejuca, L. J.; Fierro, J. L. G. *Properties and Application of Perovskite Type Oxides*; Marcel Dekker: New York, 1993.
[4] Voorhoeve, R. J. H.; Jr., Johnson, D. W.; Remeika, J. P.; Gallagher, P. K. *Science* 1977, *195*, 827-833.
[5] Zwinkels, M. F. M.; Järås, S. G.; Menon, G. P.; Griffin, T. A. *Catal. Rev. -Sci. Eng.* 1993, *35*, 319-358.
[6] Zhang, R. D.; Kaliaguine, S. In *Heterogeneous Catalysis Research Progress*; Gunther, M. B.; Ed.; Nova Publishers: New York, 2008; pp. 1-79.
[7] O'Brien, S.; Brus. L.; Murray, C. B. *J. Am. Chem. Soc.* 2001, *123*, 12085-12086.
[8] Mao, Y. B.; Wong, S. S. *Adv. Mater.* 2005, *17*, 2194-2199.
[9] Xu, H.; Hu, X. L.; Zhang, L. Z. *Cryst. Growth Des.* 2008, *8*, 2061-2065.
[10] Shabbir, G.; Qureshi, A. H.; Saeed, K. *Mater. Lett.* 2006, *60*, 3706-3709.
[11] Gao, F.; Chen, X. Y.; Yin, K. B.; Dong, S.; Ren, Z. F.; Yuan, F.; Yu, T.; Zou, Z. G.; Liu, J. M. *Adv Mater.* 2007, *19*, 2889-2892.
[12] Spinicci, R.; Faticanti, M.; Marini, P.; Rossi, S. D.; Porta, P. *J. Mol. Catal. A* 2003, *197*, 147-155.
[13] Merino, N. A.; Barbero, B. P.; Ruiz, P.; Cadús, L. E. *J. Catal.* 2006, *240*, 245-257.

[14] Rousseau, S.; Loridant, S.; Delichere, P.; Boreave, A.; Deloume, J. P.; Vernoux P. *Appl. Catal. B* 2009, *88*, 438-447.
[15] Blasin-Aubé, V.; Belkouch, J.; Monceaux, L. *Appl. Catal. B* 2003, *43*, 175-186.
[16] Sinquin, G.; Petit, C.; Hindermann, J. P.; Kiennemann, A. *Catal. Today* 2001, *70*, 183-196.
[17] Bialobok, B.; Trawczyński, J.; Miśta, W.; Zawadzki, M. *Appl. Catal. B* 2007, *72*, 395-403.
[18] Irusta, S.; Pina, M. P.; Menéndez, M.; Santamaría, J. *J. Catal.* 1998, *179*, 400-412.
[19] Wang, X.; Zhuang, J.; Peng, Q.; Li, Y. D. *Nature* 2005, *437*, 121-124.
[20] Musialik-Piotrowska A.; Landmesser, H. *Catal. Today* 2008, *137*, 357-361.
[21] Huang, H. F.; Liu, Y. Q.; Tang, W.; Chen, Y. F. *Catal. Commun.* 2008, *9*, 55-59.
[22] Levasseur, B.; Kaliaguine, S. *Appl. Catal. B* 2009, *88*, 305-314.
[23] Levasseur, B.; Kaliaguine, S. *Appl. Catal. A* 2008, *343*, 29-38.
[24] Giannakas, A. E.; Ladavos, A. K.; Pomonis, P. J. *Appl. Catal. B* 2004, *49*, 147-158.
[25] Giannakas, A. E.; Leontiou, A. A.; Ladavos, A. K.; Pomonis, P. J. *Appl. Catal. A* 2006, *309*, 254-262.
[26] He, H.; Liu, M.; Dai, H. X.; Qiu, W. G.; Zi, X. H. *Catal. Today* 2007, *126*, 290-295.
[27] Lima, R. K. C.; Batista, M. S.; Wallau, M.; Sanches, E. A.; Mascarenhas, Y. P.; Urquieta-González, E. A. *Appl. Catal. B* 2009, *90*, 441-450.
[28] Bruechey, R. L.; Morse, D. E. *Angew. Chem. Int. Ed.* 2006, *45*, 6564-6566.
[29] Niederberger, M.; Pinna, N.; Polleux, J.; Antonietti, M. *Angew. Chem. Int. Ed.* 2004,*43*, 2270-2273.
[30] Niu, J. R.; Liu, W.; Dai, H. X.; He, H.; Zi, X. H.; Li, P. H. *Chin. Sci. Bull.* 2006, *51*, 1673-1681.
[31] Niu, J. R.; Deng, J. G.; Liu, W.; Zhang, L.; Wang, G. Z.; Dai, H. X.; He, H.; Zi, X. H. *Catal. Today* 2007, *126*, 420-429.
[32] Deng, J. G.; Zhang, L.; Dai, H. X.; He, H.; Au, C. T. *Ind. Eng. Chem. Res.* 2008, *47*, 8175-8183.
[33] Alifanti, M.; Florea, M.; Somacescu, S.; Pârvulescu, V. I. *Appl. Catal. B* 2005, *60*, 33-39.
[34] Alifanti, M.; Florea, M.; Pârvulescu, V. I. *Appl. Catal. B* 2007, *70*, 400-405.
[35] Alifanti, M.; Florea, M.; Cortes-Corberan, V.; Endruschat, U.; Delmon, B.; Pârvulescu, V. I. *Catal. Today* 2006, *112*, 169-173.
[36] Nguyen, S. V.; Szabo, V.; Trong On, D.; Kaliaguine, S. *Micropor. Mesopor. Mater.* 2002, *54*, 51-61.
[37] Makshina, E. V.; Nesterenko, N. S.; Siffert, S.; Zhilinskaya, E. A.; Aboukais, A.; Romanovsky, B. V. *Catal. Today* 2008, *131*, 427-430.
[38] Makshina, E. V.; Sirotin, S. V.; van den Berg, M. W. E.; Klementiev, K. V.; Yushchenko, V. V.; Mazo, G. N.; Grünert, W.; Romanovsky, B. V. *Appl. Catal. A* 2006, *312*, 59-66.
[39] Yi, N.; Cao, Y.; Su, Y.; Dai, W. L.; He, H. Y.; Fan, K. N. *J. Catal.* 2005, *230*, 249-253.
[40] Deng, J. G.; Zhang, L.; Dai, H. X.; Au, C. T. *Appl. Catal. A* 2009, *352*, 43-49.
[41] Hurst, S. J.; Payne, E. K.; Qin, L. D.; Mirkin, C. K. *Angew. Chem. Int. Ed.* 2006, *45*, 2672-2692.
[42] Xia, Y. N.; Yang, P. D.; Sun, Y. G.; Wu, Y. Y.; Mayers, B.; Gates, B.; Yin, Y. D.; Kim, F.; Yan, H. Q. *Adv. Mater.* 2003, *15*, 353-389.

[43] Murphy, C. J.; Jana, N. R. *Adv. Mater.* 2002, *14*, 80-82.
[44] Rao, C. N. R.; Deepak, F. L.; Gundiah, G.; Govindaraj, A. *Prog. Solid State Chem.* 2003, *31*, 5-147.
[45] Xia, Y. N.; Rogers, J. A.; Paul, K. E.; Whitesides, G. M. *Chem. Rev.* 1999, *99*, 1823-1848.
[46] Cao, G. Z.; Liu, D. W. *Adv. Colloid Interface Sci.* 2008, *136*, 45-64.
[47] Martin, C. R. *Chem. Mater.* 1996, *8*, 1739-1746.
[48] Martin C. R. *Science* 1994, *266*, 1961-1966.
[49] Zhou, Y. K.; Shen, C. M.; Huang, J.; Li, H. L. *Mater. Sci. Eng. B* 2002, *95*, 77-82.
[50] Keller, N.; Pham-Huu, C.; Estournè, C.; Grenèche, J. M.; Ehret, G.; Ledoux, M. J. *Carbon* 2004, *42*, 1395-1399.
[51] Ji, G. B.; Tang, S. L.; Xu, B. L.; Gu, B. X.; Du, Y. W. *Chem. Phys. Lett.* 2003, *379*, 484-489.
[52] Zhang, G. Y.; Guo, B.; Chen, J. *Sensor. Actuat. B* 2006, *114*, 402-409.
[53] Zhao, L. L.; Steinhart, M.; Yosef, M.; Lee, S. K.; Schlecht, S. *Sensor. Actuat. B* 2005, *109*, 86-90.
[54] Yang, Z.; Huang, Y.; Dong, B.; Li, H. L.; Shi, S. Q. *Appl. Phys. A* 2006, *84*, 117-122.
[55] Yang, Z.; Huang, Y.; Dong, B.; Li, H. L. *Appl. Phys. A* 2005, *81*, 453-457.
[56] Yang, Z.; Huang, Y.; Dong, B.; Li, H. L. *Mater. Res. Bull.* 2006, *41*, 274-281.
[57] Yang, Z.; Huang, Y.; Dong, B.; Li, H. L. *J. Solid State Chem.* 2005, *178*, 1157-1164.
[58] Zhang, X. Y.; Dai, J. Y.; Lai, C. W. *Prog. Solid State Chem.* 2005, *33*, 147-151.
[59] Ma, X. Y.; Zhang, H.; Xu, J.; Niu, J. J.; Yang, Q.; Sha, J.; Yang, D. R. *Chem. Phys. Lett.* 2002, *363*, 579-582.
[60] Zhang, X. Y.; Zhao, X.; Lai, C. W.; Wang, J.; Tang, X. G.; Dai, J. Y. *Appl. Phys. Lett.* 2004, *85*, 4190-4192.
[61] Tagliazucchi, M.; Sanchez, R. D.; Troiani, H. E.; Calvo, E. J. *Solid State Commun.* 2006, *137*, 212-215.
[62] Wei, J.; Xue, D. S.; Xu, Y. *Scripta Mater.* 2008, *58*, 45-48.
[63] Zhang, X. Y.; Lai, C. W.; Zhao, X.; Wang, D. Y.; Dai, J. Y. *Appl. Phys. Lett.* 2005, *87*, 143102(1)-143102(3).
[64] Wang, J.; Manivannan, A.; Wu, N. Q. *Thin Solid Films* 2008, *517*, 582-587.
[65] Hernandez B. A.; Chang, K. S.; Fisher, E. R.; Dorhout, P. K. *Chem. Mater.* 2002, *14*, 480-482.
[66] Liu, L. F.; Ning, T. Y.; Ren, Y.; Sun, Z. H.; Wang, F. F.; Zhou, W. Y.; Xie, S. S.; Song, L.; Luo, S. D.; Liu, D. F.; Shen, J.; Ma, W. J.; Zhou, Y. L. *Mater. Sci. Eng. B* 2008, *149*, 41-46.
[67] Rørvik, P. M.; Tadannaga, K.; Tatsumisago, M.; Grande, T.; Einarsrud, M. A. *J. Eur. Ceram. Soc.* 2009, *29*, 2575-2579.
[68] Hua, Z. H.; Li, D.; Fu, H. *Acta Phys. -Chim. Sin.* 2009, *25*, 145-149.
[69] Hua, Z. H.; Yang, P.; Huang, H. B.; Wan, J. G.; Yu, Z. Z.; Yang, S. G.; Lu, M.; Gu, B. X.; Du, Y. W.; *Mater. Chem. Phys.* 2008, *107*, 541-546.
[70] Singh, S.; Krupanidhi. S. B. *Phys. Lett. A* 2007, *367*, 356-359.
[71] Liu, W.; Sun, X. H.; Han, H. W.; Li, M. Y.; Zhao, X. Z. *Appl. Phys. Lett.* 2006, *89*, 163122(1)-163122(3).
[72] Hu, Z. A.; Wu, H. Y.; Shang, X. L.; Lü, R. J.; Li, H. L. *Mater. Res. Bull.* 2006, *41*, 1045-1051.

[73] Hsu, M. C.; Leu, I. C.; Sun, Y. M.; Hon, M. H. *J. Solid State Chem.* 2006, *179*, 1420-1424.
[74] Wen, T. L.; Zhang, J.; Chou, T. P.; Limmer, S. J.; Cao, G. Z. *J. Sol-Gel Sci. Technol.* 2005, *33*, 193-200.
[75] Limmer, S. J.; Seraji, S.; Forbess, M. J.; Wu, Y.; Chou, T. P.; Nguyen, C.; Cao, G.. Z. *Adv. Mater.* 2001, *13*, 1269-1272.
[76] Kim, J.; Yang, S. A.; Choi, Y. C.; Han, J. K.; Jeong, K. O.; Yun, Y. J.; Kim, D. J.; Yang, S. M.; Yoon, D.; Cheong, H.; Chang, K. S.; Noh, T. W.; Bu, S. D. *Nano Lett.* 2008, *8*, 1813-1818.
[77] Nourmohammadi, A.; Bahrevar, M. A.; Hietschold, M. *Mater. Lett.* 2008, *62*, 3349-3351.
[78] Nourmohammadi, A.; Bahrevar, M. A.; Hietschold, M. *J. Alloy. Compd.* 2009, *473*, 467-472.
[79] Hsu, M. C.; Leu, I. C.; Sun, Y. M.; Hon, M. H. *J. Solid State Chem.* 2006, *179*, 1421-1425.
[80] Ugarte, D.; Châtelain, A.; de Heer, W. A. *Science* 1996, *274*, 1897-1899.
[81] Ajayan, P. M.; Lijima, S. *Nature* 1993, *361*, 333-334.
[82] Dujardin, E.; Ebbessen, T. W.; Hiura, H.; Tanigaki, K. *Science* 1994, *265*, 1850-1852.
[83] Gao, L. Z.; Chua, H. T.; Kawi, S. *J. Solid State Chem.* 2008, *181*, 2804-2807.
[84] Gao, L. Z.; Sun, G. B.; Kawi, S. *J. Solid State Chem.* 2008, *181*, 7-13.
[85] Gao, L. Z.; Wang, X. L.; Chua, H. T.; Kawi, S. *J. Solid State Chem.* 2006,*179*, 2036-2040.
[86] Eder, D.; Kinloch, I. A.; Windle, A. H. *Chem. Commun.* 2006, 1448-1450.
[87] Teng, F.; Liang, S. H.; Gaugeu, B.; Zong, R. L.; Yao, W. Q.; Zhu, Y. F. *Catal. Commun.* 2007, *8*, 1748-1754.
[88] Teng, F.; Gaugeu, B.; Liang, S. H.; Zhu, Y. F. *Appl. Catal. A* 2007, *328*, 156-162.
[89] Dolz, M. I.; Bast, W.; Antonio, D.; Pastoriza, H.; Curiale, J.; Sánchez, R. D.; Leyva, A. G. *J. Appl. Phys.* 2008, *103*, 083909(1)-083909(5).
[90] Leyva, A. G.; Stoliar, P.; Rosenbusch, M.; Lorenzo, V.; Levy, P.; Albonetti, C.; Cavallini, M.; Biscarini, F.; Troiani, H. E.; Curiale, J.; Sanchez, R. D. *J. Solid State Chem.* 2004, *177*, 3949-3953.
[91] Curiale, J.; Sánchez, R. D.; Troiani, H. E.; Pastoriza, H.; Levy, P.; Leyva, A. G. *Physica B* 2004, *354*, 98-103.
[92] Sacanell, J.; Bellino, M. G.; Lamas, D. G.; Leyva, A.G.. *Physica B* 2007, *398*, 341-343.
[93] Limmer, S. J.; Hubler, T. L.; Cao, G. Z. *J. Sol-Gel Sci. Technol.* 2003, *26*, 577-581.
[94] De Jong, K. P.; Geus, J. W. *Catal. Rev. -Sci. Eng.* 2000, *42*, 481-510.
[95] Yang, S.; Chen, X.; Kusunoki, M.; Yamamoto, K.; Iwanaga, H.; Motojima, S. *Carbon* 2005, *43*, 916-922.
[96] Otsuka, K.; Kobayashi, S.; Takenaka, S. *Appl. Catal. A* 2001, *210*, 371-379.
[97] Takenaka, S.; Shigeta, Y.; Tanabe, E.; Otsuka, K. *J. Phys. Chem. B* 2004, *108*, 7656-7664.
[98] Takenaka, S.; Ishida, M.; Serizawa, M.; Tanabe, E.; Otsuka, K. *J. Phys. Chem. B* 2004, *108*, 11464-11472.
[99] Ueda, W.; Sadakane, M.; Ogihara, H. *Catal. Today* 2008, *132*, 2-8.
[100] Ogihara, H.; Sadakane, M.; Nodasaka, Y.; Ueda, W. *Chem. Mater.* 2006, *18*, 4981-4983.

[101] Ogihara, H.; Sadakane, M.; Nodasaka, Y.; Ueda, W. *Chem. Lett.* 2007, *36*, 258-259.
[102] Ogihara, H.; Sadakane, M.; Wu, Q.; Nodasaka, Y.; Ueda, W. *Chem. Commun.* 2007, 4047-4049.
[103] Zhang, S. Y.; Jiang, F. S.; Qu, G.; Lin, C. Y.; *Mater. Lett.* 2008, *62*, 2225-2228.
[104] Kwan, S.; Kim, F.; Akana, J.; Yang, P. D. *Chem. Commun.* 2001, 447-448.
[105] Li, M.; Schnablegger, H.; Mann, S. *Nature* 1999, *402*, 393-395.
[106] Xu, G.; Ren, Z. H.; Du, P. Y.; Weng, W. J.; Shen, G.; Han, G. R. *Adv. Mater.* 2005, *17*, 907-910.
[107] Cheng, H.; Ma, J.; Zhu, B.; Cui, Y. *J. Am. Ceram. Soc.* 1993, *76*, 625-629.
[108] Vayssieres, L. *Int. J. Nanotechnol.* 2004, *1*, 1-41.
[109] Joshi, U. A.; Lee, J. S. *Small* 2005, *1*, 1172-1176.
[110] Joshi, U. A.; Yoon, S.; Baik, S.; Lee, J. S. *J. Phys. Chem. B* 2006, *110*, 12249-12256.
[111] Gu, H. S.; Hu, Y. M.; Wang, H.; Yang, X. R.; Hu, Z. L.; Yuan, Y.; You, J. *J Sol-Gel Sci. Technol.* 2007, *42*, 293-297.
[112] Gu, H. S.; Hu,Y. M.; You, J.; Hu, Z. L.; Yuan, Y.; Zhang, T. J. *J. Appl. Phys.* 2007, *101*, 024319(1)-024319(7).
[113] Magrez, A.; Vasco, E.; Seo, J. W.; Dieker, C.; Setter, N.; Forró, L. *J. Phys. Chem. B* 2006, *110*, 58-61.
[114] Ke, T. Y.; Chen, H. A.; Sheu, H. S.; Yeh, J. W.; Lin, H. N.; Lee, C. Y.; Chiu, H. T. *J. Phys. Chem. C* 2008, *112*, 8827-8831.
[115] Ding, Q. P.; Yuan, Y. P.; Xiong, X.; Li, R. P.; Huang, H. B.; Li, Z. S.; Yu, T.; Zou, Z. G.; Yang, S. G. *J. Phys. Chem. C* 2008, *112*, 18846-18848.
[116] Deng, J. G.; Zhang, L.; Dai, H. X.; He, H.; Au, C. T. *Catal. Lett.* 2008, *123*, 294-300.
[117] Cheng, L.; Shao, Q.; Shao, M. W.; Wei, X. W.; Wu, Z. C. *J. Phys. Chem. C* 2009, *113*, 1764-1768.
[118] Zhu, H. L.; Yang, D. R.; Yu, G. X.; Zhang, H.; Jin, D. L.; Yao, K. H. *J. Phys. Chem. B* 2006, *110*, 7631-7634.
[119] O'Brien, S.; Brus, L.; Murray, C. B. *J. Am. Chem. Soc*. 2001, *123*, 12085-12086.
[120] Urban, J. J.; Yun, W. S.; Gu, Q.; Park, H. *J. Am. Chem. Soc.* 2002, *124*, 1186-1187.
[121] Urban, J. J.; Spanier, J. E.; Ouyang, L.; Yun, W. S.; Park, H. *Adv. Mater.* 2003, *15*, 423-426.
[122] Yun, W. S.; Urban, J. J.; Gu, Q.; Park, H. *Nano Lett.* 2002, *2*, 447-450.
[123] Zhu, D. L.; Zhu, H.; Zhang, Y. H. *J. Cryst. Growth* 2003, *249*, 172-175.
[124] Liu, J. B.; Wang, H.; Zhu, M. K.; Wang, B.; Yan, H. *Mater. Res. Bull.* 2003, *38*, 817-822.
[125] Zhu, D.; Zhu, H.; Zhang, Y. H. *J. Phys.-Condens. Mater.* 2002, *14*, L519-L524.
[126] Zhang, T.; Jin, C. G.; Qian, T.; Lu, X. L.; Bai, J. M.; Li, X. G. *J. Mater. Chem.* 2004, *14*, 2787-2789.
[127] Urban, J. J.; Ouyang, L.; Jo, M. H.; Wang, D. S.; Park, H. *Nano Lett.* 2004, *4*, 1547-1550.
[128] Teng, F.; Han, W.; Liang, S. H.; Gaugeu, B.; Zong, R. L.; Zhu, Y. F. *J. Catal.* 2007, *250*, 1-11.
[129] Deng, J. G.; Zhang, Y.; Dai, H. X.; Zhang, L.; He, H.; Au, C. T. *Catal. Today* 2008, *139*, 82-87.
[130] Deng, J. G.; Zhang, L.; Dai, H. X.; He, H.; Au, C. T. *J. Mol. Catal. A* 2009, *299*, 60-67.
[131] Deng, J. G.; Zhang, L.; Dai, H. X.; Au, C. T. *Catal. Lett.* 2009, *130*, 622-629.

[132] Mao, Y. B.; Banerjee, S.; Wong, S. S. *Chem. Commun.* 2003, 408-409.
[133] Yang, Y.; Wang, X. H.; Sun, C. K.; Li, L. T. *J. Am. Ceram. Soc.* 2008, *91*, 3820-3822.
[134] Li, Y.; Gao, X. P.; Li, G. R.; Pan, G. L.; Yan, T. Y.; Zhu, H. Y. *J. Phys. Chem. C* 2009, *113*, 4386-4394.
[135] Bao, N. Z.; Shen, L. M.; Srinivasan, G.; Yanagisawa, K.; Gupta, A. *J. Phys. Chem. C* 2008, *112*, 8634-8642.
[136] Kang, S. O.; Park, B. H.; Kim, Y. I. *Cryst. Growth Des.* 2008, *8*, 3180-3186.
[137] Pinna, N.; Niederberger, M. *Angew. Chem. Int. Ed.* 2008, *47*, 5292-5304.
[138] Jun, Y. W.; Choi, J. S.; Cheon, J. *Angew. Chem. Int. Ed.* 2006, *45*, 3414-3439.
[139] Wang, H.; Wang, L.; Liu, J. B.; Wang, B.; Yan, H. *Mater. Sci. Eng. B* 2003, *99*, 495-498.
[140] Hou, L.; Hou, Y. D.; Song, X. M.; Zhu, M. K.; Wang, H.; Yan, H. *Mater. Res. Bull.* 2006, *41*, 1330-1336.
[141] Hou, Y. D.; Zhu, M. K.; Hou, L.; Liu, J. B.; Tang, J. L.; Wang, H.; Yan, H. *J. Cryst. Growth* 2005, *273*, 500-503.
[142] Zhu, X. H.; Wang, J. Y.; Zhang, Z. H.; Zhu, J. M.; Zhou, S. H.; Liu, Z. G.; Ming, N. B. *J. Am. Ceram. Soc.* 2008, *91*, 2683-2689.
[143] Hou, Y. D.; Hou, L.; Zhang, T. T.; Zhu, M. K.; Wang, H.; Yan, H. *J. Am. Ceram. Soc. 2007, 90*, 1738-1743.
[144] Hayashi, Y.; Kimura, T.; Yamaguchi, T. *J. Mater. Sci.* 1986, *21*, 757-762.
[145] Mao, Y. B.; Banerjee, S.; Wong, S. S. *J. Am. Chem. Soc.* 2003, *125*, 15718-15719.
[146] Deng, H.; Qiu, Y. C.; Yang, S. H. *J. Mater. Chem. 2009, 19*, 976-982.
[147] Qi, S. Y.; Feng, J.; Xu, X. D.; Wang, J. P.; Hou, X. Y.; Zhang, M. L. *Chem. Res. Chin. Univ.* 2008, *24*, 672-674.
[148] Feng, J.; Qi, S. Y.; Hou, X. Y.; Zhang, M. L. *Solid State Sci.* 2007, *9*, 1033-1035.
[149] Qi, S. Y.; Feng, J.; Xu, X. D.; Wang, J. P.; Hou, X. Y.; Zhang, M. L. *J. Alloy. Compd.* 2009, *478*, 317-320.
[150] Liu, H.; Hu, C. G.; Wang, Z. L. *Nano Lett.* 2006, *6*, 1535-1540.
[151] Hu, C. G.; Liu, H.; Lao, C. S.; Zhang, L. Y.; Davidovic, D.; Wang, Z. L. *J. Phys. Chem. B* 2006, *110*, 14050-14054.
[152] Wang, N.; Hu, C. G.; Xia, C. H.; Feng, B.; Zhang, Z. W.; Xi, Y. *Appl. Phys. Lett.* 2007, *90*, 16311(1)-16311(3).
[153] Jiang, W. Q.; Gong, X. Q.; Chen, Z. Y.; Hu, Y.; Zhang, X. Z.; Gong, X. L. *Ultrason. Sonochem.* 2007, *14*, 208-212.
[154] Lu, X. F.; Zhang, D. L.; Zhao, Q. D.; Wang, C.; Zhang, W. J.; Wei, Y. *Macromol. Rapid Commun.* 2006, *27*, 76-80.
[155] Wang,Y.; Santiago-Avilés, J. J. *Nanotechnology* 2004, *15*, 32-36.
[156] Maensiri, S.; Nuansing, W.; Klinkaewnarong, J.; Laokul, P.; Khemprasit, J. *J. Colloid Interf. Sci.* 2006, *297*, 578-583.
[157] Yuh, J.; Nino, J. C.; Sigmund, W. M. *Mater. Lett.* 2005, *59*, 3645-3647.
[158] Li, C.; Lei, B.; Luo, Z. C.; Han, S.; Liu, Z. Q.; Zhang, D. H.; Zhou, C. W. *Adv. Mater.* 2005, *17*, 1548-1553.
[159] Lei, B.; Li, C.; Zhang, D. H.; Han, S.; Zhou, C. W. *J. Phys. Chem. B* 2005, *109*, 18799-18803.
[160] Han, S.; Li, C.; Liu, Z. Q.; Lei, B.; Zhang, D. H.; Jin, W.; Liu, X. L.; Tang, T.; Zhou, C. W. *Nano Lett.* 2004, *4*, 1241-1246.

[161] Miyauchi, M. *J. Phys. Chem. C* 2007, *111*, 12440-12445.
[162] Nelson, J. A.; Wagner, M. J. *J. Am. Chem. Soc.* 2003, *125*, 332-333.
[163] Pribošič, I.; Makovec, D.; Drofenik, M. *Chem. Mater.* 2005, *17*, 2953-2958.
[164] Peng, X. G.; Manna, L.; Yang, W. D.; Wickham, J.; Scher, E.; Kadavanich, A.; Alivisatos, A. P. *Nature* 2000, *404*, 59-61.
[165] Buhro, W. E.; Colvin, V. L. *Nat. Mater.* 2003, *2,* 138-139.
[166] Chu, X. F.; Jiang, D. L.; Zheng, C. M. *Sensor. Actuat. B* 2007, *123*, 793-797.
[167] Sun, Y. G.; Xia, Y. N. *Science* 2002, *298*, 2176-2179.
[168] Jin, S.; Tiefel, T. H.; McCormack, M.; Fastnacht, R. A.; Ramesh, R.; Chen, L. H. *Science* 1994, *264*, 413-415.
[169] von Helmolt, R.; Wecker, J.; Holzapfel, B.; Schultz, L.; Samwer, K. *Phys. Rev. Lett.* 1993, *71*, 2331-2333.
[170] Chen, Y.; Yuan, H. M.; Tian, G.; Zhang, G. H.; Feng, S. H. *J. Solid State Chem.* 2007, *180*, 167-172.
[171] Spooren, J.; Walton, R. I. *J. Solid State Chem.* 2005, *178*, 1683-1691.
[172] Spooren, J.; Walton, R. I.; Millange, F. *J. Mater. Chem.* 2005, *15*, 1542-1551.
[173] Chai, P.; Liu, X. J.; Wang, Z. L.; Lu, M. F.; Cao, X. Q.; Meng, J. *Cryst. Growth Des.* 2007, *7*, 2568-2575.
[174] Li, J. Q.; Sun, W. A.; Ao, W. Q.; Tang, J. N. *J. Magn.Magn. Mater.* 2006, *302*, 463-466.
[175] Spooren, J.; Rumplecker, A.; Millange, F.; Walton, R. I. *Chem. Mater*. 2003, *15*, 1401-1403.
[176] Wang, X.; Li, Y. D. *Angew. Chem. Int. Ed.* 2002, *41*, 4790-4793.
[177] Zheng, W. J.; Liu, R. H.; Peng, D. K.; Meng, G. Y. *Mater. Lett.* 2000, *43*, 19-22.
[178] Sun, C.; Xing, X. R.; Chen, J.; Deng, J. X.; Li, L.; Yu, R. B.; Qiao, L. J.; Liu, G. R. *Eur. J. Inorg. Chem.* 2007, 1884-1888.
[179] Wiley, B.; Sun, Y. G.; Mayers, B.; Xia, Y. N. *Chem. Eur. J.* 2005, *11*, 454-463.
[180] Cheng, H.; Lu, Z. G. *Solid State Sci.* 2008, *10*, 1042-1048.
[181] Lu, Z. G.; Liu, J. F.; Tang, Y. G.; Li, Y. D. *Inorg. Chem. Commun.* 2004, *7*, 731-733.
[182] Yang, X. F.; Williams, I. D.; Chen, J.; Wang, J.; Xu, H. F.; Konishi, H.; Pan, Y. X.; Liang, C. L.; Wu, M. M. *J. Mater. Chem.* 2008, *18,* 3543-3546.
[183] Zhou, H. J.; Mao, Y. B.; Wong, S. S. *Chem. Mater.* 2007, *19*, 5238-5249.
[184] Chen, J.; Yu, R. B.; Li, L. H.; Sun, C.; Zhang, T.; Chen, H. W.; Xing, X. R. *Eur. J. Inorg. Chem.* 2008, 3655-3660.
[185] Zhou, H. J.; Mao, Y. B.; Wong, S. S. *J. Mater. Chem.* 2007, *17*, 1707-1713.
[186] He, X. S.; Hu, C. G.; Xi, Y.; Wan, B. Y.; Xia, C. H. *Sensor. Actuat. B* 2009, *137*, 62-66.
[187] Pileni, M. P. *Nat. Mater.* 2003, *2*, 145-150.
[188] Lu, Z. G.; Tang, Y. G.; Chen, L. M.; Li, Y. D. *J. Cryst. Growth* 2004, *266*, 539-544.
[189] Wang, Y. W.; Xu, H.; Wang, X. B.; Zhang, X.; Jia, H. M.; Zhang, L. Z.; Qiu, J. R. *J. Phys. Chem. B* 2006, *110*, 13835-13840.
[190] Xu, H. F.; Wei, W.; Zhang, C. L.; Ding, S. J.; Qu, X. Z.; Liu, J. G.; Lu, Y. F.; Yang, Z. Z. *Chem. Asian J.* 2007, *2*, 828-836.
[191] Wang, G. Z.; Sæterli, R.; Rørvik, P. M.; van Helvoort, A. T. J.; Holmestad, R.; Grande, T.; Einarsrud, M, -A. *Chem. Mater.* 2007, *19*, 2213-2221.

[192] Moreira, M. L.; Andrés, J.; Varela, J. A.; Longo, E. *Cryst. Growth Des.* 2009, *9*, 833-839.
[193] Macquart, R. B.; Smith, M. D.; zur Loye, H. C. *Cryst. Growth Des.* 2006, *6*, 1361-1365.
[194] Toshima, T.; Ishikawa, H.; Tanda, S.; Akiyama, T. *Cryst. Growth Des.* 2008, *8*, 2066-2069.
[195] Wang, Y. G.; Xu, G.; Yang, L. L.; Ren, Z. H.; Wei, X.; Weng, W. J.; Du, P. Y.; Shen, G.; Han, G. R. *Mater. Lett.* 2009, *63*, 239-241.
[196] Byrne, D.; Schilling, A.; Scott, J. F.; Gregg, J. M. *Nanotechnology* 2008, *19*, 165608(1)-165608(5).
[197] Xie, X. W.; Li, Y.; Liu, Z. Q.; Haruta, M.; Shen, W. J. *Nature* 2009, *458*, 746-749.
[198] Zhou, K. B.; Wang, X.; Sun, X. M.; Peng, Q.; Li, Y. D. *J. Catal.* 2005, *229*, 206-212.
[199] Zhou, W.; Ran, R.; Shao, Z. P. *J. Power Sources* 2009, *192*, 231-246.
[200] Liu, Q.; Chen, F. L. *Mater. Res. Bull.* 2009, *44*, 2056-2061.
[201] Velev, O. D.; Tessier, P. M.; Lenhoff, A. M.; Kaler, E. W. *Nature* 1999, *401*, 548-548.
[202] Yan, H. W.; Blanford, C. F.; Smyrl, W. H.; Stein, A. *Chem. Commun.* 2000, 1477-1478.
[203] Holland, B. T.; Blanford, C. F.; Stein, A. *Science* 1998, *281*, 538-540.
[204] Yang, P. D.; Deng, T.; Zhao, D. Y.; Feng, P. Y.; Pine, D.; Chmelka, B. F.; Whitesides, G. M.; Stucky, G. D. *Science* 1998, *282*, 2244-2246.
[205] Holland, B. T.; Blanford, C. F.; Do, T.; Stein, A. *Chem. Mater.* 1999, *11*, 795-805.
[206] Sorensen, E. M.; Barry, S. J.; Jung, H. K.; Rondinelli, J. R.; Vaughey, J. T.; Poeppelmeier, K. R. *Chem. Mater.* 2006, *18*, 482-489.
[207] Woo, S. W.; Dokko, K.; Kanamura, K. *Electrochim. Acta* 2007, *53*, 79-82.
[208] Tonti, D.; Torralvo, M. J.; Enciso, E.; Sobrados, I.; Sanz, J. *Chem. Mater.* 2008, *20*, 4783-4790.
[209] Vlasov, Y. A.; Yao, N.; Norris, D. J. *Adv. Mater.* 1999, *11*, 165-169.
[210] Velev, O. D.; Jede, T. A.; Lobo, R. F.; Lenhoff, A. M. *Nature* 1997, *389*, 447-448.
[211] Holland, B. T.; Abrams, L.; Stein, A. *J. Am. Chem. Soc.* 1999, *121*, 4308-4309.
[212] Zakhidov, A. A.; Baughman, R. H.; Iqbal, Z.; Cui, C. X.; Khayrullin, I.; Dantas, S. O.; Merti, J.; Ralchenko, V. G. *Science* 1998, *282*, 897-901.
[213] Woo, S. W.; Dokko, K.; Sasajima, K.; Takei, T.; Kanamura, K. *Chem. Commun.* 2006, 4099-4101.
[214] Johnson, S. A.; Ollivier, P. J.; Mallouk, T. E. *Science* 1999, *283*, 963-965.
[215] Park, S. H.; Xia, Y. N. *Chem. Mater.* 1998, *10*, 1745-1747.
[216] Zhou, L. Y.; Wang, D. P.; Huang, W. H.; Yao, A. H.; Xia, C. H.; Duan, X. *Mater. Res. Bull.* 2009, *44*, 259-262.
[217] Sadakane, M.; Horiuchi, T.; Kato, N.; Takahashi, C.; Ueda, W. *Chem. Mater.* 2007, *19*, 5779-5785.
[218] Sadakane, M.; Asanuma, T.; Kubo, J.; Ueda, W. *Chem. Mater.* 2005, *17*, 3546-3551.
[219] Sadakane, M.; Takahashi, C.; Kato, N.; Ogihara, H.; Nodasaka, Y.; Doi, Y.; Hinatsu, Y.; Ueda, W. *Bull. Chem. Soc. Jpn.* 2007, *80*, 677-685.
[220] Yan, H. W.; Blanford, C. F.; Holland, B. T.; Smyrl, W. H.; Stein, A. *Chem. Mater.* 2000, *12*, 1134-1141.
[221] Sokolov, S.; Bell, D.; Stein, A. *J. Am. Ceram. Soc.* 2003, *86*, 1481-1486.
[222] Zhang, Y. G.; Lei, Z. B.; Li, J. M.; Lu, S. M. *New J. Chem.* 2001, *25*, 1118-1120.

[223] Chen, F. L.; Xia, C. R.; Liu, M. L. *Chem. Lett.* 2001, *30*, 1031-1033.
[224] Kim, Y. N.; Kim, S. J.; Lee, E. K.; Chi, E. O.; Hur, N. H.; Hong, C. S. *J. Mater. Chem.* 2004, *14*, 1774-1777.
[225] Chi, E. O.; Kim, Y. N.; Kim, J. C.; Hur, N. H. *Chem. Mater.* 2003, *15*, 1929-1931.
[226] Dokko, K.; Akutagawa, N.; Isshiki, Y.; Hoshina, K.; Kanamura, K. *Solid State Ionics* 2005, *176*, 2345-2348.
[227] Hara, M.; Nakano, H.; Dokko, K.; Okuda, S.; Kaeriyama, A.; Kanamura, K. *J. Power Sources* 2009, *189*, 485-489.
[228] Kanamura, K.; Akutagawa, N.; Dokko, K. *J. Power Sources* 2005, *146*, 86-89.
[229] Ruiz-Morales, J. C.; Canales-Vázquez, J.; Peña-Martínez, J.; Marrero-López, D.; Irvine, J. T. S.; Núñez, P. *J. Mater. Chem.* 2006, *16*, 540-542.
[230] Li, H. N.; Dai, H. X.; He, H. *J. Sci. Conf. Proc.* 2009, *1*, 186-189.
[231] Li, H. N.; Zhang, L.; Dai, H. X.; He, H. *Inorg. Chem.* 2009, *48*, 4421-4434.
[232] Yang, P. D.; Zhao, D. Y.; Margolese, D. I.; Chmelka, B. F.; Stucky, G. D. *Nature* 1998, *396*, 152-155.
[233] Grosso, D.; Boissière, C.; Smarsly, B.; Brezesinski, T.; Pinna, N.; Albouy, P. A.; Amenitsch, H.; Antonietti, M.; Sanchez, C. *Nat. Mater.* 2004, *3*, 787-792.
[234] Hou, R. Z.; Ferreira, P.; Vilarinho, P. M. *Chem. Mater.* 2009, *21*, 3536-3541.
[235] Hou, R. Z.; Ferreira, P.; Vilarinho, P. M. *Micropor. Mesopor. Mater.* 2008, *110*, 392-396.
[236] Yue, W. B.; Zhou, W. Z. *Prog. Nat. Sci.* 2008, *18*, 1329-1338.
[237] Tüysüz, H.; Lehmann, C. W.; Bongard, H.; Tesche, B.; Schmidt, R.; Schüth, F. *J. Am. Chem. Soc.* 2008, *130*, 11510-11517.
[238] Xia, Y. D.; Mokaya, R. *J. Mater. Chem.* 2005, *15*, 3126-3131.
[239] Cabo, M.; Pellicer, E.; Rossinyol, E.; Castell, O.; Suriñach, S.; Baró, M. D. *Cryst. Growth Des.* 2009, *9,* 4814-4821.
[240] Li, G. S.; Zhang, D. Q.; Yu, J. C. *Chem. Mater.* 2008, *20*, 3983-3992.
[241] Bocher, L.; Rosa, R.; Aguirre, M. H.; Malo, S.; Hébert, S.; Maignan, A.;Weidenkaff, A. *Solid State Sci.* 2008, *10*, 496-501.
[242] Bednorz, J. G.; Müller, K. A. *Rev. Mod. Phys.* 1988, *60*, 585-600.
[243] Hong, J. W.; Fang, D. N. *Appl. Phys. Lett.* 2008, *92*, 012906(1)-012906(3).
[244] Roy, S.; Hegde, M. S.; Madras, G. *Appl. Energy* 2009, *86*, 2283-2297.
[245] Hu, Y. H.; Griffiths, K.; Norton, P. R. *Surf. Sci.* 2009, *603*, 1740-1750.
[246] Zhu, J. J.; Thomas, A. *Appl. Catal. B* 2009, *92*, 225-233.
[247] Russo, N.; Mescia, D.; Fino, D.; Saracco, G.; Specchia, V. *Ind. Eng. Chem. Res.* 2007, *46*, 4226-4231.
[248] Dacquin, J. P.; Lancelot, C.; Dujardin, C.; Costa, P.; Djega-Mariadassou, G.; Beaunier, P.; Kaliaguine, S.; Vaudreuil, S.; Royer, S.; Granger, P. *Appl. Catal. B* 2009, *91*, 596-604.
[249] Zhang, R. D.; Alamdari, H.; Kaliaguine, S. *J. Catal.* 2006, *242*, 241-253.
[250] Zhang, R. D.; Villanueva, A.; Alamdari, H.; Kaliaguine, S. *J. Mol. Catal. A* 2006, *258*, 22-34.
[251] Zhang, R. D.; Villanueva, A.; Alamdari, H.; Kaliaguine, S. *J. Catal.* 2006, *237*, 368-380.
[252] Zhang, R. D.; Villanueva, A.; Alamdari, H.; Kaliaguine, S. *Appl. Catal. B* 2006, *64*, 220-233.

[253] Zhang, R. D.; Alamdari, H.; Kaliaguine, S. *Catal. Lett.* 2007, *119*, 108-119.
[254] Zhang, R. D.; Alamdari, H.; Kaliaguine, S. *Appl. Catal. A* 2008, *340*, 140-151.
[255] Zhang, R. D.; Alamdari, H.; Kaliaguine, S. *Appl. Catal. B* 2007, *72*, 331-341.
[256] Zhang, R. D.; Villanueva, A.; Alamdari, H.; Kaliaguine, S. *Appl. Catal. A* 2006, *307*, 85-97.
[257] Nishihata, Y.; Mizuki, J.; Akao, T.; Tanaka, H.; Uenishi, M.; Kimura, M.; Okamoto, T.; Hamada, N. *Nature* 2002, *418*, 164-167.
[258] Royer, S.; Bérubé, F.; Kaliaguine, S. *Appl. Catal. A* 2005, *282*, 273-284.
[259] Petrović, S.; Terlecki-Baričević, A.; Karanović, L.; Kirilov-Srefanov, P.; Zdujić, M.; Dondur, V.; Paneva, D.; Mitov, I.; Rakić, V. *Appl. Catal. B* 2007, *79*, 186-198.
[260] Hammami, R.; Aïssa, S. B.; Batis, H. *Appl. Catal. A* 2009, *353*, 145-153.
[261] Koponen, M. J.; Venäläinen, T.; Suvanto, M.; Kallinen, K.; Kinnunen, T. J.; Härkönen, M.; Pakkanen, T. A. *J. Mol. Catal. A* 2006, *258*, 246-250.
[262] Saracco, G.; Geobaldo, F.; Baldi, G. *Appl. Catal. B* 1999, *20*, 277-288.
[263] Deng, J. G.; Zhang, L.; Dai, H. X.; He, H.; Au, C. T. *Appl. Catal. B* 2009, *89*, 87-96.
[264] Oliva, C.; Cappelli, S.; Rossetti, I.; Kryukov, A.; Bonoldi, L.; Forni, L. *J. Mol. Catal. A* 2006, *245*, 55-61.
[265] Oliva, C.; Bonoldi, L.; Cappelli, S.; Fabbrini, L.; Rossetti, I.; Forni, L. *J. Mol. Catal. A* 2005, *226*, 33-40.
[266] Fabbrini, L.; Kryukov, A.; Cappelli, S.; Chiarello, G. L.; Rossetti, I.; Oliva, C.; Forni, L. *J. Catal.* 2005, *232*, 247-256.
[267] Liang, S.; Teng, F.; Bulgan, G.; Zhu, Y. *J. Phys. Chem. C* 2007, *111*, 16742-16749.
[268] Zhang, Y.; Zhang, L.; Deng, J. G.; Wei, L.; Dai, H. X.; He, H. *Chin. J. Catal.* (Chinese) 2009, *30*, 347-354.
[269] Zhang, Y.; Zhang, L.; Deng, J. G.; Dai. H. X.; He, H. *Catal. Lett.* 2010, in press.
[270] Armor, J. N. *Appl. Catal. B* 1992, *1*, 221-256.
[271] Wang, W.; Zhang, H. B.; Lin, G. D.; Xiong, Z. T. *Appl. Catal. B* 2000, *24*, 219-232.
[272] Agarwal, D. D.; Goswami, H. S. *React. Kinet. Catal. Lett.* 1994, *53*, 441-449.
[273] Spinicci, R.; Tofanari, A.; Faticanti, M.; Pettiti, I.; Porta, P. *J. Mol. Catal. A* 2001, *176*, 247-252.
[274] Deng, J. G.; Dai, H. X.; Jiang, H. Y.; Zhang, L.; Wang, G. Z.; He, H.; Au, C. T. *Environ. Sci. Technol.* 2009, under review.
[275] Lee, Y. N.; Lago, R. M.; Fierro, J. L. G.; Cortés, V.; Sapiña, F.; Martínez, E. *Appl. Catal. A* 2001, *207*, 17-24.
[276] Pecchi, G.; Reyes, P.; Zamora, R.; Cadús, L. E.; Fierro, J. L. G. *J. Solid State Chem.* 2008, *181*, 905-912.
[277] Pecchi, G.; Campos, C. *React. Kinet. Catal. Lett.* 2007, *91*, 353-359.
[278] Szabo, V.; Bassir, M.; Neste, A. V.; Kaliaguine, S. *Appl. Catal. B* 2002, *37*, 175-180.
[279] Szabo, V.; Bassir, M.; Gallot, J. E.; Neste, A. V.; Kaliaguine, S. *Appl. Catal. B* 2003, 42, 265-277.
[280] Pereñíguez, R.; Hueso, J. L.; Holgado, J. P.; Gaillard, F.; Caballero, A. *Catal. Lett.* 2009, *131*, 164-169.
[281] Mizuno, N.; Yamato, M.; Misono, M. *J. Chem. Soc., Chem. Commun.* 1988, 887-888.
[282] Matsukuma, I.; Kikuyama, S.; Kikuchi, R.; Sasaki, K.; Eguchi, K. *Appl. Catal. B* 2002, *37*, 107-115.

[283] Hodjati, S.; Vaezzadeh, K.; Petit, C.; Pitchon, V.; Kiennemann, A. *Catal. Today*, 2000, *59*, 323-334.
[284] Zahir, M, H.; Suzuki, T.; Fujishiro, Y.; Awano, M. *Appl. Catal. A* 2009, *361*, 86-92.

In: Perovskites: Structure, Properties and Uses
Editors: Maxim Borowski, pp. 67-178
ISBN: 978-1-61668-525-6

Chapter 2

PEROVSKITES AND THEIR NANOCOMPOSITES WITH FLUORITE-LIKE OXIDES AS MATERIALS FOR SOLID OXIDE FUEL CELLS CATHODES AND OXYGEN-CONDUCTING MEMBRANES: MOBILITY AND REACTIVITY OF THE SURFACE/BULK OXYGEN AS A KEY FACTOR OF THEIR PERFORMANCE

V.A. Sadykov [1,2], S. N. Pavlova[1], T. S. Kharlamova[1], V. S. Muzykantov[1], N.F. Uvarov [2,3], Yu. S. Okhlupin[3], A. V. Ishchenko[1], A. S. Bobin[1], N. V. Mezentseva[1], G.M. Alikina[1], A.I. Lukashevich[1], T.A. Krieger[1], T. V. Larina[1], N. N.Bulgakov[1], V. M. Tapilin[1], V.D. Belyaev[1], E.M. Sadovskaya[1], A. I. Boronin[1], V. A. Sobyanin[2], O. F. Bobrenok[4], A. L. Smirnova[5], O. L. Smorygo[6] and J. A. Kilner[7]

[1] Boreskov Institute of Catalysis SB RAS, Novosibirsk, Russia
[2]Novosibirsk State University, Novosibirsk, Russsia
[3]Institute of Solid State Chemistry and Mechanochemistry SB RAS, Novosibirsk, Russia
[4] Institute of Thermophysics SB RAS, Novosibirsk, Russia
[5]Eastern Connecticut State University, Willimantic, CT, USA
[6]Institute of Powder Metallurgy, Minsk, Belarus
[7]Department of Materials, Imperial College, London, United Kingdom

ABSTRACT

This paper presents results of research aimed at elucidating factors controlling mobility and reactivity of the surface and bulk oxygen of complex perovskite-like

$A_nB_mO_z$ oxides (manganites, ferrites, cobaltites, nickelates of La/Sr) and their nanocomposites with fluorite-like oxides (doped ceria or zirconia) as related to their performance in the intermediate temperature solid oxide fuel cells (IT SOFC) cathodes and oxygen separation membranes. Real/defect structure and surface properties of these materials as a function of both composition, preparation route and sintering temperature were studied by combination of TEM with EDX, XRD, EXAFS, UV-Vis and XPS methods. Lattice oxygen mobility, strength of oxygen species bonding with the surface sites and their reactivity for both dispersed and dense materials were estimated by oxygen isotope exchange, temperature-programmed desorption and reduction by H_2 and CH_4. Coefficients of oxygen diffusion in dense materials were estimated by analysis of dynamics of the oxygen loss monitored by measurements of the weight loss or conductivity relaxations. For analysis of atomic-scale factors controlling oxygen bonding strength and mobility, quantum-chemical approaches including the Density Functional Theory (DFT) in spin-polarized SLDA approximation and semiempirical Interacting Bonds Method were applied.

For simple perovskites, along with well-known effects of anion vacancies/interstitial oxygen atoms and high- charge transition metal cations generated due to the oxygen non-toichiometry, pronounced effects of the surface faces termination, ordering of oxygen vacancies and appearance of extended defects were found to affect the oxygen mobility and reactivity as well. From the microscopic point of view, decreasing the Me-O bonding strength and increasing the distance between A and B cations due to the lattice parameter increase helps to decrease the activation barriers for the oxygen diffusion in the perovskite-like lattice.

For perovskite-fluorite nanocomposites, interfaces were shown to be paths for fast oxygen diffusion due to redistribution of cations between contacting phases.

The most promising combinations of perovskites and perovskite-fluorite nano-composites possessing a high lattice oxygen mobility and conductivity were used for synthesis of functionally graded cathodes of IT SOFC with thin layers of doped zirconia electrolytes as well as for manufacturing asymmetric Ni-Al compressed foam supported membranes for oxygen separation and syngas generation. High and stable performance of these materials promising for the practical application was demonstrated.

1. INTRODUCTION

Perovskites comprise a large class of complex oxides. Perovskite structure has ideal formula ABO_3 and consists of large-sized 12-coordinated cations at the A-site and small-sized 6-coordinated cations at the B-site. Perovskite compounds with different combinations of cations in the A and B sites, e.g., 1-5, 2-4 or 3-3 and their more complex combination are known. A remarkable feature of perovskites is a possibility of cationic substitutions in both A and B-sites over a wide concentration ranges. Cationic substitution by lower charge cations results in generation of oxygen vacancies in the oxygen sublattice that favors ionic conductivity. Usually ABO_3 compounds crystallize in polymorphic structures, which show small distortion from the most symmetrical form of the perovskite structure. There are many perovskite-related structures, like brownmillerite, K_2NiF_4-type structure, Ruddlesden–Popper phases $A_{n+1}B_nO_{3n+1}$, etc., which can be obtained as a result of the ordering of cations, defects, inclusion of other crystallographic units into the ideal perovskite lattice, etc. [1, 2]. Because

of the variety of structures and chemical compositions, perovskite oxides exhibit a large diversity of properties, such as ferroelectricity, piezoelectricity, magnetic, catalytic properties and even superconductivity. In addition to these well-known properties, several perovskite oxides exhibit high ionic, electronic and mixed ionic-electronic conductivity required for such applications as solid oxide fuel cells (SOFC) and permselective membranes [3, 4]. Perovskite oxides containing transition metal cations exhibit high catalytic activity in various reactions, in particular, oxidation reactions [5, 6].

The most efficient electrodes for SOFC are usually composites comprised of perovskites and oxygen-conducting electrolytes (doped ceria, zirconia etc) as only composite materials can meet the most of requirements for proper functioning of the electrode. For SOFC cathodes, main requirements are [3]

- morphological and thermodynamic stability at relevant temperatures and oxygen pressures;
- thermal expansion coefficient (TEC) should be close to that of other stack materials;
- good adhesion and stable electrical (ionic) contact to the electrolyte;
- chemical compatibility with other cell and stack components;
- high catalytic activity in the reaction of the dissociative adsorption of oxygen;
- low (less than 0.1 Ohm/cm^2) polarization resistance;
- high electronic (usually, p-type) conductivity, $\sigma > 100$ S/cm;
- low cost of materials and the fabrication process.

For Intermediate Temperature (IT) operation, materials should also possess a high ionic conductivity, i.e. to be mixed ionic-electronic conductors.

Most of these requirements are also applied to materials used for manufacturing of oxygen permeable membranes. However, in conditions of a very high oxygen chemical potential gradient such as in the case of syngas generation reactors, where membrane operates under contact with methane from one side and air from the other side, functionally graded multilayer (at least, bi-layer) design is required to prevent complete destruction of complex perovskites in reducing conditions [7]. Note, though, that a similar concept of functionally graded cathode materials with spatially varying composition and porosity of layers successively deposited on a thin layer of electrolyte was shown to be the most promising in design of anode-supported SOFC operating at decreased temperatures [8]. Tailor-made design of these functionally graded composite materials and their performance modeling should be based upon fundamental studies of the oxygen mobility and reactivity of both dense ceramics and a porous/dispersed samples of both perovskites and their composites with electrolytes [9]. However, traditional techniques for estimation of oxygen diffusion and surface reactivity parameters such as Secondary Ions Mass-Spectrometry (SIMS) oxygen isotope depth profiling, conductivity or weight relaxation analysis can be applied only to dense ceramics, and their sensitivity to the real atomic-scale structure of the surface (defects, impurities etc) is a matter of debate [3, 9]. For powders, mass-spectrometric (MS) analysis of the gas phase composition during isotope exchange allows the estimation of parameters characterizing both the surface reaction and oxygen diffusion in the bulk, though this method is not yet commonplace for the latter application [4-8]. Combination of this technique with temperature-programmed oxygen desorption (TPD O_2) and temperature –programmed

reduction by H_2 or CH_4 (TPR) [6] allows to characterize transport properties and reactivity of mixed ionic-electronic conducting materials under variable gradient of oxygen chemical potential which is important for the proper modeling of their performance in a broad range of operation parameters. Certainly, for design of mixed ionic-electronic conducting materials with graded porosity, these studies are to be carried out for composite materials progressively sintered from dispersed state to a dense ceramics, so that in the boundary region characterization techniques for powdered and dense materials can be applied simultaneously. Moreover, such a study will also allow to elucidate the role of interfaces suggested to be important for transport properties of mixed ionic-electronic conducting oxides [10] or composites [11]. To provide a noticeably impact on transport properties of a dense material, interfaces should be sufficiently extended, so the sizes of respective domains should remain in the nanorange. Certainly, this requires development of special procedures for synthesis of MIEC nanocomposites as well as application of modern sophisticated techniques for characterization of the structure and composition of these nanodomains and their boundaries.

This work reviews results of such research aimed at elucidating factors controlling mobility and reactivity of the surface and bulk oxygen of complex perovskite-like $A_nB_mO_z$ oxides (manganites, ferrites, cobaltites, nickelates of La/Sr) and their nanocomposites with fluorite-like oxides (doped ceria or zirconia) prepared using new experimental approaches. The first part considers characteristics of complex perovskites prepared via polymerized polyester precursors (Pechini) route with a due attention paid to known concepts and published data on the specificity of their real/defect structure as related to transport properties and reactivity. In the second part properties of nanocomposites comprised of selected perovskites with doped ceria or zirconia and prepared via powerful ultrasonic treatment of suspensions in organic solvents with additions of surfactants will be discussed. The last part presents results of application of these materials for design of functionally graded cathodes of IT SOFC and oxygen-conducting membranes for syngas generation and their pilot-scale testing.

2. PEROVSKITES

2.1. Theory and Experimental Procedures

Defect formation mechanisms and concentrations. In the perovskite structure ABO_3 there are three sublattices: two cationic and one anionic. Therefore, the total defect equilibrium conditions include contribution of all possible defects (vacancies and substituting ions) in each sublattice. For simplicity let us consider the defect formation in typical perovskite solid solutions of the $La_{1-x}Sr_xBO_{3-\delta}$ composition widely used in SOFC. As the perovskite lattice is formed by cubic close packing of mixed AO_3 layers, intrinsic defects are Schottky ones which together with electron-hole pairs are formed in both pure and doped perovskites. Quasichemical reactions of formation of intrinsic defects may be written as follows [12, 13]:

$$0 \rightarrow V''''_{La} + V''''_{B} + 3V^{\bullet\bullet}_{O} \qquad (1)$$

$$0 \rightarrow n' + p^{\bullet} \tag{2}$$

The cationic vacancies are much less mobile than oxygen vacancies. The oxygen vacancies together with electrons and holes determine transport properties of perovskites. For practical purposes it would be desirable to obtain a solid solution with high concentrations of both electronic defects and oxygen vacancies. The first option is to increase the concentration of Sr-cations in A-sublattice through dissolution of SrO in the perovskite lattice:

$$2SrO \rightarrow 2Sr'_{La} + 2O_O^{\times} + V_O^{\bullet\bullet} \tag{3}$$

The second approach is the doping of B-sublattice with low-charged cations, for example, substitution of Ga^{3+} cations in $LaGaO_3$:

$$2MgO \rightarrow 2Mg'_{La} + 2O_O^{\times} + V_O^{\bullet\bullet} \tag{4}$$

Reactions (3) and (4) proceed in solid electrolytes, for instance, in solid solutions based on lanthanum gallate of the general formula: $La_{1-x}A_xGa_{1-y}B_yO_{3-(x+y)/2}$ (A = Ca, Sr, Ba; B = Mg, Zn). These systems have high ionic conductivity caused by high concentration of oxygen vacancies [14, 15] and they are wide gap semiconductors, hence, concentrations of intrinsic electronic defects in these compounds are very low.

Other situation takes place in the perovskites with transition metals in B-sites. In frames of crystal-field theory, the electronic structure of these materials is described in terms of partially delocalized band states formed by t_{2g} and e_g levels [16]. For $x > 0.1$ the Fermi level falls within the half-filled band, therefore, the compound exhibits metallic or semimetallic conductivity at high temperature. The generation of electron-hole pairs proceeds via electron excitation from the effectively neutral B^{3+} cation with formation of two different electronic defects, corresponding to B^{2+} and B^{4+} cations. Hence Eqn. (2) can be rewritten as:

$$2B_B^{\times} \rightarrow B'_B + B_B^{\bullet} \tag{5}$$

Besides the process (5) the direct oxidation of B-cations also can take place following possible reaction [17]:

$$\frac{3}{2}O_2 + 6B_B^{\times} \rightarrow V_A''' + V_B''' + 3O_O^{\times} + 6B_B^{\bullet} \tag{6}$$

From (1) and (6) it follows that when this reaction prevails, concentration of oxygen vacancies strongly decreases.

Oxidation process may be realized by another mechanism:

$$SrO + \frac{1}{2}O_2 + 2B_B^{\times} \rightarrow 2Sr'_{La} + 3O_O^{\times} + 2B_B^{\bullet} \tag{7}$$

Finally, in $La_{1-x}Sr_xBO_{3-d}$ perovskites five basic processes expressed by reactions (1, 3, 5, 6 and 7), together with electrical neutrality condition

$$3[V_A'''] + 3[V_B'''] + [Sr_{La}'] + [B_B'] = 2[V_O^{\bullet\bullet}] + [B_B^{\bullet}] \quad (8)$$

define equilibrium concentrations of all ionic and electronic defects. Concentrations of electrons $[n']$ and holes $[p^{\bullet}]$ will be equal to $[B_B']$ and $[B_B^{\bullet}]$, respectively. Substituting corresponding concentrations into the expressions for equilibrium constants and solving a system of non-linear equations, one can find numerous values of all concentrations as a function of the oxygen activity or partial pressure P_{O2}. The analysis shows that general dependence of concentration on p_{O2} can be divided into several domains, where some particular neutrality conditions are fulfilled [18]:

I. Very high oxygen pressure or strongly oxidizing conditions. The process (6) dominates corresponding to electroneutrality condition: $3[V_A'''] + 3[V_B'''] = [p^{\bullet}]$. As a result, perovskite contains cation vacancies and, consequently, the excess of oxygen ions so that $\delta > 0$;

II. High oxygen pressure, oxidizing conditions when reaction (7) prevails. In this case $[Sr_{La}'] = [p^{\bullet}]$, strontium behaves like acceptor impurity in semiconductors and $\delta = 0$;

III. Intermediate oxygen pressures or weakly oxidizing conditions. Here two competitive reactions (7) and (3) proceed simultaneously so that resulting neutrality condition $[Sr_{La}'] = 2[V_O^{\bullet\bullet}] + [p^{\bullet}]$ should be held. The material becomes non-stoichiometric, contains oxygen vacancies and the parameter δ varies within the range $-x/2 < \delta < 0$;

IV. Pressure range where 'neutral' (neither oxidizing nor reducing) conditions are fulfilled, where the charge of dopant cations is compensated by oxygen vacancies as in the case of purely ionic conductors: $[Sr_{La}'] = 2[V_O^{\bullet\bullet}]$, the parameter δ is fixed at $\delta = -x/2$;

V. Low oxygen pressure, reducing conditions, the electrical neutrality is provided by oxygen vacancies and electrons $[n'] = 2[V_O^{\bullet\bullet}]$, the parameter $\delta < -x/2$ is negative and its absolute value increases with the decrease of p_{O2}. Finally, at very low p_{O2} the perovskite may irreversibly decompose due to the reduction process with formation of other phases. This decomposition pressure depends on the material type and temperature.

The five regions I-V are shown in Fig. 1 for A-doped $RE_{1-x}A_xBO_3$ perovskite with the rare earth ion (RE) in the A site. The comparison of model diagrams with experimental data for acceptor doped $La_{1-x}Sr_xBO_{3-\delta}$ perovskites with B = Mn, Fe, and Co shows [19, 20] that at high oxygen pressures the manganite is hyperstoichiometric ($\delta > 0$, region I). As p_{O2} decreases, the parameter δ falls to zero and does not change within the pressure range of 10^{-4}-10^{-10} atm (region II). This behavior implies that the oxygen vacancy concentration will be very low, and this remains true even for quite heavily acceptor doped material, while

concentration of cation vacancies is high. No appreciable concentration of oxygen vacancies is formed until oxygen partial pressures approaching 10^{-10} atm (region III). Thus, under normal SOFC cathode operating conditions, the manganite materials are expected to have low vacancy concentrations and, consequently, low oxygen diffusion coefficients. However, rather low (~ 120 kJ/mol O_2) values of the partial enthalpy of oxygen removal from the lattice of undoped or Sr-doped lanthanum manganite not depending upon the oxygen excess as estimated by Kuo et al from the results of detailed gravimetric studies [20] suggest that under large gradient of oxygen concentration (i.e. big cathodic polarization) oxygen flux in the lanthanum manganite lattice can be rather high.

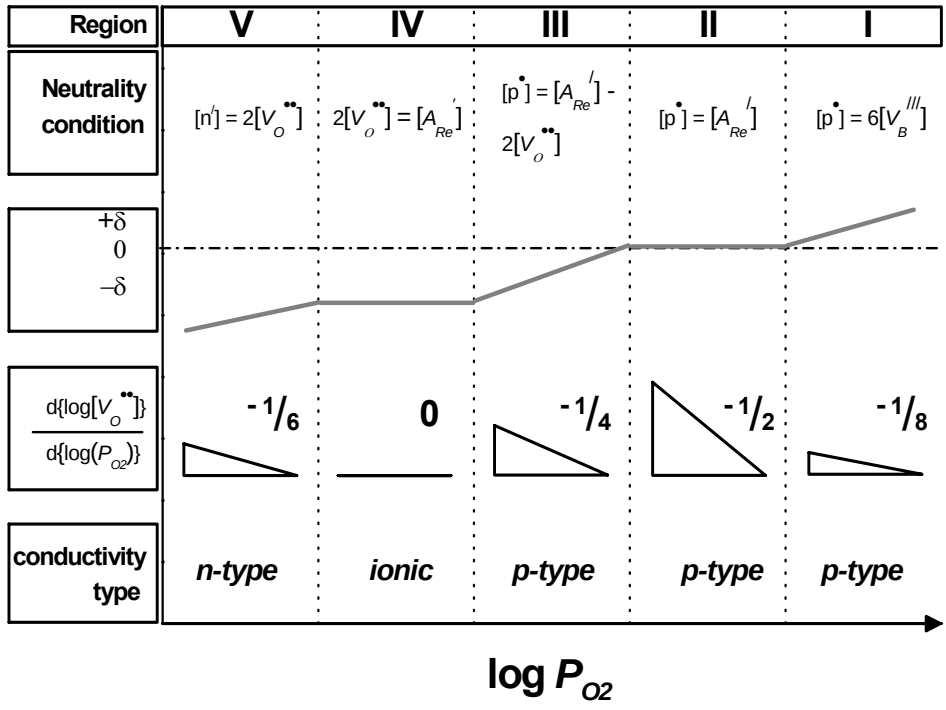

Figure 1. Schematic representation of dependences of the non-stoichiometry parameter δ, the concentration of oxygen vacancies and total conductivity on the oxygen partial pressure p_{O2} in an acceptor-doped $RE_{1-x}A_xBO_{3-\delta}$ oxide.

In contrast to the manganites, cobaltites and ferrites at normal pressure are in the mixed compensation region III, where the value of δ lies between 0 and −x/2. Thus, high oxygen vacancy concentrations and, consequently, oxygen diffusivities are expected under normal cathode conditions. For the ferrite, a plateau in the oxygen stoichiometry is observed at low P_{O2} (Fig. 2) that corresponds to the range IV, indicating that the acceptor is vacancy compensated and the material would exhibit ionic conductivity [9]. From this analysis, it is obvious that there are significant changes in the defect populations in these acceptor-doped materials. The properties of perovskites depend on the temperature, oxygen partial pressure, and first of all, on the type of the transition metal in the B-cation site.

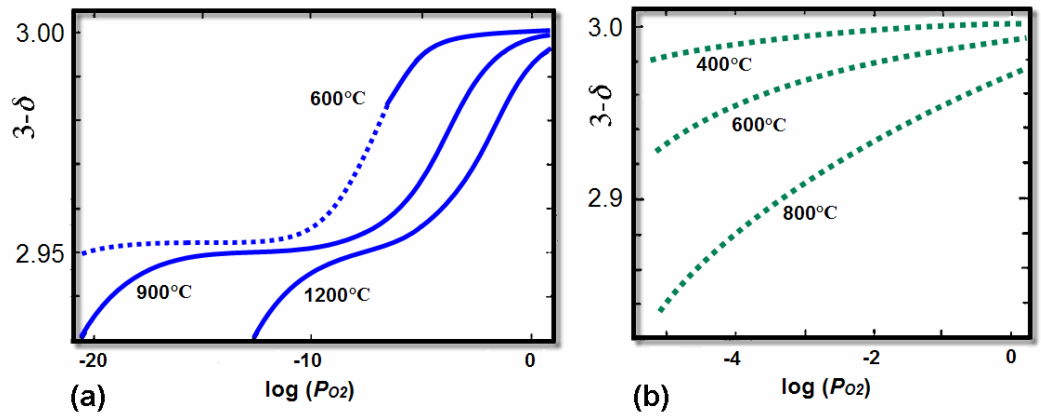

Figure 2. Oxygen stoichiometry in (a) LSF (x = 0.1) and (b) LSC (x = 0.3) as a function of O_2 and temperature.

Electrical properties. As it was mentioned above, to provide a low electrode resistance of SOFC, the electrode materials should have sufficiently high electronic conductivity, $\sigma > \sim$ 100 S/cm. To provide such a high conductivity the concentration of mobile carriers (holes, electrons) should be sufficiently high. Electronic structure of undoped perovskites $LaBO_3$, where B is the transition metal cation, is determined by the energy diagram for B cations octahedrally coordinated by the oxygen anions. In terms of the ligand field model the electronic bands are formed by bonding and antibonding molecular orbitals resulted form the overlapping of cations d-orbitals (B_d) with 2p-orbitals of ligand anions (O_{2p}). Bonding molecular orbitals are mainly composed of O_{2p} levels, whereas antibonding levels are mainly formed by d-orbitals split into three t_{2g} and two e_g crystal field levels (d_ε and d_γ electron states, respectively). In systems with unpaired electrons, especially in B cations occurring in the high-spin state, the degeneracy of t_{2g} or e_g may be removed due to the Jahn-Teller effect resulting also in the lattice distortion and lowering its symmetry. In perovskites, energies of d_ε and d_γ states lie near the bonding orbitals (top of O_{2p} bands). Moreover, metal cations may exist in several valence states which differ not strongly by energy. In this case d-electron levels of the high-charged state may be located a little below the top of O_{2p} band creating antibonding states at the top of the O_{2p} bands that results in a pinning of high-valence state that transforms the electrons and holes from localized to itinerant electronic behavior [21].

As the most effective cathode materials for SOFC are based on perovskites containing Mn, Fe, Co and Ni, let us shortly characterize transport properties of these compounds. In $La_{1-x}Sr_xMnO_{3-\delta}$ (LSM) and $La_{1-x}Sr_xFeO_{3-\delta}$ (LSF) the metal (III) cations have high-spin t^3e^1 and t^3e^2 configurations. Long-range Jahn-Teller spin-orbital ordering leads to the orthorhombic distortion of their perovskite structures and splitting of d_g levels. As a result, there are several half-filled bands leading to strong antiferromagnetic coupling and insulating properties. The electronic transport proceeds by thermally activated small polaron mechanism, the activation energy decreasing with temperature from 0.55 to 0.15 eV [21, 22]. At high temperatures or on doping, the Jahn-Teller effect decreases, the structure transforms from the orthorhombic to a cubic one, and the oxide becomes ferromagnetic. For perovskite-type solid solutions $La_{1-x}A_xMnO_{3-\delta}$ and $La_{1-x}A_xFeO_{3-\delta}$ (A = Ca, Sr, Ba), the introduction of A-cations leads to the formation of Mn (IV) and Fe(IV) cations. In manganites, Jahn-Teller

effect for Mn(IV) cation is not displayed that leads to less distortion of the structure. At some critical concentration of x = ~0.1, the oxide becomes ferromagnetic with metallic-type conductivity provided by itinerant electron-hole pairs via Zener small polaron mechanism [21]. In ferrites Fe(IV) t^3e^1 state is pinned to the top of O_{2p} band, so that d_γ electrons and holes are itinerant resulting in conductivity of the metallic type occurring via de Gennes small polaron mechanism [22, 23]. In $LaNiO_3$ Ni(III) ions occur in the low-spin state t^6e^1 with a single electron per Ni cation, d_γ-electrons form a narrow conducting band providing metallic conductivity of order of 10^3 S/cm decreasing with temperature. Ni (III) state is pinned at the top of the O_{2p} band that leads to the stabilization of this oxidation state of nickel; however, at high temperatures $LaNiO_3$ is not stable. The lanthanum cobaltite $LaCoO_3$ exhibits unusual behavior: at low temperatures Co(III) occurs in a low-spin t^6e^0 state, and the compound is a diamagnetic insulator. As the energy difference between the low-spin and high-spin t^4e^2 states is small, a transition is observed to a high-spin state at elevated temperatures. Due to strong Jahn-Teller effect, cobalt cations are first stabilized in a phase with intermediate spin state t^5e^1 of cobalt cation. At high temperatures this phase transforms into a ferromagnetic highly-conducting phase where metal cations are in a high-spin state. Substitution of lanthanum for alkali earth metal leads to a phase segregation with formation of the phase with Co (III) intermediate spin and metallic state.

Hence, there are many specific mechanisms controlling conductivity of binary perovskites $LaBO_3$ as a function of the B-cation type and temperature. Substitution of lanthanum for alkali-earth metal leads to generation of B cations in a higher oxidation state stabilized by pinning of the O_{2p} band. In the case of manganites and ferrites, it leads to weakening of Jahn-Teller effect and antiferromagnetic coupling. It results in delocalization of electrons and increase in the hole conductivity. Introduction of two transition metals into B-sublattice allows fine tuning the electronic structure of perovskites. For example, solid solutions of $La_{0.8}Sr_{0.2}Co_{1-y}Fe_yO_3$ (LSCF) have more complex electronic structure but generally exhibits more semiconductor-like behavior at a high iron content ($y > 0.8$) while being more metallic with a high Co content ($y < 0.1$) [9].

More complex defect models were also considered for $LaMnO_3$ suggesting antisite disordering (i.e. incorporation of Mn cations into La vacancies) [24, 25].

Oxygen diffusion. The total conductivity of Sr-doped lanthanum manganites, cobaltites and ferrites is much higher than the oxygen ionic conductivity. Therefore, to ensure good electrode performances it would be desirable to increase the ionic conductivity (σ_i) or diffusion coefficients which are interrelated via the Nernst-Einstein relation

$$D^* = D_v \cdot [V_O^{\bullet\bullet}] = \sigma_i \cdot \frac{fkT}{4e^2} N \tag{9}$$

Here D* is the tracer diffusion coefficient; D_v is the diffusion coefficient of oxygen vacancy; *f* is the correlation factor; *N* is the total volume concentration of oxygen ions in the substance. Eqn. (9) includes only free oxygen vacancies, i.e. not associated with the dopant cation. The diffusion coefficient is defined by ionic mobility mechanism and may be expressed in terms of ion hopping parameters:

$$D^* = \frac{1}{6} f[V_O^{\bullet\bullet}] a^2 \nu_0 \exp\left(\frac{S_m}{k}\right) \exp\left(-\frac{H_m}{kT}\right) \quad (10)$$

where a is the hopping distance; ν_0 is the attempt frequency; S_m and H_m is the migration entropy and enthalpy, respectively. It is evident that the presence of oxygen vacancies is necessary for the oxygen diffusion. Let us consider other factors affecting the diffusion coefficient. As shown in the literature [26, 27], doping of $LaBO_3$ perovskite in both La- and B-sublattices leads to a considerable, by several orders of magnitude, increase in the oxygen diffusion coefficient. The most probable reason of low diffusion coefficients in undoped perovskites is a high formation energy of oxygen vacancies by Eqn. (1). Substitution of La (or B-cation) for low-charged cations may lead to the formation of vacancies, but even in this case they may be associated with doping cations to form immobile complexes which do not participate in the oxygen transport. The contribution of association effects is the most pronounced in lanthanum chromites and manganites, where the activation energy for diffusion increases with x. In contrast, in lanthanum cobaltites and ferrites the activation energy of oxygen diffusion monotonically decreases with x due to decrease of vacancy formation energy, ΔH_f, which is accompanied by a huge increase in the oxygen diffusion coefficients [26, 27]. Fig. 3 shows temperature dependences of the diffusion coefficient of oxygen vacancies in different perovskite materials [18]. One sees that D_v values are very high and comparable with fluorite-type solid solutions known as typical ionic conductors. It makes perovskite solid solutions promising materials for oxygen separation membranes or electrode materials.

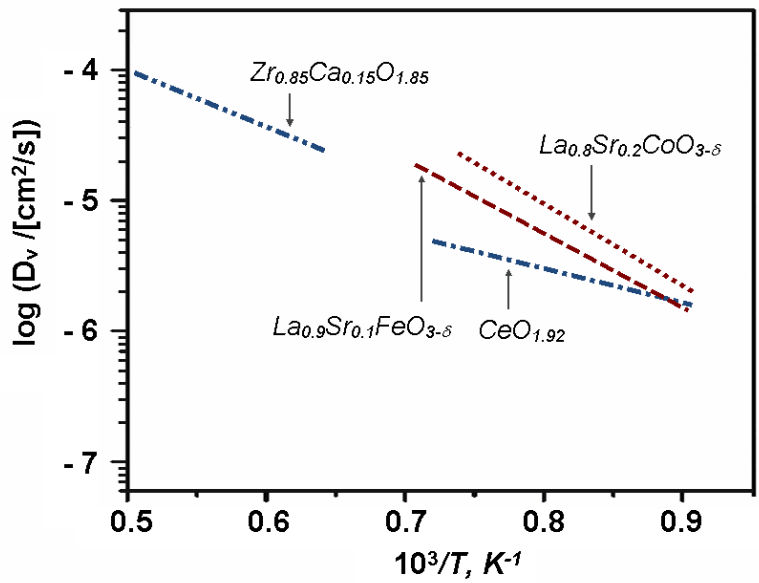

Figure 3. Typical temperature dependence of the oxygen vacancy diffusion coefficient in perovskites and fluorite-like oxides.

For oxygen diffusion under gradient of its chemical potential μ, the chemical diffusion coefficient $\tilde{D}$ is used instead of D^*. In this case the Fick's law will be expressed using the Wagner equation as a function of the oxygen chemical potential in the form:

$$J_{O_2} = -\tilde{D}\frac{\partial c_{O_2}}{\partial x} = -\left[\frac{1}{4^2F^2}\left(\frac{\sigma_e\sigma_i}{\sigma_e+\sigma_i}\right)\frac{\partial \mu_{O_2}}{\partial c_{O_2}}\right]\frac{\partial c_{O_2}}{\partial x} \tag{11}$$

where F is the Faraday constant, and the expression in round brackets is an ambipolar conductivity of electronic and ionic charge carriers. From this equation it follows that

$$\tilde{D} = \frac{1}{8F^2}\left(\frac{\sigma_e\sigma_i}{\sigma_e+\sigma_i}\right)\frac{\partial \mu_{O_2}}{\partial c_O} \tag{12}$$

If $\sigma_e >> \sigma_i$, Eqn. (12) may be represented as

$$\tilde{D} = \frac{D^*}{f}\cdot\frac{\partial \ln a_O}{\partial \ln c_O} \tag{13}$$

where the last multiplier is the thermodynamic factor which is equal to unity for ideal solutions and may strongly differ from 1 for real systems. According to the theoretical analysis [28], the limiting value of the thermodynamic factor is $\left[V_O^{\bullet\bullet}\right]^{-1}$ and from Eqn. (9) it follows that in this case $\tilde{D} = D_V$.

Surface exchange reaction. The oxygen surface exchange coefficient, k, is another important kinetic parameter characterizing oxygen transport rates in the oxide materials. It is a measure of the rate of the neutral oxygen flux J_O crossing the surface of the oxide as a result of the process [26]:

$$O_O^{\times} = \frac{1}{2}O_2 + V_O^{\bullet\bullet} + 2n';\ k = \frac{\left[V_O^{\bullet\bullet}\right]n^2 a_{O_2}^{1/2}}{[O_O^x]} \tag{14}$$

As follows from equation (14), this flux depends on the surface vacancy concentration, the surface electron concentration, and the dissociation rate of O_2 molecule. The expression for k can be formally written in the simple form [29]

$$k = \frac{J_O}{[O]} \tag{15}$$

The flux can be expressed through the exchange frequency ν and the concentration of the oxygen vacancies. Assuming that the exchange frequency is thermally activated

$$\nu = \nu_e \exp\left(\frac{S_e}{k}\right)\exp\left(-\frac{H_e}{kT}\right) \tag{16}$$

the following expression for the oxygen surface exchange coefficient was obtained [29]:

$$k = a_0 m^{-1/3}[V_O^{\bullet\bullet}]^{2/3}\nu_e \exp\left(\frac{S_e}{k}\right)\exp\left(-\frac{H_e}{kT}\right) \tag{17}$$

where a_0 is the cubic cell parameter; m is the number of oxygen sites per cell; ν_e, S_e and H_e are the attempt frequency, the entropy and the enthalpy of the elementary process of the surface exchange. This expression bears similarities to the atomistic expression for the diffusion (10) and explains the experimental observation that higher vacancy concentration leads to faster ion transport and surface exchange. Hence, the vacancy concentration is clearly a very important parameter. Other important parameter is the electronic conductivity. It was observed that oxygen exchange correlates with electronic conduction: materials with high concentrations and/or more mobile electronic carriers tend to have much better surface catalytic properties (k) than purely ionic conductive materials with similar rates of bulk ion transport (D*) [9].

The influence of the surface exchange on cathode performance may be expressed in terms of the characteristic length L_c defined as the ratio *D/k*. This length is the point at which the permeation behavior of oxygen through a mixed conducting membrane (such as a cathode) changes from diffusion-controlled to one limited by the surface exchange process [30, 31].

Experimental Techniques for Investigation of Transport Properties and Surface Exchange

Transport properties (separate determination of electronic and ionic conductivity, oxygen tracer diffusion and chemical diffusion) and surface stages (rate/constant of exchange) parameters of dense ceramics can be studied by several methods, such as electronic blocking polarization methods [32-34], ^{18}O tracer profile analysis by SIMS [26, 27, 29, 35], study of the $^{18}O/^{16}O$ isotope exchange kinetics by gas-phase analysis of the isotope composition [27, 35] or even by monitoring the change in weight of an oxide during the isotope exchange by a microbalance [36]; relaxation methods involving the measurement of change in conductivity, mass or other properties after a sudden change of p_{O2} [37-40]; or by direct study of permeation of oxygen through a dense membrane [41-47]. For powdered samples, oxygen isotope heteroexchange with mass-spectometric control of the gas-phase isotope compositions (both in static and flow modes) is a well-established technique allowing to estimate main parameters of the surface reaction steps and surface/bulk oxygen diffusion [48-62]. For powdered samples, the strength of oxygen bonding with the surface sites, amount of different surface/bulk oxygen forms and dynamics of their migration from the bulk of particles to their surface can be estimated by using temperature--programmed desorption (TPD) of oxygen or temperature--programmed reduction (TPR) by a reducing agent (H_2, CH_4) [11, 60-63].

Let's consider some of these techniques in detail.

Electrical conductivity relaxation (ECR) method. ECR method is rather simple, it does not require expensive equipment and provides high precision in determination of the oxygen chemical diffusion and surface exchange coefficients in mixed ionic-electronic conductors [64-66].

When a mixed ionic-electronic conductor (i.e. $La_{1-x}Sr_xBO_{3-\delta}$) is subjected to an oxygen chemical potential gradient, there arises a chemical diffusion of oxygen ions down the gradient (or the diffusion of oxygen vacancies in the opposite direction) and redistribution of electronic carriers. At typical values of x ($0.1 < x < 0.5$), the charge neutrality condition stipulates that

$$\left[Sr'_{La}\right] = 2\left[V_O^{\bullet\bullet}\right] - n' \tag{18}$$

for n-type regime, or

$$\left[Sr'_{La}\right] = 2\left[V_O^{\bullet\bullet}\right] + p^{\bullet} \tag{19}$$

for p-type regime; the contribution of other defects may be neglected. The defect concentration gradient will be determined by ambipolar diffusion of $V_O^{\bullet\bullet}$ and e' (in parallel direction) or $h^{\bullet}$ (in counter direction for a *p*-type regime). The total conductivity is a sum of the electronic and ionic contributions and may be written as

$$\sigma = eu_n n' + 2eu_v\left[V_O^{\bullet\bullet}\right] \tag{20}$$

(contributions of other carriers are neglected), u_k denote the mobility of the *k*-type carriers [37]. Taking time derivatives and assuming that $\partial\left[R'_B\right]/\partial t = 0$, one has

$$\frac{\partial\sigma}{\partial t} = 2e\left(u_n + u_V\right)\frac{\partial\left[V_O^{\bullet\bullet}\right]}{\partial t} \tag{21}$$

Due to Fick's second law,

$$\frac{\partial\left[V_O^{\bullet\bullet}\right]}{\partial t} = \nabla\left(\tilde{D}_O\nabla\left[V_O^{\bullet\bullet}\right]\right), \tag{22}$$

where $\widetilde{D}_O$ is the oxygen chemical diffusion coefficient. In relaxation experiments, the oxygen activity windows are chosen to be small enough (typically $|\Delta\log(a_{O2})| < 1$) so that $\widetilde{D}_O$ may be assumed to be constant. The effect of the surface reaction should be considered as the boundary condition for obtaining a solution to Fick's second law. Then an analytical solution may be obtained in the approximation that the surface reaction kinetics is linear with respect

to the oxygen concentration at the surface. For a rectangular sample with dimensions $2h$, $2w$ and $2l$ the exact solution has a form [65]:

$$\frac{\sigma(t)-\sigma_0}{\sigma_\infty-\sigma_0}=1-\sum_{i=1}^{\infty}\sum_{m=1}^{\infty}\sum_{n=1}^{\infty}\frac{2L_1{}^2\exp\left(-\frac{\beta_i^2\tilde{D}t}{h^2}\right)}{\beta_i^2(\beta_i{}^2+L_1{}^2+L_1)}\cdot\frac{2L_2{}^2\exp\left(-\frac{\gamma_m^2\tilde{D}t}{w^2}\right)}{\gamma_m^2(\gamma_m^2+L_2{}^2+L_2)}\cdot\frac{2L_3{}^2\exp\left(-\frac{\delta_n^2\tilde{D}t}{l^2}\right)}{\delta_n^2(\delta_n^2+L_3{}^2+L_3)} \tag{23}$$

where σ(t) is the time–dependent conductivity, σ_0 and σ_∞ are initial ($t \to 0$) and limiting ($t \to \infty$) conductivity values, respectively. The dimensionless parameters L_1, L_2, and L_3 are defined using the surface exchange coefficient k and the chemical diffusion coefficient as

$$\frac{L_1}{h}=\frac{L_2}{w}=\frac{L_3}{l}=\frac{k}{\tilde{D}} \tag{24}$$

which can be used for the estimation of relative contribution of surface reaction to the conductivity relaxation; coefficients β_i, γ_m, and δ_n are i-th, m-th or n-th roots of the equations:

$$\begin{aligned}\beta_i\tan\beta_i&=L_1\\ \gamma_m\tan\gamma_m&=L_2\\ \delta_n\tan\delta_n&=L_3\end{aligned} \tag{25}$$

For a specimen in the form of the infinite bar with a cross-section of 2a×2a one obtains [66]:

$$\frac{\sigma(t)-\sigma_\infty}{\sigma_0-\sigma_\infty}=\left[\sum_{n=1}^{\infty}\frac{2L^2}{\beta_n^2(\beta_n{}^2+L^2+L)}\exp\left(-\frac{\beta_n^2\tilde{D}_O t}{a^2}\right)\right]^2 \tag{26}$$

with β_n given by

$$\beta_n\tan\beta_n=L\equiv a\frac{k}{\tilde{D}} \tag{27}$$

Particularly when L<<1 the conductivity relaxation is diffusion controlled and Eqn. (23) takes the form [66]

$$\frac{\sigma(t)-\sigma_\infty}{\sigma_0-\sigma_\infty}=\frac{64}{\pi^4}\left[\sum_{j=0}^{\infty}\frac{1}{(2j+1)^2}\exp\left(-\frac{(2j+1)^2\pi^2\tilde{D}_O t}{4a^2}\right)\right]^2 \tag{28}$$

An example of the electrical conductivity relaxation curve for $La_{0.8}Sr_{0.2}Fe_{0.8}Ni_{0.2}O_{3-\delta}$ is shown in Fig. 4.

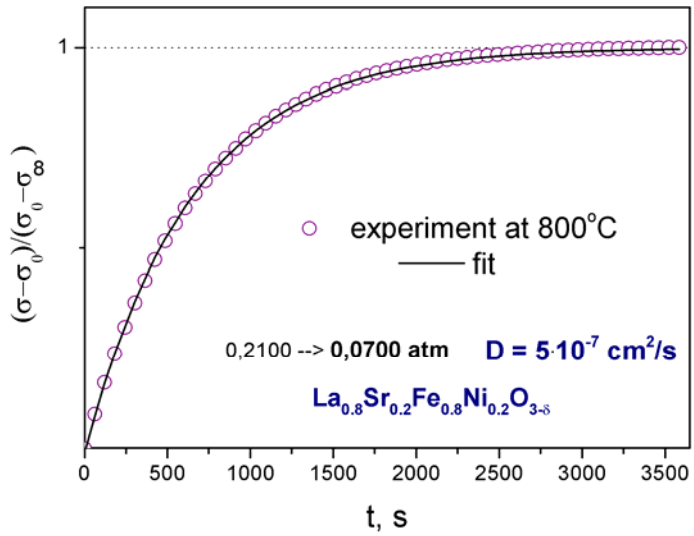

Figure 4. Conductivity relaxation curve for $La_{0.8}Sr_{0.2}Fe_{0.8}Ni_{0.2}O_{3-\delta}$ perovskite at 800°C after changing pO_2 from 0.210 to 0.070 atm. Points –experiment, line – fitting to Eqn. 28.

Oxygen isotope exchange. For dense ceramics, such technique as SIMS depth profiling can be applied. The sample with a natural oxygen isotope composition is first kept for a fixed time at the operation temperature under contact with oxygen enriched with the ^{18}O isotope. Then the ^{18}O oxygen profile across the sample depth is measured by SIMS and analyzed using the following equation [26, 66]

$$C'(x)\frac{C(x)-C_\infty}{C_g-C_\infty}=erfc\left(\frac{x}{2\sqrt{D^*t}}\right)-\exp\left(hx+h^2D^*t\right)erfc\left(\frac{x}{2\sqrt{D^*t}}+h\sqrt{D^*t}\right) \quad (29)$$

where C'(x) is the normalized fraction of ^{18}O, C(x) is the isotopic fraction as a function of depth x which is obtained from SIMS measurements, C_∞ is the background level of ^{18}O in the sample, C_g is the fraction of ^{18}O in the gas phase, and D^* is the bulk tracer diffusion coefficient. The parameter h is given by $h = k/D^*$, where k is the oxygen surface exchange coefficient. The values of D^* (cm^2/s) and k (cm/s) may be determined using a nonlinear least squares fit.

For powdered samples, mass-spectrometric (MS) analysis of the gas phase composition during isotope exchange is used for the estimation of parameters characterizing both the surface reaction and oxygen diffusion in the bulk.

In the analysis of O_2 isotopic redistribution between molecules of the gas phase, and isotopic heteroexchange between the gas phase and surface oxygen atoms of a solid oxide $(O)_S$, three routes of exchange must be taken into account [52-56]:

$$^{18}O_2 + {}^{16}O_2 = 2\ {}^{18}O^{16}O \quad (I)$$

$$^{18}O_2 + (^{16}O)_S = {}^{18}O^{16}O + (^{18}O)_S \quad (II)$$

$^{18}O_2 + 2\ (^{16}O)_S = {}^{16}O_2 + 2\ (^{18}O)_S$ (III)

The distribution of the molecules $^{18}O_i{}^{16}O_{2-i}$ (i = 0, 1, 2), characterized by their molar fractions $\boldsymbol{x}_i$, is determined by two independent composition variables (isotope variables), since $x_0 + x_1 + x_2 = 1$. The ^{18}O fraction of the oxygen gas, $\alpha = 0.5\ x_1 + x_2$, is usually selected as the first variable, while the second independent variable can be chosen as a fraction of any of the oxygen molecules, i.e. $^{18}O^{16}O$ (x_1)

With these variables, the redistribution of the isotopes in the system under consideration is described by the following isotope-kinetic equations [52-56]:

$$\frac{N}{S}\frac{d\alpha}{dt} = -R(\alpha - \alpha_s) \tag{30}$$

$$\frac{N}{S}\frac{dx_1}{dt} = K_1[2\alpha(1-\alpha) - x_1] + K_2[\alpha(1-\alpha_s) + \alpha_s(1-\alpha) - x_1] + K_3[2\alpha_s(1-\alpha_s) - x_1] \tag{31}$$

Here N is the number of O_2 molecules, S – the surface area of oxide, t – time, $R = 0.5K_2 + K_3$ – the rate of heteroexchange, K_1, K_2 and K_3 – the rates of exchange of the 1st, 2nd and 3rd type, respectively, their sum giving the total rate of exchange K.

The system of isotope-kinetic equations (30)-(31) is not closed since, along with the variables describing the gas phase composition, they contain the 3rd independent variable, α_s, the fraction of ^{18}O in the oxide surface.

For a complete description of the isotope redistribution, differential equations reflecting the isotope transfer in the solid phase should be added to this system

$$\frac{N_s}{S}\frac{\partial\alpha_s}{\partial t} = R(\alpha - \alpha_s) - r_D\frac{N_e}{S}\frac{\partial\alpha_v}{\partial\eta}\bigg|_{\eta=0} \tag{32}$$

$$\frac{\partial\alpha_v}{\partial t} = r_D\frac{\partial^2\alpha_v}{\partial\eta^2} \tag{33}$$

with the initial and boundary conditions:

t=0: $\alpha = \alpha^0$, $\alpha_s = \alpha_v = \alpha_s{}^0$

$\eta = 0$: $\alpha_v = \alpha_s$

where α_v is the fraction of ^{18}O in the oxide bulk, N_S and N_e are the number of oxygen atoms in the surface layer of oxide and the number of exchangeable atoms in the bulk of the oxide, respectively; η is the reduced depth (z) of the oxide layer η=z/h, where h is the

characteristic size of oxide particles; $r_D = \frac{D}{h^2}$ is the effective diffusion coefficient (diffusion relaxation constant), *D* is the oxygen self-diffusion coefficient.

The isotope-kinetic equations (30) - (31) allow the elucidation of the mechanism of surface reactions (adsorption-desorption and other processes) and the estimation of the bond strength of the surface oxygen [48-56] considered to be important parameters in analysis of porous MIEC cathodes performance [9].

In the case of equivalent exchangeable oxygen atoms (N_e), the time dependence of the gas phase isotopic fraction, **α(t),** is well described by an exponential function. By using the isotope balance equation $2N\alpha^0 + N_e\alpha_s^0 = 2N\alpha + N_e\alpha_s = (2N + N_e)\gamma$ (where α_s^0 is the initial value of α_s, γ-isotope fraction at equilibrium), the variable α_s can be excluded from Equation (30). This allows the estimation of the rate of heteroexchange R by using the integral form of isotope-kinetic equation (30)

$$\ln\frac{\alpha-\gamma}{\alpha^0-\gamma} = -(1+\lambda)\frac{S}{N}Rt \qquad (34)$$

$$\text{Here, } \lambda = 2N/N_e$$

The complete system of equations (30) - (34) can be used to estimate the self diffusion coefficient for oxygen in the bulk of the solid oxide. For this purpose, numerical analysis of the time dependence of the isotope variables, which corresponds to the solution of the inverse problem of the system of equations (30)-(34), was carried out through the minimization of the next objective functional:

$$F(\bar{\vartheta}) = \left(\int_o^{t_{end}} (\alpha^{calc}(t) - \alpha^{exp}(t))^2 dt + \int_o^{t_{end}} (x_1^{calc}(t) - x_1^{exp}(t))^2 dt\right) \to \min$$

where $\alpha^{exp}(t)$, $x_1^{exp}(t)$ are experimental and $\alpha^{calc}(t)$, $x_1^{calc}(t)$ - calculated dependencies of the isotope fractions in the gas phase oxygen.

To evaluate the quality of the fit between experimentally determined transient curves and calculated ones, the least square deviation was evaluated as follows:

$$Sq = \left(\sum_{i=1}^{N}(\alpha_i^{calc} - \alpha_i^{exp})^2/N + \sum_{i=1}^{N}(x_1^{calc}{}_i - x_1^{exp}{}_i)^2/N\right)^{1/2}$$

where N is the number of experimental points.

In the case of temperature-programmed oxygen exchange (TPIE), data analysis was carried out using specially derived equations. Thus, by transformation of isotope equations (30) and (31), the time-independent isotope-mechanistic equation was obtained [51-60]

$$\ln[(\mathbf{v}+\mathbf{b})/(\mathbf{v^0}+\mathbf{b})] = -\,\mathbf{a}\,\ln(\mathbf{s}/\mathbf{s^0}) \quad (35),$$

Here $\mathbf{v = z/s^2}$, $\mathbf{s = \alpha - \alpha_s}$, $\mathbf{z} = x_2 - \boldsymbol{\alpha}^2$, x_2 –fraction of $^{18}O_2$ molecules, and parameters **a** and **b** are determined by the type of mechanism (vide supra):

$$a = 2\frac{k}{r} = \frac{\kappa_2 + 2\kappa_3 - 1}{0.5\kappa_2 + \kappa_3}\ ;\ b = \frac{k_3}{2r-k} = \frac{\kappa_3}{\kappa_2 + 2\kappa_3 - 1}$$

Hence, Equation (35) can be used for estimation of the share of different types of exchange characterized by parameters K_2 and K_3.

Cheselske, Hall et al [67, 68] derived an equation to estimate the apparent activation energy of heteroexchange in experiments with a linear temperature ramp and equivalent exchangeable atoms:

$$\mathbf{E = -\,[RT^2(d\alpha/dT)/(\alpha - \gamma)]_I} \quad (36)$$

Here, $-d\alpha/dT$ is taken at the inflection point where it achieves a maximum value, α is the respective isotope fraction at this point (vide infra).

TPIE experiments also allow a semi-quantitative characterisation of the oxygen mobility. Thus, the depth of isotope penetration from the gas phase into the oxide in the course of TPIE can be characterized by the value N_X determined by the isotope balance equation in the closed system:

$$2N\alpha^0 + N_X\alpha_S^0 = \alpha(2N + N_X) \quad (37)$$

This quantity varying from 0 to the total number of exchangeable atoms is used as the measure of the number of exchanged oxygen atoms in the solid oxide. It is more conveniently expressed in relative units

$$X_S = \frac{N_X}{N_S} \text{ and } X_V = \frac{N_X}{N_V} \quad (38)$$

corresponding, respectively, to the number of exchanged oxygen monolayers X_s, (1 monolayer = $1.4\bullet10^{19}$ atoms/m^2) and the exchanged fraction of the bulk oxygen, X_v. For a given series of samples, these parameters known as the "dynamic extent of isotope exchange" [63] correlate with the oxygen diffusion coefficients [11, 60-63].

Temperature-Programmed Desorption of Oxygen From Powdered Samples (Oxygen TPD). Temperature-programmed desorption of oxygen from oxides is used to characterize the bonding strength of oxygen with the surface (as estimated by the temperature of the noticeable oxygen desorption into the stream of He or by position of the maximum of respective desorption peak) as well as the amount of easily desorbed oxygen [69]. For Sr-doped perovskite oxides (cobaltites, nickelates, manganites etc) high-temperature peaks of oxygen evolution (so called β-form) are usually assigned to a loss of oxygen from the lattice

accompanied by a change of the charge state of transition metal cations [6]. For perovskite-like oxides or their composites with fluorite-like oxides (GDC etc) with a high lattice oxygen mobility, the specific rate of oxygen desorption estimated at T_{max} of respective peak varies in parallel with the lattice oxygen mobility estimated by the oxygen isotope exchange [62]. Apparently, the maximum rate of desorption in the temperature-programmed mode is achieved when the effect of the increase of the oxygen mobility in the lattice with temperature (determined by the activation energy of the oxygen chemical diffusion) is prevailed by the effect of depletion of the amount of oxygen "stored" in the bulk of particle. Hence, this method allows to estimate (at least, qualitatively) the lattice oxygen mobility in conditions of a moderate oxygen chemical potential gradient between the surface and the bulk of particles.

Oxygen permeability. The measurement of oxygen permeability in a gradient of the oxygen pressure or activity is a direct method for determination of the oxygen diffusion coefficients in solids [70-73]. The permeability is numerically estimated from the value of stationary oxygen flux J_{O2} through a dense oxygen-permeable membrane. The value of J_{O2} should satisfy the Fick's law, Eqn. (11), which can be rewritten in a more suitable form [72]:

$$J_{O_2} = -\frac{1}{4^2 F^2 L}\int_{\ln P'_{O2}}^{\ln P''_{O2}} \left(\frac{\sigma_e \sigma_i}{\sigma_e + \sigma_i}\right) d\ln P_{O_2} \tag{39}$$

For the case of high electronic conductivity ($\sigma_e >> \sigma_i$) when ionic conductivity depends on P_{O2} by the power law $\sigma_i \approx \sigma_i \cdot p_{O2}^{n}$, after integration of Eqn. (32) one finds:

$$J_{O_2} = -\frac{\sigma_i^0 RT}{4^2 F^2 nL}\left[\left(P''_{O2}\right)^n - \left(P''_{O2}\right)^n\right] \tag{40}$$

This equation does not take the surface reaction into account. More correct expression for the oxygen flux [72] has the form:

$$J_{O_2} = -\frac{L}{L + 2L_c} \cdot \frac{t_e t_i \sigma}{4^2 F^2} \frac{\Delta\mu_{O_2}}{L} \tag{41}$$

where L_c is the characteristic length (or the membrane thickness). If $L >> L_c$, then the flux obeys ordinary Fick's law. In the opposite case the permeability is limited by the surface exchange reaction. It is seen that the oxygen flux across the membrane is reduced by a factor $(1 + 2L_c/L)^{-1}$, relative to that in the absence of transfer limitations across the interfaces. This problem is solved by supporting porous layers of the same or different composition on the oxygen-lean and oxygen rich sides of a dense membrane [7, 70, 71]. For oxygen separation, a thin porous layer of a complex perovskite (Sr-Co-Fe etc) with a high catalytic activity supported on the air side of membrane allows to change membrane operation mode from the surface-controlled to the bulk controlled one. For membranes designed for methane selective oxidation into syngas by oxygen separated from air, supporting a thin layer of Sm-doped ceria on the fuel side of perovskite membrane allows to prevent destruction of perovskite structure

caused by reduction. Supporting a porous layer of Ni or Pt catalyst allows to increase the rate of CH_4 oxidation and syngas selectivity.

There are several comprehensive reports [7, 74-79] devoted to mixed ionic–electronic conducting ceramic membranes for gas separation and selective catalytic reactions. The requirements to membrane materials differ from those to SOFC cathodes. For membranes, the most promising concept is based upon supported asymmetric functionally graded design combining a dense permselective layer and layers with different porosity. Cathode materials may be not dense, they operate in air and may be unstable in a reducing atmosphere. On the other hand, cathode materials should be chemically inert towards other SOFC components and keep their characteristics under the working conditions.

Temperature-Programmed Reduction. Temperature-programmed reduction of powdered perovskite samples by H_2 allows to estimate the reactivity of surface/bulk oxygen species, determine oxygen stoichiometry and elucidate specificity of the reaction mechanism [80]. Usually, reduction of perovskites containing redox transition metal cations (Co, Mn, Fe) proceeds in steps corresponding to Me^{4+}-Me^{3+}, Me^{3+}-Me^{2+}, or Me^{2+}-Me^{o} transitions [7, 80]. Thus, peaks corresponding to Mn^{4+} and Co^{3+} or Ni^{3+} reduction are usually situated at temperatures below 600 ^{o}C, and reduction proceeds by cooperative rearrangement of perovskites structure without new phases nucleation. In this case, variation of the lattice oxygen mobility with the composition/defect structure of perovskites affects both positions of peaks and their intensity (rates at $T_{max.}$). Reduction with formation of MnO or Me^{o} particles dispersed in matrix of irreducible rare-earth oxides proceeds via nucleation/growth stages following typical topochemical kinetics (contracting spheres, etc) in isothermal experiments [80].

Synthesis of perovskites

In frames of this work the following systems were synthesized via Pechini route:

- perovskite-type compounds and solid solutions: $La_{0.8}Sr_{0.2}Fe_{1-x}Ni_xO_{3-\delta}$ (x = 0.1-0.4) (LSFNx), $LaMnO_3$, $La_{0.8}Ca_{0.2}MnO_{3+x}$, $La_{0.8}Sr_{0.2}MnO_{3+x}$ (LSM), $La_{0.8}Sr_{0.2}Fe_{0.8}Co_{0.2}O_{3-\delta}$ (LSFC), $La_{0.8}Sr_{0.2}Fe_{0.5}Co_{0.5}O_{3-\delta}$ (LSFC), $LaNiO_3$ (LN);
- -Ruddlesden-Popper perovskite-related structures: La_2NiO_4, $La_2Ni_{0.8}Cu_{0.2}O_4$, $Pr_2Ni_{0.75}Fe_{0.25}O_4$ and $Pr_4Ni_3O_{10}$.

In Pechini method, metal nitrates (MeN), citric acid (CA), ethylene glycol (EG) and ethylenediamine (ED) were used as reagents. The molar ratio of CA:EG:ED:MeN was 3.75:11.25:3.75:1. CA and MeN were dissolved in ethylene glycol at 80 °C and in distilled water at room temperature, respectively. The prepared solutions were mixed together at room temperature under stirring followed by addition of ED. The prepared solution was stirred for 60 min and then heated at 70 °C for 24 h allowing for the gel formation. The gel was calcined at 25-700 °C.

Complex oxides in the Sr-Ba-Fe-Co-(Zr) -O system were prepared by 5 min mechanical milling of the starting reagents ($SrCO_3$, $BaCO_3$, Fe_2O_3, Co_3O_4, zirconium hydroxide) blends in an AGO-2 planetary mill with the powder/steel ball ratio of ~ 12/200 followed by calcinations at 1000-1100 ^{o}C [60]. For comparison, $LaCoO_3$ and $LaFeO_3$ samples were

prepared via ceramic route [60]. The specific surface area of samples obtained via ceramic and MA routes was in the range of 0.2-2 m^2/g.

Characterization methods. X-ray diffraction (XRD) patterns were obtained with an URD-6 an ARLX'TRA diffractometers using Cu K_α monochromatic radiation (λ=1.5418 Å). The 2θ scanning region was $5\text{-}90^0$. Transmission electron microscopy (TEM) micrographs were obtained with a JEM-2010 instrument (lattice resolution 1.4 Å) and acceleration voltage 200 kV. The morphology of sintered cell samples was studied by SEM using a BS-350 "Tesla" scanning electron microscope. X-ray photoelectron spectra (XPS) were acquired using an ES-300 electron spectrometer (Kratos Analytical, UK, AlK_α and MgK_α anodes). Samples were mounted on a holder using double-side scotch tape. Spectra were calibrated relative C1s binding energy (BE) 284.8 eV ± 0.2 eV. Quantitative analysis of the surface layers composition was made using integral line intensities and known values of atomic sensitivities factors with the relative accuracy ~10%. BET specific surface area (S_{sp}) was determined from the Ar thermal desorption data.

Isotope oxygen exchange was carried out in a static installation with MS control both in the temperature-programmed and isothermal modes as described elsewhere [60-63]. The surface/bulk oxygen mobility for samples pretreated in O_2 at 500 °C was characterized by the temperature-programmed desorption (TPD) in He flow. Reactivity of perovskites was estimated by temperature-programmed reduction (TPR) by H_2 or CH_4 (1% in Ar, heating rate of 5 K/min from 25 up to 880 °C) carried out in kinetic installations equipped with GC and PEM-2M analyzer (IR absorbance and electrochemical sensors) [11, 60-63].

Conductivity studies of samples were carried out on pellets using two-terminal scheme with silver paste electrodes at temperatures from 50 to 750 °C in air. Electric properties were measured with a Hewlett Packard HP 4284A Precision LCR Meter in the frequency range 20 Hz – 1MHz. Powders of perovskites and composites were pressed into disks (15 mm in diameter and about 1 mm thickness) and calcined at 1100ºC-1300 ^oC.

Electrical conductivities of cathode materials and relaxation profiles were measured using the four-probe Van der Pauw method with platinum wires as current and voltage electrodes. The measuring cell included $Zr(Y)O_2$ test tube with the electrochemical oxygen pump. Instrument/ device control and data acquisition used LabVIEW (National Instruments). For the abrupt change in the oxygen pressure at the beginning of the reducing/oxidation step the sample inside the electrochemical pump was blown by a pulse of the helium/oxygen flow with a maximal rate of 200 ml/min^{-1}. Then the pressure was regulated by the PID regulator of the electrochemical oxygen pump with an accuracy of $\Delta P=10^{-5}$ bar. The holder accommodates a sample with the maximum length of the side of a square sample of 0.5 cm and holds all four platinum electrodes and an K-type thermocouple.

2.2. Phase Composition, Morphology and Structural Features of Perovskites

XRD patterns of some samples of perovskites and perovskite-like oxides prepared via Pechini route are shown in Figures 5-7. According to XRD data, mainly $La_2O_2CO_3$ reflections are present in XRD patterns of samples calcined at 500°C. Phases of perovskites and K_2NiF_4-type structures are formed after polymeric precursor calcination at 700°C (Figs. 5, 6). LSM

calcination at higher temperatures results only in ordering of its structure, which leads to splitting of reflections due to lattice distortion caused by cooperative Jan-Teller effect.

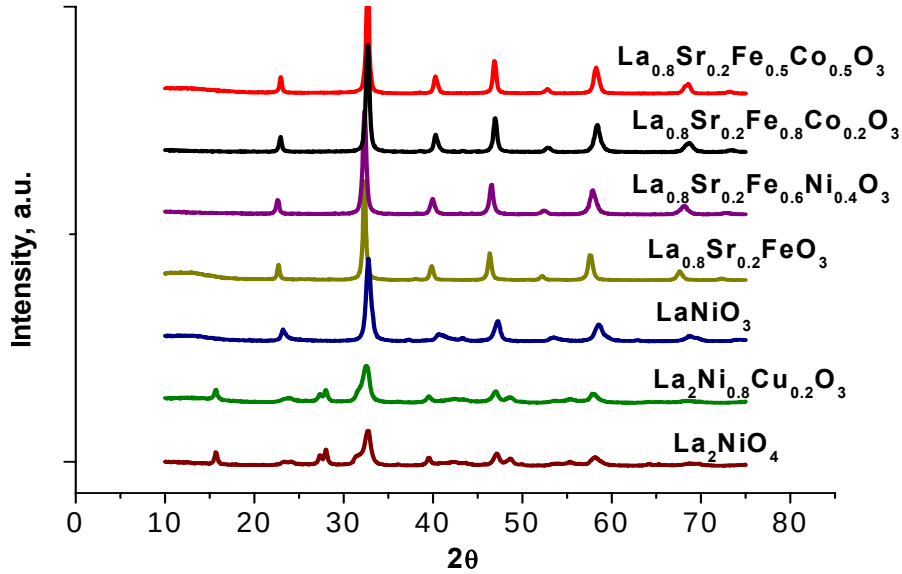

Figure 5. XRD patterns of complex perovskites after calcination at 700°C.

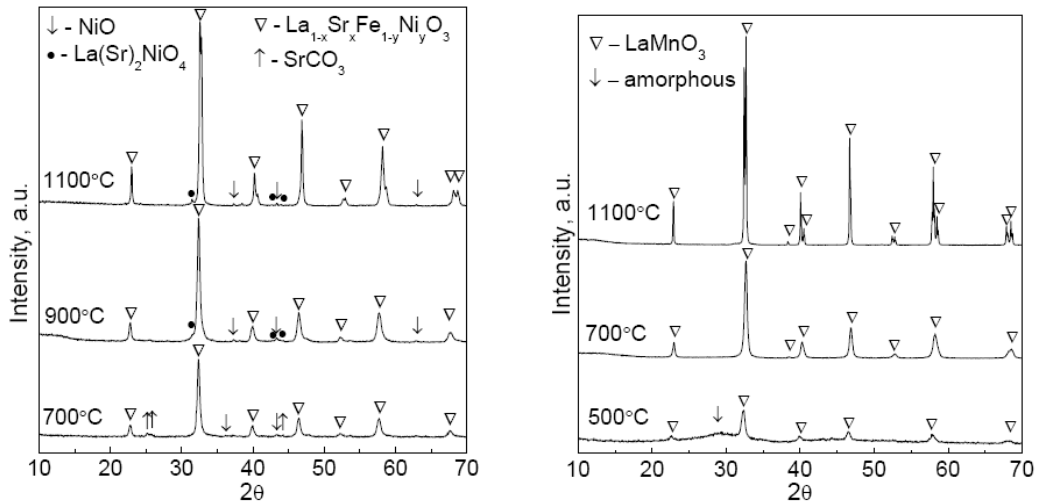

Figure 6. Powder XRD patterns showing the phase and structure evolution of LSFN (left) and LSM (right) samples with temperature of calcination.

Annealing at 900°C results in the disappearance of $SrCO_3$ reflections in the corresponding XRD patterns of Sr-doped samples. For LSNF perovskites, weak reflections of NiO are still present and a new weak reflection of tetragonal $La(Sr)_2NiO_4$ phase appears (Fig. 6). The perovskite structure of $LSFN_{0.3}$ remains orthorhombic after annealing at 900°C, but its lattice parameters decrease (Table 1). The symmetry of perovskite improves becoming rhombohedral after calcination at 1100°C, with admixtures of $La(Sr)_2NiO_4$ and NiO appreciably decreasing.

Table 1. Lattice parameters and symmetry of $LSFN_{0.3}$ perovskite phase

Sample	T, °C	Lattice parameters			
		a, Å	b, Å	c, Å	Symmetry[1]
$LSFN_{0.3}$	700	5.5299	7.8259	5.5389	O
	900	5.5271	7.8217	5.5365	O
	1100	5.5033	5.5033	13.3295	R

[1] O – orthorhombic, R – rhombohedral

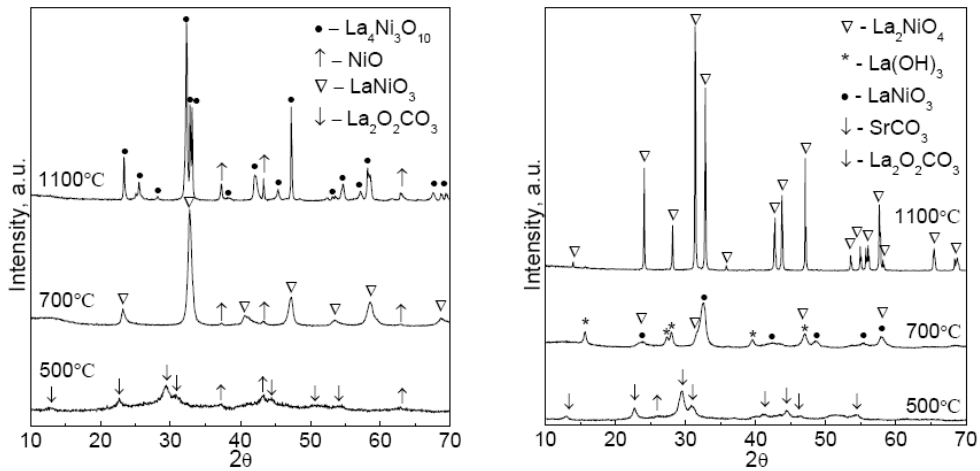

Figure 7. Typical powder XRD patterns showing the phase evolution of LN (left) and L2N (right) samples with temperature of calcination

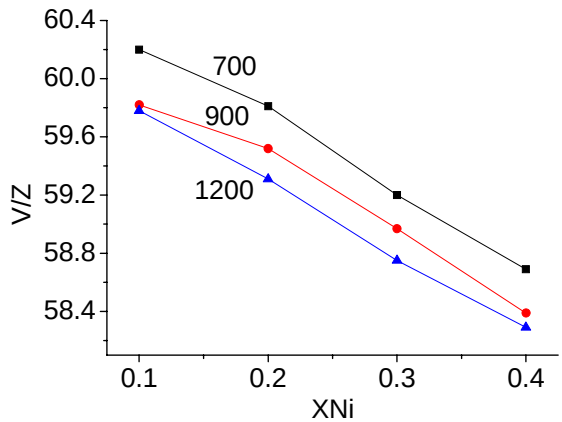

Figure 8. Effect of Ni content in $La_{0.8}Sr_{0.2}Fe_{1-x}Ni_xO$ on the lattice cell volume related per the formula unit V/Z ($Å^3$).

For LN sample some NiO is present after sample calcination at 700°C. After calcination at 1100 °C (Fig. **7**), decomposition of the perovskite $LaNiO_3$ phase was observed which is explained by instability of Ni^{3+} cations at high temperatures [81]. In the case of L2N and L2NCu samples mainly $La(OH)_3$ and $LaNiO_3$ are formed after calcination at 700 °C, with only traces of a target tetragonal phase $La_2Ni(Cu)O_4$ being observed (Fig**. 7**, right). However, single-phase $La_2Ni(Cu)O_4$ samples are formed after calcination at 1100 °C

Chiba at el shown that under air LSNF perovskites are stable single phase systems even at 1400°C when Fe mole fraction is higher than 0.5 [82]. In agreement with their data, the structure of $La_{1-y}Sr_yNi_{1-x}Fe_xO_3$ perovskite is rhombohedral at a high Ni content at all calcination temperatures (Table 2). The increase of Ni content and sintering temperature leads to LSFN lattice contraction (Fig. 8), as was earlier observed by other authors [83, 84] and explained by a smaller size of Ni^{3+} cation and removal of residual Sr carbonates accompanied by Sr incorporation into the lattice. For samples sintered at 1200 ^{0}C (Fig. 8), the trend is less strong in the range of Ni content 0.3-0.4. This clearly correlates with some segregation of NiO and tetragonal R-P type phase for $LSFN_{0.4}$ sample at 1200 ^{o}C (Fig. 9).

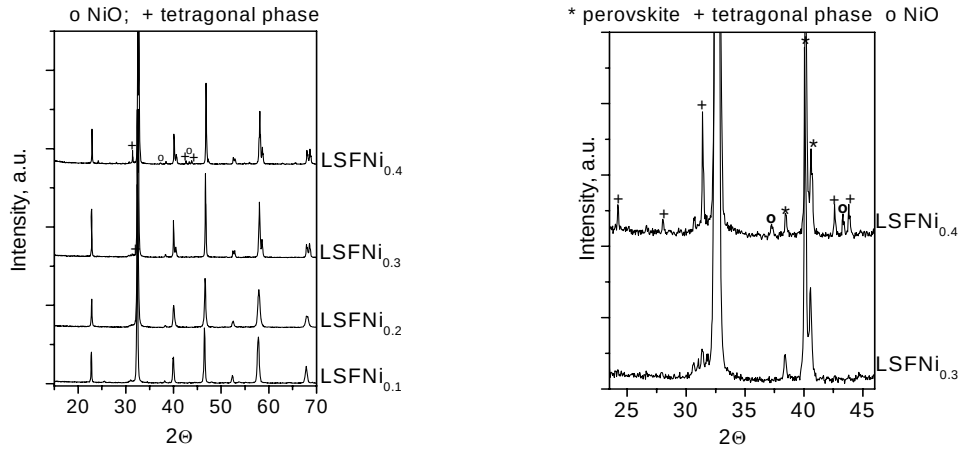

Figure 9. XRD patterns of $La_{0.8}Sr_{0.2}Fe_{1-x}Ni_xO_3$ calcined at 1200 ^{0}C (left) and the patterns of the samples with x = 0.3 and 0.4 with reflections of the impurity phases (right).

Note (Table 2) that a strong decline of specific surface area of LSFC and LSFN samples with increasing calcination temperature is accompanied by rather moderate increase of X-ray particle sizes (domains), so the extension of domain boundaries apparently increases with the sintering temperature.

Table 2. Some characteristics of $LSFN_{0.4}$ and $LSFC_{0.2}$ samples

Sample / T_c (°C)	S_{BET} (m^2/g)	Structural characteristics*			
		d XRD, nm	Lattice parameter (Å)		
			a	b	c
LSFN /700	21.6	20.5	5.516	5.516	13.364
LSFN / 900	12	30.8	5.502	5.502	13.364
LSFN / 1200	1.4	74.0	5.503	5.503	13.336
LSFC/700	18.0	32.0	5.4935	7.7903	5.5307
LSFC/900	9.2	38.5	5.4946	7.7907	5.5335
LSFC/1200	2.1	58.5	5.4983	7.7856	5.5371

Rhombohedral structure of LSNF and orthorhombic structure of LSFC

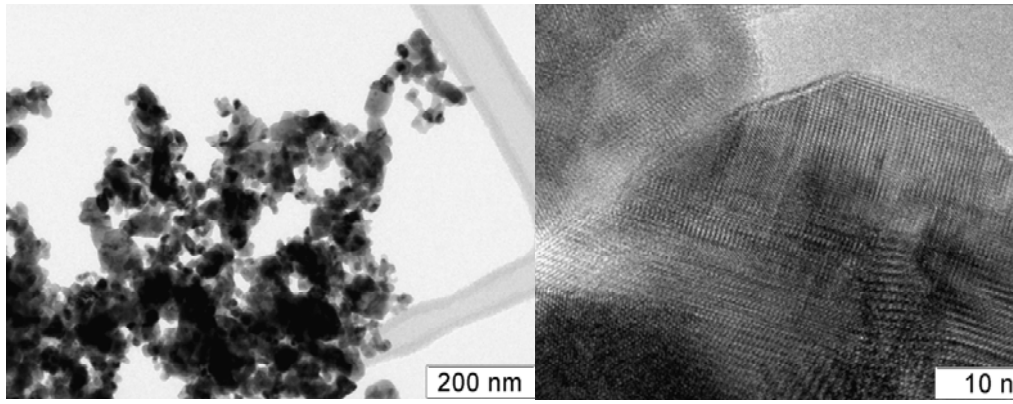

Figure 10. Morphology and HREM image of the structure of $La_{0.8}Sr_{0.2}Fe_{0.6}Ni_{0.4}O_3$ particle synthesized via Pechini method after calcination at 700ºC for 2 h.

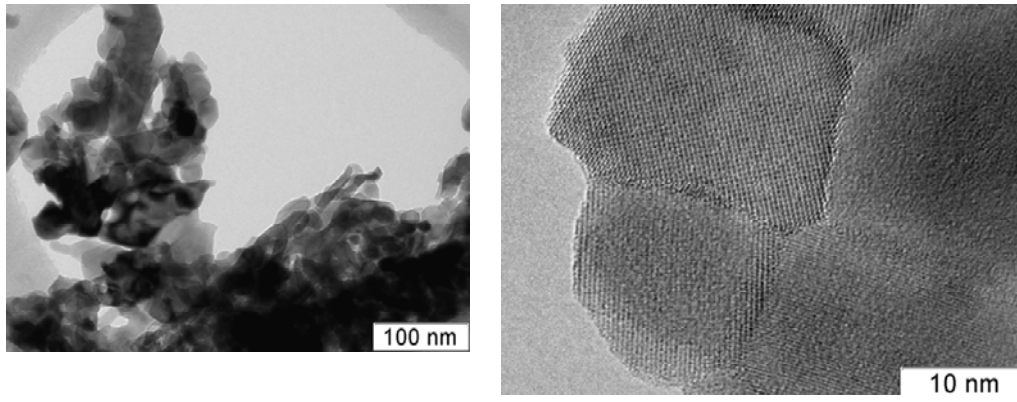

Figure 11. Morphology and structure of $La_{0.8}Sr_{0.2}MnO_3$ sample synthesized via Pechini method after calcination at 700ºC for 2 h.

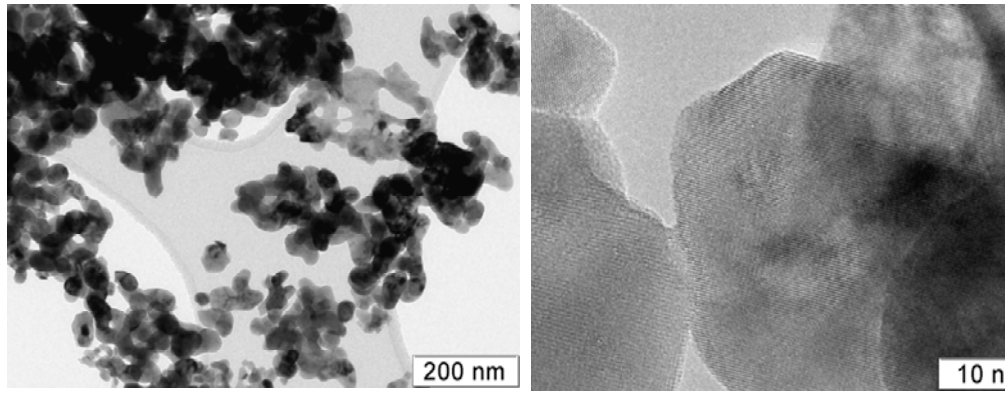

Figure 12. Morphology and structure of $La_{0.8}Sr_{0.2}Fe_{0.8}Co_{0.2}O_3$ sample synthesized via Pechini method after calcination at 700ºC for 2 h.

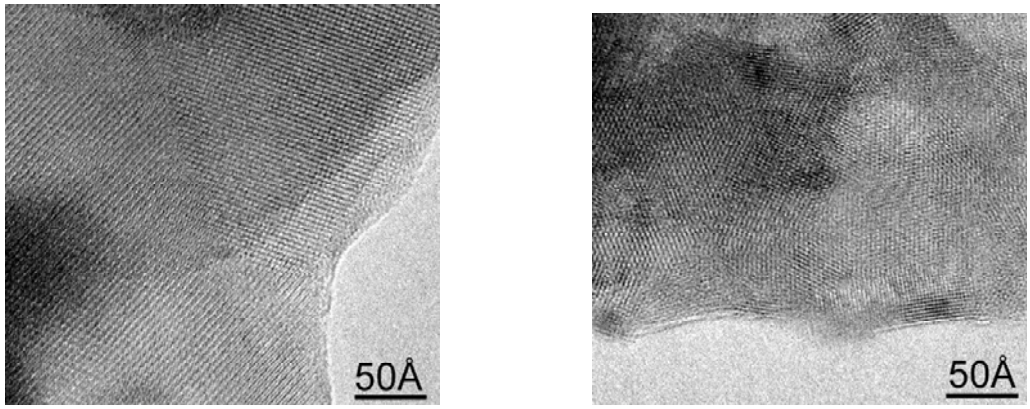

Figure 13. High resolution TEM images of particles of complex perovskites (a) $BaFe_{0.4}Co_{0.4}Zr_{0.2}O_y$ and (b) $Sr_{3.5}Ba_{0.5}Fe_{2.5}Co_{1.5}O_{10}$ prepared via MA route.

According to TEM data, perovskites prepared via Pechini route consist of crystalline nano-sized (10-50 nm) particles (Figures 10-12). There are a lot of structural defects and domain boundaries in such samples. This resembles the domain structure of disordered complex Sr-Ba-Fe-Co-(Zr) -O perovskites prepared via MA route (Fig. 13) [60]. For all these samples but those containing Zr, a cubic structure was observed, while particles were comprised of disorderly stacked microdomains. The $BaFe_{0.4}Co_{0.4}Zr_{0.2}O_y$ sample particles were comprised of the coherent intergrowth of domains with hexagonal $BaFeO_{3-x}$ [JCPDS 23-1024] and monoclinic $Ba_2Fe_2O_5$ [JCPDS 43-0256] structures.

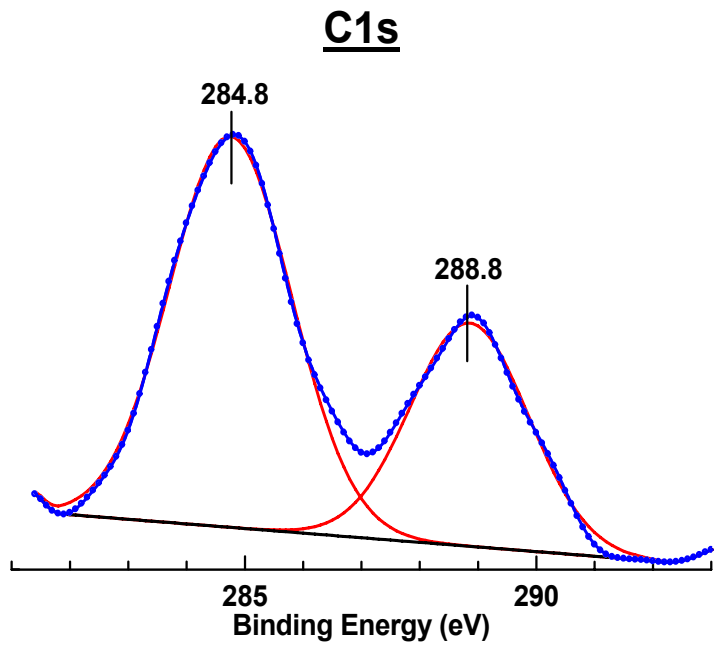

Figure 14. C1s spectrum of $La_{0.8}Sr_{0.2}Fe_{0.6}Ni_{0.4}O_3$ sample calcined at 700°C.

2.3. Surface Composition and Chemical State of Elements in Complex Perovskites

For all perovskites at room temperature after calcination in air, XPS analysis revealed substantial accumulation of carbonate species in the surface layer. In addition, the surface of the samples contains considerable amount of adsorbed hydrocarbon species trapped from the air. Typical C1s spectrum (sample $La_{0.8}Sr_{0.2}Fe_{0.6}Ni_{0.4}O_3$- 700°C) presented in Fig 14 consists of two components. The more intense component with E_b(C1s) = 284.8 eV is attributed to the elementary carbon or hydrocarbons on the surface of samples. The component with E_b(C1s) ~ 288.5 eV is unambiguously relates with carbonate species, and its share increases with the calcination temperature. Since samples after calcination were cooled under air, and XPS spectra were recorded without any pretreatment of samples, these carbonates are clearly formed due to capture of CO_2 from air by the surface layer of perovskites forming carbonate species.

For Sr-containing samples, the increase of calcination temperature from 700 to 1100 °C was accompanied by the surface enrichment with Sr, as is shown for the case of $La_{0.8}Sr_{0.2}Fe_{0.6}Ni_{0.4}O_3$ sample in Fig. 15. While the relative content of Fe and Ni cations varies rather slightly (in the range of 10-20 relative %) (Fig. 16, 17), more pronounced effects were observed for the charge state of both lanthanum and oxygen (Fig. 18, 19).

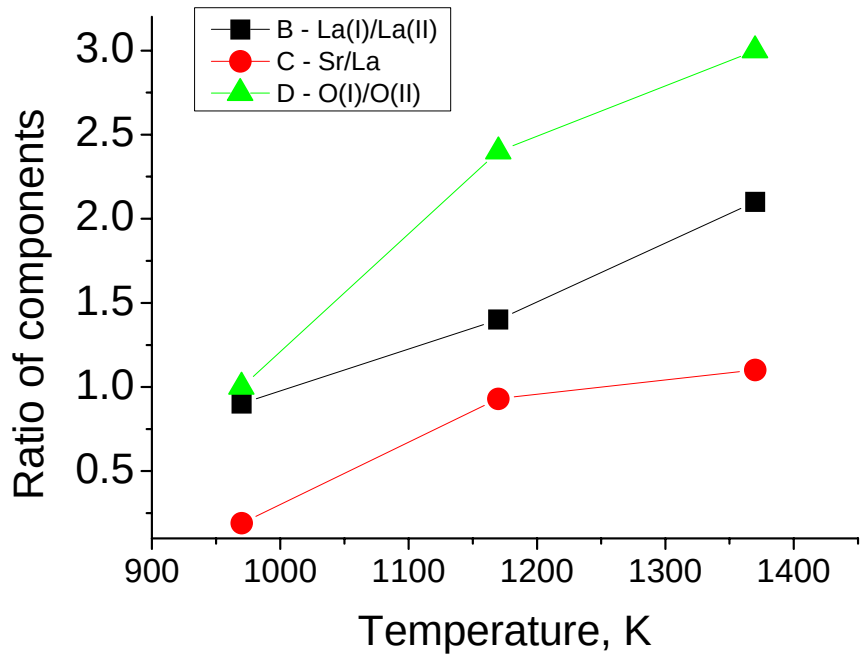

Figure 15. XPS data for the surface composition of $La_{0.8}Sr_{0.2}Fe_{0.6}Ni_{0.4}O_{3-\delta}$ sintered at different temperatures; La(I) and La(II) are La cations with a lower and normal binding energy, respectively; O(I) and O(II) are oxygen ions with a higher and normal covalency, respectively.

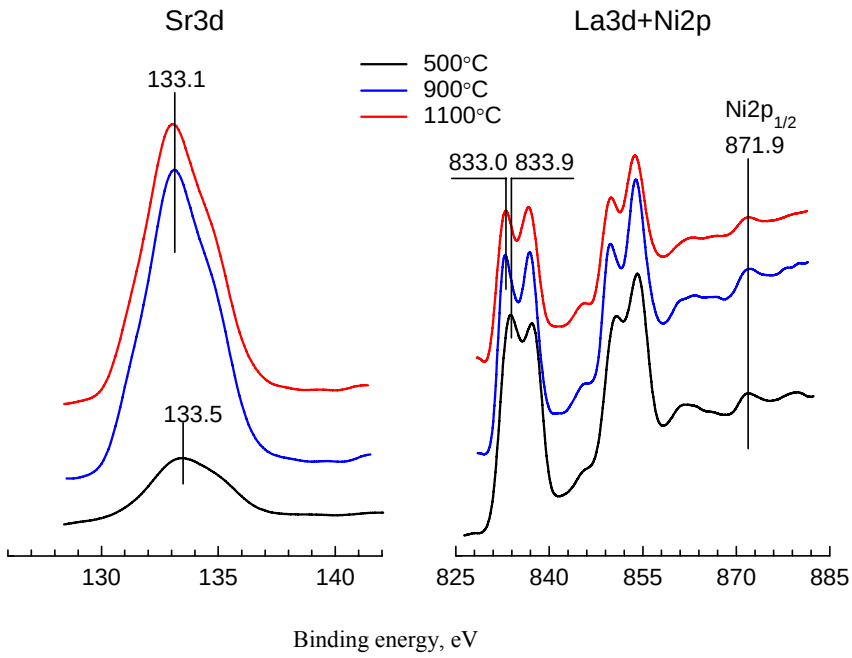

Figure 16. XPS spectra of $La_{0.8}Sr_{0.2}Fe_{0.6}Ni_{0.4}O_{3-\delta}$ sample in the range of Sr 3d (left) and La and Ni (right) binding energies.

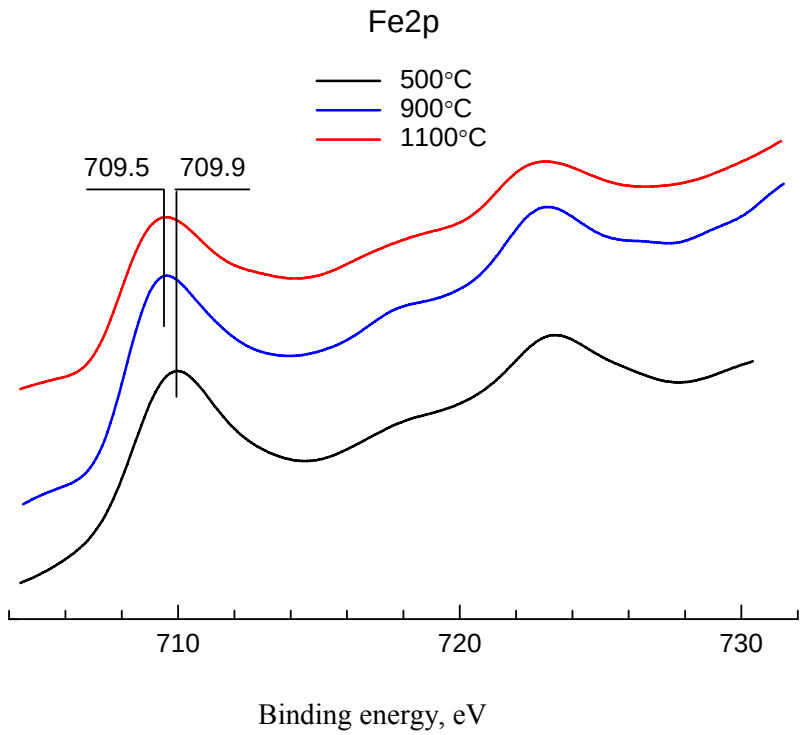

Figure 17. XPS spectra of $La_{0.8}Sr_{0.2}Fe_{0.6}Ni_{0.4}O_{3-\delta}$ sample in the range of Fe 2p binding energies.

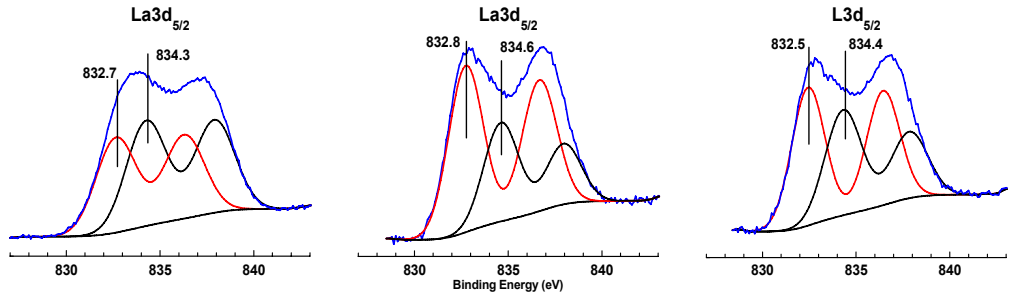

Figure 18. La3d5/2 spectra of $La_{0.8}Sr_{0.2}Fe_{0.6}Ni_{0.4}O_3$ calcined at 700°C (a), 900°C (b) and 1100°C(C).

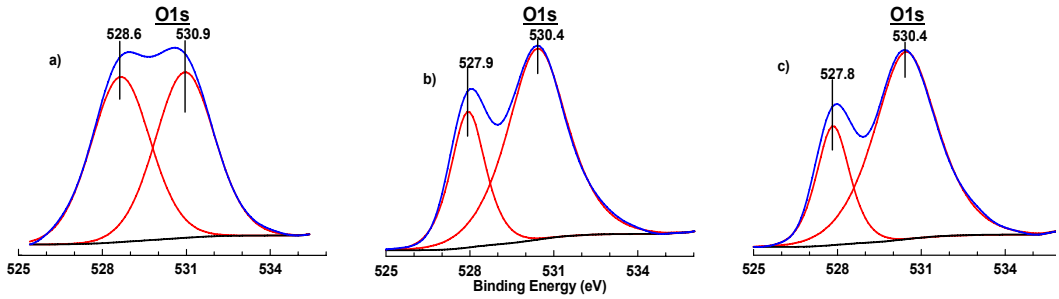

Figure 19. O1s spectra of $La_{0.8}Sr_{0.2}Fe_{0.6}Ni_{0.4}O_3$ calcined at 700°C (a), 900°C (b) and 1100°C (c).

The curve fitting of the $La3d_{5/2}$ lines shape (Fig. 18) resulted in two doublets with E_b ~ 832.7 eV (LaI) and ~ 834.5 eV (LaII). The observed La(I) and La(II) states are assigned to La^{3+} cations located in different oxygen environment.

The ratio of La(I) to La(II) increases with the calcination temperature (Fig. 15). Similarly, two states of La cations were observed for other perovskites studied here.

Two states of oxygen anions are also clearly seen from O1s spectra presented in Fig. 19. These oxygen states with E_b(O1s) ~528 eV and ~530.5 eV can be interpreted in terms of ionic and covalent bonding of oxygen in two different cations sublattices. As is shown in many papers, the O1s band shift reflects ionicity of metal- oxygen bonding. In general, oxygen with a lower E_b(O1s) is characterized by more negative charge.

All these XPS features suggest that Sr enrichment in the surface layer favors accumulation of oxygen vacancies, which decreases effective charge of La cations and increases covalence of oxygen forms filling these vacancies. As is seen from Fig. 19, the increase of the calcination temperature results in preferential growth of the surface oxide layer where oxygen is in the covalent state. Moreover, increased intensity of component with E_b(O1s) ~530.5 eV can be also caused by a higher content of carbonate species $–CO_3$ characterized by the same value of E_b(O1s) ~530.5 eV. For correct calculation of quantitative dependence of ratio O(I)/O(II) (O(I) – E_b(O1s) ~ 528 eV; O(II) - E_b(O1s) ~ 530.5 eV), the contribution of carbonate species was subtracted from the total integral intensity of O1s component with E_b(O1s) ~530.5 eV giving ratio O_I/O_{II} presented in Fig. 15.

Hence, for Sr-containing complex perovskites, substantial accumulation of oxygen vacancies in the surface is suggested by XPS data. The same feature can take place within

domain boundaries known to possess less dense structure as compared with the bulk of domains.

2.4. Conductivities of Perovskites

A high level of the total conductivity (>10^2 S/cm) at ~ 1000 K was revealed for LSFC and LSFN samples sintered at sufficiently high (1100-1300 °C) temperatures (Fig. 20-21). A close level of conductivity was determined for LSM in agreement with known results [85, 86]. The conductivity of LSFN perovskites is thermally activated exhibiting a polaronic behavior within the studied temperature range. The character of the temperature dependence of conductivity of doped nickelates is similar to that reported earlier [87-90]. According to Huang et al [91], this polaronic conductivity is explained by an overlap of Fe^{4+}/Fe^{3+} and Ni^{3+}/Ni^{2+} couples which provides two types of polaronic conduction, p-type and n-type, with the p-type carriers moving on the Fe-atom array, and the n-type carriers moving on the Ni-atom array.

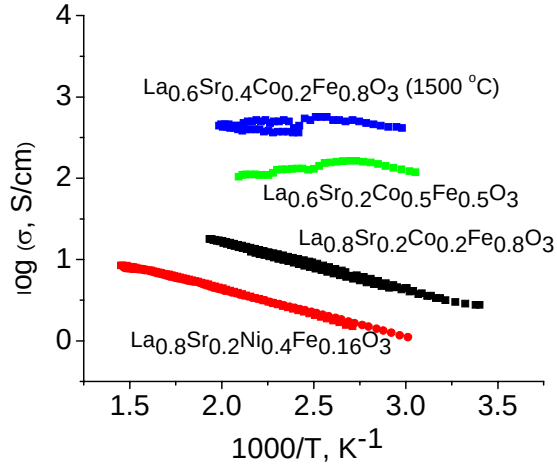

Figure 20. Temperature dependence of conductivity for LSFC samples and LSNF sample with a layered perovskite- related structure sintered at 1500 ($LSFC_{0.2}$) or 1100ºC (all other samples).

In general, different R-P type phases possess a lower conductivity than LSNF or LSFC (Fig. 22). The temperature dependence of conductivity observed for $La_2Ni_{0.8}Cu_{0.2}O_4$ is similar to that reported by Kharton et al [92], with σ values being somewhat lower. The latter might be caused by lower sintering temperatures used for the pellets preparation in our case. Hence, the data obtained suggest that $La_2Ni_{0.8}Cu_{0.2}O_4$ as well La_2NiO_4 and $La_{0.8}Sr_{0.2}Ni_{0.4}Fe_{0.6}O_3$ provide a semiconductor-type behavior at low temperatures and a pseudometallic conduction at high temperatures. In agreement with [93, 94], a partial substitution of Ni for Cu and/or Fe increases conductivity of R-P type phases. La substitution for Sr and increase of the transition metal cations content in R-P type phase up to $Ln_4Ni_3O_{10\pm\delta}$ composition was shown to increase conductivity as well [95, 96]. However, in our case conductivity of the R-P type mixed oxide with the excess of transition metal cations $La_{0.8}Sr_{0.2}Ni_{0.4}Fe_{0.16}O_{3-\delta} = (La_{0.8}Sr_{0.2})_2Ni_{0.8}Fe_{0.32}O_{4+\delta} = (La_{0.8}Sr_{0.2})_4(Ni+Fe)_{2.24}O_{8+\delta}$ is not improved appreciably (Fig. 20), perhaps, due to

insufficient content of transition metal cations. A low pellet density could be important as well, since conductivity of this sample is rather close to the specific conductivity of $LSFC_{0.2}$ perovskite sintered at the same (1100 ^{o}C) temperature.

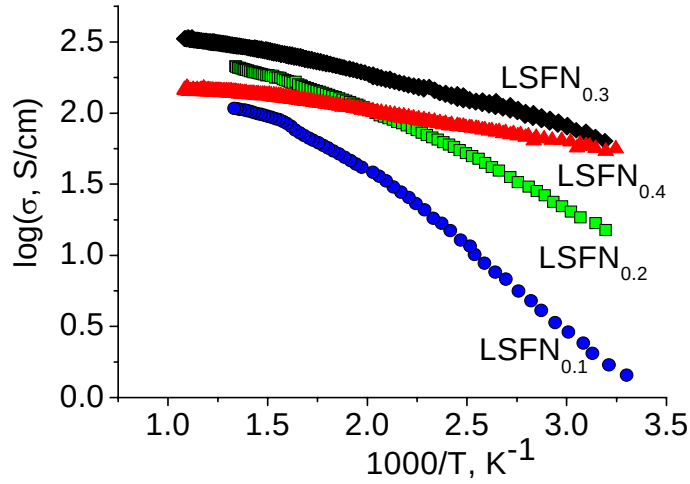

Figure 21. Temperature dependence of conductivity for LSFN samples with different Ni content sintered at 1300^{0}C.

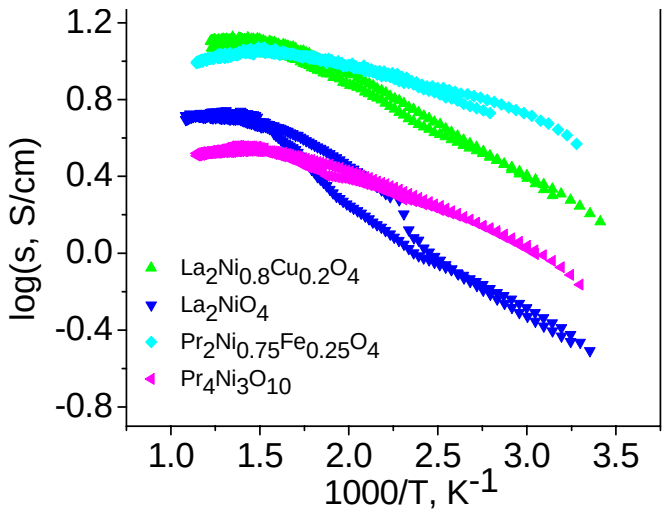

Figure 22. Temperature dependence of conductivity for samples with R-P perovskite-type structure sintered at 1100^{0}C.

In general, perovskite-like complex oxides Ba(Sr)-Fe(Co)-O comprised of disordered intergrown perovskite- braunmillerite domains possessing a high lattice oxygen mobility/oxide ionic conductivity demonstrate also not too high (1-10 S/cm) specific total conductivity at 1000 K [97, 98].

2.5. Oxygen Mobility and Reactivity of Perovskites

2.5.1. Oxygen Isotope Exchange

As shown in Fig. 23, for Co- and Ni-containing perovskites calcined at 700 °C, noticeable oxygen exchange starts at 300ºC. The dynamic extent of exchange (DEE) exceeds the monolayer capacity at ~ 400 °C and reaches 10-15 monolayers at 550ºC, somewhat higher values of DEE (and, hence, oxygen mobility) being observed for LSNF. This clearly demonstrates a high lattice oxygen mobility for these perovskites, with the rate of bulk diffusion exceeding that of the surface reaction. The increase of LSNF sintering temperature to 900 °C shifts the start of exchange to higher temperatures and somewhat decreases DEE in all studied temperature range (Fig. 24). After annealing at 1100 °C the surface steps apparently proceed with a high rate only at temperatures exceeding 500 °C. However, at temperatures exceeding 600 °C bulk diffusion occurs faster than for samples sintered at lower temperatures, so DEE exceeds 30 monolayers at 700 °C. This increase of the lattice oxygen mobility with sintering temperature can be explained by removal of carbonates from the surface as well as from the vicinity of domain boundaries thus providing coherently stacked domain boundaries as paths for the rapid oxygen migration. Moreover, as was revealed by XRD data (vide supra), the extension of domain boundaries increases with the sintering temperature, so this feature could indeed explain the increase of the lattice mobility in perovskites with sintering temperature.

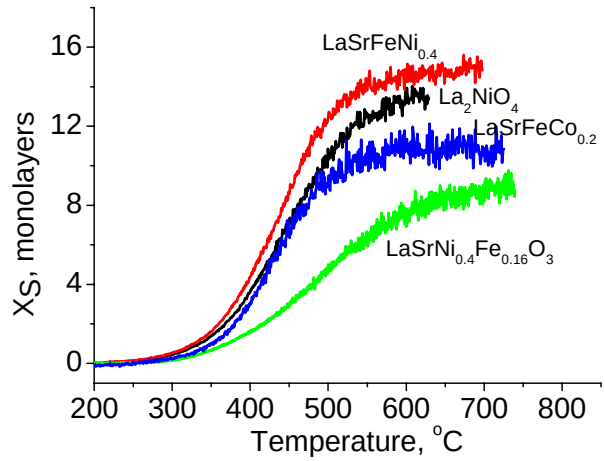

Figure 23. Temperature dependence of the dynamic degree of oxygen exchange for perovskites calcined at 700° C.

Fig. 25 compares X_S at 650 °C for some studied perovskites. It varies in a rather broad range with the chemical composition and sintering temperature. Clearly, doped chromite demonstrates rather low lattice oxygen mobility in the oxidized state. Rather low DEE values were obtained for Gd-Sr-Co-O perovskite [99], despite report about a low polarization resistance of this oxide as a cathode material [100]. As was considered by Mogensen et al [101], the highest oxygen mobility in perovskites is provided by La in A sites due to the minimum lattice distortion, which can explain the results obtained for Gd-Sr-Co-O perovskite. Similarly, Cu-doped Pr_2NiO_4 oxide demonstrates a lower oxygen mobility than

Cu-doped La_2NiO_4 oxide. La_2NiO_4 shows a higher oxygen mobility than $LaNiO_3$, which correlates with a higher ionic conductivity of the former oxide due to interstitial conductivity mechanism [102]. In agreement with the data of SIMS depth profile analysis [103, 104], the oxygen mobility in La_2NiO_4 characterized by DEE exceeds that of LSFC calcined at the same temperature. Moreover, decline of ionic conductivity in La_2NiO_4 due to Cu doping [105] is also reflected in the decrease of DEE. LSFC annealed at 1100 °C apparently possesses the highest lattice oxygen mobility which agrees with known data for dense samples [106]. However, LSFN sintered at the same temperature has at least comparable level of the lattice oxygen mobility promising for the practical application. DEE values for these complex perovskites are close to the values estimated for well-known complex perovskite systems with the highest lattice oxygen mobility such as $BaFe_{0.4}Co_{0.4}Zr_{0.2}O_x$ and $Sr_4FeCo_3O_{10}$ (Fig. 26) [60].

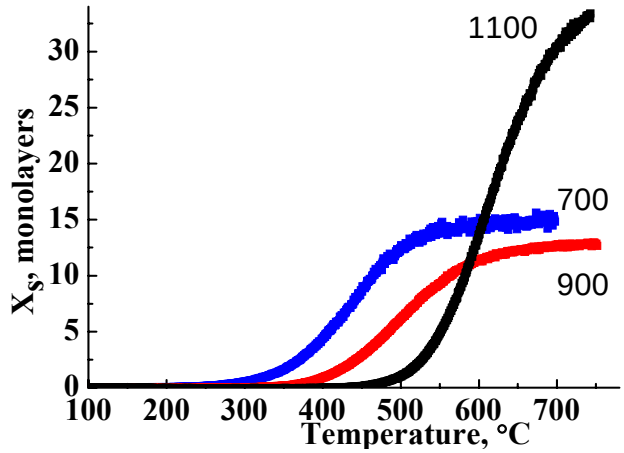

Figure 24. Temperature dependence of the dynamic degree of exchange for $La_{0.8}Sr_{0.2}Fe_{0.6}Ni_{0.4}O_3$ calcined at 700-1100°C.

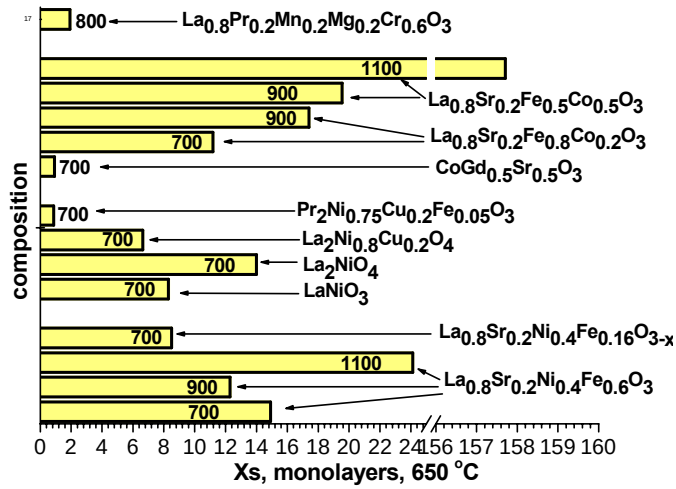

Figure 25. Dynamic degree of the oxygen heteroexchange at 650 °C and 4 Torr O_2 versus samples composition and sintering temperature.

The lowest values of the oxygen mobility estimated by oxygen isotope exchange for powders were found for lanthanum manganite either pure or doped by Ca or Sr (Fig. 26). Manganites are well known to possess a low oxygen mobility in oxidizing conditions due to the absence of oxygen vacancies in the lattice [24, 25]. Doping by Ca somewhat increases oxygen mobility though not substantially.

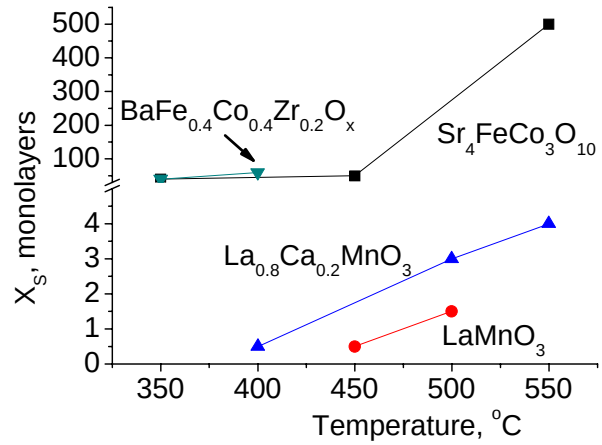

Figure 26. Temperature dependence of X_S for lanthanum manganites and complex perovskites $BaFe_{0.4}Co_{0.4}Zr_{0.2}O_x$ and $Sr_4FeCo_3O_{10}$.

Isothermal exchange experiments carried out for the same powdered samples allowed to estimate specific rates of the oxygen heteroexchange (vide supra). In general, these rates tend to increase with sintering temperature for Sr-doped complex perovskites (Fig. 27, 28) reflecting, perhaps, accumulation of oxygen vacancies in the surface layer of perovskite particles revealed by XPS (vide supra). For LSNF sample, this is true for temperatures of exchange exceeding 550 °C, while for lower temperatures specific rate of exchange decreases with the increase of sintering temperature from 900 to 1100 °C (Fig. 27). This explains variation of the temperature dependence of dynamic degree of exchange for this sample with the sintering temperature (Fig. 25). With a due regard for segregation of Ni oxide species in this sample after high-temperature annealing (vide supra), decreased low-temperature specific rate of exchange can be assigned to this phenomenon, so annealing of some surface defects as active sites of low-temperature exchange could be important as well. However, in the intermediate temperature range of SOFC operation (600-700 °C), specific rate of the oxygen exchange for LSNF sample is close to that of LSCF (Fig. 27). All other Ni- or Co-containing complex perovskites studied here demonstrate a lower specific rate of exchange (Figs. 27, 28). In general, the scale of the specific rate of exchange variation is smaller than that of DEE (cf. Figs. 25 and 28, 29). Indeed, $LaMnO_3$ having much lower lattice oxygen mobility as compared with mixed ferrite-cobaltites of Sr (Fig. 26) has rather close values of the specific rate of oxygen heteroexchange (Fig. 29). From the point of view of surface chemistry and heterogeneous catalysis [6, 55, 59, 80], comparable rates of the surface oxygen heteroexchange are expected if the surface concentration of transition metal cations and bonding strength of surface oxygen forms are close for different perovskites. While for simple oxides of Mn, Co and Ni the bonding strength of the most reactive on-top (terminal) Me-O oxygen forms was shown to be indeed comparable [107, 108], the situation is not so

straightforward for perovskites due to strong effect of the perovskite structure and chemical composition on the types and fraction of the most developed surface planes (faces), different terminations of the same face and possibility of its reconstruction/relaxation depending on the oxygen stoichiometry and gas phase composition [108, 109]. Though usually observed correlation between the oxygen surface exchange and bulk diffusion coefficients is explained by importance of both surface and bulk oxygen vacancies for the surface reaction and bulk diffusion, strong deviations are possible if detailed mechanism of the oxygen exchange is considered [48-56].

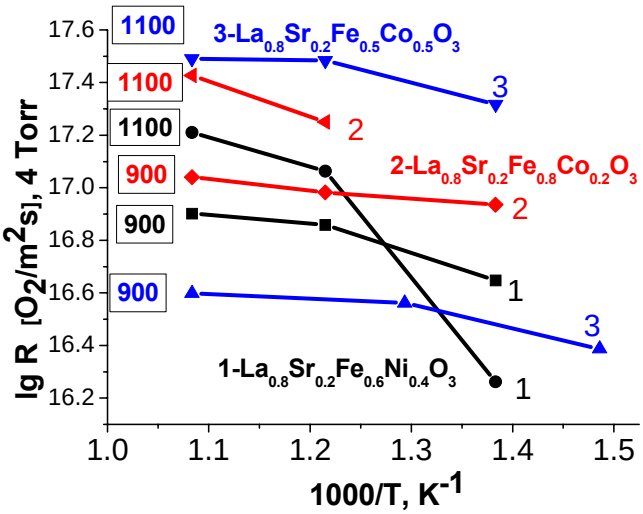

Figure 27. Temperature dependence of the specific rate of the oxygen heteroexchange at 4 Torr O_2 for $La_{0.8}Sr_{0.2}Fe_{0.6}Ni_{0.4}O_3$ (1), $La_{0.8}Sr_{0.2}Fe_{0.8}Co_{0.2}O_3$ (2) and $La_{0.8}Sr_{0.2}Fe_{0.5}Co_{0.5}O_3$ (3) sintered at 900 or 1100 ^oC (numbers at the left side of curves).

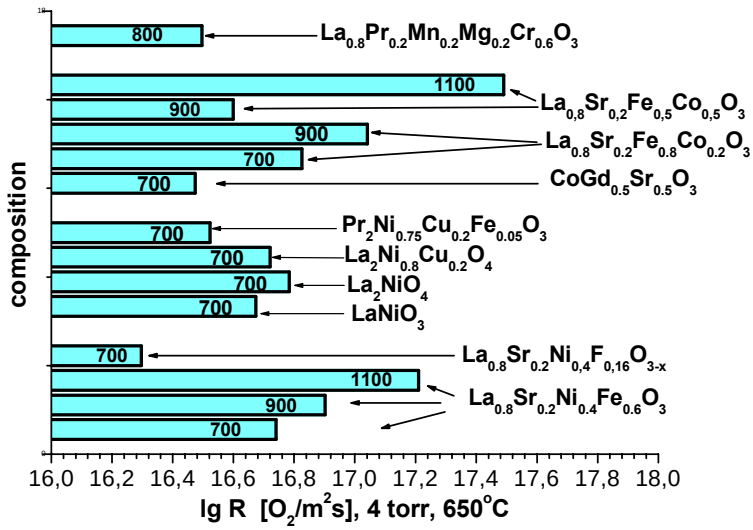

Figure 28. Specific rate of the oxygen heteroexchange at 650 ^oC and 4 Torr O_2 versus samples composition and sintering temperature.

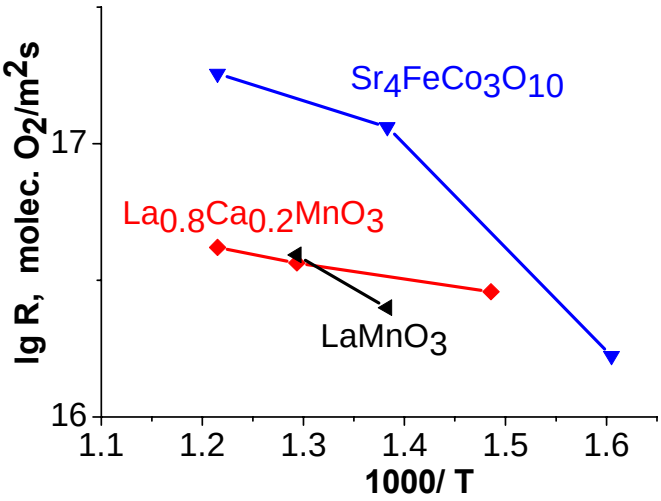

Figure 29. Temperature dependence of the specific rate of the oxygen heteroexchange at 4 Torr O_2 for $Sr_4FeCo_3O_{10}$ calcined at 1000 °C, $LaMnO_3$ and $La_{0.8}Ca_{0.2}MnO_3$ calcined at 700 °C.

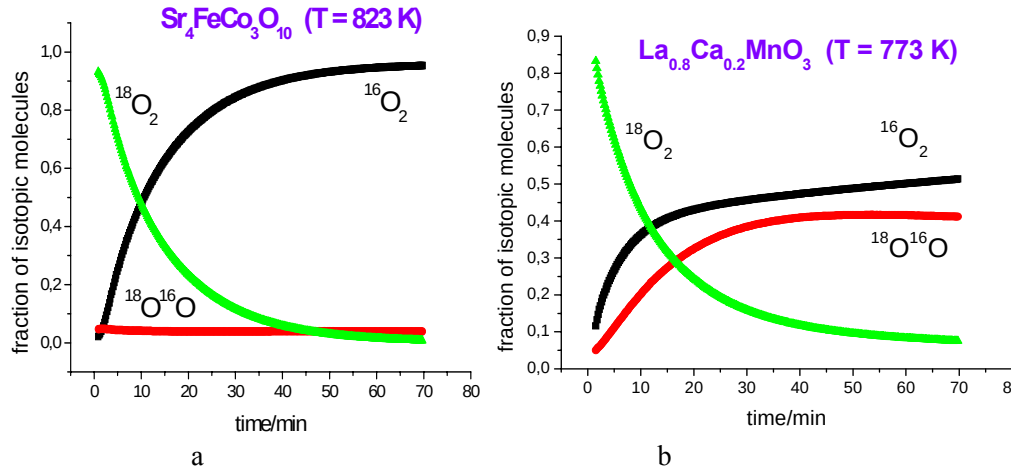

Figure 30. Typical dynamics of the oxygen exchange for perovskite catalysts in isothermal experiments.

The possibility of exchange mechanism discrimination is clearly illustrated by Fig. 30, in which the variation of the mole fractions of isotope dioxygen molecules with time is shown for two samples greatly differing by the lattice oxygen mobility. In both cases the initial gas was entirely comprised of the $^{18}O_2$ molecules. However, for the Sr-Fe-Co-O sample (Fig. 30a), asymmetric isotope $^{18}O^{16}O$ molecules were not formed while for La-Ca-Mn-O sample they appeared in considerable amounts (Fig. 30b). The complete absence of the asymmetric isotope $^{18}O^{16}O$ molecules is the unequivocal evidence that only the 3rd type of exchange operates (κ_3 = 1). Indeed, in this case, according to Eq. (III) (vide supra) the dioxygen molecule is exchanged for two atoms of oxygen from the oxide (which in the initial state was characterized by the natural oxygen isotope abundance, i.e. the heavy isotope was practically absent), and the number of emerging $^{16}O_2$ molecules is equal to the number of consumed $^{18}O_2$ molecules. For Ca-doped lanthanum manganite (as well as for $LaMnO_3$) the 2nd type of

exchange apparently dominates since, according to Eq. (II), it generates asymmetric molecules.

Analysis of the mechanism of exchange for various perovskites revealed that contribution of the 1st type of exchange is very small being noticeable (~0.4) only for $LaMnO_3$ at rather low (~ 723 K) temperatures. The 3rd type of exchange usually dominates, while in some cases (manganites, doped manganites) the contribution of the 2nd type (~ 0.6) becomes substantial as well. The higher is the lattice oxygen mobility (the bigger amount of exchangeable oxygen), the larger is the contribution of the 3rd type, which entirely determines exchange at high temperatures.

The interrelation between the types of exchange and possible mechanism of this process is considered in detail in [56]. The results obtained in the present work agree well with the most commonly encountered two-step mechanism of dioxygen exchange with oxides [56]:

$$\text{Step 1: } O_2 + Z_{ads} + (\ )_s \Leftrightarrow ZO_{ads} + (O)_s \tag{42}$$

$$\text{Step 2: } ZO_{ads} + (\ )_s \Leftrightarrow Z_{ads} + (O)_s \tag{43}$$

Here, a weakly bound form of adsorbed oxygen ZO_{ads} and a strongly bound oxygen of the surface layer $(O)_s$ participate.

When this mechanism operates, oxygen exchange of the 1st type is absent, and contributions of the 2nd and 3rd types are determined by the ratio of rates of steps (1) and (2):

$$\kappa_2 = \rho_1/(\rho_1 + \rho_2) \text{ and } \kappa_3 = \rho_2/(\rho_1 + \rho_2); \tag{44}$$

Here ρ_i (i = 1, 2) — the unidirectional rate of the i–th step (the number of events per unit of time) at equilibrium, (i.e. the rate of forward and backward reactions in conditions when they are equal).

When the 1st type of exchange is observed, a reversible dissociative adsorption of oxygen into a weakly bound form is suggested:

$$O_2 + 2\ Z_{ads} \Leftrightarrow 2\ ZO_{ads} \tag{45}$$

At last, a high oxygen mobility in the lattice suggests that there is a reversible transfer between the surface and bulk oxygen atoms:

$$(O)_s + [\ ]_v \Leftrightarrow (\ )_s + [O]_v \tag{46}$$

By itself, the isotope-exchange method does not allow to elucidate the physical nature of the participating oxygen forms. However, it allows one to make certain conclusions about their amount, atomic composition, bonding strength with the surface, mobility, types of elementary steps and relation between their rates. To elucidate the nature of the active oxygen forms, the isotope exchange method should be applied in combination with other experimental (O_2 TPD, TPR) and theoretical techniques (vide infra).

So, for manganites, operation of the 1 and 2 type of exchange at relatively low temperatures provides a high overall rate of exchange despite a low concentration of surface/bulk vacancies.

2.5.2. Oxygen TPD

Typical O_2 TPD spectra are shown in Fig. 31-35, while their parameters (W_{max} and θ, amount of oxygen desorbed in the TPD run) are given in Table 3 and in Fig. 36.

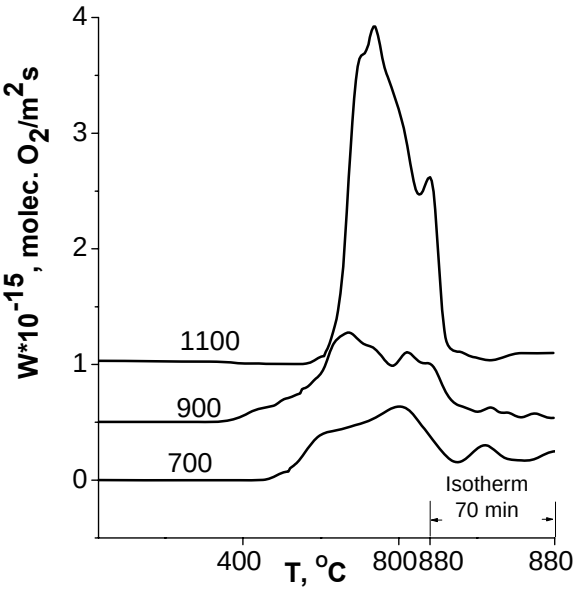

Figure 31. Typical TPD spectra for $La_{0.8}Sr_{0.2}MnO_{3-x}$ perovskite calcined at 700, 900 and 1100°C.

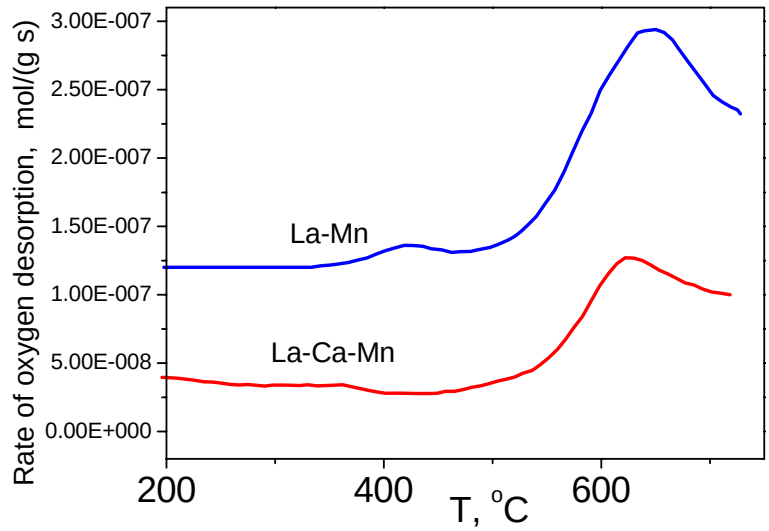

Figure 32. Typical TPD spectra for $LaMnO_{3+x}$ and $La_{0.8}Ca_{0.2}MnO_{3+x}$ perovskites calcined at 700 °C.

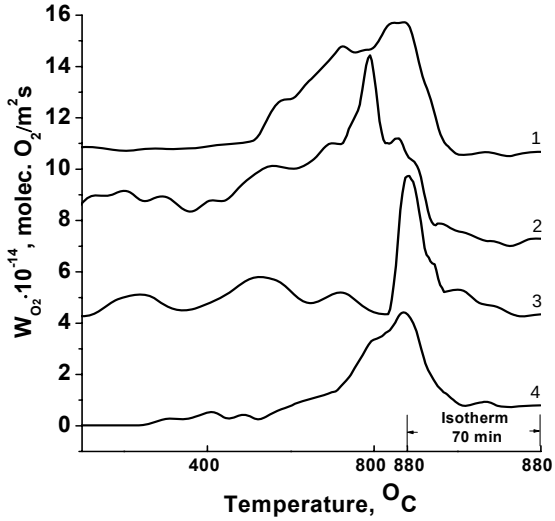

Figure 33. Typical TPD spectra for some complex perovskites. 1-$La_{0.8}Sr_{0.2}Fe_{0.8}Co_{0.2}O_3$, 2-$La_{0.8}Sr_{0.2}Fe_{0.5}Co_{0.5}O_3$, 3-$La_{0.8}Sr_{0.2}Fe_{0.6}Ni_{0.4}O_3$ calcined at 700°C, 4-$La_{0.8}Sr_{0.2}Fe_{0.6}Ni_{0.4}O_3$ calcined at 1000°C (x0.1)

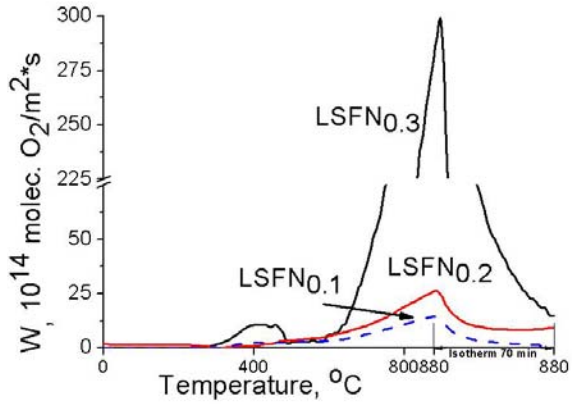

Figure 34. Effect of Ni content in $La_{0.8}Sr_{0.2}Fe_{1-x}Ni_xO_3$ perovskites annealed at 1200 ^{0}C on O_2 TPD spectra.

Table 3. Parameters of O_2 TPD for some perovskites

System	Temperature of calcination, °C	$W_{max}\cdot10^{-15}$, molec. $O_2/(m^2\cdot s)$	T_{max}, °C	θ,* monolayers
$La_{0.8}Sr_{0.2}Fe_{0.8}Co_{0.2}O_3$	700	0.5	876	0.36
$La_{0.8}Sr_{0.2}Fe_{0.5}Co_{0.5}O_3$	700	0.7	790	0.61
$La_{0.8}Sr_{0.2}Fe_{0.6}Ni_{0.4}O_3$	700	0.6	880	0.20
	1100	4.4	872	2.88
$La_{0.8}Sr_{0.2}MnO_3$	700	0.7	817	0.76
$La_{0.8}Sr_{0.2}MnO_{2.98}$	1100	2.9	723	1.32
$La_2Ni_{0.8}Cu_{0.2}O_4$	700	3.4	764	0.56

*Desorbed in the course of TPD run

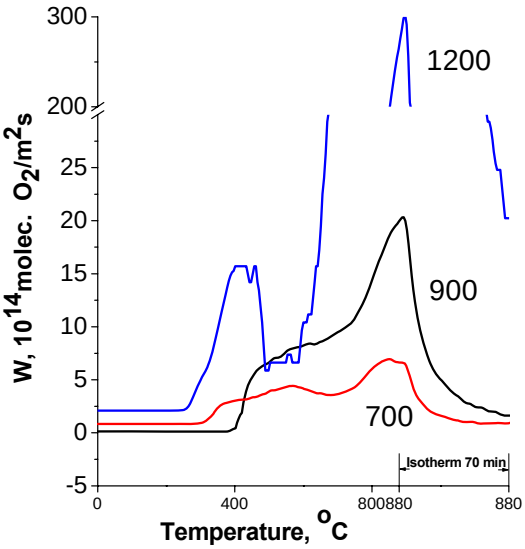

Figure 35. Effect of sintering temperature on O_2 TPD spectra of $La_{0.8}Sr_{0.2}Fe_{0.7}Ni_{0.3}O_3$ perovskites.

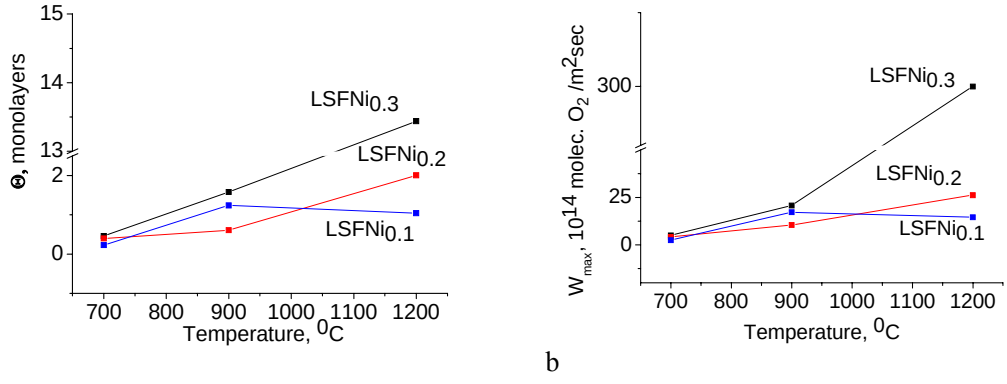

a b

Figure 36. Effect of $La_{0.8}Sr_{0.2}Fe_{1-x}Ni_xO_3$ perovskites sintering temperature on the amount of oxygen removed during TPD run (a) and the maximum rate of oxygen desorption (b).

According to these data, perovskites of a different chemical composition containing Co, Ni, and Mn cations able to change their charge state in studied temperature range accompanied by the loss of oxygen from the lattice show similar rates of O_2 desorption in the main peak situated at 700-880°C. Traditionally, this rather narrow high-temperature peak is termed as β-form [6] related (at least, in part) to oxygen desorption from the bulk of perovskite particles. Oxygen forms desorbed at lower temperatures (α-forms) are assigned to surface oxygen species [6]. Though in our experiments θ is below monolayer for samples calcined at 700°C (Table 3), this does not mean that only the surface oxygen is desorbed. Indeed, for R-P type phase $La_2Ni_{0.8}Cu_{0.2}O_4$ calcined at 700 °C a higher maximum rate of O_2 desorption can be explained by a higher lattice oxygen mobility provided by the oxygen interstitials (vide supra). Usually the surface terminal oxygen forms with the heats of adsorption up to 60 kcal/mol are desorbed at temperatures up to 600-700 °C [60, 107, 108].

Hence, several peaks situated in the 300-700 ^{o}C temperature range (Fig. 33-35) can be assigned to desorption of various surface oxygen forms including those bound with the regular and defect surface sites. Indeed, for manganites (Table 4), the surface coverage by forms desorbed at low temperatures is quite small, so they are to be bound with defect sites. The surface coverage by oxygen MO forms which can be desorbed before the main peak is in the range of 10 % of monolayer, which agrees with results for simple transition metal oxides [107, 108]. Doping lanthanum manganite with Ca cation decreases the amount of desorbed oxygen which is mainly determined by respective decrease of the oxygen excess controlled by the defect chemistry of this perovskite (Table 4). Doping with bigger Sr cation apparently increases lattice oxygen mobility, especially for sample sintered at high temperatures.

For Co-containing system the intense oxygen desorption starts at lower temperatures as compared with nickelates calcined at the same temperature, and a larger amount of oxygen is desorbed correlating with a lower bonding strength of oxygen with Co cations than with Ni, Fe or Mn cations [60, 107, 108]. Calcination of samples at higher (up to 1200°C) temperature results in increasing the rates of O_2 desorption and amount of desorbed oxygen as well as in shift of T_{max} to lower temperatures. This suggests that sintering at higher temperatures facilitates oxygen desorption and increases the lattice oxygen mobility which agrees with the results of oxygen isotope exchange obtained in conditions of oxygen chemical equilibrium between the gas and solid phases. LSNF perovskite in these conditions again demonstrates a high oxygen mobility promising for the application as cathode material. Since the increase of the desorption rate and amount of desorbed oxygen is clearly sensitive to the Ni content being the most pronounced for $La_{0.8}Sr_{0.2}Fe_{0.7}Ni_{0.3}O_3$ sample (Fig. 36), this suggests that indeed high temperature sintering really accelerates the lattice oxygen mobility, perhaps, by providing developed domain boundaries as paths for fast oxygen chemical diffusion. Since the amount of desorbed oxygen is usually smaller than the amount of easily exchanged oxygen (vide supra), preferential removal of oxygen from the vicinity of domain boundaries can be suggested. Hence, O_2 TPD data are in favor of domain boundaries as paths for fast oxygen diffusion.

Table 4. Amount of oxygen desorbed from lanthanum manganite samples

Sample/$S_{specific}$, m^2/g	Amount of oxygen desorbed, % monolayer		
	Weak surface forms[a]	Strong surface forms[b]	Lattice oxygen[c]
$LaMnO_{3.19}$/20	0.7	11	40
$La_{0.8}Ca_{0.2}MnO_{3.07}$/24	0.8	6.5	25

[a]-removed up to 500 ^{o}C;[b] removed before the main desorption peak; [c] -removed in the main desorption peak and during isothermal desorption at 880 ^{o}C.

2.5.3. Theoretical Analysis of The Heats of Oxygen Adsorption and Migration

To understand molecular-scale factors controlling oxygen mobility in perovskites, theoretical analysis of possible types of surface adsorption sites and paths for oxygen migration is very helpful [60, 102, 109-112]. For this purpose, semiempirical Interacting Bonds method [60, 110] and DFT method [112] were applied for analysis of these features for manganites, ferrite and cobaltites of La and Sr. Calculations by the Interacting Bonds method have revealed the lowest surface energy for the (100) and (111) faces of perovskites (Table

5), which are thus expected to be the most developed under equilibrium conditions. For the same face of a perovskite, different terminations can be realized.

Table 5. Surface energies (H_s) and heats (qO_2) of oxygen adsorption (kcal/mol) on perovskites

Parameter	Face					
	(100)		(110)		(111)	
H_s ($LaMnO_3$)	69.6		126.9		110.7	
Face composition	MeO_2	LaO	LaMeO	O_2	LaO_3	Me
qO_2						
O-Mn	53		65			68
O-La		72	79	46	58	64
O-La_2		177				
O-La_2Mn			234			
O-MnLa						160
O-Fe	51		68			72
O-Co	43		60			63

Due to steric reasons, bridging (O-Me_n) oxygen forms could not exist on a (100) face with MeO_2 termination, on a (110) face with O_2 termination and on a (111) face of LaO_3 composition. For the regular sites, the minimum heats of oxygen adsorption in the terminal (O-M) form on Mn and La cations are comparable (Table 5), being in the range of 50 kcal/mol. This value is close to the activation energy of O_2 desorption estimated for the main TPD peak (β-form, vide supra). However, since oxygen desorption from oxides is associated with the reduction of cations, desorption of oxygen forms bound with La cations is considered to be impossible. Bridging forms are too strongly bound to be desorbed up to 800 ^oC. Since the enthalpy of oxygen removal from the bulk of lanthanum manganite or LSM is ~ 30 kcal/mol [20], this suggests that indeed desorption of the terminal Mn-O oxygen in the main TPD peak is accompanied by fast replenishment of the surface vacancy by oxygen transferred from the near-surface layers. All desorption forms observed at lower temperatures are assigned to oxygen atoms bound with defect centers.

As a model for such a center, Mn cation migrating from the subsurface layer and filling the La vacancy on the (100) face is suggested. Such a process was estimated to be energetically favorable (~ 40 kcal/mol is gained). It could be even more favorable in the vicinity of extended defects and in lanthanum manganites with a big oxygen excess. Indeed, calculations by DFT [112] revealed that for lanthanum manganite with a big concentration of La vacancies ($La_{0.75}MnO_3$), a stable local structure is formed by the shift of Mn cation from the regular position towards the defect La-O plane. As the result, Mn^{4+} cation appears, and oxygen bound with this cation decreases its effective charge to O^-. In the surface defect position, a Mn cation is 5-coordinated. The oxygen adsorption on such a center should proceed with preservation of 5-fold Mn coordination, which can only be satisfied by simultaneous breaking of the Mn-O bond with one of the surface oxygen. As the result, the heat of oxygen adsorption on such a defect center decreases to 35 kcal/mol.

For Ca- or Sr-modified samples, Ca (Sr) migration from the bulk to the surface (100) faces was found to be energetically favorable as well, which agrees with SIMS data [110]. As

a result, a part of the terminal O-Mn oxygen forms is converted into the bridging (Mn-O-Ca) ones. This explains a decline of intensity of the high-temperature O_2 TPD peak observed for these samples.

For lanthanum ferrite and cobaltites, the energies of the oxygen adsorption were found to be comparable with those in lanthanum manganite (Table 5).

Since lanthanum manganites with the oxygen excess are characterized by the presence of cation vacancies in the lattice, it is worth to consider their effect on oxygen diffusion. It is well known that the saddle-point for the oxygen atom jump in the perovskite lattice is a triangle formed by two La and one Me cations [26, 27]. Though no diffusion is apparently possible in stoichiometric perovskites without anion vacancies, however, in the course of oxygen desorption or reduction, anion vacancies are generated at the surface and rapidly migrate into the bulk. At moderate temperatures in dynamic conditions of desorption/reduction, cation vacancies are not annealed due to a low mobility of cations, so they could facilitate the oxygen atoms migration by decreasing the activation barrier. Moreover, domain boundaries are usually characterized by less dense structure than domains, which can be due to a high concentration of cation and anion vacancies.

To quantify this hypothesis, semiempirical Interacting Bonds method was applied to estimate the oxygen migration energies for different configurations of the saddle point for simple perovskites (Table 6).

Table 6. Migration energies for different saddle-point configurations

Metal	E_m, kcal/mole			
	Regular	V_{Me}	V_{La}	$2V_{La}$
Cr	47	35	34	21
Mn	43	36	30	16
Fe	45	36	31	17
Co	43	36	28	14

As follows from the results shown in Table 6, cation vacancies indeed considerably decrease the potential barrier for the oxygen migration in the lattice. For the case of two lanthanum vacancies, calculated values are rather close to the experimental enthalpies of oxygen vacancies migration [35].

To elucidate the effect of the local structure of perovskite-like Sr-Fe(Co)-O systems with the oxygen deficiency on their oxygen mobility, $SrCoO_x$ (x=2.875, 2.75, 2.5 and 2) and $SrFeO_x$ (x=2.875, 2.75 and 2) systems were analyzed by DFT technique. For $SrCoO_x$ two kinds of oxygen vacancy ordering were revealed with energies 0.17 and 0.39 eV lower in comparison with random vacancy distribution (Fig. 37). As the result of such ordering, pairs of five-coordinated Co cations and string of 4-coordinated Co cations are formed. Transition between these ordered vacancy systems could be a step in ionic conductivity mechanism with activation energies of 0.61 and 0.78 eV depending on the direction of transformation. For $SrFeO_x$ the oxygen vacancy formation is more energy consuming, and only one type of vacancy ordering is preferable than a random distribution. Hence, these results agree in general with hypothesis about interstitial mechanism of oxygen conduction in mixed Sr-Fe-Co-O oxides with intergrown structure, where variation of the local coordination of Fe and Co cations provides low energy barriers for the oxygen migration [111, 113].

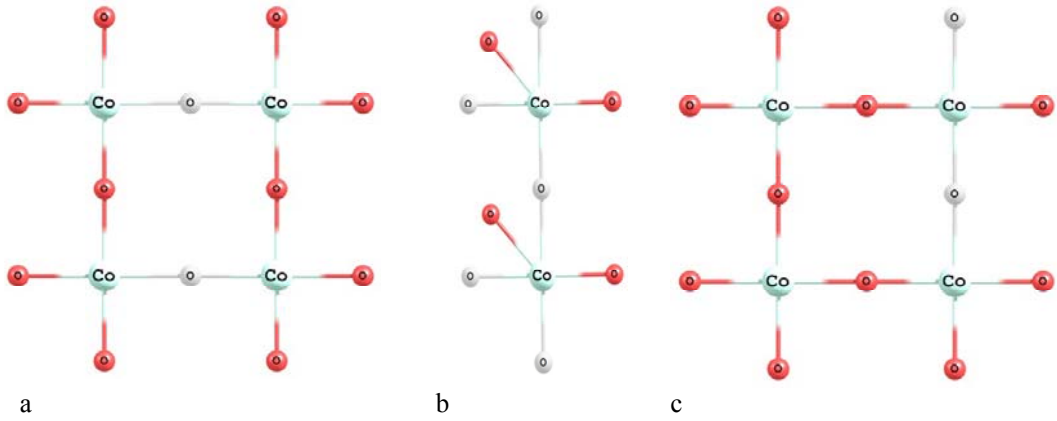

Figure 37. Two types of oxygen vacancy ordering in $SrCoO_x$ perovskite-like oxide and a transition configuration between them. a-pairs of 5-coordinated Co, E_5-E_4=0.18 eV; b-transition configuration, E_t-E_4=0.78 eV; c-4-coordinated Co, E_4=0.39 eV. Oxygen atoms outside the plane of Figure are not shown. Oxygen atoms are marked by red, oxygen vacancies – by white.

2.5.4. H_2 TPR

The temperature-programmed reduction by H_2 characterizes the surface oxygen reactivity and lattice oxygen mobility in oxide systems under large gradient of the oxygen chemical potential typical for operation of membranes for syngas production. Typical H_2 TPR spectra for basic types of studied perovskites are shown in Figs. 38-43. Usually, several peaks are observed corresponding to main steps of transition metal cations reduction up to Me^{2+} (Mn) or Me^o (Ni, Co, Fe) state.

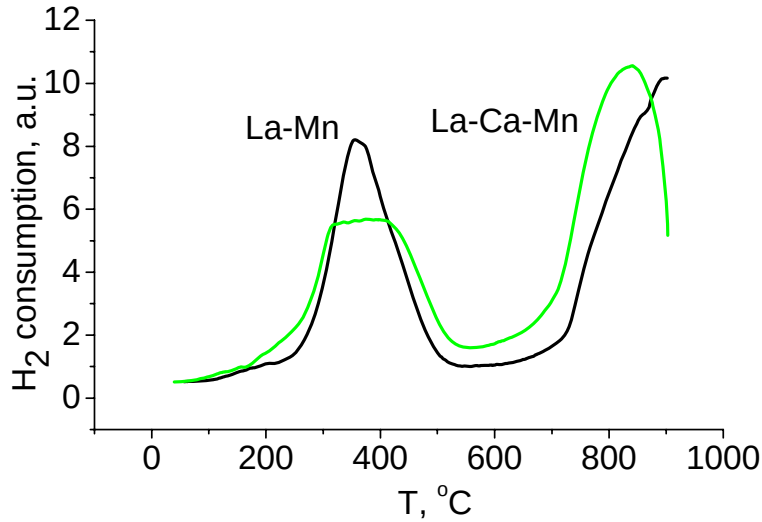

Figure 38. Typical H_2 TPR spectra for $LaMnO_{3.19}$ and $La_{0.8}Ca_{0.2}MnO_{3.07}$ samples calcined at 700 °C.

The first peak of the lanthanum manganite sample bulk reduction at ~ 350 °C (Fig. 38) corresponds to reduction of Mn^{4+} cations into Mn^{3+} state without destruction of perovskite lattice. The second TPR peak corresponds to the $LaMnO_3$ perovskite reduction into a mixture

of simple oxides (MnO +La_2O_3). Ca addition broadens the first TPR peak, which correlates with the decline of the intensity of O_2 TPD peak (Fig. 32). Sr doping produces similar but more pronounced effect (Fig. 39), so the first peak splitting is apparent, which agrees with earlier published results [114]. While position of the low-temperature component of this peak at ~ 300 ^oC does not vary with the sintering temperature, the second component position is shifted to higher temperatures. This suggests some heterogeneity of the state of easily reducible Mn^{4+} cations in doped lanthanum manganite. To clarify the reason of this heterogeneity, the amount of oxygen removed from the sample at different stages of reduction was calculated.

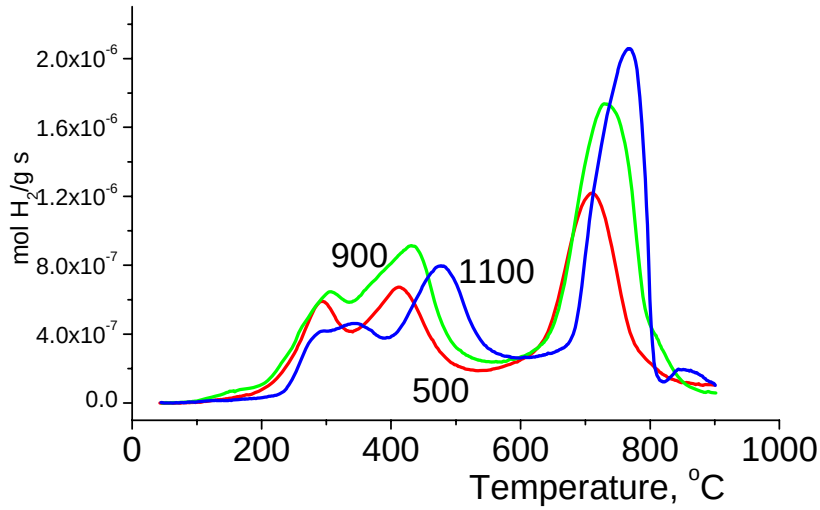

Figure 39. Typical H_2 TPR spectra for $La_{0.8}Sr_{0.2}MnO_3$ samples calcined at 500 -1100 ^oC.

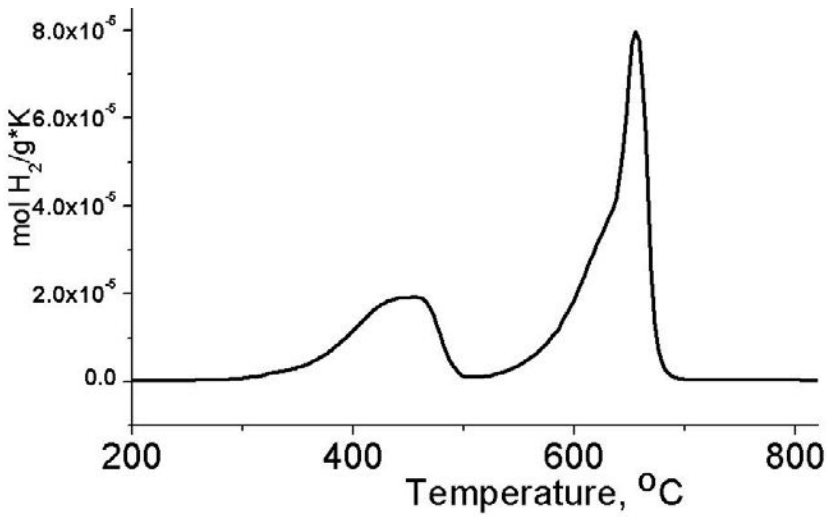

Figure 40. Typical H_2 TPR spectra for $LaCoO_3$ sample calcined at 1100 ^oC.

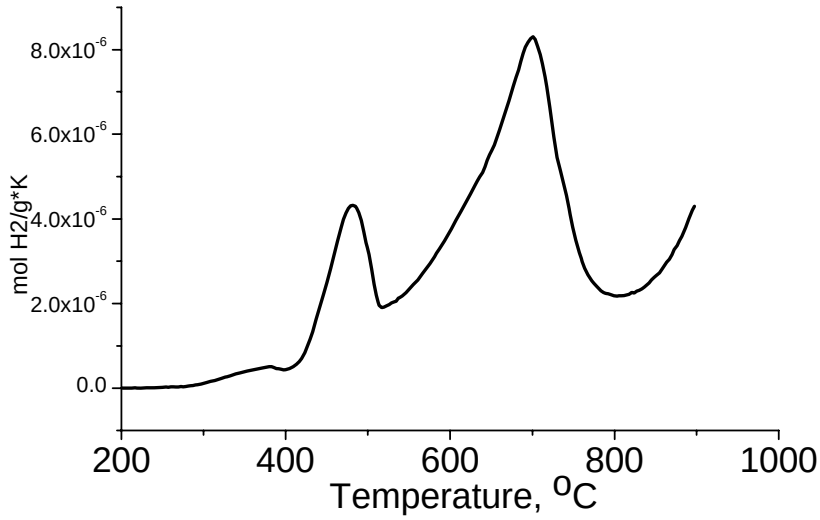

Figure 41. Typical H_2 TPR spectra for $LaFeO_3$ sample calcined at 1100 °C.

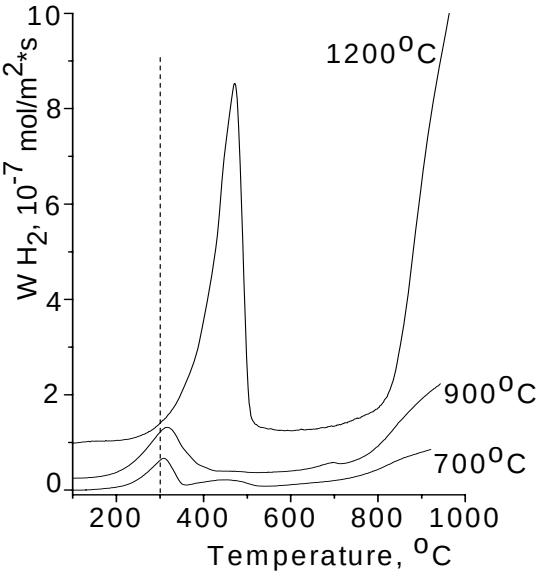

Figure 42. Effect of sintering temperature on H_2 TPR spectra for $La_{0.8}Sr_{0.2}Fe_{0.7}Ni_{0.3}O_3$ perovskites.

In estimation of the amount of oxygen required to be removed for reduction of all Mn^{4+} cations in a sample to the Mn^{3+} state, Mn^{3+} disproportionation into Mn^{2+} and Mn^{4+} by the model of Roosmalen et al [115] was taken into account. For $La_{1-x}Ca_xMnO_{3+\delta}$ the degree of disproportionation ξ was estimated by the equation [110, 115]:

$$\xi\,(x+2\delta+\xi)/(1-x-2\delta-2\xi)^2 = K;\ \text{here } K = 1.414$$

Comparison of experimental and theoretical amounts of oxygen removed in the low-temperature peak revealed their good agreement for $LaMnO_{3.15}$ and $La_{0.8}Ca_{0.2}MnO_{3.07}$

samples [110]. For these samples, the total amount of Mn^{4+} due to the oxygen excess, Ca substitution and disproportionation is ~ $6*10^{-4}$ mol O/g (Table 7). Complete reduction of all Mn^{4+} cations in the bulk of particles at moderate temperatures in a narrow peak suggests a high lattice oxygen mobility, which is not expected in stoichiometric undoped lanthanum manganite where oxygen vacancies are absent (vide supra). As follows from Table 7, a similar conclusion on a high rate of oxygen diffusion from the surface to the bulk of lanthanum ferrite and cobaltite particles in the course of reduction without destruction the perovskite lattice can be made. The maximum rates of reduction are comparable for lanthanum manganite and ferrite, which agrees with similar heats of oxygen adsorption in the reactive MO form (Table 5) and close values of oxygen migration energy (Table 6). A higher reduction rate for lanthanum cobaltite agrees with a lower bonding strength of the MO oxygen form (Table 5) as well as a lower oxygen migration energy (Table 6). Hence, under conditions of very high oxygen chemical potential gradient between the surface and the bulk of perovskites, the oxygen flux is determined by fast migration of oxygen vacancies from the surface into the bulk of particles facilitated also by a lower bonding strength of oxygen with transition metal cations in the high oxidation state as well as by the presence of cations vacancies decreasing the oxygen migration energies in strongly non-equilibrium conditions of TPR experiments [110].

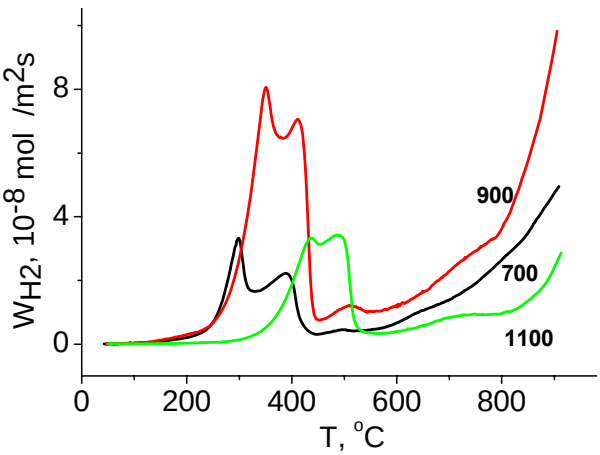

Figure 43. Effect of sintering temperature on H_2 TPR spectra for $La_{0.8}Sr_{0.2}Fe_{0.8}Co_{0.2}O_3$ perovskites.

For Sr-doped manganites the amount of oxygen removed in peaks situated in 300-500 °C range exceeds that for $LaMnO_{3.15}$ and $La_{0.8}Ca_{0.2}MnO_{3.07}$ samples (Table 7). Hence, for Sr-doped samples a part of Mn^{3+} cations is apparently reduced in the low-temperature range as well. The increase of the maximum reduction rate with sintering temperature (Table 7) correlates with respective increase of oxygen desorption rates (Fig. 31). This suggests that facile paths of oxygen vacancies migration from the surface of LSM particles into the bulk are associated with domain boundaries since their density increases with sintering (vide supra). Generation of bulk oxygen vacancies due to Sr doping and sintering at higher temperatures (Table 7) could facilitate reduction as well. However, since $SrMnO_3$ is more stable at low oxygen partial pressures than $LaMnO_3$ [20], Mn cations having Sr cations as next –nearest neighbors could be less reactive than those neighboring with a cation vacancy

or generated by Mn^{3+} disproportionation. This seems to explain superposition of two H_2 TPR peaks of LSM reduction in the low-temperature range.

Table 7. Some characteristics of perovskites reduction by hydrogen

Sample	Amount of oxygen removed in 1st peak(s), 10^{-4} mol/g	Rate at T_{max}, 10^{16} molec. H_2/m^2s
$LaMnO_{3.19}$	5.8	4.3*
$La_{0.8}Ca_{0.2}MnO_{3.07}$	5.5	2.7
$La_{0.8}Sr_{0.2}MnO_3$, 500 °C	6.8	1.8
$La_{0.8}Sr_{0.2}MnO_3$, 900 °C	10	3.5
$La_{0.8}Sr_{0.2}MnO_3$, 1100 °C	8.2	27
$LaFeO_3$ 1100 C	17% of Fe^{3+} to Fe^{2+}	17 (480 °C)
$LaCoO_3$	All Co^{3+} to Co^{2+}	2000 (470 °C)

*An order of magnitude higher rate at T_{max} ~ 450 °C was obtained for a sample with $S_{sp.} = 1$ m^2/g

The reduction of LSFN perovskite is characterized by two peaks located in the temperature range 200–400°C followed by continuous reduction at temperatures exceeding 600 °C (Fig. 42). Similar pattern was earlier observed for $LaNi_xFe_{(1-x)}O_3$ perovskites [80, 116]. The low-temperature peaks were shown to correspond to reduction of Ni^{3+} and Fe^{3+} into 2+ state thus producing a defect perovskite structure, while the high-temperature peak –to reduction of Ni and Fe cations to Me^o state forming an alloy dispersed on lanthana particles. As judged by the balance of removed oxygen for LSNF sample (not shown for brevity), this scheme is also valid in our case. The increase of LSFN calcination temperature also increases the peak reduction rate (Fig. 42) and shifts reduction peak to higher temperatures. This correlates with the increase of the specific rate of oxygen desorption from this perovskite with the increase of sintering temperature (Fig. 36b). Hence, for this system the oxygen mobility in the oxidized and reduced state apparently correlates.

For $La_{0.8}Sr_{0.2}Fe_{0.8}Co_{0.2}O_3$ perovskites (Fig. 43) H_2 TPR spectra are more complex consisting of several overlapping peaks due to simultaneous reduction of Co and Fe cations. The peak rate of reduction in the middle-temperature range goes through the maximum with the sintering temperature, perhaps, reflecting rearrangement of the real structure.

2.5.5. CH_4 TPR

Reduction of perovskites by methane (Figs. 44-47) usually proceeds at higher temperatures as compared with the reduction by H_2 (Figs. 38-43) due to strong C-H bond in CH_4 molecule. Isothermal reduction kinetics corresponds to that of a typical topochemical process with nucleation of reduced phases (oxides or metals), growth of nuclei with time described by the Avrami- Erofeyev equation followed by their overlapping and decline of observed reduction rate described by the contracting spheres model [80] (vide infra examples of isothermal reduction for LSFN-GDC composites). So the maximum rate of perovskites reduction in isothermal experiments is expected to be determined both by the density of possible nucleation sites (usually, sites with enhanced reactivity associated with defects such as dislocations, including those located at domain boundaries etc, vide supra), as well as the bulk oxygen mobility. Since O_2 TPD and oxygen isotope exchange studies suggest that oxygen mobility correlates with the extension of domain boundaries, the maximum rate of

perovskites reduction by methane is expected to correlate with the bulk oxygen mobility as well. For CH_4 as reductant, another important parameter is selectivity of methane transformation into products of deep oxidation (H_2O and CO_2) and selective oxidation (CO and H_2) [11, 60, 63]. It is determined both by bonding strength of reactive surface oxygen forms (determines primary selectivity of CH_4 activation) and by the flux of oxygen from the bulk of particles to their surface (determines possibility of CO and H_2 combustion). Moreover, for some perovskites containing Ni, Fe and Co cations, dissociation of CH_4 molecules yielding H_2 and surface carbon proceeds on metal particles even after complete reduction of samples [117]. All this determines a complex shape of CH_4 TPR spectra shown in Figs. 44-47. Reduction process starts by formation of deep oxidation products at 400-500 ^oC. Several overlapping peaks of CO and H_2 evolution are usually observed reflecting step-wise reduction of perovskites discussed above. Similarly, several peaks of products formation are also observed in CH_4 TPR spectra of MnO_2, apparently reflecting sequence of phase transitions MnO_2-Mn_2O_3-Mn_3O_4-MnO in the course of reduction (Fig. 45). A higher selectivity of CO + H_2 formation in the course of La-Sr-Mn-O reduction by CH_4 (Fig. 46) versus that for the MnO_2 case is the most probably explained by dilution effect of irreducible La cations and a higher, in general, bonding strength of oxygen forms bound with Mn cations in perovskite. Coordinatively unsaturated Mn^{2+} cations located at the surface of lanthana particles continue to dissociate CH_4 molecules even after complete reduction of manganite forming carbonaceous deposits.

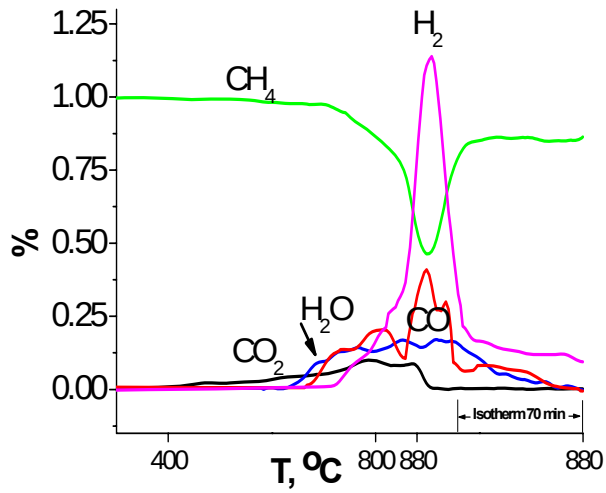

Figure 44. CH_4 TPR spectra for $La_{0.8}Sr_{0.2}MnO_3$ sample calcined at 900 ^oC.

Maximum rates of CO and CO_2 evolution for manganites (Table 8) are usually achieved in the isothermal part of TPR run at 880 ^oC. Maximum rates of CO and CO_2 formation are not sensitive to the $LaMnO_3$ surface modification by Pt, which agrees with suggestion about their control by the rate of oxygen diffusion from the bulk of particles to their surface. Higher maximum rates of both CO and CO_2 formation for Sr – and Ba- containing systems (Table 8) correlate with their higher lattice oxygen mobility (vide supra). For these systems as well as for $LaCoO_3$, a lower CO selectivity seems to be determined by a high oxygen flux leading to oxidation of syngas into CO_2 and H_2O.

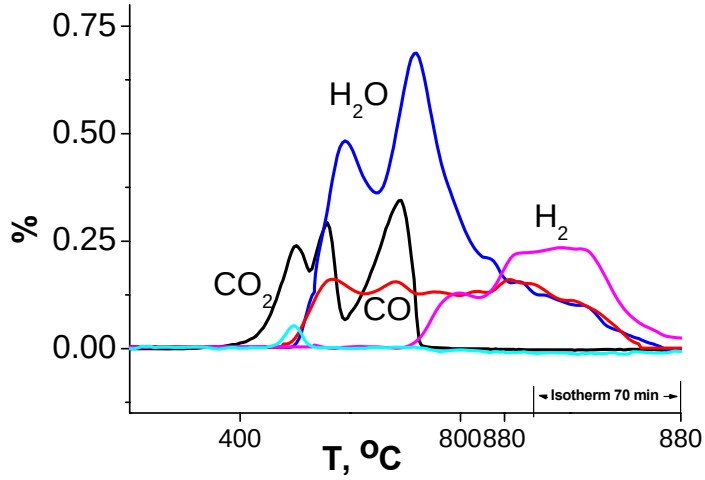

Figure 45. CH_4 TPR spectra for sample MnO_2 ($S_{sp.}$ 10 m^2/g).

Table 8. Maximum rates of some perovskites reduction by CH_4.

Sample W_{max}, 10^{16} at. O/m^2s, 880 °C	$LaMnO_{3.15}$	0.3%Pt/ $LaMnO_3$	$La_{0.8}Ca_{0.2}MnO_{3.07}$	$LaCoO_3$.	$LaFeO_3$	Sr_4FeCo_3	$Sr_{3.5}Ba_{0.5}Fe_{2.5}Co_{1.5}$
CO	1.1	1.2	0.6	3.7	15	10	20
CO_2	1.5	1.3	1.4	100	9.4	51	90

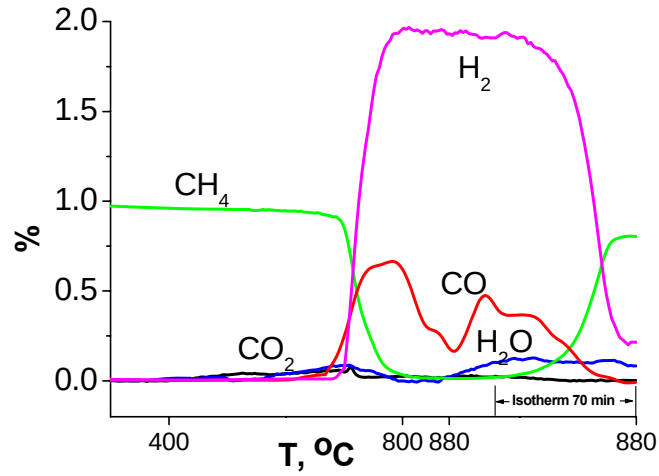

Figure 46. CH_4 TPR spectra for LSFC sample calcined at 900 °C.

For Ni- or Co-substituted La-Sr-ferrites (Figs. 46, 47) selectivity of CH_4 transformation into deep oxidation products is clearly lower than that for LSM. At 880 °C, complete conversion of CH_4 is accompanied by formation of stoichiometric amount of H_2 (2% H_2 for 1% CH_4 in He) while CO content is substantially lower (~ 0.5% or less. Hence, carbon deposition on the surface of these samples takes place.

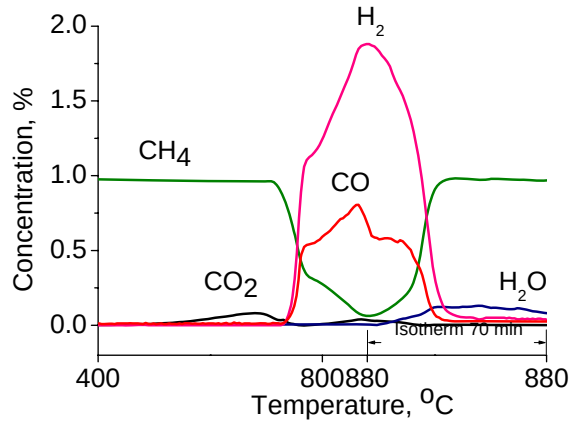

Figure 47. CH_4 TPR spectra for $LSFN_{0.3}$ sample calcined at 1200 °C.

The increase of the maximum rates of CO and CO_2 evolution with sintering temperature of perovskites (Fig. 48) clearly correlates with the increase of the oxygen mobility estimated by oxygen isotope exchange, O_2 TPD and H_2 TPR (vide supra).

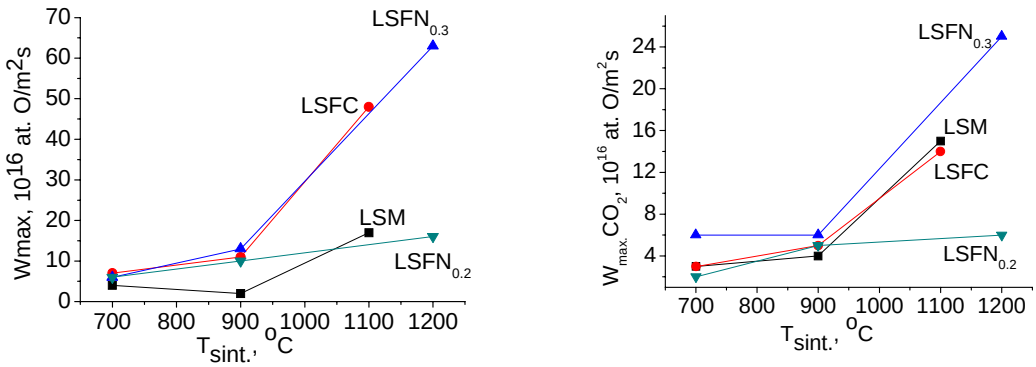

Figure 48. Effect of perovskites sintering temperature on the maximum rates of CO (a) and CO_2 (b) formation in the course of CH_4 TPR.

Hence, among studied perovskites, such systems as LSM, LSFC and LSFN appear to be promising for their application as electronic-conducting components in nanocomposite systems with a high mixed ionic –electronic conductivity in combination with ionic-conducting oxides (doped ceria or zirconia), since they possess a high conductivity along with reasonably high lattice oxygen mobility in conditions of broadly varying gradient of oxygen chemical potential.

3. PEROVSKITE-FLUORITE NANOCOMPOSITES

As it has been mentioned above, composite electrodes have many advantages compared to single-phase materials. Combination of high catalytic activity, mixed electronic and ionic

conductivity can provide excellent electrochemical properties of such materials. That is why composite materials based on perovskite solid solutions are regarded as the most promising cathode materials. In order to be used in real SOFC, the material should be compatible with solid electrolyte, interconnect and sealing materials. Mechanical compatibility of two or several densely contacting solid state materials is limited by difference in the thermal expansion coefficients which should be as small as possible. Mechanical stresses accumulated in the bulk of the material may lead to the break and pilling of cathode layers. The use of composites allows to redistribute stress directions by variation of the electrode microstructure thus diminishing the probability of the accumulation of the critical stress and avoiding fast degradation of the material.

Though in literature there are a lot of data on application of MIEC composites as cathode materials of SOFC and oxygen-conducting membranes [118-129], their synthesis procedures were usually based on mixing and milling of rather coarse-grained oxides. As the result, the interface between oxides with different predominant type of conductivity is usually not developed even in dense materials. On the other hand, the most pronounced non-additive effects related to the oxygen mobility are expected in the case of nanocomposites. It is explained by morphological instability of nanosystems at elevated temperatures. Indeed, nanocrystals or nanoceramics of pure oxides rather easily recrystallize into coarse-grained powders or ceramics. It is caused by large thermodynamic affinity to recrystallization and sintering due to high value of excess surface energy. In nanocomposite materials there are many interfaces and the excess surface energy of both components is partially compensated by the adhesion energy between the phases. It results in much lower affinity to the recrystallization process and a higher stability of the morphology of nanocomposites. With a due regard for the possible advantage of these materials, new procedures for synthesis of perovskite –fluorite nanocomposites were elaborated [11, 61, 62, 98, 99, 130-134], and results on studies of their structural characteristics and transport properties are presented below.

3.1. Preparation and Characterization of Nanocomposites

The methods of the preparation of perovskites are given above. Fluorites were synthesized similarly to perovskites using Pechini route. The ethylene glycol and distilled water solutions prepared from metal nitrates were mixed together at room temperature under stirring followed by addition of ED. The prepared solution was stirred for 60 min and then heated at 70°C for 24 h allowing for the gel formation. The gel was calcined at 25- 500°C in the case of GDC. Commercially available powders of ScCeSZ (DKKK corporation, Japan) or other fluorite phase and nano-sized powder of GDC, LSM, LSFC and LSFN synthesized via Pechini route were used for nanocomposites preparation via mixing in 1:2 (GDC:LSFC) or 1:1 ratio (all other composites) by weight.

It was found that the use of organic surfactants leads to smaller crystallite size of fluorite. Powders were ultrasonically dispersed in a solvent (distilled water, acetone) with addition of 2 wt% of a surfactant (polymethylmetacrylate, polyethylene glycol, polyvinyl butiral) using a Ika T25 ULTRA-TURRAX basic (IKA, Germany) generator. The dispersed mixture was filtered, dried in air at 25-200°C, pressed into pellets (d=15 mm, h=1 mm) under ~150 kgf/cm^2 and calcined at temperatures up to 1350°C for 5 h.

For comparison, $La_{0.6}Sr_{0.4}Fe_{0.8}Co_{0.2}O_{3+x}$ –$Ce_{0.9}Gd_{0.1}O_{2-x}$ (1:2) composite ($LS_{0.4}FC$-GDC) prepared at Imperial College (London, UK) was characterized as well. For this composite synthesis, commercially available powders of $La_{0.6}Sr_{0.4}Co_{0.2}Fe_{0.8}O_{3-\delta}$ (Praxair Specialty Ceramics, Seattle, USA) and $Ce_{0.9}Gd_{0.1}O_{1.95}$ (Fuelcellmaterials.com, Ohio, USA) were mixed in the appropriate amounts by ball-milling in ethanol. After drying, the composite powders were pressed into pellets and densified by sintering at 1250°C for 4 hours. Further details have been given in a previous publication [118, 119, 135]. Some pellets were crushed and ground with a pestle and mortar into powder ($S_{sp.}$ 0.2 m^2/g, average particle diameter 3 microns).

The samples of nanocomposites were mainly characterized by the same techniques as pure perovskites. In addition, UV-vis spectra were recorded relative $BaSO_4$ standard in the 11000–54000 cm^{-1} range using a UV-2501 PC "Shimadzu" spectrometer equipped with the diffuse reflectance ISR-240 unit. Powdered samples were put into quartz cell of 2 mm optical length. Spectra were presented as Kubelka- Munk function of the wave number.

For comparison with results of conductivity relaxation studies, values of the oxygen chemical diffusion coefficient, D_{chem}, were estimated by following the pellet weight relaxation using a STA 409 PC "LUXX" NETZSCH machine after a step-wise change of O_2 content in the N_2 stream from 14 to 1.4%**.**

The heats of oxygen absorption in the surface layers of perovskites and composites reduced by high-temperature pretreatment in He were estimated using a SEN SYS TG-DSC flow microcalorimeter and pulses of O_2 in He at 450 °C.

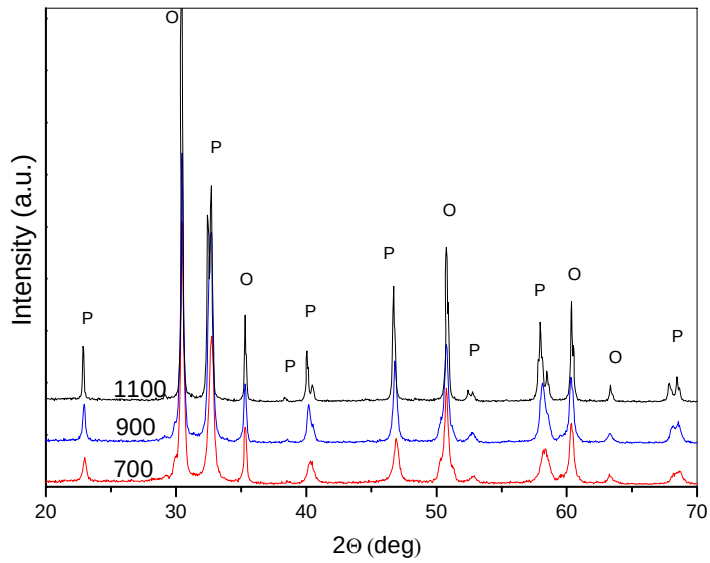

Figure 49. XRD patterns of LSM +ScCeSZ nanocomposite sintered at 700-1100 °C. P-perovskite, O-fluorite phase reflections.

3.2. Phase Composition and Structure

XRD. As follows from XRD data (Figs. 49-54), all composites are mainly comprised of a mixture of perovskite and fluorite phases. However, the structural peculiarities of samples

depend on their composition, preparation conditions and annealing temperature. Results of structural investigations showed that in all composites sintered at temperatures below 1000°C, only initial perovskite and fluorite-like phases are observed. In LSM-ScCeSZ (Fig. 49) and LSFC-GDC (Fig. 50) composites new phases were not revealed even at high sintering temperatures. However, lattice parameters of both phases vary with the sintering temperature (Table 9) reflecting redistribution of elements between phases. The increase of the lattice parameters of LSM in LSM-ScCeSZ nanocomposite with $T_{sint.}$ clearly demonstrates incorporation of bigger cations into the perovskite lattice. This can be explained only by incorporation of large Sc^{3+} and Zr^{4+} cations into the B sublattice of perovskite.

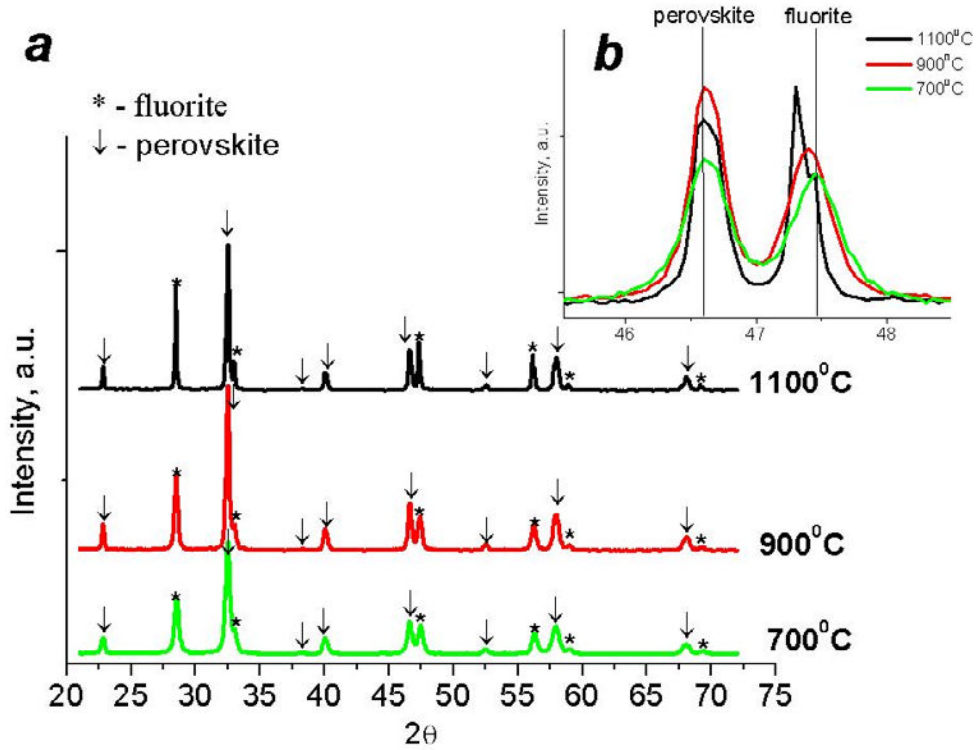

Figure 50. Typical XRD patterns of composite 70%$La_{0.8}Sr_{0.2}Fe_{0.8}Co_{0.2}O_{3-x}$+30%$Ce_{0.9}Gd_{0.1}$ calcined at different temperatures (a) and expanded range 2θ 46-48° (b).

XRD patterns of 50%$LSFN_{0.3}$ + 50%GDC composite calcined at different temperatures are shown in Fig. 51. In the composites dried after ultrasonic treatment in solvent and calcined at 700 °C, reflections corresponding to the cubic lattice of GDC and orthorhombic or rhombohedral lattice of perovskite are observed. For both phases in this composite, X-ray particle sizes are close to those for starting powders (Table 9). Sintering of composites at 900 °C increases the intensity of all reflections and narrows them (Fig. 51) due to lattice ordering and particle size increase (Table 9), without any apparent change of peaks positions.

At sintering temperature 1200 °C, for composites with $LSFN_x$ (x=0.1-0.2) only reflections of perovskite and fluorite phases are observed (Fig. 51). For $LSFN_{0.3}$ –GDC composite, weak NiO reflections appear, while for $LSFN_{0.4}$-GDC composite intensity of NiO reflections increases, which is determined by the thermodynamic instability of corresponding perovskites

[136, 137]. Note that in contrast to individual perovskites $LSFN_x$ (x=0.3-0.4) (vide supra), in the patterns of their composites the reflections of tetragonal phase are absent (Figs. 51-53). This can be explained by incorporation of La into GDC leading, among other consequences, to La_2NiO_4 consumption. Indeed, reflections corresponding to $Ce_{0.9}Gd_{0.1}O_{1.9}$ phase are shifted to lower angles (Figs. 50, 53) and the lattice parameter of fluorite phase in composites increases in all cases (Table 9) that is determined by incorporation of La and Sr cations [128] as well as a part of Ni into the fluorite lattice [138]. Similarly, parameters of perovskite phase in composites are changed as well (Table 9). Furthermore, the structure of perovskite in the composite with $LSFN_{0.3}$ changes from the orthorhombic to the rhombohedral type.

Table 9. Some structural characteristics of nanocomposite samples

Sample / T_c (°C)	S_{BET} (m^2/g)	Fluorite		Perovskite			
		d XRD (nm)	Lattice parameter **a** (Å)	d XRD (nm)	Lattice parameter (Å)		
					a	b	c
GDC/500	32	9	5.413				
GDC/700	32	24	5.420				
GDC/900	12	40	5.418				
GDC/1200	3	72	5.418				
$LSFNi_{0.1}$+GDC/700	24	18	5.420	27	5.516	5.566	7.860
$LSFNi_{0.1}$+GDC/900	9.4	32	5.434	42	5.538	5.522	7.813
$LSFNi_{0.1}$+GDC/1200	2.6	65	5.444	65	5.525	5.545	7.850
$LSFNi_{0.2}$+GDC/700	23	19	5.418	22	5.548	5.498	7.814
$LSFNi_{0.2}$+GDC/900	22	32	5.417	31	5.540	5.495	7.796
$LSFNi_{0.2}$+GDC/1200	2	44	5.438	59	5.540	5.501	7.806
$LSFN_{0.3}$+GDC/700	30	14	5.418	21	5.493	5.560	7.790
$LSFN_{0.3}$+GDC/900	12	30	5.424	29	5.480	5.532	7.789
$LSFN_{0.3}$+GDC/1200	2.4	39	5.445	50	5.491	5.535	7.802
$LSFN_{0.4}$+GDC/700	27	18	5.418	20	5.508	5.508	13.364
$LSFN_{0.4}$+GDC /900	9.5	36	5.423	35	5.500	5.500	13.363
$LSFN_{0.4}$+GDC /1200	1.0	37	5.454	59	5.501	5.501	13.344
LSFC+GDC /700	23	23	5.421	27	5.523	5.523	13.448
LSFC+GDC /900	9.2	29	5.425	41	5.519	5.519	13.452
LSFC+GDC /1100	2.1	100	5.432	54	5.517	5.517	13.450
LSM-ScCeSZ /700	26	13	5.093	33	5.499	5.499	13.365
LSM-ScCeSZ /900	8.1	24	5.097	48	5.513	5.513	13.378
LSM-ScCeSZ /1100	1.8	52	5.099	71	5.526	5.526	13.381
$LSFN_{0.2}$-ScCeSZ							
700					5.513	5.545	7.827
900					5.548	5.522	7.808
1200					5.631	5.576	7.879

For composite with ScCeSZ sintered at high temperatures (Fig. 54), along with NiO, a pyrochlore-type $La_2Zr_2O_7$ and a layered perovskite $LaSrFeO_4$ phases were formed as well. Hence, for Ni-containing composites, both Ni content in the perovskite phase and sintering temperature should be optimized to avoid segregation of low-conducting pyrochlore-type phases. The lattice parameters of LSNF phase increased with composite sintering temperature, which can be explained by a partial reduction of small Ni^{3+} cations to larger Ni^{2+} cations accompanied by the oxygen loss at high temperatures as well as by a partial incorporation of larger Zr and Sc cations into the perovskite lattice.

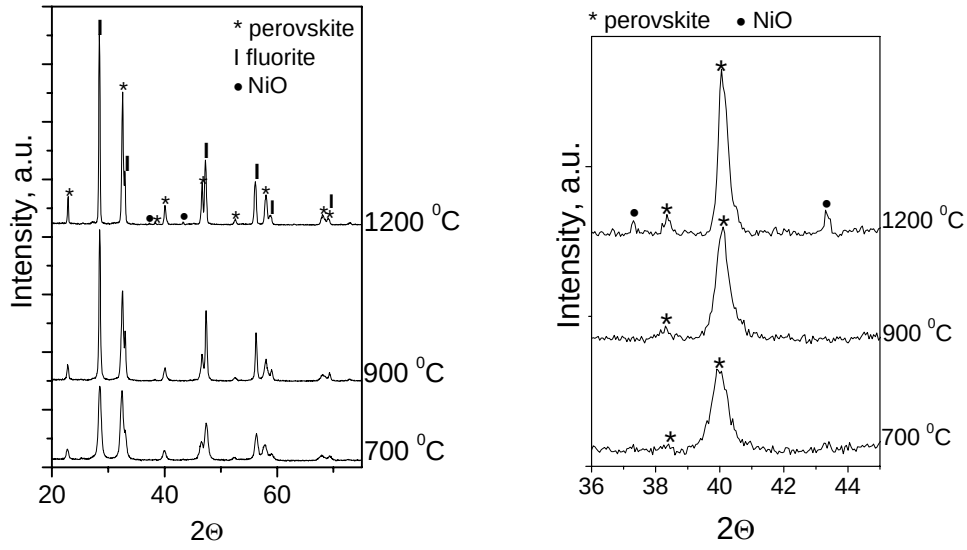

Figure 51. XRD patterns of composite $La_{0.8}Sr_{0.2}Fe_{0.7}Ni_{0.3}O_3$ +$Ce_{0.9}Gd_{0.1}O_{1.95}$ sintered at different temperatures.

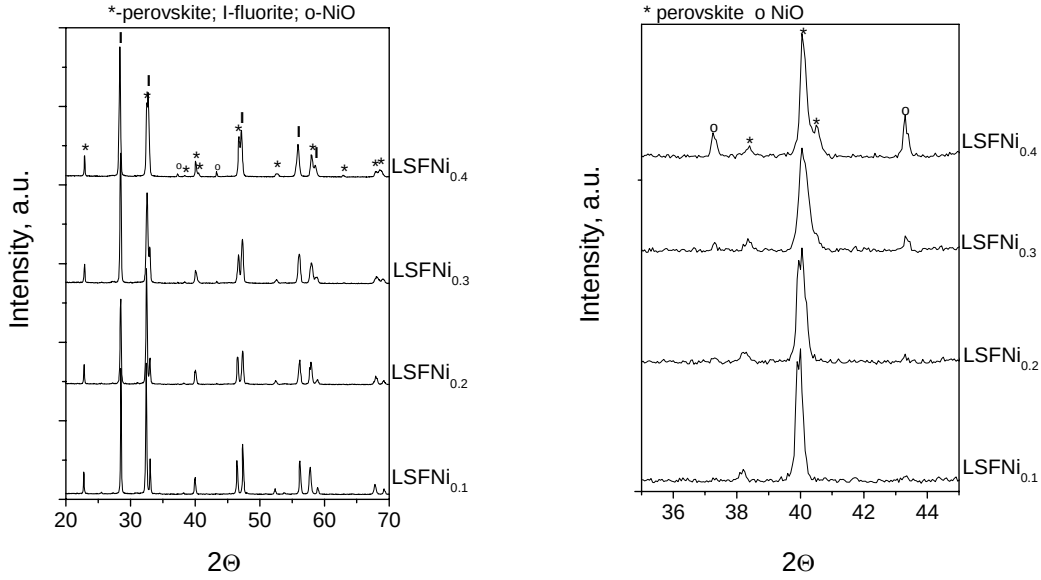

Figure 52. XRD patterns of composites $La_{0.8}Sr_{0.2}Fe_{1-x}Ni_xO_3$ + $Ce_{0.9}Gd_{0.1}O_{1,95}$ calcined at 1200 °C.

TEM and EDX. According to XRD (Table 9) and TEM data (Fig. 55), the increase of calcination temperature is accompanied by porosity annealing and the increase of particle size of both components. Estimation of the particle sizes for separate phases in nanocomposites from X-ray diffraction patterns using Sherrer equation revealed that for composite systems domain sizes of P and F phases remain on a nanoscale level even after sintering at 1200 °C (Table 9). As judged by TEM data, the nanocomposites prepared via ultrasonic dispersion route are characterized by uniform spatial distribution of P and F domains in composites (Fig.

55- 57). Such spatial uniformity allows formation of developed nearly coherent P/F interfaces at high temperatures, though sizes of P and F domains increase. As follows from EDX data, pronounced redistribution of elements between P and F domains takes place (Fig. 56- 58): transition metal cations are incorporated into F domains (mainly, surface layers), while Sc, Ce and Zr cations migrate into P domains (much stronger for LSNF phase). Domain interfaces appear to be rather coherent demonstrating a good epitaxy between P and F phases.

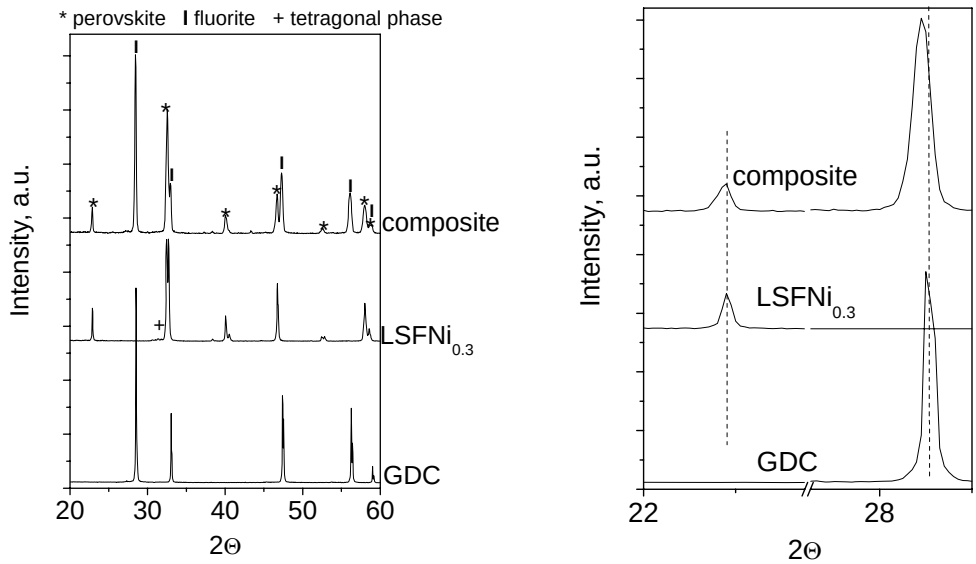

Figure 53. XRD patterns of $La_{0.8}Sr_{0.2}Fe_{0.7}Ni_{0.3}O_3$, $Ce_{0.9}Gd_{0.1}O_{1.95}$ and composite $50\%La_{0.8}Sr_{0.2}Fe_{0.7}Ni_{0.3}O_3 + 50\%Ce_{0.9}Gd_{0.1}O_{1.95}$ calcined at 1200 °C.

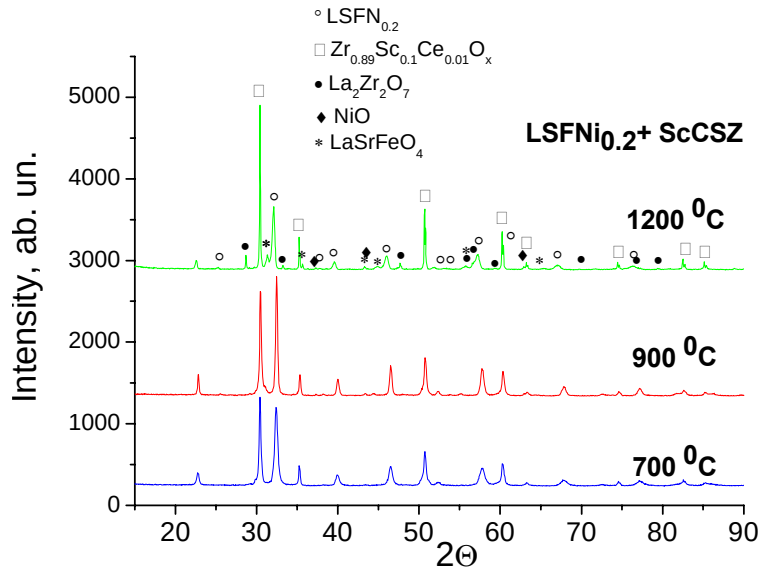

Figure 54. X-ray diffraction patters of $LSFNi_{0.2}$ -ScCeSZ composite sintered at different temperatures.

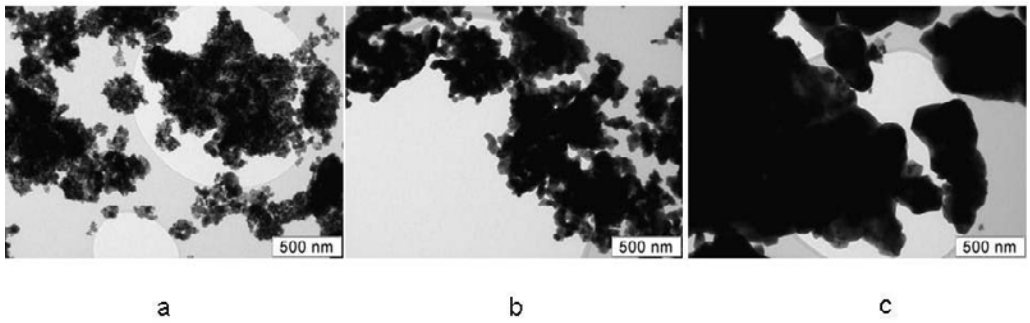

Figure 55. Typical morphology of LSNF-GDC composite particles sintered at 700 (a), 900 (b) and 1200 °C (c).

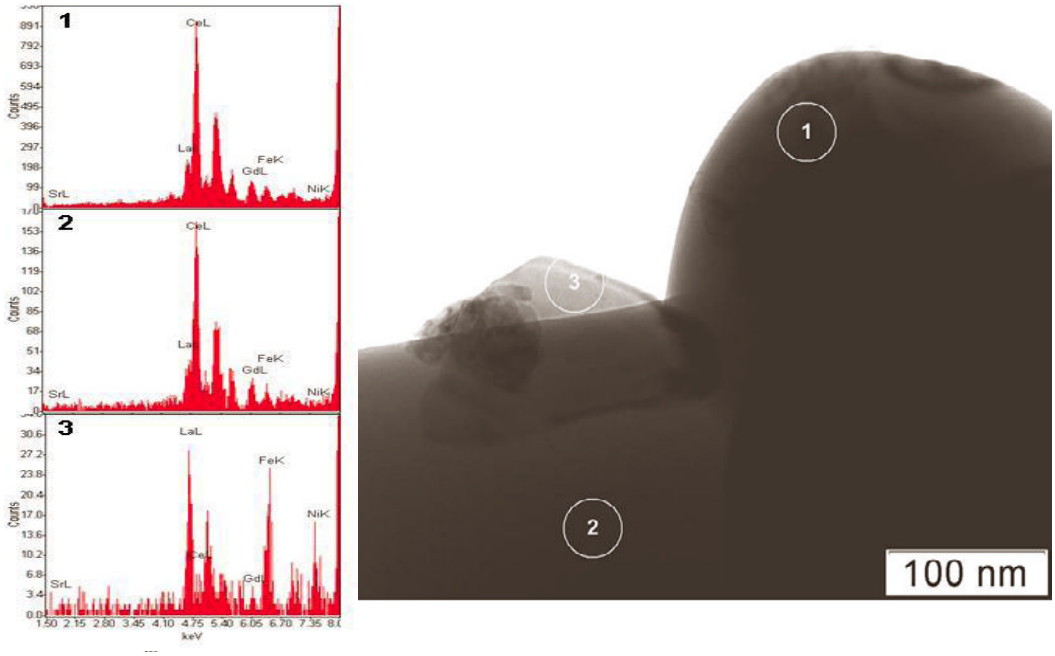

Figure 56. Typical morphology of particles in LSNF-GDC composite sintered at 1200 °C and respective EDX spectra from regions 1-3. Elemental composition: 1 - 19 wt.% $La_{0.97}Sr_{0.03}Fe_{0.68}Ni_{0.32}O_3$ + 81 wt.% $Ce_{0.93}Gd_{0.07}O_2$, 2 - 21 wt.% $La_{0.94}Sr_{0.06}Fe_{0.74}Ni_{0.26}O_3$ + 79 wt.% $Ce_{0.93}Gd_{0.07}O_2$, 3 - 82 wt.% $La_{0.98}Sr_{0.02}Fe_{0.63}Ni_{0.37}O_3$ + 18 wt.% $Ce_{0.68}Gd_{0.32}O_2$.

UV-Vis. Spectra of $La_{0.8}Sr_{0.2}MnO_{3-x}$ samples are shown in Fig. 59. The bands in the visible range can be assigned to d-d $^4A_{2g}$–$^4T_{2g}$ (16000 cm^{-1}) and $^4A_{2g}$–$^4T_{1g}$ (F) (19000 cm^{-1}) transitions in Mn^{4+} cations (d^3 configuration, basic term $^4A_{2g}$ in the octahedral crystal field) [139]. Presence of Mn^{4+} cations in LSM can be explained both by charge compensation due to Sr doping and Mn^{3+} disproportionation (vide supra). Note, though, that a proper interpretation of LSM spectra requires taking into account spin dependent hybridization between Mn *d* states and O *p* states [140, 141]. As the result, the majority Mn *d* bands overlap the O *p* bands while the minority Mn *d* bands are separated by a gap from the O *p* bands.

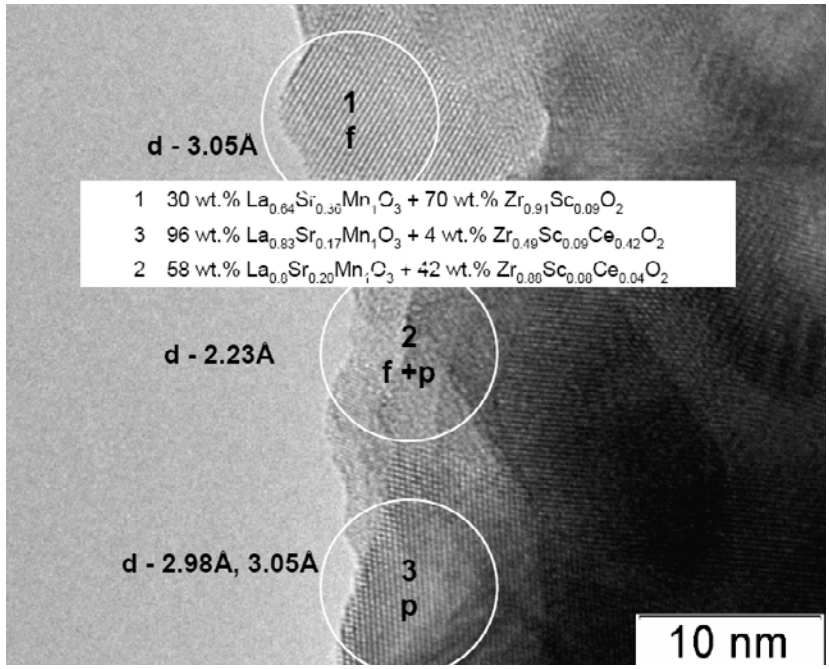

Figure 57. High resolution image of LSM-ScCeSZ nanocomposite sintered at 900 °C and composition of neighboring domains. f—fluorite phase, p-perovskite phase.

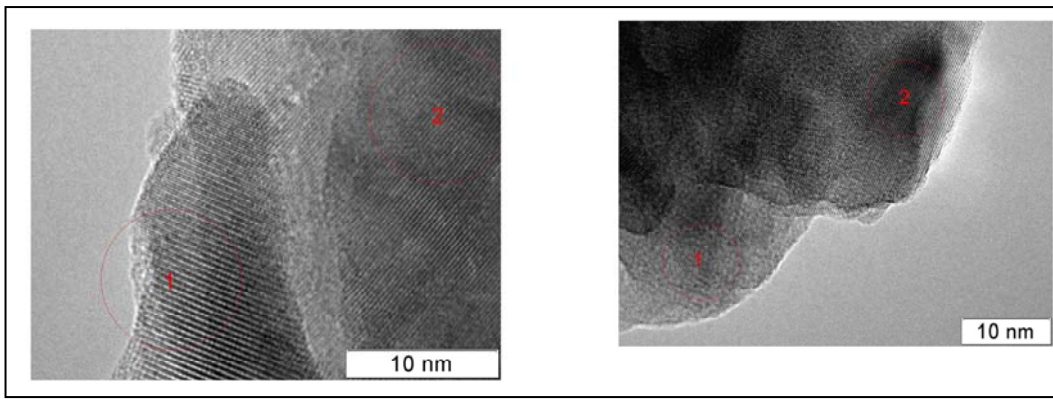

Figure 58. Lattice spacing and elemental composition of neighboring domains in $LS_{0.4}FC$-GDC composite by TEM with EDX. Left: 70%wt. $La_{0.82}Sr_{0.18}Fe_{0.78}Co_{0.22}O_3$ + 30%wt. $Ce_{0.82}Gd_{0.18}O_2$, d =1.96Å, 3.90Å (1) and 17%wt. $La_{0.87}Sr_{0.13}Fe_{0.66}Co_{0.34}O_3$ + 83%wt. $Ce_{0.92}Gd_{0.08}O_2$, d= 2.76Å (2). Right : 86%wt. $La_{0.59}Sr_{0.41}Fe_{0.78}Co_{0.22}O_3$ + 14%wt. $Ce_{0.60}Gd_{0.40}O_2$; d = 2.78Å (1) and 80%wt. $La_{0.63}Sr_{0.37}Fe_{0.79}Co_{0.21}O_3$ + 20%wt. $Ce_{0.55}Gd_{0.45}O_2$, d =2.72Å (2).

LSM samples calcined at 700 and 900°C (curves 1-2) are characterized by a broad absorption band at 13700 cm^{-1} corresponding to Mn cations in weakly distorted octahedral coordination of pseudocubic disordered perovskite phase (vide supra XRD data). For samples sintered at 1100-1200°C (curves 3-4) the oxygen excess declines, structure becomes more ordered (orthorhombic) and domain sizes increase (vide supra). This is reflected in the

decrease of the intensity of band in the visible range, its shift to 15000 cm^{-1} and appearance of a shoulder at 19800 cm^{-1} caused by cooperative Jan-Teller distortion of octahedra in LSM.

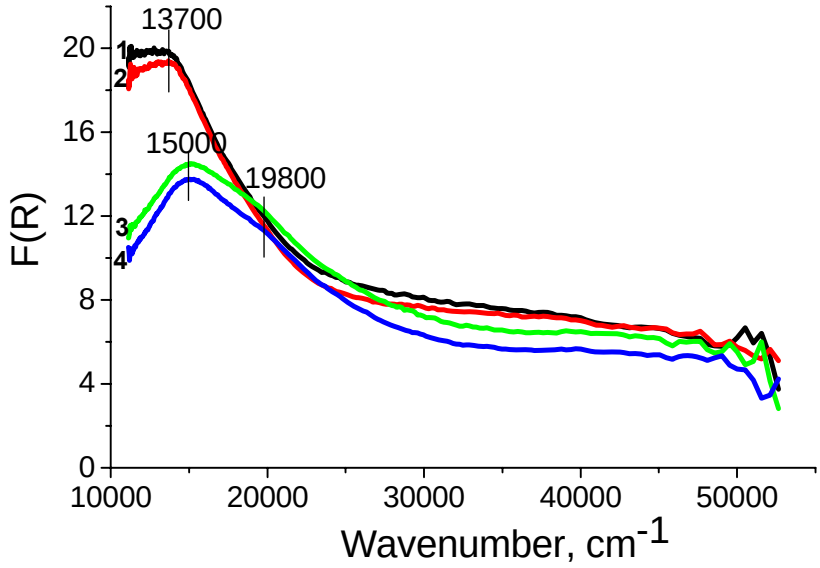

Figure 59. UV-vis spectra of $La_{0.8}Sr_{0.2}MnO_{3-x}$ calcined at 700°C (1), 900°C (2), 1100°C (3) and 1200°C (4).

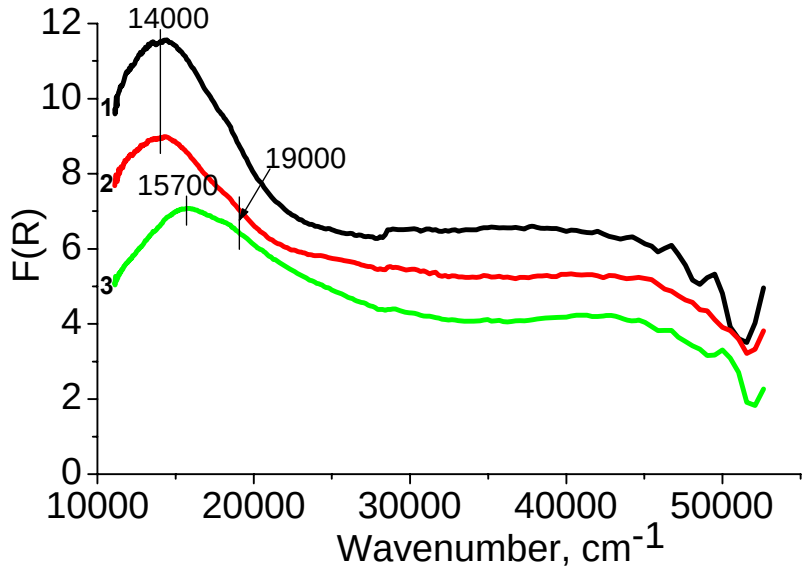

Figure 60. UV-vis spectra of LSMn-ScCeSZ composite sintered at 700°C (1), 900°C (2), 1100°C (3).

Similar variations with increasing the sintering temperature were observed in UV –Vis spectra of LSM-ScCeSZ composite (Fig. 60). However, in composite the blue shift and splitting of the band is observed already after sintering at 700 °C. After sintering at 1100 °C the shift of band in composite is more pronounced than in LSM, suggesting a stronger

distortion of oxygen octahedra around Mn cations. This can be explained by incorporation of bigger Sc and Zr cations into the B sublattice of LSM.

In spectra of $LFN_{0.3}$ samples a band at 12500-14100 dominates shifting to higher wavenumbers with the increase of sintering temperature (Fig. 61). This band is absent in the spectra of $LaFeO_3$ sample (Fig. 62), so it can be assigned to d-d transitions in Ni^{3+} (d^7) cations. Indeed, this band is present in the spectra of NiO calcined at 900 °C due to some oxygen excess (and, hence, presence of Ni^{3+}) in this sample (Fig. 63). Blue shift of this band position with sintering temperature can be explained by ordering of the LFN structure. Substitition of La for Sr does not affect appreciably the shape and position of this band (Fig. 64). Decrease of Ni content in LSFN leading to the lattice expansion, and, hence, increasing Ni-O bond length and decreasing its strength is accompanied by the red shift of the band position (Fig. 65).

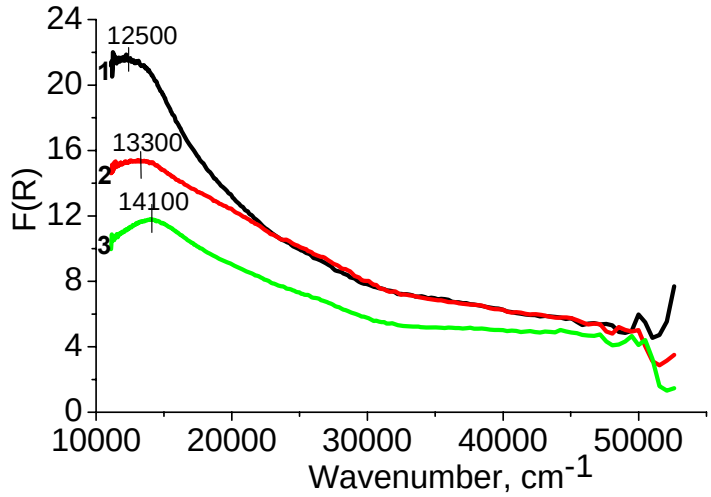

Figure 61. UV-Vis spectra $LaFe_{0.7}Ni_{0.3}O_{3-x}$ sintered at 700°C (1), 900°C (2) and 1200°C (3).

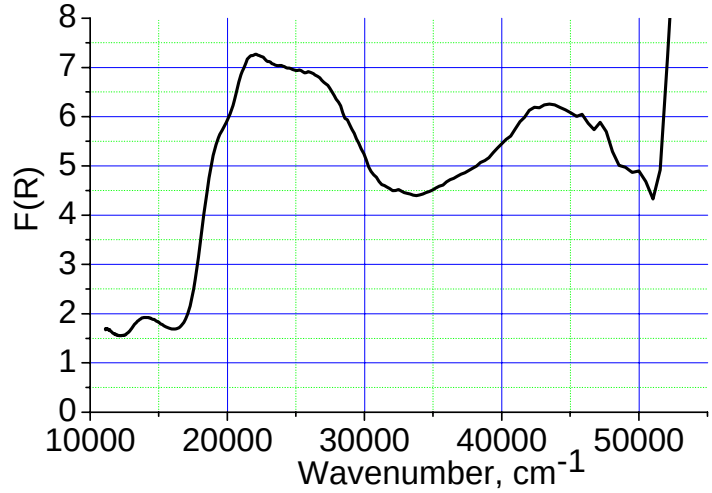

Figure 62. UV-Vis spectrum of $LaFeO_3$ calcined at 1100 °C.

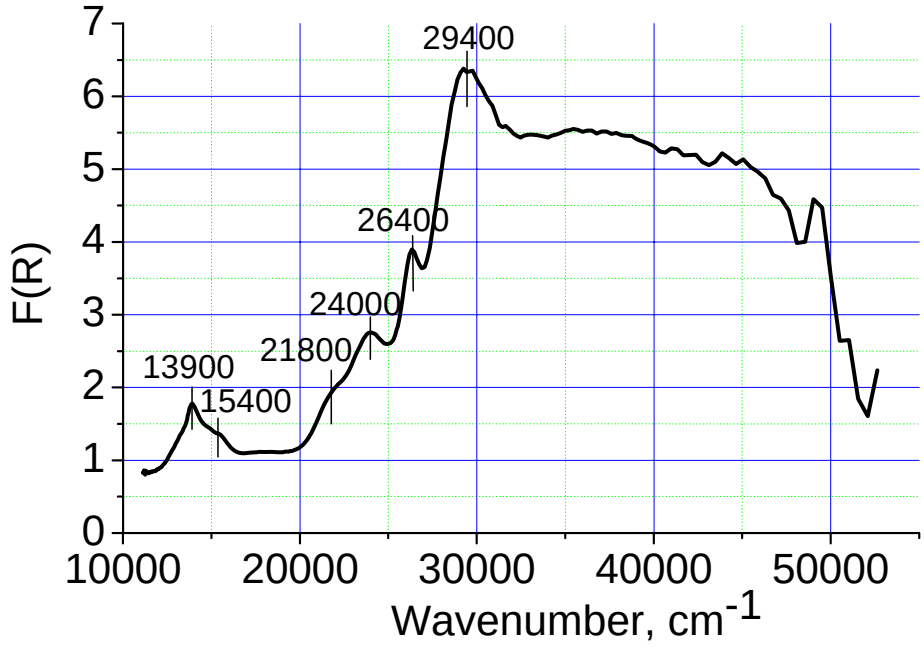

Figure 63.UV-Vis spectrum of NiO calcined at 900 °C.

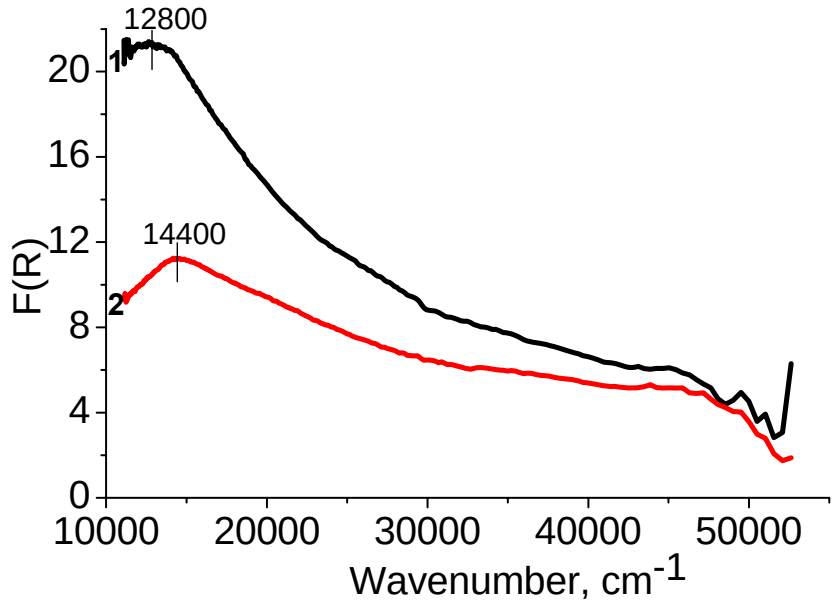

Figure 64. UV-Vis spectra of $La_{0.8}Sr_{0.2}Fe_{0.7}Ni_{0.3}O_{3-x}$ sintered at 700°C (1) and 1200°C (2).

Spectra of $Ce_{0.9}Gd_{0.1}O_{1.95}$ sintered under air are comprised of charge transfer bands (Fig. 66). The increase of sintering temperature improves spectra resolution without any shift of the absorption edge position.

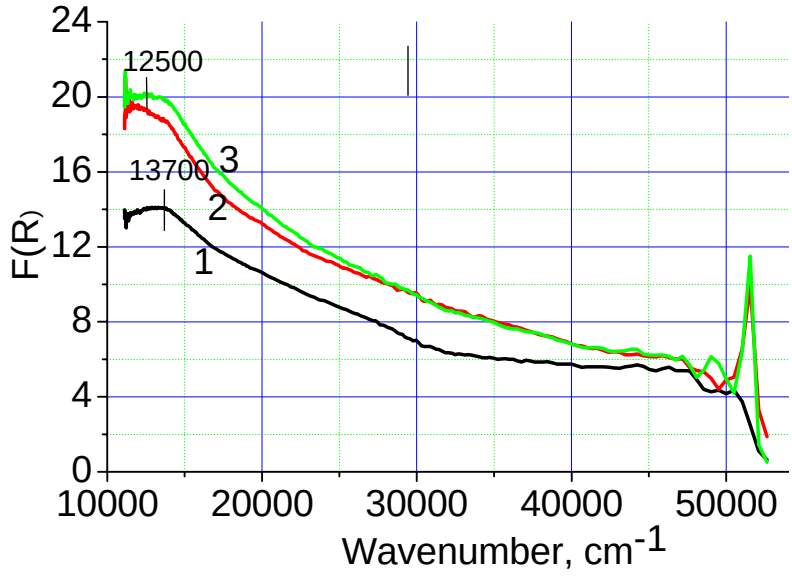

Figure 65. UV-vis spectra of $LSFN_{0.1}$ (1) and $LSFN_{0.2}$ (2, 3) sintered at 900 °C (2) and 1200 °C (1, 3).

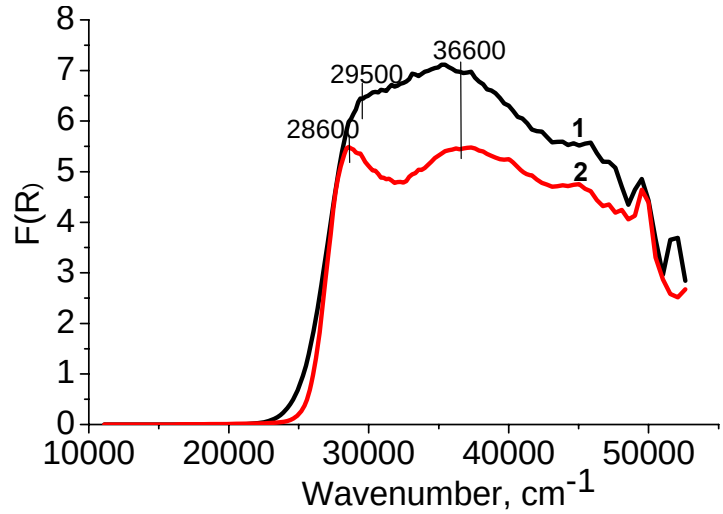

Figure 66. UV-vis spectra of $Ce_{0.9}Gd_{0.1}O_{1.95}$ sintered at 500°C (1) and 1200°C (2).

In the spectra of $LSFN_{0.3}$ + GDC composite sintered at 700-900 C (Fig. 67) the bands in the UV range are due to GDC. A poor resolution of these bands suggests disordering of GDC lattice due to smaller domain size and incorporation of La and Sr cations from the perovskite domains. The most striking feature is a strong red shift of bands corresponding to d-d transition in Ni^{3+} cations (Figs. 67, 68) even for samples calcined at moderate temperatures. This suggests considerable weakening of Ni-O bond due to disordering of LSFN structure as well. At high sintering temperatures (Fig. 68) a shift of GDC absorption observed as well indicating a strong disordering of GDC surface layer due to incorporation of transition metal cations along with La and Sr .

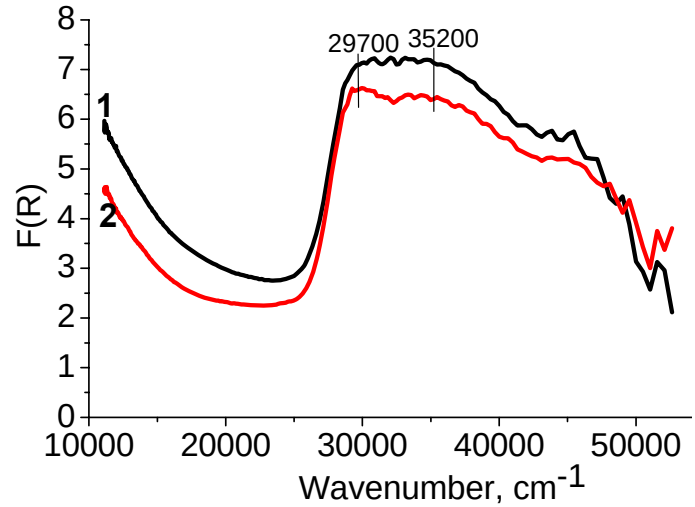

Figure 67. UV-Vis spectra of $La_{0.8}Sr_{0.2}Fe_{0.7}Ni_{0.3}O_{3-x}$+$Ce_{0.9}Gd_{0.1}O_{1.95}$ composite sintered at 700°C (1) and 900°C (2).

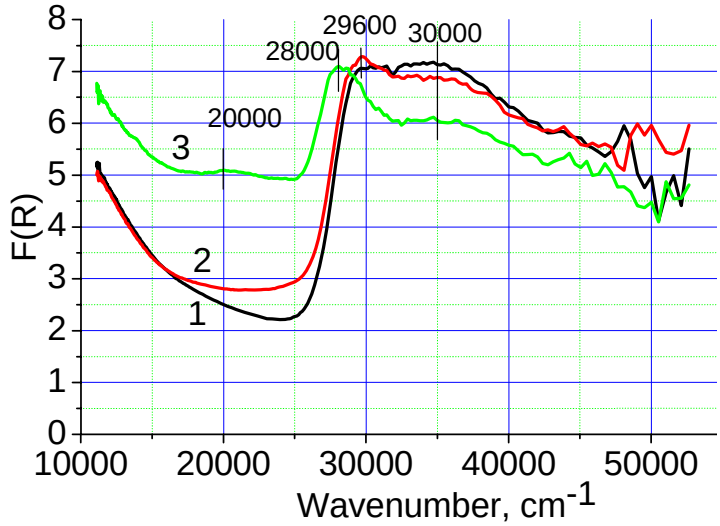

Figure 68. UV-vis spectra of $LSFN_{0.2}$+GDC (1) and $LSFN_{0.1}$+GDC (2, 3) composites sintered at 900°C (1, 2) and 1200°C (3).

3.3. Surface Composition of Composites

LSM-ScCeSZ. Mn 2p spectra (Fig. 69) can be decomposed into two doublets with $Mn2p_{3/2}$ BE ~642 eV and ~645 eV (≤20%). Their position and relative intensity are independent upon the sintering temperature, so they can be tentatively assigned to co-existing Mn^{3+} and Mn^{4+} cations in the LSM lattice and/or on the surface of fluorite-like doped zirconia phase. Indeed, according to Choudhary et al [142], Mn^{4+} cations incorporated into the surface layer of cubic ZrO_2 are characterized by $Mn2p_{3/2}$ BE 642.3 eV, hence, it is not possible to differentiate location of Mn cations in this system. For Sr and La cations (Fig. 69, 70), both

position and intensity of components at a higher BE vary with T_{sint}. This suggests redistribution of these cations between sites with different coordination environment in coexisting P and F phases. An apparent increase with $T_{sint.}$ of high-energy component of Sr 3d peak (~ 135 eV) (Fig. 69b) and high-energy shift of La 3d peak from 835.4 to 836.4 eV (Fig. 70a) suggest progressive incorporation of these cations into F phase in agreement with XRD data (Table 9). Appearance of high-charge Zr^{4+} cations as neighbors and change of the average coordination number (CN) by oxygen from 12 in perovskite to 7-8 in fluorite decrease the electron density on Sr and La cations, and, hence, increase their effective charge and BE, respectively.

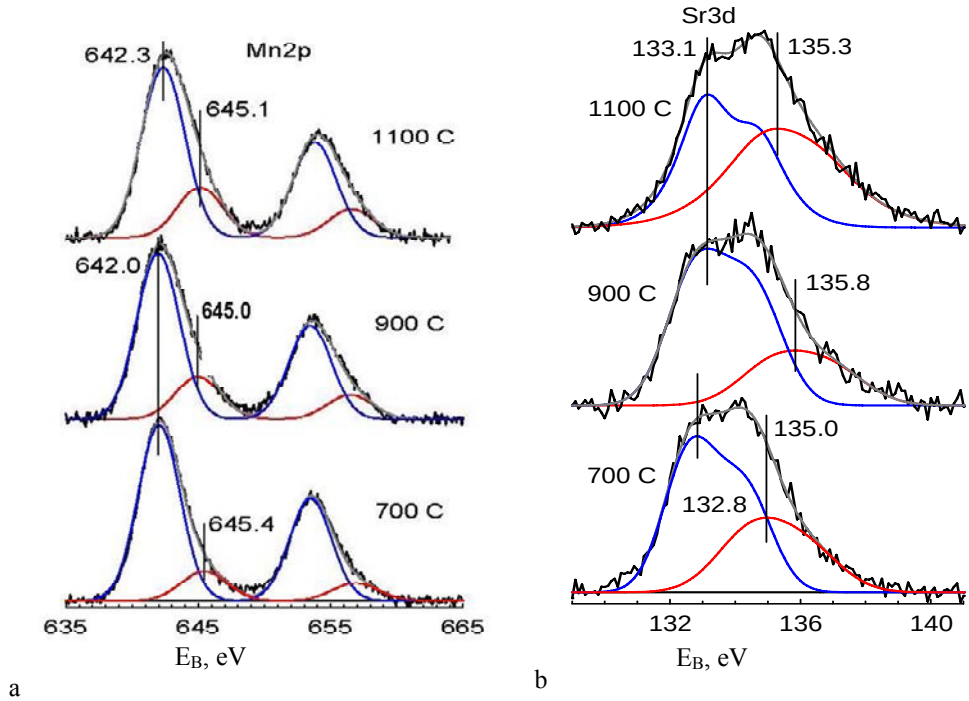

Figure 69. XPS spectra of Mn (a) and Sr(b) cations in the surface layer of LSM-ScCeSZ nanocomposite sintered at different temperatures.

In Zr 3d spectra, a low- energy component at ~ 182.6 eV corresponds to Zr cations in the surface layer of cubic zirconia [142], while the high –energy component at ~ 184 eV should be assigned to Zr cations with a higher effective charge. Hence, the increase of the relative intensity of high BE component of Zr 3d spectra with $T_{sint.}$ (Fig. 70) can be explained by progressive transfer of Zr cations from ScCeSZ (CN 8) into B positions of LSM (CN 6).

A much larger content of La and Mn as compared with Zr within the probing depth of XPS ~ 20 Å (Fig. 71a) reveals preferential presence of the perovskite phase in the surface layers of nanocomposite particles, especially those sintered at high temperatures. As the result, mainly Zr cations incorporated into the LSM surface layer and characterized by the high BE component are detected by XPS in the nanocomposite annealed at 1100 ^{o}C (Fig. 70).

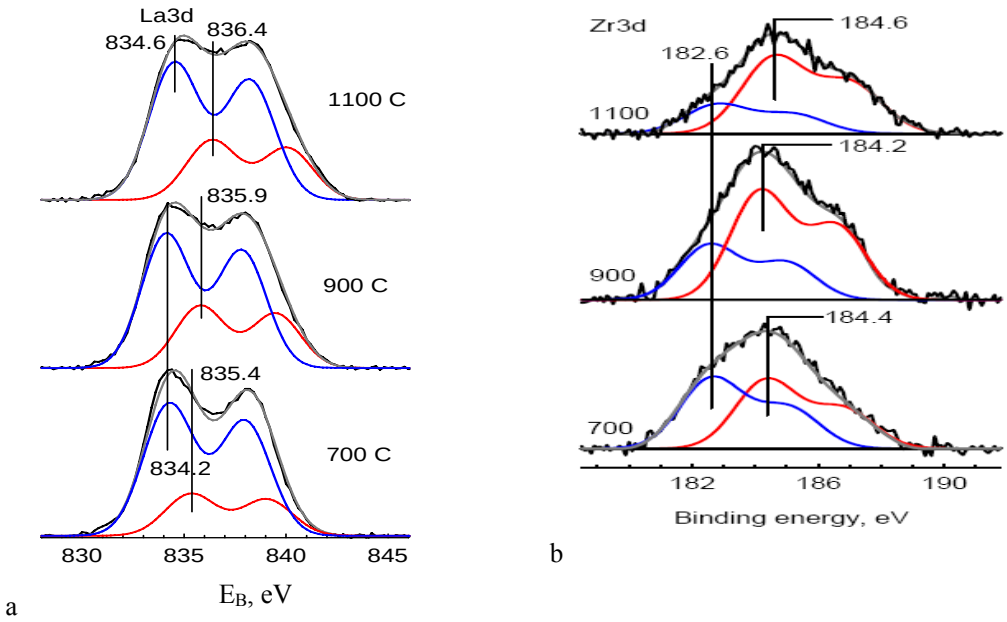

Figure 70. XPS spectra of La (a) and Zr (b) in the surface layer of LSM-ScCeZs nanocomposite sintered at different temperatures.

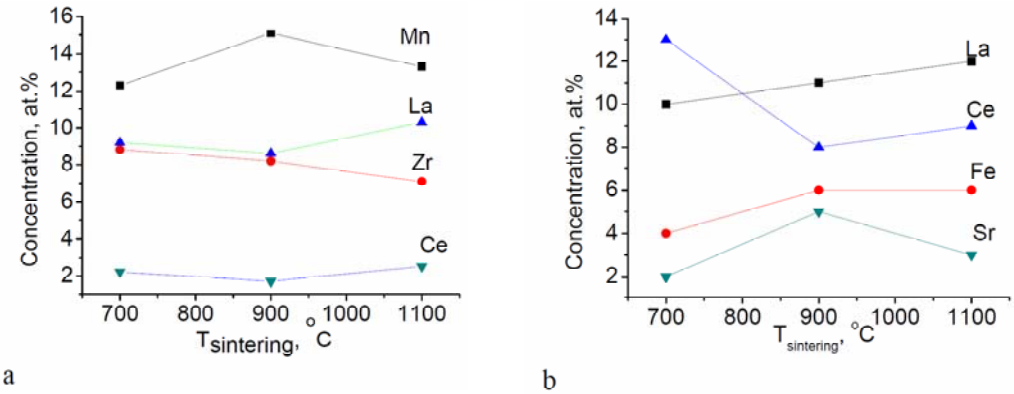

Figure 71. Sintering temperature effect on the concentration of elements in the surface layer of LSM-ScCeSZ (a) and LSFNi$_{0.4}$-GDC (b) composites.

LSFN-GDC. For better presentation all spectra for this composite are related to the same area of integral spectrum Ce^{3+} and Ce^{4+}. Calibration of spectra by binding energy was carried out by assigning the same binding energy 916.7 eV for the $3d_{1/2}$ Ce^{4+} component.

The "shake-down" processes in the course of photoemission from Ce^{4+} cations determine the shape of spectrum as well-resolved multiple structure (Fig. 72). For composites annealed at different temperatures, the gaps between neighboring peaks somewhat differ, which is caused by the varying content of Ce^{3+} cations [143]. A slight difference observed between spectra of composite sintered at increasing temperatures indicates that this content is rather small to cause any substantial effect.

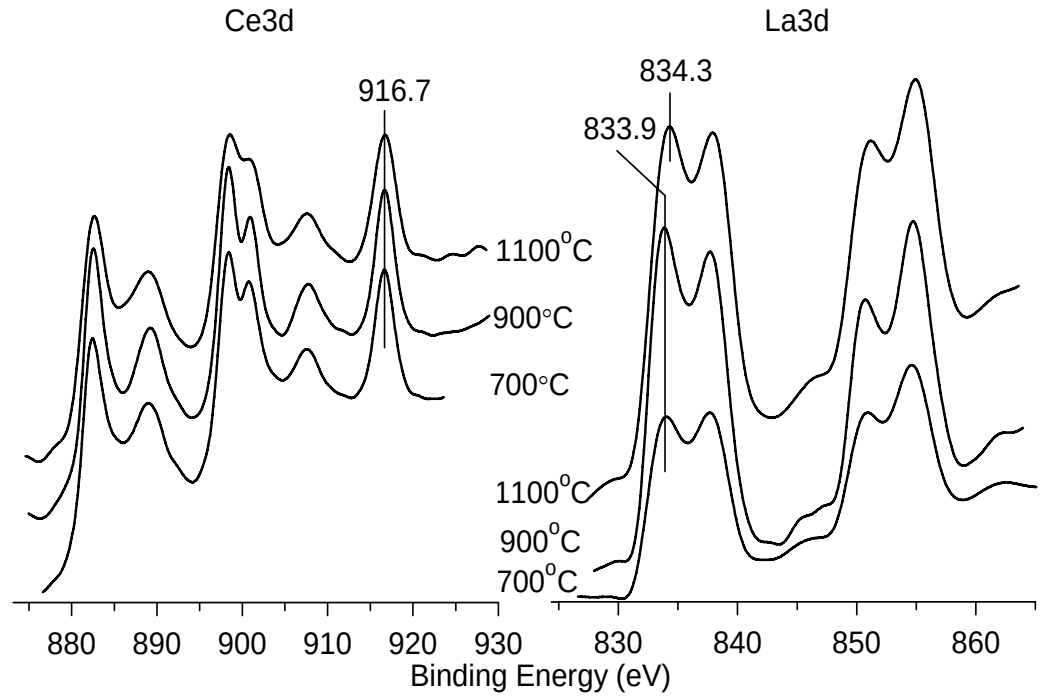

Figure 72. XPS spectra of Ce3d and La3d regions for LSFN-GDC composite sintered at 700-1100 °C.

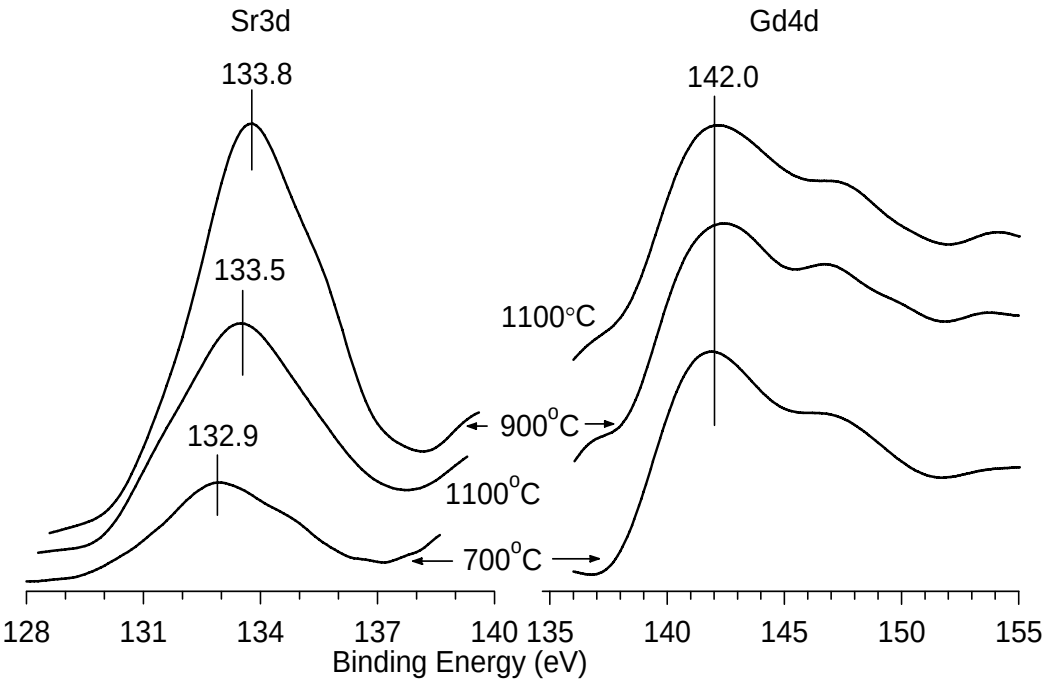

Figure 73. XPS spectra of Sr 3d и Gd 4d regions for LSFN-GDC composite sintered at 700-1100 °C.

Spectral data for La 3d (Fig. 72) demonstrate small shifts and broadening of peaks as well as increase of La/Ce ratio with the sintering temperature. By analogy with LSM-ScCeSZ

system this suggests transfer of La from the perovskite into the surface layers of GDC particles, which agrees with XRD and EDX data.

As judged by the spectra of Gd4d (Fig. 73), both the chemical state of this element as well as the Gd/Ce ratio are not affected by the temperature of composite sintering. This suggests small (if any) incorporation of Gd into the perovskite phase, which agrees with well-known higher stability of La cations in the mixed LnO_3 layers of the perovskite structure [101].

Sr 3d peaks increase by intensity and shift to higher energy with the sintering temperature (Fig. 73) following similar trend for LSM-ScCeSZ composite (Fig. 69). Based upon EDX results (vide supra), this feature can be assigned to incorporation of Sr cations into the surface layer of fluorite particles.

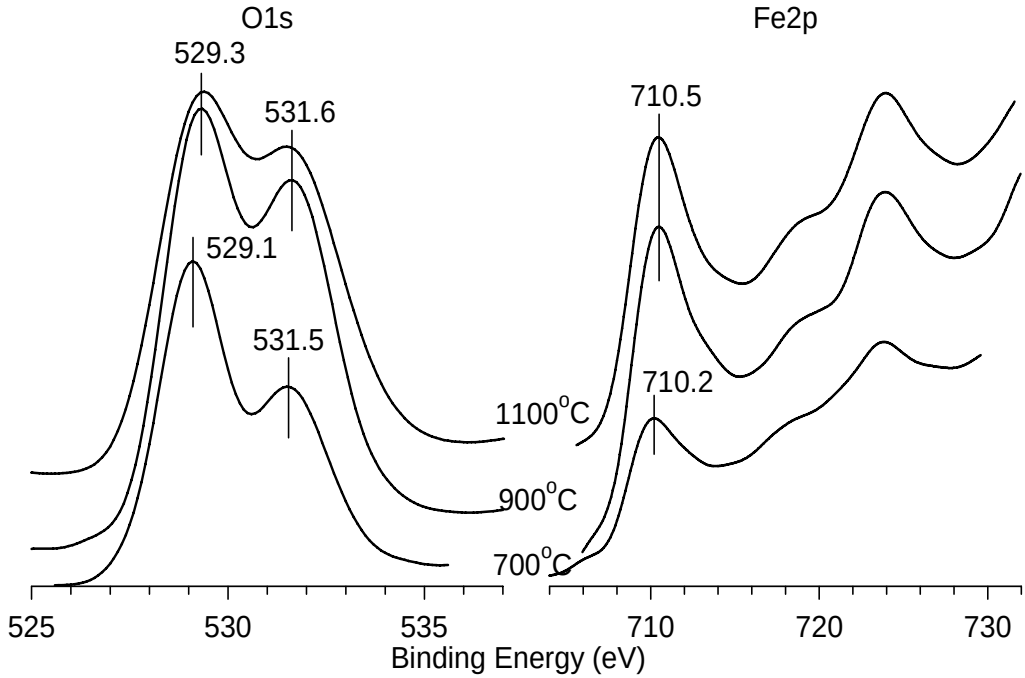

Figure 74. XPS spectra of O1s and Fe2p regions for LSFN-GDC composite sintered at 700-1100 °C.

In Fe2p spectra (Fig. 74), peaks position and their shape are not affected by sintering temperature. The increase of the spectra intensity with sintering temperature suggests segregation of Fe cations in the surface with formation of new oxide phase. Concomitant increase of the intensity of O1s line with E_B ~531.5 eV implies that this new phase is enriched by Fe and Sr. Based upon EDX results (vide supra), such a new phase can be assigned to the surface layers of some GDC particles with incorporated La, Sr and Fe cations. In Sr-containing perovskites ($SrFeO_3$, LSCF etc), a part of Fe cations is known to be in the 4+ state [144]. At least, position of Fe $2p_{3/2}$ peak at ~ 710 eV does not exclude coexistence of Fe^{3+} and Fe^{4+} cations in LSFN sample [144], though more detailed studies are further required.

Resulting variation of the surface concentration of elements in LSFN-GDC composite with sintering temperature is given in Fig. 71. In general, for both composites effects are rather weak agreeing with reasonable stability of perovskite and fluorite phases and their

moderate interaction in studied temperature range, though exceeding the relative error of XPS analysis of the surface concentration ~ 10 rel. %. In all cases a clear trend in increasing the surface content of transition metal cations and La with sintering temperature was observed. This agrees with EDX data thus demonstrating that certainly transition metal cations along with La are transferred into the surface layers of F phases. Since composition of the surface layer of composite particles comprised of perovskite and fluorite domains reflects processes of elements redistribution between this domains, it is apparent that similar (and even stronger) redistribution takes places at P-F interfaces in the bulk of composite particles.

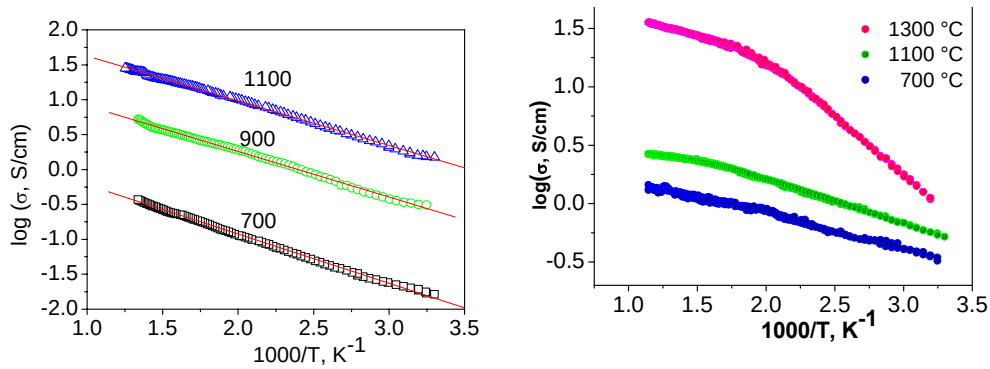

Figure 75. Temperature dependences of conductivity of LSM-GDC (a) and $LSFN_{0.4}$ – GDC (b) composites sintered at different temperatures.

3.4. Electronic and Oxygen Transport in Nanocomposites

3.4.1. Electronic Conductivity

Total conductivity of nanocomposites is mainly determined by electronic conductivity of P phase and usually increases with the sintering temperature (Fig. 75) due to densification of samples that favors percolation and improves contacts between domains provided isolating pyrochore phase is not formed [125, 145]. For LSFN-based composites, the total conductivity tends to increase with the Ni content in perovskite (Fig. 76), though for pure perovskites this trend is not so straightforward (Fig. 21) due to NiO segregation at a high Ni content (vide supra). Hence, incorporation of La, Sr, Ni and Fe cations into the surface layers of GDC generating layers of mixed cerates with a high MIEC conductivity seems to prevent segregation of NiO as a low conducting inter-granular phase. In general, conductivity of even dense nanocomposite remains several times lower than conductivity of pure P phase (Fig. 77) both due to the effect of dilution with F phase possessing a lower specific conductivity as well as due to incorporation of Zr, Ce or Sc cations into the P lattice. For LSM-ScCeSZ (Fig. 75), $LS_{0.2}FC_{0.2}$ -GDC and $LSFN_{0.4}$-GDC composites sintered at optimal (1100 -1200 ^{o}C) temperatures (Table 10), the total specific conductivity is reasonably high for their application as IT SOFC cathode materials, which agrees with results of Kharton et al [127, 129]. A higher specific conductivity in air ($lg\sigma$ ~ 2.4 at 1000 K) was measured for $LS_{0.4}FC$-GDC (30%) composite sintered at 1250 ^{o}C [61] (Table 10), which can be explained by a higher Sr and

lower GDC content. Substantially lower (lgσ ~ -2÷1 at 1000 K) specific conductivities were found for $GdMnO_3$-GDC and $La(Pr,Nd)MnO_3$-$Ce(Pr,Nd,Sm)O_2$ composites [11, 133, 134] and $Ce_{0.8}Gd_{0.2}O_{1.9}$ - $Gd_{0.7}Ca_{0.3}CoO_{3+\delta}$ composites [128]. For LSFN-GDC and LSM-ScCeSZ composites the activation energy of conductivity at low-temperatures is slightly higher than in the corresponding pure perovskites. It may be caused by influence of the intergrain barriers or by decrease in the Ni or Mn content in P due to redistribution of the elements between the phases in nanocomposites. For LSNF-ScCeSZ nanocomposite sintering at high (1330 ^oC) temperature, formation of isolating pyrochlore phase (vide supra) is reflected in a drastic decline of conductivity (Fig. 78).

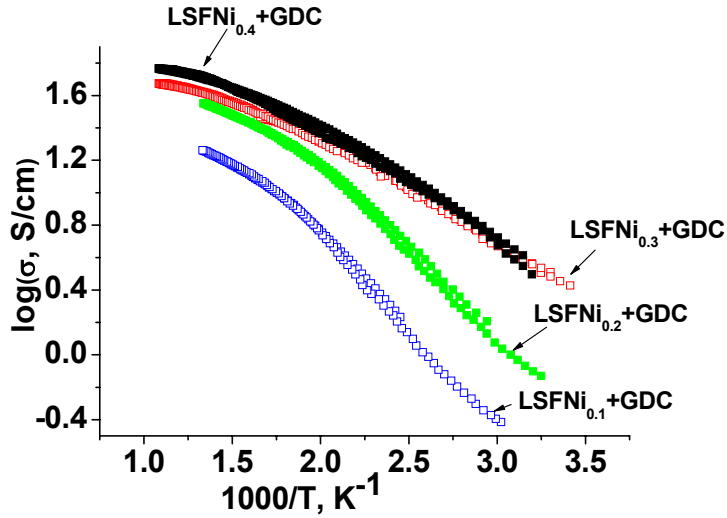

Figure 76. Temperature dependence of conductivity for $La_{0.8}Sr_{0.2}Fe_{1-x}Ni_xO_3$ -GDC composites sintered at 1330 ^oC.

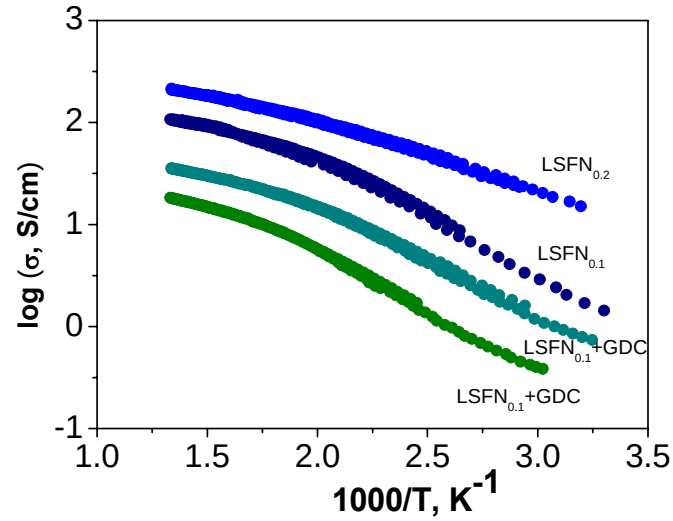

Figure 77. Temperature dependences of conductivity of composites $La_{0.8}Sr_{0.2}Fe_{0.8}Ni_xO_{3-\delta}$ – GDC ($LSFN_x$–GDC, x = 0.1, 0.2) sintered at 1300 °C in comparison with corresponding pure $LSFNi_x$ perovskites.

Table 10. Transport properties of perovskite and nanocomposite materials

Sample/* T_c (°C)	lgσ[i] (S/cm)	X_S[ii] (ML)	lg(R)[iii] ($O_2/m^2 \cdot s$)	θ_{O2}[iv] (ML)	W_{max} O_2[v]	$W_{max.}$ CH_4 TPR[vi]	
						CO	CO_2
Comp1/700		15		0.3	0.4	0.5	0.7
Comp1/900	0.9	44	16.7	1.4	1.5	1.8	1.5
Comp1/1200	1.9	100	17.9	15	14	14	9.3
Comp2/700	0	20		0.1	0.1	0.5	0.1
Comp2/900	0.8	43	17.2	0.7	0.9	1.0	0.3
Comp2/1100	1.5	175	17.6	3.9	3.6	3.8	1.6
Comp3/1250	2.4	450	17.8	17	17	5	6

* Comp1-$LSFN_{0.4}$–GDC; Comp2- $LSFC_{0.2}$ –GDC; Comp3- $LS_{0.4}FC$ –GDC

[i]-specific conductivity at 1000K;

[ii]-dynamic degree of exchange X_S (monolayers);

[iii]- the rate of oxygen isotope exchange at 650°C;

[iv]-amount of oxygen desorbed in TPD run (monolayers);

[v]- rate of O_2 desorption at T_{max} of TPD peak (10^{15} molecules O_2/m^2s);

[vi] -rate of CO or CO_2 evolution at T_{max} of CH_4 TPR peaks (10^{17} atoms O/m^2s).

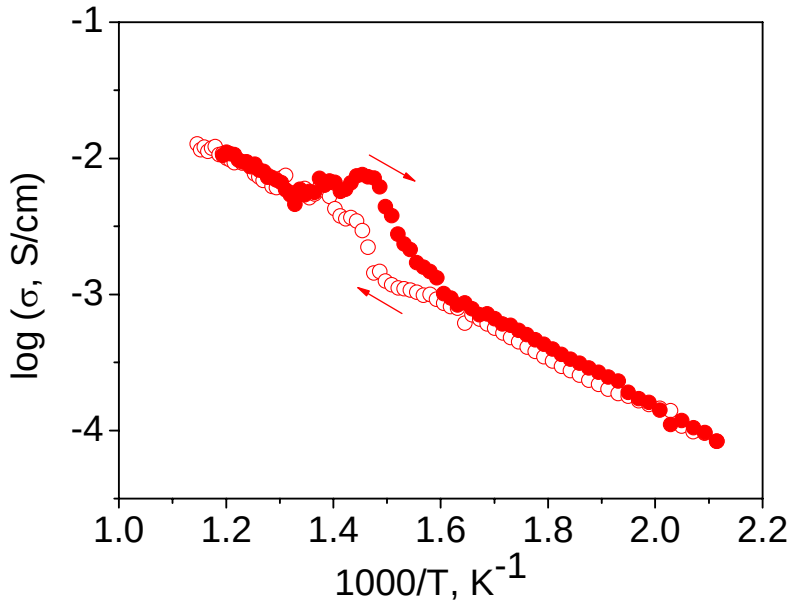

Figure 78. Temperature dependence of conductivity for $LSFNi_{0.2}$-ScCeSZ composite sintered at 1330 °C.

The dependences of conductivity on the oxygen partial pressure for composites $La_{0.8}Sr_{0.2}Fe_{0.8}Ni_{0.2}O_{3-\delta}$ - 50 wt.% $Ce_{0.9}Gd_{0.1}O_{1.95}$ and $La_{0.8}Sr_{0.2}Fe_{0.9}Ni_{0.1}O_{3-\delta}$ - 50 wt.% $Ce_{0.9}Gd_{0.1}O_{1.95}$ sintered at 1330 °C in comparison with the conductivities of pure perovskite phase are shown in Fig. 79. The slope $d\log(\sigma)/d\log(P_{O2}) \sim 0.03$ is very low, that corresponds to the Region II on a general pressure dependence (vide supra Fig. 1) where reaction (7) prevails and $[Sr'_{La}] = [p^{\bullet}]$, i.e. strontium behaves like acceptor impurity.

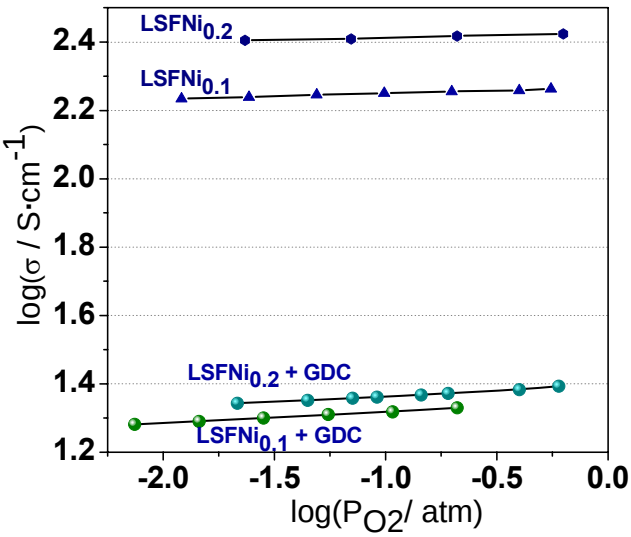

Figure 79. Dependences of electrical conductivity of $La_{0.8}Sr_{0.2}Fe_{0.8}Ni_{0.2}O_{3-\delta}$ and $La_{0.8}Sr_{0.2}Fe_{0.9}Ni_{0.1}O_{3-\delta}$ as well as the composites of the same compounds with 50 wt.% of $Ce_{0.9}Gd_{0.1}O_{1.95}$ on the oxygen pressure at 800°C.

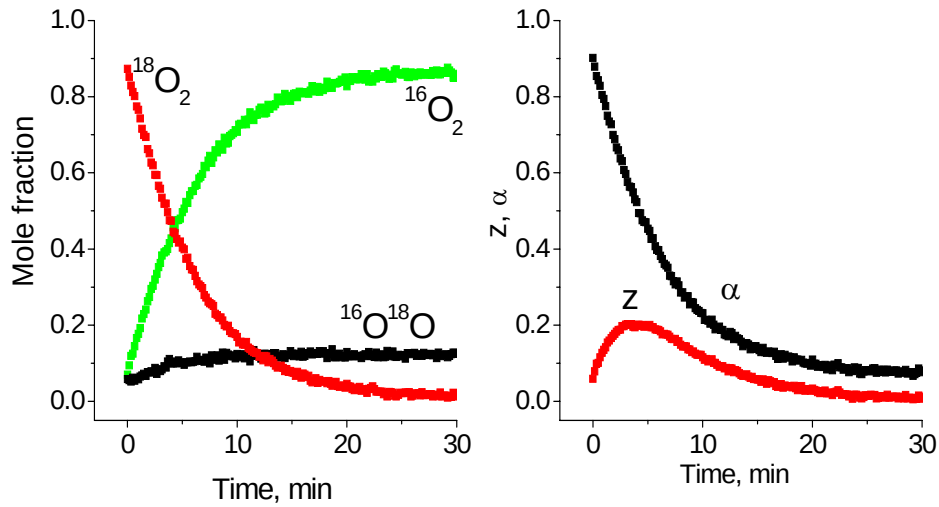

Figure 80. Time dependence of concentration of isotope molecules (left) and isotope variables (right) in the isothermal experiments (650 °C, 1.7 Torr) for 70%$La_{0.8}Sr_{0.2}Fe_{0.8}Co_{0.2}O_x$+ 30%$Ce_{0.9}Gd_{0.1}O_x$ composite sintered at 900 °C.

3.4.2. Oxygen Isotope Exchange

Figs. 80 and 81 show typical variation of the fractions of oxygen isotope molecules and respective isotope variables in the course of isothermal (Fig. 80) or temperature-programmed (Fig. 81) oxygen isotope exchange for LSFC-GDC composite. In both cases, the fraction of $^{16}O^{18}O$ molecules is quite low which is typical for samples with a high lattice oxygen mobility (cf. Fig. 30). Estimation of the type of exchange using results of isothermal experiments and TPIE experiments fitted in coordinates of isotope-mechanistic Equation (35)

(Fig. 82) revealed that for all composites a share of the 3rd type of exchange is in the range of 0.75 ±0.05. Since for manganites the share of the second type of exchange can be up to 0.6 (vide supra), a big share of the 3rd type of exchange for LSM-ScCeSZ composite apparently correlates with much higher lattice oxygen mobility (Fig. 83), in agreement with Eq. (42)-(46).

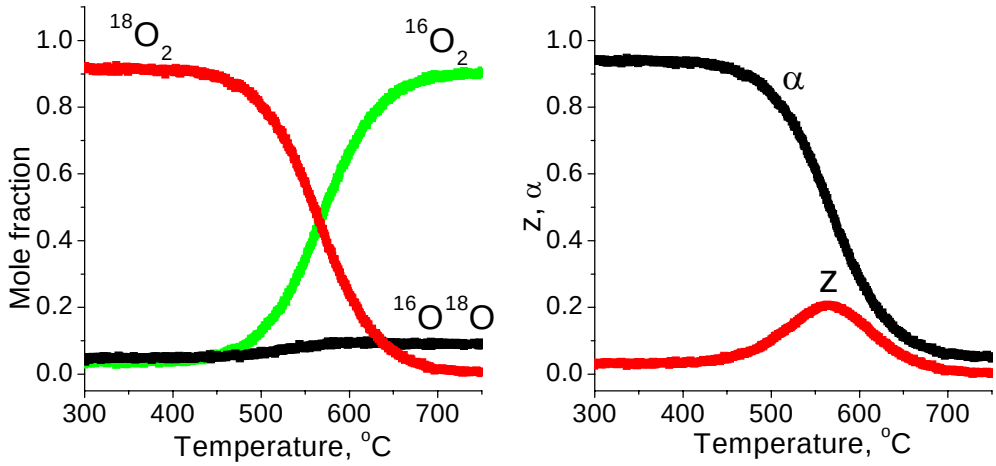

Figure 81. Temperature dependence of isotope molecules fraction (left) and isotope variables (right) in the course of temperature-programmed isotope exchange experiment for 70%$La_{0.8}Sr_{0.2}Fe_{0.8}Co_{0.2}O_x$+ 30%$Ce_{0.9}Gd_{0.1}O_x$ composite sintered at 900 °C. Temperature ramp 5°/min from 100 to 750 °C, pO_2 1.7 Torr.

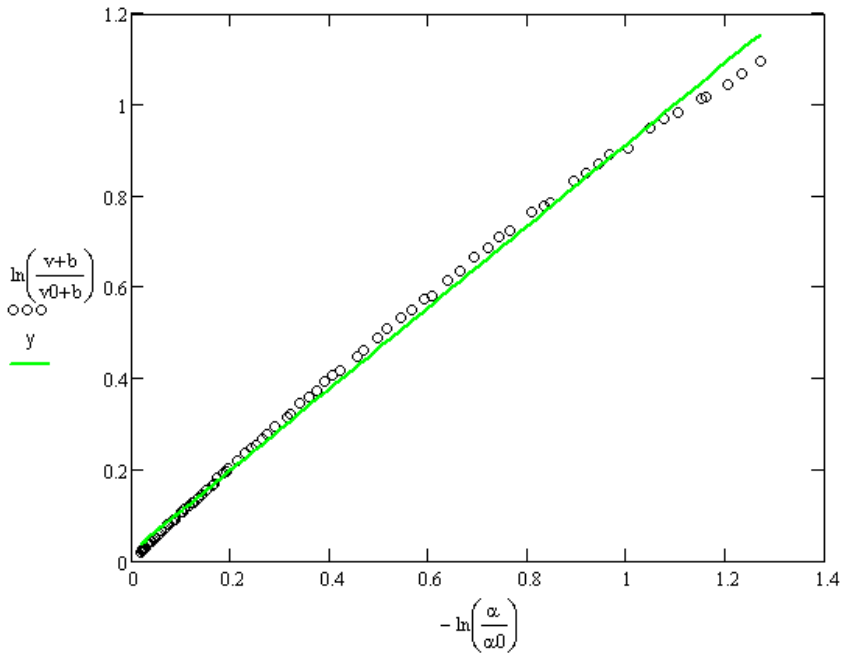

Figure 82. Estimation of the oxygen exchange type for LaSMn-ScCeSZ composite sintered at 1100 °C from results of TPIE experiments using Eq. (35).

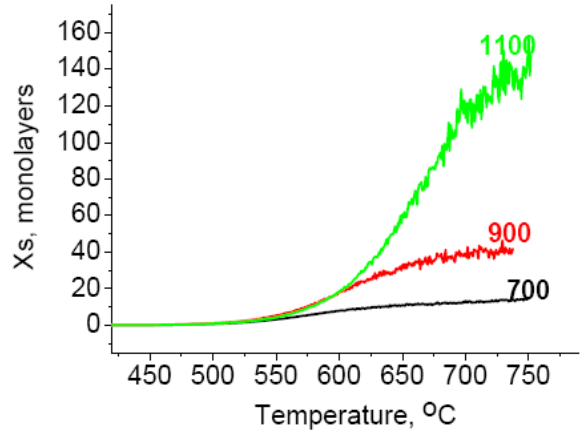

Figure 83. Temperature dependence of X_S for LSM-ScCeSZ composites sintered at 700° -1100 °C. PO_2 1.8 Torr.

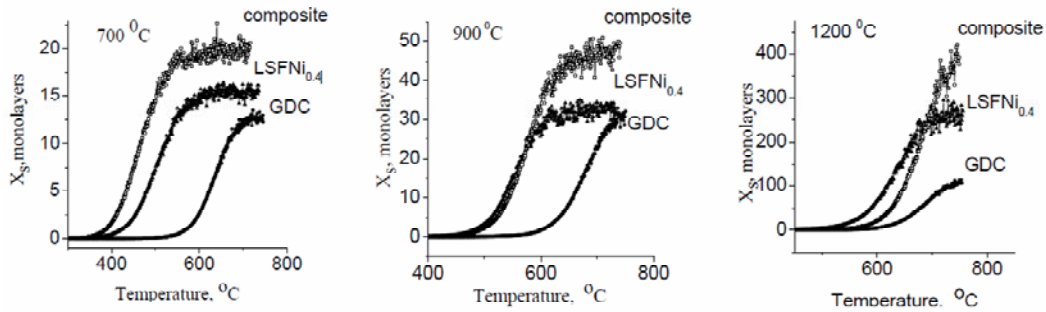

Figure 84. The dynamic degree of oxygen isotope exchange (Xs) for: 1 – $Ce_{0.9}Gd_{0.1}O_{1.95}$, 2 – $La_{0.8}Sr_{0.2}Fe_{0.6}Ni_{0.4}O_3$, 3 – composite 50% $La_{0.8}Sr_{0.2}Fe_{0.6}Ni_{0.4}O_3$+ 50% $Ce_{0.9}Gd_{0.1}O_{1.95}$ calcined at different temperatures.

For doped ceria the noticeable exchange in the dynamic mode starts from ~ 600 °C (Fig. 84) which is apparently explained by a lower specific rate of the oxygen heteroexchange [63]. For this oxide, high-temperature sintering apparently facilitates lattice oxygen mobility due to annealing of extended defects (domain boundaries) and more uniform distribution of Gd cations in the lattice increasing concentration of free anion vacancies [63, 146]. For doped ceria, the 3rd type of exchange (share ~ 90%) dominates as well [63].

For LSNF-GDC composite samples, exchange starts at nearly the same temperatures as for LSNF (Fig. 84). This suggests close specific rates of oxygen heteroexchange for LSNF and composite samples sintered at temperatures ≥ 900 °C, when interaction between perovskite and fluorite components is pronounced. Already at temperatures ≥ 550 °C, the dynamic degree of exchange for composite sintered at 1200 °C (> 10 monolayers, Fig. 84, Table 10) considerably exceeds the additive value of individual components contributions. This result suggests very high oxygen mobility in the bulk of composite particles. It can be explained only by pronounced role played by interfaces between the fluorite and perovskite domains providing fast diffusion paths. Indeed, the high-temperature sintering of composite into nearly dense ceramics provides a plenty of such interfaces, since domain sizes of both

perovskite and fluorite particles remain in the nano-scale (Table 9). The values of X_S obtained for LSFN-GDC, LSFC-GDC and LSM-ScCeSZ composite sintered at high temperatures (Figs. 83-84, Table 10) far exceed values for earlier studied $GdMnO_3$ –GDC or Ln-Mn perovskite –fluorite nanocomposites (below 20 monolayers) [11], while being close to those for typical mixed ionic –electronic conductor Sr-Fe-Co-O (>40-100 monolayers) [60]. As shown in Fig. 85, for LSFC-GDC composite with a high lattice oxygen mobility practically all oxygen in the solid is equilibrated with the gas –phase oxygen at rather moderate temperatures (X_V~ 1).

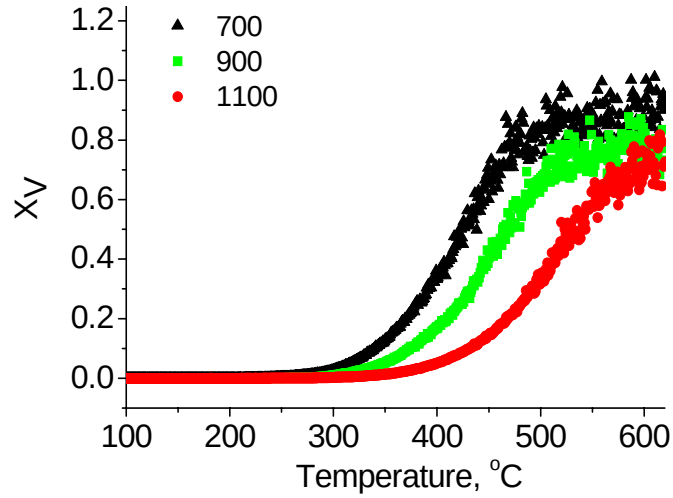

Figure 85. Temperature dependence of X_V for $LS_{0.2}FC$-GDC composite sintered at 700° -1100 °C. PO_2 1.8 Torr.

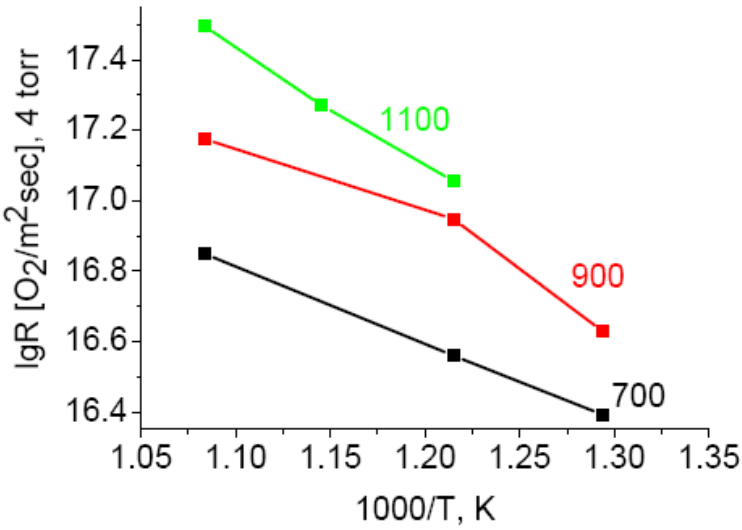

Figure 86. Temperature dependence of the specific rate of oxygen heteroexchange for samples of LSMn-ScCeSZ nanocomposite sintered at 700-1100 °C.

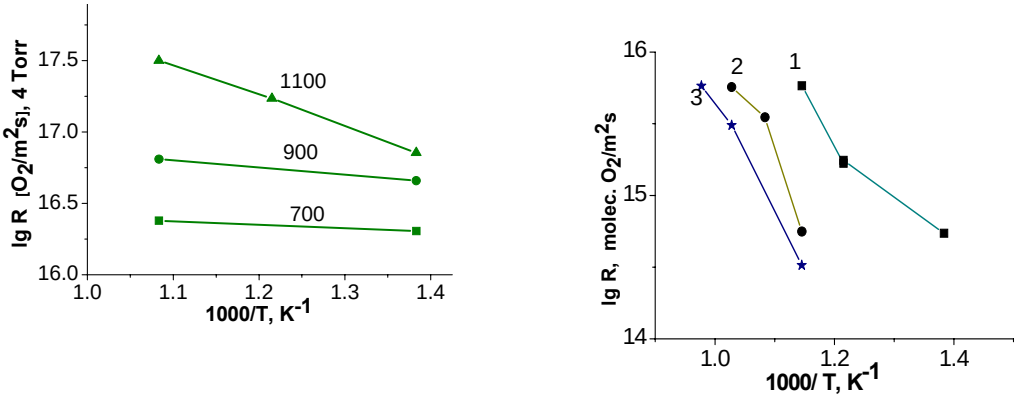

Figure 87. Temperature dependence of the specific rate of oxygen heteroexchange for samples of $LSFNi_{0.4}$-GDC nanocomposite sintered at 700-1100 oC (a) and fluorite-like oxide electrolytes (b): Sm (20%)-doped ceria (1), 2- ScCeZr, 3-ScZr.

The specific rate of oxygen heteroexchange R characterizing ability of surface sites to dissociate O_2 molecules also increases with the sintering temperature (Figs. 86-87, Table 10) achieving a level exceeding that of pure perovskites (cf. Fig. 27, 28). This occurs despite dilution of perovskite with electrolyte possessing a lower specific rate of exchange (Fig. 87). This can be explained with a due regard for EDX and XPS data demonstrating pronounced redistribution of transition metal cations between perovskite and fluorite domains. As the result, new active surface sites are created due to incorporation of transition metal cations in the surface of fluorite domains. This is reflected in the increase of apparent activation energy of exchange with the composite sintering temperature.

To estimate the oxygen diffusion coefficient from the results of oxygen isotope exchange experiments for powders, the isothermal isotope exchange curves were fitted using a complete system of isotope-kinetic and diffusion equations (30-34). In modeling, the values of diffusion coefficients (coefficients of diffusion relaxation $r_D = D/h^2$) and the share of the 3rd type of exchange $\kappa_3 = K_3 / (K_2 + K_3)$ were varied. The $\alpha(t)$ curves were found to be not sensitive to any variation of the fitting parameters, which agrees with the exponential-type kinetics of the exchange of equivalent oxygen atoms (Fig. 80). The second isotope variable x_1 (fraction of $^{16}O^{18}O$ molecules) is much more sensitive to the modeling parameters increasing more steeply with a decrease in the oxygen diffusion coefficient and a share of the 3rd type of exchange. The minimum values of k_3 thus estimated are in the range of 0.75-0.9.

For composite $LS_{0.4}FC$-GDC prepared in Imperial College and characterized in details by variety of techniques [39, 40, 118, 119, 135], coefficients of oxygen self-diffusion (D_{min}) estimated by fitting the results of isothermal isotope exchange for a powder with the characteristic size ~$3*10^{-4}$ cm are compared in Fig. 88 with the results obtained by isotope exchange depth profiling (IEDP) technique for the same composite as a dense material (D*) [119]. With a due regard for the inherent problems of fitting the results of isotope exchange for powders, the agreement between both methods is quite satisfactory.

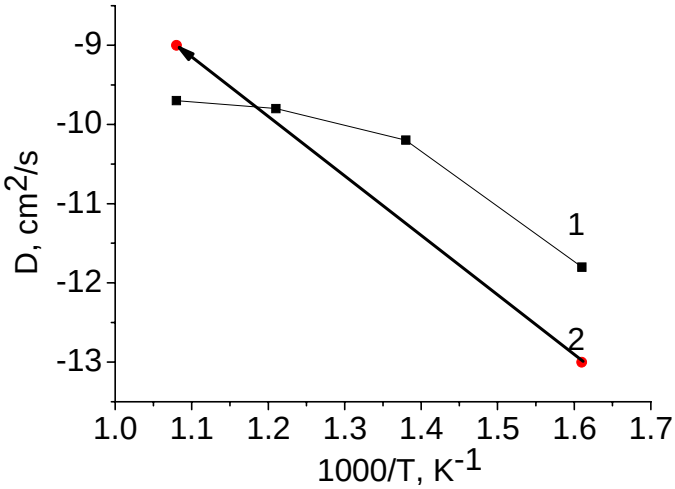

Figure 88. Comparison between coefficients of oxygen self-diffusion in $LS_{0.4}FC$-GDC composite estimated for powders (D_{min}) (1) and extrapolated values of D* for dense material (2).

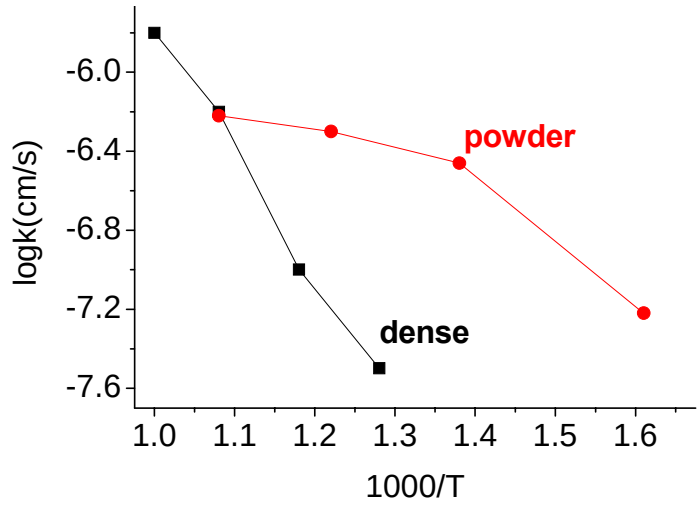

Figure 89. Comparison between coefficients of oxygen exchange in $LS_{0.4}FC$-GDC composite estimated for powdered and dense material.

Another important parameter estimated by IEDP -the surface exchange coefficient k is related to the rate of heteroexchange R (estimated for powders) by the relationship $k = 6*R/n_O*V_X$ derived by transformation of diffusion Equation (32) to parameters used in [119]. Here, n_O is the number of oxygen atoms per unit volume ($3.6*10^{22}$ at/cm^3), V_X the fraction of easily exchangeable oxygen in the bulk (an averaged value in these experiments is equal to 0.15). Comparison of k and k* values related to the same oxygen pressure (~ 1 bar) as used in IEDP SIMS studies [40, 119] revealed that k values estimated for powder exceed the k* values (estimated by IEDP) across the whole range of temperatures studied, being close only at the highest temperatures. This can be explained by the much higher sensitivity of the isotope exchange experiments on powders carried out at low pressures to the highly active surface sites which occupy perhaps only a small part of the surface due to their association

with defects either generated by grinding or situated in the vicinity of the perovskite-fluorite interfaces, domain boundaries etc. Due to a lower oxygen bonding strength, these defects could play a prominent role at lower temperatures, while their impact is not substantial at high temperatures. This would be consistent with a lower activation energy of heteroexchange (~ 80 kJ/mol) estimated for this composite as a powder (by using results of isothermal experiments as well as temperature –programmed exchange data analyzed by Eq. 36) compared to the activation energy of the surface exchange coefficient obtained by IEDP (~ 130 kJ/mol) [119].

3.4.3 Oxygen Temperature-Programmed Desorption (TPD) From Powders

O_2-TPD spectra for $LSFN_x$-GDC composites show that the increase of Ni content in $LSFN_x$ shifts beginning of desorption to lower temperatures and increases the rate of oxygen desorption (Fig. 90). Since the amount of oxygen desorbed in TPD run exceeds several monolayers (Table 10), the oxygen release from the sample caused by reduction of Ni^{3+} to Ni^{2+} is apparently controlled by the bulk diffusion. Direct estimation of heat of oxygen adsorption on perovskite or $LSFN_{0.3}$-GDC composite after high-temperature oxygen desorption by using microcalorimetric installation (Fig. 91) confirmed that indeed it varies in the range of 120-260 kJ/mole O_2 corresponding to terminal M-O forms including those fixed at defect centers (vide supra). Indeed, desorption of oxygen from LSFN perovskite in a broad temperature range (Fig. 35) suggests existence of surface sites with broadly varying oxygen bonding strength. Identical dependence of adsorption heat on the amount of desorbed oxygen for perovskite and perovskite-fluorite composite, despite twice as low content of perovskite in composite, demonstrates very fast redistribution of oxygen between perovskite and fluorite phases.

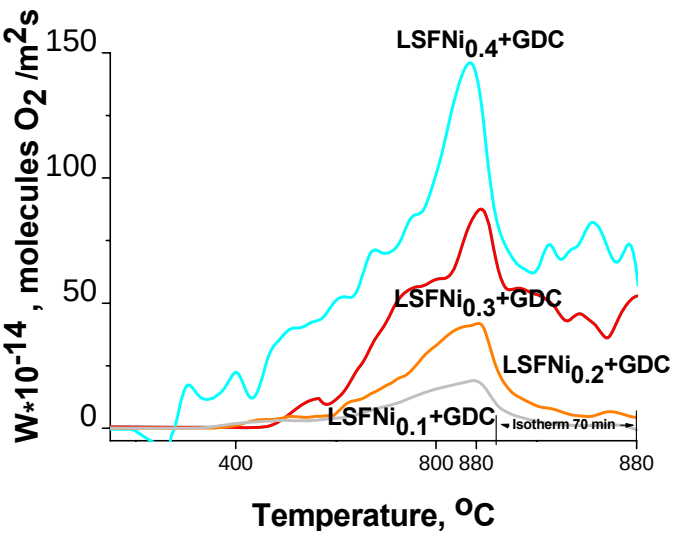

Figure 90. Effect of Ni content in LSFN perovskite on the O_2 TPD spectra for LSFN-GDC composites sintered at 1200 °C.

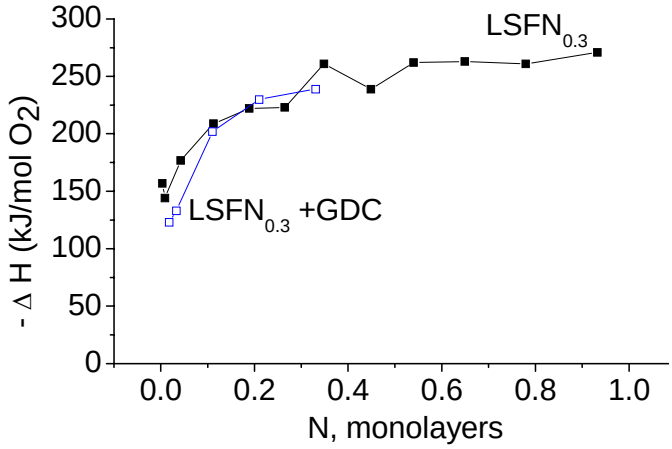

Figure 91. Heat of oxygen adsorption vs. amount of desorbed O_2 for $LSFN_{0.3}$ and $LSFN_{0.3}$ + GDC composite sintered at 1200 ^oC and pretreated in He at 750^oC. Pulses of O_2 in He at 450 ^oC.

The increase of the peak rate of oxygen desorption from composites with the sintering temperature (Fig. 92) apparently correlates with the porosity annealing thus increasing P-F interface. This suggests that P-F interface indeed provides a path for fast oxygen migration in the bulk and surface sites for reversible dissociation/recombination of oxygen molecules/atoms. In this case, a higher Ni content in perovskite provides a higher rate of oxygen desorption (Fig. 92), so for the air side of membrane composites with a higher Ni content could be more efficient in the oxygen activation. Hence, sintering temperature is to be optimized if porous composite materials are used in design of functionally graded SOFC cathodes.

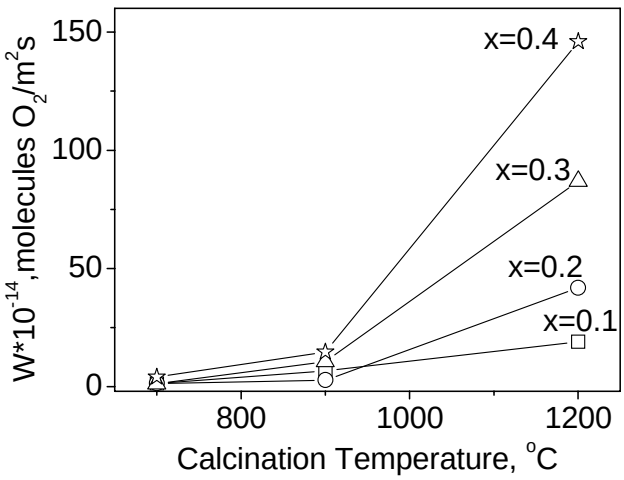

Figure 92. Temperature dependence of the maximum rate of O_2 desorption for $LSFN_x$-GDC composites.

The same trend of lattice oxygen mobility increasing with sintering temperature was observed for other nanocomposites (LSCF-GDC, LSM-ScCeSZ) both by oxygen isotope exchange and O_2 TPD (Fig. 93, Table 10). This suggests that P-F interface could indeed provide a path for fast oxygen migration. The maximum rates of oxygen desorption are comparable for composites of GDC with LSFC and LSFN (Table 10), while being several times lower for LSM-ScCeSZ composites (Fig. 93). This certainly correlates with a higher lattice oxygen mobility in the former composites estimated by the oxygen heteroexchange (vide supra).

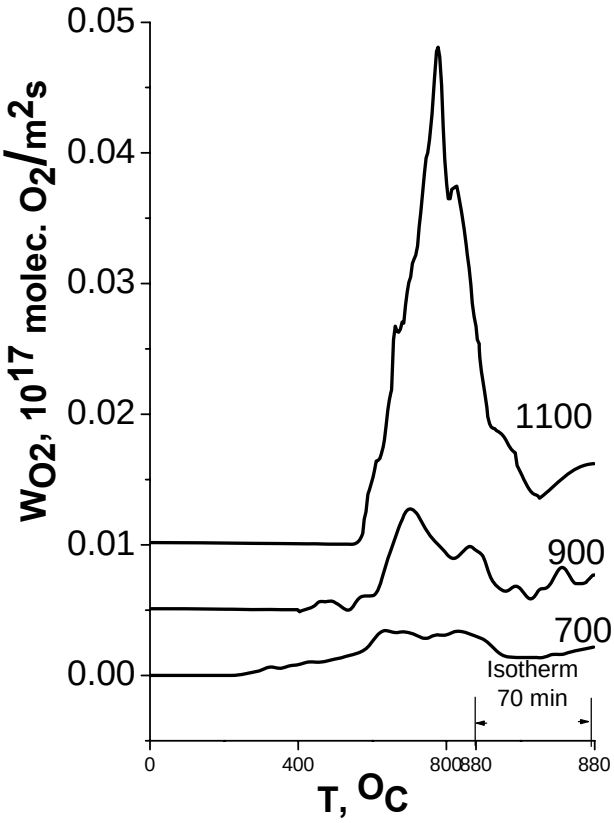

Figure 93. Temperature dependence of specific rates of O_2 TPD for LSM+ScCeSZ nanocomposite sintered at 700-1100 °C.

To verify whether the increase of the specific rate of oxygen desorption with the sintering temperature of nanocomposites can be indeed explained by increasing the oxygen bulk mobility, modeling of oxygen temperature-programmed desorption from powdered samples has been carried out. The model of oxygen temperature-programmed desorption accompanied by the oxygen diffusion from the bulk of oxide particles to the surface is represented by the system of differential equations:

$$\frac{1}{\beta}\frac{dC_{O_2}}{dT} = -\frac{1}{\tau}C_{O_2} + \frac{gSN_{O_S}}{N_G}k_{DES}\theta_{O_S}^2 \tag{47}$$

$$\frac{1}{\beta}\frac{d\theta_{O_S}}{dT} = -2k_{DES}\theta_{O_S}^2 + \frac{N_{O_{BULK}}V}{N_{O_S}S}D\left.\frac{\partial\theta_{O_{BULK}}}{\partial h}\right|_{\eta=0} \tag{48}$$

$$\frac{\partial\theta_{O_{BULK}}}{\partial t} = D\frac{\partial^2\theta_{O_{BULK}}}{\partial h^2} \tag{49}$$

Here β is the heating rate (grad/s); N_G – the total number of gas molecules in the volume of a flow reactor, C_{O_2} is the concentrations of oxygen in the gas phase; T is the reactor temperature; τ (s) is the contact time (a ratio between the reactor volume, V_R, m^3, and the feed rate of inert sweeping gas, $V_{He,}$ m^3/s); g – weight of sample, S – specific surface area (m^2/g); V– volume of sample (m^3); N_{O_S} and $N_{O_{BULK}}$ - the maximum oxygen capacity per the unit of the surface and the bulk, respectively; k_{DES} is the rate constant of desorption; D is the diffusion coefficient of oxygen in the oxide bulk (m^2s^{-1}) ; h is the characteristic size of oxide particle (m).

Calculations carried out within the frames of this model using some typical values of k_{DES} known for transition metal oxides and considering surface and bulk oxygen atoms to be uniform by bonding strength and mobility revealed that:

- In the absence of oxygen diffusion from the bulk of oxide particles, the maximum concentration of oxygen in the gas phase monitored continuously decreases proportionally to the specific surface area provided the surface adsorption capacity remains constant (Fig. 94 a), while the position of desorption peak remains the same. This provides independence of the maximum specific rate of desorption defined for the flow reactor as the product of the C_{O2}. and the flow rate of He related to the oxide surface unit.
- The oxygen desorption from the surface accompanied by a slow oxygen diffusion from the bulk of oxide particles is characterized by two desorption peaks situated at low temperatures (corresponds to oxygen desorption from the surface) and at high temperatures (corresponds to oxygen desorption from the bulk). With the increase of the bulk oxygen mobility in the oxide approaching the rate of diffusion to that of desorption from the surface (or even exceeding it), position of the high-temperature peak shifts to lower temperatures superimposing with the low-temperature peak (Fig. 94b). With decreasing specific surface area position of this peak shifts to higher temperatures due to decreasing the efficient diffusion coefficient D/h^2 as well as

decline of the oxygen flux at gas-solid interface determined by expression $\frac{N_{O_{BULK}} V_{CAT}}{N_{O_S} S} D \frac{\partial \theta_{O_{BULK}}}{\partial h}\Big|_{\eta=0}$.

In this case, the maximum oxygen content in the gas phase decreases rather slightly (Fig. 94b) which corresponds to some increase of the maximum specific rate of desorption. Hence, identical position of oxygen desorption peak for samples with broadly varying specific surface areas (particle sizes) observed in the case of perovskite-fluorite composites calcined at different temperatures (Figs. 92, 93) are expected only in the case when both oxygen bulk diffusion coefficients and specific constants of oxygen desorption increase with the particle size (sintering temperature). This apparently agrees with the data of oxygen isotope heteroexchange demonstrating the increase of the dynamic degree of exchange X_S (Figs. 83-85) and specific rates of heteroexchange (Figs. 86, 87) with the nanocomposites sintering temperature.

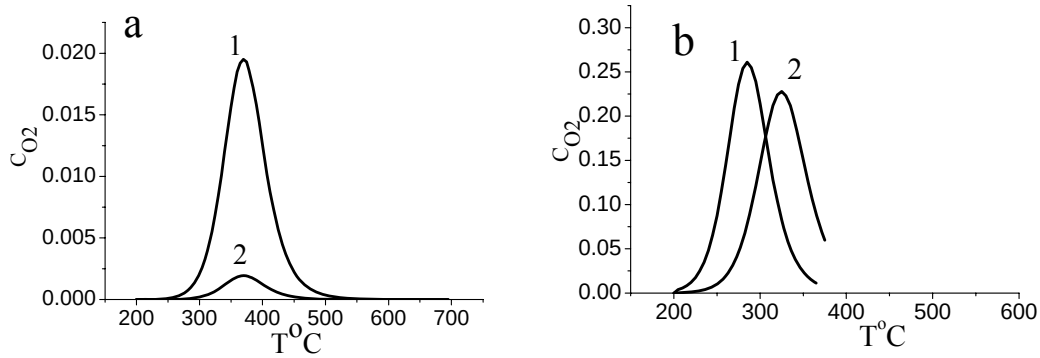

Figure 94. Oxygen TPD spectra calculated for the case of very slow (a) and fast (b) oxygen chemical diffusion in the bulk for samples with specific surface area 10 m^2/g (1) and 1 m^2/g (2).

3.4.4. Dynamics of Oxygen Desorption from Dense Samples

Gravimetric studies. Typical weight loss curves for the pellet of $LS_{0.4}FC$-GDC composite after step-wise changing the oxygen content in the feed are shown in Fig. 95. As judged by the whole weight loss (Fig. 96), only a small part of oxygen (~1-3%) is removed from sample in this temperature range, which agrees with O_2 TPD data for powder (Table 10). Kinetic curve (Fig. 97) is comprised of two characteristic parts intersecting approximately at the point of half conversion. The initial stage is described by the dependence proportional to the square root of time, while the final stage is described by the exponential time dependence. This picture qualitatively agrees with the model of pure diffusion controlled kinetics of oxygen removal from the pellet of a finite size. The initial stage corresponds to the movement of diffusion profiles from the two sides of pellet until they meet in the middle. At this stage, kinetics is described by the equation

$$\Delta M = 4\Delta M_{\max} \sqrt{\frac{D_{chem} t}{\pi d^2}} \qquad (50)$$

where ΔM is the current change of mass, ΔM_{max} - the change of mass at complete conversion (desorption), D_{chem} – the chemical diffusion coefficient, d - pellet thickness. This equation is valid for the plate with infinite thickness at $Dt<<d^2$ but approximation is satisfactory up to 30% conversion. At the final stage, kinetics is determined by the exponential decay of the most long-wave Fourier component of the concentration profile (with wavelength 2*d*). Respective temperature dependence is given by the equation

$$\Delta M = \Delta M_{max}\left(1-\exp\left(-\frac{\pi^2 D(t-t_0)}{d^2}\right)\right) \quad (51)$$

where t_0 - an efficient time of start-up of kinetics of this type provided it operates from the very beginning and is responsible for the whole mass loss ΔM_{max}. Fitting curves corresponding to equations 50 and 51 are shown in Fig. 97. Diffusion coefficients estimated from these two parts 1 and 2 were found to be close to each other and equal to $3*10^{-5}$ and $2*10^{-5}$ cm^2/s, resp.

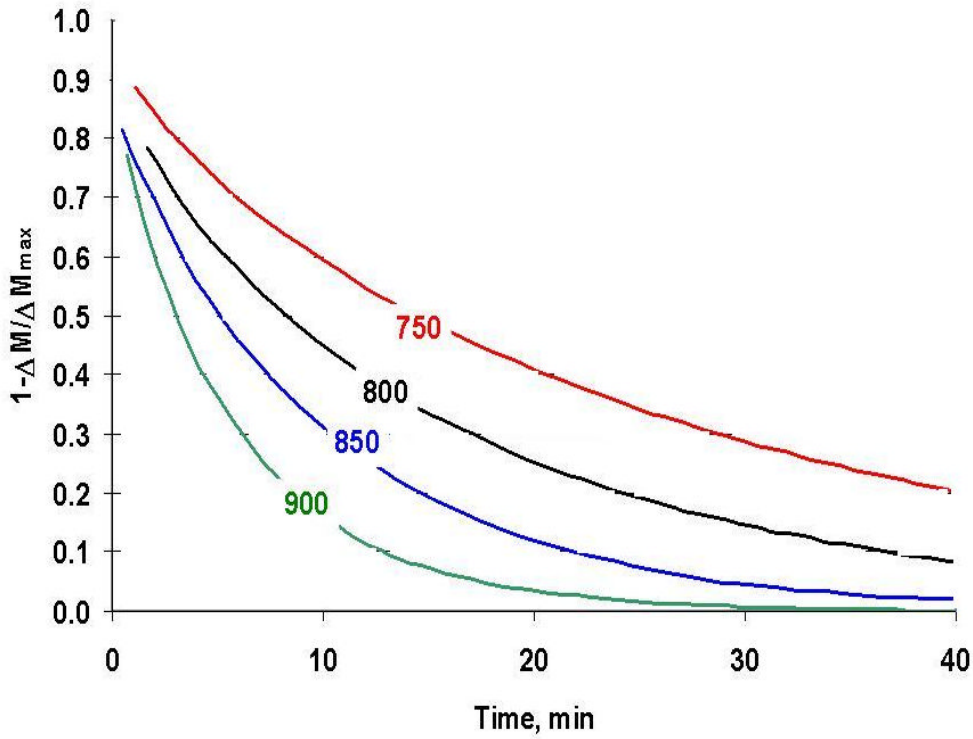

Figure 95. Weight loss curves for the pellet of $LS_{0.4}FC$-GDC composite after switching the stream of $14\%O_2+53\%N_2+$ 33%He to $1.4\%O_2+5.3\%N_2$ +93.3% He.

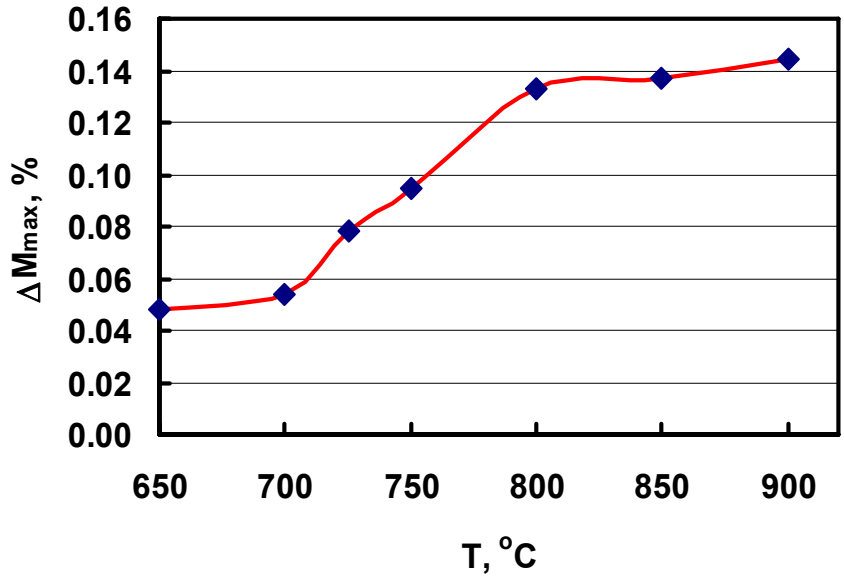

Figure 96. Temperature dependence of the maximum weight loss for gravimetric experiments of Fig. 95.

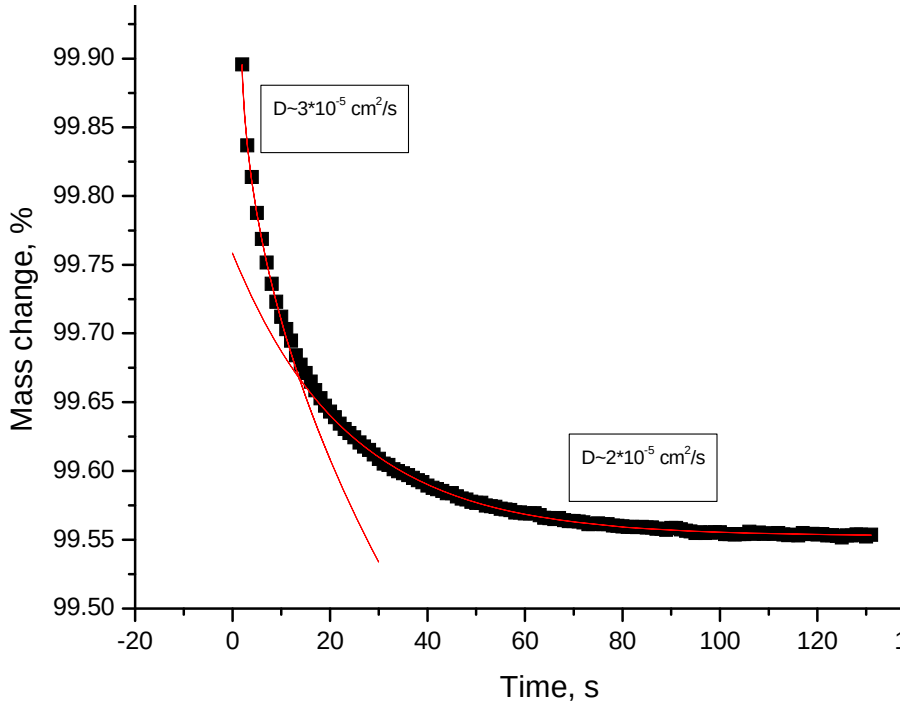

Figure 97. Typical results of fitting the weight loss curve for the pellet of $LS_{0.4}FC$-GDC composite at 900 °C by Equations (47-48).

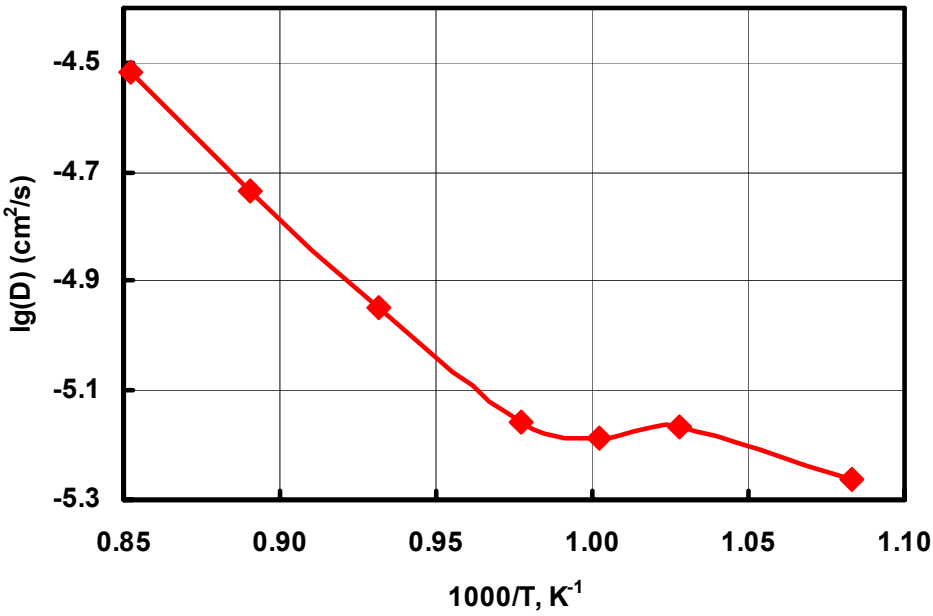

Figure 98. Temperature dependence of the oxygen chemical diffusion coefficient for the pellet of $LS_{0.4}FC$-GDC composite.

The temperature dependence of oxygen chemical diffusion coefficients for this composite is shown in Fig. 98. At 1073 K, the value of $D_{chem.}$~ 10^{-5} cm^2/s and activation energy ~ 110 kJ/mol are identical to those estimated for $LS_{0.4}FC$ perovskite by the weight relaxation method [41] and conductivity relaxation [39]. At lower temperatures, lower (~ 30 kJ/mol) activation energies of oxygen chemical diffusion provides higher values of $D_{chem.}$ for the composite found in this work (Fig. 98) as compared with pure $LS_{0.4}FC$ [39, 44]. This effect can be explained by impact of perovskite-fluorite interfaces as paths for fast oxygen diffusion. Indeed, this agrees with a small amount of oxygen desorbed in this temperature range (Fig. 96), which apparently differs by migration and/or bonding energy with majority of the lattice oxygen. Note that in the same intermediate temperature range low activation energies of oxygen self-diffusion were estimated for powdered composite by analysis of oxygen isotope exchange data (Fig. 88). From the structural point of view, diffusion of La and transition metal cations onto the surface of GDC domains revealed by TEM with EDX and XPS studies (vide supra) favours the formation of surface cerate layers with high mixed ionic-conductivity and, hence, oxygen mobility.

The values of the oxygen self-diffusion coefficient, D*, calculated from $D_{chem.}$ using known relations [39, 41, 44, 119] and taking the same value for the thermodynamic factor $\gamma=1/2(\partial \ln pO_2 / \partial \ln Co)$ for LSCF-GDC composite as for LSCF (~ 10^2) [41], are shown in Fig. 99. In the high-temperature range (~ 1100 K), the values of D (~ 10^{-7} cm^2/s) and their activation energy (~ 110 kJ/mol) estimated by the weight relaxation method correspond well to the values found by Esquirol et al for the same composite using IEDP-SIMS method [119].

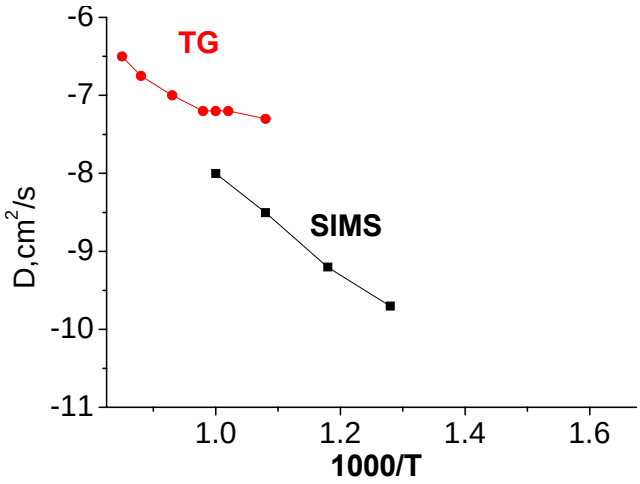

Figure 99. Comparison of oxygen self-diffusion coefficients for the pellet of $LS_{0.4}FC$-GDC composite estimated by SIMS [119] and TG (this work).

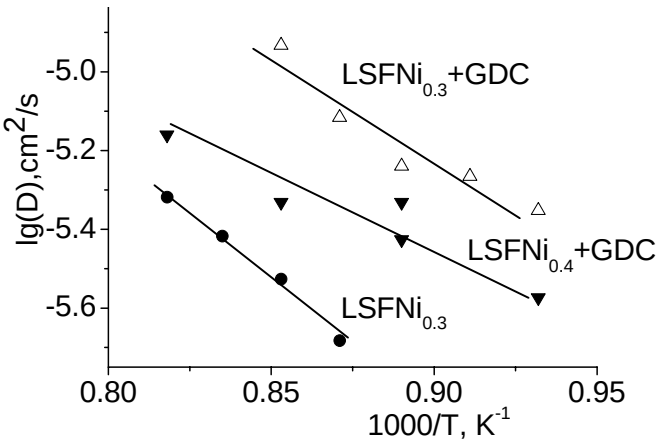

Figure 100. Temperature dependence of chemical diffusion coefficient for dense pellets of composites and perovskites sintered at 1330°C.

Fig. 100 shows temperature dependence of chemical diffusion coefficient for dense pellets of $LSFN_{0.3}$ perovskites and $LSFN_x$ –GDC composites sintered at 1330°C. In this case, higher values of $D_{chem.}$ for composites as compared with those for perovskite were found in the high-temperature range, which can be explained by a higher content of GDC (50%) in these composites (and, hence, more developed perovskite-fluorite interface) as compared with LSFC-GDC composite (30%). The activation energy of the oxygen chemical diffusion for $LSFN_x$ –GDC composites (~ 120-140 kJ/mol) is close to that for LSFC-GDC composite, though values of $D_{chem.}$ are somewhat lower (cf. Figs. 98 and 100). A higher value of D_{chem} for composite with a lower Ni content can be due to some segregation of NiO phase from $LSFN_{0.4}$ perovskite under high-temperature sintering (vide supra).

Conductivity relaxation studies. In agreement with weight relaxation studies, electrical conductivity relaxation method revealed that oxygen chemical diffusion coefficients in composites are approximately an order of magnitude higher than those in pure perovskite

phases (Fig. 101). This increase of chemical oxygen diffusivity is easily explained in terms of the effect of fast diffusion along the perovskite-fluorite interfaces. Note that the absolute values of these coefficients are somewhat higher that the values obtained by gravimetric studies (cf. Figs. 100 and 101). Hence, either conductivity relaxation method is more sensitive to the loss of oxygen from the surface layers of samples, or effect of perovskite-fluorite interfaces should be considered in frames of more detailed model considering fast transfer of oxygen along domain boundaries with a much slow diffusion within domains [10, 147]. At least, the difference between estimations made by different techniques could not be explained by the pressure difference effect, since the dependence of the oxygen chemical diffusion coefficient $\tilde{D}$ on the oxygen pressure is rather moderate for both perovskites and composites (Fig. 102).

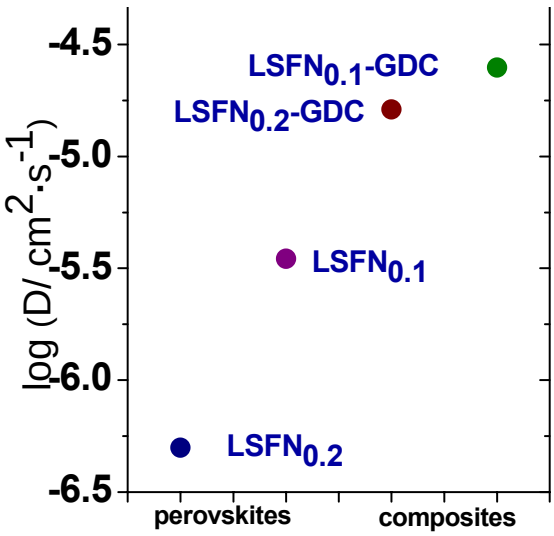

Figure 101. Oxygen diffusion coefficient values at 800°C for perovskites $LSFN_x$ and their composites with GDC.

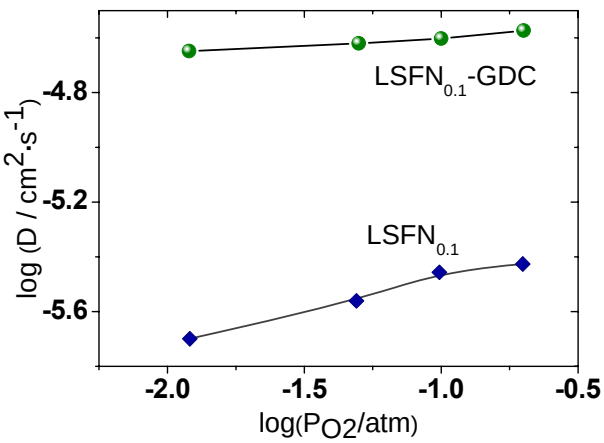

Figure 102. The dependence of chemical diffusion coefficients on the oxygen pressure for $LSFN_{0.1}$ and $LSFN_{0.1}$-GDC composite an 800 °C.

3.4.5. Temperature--Programmed Reduction

H_2 TPR spectra for studied composites are presented in Fig. 103-106. The spectra profiles and peak positions depend on the composition and calcination temperature of samples. For composites sintered at high temperatures, the low-temperature peaks are situated at lower temperatures as compared with perovskites (Fig. 104). Furthermore, for $LSFN_{0.3-0.4}$ –GDC composites sintered at 1200 °C, several peaks in the region 400-800 °C appear (Figs. 104-105). These features can be assigned to bulk reduction of GDC domains accelerated due to H_2 activation on small Ni^o clusters formed by reduction of Ni cations on the GDC surface (vide supra). The fastest reduction in the low-temperature range is observed for $LSFN_{0.3}$ –GDC composite possessing the highest oxygen mobility (Fig. 105). In general, specific rates of composites reduction increase with the sintering temperature thus correlating with the lattice oxygen mobility (vide supra). For $LSFN_{0.3}$ -GDC and LSFC -GDC nanocomposites sintered at 1200 ^oC, the maximum rate of reduction by H_2 exceeds at least several times that for Mn-containing fluorite –perovskite composites [11]. Hence, a high oxygen flux in composites under high oxygen chemical potential gradient makes these materials attractive for design of membranes for syngas generation from hydrocarbons via their selective oxidation with oxygen transferred from the air side to the fuel side of these membranes.

CH_4-TPR. Typical curves of product evolution in CH_4 temperature-programmed reduction of $LSFN_{0.3}$-GDC composite calcined at 1200°C are shown in Fig. 107. First CO_2 appears at ~ 700 ^oC, then CO and H_2 simultaneously evolve. Isothermal experiments (Fig. 108) revealed that CO and H_2 formation is described by typical topochemical kinetics even at 700 ^oC, i.e. reduction of nanocomposite by methane proceeds via nucleation and growth of reduced phases (Ni or Ni alloy particles). CO_2 appears immediately after CH_4 contact with the catalyst surface evidencing a high reactivity of the surface oxygen of these composites.

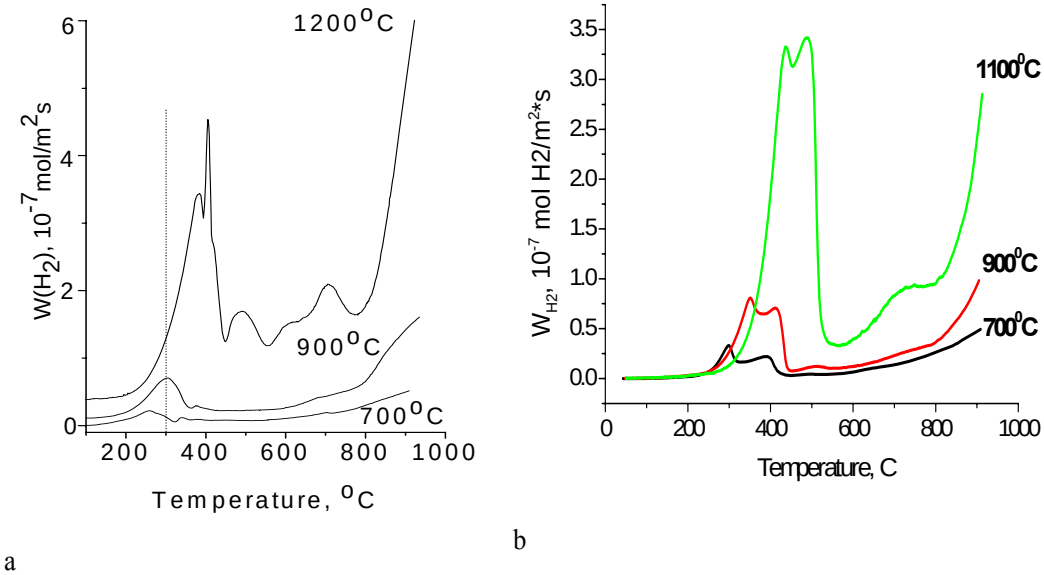

Figure 103. H_2 TPR spectra of $LSFNi_{0.3}$ –GDC (a) and $LSFNi_{0.4}$ –GDC (b) calcined at different temperatures.

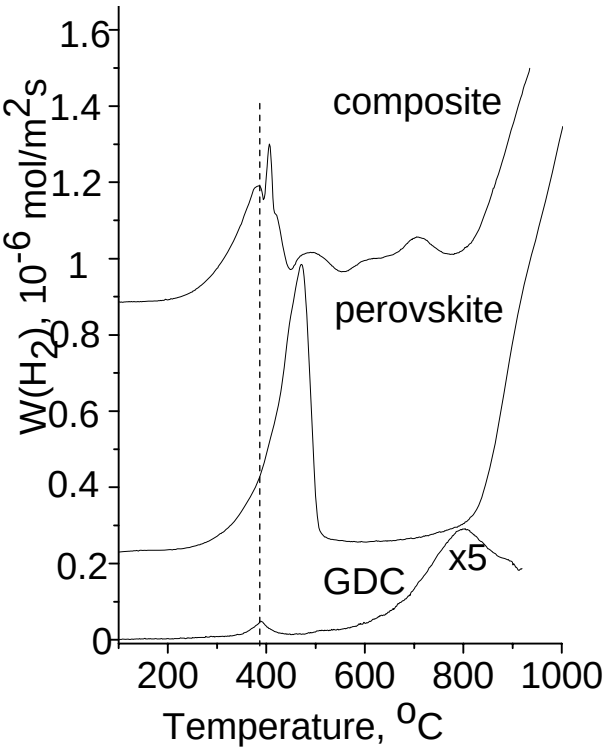

Figure 104. H_2 TPR spectra for $La_{0.8}Sr_{0.2}Fe_{0.7}Ni_{0.3}O_3$ (perovskite), $Ce_{0.9}Gd_{0.1}O_{1.95}$ (GDC) and their composite calcined at 1200 ˚C.

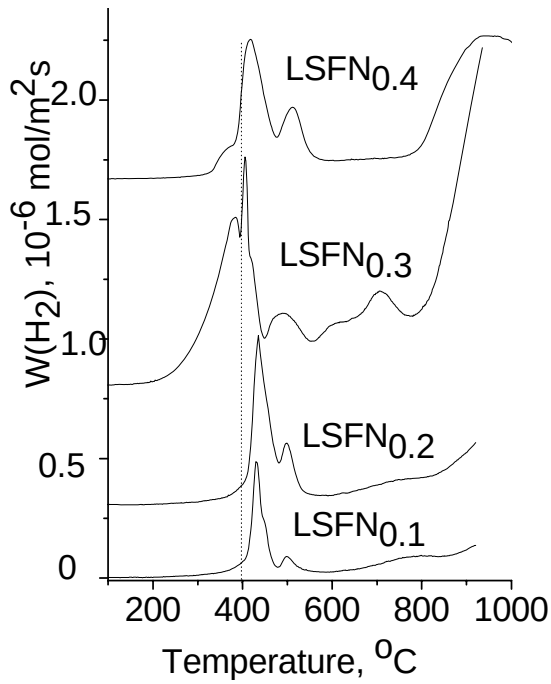

Figure 105. H_2 TPR spectra for $LSFNi_x$ –GDC composites calcined at 1200 ˚C.

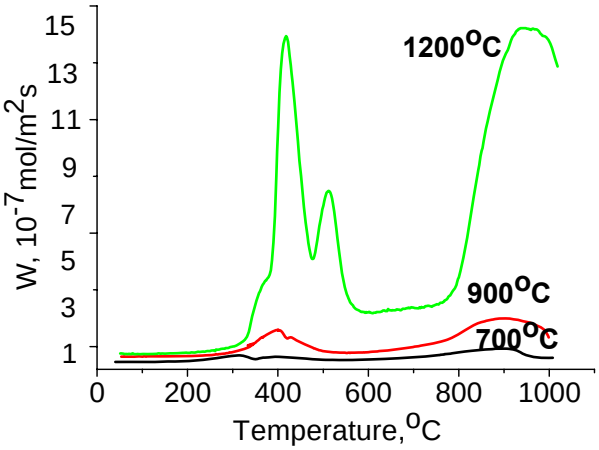

Figure 106. H_2 TPR spectra for LSFC-GDC composite calcined at 700 °C, 900 °C and 1100 °C.

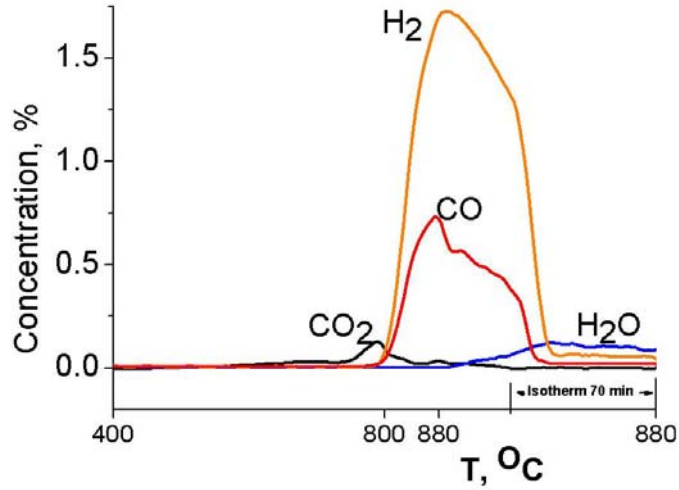

Figure 107. CH_4 TPR spectra for $LSFN_{0.3}$-GDC composite sintered at 1200 °C.

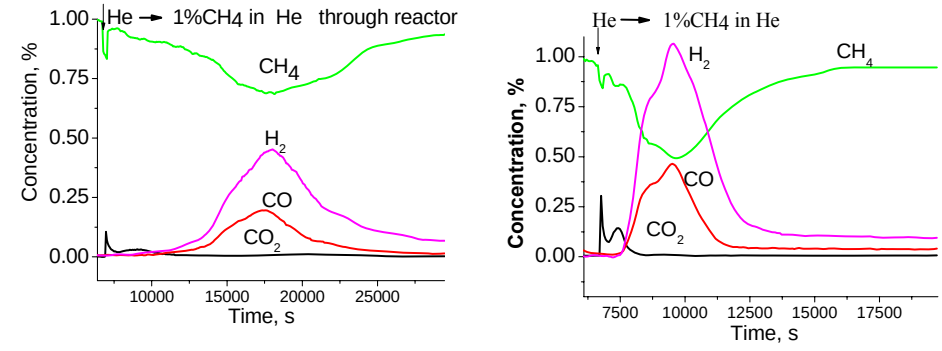

a b

Figure 108. Dynamics of isothermal reduction of sintered at 1200 °C $LSFN_{0.3}$-GDC composite in the flow of 1% CH_4 in He at 700 °C (a) and 800 °C (b).

The peak rates of CO/CO_2 evolution during CH_4-TPR for $LSFN_x$ - GDC composites (Fig. 109) and LSFC-GDC composites (Table 10) increase with their sintering temperature. This certainly correlates with the increase of the lattice oxygen mobility characterized by oxygen isotope exchange or O_2 TPD (Table 10).

The dependence of peak rate of CO/CO_2 evolution during CH_4-TPR on Ni content in composites calcined at 1200°C is presented in Fig. 110. Increasing Ni content up to x=0.3 leads to a little increase of the peak rate values for both CO and CO_2 evolution, and only at x=0.4 they increase substantially. In all cases, CO peak rates exceed those of CO_2 evolution.

Similarly, peak rates of CO_2, CO and H_2 formation in the course of CH_4 TPR for LSM-ScCeSZ composite sample increase with the sintering temperature (Fig. 111).

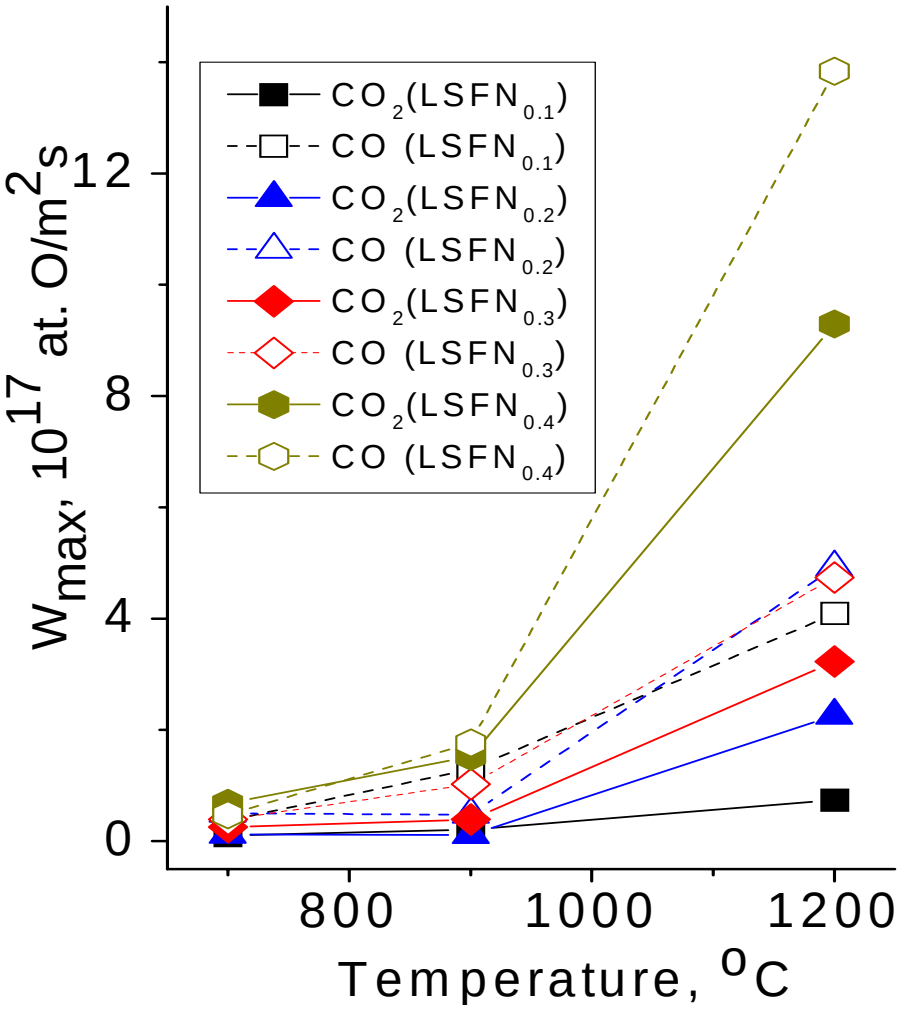

Figure 109. Dependence of the peak rate of CO/CO_2 evolution during CH_4-TPR on calcination temperature of composites 50%$LSFN_x$+50%GDC.

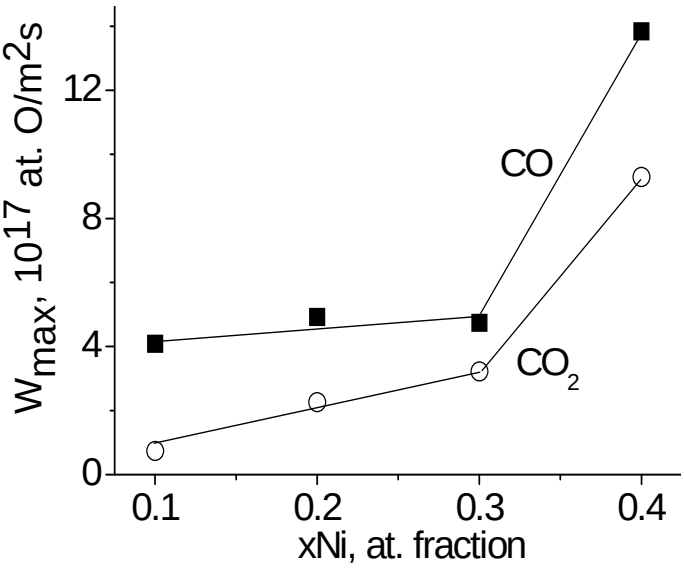

Figure 110. Dependence of peak rate of CO/CO_2 evolution during CH_4-TPR on Ni content in $LSFN_x$ composite calcined at 1200°C.

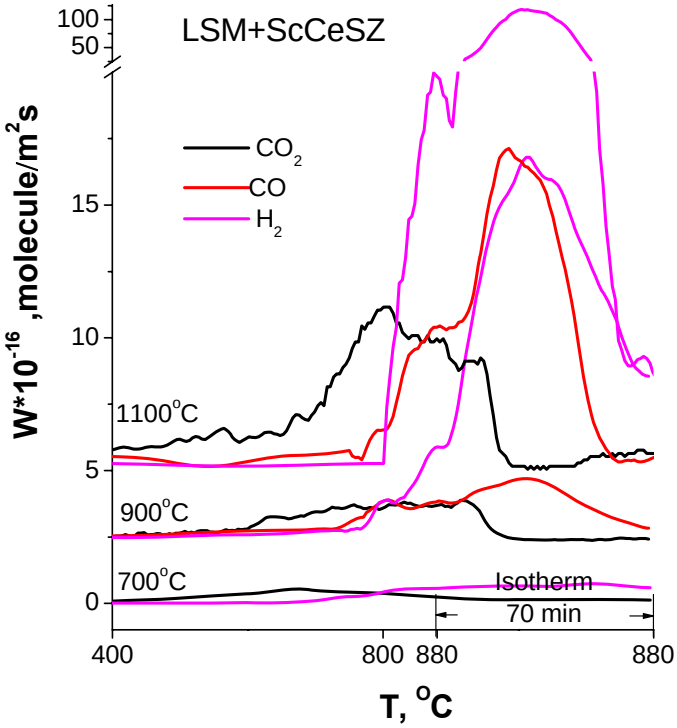

Figure 111. Typical curves of CO_2, CO and H_2 evolution during CH_4 TPR for LaSrMn- ScCeSZ composites calcined at 700, 900 and 1100°C.

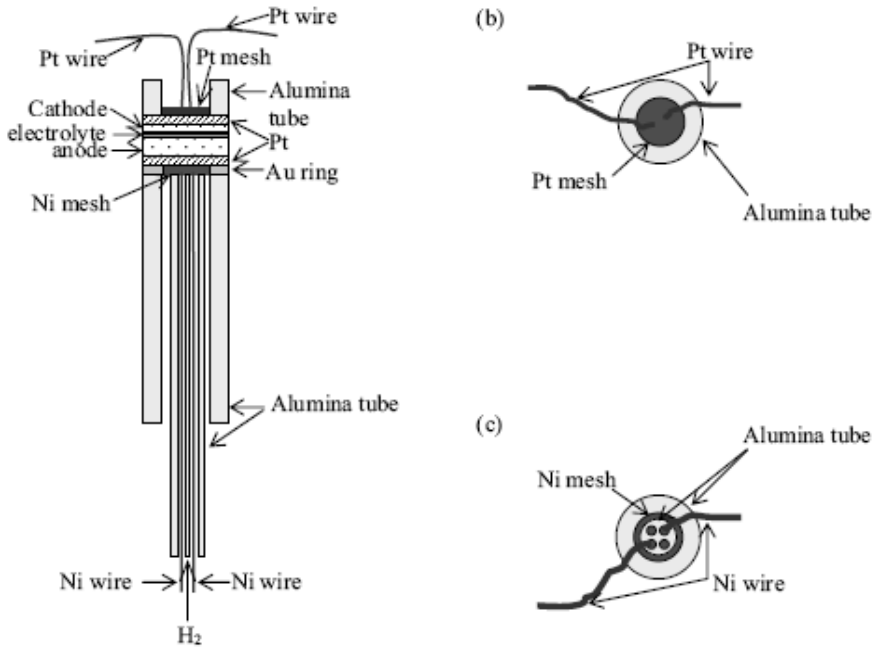

Figure 112. Schematic illustration of the SOFC test rig and the pellet assembly: cross sectional view (a), top (b) and bottom (c) of the cell (1.3 cm^2).

4. Design and Testing of IT SOFC Cathodes

Details of button-size cells assembling and their testing procedures are given in [148]. NiO-YSZ/YSZ(ScYSZ)/cathode fuel cells with and without GDC functional layer between electrolyte and cathode were assembled using prefabricated anode-supported planar half cells manufactured either in Research Center Juelich, Germany, or at the Institute of Thermophysics SB RAS (Novosibirsk). In the last case, either YSZ or ScYSZ layers (10 microns) were supported by chemical vapor deposition (CVD).

Schematic sketch of the setup is shown in Fig. 112. Humidified (5% RH) hydrogen at 0.03-0.2 L/min and air at ambient conditions were used as a fuel and an oxidant, respectively. Pt paste and Pt mesh from the cathode and Pt paste and Ni mesh from the anode side were used as current collectors.

The morphological characterization and chemical composition of the tested SOFCs was performed using SEM equipped with EDX analyzer. The SOFC samples were embedded in epoxy resin and polished using Cr_2O_3. The SEM images of SOFCs cross –sections were made with a JSM-6460 LV (Jeol, Japan) microscope.

Compositions of cells are given in Table 11.

4.1. Single Layer Cathodes

As can be seen from data presented in Figures 113, 114, performance of cells with a single layer cathode (without GDC functional layer) is low. Using LSNF+GDC composite

results in some improvement of performance (Fig. 113). However, the cell performance decreases gradually after increase of the temperature of testing (Fig. 113).

Table 11. Some characteristics of cells

Fuel cell #	Cathode layer	Functional layer
1	50% GDC + 50% LSFN	No
2	LSFN	No
3	LSFN	GDC
4	50% GDC + 50% LSFN	GDC
5	LSFN; 50% GDC + 50% LSFN (two- layered cathode)	No
6	LSFN; 50% GDC + 50% LSFN (two- layered cathode)	GDC
7	LSCF	No
8	LSCF	GDC
9	LSFN; 50% GDC + 50% LSFN (two- layered cathode)	GDC
10	LSFN	LSM-ScCeSZ
11	LSFN	LSFN-ScCeSZ

In the case of LSCF cathode, a much lower power density of the cell (Fig. 114) as compared with that provided by LSNF cathode (Fig. 113) is obviously caused by peeling of the cathode layer due to a higher LSCF thermal expansion coefficient (TEC), and, hence, its bigger mismatch with YSZ. However, decline of performance of cell with LSCF cathode in isothermal conditions clearly indicates on the pronounced chemical interaction between YSZ electrolyte and LSCF with formation of low conducting $La_2Zr_2O_7$ and $SrZrO_3$ layers. Such an interaction clearly takes place with LSNF cathode as well, which is confirmed by SEM/EDX analysis of cells after testing (Fig. 115). According to this data, diffusion of Zr atoms through the cathode layer takes place. In the case of the cell 1 with LSFN cathode, Zr atoms are distributed throughout the cathode layer (Fig. 115).

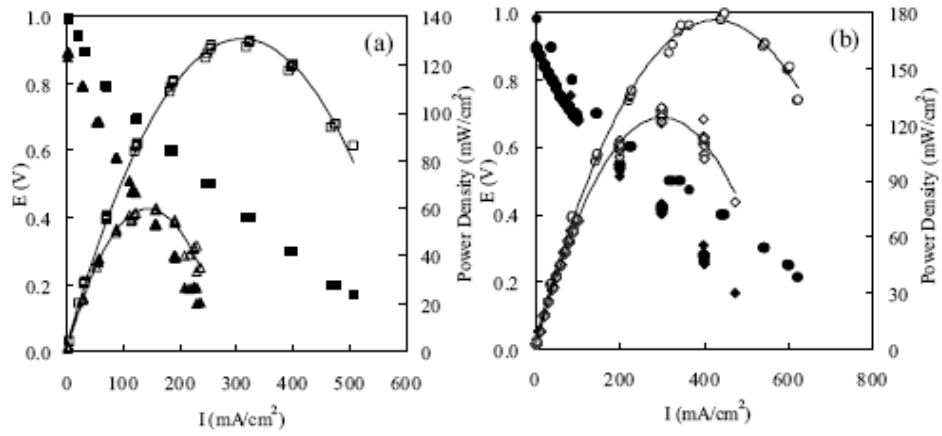

Figure 113. (a) -voltage and power density vs. current density for SOFCs at 700 °C with single layer cathode: Δ – LSFN, □ – LSNF-GDC composite; (b)- performance of the cell 2 with composite cathode at 750: • – in 1 h; ◊ – in 2.5 h.

Besides, a new rather dense layer mainly containing Zr and La cations was formed between the electrolyte and porous cathode layers. Being morphologically different from the porous cathode, this new dense layer was well visible in the SEM image (Fig. 115). This new layer can be a reason for delamination of the cathode layer during heating-cooling cycles. However, it should be mentioned that peeling observed in the SEM images is caused by the samples preparation including their fixing in epoxy resin.

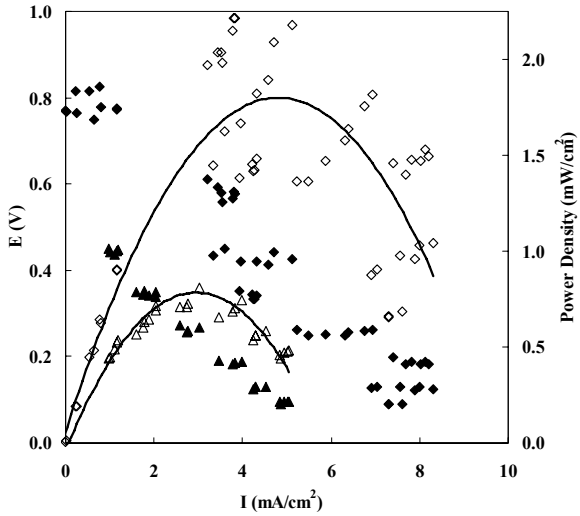

Figure 114. Performance of the SOFC with LSCF as the single layer cathode at 700 ºC after load of 0.5 V for 1 h (♦) and 4.5 h (▲) at 700 ºC.

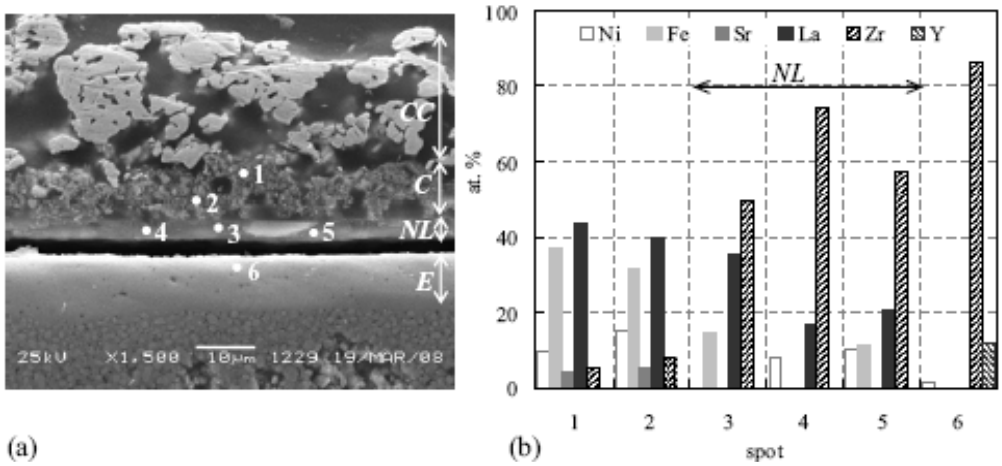

Figure 115. SEM micrographs for the cell 1 after testing: cross-section (a) and EDX analysis data in different spots near the cathode-electrolyte interface (b); CC – current collector, C – cathode, NL – new low conducting layer, E – electrolyte.

Hence, main problems for using LSFN and LSCF complex peroskites as cathode materials for IT SOFC based on YSZ as electrolyte layer are their chemical interaction and TEC mismatch with the electrolyte. To prevent strong chemical interaction of the cathode

material and YSZ resulting in formation of undesirable phases and/or destruction of dense electrolyte layer, a GDC functional layer was used.

4.2. Cathodes with GDC Functional Layer

As follows from data of Fig. 116, supporting of GDC functional layer considerably improved performance of cells with all types of cathode materials. The cell with LSFN cathode has the best performance among tested cells. According to the data of SEM with EDX (Fig. 117), a positive effect of GDC interlayer seems to be primary associated with hampering of Zr cations migration into cathodes layers this suppressing formation of dense La-Zr-O layers with a low conductivity. Another factor is *in situ* formation of nanocomposite when supporting perovskite layers on porous GDC layer. This clearly helps to match the thermal expansion coefficients of composite cathodes and YSZ, thus improving contact and providing developed three-phase boundary required for a good performance. However, another important factor could be a chemical interaction between LSNF and GDC nanoparticles under load (Fig. 118) leading to increase of the power density with time. This feature can be assigned to migration of Ni cations onto the surface of GDC and/or YSZ creating new sites for O_2 molecules dissociation as earlier revealed for nanocomposite powders by oxygen isotope exchange studies (vide supra). A driving force for this migration could be an inherent instability of Ni^{2+} cations in the cubic perovskite structure reflected also in appearance of some traces of NiO phase in the course of LSNF-GDC nanocomposites sintering (vide supra). From these point of view, a lower performance of cells with LSNF+GDC nanocomposite cathode and porous GDC functional layer can be assigned to a lower LSNF concentration at GDC interface decreasing mixed ionic-electronic conductivity and weakening positive effects of LSNF-GDC interaction under load.

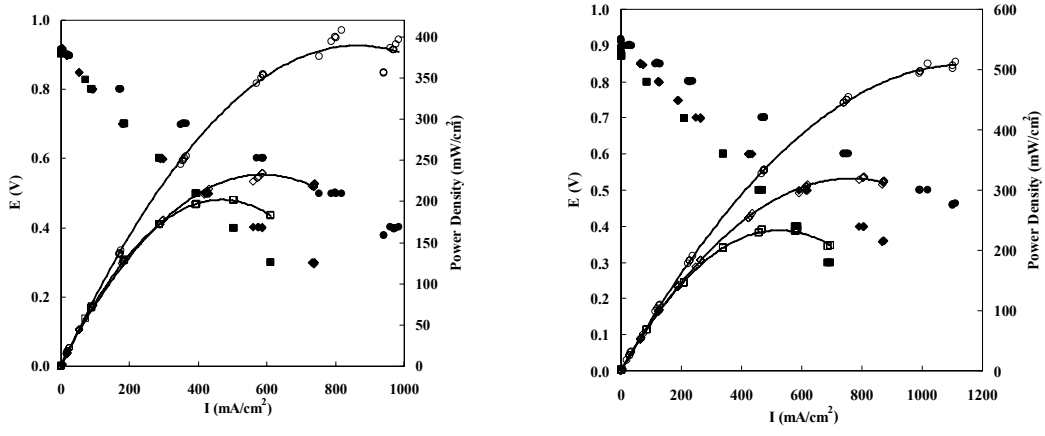

Figure 116. Performance of cells with the GDC functional layer between the cathode and YSZ at 700 (a) and 750ºC (b) after 0.5 V load for 15 h at 700ºC: ● - LSFN; ♦ – 50% LSFN + 50% GDC; ■ - LSCF.

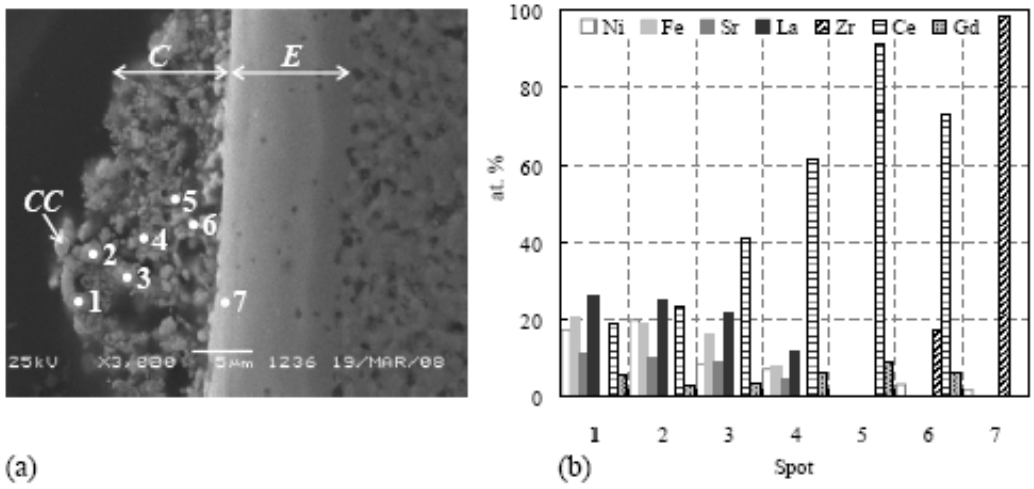

Figure 117. *SEM* micrographs of a cell cross-section for the cell #4 with composite LSNF+GDC cathode after testing (a) and data of the EDX analysis in different spots near the cathode electrolyte interface (b); CC – current collector, C – cathode, E – electrolyte. Note that the current collector was peeled off during the sample preparation for SEM study.

On the contrary, for LSCF cathode interaction of perovskite with GDC results in performance decline with time-under-load (Fig. 119). Perhaps, in this case a negative effect of time-under-load can be assigned to a higher Sr content in used sample of $La_{0.58}Sr_{0.4}Co_{0.2}Fe_{0.8}O_{3-\delta}$, so mainly Sr migration on the surface of CDC occurs leading to formation of surface cerate layers with a low conductivity. A small difference between the maximum power densities at different temperatures (Fig. 119) suggests progressing transfer of Sr with the temperature increase.

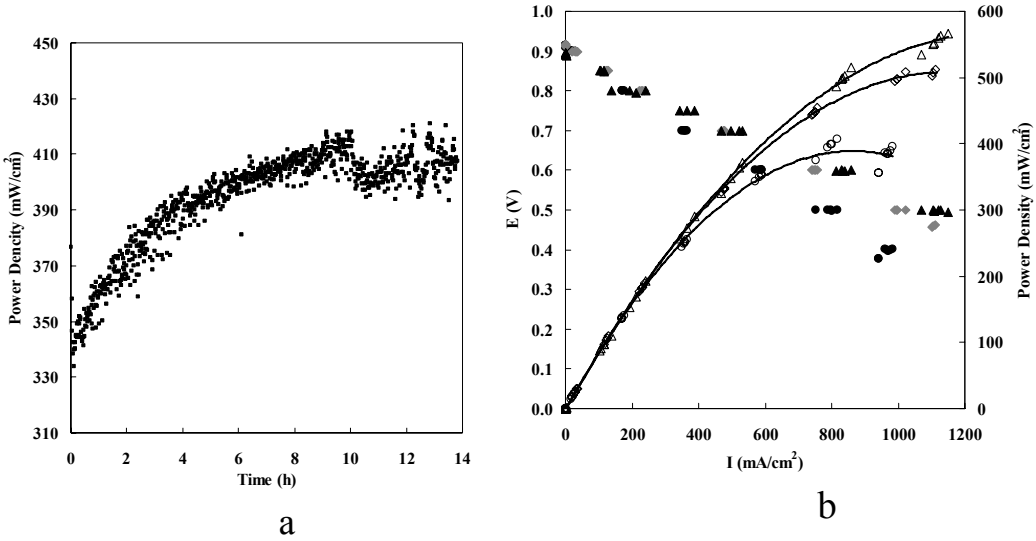

Figure 118. Time dependence of the power density of the SOFC with the GDC functional layer between the LSFN cathode and the electrolyte under load of 0.5 V at 700 ºC (a) and performance of the SOFC with the GDC functional layer between the cathode and LSFN electrolyte at different temperatures after 0.5 V load for 15 h at 700 ºC (b): ● – 700 ºC; ♦ - 750 ºC and ▲ – 800 ºC.

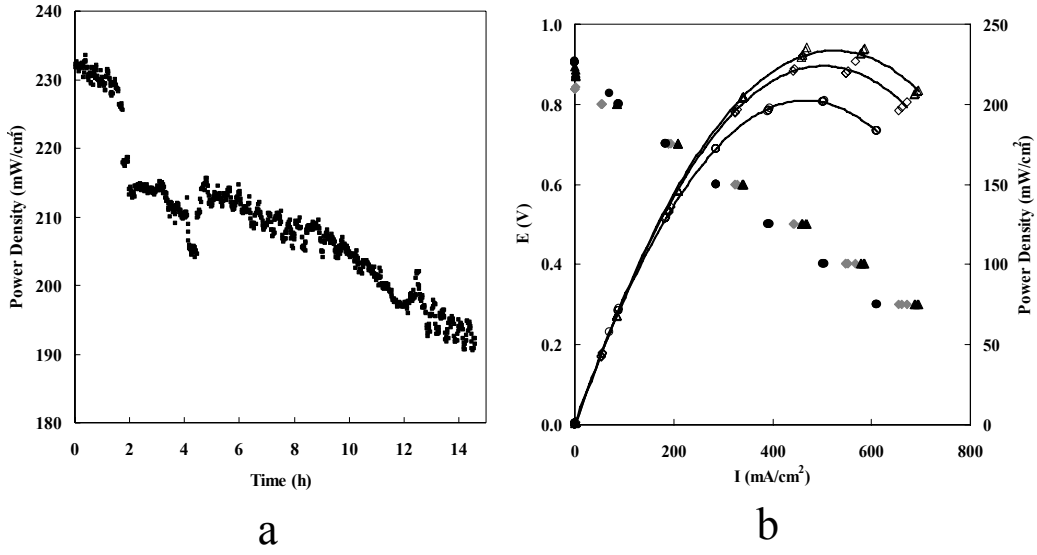

Figure 119. Time dependence of the power density of the SOFC with the GDC functional layer between the LSCF cathode and the electrolyte under load of 0.5 V at 700 ºC and performance of the SOFC with the GDC functional layer between the LSCF cathode and the electrolyte after 0.5 V load for 15 h at 700 ºC (●); 750 ºC (▲) and 800 ºC (♦).

4.3. SOFCs with Thin Nanocomposite Functional Layers

In designing functionally graded cathodes, one of the most important problems is providing a good sintering of GDC interlayer with YSZ dense layer required for ensuring a low area specific resistance (ASR) at intermediate temperatures. Though different sintering agents (Li salts, Co oxide etc) were suggested [149, 150], the problem is still far from being solved.

As alternative approach, nanocomposites LSM-ScCeSZ and LSNF-ScCeSZ were supported as thin (ca 5 microns) layers on thin dense YSZ or ScYSZ layers (Table 11). Additional advantage of these nanocomposites is their good sinterability at reasonable low (1000 ^{o}C) temperatures.

As follows from Figs. 120 and 121, performance of cells with these functional layers and LSFN as thick porous cathode layers is rather good even exceeding that for cells with GDC interlayers. For our graded design of cathodes, the maximum power density values (Figs. 120, 121) are comparable with the best published results obtained with composite cathode layers in cells with thin YSZ electrolytes [126, 151, 152]. In all cases, performance was stable at least for 10-30 hours. SEM studies with EDX analysis of cells discharged after tests has not revealed formation of isolating pyrochlore layers between composite interlayers and electrolyte, though some additional transfer of Zr cations into the interlayer takes place.

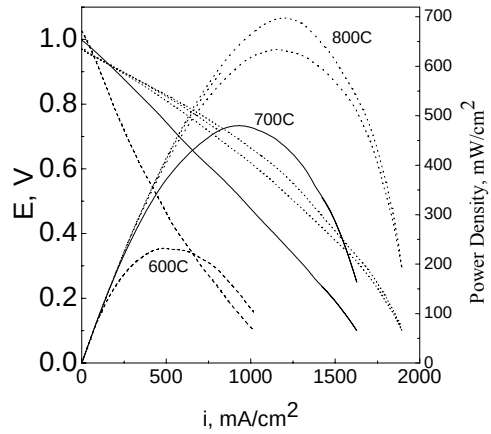

Figure 120. Typical performance of button-type cell with LSM-ScCeSZ interlayer and $LSFN_{0.2}$ cathode.

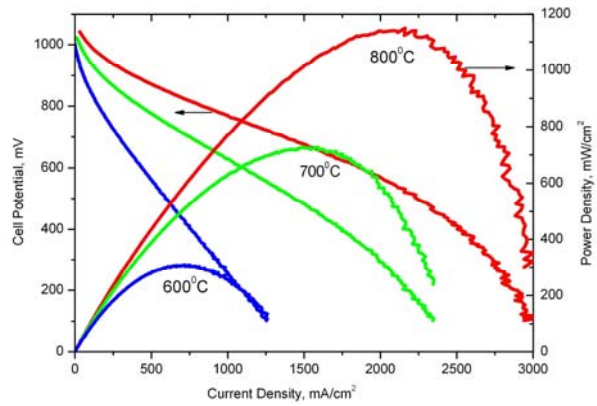

Figure 121. Typical performance of button-type cell with LSNF-ScCeSZ interlayer and $LSFN_{0.2}$ cathode.

Hence, interlayers comprised of GDC or nanocomposites of perovskites with ScCeSZ allow to provide a high and stable performance of anode-supported SOFC in the IT range.

5. Design of Asymmetric Multilayer Membranes Based on Mixed Ionic-Electronic Conducting Composites

It is well known that for thick dense oxygen permeable membranes the oxygen flux is limited by the oxygen diffusion [4, 44-47]. A number of studies clearly showed the promising features of asymmetric supported membranes with a thin dense layer for high-performance oxygen separation [44, 153-156]. However, fabrication of such membranes is still a challenge because of difficulty in obtaining porous supports with desirable properties in terms of pore size, gas permeability, thermal/mechanical stability and compatibility with MIEC materials by thermal expansion coefficients (TEC) [157, 158]. One of the promising solutions is to use a robust macroporous substrate on which MIEC nanocomposite layers with graded porosity

and chemical composition would be consecutively deposited [157]. Combination of meso- and micro-porous MIEC layers with a thin gas-tight layer provides a maximal oxygen flux under mixed surface exchange kinetics/bulk diffusion control [159, 160].

In our research, LSFN-GDC nanocomposites (vide supra) were supported as layers with a graded porosity onto macroporous metallic plates made from Ni-Al alloy compressed foam possessing a high thermal stability and mechanical strength due to segregated corundum surface layer [117]. From the fuel side, a dense layer of $MnFe_2O_4$ (MF) - GDC nanocomposite possessing required phase stability and oxygen mobility in strongly reducing conditions [161] was supported. This layer was covered by a porous layer of La-Ni-Pt/Ce-Zr-Pr-O catalyst known to be efficient and stable to coking in the reaction of methane transformation into syngas in stoichiometric CH_4/H_2O feeds [117, 162].

5.1. Preparation of Membrane

Macroporous open-cell nickel foam substrate was manufactured by the nickel electroplating of the polyurethane foam samples (cell density 60 ppi) followed by sintering in the dissociated ammonia atmosphere at 1100^{o}C for 1 h. The foam samples were then deformed by a uniaxial compression to 1 mm thickness modifying the cell morphology and decreasing porosity from 95.5 % to 60-80 %. Deformed foams were subjected to the pack aluminizing and then annealed at 1000 C for 1 h under air to form a thin α-alumina layer over the foam cell walls/ribs for a better adhesion of composite layers.

Fabrication of a supported multilayer membrane followed the next steps. First, a disc cut from membrane was pressed and spark-welded into the stainless steel ring to prevent its bending under subsequent manipulation procedures. Then the cells of a foam support from one side of a membrane were filled with macroporous layer of a coarse (fraction up to 10 microns) particles of $LSFN_{0.3}$+GDC composite presintered at 1200 ^{o}C and ball milled. A thick viscous slurry of these particles in isopropanol with addition of PVB was supported on the substrate via slip casting. This procedure was repeated several times with intermediate drying and calcination at 900-1000°C after each supporting until required uniform filling of foam cells for depth ~ 0.1 mm was achieved. For filling macropores between the coarse particles of composite (thus forming a mesoporous layer with thickness 10-20 microns), a highly dispersed $LSFN_{0.3}$+GDC composite precalcined at 700°C was next supported several times from suspension prepared by ultrasonic dispersion of nanocrystalline powders in isopropanol with addition of PVB. Next the gas-tight layer (thickness ~ 10 micron) comprised of GDC+$MnFe_2O_4$ (MF) 1:1 nanocomposite was supported via slip casting of a slurry in isopropanol with addition of PVB prepared using nanocrystalline MF synthesized via Pechini route. A special smoothing procedure was applied to restrict the thickness of this layer, thus keeping its upper surface at the outside level of the foam cell ribs. To attain complete densification of this layer by sintering at 1200°C under Ar flow, such additives as Cu, Bi or Ag nitrates were used. The gas-tight layer was washcoated by a porous catalytic layer comprised of $Pr_{0.3}Ce_{0.35}Zr_{0.35}O_{2-x}$ complex oxide with La-Ni-Pt active component (~ 10 wt.% of $LaNi_{0.9}Pt_{0.1}O_3$) supported by the incipient wetness impregnation with the mixed solution of H_2PtCl_6 and La and Ni nitrates followed by calcination at 1000 ^{o}C. Finally, the main bulk of foam substrate and the surface of macropores in the coarse nanocomposite layer were covered

with a thin layer of $LSFN_{0.4}$ by membrane impregnation from the air side by a suspension of perovskite in isopropanol with addition of PVB followed by drying and calcination at 1000 ^{o}C.

5.2. Membrane Reactor Testing

To ensure the gas-tight sealing of supported disc membrane in titanium lab-scale reactor, it was first placed in specially designed copper washers, pre-sealed using Ag paste, pressed and preheated under Ar flow at 900 ^{o}C to provide a hermetic junction between the membrane steel ring and a copper washer/ring (Fig. 122a, b). Such a disc was inserted between two halves of specially designed Ti reactor (Fig. 122c), and the copper ring was compressed by using bolts and nuts ensuring required sealing.

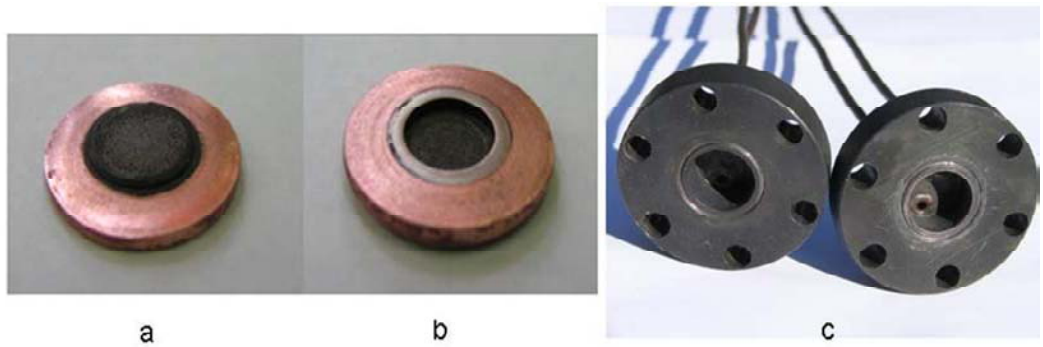

Figure 122. Typical images of small-size membrane disc embedded into the copper washer (a, b) and titanium lab-scale reactor for lab-scale membrane testing (c). a-fuel side, b-air side of membrane.

The testing results were obtained for membrane with the working surface area of 1.1 cm^2. At the outlet from the fuel side of the reactor, the reactor was loaded by a layer (about 1 cm^3) of the catalyst with the same active component $LaNi_{0.9}Pt_{0.1}O_3/Pr_{0.3}Ce_{0.35}Zr_{0.35}O_{2-x}$ supported on the microspherical γ-alumina fixed between two Fechraloy gauzes protected by corundum layer supported by dust blasting technique [162].

The membrane reactor was tested in the flow kinetic installations using feeds containing 4.5-20 vol.% CH_4 (1-15 L/h) and purified air (0.7-60 L/h) supplied into the fuel and air parts of the reactor, respectively. Concentrations of reagents and products were determined by using gas chromatographic analysis and on-line IR absorbance gas analyzer PEM-2M equipped with an electrochemical H_2 sensor [162].

In all experiments, periodical checking of the exit feed by gas chromatographic analysis on the N_2 admixture revealed its absence within the limit of analysis sensitivity (~ 0.1%). Hence, membrane retained its integrity and oxygen permselectivity in studied conditions.

As follows from Fig. 123, for feeds with a low CH_4 content, at a low feed rate mainly deep oxidation of CH_4 occurs. The increase of the flow of the fuel mixture results in the increase of selectivity of methane conversion into syngas, which is associated with the change of balance between the oxygen flux through the membrane and methane supply. H_2/CO ratio ~ 2 observed at high flow rates agrees with the stoichiometry of methane partial oxidation into syngas, though a part of CH_4 is also combusted into CO_2 and H_2O.

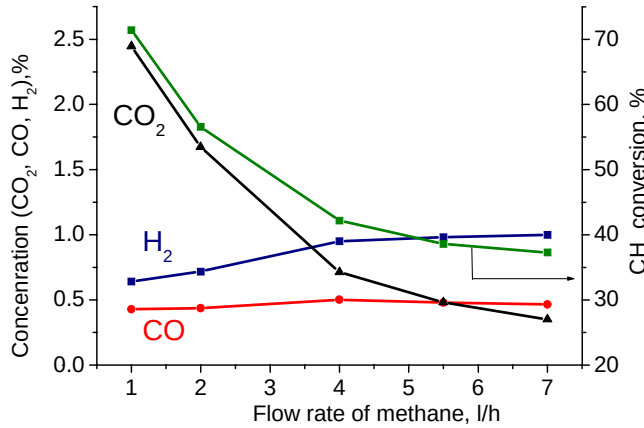

Figure 123. Dependence of methane conversion, CO and H_2 concentration on the flow rate of 4.5%CH_4 in He at 900°C. The air flow rate 1.33 L/h.

At a fixed ratio of methane and air flows, the increase of methane concentration in the fuel mixture from 1 to 5 vol.% insignificantly affects the degree of its conversion, while increasing syngas selectivity (Fig. 124). Hence, in this case, the increase of the rate of CH_4 activation on the layer of catalyst supported on membrane helps to consume the oxygen transferred through membrane forming mainly selective oxidation products.

In the process of membrane reactor start-up via its heating up to 900 ^oC in the flow of 4.5% CH_4 in He with the flow rate of 1 L/h followed by its increasing up to 5 L/h, both methane conversion degree and syngas yield were 1.5-2 times higher than stationary values. This suggests that at a low air flow rate nitrogen accumulation in meso- micropores of the membrane occurs, which hampers the oxygen transfer. Indeed, the increase of the air feed rate has resulted in the increase of the fraction of deep oxidation products due to a higher oxygen flux through the membrane (Fig. 125). According to well-known experience in design of supported membranes, limitation of oxygen viscous flow in pores of supports caused by nitrogen accumulation is indeed the vital problem which is to be dealt with by optimizing the pore structure of substrate and tuning the air feed rate [154].

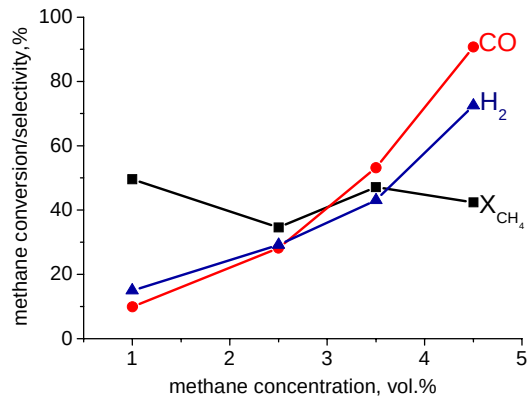

Figure 124. Dependence of methane conversion, CO and H_2 selectivity on methane concentration in the feed at 900°C. The fuel flow rate 5 L/h, the air flow rate 1.2 L/h.

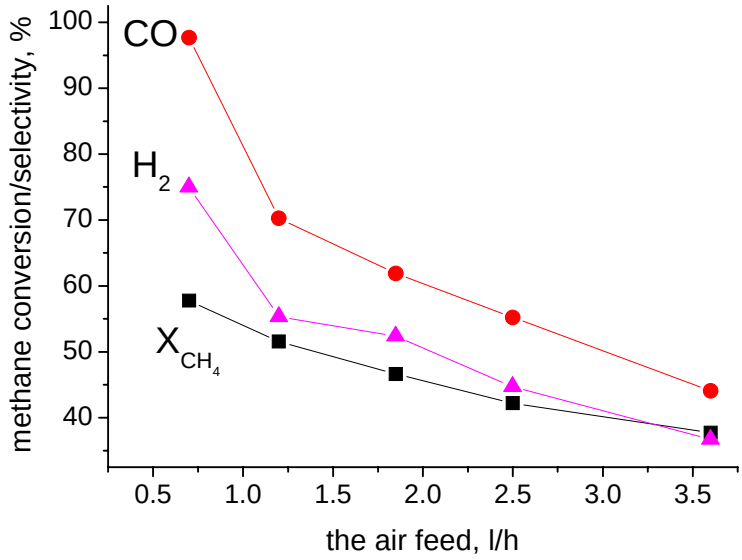

Figure 125. Dependence of methane conversion, CO and H_2 selectivity on the air flow rate at 900°C. The flow rate of 4.5% CH_4 in He 5 L/h.

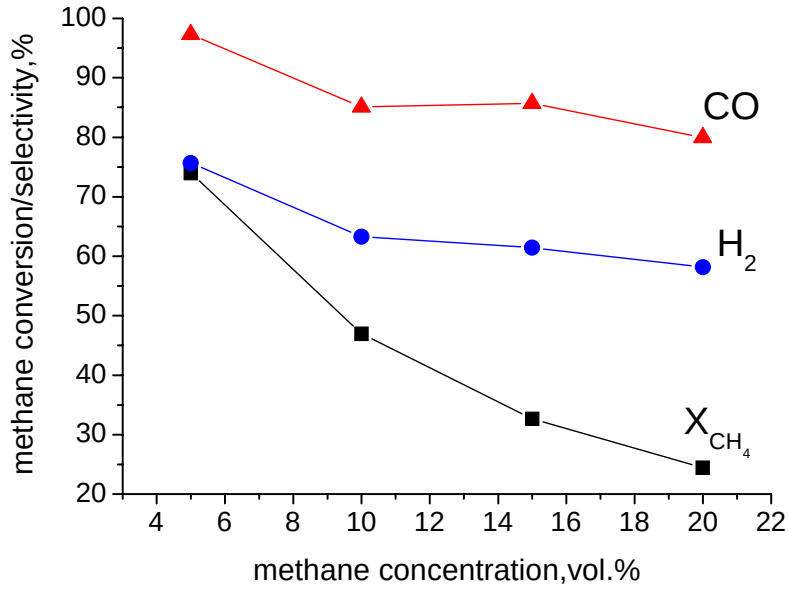

Figure 126. Dependence of methane conversion, CO and H_2 selectivity on methane concentration in the feed at 900°C. The flow rate of CH_4+He 5 L/h. The air flow rate 2 L/h.

Fig. 126 shows effect of methane concentration in the feed on its conversion and CO and H_2 selectivity. While selectivities change rather moderately, methane conversion declines as expected for the constant air feed rate. In part, decline of methane conversion can be explained by a partial coking of both supported and inserted microspherical catalytic layers. Indeed, as follows from Fig. 127, for a high CH_4 content in the feed, the increase of air flow

rate favors the increase of methane conversion and CO selectivity at a constant methane feed rate.

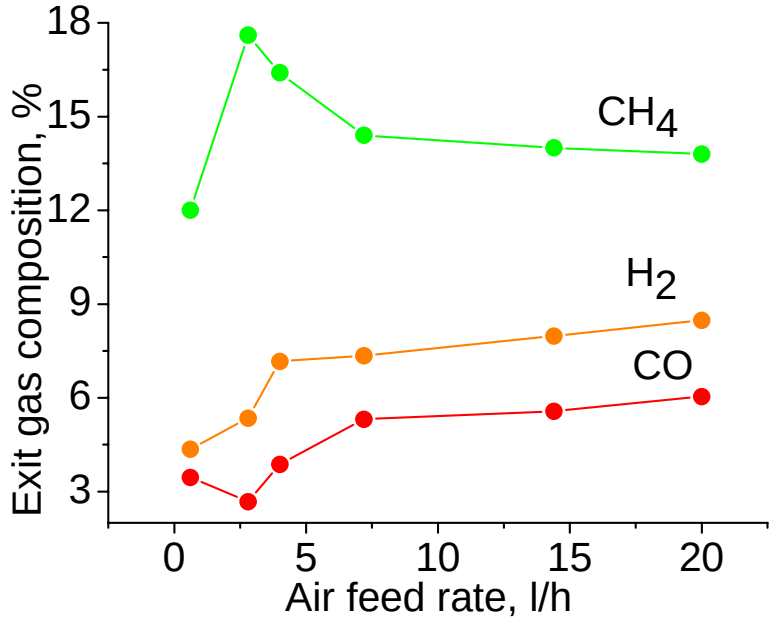

Figure 127. Effect of air feed rate on exit gas composition. 980°C, feed 20% CH_4 in He at 5 L/h.

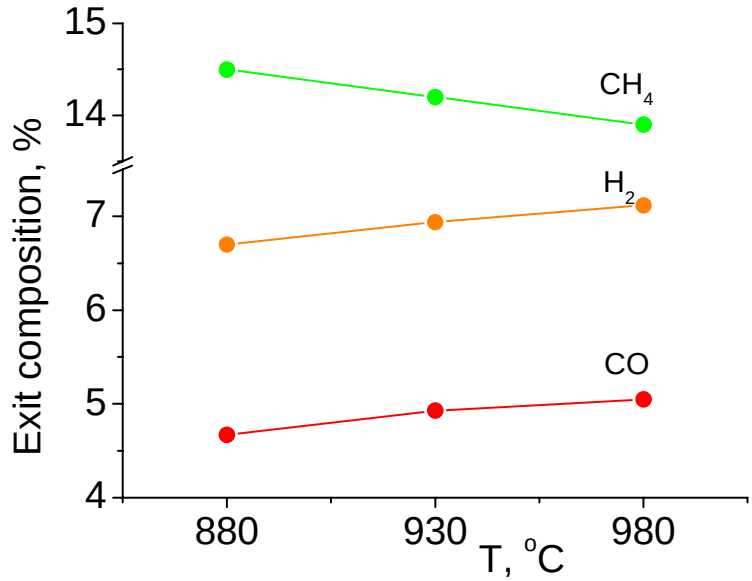

Figure 128. Temperature dependence of exit gas composition for transformation of 20% CH_4 in He at feed rate 5 L/h. Air feed rate 3.2 L/h.

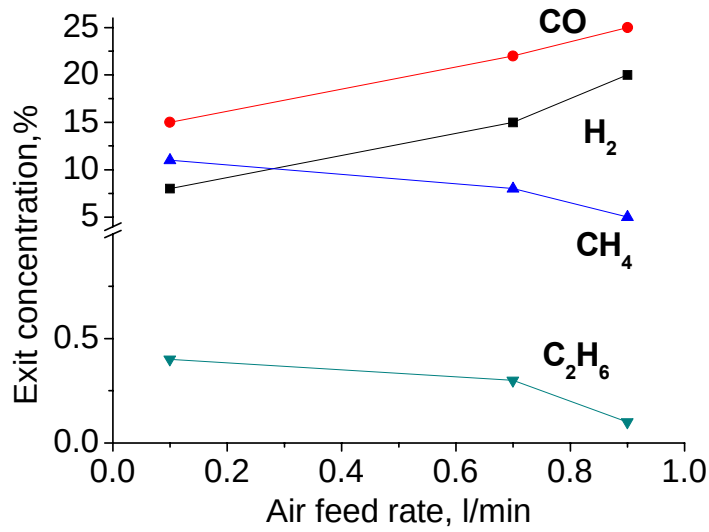

Figure 129. Effect of air feed rate on exit gas composition for oxi-dry reforming of CH_4 in membrane reactor. 20%CO_2 + 20%CH_4 in N_2, feed rate 0.25 L/min, 930 ^oC.

Balance estimation revealed that under given conditions the maximum oxygen flux through the membrane is within the limits of 1-2 mlO_2/cm^2min for 4.5% CH_4 in He and ~ 5-7 mlO_2/cm^2min for 20% CH_4 in He, i.e. increasing with methane concentration. That is associated with the increase of gradient of oxygen chemical potential across the membrane with the increase of reducing potential of the fuel mixture, which is a driving force for its transfer through the membrane. Therefore, at methane concentration in the input mixture about 50-100% provided a proper tuning of the air feed, the oxygen flow is expected to increase at least up to 10-15 ml/cm^2min, which corresponds to the criterion of membrane suitability for the practical application [4, 160]. The increase of operation temperature further increases methane conversion and syngas conversion due to higher oxygen flux through membrane (Fig. 28).

For CH_4 dry reforming, a well-known problem is the catalyst coking leading to its deactivation. Additional supply of oxygen through dense membrane could alleviate this problem helping to remove coke precursors from the surface of catalysts supported on membrane. Indeed, in the case of feed 20% CH_4 +20% CO_2 in N_2, the increase of the air feed through reactor results in increasing CH_4 conversion and syngas content in the exit stream (Fig. 129), which can be explained by a positive effect of a higher oxygen flux through membrane.

6. CONCLUSION

For nanocrystalline perovskites (manganites, cobaltites, ferrites and nickelates of La with a partial substitution by Sr) prepared via Pechini route and their nanocomposites with fluorite-like oxides (doped ceria or zirconia) mobility and reactivity of the surface/lattice oxygen was studied under a broad variation of oxygen chemical potential gradient applying variety of experimental techniques (oxygen isotope exchange, isothermal and temperature programmed

desorption/reduction) for both powdered samples and dense materials. The real/defect structure and surface composition of these materials characterized by applying TEM with EDX, XRD, UV-Vis and XPS revealed redistribution of elements between perovskite and fluorite domains remaining in nanorange even in dense nanocomposites, while isolating pyrochlore-like phases were not observed. Analysis of the interrelation between the transport characteristics of these materials and their structural features including theoretical quantum-chemical methods allowed to demonstrate a pronounced role played by nanostructuring of these systems (especially, by developed perovskite-fluorite interface in nanocomposites) in providing enhanced oxygen mobility and reactivity. Procedures of perovskite –fluorite nanocomposites preparation via the ultrasonic dispersion of powders in organic solvents with addition of surfactants were successfully applied for design of functionally graded cathodes for IT SOFC and asymmetric supported oxygen-conducting membranes which demonstrated high and stable performance promising for the up-scaling and practical application.

ACKNOWLEDGMENTS

Different parts of this work were supported by NATO SFP 980878 and ISTC 3234 Projects, Integration Project 57 SB RAS-NAN of Belarus, Project 57 of RAS Presidium Program No.27, RFBR-ofi_m 09-03-12317 and Russian-French Associated European laboratory on catalysis (RFBR –CNRS 09-03-93112 Project).

REFERENCES

[1] Well, A.F.*; ''Structural Inorganic Chemistry''*, 5-th Edition, Oxford University Press (1986), Pt. 2, Chapter 13.

[2] Aleksandrov, K.S.; Beznosikov, B.V. *Perovskite-related crystals (structural hierarchy, variety of physical properties, synthesis of new compounds).* Siberian Branch of the Russian Academy of Sciences Pbls., Novosibirsk, 1997.

[3] Mogensen M.; Primdahl S.; Jorgensen M. J.; Bagger C. *J. Electroceramics.* 2000, *5*, 141-152.

[4] Bouwmeester, H. J. M. *Catal. Today.* 2003, *82,* 141-150.

[5] Arai, H.; Yamada, T.; Eguchi, K.; Seiyama, T.; *Appl. Catal*. 1986, *26*, 265-276.

[6] Yamazoe, N.; Teraoka, Y. *Catal. Today*. 1990, *8***,** 175-199.

[7] Wachsman, E.D. *Solid State Ionics*. 2002, *152- 153*, 657- 662.

[8] Wang, W. G.; Mogensen, M. *Solid State Ionics*. 2005, *176*, 457-462.

[9] Adler, S.B. *Chem. Rev*. 2004, *104*, 4791-4843.

[10] Goldberg, E.; Nemudry, A.; Boldyrev, V.; Schöllhorn, R. *Solid State Ionics.* 1999, *122*, 17-22.

[11] Sadykov, V.A.; Borchert, Yu.V.; Alikina, G.M.; Lukashevich, A.I.; Mezentseva, N.V.; Muzykantov, V.S.; Moroz, E.M.; Rogov, V.A.; Zaikovskii, V.I.; Zyuzin, D.A.; Uvarov, N.F.; Ishchenko, A.V.; Zyryanov, V. V.; Smirnova, A. *Glass Physics and Chemistry*. 2007, *33*, 320-334.

[12] De Souza, R.A. *Ionic Transport in Acceptor Doped Perovskites*. PhD Thesis, University of London, London (1996).
[13] De Souza, R.A.; J. Maier. *Phys. Chem. Chem. Phys.* 2003, *5*, 740-748.
[14] Ishihara, T.; Matsuda, H.; Takita, Y. *J. Am. Chem. Soc*. 1994, *116* 3801-3803.
[15] Huang, K.; Tichy, R.; Goodenough, J.B. *J. Am. Ceram. Soc*. 1998, *81*, 2565-2575.
[16] Bhide, V.G.; Rajoria, D.S.; Rao, C.N.R.; Rao, G.R.; Jadhao, V.G. *Phys. Rev. B*. 1975, *12*, 2832-2843.
[17] Van Roosmalen, J.A.M.; Cordfunke, E.H.P.; Helmholdt, R.B.; Zandberg H.W. *J. S olid State Chem*. 1994, *110*, 100-105.
[18] Anderson, H.U. "Defect chemistry of p-type perovskites". In: *Proc. 14th Riso In. Symp.on Materials Science*. (Poulsen F.W.; Bentzen J.J.; Jacobsen, T.; Skou, E.; Ostergard, M.J.L. Eds.) Riso National Laboratory, Roskilde, 1993, 1-18.
[19] Mizusaki, J.; Minima, Y.; Yamauchi, S.; Fueki, K.; Tagawa H. *J. Solid State Chem*. 1989, *80*, 102-111.
[20] Kuo, J.H.; Anderson, H.U.; Sparlin, D.M. *J. Solid State Chem*. 1989, *83*, 52-60.
[21] Goodenough, J.B. *Rep. Prog. Phys.* 2004, *67*, 1915-1993.
[22] Vechersky, S.I.; Batalov, N.N.; Esina, N.O.; Shehtman, G.S. *Fizika Tverdogo Tela*, 2004, *46*, 1433-1440.
[23] De Gennes, P.G. *Phys. Rev*. 1960, *118*, 141-154.
[24] Grundy, A.N.; Hallstedt, B.; Gauckler, L.J. *Solid State Ionics*. 2004, *173*, 17-21.
[25] Nakamura, K. in "*Mixed Ionic Electronic Conducting Perovskites for Advanced Energy System"* (N. Orlovskaya, N. Browning Eds), Kluwer Academic Publ., Boston, Dordrecht, London (2004), pp. 191-204.
[26] Kilner, J.A.; Berenov, A.; Rossiny, J. *Diffusivity of the Oxide Ion in Perovskite Oxides, In: „Perovskite Oxide for Solid Oxide Fuel Cells"* (Ishihara, T. Ed.), Springer, 2009, 95-116.
[27] Ishigaki, T.; Yamauchi, Sh.; Kishio, K.; Mizusaki, J.; Fueki, K. *J. Solid State Chem.* 1988, *73,* 179-187.
[28] Chebotin, V.N. „Chemical Diffusion in Solids". Nauka Pbls., Moscow, 1989.
[29] Kilner, J.A.; De Souza, R.A.; Fullarton, I.C. *Solid State Ionics*. 1996, *86-88*, 703-709.
[30] Adler, S.B.; Lane J.A.; Steele B.C.H. *J. Electrochem. Soc*. 1996, *143*, 3554-3564.
[31] Steele, B.C.H. *Solid State Ionics*. 1997, *94*, 239-248.
[32] Teraoka, Y.; Zhang, H. M.; Okamoto, K.; Yamazoe, N. *Mater. Res. Bull.* 1988, *23*, 51-58.
[33] Teraoka, Y.; Nobunaga T.; Okamoto, K.; Miura N.; Yamazoe, N. *Solid State Ionics* 1991, *48*, 207-212.
[34] Diethelm, S.; Closset, A.; Nisancioglu, K.; van Herle, J.; McEvoy, A. J.; Gur, T. M. *J. Electrochem. Soc.* 1999, *146*, 2606-2612.
[35] Ishigaki, T.; Yamauchi, Sh.; Kishio, K.; Mizusaki, J.; Fueki, K. *J. Solid State Chem.* 1984, *54,* 100-107.
[36] Komatsu, W.; Ikuma, Y.; Kato, M.; Uematsu, K. *J. Amer. Ceram. Soc*. 1982, *65*, C211-212.
[37] Yoo, H.-I.; Lee, Ch.-E. *Solid State Ionics*. 2009, *180*, 326-337.
[38] Diethelm, S.; Closset. A.; Van Herle, J.; Nisancioglu, K. *Solid State Ionics.* 2000, *135*, 613-618.
[39] Lane, J.A.; Kilner, J.A. *Solid State Ionics.* 2000, *136-137,* 997-1001.

[40] Lane, J.A.; Benson,S.J.; Waller, D.; Kilner, J.A. *Solid State Ionics.* 1999, *121,* 201-208.
[41] Katsuki M.; Wang S.; Dokiya M.; Hashimoto T. *Solid State Ionics*. 2003, *156*, 453-461.
[42] Lankhorst, M.H.R.; Bouwmeester, H.J.M. *J. Electrochem. Soc*. 1997, *144,* 1261-1272.
[43] Van Hassel, B.A.; Kawada, T.; Sakai, N.; Yokokawa, H.; Dokiya, M.; Bouwmeester, H.J.M. *Solid State Ionics.* 1993, *66,* 295-305.
[44] Bouwmeester, H.J.M.; Kruidhof, H.; Burggraaf, A.J. *Solid State Ionics.* 1994, *72,* 185-194.
[45] Chen, C.H.; Bouwmeester, H.J.M.; Van Doorn, R.H.E.; Kruidhof, H.; Burggraaf, A.J.; *Solid State Ionics*. 1997, *98,* 7-13.
[46] Lee, T.H.; Yang, Y.L.; Jacobson, A.J.; Abeles, B.; Zhou, M. *Solid State Ionics.* 1997, *100,* 77-85.
[47] Kim, S.; Yang, Y.L.; Jacobson, A.J.; Abeles, B. *Solid State Ionics.* 1998, *106,* 189-195.
[48] Klier, K.; Novakova, J.; Jiru, P. *J. Catal*. 1963, *2*, 479-484.
[49] Klier, K.; Kucera, E. *J. Phys. Chem. Solids*. 1966, *27*, 1087-1095.
[50] Sadovskaya, E.M.; Ivanova, Yu.A.; Pinaeva, L.G.; Grasso, G.; Kuznetsova, T.G.; Van Veen, A.; Sadykov, V.A.; Mirodatos, C. *J. Phys. Chem. A: Gen.*. 2007, *111*, 4498-4505.
[51] Muzykantov, V.S.; Kemnitz, E.; Sadykov, V.A.; Lunin, V.V. *Kinetika i Kataliz*. 2003, *4*, 349-352.
[52] Muzykantov, V.S.; Popovsky, V.V.; Boreskov, G.K. *Kinetika i Kataliz*. 1964, *5*, 624-629.
[53] Muzykantov, V.S.; Jiru, P.; Klier, K.; Novakova*, J. Collect. Czech. Chem. Commun*. 1968, *33*, 829-835.
[54] Muzykantov, V.S.; Ewald, G.; von Levis, G. *Kinetika i Kataliz*. 1974, *15,* 1512-1518.
[55] Boreskov, G.K.; Muzykantov V.S. *Ann. N.Y. Acad. Sci*. 1975, *213*, 137-160.
[56] Muzykantov, V.S. *React. Kinet. Catal. Lett.* 1987, *35*, 437-447.
[57] Galdikas, A.; Descorme, C.; Duprez D. *Solid State Ionics*. 2004, *166*, 147-155.
[58] Galdikas, A.; Duprez, D.; Descorme, C. *Appl. Surf. Sci*. 2004, *236*, 342-355.
[59] Duprez, D. „*Isotopes in Heterogeneous Catalysis*", Imperial College Press, London, 2006, p. 133.
[60] Sadykov, V.A.; Bulgakov, N.N.; Muzykantov, V.S.; Kuznetsova, T. G.; Alikina, G. M.; Lukashevich, A.I.; Potapova, Yu.V.; Rogov, V.A.; Burgina, E. B.; Zaikovskii, V. I.; Moroz, E.M.; Litvak, G.S.; Yakovleva, I.S.; Isupova, L.A.; Zyryanov, V.V.; Kemnitz, E.; Neophytides, S. in: „*Mixed Ionic Electronic Conducting Perovskites for Advanced Energy Systems"* (Orlovskaya, N.; Browning, N., Editors), Kluwer Academic Publishers, Boston/Dordrecht/London, 2004, p. 53-70.
[61] Sadykov, V.; Kharlamova, T.; Batuev, L.; Mezentseva, N.; Alikina, G.; Muzykantov, V.; Krieger, T.; Pavlova, S.; Zaikovskii, V.; Ishchenko, A.; Zarubina, V.; Rogov, V.; Bobrenok, O.; Uvarov, N.; Kilner, J.; Druce, J.; Smirnova, A. *Mater. Res. Soc. Symp. Proc*. 2008, *1098,* HH07-06. 1-6.
[62] Sadykov, V.; Kharlamova, T.; Batuev, L.; Muzykantov, V.; Mezentseva, N.; Krieger, T.; Alikina, G.; Lukashevich, A.; Rogov, V.; Zaikovskii, V.; Ishchenko, A.; Salanov, A.; Boronin, A.; Koscheev, S.; Pavlova, S.; Uvarov, N.; Smirnova, A.; Vasylyev, O. *Composite Interfaces*. 2009, *16*, 407-431.
[63] Sadykov, V.A.; Frolova,Yu. V.; Alikina, G.M.; Lukashevich, A.I.; Muzykantov, V.S.; Rogov, V.A.; Moroz, E.M.; Zyuzin, D.A.; Ivanov V.P.; Borchert, H.; Paukshtis, E. A.;

Bukhtiyarov, V. I.; Kaichev, V. V.; Neophytides, S.; Kemnitz, E.; Scheurell K. *React. Kinet. Catal. Lett.* 2005, *85***,** 367-374.
[64] Yasuda, I.; Hishinuma M. *J. Solid State Chem*. 1996, *123*, 382-390.
[65] Song, C.-R.; Yoo, H.-I. *Solid State Ionics*. 1999, *120*, 141-153.
[66] Ji, Y.; Kilner, J.A.; Carolan, M.F. *Solid State Ionics*. 2005, *176*, 937-943.
[67] Cheselske, F.J.; Wallage, W.E.; Hall, W.K. *J. Phys. Chem*. 1959, *63*, 505-512.
[68] Hall, W.K.; Leftin, H.P.; Cheselske, F.J.; O'Reilly, D.E. *J. Catal*. 1963, *2*, 506-517.
[69] Gaillard, F.; Joly, J.-P.; Li, N.; Boreave, A.; Deloume, J.-P. *Solid State Ionics*. 2008, *179*, 941-945.
[70] Huang, K.; Goodenough, J.B. *J. Electrochem. Soc.* 2001, *148,* 203-214.
[71] Schroeder, M.; Huang, K.Q.; Goodenough, J.B. Ceramic Bilayer Membranes for High Temperature Oxidation of Methane. In: Mass and Charge Transport in Inorganic Materials. Fundamentals to Devices (Vincencini, P, Buscaglia, V, Eds.), Jesolo di Lido, Venice, Italy, 2000, p. 1507-1514.
[72] Bouwmeester, H.J.M.; Burggraaf , A.J. „Dense Ceramic Membranes for Oxygen Separation". In: „The CRC Handbook of Solid State Electrochemistry" (P.J. Gellings, H.J.M. Bouwmeester, Eds), CRC Press, Inc. 1997, 485-557.
[73] Sunarso, J.; Baumann, S.; Serra, J.M.; Meulenberg W.A.; Liu S.; Lin Y.S.; Diniz da Costa J.C. *J. Membrane Sci*. 2008, *320*,13-41.
[74] Saracco, G.; Specchia, V. *Catal. Rev.-Sci. Eng.* 1994, *36*, 305-384.
[75] Balachandran, U.; Dusek.; J.T.; Mieville, R.L.; Poeppel, R.B.; Kleefisch, M.S.; Pei, S.; Kobylinski, T.P.; Udovich, C.A.; Bose, A.C. *Appl. Catal. A:Gen.* 1995, *133,* 19-29.
[76] Tsai, Ch.-Y.; Dixon, A.G.; Moser, W.R.; Ma, Y.H. C*eramics Processing.* 1997, *43,* 2741-2750.
[77] Li, Sh.; Jin, W.; Huang, P.; Xu, N.; Shi, J.; Hu, M. Z.-C.; Pauzzant, E.A.; Ma, Y.H. *AIChE J.* 1999, *45,* 276-284.
[78] Tong, J.; Yang, W.; Cai, R.; Zhu, B.; Lin, L. *Catal. Lett.* 2002, *78,* 129-137.
[79] Liu, Y.; Tan, X.; Li, K. *Catal. Rev.* 2006, *48,* 145-198.
[80] Peña, M.A.; Fierro, J.L.G. *Chem. Rev.* 2001, *101,* 1981-2017.
[81] Cotton, F.A.; Wilkinson, G. Advanced Inorganic Chemistry, Interscience, New York, 1972.
[82] Chiba, R.; Yoshimura, F.; Sakurai, Y. *Solid State Ionics*. 2002, *152-153*, 575-582.
[83] Rida, K.; Benabbas, A.; Bouremmad, F.; Pena, M.A.; Martinez-Arias, A. *Catal. Commun.* 2006, *7*, 963-968.
[84] [84].
[85] Van Roosmale, J. A.M.; Huijsmans, J.P.P.; Plomp, L. *Solid State Ionics.* 1993, *66,* 279-284.
[86] Hildrum, R.; Aasland, S.; Johannesen, Ø. *Solid State Ionics.* 1993, *66,* 207-218.
[87] Chiba, R.; Yoshimura, F.; Sakurai, Y. *Solid State Ionics*. 1999, *124*, 281-288.
[88] Kumar, R.; Choudhary, R. J.; Khan, M. W.; Srivastava, J. P.; Bao, C.W.; Tsai, H. M.; Chiou, J. W.; Asokan, K.; Pong, W. F. *J. Appl. Phys.*. 2005, *97*, 093526.
[89] Chiba, R.; Yoshimura, F.; Sakurai, Y. *Solid State Ionics*. 1999, *124*, 281-288.
[90] Świerczek, K.; Marzec, J.; Pałubiak, D.; Zając, W.; Molenda, J. *Solid State Ionics*. 2006, *177*, 1811- 1817.
[91] Huang, K.; Lee, H.Y.; Goodenough, J.B. *J. Electrochem. Soc.* 1998, *145,* 3220-3227.

[92] Kharton, V.V.; Yaremchenko, A.A.; Shaula, A.L.; Patrakeev, M.V.; Naumovich, E.N.; Logvinovich, D.I.; Frade, J.R.; Marques, F.M.B. *J. Solid State Chem*. 2004, *177*, 26-37.
[93] Miyoshi, S.; Furuno, T.; Matsumoto, H.; Ishihara,T. *Solid State Ionics*. 2006, *177*, 2269 -2273.
[94] Ishihara, T.; Nakashima, K.; Okada, S.; Enoki, M.; Matsumoto, H. *Solid State Ionics.* 2008, *179*, 1367-1371.
[95] Vashook, V.; Zosel, J.; Wen, T.-L.; Guth, U. *Solid State Ionics.* 2006, *177*, 1827-1830.
[96] Amow, G.; Au, J.; Davidson, I. *Solid State Ionics*. 2006, *177*, 1837-1841.
[97] Liu, W.; Zhang, G.G.; Xie, S.; Chen, C.S.; Meng, G.Y.; Peng, D.K . *Solid State Ionics.* 2000, *135*, 727-730.
[98] Zyryanov, V.V.; Sadykov, V.A.; Uvarov, N.F.; Alikina, G.M.; Lukashevich, A.I.; Ivanovskaya, M.I.; Neophytides, S.; Criado, J.M. *Solid State Ionics*. 2005, *176*, 2813-2818.
[99] Sadykov, V.; Mezentseva, N.; Muzykantov, V.; Sammes, N.; Kilner, J.; Smirnova, A. *Proc.Int. Symp. on Innovative Materials for Processes in Energy Systems (IMPRES),* 28-31 October, 2007, Kyoto, Japan, A. 1-5.
[100] Rossignol, C.; Ralph, J.M.; Bae, J.M.; Vaughey, J.T. *Solid State Ionics* 2004, *175*, 59-61.
[101] Mogensen, M.; Lybye, D.; Bonanos, N.; Hendriksen, P.V.; Poulsen, F.W. *Solid State Ionics.* 2004, *174*, 279-286.
[102] Frayret, C.; Villesuzanne, A.; Pouchard, M. *Chem. Mater.* 2005**,** *17,* 6538-6544.
[103] Zhao, H.; Mauvy, F.; Lalanne, C.; Bassat, J.-M.; Fourcade, S.; Grenier, J.-C. *Solid State Ionics.* 2008, *179*, 2000-2005.
[104] Skinner, S.J.; Kilner, J.A.; *Solid State Ionics.* 2000, *135*, 709-712.
[105] Mauvy, F.; Boehm, E.; Bassat, J.-M.; Grenier, J.-C.; Fouletier, J. *Solid State Ionics.* 2007, *178*, 1200-1204.
[106] Liu, J.; Co, C.A.; Paulson, S.; Birss, V.I. *Solid State Ionics*. 2006, *177*, 377-387.
[107] Sadykov, V.A.; Tikhov, S.F.; Tsybulya, S.V.; Kryukova, G.N.; Veniaminov, S.A.; Kolomiichuk, V.N.; Bulgakov, N.N.; Paukshtis, E.A.; Ivanov, V.P.; Koshcheev, S.V.; Zaikovskii, V.I.; Isupova, L. A.; Burgina*,* E.B.; *J. Molec. Catal. A*. 2000, *158,* 361-365.
[108] Sadykov, V.A.; Isupova, L. A.; Zolotarski, I. A.; Bobrova, L. N.; Noskov, A. S.; Parmon, V. N.; Brushtein, E. A.; Telyatnikova, T. V.; Chernyshev, V. I.; Lunin, V. V. *Appl. Catal. A*. 2000, *204***,** 59-87.
[109] [Read, M. S. D.; Islam, M. S.; Watson, G. W. and Hancock, F. E. *J. Mater. Chem*. 2001, *11,* 2597-2602.
[110] Sadykov, V.A.; Kuznetsova, T.G.; Bulgakov, N.N.; Lunin, V.V., Kemnitz, E. *Mater. Res. Soc. Symp. Proc.* 2003, *751,* Z3.27.1-6.
[111] Fisher, C.A.J.; Islam, M.S. *J. Mater. Chem.* 2005, *15,* 3200-3207.
[112] Tapilin, V.M. *J. Struct. Chem.* 2007, *48,* 212-218.
[113] Guggilla, S.; Manthiram, A. *J. Electrochem. Soc.* 1997, *144,* 120-121.
[114] Wang, W.; Zhang, H.; Lin, G.; Xiong, Zh. *Appl. Catal. B: Envir*. 2000, *24,* 219-232.
[115] van Roosmalen, A. M.; Gordfunke, E. H. P. *J. Solid State Chem*. 1994, *110*, 113-117.
[116] Provendier, H.; Petit, C.; Kiennemann, A. *Chemistry*, 2001, 4, 57-66.
[117] Sadykov, V.; Mezentseva, N.; Alikina, G.; Bunina, R.; Pelipenko, V.; Lukashevich, A.; Tikhov, S.; Usoltsev, V.; Vostrikov, Z.; Bobrenok, O.; Smirnova, A.; Ross, J.R.H.; Smorygo, O.; Rietveld, B.; *Catal. Today*. 2009, *146*, 132-140.

[118] Dusastre, V.; Kilner, J. A. *Solid State Ionics*. 1999, *126*, 163-174.
[119] Esquirol, A.; Kilner, J.; Brandon N. *Solid State Ionics*. 2004, *175*, 63-67.
[120] Murray, E. P.; Barnett, S. A. *Solid State Ionics*. 2001, *143*, 265-273.
[121] Figueiredo, F. M.; Frade, J. R.; Marques F. M. B. *Solid State Ionics*. 2000, *135*, 463-467.
[122] Matsuzaki, Y.; Yasuda, I. *Solid State Ionics*. 2002, *152-153*, 463- 468.
[123] Wang, W. G.; Mogensen, M.; *Solid State Ionics* 2005, *176*, 457-462.
[124] Oishi, N.; Yoo, Y.; Davidson, I. *Electrochem. Soc. Proc*. 2005, *07*, 1645-1651.
[125] Jorgensen, M.J.; Primdahl, S.; Bagger, C.; Mogensen, M. *Solid State Ionics*. 2001, *139*, 1-11.
[126] Wang, Zh.; Cheng, M.; Dong, Y.; Zhang, M.; Zhang, H. *Solid State Ionics*. 2005, *176*, 2555 - 2561.
[127] Kharton, V. V.; Kovalevsky, A. V.; Biskup, A. P.; Shaula, A. L.; Figueiredo, F. M.; Naumovich, E. N.; Marques, F. M. B. *Solid State Ionics*. 2003, *160*, 247-258.
[128] Nigge, U.; Wiemhöfer, H.-D.E.; Römer, W. J.; Bouwmeester, H. J. M.; Schulte T. R. *Solid State Ionics*. 2002, *146*, 163-174.
[129] Kharton, V. V.; Kovalevsky, A. V.; Biskup, A. P.; Figueiredo, F. M.; Yaremchenko, A.A.; Naumovich, E. N.; Marques, F. M. B. *J. Electrochem. Soc.* 2000, *147***,** 2814-2821.
[130] Sadykov, V.; Pavlova, S.; Zarubina ,V.; Bobin, A.; Alikina, G.; Lukashevich, A.; Muzykantov, V.; Usoltsev, V.; Kharlamova, T.; Boronin, A.; Koscheev, S.; Krieger, T.; Ishchenko, A.; Mezentseva, N.; Salanov, A.; Smirnova, A.; Bobrenok, O.; Uvarov, N. *ECS Trans*. 2009, *25*, 2403-2412.
[131] Sadykov, V.; Muzykantov, V.; Bobin, A.; Batuev, L.; Alikina, G.; Lukashevich, A.; Boronin, A.; Krieger, T.; Ishchenko, A.; Bobrenok, O.; Uvarov, N.; Smirnova, A.; Vasylyev, O. *Mater. Res. Soc. Symp. Proc*. 2009, *1126*, S13-03. 1-6.
[132] Kharlamova, T.; Pavlova, S.; Sadykov, V.; Krieger, T.; Mezentseva, N.; Muzykantov, V.; Alikina, G.; Boronin, A.; Zaikovskii, V.; Ishchenko, A.; Rogov, V.; Uvarov, N.; Frade, J.; Argirusis, Chr. *Mater. Res. Soc. Symp. Proc*. 2008, *1056.* HH03-64. 1-6.
[133] Frolova-Borchert, Yu.V.; Sadykov, V.A.; Alikina, G.M.; Lukashevich, A.I.; Moroz, E.M.; Kochubey, D.I.; Kriventsov, V.V.; Zaikovskii, V.I.; Zyryanov, V.V.; Uvarov, N.F. *Solid State Ionics*. 2006, *177*, 2533-2538.
[134] Isupova, L.A.; Obyskalova, E.A.; Rogov, V.A.; Tsybulya, S.V.; Dovlitova, L.S.; Burgina, E.B.; Ischenko, A.V.; Zaikovskii, V.I.; Sadykov, V.A.; Orlovskaya, N. *Mater. Res. Soc. Symp. Proc.* 2006, *885E*, A03-04.1-6.
[135] Druce, J.; Kilner, J.A. *ECS. Trans*. 2009, 16, 327-336.
[136] Bannikov, D.O.; Cherepanov, V.A. J. *Solid State Chem*. 2006, *179*, 2721-2727.
[137] Zinkevich, M.; Aldinger, F. *J. Alloys and Compounds*. 2004, *375*, 147-161.
[138] Dong, W.-S.; Roha, H.-S.; Jun, K.-W.; Park, S.-E.; Ohb, Y.-S. *Appl. Cata. A: Gen*. 2002, *226*, 63-72.
[139] Lever, A.B.P. "Inorganic Electronic Spectroscopy*"*. 2nd Ed. Amsterdam-Oxford-New York-Tokyo: Elsevier. 1987. Part 1 and 2.
[140] Pickett, W.E.; Singh, D.J. *Phys. Rev. B.*1996, *53,* 1146-1160.
[141] Ravindran, P.; Kjekshus, A.; Fjellva, H.; Delin, A.; Eriksson, O. *Phys. Rev. B.* 2002, *65,* 064445.1-19.
[142] Choudhary, V.R.; Uphade, B.S.; Pataskar, S.G. *Appl. Catal. A:Gen.* 2002, *227*, 29-41.

[143] Borchert, H.; Borchert, Yu.; Kaichev, V.V.; Prosvirin, I.P.; Alikina, G.M.; Lukashevich, A.I.; Zaikovskii, V.I.; Moroz, E.M.; Paukshtis, E.A.; Bukhtiyarov, V.I.; Sadykov, V.A. *J. Phys. Chem.* 2005, *109*, 20077-20086.
[144] Mineshige, A.; Abe, J.; Kobune, M.; Uchimoto, Y.; Yazawa, T. *Solid State Ionics*. 2006, *177***,** 1803-1806.
[145] Zheng, Ya.; Ran, R.; Gu, H.; Cai, R.; Shao, Z. *J. Power Sources*. 2008, *185*, 641-648.
[146] Borchert, H.; Borchert, Yu.; Kaichev, V.V.; Prosvirin, I.P.; Alikina, G.M.; Lukashevich, A.I.; Zaikovskii, V.I.; Moroz, E.M.; Paukshtis, E.A.; Bukhtiyarov, V.I.; Sadykov, V.A. *J. Phys. Chem.* 2005, *109*, 20077-20086.
[147] Zhogin, I.L.; Nemudry, A.P.; Glyanenko, P.V.; Kamenetsky, Yu.M.; Bouwmeester, H.J.M.; Ismagilov, Z.R. *Catal. Today*. 2006, *118*, 151-157.
[148] Kharlamova, T.; Smirnova, A.; Sadykov, V.; Zarubina, V.; Krieger, T.; Batuev, L.; Ishchenko, A.; Salanov, A.; Uvarov, N.; *ECS Trans*. 2008, *13*, 275-284.
[149] Nicholas, J. D., and De Jonghe, L. C. *Mater. Res. Soc. Symp. Proc*. 2007, *1023,* JJ05-09.1-6.
[150] Lewis, G.S.; Atkinson, A.; Steele, B.C.H.; Drennan, J. *Solid State Ionics*. 2002, *152–153*, 567– 573.
[151] Leng, Y. J.; Chan, S. H.; Khor, K. A.; Jiang, S. P. *Int. J. Hydrogen Energy.* 2004, *29*, 1025–1033.
[152] Yoon, S. P.; Han, J.; Nam, S.W.; Lim, T.-H.; Oh, I.-H.; Hong, S.-A.; Yoo, Y.-S., Lim, H. C. *J. Power Sources.* 2002, *106,* 160–166.
[153] Kovalevsky, A. V.; Kharton, V. V.; Snijkers, F. M. M.; Cooymans, J. F. C.; Luyten, J.J.; Frade, J. R. *Solid State Ionics.* 2008, *179*, 61-65.
[154] van Hassel, B. A. *Solid State Ionics*, 2004, *174*, 253-260.
[155] Watanabe, K.; Yuasa, M.; Kida,T.; Shimanoe, K.; Teraoka, Y.; Yamazoe, N. *Solid State Ionics.* 2008, *179,* 1377–1381.
[156] Takamura, H.; Kobayashi, T.; Kasahara, T.; Kamegawa, A.; Okada, M. *J. Alloys Comp.* 2006, *408-412*, 1084-1089.
[157] Zyryanov, V. V.; Sadykov,V. A.; Alikina, G. M. *Separ. Sci. Tech*. 2007, *42*, 2849-2861.
[158] Li, Ch.; Hu, T.; Zhang, H.; Chen, Y.; Jin, J.; Yang, N.; *J. Membr. Sci*. 2003, *226,* 1–7.
[159] Deng, H.; Zhou, M.; Abeles, B. *Solid State Ionics.* 1994, *74*, 75-84.
[160] Liu, Y.; Tan. X.; Li, K. *Catalysis Reviews.* 2006, *48,* 145-198.
[161] Takamura, H.; Ogawa, M.; Suehiro, K.; Takahashi, H.; Okada, M. *Solid State Ionics.* 2008, *179,* 1354-1359.
[162] Sadykov, V.; Sobyanin, V.; Mezentseva, N.; Alikina, G.; Vostrikov, Z.; Fedorova, Y.; Pelipenko, V.; Usoltsev, V.; Tikhov, S.; Salanov, A.; Bobrova, L.; Beloshapkin, S.; Ross, J. R. H.; Smorygo, O.; Ulyanitskii, V.; Rudnev, V. *Fuel*, 2010, *89,* 1230–1240, doi:10.1016/j.fuel.2009.12.015.

In: Perovskites: Structure, Properties and Uses
Editor: Maxim Borowski, pp. 179-211
ISBN 978-1-61668-525-6

Chapter 3

ON THE NATURE OF LOW-TEMPERATURE RESISTIVE PEAK IN COLOSSAL MAGNETORESISTANT MATERIALS

A.I. Tovstolytkin*
Institute of Magnetism, 36-b Vernadskogo Blvd., Kyiv 03142, Ukraine

ABSTRACT

Strong interplay between electronic behavior, structure and magnetism in doped perovskite manganites gives rise to the enhanced sensitivity of transport properties to magnetic and structural peculiarities. The optimally doped manganite compounds are metallic and ferromagnetic at low temperatures, while their conductivity displays activated behavior at high temperatures. The metal-insulator transition between these two states is strongly associated with the magnetic ordering one, and this manifests itself in the formation of a resistivity peak in the vicinity of Curie temperature T_C. However, in some peculiar cases, manganite samples exhibit an additional low-temperature resistivity peak (LT-peak) (or a tendency to its emergence in a form of a plateau), which is not associated with any magnetic or structural transition and nature of which remains unclear hitherto. In this chapter, based on a simple phenomenological model, we demonstrate that the formation of the LT-peak may be a result of a strong broadening of the ferromagnetic transition. The approach developed examines the electrical properties of a system consisting of paramagnetic and ferromagnetic phases which exhibit opposite trends in the temperature dependences of resistivity and coexist over a wide temperature range. It is shown that, as the region of the phase coexistence increases, the resistive transition first broadens, then, in addition to the resistive peak near T_C, the LT-peak emerges and begins to grow, later on it becomes dominant and, eventually, only a weak shoulder-like feature remains at T_C. Such an approach is shown to be applicable to the description of the magnetic and electric properties of a number of inhomogeneous and phase-separated

* E-mail: atov@imag.kiev.ua

manganite systems, including micro- and nanocrystalline samples, ultrathin epitaxial films, etc.

INTRODUCTION

The doped perovskite manganites $La_{1-x}A_xMnO_{3\pm\delta}$ (A = Ca, Sr, Ba, …) have attracted much recent attention primarily due to the discovery of negative colossal magnetoresistance (CMR) around the Curie temperature T_C [1,2]. Although it was recognized long ago that the essential physics of these materials mainly stems from the double exchange resulting from the motion of an electron between Mn^{3+} and Mn^{4+} ions [3], recent studies have highlighted the important role of the Jahn-Teller distortion associated with the Mn^{3+} ion as well as charge ordering effects opposing double exchange (for a review see [4,5]). In view of the competing character of these interactions, a change in the Mn^{4+}/Mn^{3+} ratio, caused either by heterovalent substitutions or by the introduction of cation (anion) vacancies, may greatly affect the properties of doped manganites, leading in some cases to the appearance of extremely complex electronic/magnetic orderings [6] or peculiar phase-separated states [7,8].

The optimally doped ($x \approx 0.3$) manganite compounds are metallic and ferromagnetic (FM) at low temperatures, while their conductivity displays activated behavior at high temperatures. The metal-insulator transition between these two states is strongly associated with the magnetic ordering one and this manifests itself in the formation of a resistivity peak in the vicinity of T_C. The origin of this peak was discussed in detail in papers [9,10,11]. In many cases, however, an additional low-temperature peak (LT-peak) (or a tendency to its emergence in a form of a plateau) appears on the resistivity ρ vs. temperature T dependences for thin film [12,13,14] as well as bulk polycrystalline [15,16,17] samples of manganites, which is not related to any kind of phase transitions, neither a magnetic nor a structural one.

In this chapter, based on a simple phenomenological model, we demonstrate that the formation of the LT-peak may be a result of a strong broadening of the ferromagnetic transition. The approach developed examines the electrical properties of a system consisting of paramagnetic (PM) and FM phases which exhibit opposite trends in the temperature dependences of resistivity and coexist over a wide temperature range. It is shown that, as the region of the phase coexistence increases, the resistive transition first broadens, then, in addition to the resistive peak near T_C, the LT-peak emerges and begins to grow, later on it becomes dominant and, eventually, only a weak shoulder-like feature remains at T_C. Such approach is shown to be applicable to the description of the magnetic and electric properties of a number of inhomogeneous and phase-separated manganite systems, including micro- and nanocrystalline samples, ultrathin epitaxial films, etc.

ELECTRONIC TRANSPORT IN MAGNETICALLY INHOMOGENEOUS MANGANITE MATERIALS

The complexity of the electronic and magnetic phase diagrams of doped manganites is a result of a strong interaction between charge, spin and orbital subsystems, with a key role being played by aliovalent manganese ions [4,7,18]. In such a complex situation there is some

attraction in attempting to use averaged parameters such as valency, tolerance factor, Mn–O distance or Mn–O–Mn bond angle to describe the electric, magnetic and magnetoresistive properties of doped manganites [5,7,19]. Although there are many examples demonstrating apparently systematic trends (for a review see [4,5,7]), there is also clear evidence that these averaged quantities mask the effects resulted from a deviation of an actual parameter from its average value [20,21,22]. To isolate these effects, one should carry out additional studies on a series of carefully prepared and characterized samples with fixed values of averaged parameters.

A manifestation of one such effect is clearly seen from Figure 1. The figure shows evolution of the ρ vs. T curves for $La_{0.775}Sr_{0.225}MnO_3$ ceramic samples, which is observed upon a change in a sintering temperature T_s (the details of the samples' preparation and characterization can be seen in [21,23,24]). All the curves exhibit a maximum at $T_p \approx 340$ K, which is related to the magnetic transition from PM to FM state [24]. Both a shape of $\rho(T)$ and T_p value are in good compliance with reference data, including those obtained on single crystalline samples [4,25]. However, an interesting feature of the $\rho(T)$ curves is an emergence of additional low-temperature peak observed as T_s decreases from 1350 to 1250 ^{o}C. As follows from our investigations, as well as from the works of other authors [21,23,26,27], the appearance of LT-peak is a phenomenon which is often encountered in doped manganites, but its nature remains unclear hitherto.

In recent years, an extra low-temperature peak (in addition to the peak near the Curie point) on the temperature dependence of electric resistance *R(T)* was reported for a number of samples belonging to the $(La,Sr)MnO_{3-\delta}$ and $(La,Ce)MnO_3$ systems [23,26,27]. Tang *et al.* [28] observed similar *R(T)* curves in polycrystalline $(La,A)(Mn,Cu)O_{3-\delta}$ (A = Sr, Ba) samples. Zhang *et al.* [16] attributed the low-temperature resistivity peak formed as a result of a decrease in a granule size in the $La_{0.85}Sr_{0.15}MnO_3$ perovskite to the tunneling between granules occurring due to different values of the Curie temperature at a granule surface and its core. Steenbeck *et al.* [29] studied films with one grain boundary (on a bicrystalline substrate) and associated the two-peak *R(T)* dependence as arising from a reduced T_C value in the boundary region. However, such approaches are unable to explain the peculiar behavior of ultrathin epitaxial films investigated, among others, by Izumi *et al.* [13]. No explanation was offered in this paper for the emergence of the second peak upon a decrease in the film thickness. It should be emphasized that in all the above cases, no magnetic or structural peculiarities which could lead to anomalies in electrical properties were observed below the Curie point. It is such kind of resistive anomalies that is a subject of the discussion in this chapter.

An absence of low-temperature resistive anomalies in bulk single crystalline counterparts of the samples studied in the above papers points to the idea that the formation of LT-peak is associated with the presence of defects, structural imperfections, strained regions and/or chemical inhomogeneities, all of them being inevitably present in polycrystalline samples and strained films. A number of experimental data testifies in favor of such point. So, there is ample evidence that the LT-peak is likely to emerge upon a decrease in a grain size (in both bulk and thin film polycrystalline samples) [16,21,26,30] or film thickness [13], in other words, upon an increase in the number of various kinds of imperfections (intergrain boundaries, structural defects, strained regions) or/and enhancement of chemical, structural or magnetic inhomogeneity. One can expect that such imperfections directly or indirectly

(through a defect-induced magnetic disordering) influence the electric conductivity. The features of the influence of various kinds of imperfections on a local magnetic order in manganites will be analyzed below. At this stage, let us only pay attention to the fact that the increase in the defect number gives rise to the enhancement of magnetic inhomogeneity [20], and consider the evolution of the electric properties of such system with the increase in the degree of magnetic inhomogeneity.

A number of experimental studies have indicated that in doped manganites, the PM and FM phases can coexist over a wide temperature range below the Curie point [27,31,32,33,34]. Chechersky *et al.* [32] and Simopoulos *et al.* [35] have described the temperature dependence of the fraction of PM phase ($T < T_C$) for some Ca-based manganites. An analysis of these data shows that the magnetic transition may be stretched down to the lowest temperatures (in the samples studied by Chechersky *et al.* [32] the fraction of the PM phase is about 20% even for T/T_C = 0.4), and a part of the sample may remain paramagnetic even at absolute zero [13,16,28]. It is reasonably to assume that the enhancement in magnetic inhmomogeneity results in a widening of the temperature range where two phases coexist. A distinguishing feature of the CMR manganites is a strong dependence of their electric properties on magnetic state: the FM phase has the metallic-type conductivity ($dR/dT > 0$), while the PM one displays the activated-type conductivity ($dR/dT < 0$) [4,5]. Accounting for the fact that the characters of the $R(T)$ dependence have opposite trends in these phases, the behavior of the resulting resistance may be quite complex in the regime of the phase coexistence. It is this situation that will be analyzed in detail below.

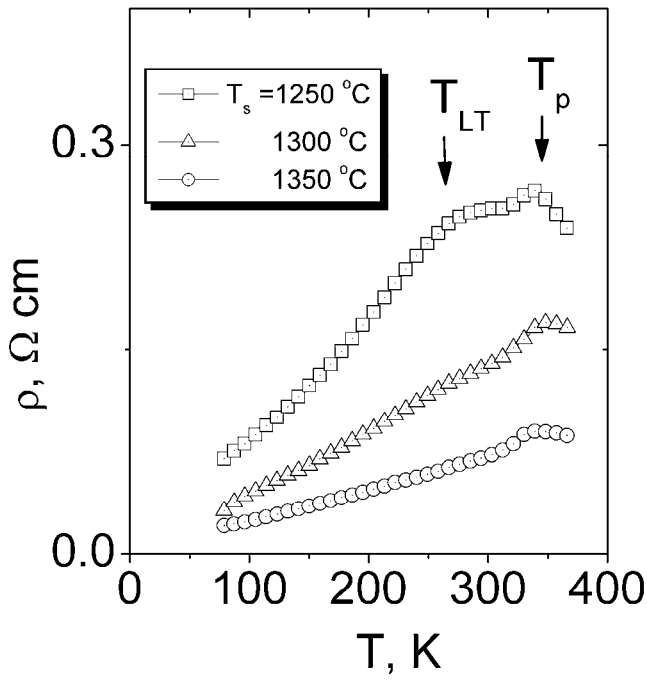

Figure 1. Resistivity vs. temperature dependences for $La_{0.775}Sr_{0.225}MnO_3$ ceramic samples synthesized at different sintering temperatures.

MODEL CALCULATIONS: ELECTRIC CONDUCTIVITY OF A TWO-PHASE MANGANITE SYSTEM

Consider the behavior of a two-phase system consisting of a mixture of PM and FM phases which have different types of conductivity (paramagnetic – activated, ferromagnetic – metallic). Denote the resistance of the material in the two phases by R_p and R_f, respectively. Consider a case where the concentration of each the phase (φ_p and φ_f, respectively) is a function of temperature, and both the phases coexist in a certain temperature interval below a temperature T_0 of the FM phase nucleation ($\varphi_p + \varphi_f = 1$). Having defined specific form of the $R_p(T)$ and $R_f(T)$ dependences, let us analyze the evolution of the resulting resistance of the system upon a variation of one of the parameters, $\varphi_p(T)$ or $\varphi_f(T)$.

Keeping in mind that we are dealing with the doped manganite systems, choose the expressions for $R_p(T)$ and $R_f(T)$ as most suitable for these materials. An analysis of extensive experimental material [4,25,36,37] shows that the temperature variation of the resistance of the FM phase can be written with a good accuracy in the form

$$R_f = B + C \cdot t^2, \tag{1}$$

which reflects the important role of the electron correlations in these materials [4,25]. Here, t is the temperature normalized to T_0, and B and C are constants.

Papers [38,39] reported on the results of a thorough experimental investigation of the electric properties of the films and bulk samples of $La_{0.67}A_{0.33}MnO_3$ (A = Ca, Sr) over a wide temperature range above the Curie point (up to 1200 K). The authors examined the range of applicability of various models, viz., variable range hopping conductivity, semiconductor-type conductivity, and small polaron hopping conductivity, the latter in both adiabatic and nonadiabatic approximations, for a description of the resistance of the PM phase of these materials. It was shown that the temperature dependence of R_p can be best described by the formula

$$R_p = A \cdot t \cdot \exp(E/t), \tag{2}$$

which corresponds to the small polaron hopping conductivity in the adiabatic approximation (E is the activation energy of a polaron and A is a constant).

The measurements of the temperature dependence of the volume fraction of the PM phase were carried out in works [32,35] with the use of Mössbauer spectroscopy for $La_{1-x}Ca_xMnO_3$ (x = 0.2; 0.3) samples. Some indirect data, for example, for samples investigated by Chen and De Lozanne [40], can be obtained by comparing the temperature dependence of the magnetization of epitaxial and polycrystalline films having the same composition and prepared under identical conditions but on different substrates. Assuming that the fraction of the FM phase in the epitaxial film is 100% below T_C, we can estimate φ_f in the polycrystalline film from the ratio between the magnetizations of the films. A similar procedure can be adopted for samples studied by Izumi *et al.* [13].

The analysis of the $\varphi_p(T)$ dependences, adopted from papers [13,40,41], has shown that the probability of the emergence of LT-peak on the $R(T)$ curve increases with an extension of

the temperature interval of the two phase coexistence. The simplest function enabling a variation of the width of this interval with the help of a single variable is an exponential function. Thus, the temperature dependence of the fraction of the PM phase is chosen to be

$$\varphi_p = 1 \ (t > 1) \tag{3a}$$

$$\varphi_p = \exp((t - 1)/d) \ (t \le 1), \tag{3b}$$

where the parameter d characterizes the transition width. It should be noted that the values of φ_p obtained in Refs. [16,28,32,40] do not equal zero even at the lowest temperatures. Hence the theoretical analysis should cover the cases of $d < 1$ as well as $d \ge 1$. A case of a more complex expression for the temperature dependence of φ_p will be considered separately.

For the calculations of the total resistance R we exploit the percolation model, which was developed in paper [42] to describe the resistance of the two-phase medium and was experimentally verified on a large number of binary media. The author of [42] obtained the equation which relates the resistance R of the system to the resistances of each of the coexisting phases, R_p and R_f, their volume fractions, φ_p and φ_f, and two parameters – the critical volume fraction of the metallic (in our case – ferromagnetic) phase φ_f^c, at which the percolation occurs, and the effective demagnetization coefficient L, which is determined by the shape of the inclusions of one phase in another one.

Being adapted to our case, this formula can be written as

$$\varphi_p \cdot (R^{1/g} - R_p^{1/g})/(R^{1/g} + K \cdot R_p^{1/g}) +$$

$$+ (1 - \varphi_p)(R^{1/g} - R_f^{1/g})/(R^{1/g} + K \cdot R_f^{1/g}) = 0, \tag{4}$$

where

$$K = (1 - \varphi_f^c)/\varphi_f^c; \ g = (1 - \varphi_f^c)/(1 - L). \tag{4a}$$

The equation (4) is valid until the condition

$$R_f << R_p \tag{4b}$$

is satisfied [42].

For simplicity, let us make calculations, assuming that the shape of the inclusions is close to spherical and, thus, $L = 1/3$. The estimations made in [42] showed that for the ellipsoids of rotation, oriented along the current flow, the changes in L are small enough for a wide range of ratios between the ellipsoid axes, $1/2 < c/a < 2$. For this reason, the results of the calculations are not particularly sensitive to the morphology of the mutual distribution of the phases and such the choice of L is well-grounded.

The critical volume fraction φ_f^c of the metallic phase at which percolation occurs is chosen to be 0.16, which is in accord with the experimental results and the theoretical analysis of the behavior of CMR manganites [43]. Such a choice of φ_f^c and L gives $g = 1.26$ and $K = 5.25$ in Eq. (4).

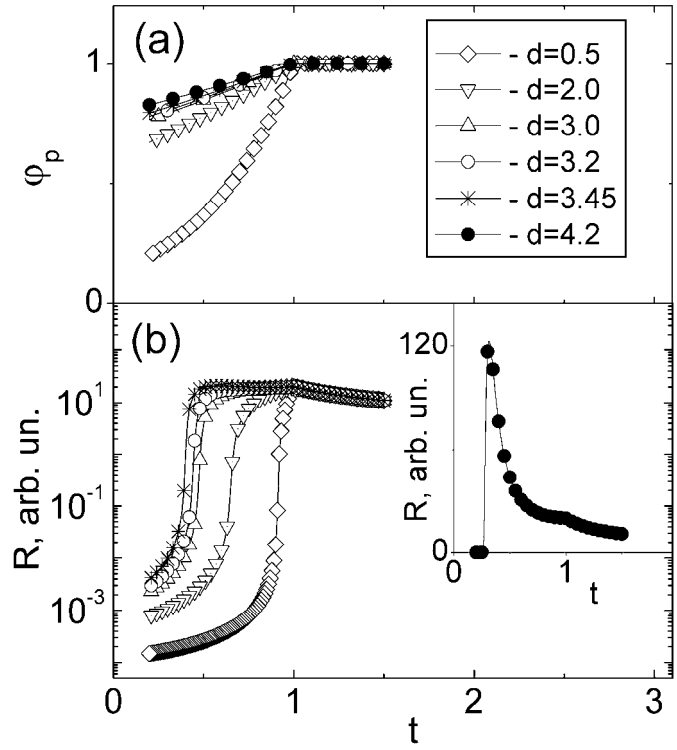

Figure 2. Temperature dependences of the volume fraction of PM phase φ_p (a) and electric resistance R (b) in a two-phase system for different values of the parameter d.

Figure 2 shows the temperature dependences of the volume fraction of the PM phase φ_p and the resulting resistance R of a two-phase system calculated by using Eq. (4) for a set of the values of the parameter d. The coefficients included in Eqs. (1) – (4) are:

$$B = C = 10^{-4},\ A = 1,\ E = 3. \tag{5}$$

Such a choice of the coefficients was made, on the one hand, based on the results of the analysis of experimental data obtained in Refs. [27,38,39] and, on the other hand, in view of the constraint imposed by the inequality (4b) on the functions R_p and R_f.

It is clearly seen from Figure 2(b) that for a sufficiently narrow ($d \leq 0.5$) transition, the R vs. t dependence exhibits a peak near t =1, as is usually observed in CMR manganites [4,5]. An increase in d gives rise to a broadening of the resistive transition. However, beginning from $d \geq 3.2$, a second peak is formed at $t < 1$, in addition to the former one. A sharp rise in the LT-peak is observed upon the further increase in d. This peak becomes dominant and eventually, for $d > 4.2$, only a weak shoulder-like feature, which may be hard to detect experimentally, remains at $t = 1$. Concerning experimental results, the situation where the temperature of the resistance maximum strongly differed from the Curie temperature has been reported in works [16,27,28,30,31,32,44]. In such cases, great care should be exercised while interpreting the experimental results and comparing the resistive data with the magnetic ones.

As our calculations show, the characteristic features of the evolution of the $R(t)$ dependences remain almost unchanged for other values of the coefficients included in Eq. (4),

as well for a more complex form of the temperature dependence of the volume fraction of PM phase. *The first stage* is the broadening of the resistive transition, *the second one* – the formation and growth of the LT-peak, and, finally, *the third stage* – almost complete disappearance of the peak near the temperature of the FM phase nucleation. Figure 3 illustrates the results of the calculations performed for the case where φ_p has the form

$$\varphi_p = \varphi_0 + (1 - \varphi_0)\cdot\exp((t - 1)/d) \quad (t < 1), \tag{6}$$

and the values of the corresponding parameters[1] are:

$$\varphi_p^c = 0.5;\ \varphi_0 = 0.49. \tag{7}$$

It should be noted that the strong temperature broadening of the magnetic transition is a phenomenon encountered quite frequently in doped manganites. Apparently, this is due to a competition between different types of interactions characteristic of these materials, as well as to a strong dependence of the magnetic properties on microstructure, mechanical stresses, degree of disorder, and chemical inhomogeneities. Strongly broadened transitions were observed experimentally in works [16,27,28,30,31,32,44]. Regarding the topic of our investigations, the most illustrative results were reported in Refs. [13,21,28,40], where a correlation between the magnetic transition width and the emergence of the low-temperature resistive anomaly could be traced clearly.

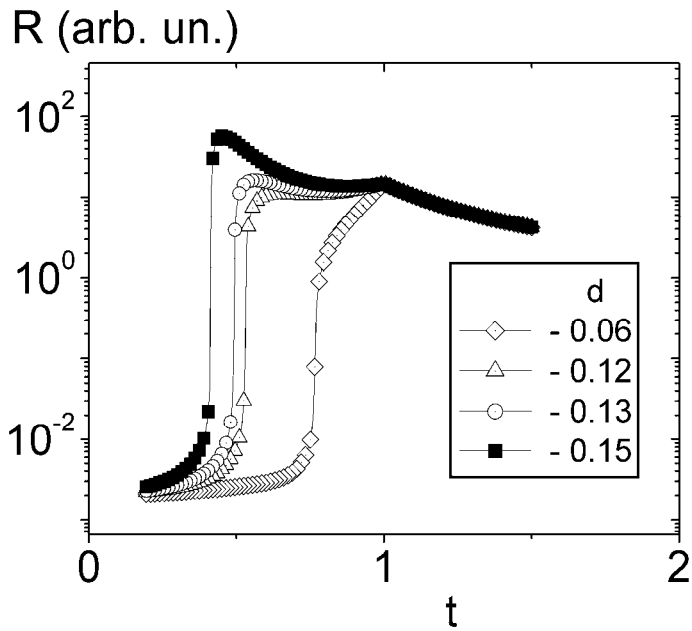

Figure 3. Temperature dependences of resistance calculated according to the expressions (4), (6) – (7). *d* is the width of the transition.

[1] The calculations show that for the case where the expression for φp has the form (6), the features of the $R(T)$ evolution are determined by the difference between φ_0 and φ_p^c, rather than by their absolute values.

Thus, we have theoretically analyzed the electrical properties of a system consisting of PM and FM phases which have different types of conductivity and coexist over a wide temperature interval. It is shown that in spite of the monotonic variation of magnetic and electric properties of each the phase, the resulting resistance may exhibit anomalies in the region of the phase coexistence. A short review of experimental data available points towards high likelihood of the emergence of such anomalies in doped manganites.

EFFECT OF MICROSTRUCTURE ON TRANSPORT PROPERTIES OF MANGANITE POLYCRYSTALS

Transport and magnetoresistance properties of manganite polycrystals have been observed to differ from those of single crystals and epitaxial films [45,46,47]. Contrary to the perfect crystals, both enhanced low-field magnetoresistance over a wide temperature range below T_C and increased overall resistivity are typical of polycrystals, and also non-coincidence of ferromagnetic and metal-insulator transition temperatures has repeatedly been reported [16,27,28,30,31,44]. In order to deeper understand the physics of such materials, one should investigate not only the properties intrinsic to single crystalline state but also those caused by microstructure, strain, disorder, and compositional variations.

This section focuses on the detailed investigation of the transport, magnetic and magnetoresistive properties of bulk manganite samples depending on microstructural changes such as grain size and intergrain connectivity. It is aimed at the elucidation of the nature of a peak on a temperature dependence of electric resistance, which emerges at $T_{LT} \approx 0.7T_C$. It is shown that the decrease in a grain size and/or deterioration of intergrain conductivity can result in a formation of such the peak. The data obtained can be well explained in terms of the coexistence of the PM and FM phases which exhibit opposite trends in the temperature dependences of resistivity, with the features of the phase coexistence being dependent on a sample microstructure.

Microstructure effects were studied in a series of $La_{0.825}Sr_{0.175}MnO_{3-\delta}$ polycrystalline samples prepared through a two-stage solid state reaction in air according to the procedure described in Refs. [21,24]. At the final stage of the samples' preparation, the obtained products were sintered for 2 hours at T_s = 1360 (pellet *A*), 1300 and 1200 ^oC (pellets *B* and *C*, respectively), and then furnace cooled down to room temperature. The details of the samples' characterization and measurements were described elsewhere [21].

Figure 4 (a-c) shows the scanning electron microscopy (SEM) pictures of the cleaved surfaces for the samples *A*, *B* and *C*, respectively. As the sintering temperature decreases, the size of the grains becomes smaller. The average intercept length over large number of grains, calculated according to the method suggested by Mendelson [48], is equal to 3.6 μm for the sample *A*, 2 μm for *B* and 1.25 μm for *C*. It is seen that the decrease in T_s gives rise to the decrease in the average grain size, and thus, to the increase in the fraction of intergrain area. As the latter is structurally and magnetically disordered [41,49], one can expect that a degree of magnetic inhomogeneity will be enhanced upon a transition from *A* to *C*. In what follows, we will present the experimental evidence of this statement.

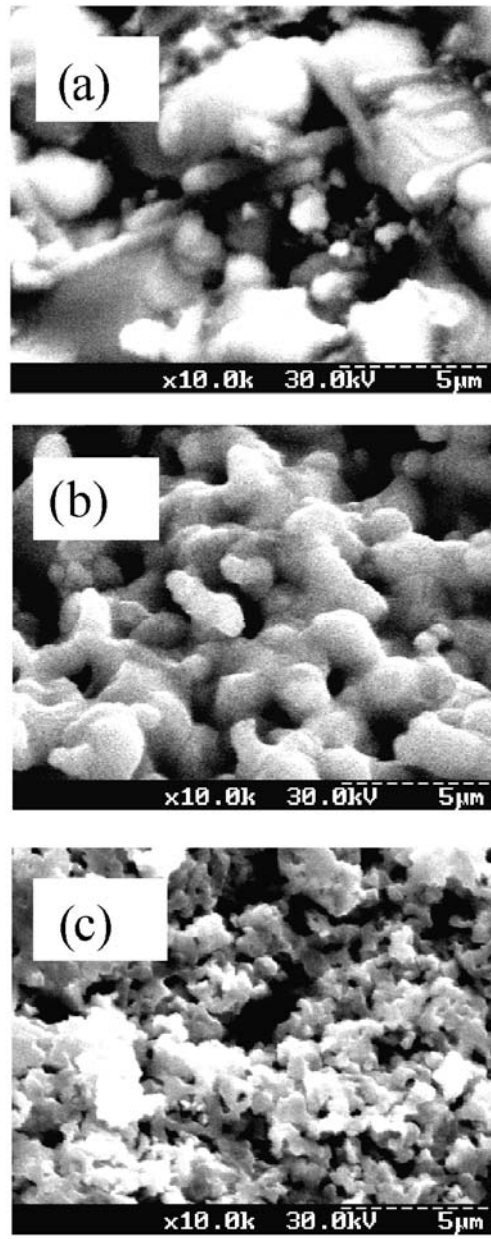

Figure 4 (a-c). SEM images of the cleaved surfaces of the samples *A*, *B*, and *C*, respectively.

Figure 5 (a-c) shows the results of the measurements of electric resistance R and magnetic susceptibility χ for the samples *A*, *B* and *C*. The character of the temperature dependences of χ indicates that all the samples become FM upon the temperature lowering. The Curie temperature T_C was calculated as a temperature of a maximum on a $-d\chi/dT$ vs. T curve. The T_C value is almost the same for all the samples and is about 250 K. For all the plots of Figure 5, the temperature is normalized to the T_C value determined in above way.

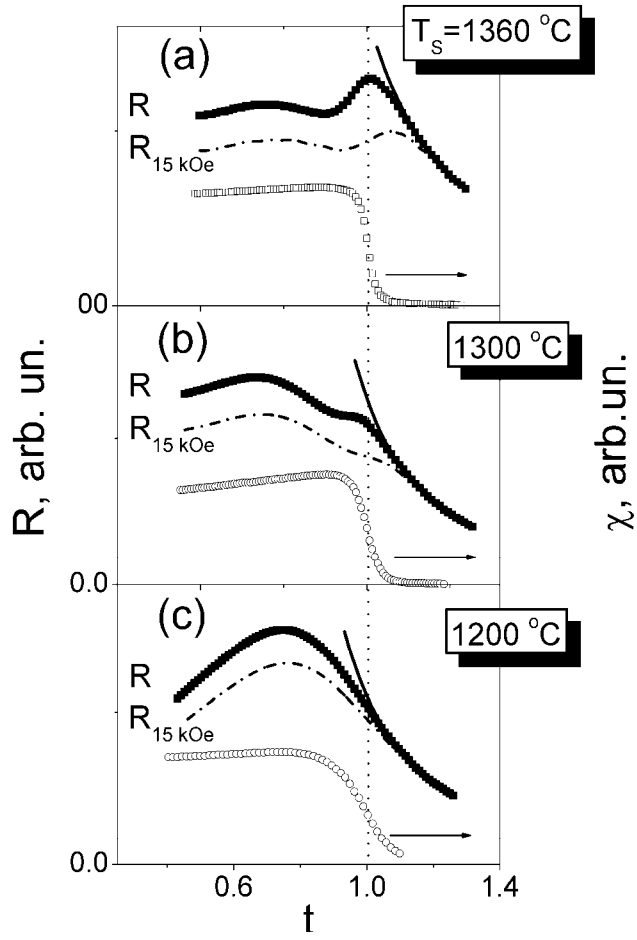

Figure 5 (a-c). Temperature dependences of electric resistance R and magnetic susceptibility χ for the samples A, B, and C, respectively. Bold solid lines denote $R(T)$ dependences extrapolated from a high-temperature region. R – resistance measured at zero external magnetic field; $R_{15\ kOe}$ – resistance under an applied field of H = 15 kOe.

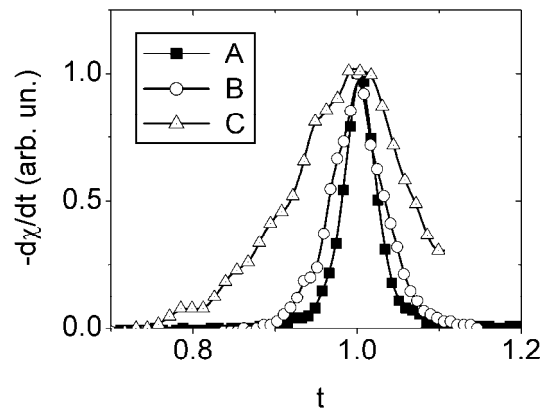

Figure 6. Normalized dependences of -dχ/dt vs. t for the samples A, B and C.

As is seen from the figure, the *R(T)* dependences are similar in the PM region but markedly differ from each other around and below Curie temperature. The resistivity of the sample *A* grows with lowering temperature, reaches a maximum at T_p slightly higher than T_C, and displays a broad peak at $T_{LT} \approx 0.7T_C$ (~ 165 K). While external magnetic field $H = 15$ kOe suppresses the first peak, giving rise to the maximum in magnetoresistance $MR = (R - R_H)/R$, there is no visible *MR* anomaly around the latter. No any peculiarity near T_{LT} is also observed on the dependence of magnetic susceptibility vs. temperature. When going from Figure 5(a) to Figure 5(c), the evolution of the transport and magnetoresistance behavior has the following features:

(a) the low-temperature resistance peak gradually grows relative to the peak at T_p, until the latter completely disappears in the sample *C*;
(b) while magnetoresistance at $T << T_C$ progressively increases, the *MR* peak near T_C becomes smaller and broader, and finally vanishes, as well.

The grain-size dependent magnetic and transport properties of polycrystalline manganites were studied in Refs. [16,47,[49]]. It has been found that the reduction in a grain size gives rise to the broadening of the FM transition and often results in the decrease in saturation magnetization. Our data show similar trend. Figure 6 presents the dependences of $-d\chi/dt$ vs. *t*, normalized to the maximal ordinate value, for the samples under investigation. The width of the transition measured at an ordinate value $y = y_0/e \cong 0.37y_0$ (y_0 is a peak value of $-d\chi/dt$ for each of the samples; $e = 2.718$) grows from 0.05 to 0.19 T_C, as the average grain size decreases from 3.6 μm to 1.25 μm. These effects can be understood taking into account evolution of the ratio of grain surface area to grain volume. The structure and composition of the surface layer differ from those of a grain core, and stronger magnetic disorder is expected far from the center of the grain [16,47]. As the particle size decreases, the contribution from the surface area increases. As a result, this brings about a degradation of the FM phase, leads to a broadening of the magnetic transition and often to a decrease in saturation magnetization.

Consider the behavior of electric resistance in more detail. It was mentioned above that at $T > T_C$, the electronic transport in manganite materials is best described by the model of small polaron hopping [39]. In adiabatic approximation the activated conduction of small polarons follows Eq. (2). We have analyzed our data using this model. Shown by bold solid lines in Figure 5 are the curves fitted according to the above expression. The results of the analysis demonstrate that activation energy *E* grows from 105 to 137 meV, when going from the sample *A* to the sample *C*.

As temperature decreases, the behavior of experimental data deviates from that predicted by adiabatic small polaron hopping model. This deviation is accompanied by a sharp growth of both susceptibility and magnetoresistance. Further temperature lowering leads to the formation of the peaks near T_C on the *R(T)* and *MR(T)* dependences for the samples *A* and *B*. It is noteworthy that, although in the case of the sample *C* the resistivity at T_C is far from its maximum value, the conduction below T_C does not obey adiabatic small polaron hopping law.

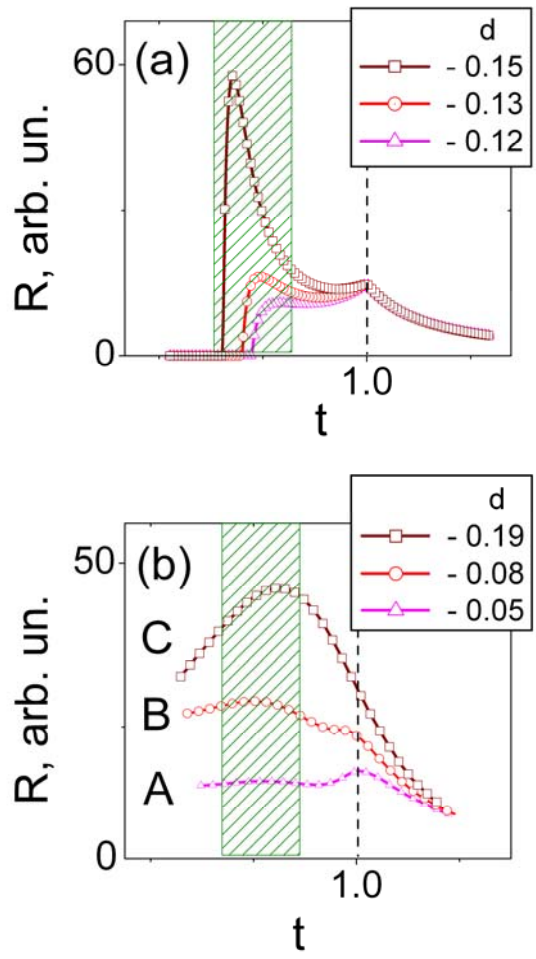

Figure 7. (a) R vs. t dependences calculated according to Eq. (4). (b) Experimental R vs. t dependences for the samples A, B and C. Shaded are the regions where the LT-peak emerges.

Close to and below the Curie temperature electronic behavior of the samples under study considerably differs from each other (see Figure 5). A and B exhibit a relatively sharp resistance peak near T_C and a broad one at $T_{LT} < T_C$, the latter only beginning to emerge in the case of the sample A. When going from A to C, the height of the LT-peak on $R(T)$ curve grows relative to the resistance at T_C. This effect is accompanied with a decrease in magnetoresistance near T_C and, as was shown above, with a broadening of magnetic transition. There is no any resemblance to the high-temperature (near T_C) peak in the sample C.

The main trends in the transformation of the $R(T)$ and $\chi(T)$ curves, observed upon the decrease in grain size, are in compliance with the results obtained in other research groups [40,45,47]. The analysis of these data confirms the ideas that the emergence of the LT-peak is a result of a broadening of magnetic transition and that it is usually observed in a region of the phase coexistence. The behavior of doped manganites for the case of the broadened magnetic transition was discussed in detail in the previous section. Figure 7 illustrates the results of the calculations made according to Eq. (4) for the following parameters:

(a) a critical volume fraction of the metallic phase, at which percolation occurs, is equal to 0.5;
(b) the temperature dependence of the PM fraction φ_p is described by the expression $\varphi_p = 0.49 + \exp((t\text{-}1)/d)$, where $t = T/T_C$ and the parameter d characterizes the transition width in units of T_C.

As is seen from Figure 7, the character of the evolution of the *R(t)* dependences, observed upon the increase in the magnetic transition width, is similar for the experimental and calculated data. With regard to the more detailed computations, it does not make sense to aspire a complete coincidence of the calculated data with the experimental ones, because the model requires $R_f << R_p$, but this is not the case for the samples under study.

The conclusions of the theory are directly applicable to the description of the transport and magnetoresistance properties of the sample *C*. It should be noted that, although there is no visible anomaly near T_C on the *R(t)* curve, the resistance at and below Curie point is far from that extrapolated from PM region.

It follows from the theoretical calculations that, as the LT-peak begins to develop, the conduction of the system becomes strongly dependent on subtle features of the electric properties of each of the phases, which, in turn, are very sensitive to the intergrain connectivity [14]. This fact can explain the evolution of the resistivity of manganite samples, which was observed to occur when the number of cooling-heating cycles increases [21].

As a result, we have correlated transport properties of $La_{0.825}Sr_{0.175}MnO_{3-\delta}$ polycrystalline samples with their magnetic and microstructure features. It has been shown that both grain size and intergrain connectivity strongly affect electric conductivity, leading in some cases to the formation of LT-peak. The analysis of the experimental data leads to the conclusion that the low-temperature resistance anomaly arises as a result of a wide-temperature-region coexistence of the phases which exhibit opposite trends in the temperature dependences of resistivity.

SELF-DOPED LANTHANUM MANGANITES AS A PHASE-SEPARATED SYSTEM: TRANSFORMATION OF TRANSPORT PROPERTIES WITH DOPING AND HYDROSTATIC COMPRESSION

Self-doped manganites $La_xMnO_{3+\delta}$ ($0.815 \le x \le 1$) are suitable model compounds for the examination of the approach developed, since for the samples synthesized under identical conditions, the character of the $R(T)$ dependences changes from activated ($x = 1$) to well pronounced double-peaked ($x = 0.90$, 0.815) with a simultaneous transformation of magnetic structure from cluster spin glass to FM [50,51,52]. At the same time, as x changes from 1 to 0.815, the concentration of the metallic phase crosses the percolation limit. Such a wide range of variation of transport and magnetic properties is brought about by a variation of both the concentration of Mn^{4+} ions and cation vacancies in lanthanum and manganese sublattices [52]. The application of high pressures makes it possible to change the character of conductivity from activated to metallic for the sample with $x = 0.94$ [51,52]. This section

analyzes the electric properties of $La_xMnO_{3+\delta}$ ($0.815 \le x \le 1.0$) polycrystalline samples at normal and high pressures up to 11.5 kbar.

A series of $La_xMnO_{3+\delta}$ (x = 0.97; 0.94; 0.90; 0.815) polycrystals (samples $L_{0.97}$, $L_{0.94}$, $L_{0.90}$, and $L_{0.815}$, respectively) was synthesized by a conventional technology of solid state reactions in air [50,52,53]. The details of the measurements carried out are described elsewhere [8,50-53].

Magnetic and resonance properties of the $La_xMnO_{3+\delta}$ ($0.815 \le x \le 1.0$) polycrystalline samples were studied as functions of temperature, La/Mn ratio, and hydrostatic compression in works [37,51,52]. It was shown that upon lowering the temperature, all the samples undergo a transition from the high-temperature PM state to a low-temperature one, with the latter being either FM for x = 0.815 – 0.94, or cluster spin glass for x = 0.97 and 1.0. Both the temperature of magnetic transition and saturation magnetization diminish and the transitions become more broadened as the La/Mn ratio grows. The hydrostatic compression strongly affects the value of the Curie temperature, which reflects the enhanced sensitivity of the double exchange interaction to the interatomic distance. It is demonstrated that in all the samples under consideration, the PM phase persists down to the lowest temperatures and its volume fraction rises with the increase in x.

The ρ vs. T dependences for the $L_{0.97}$, $L_{0.94}$, $L_{0.90}$, and $L_{0.815}$ samples are depicted in Figure 8. For the $L_{0.97}$ sample, the electric conductivity exhibits the activated character ($d\rho/dT < 0$) over the whole temperature range under discussion (77 – 300 K). For this sample, the application of high pressure strongly reduces resistivity, but does not change the character of its temperature dependence. On the contrary, a strong transformation of the $\rho(T)$ curve under the influence of pressure is observed for the $L_{0.94}$ sample (Figure 9). At normal pressure, a broad maximum at $T_{LT} \cong 105$ K and slightly noticeable tendency towards metallic ($d\rho/dT > 0$) conductivity below T_{LT} are characteristic of the ρ vs. T dependence. Only a slight shoulder-like anomaly is observed at T_C. High pressures diminish resistivity approximately by one order of magnitude at low temperatures and essentially widen the region of the metallic state. It is noteworthy that a similar result was also reported in work [54], where the application of a pressure of 9.4 kbar induced the metallic state in $La_{0.94}Mn_{0.98}O_3$ single crystal below $T_C \cong 210$ K.

For the case of the $L_{0.90}$ and $L_{0.815}$ samples, the ρ vs. T dependence shows two strongly pronounced peaks: the first one near T_C and the second, the LT-peak, at 200 and 173 K for the former and latter samples, respectively. High pressures do not change the character of the curves and to a lesser extent affect the absolute values of resistivity.

To gain a deeper insight into the phenomena observed, let us analyze the behavior of these materials based on the approach described above. To calculate the ρ vs. T dependence within the region of the PM-FM phase coexistence, we use the $\rho_f(T)$ and $\rho_p(T)$ dependences obtained experimentally at low and high temperatures, respectively. For each the sample, the volume fraction of the PM phase at low temperatures, φ_0, (see Eq. (6)) can be found from the magnetic measurements [37,52]. For calculations, we set $\varphi_f^c = 0.45$, as follows from the analysis of the experimental data for the samples of this system [37].

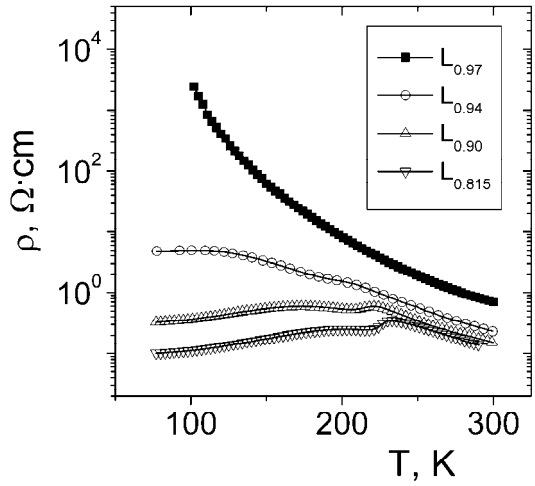

Figure 8. ρ vs. *T* dependences for the $L_{0.97}$, $L_{0.94}$, $L_{0.90}$, and $L_{0.815}$ samples.

Before proceeding further, let us discuss how strongly the intrinsic transport properties of the samples under investigation might be affected by porosity effects.

To date, various aspects of the porosity effects on electric and heat transport properties have been analyzed in Refs. [55,56,57,58,59] with the use of a number of approaches and calculation techniques. In particular, a simple analytical model developed by Mizusaki *et al.* [56] relates the conductivity of highly porous but simply connected ceramics to its porosity. A numerical method developed by Zinchenko [57] is capable of calculating the effective conductivity of randomly packed granular materials with a high particle-to-medium conductivity ratio. The features of the influence of tunneling effects on the electric conductivity of porous materials were specified in papers [60,61]. All the above results can be summarized as follows. For the cases where the tunneling effects do not play an important role in the charge transfer processes, the porosity affects the absolute value of resistivity and scarcely transforms its temperature dependence. Otherwise, it is the tunneling effects that govern the temperature, electric field and stress dependences of the electric resistivity [46,60,61]

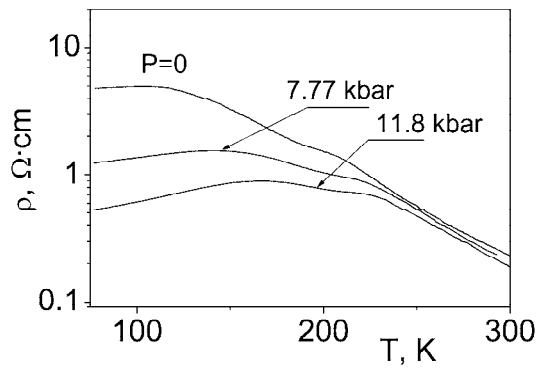

Figure 9. ρ vs. *T* curves at different pressures for the $L_{0.94}$ sample.

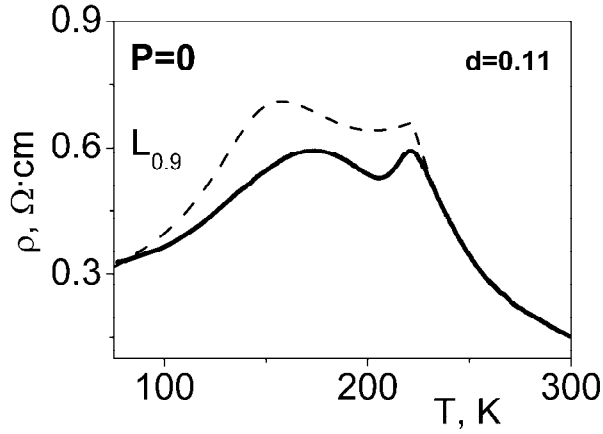

Figure 10. Simulated ρ vs. *T* dependence (dash line) along with the experimental data (bold solid line) for the $L_{0.90}$ sample at normal pressure.

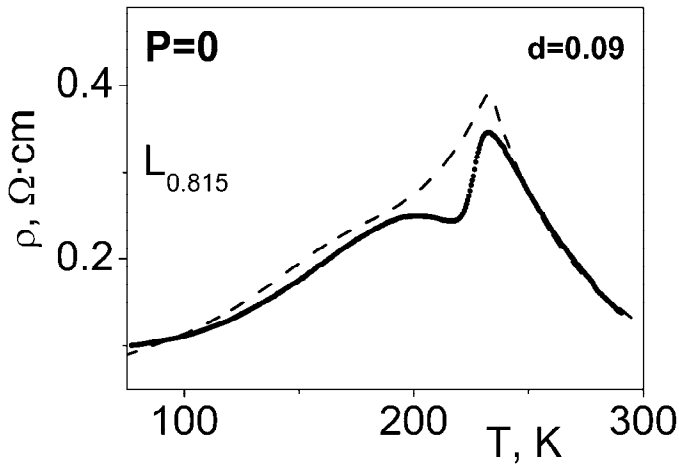

Figure 11. The same as in Figure 10 for the $L_{0.815}$ sample.

As follows from the data of work [37], the characteristic feature of the microstructure of the $La_xMnO_{3+\delta}$ samples with $x = 0.815$ and 0.90 is the presence of simply connected domains containing a number of grains. The porosity of these samples does not exceed 7 %. In both the cases, the peak resistivity is comparable to the values which were observed in polycrystalline samples for which the negligible role of tunneling effects was proved experimentally [26,62,63]. All these facts imply that for the $L_{0.815}$ and $L_{0.90}$ samples, the porosity affects the absolute value of resistivity but hardly modifies its temperature dependence. For the other samples, however, the role of porosity as well as the contribution of tunneling effects to the conductivity should be discussed separately. This will be done below while discussing the resistivity of the $L_{0.94}$ sample.

The $L_{0.90}$ sample is most suitable for the comparison of the experimental and calculated ρ vs. *T* dependences, since for this, a complete set of the parameters necessary for calculations is deduced from experiment [33] and only the parameter *d*, which characterizes a transition width, should be fitted. As follows from the calculations, it is for $d = 0.11$ that the calculated

curve is closest to the experimental one, concerning both the LT-peak position and its height. Figure 10 compares the results of the calculations with the experimental $\rho(T)$ dependence at normal pressure. The fact that the calculated $\rho(T_C)$ value is somewhat higher than the experimental one can be explained by the presence of a small fraction of the FM phase at $T \geq T_C$. To date, there has been ample direct evidence that in doped manganites, the FM clusters may be present above T_C [64,65].

The results obtained for the $L_{0.90}$ sample are in compliance with the SEM investigations [37]. The latter show that, due to a relatively large average grain size and ample amount of simply connected metallic domains, the role of intergrain charge transfer in the total conductivity does not prevail. In fact, it turns out that the double-peaked character of ρ vs. T dependence can be naturally explained within the frames of the simple model which accounts for the coexistence of two magnetic phases with different characters of temperature dependence of resistivity.

Figure 11 shows the results of a similar simulation for the $L_{0.815}$ sample. It can be seen that for d = 0.09 (the best choice), the calculated dependence quite well describes the experimental data. It should be noted that the fact that the fitted value of the parameter d decreases from 0.11 to 0.09 upon a transition from $L_{0.90}$ to $L_{0.815}$ sample is in accordance with the data of magnetic susceptibility measurements [52]: the magnetic transition becomes sharper as the La content diminishes.

A comparison of the calculated and experimental data for the $L_{0.94}$ sample is made in Figure 12. The best agreement in the range 130 – 300 K is achieved for d = 0.11. The calculated data describe well both the shoulder-like anomaly at T_C = 205 K and the activated character of resistivity down to ~130 K. However, at lower temperatures, the difference between the calculated and experimental data is essential: for all reasonable values of d, the calculations show a distinctive "metallization", instead of a plateau, and, as a result, the calculated and experimental data differ by about 5 times. As was noted above, the analysis of the SEM pictures is indicative of the increased contribution of intergrain charge transfer processes in the samples with greater x. Thus, although the grain cores may display metallic conductivity at low temperatures, the contribution from the surface layers, which usually have degraded magnetic properties and raised resistivity, impedes a strong resistivity reduction, which eventually results in a formation of a plateau.

Let us consider how well the approach under consideration can describe the $\rho(T)$ dependence at high hydrostatic pressures. Analyze the experimental curves, obtained at a maximal pressure for two characteristic samples: the $L_{0.90}$ sample, which displays metallic conductivity with negligible changes under high pressure, and the $L_{0.94}$ sample whose "metallization" under high pressures is most pronounced. A comparison of the concentration dependences of ρ^{-1}(La/Mn) at normal and high pressure (~11 kbar) [37] shows that the value of the La/Mn ratio, at which percolation occurs, is not changed with pressure and approximately equals ≈ 0.95. This, however, does not automatically mean that also the value of φ_f^c remains the same, i.e. 0.45. As follows from the experimental data [66,67], in manganites, the application of even moderately high pressures (<10 kbar) gives rise not only to the T_C growth, but also to the increase in φ_f. So, the pressure-effect coefficient for the FM volume fraction of $LaMnO_{3.05}$ manganite was shown to be ~$8.7 \cdot 10^{-3}$ kbar^{-1} [66]. As follows from the recent data [67], the application of the pressure of 9.3 kbar to $La_{0.7}Sr_{0.3}MnO_{2.85}$ manganite leads to the increase in the φ_f value from 13 % to 18 %. For this reason, in further

calculations, we should take into account the likely effect of the high pressure on the change of the FM volume fraction and vary not only the parameter d, but also φ_f. Based on the data available, we set a restriction that the increase in φ_f, caused by the application of a pressure ~11 kbar, cannot be less than 5 % and more than 10 %.

As follows from the calculations, the activation energy E (see (2)) for the $L_{0.90}$ sample decreases from 130 meV at normal pressure to 126 meV at high pressure. This change in E corresponds to the rate dE/dP = -0.34 meV/kbar, which is close to the value -0.6 meV/kbar obtained in paper [68] for $La_{0.75}Ca_{0.25}MnO_3$. The best agreement between the calculated and experimental data is achieved when the increment in both φ_0 and φ_f^c is the same and equals 5 %. Figure 13 compares the results of the calculations with the experimental data obtained at P = 10.8 kbar. The best correspondence is observed for d taking the value 0.11. It should be noted that the correspondence becomes far worse when only the increment in φ_0 is taken into account with φ_f^c set to be constant, or vice versa.

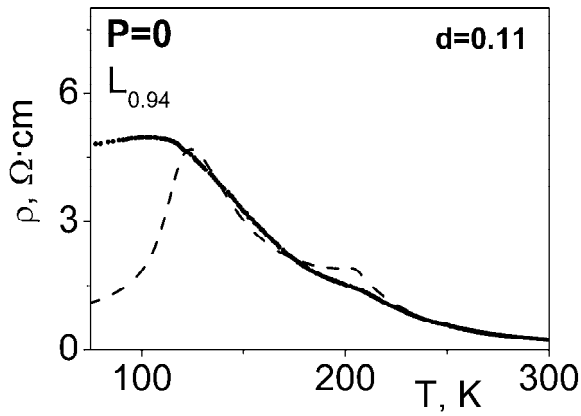

Figure 12. The same as in Figure 10 for the $L_{0.94}$ sample.

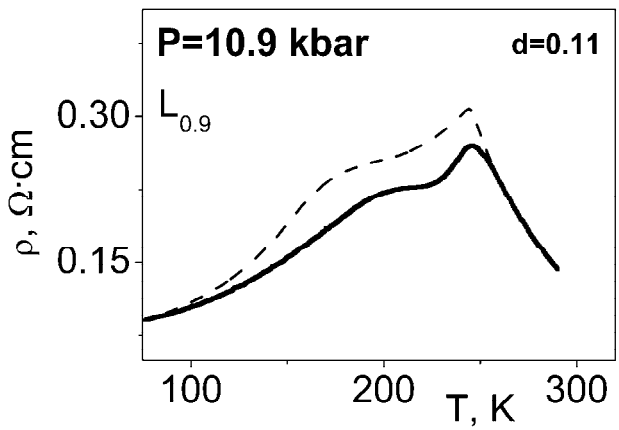

Figure 13. Simulated ρ vs. T dependence (dash line) along with the experimental data (bold solid line) for the $L_{0.90}$ sample at a pressure of 10.9 kbar.

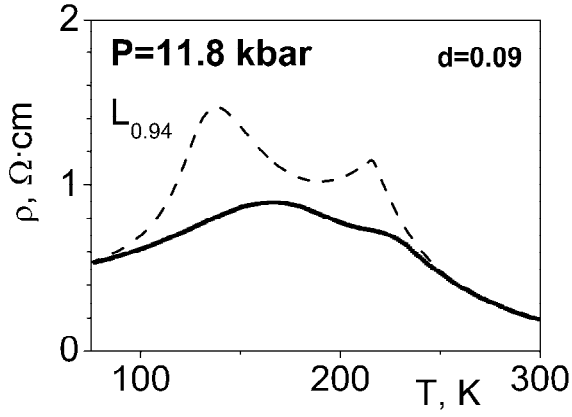

Figure 14. Simulated ρ vs. *T* dependence (dash line) along with the experimental data (bold solid line) for the $L_{0.94}$ sample at a pressure of 11.8 kbar.

Thus, the approach employed not only allows us to describe the effect of high pressure on the magnetic and transport properties of doped manganites, but also provides a deeper insight into the nature of the changes induced by the pressure. So, as follows from the calculations, for the case of the $L_{0.90}$ sample, both the relative volume fractions of the coexisting phases and the parameters of each of the phases turn out to be drastically affected. In particular, the changes the FM phase undergoes are the 5 % increment in the volume fraction and 3 times resistivity drop under a pressure of 10.9 kbar.

For the case of the $L_{0.94}$ sample, the activation energy displays a slight increase with the pressure rise with a rate $dE/dP = 0.29$ meV/kbar. At none of the fitting parameter values can a satisfactory agreement be achieved between the calculated and experimental ρ vs. *T* dependences obtained at $P = 11.8$ kbar (Figure 14). At $d \geq 0.1$, the LT-peak resulted from simulations is a few times higher than its actual value. The smaller *d* values neither go along with the results of the calculations at normal pressure (see Figure 12), nor agree with the data of magnetic susceptibility measurements [52]. Thus, the fact that neither at normal pressure, nor at high one, can the behavior of the resistivity be satisfactory described within the frames of the model that we successfully employed earlier, testifies to the enhanced role of the processes of intergrain charge transfer in $L_{0.94}$ and this is likely to be associated with a small grain size and poor intergrain connectivity. Therefore, a pronounced "metallization" under high pressure results from the transformation of the processes of charge transfer through the intergrain area, rather than from the change in the character of the grain core resistivity.

As a result, the electric properties of $La_xMnO_{3+\delta}$ ($0.815 \leq x \leq 1.0$) polycrystalline samples have been studied in the temperature range 77 – 370 K and at high pressures up to 11.8 kbar. It is shown that the increase in La/Mn ratio gives rise to a change in the low temperature magnetic state from FM to cluster spin glass, as well as to a drastic transformation of electric properties. A peculiar double-peaked shape is characteristic of the resistivity vs. temperature curves for the intermediate range of *x* values. Within this range, the application of high pressures drastically changes both the value of resistivity and the character of its temperature dependence. It is shown that the approach, which regards the state of the $La_xMnO_{3+\delta}$ polycrystals as a mixture of interpenetrating PM insulating and FM metallic phases, is able to successfully describe the peculiarities of the temperature dependence of total resistivity, as

well as the features of its transformation under hydrostatic compression. It is demonstrated that the formation of a low temperature resistance peak is a result of a wide-temperature-region coexistence of the phases which exhibit opposite trends in the temperature dependences of resistivity. The conclusion is made that not only does the hydrostatic compression result in drastic changes in the relative volume fractions of the coexisting phases, but it also affects the intrinsic parameters of each of the phases.

TRANSPORT AND MAGNETORESISTANCE PROPERTIES OF NANOCRYSTALLINE MANGANITE SAMPLES

It was shown above that the properties of doped manganites are very sensitive to the microstructural features of these materials. It is appealing to find the ways for a wide-ranging governing of the material microstructure. In most cases, however, manganese oxides are synthesized at high temperatures using a standard ceramic technique, which allows one to prepare the samples with a grain size of the order of 1 μm. Recently, chemical preparation methods such as sol-gel and coprecipitation from solutions have been introduced to synthesize the CMR oxides [49,63]. All these methods maintain the metal precursors in a highly dispersed state and offer unique advantages including more purity, homogeneity and precise composition control. What is more, such methods make it possible to synthesize the samples with a grain size of the order of tens nanometers [49,63].

In this section, we report the magnetic, transport and magnetoresistance properties of nanocrystalline $La_{0.7}Ca_{0.3}MnO_3$ synthesized by a method of coprecipitation from solutions. The details of the sample preparation and characterization were described elsewhere [24,63]. The average grain size estimated from the tunneling electron microscopy studies is about 20 nm [63].

Figure 15 presents the temperature dependences of resistivity of $La_{0.7}Ca_{0.3}MnO_3$ sample measured at $H = 0$ and 15 kOe. The $\rho(T)$ curve shows a broad peak at $T_{LT} \cong 230$ K and a shoulder-like feature at $T_p \cong 264$ K. Magnetic field does not change the nature and position of the broad peak very much, but suppresses the second one greatly. The difference in the magnetic field response of the two peaks indicates that they may have different origins. Near T_p, the low-field AC susceptibility χ exhibits a sharp increase with a decrease of temperature (Figure 16), indicating an occurrence of magnetic ordering. The onset of the magnetic ordering corresponds to a PM-FM transition at $T_C \cong 266$ K, which is consisted with other reports [4,7]. As can be seen from Figure 16, the susceptibility changes monotonically with further lowering temperature, and neither χ nor $-d\chi/dT$ displays any anomaly in the vicinity of T_{LT}. Similarly, the magnetization M measured at 10 kOe as a function of temperature (not shown here) does not exhibit peculiarities below T_C.

Figure 17 shows the magnetic hysteresis loop $M(H)$ at $T = 5$ K. As a function of field, M tends to saturate at $H \geq 6$ kOe, and the saturation magnetization M_s is equal to 3.4 μ_B/Mn. This value, being lower than that predicted by theory for the given composition (3.7 μ_B/Mn), suggests that not all the volume of the sample is in FM state even at temperatures close to absolute zero. Such result is not surprising for materials with sizeable amount of intergrain boundaries area. A significant decrease in M_s upon reducing the particle size was reported by

Huang *et al.* [30] and Balcells *et al.* [69] for granular $La_{0.7}Sr_{0.3}MnO_3$ perovskites. This phenomenon may be related to a discrepancy in magnetic behavior between the grain core and intergrain region. Indeed, since the grain boundary is expected to be similar to the glassy or amorphous state and the magnetic configuration in the grain surface is more chaotic than that in the core, the coupling between the magnetic ions in the surfaces should be weaker than that in the cores.

Magnetoresistance ratio *MR* shows a steady decline with increasing *T*, interrupted by an increase near T_p, before finally dropping to zero above 285 K (see Figure 15). Two contributions to the magnetoresistance are clearly seen from the figure, one is the cusplike *MR* near T_C, related to the intrinsic properties of the system, and the other is low-temperature *MR*, extrinsic in nature, whose origin lies in the existence of interfaces and grain boundaries [45,46,47]. In our case, the latter component reaches a value of 24 % at $T = 80$ K, indicating a substantial contribution of intergrain area to the transport and magnetotransport of the samples under investigation.

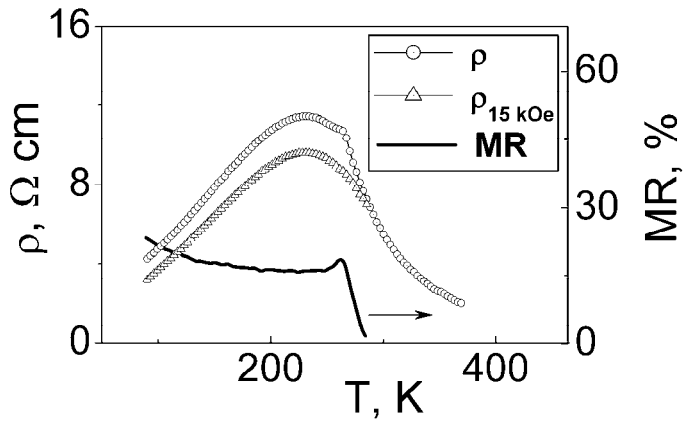

Figure 15. Temperature dependences of resistivity and magnetoresistance for the nanocrystalline $La_{0.7}Sr_{0.3}MnO_3$. ρ – resistivity measured at zero external magnetic field; $\rho_{15\ kOe}$ – resistivity under an applied field of $H = 15$ kOe.

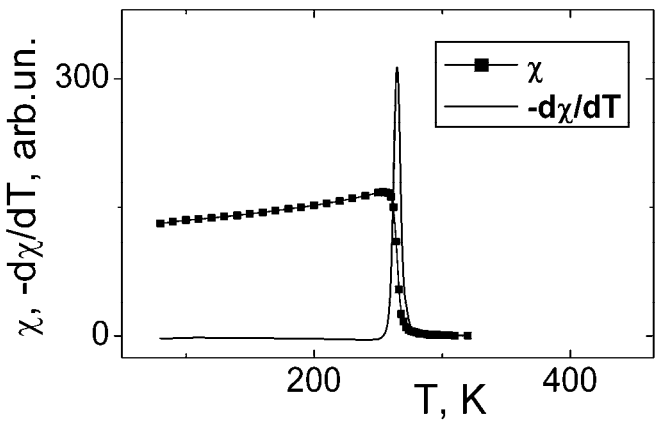

Figure 16. Dependences of magnetic susceptibility χ and -dχ/d*T* vs. *T*.

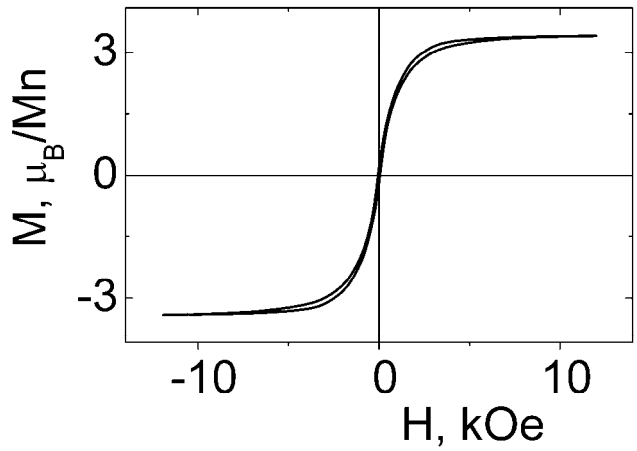

Figure 17. Magnetic hysteresis loop at $T = 5$ K.

With regard to the mechanisms lying behind the low-temperature component of *MR*, two different interpretations have been given to date, namely, spin-polarized intergrain tunneling [46,47] and spin-dependent scattering at the grain boundaries [45]. Gross *et al.* studied electrical transport properties of artificial grain boundaries in $La_{2/3}Ca_{1/3}MnO_3$ films and explained the results within a model implying the presence of a disordered PM grain boundary layer that is depleted below T_C [46]. The authors concluded that the transport across the depleted layer is dominated by multi-step tunneling via localized states. Nevertheless, for tunneling to be a dominant conduction mechanism, one should expect strongly non-Ohmic current I vs. voltage V characteristics [46,47]. As can be seen from Figure 18, this is not the case for the nanocrystalline $La_{0.7}Ca_{0.3}MnO_3$ samples. The linear $I(V)$ dependence over more than two orders of V is strong evidence excluding tunneling as the dominant conduction mechanism in the samples under study.

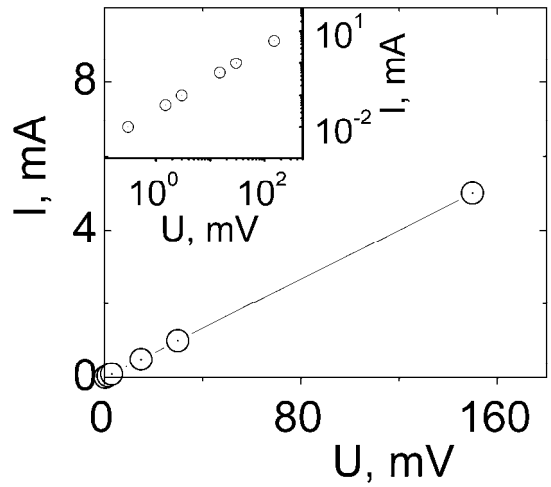

Figure 18. Current vs. voltage characteristics at 77 K. Inset shows the same dependence on a logarithmic scale.

In a recent paper devoted to spin-polarized transport in magnetic oxides Gupta *et al.* [70] pointed out that the grain boundary conductivity might be quite inhomogeneous, with insulating microscopic regions separated by more conducting regions. Conduction in this parallel channel network can then occur by a combination of spin-scattering and inelastic tunneling processes, with the relative contribution varying for different materials. In a general case, it is difficult to directly convert this picture into mathematical equations. However, this is possible for the cases where one of the processes is prevailing. When neglecting tunneling processes, the approach developed in this chapter, which regards the samples under discussion as a random mixture of the high-resistive PM and the low-resistive FM phases (or regions), is able to describe all the peculiarities observed.

Thus, transport, magnetic and magnetoresistance properties of $La_{0.7}Ca_{0.3}MnO_3$ nanocrystalline samples have been systematically studied. It is shown that temperature dependences of both electric resistivity and magnetoresistance exhibit peaks near Curie temperature $T_C \cong 266$ K. In addition, a broad resistivity peak, which is not accompanied with any anomaly on $\chi(T)$ and $MR(T)$ curves, is observed at $T_{LT} \cong 230$ K. Relatively low value of the saturation magnetization at 5 K suggests that FM metallic phase does not occupy the whole sample. Current-voltage $I(V)$ characteristics are linear over more than two orders of V at $T < T_C$, in rather contrast to the picture when intergrain tunneling is the dominant conduction mechanism. The results are well explained in terms of an inhomogeneous transport through a mixture of high-resistive PM regions separated by more conducting FM regions, where increased amount of the PM phase is provided by the expanded intergrain area.

PECULIAR FEATURES OF ELECTRIC PROPERTIES OF ULTRATHIN EPITAXIAL FILMS

This section analyzes features of the transformation of magnetic and transport properties of epitaxial manganite films upon a decrease in the film thickness. It is shown that the anomalous resistive behavior of very thin films may result from the degradation of magnetic transition and development of inhomogeneous magnetic state consisting of PM high-resistive and FM metallic phases coexisting over a wide temperature region. Theoretical calculations performed within the frames of the approach developed in this chapter are concluded to well describe the main features of the properties of the objects under consideration.

Recent investigations conducted on epitaxial films of doped manganites have shown that these films have degraded magnetic and electrical properties near a substrate-film interface [12,13,71]. Depending on substrate material, interface roughness and lattice mismatch between a film and substrate, the thickness of the "dead" layer was estimated to vary from 1 to 11 nm at $T = 77$ K. Furthermore, a thin surface layer with degraded magnetic properties was revealed by spin-polarized photoemission measurements carried out on $La_{0.67}Sr_{0.33}MnO_3$ epitaxial film [72]. In other work, Blamire *et al.* [73] concluded that magnetic state of ultrathin (5 – 6 nm) $La_{0.7}Ca_{0.3}MnO_3$ epitaxial films can be modeled on the basis of a high density of small magnetically ordered regions separated by a matrix of disordered spins. All these observations show that even the properties of high quality epitaxial films are far from those of ideal homogeneous systems, and at least the *magnetic* inhomogeneity should be taken into account to correctly analyze the behavior of manganite systems.

Izumi *et al.* [13] reported on the growth, structure, and properties of $La_{0.6}Sr_{0.4}MnO_3$ thin films fabricated on $SrTiO_3$ (001) substrates using pulsed laser deposition. Such analyses as reflection high-energy electron diffraction, coaxial impact collision ion scattering spectroscopy, atomic force microscopy, and four-circle x-ray diffraction were carried out to characterize the surface and crystal structure of the films. By atomic force microscopy, the surface of resulting films was confirmed to be extremely flat, showing atomically smooth terraces and 0.4 nm high steps. The direction and spacing of the steps were the same as those for the original substrate. The authors concluded that perfect layer-by-layer growth took place for the films used for further investigation. Transport and magnetic properties were compared for the two films with the thicknesses of 100 and 4 nm (denoted here as films *A* and *B*, respectively). The thick film showed saturation magnetization M_s of about 3.5 μ_B/Mn atom at 5 K and relatively sharp change in magnetization near T_C = 310 K. The properties of a 4-nm-thick film were considerably different – both reduced M_s at 5 K and broadened magnetic transition were characteristic of the film. Two bumps, one near T_C and another one at $T \approx 0.48T_C$, were observed on resistivity vs. temperature curve. It was noted by Izumi *et al.* that such modification of the properties might be attributed to interface and/or surface effects but the detailed analysis of the phenomena was not performed.

Let us analyze the results by Izumi *et al.* from the viewpoint of the approach described above. At $T > T_C$ the resistance of the film *B* can be well fitted by the expression:

$$R_p^B(t) = 9.7\times10^{-4}\cdot t\cdot\exp(3.6/t). \tag{8}$$

A fraction of the PM phase persisting in the film *B* below T_C can roughly be estimated from the ratio between the magnetization of the film *B* (M^B) and that of the film *A* (M^A). Taking into account that M_s of the thick film is close to the theoretical value (3.6 μ_B/Mn for the given composition) and that magnetic transition is sufficiently sharp in the film *A*, it is reasonably to assume that below T_C the whole volume of the film *A* is in FM state (corresponds to $\varphi_0 = 0$ and $d << 1$ in Eq (6)). Since the magnetization of the PM phase is sufficiently smaller than that of the FM one, a ratio of M^B/M^A corresponds to the fraction of the FM phase in the film *B*, and the temperature dependence of the PM fraction can be expressed as

$$\varphi_p^B(t) = 1 - M^B(t)/M^A(t) \ (t < 1). \tag{9}$$

Inset of Figure 19 shows the dependence of φ_p^B vs. T/T_C calculated from the experimental data of Ref. [5] (circles) and that fitted according to Eq. (6) (solid line):

$$\varphi_p^B(t) = 0.5 + 0.5\cdot\exp((t - 1)/0.2) \tag{10}$$

As a next step, let us estimate the critical volume fraction of the FM phase at which percolation occurs. There is good reason to think that, as temperature decreases, $\varphi_f^B(t)$ reaches its critical value φ_f^c at a temperature, at which a sharp drop in resistance is observed (shown by bold arrow in Figure 19). The value of φ_f^c determined in such a way is equal to 0.46.

It was noted above that, to calculate the total resistance of the two-phase system, we used the formula (4). To correctly apply this formula, the following condition has to be satisfied:

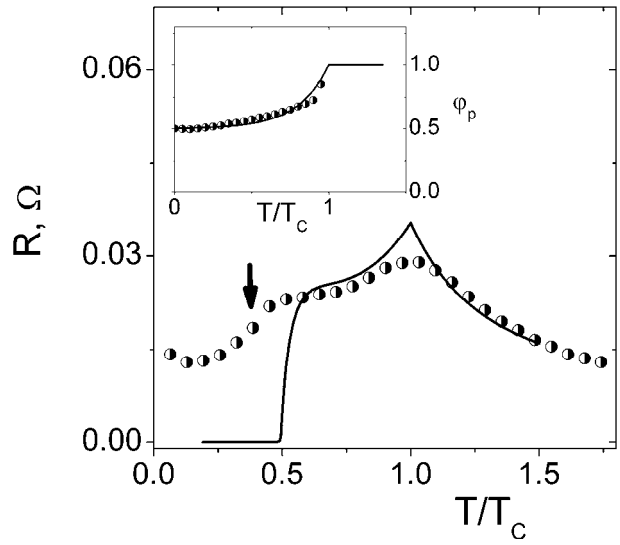

Figure 19. Resistance vs. T/T_C for the 4-nm-thick $La_{0.6}Sr_{0.4}MnO_3$ epitaxial film (circles – experimental data adopted from Ref. [5], solid line – calculated as described in text). Inset: temperature dependence of the fraction of PM phase φ_p for the same film (circles – calculated from Ref. [5], solid line – fitted according to Eq. (6)).

$R_f << R_p$.

It follows from the experimental data by Izumi *et al.* that this condition is not valid for the film *B*. Nevertheless, our calculations indicate that over the temperature region where two phases coexist, the total resistance is largely determined by the value of R_p and is weakly sensitive to the specific form of R_f. Thus, we have put R_f of the film *B* in the following form:

$$R_f^B(t) = 10^{-6} \cdot (1 + t^2). \tag{11}$$

As can be seen from Figure 19, such choice of $R_f^B(t)$ leads to a discrepancy between the experimental data (circles) and calculated ones (solid line) at very low temperatures. However, at intermediate and high temperatures, the behavior of the total resistance derived from Eqs. (4), (8) – (11) well reflects the main features of the resistance of the film *B*.

Thus, we have analyzed the transport and magnetic behavior of $La_{0.6}Sr_{0.4}MnO_3$ ultrathin epitaxial films. It is shown that over a wide temperature region, the state of the film can be well modeled as a mixture of the PM high-resistive and FM metallic phases. In this state, the resistance is preferentially determined by magnetically disordered regions and does not reflect the behavior of magnetization which measures an average spin alignment. Calculations performed in the framework of the approach developed in this chapter have been shown to well describe the main features of magnetic and transport properties of the film under consideration.

ANALYSIS OF EXISTENT APPROACHES TO DESCRIBE ELECTRIC PROPERTIES OF DOPED MANGANITES

It was stressed above that the properties of doped CMR manganites cannot be in full measure understood without accounting for the effects induced by various kinds of imperfections (grain boundaries, chemical inhomogeneities, strained regions, etc.). It is this topic that has been under intensive investigation in a number of recent papers.

The role of intergrain boundaries in the formation of the properties of doped CMR manganites has been investigated in detail in papers [20,45,46,70,74,75]. There has been ample experimental evidence of the perturbations of deformation fields and variations in stoichiometry, induced by boundaries. So, Chisholm *et al.* [76] calculated stress distribution near a low-angle intercrystallite boundary and showed that the region within which the deformation exceeds 1 % extends at least a few nanometers (4.4 nm for the 5°-angle boundary). Browning *et al*. [77] came to a conclusion that the peculiar features of intergrain boundaries in perovskites include the variations of oxygen stoichiometry over the area exceeding several nanometers. Recently, Gross *et al*. presented strong arguments in favor of the important role of the effects of energy band bending and charge depletion in the formation of electric and magnetoresistive parameters of the boundaries in doped manganites [46].

It is noteworthy that hydrostatic pressure, which causes a 1 %-deformation in $La_{2/3}Ca_{1/3}MnO_{3-\delta}$ for example, gives rise to the change in the Curie temperature $\Delta T_C \approx 10$ K [78]. At the same time, the minor changes in the parameter δ lead to $\Delta T_C \approx 15$ K [79]. For this reason, the local values of the Curie temperature and magnetization in the vicinity of grain boundaries strongly differ from those characteristic of a homogeneous phase. What is more, the perturbations grow with the rise in the angle between crystalline lattices on different sides of the boundary [20].

Similar effects are expected to result from other defects of crystalline structure, strained regions, chemical inhomogeneities, interfaces between a film and substrate, etc. [20,71,80]. So, even a high-quality single crystal displays a low-field *MR* component near T_C, which is thought to originate from heterogeneity caused by local clustering [20,70]. Thus, the enhancement in the defectiveness of doped manganite materials gives inevitably rise to the increase in their magnetic inhomogeneity. At the same time, the characteristic size of the regions where magnetic parameters deviate from their average values exceeds, as a rule, the dimensions of the defects themselves. Accounting for a strong interplay between magnetic and electric parameters in manganites, a similar picture is also characteristic of the distribution of conductivity. Moreover, in this case one should expect even stronger inhomogeneity because, in addition to the indirect influence through the fluctuations of magnetization, the defects will serve as additional centers for the charge carrier scattering.

As indicated above, there has been clear evidence that the inhomogeneity of magnetic and electric parameters is an important integral part of all the samples of doped manganites (including high-quality single crystals), and it has to be taken into account while considering the processes of charge transfer in such materials. Let us analyze the theoretical approaches which include the consideration of the effects induced by various kinds of imperfections.

Paper [81] reports the approach whose idea is very close to that developed in this chapter. Within the frames of the effective medium theory, Song *et al.* calculated the resistance of a two-phase system which is a mixture of the high-resistive PM and low-ohmic FM phases. The

calculations are based on an assumption that a manganite sample is not characterized by a single Curie point; there is a Gauss distribution of the T_C around an average value. This model was shown to fit very well to the measured resistance-temperature curves for polycrystalline $La_{0.7}Ca_{0.3}MnO_3$. Unfortunately, the authors did not consider the case of a highly broadened magnetic transition. It is in the latter case that the temperature dependences of resistance should necessarily exhibit the LT-peak.

The model developed by Yuan *et al.* [82] is close in concept to the preceding one but differs from it in a computational approach used. The authors employ a random resistor-network model in which FM metallic particles with the number density p randomly fill the space of a sample. The computations are carried out with the use of the Monte Carlo method. The authors obtained the results close to those we described in this chapter, but they did not carry out the detailed analysis of the data.

The different sources and types of defect–induced spin disorder are discussed in paper [20] and an assessment is made of transport phenomena that contribute to the magnetoresistive response. The authors succeeded in an isolation of the intergrain-boundary-induced contributions to electric- and magnetoresistance. They concluded that spin–polarized tunnelling and spin scattering at interfaces play a relatively minor role, the dominant low–field contribution to magnetoresistance coming from the response of mesoscale magnetic inhomogeneity induced by the grain boundary. A successful description of magnetoresistance as a function of magnetic field is achieved in the paper. However, the temperature dependence of electric resistance was not analyzed in this work. It should be noted that experimental results obtained in Ref. [20] correlate with those we reported in this chapter: although the low-field magnetoresistance changes monotonously with temperature, the R vs. T curves exhibit a peak below T_C. The authors analyze alternative approaches to describe electronic transport in magnetically inhomogeneous manganites and show that such approaches are unable to describe the whole complex of experimental data, but usually reflect only one side of the phenomena observed.

The grain-size-dependent transport properties in the granular perovskite $La_{0.85}Sr_{0.15}MnO_3$ were investigated by Zhang *et al*. [16]. The authors show that the decrease in a grain size from ~1 μm to 50 nm results in both the magnetization reduction and magnetic transition broadening. The LT-peak was observed to emerge when the grain size becomes less than 190 nm. Zhang *et al*. developed an approach to describe such behavior of electric resistance. Their model is based on following assumptions: (a) the conductivity of a grain core differs from that of a surface layer; (b) the Curie temperature of the latter is much lower than that of the former; (c) the mechanism of charge transfer through a surface layer is a spin-dependent tunneling. The authors succeeded in a satisfactory description of electric and magnetoresistance properties of the samples with nanoscale grain size. However, they do not provide evidence for the statement that it is the tunneling that is the dominant charge transfer mechanism through the surface layer.

The approaches developed in Refs. [7,9,83,84,85] deal with the two-phase systems, for which the conductivity of each the phases depends on magnetic state and is of activated character for the case of non-ferromagnetic ordering. However, these works mainly focus on the elucidation of the nature of the resistivity peak near T_C, on the description of the behavior of magnetoresistance or concentration dependence of electric resistance. So, the author of paper [85] admits the existence of magnetically multiphase state in perovskite manganites and considers magnetoresistive properties of a mixture of FM metallic and antiferromagnetic

semiconducting phases. The model developed makes it possible to calculate the magnetoresistance of the system for the cases where one of the phases is prevailing. However, the author did not perform the analysis of the temperature dependences of electric resistance.

As a result, the approach we developed in this chapter is based on the ideas which are close to those suggested by other authors, but it also covers the case of a strongly broadened magnetic transition, i.e. the topic which has not been considered by them.

Taking into account a considerable interest of researchers in understanding the CMR effect in doped manganites, a number of experimental and theoretical works have been devoted to the investigation of these materials (see review papers [4,5,7]). However, the theoretical works have largely been aimed at the development of the approaches enabling a description of particular behavioral features of these materials. In most cases, the ranges of applicability of these approaches to describe other physical properties have been analyzed superficially. Review and critical analysis of the available views on the nature of unusual properties of manganites, as well as a comparison of the conclusions of the theories with the experiment has been made in Refs. [7,20,46,70,86].

In general, the approaches, developed for a description of electric and magnetoresistive properties of doped manganites with account for inhomogeneity of magnetic and electric parameters, can be divided into three groups according to the dominant mechanism of charge transfer through the high-resistive regions:

1. Spin-polarized tunneling of charge carriers through weakly conducting barriers (intergrain boundaries, defect-induced regions of degraded magnetic ordering and depressed conductivity, and others).
2. Spin-dependent scattering of polarized charge carriers (a scattering of conductivity electrons on phonons or impurities into corresponding available states of spin-polarized energy bands).
3. Activated charge transfer through the weakly conductive regions.

A critical analysis of the ranges of applicability of each of the above models has been made in Refs. [7,20,46,70,86,87]. The authors have come to the conclusion that each of the above mechanisms may occur in manganite materials, but the question of which of these mechanisms is dominant is not easy to be answered. For this reason, in each particular case, one should perform a comprehensive analysis of the behavior of a sample, find a prevailing charge transfer mechanism, and only after that it may become possible to reliably predict the regularities of the behavior upon a change of one or a few parameters.

Let us illustrate such conclusion with the results obtained in work [64]. Fäth *et al.* used scanning tunneling spectroscopy to investigate single crystals and thin films of $La_{1-x}Ca_xMnO_3$ with x near 0.3. Below the bulk transition temperature T_C, a phase separation picture was observed, where inhomogeneous structures of metallic and insulating areas coexisted and were strongly field dependent in their size and structure. Insulating areas were found to persist far below T_C. In this case, the charge transfer through the high-resistive regions can occur by a combination of spin-scattering and inelastic tunneling processes (including multi-step tunneling via localized states), with the relative contribution depending on a number of factors, including field and temperature. It is almost impossible to convert this picture into a system of mathematical equations and, thus, one should look for adequate approaches, one of which is developed in this chapter.

CONCLUSION

The chapter focuses on the nature of low-temperature resistive peak, which is often observed in colossal magnetoresistant manganites below Curie temperature. Based on a review of the experimental data available, it is concluded that the presence of the LT-peak is a consequence of the enhanced inhomogeneity of manganite materials. An approach, which regards the state of doped manganites as a mixture of interpenetrating paramagnetic insulating and ferromagnetic metallic phases, is shown to be able to successfully describe the peculiarities of the temperature dependence of total resistivity. It is shown that in spite of the monotonic variation of magnetic and electric properties of each the phase, the resulting resistance may exhibit resistive anomaly (the LT-peak) within the region of the phase coexistence. Such an approach is concluded to be applicable to the description of the magnetic and electric properties of a number of inhomogeneous and phase-separated manganite systems, including micro- and nanocrystalline samples, ultrathin epitaxial films, etc.

ACKNOWLEDGMENTS

The author expresses deep gratitude to all those who contributed to the works underlying this chapter. These include: G. Bondarkova, S. Cherepov, I. Lezhnenko, A. Matviyenko, D. Podyalovskii, A. Pogorily, A. Vovk (Institute of Magnetism); A. Belous, E. Pashkova, O. V'yunov, O. Yanchevskii (V.I. Vernadsky Institute of General and Inorganic Chemistry); V. Borodin, V. Doroshev, V. Kamenev, A. Mazur, and T. Tarasenko (O.O. Galkin Institute of Physics and Engineering).

REFERENCES

[1] Helmolt, R.; Wecker, J.; Samwer, K.; Haupt L.; Bärner, K. *J. Appl. Phys.* 1994, *76*, 6925 – 6928.
[2] Jin, S.; Tiefel, T.H.; McCormack, M.; Fastnacht, R.A.; Ramesh, R. *Science* 1994, *264*, 413 – 415.
[3] Zener, C. *Phys. Rev.* 1951, *82*, 403 – 405.
[4] Haghiri-Gosnet, A.-M. and Renard, J.-P. *J. Phys. D: Appl. Phys.* 2003, *36*, R127 – R150.
[5] Dörr, K. *J. Phys. D: Appl. Phys.* 2006, *39*, R125 – R150.
[6] Yoo, Y.-K.; Duewer, F.; Yang, H.; Yi, D.; Li, J.-W.; Xiang, X.-D. *Nature* 2000, *406*, 704 – 708.
[7] Dagotto, E.; Hotta, T.; Moreo, A. *Phys. Rep.* 2001, *344*, 1 – 153.
[8] Tovstolytkin, A.; Pogorily, A.; Vovk, A.; Podyalovskii, D.; Lezhnenko, I.; Matviyenko, A. *J. Magn. Magn. Mater.* 2004, *272-276*, 1839 – 1840.
[9] Cen, C.; Alvarez, G.; Dagotto, E. *Phys. Rev. Lett.* 2007, *98*, 127202 (1 – 4).
[10] Verges, J.A.; Martin-Mayor, V.; Brey, L. *Phys. Rev. Lett.* 2002, *88*, 136401 (1 – 4).
[11] Kumar, S.; Mayumdar, P. *Phys. Rev. Lett.* 2006, *96*, 016602 (1 – 4).

[12] Tovstolytkin, A.I. *Mater. Science Forum* 2001, *373-376*, 613 – 616.
[13] Izumi, M.; Konishi, Y.; Nishihara, T.; Hayashi, S.; Shinohara, M.; Kawasaki, M.; Tokura, Y. *Appl. Phys. Lett.* 1998, *73*, 2497 – 2499.
[14] Tovstolytkin, A.I.; Pogorily, A.N.; Kovtun, S.M. *Low. Temp. Phys.* 1999, *25*, 962 – 965.
[15] Arulraj, A.; Manesh, R.; Subbara, G.N.; Mahencliran, R.; Raychaundhure, A.K.; Rao, C.N.R. *J. Sol. St. Chem.* 1996, *127*, 87 – 91.
[16] Zhang, N.; Ding, W.; Zhong, W.; Xing, D.; Du, Y. *Phys. Rev. B.* 1997, *56*, 8138 – 8142.
[17] Troyanchuk, I.O.; Khomchenko, V.A.; Tovar, M.; Szymczak, H.; Bärner, K. *Phys. Rev. B* 2004, *69*, 054432 (1 – 12).
[18] Millis, A.J.; Darling, T.; Migliori, A. *J. Appl. Phys.*1998, *83*, 1588 – 1591.
[19] Hwang, H.Y.; Cheong, S-W.; Radaelli, P. G.; Marezio, M.; Batlogg, B. *Phys. Rev. Lett.* 1995, *75*, 914 – 917.
[20] Evetts, J.E.; Blamire, M.G.; Mathur, N.D.; Isaac, S.P.; Teo, B.-S.; Cohen, L.F.; MacManus-Driscoll, J.L. *Philos. Trans. Roy. Soc. Lond. A* 1998, *356*, 1593 – 1615.
[21] Tovstolytkin, A.I.; Pogorily, A.N.; Cherepov, S.V.; Bondarkova, G.V.; Silantiev, V.I. *Metallofizika i Noveishie Tekhnologii* 2000, *22*, 23 – 31.
[22] Sun, J.R.; Rao, G.H.; Liang, J.K. *Appl. Phys. Lett.* 1997, *70*, 1900 – 1902.
[23] Pogorilyi, A.N.; Belous, N.A.; Tovstolytkin, A.I.; Belous, A.G.; Yanchevski, O.Z. *Low Temp. Phys.* 1999, *25*, 74 – 75.
[24] Belous, A.G.; V'yunov, O.I.; Pashkova, E.V.; Yanchevskii, O.Z.; Tovstolytkin, A.I.; Pogorily, A.N. *Inorg. Mater.* 2003, *39*, 161 – 170.
[25] Urushibara, A.; Moritomo, Y.; Arima, T.; Asamitsu, A.; Kido, G.; Tokura, Y. *Phys. Rev. B* 1995, *51*, 14103 – 14109.
[26] Surthi, S.; Kotru, S.; Pandey, R.K.; Fournier, P. *Sol. St. Commun.* 2003, *125*, 107– 110.
[27] Mandal, P.; Das, S. *Phys. Rev. B.* 1997, *56*, 15073 – 15080.
[28] Tang, Y.; Shaltout, I.; Braunstrin, R.; Helmolt, R.; Haupt, L.; Bärner, K. *Phys. Stat. Sol. (b)* 1994, *182*, 509 – 519.
[29] Steenbeck, K.; Eick, T.; Kirsch, K.; Schmidt, H.-G.; Strinbeiβ, E. *Appl. Phys. Lett.* 1998, *73*, 2506 – 2508.
[30] Huang, Y.-H.; Xu, Z.-G.; Yan, C.-H.; Wang, Z.-M.; Zhu, T.; Liao, C.-S.; Gao, S.; Xu, G.-X. *Solid State Commun.* 2000, *114*, 43 – 47.
[31] Archibald, W.; Zhou, J.-S.; Goodenough, J.B. *Phys. Rev. B* 1996, *53*, 14445 – 14449.
[32] Chechersky, V.; Nath, A.; Ju, H.; Greene, R.L. *Low Temp. Phys.* 1997, *23*, 536 – 540.
[33] Savosta, M.M.; Doroshev, V.D.; Kamenev, V.I.; Borodin, V.A.; Tarasenko, T.N.; Mazur, A.S.; Maryško, M. *JETP* 2003, *97*, 573 – 586.
[34] Tovstolytkin, A.I.; Pogorily, A.M.; Dzhezherya, Yu.I.; Dzyublyuk, V.V.; Mapps, D.J. *J. Phys.: Condens. Matter.* 2009, *21*, 386003 (1 – 7).
[35] Simopoulos, A.; Kallias, G.; Devlin, E.; Panagiotopoulos, I.; Pissas, M. *J. Magn. Magn. Mater.* 1998, *177-181*, 860 – 861.
[36] Rubinstein, M.; Gillespie, D.J.; Snyder, E.J.; Tritt, M.T. *Phys. Rev. B* 1997, *56*, 5412 – 5423.
[37] Doroshev, V.D.; Borodin, V.A.; Kamenev, V.I.; Mazur, A.S.; Tarasenko, T.N.; Tovstolytkin, A.I.; Trukhanov, S.V. *J. Appl. Phys*. 2008, *104*, 093909 (1 – 13).

[38] Snyder, G. J.; Hiskes, R.; DiCarolis, S.; Beasley, M.R.; Geballe, T.H. *Phys. Rev. B* 1996, *53*, 14434 – 14444.
[39] Worledge, D.C.; Snyder, G.J.; Beasley, M.R.; Geballe, T.H.; Hiskes, R.; DiCarolis, S. *J. Appl. Phys.* 1996, *80*, 5158 – 5161.
[40] Chen, C.C.; De Lozanne, A. *Appl. Phys. Lett.* 1998, *73*, 3950 – 3952.
[41] Zhang, L.W.; Gong, F.; He, L.; Cao, B.S.; Zhu M.; Zhao Y.G. *J. Magn Magn. Mater.* 2000, *219*, 236 – 240.
[42] McLachlan, D.S. *J. Phys. C: Sol. St. Phys.* 1987, *20*, 865 – 877.
[43] Gor'kov, L.P. *Physics-Uspekhi* 1998, *41*, 589 – 594.
[44] Mitchell, J.F.; Argurion, D.N.; Potter, C.D.; Hinks, D.G.; Jorgensen, J.D.; Bader, D. *Phys. Rev. B* 1996, *9*, 6172 – 6183
[45] Gupta, A.; Gong, G.Q.; Xiao, G.; Duncombe, P.R.; Lecoeur, P.; Trouilloud, P.; Wang, Y.Y. *Phys. Rev. B.* 1996, *54*, R15629 – R15632.
[46] Gross, R.; Alff, L.; Büchner, B.; Freitag, B. H.; Höfener, C.; Klein, J.; Yafeng, Lu, Mader, W.; Philipp, J. B.; Rao, M. S. R. *J. Magn. Magn. Mater.* 2000, *211*, 150 – 159.
[47] Hwang, H.Y.; Cheong, S.-W.; Ong, N.P.; Batlogg, B. *Phys. Rev. Lett.* 1996, *77*, 2041 – 2044.
[48] Mendelson, M.I. *J. Amer. Cer. Soc.* 1969, *52*, 443 – 446.
[49] Sanchez, R.D.; Rivas, J.; Vasquez-Vasquez, C.; Lopez-Quintela, A.; Causa, M.T.; Tovar, M.; Oseroff, S. *Appl. Phys. Lett.* 1996, *68*, 134 – 136.
[50] Savosta, M.M.; Kamenev, V.I.; Borodin, V.A.; Novak, P.; Maryško, M.; Hejtmanek, J.; Dörr, K.; Sahana, M. *Phys. Rev. B* 2003, *67*, 094403 (1 – 9).
[51] Savosta, M.M.; Doroshev, V.D.; Kamenev, V.I.; Borodin, V.A.; Tarasenko, T.N.; Mazur, A.S.; Maryško, M. *JETP* 2003, *97*, 573 – 586.
[52] Borodin, V.A.; Doroshev, V.D.; Kamenev, V.I.; Mazur, A.S.; Tarasenko, T.N. *High-Pressure Physics and Technology* 2007, *17*, 52 – 64.
[53] Tovstolytkin, A.I.; Pogorily, A.M.; Podyalovskii, D.I.; Kalita, V.M.; Lozenko, A.F.; Trotsenko, P.O.; Ryabchenko, S.M.; Belous, A.G.; V'yunov, O.I.; Yanchevskii, O.Z. *J. Appl. Phys.* 2007, *102*, 063902 (1 – 7).
[54] Markovich, V.; Rozenberg, E.; Gorodetsky, G.; Greenblatt, M.; McCarroll, W.H. *Phys. Rev. B* 2001, *63*, 054423 (1 – 4).
[55] Batchelor, G.K.; O'Brien, R.W. *Proc. R. Soc. Lond. A* 1977, *355*, 313 – 318.
[56] Mizusaki, J.; Waragai, K.; Tsuchiya, S.; Tagawa, H.; Arai, Y.; Kuwayama, Y. *J. Amer. Cer. Soc.* 2005, *79*, 109 – 116.
[57] Zinchenko, A.Z. *Phil. Trans. R. Soc. Lond. A* 1998, *356*, 2953 – 2978.
[58] Gonzo, E.E. *Chem. Eng. J.* 2002, *90*, 299 – 306.
[59] Kupkova, M.; Kupka, M. *Metalurgija* 2004, *43*, 97 – 102.
[60] Sheng, P. *Phys. Rev. B* 1980, *21*, 2180 – 2183.
[61] Balberg, I. *Phys. Rev. Lett.* 1987, *59*, 1305 – 1307.
[62] Li, X.W.; Gupta, A.; Xiao, G.; Gong, G.Q. *Appl. Phys. Lett.* 1997, *71*, 1124 – 1126.
[63] Pogorily, A.N.; Tovstolytkin, A.I.; Vovk, A.Ya.; Bondarkova, G.V.; Silantiev, V.I.; Cherepov, S.V.; Belous, A.G.; Yanchevski, O.Z. *Mater. Sci. Forum* 2001, *373-376*, 621 – 624.
[64] Fäth, M.; Freisem, S.; Menovsky, A.A.; Tomioka, Y.; Aarts, J.; Mydosh, J.A. *Science* 1999, 285, 1540 – 1542.

[65] Matveev, V.V.; Ylinen, E.; Zakhvalinskii, V.S.; Laiho, R. *J. Phys.: Cond. Matt.* 2007, *19*, 226209 (1 – 4).
[66] Fita, I.M.; Szymczak, R.; Baran, M.; Markovich, V.; Puzniak, R.; Wisniewski, A.; Shiryaev, S.V.; Varyukhin, V.N.; Szymczak, H. *Phys. Rev. B* 2003, *68*, 014436 (1 – 7).
[67] Trukhanov, S.V.; Troyanchuk, I.O.; Trukhanov, A.V.; Fita, I.M.; Vasil'ev, A.N.; Maignan, A.; Szymczak, H. *JETP Lett.* 2006, *83*, 33 – 38.
[68] Kozlenko, D.P.; Ovsyannikov, S.V.; Shcheninnikov, V.V.; Voronin, V.I.; Savenko, B.N. *JETP Lett.* 2007, 85, 203 – 209.
[69] Balcells, Ll.; Martinez, B.; Sandiumenge, F.; Fontcuberta, J. *J. Magn. Magn. Mater.* 2000, *211*, 193 – 199.
[70] Gupta, A.; Sun, J.Z. *J. Magn. Magn. Mater.* 1999, *200*, 24 – 43.
[71] Liang, S.; Sun, J.R.; Wang, J.; Shen, B.G. *Appl. Phys. Lett.* 2009, *95*, 182509 (1 – 3).
[72] Park, J.-H.; Veskovo, E.; Kim, H.-J.; Kwon, C.; Ramesh, R.; Venkatesan, T. *Nature* 1998, *392*, 794 – 796.
[73] Blamire, M.G.; Teo, B.-S.; Durrell, J.H.; Mathur, N.D.; Barber, Z.H.; MacManus-Driscoll, J.L.; Cohen, L.F.; Evetts, J.E. *J. Magn. Magn. Mater.* 1999, *191*, 359 – 367.
[74] Fontcuberta, J.; Bibes, M.; Martínez, B.; Trtik, V.; Ferrater, C.; Sánchez, F.; Varela, M. *J. Magn. Magn. Mater.* 2000, *211*, 217 – 225.
[75] Wang, X.L.; Dou, S.X.; Liu, H.K.; Ionescu, M.; Zeimetz, B. *Appl. Phys. Lett.* 1998, *73*, 396 – 398.
[76] Chisholm, M.F.; Pennycook, S.J. *Nature* 1991, *351*, 47 – 49.
[77] Browning, N.D.; Chisholm, M.F.; Pennycook, S.J.; Norton, D.P.; Lowndes, D.H. *Phys. C.: Supercond.* 1993, *212*, 185 – 190.
[78] Laukhin, V.; Fontcuberta, J.; García-Muñoz, J.L.; Obradors, X. *Phys. Rev. B* 1997, *56*, R10009 – R10012.
[79] Malde, N.; de Silva, P.; Hossain, A.; Cohen, L.F.; Thomas, K.A.; MacManus-Driscoll, J.L.; Mathur, N.D.; Blamire, M.G. *Solid State Commun.* 1998, *105*, 643 – 648.
[80] Kovalenko, V.F.; Tychko, A.V. *Functional Materials* 2004, *11*, 521 – 527.
[81] Song, H.; Kim, W.J.; Kwon, S.-J. *J. Magn. Magn. Mater.* 2000, *213*, 126 – 134.
[82] Yuan, S.L.; Liu, M.H.; Li, Z.Y.; Peng, G.; Xia, Z.C.; Yang, Y.P.; Tu, F.; Zhang, G.Q.; Liu, J.; Liu, L.; Tang, J.; Zhang, G.H.; Zhang, L.J.; Feng, W.; Xiong, C.S.; Xiong, Y.H. *Solid State Commun.* 2002, *121*, 291 – 294
[83] Nagaev, E.L. *Phys. Rep.* 2001, *346*, 387 – 531.
[84] Tovstolytkin, A.I.; Pogorily, A.N.; Lezhnenko, I.V.; Matviyenko A.I.; Podyalovski, D.I.; Kravchik, V.P. *Phys. Sol. St.* 2003, *45*, 1952 – 1956.
[85] Krivoruchko, V.N. *Low Temp. Phys.* 1996, *22*, 798 – 802.
[86] Ahn, K.H.; Lookman, T.; Bishop, A.R. *Nature* 2004, *428*, 401 – 404.
[87] Shenoy, V.B.; Rao, C.N.R. *Philos. Trans. Roy. Soc. Lond. A* 2008, *366*, 63 – 82.

In: Perovskites: Structure, Properties and Uses
Editor: Maxim Borowski, pp. 213-250
ISBN 978-1-61668-525-6

Chapter 4

STRUCTURAL, MAGNETIC AND ELECTRON TRANSPORT PROPERTIES OF ORDERED-DISORDERED PEROVSKITE COBALTITES

Asish K. Kundu[1] and B. Raveau[2]

[1]Indian Institute of Information Technology Design & Manufacturing, Dumna Airport Road, Jabalpur –482005, India

[2]Laboratoire CRISMAT, ENSICAEN UMR6508, 6 Boulevard Maréchal Juin, Cedex 4, Caen-14050, France

ABSTRACT

Rare earth perovskite cobaltites are increasingly recognized as materials of importance due to rich physics and chemistry in their ordered-disordered structure for the same composition. Apart from colossal magnetoresistance effect, like manganites, the different forms of cobaltites exhibit interesting phenomena including spin, charge and orbital ordering, electronic phase separation, insulator-metal transition, large thermoelectric power at low temperature. Moreover, the cobaltites which display colossal magnetoresistance effect could be used as read heads in magnetic data storage and also in other applications depending upon their particular properties. The A-site ordered-disordered cobaltites exhibit ferromagnetism and metal-insulator transitions as well as other properties depending on the composition, size of *A*-site cations and various external factors such as pressure, temperature, magnetic field etc. Ordered cobaltites, having a *112*-type layered structure, are also reported to have an effectively stronger electron coupling due to layered *A*-site cationic ordering. Most importantly for the present article we focus on *La-Ba-Co-O* based ordered-disordered perovskite phases, which exhibit interesting magnetic and electron transport properties with ferromagnetic transition, $T_C \sim 177K$, and it being the first member of lanthanide series. *Zener* double exchange mechanism considered to be crucial for understanding basic physics of the ferromagnetic-metallic phase, yet does not explain clearly the insulating-type phase. In terms of electron transport the ferromagnetic-metallic or insulating/semiconducting states have been discussed in the present article with different types of hopping model.

INTRODUCTION

Last few decades, there has been extensive research on ABO_3-type perovskite oxides of the general formula $Ln_{1-x}Ak_xBO_3$ (*Ln* = trivalent lanthanide, *Ak* = divalent alkaline earth, *B* = transition metal) [1]. Particularly the perovskite cobaltites were discovered in *1950's* and the magnetic ordering was first reported in *1960's* [2], since then there are lots of interesting phenomena reported in the literature. Some of the novel properties of the perovskite cobaltites are known for some time, especially the crystal structure transformation, the paramagnetic *(PM)* to ferromagnetic *(FM)* transition at *Curie* temperature (T_C) and the associated insulator-metal transition (T_{IM}) and so on. The discovery of colossal magnetoresistance (*CMR*) in doped manganites has renewed great interest in perovskite oxides since the early *90's* [1]. In *1997*, large value of magnetoresistance was reported for newly discovered ordered cobaltite, $LnBaCo_2O_{5.4}$ *(Ln=Eu, Gd)* known as layered *112*-phases [3]. This leads to enhanced interest because of their potential applications in improving magnetic data storage. Moreover, the perovskite cobaltites have also attracted attention because of their possible applications as oxidation catalysts, gas sensors, solid oxides fuel cells and oxygen separation membranes due to their stability in a wide range of oxygen contents, high oxygen diffusivity and electron conduction [4]. Consequently superconductivity was discovered in hydrated sodium cobaltite phase in *2003*, since then cobaltites have received even more attention [5]. Aside from potential applications, the cobaltites exhibit rich phase diagram spanning a wide range of magnetic properties and phenomena like charge ordering, orbital ordering, spin/cluster-glass behavior, electronic phase separation etc [6-11]. These phenomena represent a combined interaction between the spin, the lattice, the charge and the orbital degrees of freedom, which will provide better understanding of strongly correlated electronic behavior. Such interactions are manifested in single crystal, polycrystalline samples as well as in thin films. The properties of perovskite cobaltites can be tuned either by external factors or by chemical means. In certain critical range of cation doping, at the *A*-site of ABO_3-perovskite, the rare earth cobaltites exhibit simultaneous occurrence of ferromagnetism and metallicity, along with *CMR* in the vicinity of T_C or T_{IM} [7].

Some of the perovskite-based cobaltites are known to exhibit electronic inhomogeneities arising from the existence of more than one phase in crystals of nominally monophasic composition. This is understood in terms of electronic phase separation described recently in the literature [1]. Such a phenomenon occurs because of the comparable free energies of the different phases. The phase-separated hole-rich and hole-poor regions give rise to anomalous properties such as weak *FM* moments in an antiferromagnetic regime [1]. A variety of magnetic inhomogeneities manifest themselves in $Ln_{1-x}Ak_xCoO_3$ depending on the various factors such as the average radius of the *A*-site cation and size-disorder as well as external factors such as temperature, magnetic field etc [6-11]. In the last few years electronic phase separation in cobaltites has attracted considerable attention.

In this article, we discuss the *A*-site cationic ordering and disordering effects on magnetic and electron transport properties for rare earth cobaltites. Perovskite cobaltites have two possible forms of the *A*-site cations distribution depending on the type of cations or the synthesis procedures [9, 12]. The first reported compounds on perovskite cobaltites are the *A*-site disordered structure [2, 13], which have been investigated for last few decades, and the other one is *A*-site ordered perovskites possessing a layered *112*-type structure [3]. The latter

one discovered few years back, consists of oxide layers *[LnO]-[CoO_2]-[AkO]-[CoO_2]* alternating along the *c*-axis [3, 9, 12, 14, 15]. The ordering of Ln^{3+} and Ak^{2+} ions is favorable if the size difference is large between the *A*-site cations, hence smaller size Ln^{3+} and bigger Ak^{2+} ions easily form a layered *112*-structure and till date it is reported only for $Ak^{2+} = Ba^{2+}$ cation i.e. $LnBaCo_2O_{5+\delta}$ *(0 ≤ δ ≤1)* series [3, 9, 12, 14-16]. In contrast, as the size difference becomes smaller, as for example between La^{3+} and Ba^{2+}, the disordered cubic perovskite becomes more stable and special treatment is required to obtain the *112* ordered structure, as reported recently for the order-disorder phenomena observed in the perovskites of the system *La-Ba-Co-O* [12, 16]. The CoO_2 layers in ordered cobaltites are free from the random potential which would otherwise arise from the *Coulomb* potential and/or local strain via the random distribution of *A*-site cations (Ln^{3+}/Ak^{2+}). Both ordered and disordered cobaltites exhibit similar features like ferromagnetism, insulator-metal transition and magnetoresistance in a certain temperature range, yet prominent differences are evidenced in their properties. The ferromagnetism in these cobaltites is considered to be due to favorable Co^{3+} - *O* - Co^{4+} interactions. The effect of random distribution of *A*-site cations or disordered perovskite structure arising from the chemical disorder as observed in the conventional random doping at the *A*-site in ABO_3-perovskite. For rare earth manganites, *Attfield et al.* [17] have reported the role of *A*-site cationic radius, $\langle r_A \rangle$, and size disorder parameter, σ^2, on the T_C and/or T_{IM} with variation of these parameters. In the present article we have also discussed the role of $\langle r_A \rangle$, and σ^2 for disordered cobaltites $Ln_{0.5}Ak_{0.5}CoO_{3+\delta}$ (*Ln = La, Nd, Gd and Ak = Ba, Sr*) which unusually influence the magnetic and electronic properties [13, 18, 19]. These interesting phenomena are related to structural disordering caused by the substitution of Ak^{2+} ions in place of Ln^{3+} and we have briefly presented the effect of size disorder σ^2 for *Ln = Nd, Gd* [18, 19]. The structural disorder in cobaltites is *3D*, while a layered *2D* structure is adopted by the *112*-phase ordered cobaltites, $LnBaCo_2O_{5+\delta}$. The crystallographic structures for perovskite cobaltites with an integral number of oxygen ions per formula unit are well known, no consensus has been reached for non-integer compounds. Basic knowledge of the crystallographic structure of a compound is of particular importance for determining magnetic structures, since these two properties are closely related. Hence we have presented first the crystal structure description for both the (ordered-disordered) cobaltites before discussing the physical properties.

CRYSTAL STRUCTURE

In general, the rare earth ordered-disordered cobaltites crystallize in the perovskites structure with various types of superstructures also evidenced. The disordered ABO_3-perovskite is a simple cubic structure (*Pm-3m*) as shown in Figure 1. However, many perovskite deviate a little from this structure even at room temperature. The perovskite structure is most stable when the *Goldschmidt* tolerance factor, *t*, is unity (for cubic structure), which is defined by, $t = (r_A + r_O)/ \sqrt{2}\,(r_B + r_O)$ where, r_A, r_B and r_O are the average ionic radius of the *A, B* and *O* ions respectively. Deviation of '*t*' from unity leads to the structural distortion. For a small deviation in *t* (i.e. $t < 1$), the crystal structure changes from cubic to tetragonal, rhombohedral or orthorhombic etc. In this situation the ⟨Co-O-Co⟩ bond angle decreases from *180°*. The perovskite structure occurs only within the range $0.75 \leq t \leq 1.00$.

The stability of the perovskite structure of cobaltites depends on the relative size of the *Ln/Ak* and *Co* ions in $Ln_{1-x}Ak_xCoO_3$. In disordered cobaltites *Ln/Ak* cation is surrounded by eight corner sharing CoO_6 octahedra, which build a *3D* network. The smaller ionic radius of the cations results in a lower value of '*t*', consequently increasing the lattice distortion. The increase in lattice distortion significantly decreases the ⟨Co-O-Co⟩ bond angle from *180*°, which strongly affects the physical properties of cobaltites. When $t < 1$, there is a compression of the *Co-O* bonds, which in turn induces a tension on *Ln-O* bonds. A cooperative rotation of the CoO_6 octahedra and a distortion of the cubic structure counteract these stresses. The rare earth cobaltites can be crystallized not only in cubic or orthorhombic structure (as reported mostly), but also in tetragonal, hexagonal, rhombohedral, and monoclinic structures as well. As a consequence, for the disordered cobaltite series $Ln_{0.5}Ba_{0.5}CoO_{3+\delta}$ the crystal structure is reported as cubic or rhombohedral for *Ln = La*, whereas for other lanthanides such as *Pr, Nd, Gd, Dy* the systems crystallize in the orthorhombic structure with different space groups [13, 18]. The structural *Rietveld* analysis for disordered $Ln_{0.5}Sr_{0.5}CoO_3$ series reveals that the structure is rhombohedral for *Ln = La, Pr Nd* and that for Gd, the structure is orthorhombic as reported for *Ba*-doped compounds [13].

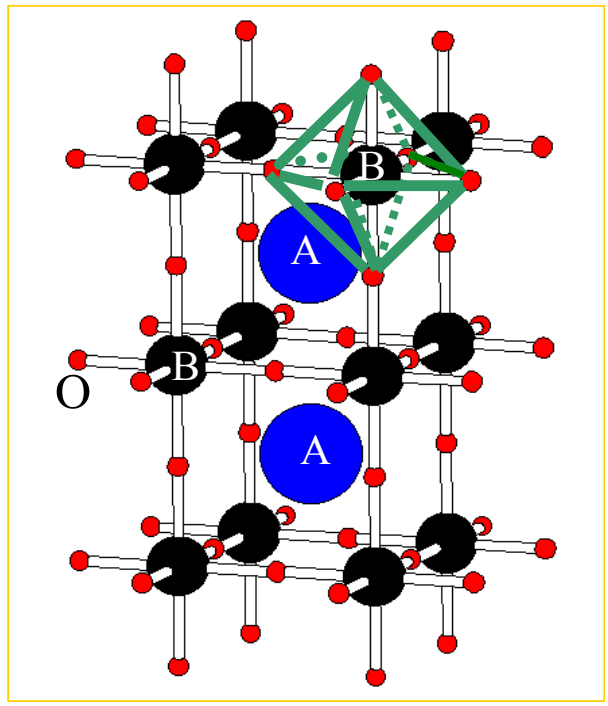

Figure 1. Rare earth ABO_3 perovskite with disorder structure.

Similarly, the layered *112*-type ordered cobaltites $LnBaCo_2O_{5+\delta}$ can be found in several crystallographic symmetries at room temperature. The variation of oxygen stoichiometry ($0 \leq \delta \leq 1$) in ordered *112*-type cobaltites lead to various structures as well as different cobalt and oxygen coordination's such as pyramidal, octahedral and/or the mixing of both environments for the *Co*-ions [14, 15]. In the following, the room temperature structures for different values

of 'δ' will be discussed. The crystal structure of the stoichiometric $LnBaCo_2O_5$ (*Ln = Eu, Gd, Tb, Ho*) cobaltite is tetragonal with *P4/mmm* space group (unit cell $a_p \times a_p \times 2a_p$; where a_p is defined as pseudo cubic cell parameters) [14, 15]. This corresponds to a doubling of the original perovskite unit cell along the *c*-direction due to alternating *BaO* and LnO_δ layers (Figure 2). The layered structure is best observed in the most oxygen deficient case $LnBaCo_2O_5$, because it is assumed that the oxygen ions are absent only in the *Ln*-layer [14, 15]. For $\delta = 0$ the Co^{2+} and Co^{3+} ions (ratio 1:1) are all within square base pyramids formed by their five oxygen neighbors.

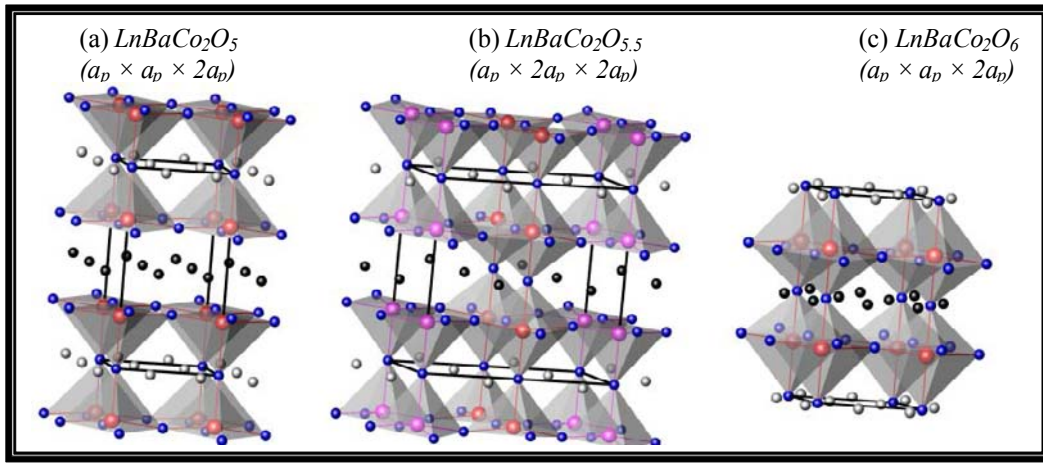

Figure 2. Layered *112*-type ordered $LnBaCo_2O_{5+\delta}$ $(0 \le \delta \le 1)$ cobaltites with (a) δ=0.0; $LnBaCo_2O_5$, (b) δ=0.5; $LnBaCo_2O_{5.5}$ and (c) δ=1.0; $LnBaCo_2O_6$.

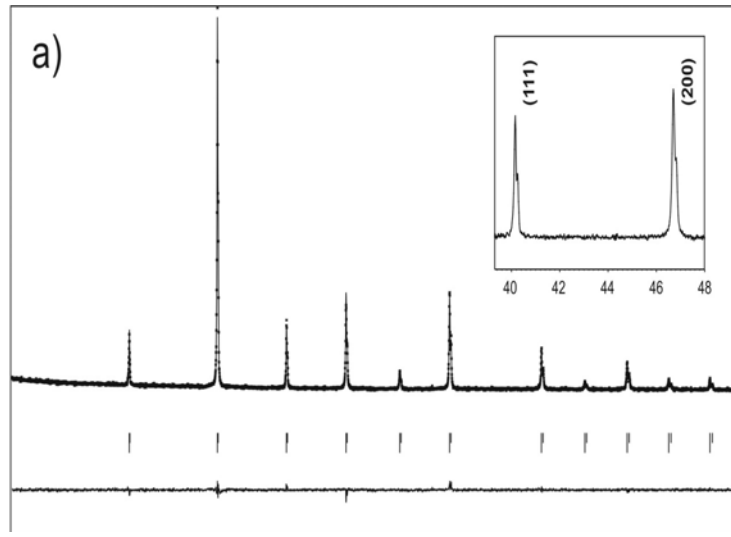

Figure 3. (Continued)

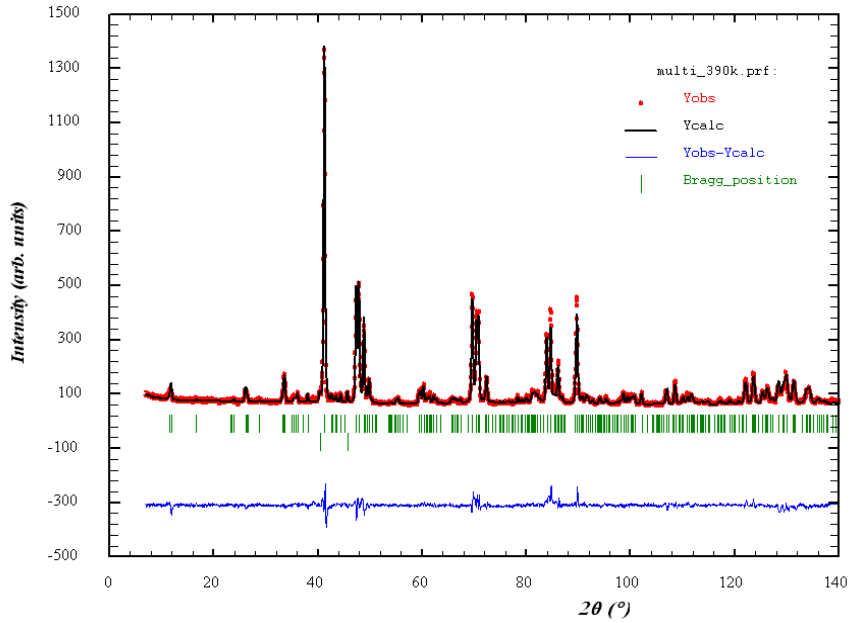

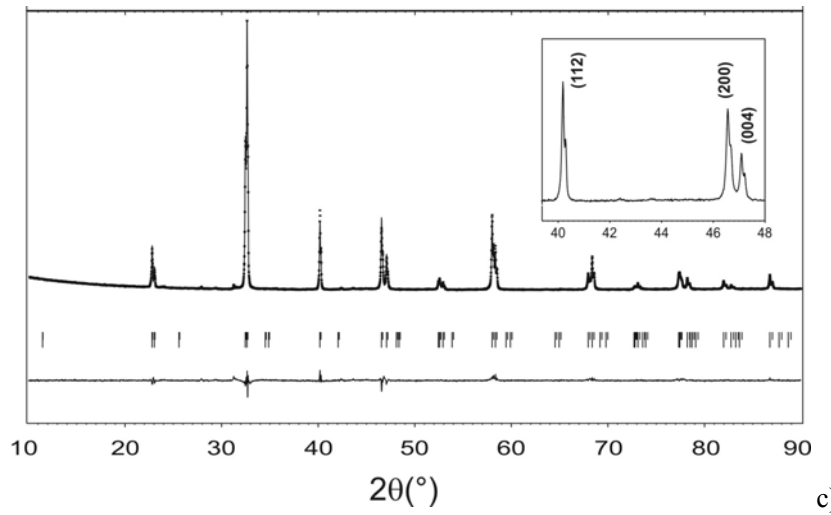

Figure 3. Rietveld refinement of X-ray diffraction pattern for (a) disordered $La_{0.5}Ba_{0.5}CoO_3$ (b) ordered $LaBaCo_2O_{5.5}$ and (c) ordered $LaBaCo_2O_6$ (Taken from Ref. 12 & 16).

For non-stoichiometric cobaltites $LnBaCo_2O_{5+\delta}$ ($0 < \delta < 1$) the crystal structure is more complex: due to oxygen vacancy ordered super-structures can arise, which vary with oxygen content. The oxygen content is strongly dependent on the size of the lanthanides [14]. Clearly, a strong correlation exists between the Ln^{3+} radius and the amount of oxygen the compound can accommodate. The first structural study of an ordered oxygen deficient perovskite of type $LnBaCo_2O_{5+\delta}$ was presented for the series *Ln = Pr to Ho* [14]. Although, the series has been investigated in details for almost all lanthanide elements of the periodic table, interestingly there was no such report on the first member of this series, i.e. for $LaBaCo_2O_{5.5}$. Very recently we have reported $LaBaCo_2O_{5.5}$ and characterized by neutron diffraction, electron microscopy and magnetic studies, showing that at room temperature the structure is *112-*

layered orthorhombic $a_p \times 2a_p \times 2a_p$ supercell with *Pmmm* space group [16]. In contrast, for *Ln = Pr – Ho*, all of the x-ray diffraction patterns could be indexed using a tetragonal structure $a_p \times a_p \times 2a_p$ with *P4/mmm* symmetry [14]. However, electron diffraction measurements additionally revealed two kinds of superstructures, depending on the radius of the lanthanide (or the oxygen content). For larger lanthanides (*Pr, Nd, Sm, Eu, Gd and Tb*) a doubling of one lattice parameter is observed, corresponding to an orthorhombic *Pmmm* $a_p \times 2a_p \times 2a_p$ supercell, whereas for smaller lanthanides (*Ho* and *Dy*) a tripling of two lattice parameters is noticed, as in a $3a_p \times 3a_p \times 2a_p$ supercell. It was suggested [14] that ordering of oxygen vacancies is at the origin of the observed superstructures. Importantly, the authors found that the oxygen vacancies are located uniquely in the LnO_δ layers (apical positions). By changing the oxygen content the superstructures either vanish or change from one to the other: Reducing oxygen content in $GdBaCo_2O_{5+\delta}$ from $\delta = 0.4$ to 0 destroys the superstructure. On the other hand in $HoBaCo_2O_{5.3}$ an increase of δ from 0.3 to 0.4 leads to a change in superstructure from $3a_p \times 3a_p \times 2a_p$ to $a_p \times 2a_p \times 2a_p$. High resolution electron microscopy supported the assumption that the ordering of the oxygen vacancies is responsible for the superstructures. *Burley et al.* and *Pralong et al.* [14] have reported $NdBaCo_2O_{5+\delta}$ for various oxygen stoichiometries. The $\delta = 0$ compound has a tetragonal structure with $a_p \times a_p \times 2a_p$ supercell where the *Nd* layer incorporates all the oxygen vacancies. For the slightly higher oxygen content $\delta = 0.38$ the structure is derived from the $\delta = 0$ one, but with oxygen ions inserted randomly into the NdO_δ layers. Oxygen vacancy ordering in *b*-direction resulting in an orthorhombic $a_p \times 2a_p \times 2a_p$ supercell unit cell with *Pmmm* symmetry is reported for $\delta = 0.5$, in agreement with other reported structure [14]. The oxidized material with $\delta = 0.69$ is again described by a tetragonal $a_p \times a_p \times 2a_p$ supercell unit cell, but a very weak peak originating from a doubling of the unit cell along the *b*-direction was detected.

Finally, for stoichiometric cobaltites $LnBaCo_2O_6$ all *Co*-ions (Co^{3+} and Co^{4+}; ratio 1:1) are in octahedral environment. In the $LnBaCo_2O_6$ series, the first member *Ln = La* could be synthesized in the two forms, ordered and disordered as shown by neutron diffraction and electron microscopy [9, 12]. At room temperature and in normal synthesis condition the crystal structure is cubic for the disordered cobaltite, which means the La^{3+} and Ba^{2+} ions are distributed randomly on the *A*-site. This is due to the smaller size differences between the cations as discussed earlier. Nevertheless, the ordered *112*-phases $LaBaCo_2O_{5.5}$ and $LaBaCo_2O_6$ are obtained for the same composition in special synthesis conditions [12, 16], which crystallize at room temperature in orthorhombic and tetragonal structures respectively. Therefore, a layered *112*-type ordered perovskite structure $LnBaCo_2O_6$ with a smaller lanthanide also exist, again with a tetragonal unit cell $a_p \times a_p \times 2a_p$ with *P4/mmm* symmetry, but require special synthesis conditions as reported by *Pralong et al.* [14]. To conclude the ordered cobaltites phase, a summary of the most commonly used models for compounds with oxygen content $\delta = 0, 0.5, 6$ at room temperature is given (Figure 2):

1. $LnBaCo_2O_5$ has the tetragonal structure with $a_p \times a_p \times 2a_p$ supercell (*P4/mmm* symmetry). Ln^{3+} layers alternate with *BaO* layers along the *c*-axis (oxygen vacancies in *Ln* layer).
2. $LnBaCo_2O_{5.5}$ has an orthorhombic structure with $a_p \times 2a_p \times 2a_p$ supercell (*Pmmm* symmetry). $LnO_{0.5}$ layers alternate with *BaO* layers along the *c*-axis. Along the *b*-direction the oxygen vacancies are ordered. This leads to an alternation of CoO_5 pyramids and CoO_6 octahedra along the *b*-direction.

3. $LnBaCo_2O_6$ is again tetragonal unit cell $a_p \times a_p \times 2a_p$ with *P4/mmm* symmetry. *LnO* layers alternate with *BaO* layers along the *c*-axis (no oxygen vacancies in *LnO* layer).

We will now discuss in brief the various parameters to obtain different phases (ordered-disordered) of *La-Ba-Co-O* cobaltites. The synthesis of $LaBaCo_2O_{5.5}$, maintaining the "$O_{5.5}$" stoichiometry and a perfect layered ordering of La^{3+} and Ba^{2+} cations, is delicate due to their small size difference which favors their statistical distribution. Moreover, the larger size of La^{3+} compared to other lanthanides allows large amounts of oxygen to be inserted, so that the disordered $La_{0.5}Ba_{0.5}CoO_3$ perovskite is more easily formed under normal conditions. Thus, the successful synthesis of ordered phase requires several steps, using soft chemistry method, and the strategy was to control the order-disorder phenomena in this system by means of two synthesis parameters, temperature and oxygen partial pressure. In order to favour the ordering of the La^{3+} and Ba^{2+} cations, the synthesis temperature was as low as possible, and consequently a soft-chemistry synthesis route was used since it allows a high reactivity at low temperature. However, this condition is not sufficient alone to achieve a perfect ordering of these cations. The formation of La^{3+} layers is in fact favoured by the intermediate creation of ordered oxygen vacancies, leading then to the *112*-type layered non-stoichiometric cobaltites $LaBaCo_2O_{5+\delta}$, built up of layers of CoO_5 pyramids between which the La^{3+} smaller than Ba^{2+} cations can be interleaved. In this process, it is rather difficult to control the oxygen stoichiometry to "$O_{5.5}$". For this reason, the synthesis of the ordered $LaBaCo_2O_6$ phase was carried out initially, using high purity argon gas, followed by annealing in an oxygen atmosphere at specific temperature. Thereafter, the layered *112* cobaltite $LaBaCo_2O_{5.5}$ was obtained from the ordered $LaBaCo_2O_6$ phase by employing temperature controlled oxygen depletion method in inert atmosphere [16].

The X-ray powder diffraction (*XRD)* patterns of the three perovskite phases (Figure 3) show their excellent crystallization. The disordered phase $La_{0.5}Ba_{0.5}CoO_3$, (Figure 3a) and the ordered phase $LaBaCo_2O_6$ (Figure 3c) exhibit sharp peaks, the patterns are indexed with the cubic *Pm*-3*m* and tetragonal *P*4/*mmm* space groups, respectively [12]. The latter corresponds to a doubling of the cell parameter along the *c*-axis related to the 1:1 ordering of the *LaO/BaO* layers (Figure 2c). More importantly, the *XRD* pattern of the ordered $LaBaCo_2O_{5.5}$ (Figure 3b) is completely different from that observed for the ordered phase (Figure 3c) and for this reason it is indexed and refined using the orthorhombic structure *Pmmm* space group [16]. The result for ordered-disordered cobaltites is slightly different from that obtained by *Nakajima et al*. [9], who observed a smaller cell volume for the ordered phase ($58.66\ Å^3/Co$) compared to the disordered one ($58.77\ Å^3$). Remarkably, the *La/Ba* ordering also involves a slight deformation of the perovskite sublattice with a dilatation of the a_p parameter within the *LaO/BaO* layers and a compression along the *LaO/BaO* layers stacking direction.

Transmission electron microscopy (*TEM*) investigations on the disordered $La_{0.5}Ba_{0.5}CoO_3$ and ordered $LaBaCo_2O_6$ cobaltites confirm their cubic and tetragonal structures respectively. The selected area electron diffraction (*SAED*) patterns of the disordered cobaltite and the corresponding high resolution electron microscopy (*HREM*) images (Figure 4a) are indeed characteristic of a classical cubic perovskite (*Pm*-3*m*) with $a \approx a_p \approx 3.9\ Å$. For ordered $LaBaCo_2O_6$, the reconstruction of the reciprocal space from the *SAED* patterns leads to a tetragonal cell, with $a \approx a_p$ and $c \approx 2a_p$, compatible with the space group *P*4/*mmm*. The doubling of one cell parameter with respect to the simple perovskite cell is clearly observed

on the *HREM* image displayed in Figure 4b and on the corresponding *SAED* [*100*] zone axis patterns (inset of Figure 4b). Beside the *SAED* investigation which gives a better view of the microstructure, bright field images are also of great interest to obtain information about the size of the *112*-type domains, taking into consideration the possibility of twinning. In the case of the disordered cubic cobaltite no twinning is observed, as expected from the symmetry. In contrast, in the long-range ordered *112*-perovskite $LaBaCo_2O_6$ twinning is clearly evidenced (Figure 5b).

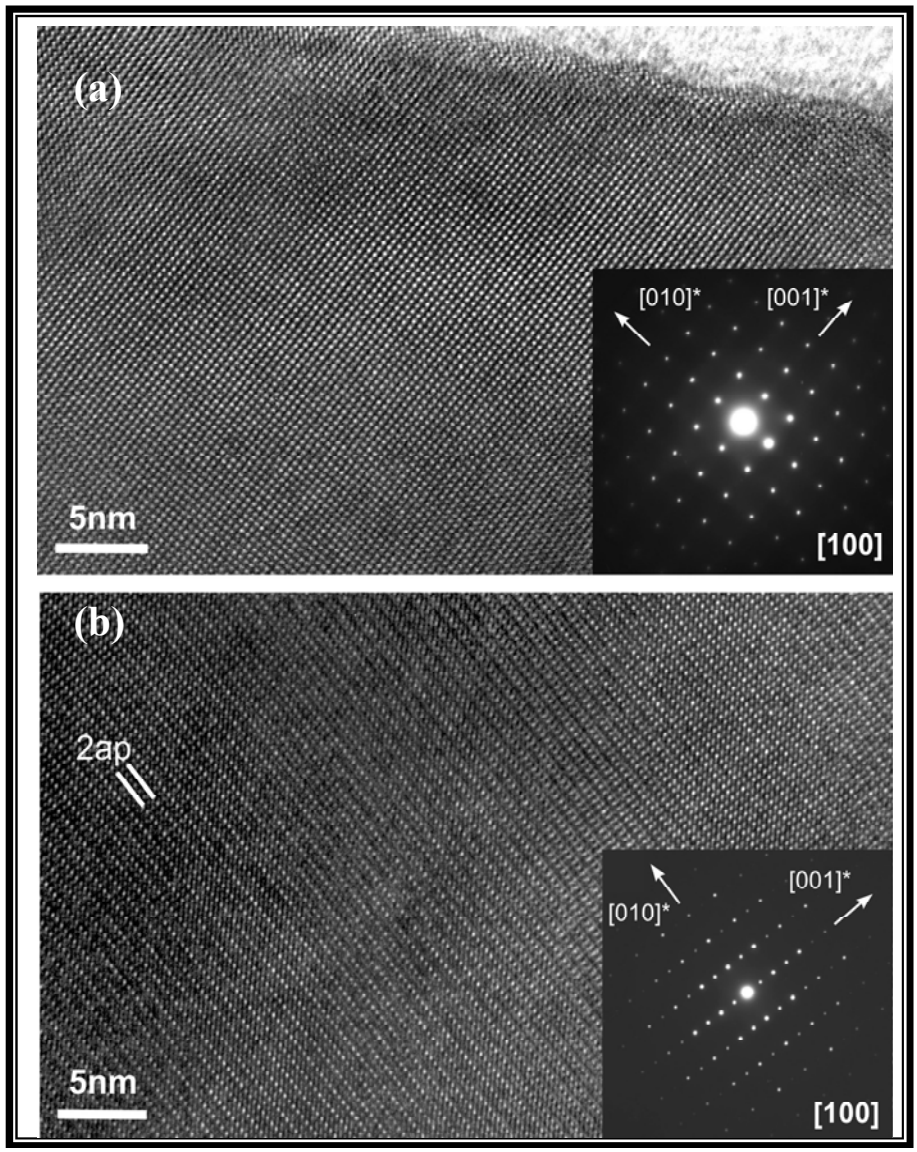

Figure 4. The HREM images and the corresponding SAED patterns for (a) disordered $La_{0.5}Ba_{0.5}CoO_3$ and (b) ordered $LaBaCo_2O_6$ (Taken from Ref. 12).

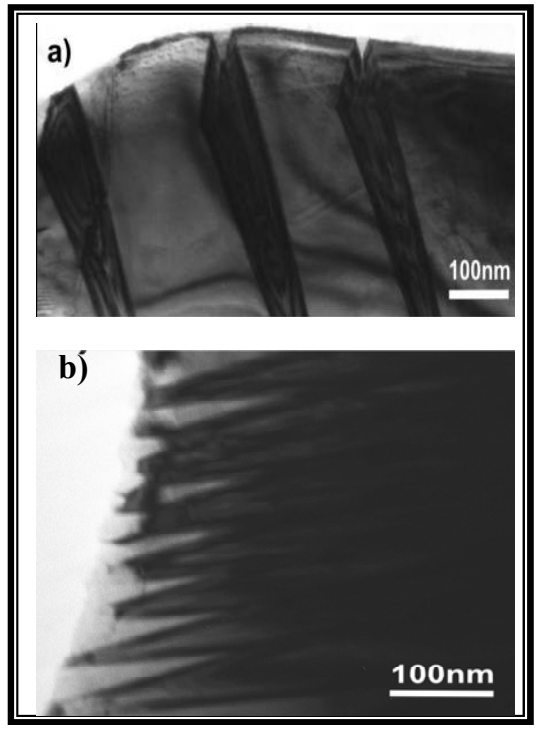

Figure 5. Bright field images for ordered cobaltites (a) $LaBaCo_2O_{5.5}$ and (b) $LaBaCo_2O_6$ (Taken from Ref. 12 & 16).

Moreover, *Rietveld* refinements of the neutron powder diffraction (*NPD*) data of $LaBaCo_2O_{5.5}$, shows a deviation from the ideal orthorhombic *Pmmm* structure due to partial disorder of the oxygen atoms at the $LaO_{0.5}$ layers. One indeed observes occupancy of about *90%* and *10%* of the *O6* and *O7* sites by oxygen, respectively, instead of the expected 100% and 0% [16]. Therefore, an investigation of ordered $LaBaCo_2O_{5.5}$ cobaltite by *TEM*, in order to identify possible secondary phase, superstructures, and/or particular microstructural features is of particular interest. In the Figure 6a, *SAED* confirms that the observed spots can be indexed with the *Pmmm* $a_p \times 2a_p \times 2a_p$ structure refined from powder diffraction. However, two additional features are also evidenced: First, one observes twinned domains at a microscale level, all over the investigated crystals regions, corresponding to the *Pmmm* $a_p \times 2a_p \times 2a_p$ structure *(112-type I)*, second, in few areas of some investigated crystals, very weak extra reflections are evidenced that cannot be indexed considering only the *Pmmm* $a_p \times 2a_p \times 2a_p$ structure. Considering the literature on the *112*-type compounds, a part of these extra spots can be indexed considering the *Cmmm* $2a_p \times 4a_p \times a_p$ cell corresponding to the $LaBaMn_2O_{5.5}$ compound [20]. This is in agreement with the results of the *NPD* refinements where the occupancies obtained for the *O6* and *O7* atomic positions can be locally attributed to a different vacancy/oxygen ordering (Figure 6b) leading notably to the existence of faulted zones having a centered structural motif *(112-type II)*. This tendency is evidenced by *SAED* but also visible in *HREM* for instance looking at one of the directions (Figure 6a). In summary, the $LnBaCo_2O_{5.5}$ structure consists mainly of 112 type I type domains (90%) combined with 112 type II (manganites) domains (10%). Finally, it is worth mentioning that

no $3a_p \times 3a_p \times 2a_p$ superstructure observed by TEM for ordered $LaBaCo_2O_{5.5}$ cobaltite, as evidenced for $HoBaCo_2O_{5.5}$ and $YBaCo_2O_{5.44}$ compounds [14, 21].

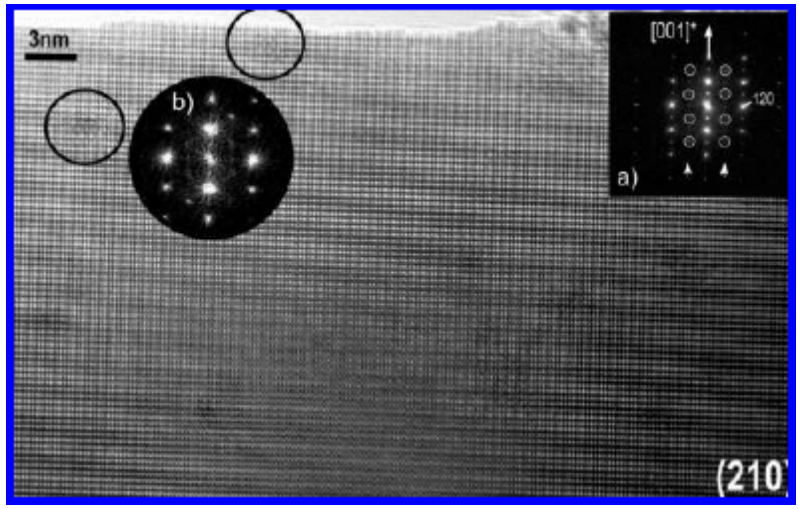

Figure 6a. The HREM images and the corresponding SAED patterns for ordered $LaBaCo_2O_{5.5}$.

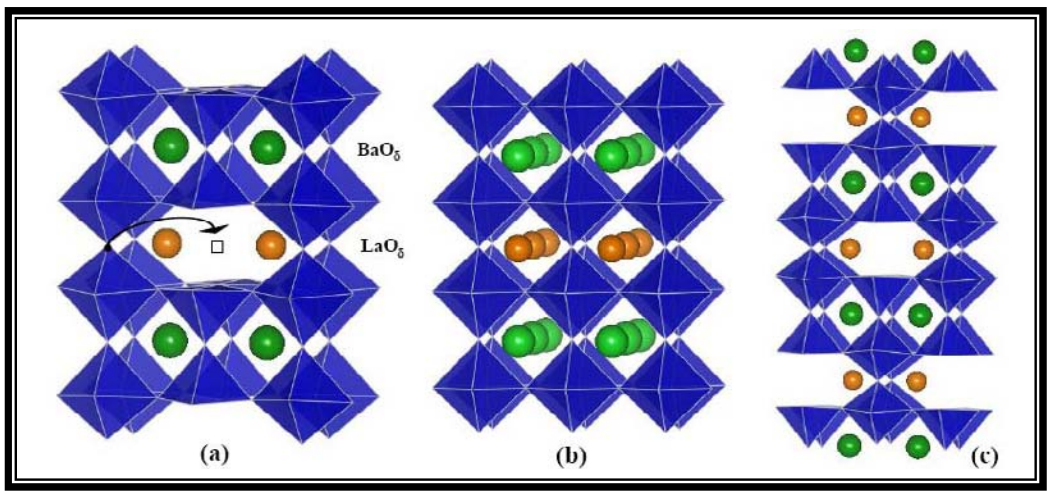

Figure 6b. Layered 112-type ordered $LaBaCo_2O_{5+\delta}$ cobaltites with (a) $\delta=0.5$; $LnBaCo_2O_5$,*(type-I)* (b) $\delta=1.0$; $LnBaCo_2O_6$ and (c) $\delta=0.5$; $LnBaCo_2O_{5.5}$ *(type-II)* (Taken from Ref. 12 & 16).

MAGNETIC AND ELECTRON TRANSPORT PROPERTIES

There are two characteristic structural distortions which influence the physical properties of doped rare earth cobaltites. The first one is cooperative tilting of the CoO_6 octahedra which is essentially established due to doping effect. This distortion is a consequence of the mismatch of the ionic radius and various factors as discussed in the previous section. The other distortion arises from the *Jahn-Teller (JT)* effect due to Co^{3+} ion, which distorts the

CoO_6 octahedra in such a way that there are long and short *Co-O* bonds (Figure 7). This occurs below a characteristic temperature for particular compounds, as for instance at *180K* for the disordered $La_{0.5}Ba_{0.5}CoO_3$ cobaltite [8]. This is well understood in terms of crystal field theory which describes how the *d*-electron of transition metal ions is perturbed by the chemical environment. The most effective distortion is the basal plane distortion (called Q_2 mode), with one diagonally opposite oxygen-pair displaced outwards and the other pair displaced inward. It is well established that a *JT* distortion involving a displacement of oxygen ions $\geq 0.1\text{Å}$ can split the e_g-band of the cobaltites (which forms the conduction band) and opens a gap at the *Fermi* level. The magnitude of the crystal field splitting of *d*-orbital determines whether the *Co*-ion occurs in the low-spin (*LS*), intermediate-spin (*IS*) or high-spin (*HS*) configuration. Figure 7, shows a scheme of the band diagram of $LaCoO_3$ to elucidate how the *JT* distortion splits the conduction band and makes the material insulating. The octahedral ligand environment around *Co*-ion splits the five *d*-orbitals into t_{2g}-triplet (d_{xy}, d_{yz} and d_{zx}) and e_g-doublet ($d_{x^2-y^2}$ and d_{z^2}) state. In this system, the resulting crystal-field splitting, Δ_{cf}, between t_{2g} and e_g orbital is around *2.06 eV* as reported by *Korotin et al.* [22] for theoretical observation, although experimentally obtained values are around *1.2 eV* and *0.9eV* [22]. Further splitting of the e_g orbitals due to the *JT* effect opens a gap at the *Fermi* level. The intra-atomic exchange energy responsible for *Hund's* highest multiplicity rule, Δ_{ex} (or J_H), is smaller than Δ_{cf} i.e. $\Delta_{ex} < \Delta_{cf}$ for Co^{3+} ion. Therefore *Co*-ions are always in low spin state below *100 K* for $LaCoO_3$ [22]. This perturbation induced electronic spin-state transition in rare earth cobaltites has been of great interest in recent years. The thermally driven spin-state transition in cobaltites is a consequence of the subtle interplay between the crystal field splitting (Δ_{cf}) and the *Hund's* coupling energy (Δ_{ex}). The Δ_{cf} usually decreases as the temperature is increased, whereas Δ_{ex} is insensitive to temperature since it is an atomic quantity. The spin-state of undoped $LaCoO_3$ (Co^{3+} ion) exhibits a gradual crossover with increasing temperature from the *LS* state ($t_{2g}^6 e_g^0$; $S = 0$) to *IS* state ($t_{2g}^5 e_g^1$; $S = 1$) at around *100 K* and finally to *HS* state ($t_{2g}^4 e_g^2$; $S = 2$) [22]. This results from the competition of the crystal field with energy Δ_{cf} (t_{2g}- e_g splitting) and the interatomic (*Hund*) exchange energy Δ_{ex}, leading to redistribution of electrons between t_{2g} and e_g levels.

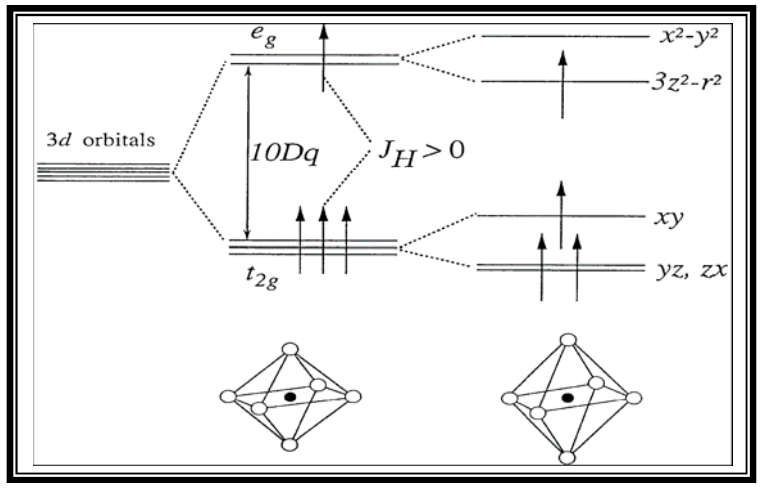

Figure 7. Field splitting of the five-fold degenerate atomic 3*d* levels for perovskite cobaltites.

In $Ln_{1-x}Ak_xCoO_3$ the doping by Ak^{2+} cation induces the formal presence of Co^{4+}, which slightly reduces the *JT* distortion leading towards cubic structure. The *JT* distortion of CoO_6 octahedra has been reported by *Fauth et al.* [8], which is favored due to the *IS* state of Co^{3+} ($t_{2g}^5e_g^1$) and Co^{4+} ($t_{2g}^4e_g^1$). The transfer interaction of e_g-electrons is greater in rhombohedral or pseudocubic phase than in the orthorhombic phase because the ⟨Co-O-Co⟩ bond angle becomes closer to *180°*. Clearly, the doping effect or the presence of Co^{4+} ion plays an important role in this material to provide the FM and metallic behavior by suppressing the *JT* distortion. The electron transport properties of cobaltites also depend on oxygen stoichiometry, and belong to the class either of metals or of semiconductors. Doped cobaltites are mixed valence materials, which mean that the Co-ions can carry different charges in the same site. The ratio between different Co-ion configurations is also determined by the oxygen stoichiometry as well as by the doping concentration, following the charge neutrality condition. Changes in the crystallographic and magnetic structures as well as the other physical properties can be induced by varying several parameters of either intrinsic hole/electron (doping, oxygen content) or extrinsic nature (temperature, pressure, magnetic field). Since only small changes of parameters (intrinsic/extrinsic) can cause a structural, magnetic or electronic transition, hence a variety of contradictory models or results exist for cobaltites. Detailed discussions are therefore required to clarify the influence of each parameter on the physical properties of the perovskite cobaltites. In this article, special emphasis has been given on the cationic ordering and oxygen stoichiometry onto the crystallographic, magnetic and electronic properties of few particular cobaltite systems. The magnetic structures, especially of the layered cobaltite systems with oxygen content of $O_{5.5}$ per unit formula, are still debated for some of the reported compounds. The determination of the magnetic structure is a complex task contrary to other materials, because the *Co*-ion in these materials can be in different spin states as discussed earlier.

I. Disordered Cobaltites

Disordered rare earth cobaltites $Ln_{1-x}Ak_xCoO_3$ have been investigated for several years due to their novel magnetic and electronic properties which include temperature-induced spin-state transitions, cluster-glass like behavior, electronic phase separation, magnetoresistance (*MR*) and so on [6-8, 11, 13]. The physical properties of perovskite cobaltites are sensitively dependent on the doping concentration of the rare-earth site. Doping brings up mixed valences in the *Co*-ions due to charge neutrality such as $(Ln^{3+}Ak^{2+})(Co^{3+}Co^{4+})O_3$. Therefore, substitution of Ln^{3+} by Ak^{2+} in $Ln_{1-x}Ak_xCoO_3$ will favor the transformation of Co^{3+} into Co^{4+} in same ratio of doping, as a result Co^{3+} and Co^{4+} will interact ferromagnetically obeying the *Zener* double-exchange (*DE*) mechanism [23]. The simultaneous observation of ferromagnetism and metallicity in cobaltites is explained by this mechanism, where the hopping of an electron from Co^{3+} to Co^{4+} via oxygen ion, i.e. where the Co^{3+} and Co^{4+} ions exchange takes place. The integral defining the exchange energy in such a system is non-vanishing only if the spins of the two *d*-orbitals are parallel. That is the lowest energy of the system is one with a parallel alignment of the spins on the Co^{3+} and Co^{4+} ions. Due to this, the spins of the incomplete *d*-orbitals of the adjacent *Co*-ion are accompanied by an increase in the rate of hopping of electrons and therefore by an increase in electrical conductivity. Thus, the mechanism which leads to enhanced electrical conductivity

requires a *FM* coupling. On the other hand, Co^{3+}-Co^{3+} and Co^{4+}-Co^{4+} couple antiferromagnetically due to super-exchange interactions. Super-exchange interaction generally occurs between localized moments of ions in insulators. *Goodenough et al.* pointed out that the *FM* interaction is governed not only by the *DE* interaction, but also by the nature of the super-exchange interactions [23]. Whether the ferromagnetism in cobaltites (similar to manganites) is mediated by a *DE* mechanism or not is clearly not understood at present. However, the absence of half filled t_{2g} orbitals is providing core spin and strong *Hund's* rule coupling, unlike manganites, making this mechanism less feasible. It seems, the *FM*-metallic phase in cobaltites can be explained by the *Zener-DE* mechanism whereas super-exchange will fit for insulating state. Hence, there will be always a competition between these two interactions to dominate one over another giving rise to a tendency of electronic phase separation in the system [1]. The growth of interest in perovskite cobaltites is due to the expectation that, in addition to the lattice, charge and spin degrees of freedom found in many other transition metal oxides, the cobalt oxides also display a degree of freedom in the "spin-state" at the *Co*-site.

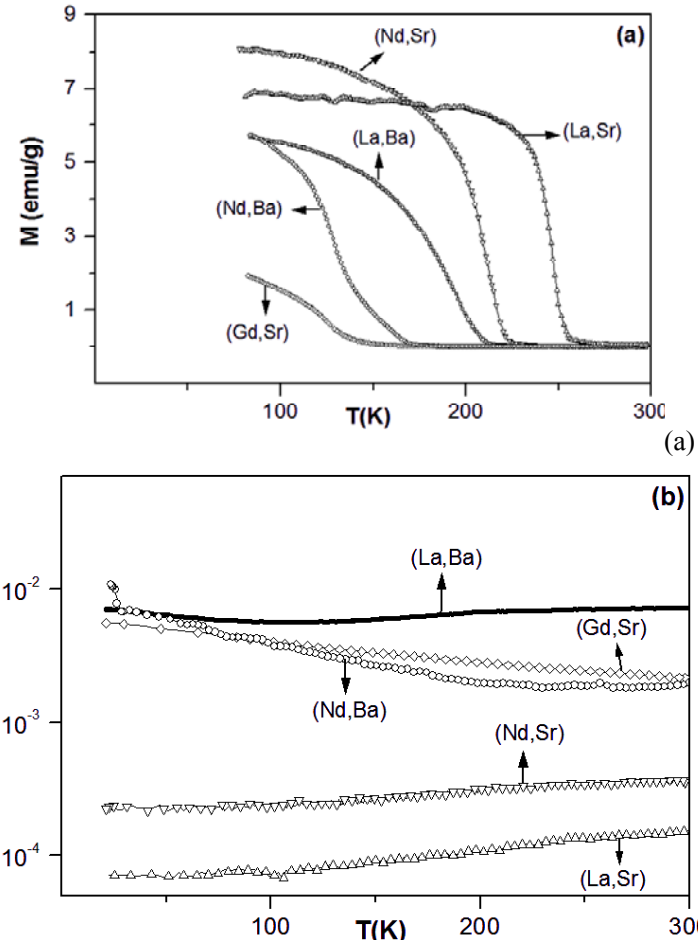

Figure 8 (Continued)

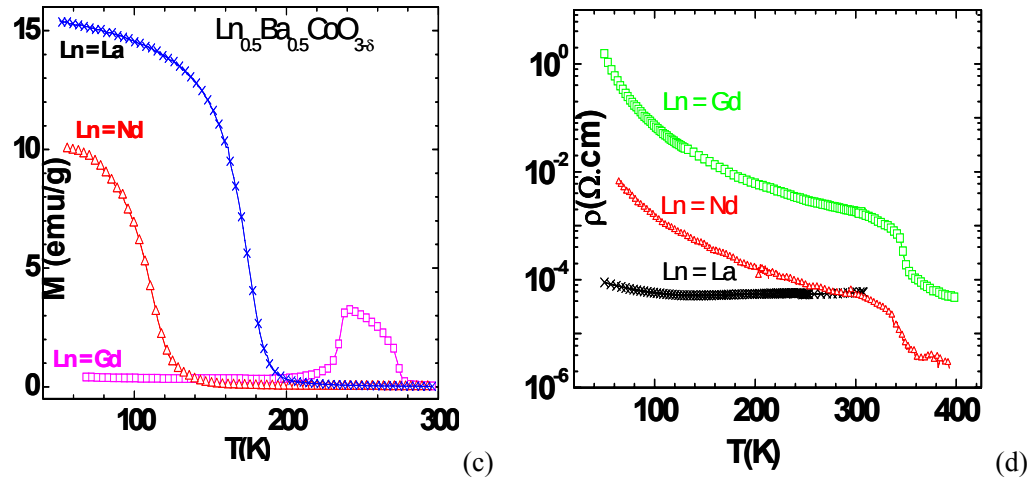

Figure 8. Temperature dependent Magnetization and Resistivity for disordered cobaltites $Ln_{0.5}Ak_{0.5}CoO_3$ (Taken from Ref. 13 & 18).

The physical properties of the cobaltites are sensitive to doping concentration at the rare earth site. Accordingly, the other parameters such as the average radius of the *A*-site cation, $\langle r_A \rangle$, and size-disorder parameter, σ^2, also vary due to doping at the perovskite *A*-site. These parameters crucially control the physical properties of disordered cobaltites. Disordered cobaltites of the type $Ln_{0.5}Ak_{0.5}CoO_3$, especially those with *Ln= La, Nd, Gd* and *Ak = Ba, Sr* are *FM*, many of them showing a metallic behavior as shown in Figure 8 [13, 18, 19]. These properties arise because of the major influence of Co^{3+}-*O*- Co^{4+} interactions in these cobaltites. The *FM* T_C increases with the increase in the size of the *A*-site cations, $\langle r_A \rangle$. In the case of *Ak = Ba*, ferromagnetism occurs when *Ln = La* ($T_C \sim 190$ *K*) and *Nd* ($T_C \sim 130$ *K*), but for *Ln = Gd*, the material shows unusual magnetic behavior (Figure 8c). Furthermore, $Gd_{0.5}Ba_{0.5}CoO_3$ is an insulator and exhibits an electronic transition around *350 K* with cationic ordering [13], whereas $La_{0.5}Ba_{0.5}CoO_3$ is metallic below *FM* T_C (Figure 8d). $Gd_{0.5}Ba_{0.5}CoO_3$ which is charge-ordered at room temperature, shows a *FM*-like feature around *280 K*, without reaching a saturation value of the magnetic moment or the highest moment achieved is rather low even in the higher applied field conditions [13, 18]. The magnetic transition around *280 K* in $Gd_{0.5}Ba_{0.5}CoO_3$, has been classified in the literature as *FM* or meta-magnetic, and other cobaltites of this family such as $La_{0.5}(Nd_{0.5})Ba_{0.5}CoO_3$ have not been distinguished, and have all been treated as *FM* transitions. There are, however, considerable differences amongst these cobaltites. The magnetic transitions in $La_{0.5}(Nd_{0.5})Ba_{0.5}CoO_3$ are distinctly *FM*, showing a sharp increase in magnetization at T_C, and the value is rather low (*130-190 K*) [13, 18]. $Gd_{0.5}Ba_{0.5}CoO_3$, with a much smaller *A*-site cation, should have been associated with an even lower T_C. In Figure 9, we present the temperature variation of the magnetization of a few compositions of $Ln_{0.5}Ak_{0.5}CoO_3$. The T_C values are plotted against $\langle r_A \rangle$ from the literature data, increasing up to $\langle r_A \rangle$ value of *1.40 Å* and decreasing thereafter. The decrease in T_C for $\langle r_A \rangle$ *1.40 Å* is likely to arise from the size-disorder. Indeed, the cations size mismatch, σ^2, is known to play an important role in determining the properties of rare earth cobaltites [13]. It appears that the large value of σ^2 in the $Gd_{0.5}Ba_{0.5}CoO_3$ (*0.033* $Å^2$)

compared to that of $La_{0.5}Ba_{0.5}CoO_3$ (0.016 $Å^2$) could be responsible for the absence of ferromagnetism and metallicity in the former [13, 18].

To understand the role of cationic size, we will now discuss the magnetic and electrical properties of several series of cobaltites. The temperature dependent magnetization and resistivity behavior of $Gd_{0.5-x}Nd_xBa_{0.5}CoO_{3-\delta}$ series is presented Figure 10. With increasing the *Nd* substitution or the $<r_A>$ value, the evolution of ferromagnetism is observed. It is interesting to note that the *280 K* magnetic transition of $Gd_{0.5}Ba_{0.5}CoO_{2.9}$ disappears even when $x \geq 0.1$. Moreover, for $x = 0.1$, a complex behavior is observed with a magnetic transition around *220 K*. The $x = 0.3$ composition shows a weak increase in magnetization value around *125 K*, and the effect is more prominent for $x = 0.4$. Similarly, for $Gd_{0.5-x}La_xBa_{0.5}CoO_{3-\delta}$, there is no clear *FM* transition in the *200-280 K* region for $0.1 < x < 0.25$. A distinct *FM* transition occurs at $x = 0.5$ in the case of *Nd*, and at $x = 0.4$ in the case of *La*. It is interesting that the *FM* characteristics start emerging at low temperatures (< *150 K*) in these cobaltite compositions around a $\langle r_A \rangle$, value of *1.30 Å*. Clearly with increasing *x*, the size of ferromagnetic clusters increases, eliminating the phase separation at lower value of *x*, caused by size disorder. It is noteworthy that in the $Ln_{0.7}Ca_{0.3}CoO_3$ (*Ln = La, Pr, Nd*) series the spin glass like behavior has been reported at low temperatures, the system approaching toward spin glass state [11] for the higher size disorder. Spin glass behavior is also reported for $La_{1-x}Sr_xCoO_3$ ($x < 0.1$), but with increase in *x* ferromagnetism manifests itself [13].

$Gd_{0.5-x}Nd_xBa_{0.5}CoO_{3-\delta}$ exhibit an insulating behavior throughout the temperature range, but the electrical resistivity decreases significantly with increase in *x*, particularly $x = 0.5$ composition exhibiting the lowest resistivity (Figure 10). Similarly for *Ln = La*, the resistivity value decreases with increasing *x*, becoming metallic for $x = 0.5$. All the other compositions are semiconducting. Considering that with increase in *x*, there is significant increase in $<r_A>$ values in these disordered $Gd_{0.5-x}Ln_xBa_{0.5}CoO_{3-\delta}$ (*Ln = La, Nd*) series of cobaltites, the changes observed can essentially be attributed to the effects of cation size which indirectly control the electronic band width and as a result the energy band gap varies.

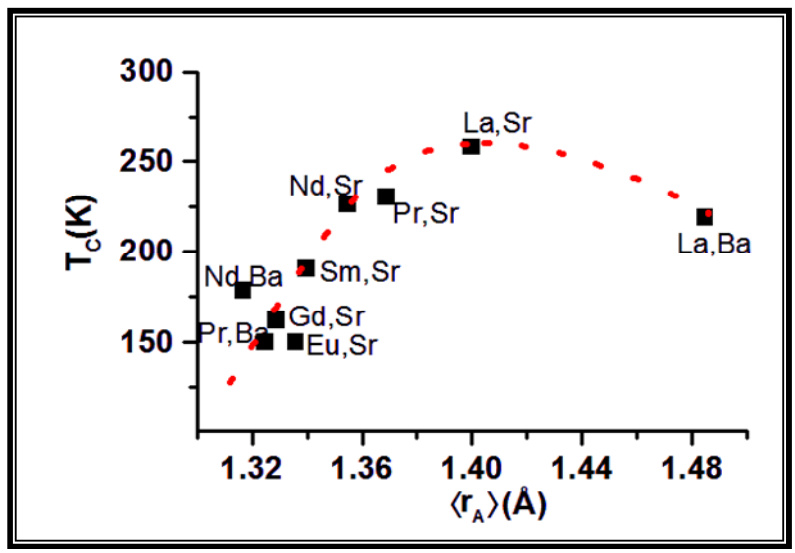

Figure 9. Variation of FM T_C with $<r_A>$ for disordered cobaltites $Ln_{0.5}Ak_{0.5}CoO_3$ (Taken from Ref. 13).

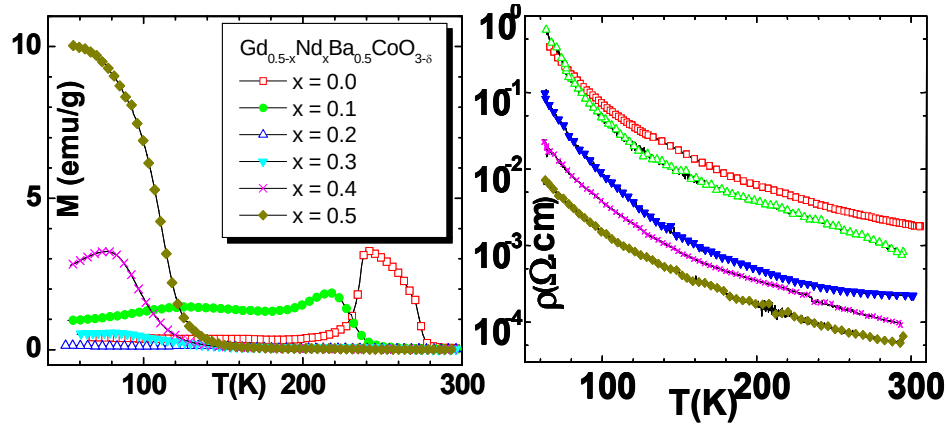

Figure 10. Temperature dependent Magnetization and Resistivity for $Gd_{0.5-x}Nd_xBa_{0.5}CoO_3$.

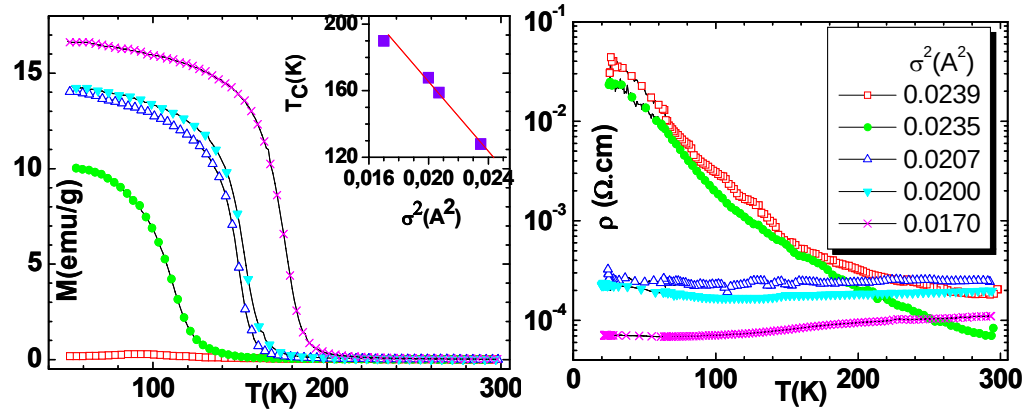

Figure 11. Temperature dependent Magnetization and Resistivity for a fixed $\langle r_A \rangle$ of *1.317 Å*, inset figure (a) shows the T_C -σ^2 plot (Taken from Ref. 18).

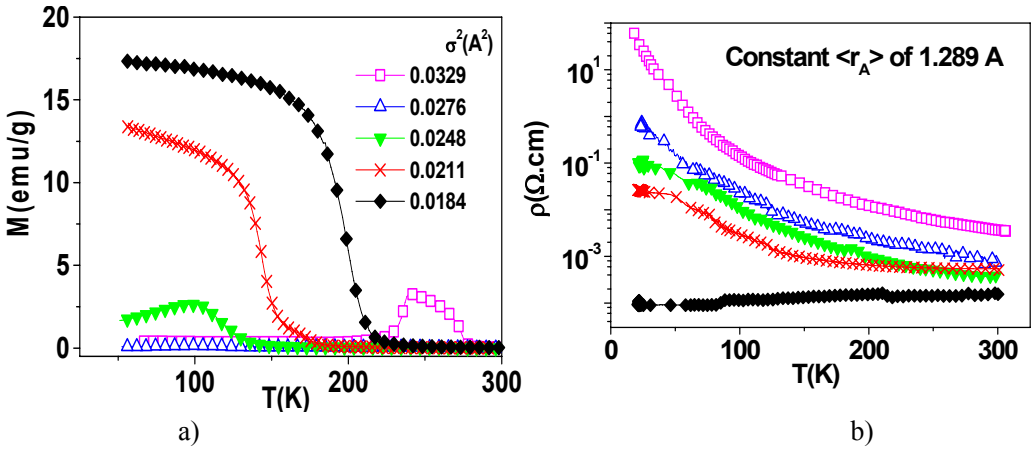

Figure 12. Temperature dependent Magnetization and Resistivity for a fixed $\langle r_A \rangle$ of *1.289 Å* (Taken from Ref. 18).

In order to understand the role of size-disorder due to cation size mismatch, σ^2, we have discussed two series of cobaltites with fixed $\langle r_A \rangle$ values of *1.317* and *1.289 Å*, corresponding to those of $Nd_{0.5}Ba_{0.5}CoO_3$ and $Gd_{0.5}Ba_{0.5}CoO_3$ respectively. The data, for a fixed $\langle r_A \rangle$ of *1.317 Å*, show that the *FM* T_C decreases with increasing σ^2 (inset Figure 11a), eventually destroying ferromagnetism at a high value of σ^2 (≈ 0.024 *Å*^{2}). Similarly, the data in Figure 12, for a fixed $\langle r_A \rangle$ of *1.289 Å*, are interesting. It is observed that with decreasing σ^2, the magnetic behavior of this system changes markedly. Thus, when $\sigma^2 = 0.028$ *Å*^{2}, there is no such magnetic anomaly as observed in the case of $Gd_{0.5}Ba_{0.5}CoO_{2.9}$ at *280 K*. When $\sigma^2 = 0.021$ *Å*^{2}, we observe a *FM* transition with a $T_C \sim 160$ *K* and for $\sigma^2 = 0.018$ *Å*^{2}, the T_C value reaches *220 K*, a value higher than that of $La_{0.5}Ba_{0.5}CoO_3$. These data clearly demonstrate that the absence of prominent ferromagnetism in $Gd_{0.5}Ba_{0.5}CoO_3$, and the unusual magnetic properties, like magnetic anomaly around *280 K*, is almost entirely due to the disorder arising from the cation size mismatch. Such size-disorder can give rise to electronic phase separation as reported for other cobaltites [18]. The electrical resistivity of these series of cobaltites corroborates the results from the magnetic measurements. In Figure 12b, we present the electrical resistivity data to demonstrate how the resistivity increases with increase in σ^2. Interestingly, disorder-induced insulator-metal transitions are noticed in both the series of cobaltites and the compositions with $\sigma^2 < 0.02$ *Å*^{2} showing metallic behavior. While disorder-induced meal-insulator transitions are common, size variance-induced insulator-metal transitions are indeed novel.

Further support of the previous discussion that cation size-disorder crucially determines the properties of $Gd_{0.5}Ba_{0.5}CoO_{2.9}$ is provided in this section by the study of $Gd_{0.5}Ba_{0.5-x}Sr_xCoO_{3-\delta}$ series of cobaltites as reported in the literature [18]. Here, $x = 0.5$ composition, corresponding to $Gd_{0.5}Sr_{0.5}CoO_3$, has a smaller $\langle r_A \rangle$ than $Gd_{0.5}Ba_{0.5}CoO_{2.9}$, and yet it shows ferromagnetic features. The *280 K* magnetic anomaly of $Gd_{0.5}Ba_{0.5}CoO_3$ disappears even when $x = 0.1$ and the apparent T_C increases with increasing x in this series. This behavior is clearly due to size disorder effect, since σ^2 decreases with increase in x. Accordingly, the present system exhibits an insulator-metal transition with increase in x or decrease in σ^2. It appears that a σ^2 value larger than *0.02 Å*^{2} generally destroys ferromagnetism in the cobaltites and changes the metal into an insulator as discussed earlier.

In view of the interesting magnetic and electrical properties of the disordered $Ln_{0.5}Ba_{0.5}CoO_3$ cobaltites, we have also presented a comparative study of *Sr*-doped disordered cobaltites $Ln_{0.5}Sr_{0.5}CoO_3$ with *Ln = La, Pr, Nd,* and *Gd*. Magnetic properties of $La_{0.5}Sr_{0.5}CoO_3$ are fairly well understood. Although it shows a sharp *FM* T_C around *240 K*, it exhibits a significant divergence between the *FC* and *ZFC* magnetization data (Figure 13a) and also shows a frequency-dependent *AC* susceptibility maximum around *165 K*, suggesting a glassy nature [19]. It was realized a few years ago that $La_{0.5}Sr_{0.5}CoO_3$, which was considered to be a good ferromagnetic metal, was actually a magnetic cluster-glass with some long-range magnetic ordering wherein frustration arose from inter-cluster interactions at low temperatures [6]. The magnetic behavior of these systems has generally been interpreted in terms of short-range magnetic ordering. Cluster-glass behavior occurs at a high concentration of *Sr* ($x > 0.3$), where the coalescence of short-range ferromagnetic clusters is proposed to occur [6, 13]. ^{139}La *NMR* studies confirm the coexistence of ferromagnetic, paramagnetic, and cluster-glass phases in $La_{1-x}Sr_xCoO_3$ [6, 13]. Electronic phase separation in the $La_{1-x}Sr_xCoO_3$ systems is associated with the formation of isolated nanoscopic ferromagnetic clusters. Thus,

the cobaltites comprise ferromagnetic clusters, paramagnetic matrices and spin-glass-like phases, all contributing to the glassy magnetic behavior. More importantly, this glassy ferromagnetism is accompanied by phase separation wherein the ferromagnetic clusters exist within a antiferromagnetic (*AFM*) matrix. In these cobaltites, the *FM* phase is conducting and the *AFM* phase is insulating. Depending on x or the carrier concentration, we can have a situation such as that shown in Figure 14. The phase separation scenario here is somewhat complex because the transition from the metallic to the insulating state is not sharp. In the presence of *Coulomb* interaction, the microscopically charged inhomogeneous state is stabilized, giving rise to clusters of one phase embedded in another. Electronic phase separation with phases of different charge densities is generally expected to give rise to nanometer scale clusters [19]. This is because large-phase separated domains would break up into small pieces because of *Coulomb* interactions. The shapes of these pieces could be droplet or stripes (see Figure 14a-d). The domains of the two phases can also be sufficiently large to give rise to well-defined signatures in neutron scattering or diffraction. One can visualize phase separation arising from disorder as well. The disorder can arise from the size mismatch of the *A*-site cations in the disordered perovskite structure [1]. Such phase separation is reported for $(La_{1-y}Pr_y)_{1-x}Ca_xMnO_3$ system in terms of a metal-insulator transition induced by disorder [1]. The size of the clusters depends on the magnitude of disorder. The smaller the disorder, the larger would be the size of the clusters. This could be the reason why high *MR* occurs in systems with small disorder.

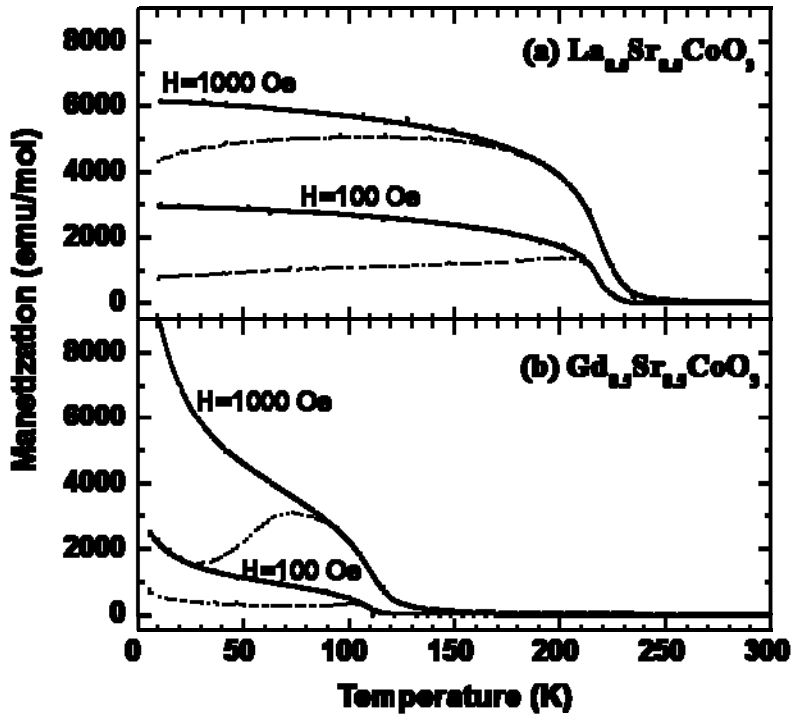

Figure 13. Temperature dependent FC-ZFC Magnetization for (a) $La_{0.5}Sr_{0.5}CoO_3$ and (b) $Gd_{0.5}Sr_{0.5}CoO_3$ (Taken from Ref. 19).

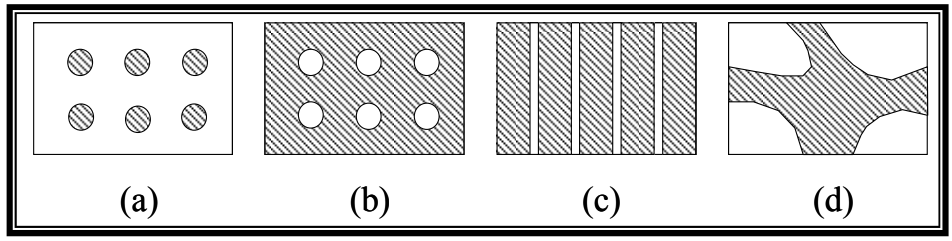

Figure 14. Schematic representation of electronic phase separation (Taken from Ref. 1).

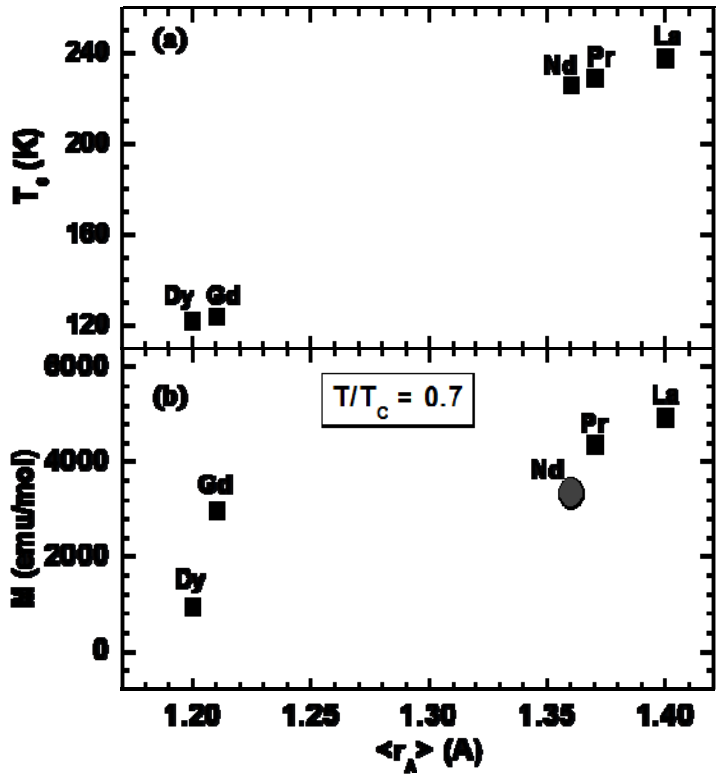

Figure 15. Variation of (a) FM T_C and (b) Magnetization with $<r_A>$ for disordered cobaltites $Ln_{0.5}Sr_{0.5}CoO_3$ at *120 K* (Taken from Ref. 19).

Electronic phase separation in the $La_{1-x}Sr_xCoO_3$ systems is associated with the formation of isolated nanoscopic *FM* clusters [6]. Evidence for the occurrence of phase separation in $La_{0.5}Sr_{0.5}CoO_3$ is provided by the *NMR* studies [6]. The *Mössbauer* spectra reported by *Bhide et al.* [13] show the presence of a paramagnetic signal in addition to the six-finger pattern due to the *FM*-type species over a range of compositions and a wide range of temperatures. The temperature variation of the ferromagnetic-paramagnetic (*FM/PM*) ratio was reported recently for $La_{0.5}Sr_{0.5}CoO_3$ [19], showing an increasing ratio with decreasing temperature, as one would expect. While the *FM/PM* ratio increases with a decrease in temperature, the *PM* phase continues to exist well below T_C in $La_{0.5}Sr_{0.5}CoO_3$. Clearly, this observation is a direct evidence for phase separation in $La_{0.5}Sr_{0.5}CoO_3$. It is of interest to examine the glassy phases and phase separation occurring in the other rare earth cobaltite compositions of the type

$Ln_{0.5}Sr_{0.5}CoO_3$. The temperature-dependent *DC* magnetization data of $Gd_{0.5}Sr_{0.5}CoO_3$ exhibits divergence in the *ZFC* and *FC* behavior just as in magnetically disordered systems. What is particularly noteworthy is that the magnetization value in $Gd_{0.5}Sr_{0.5}CoO_3$ is much smaller than the *Pr* and *La* counterparts below their T_C's, especially at temperatures below the relatively sharp transition around *110 K*. Since the carrier concentration or the Co^{3+}/Co^{4+} ratio remains constant in these cobaltites, the only possible explanation for such a decrease in magnetization is that the proportion of *PM* species relative to that of the *FM* species increases with the decrease in the size of the rare earth ion. It is entirely understandable that the proportion of the clusters responsible for ferromagnetism decreases with decrease in $<r_A>$. In the $Ln_{0.5}Sr_{0.5}CoO_3$ series, the *FM* T_C decreases with decreasing $<r_A>$ (Figure 15) which is a well-established behavior for disordered cobaltites [13, 19]. Since the magnetic moment below T_C is related to the proportion of the *FM* clusters, the variation of magnetization with $<r_A>$ at *120 K* in a series of $Ln_{0.5}Sr_{0.5}CoO_3$ compounds is shown in Figure 15. We have presented the size disorder effect in the $Ln_{0.5}Sr_{0.5}CoO_3$ system as well. For this purpose, the data were presented for fixed $<r_A> = 1.196$ *Å* as equal to that of $Dy_{0.5}Sr_{0.5}CoO_3$ and varying the σ^2 values for different cobaltite compositions. The plot of T_C values against σ^2 is shown in Figure 16. The *FM* T_C increases with a decreasing σ^2 and the T_C^0 value corresponding to the disorder-free case ($\sigma^2 = 0.0$) is 217 ± 2 *K*. The linear relation between T_C and σ^2 gives a slope of 9667 ± 192 *K* $Å^{-2}$, which is comparable to that reported in the literature [13, 18]. Thus, it can be concluded for disordered cobaltites that, increasing size disorder favors electronic phase separation, giving rise to magnetic clusters of different size ranges, while decreasing size disorder increases the *FM/PM* ratio.

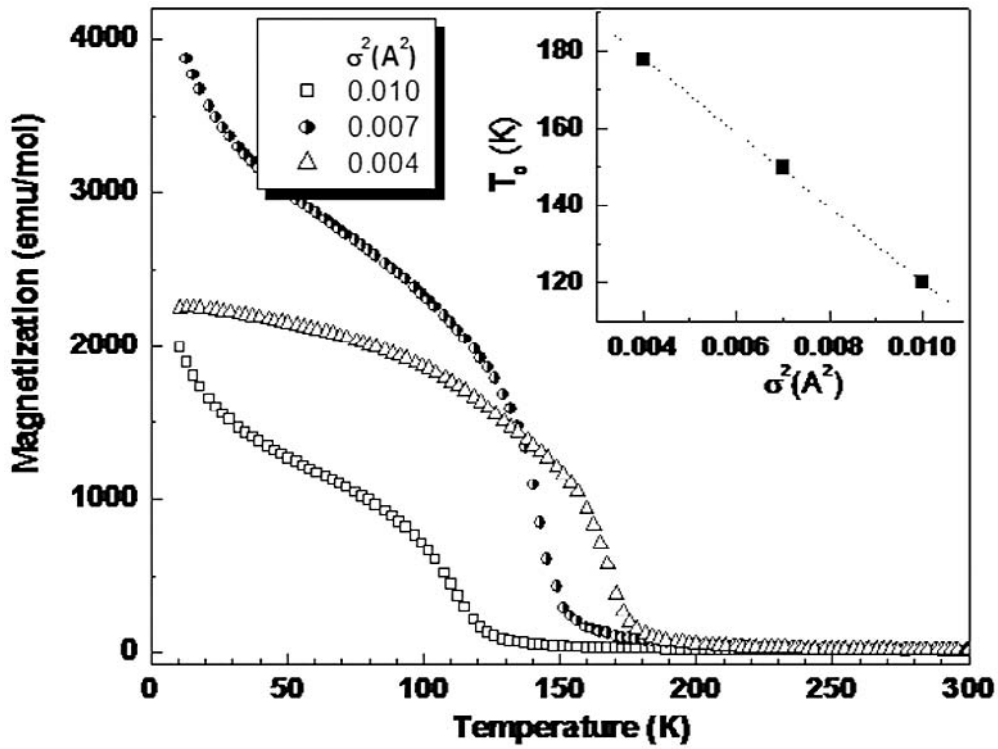

Figure 16. Magnetic properties for a fixed $<r_A>$ of *1.196 Å* (same as $Dy_{0.5}Sr_{0.5}CoO_3$) (Taken from Ref. 19).

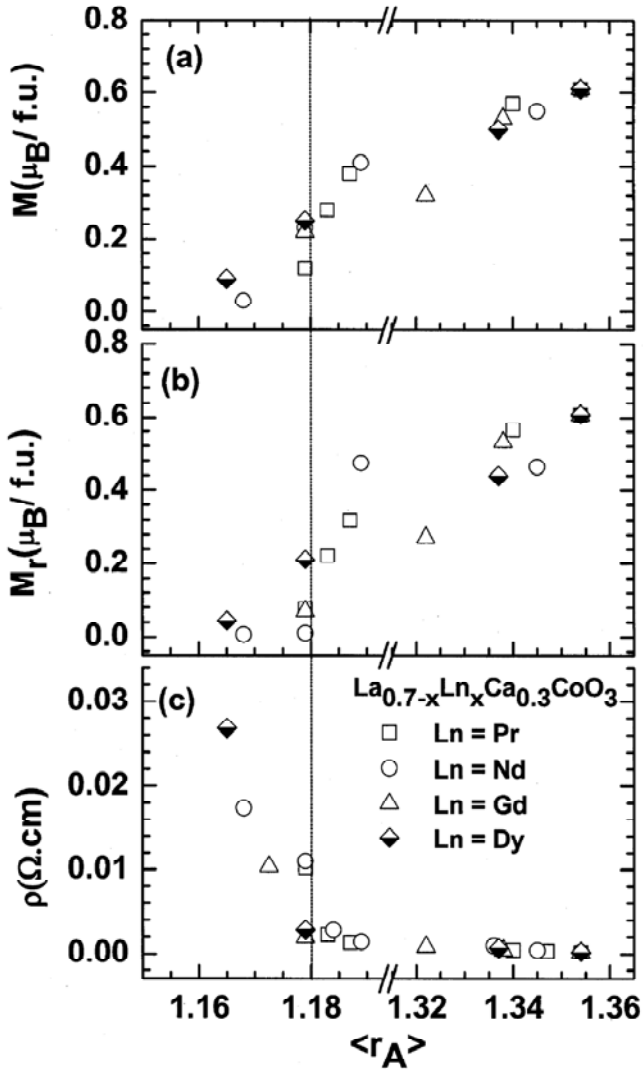

Figure 17. Magnetization and Resistivity behavior for disordered $La_{0.7-x}(Pr/Nd/Gd/Dy)_xCa_{0.5}CoO_3$ series with the variation of $<r_A>$ at *50 K* (Taken from Ref. 11).

The value of *MR* for disordered cobaltites (even at T_C/T_{IM}) is much smaller in magnitude than for the manganites [7]. However, in disordered cobaltites the large and negative *MR* has been reported in the insulating compositions of $La_{0.5}Sr_{0.5}CoO_3$ [7]. In such system, the maximum *MR* is observed where it shows *SG*-like behavior [7, 13]. Disordered cobaltites of the type $Ln_{1-x}Ca_xCoO_3$ show no long-range ferromagnetism or insulator-metal transition, instead they exhibit electronic phase separation and/or glassy magnetic behavior at low temperatures [11, 13]. Studies on $La_{1-x}Ca_xCoO_3$ samples have suggested that there are no major differences from the *Sr*-doped system. Ferromagnetism is observed in both systems, with the Curie temperature being lower in *Ca*-doped materials at a fixed doping level. Magnetic and electron transport properties of different rare earth cobaltites have been investigated to examine the effect of $\langle r_A \rangle$, and σ^2 on these systems as presented in Figure 17.

Thus, while $La_{0.7}Ca_{0.3}CoO_3$ ($\langle r_A \rangle$, = *1.354 Å*) shows glassy ferromagnetism associated with metallicity at low temperature, $Ln_{0.7}Ca_{0.3}CoO_3$ with a smaller $\langle r_A \rangle$, of *1.179 Å* (*Ln = Pr*) and *1.168 Å* (*Ln = Nd*) shows no long-range ferromagnetism or insulator-metal transition [11]. Instead, the latter two systems exhibit electronic phase separation and/or spin-glass like behavior at low temperatures. The electronic phase separation and associated magnetic properties of $Pr_{0.7}Ca_{0.3}CoO_3$ and $Nd_{0.7}Ca_{0.3}CoO_{2.95}$ arise because of the small average size of the A-site cations [11]. In these two cobaltites, the average radius (for orthorhombic structure) is less than *1.18 Å*, which is the critical value only above which long-range ferromagnetism manifests itself. A detailed study on disordered rare earth cobaltites has shown the occurrence of electronic phase separation and glassy magnetic behavior for small $\langle r_A \rangle$, and a large σ^2 value [11].

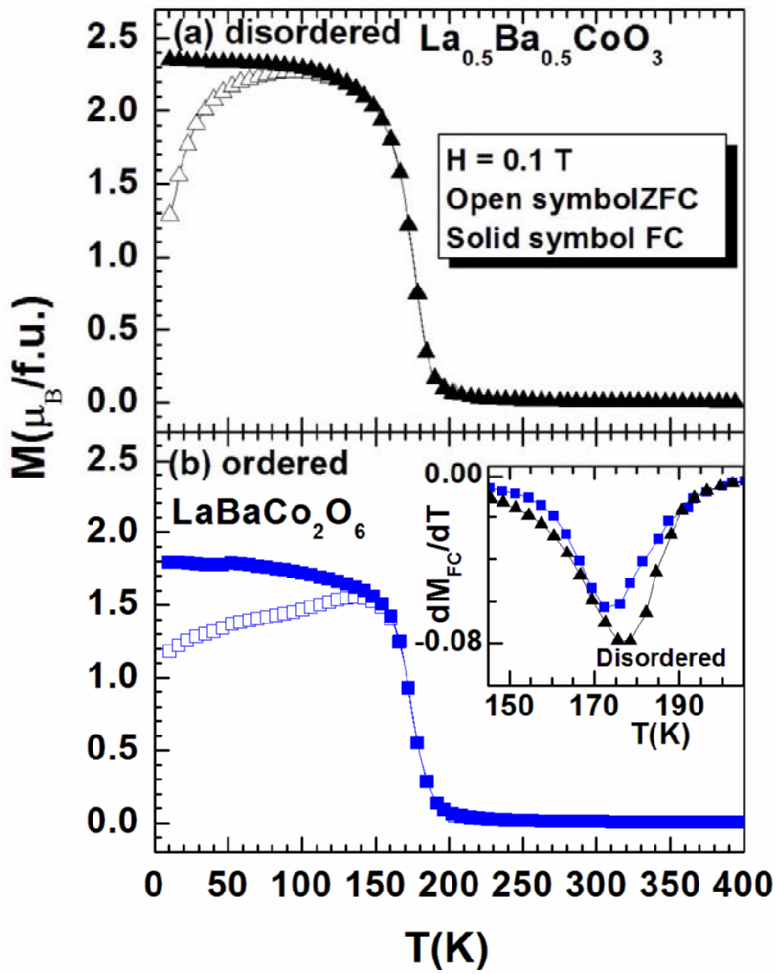

Figure 18. Temperature dependence ZFC (open symbol) and FC (solid symbol) Magnetization (H = 0.1 Tesla) for (a) disordered $La_{0.5}Ba_{0.5}CoO_3$ and (b) ordered $LaBaCo_2O_6$. The inset figure shows dM_{FC}/dT vs temperature plot.

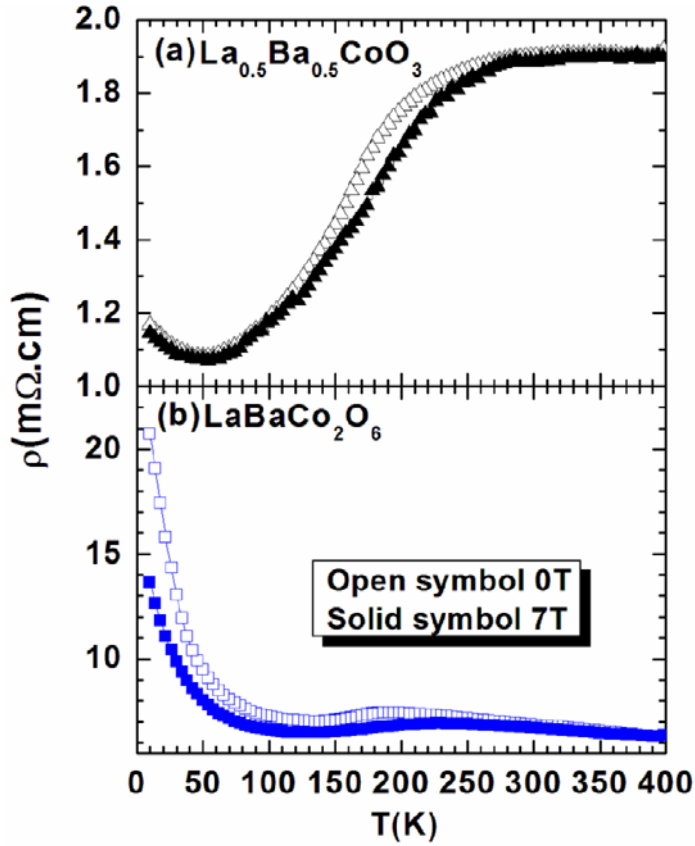

Figure 19. Temperature dependence electrical resistivity, ρ, for (a) disordered $La_{0.5}Ba_{0.5}CoO_3$ and (b) ordered $LaBaCo_2O_6$ cobaltites (Taken from Ref. 12).

II. Ordered Cobaltites

The cationic order-disorder phenomena in the perovskite cobaltites do not affect much their *PM-FM* transition temperature T_C [9], in contrast to the ordered $LaBaMn_2O_6$ and disordered $La_{0.5}Ba_{0.5}MnO_3$ manganites [20]. However, the influence of the cationic ordering upon the T_C seems to be reverse since, according to *Nakajima et al.* [9], the disordered cobaltites exhibit a higher T_C of *190 K* than the ordered phase *(175 K)*. Figure 18, shows the temperature dependent magnetization measurements for the disordered $La_{0.5}Ba_{0.5}CoO_3$ and ordered $LaBaCo_2O_6$ also indeed exhibit T_C of *177 K* and *174 K* respectively [12]. Moreover, other magnetic behaviors such as the field and the temperature dependent magnetization are similar to expected for *PM/FM* phases [9, 12]. The coercive field, H_C, for disordered $La_{0.5}Ba_{0.5}CoO_3$ and ordered $LaBaCo_2O_6$ are *0.08* and *0.05 Tesla (T)* respectively (at *10 K*); the low value of H_C signifies the nature of soft *FM* material [12]. There is one more cobaltite compound reported in the literature as ordered-disordered phases, with a FM T_C of 250 K in the ordered $NdBaCo_2O_6$ phase [14] whereas for disordered $Nd_{0.5}Ba_{0.5}CoO_3$ phase [13] the value is 130 K. Since those compounds are reported by two different groups so we will not elaborate our discussion on those phases for the present article.

Figure 19 shows the temperature dependence of electrical resistivity for both ordered-disordered phases in the presence and absence of an applied magnetic field of ±7 *Tesla(T)*. Note that the resistivity, *ρ(T)*, behavior of the disordered $La_{0.5}Ba_{0.5}CoO_3$ and ordered $LaBaCo_2O_6$ are different from those reported by *Nakajima et al*. [9], and corroborate the result reported by *Fauth et al*. [8] for the disordered $La_{0.5}Ba_{0.5}CoO_3$. The *ρ(T)* curve in *10-400 K* temperature range depicts that at high temperature (*T>300K*) the disordered $La_{0.5}Ba_{0.5}CoO_3$ (Figure 19a) phase is semi-metallic, whereas the ordered $LaBaCo_2O_6$ is semiconducting down to *190 K* (Figure 19b). This feature is explained by the fact that the disordered cobaltite exhibits *180°* ⟨Co-O-Co⟩ bond angle in this temperature range, in agreement with its cubic or pseudo cubic structural symmetry, favoring a perfect overlapping of the *Co 3d* orbitals and oxygen *2p* orbitals. This is in contrast to the ordered $LaBaCo_2O_6$, where the ⟨Co-O-Co⟩ bond angles of *174°* in the equatorial planes of the $[CoO_2]_\infty$ layers are observed at room temperature [9]. In this case the conduction of charge carriers will be more favorable for linear bond angle, as a result metallic type of conductivity is noticed for the disordered cobaltite. With decreasing temperature a transition to a nearly metallic state is observed for both phases. It is characterized by a change in slope of *ρ(T)* at T_C for the disordered $La_{0.5}Ba_{0.5}CoO_3$ (Figure 19a), or by a flat maximum at T_C for the ordered $LaBaCo_2O_6$ (Figure 19b). Thus, these results show that irrespectively of their structural nature, the different forms of cobaltites exhibit a *FM* metallic behavior below T_C. Moreover, both phases depict an upturn in the resistivity behavior at low temperature. This feature is interpreted as a weak localization contribution associated with electron-electron interaction. In the present case, the magnetoresistance measurements, that will be discussed later, suggest that the upturn is rather due to grain boundary effects.

It is now important to discuss about the oxygen deficient ordered cobaltites $LaBaCo_2O_{5.5}$, which have been of great interest due to their rich physical properties and interesting structural phenomena associated with them. In these phases the oxygen stoichiometry is *"5.5"*, hence the average valency of cobalt ion is Co^{3+} unlike the presence of mixed valences in the other two phases. This is particularly interesting because of the ordering of Co^{3+} ions in two different crystallographic sites corresponding to pyramidal and octahedral oxygen coordination as discussed earlier. The magnetization and susceptibility curves versus temperature, *M (T)*, measured in the range *10-400 K*, under external fields between *0.01* and *5 T* (Figure 20) were reported recently by *Rautama et al.* [16] to be similar to those previously observed for other lanthanides [3, 14]. In the whole temperature range the system exhibits several magnetic transitions from *PM* to *FM*-like to antiferromagnetic as the temperature decreases from *400 K* to *10 K*. The sudden increase of the magnetic susceptibility at $T_C = 326$ *K* indicates a *PM/FM* transition and a sharp decrease in the magnetization at $T_N = 295$ *K* indicates a *FM/AFM* transition. The interactions between Co^{3+} ions, both in pyramidal and octahedral coordination, are found to be *AFM* at low temperature. Moreover, the thermomagnetic irreversibility between *ZFC* and *FC* in the low temperature *AFM* state remains well discernible even at higher field ($H \geq 5$ *T*). It is reported that a high field basically affects the *FM-AFM* competition, which in turn suppresses the magnetization drop below the T_N. Thus, with increasing the external magnetic field, the *FM* state ($260\ K \leq T \leq 326\ K$) becomes more stable (indeed T_C increases and the *FM* region expands in the temperature scale), but T_N shifts to lower temperature. In the *AFM* phase, the nonzero value of magnetization down to low temperature signifies the presence of some kind of *FM*-like

interactions, where some weak magnetic transition is evidenced. Inset of Figure 20 depicts the inverse magnetic susceptibility versus temperature plot in the temperature range of *220-400 K*. This follows a simple *Curie-Weiss* behavior in the $335\ K \leq T \leq 400\ K$ range giving a *PM Weiss* temperature (θ_p) of ~ *-290 K* and an effective *PM* magnetic moment (μ_{eff}) of *5.27* μ_B*/f.u.* The large negative θ_p value for ordered $LaBaCo_2O_{5.5}$ sample indicates the existence of *AFM* type interactions in the high temperature region. The obtained μ_{eff} value (*5.27* μ_B*/f.u.*) from the high temperature region magnetic data corresponds to a situation where the Co^{3+} ions are most probably in the *IS* state, which corroborate the results of *NPD* [16]. The sharp drop in inverse susceptibility near T_C, is similar to that observed for $YBaCo_2O_{5.5}$ and $GdBaCo_2O_{5.5}$ [21, 24].

The *FM*-like features below T_C ~ *326 K*, have been confirmed by the magnetic field dependent isotherm magnetization, *M(H)*, studies at six different temperatures as shown in Figure 21. The *M(H)* curve at *300 K* shows a prominent hysteresis loop with a remanent magnetization, M_r, and a coercive field, H_C, values of *0.02* μ_B*/f.u* and *0.1T* respectively, indicating a *FM*-like state below T_C. Nevertheless, the maximum value of the magnetic moment measured in *5T* (*0.23*μ_B*/f.u.*) at *275 K* is much smaller than the theoretical spin-only value (*4*μ_B*/f.u.*) of Co^{3+} in *IS* state. Therefore, the *FM*-like behavior of this compound is most probably due to the canting of the magnetic spin alignment in the *AFM* phase, often observed in other systems [14]. Although there are some controversies in the literature to explain these *FM*-like features, yet this behavior is prominent for this ordered cobaltite and subject to further investigations. It is worth pointing out that at low temperature in the *AFM* state, some *FM*-like phase is still present as evidenced from the *M(H)* behavior, with a finite value of the coercive field. Interestingly, the highest moment of *0.23* μ_B*/f.u.* (at *275 K*) and highest coercive field value of *0.4 T* (at *245 K*) are obtained in the *AFM* region compared to the values of *0.16* μ_B*/f.u.* and *0.1 T* in the *FM* region (at *300 K*). For comparison the H_C values have been re-plotted for lower fields at *245* and *300 K* in the inset of Figure 21. The H_C values in the *AFM* region (*275-200 K*) are larger than in the *FM* region and finally at *10 K*, the *M(H)* behavior becomes linear akin to *AFM* state.

Figure 22 shows *ρ(T)* for $LaBaCo_2O_{5.5}$ in the temperature range of *10-400 K* (re-plotted *M(T)* for comparison), which is plotted for heating and cooling cycle of the measurements in the presence and absence of the external magnetic field of 7 T. The zero field *ρ(T)* curve shows a significant change in slope corresponding to the semiconductor-semiconductor transition (T_{SC}) around *326 K* (Figure 22a). This type of transition is previously reported for the other series of $LnBaCo_2O_{5.5}$ [14, 24, 26], and referred to as T_{IM} albeit the true nature of this transition is semiconducting to semiconducting type. For $LaBaCo_2O_{5.5}$ system, in contrast to a metallic behavior, the slope of the resistivity curve ($d\rho/dT$) is negative above the transition temperature ($T > T_{SC}$). Furthermore, for $LaBaCo_2O_{5.5}$ there is absence of any significant change in the resistivity behavior through out the temperature range, apart from a slight decrease in the magnitude below T_{SC}. It is noticed that, the electronic and magnetic transition temperatures for $LaBaCo_2O_{5.5}$ are almost the same (T_C & $T_{SC} \approx 326\ K$), in contrast to other ordered cobaltites $LnBaCo_2O_{5.5}$, which exhibit a large shift between them [14, 24, 26, 27]. Hence, the sample is magnetic-semiconductor below T_{SC} and the resistivity increases exponentially with decreasing temperature.

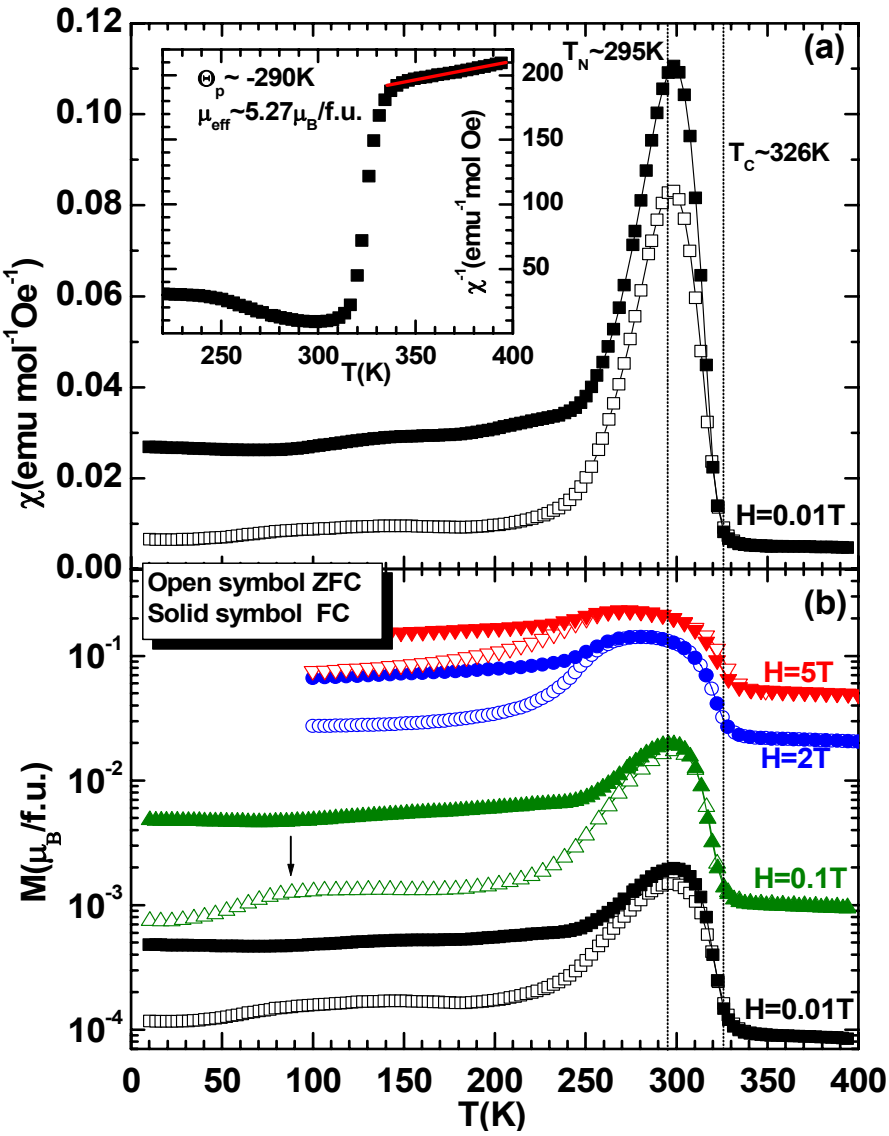

Figure 20. Temperature dependent ZFC (open symbol) and FC (solid symbol) Magnetization behavior of ordered $LaBaCo_2O_{5.5}$; (a) magnetic susceptibility, χ, under H=0.01 Tesla (inset figure shows the inverse magnetic susceptibility, χ^{-1}, versus temperature plot and solid line is Cuire-Weiss fitting) and (b) Magnetic moment in different magnetic fields (H=0.01, 0.1, 2 and 5 Tesla).

In general, the semiconductor or insulator like transport properties in perovskite cobaltites were characterized by three possible models [11, 25] namely thermal activation (*TA*): $log\ \rho\ \alpha\ 1/T$, *Efros-Shklovskii* type hopping (*ESH*): $log\ \rho\ \alpha\ T^{1/2}$ and *Mott's* variable range hopping (*VRH*): $log\ \rho\ \alpha\ T^{1/4}$. To understand the transport mechanism for $LaBaCo_2O_{5.5}$, the data have been analyzed based on these models. The zero field resistivity data is plotted in Figure 23a, which shows that the *VRH* model fits better than the other two models in $40\ K \leq T \leq 270\ K$ range, and is consistent with the preceding studies on perovskite cobaltites [11, 25]. This type of transport mechanism is typical for disordered systems as shown in Figure 23b, where the charge carrier's move by hopping between localized states [11]. *Taskin et al* [26]

have described the formation of localized states in terms of oxygen defects in *112*-type ordered $GdBaCo_2O_{5.5}$, which inevitably generate electrons or holes in the CoO_2 planes. Furthermore, we consider *ESH* and *TA* models, which are expected to describe the dominant conduction process. The transport mechanism is very complicated in the whole temperature region and does not satisfy entirely any of the above models for $LaBaCo_2O_{5.5}$. From the nearly linear region of the *TA* model ($\leq 250\ K$) we have calculated the approximate activation energy (E_a) of around *21 meV*, yet less than the value reported for $GdBaCo_2O_{5.5}$ [26].

The magnetoresistance (*MR*) behavior of the stoichiometric ordered-disordered phases (Figure 24) shows a clear magnetic field dependent change in the resistivity below T_C. The *MR* value is calculated as $MR\ (\%) = [\{\rho(7)-\rho(0)\}/\rho(0)]x100$, where $\rho(0)$ is the sample resistivity at *0 T* and $\rho(7)$ under an applied field of $\pm 7\ T$. For the disordered $La_{0.5}Ba_{0.5}CoO_3$ (Figure 24a), the maximum *MR* value is obtained around T_C and the corresponding value is indeed *7 %* at *179 K*. The ordered $LaBaCo_2O_6$ exhibits (Figure 24b) a rather close value of *6 %* around T_C (at *179 K)*. But importantly, the ordered $LaBaCo_2O_6$ depicts an *MR* value up to *14.5%* at *10 K* in an applied field of $\pm 7\ T$ which is much larger than an *MR* value of *4%* at the same temperature (*10 K*) for the disordered phase. This difference suggests that at low temperature ($T < 50\ K$), the grain boundary effect plays an important role in the anisotropic *MR* behavior for the ordered $LaBaCo_2O_6$ perovskite. This is in agreement with its much larger upturn of resistivity, which is almost *10* times larger (at *10 K*) than the disordered $La_{0.5}Ba_{0.5}CoO_3$ cobaltites. Thus, the larger *MR* observed for the ordered $LaBaCo_2O_6$ is interpreted as tunnelling magnetoresistance (*TMR*) effect due to the increase of the intergrain insulating barriers [28], rather than an intrinsic effect, and is dominant at *10 K* over the *TMR* effect for the disordered phase. Therefore the spin-polarized tunnelling of carriers across the insulating boundaries occurring at the interfaces between polycrystalline grains give rise to the *TMR* effect in these phases. Figure 25, shows the *MR* effect for ordered $LaBaCo_2O_{5.5}$ at five different temperatures. Unfortunately, in the case of temperature dependent resistivity data (with field), there is no major change in the $\rho(T)$ curve even though the *M(T)* behavior reveals some kind of *FM* and *AFM* ordering. The charge transport for this kind of system is expected to be very sensitive due to the co-existence of *FM* and *AFM* state and the external magnetic fields readily induces an *MR* effect by affecting the subtle balance between *FM-AFM* phases. Unlike, disordered $La_{0.5}Ba_{0.5}CoO_3$ and ordered $LaBaCo_2O_6$ cobaltites, the highest negative *MR* value is obtained at *245 K* around *5 %* in an applied field of *7 T* and near room temperature the value is only *1.6 %.* At low temperatures, the *MR* values are only *2.8 %* (at *150 K*) and *2.5 %* (at *50 K*) respectively. The evidence of negative MR at low temperatures, similar to the *TMR* observed usually in polycrystalline samples, in the case of ordered cobaltites, is considered to be related to the spin-dependent scattering at grain boundaries. Nevertheless, in the case of ordered $LaBaCo_2O_{5.5}$, the highest *MR* value is noticed near the *FM-AFM* phase boundary, hence the grain boundary effect can be ignored and considered to be as an intrinsic effect.

Interestingly, the isothermal *MR* behavior at *245 K* exhibits an irreversible effect analogous to those of isothermal magnetization, *M(H)*, behavior (inset Figure 25), also present in *300 K* isothermal *MR* data. The peak in the isothermal *MR* data occurs around the coercive field value, which corresponds to the state of maximum disorder in the orientation of the neighbouring magnetic spins.

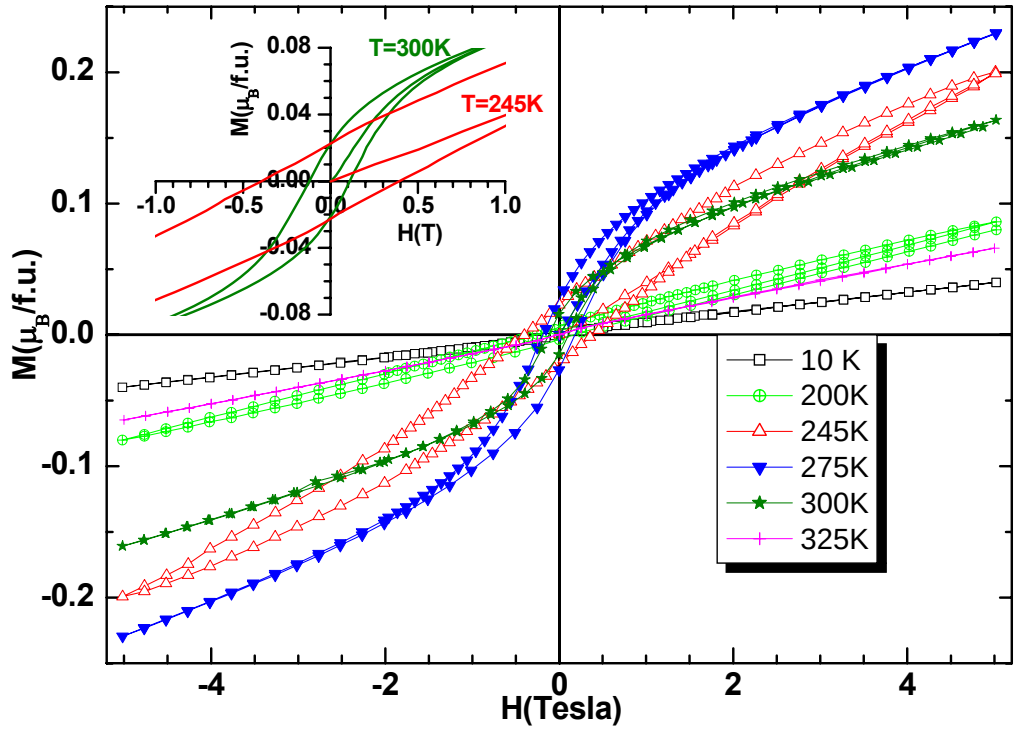

Figure 21. Magnetic field dependent isotherm magnetization, M(H), of ordered $LaBaCo_2O_{5.5}$ at six different temperatures. The inset figure shows the expanded version for lower magnetic fields at 245 and 300K (Taken from Ref. 25).

Hence, the field dependent *MR* data that is indirectly related to the alignment between magnetic spins, reaches a maximum value. This effect is prominent for *300 K* data, compared to *245 K* as evidenced from the inset Figure 25 (dotted vertical lines), which may be due to *FM*-like state near *300 K* whereas latter one corresponds to magnetic phase boundary. Additionally, the isothermal *MR* data exhibit hysteresis effects that resemble the "butterfly-like" feature, although the effect is rather weak at low temperature (*50 K*). It is clear from the obtained data that the *MR* effect is strongly irreversible near the *FM-AFM* phase boundary. The "butterfly-like" feature appears only near the magnetic phase boundary. Correspondingly, the magnetic field dependent isotherm *MR* behavior at *10 K* for stoichiometry ordered-disordered phases exhibits an anisotropic effect similar to those of the magnetization behavior. Nevertheless, the isotherm *MR* data at low temperature for all three phases exhibit hysteresis effects, which resemble the "butterfly-like" feature, although the effect is rather weak for the disordered phase. It is noticed that the *MR* effect is almost isotropic for temperatures near or above the T_C. Hence, the butterfly-like feature appears only at low temperatures, which is prominent for ordered $LaBaCo_2O_{5.5}$ and $LaBaCo_2O_6$ phases. The origin of the magnetic field induced maximum *MR* near T_C for the disordered $La_{0.5}Ba_{0.5}CoO_3$ and ordered $LaBaCo_2O_6$ are explained by the mechanism of suppression of spin fluctuations below T_C. On the other hand, the highest obtained *MR* value, obtained at *10 K* for the ordered $LaBaCo_2O_6$ is explained by the *TMR* effect due to the presence of more insulating grain boundaries. Hence, the occurrence of irreversible *MR* behavior nearly at similar temperatures

as those for magnetic field variation isothermal *M(H)* studies suggest the strongly correlated nature of field-induced magnetic and electronic transitions [12, 25].

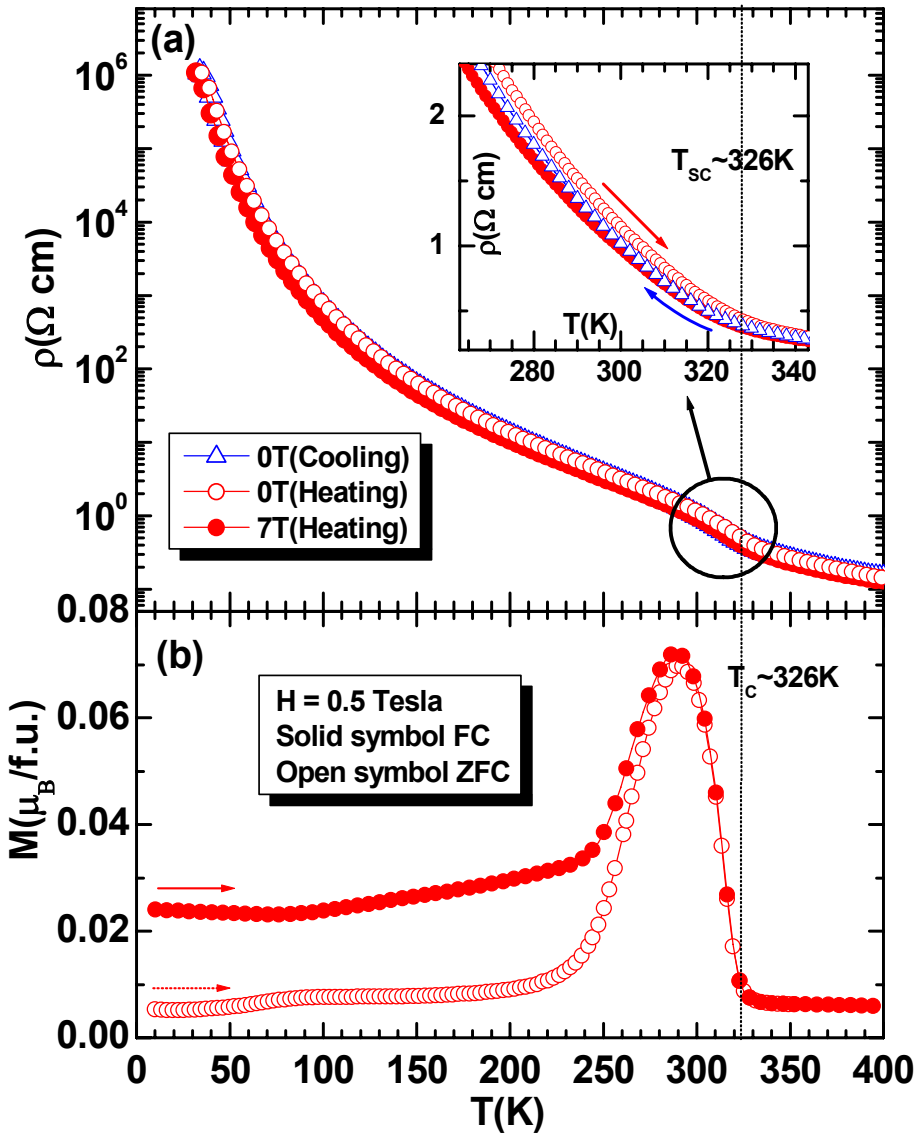

Figure 22. Temperature dependent physical properties for ordered $LaBaCo_2O_{5.5}$: (a) electrical resistivity, ρ(T), in the presence (solid symbol) and absence (open symbol) of magnetic field (7 Tesla) during heating and cooling cycles (inset shows the expanded version near the transition temperature, T_{IM}), and (b) ZFC (open symbol), FC (solid symbol) Magnetization in an applied field of 0.5 Tesla (Taken from Ref. 25).

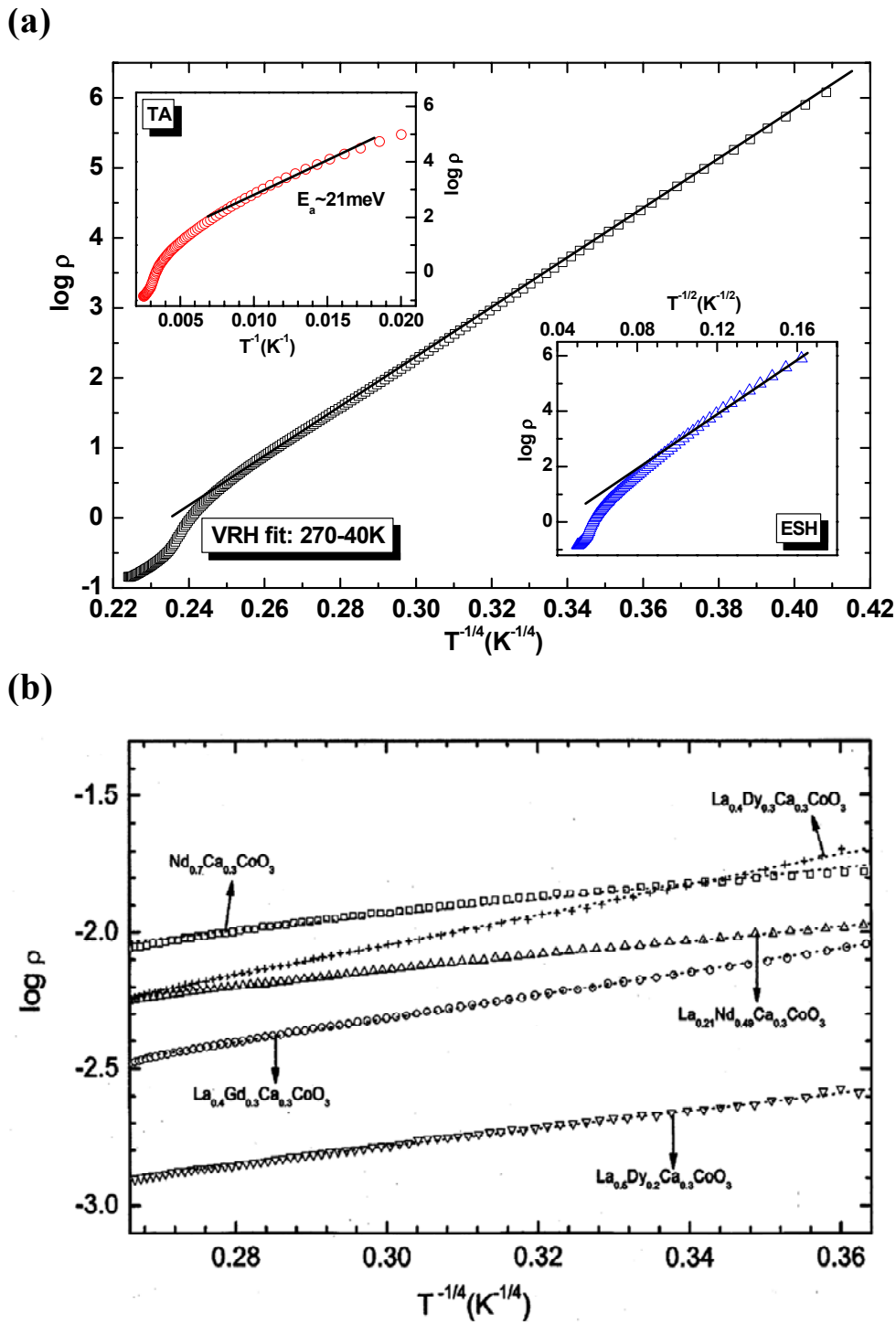

Figure 23. Logarithm of the resistivity versus $T^{-1/n}$ plots for (a) ordered $LaBaCo_2O_{5.5}$ and (b) disordered $Ln_{0.7}Ca_{0.3}CoO_3$ cobaltites (where n = 1, 2 or 4): open symbols and solid lines represent the experimental data and apparent fit to the hopping models as described in the text (Taken from Ref. 11 & 25).

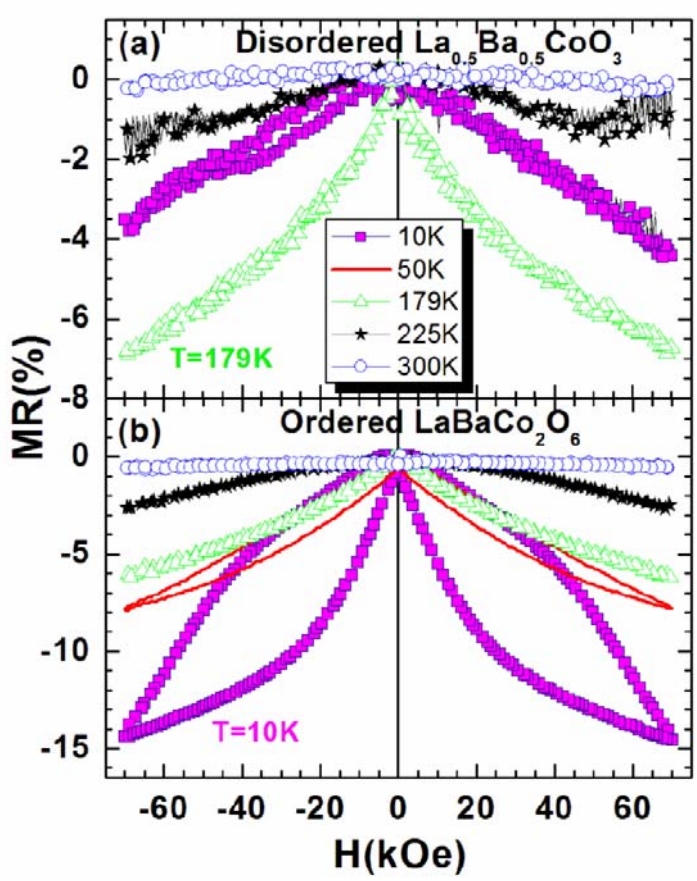

Figure 24. Temperature variation marnetoresistance for (a) disordered $La_{0.5}Ba_{0.5}CoO_3$ (b) ordered $LaBaCo_2O_6$ cobaltites (Taken from Ref. 12).

In order to get more insight into the nature of the conduction mechanism below T_{SC}, we have also discussed the thermopower (*Seebeck* coefficient), *S(T)*, and thermal conductivity, *κ(T)*, measurements for ordered $LaBaCo_2O_{5.5}$. These are sensitive to the magnetic and electrical nature of charge carriers (hole/electron) and can give some valuable information, which are absent in the magnetotransport measurements. Additionally, the *S(T)* data is less affected due to the presence of grain boundaries, which often complicates the *ρ(T)* data interpretation for polycrystalline samples. We noticed that, at room temperature the system shows a relatively large positive value of the thermoelectric power (*91 μV/K)*, while it has a low resistivity (*~1.14 Ω cm* at *300 K*). The *S(T)*, for cooling and heating cycles is shown in Figure 26. It is observed that, the *S(T)* value is positive below T_{SC} and with decreasing temperature the value increases gradually and reaches a maximum value of *~303 μV/K* at around *120 K* (marked by an arrow in the figure). Below that, the *S(T)* value decreases continuously and similar to the literature behaviors (i.e. for $NdBaCo_2O_{5.5}$, $GdBaCo_2O_{5.5}$ and $HoBaCo_2O_{5.5}$ the peak values are *105, 88* and *70 K* respectively [26, 27]).

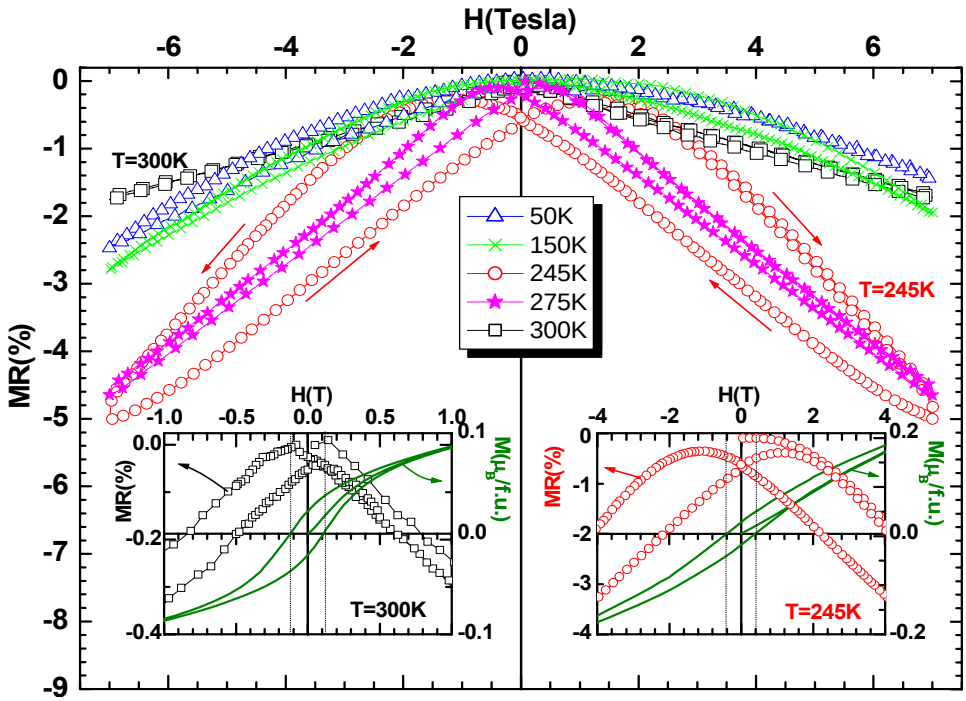

Figure 25. Magnetic field dependent isotherm magnetoresistance, MR, effect for ordered $LaBaCo_2O_{5.5}$ at five different temperatures (H= ±7 Tesla). Inset figures show the isotherm magnetization, M(H), and MR plot at 245 and 300 K for comparison (Taken from Ref. 25).

The *S(T)* data implies that the $LnBaCo_2O_{5.5}$ systems show a semiconducting type behavior of the thermopower down to low temperature akin to resistivity behavior and below the *S(T)* behavior is complex, decreasing abruptly at low temperature. In fact, with decreasing temperature the *S(T)* value should increase due to trapping or localization of charge carriers. This type of *S(T)* behavior is quite unexpected for semiconducting thermoelectric materials and there is no general explanation till date. Following the general approach in analyzing the semiconducting behavior we have plotted the *S(T)* data in the $T^{1/n}$ scale similar to $\rho(T)$. Since for semiconductors the *S(T)* is expected to be linear in T^1 behavior (according to *TA* model) or to follow either of the described hopping models similar to resistivity behavior [11, 25]. It is noticed that the *S(T)* data can not be described by the previous mentioned models and one observes *p*-type conductivity throughout the temperature range. Many authors have already explained the *S(T)* behavior at higher temperature and their sign reversal near the electronic transition [26, 27]. However, the low temperature *S(T)* evolution, basically the appearance of the broad maximum in the metastable *AFM* phase and the decreasing nature with temperature (in spite of semiconducting behavior) has not been explained properly. We have analysed the obtained thermopower data using an expression $S(T) = S_0 + S_{3/2}T^{3/2} + S_4T^4$ defined by *P. Mandal* [29], which can be understood on the basis of electron magnon scattering (spin wave theory). In ferro- and antiferromagnets, electrons are scattered by spin wave as explained earlier for perovskite manganites [29] and hence it is expected that this theory may explain the *S(T)* behavior for the present system. However, the obtained thermopower value is higher than the one reported for manganites. The *S(T)* data in $60\ K \square T \square 105\ K$ range follows $T^{3/2}$ behavior and in the *120-320 K* range, it fits linearly with the T^4 behavior (insets of Figure 26).

At low temperature the second term ($S_{3/2}$) will dominate over S_4 ($S_{3/2}>>S_4$), hence the *S(T)* will depict downward trend at low temperature. Although we do not have sufficient experimental data points below the broad peak, yet the *S(T)* curve fits linearly to the $T^{3/2}$ term (inset of Figure 26b), as expected from the spin wave theory. Additionally, the downward feature in *S(T)* data is present in all studied $LnBaCo_2O_{5.5}$ cobaltites [25-27]. Hence, the broad peak at low temperature and downward trends for layered cobaltites are considered to be the result of the electron magnon scattering akin to perovskite manganite as explained by *P. Mandal* [29].

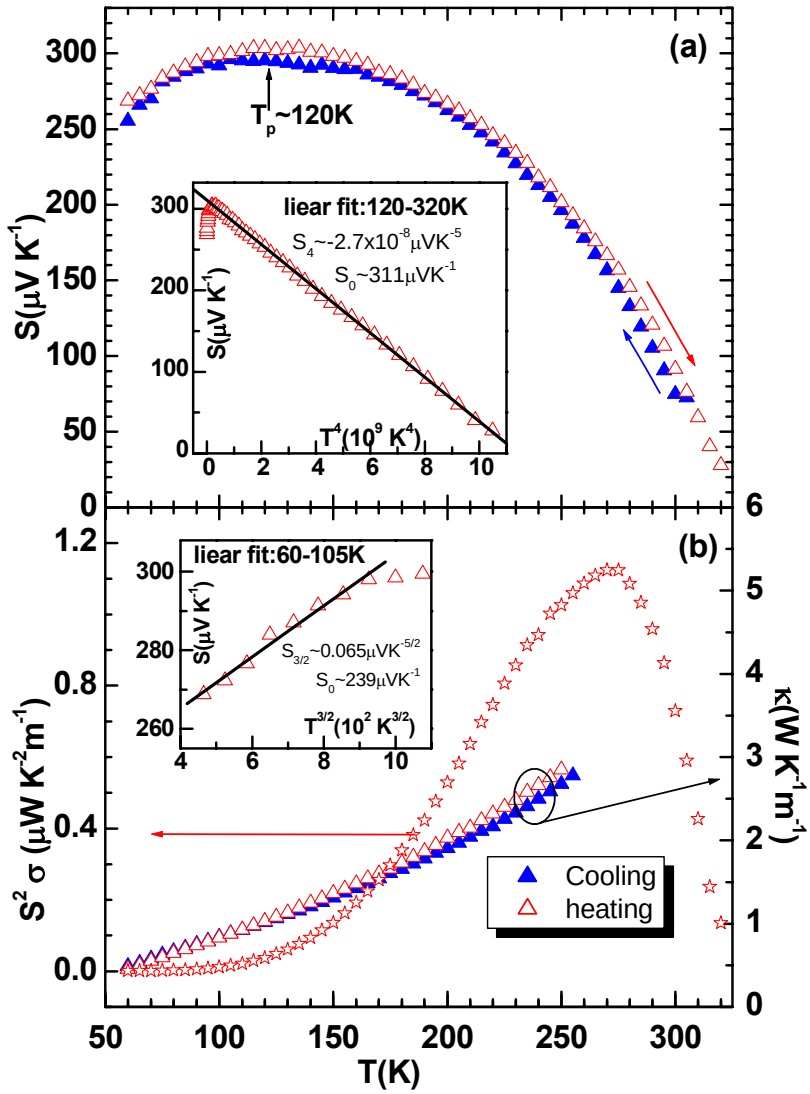

Figure 26. Temperature dependent transport measurements for ordered $LaBaCo_2O_{5.5}$: (a) thermoelectric power, S(T), during cooling (solid triangle) and heating (open triangle) cycles and inset shows the S-T^4 plot in the 120-320K range, (b) thermal conductivity, κ(T), and power factor, $S^2\sigma(T)$, in the temperature range of 60-320K (inset shows the S-$T^{3/2}$ plot in the 60-105K range) (Taken from Ref. 25).

Thermal conductivity, $\kappa(T)$, measurements of $LaBaCo_2O_{5.5}$ during cooling and heating cycles are shown in Figure 26b. The $\kappa(T)$ value increases with increasing temperature, indicating an usual phonon mediated scattering mechanism of charge carriers, which is the sum of phonon (κ_p) and electronic (κ_e) contribution [*i.e.* $\kappa(T) = \kappa_p(T) + \kappa_e(T)$]. Therefore, from the *Wiedemann-Franz* law we have calculated the electronic contribution (κ_e) at *250 K*, which is around $\sim 1.5x10^{-4}\ WK^{-1}m^{-1}$ [whereas $\kappa(250\ K) \sim 2.8\ WK^{-1}m^{-1}$]. This implies that, the lattice modulated phonon contribution (κ_p) is dominant near room temperature *i. e.* $\kappa_p(T) >> \kappa_e(T)$. We have also calculated the temperature dependence of power factor ($S^2\sigma$) from the obtained resistivity and thermopower data as shown in Figure 26b, which depicts a clear maximum near *270 K* and decreases rapidly on both sides of the temperature scale ($60K \leq T \leq 320K$). It is important to note that, this maximum is in the region of *FM-AFM* phase boundary. This suggests that the electron magnon scattering at low temperature strongly affects the *S(T)* behavior of $LaBaCo_2O_{5.5}$ system. The calculated figure of merit (*ZT*) shows too small values close to room temperature ($\sim 10^{-5}$) for applications as expected from 112-type cobaltite systems.

CONCLUSION

The discussion in the earlier sections clearly brings out the varied effects of magnetization, magneto-transport properties, electronic phase separation, thermopower etc, in the ordered-disordered rare earth cobaltites. This paper shows that the method of synthesis – precursor reactivity and oxygen pressure – plays a crucial role for controlling the cationic order-disorder phenomena in the non-stoichiometry ordered $LaBaCo_2O_{5.5}$ and the stoichiometric disordered $La_{0.5}Ba_{0.5}CoO_3$ and ordered $LaBaCo_2O_6$. From the viewpoint of the transport properties, the ordered $LaBaCo_2O_{5.5}$ is semiconducting throughout and the disordered $La_{0.5}Ba_{0.5}CoO_3$ exhibits a semi-metal to metal transition around T_C, whereas the layer-ordered $LaBaCo_2O_6$ is characterized by semi-conductor to metal transition around T_C. As a consequence, they exhibit a similar intrinsic magnetoresistance, maximum at the vicinity of T_C (*6* to *7 %*), whereas the ordered $LaBaCo_2O_6$ exhibits a much larger *MR* value, indicating *TMR* at low temperature due to different grain boundary effects. It appears that the phenomenon is much more common than anticipated, to the extent that some workers suggest that even the physical properties of these cobaltites, showing different types of interesting behavior, is a consequence of cationic ordering. It is noteworthy that the large thermopower value caused by lowering temperature in ordered $LaBaCo_2O_{5.5}$ may indeed be due to semiconducting behavior. The unusual *S(T)* behavior and the appearance of a broad peak at low temperature with a maximum value of $\sim 303\ \mu V/K$ is explained by electron magnon scattering mechanism. This is expected to be applicable to all series of $LnBaCo_2O_{5.5}$ cobaltites at low temperature. It would be worthwhile to study the relevance of this phenomenon to other transition metal oxide systems.

ACKNOWLEDGMENTS

AKK gratefully acknowledges Prof. A. Ojha, Director of IIITDM-J, for sanctioning faculty research grant.

REFERENCES

[1] Rao C. N. R.; B. Raveau (Eds.), Colossal Magnetoresistance, Charge-Ordering and Related Properties of Manganese Oxides, World Scientific, Singapore, 1998; Dagotto E., Nanoscale Phase Separation and Colossal Magnetoresistance: The Physics of Manganites and Related Compounds, Springer-Verlag, Berlin, New York, 2003; Rao, C. N. R.; Kundu, A. K.; Seikh, M. M.; Sudheendra, L. *Dalton Trans.* 2004, *19*, 3003.

[2] Jonker, G. H.; van Santen, J. H.; *Physica* 1953, *19*, 120; Goodenough, J. B. *J. Phys. Chem. Solids* 1958, *6*, 287; Jonker, G. H. *J. Appl. Phys.* 1966, *37*, 1424.

[3] Martin, C.; Maignan, A.; Pelloquin, P.; Nguyen, N.; Raveau, B. *Appl. Phys. Lett.* 1997, *71*, 1421.

[4] Teraoka Y.; Nobunaga T.; Okamoto K.; Miura N.; Yamazoe N. *Solid State Ionics* 1991, *48*, 207; Kruidhof H.; Bouwmeester H. J. M.; van Doorn R. H. E.; Burggraaf A. J. *Solid State Ionics* 1993, *63*, 816; van Doorn R. H. E.; Burggraaf A. J. *Solid State Ionics* 2000, *128*, 65; Kim, G.; Wang, S.; Jacobson, A. J.; Reimus, L.; Brodersen, P.; Mims, C. A. *J. Mater. Chem.* 2007, *17*, 2500.

[5] Takada K.; Sakurai H.; Takayama-Muromachi E.; Izumi F.; Dilanian R.; Sasaki T. *Nature* 2003, *422*, 53.

[6] Itoh M.; Natori I. ; Kubota S.; Matoya K. *J. Phys. Soc. Jpn.*1994, *63***,** 1486; Anil Kumar P. S. ; Joy P. A. ; Date S. K. *J. Phys.: Condens. Matter* 1998, *10*, L487; Nam, D. N. H.; Jonason, K.; Nordblad, P.; Khiem, N. V.; Phuc, N. X.; *Phys. Rev. B*, 1999, *59*, 4189; Kuhns, P. L.; Hoch, M. J. R.; Moulton, W.G.; Reyes, A. P.; Wu, J.; Leighton, C. *Phys. Rev. Lett.* 2003, *91*, 127202; Burley, J. C.; Mitchell, J. F.; Short, S. *Phys. Rev. B* 2004, *69*, 054401; Troyanchuk, I. O.; Kasper, N. V.; Khalyavin, D. D.; Szymczak, H.; Szymczak, R.; Baran, M. *Phys. Rev. Lett.*1998, *80*, 3380.

[7] Mahendiran, R.; Raychaudhuri, A. K. ; Chainani, A. ; Sarma, D. D. *J. Phys.: Condens. Mater.* 1995, *7*, L561; Mahendiran, R.; Raychaudhuri, A. K. *Phys. Rev. B* 1996, *54*, 16044.

[8] Fauth, F.; Suard, E.; Caignaert, V. *Phys. Rev. B* 2001, *65*, 60401.

[9] Nakajima, T.; Ichihara, M.; Ueda, Y. *J. Phys. Soc. Jpn.* 2005, *74*, 1572.

[10] Wu, J.; Lynn, J.W.; Glinka, C.J.; Burley, J.; Zheng, H.; Mitchell, J.F.; Leighton, C. *Phys. Rev. Lett.* 2005, *94*, 037201.

[11] Kundu, A. K.; Ramesha, K.; Seshadri, R.; Rao, C. N. R. *J. Phys. Condens. Matter* 2004, *16*, 7955; Kundu, A. K.; Sampathkumaran, E. V.; Gopalakrishnan, K. V.; Rao, C. N. R. *J. Mag. Mag. Mater.* 2004, *281*, 261; Kundu, A. K.; Nordblad, P.; Rao, C. N. R. *Phys. Rev. B* 2005, *72*, 144423; Kundu, A. K.; Nordblad P.; Rao C. N. R.; *J. Solid State Chem.* 2006, *179*, 923.

[12] Rautama, E-L; Boullay, P.; Kundu, A. K.; Pralong, V.; Caignaert, V.; Karppinen, M.; Raveau, B. *Chem. Mat.* 2008, *20*, 2742.

[13] Rao, C. N. R.; Bhide, V. G.; Mott, N. F. *Phil. Mag.* 1975, *32*, 1277; Bhide, V. G.; Rajoria, D. S.; Rao, C. N. R.; Rao, G. R.; Jadhao, V. G. *Phys. Rev. B* 1975, *12*, 2832; Rao, C. N. R.; Prakash, O.; Bahadur, D.; Ganguly, P.; Nagabhushana, S. *J. Solid State Chem.* 1977, *22*, 353; Senaris-Rodriguez, M.A.; Goodenough, J.B. *J. Solid State Chem.* 1995, *118*, 323; Moritomo, Y.; Takeo, M.; Liu, X. J.; Akimoto, T.; Nakamura, A. *Phys. Rev. B* 1998, *58*, R13334; Troyanchuk, I.O.; Kasper, N.V.; Khalyavin, D.D.; Szymczak, H; Szymczak, R.; Baran, M. *Phys. Rev. B* 1998, *58*, 2418; Vanitha, P. V.; Arulraj, A.; Santosh, P. N.; Rao, C. N. R. *Chem. Mater.* 2000, *12*, 1666; Ganguly, R.; Maignan, A.; Martin, C.; Hervieu, M.; Raveau, B. *J. Phys.: Condens. Matter* 2002, *14*, 8595.

[14] Maignan A, Martin C, Pelloquin D, Nguyen N and Raveau B *J. Solid State Chem.* 1999, *142*, 247; Moritomo, Y.; Akimoto, T.; Takeo, M.; Machida, A.; Nishibori, E.; Takata, M.; Sakata, M.; Ohoyama, K.; Nakamura, A. *Phys. Rev. B* 2000, *61*, R13325; Roy, S.; Khan, M.; Guo, Y. Q.; Craig, J.; Ali, N. *Phys. Rev. B* 2002, *65*, 064437; Burley, J. C.; Mitchell, J. F.; Short, S.; Miller, D.; Tang, Y. *J. Solid State Chem.* 2003, *170*, 339; Roy, S.; Dubenko, I. S.; Khan, M.; Condon, E. M.; Craig, J.; Ali, N. *Phys. Rev. B* 2005, *71*, 024419; Pralong, V.; Caignaert, V.; Hebert, S.; Maignan, A.; Raveau, B. *Solid State Ionics* 2006, *177*, 1879; Seikh, M. M.; Simon, C.; Caignaert, V.; Pralong, V.; Lepetit, M. B.; Boudin, S.; Raveau, B. *Chem. Mat.* 2008, *20*, 231.

[15] Vogt, T.; Woodward, P. M.; Karen, P.; Hunter, B. A.; Henning, P.; Moodenbaugh, A. R. *Phys. Rev. Lett.* 2000, *84*, 2969; Suard, E.; Fauth, F.; Caignaert, V.; Mirebeau, I.; Baldinozzi, G. *Phys. Rev. B* 2000, *61*, R11871.

[16] Rautama, E-L.; Caignaert, V.; Boullay, P.; Kundu, A. K.; Pralong, V.; Karppinen, M.; Ritter, C.; Raveau, B.; *Chem. Mat.* 2009, *21*, 102.

[17] Rodriguez-Martinez, L. M.; Attfield, J. P. *Phys. Rev. B* 1996, *54*, R15622; Attfield, J. P. *Chem. Mater.* 1998, *10*, 3239.

[18] Kundu, A. K.; Rao, C. N. R. *J. Phys.: Condens. Matter* 2004, *16*, 415; Kundu, A. K.; Sampathkumaran, E. V.; Rao, C. N. R. *J. Phys. Chem. Solids* 2004, *65*, 95.

[19] Kundu, A. K.; Sarkar, R.; Pahari, B.; Ghoshray A.; Rao C. N. R. *J. Solid State Chem.* 2007, *180*, 1318 and references therein.

[20] Millange, F.; Caignaert, V.; Domengès, B.; Raveau, B.; Suard, E. *Chem. Mater.* 1998, *10*, 1974.

[21] Akahoshi, D.; Ueda, Y. *J. Solid State Chem.* 2001, *156*, 355.

[22] Abbate, M.; Fuggle, J. C.; Fujimori, A.; Tjeng, L. H.; Chen, C. T.; Potze, R.; Sawatzky, G. A.; Eisaki, H.; Uchida, S. *Phys. Rev. B* 1993, *47*, 16124; Korotin, M. A. ; Ezhov, S. Y. ; Solovyev, I. V. ; Anisimov, V. I.; Khomskii, D. I.; Sawatzky, G. A. *Phys. Rev. B* 1996, *54*, 5309; Wu, H. *Phys. Rev. B* 2000, *62*, R11953.

[23] Zener, C. *Phys. Rev.* 1951, *82*, 403; Goodenough, J. B.; Wold, A.; Arnott, R. J.; Menyuk, M. *Phys. Rev.* 1961, *124*, 373.

[24] Taskin, A. A.; Lavrov, A. N.; Ando, Y. *Phys. Rev. Lett* 2003, *90*, 227201.

[25] Kundu, A. K.; Raveau, B.; Caignaert, V., Rautama, E-L.; Pralong, V. *J. Phys.: Condens. Matter* 2009, *21*, 056007.

[26] Taskin, A. A.; Lavrov, A. N.; Ando, Y. *Phys. Rev. B* 2005, *71*, 134414; Taskin, A. A.; Lavrov, A. N.; Ando, Y. *Phys. Rev. B* 2006, *73*, R121101.

[27] Maignan, A.; Caignaert, V.; Raveau, B.; Khomskii, D.; Sawatzky, G. *Phys. Rev. Lett.* 2004, *93*, 26401.

[28] Niebieskikwiat, D.; Prado, F.; Caneiro, A.; Sanchez, R. D. *Phys. Rev. B* 2004, *70*, 132412.
[29] Mandal, P. *Phys. Rev. B* 2000, *61*, 14675.

In: Perovskites: Structure, Properties and Uses
Editor: Maxim Borowski, pp. 251-282
ISBN 978-1-61668-525-6

Chapter 5

ELECTRICALLY TUNABLE DIELECTRIC AND CONDUCTION PROPERTIES IN PEROVSKITE THIN FILMS

Yidong Xia*, Xiangkang Meng and Zhiguo Liu
Department of Materials Science and Engineering, and National Laboratory of Solid State Microstructures, Nanjing University, Nanjing 210093, People's Republic of China

ABSTRACT

Perovskite thin films are widely employed in today's advanced technology. The broad range of physical properties in such category of materials has offered various functionalities in devices ranging from dynamic random access memories and ferroelectric nonvolatile memories to piezoelectric and optical devices. In addition to the aforementioned applications, perovskites have been revealed to be promising candidate materials in many novel applications including electrically tunable microwave devices and resistive switching memories. Thin films of the perovskite ferroelectrics are being used to develop the tunable microwave devices owing to their strong electric field dependent dielectric constant in the paraelectric state. Reversible switching between high- and low- resistance states induced by electric field makes perovskite thin films suitable for the applications in resistive switching memories. This chapter focuses on our recent progress on these two kinds of electrically tunable properties in perovskite thin films. Based on the origin of dielectric tunability that is defined as the variation of dielectric constant in a certain electric field range, approaches to improve the tunable dielectric properties will be introduced. On the other hand, although resistive switching behaviors have been discovered in many perovskites during the last decade, the origin of such switching is not well understood yet. In this chapter, some proposed mechanisms responsible for the resistive switching will be discussed.

* Author to whom correspondence should be addressed; electronic mail: xiayd@nju.edu.cn

I. DIELECTRIC TUNABLE PROPERTIES IN PEROVSKITE THIN FILMS BASED ON (BA,SR)TIO$_3$

In the last two decades, much attention has been paid to ferroelectrics thin films based on (Ba,Sr)TiO_3 (BST) and $SrTiO_3$ (STO) for their applications in high density dynamic random access memory because of its high dielectric constant ε [1]. With the development of these storage capacitor dielectrics for the memory applications, it has been revealed that such perovskites show strong electric-field dependent dielectric constant, where typically ε decreases with increasing field [2-4]. Such behavior is usually described by a quantity termed as tunability, which is defined as [5-7]

$$(\varepsilon_{\max} - \varepsilon_{\min})/\varepsilon_{\max} \tag{1}$$

to characterize the variation of dielectric constant in a certain electric field range. Here, $\varepsilon_{\max}$ is the maximum dielectric constant, generally obtained at zero applied bias, and $\varepsilon_{\min}$ is the minimum dielectric constant measured at the bias applied to the dielectrics. The field-dependent dielectric properties are essential in designing a new class of electrically tunable microwave devices, such as phase-shifters, tunable filters, and voltage-controlled oscillators [5-15].

Generally, the perovskite thin films are integrated in capacitor configuration for these applications. In most practical cases the tunability of the capacitance $T_C(V) = (C_{\max} - C_{\min})/C_{\max}$ rather than the tunability of dielectric constant $T_\varepsilon(V)$ defined by Eq. 1 is used to estimate the effective parameters of the materials [7]. Two capacitor structures are usually employed [13]. One is the sandwich-type with parallel-plate electrode, i.e. a layer of ferroelectric thin film sandwiched between two electrodes (metal or conducting oxide electrodes). The other is the planar capacitor with interdigital electrode, i.e. a gap between electrodes on the surface of a ferroelectric film. For sandwich-type capacitors $T_C(V)$ is approximately the same as $T_\varepsilon(V)$, while it is smaller than $T_\varepsilon(V)$ for planar capacitors. It has to be concerned for the planar capacitors that measured effective dielectric constant, tunability, and dielectric loss are often lower than those of the film itself [7]. This is because in planar structures, a considerable part of the field is outside the ferroelectric films and locates in the substrates. The field outside the ferroelectric layers with given film thickness depends on the gap between the planar electrodes, which makes the applied field inefficient to adjust the dielectric constant and higher control voltages are accordingly necessary to obtain the desired tunable parameters as compared with the sandwich capacitors. As a result, in general the sandwich-type capacitors are especially attractive in these electrically tunable devices although the planar capacitors are simpler to fabricate and integrate into circuits [7,13].

1. Thickness-dependent Dielectric Characteristics of Perovskite Thin Films

A critical issue as to the sandwich capacitors based on ferroelectric thin films is the thickness-dependence of dielectric properties. The development of portable and agile devices requires the reducing size of capacitor components. Unlike their predecessor, bulk ceramics, however, thin films show far lower effective dielectric constant and tunablity as what is expected [16-28]. The dielectric properties of ferroelectric thin films degrade with decreasing thickness, markedly in the case of metals used as the electrodes [16,17]. Several mechanisms have been proposed to account for the microscopic origin of this thickness dependence. Among them, the most employed one is the so-called interfacial "dead layer" model [17-19,24-28], which assumes the existence of an interfacial layer with low dielectric constant at film/electrode interface, acting as a smaller capacitance in series with the film bulk capacitance. The effective dielectric constant in thin film capacitors is usually experimentally derived from the measured capacitance density. Consequently, according to the principle of "dead layer" model, the reduction in effective dielectric constant can be expressed in terms of the limited overall capacitance density C as [28]

$$\frac{1}{C}=\frac{1}{C_i}+\frac{1}{C_b}+\frac{1}{C_i}, \tag{2}$$

where C_i and C_b stand for the low capacitance density of the electrode/film interfacial regions and the capacitance density of the bulk film, respectively.

But, the origins of such "dead layer" are not well understood yet. Debates focused on whether such dead layer exists at all, and if so, whether it is an intrinsic property as films contacted with electrodes or a result of processing issues such as defects and strains [28]. First-principles calculations, recently reported by Stengel and Spaldin, conjectured that excellent screening properties at the interface are crucial to reducing the dead layer [28]. They demonstrated the existence of a dielectric dead layer by calculating the dielectric profile across the interface and analyse its origin by extracting the ionic and electronic contributions to the electrostatic screening. They further predicted that metals, *e.g.* Pt, not the metallic oxide electrodes (*e.g.* $SrRuO_3$), should be the best candidates for reducing the dead layer, because of their shorter electronic screening length. Accordingly, the experimentally observed dielectric degradation with film thickness for Pt/BST/Pt structure is attributed to the structural mismatching or defects at interfaces.

Studies on the interfacial microstructure via high resolution transmission electron microscopy (HRTEM) have been performed to verify the existence of "dead layer" between BST films and Pt or $SrRuO_3$ electrodes. Formations of misfit dislocations, planar fault, and disordered or amorphous regions have been reported [19,27,29-33]. More recently, we have observed two distinct types of interfaces between BST films and Pt electrodes via HRTEM [34]. One case is the presence of interfacial layer with distorted structure (type I), as shown in Figure 1 (a). Another case, called type II, is exhibited in Figure 1 (b), in which good interfacial match with no interfacial layer is observed.

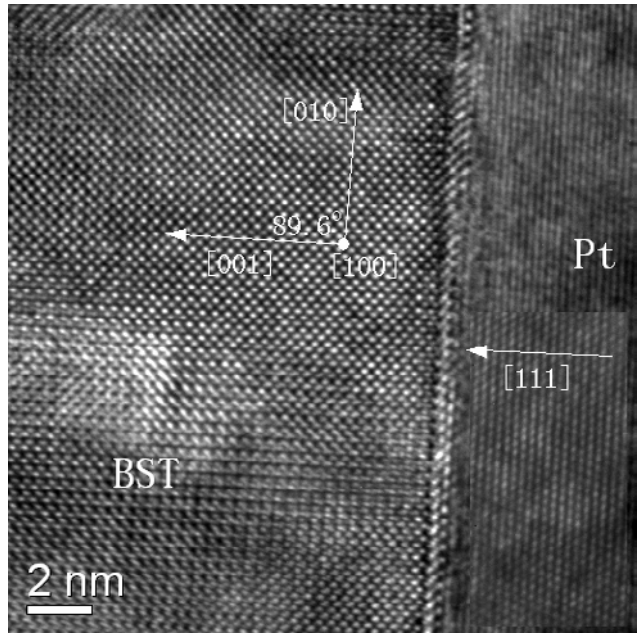

(a)

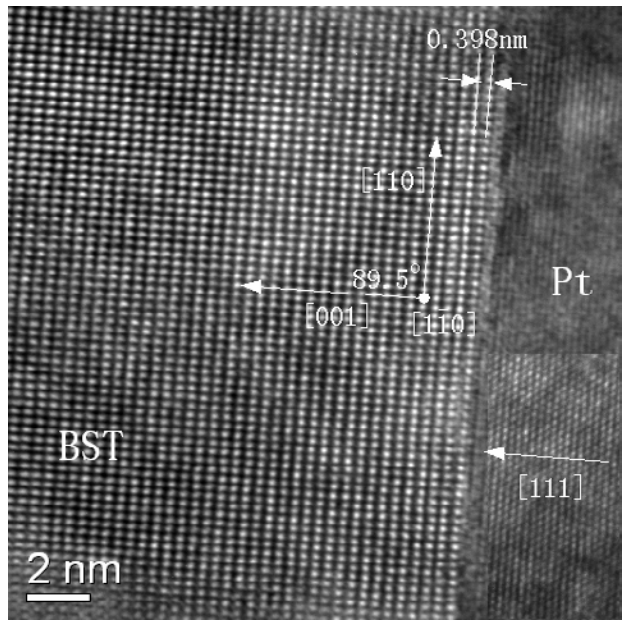

(b)

Figure 1. (Ref. [34])

The origin of such dissimilar interfaces has been analyzed based on the crystallographic relationships between BST and Pt. It is concluded that the atomic arrangement in the plane parallel to the interfacial plane plays an important role in determining the feature of the interfaces. For BST films, the directions perpendicular to the BST/Pt interfaces in the two cases are both determined to be [001], while for Pt electrodes the normal direction is [111], as illustrated in the insets in Figs. 1 (a) and (b). This indicates that the influence of the out-of-plane lattice constants is negligible due to the same mismatch of lattice constants between BST and Pt in the normal direction in these two cases. However, the BST orientations parallel

to the BST/Pt interfaces are dissimilar. For type I, the atomic arrangement is along the [010] direction, whereas [110] is the direction parallel to the interface for type II.

No amorphous areas at the interfaces can be detected in both Figs. 1 (a) and (b). The amorphous regions were demonstrated to be the Ti-excess amorphous phase compared with the BST film matrix [32]. The absence of such amorphous regions indicates that the effect of excess titanium caused by the deposition process can be ruled out. On the other hand, Yoo *et al.* reported that the crystallization of amorphous BST at the interfaces can distort the lattice structure during the annealing process [31]. By calculating the angle between [001] and [010] (89.6^o, for type I) and the angle between [001] and [110] (89.5^o, for type II), respectively, no distorted structure is observed in the regions approaching the BST/Pt interfaces for both samples. Along the [001] direction from the BST/Pt interfaces, the separation of the two planes next to the interface is consistent with the separation of the planes more far away from the interface. It is not the case reported by Jin *et al.* [27] In their work, the separation of the last two planes was observed to be much larger than those in the film bulk, which was attributed to Ruddlesden-Popper planar fault [35]. As a result, the above-mentioned effects cannot fit this case very well.

Taking into account the above discussions, the study on the origin of interfacial layer is hence focused on the relationships of the in-plane lattice structure between BST film and Pt. Pt is an elemental metal with *fcc* structure. A schematic representation of [111] projected lattice structure of Pt is shown in Figure 2 (a). The Pt atoms are arranged according to equilateral triangle lattice structure in Pt (111) plane. The atomic separation between the nearest neighbor Pt atoms is calculated to be 0.274 nm along the <110> direction. BST is a typical perovskite dielectric with ABO_3 structure. In such crystal structure, Ti ions are located at the body center (*B* site), each surrounded by six oxygen ions at the face centers to structure the oxygen octahedral, while the *A* site ions (Ba and Sr) occupy the corners. *A*-O planes alternate with *B*-O planes along <001> direction to form the BST crystal structure. Figure 2 (b) and (c) show the schematic diagram of [001] projected lattice structure of BST, depicting the *B*-O plane and the *A*-O plane, respectively. In *B*-O plane, *B* and O atoms are arranged along the <010> direction with the *B* atomic separation of 0.394 nm. In *A*-O plane, the *A* atomic separation is twice of the (110) interplanar distance that is determined to be 0.276 nm. For ABO_3 films, the first atomic plane grown onto the Pt can be either *A*-O plane or *B*-O plane, as demonstrated by the atomic resolution HAADF/STEM investigations [19]. So, it can be speculated that, if *B*-O plane is the first plane onto the Pt plane, according to the obtained atomic separations, the two in-plane lattices are evidently mismatched. However, in the case of *A*-O plane as the first plane, good matching can be expected with the mismatch smaller than 1%, as the *A* atomic separation along <110> can be adequate to the twice that in Pt. The effects of terminations on the interface energetics were theoretically demonstrated [36], where different cases of Pt occurred when Pt films were grown on SrO- and TiO_2-terminated surfaces of $SrTiO_3$.

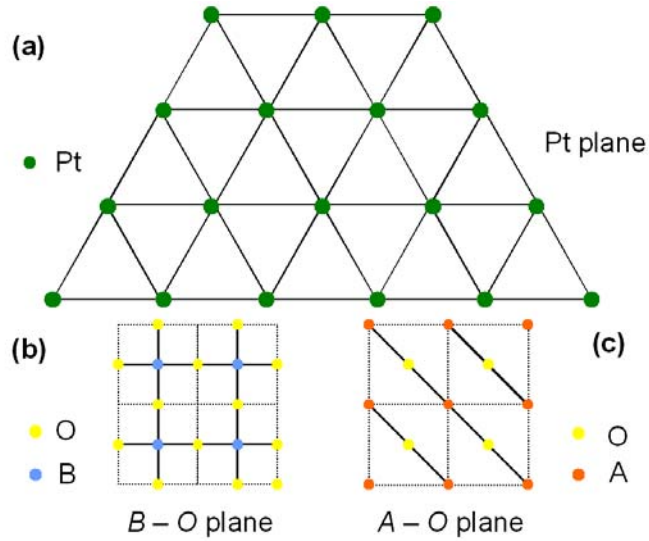

Figure 2. (Ref. [34])

Back to the crystallographic relationships between BST and Pt in Figs. 1 (a) and (b), the origin of two distinct interfacial cases with identical normal crystal orientation can be proposed based on the in-plane mismatch. The first grown atomic plane is crucial to determining the crystal growth. As *B*-O plane is the first growth plane, [010] is the direction parallel to the interface. Similar case was found in BST/$LaAlO_3$ structures by the Z-contrast STEM dark field image [33]. Therefore, large mismatch gives rise to a distorted lattice in several atomic layers adjacent to the interface. It is the case of type I interfacial layer, as illustrated in Figure 1 (a). When the growth initiates with *A*-O plane, type II interface occurs. Good matching takes place as the atoms are arranged along the [110] direction to form the in-plane lattice. However, it is also noticed that there is no good matching in the perpendicular direction, while no indication of interfacial layer exists in this case. Thus, the results presented herein imply that the quality of the BST/Pt interface can be improved when there is a good film/electrode lattice matching at least in one direction. It can be expected that appropriate fabrication of films on Pt electrodes can avoid the presence of interfacial layers and obtain atomically sharp interfaces [28].

2. Approaches to Enhance the Tunability of BST Thin Films

Dielectric tunability and dielectric loss are the basic parameters characterizing ferroelectrics for applications in electrically tunable devices [7,13-15]. Earlier viewpoint considered the loss as the more critical issue in device applications. Much effort has focused on lowering the dielectric loss in thin films, but no substantial reduction of loss has been achieved yet. Moreover, such lowering of loss is usually at the expense of reduced tunability [37,38].

More recently, Pervez *et al*. pointed out that [39], as in phase shifter circuit, higher tunability allows for fewer tuning elements, which are cascaded to achieve the desired phase shifting. The decrease of the amount of the tuning units directly reduces the net circuit loss.

As a result, the tunability should be more crucial in practical applications than the dielectric loss. However, as discussed in the above section, dielectric properties degrade dramatically in ferroelectric thin films. How to enhance the dielectric tunability is consequently the key issue to be solved for the tunable devices based on ferroelectric thin films. In the following, we will introduce some approaches to enhance the tunable properties based on the origin of the tunability of perovskites.

2.1. Origin of Dielectric Tunability in Perovskites

Tunability of perovskites is defined according to the dielectric nonlinearity of ε as functions of electric field above the Curie temperature. Ferroelectrics for applications in electrically tunable devices are generally in the paraelectric phase [3,4,7-10,13]. The reason is that most of the ferroelectrics in polar phase are also piezoelectric. Piezoelectric transformations cause large losses at relatively low microwave frequencies, and additional losses in polar phase are associated with the domain wall movements. Another reason hindering the applications of a ferroelectric in a polar phase is the hysteresis in field-dependent dielectric characteristics [7].

It is known that the displacive ferroelectrics have quite perceptible dielectric nonlinearity at the temperature range of 50°C ~ 100°C above T_c [4]. Marked tunability takes place near the phase transition point, which decreases with the increasing temperature. In particular, a wide temperature range of nonlinearity can be obtained in material with a diffused phase transition.

The explicit functional relationship between dielectric constant and electric field for a ferroelectric in the paraelectric state is derived by K. M. Johnson in 1961 based on Slater's and Devonshire's work [3,40,41]. In the light of the phenomenological theory of Devonshire [41], the free energy F is expanded as [3]

$$F(T,P) = F(T,0) + \frac{(T-\theta)}{2\varepsilon_0 C}P^2 + \frac{B(T)}{12}P^4 + \ldots, \tag{3}$$

where T is the absolute temperature, P is the polarization developed by the external field, $F(T,0)$ is the zero-field free energy, C and θ are the Curie-Weiss constant and temperature, $B(T)$ is a phenomenological constant, and ε_0 is the dielectric constant of vacuum. The dielectric constant ε_r follows Curie-Weiss law above the Curie temperature in the paraelectric state. Since the dielectric constant of BST $\varepsilon_r(T,E) >> 1$, we can express $\varepsilon_r(T,E)$ as [10]

$$\frac{1}{\varepsilon_r(T,E)} \approx \varepsilon_0\left(\frac{\partial E}{\partial P}\right)_T = \frac{1}{\varepsilon_r(T,0)} + \varepsilon_0 B(T)P^2 + \ldots, \tag{4}$$

where the electric field is given by

$$E = \left(\frac{\partial F}{\partial P}\right)_T = \frac{(T-\theta)}{\varepsilon_0 C}P + \frac{B(T)}{3}P^3 + \ldots \tag{5}$$

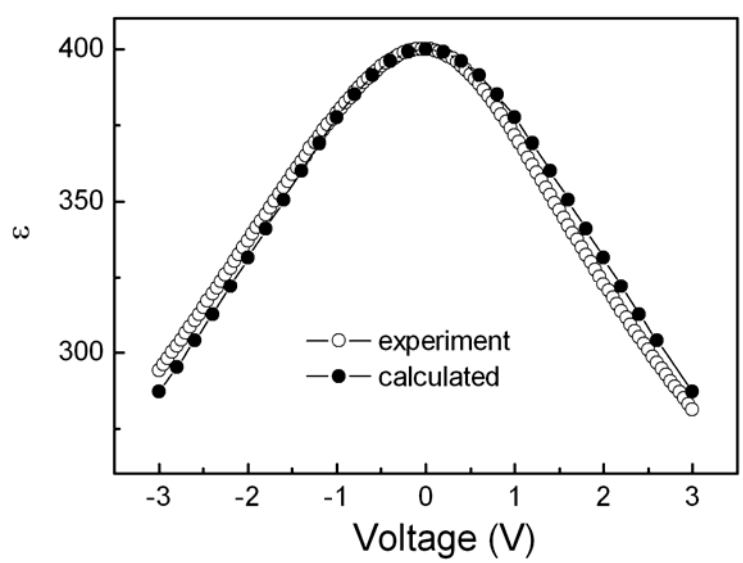

Figure 3.

In the case of small field, we can assume that $P = \varepsilon_0 \varepsilon_r E$ and neglect terms in P^4 or greater. Based on Eqs. 4 and 5, Johnson proposed the variation of dielectric constant ε_r with the electric field E as

$$\varepsilon_r(T,E) = \frac{\varepsilon_r(T,0)}{\{1+[\varepsilon_0 \varepsilon_r(T,0)]^3 B(T) E^2\}^{1/3}} . \tag{6}$$

This expression demonstrates the decreasing dielectric constant with increasing E. The comparison of experimental and calculated data of $\varepsilon_r - E$ characteristics is shown in Figure 3. The agreement between experimental and theoretical results, especially the data under lower electric field, verifies the validity of illuminating the field-dependent dielectric constant by using Eq. 6. If we rewrite Eq. 6 as

$$tunability = 1 - \frac{\varepsilon_r(T,E)}{\varepsilon_r(T,0)} = 1 - \frac{1}{\{1+[\varepsilon_0 \varepsilon_r(T,0)]^3 B(T) E^2\}^{1/3}} , \tag{7}$$

we thus have the expression of tunability which shows dependence on $\varepsilon_r(T,0)$. The larger $\varepsilon_r(T,0)$ in the right site of Eq. 7 directly results in the higher tunability.

The above analyses is based on the thermodynamical theory, while G. Rupprecht *et al.* and Johnson also discussed the origin of such field-dependent behavior according to the ion oscillating in a lattice anharmonic potential in perovskites [3,42]. It has been concluded that the anharmonic restoring forces on the Ti ion when it is displaced from its equilibrium position, is responsible for the dielectric tuning in BST and STO. G. Rupprecht *et al.* also evaluated the nonlinear constant of $A(=\varepsilon_0^3 B(T))$ in Eq. 6. Their theoretical results indicated

that the nonlinearity of the dielectric constant has a marked dependence on the direction of an external field with respect to the crystallographic axes [42]. *A* is largest for the <100> directions, while *A* takes the smallest value along the <111> directions. This direction-dependent nonlinearity is consistent with the studies on ion displacements by Neville *et al*. [43] They considered the crystal structure of perovskite STO and arrived at the conclusions that Ti ion motion determines the nonlinearity of dielectric constant. Their results revealed that the nearest-neighbor Ti-O distance decreases fastest if the Ti ion is displaced in the [001] direction, and least if the Ti ion is displaced in the [111] direction. Consequently, the greatest nonlinearity can be expected if Ti ion displacements are significant for electric fields applied in the [001] direction, and the smallest one takes place for fields applied in the [111] direction. It is thus evident that perovskite BST and STO films with (100) texture can exhibit strongest tunable behaviors as the fields are generally applied to the capacitors in <100> directions.

According to the above discussions, the dielectric tunable properties of perovskites are highly associated with the phase transition of ferroelectrics, crystal texture, and lattice anharmonic interactions. These accordingly provide us approaches to enhance the tunable properties of perovskites thin films.

2.2. Effects of Electric Annealing on the Tunable Properties of BST Thin Films

It has been discussed in section 2.1 that the anharmonic restoring forces on the Ti ion when it is displaced from its equilibrium position, is responsible for the dielectric tuning in perovskites. For BST, the Ti ion is displaced toward the oxygen ions at the apices of the octahedron, even in the paraelectric state, resulting in asymmetry of the Ti-O bond lengths [44]. A large dielectric constant is often associated with a high value of tunability, because when the dielectric constant is larger, the asymmetry of the bonds is greater to begin with, so further displacement becomes even more difficult [44]. In addition, Hyun *et al.* reported that the tensile strain along the direction of the applied field increases the ionic displacement, and hence enhance the tunability [45]. All of these indicate that the displacement of the Ti ion from its equilibrium position plays a crucial role in determining the tuning properties of BST films.

Since the applied voltage has an impact on the ionic displacement, Xia *et al.* has introduced an electric field to the process of thermal annealing in an attempt to improve the tunable properties of BST thin films [46], whereafter this approach was further confirmed by Cho *et al.* [47] $Ba_{0.5}Sr_{0.5}TiO_3$ thin films derived by rf magnetron sputtering technique were rapid thermal annealed with electric field applied. The set-up composed of two parallel plates acting as electrodes for applying the electric field is placed in a quartz tube furnace to experience the thermal annealing. The bottom plate is electric grounded, and voltages with different values were applied onto the top plate. The voltage was still applied during the cooling process. In addition, the annealing under 0 V is simplified as conventional annealing, and the annealing under non-zero voltage is called as electric annealing.

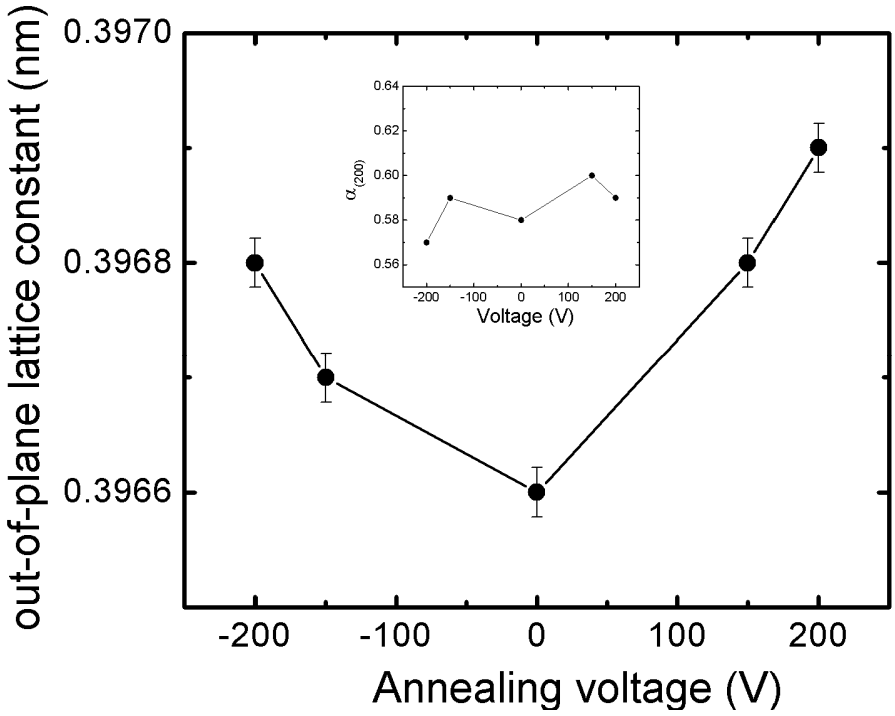

Figure 4. (Ref. [46])

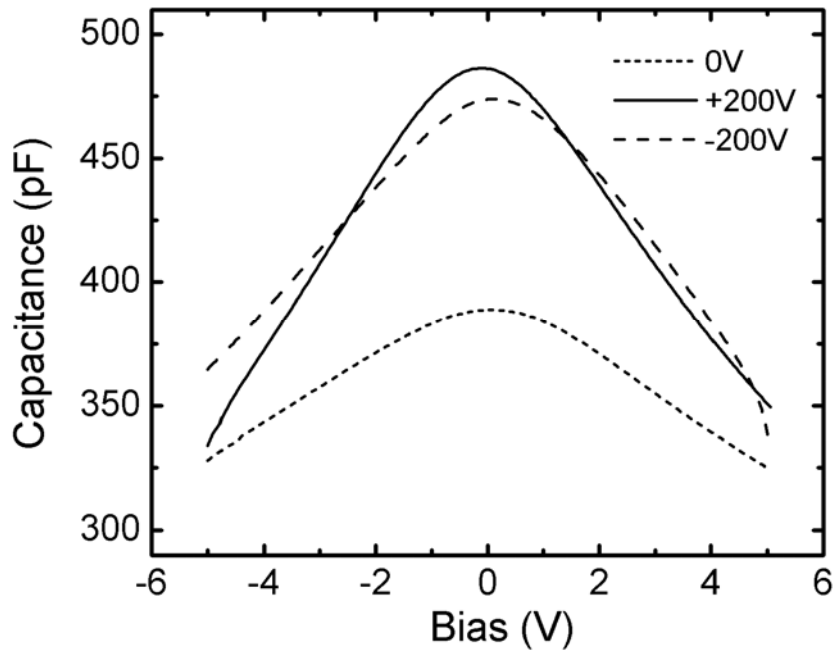

Figure 5. (Ref. [46])

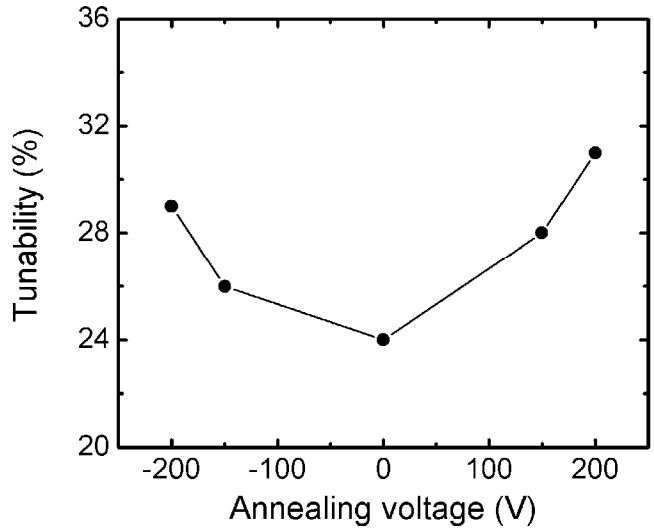

Figure 6. (Ref. [46])

The effects of electric annealing on the film microstructures have been investigated based on the x-ray diffraction (XRD) patterns. The in-plane lattice constant is barely changeable as the applied electric field [47], whereas the out-of-plane lattice constants are increased after the films were subjected to electric annealing under both the positive and the negative voltage applied, as shown in Figure 4. As the applied voltage increases, the out-of-plane lattice constants also increase. But the degree of the (200) orientation, α_{200}, has no obvious change with respect to the electric annealing. Here, α_{200} is defined as the relative intensity ratio $\alpha_{200} = I_{200}/(I_{200} + I_{110})$, where I_{hkl} is the integrated intensity of the (*hkl*) peaks recorded in $\theta - 2\theta$ scans. This indicates that the electric annealing has no contribution for the improvement of the film orientation and the crystallization compared to the conventional annealing, but just results in a slight elongation of the lattice constant along the surface normal direction. This elongation could be attributed to the enlarged ionic displacement in the field direction caused by the electric field, considering the only difference between the electric and conventional annealing is the applied electric filed. Furthermore, AFM observations reveal that the electric annealing also affects the surface morphology of the BST films. The electric annealing leads to slightly smooth surface compared to the conventional annealing [47].

The dielectric properties of the BST films are correlated to the electric annealing. Figure 5 shows the capacitance-bias (*C-V*) characteristics of BST films annealed with applied voltage of $\pm$ 200 V and 0 V, measured at room temperature. The zero-capacitance is found to increase with the introduction of applied voltage when annealed. The calculated zero-voltage dielectric constant are 345, 424 and 415 for the annealing voltage of 0 V, +200 V and –200 V, respectively. This increase could be attributed to the elongated ionic displacement. A larger zero-electric-field dielectric constant is often associated with a higher value of tunability [44]. The tunability is calculated from the *C-V* curves, and the tunability measured at +5 V as the function of the annealing voltage is exhibited in Figure 6. The tunability of electric-annealed BST films shows a noticeable increase compared to that of BST annealed without electric

field. The field dependence of the dielectric constant at paraelectric state is caused by the anharmonic interaction of Ti ion. For the samples subjected to electric annealing, which have elongated ionic displacement compared to those subjected to conventional annealing, the asymmetry of the bonds is greater to begin with, so the ionic vibration and further displacement become even more difficult when voltage is applied, and hence enhances the tunability. Cho *et al.* also studied the dielectric loss of BST films at microwave range (1-3 GHz). As the applied voltage increases, the dielectric loss slightly increases, which can be explained by mechanism of energy scattering on the ferroelectric mode that is connected with the relaxation of phonon distribution function [47].

It is reported that the sputtered films deposited from a stoichiometric ceramic are often Sr-deficient films and have O vacancies [48]. Ti^{4+} ions located near the O vacancy can capture one electron and change to Ti^{3+}. For the Sr-deficient films, some Ti^{3+} ions will occupy the Sr vacancies [48,49]. When the films are annealed under an applied electric field, the Ti^{3+} ions could trend to distribute against the direction of electric field compared to the Ti^{4+} ions. This results in the different distributing regions of Ti^{3+} and Ti^{4+} ions in the films, which changes the former random ionic distribution. It can be hypothesized that the regions at which Ti^{3+} ions located could be Ba-rich because the Ti^{3+} can occupy the Sr site, and display some $BaTiO_3$-like behavior and become polar, whereas other regions remain paraelectric at room temperature. This indicates that a polar nano-region phase might appear in the BST films during the electric annealing. The polar-regions have the tetragonal phase structures with larger *c*-lattice constants, which is consistent with the calculated out-of-plane lattice constants. The existence of the nano-polar-regions could be related to the relaxor-like characteristics, and result in the hysteresis loops even in the paraelectric state at room temperature [50]. The existence of polar phases in the annealed films has been confirmed by the observed polarization hysteresis loops even though the electric-annealed films are still in paraelectric state at room temperature. And hence, larger tunability could be obtained, as expected, due to the large dielectric constants that relaxors usually have.

Furthermore, it is also noticed, in Figure 5, that the symmetry of *C-V* curves is destroyed after the films electric-annealed. For the films annealed at +200 V, the negative part of the *C-V* curve exhibits slightly stronger tuning property than the positive part, whereas the films annealed at –200 V shows the opposite phenomenon. Such asymmetry of the *C-V* characteristics might also result from the appearance of the nano-polar-regions in the paraelectric state, since the similar asymmetries observed in ferroelectric films due to the hysteresis effects.

2.3. Effects of A-site Doping on the Tunable Properties

The phase transition temperature (T_c) plays a critical role in determining the tunable properties of perovskites. O. G. Vendik pointed out that marked tunability takes place near the phase transition point [4], which decreases with the increasing temperature. So, if the T_c can be modulated to be closer to the operation temperature, higher tunability could be obtained. On the other hand, the microwave devices made of these tunable materials would be operated at environment with different temperatures, requiring the tunability of thin films to be low temperature dependent over a broad temperature range.

An effective approach to modulate the T_c is chemical substitution in such films. Moreover, it is also known that adding more kinds of cations to the *A*-site in perovskite structure (ABO_3) usually results in diffuse phase transition, which can broaden the transition

peak and induce low temperature-dependence. Recently, the *A*-site doping of PbO, Bi_2O_3, and CaO in (Ba,Sr)TiO_3 thin films has been reported to modulate the T_c and result in enhanced diffuse phase transition in BST [51-54]. Herein, Pb doping is introduced as a typical example.

Figure 7 shows the dielectric constant-temperature ($\varepsilon - T$) characteristics of the Pb doped BST (BPST) thin films at 1MHz. For comparison, the $\varepsilon - T$ behavior of BST films is also shown in the inset of Figure 7. It is noticed that the dielectric constant of BPST exhibits a maximum at the temperature of 7 ^{o}C, whereas, in the case of BST, the maximum occurs at –79 ^{o}C. The temperature corresponding to this peak of dielectric constant is considered to be T_c. As is known, BST is a continuous solid solution between $BaTiO_3$ (BTO) and STO. $PbTiO_3$ (PTO) has a higher T_c of 485 ^{o}C than that of BTO of 120 ^{o}C. That's why, with the adding of PTO into BST system, the T_c of the solid solution BPST could be adjusted to shift to a higher temperature.

As more kinds of cations were added to the *A*-site in perovskite structure, enhanced relaxor behavior and diffuse phase transition are to be expected for BPST films. Figure 7 also gives the characteristics of $\varepsilon - T$ at different frequencies for BPST films. An obvious increase of peak temperature with increasing frequency, together with the broadening of the transition peak, is observed. This indicates a typical behavior of relaxor ferroelectrics. However, no clear shift of T_c of BST films is found, as illustrated in the inset of Figure 7. It is now known that the relaxor behavior is related to the heterogeneity of the nanoscale composition [50]. As a result, adding Pb ions into the *A*-site of pervoskite structure of BST system could be responsible for the relaxor behavior of BPST films. The regions with *A*-site rich in Pb^{2+} would display some PTO-like behavior and become polar at room temperature, whereas other regions could have a tendency to remain paraelectric (BST with Sr rich is paraelectric at room temperature). The existence of nanopolar regions in paraelectric environment results in the distribution of T_c in BPST films, giving rise to the broadening of the transition peak and low temperature-dependent dielectric constant.

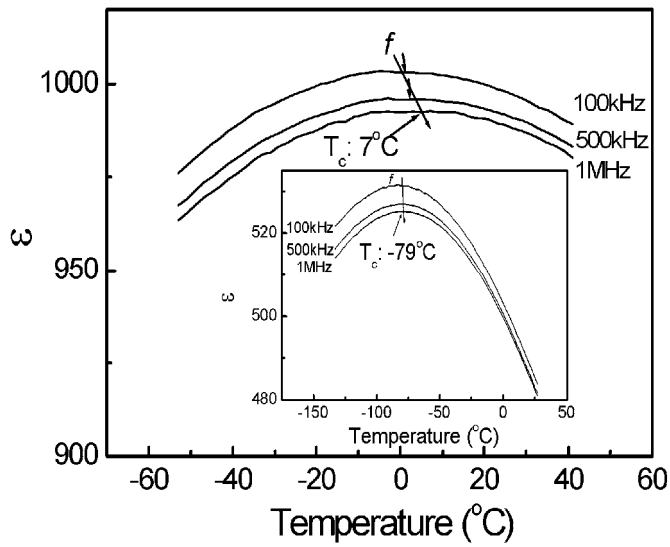

Figure 7. (Ref. [52])

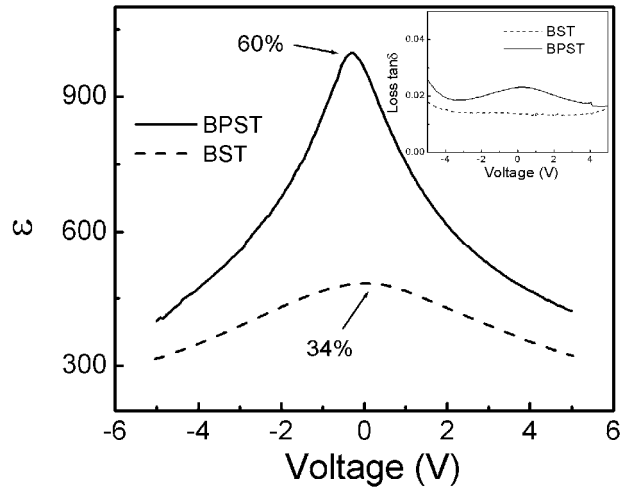

Figure 8. (Ref. [52])

As the T_c of BPST films is much closer to the room temperature, the enhanced tunable properties would be obtained at room temperature. The tunability is calculated from the dielectric constant-voltage ($\varepsilon - V$) characteristics by using the Eq. 1. Figure 8 shows the $\varepsilon - V$ curves of the BPST and BST films, measured at room temperature and 1MHz. As expected, the calculated tunabilty of BPST is much larger than that of the undoped BST. Furthermore, such enhanced tunability could also be related with the existence of nanopolar regions in BPST films, since the nanodomains may be affected by the external field through changing the nonferroelectric states into ferroelectric ones [2,50,55]. In addition, the dielectric loss is shown in the inset of Figure 8. The loss tan δ increases slightly, also due to the T_c of BPST closer to the measured temperature.

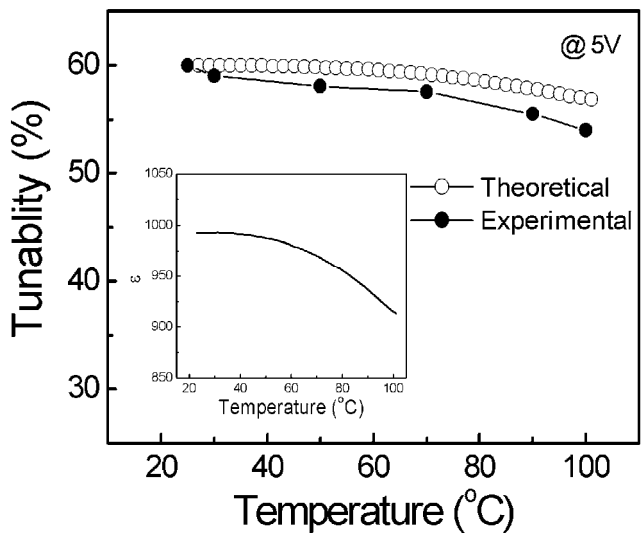

Figure 9. (Ref. [52])

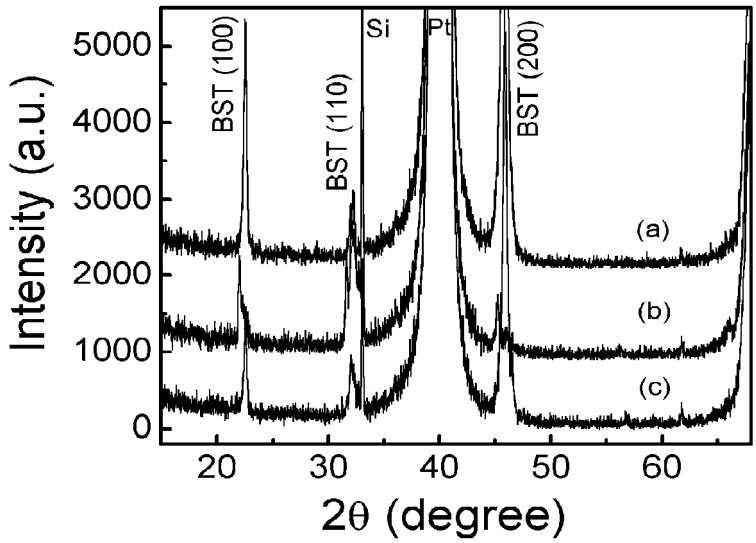

Figure 10. (Ref. [60])

As aforementioned, microwave devices require the materials to be stable against the change of temperature. It has been discussed in section 2.1 that the dependence of tunability on the temperature can be elucidated according to the phenomenological theory of Devonshire [41]. Eq. 7 indicates that the decreased $\varepsilon_r(T,0)$ directly results in the lower tunability. The temperature dependence of the tunability (at 5 V) is presented in Figure 9, and the inset shows the $\varepsilon - T$ characteristics (T larger than room temperature) without applied bias. It is worth noting that, in the temperature range from 25 ^{o}C to 100 ^{o}C, the BPST films still exhibits relatively high tunability from 60 % slightly down to 54 %. This no steep variation of tuning property with regard to temperature could be attributed to the broadened dielectric constant peak caused by the diffuse phase transition, as illustrated in the $\varepsilon - T$ curve. Since the dielectric constant decreases slowly with the increasing temperature, the relatively stable tunability can be obtained. Figure 9 also gives the theoretical data based on Eq. 7 and $\varepsilon - T$ curve. The agreement between the experimental and the theoretical results verifies the validity of illuminating the low temperature-dependent tunability by using Eq. 7. These results demonstrated that Pb substitution can be a simple and effective method to obtain high tunability and low temperature-dependence simultaneously. This stability of high tuning property bodes well for tunable devices made of BPST films, which would be operated at environment with different temperature.

2.4. Effects of Bilayer Thin Films on the Tunable Properties

The (100) orientation has been found to produce large dielectric constant and high tunability [44,56]. BST films have been successfully fabricated on Pt coated silicon substrates by sputtering [56], chemical vapor deposition (CVD) [57], and pulsed laser deposition (PLD) [58]. Compared to other deposition methods, the sputtering process offers some special characteristics, for example, controlling the Ar/O_2 ratio and the total ($Ar + O_2$) pressure during the deposition could attain the (100) preferred orientation [56] and adjust the

stoichiometry [59]. A highly (100) preferred orientation has been developed with the introduction of the compositional bilayer structure.

BST films with different Ba/Sr and (Ba + Sr)/Ti ratios have been fabricated using rf magnetron sputtering by controlling the deposition conditions. The variation in thin film composition can be controlled by the gas pressure in sputtering process [59,60]. BST films with a Ba/Sr ratio of ~ 0.80 and (Ba + Sr)/Ti ratio of ~ 0.91 were deposited at 600 ^{o}C at a total process gas pressure of 3 Pa, while at a total pressure of 9 Pa a Ba/Sr ratio of ~ 0.97 and (Ba + Sr)/Ti ratio of ~ 0.98 was obtained. This makes it advantageous to fabricate BST compositional multilayer films by stacking different chemical compositional layers under different sputtering conditions.

In this approach, a bilayer film with the same individual thicknesses has been fabricated according to the following procedure. A first layer with a thickness of 120 nm was deposited at 600 ^{o}C at a total process gas pressure of 3 Pa on the Pt bottom electrode, and was immediately annealed *in situ* at 600 ^{o}C in the same ambience for 30 min. Then, an upper layer was deposited at 600 ^{o}C at a total process gas pressure of 9 Pa onto the lower layer with the same thickness of 120 nm. For comparison, some monolayer BST films were deposited at 600 ^{o}C at a total pressure of 9 Pa. They have the same thickness as the 240 nm bilayer films.

The crystalline structures of BST bilayer and monolayer films, analyzed by x-ray $\theta - 2\theta$ scans, are shown in Figure 10. The bilayer case exhibits a polycrystalline structure with a highly (100) preferential orientation, while in the monolayer case the structure was characterized by a strong (110) orientation. The (100)-orientation parameter, α_{100}, is calculated from the relative heights of the (100) and (110) diffraction peaks, i.e., $\alpha_{100} = I_{100}/(I_{100} + I_{110})$, and α_{100} = 0.84 was obtained for the bilayer BST thin films. The change in the orientation indicates that the crystallization and growth of the films are significantly influenced by the introduction of the bottom layer. The (100) preferred orientation of BST films could be attained by controlling the Ar/O_2 ratio, the deposition gas pressure, and the deposition rate during deposition in rf sputtering. As can be seen in Figure 10 (c), the bottom layers with an *in situ* annealing, after being deposited at a total gas pressure of 3 Pa, show a structure with a strong (100) peak and a weaker (110) peak, which is similar to the report of P. Padmini *et al*. [56] It is well known that at higher deposition pressures, the atom mean free path can be reduced, which results in the lower deposition rate. The average energies of the atoms forming the films will also be reduced, so that the growth orientation may be more determined by the substrate structure [61,62]. So when the upper layer was deposited onto the (100) preferred layer at a total gas pressure of 9 Pa, the bottom layer could act as a nucleation site to determine the texture of the upper layer and a highly developed (100) orientation could be obtained.

The (100) texture leads to high tunability in sputtered BST on $Pt/TiO_2/SiO_2/Si$ substrates [44,56]. Figure 11 (a) shows the *C-V* characteristics measured at 1 MHz of BST bilayer and monolayer films. The zero-bias dielectric constant in bilayer case as calculated from the result shown in Figure 11 (a) is 600, which shows a significant increase compared to that of the monolayer of 387. The (100) orientation has a larger dielectric constant because Ti ion is preferentially displaced along the (100) direction towards the oxygen ions at the apices of the octahedron, even in the paraelectric state, resulting in the maximum polarization and dielectric constants along this direction [44]. So in bilayer case the highly (100) oriented film exhibits a considerable enhancement of the dielectric constant. A large dielectric constant is

often associated with a high value of the tunability. The tunability of the bilayer films calculated from Figure 11 (a) was about 44% at an applied electric field of 210 kV/cm, which is double the value of 21% for the monolayer films. It has been demonstrated that the vibration of Ti ion in oxygen octahedral is responsible for the tuning of the BST [3,63]. The displacement of the Ti ion induces the asymmetry in the Ti-O bond, which results in the anharmonic restoring forces on the Ti ion. The more highly (100) texture is, the greater the asymmetry of the bonds will be. As the Ti ion is displaced more from the center position, its vibration is softened more easily with increasing applied voltage, and hence the tunability increases.

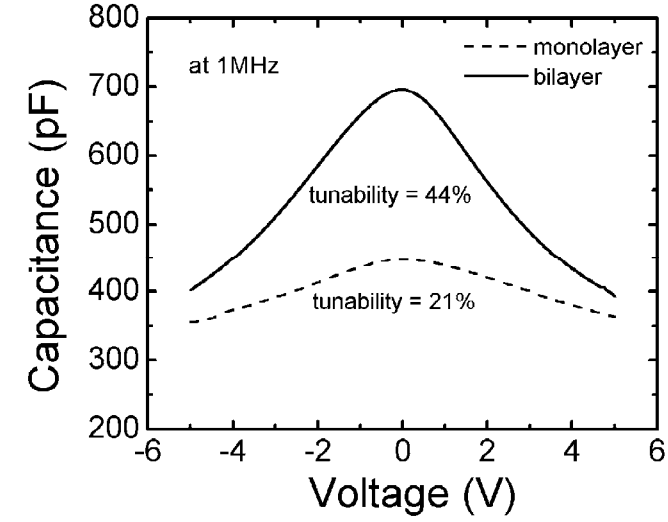

(a)

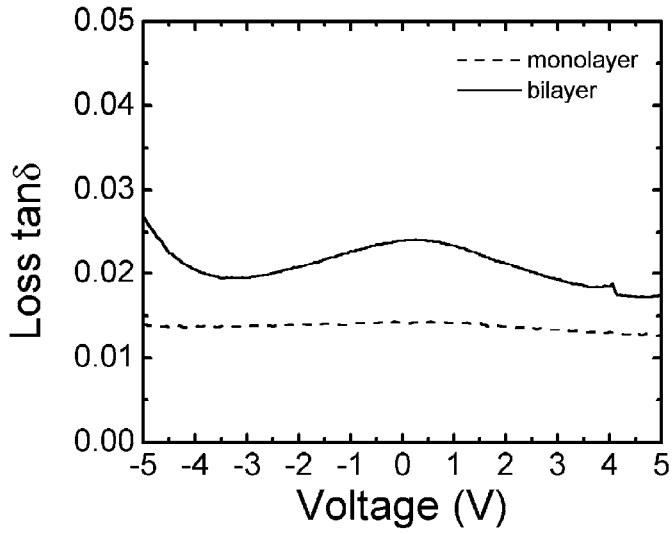

(b)

Figure 11. (Continued)

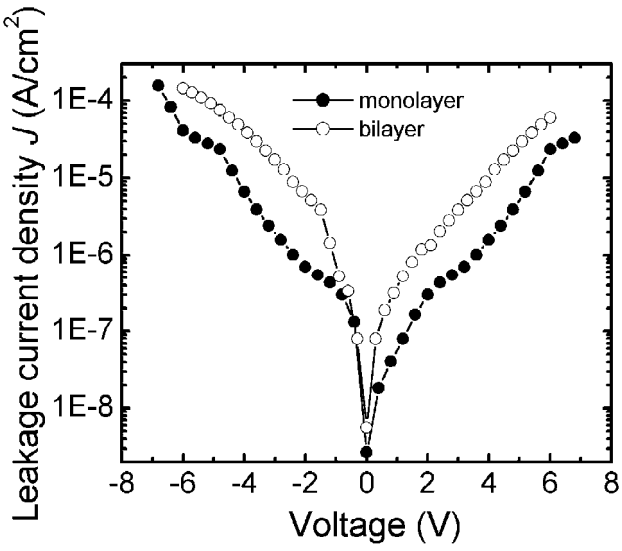

(c)

Figure 11. (Ref. [60])

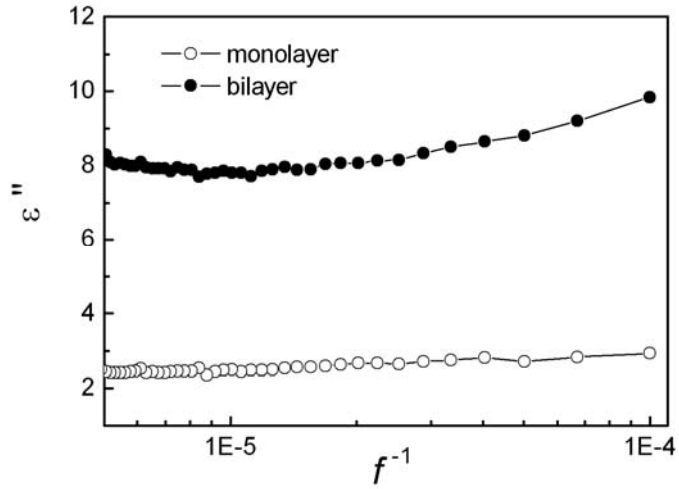

Figure 12.

On the other hand, the interface between two successive dielectric layers must also be considered for the dielectric enhancement, which was associated with an increased loss tan δ, from 0.014 to 0.024, as shown in Figure 11 (b). A compositional gradient can be formed at this interface zone due to the different composition of the two layers. It will induce more space charges to be located in this region. Hence, the resistivity of the interfacial material is reduced, resulting in the increased leakage current density, as shown in Figure 11 (c). These results can be correlated to a Maxwell-Wagner (MW) like dielectric enhancement effect. As proposed by Catalan and O'Neill *et al* [64,65], the dielectric enhancement of the mulitilayer film system can be associated with the onset of MW behavior as long as a low resistivity interfacial region is formed between two bulk-like insulating dielectric layers. The effective structure is thus treated as consisting of interfacial, semiconducting regions intercalated

between a bulk-like, insulating ferroelectric [65]. Such a system is well described by the MW series capacitor, which yields imaginary part of dielectric constant ε''

$$\varepsilon''(\omega) = \frac{1}{\varpi C_0 (R_i + R_b)} + \frac{(\varepsilon_0 - \varepsilon_\infty)\varpi\tau}{1 + \varpi^2\tau^2}, \tag{8}$$

where ϖ is frequency, C_0 is a geometric factor, R_i and R_b are resistances of the two dielectric components, ε_0 and ε_∞ are dielectric constant at zero and infinite frequency, and τ is the relaxation time of the entire MW capacitor [64]. Figure 12 illustrates the dependence of ε'' on frequency. The ε'' of bilayer films increases with the decreasing frequency, which is the typical MW behavior according to Eq. 8, whereas for the monolayer case ε'' does not exhibit such dependence.

Some of the samples of bilayer were subjected to a long high-temperature furnace post-annealing. Such a long annealing could result in the destruction of the bilayer structure. The diffusion caused by the thermal annealing gradually eliminates the non-uniform composition distribution at the interface, and so destroys the interface between the two layers. As expected, the enhanced tuning properties were degraded after post-annealing at 800 ^{o}C for 1.5 h due to the destruction of the bilayer structure. This indicates that the interface has a more dominating influence on the dielectric characteristics of the bilayer structure compared with the orientation. The longer annealing time is, the lower the tunability and zero-bias dielectric constant will be. The films after 2.5 h of annealing have a tunability and zero-bias dielectric constant of 28% and 460, respectively, as shown in Figure 13, which are still larger than those of the monolayer films because of the remaining highly (100) orientation.

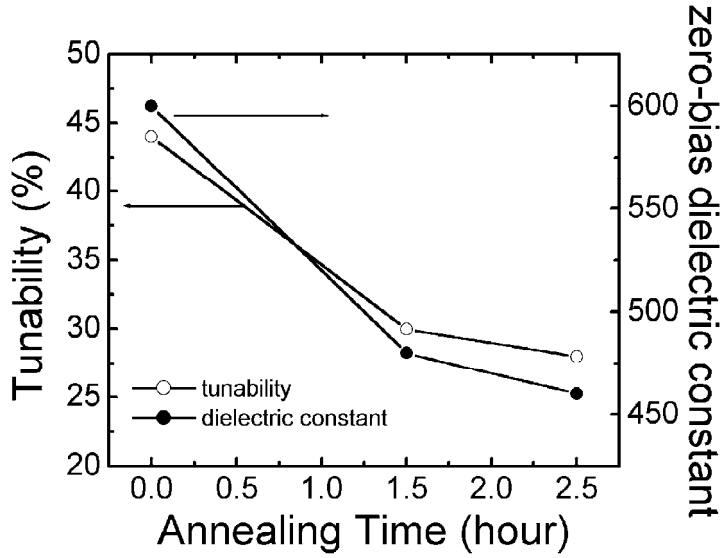

Figure 13. (Ref. [60])

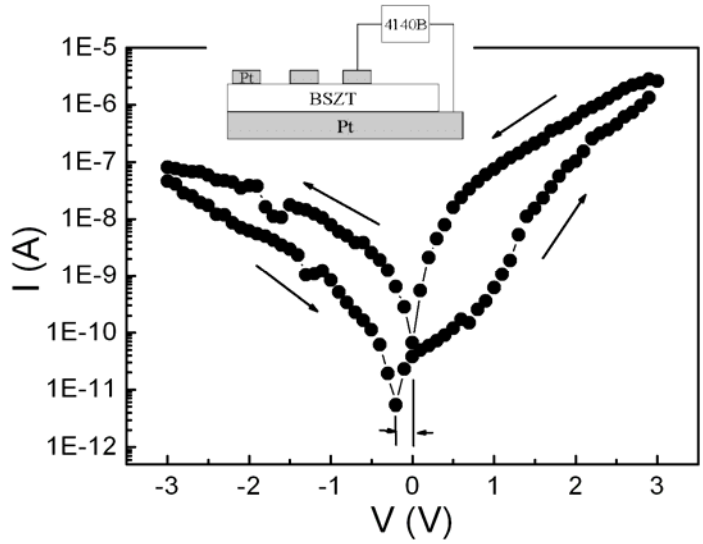

Figure 14. (Ref. [79])

3. Conclusions

Perovskites based on BST, because of their strong electric-field dependent dielectric constant in the paraelectric state, are being used to develop a new class of electrically tunable microwave devices. The dielectric tunability is a critical parameter for such applications. The anharmonic restoring forces on the Ti ion when it is displaced from its equilibrium position in the lattice of perovskites is responsible for the dielectric tuning in BST. Unfortunately, the tunable dielectric properties degrade dramatically in perovskite thin films. As the dielectric tunable properties are highly associated with the phase transition of ferroelectrics, crystal texture, and lattice anharmonic interactions, in this section some approaches to enhance the tunable properties of BST thin films have been introduced. It has been demonstrated that post-annealing in proper electric field can increase the dielectric constant and the tunability remarkably and destroy the symmetry of *C-V* characteristics of the films. The increased out-of-plane lattice constant and the appearance of the hysteresis loops in the electric-annealed films indicated the formation of small polar regions with tetragonal structure, which are responsible for the increased dielectric constant and tunability. The substitution of Pb for Ba in BST system has been revealed to raise the transition temperature close to room temperature, which results in the enhanced tuning property. The adding of lead into BST leads to the relaxor behavior and diffuse phase transition. The tunability of BPST films consequently displays good stability against the temperature. This stability of high tuning property bodes well for tunable devices made of BPST films, which would be operated at environment with different temperature. In addition, a highly (100) preferred orientation can be developed, and enhanced tunability is obtained with the introduction of compositional bilayer structure. A Maxwell-Wagner like effect is also considered to result in enhanced dielectric properties and increased loss $\tan\delta$. These results provide effective approaches to obtain high tunability, and are of importance to develop BST thin films in the dielectric tunable applications.

II. Resistive Switching in Perovskite Thin Films

Leakage behaviors in perovskite thin films are usually treated as an adverse factor for memory applications. Efforts have focused on the reduction of leakage current in perovskite thin films for DRAM and ferroelectric memory applications. This is because high leakage current (or low resistance) generally leads to the loss of data. But, recently the leakage behavior has been utilized to construct a novel memory concept of resistive switching memory (RRAM), which has triggered scientific and technological attentions. The basic principle of RRAM is that the conduction behaviors of a metal-insulator-metal (MIM) device can be electrically modulated in a simple way. Consequently the different resistance states (normally high- and low- resistances) controlled by the applied electric fields can act as data of "0" and "1" in the memory processes. RRAMs, due to the nonvolatile characteristics and the simplified device structure, are considered to be the most promising candidates for the next-generation nonvolatile memory [66-69].

The candidate materials for RRAMs include chalcogenide semiconductors, organic materials, and transition-metal oxides. Recently, such reversible switching behaviors were also discovered in perovskite type materials, such as manganates, zirconates, and titanates, which are of increasing interest during the last decade [70-75]. Well-developed two state or multilevel switching performances have been reported not only in epitaxial thin films but also in polycrystalline thin films. Efforts have been put forth to make clear the origin of the switching characteristics in perovskite thin films. Several models have been proposed: (1) charge-transfer processes via donor and acceptor levels (Cr^{3+} and Cr^{4+}), (2) conductivity changes related to the spontaneous polarization, (3) formation of local conducting filaments, and (4) process of charge accumulation [70-78]. However, some inconsistent results still remain in previous reported papers (for example, whether the interface or the film bulk dominates the resistive switching) [74]. Several conduction mechanisms control the leakage characteristics in dielectric thin films, and consequently can determine the resistance features. Therefore, it's worthwhile to further comprehend the switching mechanisms with regard to the conduction characteristics in such films.

1. Resistive Switching Based on Space-charge-limited Current

More and more evidence indicates that space-charge-limited current (SCLC) plays an important role in the conduction transition between high- and low- resistance states [79-83]. The Lampert's theory of SCLC predicts that valuable information can be obtained from the current-voltage (*I-V*) dependence of the material [84]. A typical *I-V* characteristic of Zr doped BST (BSZT) polycrystalline film is illustrated as a semilogarithmic plot in Figure 14. By sweeping the voltage *V*, hysteresis of *I-V* curve is obtained, indicating different resistance states occur during the voltage sweeping. It is noteworthy that a shift of the current minimum to negative from zero voltage exists in forward *I-V* curve, demonstrating the presence of internal field in the film due to nonuniform distribution of space charges contained in the film. But, this shift vanishes when reverse swept, indicating the charge neutralization takes place during the scan cycle. It can be assumed that negative charges, i.e. electrons, are trapped in the film to diminish this negative shift.

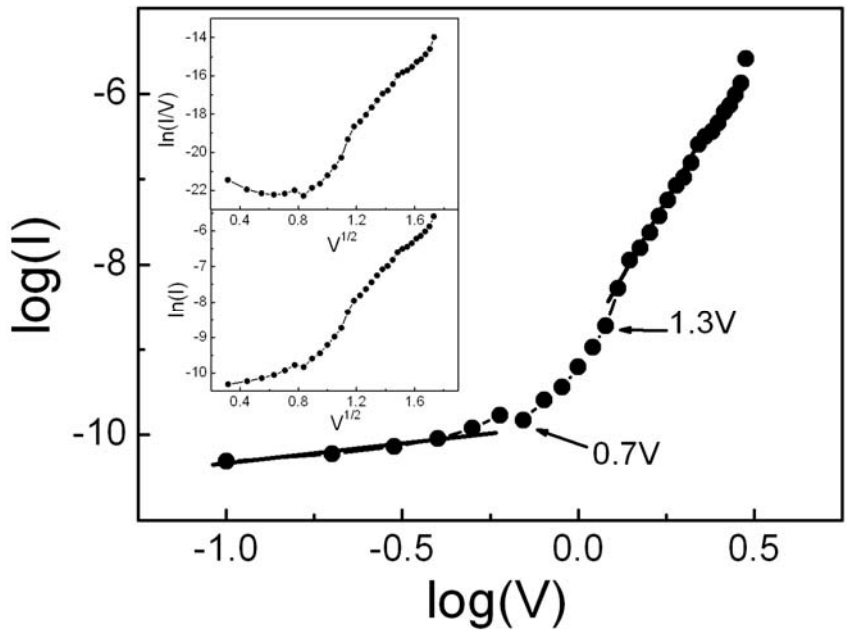

Figure 15. (Ref. [79])

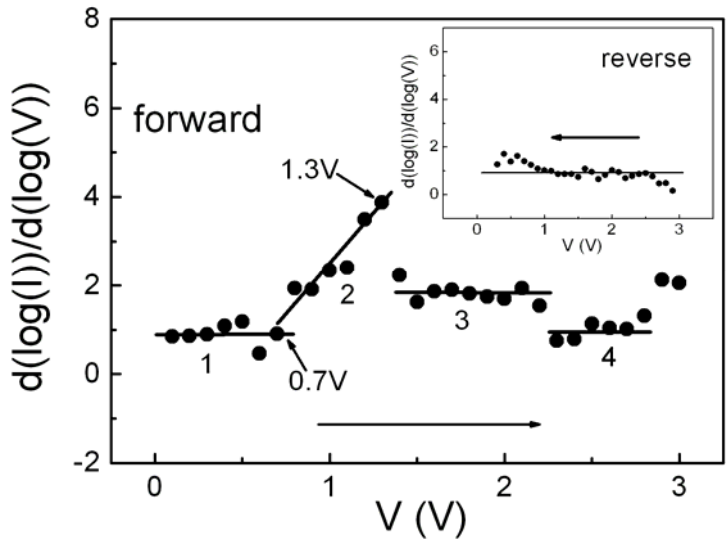

Figure 16. (Ref. [79])

Nonlinear *I-V* characteristics occur at higher voltages in forward curve, as shown in Figure 14. Classic nonlinear conduction mechanisms include SCLC, Schottky emission, and Poole-Frenkel (PF) emission. These mechanisms can be distinguished via the isothermal logarithmic plot of *I-V* correlation. Figure 15 exhibits the replot of the positive branch of the forward curve (from 0 to +3 V) in Figure 14 as a log(*I*)-log(*V*) curve. There are three regions observed in this logarithmic curve: two linear regions for smaller voltages (< 0.7 V) and higher voltages (>1.3 V) and a nonlinear increase region for the in-between voltages. This is

the well-known SCLC feature as described in Refs. [85 – 87]. According to the SCLC theory, linear dependence for voltages smaller than 0.7 V is corresponded to the ohmic law region [85,88]:

$$I = \frac{qn\mu AV}{d}, \tag{9}$$

where q is the electronic charge, d is the film thickness, n is the concentration of charge carriers, μ is the mobility, and A is the area of the electrode. This indicates that the injected carrier concentration is lower than the equilibrium concentration at lower fields. At higher fields (voltages larger than 1.3 V in Figure 15), a strong injection of the charge carriers in the bulk of the film takes place, and current follows a square dependence on voltage: $I \propto V^2$, which is corresponded to the Child's law region. In the presence of shallow trapping level, the current is given by [85,88]:

$$I = \frac{9\theta A\mu\varepsilon_r\varepsilon_0}{8d^3}V^2, \tag{10}$$

where θ is the ratio of the free electron density and the density of the filled trapping sites, ε_r is the dielectric constant of the film and ε_0 is the permittivity of free space. This equation also holds well for an exponential distribution of traps. If sufficient charge is injected into the insulator, all the traps will become filled. Further injected charge then exists as free charge in the conduction band and contributes to the current [85].

The voltage values of 0.7 and 1.3 V denote the ohmic-boundary voltage and the square-law onset voltage, respectively. The intermediate region represents the transition between ohmic and SCLC behaviors, providing information about the trap distribution in the films. Electron traps formed by defects in polycrystalline films locate below the conduction band can absorb injected electrons [86]. Such defects in pervoskite films mainly come from oxygen vacancies, and also from other types of defects, such as *A*-site vacancies and Ti^{4+} interstitials [74]. When the voltage reaches the value to fill the traps, a large-voltage square-law conduction occurs, and this voltage is defined as the so-called trap-filled-limit voltage (V_{TFL}). Such electron trapping is in accord with the above assumption about the shift of the current minimum. Instead of the clearly defined V_{TFL}, a small voltage range is found in Figure 15, indicating the presence of traps exponentially distributed in energy [89], such as different trapping levels below the conduction band edge in the *B*-O plane and the *A*-O plane in perovskite dielectrics [90].

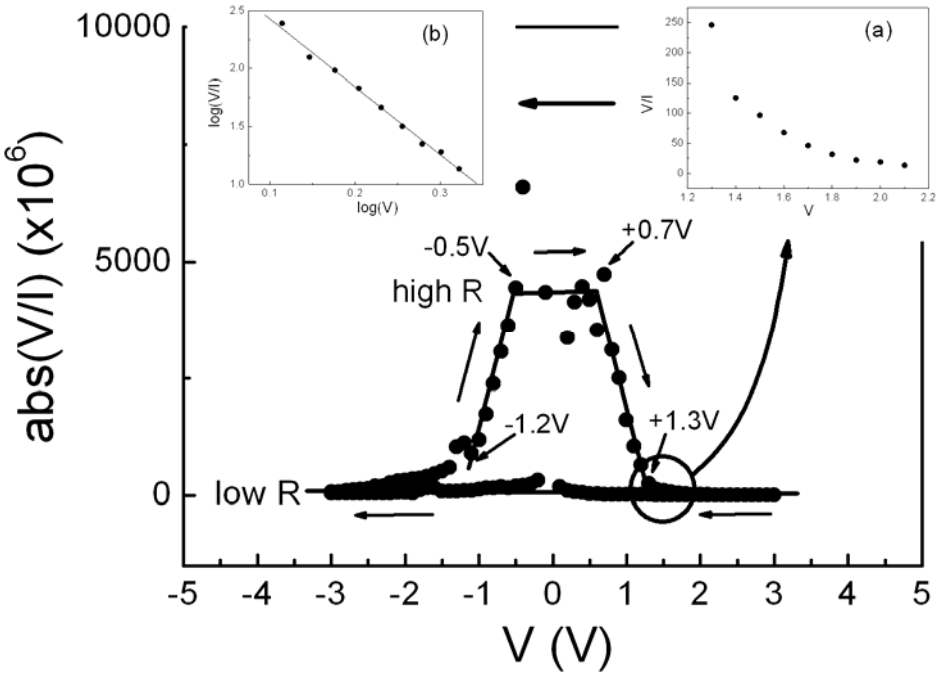

Figure 17. (Ref. [79])

The slope of the log(*I*)-log(*V*) curve, i.e. $d\log(I)/d\log(V)$, is used for further confirmation of the SCLC mechanism, as presented in Figure 16. Numbers from 1 to 4 represent four different regions in this slope curve. For small voltage (< 0.7 V), the slopes approximately equal unity, indicating the ohmic behavior. When the voltage larger than 1.3 V (region 3), $d\log(I)/d\log(V)$ values are around 2, demonstrating the domination of SCLC. The increasing slope value in region 2 is corresponded to the trap-filled process. Similar treatment is executed for the positive branch of reverse sweep in Figure 14, and the $d\log(I)/d\log(V)$ values are ploted in the inset of Figure 16. These values around 1 through most of the voltage range are consistent with those in the highest voltage region (region 4) in Figure 16, indicating that the conduction mechanism in these two voltage ranges might be the same. This means that the difference between forward and reverse scan is eliminated in region 4, and the low-resistance state is formed in this region. The dominant conduction mechanism for the low-resistance state is thus concluded to be ohmic conduction, which is coincident with the conclusions in other literatures (Refs. [72] and [81]). The other two conduction models (PF emission and Schottky emission) are characterized by linear $\ln(I/V) \propto \sqrt{V}$ for PF and linear $\ln(I) \propto \sqrt{V}$ for Schottky emission. No straight lines in both $\ln \sim \sqrt{V}$ curves can be found in the inset of Figure 15, indicating that these two mechanisms can be ruled out or they play minor role in determining the *I-V* characteristics than SCLC, if they exist. SCLC is a bulk-limited mechanism, demonstrating the bulk-limited effect dominates the transition of resistance states in BSZT films.

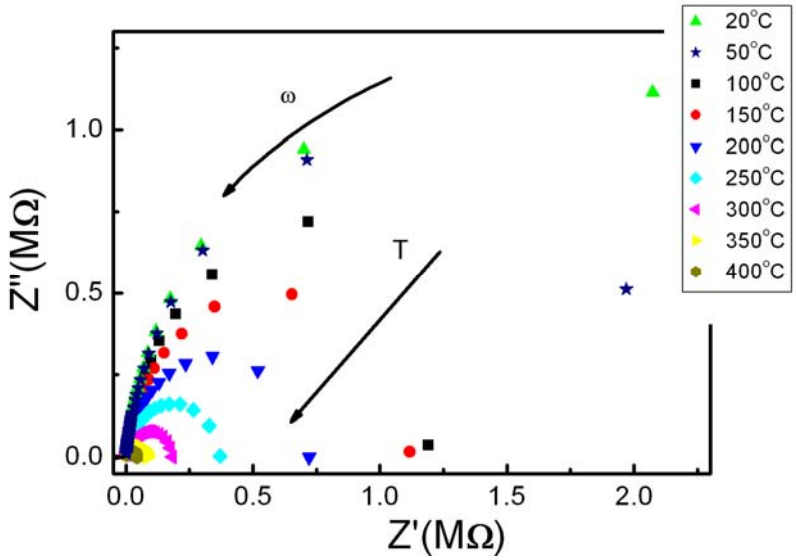

Figure 18. (Ref. [93])

Two resistance states are illustrated in Figure 17 as a $|V/I|$ (resistance) – V plot. The zero voltage data were deleted in this figure due to V/I value equals 0 (at 0 V). It is clearly seen that high- and low-resistance states exist during the voltage sweeping. The state transition is characterized by the resistance drop over the voltage range from 0.7 to 2.2 V, corresponded to region 2 and 3 in Figure 16. A nonlinear region is found in Figure 17 and enlarged in the inset figures. The V/I vs V curve exhibits an inverse proportion characteristic from 1.3 to 2.2 V, indicating the $I \propto V^2$ characteristic and further demonstrating the SCLC mechanism. Beyond this region, the two resistance states are superposed, and the sample is positioned in the low-resistance state.

2. Behaviors of Oxygen Vacancies Responsible for the Resistive Switching

It is now accepted that oxygen vacancies play critical role in the conduction in oxides [75,79,91-93]. As above discussed, electron traps in films, mostly the oxygen vacancies in perovskite oxides, were employed to structure the SCLC model for the elucidation of bulk-limited effect. There are still issues to be further interpreted. As the BSZT films investigated are polycrystalline in nature, it is known that the electron traps can locate in the grain bulk and/or at the grain boundaries. It is required to make clear whether the grain bulk or the grain boundary dominates the conduction. On the other hand, we still need to know the exact behaviors of oxygen vacancies responsible for the high- and low- resistance states, respectively.

Impedance spectroscopy (IS) is a powerful tool used to study the electrical characteristics in oxide dielectrics [94-97], and is progressively utilized to analyze the resistive switching [70,93,98]. Complex impedance spectroscopy can be employed to identify the response of grain bulk from those of grain boundary and electrode interface by representing the samples

as an analogous circuit consisting of a series of parallel RC combinations. Different responses of the grain bulk, grain boundary and electrode interface, each contributing to a parallel combination of a resistance and a capacitance, correspond to the individual semicircle in the complex plots [94-96]. Figure 18 shows the complex impedance plots of BSZT samples set at low-resistance state in the temperature range from 20 ^{o}C to 400 ^{o}C. Although whole semicircle cannot be obtained at room temperature due to the measurements at low frequency beyond the frequency range of our equipment, only one semicircular arc can be detected in the Z" vs Z' curves at higher temperatures. The absence of more than one semicircle certainly demonstrates that the response arising from the electrode interface can be excluded, and furthermore, indicates the conduction in such polycrystalline films is more controlled by the grain bulk rather than the grain boundary effect [96].

The activation energies for the conduction in the low- and high- resistance states can be derived from the variation of conductivity as a function of temperature. The conductivity increases with the increasing temperature, as shown in Figure 19 (a). According to the relationship

$$\sigma = \sigma_0 \exp(-\frac{E_a}{kT}) \tag{11}$$

where σ is the conductivity, σ_0 is the pre-exponential factor, E_a is the activation energy, k is the Boltzmann's constant, and T is the absolute temperature, the curve in Figure 19 (a) can be fitted with two linear lines in low and high temperature regions. The calculated activation energy for the low temperature region is 0.093 eV, and 0.44 eV for the high temperature region.

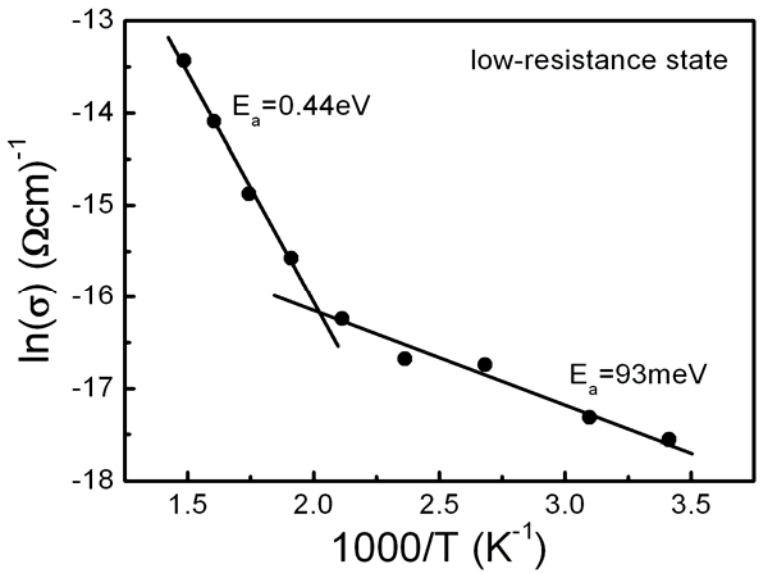

a)

Figure 19 (Continued)

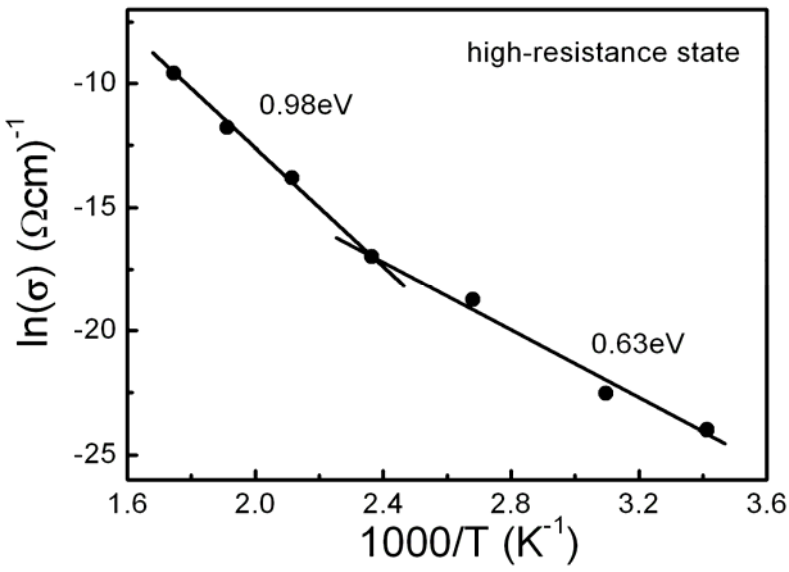

(b)

Figure 19. (Ref. [93])

It is well known that in the titanate-based perovskite oxides, the ionization of the oxygen vacancies will create the conducting electrons

$$O_o \Leftrightarrow V_o + 1/2\, O_2 \tag{12}$$

$$V_o \Leftrightarrow V_o^{\cdot} + e' \tag{13}$$

$$V_o^{\cdot} \Leftrightarrow V_o^{\cdot\cdot} + e' \tag{14}$$

or these electrons might be bonded to Ti^{4+} in the form of

$$Ti^{4+} + e' \Leftrightarrow Ti^{3+}. \tag{15}$$

Here, the notation defined by Kröger and Vink is adopted; $V_o^{\cdot}$ and $V_o^{\cdot\cdot}$ represent the oxygen vacancies carrying one and two positive charges, respectively [99-101]. It has been concluded by Chen Ang *et al*. that the oxygen vacancies lead to shallow level electrons, which may be trapped by Ti^{4+} ions or oxygen vacancies and are easy to be activated becoming conducting electrons [100].

In perovskite oxides, the activation energy of the first ionization of oxygen vacancies as expressed in Eq. 13 was reported to be 0.1 eV [100-102]. In BSZT films, for the samples set at low-resistance state, the obtained activation energy of 0.093 eV in the low temperature region indicates that at room temperature, the first ionization of oxygen vacancies is responsible for the conduction.

For comparison, the conductivity of BSZT samples positioned at high-resistance state is also plotted in Figure 19 (b). Larger activation energies for conduction are obtained from the

$\ln\sigma$ vs 1000/T curve. If the electrical conduction is governed by the thermal excitation of carriers from the second ionization of oxygen vacancies (as described in Eq. 14) to the conduction band, the activation energy for conduction was demonstrated to be around 0.7 eV [99,100], near the activation energy of 0.63 eV obtained in the low temperature region. This implies that at high-resistance state, the conducting electrons at room temperature are dominated by the second ionization of oxygen vacancies. In the higher temperature region, the activation energy is calculated to be 0.98 eV. According to the literatures, the activation energy for the motion of $V_o^{\cdot\cdot}$ in Ti-based perovskite materials is 0.9 - 1.1 eV [94,96]. This means that the extra contribution to the conduction from the doubly ionized oxygen vacancies leads to the increase in σ, which is the typical behaviors in such perovskite oxides.

Consequently, it can be concluded that in the low-resistance state, the first ionization of oxygen vacancies determines the conduction in the low temperature region. The conduction in the high-resistance state is the normal case for perovskite oxides, i.e. the second ionization of oxygen vacancies is responsible for the conduction at low temperature and the motion of $V_o^{\cdot\cdot}$ contributes to the conduction at higher temperature.

The electron trapping accountable for the transition of resistance states can be deduced in the light of the defect formations and the obtained activation energies. Based on the above discussions, at room temperature, the higher E_a for the second ionization of oxygen vacancies compared to that for the first ionization indicates that it is more difficult to activate the conducting electrons without any applied field, and hence the low free electron concentration is in agreement with the high-resistance state at which the initial samples were set. $V_o^{\cdot\cdot}$ acts as the carriers in such case and *p*-like behaviors can be expected [101]. After the samples were set at low-resistance state, according to the first ionization process, the existence of V_o is in accord with the assumption about the electrons trapped by the oxygen vacancies. The activated conducting electrons increase the free electron concentration, representing the *n*-like conduction. Such conductive transition can be confirmed by the different dc conduction characteristics. The transition of SCLC, Ohmic conduction, and Schottky emission were also demonstrated in other reports [81]. Accordingly this electron trapping effect and the transition of conduction behavior can be expected to fit the resistive switching observed in other perovskite oxides.

3. CONCLUSIONS

In this section, hysteretic *I-V* characteristics and resistive switching have been demonstrated in perovskite BST films, which provides the potential applications of perovskites in resistive switching memory. Detailed study of *I-V* characteristics reveals SCLC is responsible for the transition of resistance states. The electron trapping and detrapping process is proposed for interpreting the resistive switching. The domination of the grain bulk effect on the resistive switching is demonstrated by the complex impedance spectroscopy. The analyses of activation energies for the conduction in the low- and high- resistance states have been executed comparatively. It is proposed that the first and the second ionization of oxygen vacancies are responsible for the conduction in the low- and high- resistance states, respectively. This electron trapping effect and the transition of conduction behavior can be

expected to fit the resistive switching observed in other perovskite oxides. It can be hypothesized that resistive switching can take place in various oxides as long as electron-trapping-assisted SCLC exists.

ACKNOWLEDGMENTS

This work was supported by a grant from the State Key Program for Basic Research of China (2004CB619305-2010CB631004), National Natural Science Foundation of China (10804048), and Research Fund for the Doctoral Program of Higher Education of China (200802841003).

REFERENCES

[1] J. F. Scott, *Annu. Rev. Mater. Sci.* 28, 79 (1998).
[30] H. Diamond, *J. Appl. Phys.* 32, 909, (1961).
[31] K. M. Johnson, *J. Appl. Phys.* 33, 2826 (1962).
[32] O. G. Vendik, *Ferroelectrics* 12, 85 (1976).
[33] Q. X. Jia, J. R. Groves, P. Arendt, Y. Fan, A. T. Findikoglu, S. R. Foltyn, H. Jiang, and F. A. Miranda, *Appl. Phys. Lett.* 74, 1564 (1999).
[34] L. A. Knauss, J. M. Pond, J. S. Horwitz, D. B. Chrisey, C. H. Mueller, and R. Treece, *Appl. Phys. Lett.* 69, 25 (1996).
[35] S. S. Gevorgian, and E. L. Kollberg *IEEE Trans. Microwave Theory Tech.* 49, 2117 (2001).
[36] V. K. Varadan, D. K. Ghodgaonker, V. V. Varadan, J. F. Kelly, and P. Glikerdas, *Microwave J.* 35, 116 (1992).
[37] R. W. Babbitt, T. E. Koscica, and W. C. Drach, *Microwave J.* 35, 63 (1992).
[38] A. Outzourhit, J. U. Trefny, T. Kito, B. Yarar, A. Naziripour, A. M. Hermann, *Thin Solid Films* 259, 218 (1995).
[39] De Flaviis, N. G. Alexopoulos, and M. Staffsudd, *IEEE Trans. Microwave Theory Tech.* 45, 963 (1997).
[40] S. Zafar, R. E. Jones, P. Chu, B. White, B. Jiang, D. Taylor, P. Zurcher, and S. Gillepsie, *Appl. Phys. Lett.* 72, 2820 (1998).
[41] R. York, A.Nagra, E. Erker, T. Taylor, P. Periaswamy, J. Speck, S. Streiffer, O. Auciello, *Proceedings of the 2000 12th IEEE International Symposium on Applications of Ferroelectrics* 1, 195 (2000).
[42] X. X. Xi, H.-C. Li, W. Si, A. A. Sirenko, I. A. Akimov, J. R. Fox, A. M. Clark, and J. Hao, *J. Electroceramics* 4, 393 (2000).
[43] X.H. Zhu, J. M. Zhu, S. H. Zhou, Z. G. Liu, N. B. Ming, S. G. Lu, H. L.-W. Chan, and C.-L. Choy, *J. Electron. Mater.* 32, 1125 (2003).
[44] J. C. Shin, J. Park, C. S. Hwang, and H. J. Kim, *J. Appl. Phys.* 86, 506 (1999).
[45] C. S. Hwang, *J. Appl. Phys.* 92, 432 (2002).
[46] J. Q. He, E. Vasco, C. L. Jia, and R. H. Wang, *Appl. Phys. Lett.* 87, 062901 (2005)

[47] S. Schmidt, D. O. Klenov, S. P. Keane, J. Lu, T. E. Mates, and S. Stemmer, *Appl. Phys. Lett.* 88, 131914 (2006).
[48] L. J. Sinnamon, M. M. Saad, R. M. Bowman, and J. M. Gregg, *Appl. Phys. Lett.* 81, 703 (2002).
[49] B. H. Park, E. J. Peterson, Q. X. Jia, J. Lee, X. Zeng, W. Si, and X.X. Xi, *Appl. Phys. Lett.* 78, 533 (2001).
[50] I. A. Akimov, A. A. Sirenko, A. M. Clark, J. H. Hao, and X. X. Xi, *Phys. Rev. Lett.* 84, 4625 (2000).
[51] C. T. Black and J. J. Welser, *IEEE Trans. Electron Devices* 46, 776 (1999).
[52] C. Zhou and D. M. Newns, *J. Appl. Phys.* 82, 3081 (1997).
[53] L. J. Sinnamon, R. M. Bowman, and J. M. Gregg, *Appl. Phys. Lett.* 78, 1724 (2001).
[54] B. Chen, H. Yang, L. Zhao, J. Miao, B. Xu, X. G. Qiu, B. R. Zhao, X. Y. Qi, and X. F. Duan, *Appl. Phys. Lett.* 84, 583 (2004).
[55] H. Z. Jin, J. Zhu, P. Ehrhart, F. Fitsilis, C. L. Jia, S. Regnery, K. Urban, and R. Waser, *Thin Solid Films* 429, 282 (2003).
[56] M. Stengel and N. A. Spaldin, *Nature* 443, 679 (2006).
[57] C. L. Chen, J. Shen, S. Y. Chen, G. P. Luo, C. W. Chu, F. A. Miranda, F. W. Van Keuls, J. C. Jiang, E. I. Meletis, and H. Y. Vhang, *Appl. Phys. Lett.* 78, 652 (2001).
[58] J. H. Chen, C. L. Lia, K. Urban, and C. L. Chen, *Appl. Phys. Lett.* 81, 1291 (2002).
[59] D. C. Yoo and J. Y. Lee, *J. Cryst. Growth* 224, 251 (2001).
[60] Y. L. Qin, C. L. Jia, K. Urban, R. Liedtke, and R. Waser, *Appl. Phys. Lett.* 80, 2728 (2002).
[61] H. -J. Gao, C. L. Chen, B. Rafferty, S. J. Pennycook, G. P. Luo, and C. W. Chu, *Appl. Phys. Lett.* 75, 2542 (1999).
[62] Y. D. Xia, K. B. Yin, C. Xu, Y. Zhang, B. Xu, W. Y. He, X. K. Meng, J. Yin, and Z. G. Liu, *Appl. Phys. Lett.* 92, 102906 (2008).
[63] S. N. Ruddlesden, and P. Popper, *Acta Cryst.* 11, 54 (1958).
[64] A. Asthagiri and D. S. Sholl, *J. Chem. Phys.* 116, 9914 (2002).
[65] M. W. Cole, P. C. Joshi, and M. H. Ervin, *J. Appl. Phys.* 89, 6336 (2001).
[66] M. W. Cole, P. C. Joshi, M. H. Ervin, M.C. Wood, and R. L. Rfeffer, *Thin Solid Films* 374, 34 (2000).
[67] N. K. Pervez, P. J. Hansen, and R. A. York, *Appl. Phys. Lett.* 85, 4451 (2004).
[68] J. C. Slater, *Phys. Rev.* 78, 748 (1950).
[69] A. F. Devonshire, *Phli. Mag.* 40, 1040 (1949).
[70] G. Rupprecht, R. O. Bell, and B. D. Silverman, *Phys. Rev.* 123, 97 (1961).
[71] R. C. Neville, B. Hoeneisen and C. A. Mead, *J. Appl. Phys.* 43, 2124 (1972).
[72] B. A. Baumert, L. –H. Chang, A. T. Matsuda, T. –L. Tsai, C. J. Tracy, R. B. Gregory, P. L. Fejes, N. G. Cave, W. Chen, D. J. Taylor, T. Otsuki, E. Fujii, S. Hayashi, and K. Suu, *J. Appl. Phys.* 82, 2558 (1997).
[73] S. Hyun and K. Char, *Appl. Phys. Lett.* 79, 254 (2001).
[74] Y. D. Xia, J. B. Chen, B. Pan, D. Wu, X. K. Meng, and Z. G. Liu, *Appl. Phys. Lett.* 87, 052902 (2005).
[75] K.-H. Cho, C.-H. Lee, C.-Y. Kang, S.-J. Yoon, and Y.-P. Lee, *Appl. Phys. Lett.* 90, 162905 (2007).
[76] X. Wang, U. Helmersson, L. D. Madsen, I. P. Ivanov, P. Munger, S. Rudner, B. Hjorvarsson, and J. –E. Sundgren, *J. Vac. Sci. Technol. A* 17, 564 (1999).

[77] K. W. Blazey, R. Koch, and K. A. Muller, *Mater. Res. Bull.* 16, 1149 (1981).
[78] J. Zhai, X. Yao, L. Zhang, and B. Shen, *Appl. Phys. Lett.* 84, 3136 (2004).
[79] P. Sun, N. Matsuura, and H. E. Ruda, *J. Appl. Phys.* 96, 3417 (2004).
[80] Y. D. Xia, C. Cai, X. Y. Zhi, B. Pan, D. Wu, and Z. G. Liu, *Appl. Phys. Lett.* 88, 182909 (2006).
[81] W. Chen, X. Yao, and X. Y. Wei, *Solid State Communications* 141, 84 (2007).
[82] W. Qin, W. B. Wu, J. R. Cheng, and Z. Y. Meng, *Materials Letters* 61, 5161 (2007).
[83] S. G. Lu, X. H. Zhu, C. L. Mak, K. H. Wong, H. L. W. Chan, and C. L. Choy, *Appl. Phys. Lett.* 82, 2877 (2003).
[84] P. Padmini, T. R. Taylor, M. J. Lefevre, A. S. Nagra, R. A. York, and J. S. Speck, *Appl. Phys. Lett.* 75, 3186 (1999).
[85] H. J. Cho, and H. J. Kim, *Appl. Phys. Lett.* 72, 2820 (1998).
[86] S. G. Yoon, J. C. Lee, and A. Safari, *J. Appl. Phys.* 76, 2999 (1994).
[87] Im Jaemo, O. Auciello, P. K. Baumann, and S. K. Streiffer, D. Y. Kaufman, and A. R. Krauss, *Appl. Phys. Lett.* 76, 625 (2000).
[88] Y. D. Xia, D. Wu, and Z. G. Liu, *J. Phys. D* 37, 2256 (2004).
[89] B. Chapman, *Glow Discharge Processes* Wiley (New York) p.203 (1980).
[90] J. A. Thornton, *Ann. Rev. Mater. Sci.* 7, 239 (1977).
[91] J. W. Liou, and B. S. Chiou, *J. Am. Ceram.* Soc. 80, 3093 (1997).
[92] D. O'Neill, R. M. Bowman, and J. M. Gregg, *Appl. Phys. Lett.* 77, 1520 (2000).
[93] G. Catalan, D. O'Neill, R. M. Bowman, and J. M. Gregg, *Appl. Phys. Lett.* 77, 3078 (2000).
[94] International Technology Roadmap for Semiconductors, 2007 Edition, www.itrs.net/Links/2007ITRS/ExecSum2007.pdf.
[95] G. I. Meijer, *Science* 319, 1625 (2008).
[96] R. Waser, M. Aono, *Nat. Mater.* 6, 833 (2007).
[97] A. Sawa, *Mater. Today*, 11, 28 (2008).
[98] S. Tsui, A. Baikalov, J. Cmaidalka, Y. Y. Sun, Y. Q. Wang, Y. Y. Xue, C. W. Chu, L. Chen, and A. J. Jacobson, *Appl. Phys. Lett.* 85, 317 (2004).
[99] A. Beck, J. G. Bednorz, Ch. Gerber, C. Rossel, and D. Widmer, *Appl. Phys. Lett.* 77, 139 (2000).
[100] J.-W. Park, K. Jung, M. K. Yang, J.-K. Lee, D.-Y. Kim, and J.-W. Park, *J. Appl. Phys.* 99, 124102 (2006).
[101] Y. Watanabe, J. G. Bednorz, A. Bietsch, Ch. Gerber, D. Widmer, A. Beck, S. J. Wind, *Appl. Phys. Lett.* 78, 3738 (2001).
[102] D. Choi, D. Lee, H. Sim, M. Chang, and H. Hwang, *Appl. Phys. Lett.* 88, 082904 (2006).
[103] K. Szot, W. Speier, G. Bihlmayer, R. Waser, *Nat. Mater.* 5, 312 (2006).
[104] R. Oligschlaeger, R. Waser, R. Meyer, S. Karthäuser, and R. Dittmann, *Appl. Phys. Lett.* 88, 042901 (2006).
[105] Y. Watanabe, *Phys. Rev. B* 59, 11257 (1999).
[106] M. Hamaguchi, K. Aoyama, S. Asanuma, Y. Uesu, and T. Katsufuji, *Appl. Phys. Lett.* 88, 142508 (2006).
[107] Y. D. Xia, W. Y. He, L. Chen, X. K. Meng, and Z. G. Liu, *Appl. Phys. Lett.* 90, 022907 (2007).

[108] R. Dong, D. S. Lee, W. F. Xiang, S. J. Oh, D. J. Seong, S. H. Heo, H. J. Choi, M. J. Kwon, S. N. Seo, M. B. Pyun, M. Hasan, and H. Hwang, *Appl. Phys. Lett.* 90, 042107 (2007).
[109] P. W. M. Blom, R. M. Wolf, J. F. M. Cillessen, and M. P. C. M. Krijn, *Phys. Rev. Lett.* 73, 2107 (1994).
[110] L.-E. Yu, S. Kim, M.-K. Ryu, S.-Y. Choi, and Y.-K. Choi, *IEEE Electron Device Letters* 29, 331 (2008).
[111] N. Das, S. Tsui, Y. Y. Xue, Y. Q. Wang, and C. W. Chu, *Phys. Rev. B* 78, 235418 (2008).
[112] M. A. Lampert and P. Mark, Current Injection in Solids (Academic, New York, 1970).
[113] P. C. Joshi and S. B. Krupanidhi, *J. Appl. Phys.* 73, 7627 (1993).
[114] G. R. Fox and S. B. Krupanidhi, *J. Appl. Phys.* 74, 1949 (1993).
[115] C. Sudhama, A. C. Campbell, P. D. Maniar, R. E. Jones, R. Moazzami, C. J. Mogab, and J. C. Lee, *J. Appl. Phys.* 75, 1014 (1994).
[116] J. G. Simmons, in *Handbook of Thin Film Technology*, edited by L. I. Maissel and R. Glang (McGraw-Hill, New York, 1970), p. 14.
[117] C. Sudhama, A. C. Campbell, P. D. Maniar, R. E. Jones, R. Moazzami, C. J. Mogab, and J. C. Lee, *J. Appl. Phys.* 75, 1014 (1994).
[118] J. D. Baniecki, R. B. Laibowitz, T. M. Shaw, C. Parks, J. Lian, H. Xu, and Q. Y. Ma, J. Appl. Phys. 89, 2873 (2001).
[119] M. Janousch, G. I. Meijier, U. Staub, B. Delley, S. F. Karg, B. P. Anderson, *Adv. Mater.* 2007, *19*, 2232.
[120] Y. B. Nian, J. Strozier, N. J. Wu, X. Chen, A. Ignatiev, *Phys. Rev. Lett.* 2007, *98*, 146403.
[121] Y. D. Xia, Z. G. Liu, Y. Wang, L. Shi, L. Chen, J. Yin, X. K. Meng, *Appl. Phys. Lett.* 2007, *91*, 102904.
[122] D. Wu, A. D. Li, and N. B. Ming, *Appl. Phys. Lett.* 84, 4505 (2004).
[123] D. C. Sinclair and A. R. West, *J. Appl. Phys.* 66, 3850 (1989).
[124] S. Saha and S. B. Krupanidhi, *J. Appl. Phys.* 87, 849 (2000).
[125] M. M. Kumar and Z. G. Ye, *J. Appl. Phys.* 90, 934 (2001).
[126] Y. H. You, B. S. So, J. H. Hwang, W. Cho, S. S. Lee, T. M. Chung, C. G. Kim, and K. S. An, *Appl. Phys. Lett.* 89, 222105 (2006).
[127] K. Morii, H. Kawano, I. Fujii, T. Matsui, and Y. Nakayama, *J. Appl. Phys.* 78, 1914 (1995).
[128] Chen Ang, Zhi Yu, and L. E. Cross, *Phys. Rev. B* 62, 228 (2000).
[129] C. C. Wang and L. W. Zhang, *Phys. Rev. B* 74, 024106 (2006).
[130] J. Daniels and K. H. Hardtl, *Philips Res. Rep.* 31, 480 (1976).

In: Perovskites: Structure, Properties and Uses
Editor: Maxim Borowski, pp. 283-317
ISBN 978-1-61668-525-6

Chapter 6

MICROWAVE DIELECTRIC PROPERTIES OF $Ca[(Li_{1/3}A_{2/3})_{1-x}M_x]O_{3-\delta}$ [A=Nb, Ta AND M=Ti, Zr, Sn] COMPLEX PEROVSKITES: A REVIEW

George Sumesh and Thomas Sebastian Mailadil*
Materials and Minerals Division, National Institute for Interdisciplinary Science and Technology (CSIR), Thiruvananthapuram - 695 019, India

ABSTRACT

The perovskite family of materials is of considerable technological importance for its excellent temperature stable microwave properties for dielectric resonator based filters, oscillators and antenna applications. In this chapter we review the preparation, characterization and the microwave dielectric properties of $Ca[(Li_{1/3}A_{2/3})_{1-x}M_x]O_{3-\delta}$ [A=Nb, Ta and M=Ti, Zr, Sn] dielectric ceramics. This family of perovskite materials shows relative permittivity in the range 20 to 56 with a quality factor up to 45000 GHz and temperature coefficient of resonant frequency (τ_f) in the range from −21 to +83 ppm/°C. The τ_f can be tailored by adjusting the titanium content. The sintering temperature can be lowered below 950 °C to suit LTCC by the addition of low melting glasses.

1. INTRODUCTION

Microwave integrated electronics play a major role in communication systems. The growth of satellite communication and cellular radio systems has led to the requirement of compact, temperature stable, and low cost filters. In the early seventies, it was difficult to find a device which could perform as filter, oscillator, and antenna with weight and size features suitable for integration in miniature circuits. For instance, for frequency stabilization, one has to rely upon the bulky expensive metallic cavities which were not integrable. These problems

* Email: mailadils@yahoo.com

were alleviated with the advent of ceramic microwave dielectric resonators and have been essential in eliminating metallic cavities and waveguides. The past 25 years have seen a rapid development in the miniaturization of microwave circuitry and this has led to the development of dielectric resonators which can replace the bulky metallic cavities. Recently, microwave dielectric materials designed for wireless communication has become a booming area of growth. Latest communication technologies including mobile multimedia systems, ultra high speed wireless local area network and intelligent transport systems require highly intelligent device that enable communication effectively between people and machines. The dielectric resonators used in filters oscillators and antennas have become indispensable component in microwave communication systems for its integration potential, size reduction, reliability and temperature stability [1]. The materials for dielectric resonators are required to excel in three characteristics, a high dielectric constant, a high quality factor, and a nearly zero temperature coefficient of resonant frequency. High dielectric constant is essential since it is the key factor for miniaturization and can thus lower the cost of production. The higher the quality factor, the lower is the insertion loss and steeper the cut off. Moreover, a high quality factor provides a narrow band width and hence enables the allocation of more number of channels within a given frequency range [1-4].

From a historical perspective, guided electromagnetic wave propagation in dielectric media received much attention in the early days of researching microwaves [5]. The possibility of using unmetallized dielectrics as resonators was first proposed by Ritchmyer [6] in 1939. The search for dielectrics for microwave applications starts from 1960. The first reported work on the adaptability of a high dielectric constant dielectric rod to generate standing wave resonance phenomena was proposed by Schlike [7]. Okaya reported that a piece of rutile (TiO_2) acted as a resonator and subsequently Okaya and Barash analyzed the different modes of a dielectric resonator [8, 9]. The first microwave filter proposed by Cohen [10] in 1968 where TiO_2 was used as the dielectric resonator. The rutile TiO_2 has a high dielectric constant (ε_r = 100), high quality factor (Qxf = 10000 GHz), and high temperature coefficient of resonant frequency (τ_f = +450 ppm/^{O}C). This filter was not put into practical use because of its large τ_f. A real breakthrough in microwave ceramic technology occurred when the first temperature stable ceramic dielectric barium tetratitanate developed by Raytheon [11] in 1970. Later, a modified barium titanate with improved performance was reported from BEL laboratories [12]. The next major breakthrough came from Japan when the Murata Manufacturing Company produced (Zr-Sn)TiO_4 ceramics with excellent microwave dielectric properties [13, 14]. These positive results led to an intensive research and actual implementation of dielectric resonator as the indispensable component in the microwave communication. With the revolution in mobile phone and satellite communication systems using microwave as propagation media, the research and development in the field of microwave dielectrics for device miniaturization and excellent performance has been one of the biggest challenges in the area of materials science.

Table 1. Microwave dielectric properties and sintering temperatures of representative materials

Material	Permittivity	Qxf (GHz)	τ_f	Sintering Temperature (^oC)	Reference
$MgTiO_3 – CaTiO_3$	20	55000	0	1400	[15]
$BaTi_4O_9$	37	22700	15	1300	[16, 17]
$Ba_2Ti_9O_{20}$	39	32000	2	1350	[12]
$(Zr_{1-x}Sn_x)TiO_4$	39	51500	0.7	1600	[13, 14]
$Ba(Zn_{1/3}Ta_{2/3})O_3$	28	168000	0.5	1500	[77-80]
$Ba(Mg_{1/3}Ta_{2/3})O_3$	24	430000	8	1640	[29, 78-80]
$BaO-Sm_2O_3-TiO_2$	77.5	11200	-3.4	1360	[19]
$BaO-Nd_2O_3-TiO_2$	83	10500	70	1450	[81]
$CaTiO_3$ - $NdAlO_3$	41	33000	-17	1450	[21, 22]
$SrTiO_3$ - $LaAlO_3$	39	32000	2	1450	[20, 23]

The microwave dielectric resonator materials with dielectric constant from 20 to about 80 with high quality factor and low τ_f are now available for practical use. The extensive research in the last three decades provides several extremely low loss ceramics suitable for resonator applications. The properties of the important DR materials such as $MgTiO_3–CaTiO_3$ [1, 15], $BaTi_4O_9$ [16, 17], $BaTi_9O_{20}$ [12], $(Zr_{1-x}Sn_x)TiO_4$ [1, 13, 14], $Ba(Zn_{1/3}Ta_{2/3})O_3$ and $Ba(Mg_{1/3}Ta_{2/3})O_3$ [18], $BaO-RE_2O_3-TiO_2$ [19], $SrTiO_3$-$LaAlO_3$, $CaTiO_3$-$LaAlO_3$ [20-23] are shown in table 1. Thirty years ago Ichinose et al. [24] investigated the A site modified $(Sr_{1-x}Ca_x)[(Li_{1/4}Nb_{3/4})_{1-y}Ti_y]O_3$ complex perovskite ceramics. This was the first low loss lithium based complex perovskite system and x = y = 0.08 composition has good dielectric properties of ε_r = 43.2, Q = 3500 GHz at 9 GHz, and τ_f = -30 ppm/°C when sintered at 1300 °C.

The current trend and the state of the art of microwave dielectric materials for telecommunication applications is discussed in the book “Dielectric materials for wireless communications” [1] authored by Sebastian. This book reports the sintering temperature and microwave dielectric properties of more than 2000 low loss dielectric ceramic compositions and discusses the ways to tailor their properties by possible substitution, dopant and glass additions. This book covers the important low loss microwave dielectric materials of the type zirconium tin titanate, $BaO-TiO_2$ systems, pseudo-tungsten bronze, perovskite type ceramics (1:1 cation ordering, 1:2 cation ordering, and the cation deficient complex perovskites) and the other materials such as tungstates, silicates, aluminates and spinals etc. Among the various type of microwave dielectric ceramics, perovskite structure has attracted much attention for their excellent microwave dielectric properties. The complex perovskite family shows the relative permittivity in the range 25-40 with high quality factor and low temperature coefficient of resonant frequency. Compared to other complex perovskite materials, $Ba(Zn_{1/3}Ta_{2/3})O_3$ and $Ba(Mg_{1/3}Ta_{2/3})O_3$ show excellent microwave dielectric properties and have been extensively studied [1]. However, they are usually made up of expensive chemicals such as tantalates and a high sintering temperature (≈1500 ^oC) is necessary for obtaining good densification and microwave dielectric properties. It is well known that the cation ordering affects the dielectric properties, especially the quality factor of the complex perovskites [1]. In order to obtain a high quality factor, a high sintering temperature together with a long annealing time is necessary for these complex perovskite systems. Hence, these resonators are

very expensive and not cost effective. The above problem can be solved by the development of low temperature sinterable low cost materials or by lowering the sintering temperature of the microwave ceramics with reasonably good dielectric properties. Most of the low loss dielectric materials have high sintering temperature [1]. Earlier reports show that addition of sintering aid is the best method to reduce the sintering temperature. Low temperature co-fired ceramics (LTCC) has been identified as an enabling solution for the fabrication of miniaturized microwave devices and modules. An advantage of LTCC technology includes shrinking circuit dimensions, high level of passive integration, exceptional high frequency performance, excellent reliability and low cost [25]. However, from table 1 it can be observed that the currently available high Q materials are having high processing temperature. However, in most of the high temperature processed high Q complex perovskites, a drastic degradation of microwave dielectric properties is observed with the reduction of sintering temperature by the glass addition [26, 27]. Reports show that, large amount of glass is necessary to lower the sintering temperature of the ceramics having high processing temperature [26-31]. As the amount of glass increases, the quality factor decreases. Hence the selection of the low loss ceramics having low processing temperature is important for glass addition. From the device design point of view, a good combination of high permittivity, high quality factor, nearly zero temperature coefficients of resonant frequency and low processing temperature are required for practical applications. Hence the development of good microwave dielectric materials with optimal balance of these properties is one of the major challenges in the microwave communication industry.

Recently, Choi *et al*. [32, 33] proposed a nonstoichiometric $Ca(Li_{1/3}Nb_{2/3})O_{3-\delta}$ complex perovskite ceramic which can sinter at 1150^{o}C with excellent microwave dielectric properties. This system is multiphase and the substitution of Sn^{4+}, Zr^{4+} and Ti^{4+} for $[Li_{1/3}Nb_{2/3}]^{3.67+}$ by forming $Ca[(Li_{1/3}Nb_{2/3})_{1-x}M_x]O_{3-\delta}$ [M=Ti, Zr, Sn] give single phase perovskites. This family of materials with excellent dielectric properties can be a promising candidate for low temperature sintering ceramics because they can be sintered at 1150^{o}C without sintering aid. However, the sintering temperature of this material is relatively high to use silver or copper as an internal electrode in multilayered structures and further there exist the possibility of evaporation of volatile lithium at such high sintering temperatures. Although some of the Li based ceramics have excellent dielectric properties, the volatile Li has a deleterious effect on the dielectric properties. The deficiency of Li leads to decrease in density and lattice defects which adversely affect the dielectric properties. This problem can be minimised by muffling the pellets in its own calcined powder or by lowering the sintering temperature by using a sintering aid. Several authors [34-45] tried to minimize the escape of volatile lithium by lowering the sintering temperature by the addition of low melting additives such as B_2O_3, Bi_2O_3, and glass frit and also tried to tailor the dielectric properties by suitable substitution. The present report reviews the microwave dielectric properties of $Ca[(Li_{1/3}A_{2/3})_{1-x}M_x]O_{3-\delta}$ [A=Nb, Ta and M=Ti, Zr, Sn] ceramics and the possible substitution and glass addition.

2. EXPERIMENTAL

The $Ca[(Li_{1/3}Nb_{2/3})_{1-x}Ti_x]O_{3-\delta}$ [CLNT] and $Ca[(Li_{1/3}Ta_{2/3})_{1-x}Ti_x]O_{3-\delta}$ [CLTT] ceramic samples were prepared by the conventional solid state ceramic route. High purity $CaCO_3$, Li_2CO_3, TiO_2 (99.9+%, Aldrich chemical company, Inc, Milwaukee, WI, USA) Ta_2O_5 and Nb_2O_5 (99.9+%, NFC Hyderabad, India) were used as the starting materials. Stoichiometric amounts of the powder samples were mixed and ball milled using zirconia balls in ethanol medium for 24 hours. Li_2CO_3 dissolve in water and hence ethanol was used as the mixing medium. The resultant slurry was then dried and calcined. The calcinations were carried out at temperatures in the range 900 to 1050 ^oC for four hours. The calcination temperature is optimized for the best density and the dielectric properties. The sintering temperature of the CLNT/CLTT ceramics were lowered by the addition of different borosilicate glasses such as lithium borosilicate (35.5:Li_2O, 31.66:B_2O_3, 33.2:SiO_2)(LBS), lead borosilicate (40:PbO,40:B_2O_3, 20:SiO_2) (PBS), barium borosilicate (30:BaO,60:B_2O_3, 10:SiO_2)(BBS), zinc borosilicate (60:ZnO,30:B_2O_3, 10:SiO_2)(ZBS), bismuth zinc borosilicate (35:Bi_2O_3, 32:ZnO, 27:B_2O_3, 6:SiO_2)(BZBS) and lithium magnesium zinc borosilicate (20:Li_2O, 20:MgO, 20:ZnO, 20:B_2O_3, 20:SiO_2) (LMZBS). The corresponding glass powders were synthesized from high purity oxide chemicals of B_2O_3, Li_2CO_3, SiO_2, PbO, $BaCO_3$, Bi_2O_3, $(MgCO_3)_4$ $Mg(OH)_2$ $5H_2O$ and ZnO (99.9 % Aldrich chemical company, U.S.A). These oxides were weighed stoichiometrically and were mixed in an agate mortar for 2 hours using ethanol as the medium. They were dried, melted in platinum crucible above their melting point, quenched and powdered. Different weight percentages of various glasses were added to the fine powder of calcined CLNT and CLTT ceramics. Polyvinyl alcohol (PVA) (Molecular Weight 22000, BDH Lab Suppliers, England) solution was then added to the powder, mixed, dried and ground well and pressed into cylindrical disks of about 14 mm diameter and 7mm thickness, by applying a pressure of about 100 MPa. These compacts were muffled by CLNT or CLTT powder of the same composition and sintered at different temperatures in the range 875^oC – 1200 ^oC for 4 hours. The sintering temperature was optimized for the best density and the dielectric properties. The samples were muffled with powders of same composition to prevent the escape of volatile lithium at elevated sintering temperatures. The crystal structure and phase purity of the powdered samples were investigated by X- ray diffraction technique using Ni-filtered Cu-Kα radiation (Rigaku Dmax-I, Japan, diffractometer). The microstructures of the sintered samples were studied using scanning electron microscope (*JEOL-JSM* 5600 LV, Tokyo, Japan). The sintered density of the specimen was measured by the Archimedes method. The microwave dielectric properties were measured in the frequency range 4 to 6 GHz by a Vector Network Analyzer (8753 ET, Agilent Technologies). The dielectric constant and unloaded quality factor of the samples were measured by Hakki and Coleman [46] and cavity method [47] respectively. Shrinkage characteristics were studied using Dilatometer (TMA- 60 H, Shimadzu, Kyoto, Japan).

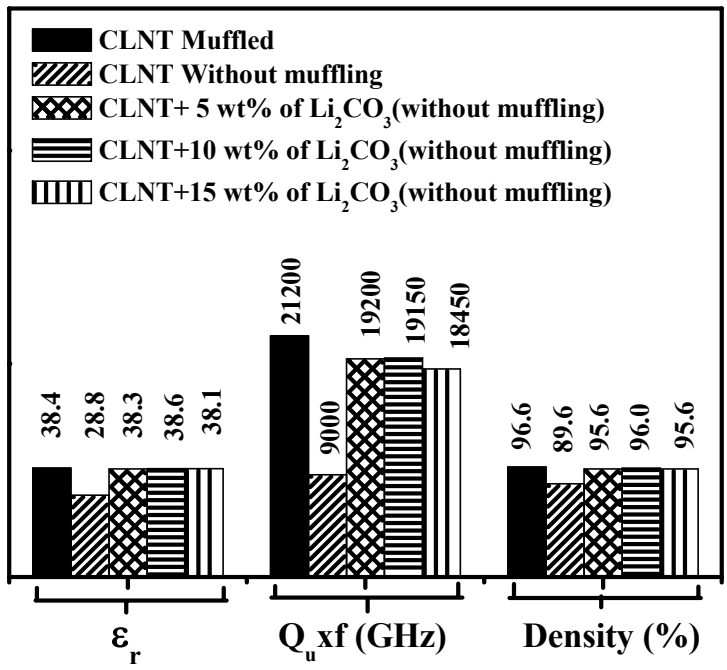

Figure 1. Relative density and dielectric properties of $Ca[(Li_{1/3}Nb_{2/3})_{0.8}Ti_{0.2}]O_{3-\delta}$ ceramics with different sintering condition.

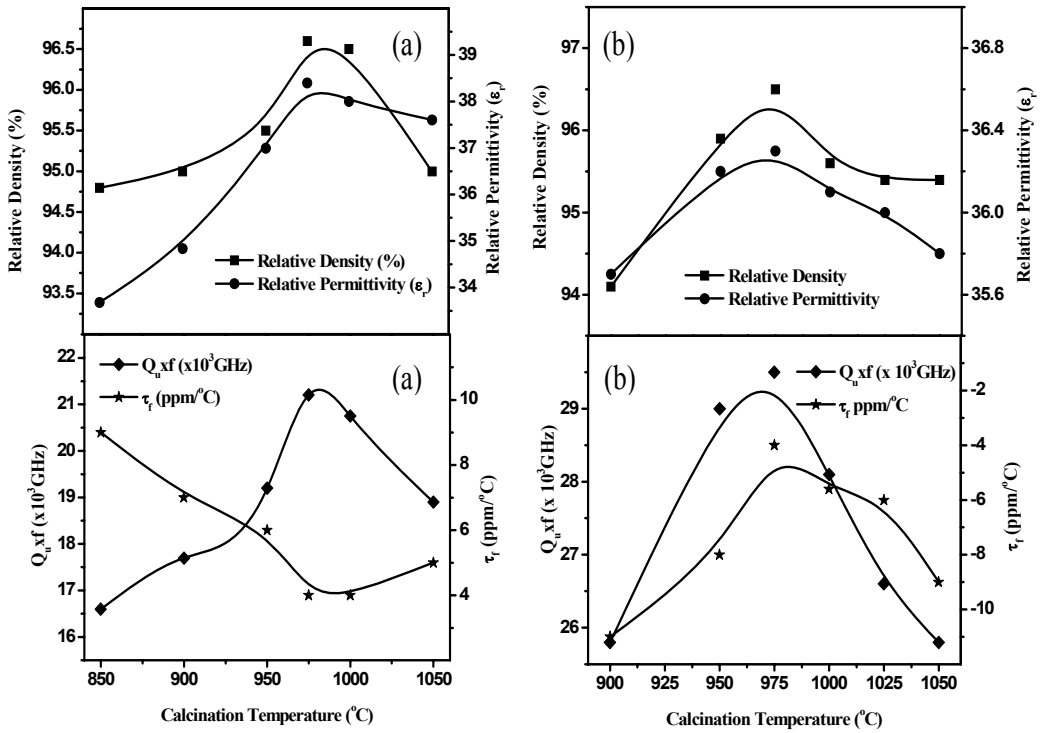

Figure 2. Variation of densification and microwave dielectric properties of (a) CLNT and (b) CLTT ceramics as a function of calcination temperature.

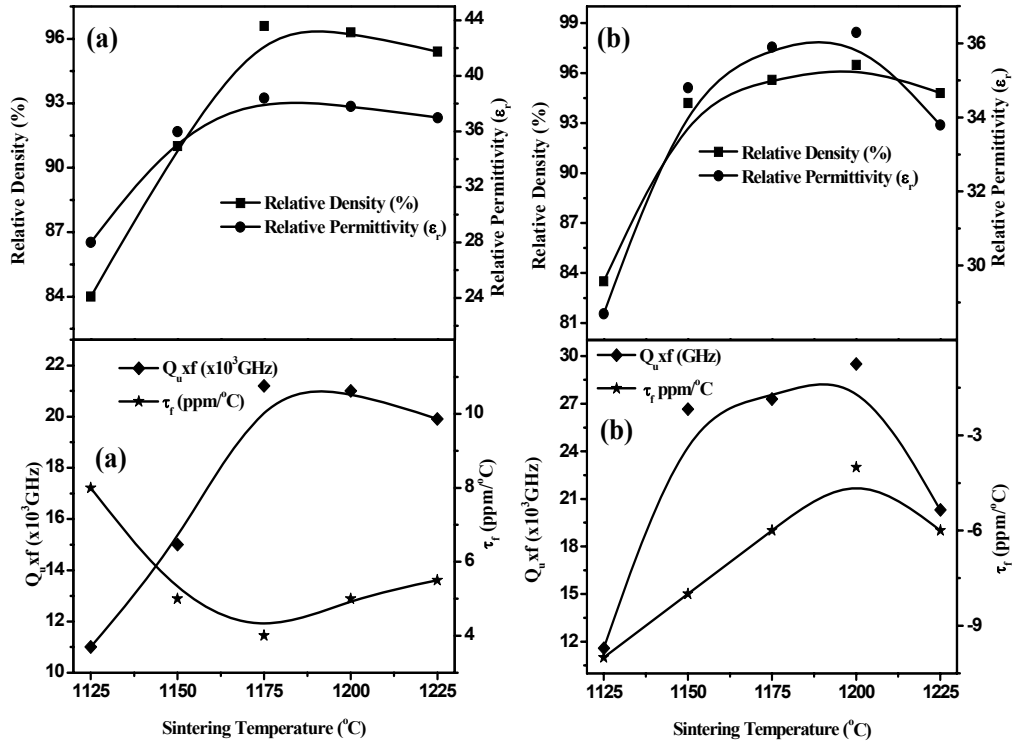

Figure 3. Variation of densification and microwave dielectric properties of (a) CLNT and (b) CLTT ceramics as a function of sintering temperature.

3. $Ca(Li_{1/3}A_{2/3})O_{3-\delta}$ Complex Perovskite [A=Nb, Ta]

The $Ca(Li_{1/3}A_{2/3})O_{3-\delta}$ [32, 38] is a nonstoichiometric perovskite and is multiphase when prepared by the conventional solid state ceramic route. The X- ray diffraction pattern of $Ca(Li_{1/3}A_{2/3})O_{3-\delta}$ [A = Nb, Ta] [32, 38] can be indexed based on $CaTiO_3$ orthorhombic perovskite structure with a small amount of second phase. However, substitution of Sn^{4+} and Ti^{4+} for $[Li_{1/3}Nb_{2/3}]^{3.67+}$ by forming $Ca[(Li_{1/3}Nb_{2/3})_{1-x}M_x]O_{3-\delta}$ [M=Ti, Sn] give single phase perovskites in the vicinity of x=0.2 [32]. The $Ca[(Li_{1/3}Nb_{2/3})_{1-x}M_x]O_{3-\delta}$ [M=Ti, Sn] dielectric resonators were prepared by calcining the ball milled raw powders at temperatures in the range 900-1000 ^oC/4h and sintering at about 1150 ^oC/4hrs [32, 38]. It was reported that lithium is volatile and escape during sintering at elevated temperature [1, 32, 38, 43]. Muffling of the samples with calcined powders of the same composition or keeping the pellets in closed box is the best method to avoid the volatilization of lithium. It is also possible to control the escape of lithium by adding extra lithium in the parent composition. Recently, Sumesh *et al*. [48] compares the microwave dielectric properties of the $Ca[(Li_{1/3}Nb_{2/3})_{0.8}Ti_{0.2}]O_{3-\delta}$ ceramics with different sintering condition such as open sintering, muffling and different wt% of lithium addition to the parent material. Figure 1 shows the densification and the microwave dielectric properties of $Ca[(Li_{1/3}Nb_{2/3})_{0.8}Ti_{0.2}]O_{3-\delta}$ ceramics with different sintering condition such as muffling, without muffling, and addition of extra

Li_2CO_3 to the parent material. It is found that the sample sintered without muffling has inferior dielectric properties compared to other sintering conditions. Addition of extra lithium in the parent material shows dielectric properties comparable to that of muffling. However, there is a possibility of the formation of second phase with the addition of extra lithium. Hence muffling is the best method to avoid the volatilization of low melting elements.

1. 3.1. Optimization of Calcination and Sintering Temperatures

The microwave dielectric properties not only depend on the chemical composition but also on the calcination and sintering temperatures. Figures 2 and 3 show the optimization of calcination and sintering temperatures of $Ca[(Li_{1/3}Nb_{2/3})_{0.8}Ti_{0.2}]O_{3-\delta}$ (CLNT) and $Ca[(Li_{1/3}Ta_{2/3})_{0.7}Ti_{0.3}]O_{3-\delta}$ (CLTT) ceramics. These compositions have been selected for its phase purity and excellent temperature stable microwave dielectric properties. The calcination and sintering temperatures were optimized for best density and dielectric properties. It can be observed that the increase in the calcination temperature improved the physical and electrical properties. The best physical and dielectric properties are observed for the compounds calcined at 975 ^oC/4hrs. Further increase in the calcination temperature degraded the physical and dielectric properties. Unreacted materials in under-calcined powder acted as an inhibitor of grain growth during sintering [43]. It is reported that higher calcination temperature lowered the reactivity of ceramic powders resulting in the increase in the number of pores. These could be the reason for the degradation of densification and dielectric properties below and above the optimized calcination temperature. Figure 3 shows the variation of the density and dielectric properties of $Ca[(Li_{1/3}Nb_{2/3})_{0.8}Ti_{0.2}]O_{3-\delta}$ and $Ca[(Li_{1/3}Ta_{2/3})_{0.7}Ti_{0.3}]O_{3-\delta}$ ceramics as a function of sintering temperature. It is found that the density and dielectric properties improve with increase in the sintering temperature. The increase in the permittivity and quality factor with sintering temperature is attributed to the improvement in densification. On the other hand the dielectric properties were degraded due to the formation of pores and escape of volatile lithium at higher sintering temperature (>1000 ^oC). The optimized sintering temperature of $Ca[(Li_{1/3}Nb_{2/3})_{0.8}Ti_{0.2}]O_{3-\delta}$ (CLNT)and $Ca[(Li_{1/3}Ta_{2/3})_{0.7}Ti_{0.3}]O_{3-\delta}$ (CLTT) ceramics are 1175 ^oC and 1200 ^oC respectively for the best density and dielectric properties. It may be noted that the calcination and sintering temperatures may vary slightly with the particle size, purity and origin of the initial raw materials.

3.2. Phase Analysis of $Ca[(Li_{1/3}A_{2/3})_{1-x}M_x]O_{3-\delta}$ [A=Nb, Ta and M=Ti, Zr, Sn] Ceramics

Figures 4, 5, and 6 show the X ray diffraction patterns of $Ca[(Li_{1/3}Nb_{2/3})_{1-x}M_x]O_{3-\delta}$ [M=Ti, Zr, Sn] ceramics sintered at 1150 ^oC with increasing amount of Ti, Sn, and Zr respectively. The XRD pattern could be indexed based on the $CaTiO_3$ type orthorhombic perovskite with four formula per unit cell. At x = 0, the composition $Ca(Li_{1/3}Nb_{2/3})O_{3-\delta}$ is multiphase. However, the stability of perovskite phase increased with increasing the Ti, Sn, or Zr content and a single phase material is obtained in the range $0.2 \leq x \leq 0.3$. Further increase of Ti, Sn, or Zr concentration results in the formation of second phases. A systematic shift in

the peak positions towards higher 2θ values observed with increasing Ti substitution (see figure 4) [32]. However, the XRD peaks shift to lower angle with an increase in Zr and Sn substitution (see Figure 5 and Figure 6) [33]. This could be due to the higher ionic radii of $(Li_{1/3}Nb_{2/3})$ (0.066 nm) compared to Ti (0.056 nm) and lower ionic radii compared to Sn (0.069 nm) and Zr (0.072 nm). The tantalum analogue also has interesting microwave dielectric properties [38]. The $Ca(Li_{1/3}Ta_{2/3})O_{3-\delta}$ ceramics is also a multiphase compound with a secondary phase of Li_3TaO_4. In order to tune the τ_f and to lower the sintering temperature, Liu *et al*. [38] made a partial replacement of $(Li_{1/3}Ta_{2/3})$ by Ti and added B_2O_3 in $Ca(Li_{1/3}Ta_{2/3})O_{3-\delta}$. The substitution of smaller Ti^{4+} for $(Li_{1/3}Ta_{2/3})$ decreased the cell volume. X-ray diffraction study showed that substitution of Ti for (Li,Ta) stabilized the orthorhombic perovskite phase but decreased the 1:2 ordering (see Figure 7). The ordering peak disappeared with Ti substitution. In addition to the formation of single phase compound, the substitution of Ti^{4+} in the B site of $Ca[(Li_{1/3}A_{2/3})]O_{3-\delta}$ [A = Nb, Ta] has an additional advantage of tuning the temperature coefficient of resonant frequency to zero.

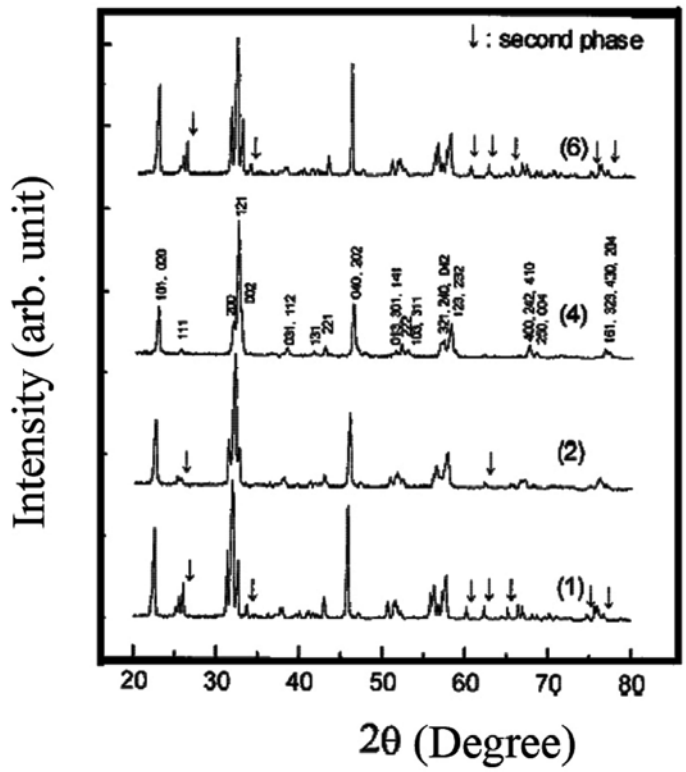

Figure 4. X-ray diffraction pattern of $Ca[(Li_{1/3}Nb_{2/3})_{1-x}Ti_x]O_{3-\delta}$ ceramics sintered at 1150°C as a function of (1) x=0.0, (2) x=0.1, (4) x=0.2, (6) x=0.5. (after ref . 32).

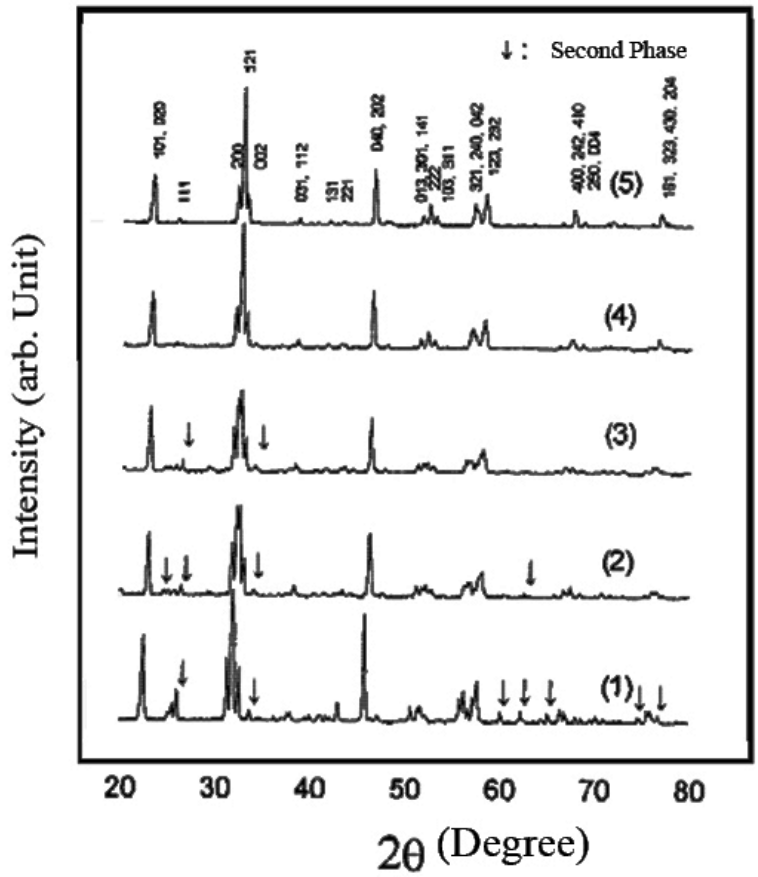

Figure 5. X-ray diffraction pattern of $Ca[(Li_{1/3}Nb_{2/3})_{1-x}Sn_x]O_{3-\delta}$ ceramics sintered at 1150^{o}C as a function of (1) x=0.0, (2) x=0.1, (3) x=0.15 (4) x=0.2, (5) x=0.3. (after ref. 32)

3.3. Microwave Dielectric Properties of $Ca[(Li_{1/3}A_{2/3})_{1-x}M_x]O_{3-\delta}$ [A=Nb, Ta and M=Ti, Zr, Sn] Ceramics

Figure 8 shows the relative permittivity of $Ca[(Li_{1/3}Nb_{2/3})_{1-x}M_x]O_{3-\delta}$ [M=Ti, Zr, Sn] [32, 33, 38] ceramics sintered at 1150 ^{o}C with increasing concentration of Ti, Sn, and Zr. The relative permittivity decreases from 29.6 to 23.5 with increasing Sn concentration from 0 to 0.3. It is expected that the decrease of relative permittivity by the substitution of Sn occurs because a slightly large Sn^{4+} ion (0.069 nm) is substituted to a B site ($Li_{1/3}Nb_{2/3}$) having slightly smaller ionic radii (0.066 nm). However, the relative permittivity increases with an increase in the substitution of Ti ions in the B site ($Li_{1/3}Nb_{2/3}$). For Ti substitution, the relative permittivity increases from 29.6 to 55.2 with an increase in x from 0 to 0.50. The increase in the relative permittivity could be due to the smaller ionic radii of Ti^{4+} ion (0.056 nm) incorporated to a B site ($Li_{1/3}Nb_{2/3}$) with larger ionic radii (0.066 nm) which may distort the unit cell. Hence it is easily displaced under electric field and the relative permittivity increases. A similar trend has been reported in the literature [49-52]. A slight decrease in the

relative permittivity is expected for the Zr substituted system because of the higher ionic radii of Zr^{4+} (0.072 nm) compared to $(Li_{1/3}Nb_{2/3})$ (0.066 nm). However, a slight increase of relative permittivity from 29.6 to 31.1 has been observed with an increase in x from 0 to 0.30. This could be due to the higher ionic polarizability of Zr^{4+} (0.325 nm) compared to $(Li_{1/3}Nb_{2/3})$ (0.305 nm).

Figure 9 shows the quality factor of $Ca[(Li_{1/3}Nb_{2/3})_{1-x}M_x]O_{3-\delta}$ [M=Ti, Zr, Sn] ceramics with increasing the amount of Ti, Sn, and Zr substitution. The quality factor increased from 40000 to 52100 GHz with increasing Sn substitution from x = 0 to 0.15 and then decreased from 52100 to 46000 GHz with increasing Sn substitution from x = 0.15 to 0.3. It is worth noting that Sn substitution significantly improves the quality factor. The quality factor decreased from 40000 to 18600 GHz with increasing Ti for x= 0 to 0.5. Similarly for Zr substitution, the quality factor decreases from 40000 to 27100 GHz with increase in x from 0 to 0.30.

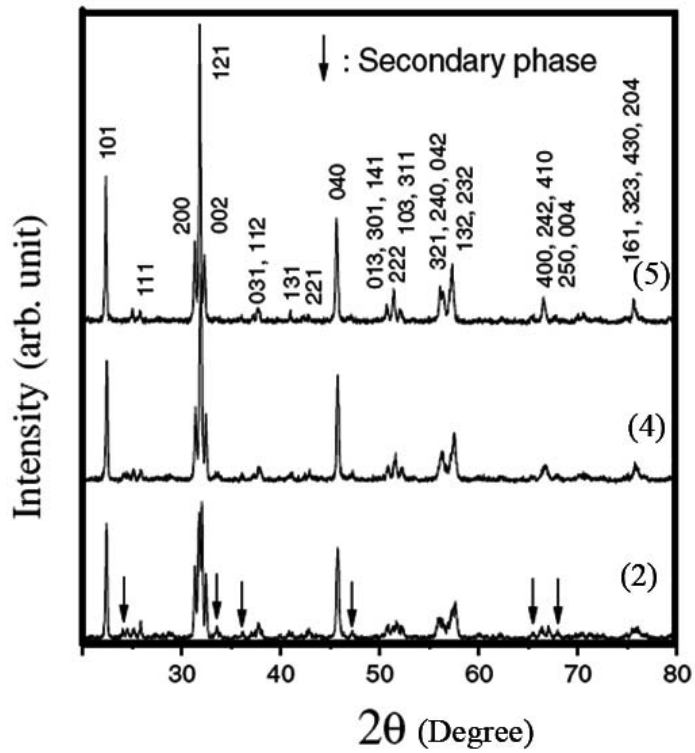

Figure 6. X-ray diffraction pattern of $Ca[(Li_{1/3}Nb_{2/3})_{1-x}Zr_x]O_{3-\delta}$ ceramics sintered at 1150°C as a function of (2) x=0.1, (4) x=0.2, (5) x=0.3. (after ref. 33)

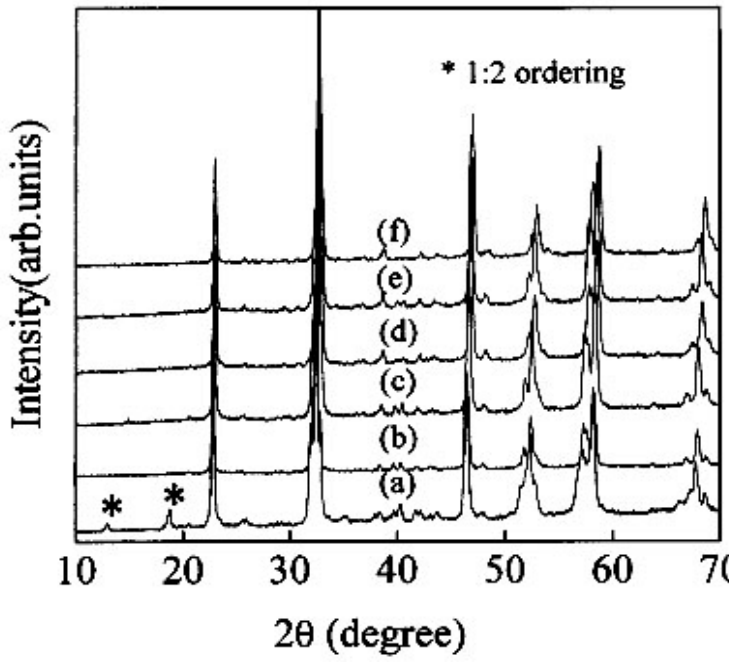

Figure 7. X-ray diffraction pattern of $Ca[(Li_{1/3}T_{2/3})_{1-x}Ti_x]O_{3-\delta}$ ceramics doped with 3 wt% of B_2O_3 sintered at 1050°C as a function of (a) x=0.05, (b) x=0.1, (c) x=0.15, (d) x=0.2, (e) x=0.3, (f) x=0.5. (After ref. 38)

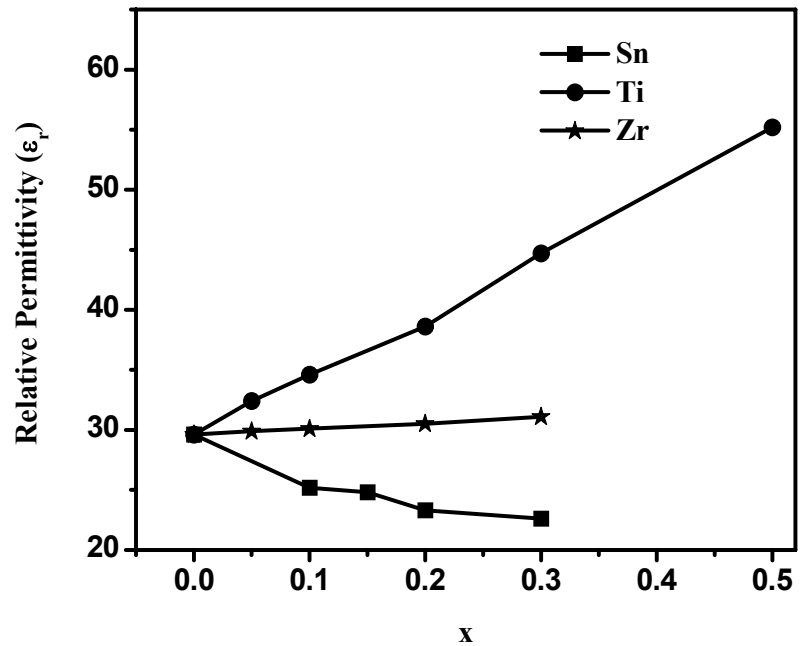

Figure 8. Variation of Relative permittivity of $Ca[(Li_{1/3}Nb_{2/3})_{1-x}M_x]O_{3-\delta}$ [M=Ti, Sn, Zr] ceramics sintered at 1150°C as a function of x.

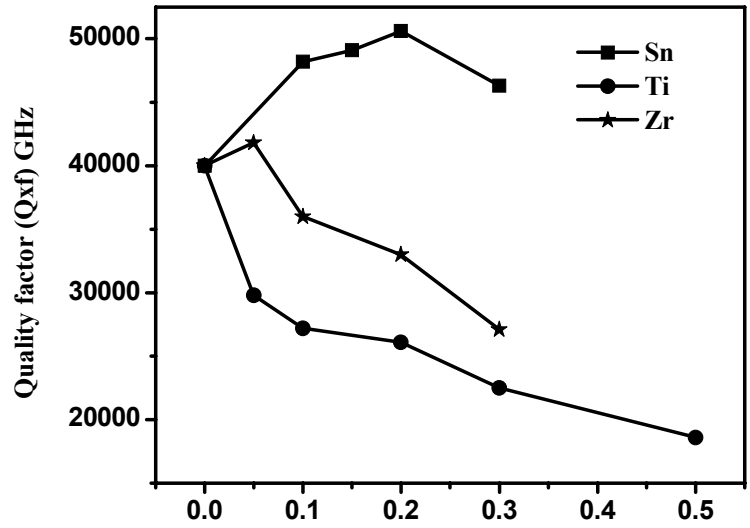

Figure 9. Variation of quality factor of $Ca[(Li_{1/3}Nb_{2/3})_{1-x}M_x]O_{3-\delta}$ [M=Ti, Sn, Zr] ceramics sintered at 1150°C as a function of x.

Figure 10 shows the variation of temperature coefficient of resonant frequency (τ_f) of the $Ca[(Li_{1/3}Nb_{2/3})_{1-x}M_x]O_{3-\delta}$ [M=Ti, Zr, Sn] ceramics sintered at 1150 °C as a function of x. The τ_f value slightly improved from −21 to −15 ppm/°C with an increase of Sn substitution (x =0.1) and then degraded from −15 to −40 ppm/°C with an increase of x > 0.1. The τ_f of the $Ca[(Li_{1/3}Nb_{2/3})_{1-x}Zr_x]O_{3-\delta}$ improved from -25.1 to-4.9 ppm/°C with increasing Zr content from (x = 0 to 0.10) and then degraded from -4.9 to -15.2 ppm/°C with x = 0.10 to 0.30. The τ_f of -4.9 ppm/°C is realized for x = 0.10 of Zr substitution. This composition has ε_r of 29.8 and Qxf value of 36300GHz. As expected, the τ_f value increased from −21 to +83 ppm/°C with an increase in Ti substitution from 0 to 50 mole%. A τ_f value of 0 ppm/°C was realized for $Ca[(Li_{1/3}Nb_{2/3})_{0.8}Ti_{0.2}]O_{3-\delta}$ (x = 0.2). This composition has ε_r and Qxf value of 38.6 and 26100 GHz, respectively. The Qxf value of this composition is relatively lower than the commonly used materials such as $Ba_2Ti_9O_{20}$ (32000 GHz) and $(Zr,Sn)TiO_4$ (49000 GHz) but this composition has a low sintering temperature (1150 °C). The temperature coefficient resonant frequency of the titanium substituted $Ca[(Li_{1/3}Nb_{2/3})_{1-x}B_x]O_{3-\delta}$ (B=Ti, Zr, Sn) shifts from negative to positive while the Sn and Zr substituted $Ca[(Li_{1/3}Nb_{2/3})_{1-x}B_x]O_{3-\delta}$ (B= Zr, Sn) remains as negative. The $Ca(Li_{1/4}Nb_{3/4})O_{3-\delta}$ ceramics sintered at 1275°C has ε_r =26 Qxf = 13000 GHz and τ_f =-49 ppm/°C. The solid solution of $0.7Ca(Li_{1/4}Nb_{3/4})O_{3-\delta}$- $0.3CaTiO_3$ [43] ceramics sintered at 1300 °C showed ε_r = 44, Qxf = 12000 GHz and τ_f = -9 ppm/°C. These properties are different from non-stoichiometric $Ca[(Li_{1/3}Nb_{2/3})_{1-x}Ti_x]O_{3-\delta}$ where the zero τ_f is for x=0.2. Table 2 shows the microwave dielectric properties of $Ca[(Li_{1/3}Nb_{2/3})_{1-x}B_x]O_{3-\delta}$ (B=Ti, Zr, Sn) complex perovskites. The tantalum analogue of $Ca[(Li_{1/3}Nb_{2/3})_{1-x}Ti_x]O_{3-\delta}$ ceramics has received less attention [38]. Liu *et al*. [38] reported the low temperature sintering and microwave dielectric properties of $Ca[(Li_{1/3}Ta_{2/3})_{1-x}Ti_x]O_{3-\delta}$ ceramics. As x increased to 0.5, ε_r increased linearly from 24 to 48 and τ_f became positive. At x=0.3, $Ca[(Li_{1/3}Nb_{2/3})_{0.7}Ti_{0.3}]O_{3-\delta}$ +3 wt% B_2O_3 sintered at 1050 °C/4hrs showed ε_r =35, Qxf = 22800 GHz and τ_f = -4 ppm/°C.

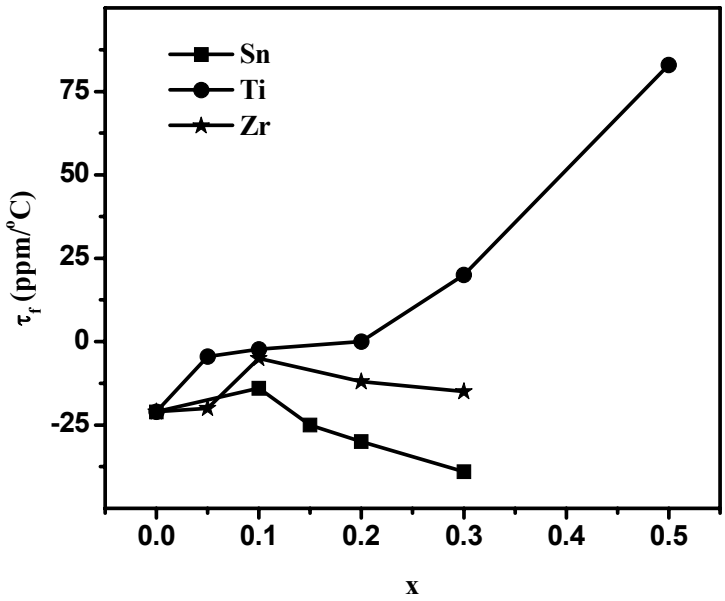

Figure 10. Variation of temperature coefficient of resonant frequency of $Ca[(Li_{1/3}Nb_{2/3})_{1-x}M_x]O_{3-\delta}$ [M=Ti, Sn, Zr]ceramics sintered at 1150°C as a function of x.

Table 2. Microwave dielectric properties of $Ca[(Li_{1/3}Nb_{2/3})_{1-x}B_x]O_{3-\delta}$ (B=Ti, Zr, Sn) complex perovskites with tolerance factor

Material	x	Tolerance factor	ε_r	$Q_u$xf (GHz)	τ_f (ppm/°C
$Ca[(Li_{1/3}Nb_{2/3})_{1-x}Ti_x]O_{3-\delta}$	0.0	0.931656	29.6	40000	-21
	0.1	0.935010	34.6	27200	-2.3
	0.2	0.938388	38.6	26100	0
	0.3	0.941792	44.7	22500	20
	0.5	0.948672	55.2	18600	83
$Ca[(Li_{1/3}Nb_{2/3})_{1-x}Sn_x]O_{3-\delta}$	0.10	0.931191	25.2	48200	-14
	0.15	0.930958	24.8	49100	-25
	0.20	0.930725	23.3	50600	-30
	0.30	0.930261	22.6	46300	-39
$Ca[(Li_{1/3}Nb_{2/3})_{1-x}Zr_x]O_{3-\delta}$	0.05	0.930750	29.9	41800	-20
	0.1	0.929850	30.1	36000	-5
	0.2	0.928051	30.5	33000	-12
	0.3	0.926258	31.1	27100	-15

4. Low Temperature Co-fired Ceramics

Telecommunication industry today requires high volume efficiency without the degradation of electrical performance of the devices. In order to reduce the size of microwave devices in communication systems, the dielectric component must also be miniaturized. The

development of multilayered structures has led to considerable volume efficiency [53, 54]. In order to use a material for incorporation into multilayer type elements, the dielectric material should be capable of being sintered along with electrode, in addition to having dielectric properties suitable for desired applications. Low Temperature Co-fired Ceramic (LTCC) technology is one of the promising technology for advanced packaging and multilayered structures with buried passive components for fast digital applications [28, 55]. LTCC is well suited for realizing the compact, multifunctional RF and microwave modules. One of the most important processes in manufacturing multilayered LTCC component involves the co-firing of electrode materials such as silver with low loss ceramics. A good combination of high permittivity, high quality factor, nearly zero temperature coefficients of resonant frequency and low processing temperature are required for the possible application of microwave dielectric materials in LTCC based devices. There are many ceramic materials with excellent microwave dielectric properties but most of them have high sintering temperature [1]. In general, the sintering temperature of most of the microwave dielectric ceramics is much higher than the melting point of commonly used electrode materials such as silver (961^oC). Hence in multilayered structure, it is necessary to lower the sintering temperature of the ceramics below the melting point of electrode materials such as silver. Generally, chemical synthesis, use of starting powder with smaller particle size and liquid phase sintering are the three methods employed to lower the sintering temperature of the ceramics [28, 56-59]. Among these, liquid phase sintering using glass addition is known to be the most effective and least expensive method of achieving high density sintered ceramics at low sintering temperatures [26, 28, 60, 61]. In the LTCC systems, addition of low melting glasses to the ceramics is commonly used to lower the sintering temperature. However, in the majority of ceramic- glass systems, the reduction of sintering temperature is usually accompanied by an abrupt degradation of dielectric properties and is due to the loss mechanism associated with the glass and the formation of second phases. To weaken the destructive effect of the glass additives on the microwave dielectric properties of the ceramics, researchers have to find a good glass flux which could decrease the sintering temperature without affecting the microwave dielectric properties. It is well known that the sintering aids containing boron oxide and silicon dioxide promotes densification by liquid phase sintering and have low dielectric loss [62]. Silica is not an effective flux for microwave dielectrics if it is used alone. To lower the melting point, the rigid bonds in silicon dioxide may be broken by modifiers such as B_2O_3, and alkali ions. In general, the B_2O_3 modifier could increase the fluidity of glass and the pores were correspondingly coalesced during melting. Reports show that single component low melting additives easily forms second phase with parent materials which may have high dielectric loss [1, 26-28, 63]. Similar phenomenon has been reported in high quality factor materials like $Ba_2Ti_9O_{20}$ (BT), $Ba(Mg_{1/3}Ta_{2/3})O_3$ (BMT), $Ba(Zn_{1/3}Ta_{2/3})O_3$ (BZT) and $(Zr_{1-x}Sn_x)TiO_4$ (ZST) etc [26, 27, 64-69]. Earlier reports show that multi component glasses are more effective than single component glasses to reduce the sintering temperature of the ceramics without much degradation of the microwave dielectric properties [28, 61]. When glass is used in microwave ceramics, the quality factor invariably degrades due to the loss mechanism associated with the glass. Therefore the development of low temperature sinterable ceramics with high relative permittivity, low dielectric loss and nearly zero temperature coefficient of resonant frequency is one of the major challenges in the electronic industry.

It has been reported that the A site and M site modified solid solution of $Ca[(Li_{1/3}A_{2/3})_{1-x}M_x]O_{3-\delta}$ [A=Nb, Ta and M=Ti, Zr, Sn] [32, 33, 38] complex perovskite ceramics show excellent microwave dielectric properties at a relatively low sintering temperatures of about 1150 ^oC/4hrs. However, the sintering temperature of this material is still too high to use silver or copper as an internal electrode in multilayered structures. In order to develop lithium based complex perovskite as a new type of LTCC, it is essential to reduce the sintering temperature without considerably affecting the microwave dielectric properties. Therefore this section focused on the sinterability and microwave dielectric properties of $Ca[(Li_{1/3}A_{2/3})_{1-x}M_x]O_{3-\delta}$ [A=Nb, Ta and M=Ti, Zr, Sn] complex perovskite ceramics with glass addition. Among the $Ca[(Li_{1/3}A_{2/3})_{1-x}M_x]O_{3-\delta}$ [A=Nb, Ta and M=Ti, Zr, Sn] complex perovskites, the Ti^{4+} substitution has a wide range of τ_f extending from -21 to +83 ppm/^oC. A single phase perovskite with zero τ_f is observed in the vicinity of x = 0.2. Hence the majority of the work based on LTCC has been done on the titanium substituted $Ca[(Li_{1/3}A_{2/3})_{1-x}Ti_x]O_{3-\delta}$ [A=Nb, Ta] complex perovskite system.

4.1. Effect of Glass Addition in $Ca[(Li_{1/3}A_{2/3})_{1-x}Ti_x]O_{3-\delta}$ [A=Nb, Ta]

Several authors [34-45] tried to control the escape of volatile lithium by lowering the sintering temperature and by the addition of low melting additives such as B_2O_3, Bi_2O_3, glass frit or LiF. Effects of B_2O_3 and/or Bi_2O_3 on the sinterability and microwave dielectric properties of nonstoichiometric $Ca(Li_{1/3}Nb_{2/3})O_{3-\delta}$ (CLN) ceramics were investigated by Liu *et al*. [37]. With the addition of B_2O_3 from 0.5 wt% to 4.0 wt%, the ε_r and Qxf value of CLN sintered at 990 ^oC were comparable to those of pure CLN sintered at 1150 ^oC. For the specimens with 1.0 wt% B_2O_3 and 9 wt% Bi_2O_3, the sintering temperature of the sample was further reduced to 900 ^oC, while the Qxf value decreased with the increase of Bi_2O_3 content. These results are due to the formation of a low-melting-point second phase between Li_2O and B_2O_3. The dielectric properties of the samples with 6.0 wt% B_2O_3 degraded significantly due to the formation of the $Li_2B_4O_7$ secondary phase. The sintering temperature of CLN ceramics was reduced by Bi_2O_3 at the expense of the Qxf value. Typically, ε_r of 30.6, Qxf of 31000 GHz, and τ_f of −17.5 ppm/◦C were obtained for the samples with 4.0 wt% B_2O_3 sintered at 1000 ^oC. Lui *et al*. [39, 40] also studied the effect of B_2O_3 addition on the microwave dielectric properties of $Ca[(Li_{1/3}Nb_{2/3})_{1-x}Ti_x]O_{3-\delta}$. Addition of 2 wt % B_2O_3 and 6 wt % Bi_2O_3 to $Ca[(Li_{1/3}Nb_{2/3})_{0.7}Ti_{0.3}]O_{3-\delta}$ ceramics sintered at 920 ^oC has ε_r = 43.1, Qxf = 10600 GHz, and τ_f = 10.7 ppm/^oC.

Ha *et al*. [34-36] reported the microwave dielectric properties of $Ca[(Li_{1/3}Nb_{2/3})_{1-x}Ti_x]O_{3-\delta}$ ceramics with Bi_2O_3 and B_2O_3-ZnO-SiO_2-PbO glass. Secondary phase has been observed when more than 5 wt% of B_2O_3 was added. The $Ca[(Li_{1/3}Nb_{2/3})_{0.8}Ti_{0.2}]$ $O_{3-\delta}$ ceramics with 5 wt.% Bi_2O_3 sintered at 900 ^oC for 3 hours has ε_r = 35, Qxf = 11000 GHz, and τ_f = 13 ppm/^oC. Addition of glass frit (B_2O_3–ZnO–SiO_2–PbO) improved the densification and decreased the sintering temperature of $Ca[(Li_{1/3}Nb_{2/3})_{1-x}Ti_x]O_{3-\delta}$ dielectric ceramics from 1150 ^oC to 900^oC. The dielectric properties of $Ca[(Li_{1/3}Nb_{2/3})_{0.8}Ti_{0.2}]$ $O_{3-\delta}$ with 12 wt% glass sintered at 900 ^oC for 3 h were ε_r = 40, Qxf = 12500 GHz, and τ_f = - 8 ppm/^oC respectively.

Tong *et al*. [41, 42] reported the low température firing and microwave dielectric properties of $Ca[(Li_{1/3}Nb_{2/3})_{0.9}Ti_{0.1}]O_{3-\delta}$ ceramics with LiF addition and the

$Ca[(Li_{1/3}Nb_{2/3})_{0.84}Ti_{0.16}]$ $O_{3-\delta}$ with the combination of LiF and ZBS glass. The $Ca[(Li_{1/3}Nb_{2/3})_{0.84}Ti_{0.16}]$ $O_{3-\delta}$ ceramics with 2 wt% LiF and 3 wt% ZBS sintered at 900°C for 2 h show excellent dielectric properties: ε_r = 34.3, Qxf = 17400 GHz, and τ_f = - 4.6 ppm/°C. Table 6 shows the microwave dielectric properties of low temperature sintered CLNT/CLTT ceramics.

4.1.2. Effect of Borosilicate Glasses in $Ca[(Li_{1/3}A_{2/3})_{1-x}Ti_x]O_{3-\delta}$ [A=Nb, Ta] Ceramics

The low temperature sintering and microwave dielectric properties of $Ca[(Li_{1/3}A_{2/3})_{1-x}Ti_x]O_{3-\delta}$ [A=Nb, Ta] complex perovskite with different borosilicate glasses such as lithium borosilicate (LBS), lead borosilicate (PBS), zinc borosilicate (ZBS), barium borosilicate (BBS), lithium magnesium zinc borosilicate (LMZBS) and bismuth zinc borosilicate (BZBS) [70-73] is discussed in detail in this section. Table 3 shows the physical and dielectric properties of various borosilicate glasses [28, 30, 44, 60, 70-75]. The $Ca[(Li_{1/3}Nb_{2/3})_{0.8}Ti_{0.2}]$ $O_{3-\delta}$ and $Ca[(Li_{1/3}Ta_{2/3})_{0.7}Ti_{0.3}]$ $O_{3-\delta}$ ceramic compositions have been taken to investigate the effect of glass addition on the sinterability and microwave dielectric properties for its phase purity and excellent temperature stable microwave dielectric properties.

Table 3. Physical and dielectric properties of various borosilicate glasses

Glass code	Composition (mole %)	Density (g/cc)	Softening Temperature (°C)	ε_r	Tan δ	Reference
PBS	40:PbO,40:B_2O_3, 20:SiO_2	4.31	448	12.9	$7.1x10^{-3}$ (12 GHz)	28
BBS	30:BaO,60:B_2O_3, 10:SiO_2	3.40	627	7.20	$4.4x10^{-3}$ (15 GHz)	28
ZBS	60:ZnO,30:B_2O_3, 10:SiO_2	3.60	582	7.50	$1.07x10^{-2}$ (15 GHz)	28
LBS	35.5:Li_2O, 31.66:B_2O_3, 33.2:SiO_2	2.34	513	6.44	$3x10^{-3}$ (1 MHz)	28
BZBS	35:Bi_2O_3, 32:ZnO, 27:B_2O_3, 6:SiO_2	4.30	950	8.80	$1.3x10^{-3}$ (1 MHz)	28
LMZBS	20:Li_2O, 20:MgO, 20: ZnO, 20:B_2O_3, 20:SiO_2	2.75	900	6.90	$1x10^{-3}$ (1 MHz)	28

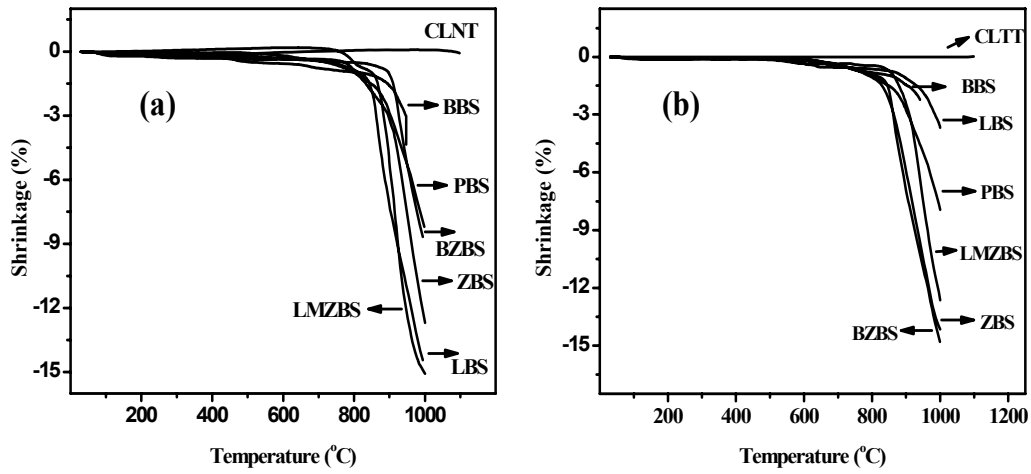

Figure 11. Shrinkage characteristics of (a) CLNT and (b) CLTT ceramics with various borosilicate glasses.

4.1.3. Shrinkage Characteristics

To identify whether the glass additive would be effective on the low temperature firing of CLNT / CLTT ceramics, the linear shrinkage of as pressed pellets as a function of temperature is to be initially measured. The dilatometry study provides insight into the densification process for the glass ceramic systems. Figure 11 (a) and (b) shows the shrinkage characteristics of CLNT / CLTT ceramics and with 12 wt% of various borosilicate glasses. It is found that there is no linear shrinkage for pure CLNT and CLTT in the temperature range of 800-1100^{o}C. This indicates that sintering does not start even at 1100 ^{o}C for both the ceramics. However, a linear shrinkage is observed as shown in Figure 11 for all the glass added ceramics which implies that all the borosilicate glass acts as a good sintering aid. Among the various glasses, BZBS, ZBS and LMZBS glasses in CLTT and LBS, LMZBS, and ZBS glasses in CLNT show a linear shrinkage of more than 12% in the temperature range 800-1000 ^{o}C.

4.1.4. Densification

Figure 12 shows the variation of sintering temperature, and the relative density of CLNT / CLTT ceramics mixed with different wt% of various borosilicate glasses. It is found that all the glasses decreases the sintering temperature. However, among the various six borosilicate glasses, LBS, LMZBS and ZBS glass could reduce the sintering temperature of CLNT ceramics. The ZBS and BZBS glasses reduced the sintering temperature of CLTT ceramics below the melting point of silver. The theoretical density (D) of the glass added CLNT was calculated using the equation

$$D = \frac{W_1 + W_2}{W_1 / D_1 + W_2 / D_2}$$

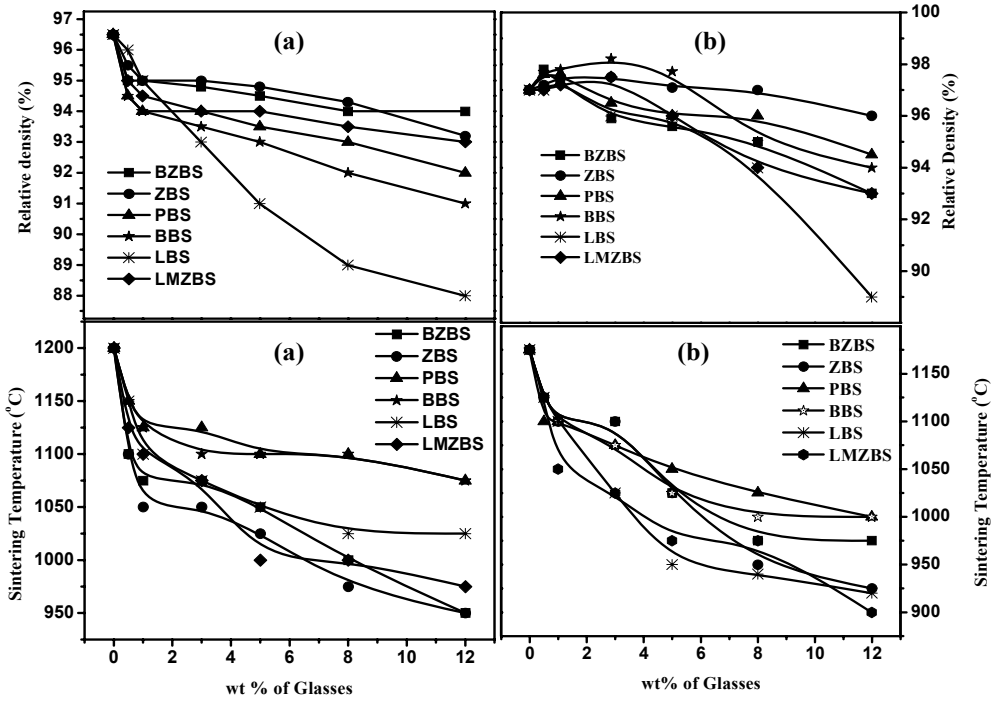

Figure 12. Variation of sintering temperature and relative density of (a) CLNT and (b) CLTT ceramics with different wt% of various borosilicate glasses.

where W_1 and W_2 are the weight percentage of ceramics and glass with densities D_1 and D_2 respectively.

The relative density of the glass-ceramic composite was calculated using the equation:

$$Densification = \frac{D_{th}}{D_{\exp t}}$$

Figure 12 also shows the variation of relative density as a function of glass content. The relative density decreases with increase of glass content in CLTT ceramics. For CLNT-glass composite, the relative density increases slightly with an increase in the glass. However, higher wt% of glass addition decreases the densification of CLNT-glass composite. The relative density and the densification temperature is different for different glasses in ceramics. The effectiveness of sintering aid depends on several factors such as sintering temperature, viscosity, solubility, and glass wettability. The densification of glass ceramic systems is due the formation of liquid phase. The glassy liquid phase at the grain boundary effectively eliminates pores and this could be the reason for the increase in the relative density of CLNT-glass system. Trapped porosity associated with grain growth and formation of pores by the evaporation of excess glass components are the reasons for the reduction in the density for higher wt% of glass fluxing [27, 28, 60]. It may be noted that the glasses have lower density as compared to CLNT / CLTT ceramics. The required densification for practical application

could be obtained by the addition of glasses. However, undesirable decomposition of host dielectric material and the formation of second phase may occur which may degrade the microwave dielectric properties. Hence the amount of glass frit has to be optimized to get the best dielectric properties.

4.1.5. Phase Analysis

Figs. 13 and 14 show the X-ray powder diffraction patterns of sintered CLNT / CLTT ceramics and the different borosilicate glass added CLNT / CLTT ceramics. The XRD patterns are indexed based on the $CaTiO_3$ type orthorhombic perovskite structure. Higher wt% of glasses resulted in the formation of a small amount of second phase which was prominent for LBS glass added CLTT ceramics. For co-firing applications, the glass ceramic composite should not react with silver. Figure 13 (h), (i) and (j) show the X-ray diffraction patterns of sintered CLNT ceramics with 20 wt% of silver and 5 wt% of LBS, 12 wt% of LMZBS, and 8 wt% of ZBS glasses respectively. Similarly, Figs. 14(h) and (i) show the X-ray diffraction patterns of 20 wt% of silver added CLTT ceramics with 12 wt% of ZBS and BZBS glasses sintered at the optimized sintering temperature. It is clear from the X-ray diffraction patterns that there is no additional phases other than the orthorhombic CLNT / CLTT ceramics and metallic silver (ICDD File No: 03-0921). This indicate that there is no chemical reactivity between the glass added CLNT/CLTT and the electrode material silver.

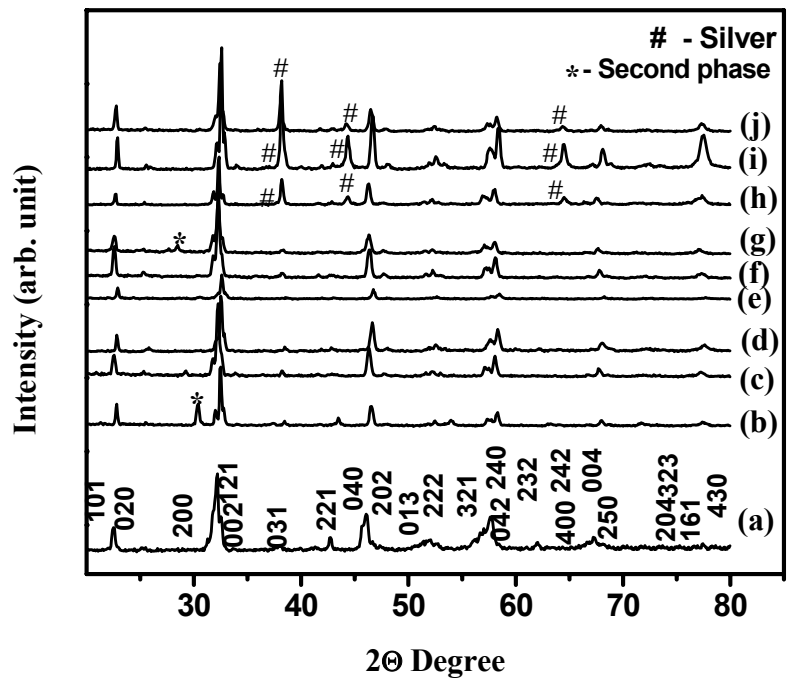

Figure 13. The X-ray powder diffraction patterns of sintered (a) CLNT ceramics, CLNT ceramics with (b) 12 wt% of BBS, (c) 12 wt% of PBS, (d) 5 wt% of LBS, (e) 12 wt% of LMZBS, (f) 8 wt% of ZBS, (g) 12 wt% of BZBS glasses, (h) CLNT ceramics with 5 wt% of LBS glass and 20 wt% of silver and (i) CLNT ceramics with 8 wt% of ZBS glass and 20 wt% of silver and (j) CLNT ceramics with 12 wt% of LMZBS glass and 20 wt% of silver using Ni-filtered Cu-Kα radiation.

4.1.6. Microstructure Analysis

Figures 15 (a) and 16 (a) shows the scanning electron micrographs of thermally etched $Ca[(Li_{1/3}Nb_{2/3})_{0.8}Ti_{0.2}]O_{3-\delta}$ ceramics and $Ca[(Li_{1/3}Ta_{2/3})_{0.7}Ti_{0.3}]O_{3-\delta}$ ceramics. The CLNT and CLTT ceramics sintered at 1175°C and 1200°C give an average grain size of 2-4 μm. It is evident from the micrographs that a small amount of glass addition helps the sintering of CLNT ceramics by liquid phase. The densification improved initially up to 1 wt% of LBS glass addition and further addition of glass degraded the densification which can be clearly seen from Figure 15 (c). Figure 15 (e), and (f) shows the SEM picture of 8 and 12 wt% of ZBS and BZBS glass added ceramics. It is also evident from both the micrograph (see Fig 15 and 16) that the glass addition decreases the grain size which is in agreement with previous reports [37]. At higher sintering temperature the glasses melts and may evaporate and generate porosity which can be seen in Figure 16 (b) and (c). Figure 15 (d) and 16 (d) shows the scanning electron micrographs of CLNT+ 5 wt% of LBS+ 20 wt% of Ag and CLTT+12 wt% of BZBS+ 20 wt% of Ag respectively. It is observed that the silver does not react with glass-ceramic composite and the absence of such reaction is required for the material for LTCC application.

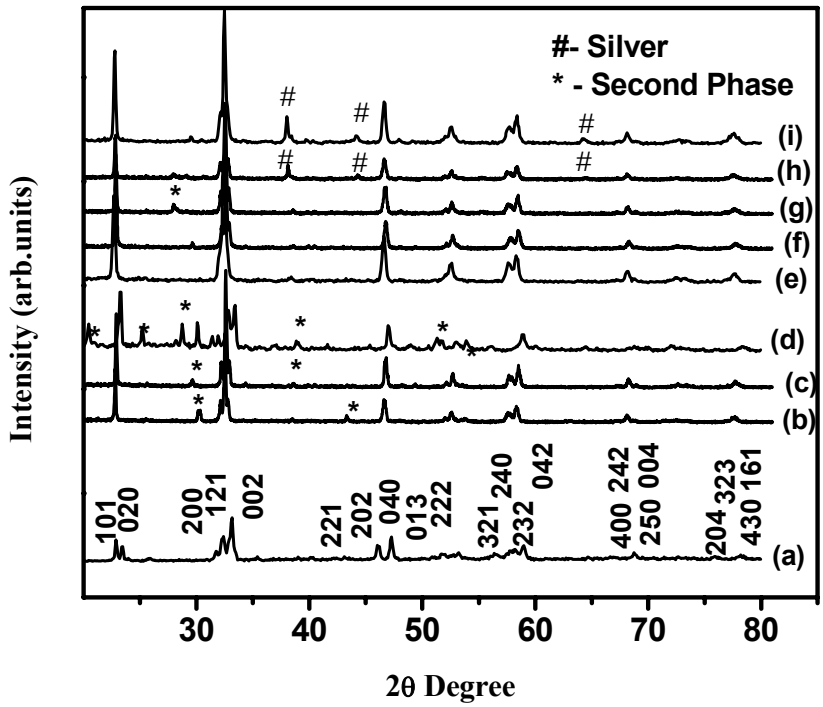

Figure 14. The X-ray powder diffraction patterns of sintered (a) CLTT ceramics, CLTT ceramics with 12 wt% of (b) BBS, (c) PBS, (d) LBS, (e) LMZBS, (f) ZBS, (g) BZBS glasses, (h) CLTT ceramics with 12 wt% of ZBS glass and 20 wt% of silver and (i) CLTT ceramics with 12 wt% of BZBS glass and 20 wt% of silver using Ni-filtered Cu-Kα radiation.

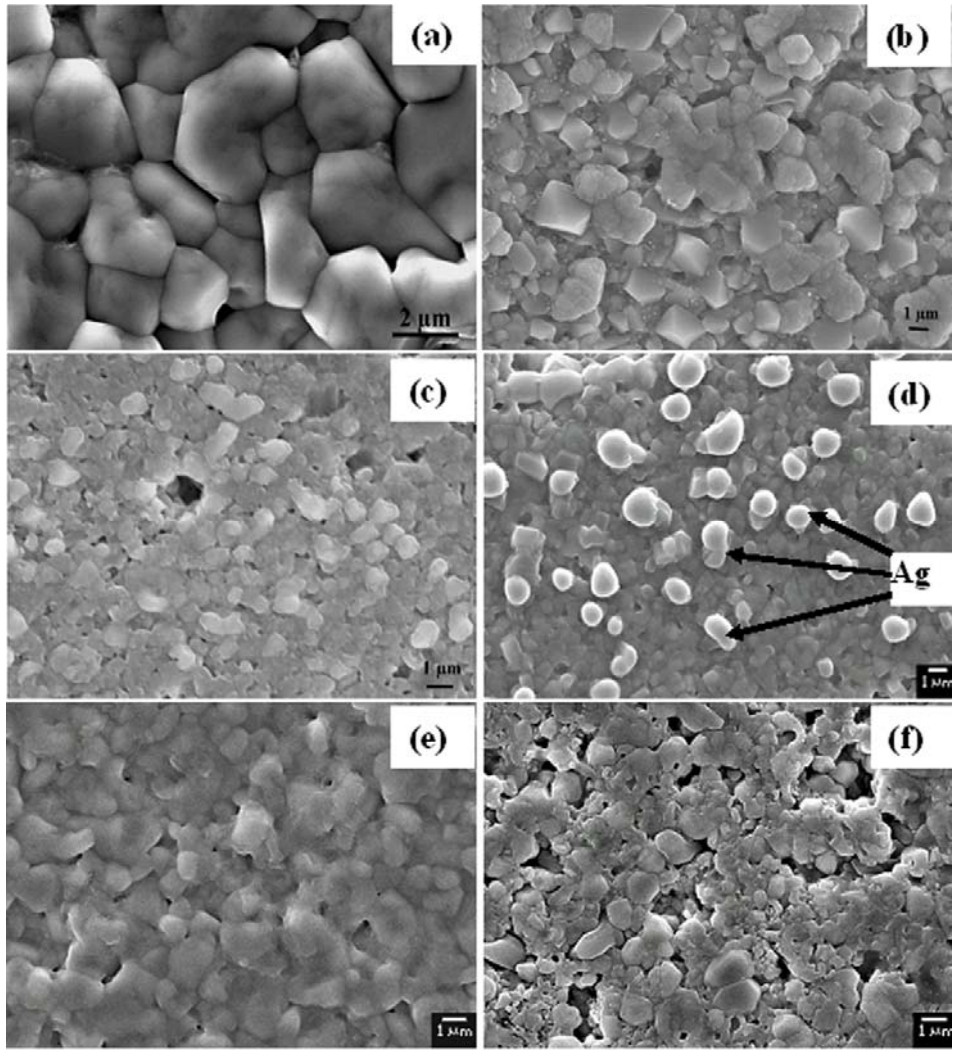

Figure 15. The microstructure of sintered $Ca[(Li_{1/3}Nb_{2/3})_{0.8}Ti_{0.2}]O_{3-\delta}$ ceramics with (a) 0wt%, (b) 1 wt% LBS (c) 5 wt% LBS, (d) 5 wt% of LBS + 20 wt% Ag, (e) 8 wt % ZBS and 12 wt% LMZBS glass.

4.1.7. Microwave Dielectric Properties

Addition of glasses not only promotes the sinterability but also affect the microwave dielectric properties. It is well known that relative density and dielectric properties are inter-related. Figure 17 shows the microwave dielectric properties CLNT / CLTT ceramic as a function of different wt% of various glasses. The relative permittivity of glass added CLNT / CLTT ceramics decreases with increase in the glass content as shown in Figure 17. The relative permittivity of all the borosilicate glasses is much lower than that of CLNT / CLTT ceramics as given from table 3. Moreover, higher wt% of glass addition increased the porosity and decreased the densification of ceramics. The low permittivity of glass and the poor densification are the reasons for the decrease in the relative permittivity of CLNT / CLTT ceramics with higher wt% of glass addition.

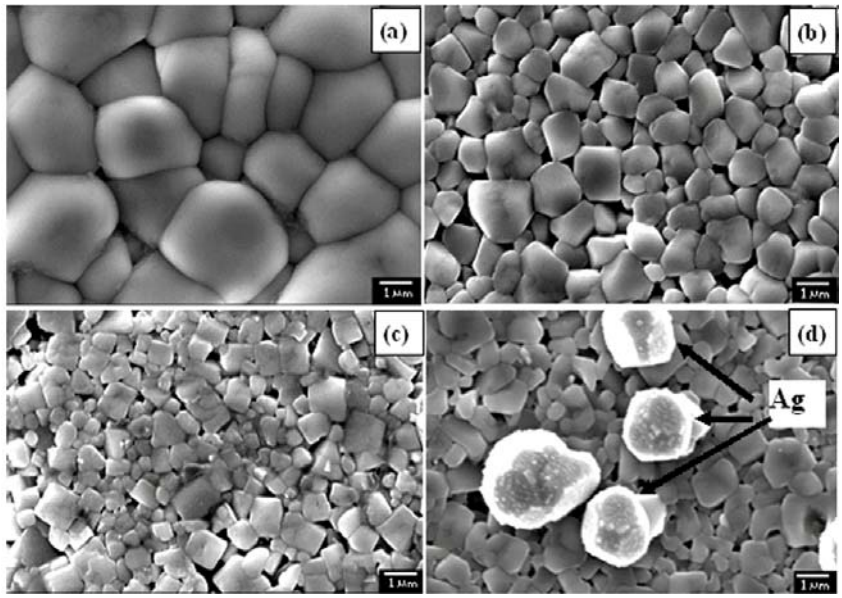

Figure 16. The microstructure of sintered $Ca[(Li_{1/3}Ta_{2/3})_{0.7}Ti_{0.3}]O_{3-\delta}$ ceramics with (a) 0wt %, (b) 12 wt% BZBS (c) 12 wt% ZBS, and (d) 12 wt% of BZBS + 20 wt% Ag.

The microwave dielectric properties of CLNT/CLTT ceramics with different amount of glass are shown in table 6. Figure 17 shows the optimized quality factor for the addition of 0-12 wt% of different borosilicate glasses in CLNT ceramics. The sintering temperature versus wt % of glass in CLNT/CLTT composite shows (see figure 12) that, all the glasses could not act as good sintering aid to lower the sintering temperature below 950 ^oC. Among the six borosilicate glasses, only the LBS, LMZBS, and ZBS glass could reduce the sintering temperature of CLNT ceramics with reasonable dielectric properties. It is observed that the addition of small amount of LBS, ZBS and LMZBS glasses increased the quality factor slightly. Maximum $Q_u$xf value of 22900 GHz, 24500 GHz, and 23500 GHz (f = 4.4 GHz) was found for the addition of 1 wt% of LBS, 3 wt% of LMZBS, and 1 wt% of ZBS glasses respectively. These could be due to the increased densification of CLNT ceramics by liquid phase sintering with small amount of glass fluxing. These compositions have relative permittivity of 34.2, 34 and 38.3 respectively with a τ_f of around -10 ppm/ ^oC. Higher wt% of glass addition in CLNT ceramics lowered the sintering temperature with further lowering of the quality factor. The CLNT ceramics with 5 wt% of LBS glass sintered at 950 ^oC shows ε_r = 30.5, Q_u x f = 14700 GHz (f = 4.6 GHz) and τ_f = -18 ppm/ ^oC. A similar trend is also observed with the addition of ZBS and LMZBS glasses in CLNT ceramics. Addition of 12 wt% of ZBS glass in CLNT ceramics gives a relative permittivity of 33.5 with Qxf of about 13200 GHz and τ_f of -28 ppm/^oC. Hence for CLNT ceramics, amoung the various six borosilicate glasses the LBS, LMZBS, and ZBS glass acts as good sintering aid to lower the sintering temperature with reasonably good microwave dielectric properties.

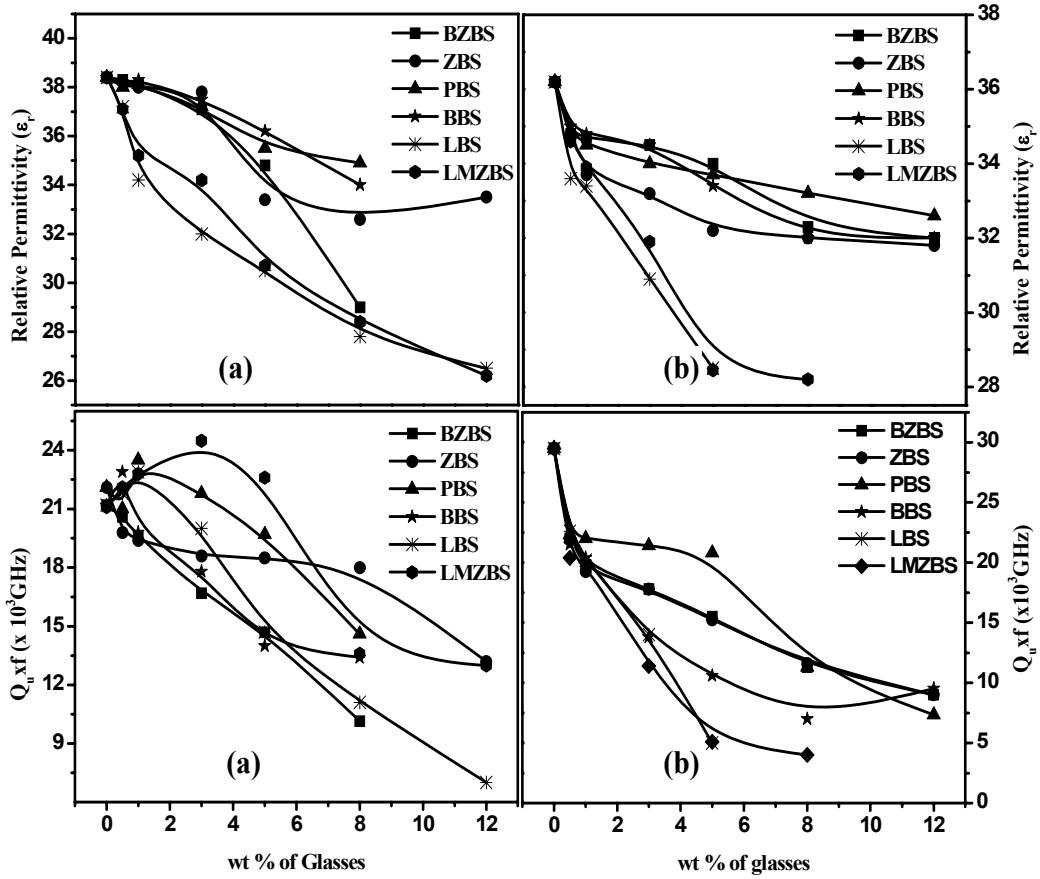

Figure 17. Variation of relative permittivity and quality factor of (a) CLNT and (b) CLTT ceramics with different wt% of various borosilicate glasses.

It can be observed from figure 17 that the quality factor of CLTT ceramics decreased with increase in borosilicate glass additions. For CLTT ceramics, the ZBS and BZBS glasses acts as good sintering aids and the glasses such as BBS, PBS, LBS, and LMZBS could not lower the sintering temperature below 950 ^{o}C with reasonably good dielectric properties. The CLTT ceramics with 12 wt% of ZBS glass sintered at 950 ^{o}C showed $\varepsilon_r = 31.8$, Q_u x f = 9000 GHz (f = 4.6 GHz). Addition of 12 wt% of BZBS glass in CLTT ceramics sintered at 950 ^{o}C showed $\varepsilon_r = 32.0$, Q_u x f = 9000 GHz (f = 4.7 GHz). It may be noted that the dielectric loss of glasses is much higher than that of pure CLTT ceramics. The added glasses not only acts as the sintering aid but also as an impurity that can adversely affect the microwave dielectric properties. It is reported that the microwave dielectric loss was mainly caused not only by the lattice vibrations but also by the pores, the grain morphology and the second phase [76]. These could be the reason for the decrease in the quality factor with glass additions.

Figure 18 shows the variation of temperature coefficient of resonant frequency of CLNT / CLTT ceramics with different wt% of various borosilicate glasses. Addition of various borosilicate glasses decreased the temperature coefficient of resonant frequency (τ_f) of CLNT ceramics +4 ppm/^{o} C to -22 ppm/^{o} C and that of CLTT ceramics from -3 ppm/^{o} C to -41 ppm/^{o} C. This is due to the high negative τ_f of all the borosilicate glasses compared to CLTT

ceramics. The CLNT / CLTT ceramics sintered below 950 ^oC with selected borosilicate glasses show excellent dielectric properties. However, the temperature coefficient of resonant frequency is slightly higher (> -20 ppm/^{o} C). Hence, it is necessary to lower the τ_f close to zero for applications in LTCC based devices. It is well known that rutile has high positive τ_f and are widely used for tuning the temperature coefficient of resonant frequency of dielectric resonators [49-52]. In order to lower the τ_f value, the $Ca[(Li_{1/3}Nb_{2/3})_{0.8}Ti_{0.2}]O_{3-\delta}$ ceramics were modified to $Ca[(Li_{1/3}Nb_{2/3})_{0.75}\ Ti_{0.25}]O_{3-\delta}$ and the $Ca[(Li_{1/3}Ta_{2/3})_{0.7}Ti_{0.3}]O_{3-\delta}$ ceramics were modified to $Ca[(Li_{1/3}Ta_{2/3})_{0.6}\ Ti_{0.4}]O_{3-\delta}$ by increasing the rutile content.

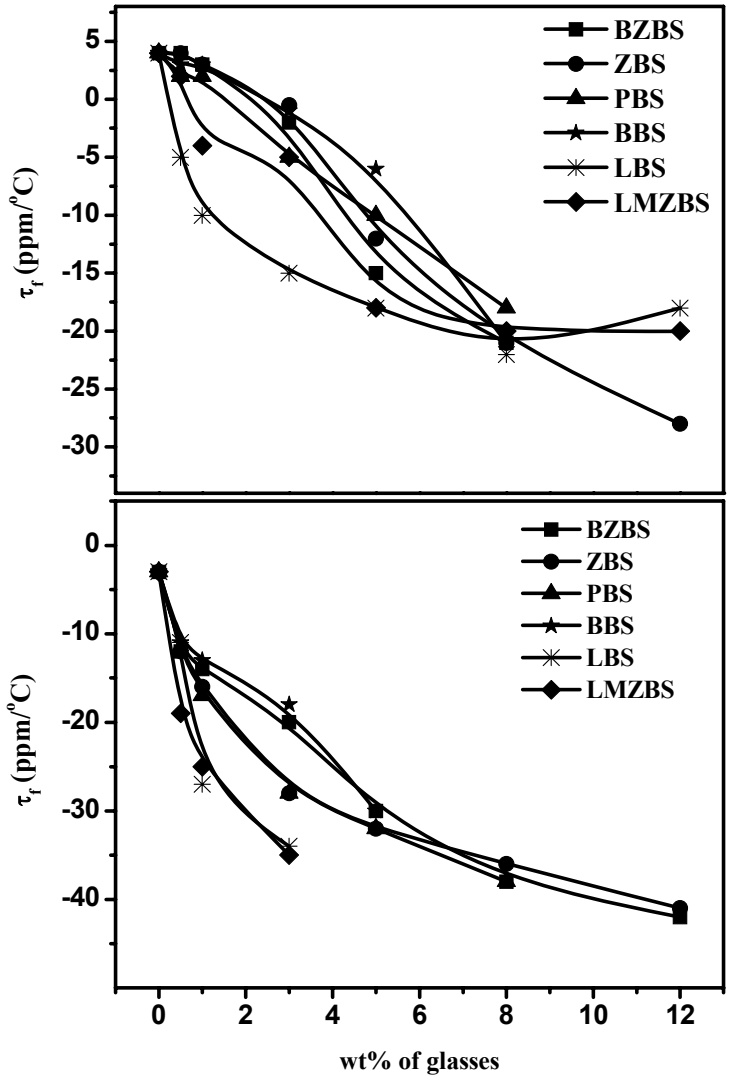

Figure 18. Variation of temperature coefficient of resonant frequency of (a)CLNT and (b) CLTT ceramics with different wt% of various borosilicate glasses.

Table 4. Densification and microwave dielectric properties of LBS and LMZBS glass added $Ca[(Li_{1/3}Nb_{2/3})_{0.75}Ti_{0.25}]O_{3-\delta}$ ceramics and the BZBS glass added $Ca[(Li_{1/3}Ta_{2/3})_{0.6}Ti_{0.4}]O_{3-\delta}$ ceramics (after Ref 44, 82)

Material	Sintering Temperature (^oC)	ε_r	$Q_u$xf (GHz)	τ_f ppm/^{o}C
$Ca[(Li_{1/3}Nb_{2/3})_{0.75}Ti_{0.25}]O_{3-\delta}$	1175	41.9	17500	+23
$Ca[(Li_{1/3}Nb_{2/3})_{0.75}Ti_{0.25}]O_{3-\delta}$ + 5 wt% LBS	950	33.0	11500	-2
$Ca[(Li_{1/3}Nb_{2/3})_{0.75}Ti_{0.25}]O_{3-\delta}$ + 8 wt% LBS	940	30.5	9750	-5
$Ca[(Li_{1/3}Nb_{2/3})_{0.75}Ti_{0.25}]O_{3-\delta}$ + 12 wt% LMZBS	920	28.5	11000	-3
$Ca[(Li_{1/3}Nb_{2/3})_{0.75}Ti_{0.25}]O_{3-\delta}$ + 15 wt% LMZBS	900	27.4	11100	-8
$Ca[(Li_{1/3}Ta_{2/3})_{0.6}Ti_{0.4}]O_{3-\delta}$	1200	38.7	15000	+15
$Ca[(Li_{1/3}Ta_{2/3})_{0.6}Ti_{0.4}]O_{3-\delta}$ + 12 wt% of BZBS glass	950	34.9	6500	-6

Table 5. Sintering temperature and microwave dielectric properties of $Ca[(Li_{1/3}A_{2/3})_{1-x}M_x]O_{3-\delta}$ [A=Nb, Ta and M=Ti, Zr, Sn] complex perovskites

SI No	Materials	Sintering Temperature (^oC)	ε_r	Qxf (GHz)	τ_f (ppm/^{o}C)	Ref
1	$Ca[(Li_{1/3}Nb_{2/3})_{1-x}Ti_x]O_{3-\delta}$ x=0- 0.5	1150/5h	29-55	40000-18000	-21 to+83	32
	x = 0.00	1150/5h	29.6	40000	-21	32
	0.05	1150/5h	32.4	29800	-4.5	
	0.10	1150/5h	34.6	27200	-2.3	
	0.20	1150/5h	38.6	26100	0	
	0.30	1150/5h	44.7	22500	+20	
	0.50	1150/5h	55.2	18600	+83	
2	$Ca[(Li_{1/3}Nb_{2/3})_{1-x}Sn_x]O_{3-\delta}$ (x=0- 0.3)	1150/3h	29-23	40000-46000	-21 to -40	32
	x = 0.00	1150/3h	29.6	40000	-21	32
	0.10	1150/3h	25.2	48200	-14	
	0.15	1150/3h	24.8	49100	-25	
	0.20	1150/3h	23.3	50600	-30	
	0.30	1150/3h	22.6	46300	-39	
3	$Ca[(Li_{1/3}Nb_{2/3})_{1-x}Zr_x]O_{3-\delta}$ (x=0- 0.5)	1150/3h	29.5- 31	40000-27000	-25 to -15	33
	x = 0.00	1150/3h	29.5	40000	-25	33
	0.10	1150/3h	29.8	36000	-4.9	
	0.20	1150/3h	30.5	32000	-13.2	
	0.30	1150/3h	31.0	27100	-15.2	

4	1-x $Ca[(Li_{1/4}Nb_{3/4})O_3$-$xCaTiO_3$, x=0- 0.5	1200-1300/2h	36-48	16000-11000	-33to +40	43
	x = 0.00	1275/2h	26.0	13000	-49	43
	0.20	1275/2h	36.0	15400	-25	
	0.25	1275/2h	39.0	12500	-21	
	0.30	1275/2h	43.0	9000	-18	
	0.35	1275/2h	45.0	8500	+10	
	0.40	1275/2h	48.0	8500	+40	
5	$Ca[(Li_{1/3}Ta_{2/3})_{1-x}Ti_x]O_{3-\delta}$ x=0- 0.5	1200/4	24-42	42000-11000	-40 to +50	38
	x=0.0	1200/4	24.0	42000	-40	38
	0.1	1200/4	26.3	-	-	
	0.2	1200/4	28.4	-	-	
	0.3	1200/4	35.0	22800	-4.1	
	0.5	1200/4	42.0	11000	+50	

Table 6. Low temperature sintered $Ca[(Li_{1/3}A_{2/3})_{1-x}Ti_x]O_{3-\delta}$ [A=Nb, Ta] complex perovskites with sintering aid

SI No	Materials	wt % of Glass (y)	Sintering Temperature (^oC)	ε_r	Qxf (GHz)	τ_f (ppm/^oC)	Ref
1	$Ca[(Li_{1/3}Nb_{2/3})O_{3-\delta}$ +1 wt% B_2O_3+ y Bi_2O_3	0	980/4	24.0	10000	-16	37
		2	980/4	28.0	17000	-20	
		4	980/4	29.0	12000	-22	
		6	980/4	30.0	11000	-23	
		8	980/4	30.2	10000	-24	
2	$Ca[(Li_{1/3}Nb_{2/3})_{1-x}Ti_x]O_{3-\delta}$ + y (B_2O_3+ZnO+SiO_2+PbO x=0	10	900/3	23.0	17000	-75	35
		12	900/3	27.0	16000	-60	
		15	900/3	28.0	13000	-50	
3	x=0.1	10	900/3	25.0	16000	-58	35
		12	900/3	30.5	15000	-52	
		15	900/3	34.0	11000	-42	
4	x=0.2	10	900/3	32.5	14000	-22	35
		12	900/3	35.5	11000	-20	
		15	900/3	38.0	7000	-18	
5	x=0.3	10	900/3	41.0	10000	+20	35
		12	900/3	43.0	7500	+30	
		15	900/3	46.0	7000	+50	
6	$Ca[(Li_{1/3}Nb_{2/3})_{1-x}Ti_x]O_{3-\delta}$ + y (Bi_2O_3) x=0.05	5	900/3	20.0	3500	-10	36
		7	900/3	22.5	5000	-	
		10	900/3	24.5	6000	-	

Table 6. Continued

7	x=0.1	5	900/3	23.0	4500	+5	36
		7	900/3	24.0	5000		
		10	900/3	27.0	6500		
8	x=0.2	5	900/3	35.0	7000	+12	36
		7	900/3	37.5	8000		
		10	900/3	40.0	10500		
9	x=0.3	5	900/3	37.0	6500	+18	36
		7	900/3	40.0	7500		
		10	900/3	42.5	8000		
10	$Ca[(Li_{1/3}Nb_{2/3})_{1-x}Ti_x]O_{3-\delta}$ x=0.0	2 wt% B_2O_3	1050/3	30.0	30000	-20	39
11	x=0.1	2 wt% B_2O_3	1000/3	34.0	25000	-10	39
12	x=0.2	2 wt% B_2O_3	1000/3	37.0	20000	+5	39
13	x=0.3	2 wt% B_2O_3	1000/3	42.0	18000	+15	39
14	x=0.5	2 wt% B_2O_3	1000/3	52.0	15000	+80	39
15	$Ca[(Li_{1/3}Nb_{2/3})_{0.7}Ti_{0.3}]O_{3-\delta}$ + 2 wt% B_2O_3	1 wt% Bi_2O_3	960	43.9	16600	+35.5	39
16	$Ca[(Li_{1/3}Nb_{2/3})_{0.7}Ti_{0.3}]O_{3-\delta}$ + 2 wt% B_2O_3	3 wt% Bi_2O_3	940	43.1	12900	+53.7	39
17	$Ca[(Li_{1/3}Nb_{2/3})_{0.7}Ti_{0.3}]O_{3-\delta}$ + 2 wt% B_2O_3	6 wt% Bi_2O_3	920	43.1	10600	+10.7	39
18	$Ca[(Li_{1/3}Nb_{2/3})_{0.9}Ti_{0.1}]O_{3-d}$ + y LiF	0	1150	35.0	16000		41
19	$Ca[(Li_{1/3}Nb_{2/3})_{0.9}Ti_{0.1}]O_{3-\delta}$ + y LiF	2	975	31.0	15000	+17	41
20	$Ca[(Li_{1/3}Nb_{2/3})_{0.9}Ti_{0.1}]O_{3-\delta}$ + y LiF	6	940	29.0	17000	+2	41
21	$Ca[(Li_{1/3}Nb_{2/3})_{0.9}Ti_{0.1}]O_{3-d}$ + y LiF	10	900	25.0	19000	-15	41
22	$Ca[(Li_{1/3}Nb_{2/3})_{0.9}Ti_{0.1}]O_{3-\delta}$ + y LiF	20	840	19.0	20000	-25	41
23	$Ca[(Li_{1/3}Nb_{2/3})_{0.84}Ti_{0.16}]O_{3-\delta}$	0	1180/3	37.8	14270	-6.2	42
24	$Ca[(Li_{1/3}Nb_{2/3})_{0.84}Ti_{0.16}]O_{3-\delta}$ + 2 wt% ZBS+ y wt%LiF	1	940/3	34.5	16000	+28	42
		2	940/3	34.0	15000	+7	
		3	940/3	32.5	14500	-5	
		5	940/3	30.5	13000	-18	
25	$Ca[(Li_{1/3}Nb_{2/3})_{0.84}Ti_{0.16}]O_{3-\delta}$ + 2 wt% LiF + y wt% ZBS	1	940/3	34.0	18000	+20	42
		2	940/3	33.5	16000	+7	
		3	940/3	33.0	15000	+5	
		5	940/3	32.4	14500	-8	
26	$Ca[(Li_{1/3}Nb_{2/3})_{0.8}$	5	1025	33.4	18500	-12	42

	$Ti_{0.2}]O_{3-\delta}$ + y wt% ZBS	8	950	32.6	18000	-21	
		12	925	33.5	13200	-28	
27	$Ca[(Li_{1/3}Nb_{2/3})_{0.8}$	3	1025	34.2	24500	-5	44
	$Ti_{0.2}]O_{3-\delta}$ + y wt%	5	975	30.7	22600	-18	
	LMZBS	8	975	28.4	13590	-20	
		12	900	26.2	13000	-20	
		15	900	24.1	11500	-21	
28	$Ca[(Li_{1/3}Nb_{2/3})_{0.8}$	3	1025	32.0	20000	-15	44
	$Ti_{0.2}]O_{3-\delta}$ + y wt% LBS	5	950	30.5	14700	-18	
		8	940	27.8	11100	-22	
		12	920	26.5	7000	-18	
29	$Ca[(Li_{1/3}Ta_{2/3})]O_3$+ y	0	1200/2	24.0	42000	-40	38
	wt% B_2O_3	1	1100/2	24.1	38900	+7	
		3	1050/2	23.4	40300	+5	
		6	1050/2	23.4	27900	-8	
30	$Ca[(Li_{1/3}Ta_{2/3})_{1-x}Ti_x]O_{3-\delta}$ x=0.05	3 wt% B_2O_3	1100/4	26.1	22000	-97	38
31	x=0.15	3 wt% B_2O_3	1050/4	29.5	20700	-57	38
32	x=0.20	3 wt% B_2O_3	1050/4	28.4	12900	-14.7	38
33	x=0.30	3 wt% B_2O_3	1050/4	35.0	22800	-4.1	38
34	x=0.50	3 wt% B_2O_3	1050/4	45.0	12300	75	38
35	$Ca[(Li_{1/3}Ta_{2/3})_{0.7}$	5	1050	34.0	15250	-30	82
	$Ti_{0.3}]O_{3-\delta}$ + y wt% ZBS	8	1000	32.2	20800	-32	
		12	950	32.3	11600	-38	
36	$Ca[(Li_{1/3}Ta_{2/3})_{0.7}$	5	1025	32.0	11300	-36	82
	$Ti_{0.3}]O_{3-\delta}$ + y wt%	8	975	32.0	9000	-42	
	BZBS	12	950	31.8	7350	-41	

Table 4 shows the densification and microwave dielectric properties of LBS and LMZBS glass added $Ca[(Li_{1/3}Nb_{2/3})_{0.75}Ti_{0.25}]O_{3-\delta}$ ceramics and the BZBS glass added $Ca[(Li_{1/3}Ta_{2/3})_{0.6}$ $Ti_{0.4}]O_{3-\delta}$ ceramics. The Ti substitution increased the dielectric constant of the CLNT / CLTT ceramics. This can be due to the incorporation of small Ti^{4+} ion (0.605 Å) to the B site $[Li_{1/3}$ $Nb/Ta_{2/3}]^{3.67+}$ with slightly larger ionic radius (0.66 Å) [52]. The $Ca[(Li_{1/3}Ta_{2/3})_{0.6}$ $Ti_{0.4}]O_{3-\delta}$ ceramics with 12 wt% of BZBS glass sintered at 950 ^oC has ε_r = 34.9, Qxf =6500 GHz (f = 4.6 GHz) and $\tau_f \approx$ -6 ppm/^oC. The $Ca[(Li_{1/3}Nb_{2/3})_{0.75}$ $Ti_{0.25}]O_{3-\delta}$ ceramics with 12 wt% LMZBS glass sintered at 900^o C has ε_r =28.5, Q_u x f =11000 GHz (f = 4.7 GHz) and τ_f = -3 ppm/^{o}C and that of LBS glass addition of 5 wt% sintered at 950^{o}C has ε_r = 33, Qxf =11500 GHz (f = 4.6 GHz) and $\tau_f \approx$ -2 ppm/^{o}C. The CLNT ceramics shows good dielectric properties at low sintering temperature compared to CLTT ceramics. Hence the $Ca[(Li_{1/3}Nb_{2/3})_{0.75}$ $Ti_{0.25}]O_{3-\delta}$ ceramics with suitable amount of glass addition can find application in LTCC based devices.

Table 5 shows the sintering temperature and microwave dielectric properties of $Ca[(Li_{1/3}A_{2/3})_{1-x}M_x]O_{3-\delta}$ [A=Nb, Ta and M=Ti, Zr, Sn] complex perovskites and table 6 shows the low temperature sintered $Ca[(Li_{1/3}A_{2/3})_{1-x}Ti_x]O_{3-\delta}$ [A=Nb, Ta] complex perovskites with sintering aid.

5. CONCLUSIONS

The present review reports the microwave dielectric properties of $Ca[(Li_{1/3}A_{2/3})_{1-x}M_x]O_{3-\delta}$ [A=Nb, Ta and M=Ti, Zr, Sn] ceramics and their composites with glass for the possible applications in LTCC based devices. $Ca[(Li_{1/3}A_{2/3})_{1-x}M_x]O_{3-\delta}$ [A=Nb, Ta and M=Ti, Zr, Sn] complex perovskites show excellent temperature stable microwave dielectric properties when sintered at about 1150°C. The $Ca[(Li_{1/3}A_{2/3})_{1-x}Ti_x]O_{3-\delta}$ [A=Nb, Ta] solid solution has an advantage of tuning the temperature coefficient of resonant frequency close to zero by adjusting the titanium content. Compared to CLTT-glass composites, the CLNT-glass composites show excellent dielectric properties with low sintering temperature suitable for LTCC applications.

ACKNOWLEDGMENT

The authors are grateful to the CSIR, New Delhi, India for the financial assistance.

REFERENCES

[1] Sebastian M. T. *Dielectric materials for wireless communications,* Elseiver Publishers, Oxford U. K (2008).

[2] Freer R. Microwave Dielectric Ceramics- An Overview, *Silicate Industriels,* (1993), 9-10, 191-197.

[3] Wersing W. Microwave ceramics for resonators and filters, *Ceramics, composites and intergrowths*, (1996), 715-731.

[4] Kajfez D. Guillon P. *Dielectric Resonators,* Noble Publishing Corporation, Atlanta, US Atlanta (1998).

[5] Fiedziuszko S. J., Hunter I. C., Itoh T., Kobayashi Y., Nishikawa T., Stitzer S. N. and Wakino K. Dielectric Materials, Devices, and Circuits, IEEE Trans. *Microwave Theory and Tech.*, (2002), 50, 706-720.

[6] Richtmyer R. D. Dielectric Resonators, *J. App. Phys.*, (1939), 15, 391-398.

[7] Schlicke H. M. Quasidegenerate modes in high-e dielectric cavities, *J. Appl. Phys.,* (1953), 24, 187-191.

[8] Okaya A. The Rutile microwave resonator, Paper presented at the Proc. IRE, vol.(1960)

[9] Okaya A. and Barash L. F. *The dielectric microwave resonator,* Paper presented at the *Proc. IRE*. (1962)

[10] Cohn S. B. Microwave bandpass filters containing high Q dielectric resonators, *IEEE Trans. Microwave Theory Tech.,* (1968), MTT-16, 218-227.

[11] Masse D. J. A new low loss high-k temperature compensated dielectric for microwave applications, Paper presented at the *Proc. IEEE*.(1971)

[12] Plourde J. K., Linn D. F., O'Bryan H. M. J. and Thompson J. J. $Ba_2Ti_9O_{20}$ as a microwave dielectric resonator, *J. Am. Ceram. Soc.,* (1975), 58, 418-420.

[13] Wolfram G. and Goebel H. E. Existence range, structural and dielectric properties of $Zr_xTi_ySn_zO_4$ ceramics (x+y+z = 4). *Mat. Res. Bull.,* (1981), 16, 1455-1463.

[14] Michiura N., Tatekawa T., Higuchi Y. and Tamura H. Role of donor and acceptor ions in the dielectric loss tangent of $(Zr_{0.8}Sn_{0.2})TiO_4$ dielectric resonator material., *J. Am. Ceram. Soc.,* (1995), 78, 793-796.

[15] Huang C.-L. and Weng M.-H. Improved high Q value of $MgTiO_3$-$CaTiO_3$ microwave dielectric ceramics at low sintering temperature, *Mater. Res. Bull*., (2001), 36, 2741-50.

[16] Nishigaki S., Yano S., Kato H., Hirai T. and Nonomura T. BaO-TiO_2-WO_3 microwave ceramics and crystalline $BaWO_4$., *J. Am. Ceram. Soc.,* (1988), 71, C-11-17.

[17] O'Bryan H. M. J., Thomson J. J. and Plourde J. K. A new BaO-TiO_2 compound with temperature-stable high permittivity and low microwave loss, *J. Am. Ceram. Soc.,* (1974), 57, 450-453.

[18] Roy R. Multiple ion substitution in perovskite lattice, *J. Am. Ceram. Soc.,* (1954), 27, 581-588.

[19] Nishigaki S., Kato H., Yano S. and Kamimura R. Microwave dielectric properties of (Ba,Sr)O-SmO -TiO ceramics, *Am. Ceram. Soc. Bull.,* (1987), 66, 1405-1410.

[20] Huang C.-L. and Weng M.-H. Dielectric properties of B_2O_3 doped (1-x)$LaAlO_3$-x$SrTiO_3$ ceramic system at microwave frequency range, *Mater. Res. Bull.,* (2002), 37, 1941-1948.

[21] Jancar B., Valant M. and Suvorov D. Solid state reactions occurring during the synthesis of $CaTiO_3$-$NdAlO_3$ perovskite solid solutions, *Chem. Mater.,* (2004), 16, 1075-1082.

[22] Moon J. H., Jung H. M., Park H. S., Shin J. Y. and Kim H. S. Sintering behaviour and microwave dielectric properties of (Ca,La)(Ti,Al)O_3 ceramics, *Jpn. J. Appl. Phys.,* (1999), 38, 6821-6827.

[23] Sun P., Nakamura T., Shan Y. J., Inaguma Y., Itoh M. and Kitamura T. Dielectric behaviour of (1-x)$LaAlO_3$-x$SrTiO_3$ solid solution system at microwave frequencies, *Jpn. J. Appl. Phys,* (1998), 37, 5625-5629.

[24] Inchinose I., Mizutani H. and Ookuma H. *Ceramics International,* (1977), 3, 100.

[25] Imanaka Y. Multylayered Low Temperature Cofired Ceramics (LTCC) Technology, Spinger, Japan (2005).

[26] Surendran K. P., Mohanan P. and Sebastian M. T. The effect of glass additives on the microwave dielectric properties of $Ba(Mg_{1/3}Ta_{2/3})O_3$ ceramics, *J. Sol. State Chem,* (2004), 177, 4031-4046.

[27] Bijumon P. V. and Sebastian M. T. Influence of glass additives on the microwave dielectric properties of $Ca_5Nb_2TiO_{12}$ ceramics, *Mater. Sci. Engg*. B, (2005), 123, 31-40.

[28] Sebastian M. T. and Jantunen H. Low loss dielectric materials for LTCC applications: a review, *International Materials Review,* (2008), 53, 57-90.

[29] Surendran K. P. Investigations on Low Loss Dielectric Materials for Wireless Communication *Faculty of Science*,(2004), (Kerala, University of Kerala).

[30] Thomas S. and Sebastian M. T. Effect of B_2O_3-Bi_2O_3-SiO_2-ZnO glass on the sintering and microwave dielectric properties of $0.83ZnAl_2O_4$-$0.17TiO_2$, *Mater. Res. Bull.,* (2008), 43, 843-51.

[31] Anjana P. S. and Sebastian M. T. Microwave Dielectric Properties and Low-Temperature Sintering of Cerium Oxide for LTCC Applications, *J. Am. Ceram. Soc.,* (2009), 92, 96-104.

[32] Choi J.-W., Kang C.-Y., Yoon S.-J., Kim H.-j. and Jung H.-J. Microwave dielectric properties of $Ca[(Li_{1/3}Nb_{2/3})_{1-x}$ $M_x]O_{3-\delta}$ (M=Sn,Ti) Ceramics, *J. Mater. Res.,* (1999), 14, 3567-3570.

[33] Choi J.-W., Ha J. Y., Yoon S.-J., Kim H.-j. and Yoon K. H. Microwave dielectric properties of $Ca[(Li_{1/3}Nb_{2/3})_{1-x}$ $Zr_x]O_{3-\delta}$ ceramics, *Jan. J. Appl. Phys,* (2004), 43, 223-225.

[34] Ha J.-Y., Choi J.-W., Kang C.-Y., Yoon S.-J., Choi D. J. and Kim H.-j. Low Temperature Sintering of $Ca[(Li_{1/3}Nb_{2/3})_{1-x}$ $Ti_x]O_{3-\delta}$ Based Microwave Dielectric Ceramics with Glass Frit, *Jpn. J. Appl. Phys.,* (2005), 44, 1322-1325.

[35] Ha J.-Y., Choi J.-W., Kang C.-Y., Yoon S.-J., Choi D. J. and Kim H.-j. Microwave Dielectric Properties of $Ca[(Li_{1/3}Nb_{2/3})_{1-x}$ $Ti_x]O_{3-\delta}$ ceramics with glass, *J. Electroceramics,* (2006), 17, 399-403.

[36] Ha J.-Y., Choi J.-W., Yoon S.-J., Choi D. J., Yoon K. H. and Kim H.-j. Microwave Dielectric Properties of Bi_2O_3 doped $Ca[(Li_{1/3}Nb_{2/3})_{1-x}$ Tix]O-δ ceramics, *J. Eur. Ceram. Soc.,* (2003), 23, 2413-2416.

[37] Liu P., Kim E. S. and Yoon K. H. Low-Temperature Sintering and Microwave Dielectric Properties of $Ca(Li_{1/3}Nb_{2/3})O_{3-\delta}$ Ceramics, *Jpn. J. Appl. Phys.,* (2001), 40, 5769-5773.

[38] Liu P., Ogawa H., Kim E. S. and Kan A. Low temperature sintering and microwave dielectric properties of $Ca(Li_{1/3}Ta_{2/3})O_{3-\delta}$-$CaTiO_3$ ceramics, *J. Eur. Ceram. Soc.,* (2003), 23, 2417-2421.

[39] Liu P., Ogawa H., Kim E. S. and Kan A. Microwave dielectric properties of low-temperature sintered $Ca[(Li_{1/3}Nb_{2/3}),Ti]O_{3-\delta}$ ceramics, *J. Eur. Ceram. Soc.,* (2004), 24, 1761-1764.

[40] Liu P., Zhang H., Ogawa H. and KIM E. S. Low temperature cofired $Ca[(Li_{1/3}Nb_{2/3})]O_{3-\delta}$ Ceramics for microwave applications, *phys. stat. sol.* (a), (2004), 201, 2175-2179.

[41] Tong J. X., Zhang Q. L., Yang H. and Zou J. L. Low-temperature sintering and microwave dielectric properties of $Ca[(Li_{1/3}Nb_{2/3})_{0.9}Ti_{0.1}]O_{3-\delta}$ ceramics with LiF addition, *Mater. Lett.,* (2005), 59, 3252-3255.

[42] Tong J. X., Zhang Q. L., Yang H. and Zou J. L. Low Temperature Firing and Microwave Dielectric Properties of $Ca[(Li_{1/3}Nb_{2/3})_{0.84}$ $Ti_{0.16}]O_{3-\delta}$ Ceramics for LTCC applications, *J. Am. Ceram. Soc.,* (2007), 90, 845-849.

[43] Yoon S. O., Kim D. M., Shim S. H., Park J. K. and Kang K. S. Microwave dielectric properties of $Ca(Li_{1/4}Nb_{3/4})O_3$–$CaTiO_3$ ceramic systems, *J. Eur. Cer. Soc.,* (2006), 26, 2023-2026.

[44] George S. and Sebastian M. T. Effect of lithium based glass addition on the microwave dielectric properties of $Ca[(Li_{1/3}Nb_{2/3})_{1-x}Ti_x]O_{3-\delta}$ ceramics for LTCC Applications, *J. All. and Comp.,* (2009), 473, 336-340.

[45] Pang L.-X., Wang H., Zhou D., Zhou H.-F. and Yao X. Low temperature firing and microwave dielectric properties of $Ca[(Li_{1/3}Nb_{2/3})_{0.8}Ti_{0.2}]O_{3-\delta}$ ceramics with ZnB_2O_4 glass addition., *Int. J. Appl. Ceram. Technol.,* (2008), 5, 341-346.

[46] Hakki B. W. and Coleman P. D. A dielectric resonator method of measuring inductive capacitance in the millimeter range, IRE Trans. *Microwave Theory Tech.,* MTT., (1960), 8, 402-410.

[47] Krupka J., Derzakowski K. D., Riddle B. and Jarvis J. B. A Dielectric Resonator for Measurements of Complex Permittivity of Low Loss Dielectric Materials as a Function of Temperature, *Meas. Sci. Technol.,* (1998), 9, 1751-56.

[48] George S. and Sebastian M. T. Unpublished data, Unpublished data.

[49] Dai S. X., Huang R. F. and Wilcos Sr D. L. Use of titanates to achieve a temperature stable low temperature cofired ceramic dielectric for wireless application, *J. Am. Ceram. Soc.,* (2002), 85, 828-832.

[50] Fukuda K., Kitoh R. and Awai I. Microwave characteristics of TiO_2-Bi_2O_3 dielectric resonator, *Jpn. J. Appl. Phys.,* (1993), 32, 4584-4587.

[51] Haga K., Ishi T., Mashiyama J. and Ikeda T. Dielectric properties of two phase mixtures ceramic composed of rutile and its compounds, *Jpn. J. Appl. Phys.,* (1992), 31, 3156-3159.

[52] Kagata H., Kato J., Nishimoto K. and Inoue T. The dielectric properties of Pb based perovskite substituted by Ti for B site at microwave frequencies, *Jpn. J. Appl. Phys.,* (1993), 32, 4332-4334.

[53] Wang Y., Zhang G. and Ma J. Research of LTCC/Cu, Ag multilayer substrate in microelectronic packaging, *Mater. Sci. Eng.* B, (2002), 94, 48-53.

[54] Zhang Q. L., Yang H., Zou J. L. and Wang H. P. Sintering and Microwave Dielectric Properties of LTCC Zinc Titanate Multilayers, *Mater. Lett.,* (2005), 59, 880-884.

[55] Shimoda H., Ishitobi N., Kawamura K. and Kobayashi M. Development of a High-Q Multilayer Ceramic Resonator, *Jpn. J. Appl. Phys.,* (1992), 31, 3160-3163.

[56] Liang M. H., Wu S.-Y., Hu C.-T. and Li I.-N. Enhancing the sinterability of $Ba(Mg_{1/3}Ta_{2/3})O_3$ dielectrics by using chemically-derived powders, *Mater. Chem. Phys.,* (2003), 79, 276-281.

[57] Lu C. H. and Tsai C. C. Homogeneous precipitation synthesis and sintering behavior of microwave dielectrics: $Ba(Mg_{1/3}Ta_{2/3})O_3$, *Mater. Sci. Eng.* B., (1998), 55, 95-101.

[58] Renoult O., Boilot J. P., Chaput F., Papiernik R. and Hubert-Pfalzgraf L. G. Sol-Gel Processing and Microwave Characteristics of $Ba(Mg_{1/3}Ta_{2/3})O_3$ Dielectrics, *J. Am. Ceram. Soc.,* (1992), 75, 3337-3340.

[59] Shirey H. M. Low temperature synthesis of the microwave dielectric material Barium Magnesium Tantalate (BMT), (2002), (University of Pittsburgh).

[60] George S., Anjana P. S., Deepu V., Mohanan P. and Sebastian M. T. Low-Temperature Sintering and Microwave Dielectric Properties of Li_2MgSiO_4 Ceramics, *J. Am. Ceram. Soc.*, (2009), 92, 1244-1249.

[61] Jantunen H. A novel low temperature cofiring ceramic (LTCC) material for telecommunication devices, Ph.D. thesis, *Faculty of Science*, (2001), (Finland, University of Oulu).

[62] Ho I.-C. Semiconducting barium titanate ceramics prepared by Boron-containing liquid-phase sintering, *J. Am. Ceram. Soc.,* (1994), 77, 829-832.

[63] Zhang Q. L. and Yang H. Low temperature firing and microwave dielectric properties of ZnO-Nb_2O_5-TiO_2-SnO_2 ceramics with CuO-V_2O_5, *Mater. Res. Bull.,* (2005), 40, 1891-1898.

[64] Huang C.-L., Weng M.-H., Lion C.-T. and Wu C.-C. Low temperature sintering and microwave dielectric properties of $Ba_2Ti_9O_{20}$ ceramics using glass additions, *Mater. Res. Bull.,* (2000), 35, 2445-2456.

[65] Huang G., Zhou D., Xu J., Chen X., Zhang D., Lu W. and Li B. Low-temperature sintering and microwave dielectric properties of $(Zr,Sn)TiO_4$ ceramics, *Mater. Sci. Eng.* B., (2003), 99, 416-420.

[66] Jantunen H., Rautioaho R., Uusimaki A. and Leppavuori S. Temperature Coefficient of Microwave Resonance Frequency of a Low-Temperature Cofired Ceramic (LTCC) System, *J. Am. Ceram. Soc.,* (2002), 85, 697-699.

[67] Kim D. W., Lee D.-G. and Hong K. S. Low-temperature firing and microwave dielectric properties of $BaTi_4O_9$ with Zn-B-O glass system, *Mater. Res. Bull.*, (2001), 36, 585-595.

[68] Lee Y.-C., Lee W.-H. and Shieu F.-S. Low temperature sintering and microwave dielectric properties of $Ba_2Ti_9O_{20}$ ceramics with $3ZnO$-B_2O_3 addition, *Jpn. J. Appl. Phys.,* (2002), 419, 6049-6053.

[69] Wang S.-F., Chiang C.-C. and Wang C.-H. Phase stability of B_2O_3 added $Ba_2Ti_9O_{20}$ ceramic: Processing effects, *J. Mater. Res.,* (2003), 18, 201-207.

[70] Jantunen H., Rautioaho R., Uusimaki A. and Leppavuori S. Composition of $MgTiO_3$-$CaTiO_3$ ceramic with two borosilicate glasses for LTCC technology, *J. Eur. Ceram. Soc.,* (2000), 20, 2331-2336.

[71] Jean J. H. and Lin S. C. Effect of borosilicate glass on densification and properties of borosilicate glass + TiO_2 ceramics, *J. Mater. Res.,* (1999), 14, 1359-1363.

[72] Shin H., Shin H. K., Jung H. S., Cho S. Y. and Hong K. S. Phase evalution and dielectric properties of $MgTi_2O_5$ ceramic sintered with lithium borosilicate glass, *Mater. Res. Bull.,* (2005), 40, 2021-2028.

[73] Takada T., Wang S. F., Yoshikawa S., Jang S.-J. and Newnham R. E. Effect of glass additions on BaO-TiO_2-WO_3 microwave ceramics, *J. Am. Ceram. Soc.,* (1994), 77, 1909-1916.

[74] Park J. H., Choi Y. J. and Park J. H. Low fire dielectric compositions with permittivity 20-60 for LTCC applications, *Mater. Chem. Phys.,* (2004), 88, 308-312.

[75] Wu J.-M. and Huang H. L. Microwave properties of zinc, barium and lead borosilicate glasses, *J. Non Cryst. Solids.*, (1999), 260, 116-124.

[76] Wersing W. Microwave ceramics for resonators and filters, *Curr. Opin. Solid State Mater. Sci.,* (1996), 1, 715-731.

[77] Kawashima S., Nishida M., Ueda I. and Ouchi H. $Ba(Zn,Ta)O_3$ ceramic with low dielectric loss, *J. Am. Ceram. Soc.,* (1983), 66, 421-423.

[78] Kawashima S., Nishida M., Ueda I., Ouchi H. and Hayakawa S. Dielectric properties of $Ba(Zn,Ta)O_3$-$Ba(Zn,Nb)O_3$ ceramic, Paper presented at the *Proc. Ferroelect.Mater. Applications*.(1977).

[79] Nomura S., Toyama K. and Tanaka K. $Ba(Mg_{1/3}Ta_{2/3})O_3$ ceramics with temperature-stable high dielectric constant and low microwave loss, *Jpn. J. Appl. Phys.*, (1982), 21, L624-626.

[80] Surendran K. P. and Sebastian M. T. Low loss dielectrics in $Ba[(Mg_{1/3}Ta_{2/3})_{1-x}\ Ti_x]O_3$ and $Ba[(Mg_{1-x}\ Zn_x)_{1/3}]Ta_{2/3}]O_3$ systems, *J. Mater. Res.,* (2005), 20, 1-7.

[81] Wakino K., Minai K. and Tamura H. Microwave characteristics of $(Zr,Sn)TiO_4$ and $BaO\text{-}PbO\text{-}Nd_2O_3\text{-}TiO_2$ dielectric resonator, *J.Am. Ceram. Soc.,* (1984), 67, 278-281.

[82] George S. and Sebastian M. T. Effect of borosilicate glass addition on the sinterability and microwave dielectric properties of $Ca[(Li_{1/3}Ta_{2/3})_{1-x}Ti_x]O_{3-\delta}$ ceramics for LTCC Applications, *J. Mater. Sci. Mater. Elect.* Communicated (2010)

In: Perovskites: Structure, Properties and Uses
Editor: Maxim Borowski, pp. 319-343
ISBN 978-1-61668-525-6

Chapter 7

PEROVSKITE-TYPE OXIDES: SYNTHESIS AND APPLICATION IN CATALYSIS

Junjiang Zhu[1,2,*] and Jinfa Chen[3]

1Technical University Berlin, Englische Str. 20, 10587 Berlin Germany
2Max Planck Institute of Colloids and Interfaces, Colloid Chemistry, Am Mühlenberg 1, 14476 Potsdam/Golm, Germany
3National Engineering Research Center of Chemical Fertilizer Catalyst, Fuzhou University, Gongye Road 523, Fuzhou, 350002, Fujian, China

ABSTRACT

Two topics of perovskite-type oxides were browed and discussed in this chapter: one is the synthesis method and the other is its application in catalysis. Because of the diverse applications of perovskite-type oxides, special properties are usually required depending on the ultimate use, while the desired properties could be achieved by choosing a proper synthesis method. For example, using coprecipitation method could lead to a well crystallized structure, while by a nanocasting method perovskite with high surface area could be achieved. Thus, an overview of synthesis method for perovskite-type oxides reported in the publications was made for better understanding the advantage of each method.

Efforts on the application of perovskite-type oxides were made exclusively in catalysis in this part. Attentions on using these oxides as catalyst are increasing year by year not only because of their low manufacturing cost but also due to the unique properties, such as high thermal stability, exchangeability of cations and of course, considerable activity. Many catalytic reactions using perovskite-type oxides as catalyst has been attempted, and although for a given reaction catalyst with different ions, either at A- or B-site, show different catalytic activities, a common point is that the presence of oxygen vacancy is necessary for the reaction to proceed. From the nature of catalytic reaction, that is the difficulty of electron transferring between reactant and catalyst, it was

* E-mail: ciaczjj@gmail.com

proposed, exampled by the reactions of NO decomposition and NO+CO reduction, that the crucial pre-requisite for a catalytic reaction to occur is that the full redox cycle of catalyst can proceed easily. Thus only when this requirement is fulfilled, other parameters, such as the amount of active sites, could come into the focus of catalyst design.

1. INTRODUCTION

Perovskite, which is first used to describe the oxides $CaTiO_3$, is now extensively referring to oxides with ABO_3 structure, and sometimes also to the oxides with A_2BO_4 structure. In some cases, carbides, nitrides, halides, and hydrides also have the ABO_3 structure,[1] but practically perovskite refers to the oxides compounds. In this context, if not specified, perovskite means an oxide compound having the ABO_3 or A_2BO_4 structure.

Ideal structure of perovskite oxides with ABO_3 or A_2BO_4 structure are shown in Figure 1. The former is cubic with space group $Pm3m\text{-}O_h$,[2] while the latter is composed of ABO_3 structure plus an AO layer. Detailed descriptions of these structures have been made in the original publications and in some previous reviews,[1-4] here we just give an initial concept of perovskite. As shown in Figure 1, A is a larger cation that locates on the edge of the structure, and B is a smaller cation locating in the center of the octahedron. The A- and/or B-site cations could be substituted by a foreign one, which would lead to the distortions of structure, however not destroying the matrix structure, if the cations in the structure could satisfy the requirement of $t = (r_A + r_O)/\{\sqrt{2}(r_B + r_O)\}$, where t is in the range of 0.75 ~ 1.0.[5]

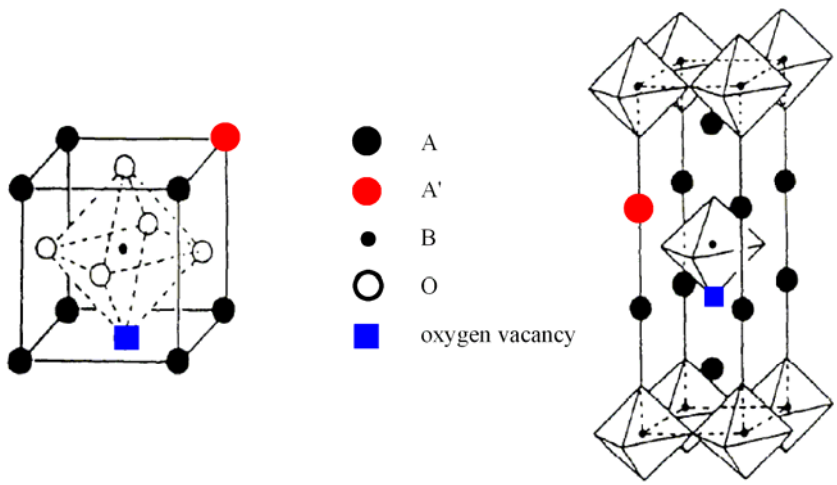

Figure 1. Ideal models of perovskite-type oxides with ABO_3 and A_2BO_4 structure. The red cycle means that A-site cation was substituted by a foreign one; the blue square means the oxygen vacancy. Note: the oxygen symbol was not shown in the A_2BO_4 structure for simplification. Reprinted from ref. 73, copyright 2009, with permission from Elsevier

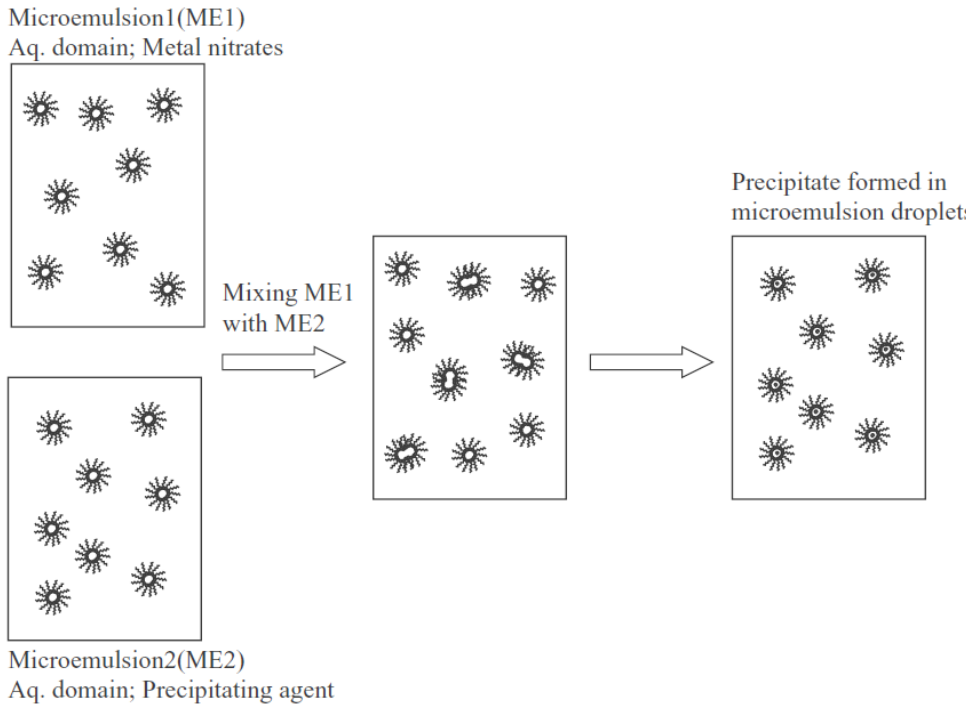

Figure 2. Schematic presentation of particle formation by precipitation in a microemulsion. Reprinted from ref. 24, copyright 2004, with permission from Elsevier

Attentions on perovskite oxides have been largely paid in the last decades due to their special structures and unique properties. It was mentioned that 90% of the metallic natural elements of the Periodic Table are stable in a perovskite structure and multicomponent perovskites could be synthesized by partial substitution of cations at either A- or B-site without destroying the matrix structure.[1] This allows tuning the oxidation state of cataions (especially for these at B-site) or creating oxygen vacancies with desired properties, thus offering the possibility of correlating these properties to the chemical performances directly. As a result, these oxides are of highly concerned in scientific research since clear and confident correlation could be plotted simply by partial substitution of the cations.

Application of perovskite oxides have been extensively studied [6-13] in such as, solid state chemistry, physics, advanced materials, and catalysis. Because of these diverse applications and special requirements in each application, perovskite-type oxides with special properties are required depending on the ultimate end use. For example, materials-oriented applications require densification by high temperature sintering to minimize both surface area and surface free energy in order to maximize mechanical strength. In contrast, catalytic materials have to maintain sufficiently high surface area in order to maximize their participation and activity in chemical reactions.[14]

The requirement for these special properties mostly could be achieved by choosing a proper synthesis method, such as the solid-state reaction, citric acid combustion or chemical vapor deposition. The synthesis of new perovskite materials has been an ongoing interest for materials scientists and a combination of perovskites with other materials has proved to be an efficient approach to enhance the desired properties and develop new applications. Therefore,

to find a synthesis method with novel processing undoubtedly is an interesting subject of future tasks. [3]

In this chapter, synthesis methods and applications of perovskite-type oxides in catalysis were reviewed. However, since the reported literatures on these two topics are really extensive, we do not have the attempt in making an exhaustive coverage for them. Here, only a series of typical examples is given to illustrate the synthesis method and efforts made on the application of perovskites concentrated mainly in the field of catalysis.

2. SYNTHESIS METHODS FOR PEROVSKITE OXIDES

The preparation route plays a critical role on the physical and chemical properties of perovskites. The approach to synthesis of perovskites must be examined in function of the specific demands concerning activity and/or selectivity, both of which depend on the arrangement of atoms at a small scale. A general objective is to locate the different constituting atoms at precise positions. The main difficulty is to transform the starting precursor into a highly porous solid without segregation of different elements that would produce tiny parts with different properties.

A. Solid-state Method

The simplest method for synthesizing perovskite is by grinding or ball-milling the mixed oxides, either in dry or wet slurry. The mixture was then calcined at temperatures of 600–1000 °C to obtain the final product. This operation sometimes needs to be repeated several times to obtain a pure pervoskite. However, it should be noted that the grinding conditions, such as the rotate rate, grinding time and grinding atmosphere, have significant effect on the surface area and catalytic performances.[15] The solid-solid reaction can be accelerated by 'priming' or catalyzing by a small amount of additive pre-mixed with the reactant oxides, presumably for increasing surface area and nucleating the desired phase.[16, 17] However, when an additive is used, the perovskite product should be thoroughly washed, in order to free the sample from the residues of the additive.

Nanoparticle perovskite could also be synthesized by this method with the assistance of oriented substrate. The surface energy of perovskite changes with the orientation of the substrates due to variation in atomic arrangements. The resulting particle shape is polyhedral, and is composed of planes that minimize the surface and interfacial energies between the individual components and that between the components and the substrates.[18]

Whereas it should be noted that the solid-state method is difficult to make the mixed oxides precursors in a uniform state, therefore, in order to prepare perovskite with homogeneous phase, other techniques, such as ultrasonic treatment, could be used to homogenize the mixture to improve the quality of the formed perovskite.

In all, this method could be easily operated but is not so preferable, especially in catalysis, as it gives wide grain size distributions, bad homogametic phases and further needs very high calcination temperatures, which is energy consuming. Also, due to the agglomeration at high temperature, it shows a relatively low surface area.

B. Wet Method

Other than that in solid-state method, the precursors could be homogeneously mixed if they are presenting in gaseous or liquid phase. Precursor in liquid phase is more convenient, because it has no long-range structure, permitting a statistical distribution at molecular scale. In addition, the movements of molecule in liquid state is of the order of magnitude of Van der Waals forces or hydrogen bond forces, that is a few kJ/mol, while diffusion in solids necessitates the loosening of ionic forces or the breaking of covalent bonds, the strength of which is much higher than that in liquid state. Therefore, perovskite synthesized by chemical solution methods show fine and homogeneous particles with relatively high specific surface areas.

B1. Coprecipitation

Coprecipitation is a common method for the preparation of mixed-oxide catalyst. Generally, nitrates, carbonates and oxalates could be used as the metal source, while NaOH, KOH or (NH_3)aq. as precipitant agent. Aqueous ammonia is preferable for precipitation, especially in the case that foreign ions (e.g. Na^+, K^+) have negative effect on the synthesized catalyst. An exception to this is when (NH_3)aq has the possibility of forming metal-ammine complexes (e.g. Ni, Co, Cu, Zn). Following is an example using coprecipitation method for the preparation of $La_{1-x}Ca_xFeO_3$ oxides: [19] 0.1N sodium hydroxide solution was dropped one by one to 0.1N of corresponding nitrates precursors at room temperature until the pH value reaches 10, which was then aged for 48 h under the same conditions. The resulting precipitate was filtered off, washed with distilled water to remove excess sodium ions until reaching constant conductivity value, and then dried in air at 110 °C overnight. The obtained solids were finally calcined in air at 700 °C for 6h.

In this method two major steps are involved in, namely, nucleation and growth. To obtain a highly dispersed precipitate, it is necessary to accelerate the nucleation rate while suppress the growth rate, which could be achieved by the following techniques:[20]

(1) A vigorous stirring of the solution when adding the chemical compound. This allows the ions reaching the over-saturation status rapidly, and hence accelerates the nucleation speed.
(2) A rapid addition of precipitating agent ensures a rapid reaching of supersaturation in the whole volume of the solution, leading to a maximum nucleation rate.
(3) Because higher temperature will promote the growth rate of new phase, precipitation is usually performed at the lowest temperature, though the situation practically is different from case to case.
(4) Other specific steps, for example the addition of an extra component, re-dispersion of hydroxide, coprecipitation in an aqueous medium by sonication, etc.

However, for compound oxides, because the precipitation point for each component is different, segregation almost invariably occurs when liquids are reacted to give solids. Hence it is difficult to control the stoichiometry and homogeneity of cationic distribution in the grains.

B2. Citrate Method

Compared to coprecipitation method, the 'citrate' one which consists of preparing stable amorphous or glassy precursors guarantees stoichiometry and homogeneity of cation distribution and tolerates wide range of compositions. The starting solution is a mixture of metallic salts and a hydroxyacid such as citric, malic, tartaric, lactic, or glycolic acid. Citric acid so far has been used most frequently because it is cheap and stable, and hence the name 'citrate' is attached to the method.

Typically, the concentrations of organic acid are higher than that of the total metals, and the solution is concentrated by rapid evaporation under vacuum, until a gel is obtained. So far, the solution can be dehydrated under vacuum at about 80 °C to give a rigid-foam (meringue) precursor, which is amorphous and hygroscopic, and exhibits the color of the metallic ions. The amorphous precursor is some sort of a three-dimensional polymer in which the multifunctional organic acids are linked to two or more cations by covalent or hydrogen bonds. The thermal decomposition of the amorphous mass could proceed continuously or in two distinct steps at 80–100 and 250–400 °C. The resulting powders, amorphous citrate precursor, were crushed and sieved to obtain the required particle size. Finally, the solids were calcined at a certain temperature for several hours to obtain the product.

According to literature [21], the hydroxy acids with one hydroxy group and two or more carboxylic groups seem to be more preferable. While at this time the properties of perovskite would be changed depending on the metal source. Metal nitrates were considered to be the best one since it will not leave any residues during thermal decomposition. Also, the use of nitrate would promote the surface area and porosity of sample, due to the large amount of gas produced during the decomposition. The metal acetates or chlorides were not as effective as nitrates in producing the perovskite phase at lower temperatures.

However, because of the violent reactions during the thermal decomposition of amorphous mass, it should be carried out carefully, taking all necessary precautions. The preparation of oxides containing metallic ions which are highly active in oxidation needs very stringent precautions and is generally not advisable, especially for copper and silver salts. In these cases, the freshly formed metal particles could be powerful catalysts for some unexpected reactions, e.g. with ammonia. Also, secondary reactions can occur even at room temperature resulting in the formation of a small amount of lethal cyanogen gas.[20]

Many attempts have been made to modify the citrate method, and a promising one is called "Pechini method", in which polyalcohol is introduced to the initial solution.[22] The role of polyalcohol is supposed to promote the formation of reticulation from the starting solution to the rigid foam. The reticulation or polymer formation is due to the esterification reaction between citric acid and the poly-alcohol.

B3. Microemulsions Method

Microemulsions are transparent, thermodynamically stable multicomponent fluids, normally are composed of an aqueous component, an oily component, an amphiphile (used as emulsifying agent) and frequently a co-surfactant. There are two different types of microemulsions: (a) oil in water microemulsion (o/w-microemulsion), in which the hydrophobic part of the surfactant is absorbed on the surface of oil microdroplets while the hydrophilic part is oriented toward the water; and (b) water in oil microemulsion (w/o-microemulsion), in which the hydrophilic part of the surfactant is absorbed at the surface of water microdroplets while the hydrophobic part is oriented toward the oil. The latter is also

called reverse microemulsion. With increasing the water concentration the nanodroplets of microemulsion increases and eventually forms aggregates or infinite clusters.[23] At this stage the microemulsion processes a bicontinuous structure. The reverse microemulsion method, utilizing aqueous solution nanodrops surrounded by surfactant molecules, has been used extensively for the synthesis of many kinds of materials including perovskites.

Figure 2 shows a schematical double microemulsion technique, where two microemulsions with equal water–surfactant–oil ratio are mixed. One contains metal ions and the other the precipitating agent.[24] Due to the dynamics of the system,[25] the water in the droplets mixed rapidly, leading to the formation of particles by precipitating inside the microemulsion droplets. The perovskite phase can then be formed at a low calcination temperature, due to the homogenous mixing of the metals and the small-size primary particles. Low calcination temperature avoids the particle growth and thus preserves high surface area. Compared to these prepared by co-precipitation in water, the materials by microemulsion technique show more homogenous morphology consisting of smaller crystallites.

B4. Combustion Method

The combustion method, which is used to synthesize oxides with fine particles, represents an interesting alternative due to the following advantages: relatively cheap starting reactants, simple and easily available organic molecules as fuel and highly exothermic and self-sustaining reactions. In this method, the appropriate amount of metal nitrates and organic fuels were first added to de-ionized water, the mixtures were then thoroughly stirred to eliminate the water at 60–70 ˚C until homogeneous sol-gel was formed, subsequently the sol-gel was ignited in air and fine oxides particles were obtained. These fine particles were finally calcined at desired temperature to form the perovskite structure.

Organic molecules (e.g. glycine, alanine, glycerol and urea) play a double role in this process: (i) as complexing agent to homogenize metal cations during evaporation and (ii) as fuel to react with the internal oxidants (nitrogen oxides formed during the decomposition of the nitrates) and/or atmospheric oxygen to form the fine oxide particles. It has been reported that $LaMnO_3$ and $LaCoO_3$ prepared by combustion technique showed the highest thermal stability and the best catalytic activity for methane combustion than that by other synthesis routes.[26] While perovskites synthesized by different organic fuels result in different temperature attained in the combustion process, and hence different BET surface areas, residual carbon contents and catalytic activities. For example, Specchia et al. [27] found that the use of glycine as a fuel for the synthesis of $LaMnO_3$-based catalysts is more preferable than that of alanine and glycerol. They also investigated the effect of fuel/oxidizer ratio and found that the optimum value is at ~1:1. Besides, Wang et al [28] recently investigated the effect of complex on the catalytic performances of perovskite for CO oxidation reaction, finding that $LaSrNiO_4$ catalyst prepared by using oxalic acid showing the best and stable activity, while that by citric acid is the lowest one.

However, the specific surface areas of perovskites synthesized by combustion method were not dramatically higher than those obtained by traditional methods. Further the sample synthesized by this way was found to be rapidly deactivated due to sintering, even by a short thermal treatment. Therefore, in this method NH_4NO_3 was usually chosen as an additive, because it can enhance the specific surface area and resistance to thermal treatment, while without leaving any residues and altering the proportion of the components.[29] The main

drawback of using NH_4NO_3 is that hazardous or polluting compounds are emitted during the synthesis (mainly NH_3 or NOx).

B5. Freeze-drying

Usually slow evaporation of a homogeneous solution containing two different precursors leads to two separate salts in the solid product. To prevent this, the elimination of physical diffusion process would be useful, which could be achieved by a rapid cooling technique, i.e. freeze-drying. Freeze-drying is a versatile method that can produce mixtures of phases with high homogeneity, although there is, in principle, no atomic level homogeneity.

Following is an example for the preparation of $NdCoO_3$ perovskite by freeze-drying method: [30] 0.005 mol neodymium sesquioxide was first dissolved in 5 ml of concentrated nitric acid, and then added to a solution of 0.01 mol of cobalt (II) acetate in 25 ml of water. The pH of the resulting solution was adjusted to 4.5 by addition of dilute ammonia. Finally, the resulting reddish solution were frozen in liquid N_2 and transferred into a freeze-dryer operated at a pressure of 7.6 torr. The resulting blue-pink powder was placed into an alumina boat and pretreated at 400 ˚C for 2 h under vacuum. The "ashes" were finally ground and treated for 24 h under a dynamic oxygen atmosphere at 700 and 900 ˚C.

The use of the freeze-drying allows obtaining a relatively high surface area and precursors show perfect homogeneity in grain composition, hence the product could be easily synthesized at lower temperatures. However, the important parameters in freeze-drying are cooling rate and the final temperature of the solidified solution. These can be controlled but only with a small scale. Hence the method is not well suited to large-scale manufacture of catalysts.

B6. Template Method

By filling the interspaces of the template with the material (precursor) to be cast, and subsequently calcinating and removing the mold, materials with replica structure can be obtained. The use of a confined space is of great importance because it restricts the growth of the material during the synthesis and facilitates the formation of nanostructures. By this way, numerous mesoporous metal oxides, including perovskite, could be synthesized.[31-33] For the synthesis of perovskite, complex (e.g. citrate acid) usually is used to guarantee stoichiometry and homogeneity of cation distribution in the mother solution.

One typical procedure for nanocasting synthesis of mesoporous $LaCoO_3$ perovskite is as below:[33] stoichiometric lanthanum and cobalt nitrates were first dissolved in the mixed citrate solution of deionized water and ethanol, with the molar ratio of citric acid to total metal cations (La + Co) at 1:1. So far, 4 mmol lanthanum nitrate, 4 mmol cobalt nitrate and 8 mmol citric acid were dissolved in a mixture of 15 mL ethanol and 5 mL deionized water. A homogeneous solution was obtained after stirring at room temperature for one night. Then 1.0 g of hard template was added to this solution, the mixture was stirred for another several hours at 40 °C until it became viscous, then dried at 80 °C for 6 h and calcined at 500 °C for 4h to decompose the nitrate species. To achieve higher loadings, the impregnation could be repeated with the same procedure. The resulting material was calcined at 700 °C for 4 h (ramp, 2 °C /min) in air. The silica framework was then etched by using 2M NaOH aqueous solution at room temperature for three times. After being centrifuged, washed with water and ethanol, and dried at 80 °C overnight, finally the black $LaCoO_3$ powder was obtained.

The advantage of this strategy is that the synthesis of the porous materials takes place in a confined space formed by the porosity of the template. Thus-synthesized perovskite has a high surface area with three-dimensional ordered mesoporous channels, which can not be achieved by conventional methods. Moreover, template-based growth is commonly a solution or colloidal dispersion based process. It is less expensive and readily scalable to mass production. It also offers the advantages of less contamination and is environmentally benign. [34]

However, the removal of template is difficult and requires severe conditions, either strong basic medium (e.g. NaOH) or acidic medium (e.g, NH_4HF_2), which may destroy the structure of the produced perovskite. Further, not all of perovskites can be successfully synthesized by templating. It is difficult to find appropriate templates with pore channels of desired diameter, length and surface chemistry and to remove the template completely without compromising the integrity of the nanostructured perovskites. Gao et al [35] concluded that the rules of choosing templates to get highly textured perovskites are: (1) Template with large anisotropy dimension can be easily prepared; (2) The elements of templates composition should be involved in the composition of matrix perovskites and can be easily removed; (3) Lattice structure of templates should be similar to that of matrix perovskites; (4) Templates should have high reactivity or diffusion with matrix particle to ensure a single phase; (5)The morphology and the size of template should be uniform for tape casting.

3. APPLICATION IN CATALYSIS

A. Photocatalysis for Water Splitting

It has been reported long time ago that some of perovskite-type oxides, e.g. $SrTiO_3$, can decompose H_2O into H_2 and O_2 with no external bias potential.[36] The principle for this process is that the conduction band (CB) edges of some of the perovskite oxides are more negative than the H^+/H_2 energy level.[1] However, only a few work on using perovskite oxides as photocatalyst is reported up to date and study on this field is still in its infancy.

In most cases however the perovskite alone shows no or little activity for water splitting and thus introduction of a foreign metal on the substrate is required, e.g. $NiO/SrTiO_3$.[37] The introduction of the foreign metal is to decrease the H_2 overvoltage in the process, since high H_2 overvoltage leads to low efficiency for water reduction. Accordingly, it was proposed that the oxidation and reduction processes in water splitting occur on two different sites: the oxidation of oxygen ($2O \rightarrow O_2$) is on the perovskite semiconductor and the reduction of hydrogen ($2H \rightarrow H_2$) is on the supported metal (Note: electron transferring was not marked for simplification).[37]

As expected the activity of perovskite catalyst for water splitting could be altered through partial substitution of cation by a foreign one. A typical example is the substitution of Ta^{5+} by Ti^{4+} in $KTaO_3$.[38] As shown in Figure 3, the activity of $KTa_{1-x}Ti_xO_{3-x/2}$ for water splitting changes with the amount of Ta being substituted and the best activity appears at $x = 0.08$.

Other parameters, such as calcination conditions and preparation methods, also have great effect on the activity of the catalyst. In a recent work Hu et al [39] investigated the preparation methods (Sol–gel, hydrothermal and solid-state methods) on the crystalline

structure and photocatalytic activity of $NaTaO_3$ perovskite for water splitting, finding that the catalyst prepared by sol-gel method, which has a monoclinic phase, shows the best activity for water splitting, as shown in Figure 4. Also they concluded that the photocatalytic activity of the $NaTaO_3$ specimens in water splitting has the same order as that of the Ta-O-Ta bond angle observed in the structure.

Other catalytic reactions, especially for those using hydrogen as reactant, are also explored in photocatalysis, due to the production of H_2 from the photocatalytic water splitting. Two typical cases are the reduction of CO_2 [40-42] by H_2O and the synthesis of NH_3 from N_2 and H_2O.[43, 44] The later indicated that the thermodynamically unfavorable reaction of NH_3 formation from N_2 and H_2O can be produced under band-gap irradiation of these catalysts.

B. Electrocatalysis

The solid oxide fuel cell (SOFC) is an electrochemical device that can be used for either stationary or mobile generation of electrical energy from a gaseous fuel.[45] Perovskite oxides could be good cathode materials for SOFC with an efficiency ranging from 50 to 65%,[46-48] because they possess high-electronic and ionic conductivities, porosity, thermal and chemical compatibilities with the electrolyte, and long-term stability, which are essential for cathode of SOFC. Also, some unique properties of perovskite oxides, such as the exchangeability of cations and the possibility of creating oxygen vacancy without destroying the matrix structure, make them a prominent candidate in fabricating the cathode of SOFC.

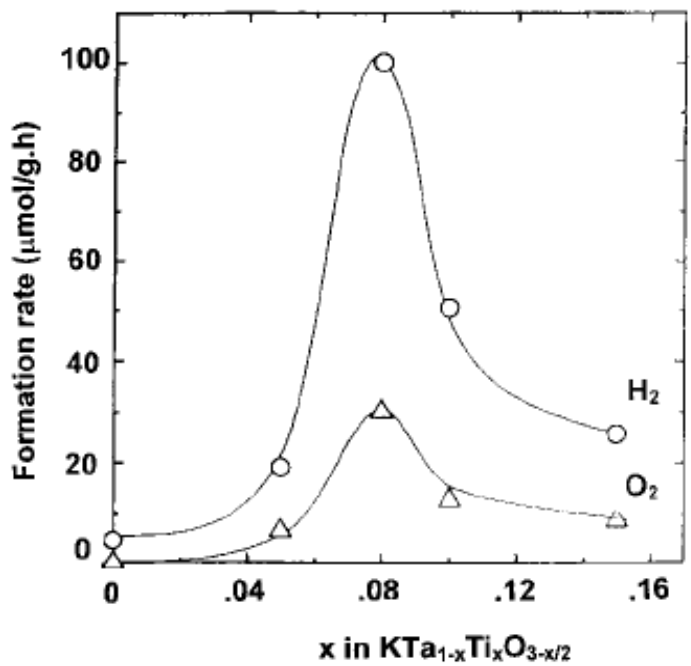

Figure 3. Formation rate of H_2 and O_2 as a function of Ti content in $KTaO_3$ (loaded with 1wt% NiO). Reprinted from ref. 38, copyright 1999, with permission from Chemical Soc. Japan.

Sr-doped $LaMnO_3$ ($La_{1-x}Sr_xMnO_3$) perovskite has been extensively studied for decades as a cathode material in ZrO_2-based SOFC, due to its relatively high electrocatalytic activity for O_2 reduction and good thermal and chemical compatibility with ZrO_2- based electrolyte. [1, 49] However the Mn-based perovskite usually are lacking of oxygen vacancy, thus the oxide-ion conduction at the working temperature, makes it necessary to use thick, porous electrodes containing an array of triple-phase boundaries where gas, electrolyte and electrode meet.

Also, because the conventional SOFC using $La_{1-x}Sr_xMnO_3$ as the cathode material usually requires high operating temperature (~1000 ˚C), which leads to some serious problems, such as a high possibility of interfacial reaction between the electrode and electrolyte to form insulating phase(s), and the densification of the electrode layer due to high-temperature sintering, thus the search for new cathode candidate that can work at a relative low temperature range is essential.[50] Shao and Haile [51, 52] recently found that $Ba_{0.5}Sr_{0.5}Co_{0.8}Fe_{0.2}O_{3-\delta}$ (BSCF) perovskite oxide can show high electrochemical activity at temperature of 600 ˚C and a detailed review regarding the using of BSCF in SOFC was given more recently.[50]

Another application of perovskite in electrocatalysis is for electrochemical reduction of some pollutes such as NO. For example, Simonsen et al [53] investigated the simultaneously reduction of NO and O_2 over $La_{2-x}Sr_xNiO_4$ based electrodes. They found that, based on CV measurement, the reduction of NO is more preferred than O_2 at -100 mV (see Figure 5) and the electrode made by $LaSrNiO_4$ showed the best result. This offers an option for NO removal in the presence oxygen, which practically is a challenging topic in heterogeneous catalysis.

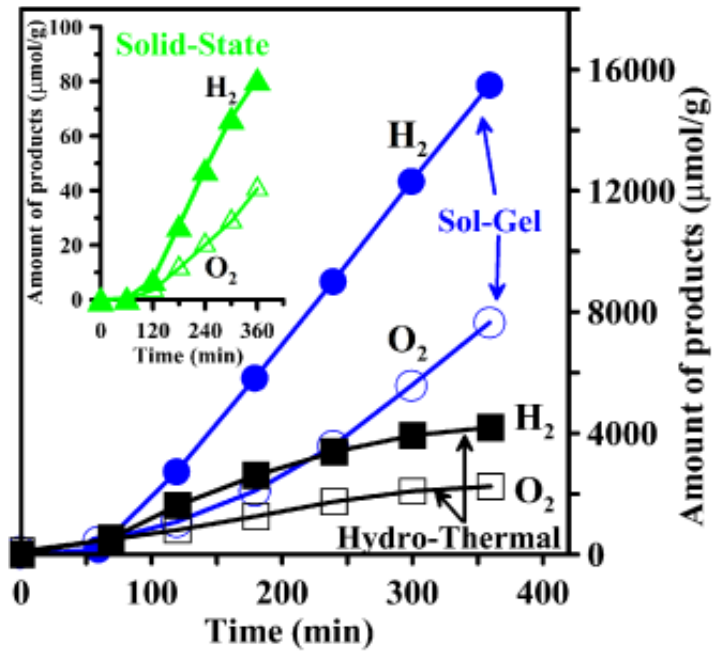

Figure 4. Photocatalytic H_2 (empty) and O_2 (full) evolution from 900 mL pure water suspended with 1 g of the sol–gel, hydro-thermal, and solidstate $NaTaO_3$ photocatalysts, which have surface areas of 23, 12, and 0.6 m^2/g, respectively. Reprinted from ref. 39, copyright 2009, with permission from Wiley

C. Heterogeneous Catalysis

Different from the two above-mentioned catalysis, heterogeneous catalysis does not involve extra substance (such as photos, electrons), and all the behaviors performed in the reaction are done by the catalyst itself. A review of literature shows that the amount of works reporting the application of perovskite catalyst in heterogeneous catalysis is far more than that in photocatalysis or in electrocatalysis. Possible reasons could be the various reactions in heterogeneous catalysis and no restriction for the catalyst is required at this time, which is different from that for Photocatalysis or Electrocatalysis, where special properties, such as negative energy level, high-electronic and ionic conductivities are usually required.

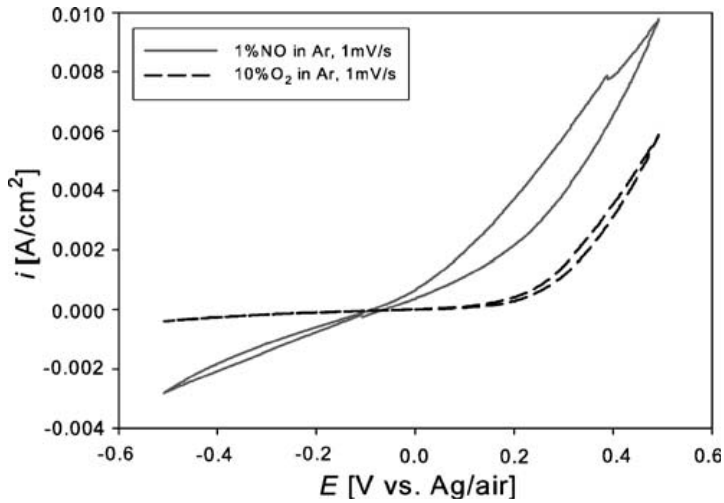

Figure 5. CVs obtained for $LaSrNiO_4$ electrode at 400 ºC. The measurements are performed in 10% O_2 in Ar and 1% NO in Ar at 1 mV/s. Reprinted from ref. 53, copyright 2009, with permission from Springer

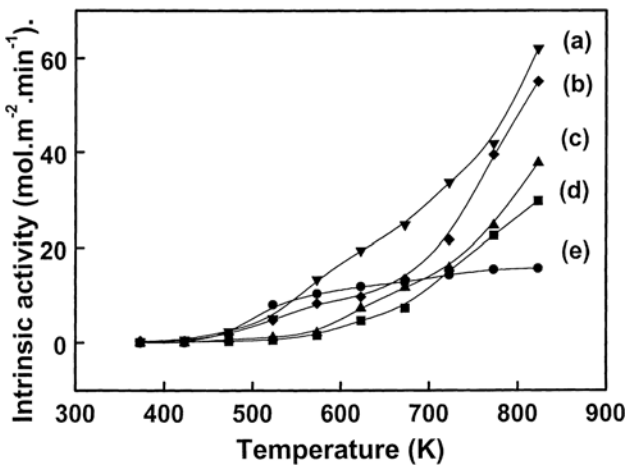

Figure 6. Temperature dependence of the intrinsic activity in the catalytic CO oxidation on $LaCuO_{3-\delta}$ catalysts: (a) $LaCuO_{2.55}$; (b) $LaCuO_{2.65}$; (c) $LaCuO_{2.73}$; (d) $LaCuO_{2.95}$ and (e) La_2CuO_4. Reprinted from ref. 63, copyright 2000, with permission from Elsevier

C1. Liquid Phase Reaction

Liquid phase reaction using solid catalyst is an interesting topic in fine chemicals. Comparing with homogeneous catalysis where liquid catalyst is used, heterogeneous reaction has the great advantage in separating catalyst from the product. Perovskite oxides due to its low cost, diverse properties and of course, considerable activity thus received great attentions. Another fact that should be pointed out is that the active site of perovskite oxides, other than that of supported noble metal catalyst, will not be leached in the reaction.

Liu et al [54] first investigated the catalytic behavior of $La_{2-x}Sr_xCuO_4$ perovskite oxides for liquid hydroxylation of phenol using H_2O_2 as the oxidant. A considerable value for phenol conversion (50.9% for La_2CuO_4) was observed and especially, they found that the activity of catalyst was unchanged even after ten runs of the reaction, indicating that perovskite oxides are very stable catalyst for liquid phase reaction. Notably, they pointed out that copper with low oxidation state is more favorable for the hydroxylation reaction, while side reactions became prominent when copper has high oxidation state.

Recently, Resini et al [55] investigated the catalytic behaviors of $La_{0.8}Sr_{0.2}Mn_{0.98}O_3$ for catalytic wet oxidation of phenol through tuning the temperature, catalyst loading, phenol concentration and stirrer speed used in the experiment. A significant activity was observed at low oxygen pressure and only a very small formation of toxic side products, e.g. hydroquinone, p- and o-benzoquinone. They showed that the reaction is first-order with respect to phenol concentration but there has a transport limitation of phenol to the catalyst surface, which however could be overcome by increasing the catalyst loading.

Also, comparison of preparation method on the catalytic behavior of perovskite oxides for liquid reaction was investigated. Kulkarni et al [56, 57] prepared a series of $La_{1-x}Sr_xFeO_3$ catalyst for reduction of nitrobenzene to aniline by microwave irradiation method, finding that the activity is similar to that prepared by conventional methods. The advantage in using microwave method is that it does not involve intermittent grindings and calcinations at elevated temperatures.

C2. Gas Phase Reaction

C2.1. CO Oxidation

The oxidation of CO over perovskite oxides has been largely investigated not only with the aim for removing this harmful gas, but also for using as a probe reaction to study the defect chemistry of these compounds. The first report using perovskite oxides as catalyst for CO oxidation was carried out by Parravano in the early 50s, [58] while it is still extensively investigated up to date.

Generally it was believed that the CO oxidation over perovskite catalyst proceeds via a suprafacial process, in which the electronic band structure near the Fermi level plays a key role. [59, 60] That is, the reaction proceeds via the adsorbed CO and oxygen. However, the lattice oxygen also plays an important role in the reaction, since it could affect the oxygen mobility in the bulk, the redox behavior of the metal ion and in some certain conditions, it could also be transferred into adsorbed oxygen.

Because molecular oxygen usually is inert, it must be activated and dissociated into atomic oxygen before participating in the reaction.[61] ^{18}O isotope experiment gave evidence that the oxygen adsorption and activation on perovskite catalyst proceeds on the oxygen

vacancy, which is formed due to the losing of lattice oxygen.[62] Hence, the amount of oxygen vacancy or the mobility of lattice oxygen would have great effect on the CO oxidation activity. Indeed, Falcon et al [63] have investigated this relationship by testing the CO oxidation activity over $LaCuO_{3-\delta}$ ($\delta = 0.05 - 0.45$) catalyst system, in which the concentration of oxygen vacancies can be gradually changed by controlled annealing under high oxygen pressures at temperatures from 800 to 1000 ˚C. The results shown in Figure 6 indicate that although all the samples show measurable and similar activity at 150 ˚C, an obvious difference in the activities is observed with increasing the reaction temperature. The orthorhombic $LaCuO_{2.55}$ with the largest oxygen defect shows the best activity for CO oxidation, while La_2CuO_4 with no oxygen vacancy shows the lowest one.

Au et al [64] investigated the influence of oxygen (both adsorbed and lattice) on the CO oxidation activity by using $ACo_{1-x}Bi_xO_{3+\delta}$ as the catalyst. They found that the incorporation of Bi could lead to the lattice oxygen desorbing at a lower temperature and improve the mobility of lattice oxygen, as evidenced by O_2-TPD and H_2-TPR experiments (see Figure 7). They also suggested that the redox reaction of cobalt ions plays an important role in the reaction, and in the present case the activity could be attributed to the extent of the redox processes:

$$2Co^{4+} + O^{2-}_{lattice} \rightleftharpoons 2Co^{3+} + (1/2)\,O_2 \quad (1)$$

$$2Co^{3+} + O^{2-}_{lattice} \rightleftharpoons 2Co^{2+} + (1/2)\,O_2 \quad (2)$$

$$Co^{2+} + O^{2-}_{lattice} \rightleftharpoons Co^{0} + (1/2)\,O_2 \quad (3)$$

$$Bi^{5+} + O^{2-}_{lattice} \rightleftharpoons Bi^{3+} + (1/2)\,O_2 \quad (4)$$

$$2Bi^{3+} + 3\,O^{2-}_{lattice} \rightleftharpoons 2B^{0} + (3/2)\,O_2 \quad (5)$$

Effect of electrochemical properties of perovskite catalyst on CO oxidation reaction was recently investigated through comparing with CH_4 complete oxidation reaction, which is usually considered to be an intrafacial reaction. Results indicate that for suprafacial CO oxidation, its activity depends mainly on the redox peak area of the catalyst, while for intrafacial CH_4 oxidation, the activity depends on the symmetry of redox potentials of the catalyst.[65, 66] Dependence of CO oxidation activity on the redox peak area was shown in Figure 8, which clearly showed that they have the same trends, indicating that the redox peak area of catalyst is a very important parameter in deciding the activity of CO oxidation.

Mechanism of CO oxidation over perovskite catalyst, according to the results of Tilset et al, [67] must involve reduction and re-oxidation of the catalyst. That is, the catalyst is first

oxidized by oxygen and then reduced by CO. At this time the oxygen must be in adsorbed state while the CO could be in gas (i.e. Eley-Rideal mechanism) or adsorbed state (i.e. Langmuir-Hinshelwood mechanism), as below: [68]

$$CO_{(g)} + O_{(s)} \rightarrow CO_{2\,(g)} \quad (1)$$

$$CO_{(g)} \rightarrow CO_{(s)} \quad (2)$$

$$CO_{(s)} + O_{(s)} \rightarrow CO_{2\,(s)} \rightarrow CO_{2\,(g)} \quad (3)$$

However, because carbonate is usually observed in the experiment, which suggests that the reaction process is not as simple as mentioned above, a new mechanism containing carbonate formation and decomposition steps were thus proposed, denoted as reactions (4) and (5): [68]

$$CO_{(s)} + 2O_{(s)} \rightarrow COOO_{(s)} \quad (4)$$

$$COOO_{(s)} \rightarrow COO_{(s)} + O_{(s)} \rightarrow COO_{(g)} + O_{(s))} \quad (5)$$

C2.2. NO Removal

Although the reaction of nitrogen oxide to nitrogen and oxygen ($NO = 1/2N_2 + 1/2O_2$) is thermodynamically favored it is kinetically hindered.[69] For NO decomposition it involves the dissociation of NO to N_2 and O_2 on a catalytic surface and that nitrogen readily desorbs as N_2 while oxygen is strongly retained on the surface. Therefore, the catalyst used for NO decomposition should possess the ability not only for NO dissociation, but also for oxygen desorption. This thus requires the presence of oxygen vacancy that are using for oxygen migrating and colliding to form oxygen molecule (i.e. $O + O \rightarrow O_2$).

Presence of oxygen vacancy in the catalyst is very important for oxidation reaction includes NO removal reaction. Besides the above-mentioned function for oxygen formation and desorption, oxygen vacancy also is the site for NO adsorption and activation. Therefore, a competitive adsorption between O_2 and NO usually is unavoidable for most of catalysts, in particular when NO decomposition reaction is carried out in the presence of oxygen. Thus, the preparation of perovskite catalyst, which possesses oxygen vacancy and with highly regeneration frequency is of great importance for NO decomposition. Zhao et al [70] reported that in NO decomposition La_2NiO_4 without oxygen vacancy showed less than 20% NO conversion even at 900 ˚C, while a ~95% NO conversion was observed over $LaSrNiO_{4+\lambda}$ that possesses large amount of oxygen vacancy ($\lambda = -0.16$). However, it should be pointed out that for $Ca_2Fe_2O_{5+\lambda}$ that have lots of oxygen vacancies, it also can not show activity for NO decomposition, but high activity could be shown when Ca was replaced by Sr, i.e. $Sr_2Fe_2O_{5+\lambda}$. The reason is that the oxygen vacancy in the former is in ordered structure, while that in the latter is disordered one.[71] That is, only for oxygen vacancy with disordered structure, can it work for NO decomposition.

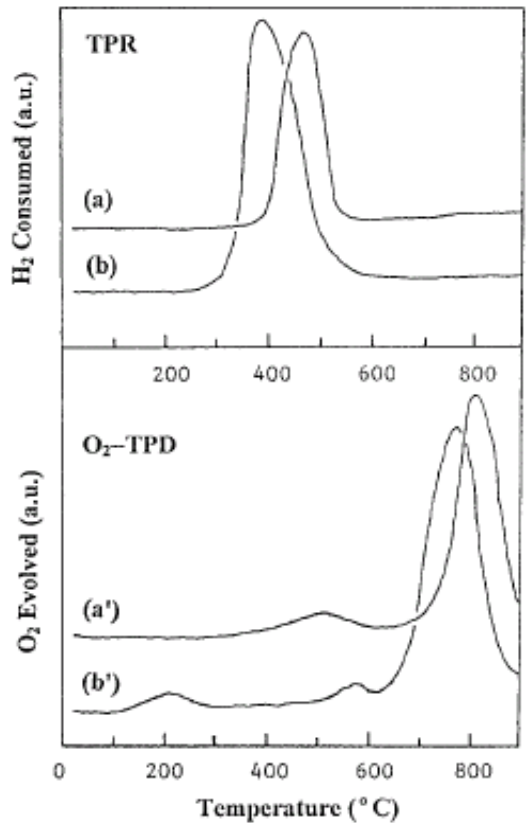

Figure 7. TPR and O_2-TPD profiles of $La_{0.8}Ba_{0.2}CoO_{2.94}$ (a, a') and $ACo_{0.8}Bi_{0.2}O_{2.87}$ (b, b'). Reprinted from ref. 64, copyright 2001, with permission from Springer

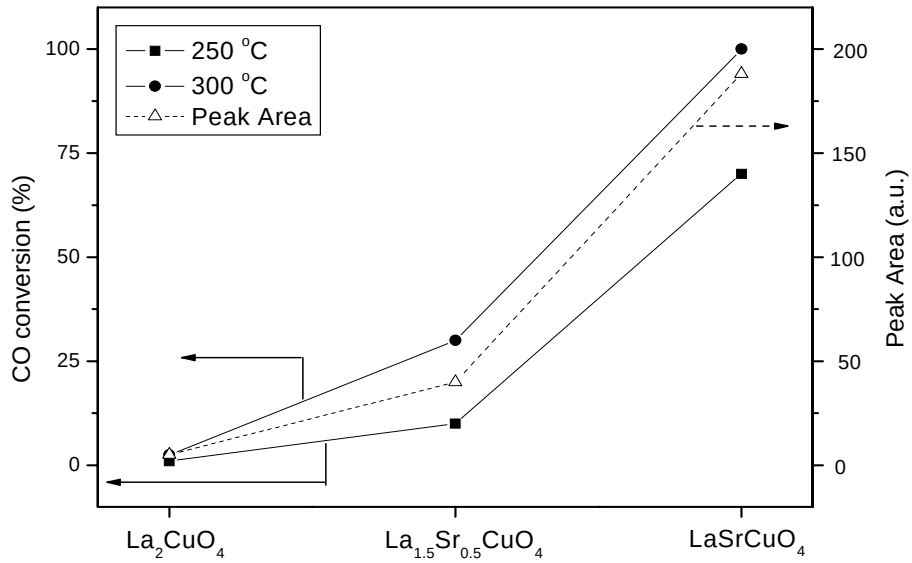

Figure 8. Relationship between CO conversion and redox peak area over $La_{2-x}Sr_xCuO_4$ (x = 0.0, 0.5, 1.0). Reprinted from ref. 66, copyright 2006, with permission from Springer

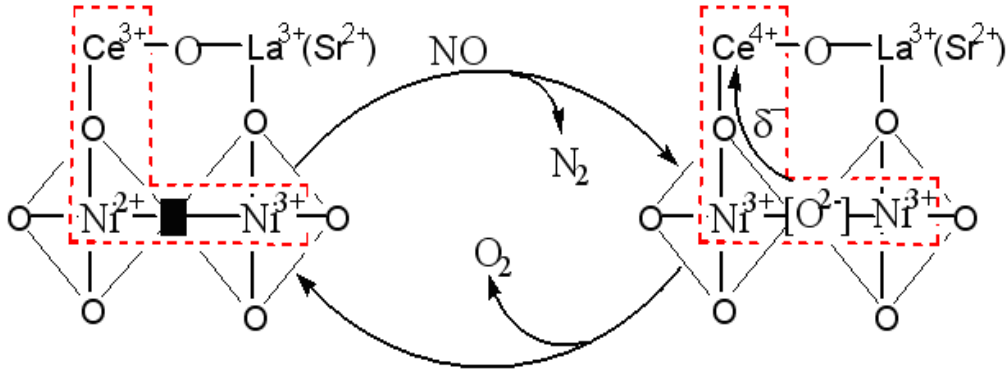

Figure 9. Active site structure of $La_{1-x}Ce_xSrNiO_4$ for NO decomposition ('■': oxygen vacancy). Reprinted from ref. 77, copyright 2005, with permission from Elsevier

Substitution of both A- and B-site cation was largely investigated [72-76] in order to correlate the relationships of physiochemical properties and NO decomposition behaviors. Usually the substitution of A-site cation is to change the physical properties of catalyst, such as the ability to adsorb NO, the amount of oxygen vacancy and/or the oxidation state of B-site cation; while the substitution of B-site cation is to change the chemical properties of catalyst, i.e. the redox behavior of catalyst. That is, the A-site cation of perovskite oxides is catalytically inactive. However, this conclusion is obtained only when the A-site cation has a permanent oxidation state (e.g. La^{3+}, Sr^{2+}) and things maybe different if the A-site cation has changeable oxidation state. Actually, it was reported [77] that the substitution of Ce for La in $La_{1-x}Ce_xSrNiO_4$ leads to a new active site for NO decomposition, as shown in Figure 9, which indicates that the A-site cation is not inactive and it can be one component of the active site for NO decomposition if it has changeable oxidation state.

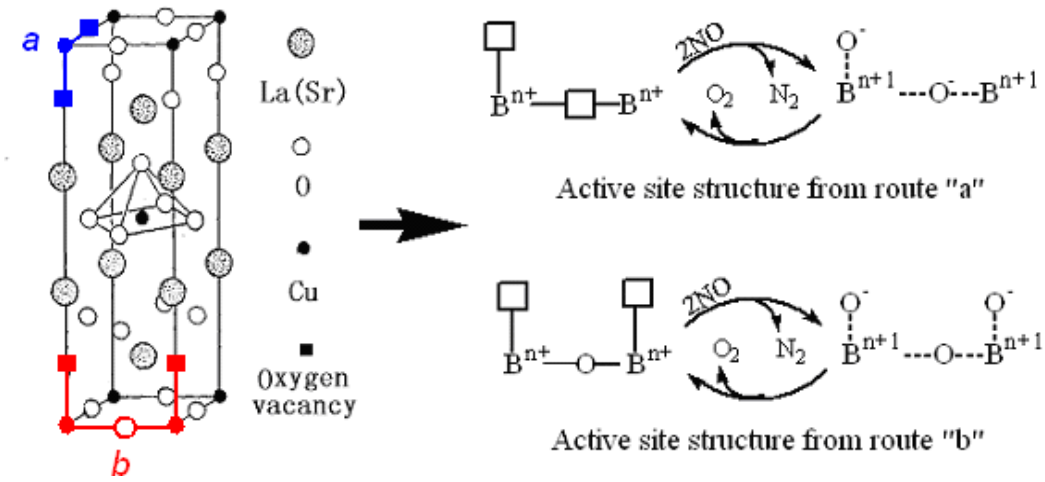

Figure 10. Two proposed active site structures for NO decomposition reaction carried out on perovskite-type catalyst. Model *a* was proposed by Shin et al [78]; model *b* was by Zhu et al. [79]. Reprinted from ref. 78 and 79, copyright 1979 and 2007, with permission from Elsevier and American Chemical Society.

The above discussion indicates that both oxygen vacancy and metal ions are component of active site, but the exact form of active site is till in controversial at present. Shin et al [78] based on IR results proposed that the active site contains two adjacent oxygen vacancies and one transitional metal, while recently Zhu et al [79] based on a theoretical calculation and the catalytic activity of $LaSrCuO_4$ with T and T* phases suggested that the active site should contain two oxygen vacancies, two transitional metals and one lattice oxygen. A comparison of the two active site structure was shown in Figure 10. In route (*b*) there involves a lattice oxygen between the two transition metals, which suggests that the properties (e.g. mobility) of lattice oxygen would have great effect on the reaction. Actually, there have lots of work suggest that the NO decomposition activity has close relation to the properties of lattice oxygen based on the measurements such as O_2-TPD and H_2-TPR.

Anyway, it means that the active site has several components and hence how to characterize it suitably becomes difficult, as the traditional method was used only for oxygen vacancy or for transitional metal. In order to solve this problem and to check the overall redox properties of catalyst, cyclic voltammetry (CV) measurement were introduced.[80-82] The use of CV has the advantage of measuring the catalytic behavior of the whole catalyst, irrespective of the influence of each component. Table 1 listed some parameters calculated from the CV curves of several perovskite catalysts, together with their activity for NO decomposition and for NO+CO reduction. Results indicate that the NO decomposition activity depends mainly on the symmetry of redox potentials, while the NO+CO activity depends on the redox peak area. Concerning the major difference in these two reactions is the presence of CO in NO+CO reaction, the change of activity in Table 1 could be explained by the following reasons: 1) for NO decomposition, in which no reducing agent (i.e. CO) was present, the closing cycle (steps of reduction and re-oxidation) depends fully on the redox ability of catalyst. The smaller the difference in the redox potentials, the faster the reaction proceeds. As a result, $LaSrNiO_4$ with the smallest ΔE shows the best activity for NO decomposition. 2) While for NO+CO reaction, the apparent redox potentials of catalyst, according to Nernst Equation, could be reduced due to the presence of CO reducing agent, that is, the reducibility of catalyst could be compensated at this time. Therefore, the role of ΔE becomes weak and that of redox peak area (which represents the amount of active sites) turns to be the major factor in deciding the activity. As a result, $LaSrCuO_4$ with the largest redox peak area shows the best activity for NO+CO reduction.

Table 1. Electrochemical properties and catalytic performance of various catalysts for NO decomposition. Reprinted from ref. 80, copyright 2005, with permission from Elsevier

Catalysts	NO conv. (%)[a]	NO conv. (%)[b]	Redox peak area (a.u.)	Red. Pot. (V)[c]	Ox. Pot. (V)[d]	ΔE (V)[e]
La_2CuO_4	1.0	1.9	5	2.49	3.35	0.86
$La_{1.5}Sr_{0.5}CuO_4$	60.0	9.8	40	2.0	2.9	0.9
$LaSrCuO_4$	*96.8*	34.3	*188*	1.30	3.13	1.77
$LaSrCoO_4$	39.9	20.3	—	—	2.15	—
$LaSrNiO_4$	80.1	*94.7*	22	2.75	3.25	*0.5*

[a] NO+CO reduction at 400˚C; [b] NO decomposition at 850˚C; [c] Red. Pot. = Reductive Potential;
[d] Ox. Pot = Oxidative Potential; ΔE: Difference between oxidative and reductive potential.

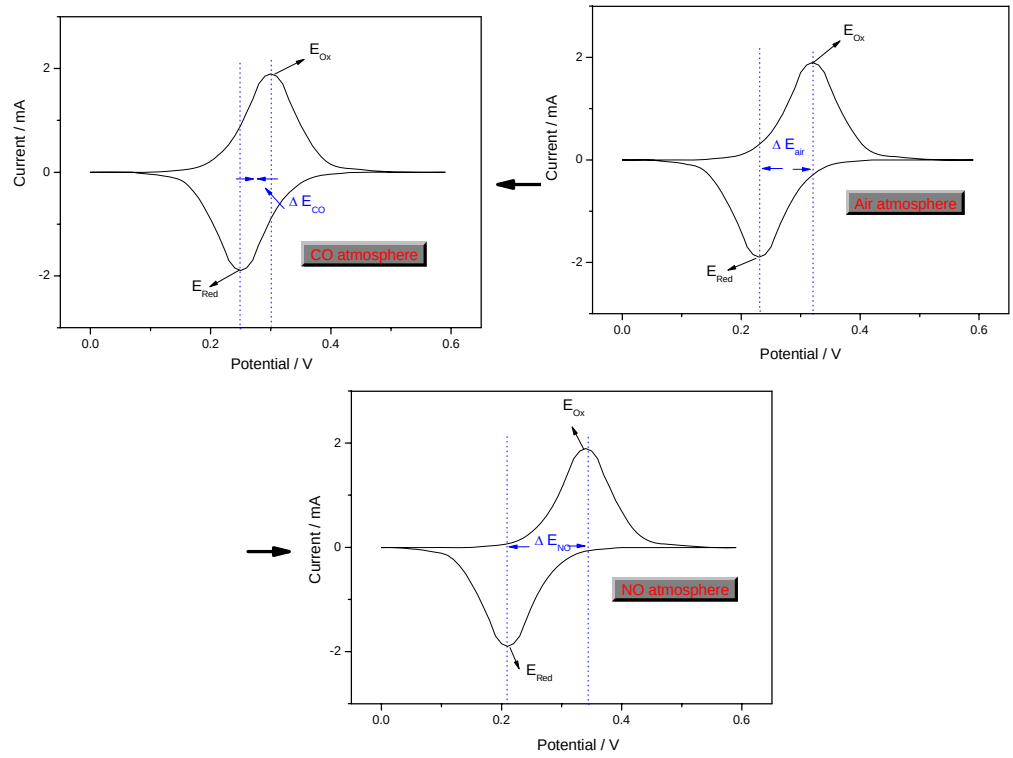

Figure 11. An imaged profile for the change of redox potentials in oxidative (e.g. NO) and reductive (e.g. CO) atmosphere. Here the change of the profiles in different atmospheres were speculated based on the Nernst Equation. Reprinted from ref. 73, copyright 2009, with permission from Elsevier

The essence of CV measurements indicates that the crucial pre-requisite for catalytic reaction to occur is that the full redox cycle can proceed easily, that is, the electrons transferring between reactant and catalyst is not a problem. Only when this requirement is fulfilled, other parameters, such as the amount of active sites, could come into the focus of the catalyst design. The apparent redox ability of catalyst would be changed depends on the reaction environment, e.g. CO or NO atmosphere, as shown in Figure 11. This explains why in NO+CO reaction the redox peak area plays the major role in the reaction, since the difference in redox potentials (i.e. the difficulty in electron transfer) could be compensated due to the presence of CO.

It was recently proposed that the redox ability of perovskite catalyst could also be evaluated from the reduction peak area measured from H_2-TPR experiments, represented as: $\Delta E = (RT/nF)\ \ln(A_F/A_S)$.[83] At this time, the ratio of the two reduction peak areas could be taken as a criterion of the difficulty of electrons transferring in $M^{(n+1)+} \leftrightarrow M^{n+}$. Results in Figure 12 indicate that the ΔE calculated by this way indeed has a close relation to the NO decomposition activity, suggesting that this new method could be an indication in predicting the catalytic performance of catalyst for NO decomposition.

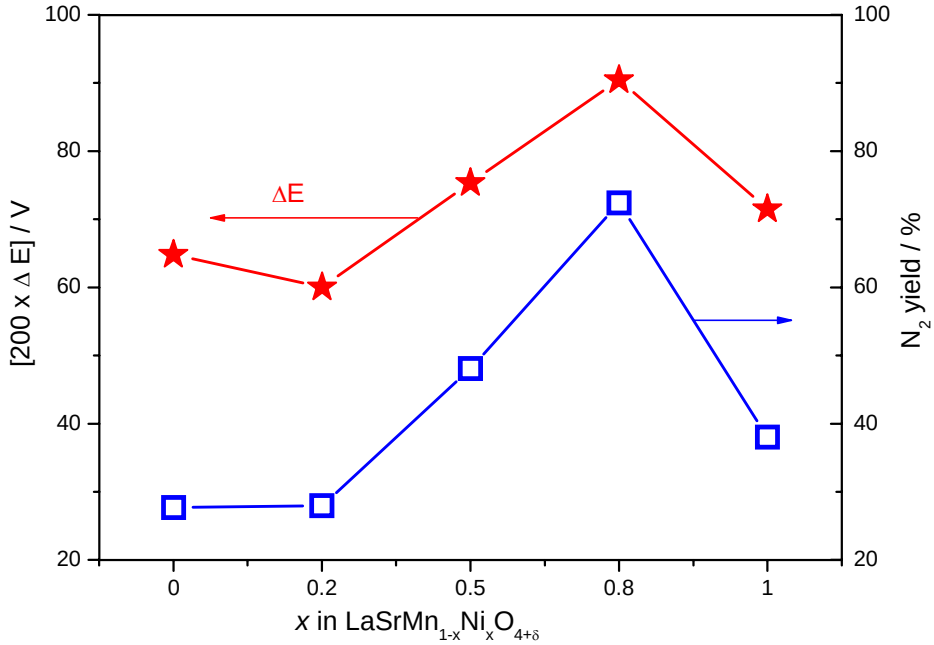

Figure 12. Relationships between the difference in redox potentials (ΔE) and NO decomposition activity (in 2.5v/v% O_2, at 850 °C) of $LaSrMn_{1-x}Ni_xO_{4+\delta}$. Reprinted from ref. 83, copyright 2009, with permission from Springer

4. Conclusion and Perspectives

Perovskite-type oxides are one kind of promising materials in practical application not only because of its low cost, but also due to its controllable properties. Synthesis of perovskite-type oxides with desired properties is still an ongoing topic in materials science and select a proper method is certainly of importance. More and more methods were explored to synthesize perovskite with desired properties to satisfy the diverse applications. One potential application of perovskite-type oxides is as catalyst for catalytic reaction, which has been broadly investigated. Although at present there have not yet found application as commercial catalysts, theses oxides offer the possibility of correlating solid-state properties with catalytic performances, and hence getting insight into the nature of catalytic reaction. By correlating the electrochemical properties with the catalytic performances, it could be concluded that the difficulty of electron transferring between catalyst and reactant (i.e. the difference in redox potentials) is the crucial pre-requisite for a catalytic reaction to occur. Thus further studies are proposed to be concentrated on searching new method for synthesizing perovskite oxides with suitable ability for electron denotation and reception, especially when used as catalyst for catalytic reactions.

REFERENCES

[1] Pena MA, Fierro JLG. (2001). Chemical structures and performance of perovskite oxides. *Chem Rev*. *101,* 1981-2017.

[2] *Catalytic Chemistry of Solid state Inorganics*. New York: New York Academy of Sciences 1976.

[3] *Properties and Applications of Perovskite-type Oxides*. New York: CRC Press 1993.

[4] Smyth DM. (1985). DEFECTS AND ORDER IN PEROVSKITE-RELATED OXIDES. *Annu Rev Mater Sci*. *15,* 329-57.

[5] Goldschmidt VM. *Skr. Nor. Viedenk.* -Akad., K1. I: Mater. Naturvidensk. K1. 1926.

[6] Kim JH, Kim Y, Connor PA, Irvine JTS, Bae J, Zhou WZ. (2009). Structural, thermal and electrochemical properties of layered perovskite SmBaCo2O5+d, a potential cathode material for intermediate-temperature solid oxide fuel cells. *J Power Sources*. *194,* 704-11.

[7] Wang HC, Wang CL, Zhang JL, Zhao ML, Liu J, Su WB, et al. (2009). Cu Doping Effect on Electrical Resistivity and Seebeck Coefficient of Perovskite-Type LaFeO3 Ceramics. *Chinese Phys Lett*. *26*.

[8] Takashima H, Shimada K, Miura N, Katsumata T, Inaguma Y, Ueda K, et al. (2009). Low-Driving-Voltage Electroluminescence in Perovskite Films. *Adv Mater*. *21,* 3699-+.

[9] Wang H, Zhao Z, Liang P, Xu CM, Duan AJ, Jiang GY, et al. (2008). Highly active La1-xKxCoO3 perovskite-type complex oxide catalysts for the simultaneous removal of diesel soot and nitrogen oxides under loose contact conditions. *Catal Lett*. *124,* 91-9.

[10] Liu J, Zhao Z, Xu CM, Duan AJ, Jiang GY. (2008). The structures, adsorption characteristics of La-Rb-Cu-O perovskite-like complex oxides, and their catalytic performances for the simultaneous removal of nitrogen oxides and diesel soot. *J Phys Chem C*. *112,* 5930-41.

[11] He H, Dai HX, Au CT. (2001). An investigation on the utilization of perovskite-type oxides La1-xSrxMO3 (M = Co0.77Bi0.20Pd0.03) as three-way catalysts. *Appl Catal B-environ*. *33,* 65-80.

[12] Zhu JJ, Mao DH, Li J, Xie XF, Yang XG, Wu Y. (2005). Recycle - new possible mechanism of NO decomposition over perovskite(-like) oxides. *J Mol Catal A-chem*. *233,* 29-34.

[13] Zhu JJ, Zhao Z, Xiao DH, Li J, Yang XG, Wu Y. (2005). CO oxidation, NO decomposition, and NO plus CO reduction over perovskite-like oxides La2CuO4 and La2-xSrxCuO4: An MS-TPD study. *Ind Eng Chem Res*. *44,* 4227-33.

[14] Tejuca LG, Fierro JLG. Properties and Applications of Perovskite-type Oxides. New York: CRC Press 1993.

[15] Szabo V, Bassir M, Gallot JE, Van Neste A, Kaliaguine S. (2003). Perovskite-type oxides synthesised by reactive grinding - Part III. Kinetics of n-hexane oxidation over LaCo(1-x)FexO3. *Appl Catal B-environ*. *42,* 265-77.

[16] Tien-Thao N, Zahedi-Niaki MH, Alamdari H, Kaliaguine S. (2007). Effect of alkali additives over nanocrystalline Co-Cu-based perovskites as catalysts for higher-alcohol synthesis. *J Catal*. *245,* 348-57.

[17] Tien-Thao N, Zahedi-Niaki MH, Alamdari H, Kaliaguine S. (2007). Conversion of syngas to higher alcohols over nanosized LaCo0.7Cu0.3O3 perovskite precursors. *Appl Catal A-gen*. *326,* 152-63.

[18] Chiodelli G, Malavasi L, Tealdi C, Barison S, Battagliarin M, Doubova LM, et al. (2009). Role of synthetic route on the transport properties of BaCe1-xYxO3 proton conductor. *J Alloy Compd*. *470,* 477-85.

[19] Pecchi G, Reyes P, Zamora R, Campos C, Caduus LE, Barbero BP. (2008). Effect of the preparation method on the catalytic activity of La1-xCaxFeO3 perovskite-type oxides. *Catal Today*. *133,* 420-7.

[20] Delmon B. (2007). Preparation of heterogeneous catalysts. *J Therm Anal Calorim*. *90,* 49-65.

[21] Teraoka Y, Kakebayashi H, Moriguchi I, Kagawa S. (1993). Hydroxy Acid-Aided Synthesis of Perovskite-Type Oxides with Large Surface-Areas. *J Alloy Compd*. *193,* 70-2.

[22] McCarty JG, Wise H. (1990). Perovskite catalysts for methane combustion. *Catal Today*. *8,* 231-48.

[23] Moulik SP, Paul BK. (1998). Structure, dynamics and transport properties of microemulsions. *Adv Colloid Interfac*. *78,* 99-195.

[24] Wallin M, Cruise N, Klement U, Palmqvist A, Skoglundh B. (2004). Preparation of Mn, Fe and Co based perovskite catalysts using microemulsions. *Colloid Surface A*. *238,* 27-35.

[25] Fletcher PDI, Howe AM, Robinson BH. (1987). The Kinetics of Solubilisate Exchange between Water Droplets of a Water-in-Oil Microemulsion. *J Chem Soc Farad T 1*. *83,* 985-1006.

[26] Campagnoli E, Tavares A, Fabbrini L, Rossetti I, Dubitsky YA, Zaopo A, et al. (2005). Effect of preparation method on activity and stability of LaMnO3 and LaCoO3 catalysts for the flameless combustion of methane. *Appl Catal B-environ*. *55,* 133-9.

[27] Specchia S, Civera A, Saracco G. (2004). In situ combustion synthesis of perovskite catalysts for efficient and clean methane premixed metal burners. *Chem Eng Sci*. *59,* 5091-8.

[28] Wang KJ, Zhong P, Zhu JJ. (2009). Preparation of Highly Active and Stable Perovskite-like Catalyst by Combustion Method: Effect of Complex. *Catal Lett*. *131,* 672-5.

[29] Civera A, Pavese M, Saracco G, Specchia V. (2003). Combustion synthesis of perovskite-type catalysts for natural gas combustion. *Catal Today*. *83,* 199-211.

[30] Gonzalez A, Tamayo EM, Porter AB, Corberan VC. (1997). Synthesis of high surface area perovskite catalysts by non-conventional routes. *Catal Today*. *33,* 361-9.

[31] Tian BZ, Liu XY, Yang HF, Xie SH, Yu CZ, Tu B, et al. (2003). General synthesis of ordered crystallized metal oxide nanoarrays replicated by microwave-digested mesoporous silica. *Adv Mater*. *15,* 1370-+.

[32] Jiao F, Bruce PG. (2007). Mesoporous crystalline beta-MnO2- a reversible positive electrode for rechargeable lithium batteries. *Adv Mater*. *19,* 657-+.

[33] Wang YG, Ren JW, Wang YQ, Zhang FY, Liu XH, Guo Y, et al. (2008). Nanocasted synthesis of mesoporous LaCoO3 perovskite with extremely high surface area and excellent activity in methane combustion. *J Phys Chem C*. *112,* 15293-8.

[34] Cao GZ, Liu DW. (2008). Template-based synthesis of nanorod, nanowire, and nanotube arrays. *Adv Colloid Interfac*. *136,* 45-64.

[35] Gao F, Hong RZ, Liu JJ, Yao YH, Tian CS. (2008). Effect of different templates on microstructure of textured Na0.5Bi0.5TiO3-BaTiO3 ceramics with RTGG method. *J Eur Ceram Soc*. *28,* 2063-70.

[36] Wrighton MS, Ellis AB, Wolczanski PT, Morse DL, Abrahamson HB, Ginley DS. (1976). Strontium-Titanate Photoelectrodes - Efficient Photoassisted Electrolysis of Water at Zero Applied Potential. *J Am Chem Soc*. *98,* 2774-9.

[37] Domen K, Naito S, Onishi T, Tamaru K. (1982). Study of the Photocatalytic Decomposition of Water-Vapor over a Nio-Srtio3 Catalyst. *J Phys Chem-Us*. *86,* 3657-61.

[38] Mitsui C, Nishiguchi H, Fukamachi K, Ishihara T, Takita Y. (1999). Photocatalytic decomposition of pure water over NiO supported on KTa(M)O-3 (M=Ti4+,Hf4+,Zr4+) perovskite oxide. *Chem Lett*. 1327-8.

[39] Hu CC, Tsai CC, Teng H. (2009). Structure Characterization and Tuning of Perovskite-Like NaTaO3 for Applications in Photoluminescence and Photocatalysis. *J Am Ceram Soc*. *92,* 460-6.

[40] Vijayakumar KM, Lichtin NN. (1984). Reduction of Co2 by H2 and Water-Vapor over Metal-Oxides Assisted by Visible-Light. *J Catal*. *90,* 173-7.

[41] Lichtin NN, Vijayakumar KM, Rubio BI. (1987). Photoassisted Reduction of Co2 by H-2 over Metal-Oxides in the Absence and Presence of Water-Vapor. *J Catal*. *104,* 246-51.

[42] Lichtin NN, Vijayakumar KM. (1983). Photocatalyzed Light-Driven Reduction of Co2 and N2 on Semiconductor Surfaces. *J Electrochem Soc*. *130,* C108-C.

[43] Miyama H, Fujii N, Nagae Y. (1980). Heterogeneous Photocatalytic Synthesis of Ammonia from Water and Nitrogen. *Chem Phys Lett*. *74,* 523-4.

[44] Li Q, Domen K, Naito S, Onishi T, Tamaru K. (1983). Photocatalytic Synthesis and Photo-Decomposition of Ammonia over Srtio3 and Batio3 Based Catalysts. *Chem Lett*. 321-4.

[45] Huang YH, Liang G, Croft M, Lehtimaki M, Karppinen M, Goodenought JB. (2009). Double-Perovskite Anode Materials Sr2MMoO6 (M = Co, Ni) for Solid Oxide Fuel Cells. *Chem Mater*. *21,* 2319-26.

[46] Huang K, Lee HY, Goodenough JB. (1998). Sr- and Ni-doped LaCaO3 and LaFeO3 perovskites - New cathode materials for solid-oxide fuel cells. *J Electrochem Soc*. *145,* 3220-7.

[47] Weston M, Metcalfe IS. (1998). La0.6Sr0.4Co0.2Fe0.8O3 as an anode for direct methane activation in SOFCS. *Solid State Ionics*. *115,* 247-51.

[48] Sfeir J, van Herle J, McEvoy AJ. (1999). Stability of calcium substituted lanthanum chromites used as SOFC anodes for methane oxidation. *J Eur Ceram Soc*. *19,* 897-902.

[49] Kuo JH, Anderson HU, Sparlin DM. (1990). Oxidation Reduction Behavior of Undoped and Sr-Doped Lamno3 - Defect Structure, Electrical-Conductivity, and Thermoelectric-Power. *J Solid State Chem*. *87,* 55-63.

[50] Zhou W, Ran R, Shao ZP. (2009). Progress in understanding and development of Ba0.5Sr0.5Co0.8Fe0.2O3-delta-based cathodes for intermediate-temperature solid-oxide fuel cells: A review. *J Power Sources*. *192,* 231-46.

[51] Shao ZP, Haile SM. (2004). A high-performance cathode for the next generation of solid-oxide fuel cells. *Nature*. *431,* 170-3.

[52] Shao ZP, Haile SM, Ahn J, Ronney PD, Zhan ZL, Barnett SA. (2005). A thermally self-sustained micro solid-oxide fuel-cell stack with high power density. *Nature*. *435,* 795-8.

[53] Simonsen VLE, Norskov L, Hagen A, Hansen KK. (2009). Electrochemical reduction of NO on La2-xSrxNiO4 based electrodes. *J Solid State Electr*. *13,* 1529-34.

[54] Liu CB, Zhao Z, Yang XG, Ye XK, Wu Y. (1996). Superconductor mixed oxides La2-xSrxCuO4+/-lambda for catalytic hydroxylation of phenol in the liquid-solid phase. *Chem Commun*. 1019-20.

[55] Resini C, Catania F, Berardinelli S, Paladino O, Busca G. (2008). Catalytic wet oxidation of phenol over lanthanum strontium manganite. *Appl Catal B-environ*. *84,* 678-83.

[56] Kulkarni AS, Jayaram RV. (2003). Liquid phase catalytic transfer hydrogenation of aromatic nitro compounds on perovskites prepared by microwave irradiation. *Appl Catal A-gen*. *252,* 225-30.

[57] Kulkarni AS, Jayaram RV. (2004). Liquid phase catalytic transfer hydrogenation of aromatic nitro compounds on La1-xSrxFeO3 perovskites prepared by microwave irradiation. *J Mol Catal A-chem*. *223,* 107-10.

[58] Parravano G. (1953). Catalytic Activity of Lanthanum and Strontium Manganite. *J Am Chem Soc*. *75,* 1497-8.

[59] Tejuca LG, Fierro JLG, Tascon JMD. (1989). Structure and Reactivity of Perovskite-Type Oxides. *Adv Catal*. *36,* 237-328.

[60] Voorhoeve RJH, Remeika JP, Trimble LE. (1976). Defect Chemistry and Catalysis in Oxidation and Reduction over Perovskite-Type Oxides. *Ann Ny Acad Sci*. *272,* 3-21.

[61] Sokolovskii VD. (1990). Principles of Oxidative Catalysis on Solid Oxides. *Catal Rev*. *32,* 1-49.

[62] Anshiz AG, Sokolovskii VD, Boreskov GK, Boronin AI. (1977). Participation of Molecular-Oxygen in Formation of Complete Oxidation-Products Via a Concerted Mechanism. *React Kinet Catal L*. *7,* 87-92.

[63] Falcon H, Martinez-Lope MJ, Alonso JA, Fierro JLG. (2000). Defect LaCuO3-delta (delta=0.05-0.45) perovskites - Bulk and surface structures and their relevance in CO oxidation. *Appl Catal B-environ*. *26,* 131-42.

[64] Dai HX, He H, Li W, Gao ZZ, Au CT. (2001). Perovskite-type oxide ACo(0.8)Bi(0.2)O(2.87) (A = La0.8Ba0.2): a catalyst for low-temperature CO oxidation. *Catal Lett*. *73,* 149-56.

[65] Zhu JJ, Yang XG, Xu XL, Wei KM. (2006). Cyclic voltammetry for predicting oxidation process in heterogeneous catalysis. *Z Phys Chem*. *220,* 1589-94.

[66] Zhu JJ, Yang XG, Xu XL, Wei KM. (2006). Study of CH4 and CO oxidation from electrochemical method. *Chinese Sci Bull*. *51,* 374-6.

[67] Tilset BG, Fjellvag H, Kjekshus A, Slagtern A, Dhal I. (1996). Properties of LaCo1-tCrtO3 .3. Catalytic activity for CO oxidation. *Appl Catal A-gen*. *147,* 189-205.

[68] Zhang-Steenwinkel Y, van der Zande LM, Castricum HL, Bliek A. (2004). Step response and transient isotopic labelling studies into the mechanism of CO oxidation over La0.8Ce0.2MnO3 perovskite. *Appl Catal B-environ*. *54,* 93-103.

[69] Kubaschewski O, Alcock CB, Spencer PJ. *Materials Thermochemistry*. 6th Edition ed. Oxford: Pergamon Press 1993.

[70] Zhao Z, Yang XG, Wu Y. (1996). Comparative study of Nickel-based perovskite-like mixed oxide catalysts for direct decomposition of NO. *Appl Catal B-environ*. *8,* 281-97.

[71] Shin S, Hatakeyama Y, Ogawa K, Shimomura KY. (1979). Catalytic Decomposition of No over Brownmillerite-Like Compounds, Ca2fe2o5 and Sr2fe2o5. *Mater Res Bull*. *14,* 133-6.

[72] Zhu YJ, Wang D, Yuan FL, Zhang G, Fu HG. (2008). Direct NO decomposition over La2-xBaxNiO4 catalysts containing BaCO3 phase. *Appl Catal B-environ*. *82,* 255-63.

[73] Zhu J, Thomas A. (2009). Perovskite-type mixed oxides as catalytic material for NO removal. *Appl Catal B-environ*. *92,* 225-33.

[74] Ishihara T, Shinmyo Y, Goto K, Nishiyama N, Iwakuni H, Matsumoto H. (2008). NO decomposition on Ruddlesden-Popper-type oxide, Sr3Fe2O7, doped with Ba and Zr. *Chem Lett*. *37,* 318-9.

[75] Iwakuni H, Shinmyou Y, Yano H, Matsumoto H, Ishihara T. (2007). Direct decomposition of NO into N-2 and O-2 on BaMnO3-based perovskite oxides. *Appl Catal B-environ*. *74,* 299-306.

[76] Ishihara T, Ando M, Sada K, Takiishi K, Yamada K, Nishiguchi H, et al. (2003). Direct decomposition of NO into N-2 and N-2 over La(Ba)Mn(In)O-3 perovskite oxide. *J Catal*. *220,* 104-14.

[77] Zhu JJ, Xiao DH, Li J, Yang XG, Wu Y. (2005). Effect of Ce on NO direct decomposition in the absence/presence of O-2 over La1-xCexSrNiO4 (0 <= x <= 0.3). *J Mol Catal A-chem*. *234,* 99-105.

[78] Shin S, Arakawa H, Hatakeyama Y, Ogawa K, Shimomura K. (1979). Absorption of No in the Lattice of an Oxygen-Deficient Perovskite Srfeo3-X and the Infrared Spectroscopic Study of the System No - Srfeo3-X. *Mater Res Bull*. *14,* 633-9.

[79] Zhu JJ, Yang XG, Xu XL, Wei KM. (2007). Active site structure of NO decomposition on perovskite(-like) oxides: An investigation from experiment and density functional theory. *J Phys Chem C*. *111,* 1487-90.

[80] Zhu JJ, Zhao Z, Xiao D, Li J, Yang XG, Wu Y. (2005). Application of cyclic voltammetry in heterogeneous catalysis: NO decomposition and reduction. *Electrochem Commun*. *7,* 58-61.

[81] Zhu JJ, Zhao Z, Xiao DH, Li J, Yang XG, Wu Y. (2005). Study of La2-xSrxCuO4 (x=0.0, 0.5, 1.0) catalysts for NO plus CO reaction from the measurements of O-2-TPD, H-2-TPR and cyclic voltammetry. *J Mol Catal A-chem*. *238,* 35-40.

[82] Zhu JJ, Zhao Z, Xiao DH, Li J, Yang XG, Wu Y. (2005). CO oxidation over the perovskite-like oxides La2-xSrxMO4 (x=0.0, 0.5, 1.0; M = Cu, Ni): A study from cyclic voltammetry. *Z Phys Chem*. *219,* 807-15.

[83] Zhu JJ, Xiao DH, Li J, Yang XG. (2009). Perovskite-Like Mixed Oxides (LaSrMn1-x Ni (x) O4+delta, 0 a parts per thousand currency sign x a parts per thousand currency sign 1) as Catalyst for Catalytic NO Decomposition: TPD and TPR Studies. *Catal Lett*. *129,* 240-6.

In: Perovskites: Structure, Properties and Uses
Editor: Maxim Borowski, pp. 345-376
ISBN 978-1-61668-525-6

Chapter 8

MECHANISM OF FORMATION OF PEROVSKITE-TYPE LAYERED OXIDES

Irina A. Zvereva [*] ***and Alexander B. Missyul***
Saint-Petersburg State University, Department of Chemistry,
Universitetsky pr., 26, Petrodvoretz, Saint-Petersburg, 198504, Russia

ABSTRACT

The chapter presents general analysis and results of experimental data on the structure-chemical investigation of process of formation of perovskite type structures in different groups of layered oxides, which exhibit a number of practically important properties. In many cases the layered perovskite-like phases are formed in a multistage way. The composition and stability of the intermediates can strongly affect both reaction rate and the structure of the final compound. Examples of such impact for several Ruddlesden-Popper and Aurivillius phases are considered. Formation of the double-perovskite layered phases for the series of high temperature aluminates $Ln_2SrAl_2O_7$ (Ln=La, Nd, Sm, Eu, Gd, Ho) is discussed in terms of the dependence of mechanism of reaction on the nature of rare earth elements. For the double-layered manganites $LnSr_2Mn_2O_7$ (Ln=La, Nd, Gd) the structure and stability of the intermediate perovskite phase affects both the reaction speed and the microstructure of the resulting Ruddlesden-Popper phase, including phase separation in the CMR manganites. The double-layered ferrites $Ln_2SrFe_2O_7$ (Ln=La, Nd, Gd) exhibit the evolution of oxidation state of iron along the process of synthesis. Mechanism of formation of the ferroelectric Aurivillius phase Bi_3TiNbO_9 demonstrates the limitations on the Bi→Ln and Ti→Mn substitution in this structure. The stability of the intermediate phase results in the substitution limitations. Investigations of the processes occurring in the reaction mixture during synthesis of the perspective ionic conductors and catalyst $(Na,Nd)_{n+1}Ti_nO_{3n+1}$ allow to explain the necessity of the excess of alkali metal containing starting compound, optimize the conditions of synthesis and significantly decrease the size of particles.

[*] E-mail: irinazvereva@yandex.ru

1. INTRODUCTION

Perovskite type layered structures and especially layered oxides are intensively studied because they exhibit a wealth of "modern" physical phenomena, such as high-T_c superconductivity, colossal magnetoresistance, ferroelectricity and quantum critical behavior. Due to this layered oxides create the basis for many technological applications including information storage and transmission, micro-electronics and micro-manipulation.

And moreover layered structures attract particular interest, not only from the point of view of promising properties but also due to broad fundamental aspects of crystal chemistry and thermodynamics. Layered compounds represent the intergrowth of blocks of different simple structure-types. The phase stability in such systems depends on extent of constrains between different types of structure and determined by equilibrium in multicomponent (different cations) microheterogeneous (different layers) system.

The best examples of layered compounds are the intergrowth of layers of more outstanding and well investigated type of structure – perovskite – and slabs of the different type of structure [1,2]. It could be slabs with rock salt or calcium fluorite type or slabs with cations of metals. Some phenomena play important role in structure of layered compounds. The first one is isomorphism of non-isovalent atoms (usually lanthanide Ln^{3+} and alkali-earth A^{2+} or alkaline A^{1+} atoms) in matrix of layered structure [3,4] resulting in the distribution of cations of different charge over one (two) equivalent sites. The variations of cationic substitution (isovalent and non-isovalent) in this type of compounds ensure such outstanding properties as superconductivity, colossal magnetoresistance and catalytical ability. The second one is the nanoscaled thickness of perovskite layers and consequently specific 2D character of electrical, magnetic and optical properties.

The influence of particularities of structure on physical and chemical properties is considered in many respects, but the mechanism of the process of formation of such compounds was hardly investigated. Moreover the knowledge of formation could be useful for the explanation of the stability of compounds and for the determination the optimal methods of synthesis.

In this chapter we will consider the structure-chemical mechanism of formation of several groups of layered oxides being among most important for applications: aluminates $Ln_2SrAl_2O_7$ (Ln=La – Ho) with high termal stability, CMR manganites $LnSr_2Mn_2O_7$ (Ln=La, Nd, Gd), ferrites $Ln_2SrFe_2O_7$ (Ln=La, Nd, Gd), ferroelectric titanoniobates Bi_3TiNbO_9 and perspective catalysts titanates $NaNdTiO_4$ and $Na_2Nd_2Ti_3O_{10}$.

We investigate in details the most typical way for synthesis of the intergrowth structures (solid state reaction starting from oxides and carbonates) by quenching-cooling method and X-ray phase analysis. The time-temperature dependence of the composition of reaction mixtures was used for interpretation of mechanism and kinetics of reactions.

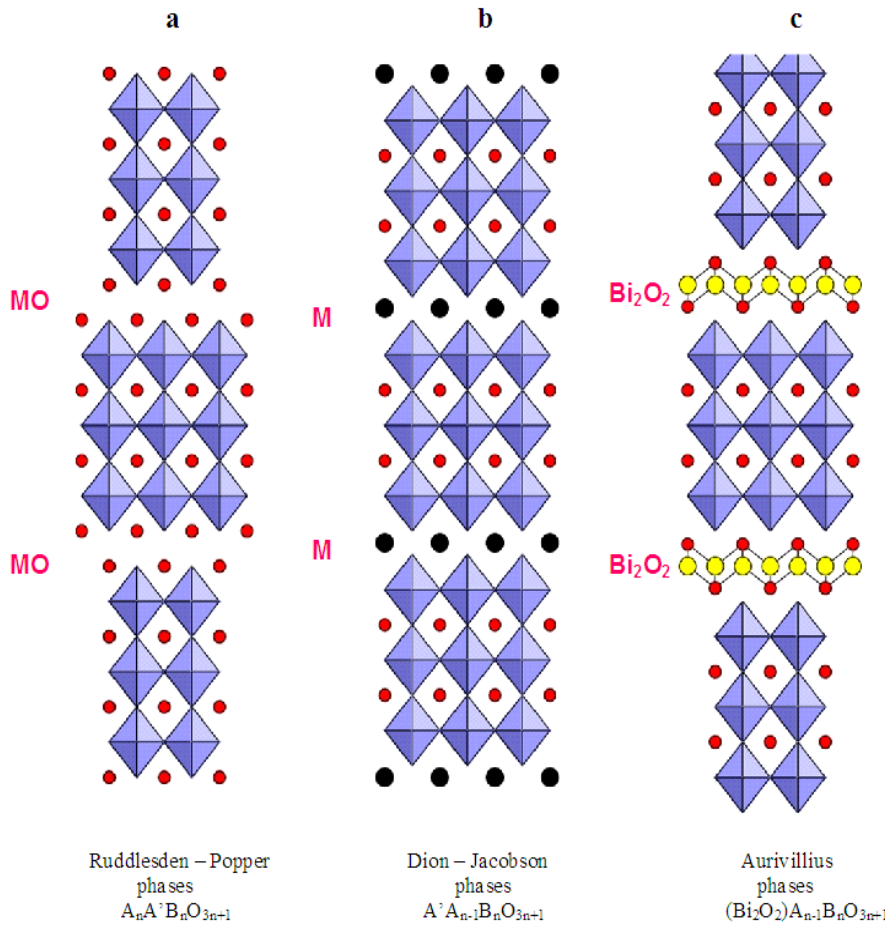

Figure 1. Layered perovskite-like oxides (n = 3).

2. PEROVSKITE-TYPE LAYERED PHASES

Perovskite-type layered compounds are the intergrowth of perovskite layers (P) ABO_3 and slabs of the differ type of structure (rock salt, calcium fluorite type, cations of metals). Depending on the nature of slabs between perovskite blocks, layered compounds belong to three big groups: Ruddlesden-Popper phases, Aurivillius phases, Dion-Jacobson phases.

Ruddlesden-Popper phases are the most well known and intensively investigated perovskite-type layered structures. In 1957 R.S. Ruddlesden and P. Popper synthesized complex oxide Sr_2TiO_4 [5] with K_2NiF_4-type of structure and then $Sr_3Ti_2O_7$ and $Sr_4Ti_3O_{10}$ [6] which gave the name of new structure types. These compounds formed new class of complex oxides $Sr_{n+1}Ti_nO_{3n+1}$ and appearance of the term "Ruddlesden-Popper phases". Particularity of Ruddlesden-Popper phases is the intergrowth of perovskite layers (P) and slabs of rock salt (RS) with consequence of layers – RS – (P-…-P) – RS – (P-…-P) – RS. Schematic representation of these phases is given in Figure 1a.

Great interest to compounds with 2D character of physical properties in 70-th [7-14] and discovering of high temperature superconductivity in 1986 for K_2NiF_4-type oxides [15] gave rise to the strong growth of investigation of perovskite-type layered oxides containing rare-earth elements $LnAMO_4$ (Ln – lanthanoid or Y; A – Sr,Ca; M – Al or 3d-cations) [16-26]. At that time compounds $Ln_2SrAl_2O_7$ (Ln – La, Nd, Gd) with $Sr_3Ti_2O_7$-type of structure [27,28] have been obtained. Later the series was prolongated till $Ho_2SrAl_2O_7$ [3,29]. In the end of 90-th the search for materials with ionic conductivity and ion-exchange properties resulted in synthesis of new titanates $LnATiO_4$ [30-32] and $Ln_2A_2Ti_3O_{10}$ [33-39], $Na_2Ca_2Ta_3O_{10}$ [40], even though $LaNaTiO_4$ have been obtained by G. Blasse as early as in 1965 [41]. Discovering the phenomena of colossal magnetoresistance moved the interest to oxides $Sr_2LnMn_2O_7$ [42] and $Sr_3Fe_2O_7$ [43] and solid solutions with partial cationic substitution [44-48]. Recently the search for new high temperature superconductors among bismuthates and plumbates results in synthesis of $Ba_{n+1}(Pb_{1-x}Bi_x)_nO_{3n+1}$ and $Ba_3Pb_2O_7$, $(Ba, K)_2BiO_4$ and $(Ba, K)_3Bi_2O_7$ [49].

Thus, today Ruddlesden-Popper phases include complex oxides containing metals from groups 1, 2, 13, 14 and 15 as well as transition (d- and 4f-) elements. The general formula of such oxides can be written as $AO(ABO_3)_n$, where A means alkaline, alkali earth or rare earth element, while B is d-element, Al, Ga, In, Pb or Bi. This formula shows the main structural feature of this class of the layered perovskite-like compounds, that is the intergrowth of the perovskite blocks AMO_3 (P) and rock salt blocks AO (RS) in a consequence -P_n-RS-P_n-RS-. In case of $n = \infty$ the perovskite structure itself is obtained. Figure 1 shows schematically the structure of the Ruddlesden-Popper phases (n=3) as compared to the other types of the layered perovskite-like compounds.

In perovskite type layered structure the consequence of perovskite layers and other blocks is not usual geometrical one, it is really the intergrowth of different structures. Stability of intergrowth depends on the extent of geometrical constrains between different types of structure, and thermodynamic equilibrium between different layers.

The Dion-Jacobson phases are chemically close to the Ruddlesden-Popper phases. They have been synthesized for the first time in 1980 by M. Dion [50], but it was not until A. Jacobson's studies [51,52] that they attracted significant attention for high reactivity of these compounds. The general formula of the Dion-Jacobson phases is $A'A_{n-1}B_nO_{3n+1}$, where A' is usually alkaline ion, A is alkali earth or rare earth ion, and B is group 5 ion or group 4 ion, for example $KCa_2Nb_3O_{10}$ or $MLa_2Ti_2TaO_{10}$. In these compounds the perovskite layers are divided by the layers of the alkaline or alkali earth ions (Figure 1b). The Dion-Jacobson phases show high catalytic activity as well as high ionic conductivity [39,53-54], and that is why they are very popular investigation objects in the last years.

The Aurivillius phases $A_{n-1}Bi_2B_nO_{3n+3}$ have been discovered by Aurivillius in 1949 [55]. In 1961 G. A. Smolenski, V. A. Isupov and A. I. Agranovskaya [56] discovered ferroelectricity in this class of oxides. Today the Aurivillius series includes a large number of oxides $A_{n-1}Bi_2B_nO_{3n+3}$, where A = Bi^{3+}, Ba^{2+}, Sr^{2+}, Ca^{2+}, Pb^{2+}, K^+, Na^+, Ln^{3+} etc., B = Ti^{4+}, Fe^{3+}, Nb^{5+}, Ta^{5+}, Mo^{6+}, W^{6+} [57-60]. The perovskite layers in the structure of the Aurivillius phases are interleaved by the fluorite-type layers Bi_2O_2 (Figure 1c). That is why in the last time their composition is usually written as $(Bi_2O_2)A_{n-1}B_nO_{3n+1}$.

3. Formation of the Double-perovskite Layered Aluminates $Ln_2SrAl_2O_7$ (Ln=La – Ho)

The mechanism of formation of the double-perovskite layered aluminates was investigated for the series of $Ln_2SrAl_2O_7$ (Ln=La, Nd, Sm, Eu, Gd, Ho) [61-65,29] in the temperature range of 1000-1500°C for the reaction of the binary oxides and strontium carbonate:

$$Ln_2O_3 + Al_2O_3 + 2\ SrCO_3 = Ln_2SrAl_2O_7 \quad (1)$$

In case of La, Nd, Sm-containing oxides, the perovskite phases $LnAlO_3$ and 1/1 intergrowth structures $LnSrAlO_4$ were obtained as intermediate phases [61,62]. Their interaction results in forming of the 2/1 intergrowth of oxides $Ln_2SrAl_2O_7$ (Ln=La,Nd,Sm). Thus intermediate reactions of overall process of $Ln_2SrAl_2O_7$ are the following:

$$Ln_2O_3 + Al_2O_3 = 2\ LnAlO_3 \quad (2)$$

$$Ln_2O_3 + Al_2O_3 + 2\ SrCO_3 = 2\ LnSrAlO_4 + 2\ CO_2 \quad (3)$$

$$LnAlO_3 + LnSrAlO_4 = Ln_2SrAl_2O_7 \quad (4)$$

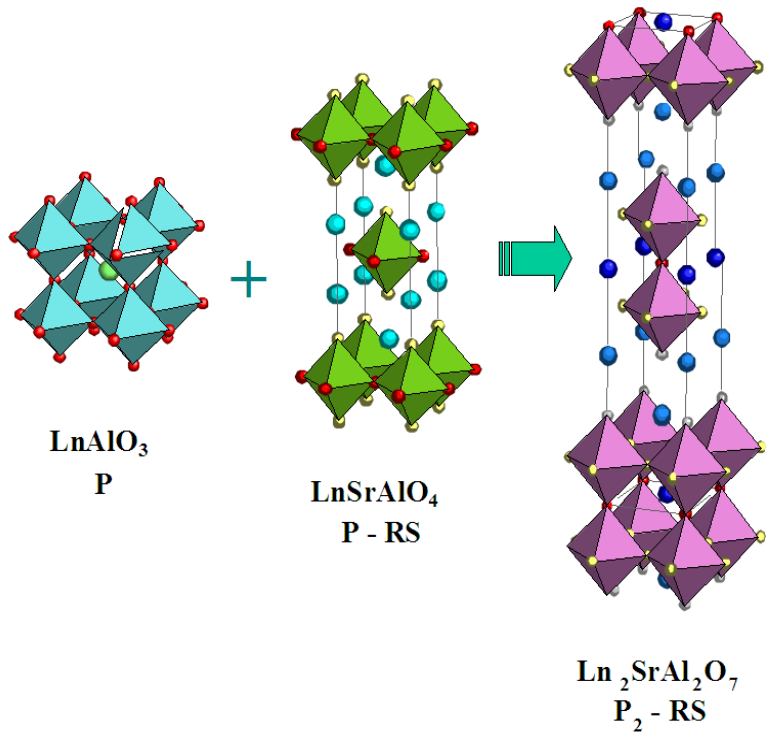

Figure 2. The structure transformation during the last stage of $Ln_2SrAl_2O_7$ formation.

To support this mechanism the consequence of reaction (2)-(4) have been performed. We can say that this is the usual way of formation of the Ruddlesden-Popper phases through the more simple perovskite-types structure if they stable at temperature of synthesis. This mechanism works for the beginning of lanthanide raw La–Sm. The structure-chemical reaction of the last stage of $Ln_2SrAl_2O_7$ formation which determines the rate of overall process is presented in Figure 2.

In the second part of the lanthanides raw (starting from gadolinium) the perovskite type structure is not stable at temperature of synthesis. Due to the instability of $GdAlO_3$ oxide $SrAl_2O_4$ with spinel type of structure occurs as the intermediate phase. Till the end of reaction the gadolinium oxide is also found in the reaction mixture. Interaction between these two compounds is the limiting reaction for the overall process of 2/1 intergrowth $Gd_2SrAl_2O_7$ formation [63]:

$$Al_2O_3 + SrCO_3 = SrAl_2O_4 + CO_2 \quad (5)$$

$$SrAl_2O_4 + Gd_2O_3 = Gd_2SrAl_2O_7 \quad (6)$$

Mechanism (5)-(6) works for the second part of lanthanides Gd-Ho. Holmium brings some novel phenomena. Its smallest atoms form the phase $SrHo_2O_4$ with tunnel structure of the $CaFe_2O_4$ type at temperature higher than 1300°C and simultaneously with reactions (5)-(6) intermediate reactions (7)-(8) take place [29].

$$Ho_2O_3 + SrCO_3 = SrHo_2O_4 + CO_2 \quad (7)$$

$$SrHo_2O_4 + Al_2O_3 = Ho_2SrAl_2O_7 \quad (8)$$

Of the special interest is the formation of the Eu-containing compound, $Eu_2SrAl_2O_7$, located between two groups with different formation mechanisms. The mechanism of formation of the Eu-containing phase depends on the temperature. Below 1400°C the intermediate reaction is

$$SrAl_2O_4 + Eu_2O_3 \rightarrow Eu_2SrAl_2O_7 \quad (9)$$

while above 1400°C the reaction goes through the stage

$$EuAlO_3 + EuSrAlO_4 \rightarrow Eu_2SrAl_2O_7 \quad (10)$$

This means that $Eu_2SrAl_2O_7$ formation goes through the P/RS ($EuSrAlO_4$) and P ($EuAlO_3$) phases only if the last one is stable at the synthesis temperature, while at lower temperatures the mechanism of the reaction changes from the one characteristic for the first members of the lanthanide series (reactions 2-4) to the one typical for the last members (reactions 5-6).

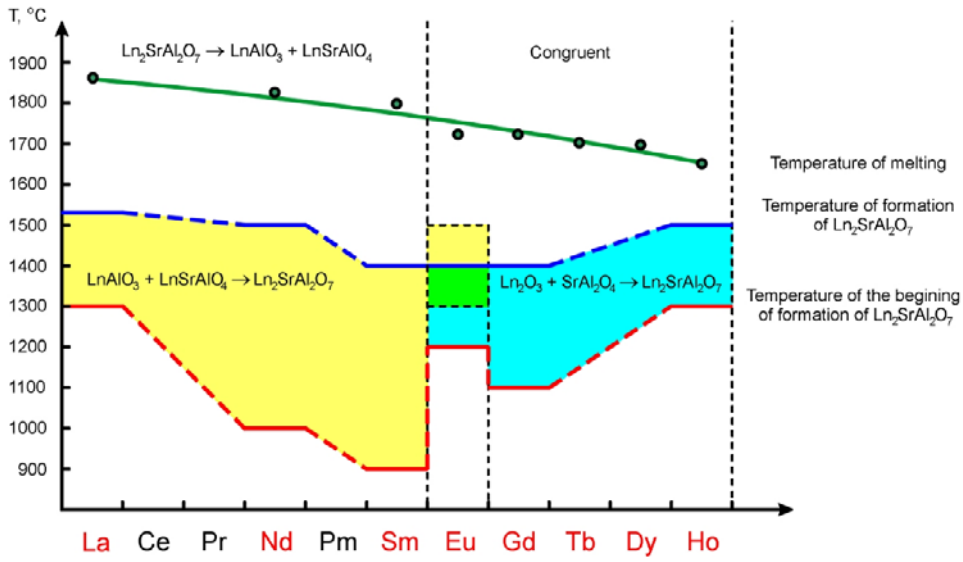

Figure 3. Temperatures and mechanisms of formation of $Ln_2SrAl_2O_7$.

Figure 3 demonstrates the difference in mechanism of formation in the raw La – Ho. Diagram also indicates the temperature of the beginning of formation of $Ln_2SrAl_2O_7$ and temperature of obtaining of single phase without impurities of intermediate compounds. It is important to mention that difference in character of $Ln_2SrAl_2O_7$ melting follows the difference in the mechanism of formation.

In the rare-earth series La-Gd there is a large increase of the formation rate of the intergrowth oxides. In Figure 4(a-d) it is possible to see that after three hours heating at 1500 °C, in La-containing system there is a mixture of perovskite, 1/1 and 2/1 intergrowth phases. Under the same conditions, in Nd and Gd-containing systems there is the only 2/1 intergrowth oxide.

After Gd the mechanism of formation of the $Ln_2SrAl_2O_7$ phases remains the same, $SrAl_2O_4$ being the intermediate compound, but the formation rate decreases significantly. $SrAl_2O_4$ is formed at 1000°C in all cases, but interaction of $SrAl_2O_4$ with Gd_2O_3 starts already at 1100°C, while Ho_2O_3 reacts only after 1300°C. At 1500°C $Gd_2SrAl_2O_7$ formation is finished already after 1 hour heating, while pure $Ho_2SrAl_2O_7$ can be obtained only after 24 hours (Figure 4e).

The effect of the cationic substitution on the formation of the Ruddlesden-Popper aluminates has been investigated for the $(La_xHo_{1-x})_2SrAl_2O_7$ and $(Nd_xHo_{1-x})_2SrAl_2O_7$ solid solutions. Figure 5 shows change of the formation rate of $(La_{0.1}Ho_{0.9})_2SrAl_2O_7$ and $(Nd_{0.15}Ho_{0.85})_2SrAl_2O_7$ compared to $Ho_2SrAl_2O_7$. It is clear that even small amounts of La or Nd strongly affect the reaction rate. The presence of Nd results in the increase of the formation rate, while the La-containing phase is formed at smaller rate. This difference corresponds to the difference in the reactivity in the systems Ln_2O_3–$SrCO_3$–Al_2O_3 (Ln=La, Nd, Ho).

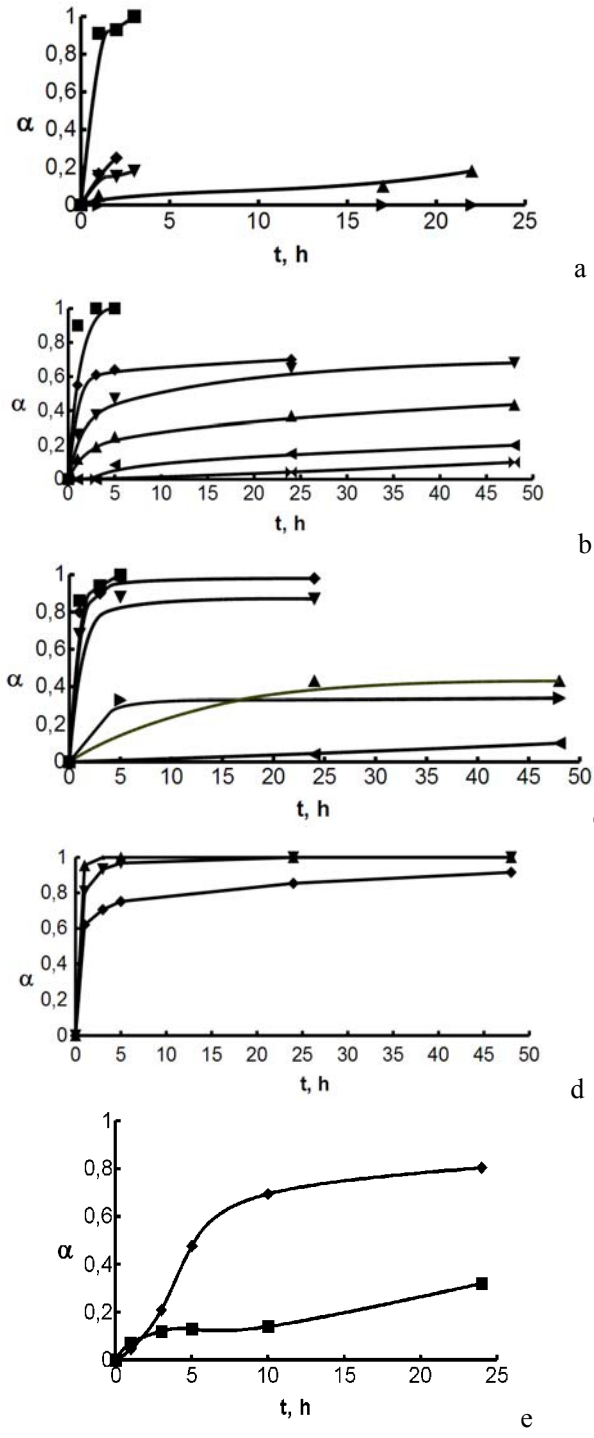

Figure 4. Degree of formation of $Ln_2SrAl_2O_7$ vs. time dependence for different temperatures: a – Ln=La; ► - 1200°C; ▲ - 1300°C; ▼ - 1400°C; ♦ - 1500°C; ■ - 1530°C; b – Ln=Nd; ►◄ - 1000°C; ◄ - 1100°C; ▲ - 1200°C; ▼ - 1300°C; ♦ - 1400°C; ■ - 1500°C; c – Ln=Sm; ◄ - 900°C; ▲ - 1000°C; ►- 1100°C; ▼ - 1200°C; ♦ - 1300°C; ■ - 1400°C; d – Ln=Gd; ♦ - 1200°C; ▼ - 1300°C; ▲- 1400°C; e – Ln=Ho; ♦ - 1200°C; ▼ - 1300°C; ▲- 1400°C.

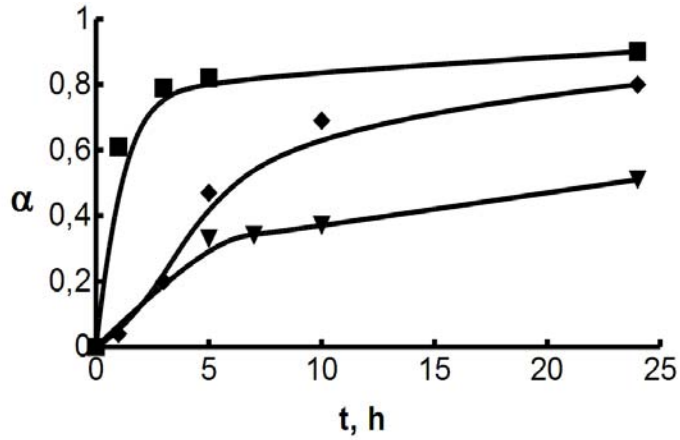

▼ - $(La_{0.1}Ho_{0.9})_2SrAl_2O_7$; ♦ - $Ho_2SrAl_2O_7$; ■ - $(Nd_{0.15}Ho_{0.85})_2SrAl_2O_7$.

Figure 5. Degree of formation of $Ho_2SrAl_2O_7$-based solid solutions vs. time dependence (1400°C).

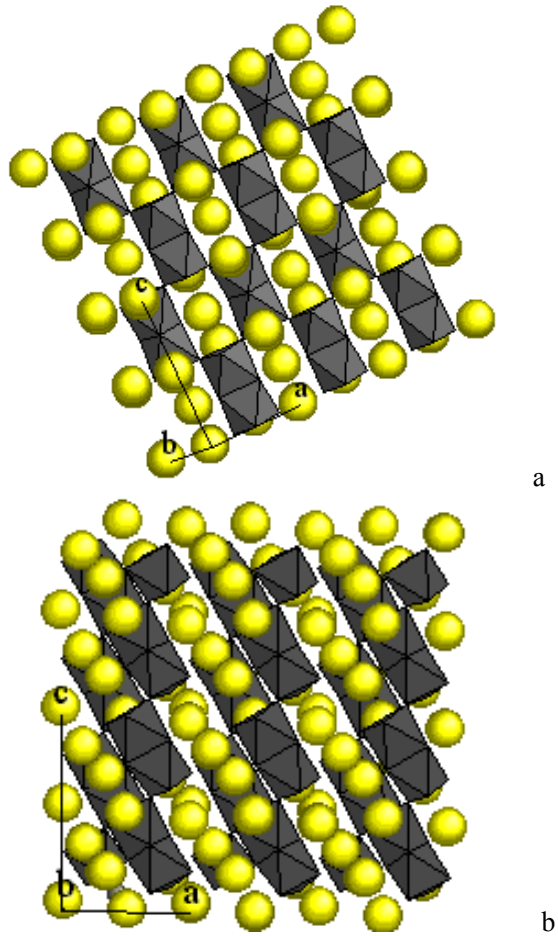

Figure 6. Comparison of the structures of 4H-$SrMnO_3$ (a) and $Sr_7Mn_4O_{15}$ (b).

4. FORMATION OF THE DOUBLE-PEROVSKITE LAYERED MANGANITES $Ln_2SrMn_2O_7$ (Ln=La, Nd, Gd).

The formation of the $NdSr_2Mn_2O_7$ from the Nd_2O_3, $SrCO_3$ and MnO_2 has been investigated under isothermal conditions at 1200°C and under constant heating rate conditions by the DSC-TGA method.

The qualitative phase analysis of the reaction mixture after 3 hrs heating at 1200°C shows that the following phases present: Nd_2O_3, $Sr_7Mn_4O_{15}$, $Nd_xSr_{1-x}MnO_3$ and $Nd_{1+x}Sr_{2-x}Mn_2O_7$. Using the analogy with the previously found mechanism of formation of the Ruddlesden-Popper phases $Ln_2SrAl_2O_7$ and $Ln_2SrFe_2O_7$ [61-67] the following mechanism had been proposed:

$$7SrCO_3 + 4MnO_2 \rightarrow Sr_7Mn_4O_{15} + 7CO_2 \quad (11)$$

$$3Nd_2O_3 + 2SrCO_3 + 8MnO_2 \rightarrow 8Nd_{0.75}Sr_{0.25}MnO_3 + 2CO_2 + 1.5O_2 \quad (12)$$

$$Nd_2O_3 + 2Sr_7Mn_4O_{15} \rightarrow 8Nd_{0.25}Sr_{1.75}MnO_4 + 0.5O_2 \quad (13)$$

$$Nd_{0.75}Sr_{0.25}MnO_3 + Nd_{0.25}Sr_{1.75}MnO_4 \rightarrow NdSr_2Mn_2O_7. \quad (14)$$

Absence of the peaks of the $Nd_{0.25}Sr_{1.75}MnO_4$ phase on the powder pattern means that its formation is the slowest stage in the reaction while the last stage is much faster.

The possibility of the proposed reaction sequence (11-14) has been confirmed by carrying out each of them independently. It should be noted that the intermediate phases are formed at higher temperatures when synthesized apart. This is analogous to the case of the formation of the $Ln_2SrAl_2O_7$ phases where the temperature of the separate formation of the intermediate perovskite phase $LnAlO_3$ is higher than the temperature of its formation as an intermediate compound. [61]

The fact that $Sr_7Mn_4O_{15}$ appears in the reaction mixture instead of the K_2NiF_4-type phase can be understood by analysis of the structure of $SrMnO_3$. While possessing the same formula as perovskites, this compound has different structure with face-sharing MnO_6 octahedra (Figure 6a). This structural feature remains unchanged when the layered structure is formed, leading to the different chemical composition (Figure 6b). It is interesting to note that 4H-$SrMnO_3$ transforms to the orthorhombic β-$SrMnO_3$ [68,69] at approximately the same temperature (about 1400°C), as the temperature of stabilization of Sr_2MnO_4 compared to $Sr_7Mn_4O_{15}$ [70]. This gives the additional confirmation to the interconnection of between the structure of $SrMnO_3$ and the layered phase.

The quantitative analysis of the reaction mixture shows that the proposed mechanism does not account for the reaction completely. The molar ratio $\nu(Sr_7Mn_4O_{15}) : \nu(Nd_2O_3)$ appears to be 0.77:1 instead of 2:1, as required by the proposed mechanism. In order to explain this fact it was proposed that the perovskite phase contains less Nd, while the excess of the Nd_2O_3 reacts with the perovskite in the same way as in case of the formation of the $Gd_2SrFe_2O_7$ [67]. This means that the perovskite phase reacts with Nd_2O_3 forming the K_2NiF_4-type phase and this K_2NiF_4-type phase reacts with the perovskite phase again yielding

the double-layered Ruddlesden-Popper phase. Again, the slowest stage of the reaction is the formation of the K_2NiF_4-type phase.

The processes that take place in the system during heating were investigated by the DSC-TGA method (Figure 7). Comparison with the literature data for the pure initial compounds and previously published results concerning the formation of the $LnSr_2Al_2O_7$ series [61-62] as well as X-ray phase analysis gives rise to the following explanation of the observed thermal effects. At 360°C small amounts of water (about 0.5%) absorbed by Nd_2O_3 are released. At 650°C MnO_2 decomposes yielding Mn_2O_3. The broad peak at 950-1030°C appears due to the series of processes: Mn_2O_3 decomposes yielding Mn_3O_4, $SrCO_3$ undergoes the phase transition and the formation of the intermediate products starts. These processes result in a large decrease in mass (14% approximately). At higher temperature the mass of the reaction mixture increases again because the formation of the intermediate compounds from Mn_3O_4 implies absorption of oxygen from air. The small peak at 1190°C corresponds to the phase transition in Mn_3O_4.

The complete mechanism of the reaction can be written as follows:

Common stages

$$2MnO_2 \rightarrow Mn_2O_3 + 0.5°O_2 \quad (15)$$
$$3Mn_2O_3 \rightarrow 2Mn_3O_4 + 0.5°O_2 \quad (16)$$
$$21SrCO_3 + 4Mn_3O_4 + 4°O_2 \rightarrow 3Sr_7Mn_4O_{15} + 21CO_2 \quad (17)$$
$$3xNd_2O_3 + 6(1-x)SrCO_3 + 2Mn_3O_4 + (4-3x)O_2 \rightarrow 6Nd_xSr_{1-x}MnO_3 + 6(1-x)CO_2 \quad (18)$$

Mechanism (I)

$$Nd_2O_3 + 2Sr_7Mn_4O_{15} \rightarrow 8Nd_{0.25}Sr_{1.75}MnO_4 + 0.5O_2 \quad (19)$$
$$Nd_xSr_{1-x}MnO_3 + Nd_{0.25}Sr_{1.75}MnO_4 \rightarrow Nd_{0.25+x}Sr_{2.75-x}Mn_2O_7 \quad (20)$$

Mechanism (II)

$$2Nd_xSr_{1-x}MnO_3 + Nd_2O_3 \rightarrow 2Nd_{1+x}Sr_{1-x}MnO_4 + 0.5O_2 \quad (21)$$
$$Nd_xSr_{1-x}MnO_3 + Nd_{1+x}Sr_{1-x}MnO_4 \rightarrow 2Nd_{1+2x}Sr_{2-2x}Mn_2O_7 \quad (22)$$

In both reaction pathways the slowest stage is the formation of the K_2NiF_4-type phase (19,21). It should be noted that the cationic composition of the double-layered Ruddlesden-Popper phases obtained by these two pathways is not the same. This means that the proposed mechanism gives explanation to the formation of two phases observed by P. D. Battle *et al*. [42,43]

The stoichiometry of the reaction allows to find the perovskite phase composition and the proportions of the product formed by each of the mechanisms simultaneously with the kinetic calculations. The following relationship between the x value in $Nd_xSr_{1-x}MnO_3$ and the molar fraction of the Ruddlesden-Popper phase obtained by the mechanism II (y) can be derived:

$$(1 - y)(x + 0.25) + y(1 + 2x)=1, \quad (23)$$

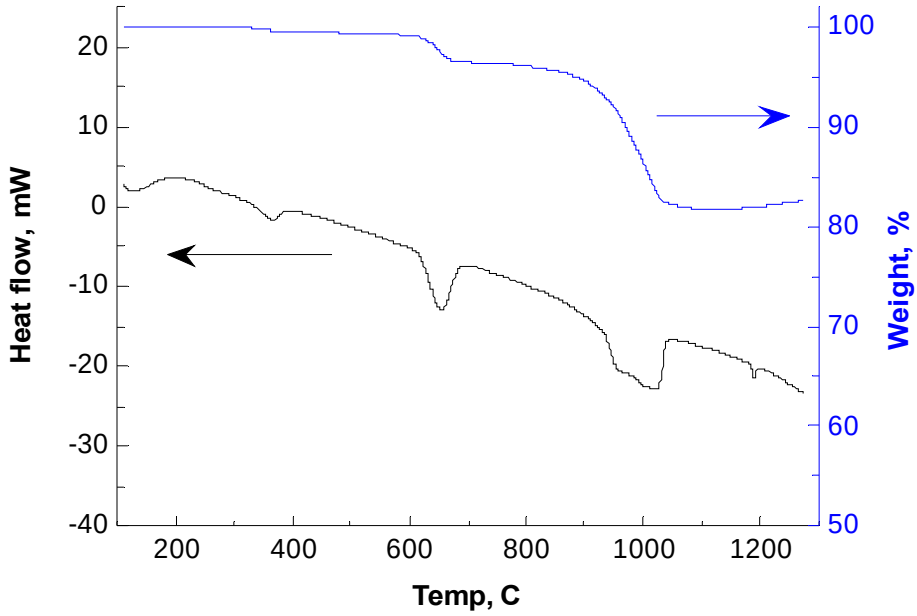

Figure 7. The DSC-TGA analysis of the reaction mixture during synthesis of $NdSr_2Mn_2O_7$.

meaning that the $Nd_{0.25+x}Sr_{2.75-x}Mn_2O_7$ and $Nd_{1+2x}Sr_{2-2x}Mn_2O_7$ phases are formed at the molar ratio $(2x)$:$(0.75 - x)$.

Using the quantitative X-ray diffraction analysis the kinetics of the reaction at 1200˚C has been investigated. As long as the amount of the perovskite phase can not be determined accurately from the X-ray diffraction data due to the peak overlapping, it was assumed that the conversion degree according to both mechanisms is almost the same after 3 hours heating. The error of such assumption is of the same order as the error of the X-ray quantitative analysis.

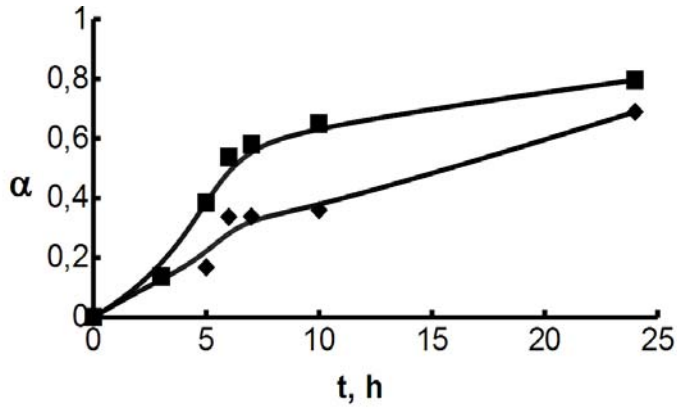

■ – mechanism I; ♦ - mechanism II.

Figure 8. The reaction rate of two mechanisms of the $NdSr_2Mn_2O_7$ formation at 1200°C.

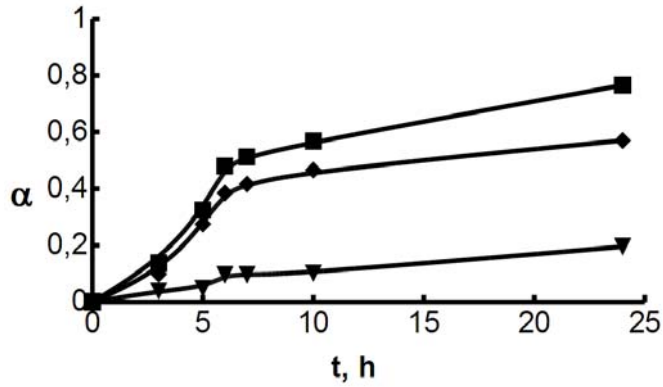

♦ – mechanism I; ▼ – mechanism II; ■ – total amount.

Figure 9. Amount of $Nd_{1-x}Sr_{2+x}Mn_2O_7$ formed by each of the reaction mechanisms and total amount of the Ruddlesden-Popper phases at 1200°C.

The composition of the intermediate perovskite phase appears to be $Nd_{0.42}Sr_{0.58}MnO_3$. Approximately 72% of the double-layered phase is formed according to the mechanism (I). The comparison of the reaction rate for each mechanism is shown on Figure 8. The amounts of the Ruddlesden-Popper phases obtained for each mechanism are shown on Figure 9.

In case of $LaSr_2Mn_2O_7$, the intermediate compounds observed in the reaction mixture after 3 hours heating at 1200°C are La_2O_3, $La_xSr_{1-x}MnO_3$, $LaSr_2Mn_2O_7$, $La_{1-x}Sr_{1+x}MnO_4$ and $Sr_7Mn_4O_{15}$. However, after 5 hours $Sr_7Mn_4O_{15}$ cannot be observed in the reaction mixture, probably due to high rate of the interaction with La_2O_3. Mechanism of formation of $LaSr_2Mn_2O_7$ is the same as for $NdSr_2Mn_2O_7$ but the comparative rates of the reaction steps are different: the K_2NiF_4-type compound forms and reacts with approximately the same rate. This holds for the Gd-containing compound too. The overall formation rate of $LaSr_2Mn_2O_7$ and $GdSr_2Mn_2O_7$ at 1200°C is shown at Figure 10.

The DSC-TGA data of the reaction mixture during the formation of $LaSr_2Mn_2O_7$ and $GdSr_2Mn_2O_7$ are qualitatively the same as for $NdSr_2Mn_2O_7$. This supports the conclusion that the formation process goes the same way or all lanthanides investigated.

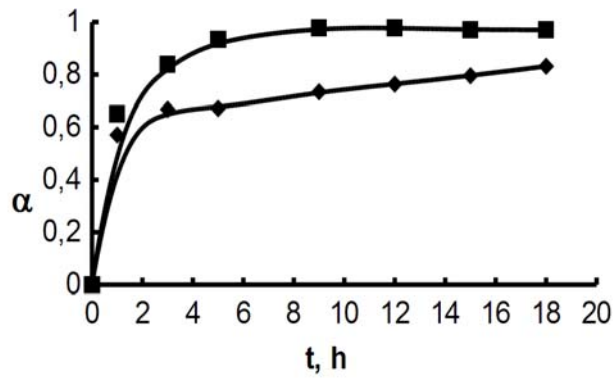

Figure 10. Degree of formation vs. time dependence for $LaSr_2Mn_2O_7$ (♦) and $GdSr_2Mn_2O_7$ (■) at 1200°C.

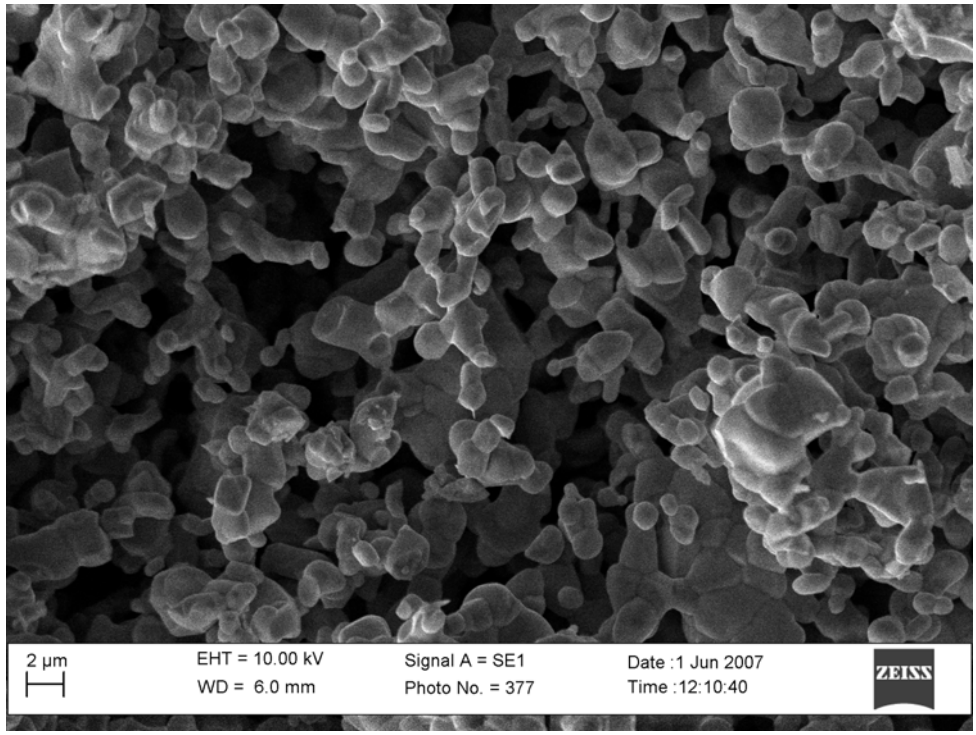

Figure 11. The SEM microphotograph of the reaction mixture during the formation of $GdSr_2Mn_2O_7$.

The reaction mixture obtained during the formation of $GdSr_2Mn_2O_7$ has been investigated by SEM. The interacting particles have the size of 1-5µm (Figure 11). The microprobe analysis of the sample has shown that the intermediate perovskite phase is $Gd_{0.5}Sr_{0.5}MnO_3$, the composition being close to the one obtained for $NdSr_2Mn_2O_7$ by means of the X-ray diffraction data.

Investigation of the formation of manganites $LnSr_2Mn_2O_7$ (Ln=La, Nd, Gd) allowed to understand the new aspects in nature of the phase separation in the double-layered Ruddlesden-Popper phases, namely that cationic composition in these compounds depends on pathways of reaction. The difference in the cationic composition of two phases obtained by the one-step synthesis is due to the difference in the mechanisms of formation.

4. Formation of the Double-perovskite Layered $Ln_2SrFe_2O_7$ (Ln=La, Nd, Gd)

Ferrite ceramics is used in memory chips of computer equipment, as catalysts in chemical industry, and also in power engineering and electronics. To develop effective technology of ferrite products with the required magnetic and other characteristics, it is necessary to provide not only the preset crystal-chemical characteristics (structure and distribution of cations over various structural positions), but also stability of the valence state of iron atoms.

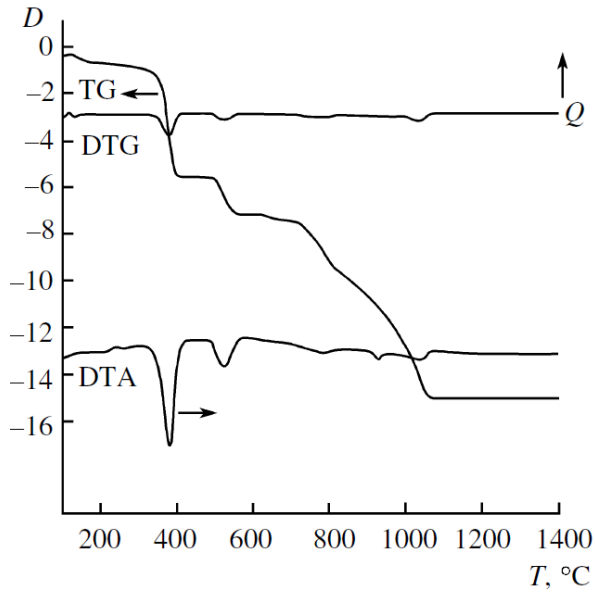

Figure 12. The DTA-TGA analysis of the reaction mixture during synthesis of $La_2SrFe_2O_7$.

Polycrystalline samples of $Ln_2SrFe_2O_7$ (Ln = La, Nd, Sm, Gd) were prepared by the solid-phase synthesis in an oxygen atmosphere [71], whereas single crystals of $Eu_2SrFe_2O_7$ were prepared from a solution in a PbO melt [72]. However, data on the mechanism and kinetics of formation of $Ln_2SrFe_2O_7$ are lacking.

The mechanism of formation of $La_2SrFe_2O_7$ and $Nd_2SrFe_2O_7$ has been investigated in [66,67]. An initial oxides mixture with the stoichiometry corresponding to the compound $La_2SrFe_2O_7$ was subjected to thermal analysis up to 1400°C (Figure 12); two strong endothermic effects at 344-422 and 489-578ºC, accompanied by weight loss of 4.59 and 1.58%, respectively, were revealed. These effects correspond to the stepwise dehydration of $La(OH)_3$ with the formation of lanthanum oxyhydroxide and oxide, respectively. The presence of lanthanum hydroxide in the starting mixture was caused by the specific procedure of sample preparation, involving powdering and mixing of components in distilled water, and by the reactivity of lanthanum oxide toward water. Starting from 730ºC, three extra endothermic effects accompanied by a weight loss are clearly seen. These effects result from the decomposition of strontium carbonate conjugated to the formation of $LaSrFeO_4$, as follows from the X-ray diffraction patterns. As the temperature is increased to 1200-1300°C, a sharp increase in the rate of formation of $LaSrFeO_4$ and $LaFeO_3$ is observed, the starting oxides completely disappear from the mixture, and the formation of $La_2SrFe_2O_7$ begins. The formation of $Nd_2SrFe_2O_7$ goes the same way.

It is known that at temperatures exceeding 1380°C iron(III) oxide dissociates to form Fe_3O_4 [73]. The thermal analysis of the mixture of the stoichiometric composition $La_2SrFe_2O_7$ (Figure 12) in air revealed no effects attributable to changes in the iron(III) oxidation state. The results of the thermal analysis and the data of the X-ray phase analysis of the samples obtained by heat treatment in the annealing-quenching mode show that the intermediate compounds $LnFeO_3$ and $LnSrFeO_4$ are formed fairly rapidly at temperatures up to 1200°C. This fact suggests that the intermediate compounds are formed at temperatures lower than the

temperature of the Fe_2O_3 conversion to Fe_3O_4 and that the iron(III) state is stabilized in $LnFeO_3$ and $LnSrFeO_4$.

When the mixtures are sintered in the range 1400-1500°C, the rate of the $Ln_2SrFe_2O_7$ formation increases. The solid-phase reaction is complete after 3 hours heating at 1500°C.

In [67] the mechanism of formation of the complex oxide $Gd_2SrFe_2O_7$ has been examined by means of X-ray phase analysis and Mossbauer spectroscopy. The phase analysis of the samples obtained after heat treatment for 3 h at 1200, 1300, and 1400°C shows that Gd_2O_3, $GdFeO_3$, $SrFeO_{3-x}$, and $Gd_2SrFe_2O_7$ present in the reaction mixture. The mechanism of formation of the complex oxide $Gd_2SrFe_2O_7$ is not similar to that of the aluminate $Gd_2SrAl_2O_7$. The complex aluminate $Gd_2SrAl_2O_7$ is formed by the reaction of an intermediate compound of the spinel structure with gadolinium oxide (6).

The composition of the reaction mixture and the structural characteristics of intermediate compounds indicate that reaction is a complex multistep process, as well as the majority of solid-phase reactions, and allows to suggest the following mechanism for the solid-phase synthesis of the complex oxide $Gd_2SrFe_2O_7$:

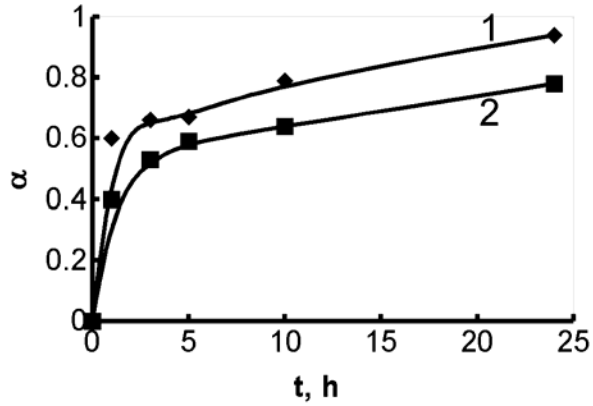

1 - 1400°C; 2 - 1300°C.

Figure 13. Degree of formation of $La_2SrFe_2O_7$ vs. time dependence for different temperatures.

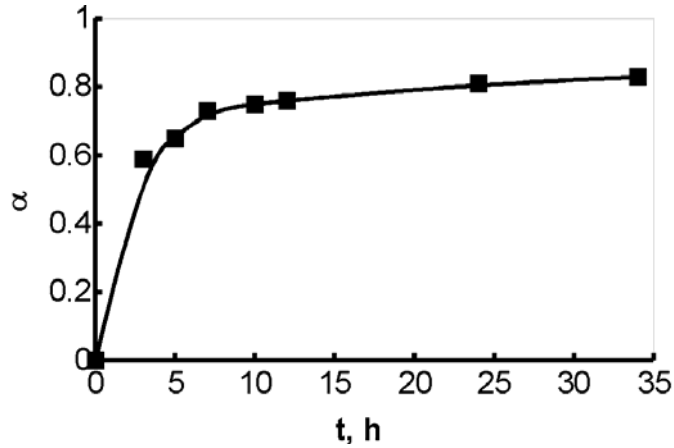

Figure 14. Degree of formation of $GdSrFeO_4$ vs. time dependence at 1300°C.

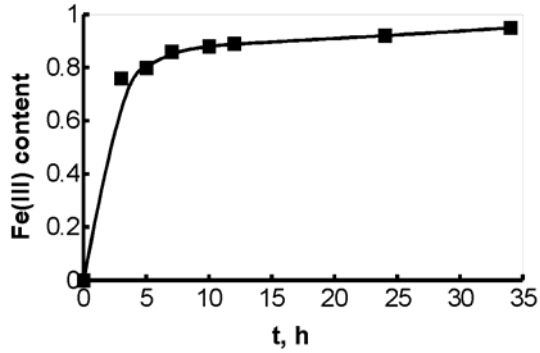

Figure 15. Fe(III) content in the reaction mixture during the formation of $GdSrFeO_4$ at 1300°C.

$$Gd_2O_3 + Fe_2O_3 \rightarrow 2GdFeO_3 \quad (24)$$

$$2SrCO_3 + (1 - 2x)O_2 + Fe_2O_3 \rightarrow 2SrFeO_{3-x} + 2CO_2 \quad (25)$$

$$Gd_2O_3 + 2SrFeO_{3-x} \rightarrow 2GdSrFeO_4 + (1 - 2x)O_2 \quad (26)$$

$$GdFeO_3 + GdSrFeO_4 \rightarrow Gd_2SrFe_2O_7 \quad (27)$$

The fact that the compound $GdSrFeO_4$ is not detected in the reaction mixture by X-ray diffraction can be accounted for by a high rate of its reaction with $GdFeO_3$.

The degree of conversion to the final product $La_2SrFe_2O_7$ was determined for temperatures of 1300 and 1400°C in relation to the reaction time in the range 1-24 h. This is illustrated by kinetic curves in Figure 13.

A comparative analysis of the kinetics of $La_2SrFe_2O_7$ and $La_2SrAl_2O_7$ formation shows that the degree of the aluminate conversion in 24 h at 1300°C does not exceed 0.2, and for the ferrite it is 0.8. This fact indicates that the rate of the ferrite formation considerably exceeds the rate of the aluminate formation and requires lower temperatures. This does not hold for Gd-containing compounds: $Gd_2SrAl_2O_7$ is formed much faster than $Gd_2SrFe_2O_7$.

The mechanism and kinetics of formation of the single-layered Ruddlesden-Popper phase $GdSrFeO_4$ has been investigated in [74] by means of X-ray diffraction and Mossbauer spectroscopy. The X-ray phase analysis shows that $SrFeO_{3-x}$ acts as an intermediate compound in this reaction. According to the Mossbauer spectrum, x is equal to 0.36±0.05.

The kinetics of the formation of $GdSrFeO_4$ has been characterized by the phase composition determined from the X–ray diffraction data (Figure 14) and by the Fe^{3+} fraction in the reaction mixture determined from the Mossbauer data (Figure 15). Both data sets are in a good agreement.

5. Formation of the Double-perovskite Layered Bi_3TiNbO_9

The kinetics of the formation of Bi_3NbTiO_9 from the initial oxides was investigated at 600°C. The interaction between intermediate compounds was investigated at 700-900°C. The DTA has been performed in order to confirm the data of the isothermal investigation.

The results of phase analysis show that, like the Ruddlesden-Popper phases, the Aurivillius phases are formed in a multistage way with more simple phases of the same class as intermediates. The peaks of Bi_3NbTiO_9, $Bi_{12}TiO_{20}$, $Bi_4Ti_3O_{12}$ and $Bi_5Nb_3O_{15}$ can be observed at the X-ray powder pattern. This means that during the formation of the n=2 phase Bi_3NbTiO_9 two other Aurivillius phases, $Bi_4Ti_3O_{12}$ (n=3) and $Bi_5Nb_3O_{15}$ (n=1.5) act as intermediates (Figure 16). The $Bi_{12}TiO_{20}$ compound has been observed earlier [75] during the investigation of the formation of Aurivillius phases in the Bi_2O_3-TiO_2-Fe_2O_3 system. It appears to be the γ-form of the bismuth oxide stabilized by titanium dioxide [76]. It is the formation of stabilized γ-Bi_2O_3 that leads to the activation of the solid state reactions in such systems. In general, the formation of the Bi_3NbTiO_9 phase can be represented as follows:

$$Bi_2O_3 \rightarrow \gamma\text{-}Bi_2O_3 \text{ (or } Bi_2O_3 + TiO_2 \rightarrow Bi_{12}TiO_{20}) \quad (28)$$

$$\gamma\text{-}Bi_2O_3 + TiO_2 \rightarrow Bi_4Ti_3O_{12} \quad (29)$$

$$\gamma\text{-}Bi_2O_3 + Nb_2O_5 \rightarrow Bi_5Nb_3O_{15} \quad (30)$$

$$Bi_4Ti_3O_{12} + Bi_5Nb_3O_{15} \rightarrow Bi_3NbTiO_9 \quad (31)$$

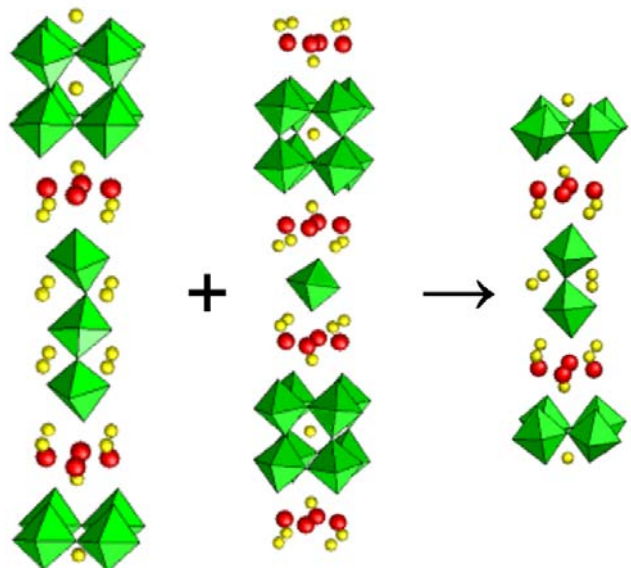

Figure 16. The structure transformation during the last stage of Bi_3NbTiO_9 formation.

The thermal analysis of the reaction mixture reveals two endothermic effects at 740˚C and 860˚C (Figure 17). The temperature of the first effect corresponds to the temperature of formation of the TiO_2-stabilized γ-Bi_2O_3 (28). The second effect corresponds to the peritectic melting of $Bi_{12}TiO_{20}$. [77] The results of the X-ray phase analysis show that after the second effect almost pure Bi_3NbTiO_9 is obtained.

The X-ray data of the sample quenched after reaching the temperature of the first endothermic effect show that besides the previously observed compounds another bismuth

niobate, $BiNbO_4$, presents in the reaction mixture. This fact could be explained by the assumption that the formation of $Bi_5Nb_3O_{15}$ is a two-step reaction:

$$\gamma\text{-}Bi_2O_3 + Nb_2O_5 \rightarrow BiNbO_4 \quad (30a)$$

$$\gamma\text{-}Bi_2O_3 + BiNbO_4 \rightarrow Bi_5Nb_3O_{15} \quad (30b)$$

The second step is much faster than the first one. This results in a very low concentration of $BiNbO_4$ after long heating time. The reaction (30a) is the limiting stage of the overall process.

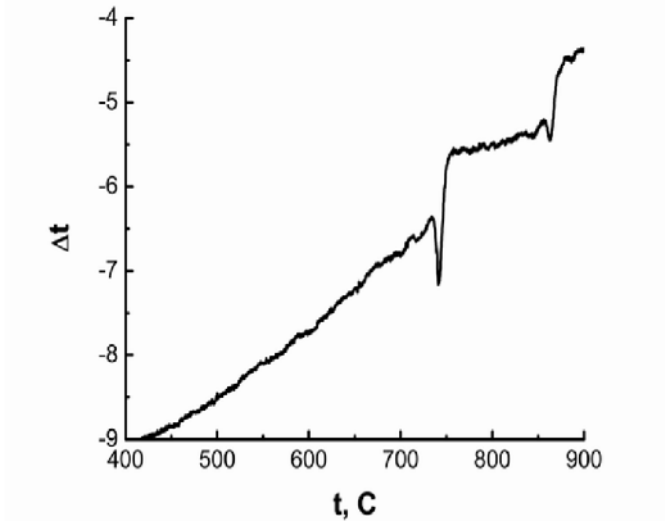

Figure 17. The DTA analysis of the reaction mixture during synthesis of Bi_3NbTiO_9.

Proposed reaction mechanism accounts for the observed limits of obtaining the substituted Aurivillius phases. It was found that the lanthanide-substituted phases $Bi_2LnNbTiO_9$ can be obtained only for Ln=La-Gd, while the Mn-substituted $Bi_3NbTi_{1-x}Mn_xO_9$ can be obtained only for $x<0.3$. These limits coincide with the limits of the cationic substitution in the intermediate compound $Bi_4Ti_3O_{12}$. Namely, investigations [78] of the substitution of Bi^{3+} for Ln^{3+} in triple-layered Aurivillius $Bi_4Ti_3O_{12}$ have shown that Aurivillius phases are not formed for the lanthanides smaller than Gd. In case of the Mn-substituted $Bi_4Ti_3O_{12}$, the Mn^{+4} cations are fully ordered in the middle perovskite layer [79]. It means that 1/3 Ti is substituted by Mn in $Bi_4Ti_3O_{12}$ and Mn content in $Bi_3NbTi_{1-x}Mn_xO_9$ is limited by the value $x=0.3$. So the Bi_3NbTiO_9 derivatives that would require formation of the unstable derivatives of $Bi_4Ti_3O_{12}$ as intermediates can not be obtained by straightforward synthesis from the binary oxides.

The kinetics of formation of Bi_3NbTiO_9 from the initial oxides has been investigated at 600°C. The conversion degree α versus time plot is shown at Figure 18. The formation of the Bi_3NbTiO_9 from the intermediate compounds (synthesized in advance by 6 hours annealing at 1000°C) according to the reaction (31) was studied at 700-900°C (Figure 19).

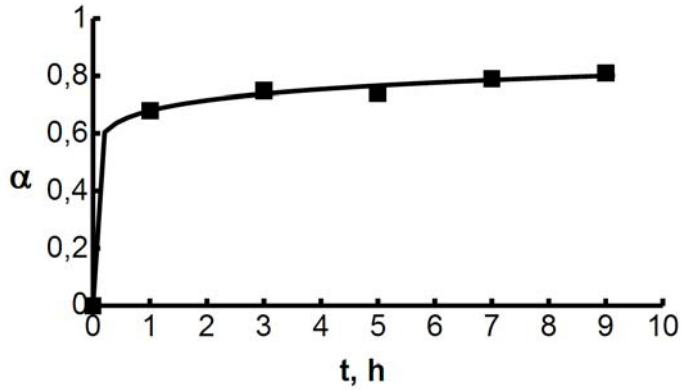

Figure 18. Degree of formation of Bi_3NbTiO_9 from the initial oxides vs. time dependence at 600°C.

The results show that Bi_3NbTiO_9 is formed much faster if the metal oxides are used as the initial materials than if Bi_3NbTiO_9 is synthesized from the intermediate compounds. This fact can be explained in terms of the microstructure of the intermediate compounds in these two cases. If Bi_3NbTiO_9 is synthesized from the metal oxides, intermediate compounds react immediately after they are formed, so they have less particle size and higher concentration of defects than if they are synthesized in advance.

The mechanism of formation of the Ln-substituted phases $Bi_2LnNbTiO_9$ appears to be the same as for the non-substituted phase. However, the limiting stage changes: for the formation of the non-substituted Aurivillius phase the reaction rate is limited by the formation of $BiNbO_4$ (reaction 30b), while for the substituted ones the reaction rate is limited by the formation of the intermediate Aurivillius phase $Bi_4LnNb_3O_{15}$ (reaction 34):

$$Bi_2O_3 \rightarrow \gamma\text{-}Bi_2O_3 \text{ (or } Bi_2O_3 + TiO_2 \rightarrow Bi_{12}TiO_{20})$$

$$\gamma\text{-}Bi_2O_3 + Ln_2O_3 + TiO_2 \rightarrow Bi_2Ln_2Ti_3O_{12} \quad (32)$$

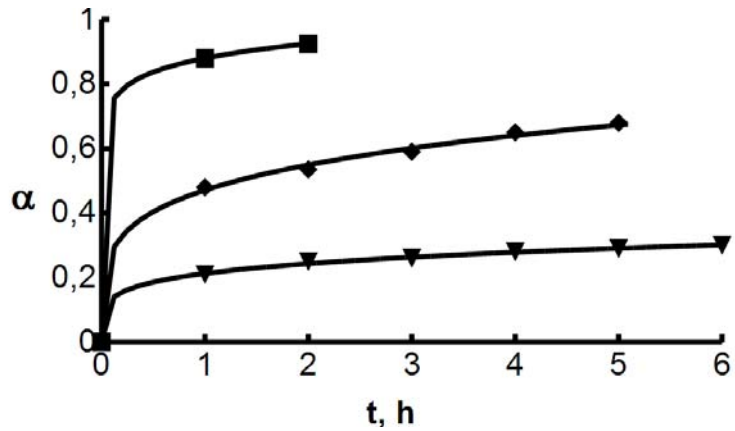

▼ – 700°C; ♦ –800°C; ■ – 900°C.

Figure 19. Degree of formation of Bi_3NbTiO_9 from the intermediate compounds vs. time dependence.

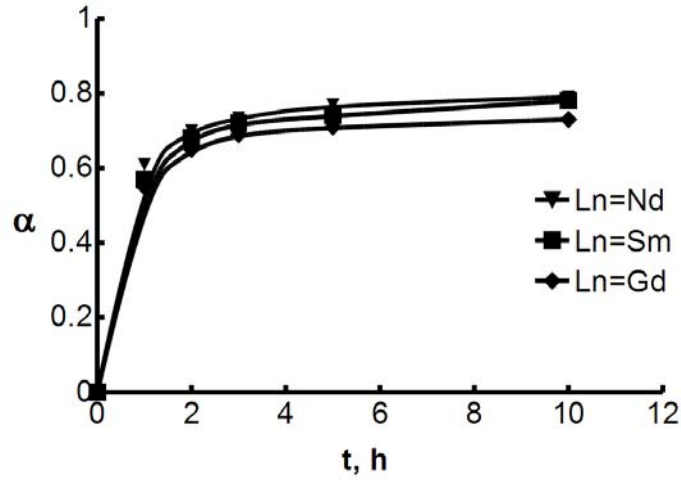

Figure 20. Degree of formation of $Bi_2LnNbTiO_9$ at 800°C.

$$\gamma\text{-}Bi_2O_3 + Nb_2O_5 \rightarrow BiNbO_4 \quad (33)$$

$$BiNbO_4 + \gamma\text{-}Bi_2O_3 + Ln_2O_3 \rightarrow Bi_4LnNb_3O_{15} \quad (34)$$

$$Bi_2Ln_2Ti_3O_{12} + Bi_4LnNb_3O_{15} \rightarrow Bi_2LnNbTiO_9 \quad (35)$$

The kinetics of the formation of the Ln-substituted Aurivillius phases has been investigated at 800˚C (Figure 20). The reaction rate is much slower than or the non-substituted phase and decreases along the lanthanide row.

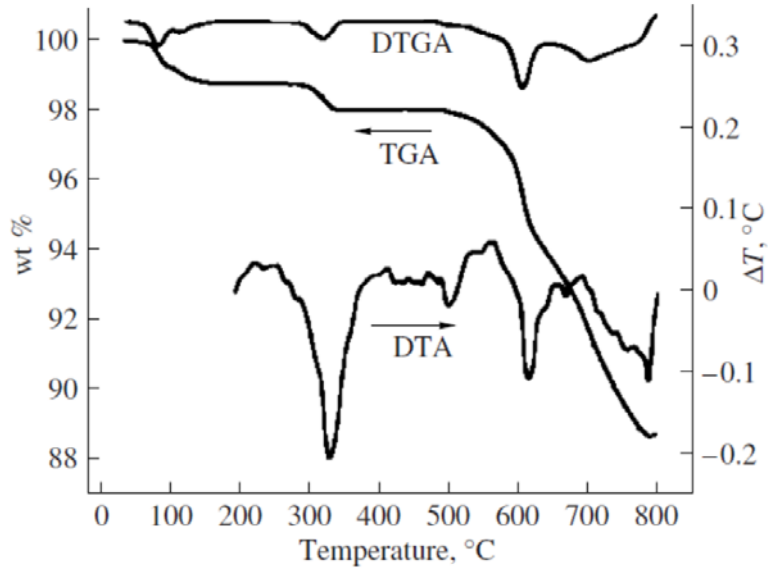

Figure 21. The DTA-TGA analysis of the reaction mixture during synthesis of $NaNdTiO_4$.

6. FORMATION OF THE RUDDLESDEN-POPPER PHASES $NaNdTiO_4$ AND $Na_2Nd_2Ti_3O_{10}$

The synthesis of $NaNdTiO_4$ is usually carried out using reaction of the sodium carbonate, neodymium oxide and titanium oxide at a temperature of 900˚C for 6 h. The experiments showed that Na_2CO_3 melts at temperatures of the order of 850˚C and leaves the reaction zone. Due to this fact the excess of Na_2CO_3 is necessary to obtain the pure compound and extra stage of washing out the residue of the sodium carbonate has to be performed. The synthesis at higher temperatures leads to the formation of the impurity compounds $Na_2Nd_2Ti_3O_{10}$ at 950˚C and $Nd_2Ti_2O_7$ at 1100˚C. The study of the thermal stability of the $NaNdTiO_4$ complex oxide showed that, at a temperature of 1150˚C, the oxide almost completely decomposes into the phases $Nd_2Ti_2O_7$ and $Nd_2Ti_3O_9$, which do not contain sodium.

The derivatographic study [81] of reaction in the temperature range 25–800˚C demonstrated that the main weight loss of the reaction system, which is equal to approximately 10% (Figure 21), is observed in the temperature range 600–780˚C and accompanied by endothermic effects at temperatures of 600, 660, and 780˚C. The endothermic effects at temperatures of 300 and 500˚C with a small weight loss correspond to the decomposition of neodymium hydroxide with the formation of neodymium oxyhydroxide and neodymium oxide, which is explained by the activity of neodymium oxide in the reaction with water. The thermal analysis of the binary mixture of sodium carbonate and titanium oxide reproduces the endothermic effects at 600 and 660˚C.

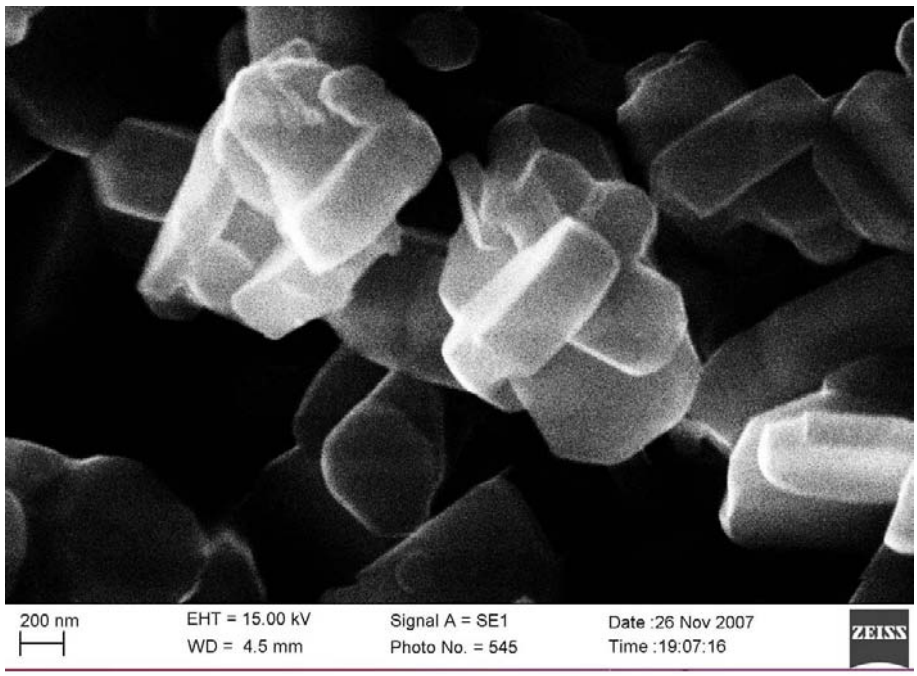

Figure 22. Electron micrograph of the $NaNdTiO_4$ sample synthesized at 750°C.

The derivatographic data agree with the results obtained by the "annealing–quenching" method [81]. The Na_2CO_3–TiO_2 system has been investigated separately, motivated by the low reactivity of the neodymium oxide at the temperature of synthesis. The X-ray diffraction patterns of the reaction mixture indicate that sodium titanate $Na_4Ti_5O_{12}$ is formed at 600˚C. At 720˚C, the X-ray diffraction patterns contain reflections of the $Na_8Ti_5O_{14}$ phase. The fraction of the $Na_8Ti_5O_{14}$ phase increases at 780˚C and reflections of $Na_2Ti_3O_7$ appear. At 900˚C, virtually only the $Na_8Ti_5O_{14}$ and $Na_2Ti_3O_7$ phases are present in the reaction mixture.

In case of the Nd_2O_3–Na_2CO_3–TiO_2 system the same processes have been observed up to 720˚C. After this temperature $NaNdTiO_4$ starts to form. At 780˚C only $NaNdTiO_4$ is observed in the reaction mixture.

The determination of the temperature intervals of the phase transformations in the Na_2CO_3–TiO_2 system and the determination of the temperature range of the reaction with Nd_2O_3 make it possible to propose the following reaction sequence of the formation of the $NaNdTiO_4$ oxide:

$$600^\circ C\ 4Na_2CO_3 + 10TiO_2 \rightarrow 2Na_4Ti_5O_{12} + 4CO_2 \tag{36}$$

$$660^\circ C\ Na_4Ti_5O_{12} + 2Na_2CO_3 \rightarrow Na_8Ti_5O_{14} + 2CO_2 \tag{37}$$

$$720\text{–}780^\circ C \begin{cases} Na_4Ti_5O_{12} \rightarrow l/7Na_8Ti_5O_{14} + 10/7Na_2Ti_3O_7, & (38) \\ 10/7Na_2Ti_3O_7 + 2Na_2O \rightarrow 6/7Na_8Ti_5O_{14}, & (39) \\ 2Na_8Ti_5O_{14} + 5Nd_2O_3 \rightarrow 10NaNdTiO_4 + 3Na_2O. & (40) \end{cases}$$

Reaction (39) requires sodium oxide (possibly, partially transformed into carbonate), which is formed in the course of reaction (40). This reaction mechanism of the formation of $NaNdTiO_4$ explains the necessity of using at least 20% excess of sodium carbonate for the reaction. The synthesis of $NaNdTiO_4$ without a sodium carbonate excess at temperatures below 780˚C is practically impossible (instead, the formation of $NaNdTi_2O_6$ slowly occurs) because $Na_8Ti_5O_{14}$ is hardly formed in the system, whereas the decomposition reaction of $Na_4Ti_5O_{12}$ proceeds very slowly. With 60% excess of sodium carbonate, only reactions (36), (37) and (40) sequentially occur.

The analysis of the phase composition of the reaction mixture at 780˚C enables one to claim that the formation of the layered $NaNdTiO_4$ oxide is almost complete after 30 minutes heating in the temperature range 720–780˚C, which is considerably lower than the melting point of Na_2CO_3 (830˚C). Therefore, the losses of sodium carbonate at this temperature are negligible.

It should be noted that the particles of the material obtained by this procedure have substantially smaller sizes and a more uniform shape than those obtained according to the methods described in the literature. Thus, the synthesis of $NaNdTiO_4$ at 750˚C makes it possible to obtain flaked particles 200 nm thick (Figure 22). At the same time the mean size of the particles obtained by the standard procedure is 1–4 μm. This fact cannot be underestimated taking into account the prospect of the use of $NaNdTiO_4$ as a catalyst.

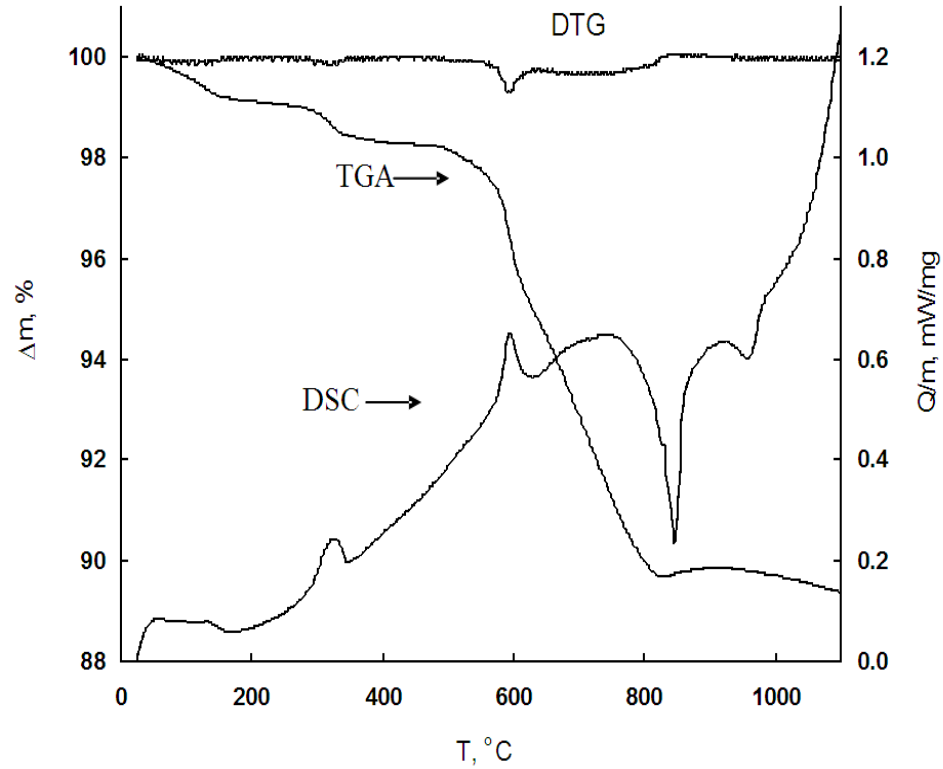

Figure 23. The DSC-TGA analysis of the reaction mixture during synthesis of $Na_2Nd_2Ti_3O_{10}$.

Another Ruddlesden-Popper phase in the Nd_2O_3–Na_2CO_3–TiO_2 system, $Na_2Nd_2Ti_3O_{10}$, attracted interest in the last years due to possible photocatalytic activity and ability to take part in the metathesis reactions [82,83]. The formation of this phase has been investigated at temperatures up to 1100°C by means of the X-ray diffraction and thermal analysis.

No chemical reactions take place in the Nd_2O_3–TiO_2–Na_2CO_3 mixture up to 500°C. Above 600°C $Na_4Ti_5O_{12}$ phase appear together with the traces of the perovskite-type $Na_{1/2}Nd_{1/2}TiO_3$. At 700°C $Na_8Ti_5O_{14}$ starts to form and the amount of $Na_{1/2}Nd_{1/2}TiO_3$ increases significantly. When the reaction mixture is heated further to 850°C the $Na_4Ti_5O_{12}$ disappears completely. At 900°C the Ruddlesden-Popper phases $NaNdTiO_4$ and $Na_2Nd_2Ti_3O_{10}$ appear. In the temperature range of 950–1050°C the amount of $Na_2Nd_2Ti_3O_{10}$ increases at the expense of $NaNdTiO_4$. At 1100°C the formation of $Na_2Nd_2Ti_3O_{10}$ is complete.

The DSC-TGA analysis (Figure 23) supports the data obtained under the isothermal heating conditions. The main mass loss (8.75%) is observed 550–820°C and can be attributed to the CO_2 evolution during the reactions involving Na_2CO_3. Four thermal effects can be found at the DTA curve. First of them appears at 325°C and can be attributed to the Nd_2O_3 dehydration. The second one at 594°C corresponds to the beginning of the solid-state reactions. The large exothermal peak at 845°C appears due to the series of reactions including the decomposition of $Na_4Ti_5O_{12}$ and the formation of $NaNdTiO_4$ and $Na_2Nd_2Ti_3O_{10}$. The last effect at 957°C corresponds to the decomposition of $NaNdTiO_4$.

The following reactions can be proposed for the formation of $Na_2Nd_2Ti_3O_{10}$:

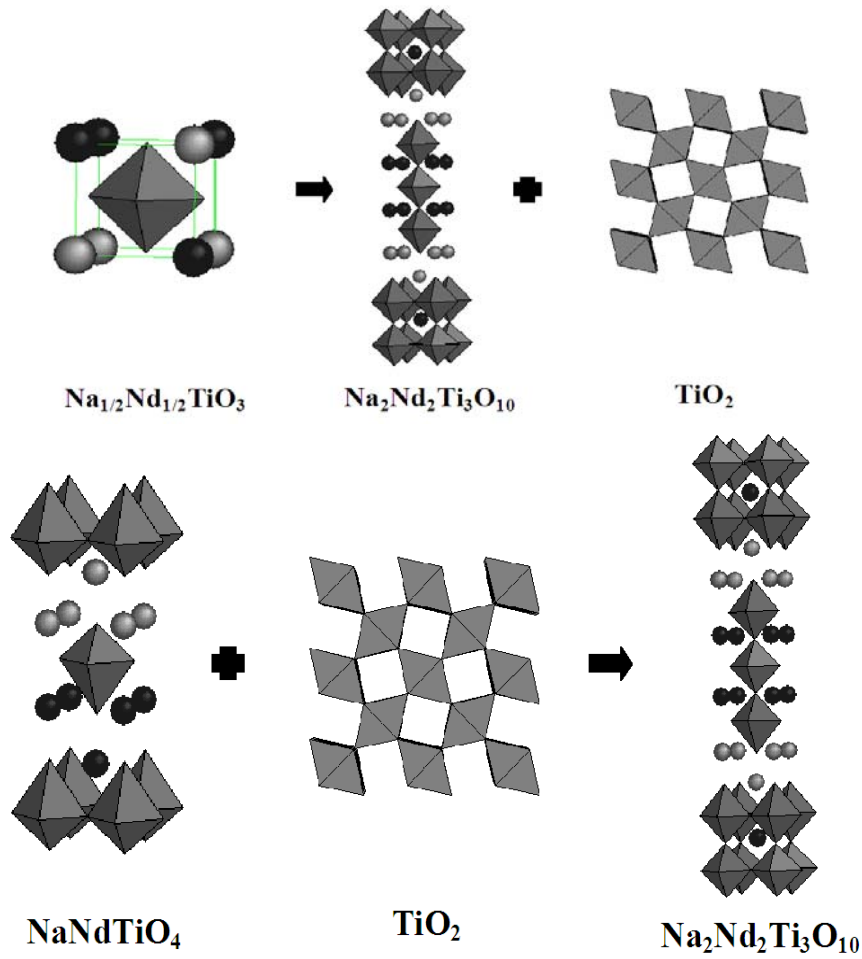

Figure 24. The structure transformations during the last stage of $Na_2Nd_2Ti_3O_{10}$ formation.

595°C $2\ Na_2CO_3 + 5\ TiO_2 \rightarrow\ Na_4Ti_5O_{12} + 2\ CO_2$ (36)

695°C
$Na_4Ti_5O_{12} + 2\ Na_2CO_3 \rightarrow Na_8Ti_5O_{14} + 2\ CO_2$ (37)
$7\ Na_4Ti_5O_{12} \rightarrow Na_8Ti_5O_{14} + 10\ Na_2Ti_3O_7$ (38)

600–820°C $Nd_2O_3 + 4\ TiO_2 + Na_2CO_3 \rightarrow 4\ Na_{1/2}Nd_{1/2}TiO_3 + CO_2$ (41)

825–895°C
$10/7Na_2Ti_3O_7 + 2Na_2O \rightarrow 6/7Na_8Ti_5O_{14},$ (39)
$2Na_8Ti_5O_{14} + 5Nd_2O_3 \rightarrow 10NaNdTiO_4 + 3Na_2O.$ (40)
$4\ Na_{1/2}Nd_{1/2}TiO_3 \rightarrow Na_2Nd_2Ti_3O_{10} + TiO_2$ (42)

960–1100°C $2\ NaNdTiO_4 + TiO_2 \rightarrow Na_2Nd_2Ti_3O_{10}$ (43)

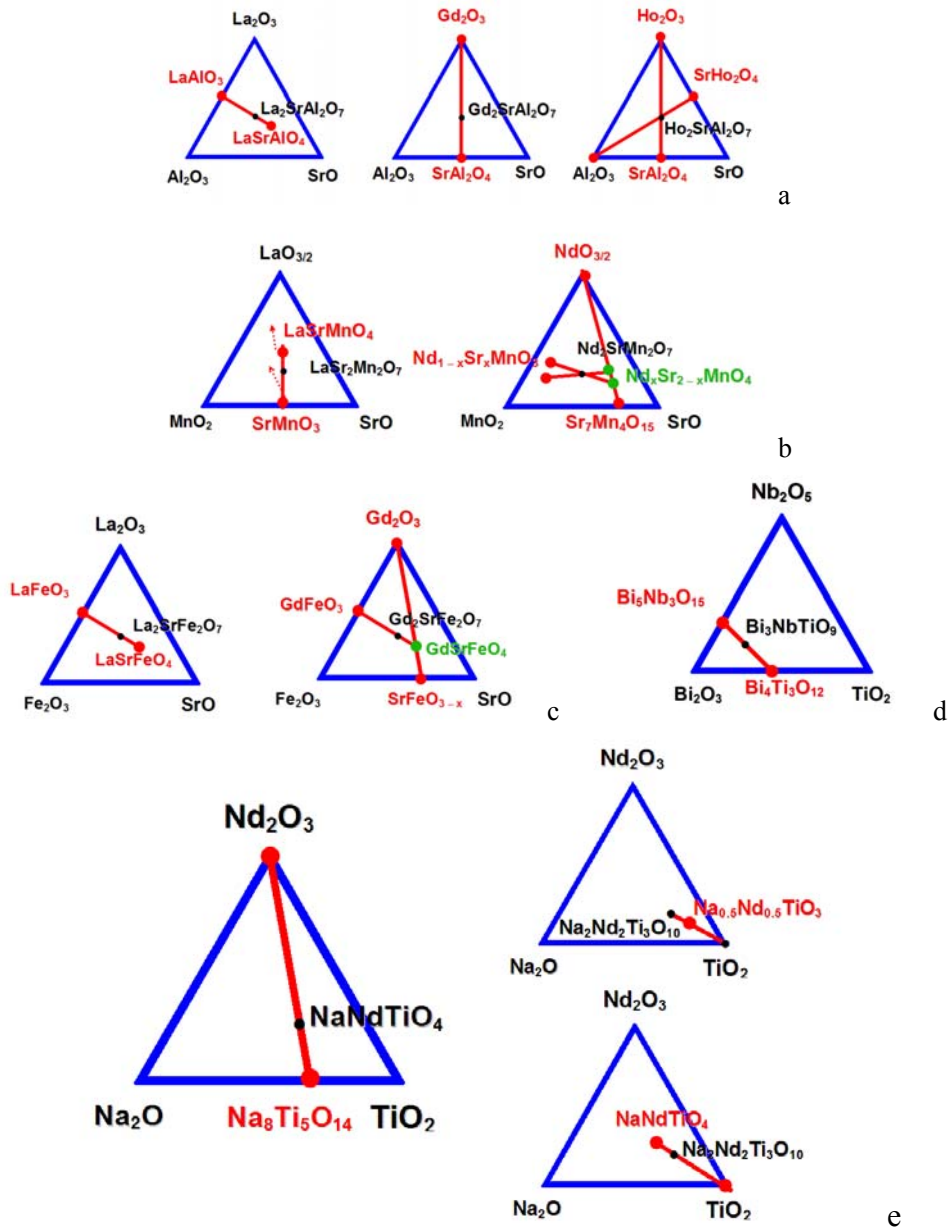

Figure 25. The reaction lines for the formation of different types of the layered perovskite-like oxides. a – double-layered Ruddlesden-Popper aluminates; b – double-layered Ruddlesden-Popper manganites; c – double-layered Ruddlesden-Popper ferrites; d – double-layered Aurivillius phases; e – single- and triple-layered Ruddlesden-Popper titanates.

The formation of $Na_2Nd_2Ti_3O_{10}$ goes by two ways: about 900°C $Na_{1/2}Nd_{1/2}TiO_3$ decomposes to form $Na_2Nd_2Ti_3O_{10}$ and TiO_2, while at 960°C $Na_2Nd_2Ti_3O_{10}$ is formed by interaction of $NaNdTiO_4$ and TiO_2 appearing at the previous stage. The structure transformations during these processes are shown at Figure 24.

It is interesting to note that during the formation of $Na_2Nd_2Ti_3O_{10}$ it is possible to observe the same reactions (36-40) as during the formation of $NaNdTiO_4$. However, the temperature necessary for these reactions is approximately 100°C higher (825–895°C instead of 780°C).

7. CONCLUSION

The formation of the layered perovskite-like oxides usually goes by a complex multistage way. The set of the intermediate compounds may strongly affect the properties of the final product or even the possibility of obtaining the pure phase. Some of the typical reaction pathways are shown at Figure 25. In the most cases the intermediates are compounds of the same family with simpler structure. However, if these compounds are not stable under the conditions of synthesis, the mechanism may become quite complex and unpredictable.

In the series of the phases containing chemically analogous elements the reaction rate changes regularly provided that the mechanism remains unchanged. On the other hand, change in the mechanism might result in the strong jump of the reaction rate.

On the whole, investigations of the process of formation of the layered perovskite-like compounds are very important for optimization of the synthesis conditions and in many cases may give explanation to the properties of the final product.

ACKNOWLEDGMENT

This work was partly supported by Russian Foundation for Basic Research (grant 09-03-00853).

REFERENCES

[1] Wells, A.F., Structural Inorganic Chemistry. Oxford: Oxford Univ. Press, 1986.

[2] Rao, C.N.R., Raveau, B. Transition metal oxides: structure, properties, and synthesis of ceramic oxides. Wiley-VCH, New York, Chichester, Weinheim, Brisbane, Singapore, Toronto, 1998.

[3] Zvereva, I., Smirnov, Yu., Gusarov, V., Popova, V., Choisnet, J. Complex aluminates $RE_2SrAl_2O_7$ (RE = La, Nd, Sm-Ho):Cation ordering and stability of the double perovskite slab-rocksalt layer P_2/RS intergrowth. *Solid State Sciences*. 2003, 5, 343-349.

[4] Smirnov, Yu. E., Zvereva, I. A., Cation Distribution and Interatomic Interactions in Oxides with Heterovalent Isomorphism: III. Complex Aluminates *Ln*$CaAlO_4$ (*Ln* =

Y, La, Nd, Gd, Ho, Er, Yb). *Russian Journal of General Chemistry*. 2001, 71, 845–852.

[5] Ruddlesden, S.N., Popper, P. New compounds of the K_2NiF_4 type. *Acta Crystallogr*. 1957, 10, 538-539.

[6] Ruddlesden, S.N., Popper, P. The compounds $Sr_3Ti_2O_7$ and its structure. *Acta Crystallogr*. 1958, 11, 54-55.

[7] Oudalov, Y.P., Daoudi, A., Jourbort, J.C., Le Flem, G., Hagenmuller P. Sur une nouvelle serie d'alluminates double de calcium et d'elements lanthanique de structure K_2NiF_4. *Bull. Soc. Chem. Fr*. 1970, 10, 3408-3411.

[8] Fava, J., Oudalov, Y.P., Reau, J.-M., Le Flem, G., Hagenmuller, P. Sur une nouvelle famille d'alluminates double de strontium ou d'europium divalent et de terres rares. *Compt. Rend*. 1972, C274, 1837-1839.

[9] Longo, J.M., Raccah, P.M. The structure of La_2CuO_4 and $LaSrVO_4$. *J. Solid State Chem*. 1973, 6, 526-531.

[10] Fava, J., Le Flem, G. Etude des oxide avec une structure lamellaire. *Mat. Res. Bull*. 1975, 10, 75-80.

[11] Demazeau, G., Pouchard, M., Hagenmuller P. Sur quelque nouveaux composes oxyges du Nickel +III de structure K_2NiF_4. *J. Solid State Chem*. 1976, 18, 159-162.

[12] Demazeau, G., Courbin, P., Main, J.C., Le Flem, G. Sur une nouvelle serie d'oxides du cobalt +III de structure K_2NiF_4. *Compt. Rend. Acan. Sci. Paris*. 1976, 233, 61-62.

[13] Fava, J., Danot, M., Dinh, N.T., Daoudi, A., Le Flem, G. Etude de radiocrystallographique et par resonance Mossbauer de $CaLaFeO_4$. *Solid State Comm*. 1977, 22, 733-736.

[14] Benabad, A., Daoudi, A., Salmon, R., Le Flem, G. Les phases $SrLnMnO_4$, $BaLnMnO_4$ $MnxLa_{1-x}MnO_4$. *J. Solid State Chem*. 1977, 22, 121-126.

[15] Bednorz, J.G., Muller, K.A. Possible high-T_c superconductivity in the Ba-La-Cu-O system. *J. Phys. B. Condesed Matter*. 1986, 64, 189-193.

[16] Soybeyroux, G.-L., Delmas, C. The 2D magnetic oxides. *J. Magn. Mat*. 1980, 15-18, 1315-1316.

[17] Le Flem, G., Demazeau, G., Hagenmuller, P. Relations between Structure and Physical properties in K_2NiF_4-type Oxides. *J. Solid State Chem*. 1982, 44, 82-88.

[18] Le Flem, G., Courbin, P., Delmas, C., Soybeyroux, J.-L. Magnetic properties of the 2D oxides. *Z. Anorg. Allg. Chem*. 1981, 476, 69-88.

[19] Ganguly, P., Rao, C.N.R. Crystal chemistry and magnetic properties of layered metal oxides possessing the K_2NiF_4 or related structure. *J. Solid State Chem*. 1984, 53, 193-216.

[20] Le Flem, G. Origine des couplages magnetique tridimensionelles dans les oxydes de type K_2NiF_4. *Compt. Rend. Acad. Sci. Paris*. 1982, 233, S.C., 29-32.

[21] Le Flem, G. Magnetic properties of ternary compounds. *Il nuova cimento*. 1983, 2B, 1814-1822.

[22] Mohan Ram, R.A., Singh, K.K., Madhusadan, W.H., Ganguly, P., Rao, C.N.R. Electronic and spin configurations of Co^{3+} and Ni^{3+} ions in oxides of K_2NiF_4 type structure: a magnetic susceptibility study. *Mat. Res. Bull*. 1983, I 8, 703-712.

[23] Kovba, M.L., Lukova, L.N., German, M.V., Antipov, E.V. Oxides with perovskite-type structure. *Russian Journal of General Chemistry*. 1986, 56, 1006-1014.

[24] Buttrey, D., Honig, J.M., Rao, C.N.R. Magnetic properties quasi-two-dimensional La_2NiO_4. *J. Solid State Chem*. 1986, 64, 287-295.

[25] Jorgensen, J.D., Dabrovski, B., Pei, S., Richrds, D.R., Hikks D.G. Structure of the interstitial oxygen defect in $La_2NiO_{4+\delta}$. *Phys. Rev. Bull*. 1989, 40, 2187-2199.

[26] Wada, S., Furukawa, Yu., Kaburagi, M., Kajitani, T., Mosoya, S., Yamada, Yo. Magnetic and electronic structure of antiferromagnetic LaNi oxide ($La_2NiLa_2NiO_{4+\delta}$) and LaSrNi oxide ($La_{2-x}Sr_xNiO_{4+\delta}$). *J. Phys.: Condens. Mater*. 1993, 5, 765-780.

[27] Fava, J., Le Flem, G., Les phases $SrLa_2Al_2O_7$ et $SrGd_2Al_2O_7$. *Mat. Res. Bull*. 1975, 10, 75-80.

[28] Oudalov, Y.P., Salmon, R, Bondar, I.A. System SrO-Nd_2O_3-Al_2O_3. *Russian Journal of Inorganic Chemistry*. 1976, 21, 541-546.

[29] Popova, V. F., Tugova, E. A., Isaeva, A. S., Zvereva, I. A., Gusarov, V. V. Phase Equilibria in the Ho_2O_3–$SrAl_2O_4$ System. *Glass Physics and Chemistry*. 2007, 33, 498

[30] Toda, K., Kameo, Y., Kurita, S., Sato, M. Crystal structure determination and ionic conductivity of layered perovskite compounds $NaLnTiO_4$ (Ln = rare earth). *Journal of Alloys Compd*. 1996, 234, 19-25.

[31] Byeon, S.-H., Park, K., Itoh, M. Structure and ionic conductivity of $NaLnTiO_4$; comparison with those of $Na_2Ln_2Ti_3O_{10}$ (Ln = La, Nd, Sm, and Gd). *J. Solid State Chem*. 1996, 121, 430-436.

[32] Schaak, R.E., Mallouk, T.E. $KLnTiO_4$ (Ln = La, Nd, Sm, Eu, Gd, Dy): A New Series of Ruddlesden-Popper Phases Synthesized by Ion-Exchange of $HLnTiO_4$. *J. Solid State Chem*. 2001, 161, 225-232.

[33] Sato, M., Toda, K., Watanabe, J., Uematsu, K. Structure determination and silver ion conductivity of layered perovskite compounds $M_2La_2Ti_3O_{10}$ (M = K and Ag). *J. Chem. Soc. Japan*. 1993, 640-646.

[34] Toda, K., Watanabe, J., Sato, M. Crystal structure determination of ion-exchangeable layered perovskite compounds, $K_2La_2Ti_3O_{10}$ and $Li_2La_2Ti_3O_{10}$. *Materials Research Bulletin*. 1996, 31, 1427-1435.

[35] Toda, K., Kameo, Y., Fujimoto, M., Sato, M. Crystal structure and ionic conductivity of a layered perovskite, $Na_2La_2Ti_3O_{10}$. *Journal of Ceram. Soc. Jpn*. 1994, 102, 737-741.

[36] Park, K., Byeon, S.-H. Correlation between structures and ionic conductivities of $Na_2Ln_2Ti_3O_{10}$ (Ln = La, Nd, Sm, and Gd). *Bulletin of the Korean Chemical Society*. 1996, 17, 168-172.

[37] Wright, A.J., Greaves, C. A neutron diffraction study of structural distortions in the Ruddlesden-Popper phase $Na_2La_2Ti_3O_{10}$. *Journal of Materials Chemistry*. 1996, 6, 1823-1825.

[38] Lalena, J.N., Falster, A.U., Simmons, W.B., Carpenter, E.E. Synthesis and characterization of new mixed-metal triple-layered perovskites, $Na_2La_2Ti_{3-x}Ru_xO_{10}$ ($x \leq 1.0$). *Chemistry of Materials*. 2000, 12, 2418-2423.

[39] Hong, Y.-S., Kim, K. New-type ordering behaviour in the layered perovskite compound $RbLa_2Ti_2NbO_{10}$. *Chemistry Letters*. 2000, 29, 690-691.

[40] Toda, K., Teranishi, T., Takahashi, M., Zuo-Guang, Ye Z.-G., Sato, M. Structural chemistry of new ion-exchangeable tantalates with layered perovskite structure: new

reduced Ruddlesden-Popper phase, $Na_2Ca_2Ta_3O_{10}$. *Solid State Ionics*. 1998, 113-115, 501-508.

[41] Blasse, G. New compounds with K_2NiF_4 structure. *J. Inorg. Nucl. Chem*. 1965, 27, 2683-2684.

[42] Battle, P.D., Green, M.A., Laskey, N.S., Millburn, J.E., Murphy, L., Rosseinsky, M.J., Sullivan, S.P., Vente, J.F. Layered Ruddlesden-Popper Manganese oxides: Synthesis and Cationic Ordering. *Chem. Mater*. 1997, 9, 552-559.

[43] Battle, P.D., Rosseinsky, M.J. Synthesis, structure, and magnetic properties of n = 2 Ruddlesden-Popper manganites. *Current Opinion in Solid State and Materials Science.* 1999, 4, 163-170.

[44] Dann, S.E., Welle,r M.T., Currie, D.B. Structure and Oxygen Stoichiometry in $Sr_3Fe_2O_{7-y}$, $0 \le y \le 1.0$. *J. Solid State Chem*. 1992, 97, 179-185.

[45] Seshadri, R., Martin, C., Maignan, A., Hervieru, M., Raveau, B. Structure and magnetotransport properties of layered manganites $RE_{1.2}Sr_{1.8}Mn_2O_7$ (RE = La, Pr, Nd). *J. Mater. Chem*. 1996, 6, 1585-1590.

[46] Floros, N., Hervieu, M., Van Tendeloo, G., Michel, C., Maignan, A., Raveau, B. The layered manganate $Sr_{4-x}Ba_xMn_3O_{10}$: synthesis, structural and magnetic properties. *Solid State sciences*. 2000, 2, 1-9.

[47] Siruguri, V., Ganguly, R., Krishna, P.S.R., Sastry, P.U., Paranjpe, S.K., Gopalakrishnan, I.K., Yakhmi, J.V. Stability of $Sr_3Ti_2O_7$ structure in $La_{1.2}(Sr_{1-x}Ca_x)_{1.8}Mn_2O_7$ and $Ca_{3-y}La_yMn_2O_7$. *J. Mater. Chem*. 2001, 11, 1158–1161.

[48] Yu, R.C., Zhu, J.L., Li, S.Y., Li, F.Y., Zhang, Z., Jin, C.Q., Voigt-Martin, I.G. HTEM studies on $La_{2-2x}Ca_{1+2x}Mn_2O_7$ (x = 0.5 and 0.25). *Materials Science and Engineering*. 2003, A345, 344-349.

[49] Kazanova, N.R., Kovba, M.L., Putilin, S.N., Antipov, E.V., Lebedev, O.I., Van Tendeloo, G. Synthesis, structure and properties of layered bismuthates: $(Ba,K)_3Bi_2O_7$ and $(Ba,K)_2BiO_4$. *Solid State Communications*. 2002, 122, 189-193.

[50] Dion, M., Ganne, M., Tournoux, M., Nouvelles familles de phases $M^IM^{II}_2Nb_3O_{10}$ a feuillets «perovskites». *Materials Research Bulletin*. 1981, 16, 1429-1435.

[51] Jacobson, A.J., Lewandowski, J.T., Johnson, J.W. Ion exchange of the layered perovskite $KCa_2Nb_3O_{10}$ by protons. *Journal of the Less-Common Metals*. 1986, 116, 137-145.

[52] Jacobson, A.J., Johnson, J.W., Lewandowski, J.T. Interlayer chemistry between thick transition-metal oxide layers: synthesis and intercalation reactions of $K[Ca_2Na_{n-3}Nb_nO_{3n+1}]$. *Inorg. Chem.* 1985, 24, 3727-3729.

[53] Thangadurai, V., Schmid-Beurmann, P., Weppner, W. Synthesis, Structure, and electrical conductivity of A'$[A_2B_3O_{10}]$ (A' = Rb, Cs; A = Sr, Ba; B = Nb, Ta): new members of Dion-Jacobson type layered perovskites. *J. Solid State Chem*. 2001, 158, 279-289.

[54] Hong, Y.-S., Han, C.-H., Kim, K. Structural characterization of new layered perovskites $MLa_2Ti_2TaO_{10}$ (M = Cs, Rb) and $NaLa_2Ti_2TaO_{10}{\cdot}xH_2O$ (x = 2, 0.9, 1.0). *J. Solid State Chem*. 2001, 158, 290-298.

[55] Hong, Y.-S., Kim, K. New-type ordering behaviour in the layered perovskite compound $RbLa_2Ti_2NbO_{10}$, *Chemistry Letters*. 2000, 29, 690-691.

[56] Aurivillius, B. Mixed bismuth oxides with layer lattices. I, II, and III. *Ark. Kemi*. 1949, 1, 463-471; 1949, 1, 499-512; 1950, 1, 519-528.

[57] Smolenski, G. A., Isupov, V. A., Agranovskaya, A. I., Ferroelectrics of the Oxygen-Octahedral Type With Layered Structure. *Sov. Phys. Solid State*. 1961, 3, 651-655

[58] Hervoches, H., Snedden, A., Riggs, R., Kilcoyne S.H., Manuel P., Lightfoot P. Structural Behavior of the Four-Layer Aurivillius-Phase Ferroelectrics $SrBi_4Ti_4O_{15}$ and $Bi_5T\ i_3FeO_{15}$. *J. Solid State Chem*. 2002, 164, 280-291.

[59] Pineda-Flores, J.L., Chavira, E., Huanosta-Tera, A. Ferroelectric characteristics in Aurivilius solid solutions: $Bi_{4-x}Ln_xTi_3O_{12}$ (Ln = Gd, Dy), $0 < x < 0.8$. *Physica C*. 2001, 364-365, 674-677.

[60] Boullay, Ph., Trolliard, G., Mercurio, D., Perez-Mato, J.M., Elcoro, L. Toward a unified approach to the crystal chemistry of Aurivillius-type compounds. *J. Solid State Chem*. 2002, 164, 252-271.

[61] Subbanna, G.N., Guru Row, T.N., Rao, C.N.R. Structure and dielectric properties of recurrent intergrowth structures formed by the Aurivillius family of bismuth oxides of the formula $Bi_2A_{n-1}B_nO_{3n+3}$. *J. Solid State Chem*. 1990, 86, 206-211.

[62] Zvereva, I. A., Popova, V. F., Vagapov, D. A., Toikka, A. M., Gusarov, V. V. Kinetics of Formation of Ruddlesden-Popper Phases: I. Mechanism of $La_2SrAl_2O_7$ Formation. *Russian Journal of General Chemistry*. 2001, 71, 1181-1185.

[63] Zvereva, I. A., Popova, V. F., Pylkina, N. S., Gusarov, V. V. Kinetics of Ruddlesden-Popper Phase Formation: II. Mechanism of $Nd_2SrAl_2O_7$ and $Sm_2SrAl_2O_7$ Formation. *Russian Journal of General Chemistry*. 2003, 73, 433-447

[64] Zvereva, I. A., Popova, V. F., Missyul, A. B., Gusarov, V. V. Kinetics of Ruddlesden-Popper Phase Formation: III. Mechanism of Formation of $Gd_2SrAl_2O_7$. *Russian Journal of General Chemistry*. 2003, 73, 684-688

[65] Isaeva, A. S., Kozhina, I. I., Toikka, A. M., Zvereva, I. A. Structural–Chemical Mechanism of Formation of Solid Solutions in the $La_2SrAl_2O_7$–$Ho_2SrAl_2O_7$ System. *Glass Physics and Chemistry*. 2006, 32, 106–112.

[66] Missyul, A. B., Marchenko, E. M., Popova, V. F., Zvereva, I. A. Mechanism and Kinetics of Formation of Solid Solutions in the $Nd_2SrAl_2O_7$–$Ho_2SrAl_2O_7$ System. *Glass Physics and Chemistry*. 2003, 29, 608–612.

[67] Tugova, E. A., Popova, V. F., Zvereva, I. A., Gusarov, V. V. Mechanism and Kinetics of Formation of $La_2SrFe_2O_7$ and $Nd_2SrFe_2O_7$. *Russian Journal of General Chemistry*. 2007, 77, 979-981.

[68] Zvereva, I. A., Otrepina, I. V., Semenov, V. G., Tugova, E. A., Popova, V. F., Gusarov, V. V. Mechanism of Formation of the Complex Oxide $Gd_2SrFe_2O_7$. *Russian Journal of General Chemistry*. 2007, 77, 973-978.

[69] Majewski, P., Benne, D., Epple, L., Aldinger, F. Phase equilibria in the system La_2O_3-SrO-Mn_3O_4 in air. Intern. *J. of Inorg. Materials*. 2001, 3, 1257–1259.

[70] Cherepanov, V. A., Barkhatova, L. Yu., Voronin, V. I. Phase Equilibria in the La-Sr-Mn-O System. *J. Solid State Chem*. 1997, 134, 38–44

[71] Kriegel, R., Feltz, A., Walz, L., Simon, A., Mattausch, H.-J. Über die Verbindung $Sr_7Mn_4O_{15}$ und Beziehungen zur Struktur von Sr_2MnO_4 und alpha-$SrMnO_3$. *Z. anor. allg. Chem*. 1992, 617, 99–104.

[72] Sharma Indu, B., Singh, D., Magotra, S.K. Effect of substitution of magnetic rare earths for La on the structure, electric transport and magnetic properties of $La_2SrFe_2O_7$. *J. Alloys Comp*. 1998, 269, 13-16.

[73] Drofenik, M., Kolar, D., Golic, L. Crystal growth and crystallographic study of $Eu_2SrFe_2O_7$. *Journal of Crystal Growth*. 1973, 20, 75-76.

[74] Darken, L.S., Gurry, R.W. The system iron-oxygen. I. The wüstite field and related equilibria. *J. Am. Chem. Soc.* 1945, 67, 1398.

[75] Otrepina, I. V., Volodin, V. S., Zvereva, I. A., Liu, J.-Sh. Investigation of the Formation of the $GdSrFeO_4$ Oxide. *Glass Physics and Chemistry*. 2009, 35, 423–430.

[76] Morozov, M. I., Gusarov, V. V. Synthesis of $A_{m-1}Bi_2M_mO_{3m+3}$ Compounds in the $Bi_4Ti_3O_{12}$–$BiFeO_3$ System. *Russian Journal of Inorganic materials*. 2002, 38, 723-729.

[77] Craiq, D. C., Stephenson, N. C. Structural studies of some body-centered cubic phases of mixed oxides involving Bi_2O_3: The structures of $Bi_{25}FeO_{40}$ and $Bi_{38}ZnO_{60}$. *J. Solid State Chem*. 1975, 15, 1-8.

[78] Bruton, T. M. Study of the liquidus in the system Bi_2O_3-TiO_2. *J. Solid State Chem*. 1974, 9, 173-175.

[79] Armstrong, R. A., Newnham, R. E. Bismuth titanate solid solutions. *Mat. Res. Bull*. 1972, 7, 1025-1034.

[80] Yu, W. J., Kim, Y. I., Ha, D. H., Lee, J. H., Park, Y. K., Seong, S., Hur, N. H. A new manganese oxide with the Aurivillius structure: $Bi_2Sr_2Nb_2MnO_{12-\delta}$. *Solid State Communications*. 1999, 111, 705–709.

[81] Zvereva, I. A., Silyukov, O. I., Markelov, A. V., Missyul, A. B., Chislov, M. V., Rodionov, I. A., Liu, J. Sh. Formation of the Complex Oxide $NaNdTiO_4$. *Glass Physics and Chemistry,* 2008, 34, 749–755.

[82] Richard, M., Brohan, L., Tournoux, M. Synthesis, characterization, and acid exchange of the layered perovskites: $A_2Nd_2Ti_3O_{10}$ (A=Na, K). Journal of Solid State Chemistry. 1994, 112, 345-354.

[83] Tai, Y.-W., Chen, J.-S., Yang, Ch.-C., Wan, B.-Z. Preparation of nano-gold on $K_2La_2Ti_3O_{10}$ for producing hydrogen from photo-catalytic water splitting. *Catalysis Today*. 2004, 97, 95-101.

Reviewed by Professor Jacques Choisnet, Laboratoire CRISMAT, CNRS ENSICAEN and Caen University, Fran*ce*

In: Perovskites: Structure, Properties and Uses
Editor: Maxim Borowski, pp. 377-435
ISBN 978-1-61668-525-6

Chapter 9

SOME THEORETICAL ASPECTS OF MAGNETIC STRUCTURE, SPIN EXCITATIONS AND MAGNETIZATION OF MANGANITES

B. V. Karpenko*
Institute of Physics of Metals, Ural Division, Russian Academy of Science,
Ekaterinburg 620041, Russia

ABSTRACT

The behavior of the system $La_{1-x}Ca_xMnO_3$ is considered theoretically at the absolute zero temperature (magnetic configurations), at the low temperatures (spin waves) and at the high temperatures (magnetization).

The appearance of the different magnetic configurations in the row $0 \le x \le 1$ is studied. Superexchange, double exchange and anisotropy energy are taken into account. The spin operator of double exchange interaction in crystal between ions with different valence Mn^{3+} and Mn^{4+} is the straight generalization of two - spin operator problem of Anderson – Hasegawa molecule. Ground state energy minimization gives 11 types of magnetic configurations: two ferromagnetic, three collinear antiferromagnetic and six non-collinear. When the concentration of Ca ions changes, then the spin configurations replace one another as the ground state. As a whole the sequence of configurations when x changes from 0 to 1 can be brought in correspondence to those observed at the experiment. The appearance of the angle configurations in the systems may occur if the Heisenberg and non – Heisenberg exchange exist simultaneously. The comparison with experiment was made by means of mixed procedure: part of the numerical values of interaction parameters and transition concentrations x were taken from the experiment while the missing values of these parameters were calculated with the help of the

* Data for correspondence: Karpenko Boris Victorovich. Senior scientific worker. Laboratory of Magnetic Semiconductors, Institute of Physics of Metals, Ural Division, Russian Academy of Science, 18 S. Kovalevskaya Street, Ekaterinburg 620041, Russia. E-mail: boris.karpenko@mail.ru

corresponding theoretical relations. The proposed dynamical alloy model of different spins can be used for description of real perovskite-like systems behavior.

The elementary spin excitations were studied in ferromagnets and antiferromagnets for the compounds with the special contents and theoretical dispersion curves were compared with experimental ones obtained by neutron inelastic scattering method for different directions in the first full Brillouin zone. Theoretical expressions are obtained for the spin-wave spectrum in a ferromagnetic cubic crystal with variable-valence ions. Interactions up to the fourth coordination shell are taken into account. Two kinds of exchange are assumed to occur in the system. As a result, the numerical values of total exchange parameters for each of the coordination shells can be found. These studies are made for ferromagnets at $x = 0.17,0.25,0.30$. Theoretical expressions are obtained for energy of spin waves in layered antiferromagnetic structure of the perovskite-like compound $LaMnO_3$. The quadratic exchange interactions of the central spin moment of the trivalent manganese ion with its eighteen neighbors from five coordination shells and single-ion magnetic anisotropy energy are taken into account. For the three principal crystallographic directions, the theoretical results are compared with the experimental data. It is shown that the in-plane ferromagnetic interaction can be more than sixteen times as great as the interplanar antiferromagnetic interaction.

The high temperature dependence of spontaneous magnetization at a separate site in the compounds with $0 \le x \le 1$ is investigated in the molecular field approximation using a homogeneous model for the magnetic sub-lattice with allowance for the Heisenberg and double exchange between nearest neighbors. Unlike with the usual magnets having one type of magnetic ions, in this case there appears a system of equations with two unknowns mean spins of manganese ions. In the vicinity of the ordering temperature, this system can be solved analytically and the expression for the ordering temperature can be obtained as well. To find the temperature dependence of magnetization in the whole temperature range the exact expression for the double exchange operator containing spin operators under square root was used. The numerical solutions were found in this case.

INTRODUCTION

It is already sixty years herovskite-like manganites continue to surprise the investigators by their unusual properties. The fundamental works [1-7], experimental and theoretical, gave the ground for subsequent studies. Up to now there are innumerable publications on this theme. The review articles [8-24] may help to navigate in this topic. So far there is no more or less common point of view on the physical essence of manganites. Therefore many results and approaches are in controversy.

In present paper it will be considered some particular problems concerning magnetic phases, elementary excitations and magnetization in manganites.

Regularly the perovskite-like manganese compounds were began to study as long as1950 years. Zener was the first who proposed the mechanism of indirect interaction of localized moments in crystal via conduction electrons [3, 4] and called it as double exchange. The experimental results by Jonker and van Santen [1, 2], that connected ferromagnetism and conductivity, were in full qualitative concordance with Zener's theory. The general idea of

Zener gave rise to appear two main approaches. The first is double exchange (DE) mechanism in the sense of Anderson and Hasegawa [6]. The second is the mechanism of indirect interaction by Ruderman-Kittel-Kasuya-Yosida (RKKY) [25-27].

DE and RKKY mechanisms use opposite initial approaches: if the DE is believed that the kinetic energy of the electron is small comparing with potential energy (interatomic exchange), but in RKKY - on the contrary, the kinetic energy (Fermi energy) is supposed to be substantially higher than the interatomic interactions. As a result RKKY mechanism leads to the effective interaction of localized moments of Heisenberg type, and DE – to non-Heisenberg one. So we can say that, DE is more suitable for semiconductors and RKKY - for metals. RKKY can lead both to ferromagnetic and antiferromagnetic interactions (the interaction of an oscillating type), while DE – only to ferromagnetic.

It must be said that the idea of a correlation between mobile and localized electrons appeared in the thirties of the last century and it was proposed by two soviet scientists Schubin and Vonsovsky in the paper [28]. In this model it is supposed that the localized electrons (d-electrons) are in magnetic order due to, for example, direct exchange interaction, while conduction electrons (s-electrons) are magnetized due to s-d interaction, which leads to a number of peculiarities in the behavior of the last. A detailed description of this model and the various effects that appear when it is used can be found in the monograph [29].

As stated above, there are large differences between the values of kinetic and potential energies in the different models, but in principle it is possible to imagine a situation where both the energy of one order of magnitude and then there appears a need to formulate new a mechanism for interaction.

With regard to the specific compounds of perovskite-like manganite, it is difficult in advance to give preference to any kind of exchange interactions that are realized in them. We can assume the existence of direct exchange interactions between magnetic cations, indirect interactions through anions (superexchange), the double exchange interaction and the interaction via phonons (as evidenced by isotopic effect). Below, if necessary, we will provide two types of exchange interactions: of Heisenberg and non-Heisenberg types. In doing so, for us it is unimportant by what interaction (direct or indirect) the Heisenberg effective spin Hamiltonian is caused. Under the non-Heisenberg Hamiltonian we will bear in mind the effective spin operator of the double exchange interaction. Only in the consideration of the dispersion curves for the spin-wave spectrum in $LaMnO_3$ the double exchange operator will not be available due to natural causes.

PART 1. MAGNETIC STRUCTURES

This part is written following the results of the papers [1, 2, 5-7, 30-40].

Since below the notion of the double exchange will be often used then it seems helpful to give the main features of this interaction mechanism.

1.1. Anderson-Hasegawa Molecule and Effective Spin Hamiltonian

So we shall briefly set main results for Anderson-Hasegawa molecule [6]. Let we have two centers a and b with localized on them $S_a = S_b = S$ and one additional electron (spin $\sigma = 1/2$), which can transfer from one center to another with transition integral $B > 0$. On each site spin $\vec{\sigma}$ is bound with spins $\vec{S}_a$ or $\vec{S}_b$ into rigid spin $S + 1/2$ due to Hund's rule (the exchange integral J). Then as it is shown in Ref. [6], the lower group of energy levels E at $J \to \infty$ is given by the expression

$$E = -\frac{1}{2}\frac{2S_0 + 1}{2S + 1}B, \tag{1.1}$$

where S_0 is the total molecule spin;

$$\vec{S}_0 = \vec{S}_a + \vec{S}_b + \vec{\sigma}. \tag{1.2}$$

S_0 takes $2S + 1$ values:

$$S_0 = 1/2, 3/2, ..2S + 1/2. \tag{1.3}$$

Each of these numbers is realized twice.
Let's consider the identity

$$S_0 = -\frac{1}{2} + \sqrt{1 + S(2S+3)}\sqrt{1 + \frac{2}{S(2S+3)}(\vec{S}_a + \vec{\sigma})\vec{S}_b}. \tag{1.4}$$

Then energy Eq. (1.1) can be treated as the eigenvalues of an effective spin operator

$$\hat{H}_D = -pB\sqrt{1 + q(\vec{S}_a + \vec{\sigma})\vec{S}_b}, \tag{1.5}$$

where

$$p = \frac{\sqrt{1 + S(2S+3)}}{2S+1}, q = \frac{2}{1 + S(2S+3)}. \tag{1.6}$$

(It is clear, that Eqs. (1.4) and (1.5) can be presented in symmetrized form.)

The operator $\widehat{H}_D$ from Eq. (1.5) we shall call the double exchange interaction operator. Its non-Heisenberg form is obvious. The operator $\widehat{H}_D$ represents interaction between rigid spins $S+1/2$ and S. Just in this form we shall use it considering the crystal.

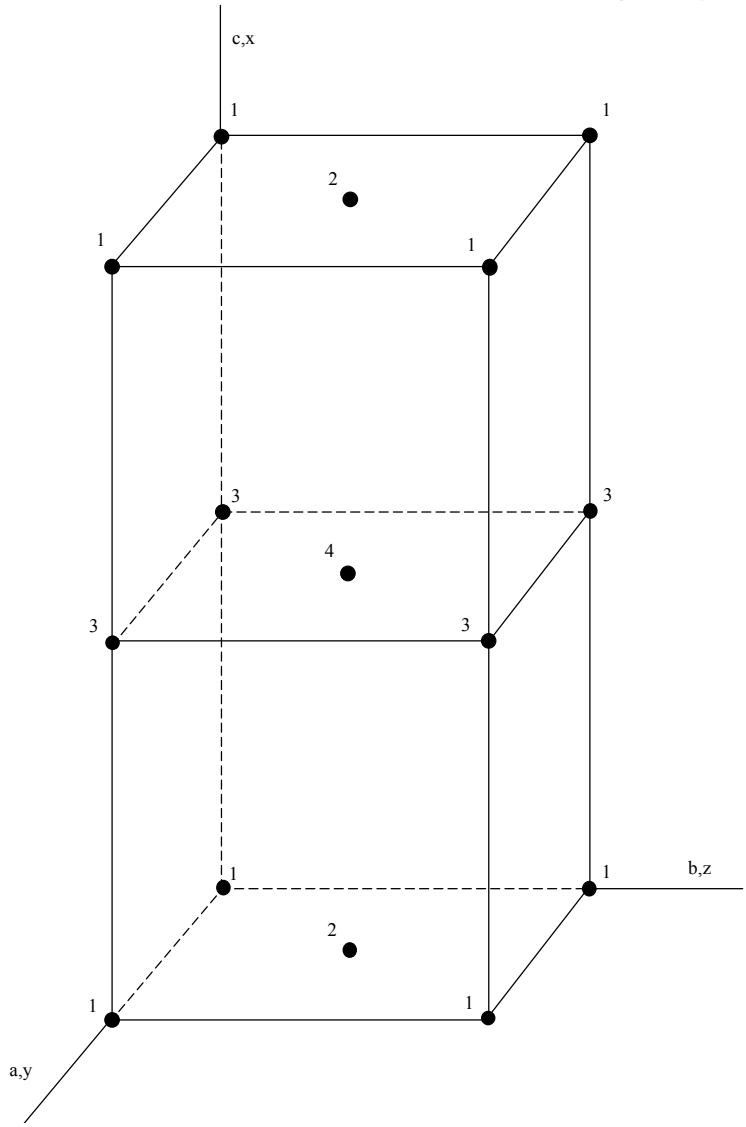

Figure 1.1. The elementary cell of $La_{1-x}Ca_xMnO_3$. Only Mn-sites are denoted. Figures 1-4 number Bravais lattices.

1.2. Hamiltonian for the Crystal

Let's write down the model Hamiltonian for the crystal. We shall use the homogeneous model for magnetic manganese sub-lattice in $La_{1-x}Ca_xMnO_3$, that is we shall suppose that each site in the manganese sub-lattice is occupied with probability x by ion Mn^{4+} and has

spin $S(Mn^{4+}) = 3/2$ and with probability $1-x$ - by ion Mn^{3+} and has spin $S(Mn^{3+}) = 2$. Thus our magnetic system represents a homogeneous dynamical spin alloy of rigid spins of $S_1 = 2$ and $S_2 = 3/2$. Further the nearest neighbor approximation will be used when each spin interacts with its nearest environment by means of two mechanisms: Heisenberg (quadratic) and non-Heisenberg (double exchange).

Let's assume that the compound $La_{1-x}Ca_xMnO_3$ has the $GdFeO_3$ type of structure in the whole range $0 \le x \le 1$. The elementary cell of orthorhombic lattice is presented on Figure 1.1 where only manganese ions sites are presented. Numbers 1, 2, 3, 4 enumerate four Bravais lattices. The base vectors of Bravais magnetic lattices (sub-lattices) are

$$\vec{\rho}_1 = 0, \vec{\rho}_2 = \frac{1}{2}(\vec{a}+\vec{b}), \vec{\rho}_3 = \frac{1}{2}\vec{c}, \vec{\rho}_4 = \frac{1}{2}(\vec{a}+\vec{b}+\vec{c}), \tag{1.7}$$

where $\vec{a}, \vec{b}$ and $\vec{c}$ are vectors of primitive translations for a simple orthorhombic lattice. Vectors of six nearest neighbors are given by the expressions

$$\vec{\Delta}_1 = \frac{1}{2}(\vec{a}+\vec{b}), \vec{\Delta}_2 = \frac{1}{2}(-\vec{a}+\vec{b}), \vec{\Delta}_3 = -\frac{1}{2}(\vec{a}+\vec{b}), \vec{\Delta}_4 = \frac{1}{2}(\vec{a}-\vec{b}), \tag{1.8}$$
$$\vec{\Delta}_5 = \frac{1}{2}\vec{c}, \vec{\Delta}_6 = -\frac{1}{2}\vec{c}.$$

Let's denote the integral of Heisenberg exchange between ions $Mn^{3+} - Mn^{3+}$ in (ab) - plane as I_1 (the nearest neighbors $\vec{\Delta}_1, \vec{\Delta}_2, \vec{\Delta}_3, \vec{\Delta}_4$), while that along c - axis as I_2 (the nearest neighbors $\vec{\Delta}_5$ and $\vec{\Delta}_6$). Similarly for interaction $Mn^{4+} - Mn^{4+}$ in (ab) - plane as I_3, while along c - axis as I_4. Interactions $Mn^{3+} - Mn^{4+}$ in (ab) - plane we shall denote as I_5, and along c - axis as I_6. The transfer integral between ions Mn^{3+} and Mn^{4+} in (ab) - plane let's be B_1, and along c - B_2. Besides we shall take into consideration anisotropy energy choosing b - axis as an easy one. We shall denote the anisotropy constant for ions Mn^{3+} as $K_1 > 0$, and for ions Mn^{4+} as $K_2 > 0$. Thus 10 interaction parameters are taken into account in our problem: $I_1, I_2, I_3, I_4, I_5, I_6, B_1, B_2, K_1$ and K_2.

With regard for all stated above let's write down spin Hamiltonian $\hat{H}$ in the form:

$$\hat{H} = \hat{H}_{1ex} + \hat{H}_{2ex} + \hat{H}_a, \tag{1.9}$$

where

$$\widehat{H}_{1ex} = \sum_{\vec{m}} \sum_{k=1}^{4} \sum_{i=1}^{6} \sum_{n=1}^{2} \sum_{l=1}^{2} I_{nl}(\vec{\Delta}_i) \vec{S}_n(\vec{m} + \vec{\rho}_k) \vec{S}_l(\vec{m} + \vec{\rho}_k + \vec{\Delta}_i), \tag{1.10}$$

$$\widehat{H}_{2ex} = -\sum_{\vec{m}} \sum_{k=1}^{4} \sum_{i=1}^{6} \sum_{n=1}^{2} \sum_{l=1}^{2} B_{nl}(\vec{\Delta}_i) \sqrt{1 + \frac{2\vec{S}_n(\vec{m} + \vec{\rho}_k)\vec{S}_l(\vec{m} + \vec{\rho}_k + \vec{\Delta}_i)}{1 + S(2S+3)}}, \tag{1.11}$$

$$\widehat{H}_a = -\sum_{\vec{m}} \sum_{k=1}^{4} \sum_{n=1}^{2} A_n (S_n^z(\vec{m} + \vec{\rho}_k))^2. \tag{1.12}$$

Here $\widehat{H}_{1ex}$ is the operator of Heisenberg exchange interaction, $\widehat{H}_{2ex}$ is the operator of double exchange and $\widehat{H}_a$ is the operator of anisotropy energy. The summation over $\vec{m}$ in Eqs. (1.10-1.2) is led upon N sites of sub-lattice (the whole number of sites is $4N$). Sum over index k means summing over four sub-lattices. Index i numbers the nearest neighbors. Indexes n and l distinguish ions $Mn^{3+}(n,l=1)$ and $Mn^{4+}(n,l=2)$. In this case we have $S_1 = S + 1/2$ (spin on ion Mn^{3+}) and $S_2 = S$ (spin of ion $Mn^{4+}, S = 3/2$). The following notations are introduced also in Eqs. (1.10-1.2):

$$I_{11}(\vec{\Delta}_i) = (1-x)^2 I_1; i = 1,2,3,4. \tag{1.13}$$

$$I_{11}(\vec{\Delta}_i) = (1-x)^2 I_2; i = 5,6. \tag{1.14}$$

$$I_{22}(\vec{\Delta}_i) = x^2 I_3; i = 1,2,3,4. \tag{1.15}$$

$$I_{22}(\vec{\Delta}_i) = x^2 I_4; i = 5,6. \tag{1.16}$$

$$I_{12}(\vec{\Delta}_i) = I_{21}(\vec{\Delta}_i) = x(1-x) I_5; i = 1,2,3,4. \tag{1.17}$$

$$I_{12}(\vec{\Delta}_i) = I_{21}(\vec{\Delta}_i) = x(1-x) I_6; i = 5,6. \tag{1.18}$$

$$B_{11}(\vec{\Delta}_i) = B_{22}(\vec{\Delta}_i) = 0. \tag{1.19}$$

$$B_{12}(\vec{\Delta}_i) = B_{21}(\vec{\Delta}_i) = x(1-x)\sqrt{\frac{S+1}{2S+1}} B_1; i = 1,2,3,4. \tag{1.20}$$

$$B_{12}(\vec{\Delta}_i)=B_{21}(\vec{\Delta}_i)=x(1-x)\sqrt{\frac{S+1}{2S+1}}B_2;i=5,6. \tag{1.21}$$

$$A_1=(1-x)K_1, A_2=xK_2. \tag{1.22}$$

The double exchange operator $\widehat{H}_{2ex}$ from Eq. (1.11) in the limit case of two sites goes to operator of Eq. (1.5) of Anderson-Hasegawa molecule.

For the following analysis it is convenient to introduce local coordinate systems according to Euler formulas for direction cosines α_{ij}:

$$\begin{aligned}
&\alpha_{11}=-\sin\phi\cos\chi-\cos\theta\cos\phi\sin\chi,\\
&\alpha_{12}=\cos\phi\cos\chi-\cos\theta\sin\phi\sin\chi,\\
&\alpha_{13}=\sin\theta\sin\chi,\\
&\alpha_{21}=\sin\phi\sin\chi,\\
&\alpha_{22}=-\cos\phi\sin\chi-\cos\theta\sin\phi\cos\chi,\\
&\alpha_{23}=\sin\theta\cos\chi,\\
&\alpha_{31}=\sin\theta\cos\phi,\\
&\alpha_{32}=\sin\theta\sin\phi,\\
&\alpha_{33}=\cos\theta.
\end{aligned} \tag{1.23}$$

Later we shall not investigate dependence upon angle χ, leaving only polar and azimuth angles θ and ϕ, leaving $\chi=0$. This is our model suggestion. So, we have

$$S_n^{x_i}(\vec{m}+\vec{\rho}_k)=\sum_{j=1}^{3}\alpha_{ji}(k)S_n^{\xi_j(\vec{\rho}_k)}(\vec{m}+\vec{\rho}_k), x_1\equiv x, x_2\equiv y, x_3=z. \tag{1.24}$$

When substitute Eq. (1.24) into Eqs. (1.10-1.12), we obtain

$$\widehat{H}_{1ex}=-\sum_{\vec{m}}\sum_{k=1}^{4}\sum_{i=1}^{6}\sum_{n=1}^{2}\sum_{l=1}^{2}I_{nl}(\vec{\Delta}_i)\sum_{\delta=1}^{3}\sum_{\lambda=1}^{3}\beta_{\delta\lambda}(\vec{\rho}_k,\vec{\Delta}_i)\times, \tag{1.25}$$
$$\times S_n^{\xi\delta(\vec{\rho}_k)}(\vec{m}+\vec{\rho}_k)S_l^{\xi\lambda(\vec{\rho}_k+\vec{\Delta}_i)}(\vec{m}+\vec{\rho}_k+\vec{\Delta}_i)$$

$$\widehat{H}_{2ex}=-\sum_{\vec{m}}\sum_{k=1}^{4}\sum_{i=1}^{6}\sum_{n=1}^{2}\sum_{l=1}^{2}B_{nl}(\vec{\Delta}_i)\times \tag{1.26}$$
$$\times\sqrt{1+\frac{2\sum_{\delta,\lambda=1}^{3}\beta_{\delta\lambda}(\vec{\rho}_k,\vec{\Delta}_i)S_n^{\xi_\delta(\vec{\rho}_k)}(\vec{m}+\vec{\rho}_k)S_l^{\xi_\lambda(\vec{\rho}_k+\vec{\Delta}_i)}(\vec{m}+\vec{\rho}_k+\vec{\Delta}_i)}{(S+1)(2S+1)}},$$

$$\widehat{H}_a = -\sum_{\vec{m}} \sum_{k=1}^{4} \sum_{n=1}^{2} A_n \Big(\sum_{\delta=1}^{3} \alpha_{\delta 3}(\vec{\rho}_k) S_n^{\xi\delta(\vec{\rho}_k)}(\vec{m}+\vec{\rho}_k) \Big)^2, \tag{1.27}$$

where

$$\beta_{\delta\lambda}(\vec{\rho}_k, \vec{\Delta}_i) = \sum_{r=1}^{3} \alpha_{\delta r}(\vec{\rho}_k) \alpha_{\lambda r}(\vec{\rho}_k + \vec{\Delta}_i). \tag{1.28}$$

Eqs. (1.9, 1.25-1.28) present the final form of our Hamiltonian.

1.3. Ground State Energies of Different Magnetic Configurations

Here we shall confine ourselves only to the case of absolute zero temperature. In order to consider energies of ground states we shall use the formula

$$S_n^{\xi_j(\vec{\rho}_k)}(\vec{m}+\vec{\rho}_k) = \delta_{j3} S_n, \; n = 1,2 . \tag{1.29}$$

Substituting Eq.(1.29) into Eqs.(1.9, 1.25-1.27), we obtain for the ground state energy E the expression

$$\begin{aligned} E = &-N\{a[\beta(12)+\beta(34)]+b[\beta(13)+\beta(24)]+ \\ &+c[\alpha^2(1)+\alpha^2(2)+\alpha^2(3)+\alpha^2(4)]+ \\ &+8Q[2(\sqrt{1+\gamma\beta(12)}+\sqrt{1+\gamma\beta(34)})B_1+ \\ &+(\sqrt{1+\gamma\beta(13)}+\sqrt{1+\gamma\beta(24)})B_2]\}, \end{aligned} \tag{1.30}$$

where

$$a = 8[(1-x)^2 S_1^2 I_1 + x^2 S_2^2 I_3 + 2x(1-x) S_1 S_2 I_5], \tag{1.31}$$

$$b = 4[(1-x)^2 S_1^2 I_2 + x^2 S_2^2 I_4 + 2x(1-x) S_1 S_2 I_6], \tag{1.32}$$

$$c = (1-x) S_1^2 K_1 + x S_2^2 K_2, \tag{1.33}$$

$$Q = x(1-x)\sqrt{\frac{S+1}{2S+1}}, \gamma = \frac{S}{S+1}, \tag{1.34}$$

$$\begin{aligned} &\alpha(i) = \cos\theta_i, \\ &\beta(ij) = \sin\theta_i \sin\theta_j \cos(\phi_i - \phi_j) + \cos\theta_i \cos\theta_j; i, j = 1,2,3,4. \end{aligned} \tag{1.35}$$

Indexes i, j number sub-lattices.

The energy of Eq. (1.30) is minimal at angles θ and ϕ, satisfying eight equations:

$$\frac{\partial E}{\partial \theta_1}=\frac{\partial E}{\partial \theta_2}=\frac{\partial E}{\partial \theta_3}=\frac{\partial E}{\partial \theta_4}=\frac{\partial E}{\partial \phi_1}=\frac{\partial E}{\partial \phi_2}=\frac{\partial E}{\partial \phi_3}=\frac{\partial E}{\partial \phi_4}=0. \tag{1.36}$$

The system (1.36) has the following solutions.

$$A:\phi_1=\phi_2=\phi_3=\phi_4=\phi;\theta_1=\theta_2=0,\theta_3=\theta_4=\pi. \tag{1.37}$$

$$A_1:\phi_1=\phi_2=\phi_3=\phi_4=\phi,\theta_1=\theta_2=\frac{1}{2}\arccos h,\theta_3=\theta_4=\pi-\theta_1. \tag{1.38}$$

$$A_2:\phi_1=\phi_2=\phi,\phi_3=\phi_4=\phi\pm\pi,\theta_1=\theta_2=\theta_3=\theta_4=\frac{1}{2}\arccos(-h_1). \tag{1.39}$$

$$B:\phi_1=\phi_2=\phi_3=\phi_4=\phi,\theta_1=\theta_2=\theta_3=\theta_4=0. \tag{1.40}$$

$$B':\phi_1=\phi_2=\phi_3=\phi_4=\phi,\theta_1=\theta_2=\theta_3=\theta_4=\pi/2. \tag{1.41}$$

$$C:\phi_1=\phi_2=\phi_3=\phi_4=\phi,\theta_1=\theta_3=0,\theta_2=\theta_4=\pi. \tag{1.42}$$

$$C_1:\phi_1=\phi_2=\phi_3=\phi_4=\phi,\theta_1=\theta_3=\frac{1}{2}\arccos g,\theta_2=\theta_4=\pi-\theta_1. \tag{1.43}$$

$$C_2:\phi_1=\phi_3=\phi,\phi_2=\phi_4=\phi\pm\pi,\theta_1=\theta_2=\theta_3=\theta_4=\frac{1}{2}\arccos(-g_1). \tag{1.44}$$

$$G:\phi_1=\phi_2=\phi_3=\phi_4=\phi,\theta_1=\theta_4=0,\theta_2=\theta_3=\pi. \tag{1.45}$$

$$G_1:\phi_1=\phi_2=\phi_3=\phi_4=\phi,\theta_1=\theta_4=\frac{1}{2}\arccos h_2,\theta_2=\theta_4=\pi-\theta_1. \tag{1.46}$$

$$G_2:\phi_1=\phi_4=\phi,\phi_2=\phi_3=\phi\pm\pi,\theta_1=\theta_2=\theta_3=\theta_4=\frac{1}{2}\arccos(-g_2). \tag{1.47}$$

(Angle ϕ is arbitrary. Here and below symbols A, B, C, G introduced by Wollan and Koehler in Ref. [5] are used in order to denote spin configurations.) The following notations are input above:

$$h=\frac{1}{\gamma}\left[1-\left(\frac{f}{b-c}\right)^2\right], \tag{1.48}$$

$$h_1=\frac{1}{\gamma}\left[1-\left(\frac{f}{b+c}\right)^2\right], \tag{1.49}$$

$$g=\frac{1}{\gamma}\left[1-\left(\frac{d}{a-c}\right)^2\right], \tag{1.50}$$

$$g_1=\frac{1}{\gamma}\left[1-\left(\frac{d}{a+c}\right)^2\right], \tag{1.51}$$

$$h_2=\frac{1}{\gamma}\left[1-\left(\frac{d+f}{a+b-c}\right)^2\right], \tag{1.52}$$

$$g_2=\frac{1}{\gamma}\left[1-\left(\frac{d+f}{a+b+c}\right)^2\right], \tag{1.53}$$

Where

$$d=\frac{8Sx(1-x)B_1}{\sqrt{(S+1)(2S+1)}}, \tag{1.54}$$

$$f=\frac{4Sx(1-x)B_2}{\sqrt{(S+1)(2S+1)}}. \tag{1.55}$$

We have for energies of the corresponding states $\varepsilon = E/4N$

$$\varepsilon_A=-\frac{1}{2}\left[a-b+2c+8\left(2B_1+\frac{B_2}{\sqrt{2S+1}}\right)x(1-x)\right], \tag{1.56}$$

$$\varepsilon_{A_1} = -\frac{1}{2}\left[a - \frac{S+1}{S} b + \frac{2S+1}{S} c + 16B_1 x(1-x) - \frac{16B_2^2 S}{(2S+1)(b-c)} x^2 (1-x)^2 \right],$$

$$b - c < 0, \tag{1.57}$$

$$\varepsilon_{A_2} = -\frac{1}{2}\left[a - \frac{S+1}{S} b - \frac{1}{S} c + 16B_1 x(1-x) - \frac{16SB_2^2}{(2S+1)(b+c)} x^2 (1-x)^2 \right],$$

$$b + c < 0, \tag{1.58}$$

$$\varepsilon_B = -\frac{1}{2}\left[a + b + 2c + 8(2B_1 + B_2) x(1-x) \right], \tag{1.59}$$

$$\varepsilon_{B'} = -\frac{1}{2}\left[a + b + 8(2B_1 + B_2) x(1-x) \right], \tag{1.60}$$

$$\varepsilon_C = -\frac{1}{2}\left[-a + b + 2c + 8\left(\frac{2B_1}{\sqrt{2S+1}} + B_2 \right) x(1-x) \right], \tag{1.61}$$

$$\varepsilon_{C_1} = -\frac{1}{2}\left[-\frac{S+1}{S} a + b + \frac{2S+1}{S} c - \frac{64SB_1^2}{(2S+1)(a-c)} x^2 (1-x)^2 + 8B_2 x(1-x) \right],$$

$$a - c < 0, \tag{1.62}$$

$$\varepsilon_{C_2} = -\frac{1}{2}\left[-\frac{S+1}{S} a + b - \frac{1}{S} c - \frac{64SB_1^2}{(2S+1)(a+c)} x^2 (1-x)^2 + 8B_2 x(1-x) \right],$$

$$a + c < 0, \tag{1.63}$$

$$\varepsilon_G = -\frac{1}{2}\left[-a - b + 2c + \frac{8}{\sqrt{2S+1}} (2B_1 + B_2) x(1-x) \right], \tag{1.64}$$

$$\varepsilon_{G_1} = -\frac{1}{2}\left[-\frac{S+1}{S} a - \frac{S+1}{S} b + \frac{2S+1}{S} c - \frac{16S(2B_1 + B_2)^2}{(2S+1)(a+b-c)} x^2 (1-x)^2 \right],$$

$$a + b - c < 0, \tag{1.65}$$

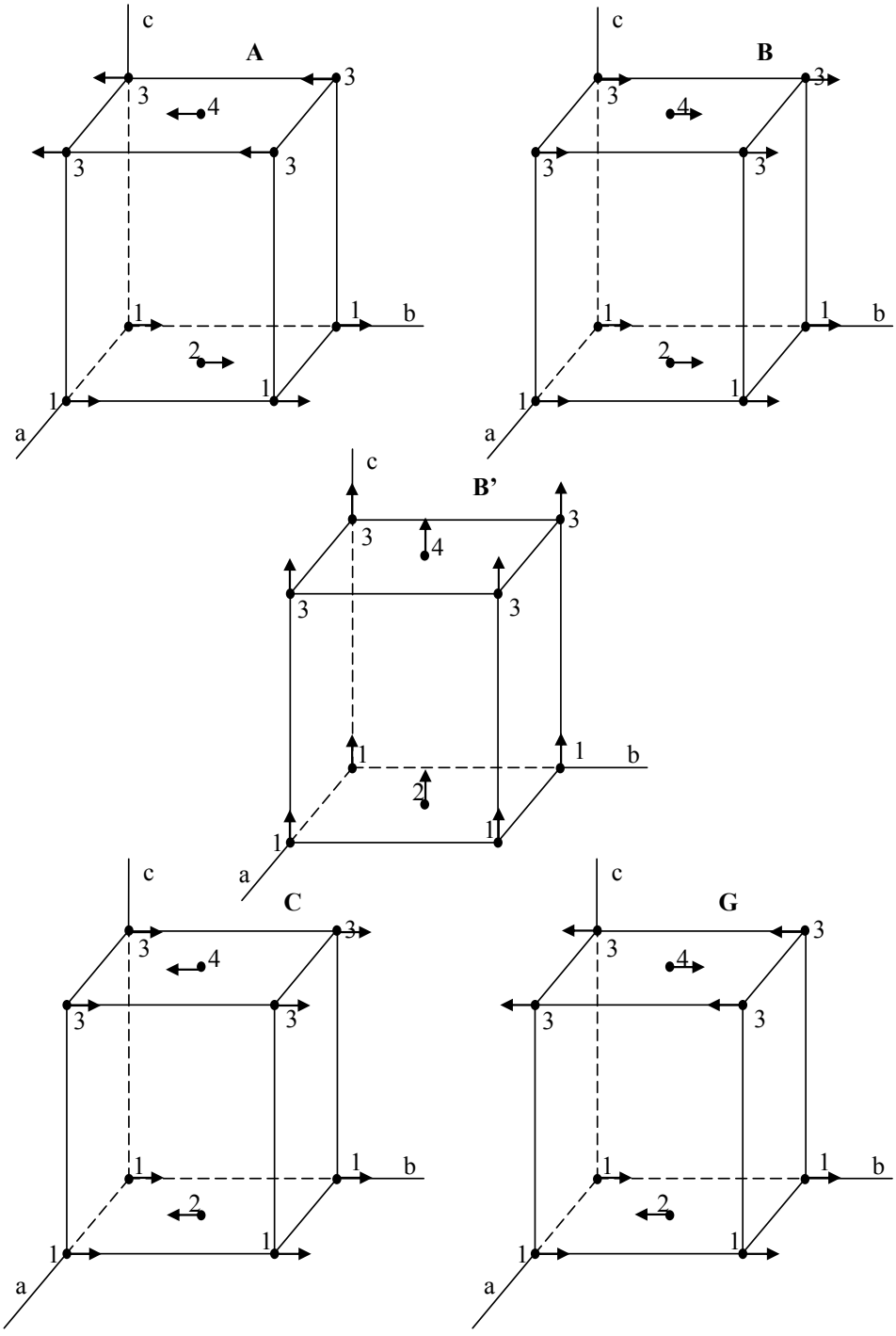

Figure 1.2. Collinear magnetic configurations A, B, B', C, G. Arrows denote the site spins.

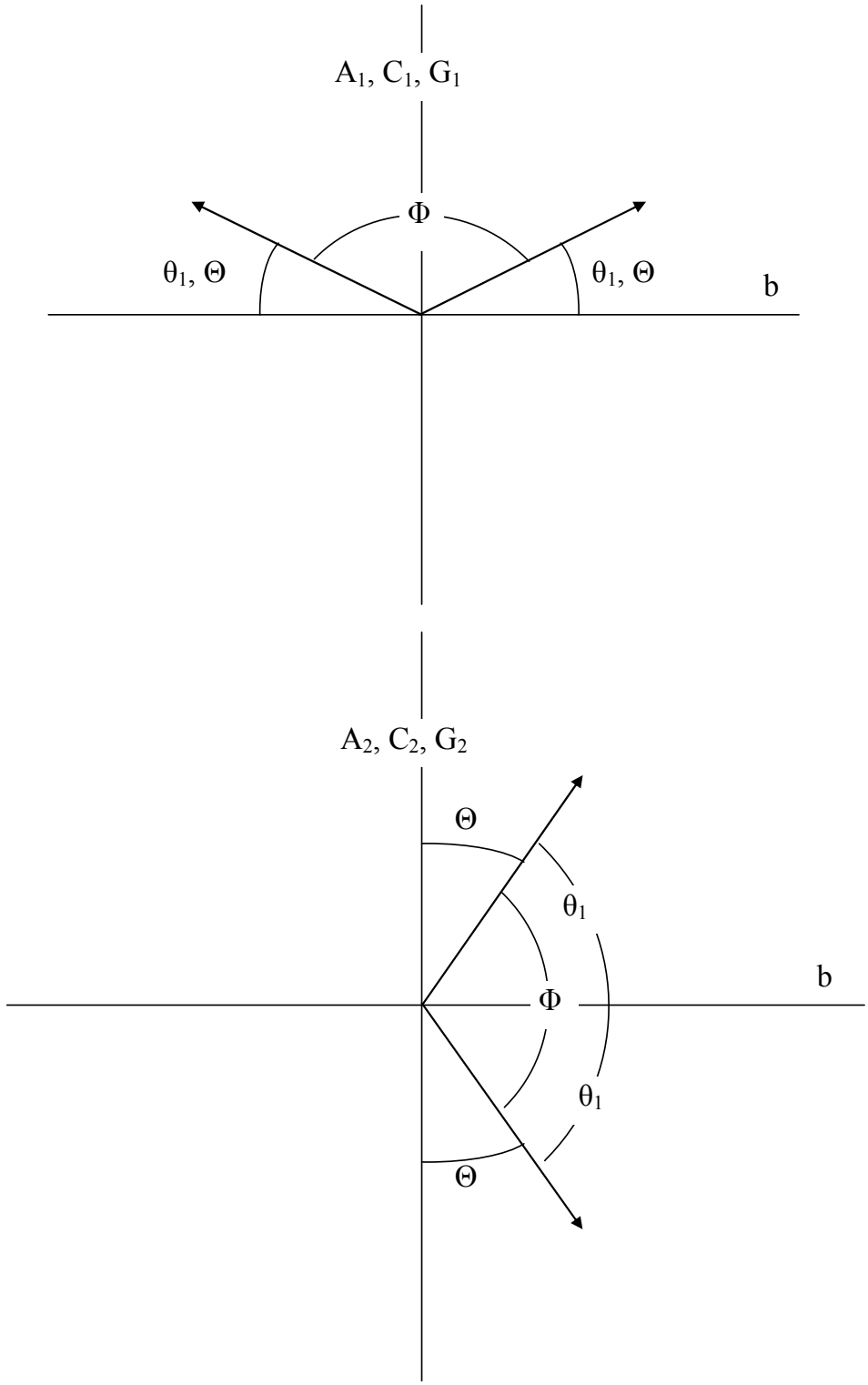

Figure 1.3. The ordering of sub-lattice moments in angle configurations A_1, C_1, G_1 and A_2, C_2, G_2.

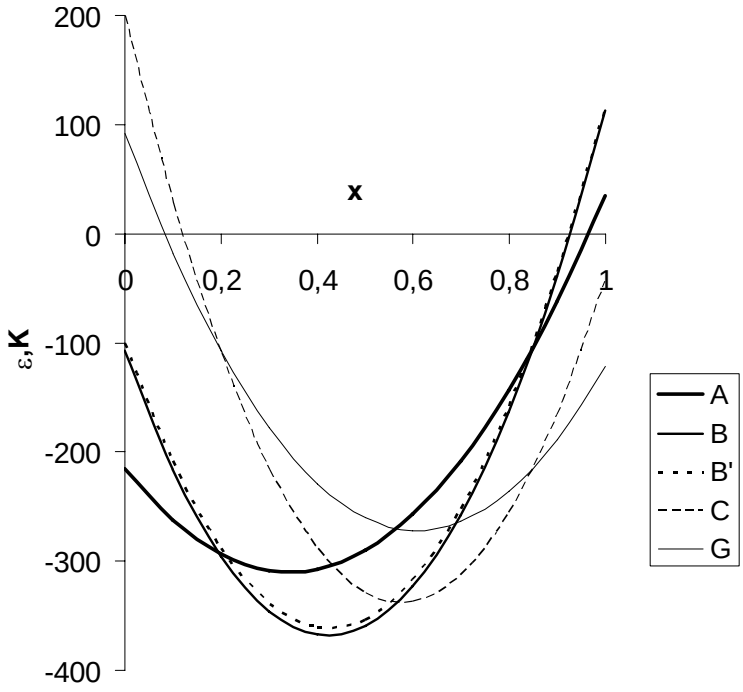

Figure 1.4. Energies $\varepsilon(x)$ for collinear structures A, B, B', C, G.

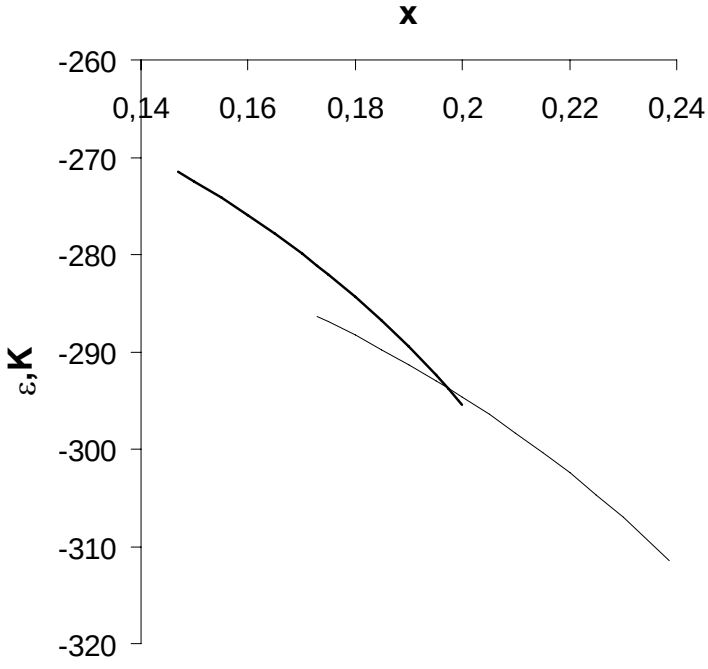

Figure 1.5. Energies $\varepsilon(x)$ for non-collinear structures A_1 (thin line) and A_2 (thick line).

$$\varepsilon_{G_2} = -\frac{1}{2}\left[-\frac{S+1}{S}a - \frac{S+1}{S}b - \frac{1}{S}c - \frac{16S(2B_1+B_2)^2}{(2S+1)(a+b+c)}x^2(1-x)^2\right], \quad (1.66)$$

$a+b+c<0.$

Thus we have obtained five collinear magnetic configurations two of which (B and B') are ferromagnetic while three are antiferromagnetic (A, C and G), and also six non-collinear structures ($A_1, A_2, C_1, C_2, G_1, G_2$). In the ferromagnetic phase B vector of magnetization is directed along the easy axis b, while in ferromagnetic phase B' vector of magnetization is perpendicular to axis b. The collinear phases A, B, B', C, G are depicted in Figure 1.2. In A state each spin is surrounded by four parallel to it spins and two antiparallel. In C state the surrounding consists of two parallel and four antiparallel spins. In configuration G all six nearest neighboring spins are antiparallel to the central spin. The figure shows that in B' state spins are parallel to c-axis, however this is not necessarily – they must only lie in the (ac)-plane. In non-collinear phases A_1, C_1, G_1 vectors of spin sub-lattices are situated symmetrically with respect to the b -axis normal, while in configurations A_2, C_2, G_2 the sub-lattices spins are situated symmetrically with respect to b -axis as it is shown in Figure 1.3. On this Figure Θ is the angle of non-collinearity (the angle of canting), and Φ is the angle between sub-lattice vectors.

The energies in Eqs. (1.56-1.66) as the functions of concentration x are shown in Figures 1.4, 1.5, 1.6, 1.7 at certain values of interaction parameters (see the next section).

1.4. Comparison with Experiment

Numerous experiments demonstrate that with increase of x in $La_{1-x}Ca_xMnO_3$ magnetic configurations change each other. Being guided the results of Refs. [1, 2, 5, 30-38] we can suppose the following scheme of magnetic transitions when x changes from 0 till 1:

$$A \to A_1 \to A_2 \to B \to C_2 \to C_1 \to C \to G. \quad (1.67)$$

The following equations should be held in the transition points

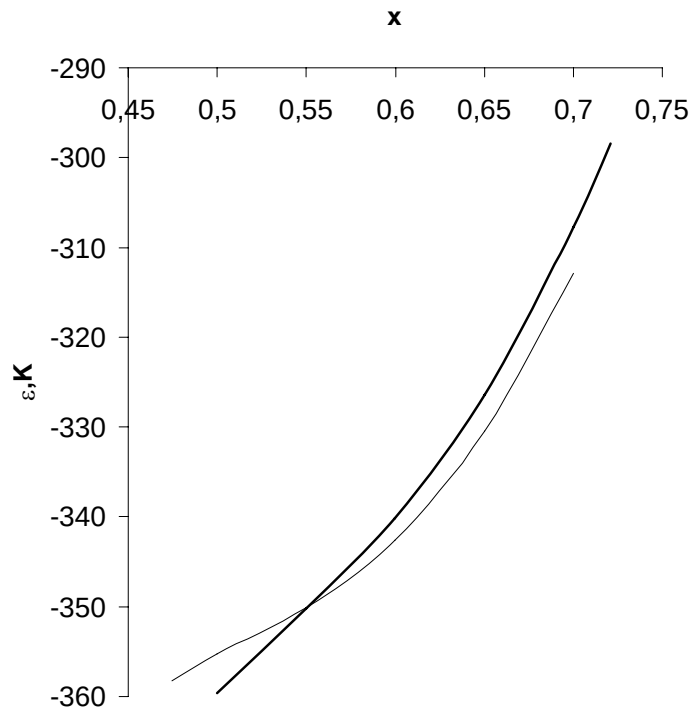

Figure 1.6. Energies $\varepsilon(x)$ or non-collinear structures C_1 (thin line) and C_2 (thick line).

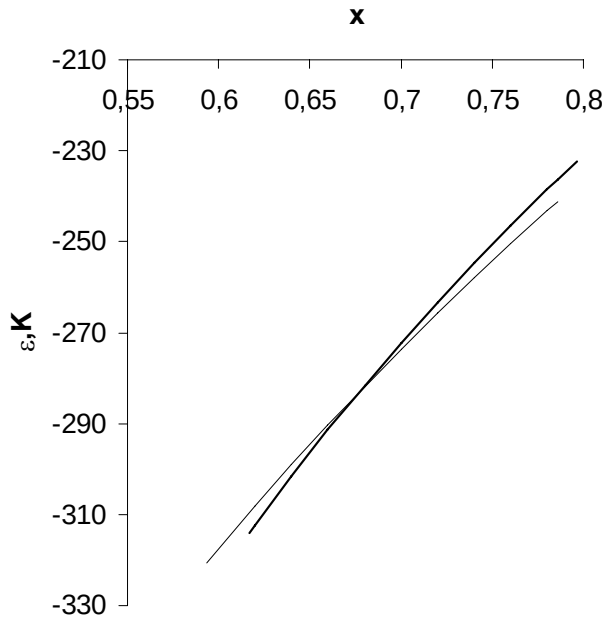

Figure 1.7. Energies $\varepsilon(x)$ or non-collinear structures G_1 (thin line) and G_2 (thick line).

$$\varepsilon_A(x_1)=\varepsilon_{A_1}(x_1), \tag{1.68}$$

$$\varepsilon_{A_1}(x_2)=\varepsilon_{A_2}(x_2), \tag{1.69}$$

$$\varepsilon_{A_2}(x_3)=\varepsilon_B(x_3), \tag{1.70}$$

$$\varepsilon_B(x_4)=\varepsilon_{C_2}(x_4), \tag{1.71}$$

$$\varepsilon_{C_2}(x_5)=\varepsilon_{C_1}(x_5), \tag{1.72}$$

$$\varepsilon_{C_1}(x_6)=\varepsilon_C(x_6), \tag{1.73}$$

$$\varepsilon_C(x_7)=\varepsilon_G(x_7)\cdot \tag{1.74}$$

Substituting energies of Eqs.(1.56-1.66) in Eqs.(1.68-1.74), then we obtain

$$b(x_1)-c(x_1)+\frac{4B_2Sx_1(1-x_1)}{\sqrt{2S+1}}=0, A\to A_1. \tag{1.75}$$

$$b^2(x_2)-c^2(x_2)-\frac{16S^2B_2^2x_2^2(1-x_2)^2}{(S+1)(2S+1)}=0, A_1\to A_2. \tag{1.76}$$

$$b(x_3)+c(x_3)+\frac{4SB_2x_3(1-x_3)}{2S+1}=0, A_2\to B. \tag{1.77}$$

$$a(x_4)+c(x_4)+\frac{8SB_1x_4(1-x_4)}{2S+1}=0, B\to C_2 \tag{1.78}$$

$$a^2(x_5)-c^2(x_5)-\frac{64S^2B_1^2x_5^2(1-x_5)^2}{(S+1)(2S+1)}=0, C_2\to C_1 \tag{1.79}$$

$$a(x_6)-c(x_6)+\frac{8B_1Sx_6(1-x_6)}{\sqrt{2S+1}}=0, C_1\to C. \tag{1.80}$$

$$b(x_7)+4B_2\left(1-\frac{1}{\sqrt{2S+1}}\right)x_7(1-x_7)=0, C\to G. \tag{1.81}$$

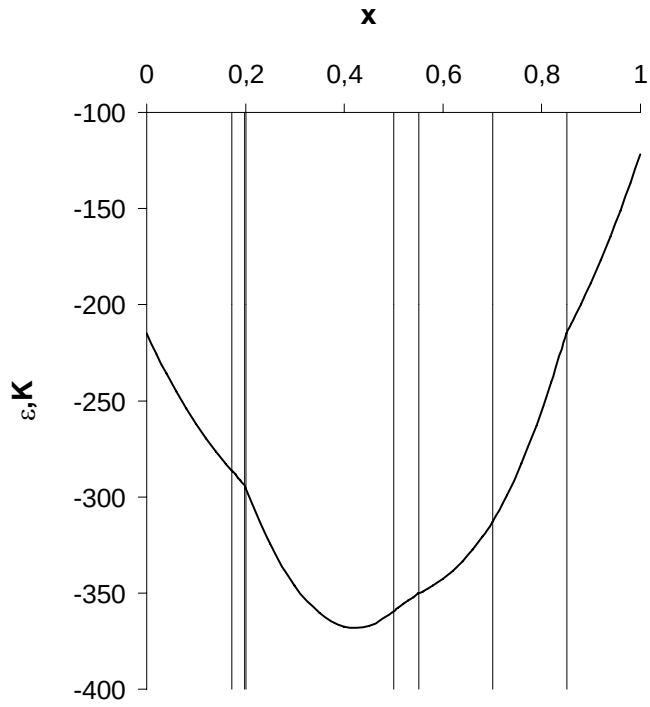

Figure 1.8. Energy $\varepsilon(x)$, consisting of energies $\varepsilon_A(x)$, $\varepsilon_{A_1}(x)$, $\varepsilon_{A_2}(x)$, $\varepsilon_B(x)$, $\varepsilon_{C_2}(x)$, $\varepsilon_{C_1}(x)$, $\varepsilon_C(x)$ and $\varepsilon_G(x)$. Vertical lines are drawn through transition points x_1-x_7.

So we have seven Eqs. (1.75-1.81) with seventeen unknowns: ten parameters $I_1 - I_6$, K_1, K_2, B_1, B_2 and seven transition concentrations $x_1 - x_7$. In order to use the system of Eqs. (1.75-1.81) in practice we should determine some ten values independently, while the missing seven ones we shall find solving the system of seven Eqs. (1.75-1.81). Let us do it in the following way. The values $I_1 = 9.6K$, $I_2 = -6.7K$, $K_1 = 1.92K$ were obtained in Ref. [30] during the analysis of spin-wave spectrum in $LaMnO_3$. We arbitrarily (not having experimental data) assumed $K_1 = K_2 = 1.92K$. If one uses data on Néel temperature for [5, 38] we shall put approximately $I_3 = I_4 = 8.7K$. Keeping in mind the results of papers [5, 34-38] let's put some mean experimental values for transition concentrations $x_3 = 0.2, x_4 = 0.5, x_6 = 0.7, x_7 = 0.85$. When substitute these ten parameters $I_1, I_2, I_3, I_4, K_1, K_2, x_3, x_4, x_6, x_7$ into the system of Eqs. (1.75-1.81), we have obtained for the missing parameters the following values:

$$I_5 = -12.673K, I_6 = 9.603K, B_1 = 144.571K, B_2 = 116.085K, \tag{1.82}$$

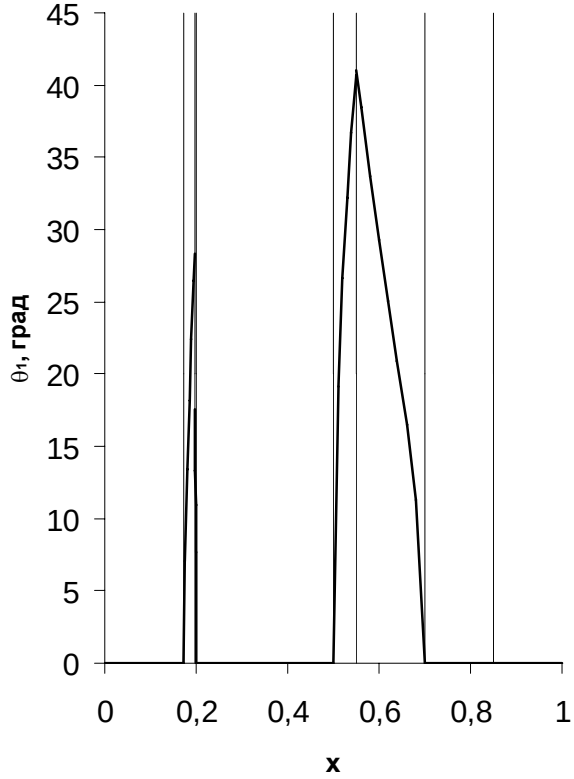

Figure 1.9. Dependence of angle θ_1 upon concentration x.

$$x_1 = 0.173, x_2 = 0.197, x_5 = 0.55 \cdot \tag{1.83}$$

Using these values we have depicted plots of energies in the whole range of x values in Figures 1.4-1.7. Figure 1.8 shows the continuous curve $\varepsilon(x)$, made up of the pieces of functions $\varepsilon_A, \varepsilon_{A_1}, \varepsilon_{A_2}, \varepsilon_B, \varepsilon_{C_2}, \varepsilon_{C_1}, \varepsilon_C$ and ε_G, closing each other consecutively in the transition points $x_1 - x_7$. Figure 1.9 shows the dependence $\theta_1(x)$. Figure 1.10 depicts the dependence of angle Φ between sub-lattices moments upon x, Figure 1.11 is the plot of canting angle $\Theta(x)$, while Figure 1.12 presents the concentration dependence of ferromagnetic momentum (on one ion of manganese) $m = 2\mu_B S_F$, where μ_B is Bohr magneton and S_F is given by formula

$$S_F = \frac{1}{2}(4 - x)\cos\frac{\Phi}{2}. \tag{1.84}$$

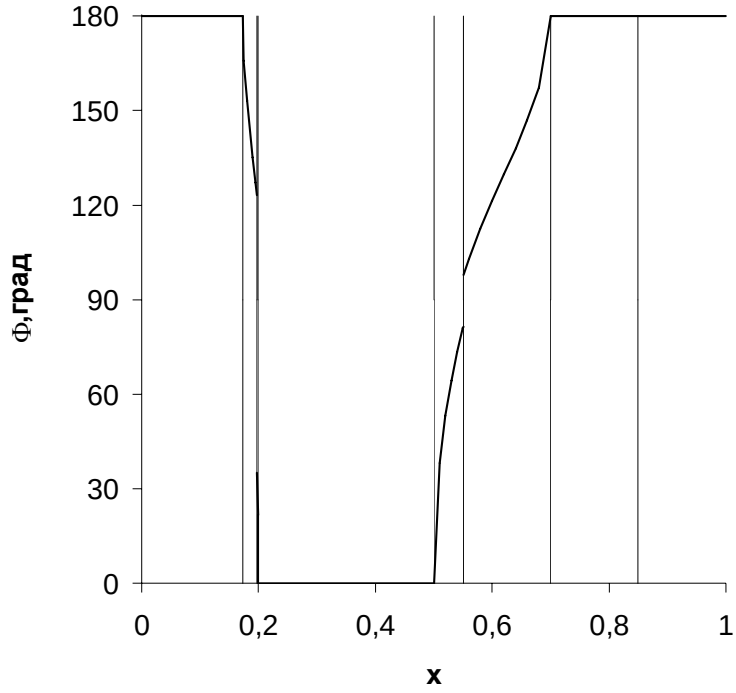

Figure 1.10. Dependence of angle Φ between sub-lattices vectors upon concentration x.

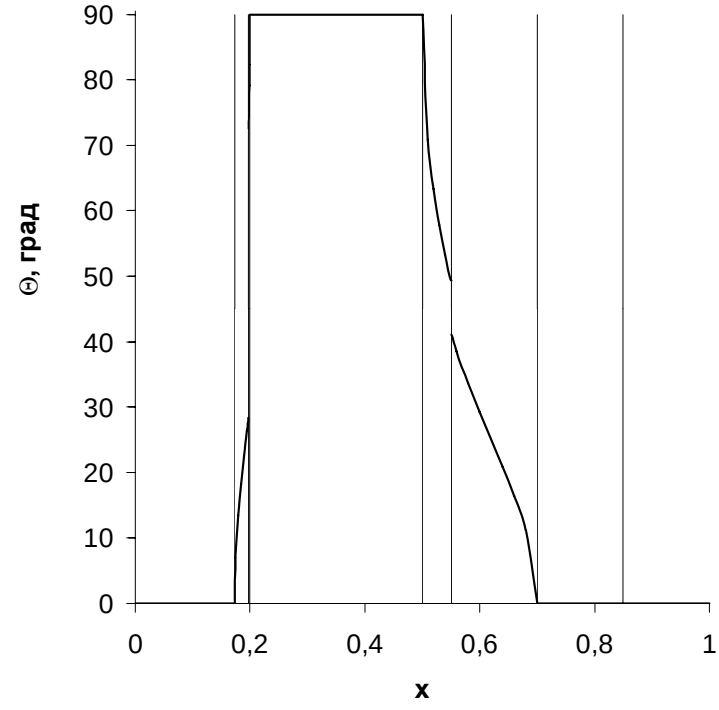

Figure 1.11. Theoretical dependence of canting angle Θ upon concentration x.

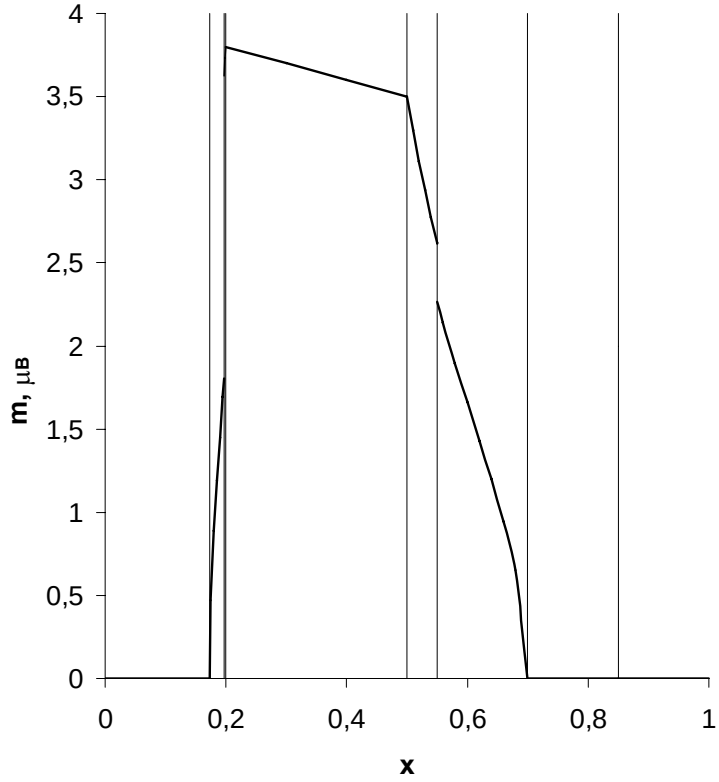

Figure 1.12. Theoretical dependence of ferromagnetic momentum m upon concentration x.

Functions $\varepsilon(x)$ for collinear states A, B, C, G have positive second derivatives $\partial^2\varepsilon/\partial x^2$ in the whole range $0 \le x \le 1$. The energies of non-collinear states $\varepsilon_{A_1}, \varepsilon_{A_2}, \varepsilon_{C_1}, \varepsilon_{C_2}, \varepsilon_{G_1}, \varepsilon_{G_2}$ are defined each in the own region of definition

$$\varepsilon_{A_1}: 0.173 \le x \le 0.239, \tag{1.85}$$

$$\varepsilon_{A_2}: 0.147 \le x \le 0.2, \tag{1.86}$$

$$\varepsilon_{C_1}: 0.474 \le x \le 0.7, \tag{1.87}$$

$$\varepsilon_{C_2}: 0.5 \le x \le 0.721, \tag{1.88}$$

$$\varepsilon_{G_1}: 0.594 \le x \le 0.786, \tag{1.89}$$

$$\varepsilon_{G_2}: 0.617 \le x \le 0.797. \tag{1.90}$$

The states A_1, A_2, G_1, G_2 have negative second derivative in their definition regions. The state C_1 has negative second derivative for $x < 0.515$ and positive one for $x > 0.515$. Respectively for C_2 the point of inflection for $\varepsilon(x)$ is equal to 0.54. Thus in the range $x_5 \le x \le x_6$ for C_1 the second derivative is positive, while for C_2 the second derivative changes sign from negative to positive with the increase of x in the range $x_4 \le x \le x_5$.

It was experimentally shown in Ref. [34], that transition from antiferromagnetic phase A at small x with increase of concentration to ferromagnetic state with $\theta_1 = \Theta = 90^\circ$ (in our terminology B') occurs rather smoothly (see Figure 1.13 [34] which should be compared with our Figure 1.11) and only through the sequence of one-type angle states (analog of our configuration A_1). So we see that the results of our theory and this experiment differ essentially: state B' does not realize in our theory at all and two intermediate angle states A_1 and A_2 exist between antiferromagnetic state A and ferromagnetic state B ($\Theta = 0$). Besides the range of transition between anti- and ferromagnetic states in Ref. [34] is much broader than we have obtained. We do not have enough experimental data about the dependence of canting angle upon concentration $\Theta(x)$ for values $x \ge 0.5$ in order to compare in details theory and experiment. Only Ref. [35] informs about angle magnetism at $x = 0.667$.

Our theoretical curve for m (see Figure 1.12) can be compared with experimental data from Refs. [1, 5] that are depicted on Figure 1.14. The type of the dependence is approximately the same while the qualitative coincidence is not good enough.

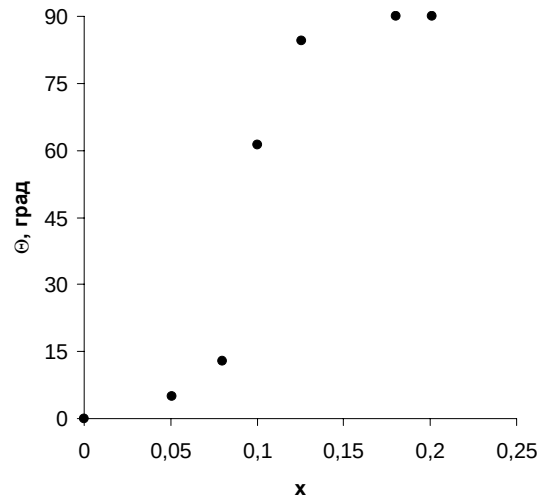

Figure 1.13. Experimental dependence of angle Θ upon concentration in $La_{1-x}Ca_xMnO_3$. The plot is taken from Ref. [34].

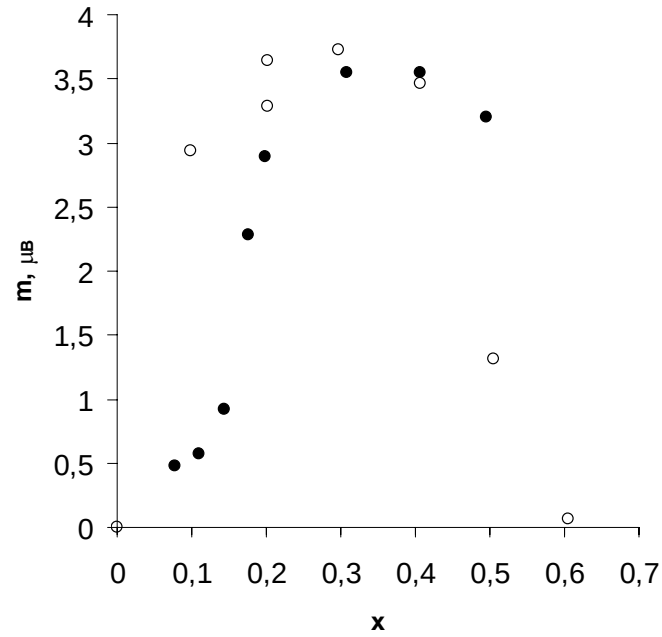

Figure 1.14. Experimental dependence of ferromagnetic momentum m per one Mn ion upon concentration x for $La_{1-x}Ca_xMnO_3$. (See Figure 12 of Ref. [5]). Clear circles are data of Ref.1, while dark ones were taken from Ref. [5].

1.5. Some Discussions

The proposed model of homogeneous dynamical spin alloy for compound $La_{1-x}Ca_xMnO_3$ has in principle allowed to explain the different magnetic configurations observed experimentally and the sequence of their change depending on the concentration x. The numerical values of interaction parameters obtained theoretically are rather plausible. Taking account of simultaneous presence of Heisenberg-type direct or superexchange and non-Heisenberg-type double exchange leads to the appearance of non-collinear (canted) structures. Heisenberg interaction can be both positive (ferromagnetic) and negative (antiferromagnetic). Double exchange is essentially positive. Canted structures appear at values of concentration x, when balance takes place between the total Heisenberg antiferromagnetic exchange interaction and ferromagnetic double exchange. Heisenberg interaction and double exchange taken separately cannot lead to canted configurations.

Presence of anisotropy energy (which is small) leads to the fact that angle states "symmetrical" with respect to the normal of b-axis turn at certain x values into states "symmetrical" with respect to b-axis. At finite values of anisotropy energies ferromagnetic state B', which is the limit case of angle states ($\theta = 90^\circ$), symmetrical with respect to normal of b-axis turns out to be unattainable. Ferromagnetic state B always has lower energy than that of ferromagnetic state B' and their difference is just anisotropy energy.

Let's note that the canting angle $\Theta(x)$ has infinite derivatives with respect to x in the points of transitions between collinear and non-cllinear structures (x_1, x_3, x_4, x_6).

Let's note that magnetic phase transitions depending upon concentration in systems with double exchange were investigated earlier by many authors with the use of band approximation which was proposed by de-Gennes in his famous work [7]. The typical feature of this approximation is the proposal that additional electron realizing exchange coupling between localized spins is the conduction electron whose transfer integral depends upon mutual orientation of localized electrons spins. The band description is used for it so it is natural to call such an approach to double exchange theory the band approximation of double exchange. Then the approximation used in our paper can be relevantly called the localized approximation of double exchange though the conditionality of such a title is obvious. We did not use the concept of bands and only different spins $S+1/2$ and S for ions Mn^{3+} and Mn^{4+} are present in our approach. (However this does not mean that our model forbids electronic conductivity. The conductivity is "hiding" here in probabilities x and $1-x$ which we have introduced. Of course they allow electron migration from site to site. It seems that in our approach it's more proper to speak about not band but jump conductivity.) The difference between ions Mn^{3+} and Mn^{4+} disappears in band model and correspondingly different superexchange parameters between ions Mn^{3+} and Mn^{4+} are absent while in our approach these parameters are present separately. This essential difference does not allow compare literally the band and localized approximations.

The following moments should be associated with difficulties of our theory. The negativity of the second derivative for angle states A_1, A_2 and partly C_2 indicates non-stability of these states. This question needs an additional investigation. It's impossible to obtain phenomenon of charge ordering in our approach because we are using homogeneous approximation. In connection with this we have simplified the situation supposing that only configurations C_1, C_2 or C are present in the range $0.5 < x < 0.85$ while experiment shows that CE states are also present in this range of x . We have called the object under investigation "*hypothetical* compound $La_{1-x}Ca_xMnO_3$" because of the fact that really at x increasing from 0 till 1 both the lattice symmetry change ($LaMnO_3$ has orthorhombic symmetry while $CaMnO_3$ is cubic) and the lattice parameters hence the exchange parameters I, B, K also change. Unfortunately the dependence of interaction parameters upon x is unknown. It is of course inconsistently to assume parameters I_1 and I_2 to be different while I_3 and I_4 equal ones as we have done above at numerical evaluations. Thus numerical values for I, B, K obtained above are approximate and averaged.

PART 2. SPIN-WAVE EXCITATIONS

The content of this part is based on the papers [30-34, 41-59].

2.1. Some General Formulas. Ferromagnets

After considering the some magnetic configurations at zero temperature and concentration transitions between them in Part 1 then the magnon spectrum will be studied now. Many papers were devoted to this problem [30-34, 41-46]. As before we'll assume that there are two kind of exchange in a system – Heisenberg and double. The energy operator for conducting ferromagnetic manganites is

$$\widehat{H} = \widehat{H}_{1ex} + \widehat{H}_{2ex} + \widehat{H}_a, \tag{2.1}$$

where the first term represents Heisenberg interaction, the second term stands for the double exchange operator, and the third term is the anisotropy energy. These are expressed as

$$\widehat{H}_{1ex} = -\sum_{\vec{m}} \sum_{\vec{\Delta}} \sum_{k,l=1}^{2} I_{kl}(\vec{\Delta}) \vec{S}_k(\vec{m}) \vec{S}_l(\vec{m} + \vec{\Delta}), \tag{2.2}$$

$$\widehat{H}_{2ex} = -\sum_{\vec{m}} \sum_{\vec{\Delta}} \sum_{k,l=1}^{2} B_{kl}(\vec{\Delta}) \sqrt{1 + \frac{2\vec{S}_k(\vec{m}) \vec{S}_l(\vec{m} + \vec{\Delta})}{1 + S(2S+3)}}, \tag{2.3}$$

$$\widehat{H}_{\alpha} = -\sum_{\vec{m}} \sum_{k=1}^{2} A_k (S_k^z(\vec{m}))^2, \tag{2.4}$$

respectively. The sense of the designations is the same as in the Part 1.

We then come from spin operators to second quantization operators in a standard manner, expand the square root in Eq. (2.3) in a bilinear operator form, and, finally, perform the Fourier transform. As a result, we obtain the following expression for the spin wave energy:

$$E(\vec{q}) = 2\left\{ \sum_{p=1}^{n} \left[z_p \widetilde{J}_p - \gamma_p(\vec{q}) J_p \right] + A \right\}, \tag{2.5}$$

where $\vec{q}$ is the spin-wave quasi-momentum, subscript p numbers n coordination shells, z_p is the number of sites in the p-th shell,

$$\gamma_p(\vec{q}) = \sum_{j=1}^{z_p} \exp(-i\vec{q}^{\,j}\vec{\Delta}_p), \tag{2.6}$$

$$J_p = (1-x)^2(S+\frac{1}{2})({}^{11}I_p) + x^2 S({}^{22}I_p) + \\ + x(1-x)\sqrt{2S(2S+1)}\left[{}^{12}I_p + \frac{B_p}{(2S+1)^2}\right], \tag{2.7}$$

$$\widetilde{J}_p = J_p + f(S)x(1-x)\left[{}^{12}I_p + \frac{B_p}{(2S+1)^2}\right],$$

$$f(S) = 2S + \frac{1}{2} - \sqrt{2S(2S+1)}, \tag{2.8}$$

and

$$A = (1-x)(S+\frac{1}{2})K_1 + xSK_2. \tag{2.9}$$

To derive Eq. (2.5), we used the relations

$$\sum_{\vec{\Delta}} I_{11}(\vec{\Delta})\exp(-i\vec{q}\vec{\Delta}) = (1-x)^2 \sum_{p=1}^{n} {}^{11}I_p \gamma_p(\vec{q}), \tag{2.10}$$

$$\sum_{\vec{\Delta}} I_{22}(\vec{\Delta})\exp(-i\vec{q}\vec{\Delta}) = x^2 \sum_{p=1}^{n} {}^{22}I_p \gamma_p(\vec{q}), \tag{2.11}$$

$$\sum_{\vec{\Delta}} I_{12}(\vec{\Delta})\exp(-i\vec{q}\vec{\Delta}) = x(1-x) \sum_{p=1}^{n} {}^{12}I_p \gamma_p(\vec{q}), \quad I_{12} = I_{21}, \tag{2.12}$$

$$\sum_{\vec{\Delta}} B_{12}(\vec{\Delta})\exp(-i\vec{q}\vec{\Delta}) = x(1-x) \sum_{p=1}^{n} B_p \gamma_p(\vec{q}),$$

$$B_{12} = B_{21},\ B_{11} = B_{22} = 0. \tag{2.13}$$

$$A_1 = (1-x)K_1,\ A_2 = xK_2. \tag{2.14}$$

Due to symmetry of the system, we assumed that all integrals of the same type inside the same coordination shell are equal to each other. Therefore we introduced for the new designations I_p^{ij}.

Table 1.

p	z_p	${}^j\vec{\Delta}_p$	$\left\|{}^j\Delta_p\right\|$	γ_p
1	6	$\pm(a00),\pm(0a0),\pm(00a)$	$a\sqrt{1}$	$2(\cos aq_a+\cos aq_b+\cos aq_c)$
2	12	$\pm(aa0),\pm(a0a),\pm(0aa),$ $\pm(-aa0),\pm(-a0a),\pm(0-aa)$	$a\sqrt{2}$	$4(\cos aq_a\cos aq_b+$ $+\cos aq_a\cos aq_c+$ $+\cos aq_b\cos aq_c)$
3	8	$\pm(aaa),\pm(aa-a),$ $\pm(a-aa),\pm(-aaa)$	$a\sqrt{3}$	$8\cos aq_a\cos aq_b\cos aq_c$
4	6	$\pm(2a00),\pm(02a0),\pm(002a)$	$a\sqrt{4}$	$2(\cos 2aq_a+\cos 2aq_b+\cos 2aq_c)$

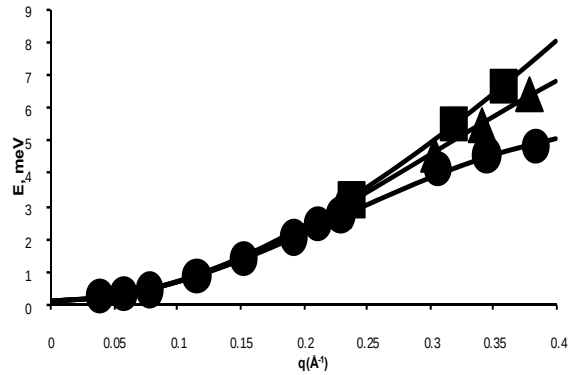

Figure 2.1. Dispersion curves for the (circles) [001], (triangles) [110] and [101] and (squares) [111] directions borrowed from [44]. The solid curves were calculated Eqs. (2.15)-(2.17).

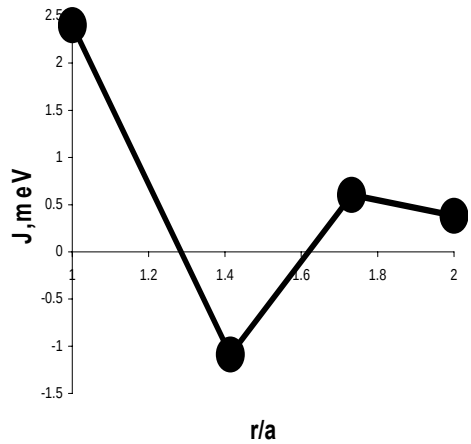

Figure 2.2. Dependences of the exchange integrals of the reduced distance r/a (a is the lattice parameter).

As will be explained below, we consider the case of four coordination shells. The main parameters for this situation are given in the table (where a is the lattice parameter).

2.2. Comparison with Experiment. Ferromagnets

First we compare above theoretical formulae with experiment from paper [44] for $La_{0.83}Ca_{0.17}MnO_3$. Dispersion curves for spin waves obtained by neutron inelastic studies for three principal crystallographic directions are shown in Figure 2.1. We now compare them with our theoretical calculations and have

$$E_{\langle 100\rangle}(q)=a_1+b_1\cos(aq)+c_1\cos(2aq), \tag{2.15}$$

$$E_{\langle 110\rangle}(q)=a_2+b_2\cos\left(\frac{aq}{\sqrt{2}}\right)+c_2\cos\left(\frac{2aq}{\sqrt{2}}\right), \tag{2.16}$$

$$E_{\langle 111\rangle}(q)=a_3+b_3\cos\left(\frac{aq}{\sqrt{3}}\right)+c_3\cos\left(\frac{2aq}{\sqrt{3}}\right)+d_3\cos\left(\frac{3aq}{\sqrt{3}}\right), \tag{2.17}$$

where

$$\begin{aligned} &a_1=2x_1+2x_2+2x_4+x_5,\\ &b_1=x_1+4x_2+4x_3,\ c_1=x_4, \end{aligned} \tag{2.18}$$

$$\begin{aligned} &a_2=x_1+x_2+2x_3+x_4+x_5,\\ &b_2=2x_1+4x_2,\ c_2=x_2+2x_3+2x_4, \end{aligned} \tag{2.19}$$

$$\begin{aligned} &a_3=3x_2+x_5,\ b_3=3x_1+3x_3,\\ &c_3=3x_2+3x_4,\ d_3=x_3, \end{aligned} \tag{2.20}$$

$$x_1=-4\tilde{J}_1,\ x_2=-4\tilde{J}_2,\ x_3=-4\tilde{J}_3,\ x_4=-4\tilde{J}_4, \tag{2.21}$$

$$x_5=2\left(\sum_{p=1}^{4} z_p\tilde{J}_p+A\right). \tag{2.22}$$

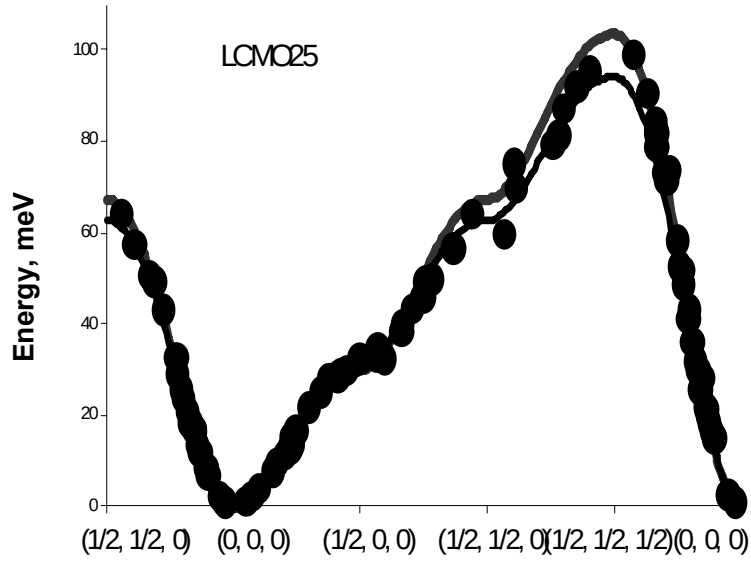

Figure 2.3. LCMO25. Dispersion curves for the main crystallographic directions. Circles – experimental points from paper [46]. Thin line is calculated curve in [46], thick line is calculated by Eqs. (2.27).

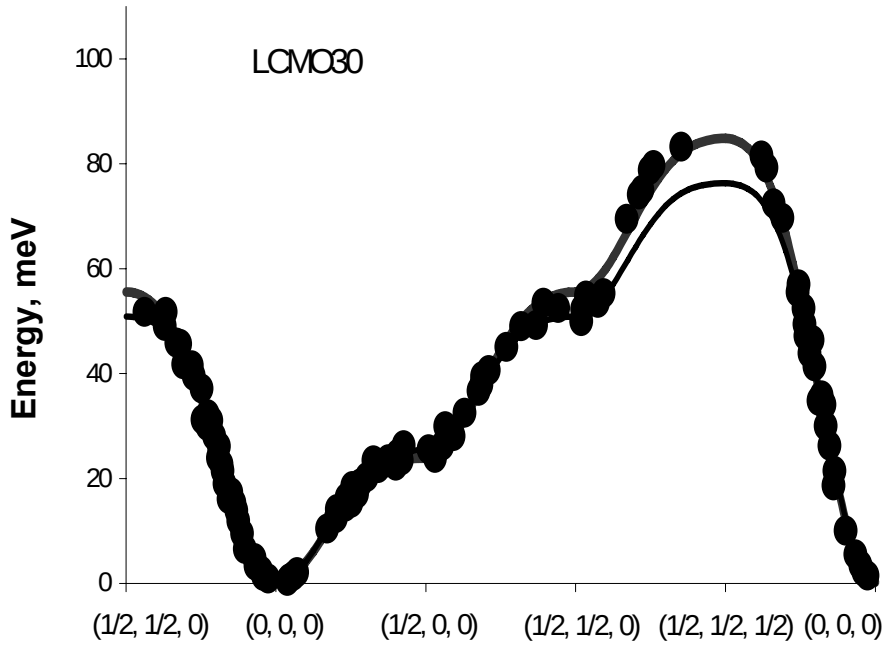

Figure 2.4. LCMO30. Dispersion curves for the main crystallographic directions. Circles – experimental points from paper [46]. Thin line is calculated curve in [46], thick line is calculated by Eqs. (2.28).

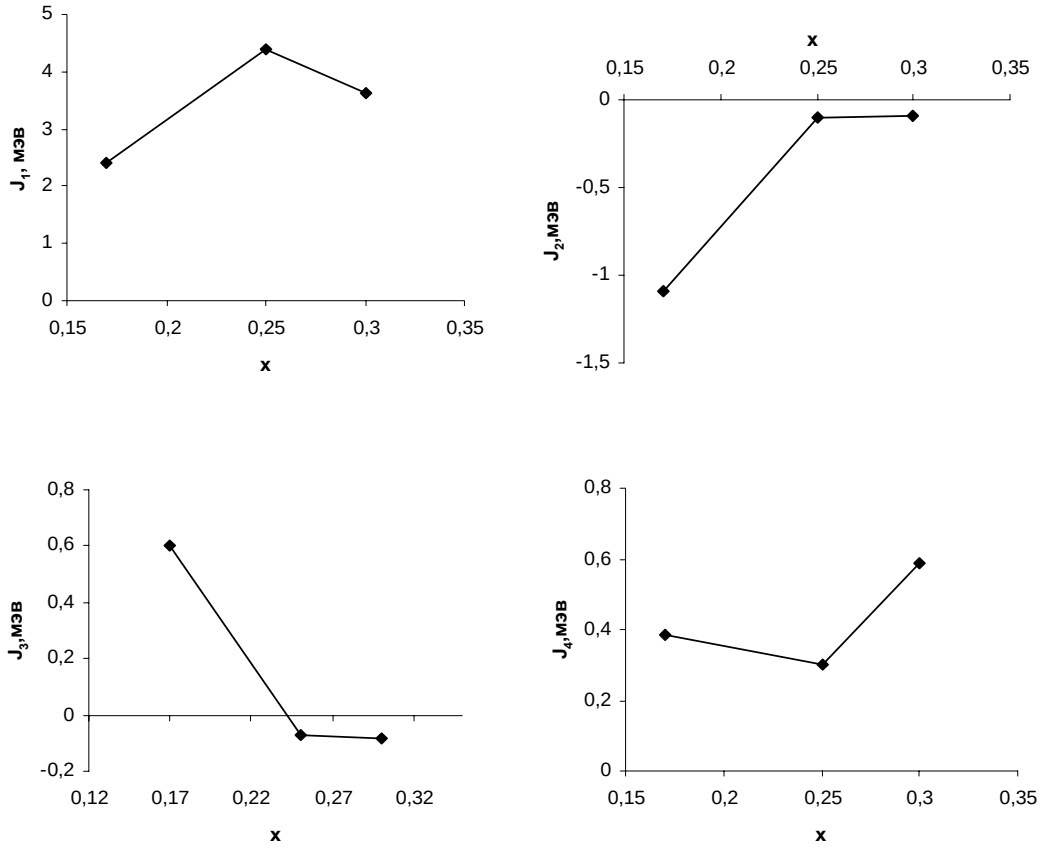

Figure 2.5. Dependences of the exchange integrals on the concentration x.

To find the unknowns $x_1 - x_5$ we use the least squares method; to this end, we set up the functional

$$F = \sum_{\langle 100 \rangle} \left(E_{theor} - E_{\exp}\right)^2 + \sum_{\langle 110 \rangle} \left(E_{theor} - E_{\exp}\right)^2 + \\ + \sum_{\langle 111 \rangle} \left(E_{theor} - E_{\exp}\right)^2 \quad . \tag{2.23}$$

We impose the minimum conditions

$$\frac{\partial F}{\partial x_1} = \frac{\partial F}{\partial x_2} = \frac{\partial F}{\partial x_3} = \frac{\partial F}{\partial x_4} = \frac{\partial F}{\partial x_5} = 0, \tag{2.24}$$

on this functional and obtain the set of five equations for five unknowns.The lattice parameter is taken to be the experimental value ($a = 3.89$ Å, see below), and we have (in meV)

$$J_1 = 2.405,\ J_2 = -1.088,\ J_3 = 0.605,\ J_4 = 0.384,\ x = 17.19. \tag{2.25}$$

The calculated dispersion curves are presented in Figure 2.1. Figure 2.2 shows the distance dependence of exchange integrals J_n. The energy gap is expressed as

$$\delta = 2A + 2f(S)x(1-x)\sum_{p=1}^{4} z_p \left({}^{12}I_p + \frac{B_p}{(2S+1)^2} \right). \tag{2.26}$$

At the numerical values of the parameters from Eq. (2.25), this gap is $\delta \approx 0.136$.

Let us discuss the approximations and results obtained.

First, we should explain why we took into account interactions up to fourth –nearest neighbors (i.e., neighbors from the fourth coordination shell). Indeed, as follows from the experimental curve for the [100] direction (Figure 2.1), the dispersion curve has an inflection point at $q < 0.4$, whereas the nearest-neighbor approximation with the $\cos(aq)$ can give an inflection only at $q > 0.4$ (at $a = 3.89$ Å). The required inflection point can be induced by the $\cos(2aq)$ harmonic. However, the next and next-next nearest neighbors cannot generate this harmonic, and it appears only when fourth-nearest neighbors are taken into account.

Second, we used in spite of the fact that the compound under study has an orthorhombic structure. However, such compounds are often approximately considered as cubic or pseudocubic crystals because of numerical relations between their lattice parameters. The compound under study was taken to be cubic, and this approximation should inevitably affect the accuracy of our calculations.

Third, the lattice parameter was assumed to be 3.89 Å which is average of the values of parameters a, b and c at low temperatures for $La_{0.83}Ca_{0.17}MnO_3$ (see [44], Figure 4).

Fourth, when analyzing the dispersion curves, we can only determine total exchange integrals J_1, J_2, J_3, and J_4 rather than ${}^{ij}I_p$ and B_p separately. It is still unclear from which experiments these exchange components could be determined.

Fifth, note that, in our model an energy gap in spin-wave spectrum appears due to both anisotropy and (quadratic and double) exchange energies, which is caused by the presence of ions with different ($S, S+1/2$) spins in the system.

Sixth, $La_{0.83}Ca_{0.17}MnO_3$ is a semiconductor, and a tendency to the metallic temperature dependence of electrical resistivity appears only in the vicinity of the Curie temperature. Compounds with $0.125 < x < 0.220$ are attributed to a precursor metallic phase [44]. The compound $La_{0.83}Ca_{0.17}MnO_3$ can serve as a basis for analyzing the dependence of the exchange parameters on concentration x in the range of “more metallic” compounds. The approach proposed in this work is suitable for any x provided that charge ordering is absent in the system.

Seventh, the system $La_{0.83}Ca_{0.17}MnO_3$ is more complex that than it is assumed here. In reality, Hennion and Moussa [44] showed that dispersion law for the lower curve in Figure 2.1 is only valid for the [001] direction and that experimental points in the range $q \geq 0.125$ in the [100] direction do not fall on the general curve. This behavior cannot be described in terms of our model.

The next objects of our attention will be the results obtained in the papers [45, 46]. Ye et al studied by the method of inelastic neutron scattering spin-wave dispersion curves in ferromagnetic metallic compounds with $x = 0.25$ and $x = 0.30$. It considered as cubic. Their data for different directions in Brillouin zone are represented in Figure 2.3 and Figure 2.4. We again will compare these experimental results with our theoretical calculations. As above the presence of Heisenberg and double exchanges are assumed to be realize in these compounds. So, we can use the formulae Eqs. (2.1-2.14). According the data of [45, 46] we'll assume that anisotropy energy is absent ($A = 0$). Using the standard square-mean method we obtain in four-shell coordination approximation and for the directions $[100]+[110]+[111]$:

$$J_1 = 4.402,\ J_2 = -0.097,\ J_3 = -0.068,\ J_4 = 0.3,\ J = 26.44 \tag{2.27}$$

for LCMO25 and

$$J_1 = 3.635,\ J_2 = -0.087,\ J_3 = -0.081,\ J_4 = 0.586,\ J = 23.755 \tag{2.28}$$

for LCMO30. The values are given in meV-units. The calculated curves are represented in Figure 2.3 and Figure 2.4 by solid lines.

The authors of [45, 46] also treated their data from theoretical point of view to obtain the numerical magnitudes of exchange parameters. Their calculated curves are given in Figure 2.3 and Figure 2.4 by thin lines. They obtained

$$I_1 = 2.088,\ I_2 = 0,\ I_3 = 0,\ I_4 = 0.136 \tag{2.29}$$

for LCMO25

and

$$I_1 = 1.719,\ I_2 = 0,\ I_3 = 0,\ I_4 = 0.335 \tag{2.30}$$

for the compound LCMO30.

The additional explanations are needed to understand the difference in the approaches – our and in [45, 46].

Although the authors of [45, 46] claimed, that they use the double exchange interaction, as a matter of fact usual Heisenberg spin-operator was treated. Contrary, in our approach Heisenberg and double exchanges are present in evident form.

In order to take into account the existence of two different manganese ions Mn^{3+} (spin 2) and Mn^{4+} (spin 3/2) the notion of average spin was introduced in [45, 46]. In our approach two different spins S and $S + 1/2$ present separately without any averaging.

In contrast to our approach the authors of [45, 46] suppose $J_2 = J_3 = 0$ in advance.

In our study the parameters J_1, J_2, J_3 and J_4 have an "internal structure", whereas these merely represent certain effective quantities in [45, 46].

Our magnitudes J_p are the analogues of I_p from [45, 46], but literally it is impossible to compare due to their different physical meaning.

Note, that really interactions with second and third coordination shells are small in comparing with first and fourth ones, as supposed the authors of [45, 46]. However since the number of second order neighbors is equal 12 and ones of third order 8 as to compare with 6 neighbors of fourth order then total contribution from second and third order may be comparable with fourth order contribution in magnetic behavior.

Let us tell about one difficulty which appears at numerical estimations of exchange parameters. The total ferromagnetic interaction the measure of which may serves the magnitude

$$J = \sum_{p=1}^{4} z_p \widetilde{J}_p \tag{2.31}$$

appears larger for LCMO25 then for LCMO30. This is in contradiction with the fact that Curie temperature of LCMO25 is lower then one of LCMO30. The same situation in [45, 46]: $I_1 + I_4$ and average spin are larger for LCMO25 then for LCMO30. Hence the problem of concordance of low-temperature and high-temperature properties demands additional investigation.

At last using results for three compounds with $x = 0.17, 0.25, 0.30$ we obtain the dependence of exchange integrals from concentration x. These dependences are shown in Figure 2.5. Take notice the nonmonotonic dependence of J_1 and J_4 and also large magnitude of J_2 and J_3 in LCMO17 as compare with LCMO25 an LCMO30. These facts need additional consideration also.

2.3. Some General Formulas. Antiferromagnet

Above we considered spin-wave spectrum in the ferromagnetic conducting compounds LCMO17, LCMO25 and LCMO30. Now we will study magnon energy in antiferromagnetic dielectric $LaMnO_3$. Naturally the mechanism of double exchange is absent here. Only the three-valence manganese ions with spin of $3/2$ are existed in this system. The crystal is orthorhombic, space group no. 62, $GdFeO_3$ structure type. The unit cell is shown in Figure 1.1. We are interested in the antiferromagnetic phase A, which is shown in Figure 1.2 together with other magnetic structures. The phase A consists of ferromagnetic (ab) planes with the total magnetic moments directed alternately along and opposite to the axis b. The antiferromagnetic structure is a two-sublattice system. One sublattice includes the first and second Bravais lattices, and the other sublattice includes third and fourth Bravais lattices.

Most frequently, an analysis of the exchange interactions has been performed with allowance made only for the interactions of the nearest neighbors, even though this inclusion can prove to be insufficient. On the other hand, it is impossible to predict how many

neighbors should be taken for describing the situation adequately. Let us, fairly arbitrarily, choose the interactions between eighteen neighbors from four coordination shells. In this case, we focus our attention only on the interstitial distances, even though it is known that the direction of the neighbor can play a decisive role. The position vectors of the neighbors can be represented as follows:

$$\vec{\Delta}_1 = -\vec{\Delta}_2 = (0, a/2, b/2),$$
$$\vec{\Delta}_3 = -\Delta_4 = (0, a/2, -b/2), \tag{2.32}$$

$$\vec{\Delta}_5 = -\vec{\Delta}_6 = (0, a, 0), \tag{2.33}$$

$$\vec{\Delta}_7 = -\vec{\Delta}_8 = (0, 0, b), \tag{2.34}$$

$$\vec{\Delta}_9 = -\vec{\Delta}_{10} = (c/2, 0, 0), \tag{2.35}$$

$$\vec{\Delta}_{11} = -\vec{\Delta}_{12} = (c/2, a/2, b/2),$$
$$\vec{\Delta}_{13} = -\vec{\Delta}_{14} = (c/2, a/2, -b/2),$$
$$\vec{\Delta}_{15} = -\Delta_{16} = (c/2, -a/2, b/2),$$
$$\vec{\Delta}_{17} = -\vec{\Delta}_{18} = (c/2, -a/2, -b/2). \tag{2.36}$$

In these formulas, a, b and c are the lattice constants. According to [30], these lattice constants are (in Å)

$$a = 5.5333, b = 5.7461, c = 7.6637. \tag{2.37}$$

Then, the magnitudes of the vectors from relationships (2.32)-(2.36) can be written as

$$\left|\vec{\Delta}_1\right| = \left|\vec{\Delta}_2\right| = \left|\vec{\Delta}_3\right| = \left|\vec{\Delta}_4\right| = 3.9886, \tag{2.38}$$

$$\left|\Delta_5\right| = \left|\vec{\Delta}_6\right| = 5.5333, \tag{2.39}$$

$$\left|\vec{\Delta}_7\right| = \left|\vec{\Delta}_8\right| = 5.7461, \tag{2.40}$$

$$\left|\vec{\Delta}_9\right| = \left|\vec{\Delta}_{10}\right| = 3.8319, \tag{2.41}$$

$$\left|\vec{\Delta}_{11}\right| = \left|\vec{\Delta}_{12}\right| = \left|\vec{\Delta}_{13}\right| = \left|\vec{\Delta}_{14}\right| = \left|\vec{\Delta}_{15}\right| = \left|\vec{\Delta}_{16}\right| = \left|\vec{\Delta}_{17}\right| = \left|\vec{\Delta}_{18}\right| = 5.531. \tag{2.42}$$

The next neighbors are at a distance of 6.7306; however, we ignore them in our consideration.

In terms of symmetry, here, we have five different parameters of the exchange interaction:

I_1 for the vectors $\vec{\Delta}_1 - \vec{\Delta}_4$, (2.43)

I_2 for the vectors $\vec{\Delta}_5, \vec{\Delta}_6$, (2.44)

I_3 for the vectors $\vec{\Delta}_7, \vec{\Delta}_8$, (2.45)

I_4 for the vectors $\vec{\Delta}_9, \vec{\Delta}_{10}$, (2.46)

I_5 for the vectors $\vec{\Delta}_{11} - \vec{\Delta}_{18}$. (2.47)

In addition to these five parameters, we also introduce the anisotropy constant D, which orients antiferromagnetic axis along the crystallographic direction b.

As was said above we assume that the exchange interaction is described by the Heisenberg Hamiltonian and that the anisotropy energy has single-ion nature. Then, we have

$$\hat{H} = \sum_{i=1}^{2} \sum_{j=1}^{18} \sum_{\vec{m}_i} I(\vec{m}_i, \vec{m}_i + \vec{\Delta}_j) \vec{S}(\vec{m}_i) \vec{S}(\vec{m}_i + \vec{\Delta}_j) - D \sum_{i=1}^{2} \sum_{\vec{m}_i} (S^z_{\vec{m}_i})^2, \tag{2.48}$$

where i denotes the sublattice number and $\vec{m}_i$ runs over N -values of radius-vectors of sites for each of sublattices. It is assumed that $D > O$ Further, following the routine of passing from the spin operators to the second quantization operators and performing the diagonalization by the Fourier transform, we obtain the following expression for the magnon energy w as a function of the reduced quasi-momentum $\vec{q}$:

$$w(\vec{q}) = \sqrt{t_1^2 - t_2^2}, \tag{2.49}$$

$$t_1 = -2S[I_1(\gamma_1 - 4) + I_2(\gamma_2 - 2) + I_3(\gamma_3 - 2) + 2I_4 + 8I_5 - D], \tag{2.50}$$

$$t_2 = -2S[I_4\gamma_4 + I_5\gamma_5], \tag{2.51}$$

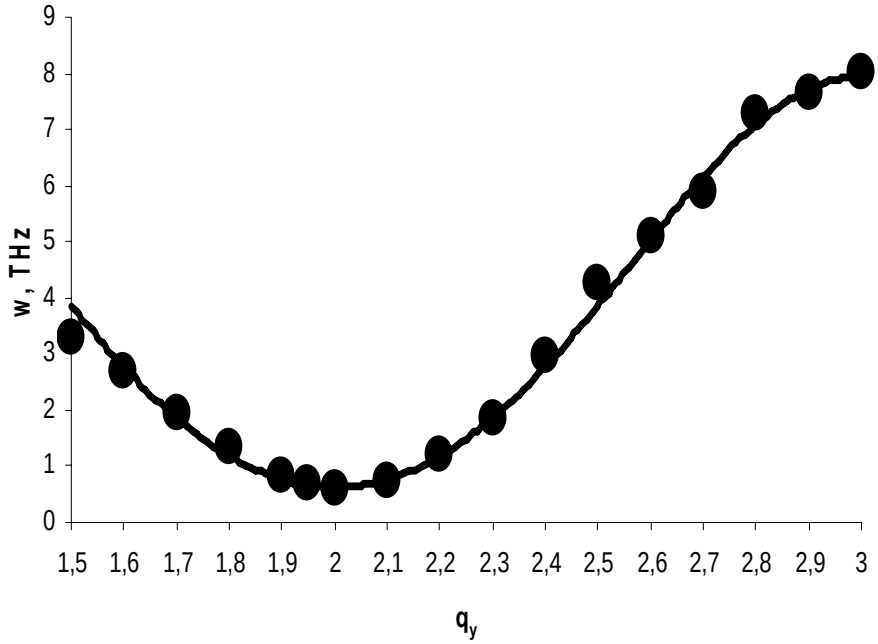

Figure 2.6. Dispersion curve for the $[100]^*$ direction. Experiment from [30].

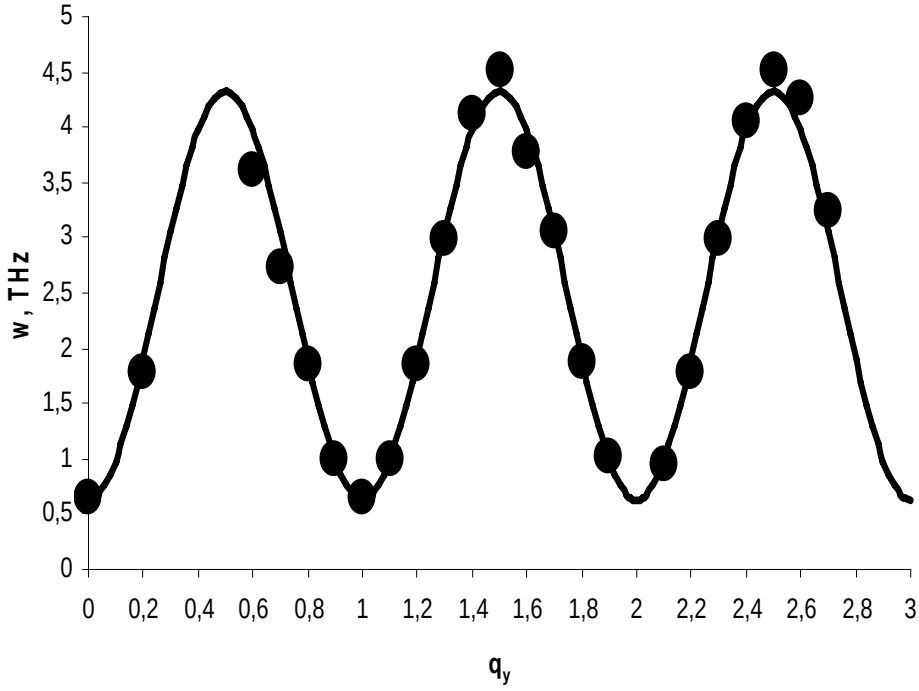

Figure 2.7. Dispersion curve for the $[110]^*$ direction. Experiment from [30].

$$\gamma_1 = 4\cos\pi q_y \cos\pi q_z, \tag{2.52}$$

$$\gamma_2 = 2\cos 2\pi q_y, \tag{2.53}$$

$$\gamma_3 = 2\cos 2\pi q_z, \tag{2.54}$$

$$\gamma_4 = 2\cos 2\pi q_x, \tag{2.55}$$

$$\gamma_5 = 8\cos\pi q_x \cos\pi q_y \cos\pi q_z. \tag{2.56}$$

The expression for w is valid over entire Brillouin zone.

2.4. Comparison with Experiment. Antiferromagnet

Moussa et al. [30] investigated inelastic neutron scattering and obtained the dispersion curves for principal crystallographic direction in $LaMnO_3$ compound. Figures 2.6-2.8 present the experimental points. Now, we compare our results with these experimental data for the directions $[100]^*, [110]^*$ and $[001]^*$. From expressions Eqs. (2.49) - (2.56), we obtain

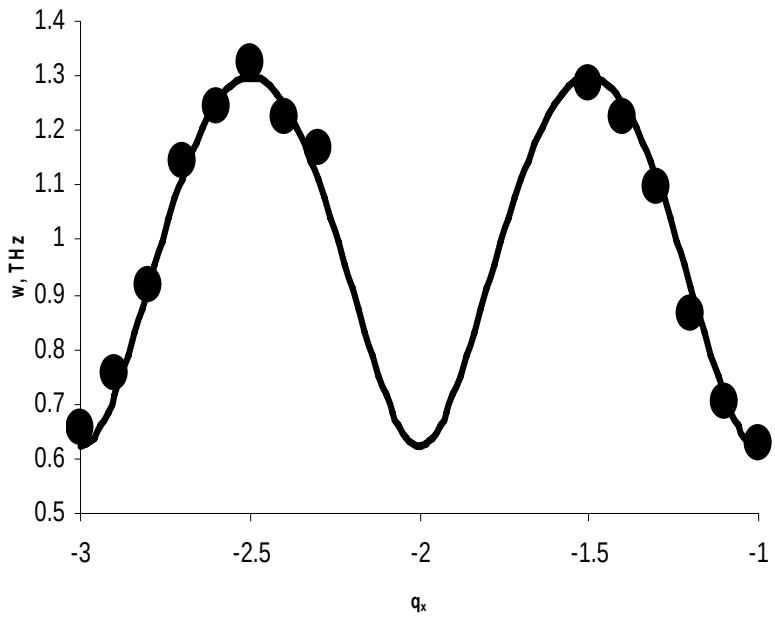

Figure 2.8. Dispersion curve for the $[001]^*$ direction. Experiment from [30].

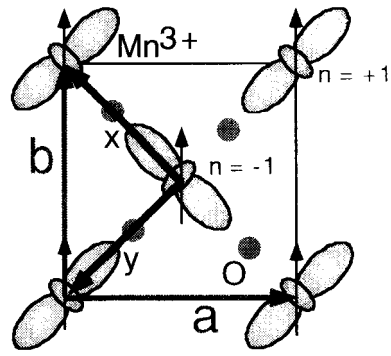

Figure 2.9. The directed lobes of wave functions. The plane picture. From [49].

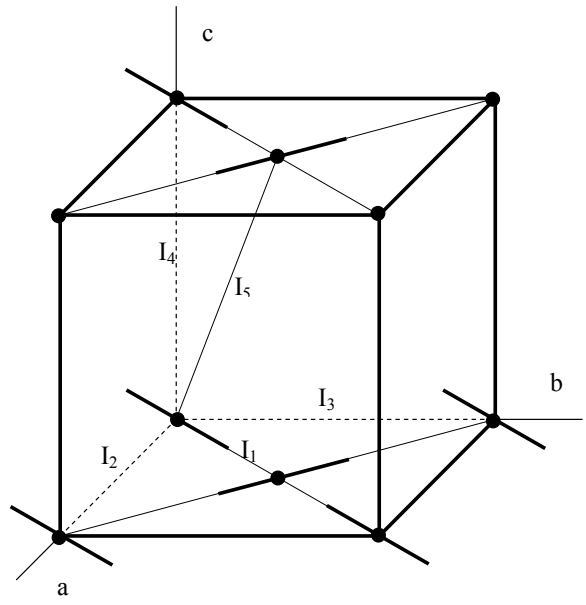

Figure 2.10. The directed lobes of wave functions. The volume picture.

$$w_{[100]^*} = (a_1 + b_1 \cos \pi q_y + c_1 \cos^2 \pi q_y + d_1 \cos^3 \pi q_y + f_1 \cos^4 \pi q_y)^{1/2}, \tag{2.57}$$

$$w_{[110]^*} = (a_2 + b_2 \sin^2 \pi q_y + c_2 \sin^4 \pi q_y)^{1/2}, \tag{2.58}$$

$$w_{[001]^*} = (a_3 + b_3 \cos^2 \pi q_x)^{1/2}, \tag{2.59}$$

where

$$a_1 = 16[16(I_1 + I_2)^2 + \\ + (2I_4 + 8I_5 - D)(2I_4 + 8I_5 - D - 8I_1 - 8I_2) - 4I_4^2], \tag{2.60}$$

$$b_1 = 128[I_1(-4I_1 - 4I_2 + 2I_4 + 8I_5 - D) - 4I_4 I_5], \tag{2.61}$$

$$c_1 = 128[2I_1^2 + I_2(-4I_1 - 4I_2 + 2I_4 + 8I_5 - D) - 8I_5^2], \tag{2.62}$$

$$d_1 = 512 I_1 I_2, \tag{2.63}$$

$$f_1 = 256 I_2^2, \tag{2.64}$$

$$a_2 = -16D[4(I_4 + 4I_5) - D], \tag{2.65}$$

$$b_2 = 128[-(I_1 + I_2 + I_3)(2I_4 + 8I_5 - D) + 4(I_4 + 4I_5)I_5], \tag{2.66}$$

$$c_2 = 256[(I_1 + I_2 + I_3)^2 - 4I_5^2], \tag{2.67}$$

$$a_3 = 16(2I_4 + 8I_5 - D)^2, \tag{2.68}$$

$$b_3 = -64(I_4 + 4I_5)^2. \tag{2.69}$$

Here we have set $S = 2$.

In order to find numerical values of the parameters $I_1 - I_5$ .and D, we employ the least-square method by minimizing the standard deviation over these parameters and using all fifty four experimental points for all three crystallographic directions simultaneously. The resulting nonlinear of six equations in six unknowns has the following solution (in THz):

$$I_1 = 0.588, I_2 = -0.010, I_3 = 0.011, I_4 = -1.226, I_5 = 0.271, D = 0.040. \tag{2.70}$$

The dispersion curves theoretically calculated with these parameters are shown in Figures 2.6-2.8 by solid lines together with the experimental points. In order to estimate the error in the calculation and the stability of the method, we assume that the relative experimental error for the energy at any quasi-momentum has a moderate value of 10% (the error are not given in [30]). Then, we scatter the experimental data (points in Figures 2.6 - 2.8) by ±10% with a random number generator and recalculate the values of I_1, I_2, I_3, I_4, I_5 and D. We have repeated this procedure 20 times. Our parameters averaged over 20 sets are as follows:

$$\langle I_1 \rangle = 0.550,\ \langle I_2 \rangle = -0.009,\ \langle I_3 \rangle = 0.011,$$
$$\langle I_4 \rangle = -1.142,\ \langle I_5 \rangle = 0.250,\ \langle D \rangle = 0.039. \tag{2.71}$$

Determining the root-mean-square deviations, we find the following relative errors δ :

$$\delta(I_1) = 18\%,\ \delta(I_2) = 59\%,\ \delta(I_3) = 32\%,$$
$$\delta(I_4) = 20\%,\ \delta(I_5) = 23\%,\ \delta(D) = 11\%. \tag{2.72}$$

The values of the parameters from solutions Eq. (2.70) are within the confidence intervals.

2.5. Discussion of Results

Let us discuss the results. First, we compare our solution Eq. (2.70) with the results reported in [30]. In [30], it is assumed, just as we do, that $I_1 > 0$ and $I_4 < 0$ (here, we use the notations accepted in present work). However, the authors of those studies allowed only for the nearest neighbor interactions (I_1 and I_4 parameters), while we consider the next-nearest neighbors (I_2, I_3 and I_5) as well. The performed in [30] mathematical treatment of the experimental data (shown here in Figures 2.6-2.8) yields the following results (in THz):

$$I_1 = 0.2, I_2 = -0.14, I_3 = 0.04. \tag{2.73}$$

A comparison of these results with the values of solutions Eq. 2.70 demonstrates that only the value of D is in agreement, while the values of I_1 and I_4 differ very greatly from solutions Eq. 2.70. Note that the authors of [30] indicated difficulties in applying their method to the determination of the I_4 parameter: if its value is determined for the $[001]^*$ direction, it amounts to -0.14 THz, whereas the corresponding value determined from curves in the (ab) plane is equal to zero.

Feiner and Oleś [47, 48] also determined I_1 and I_4 . They did not analyze the dispersion curves but calculated I_1 and I_4 from their theoretical model. They obtained 0.28 THz for I_1 and -0.21 THz for I_4 . These values also disagrees with our data (solutions Eq. 2.70).

Reasons for disagreement of our results with those obtained in [30] are most likely as follows: first, we have taken into account a large number of interaction parameters, and, second, we have determined these parameters for all the three crystallographic directions simultaneously rather than separately. As regard the discrepancies with results obtained in [47, 48], we can only remark that the model microscopic calculation and the results of mathematical treatment of dispersion curves have not reached a fairly good agreement.

It is evident from solutions Eqs. (2.70) and (2.71) that the exchange interaction is significantly anisotropic. This fact agrees well with the orbital ordering phenomenon, which was revealed in the $LaMnO_3$ compound by resonant x-ray scattering in [49]. The magnitudes of the exchange integrals are determined by both the distance between ions and the mutual orientation of the 3d functions. We see in Figure 2.9, reproduced from the work by Murakami et al [49] the direction of wave function is shown. In volume picture Figure 2.10 it is seen that I_1 and I_5 correspond to the mutual "perpendicularity" of the lobes of the wave functions, whereas I_2, I_3 and I_4 correspond to their "parallelism". This is responsible for the strong anisotropy of the exchange interaction. This effect is especially strong for I_2 and I_5 interactions: the distances are practically the same (5.5333 Å and 5.531 Å), but they have different signs and different absolute values.

Now, we note the following circumstance. The Néel temperature T_N calculated from the known formula of the molecular field theory with the use of our solutions Eq. (2.70) is equal to 500 K, whereas the corresponding experimental temperature is 140 K [30]. In our opinion, such a large difference can be explained as follows. First, the molecular field theory is known to lead to overestimate values for the ordering temperature. Second, this theory should not be applied to our case at all. Indeed, we introduce two quantities J_1 and J_2 as follows:

$$J_1 = 4I_1 + 2I_2 + 2I_3,\ J_2 = I_4 + 4I_5. \tag{2.74}$$

The quantity J_1 is the total interaction in the ferromagnetic plane, and the quantity J_2 is the interplanar interaction. Using solution Eq. (2.70) we obtain $J_1 = 2.354,\ J_2 = -0.142$, and $y \equiv |J_2|/J_1 = 0.06$. Such a small value of the ratio y allows us to treat our system as a quasi-two-dimensional magnet. In this case, the ordering temperature should be calculated by a method that differs from the method used in the molecular field theory. In [50-53], the approach based on the temperature Green's function method was developed to calculate the temperatures T_N and T_C in layered quasi-two dimensional structures. It was shown that, as the ratio between the interplanar exchange interaction parameter changes from 1 to 0, ordering temperature changes from a maximal temperature to zero. Unfortunately, we cannot use these calculations, because were performed for a particular case of $S = 1/2$ and included only two interaction parameters. However, we can assume with confidence that a small value of y in our case, undoubtedly, leads to a decrease in the calculated temperature T_N (possible, even a severalfold decrease).

For the parameters corresponding to solution Eq. (2.70), the calculated paramagnetic Néel temperature Θ_N amounts to 400 K. One should not expect that this value can be confirmed in the experiment. The point is that, in order to determine the Néel temperature Θ_N, it is necessary to perform high-temperature measurements of the magnetic susceptibility. However, an increase in the temperature results in a change in the lattice parameters and occurrence of phase transitions. Therefore, there arises an uncertainty in the

determination of the Néel temperature Θ_N. Two paramagnetic Néel temperatures, i.e., the "low Néel temperature" (75 K) and the "high Néel temperature" (205 K) were obtained in [54-56].

The check of solution Eq. (2.70) for stability has shown that the average values Eq. (2.71) are close to the initial values Eq. (2.70). The relative errors $\delta(I_2)$ and $\delta(I_3)$ are very large; however, the values of I_2 and I_3 are small and do not make a substantial contribution to the total exchange interaction. The exchange integrals I_1, I_4 and I_5 determine the magnetism of the $LaMnO_3$ compound.

Note, when we use the mean square method to determine the $I_1 - I_5, D$, the very complicated nonlinear system of equations was obtained. The procedure of solving is rather cumbersome and therefore is not present here.

So, the performed analysis of the dispersion curves for spin waves in the $LaMnO_3$ compound has demonstrated that the exchange interactions are characterized by a strong anisotropy: the interactions are opposite in sign for the nearest neighbors and can both be opposite in sign and differ in absolute value by many factors for the next-nearest neighbors. Such anisotropy, which is caused by orbital ordering phenomenon, leads to the quasi-two dimensionality of the magnet. By and large, the theoretical curves agree with experimental data.

PART 3. MAGNETIZATION

In this part the high temperature magnetization in systems with double exchange will be considered. The molecular field method will be used. Formally, this method is applicable at all temperatures, but since at low temperatures it gives incorrect results, we call our approach as a high-temperature one. As above, we will use our model of homogeneous spin alloy with spins $S_1 = S + 1/2$ for Mn^{3+} and $S_2 = S$ for Mn^{4+} where $S = 3/2$. Only collinear configurations will be considered here: one ferromagnetic B and three antiferromagnetic A, C and G (see Figure 1.2). The nearest neighbor approximation will be used and two interaction mechanisms– Heisenberg and double exchange – are to be present. The needed coordinates of sites and operators of the exchange interactions are given in Part 1.

3.1. The Near Ordering Temperatures

If one expands the square root in Hamiltonian $\widehat{H}_{2ex}$ (see Eqs. (1.11) and (1.26)) up to the first degree of spin operator scalar product then in Weis molecular field approximation we obtain

$$\left\langle S_l^z(k) \right\rangle = S_l B_{S_l}(Z_{lk}), \tag{3.1}$$

where

$$B_S(Z)=\frac{2S+1}{2S}\coth\left(\frac{2S+1}{2S}Z\right)-\frac{1}{2S}\coth\left(\frac{Z}{2S}\right) \tag{3.2}$$

is the Brillouin function. (As above $l=1,2$ differs Mn^{3+} and Mn^{4+}; $k=1,2,3,4$ numerates the sublattices.) Let us introduce the following notations for spins of ions Mn^{3+} and Mn^{4+}, being in one of four magnetic sublattices:

$$\begin{aligned}&\left\langle S_1^z(1)\right\rangle=x_1,\left\langle S_1^z(2)\right\rangle=x_3,\ \left\langle S_1^z(3)\right\rangle=x_5,\ \left\langle S_1^z(4)\right\rangle=x_7,\\&\left\langle S_2^z(1)\right\rangle=x_2,\ \left\langle S_2^z(2)\right\rangle=x_4,\ \left\langle S_2^z(3)\right\rangle=x_6,\ \left\langle S_2^z(4)\right\rangle=x_8.\end{aligned} \tag{3.3}$$

Then we obtain the following system of equations for sublattices magnetizations

$$\begin{aligned}x_1&=S_1B_{S_1}(Z_{11}),\\x_2&=S_2B_{S_2}(Z_{21}),\\x_3&=S_1B_{S_1}(Z_{12}),\\x_4&=S_2B_{S_2}(Z_{22}),\\x_5&=S_1B_{S_1}(Z_{13}),\\x_6&=S_2B_{S_2}(Z_{23}),\\x_7&=S_1B_{S_1}(Z_{14}),\\x_8&=S_2B_{S_2}(Z_{24}).\end{aligned} \tag{3.4}$$

The following notations for molecular fields are accepted here:

$$\begin{aligned}Z_{11}&=\frac{2S_1}{T}\{(1-x)^2[4I_1x_3+2I_2x_5]+x(1-x)[4\widetilde{I}_5+2\widetilde{I}_6x_6]\},\\Z_{21}&=\frac{2S_2}{T}\{x^2[4I_3x_4+2I_4x_6]+x(1-x)[4\widetilde{I}_5x_3+2\widetilde{I}_6x_5]\},\\Z_{12}&=\frac{2S_1}{T}\{(1-x)^2[4I_1x_1+2I_2x_7]+x(1-x)[4\widetilde{I}_5x_2+2\widetilde{I}_6x_8]\},\\Z_{22}&=\frac{2S_2}{T}\{x^2[4I_3x_2+I_4x_8]+x(1-x)[4\widetilde{I}_5x_1+2\widetilde{I}_6x_7]\},\end{aligned}$$

$$Z_{13}=\frac{2S_1}{T}\{(1-x)^2[4I_1x_7+2I_2x_1]+x(1-x)[4I_5x_8+2\widetilde{I}_6x_2]\},$$
$$Z_{23}=\frac{2S_2}{T}\{x^2[4I_3x_8+2I_4x_2]+x(1-x)[4\widetilde{I}_5x_7+2\widetilde{I}_6x_1]\},$$
$$Z_{14}=\frac{2S_1}{T}\{(1-x)^2[4I_1x_5+2I_2x_3]+x(1-x)[4\widetilde{I}_5x_6+2\widetilde{I}_6x_4]\},$$
$$Z_{24}=\frac{2S_2}{T}\{x^2[4I_3x_6+2I_4x_4]+x(1-x)[4\widetilde{I}_5x_5+2\widetilde{I}_6x_3]\}, \tag{3.5}$$

where

$$\widetilde{I}_5=I_5+\frac{B_1}{1+S(2S+3)}\sqrt{\frac{S+1}{2S+1}}, \tag{3.6}$$

$$\widetilde{I}_6=I_6+\frac{B_2}{1+S(2S+3)}\sqrt{\frac{S+1}{2S+1}} \tag{3.7}$$

To find the temperature dependence of spontaneous magnetization at temperature approaching the ordering temperature from below let's expand all Brillouin functions at small Z

$$B_S(Z)=\frac{(2S+1)^2-1}{(2S)^2}\left(\frac{Z}{3}\right)-\frac{(2S+1)^4-1}{3(2S)^4}\left(\frac{Z^3}{45}\right), Z<<1. \tag{3.8}$$

The system of equations for sub-lattices magnetizations Eq. (3.4) is essentially simplified if one chooses the concrete type of ordering.

B-structure

As it can be seen from Figure 1.2, at ferromagnetic ordering one has

$$x_3=x_5=x_7=x_1,\ x_4=x_6=x_8=x_2. \tag{3.9}$$

As a result system Eq. (3.4) will consist of two equations

$$x_1=S_1B_{S_1}(Z_{11}),\qquad x_1=S_1B_{S_1}(Z_{11})$$
$$x_2=S_2B_{S_2}(Z_{21}), \tag{3.10}$$

where

$$Z_{11} = \alpha x_1 + \beta x_2,\ Z_{21} = \gamma x_1 + \delta x_2, \tag{3.11}$$

$$\alpha = \frac{2S_1}{T}(1-x)^2(4I_1 + 2I_2), \tag{3.12}$$

$$\beta = \frac{2S_1}{T}x(1-x)(4\tilde{I}_5 + 2\tilde{I}_6), \tag{3.13}$$

$$\gamma = \frac{2S_2}{T}x(1-x)(4\tilde{I}_5 + 2\tilde{I}_6), \tag{3.14}$$

$$\delta = \frac{2S_2}{T}x^2(4I_3 + 2I_4). \tag{3.15}$$

As a result we obtain the following system for magnetizations of the first sub-lattice x_1 and x_2 near Curie temperature

$$x_1 = t_1(\alpha x_1 + \beta x_2) - a_1(\alpha x_1 + \beta x_2)^3, \tag{3.16}$$

$$x_2 = t_2(\gamma x_1 + \delta x_2) - a_2(\gamma x_1 + \delta x_2)^3, \tag{3.17}$$

where

$$t_1 = \frac{S_1+1}{3},\ t_2 = \frac{S_2+1}{3}, \tag{3.18}$$

$$a_1 = \frac{(S_1+1)[1+(2S_1+1)^2]}{45(2S_1)^2},\ a_2 = \frac{(S_2+1)[1+(2S_2+1)^2]}{45(2S_2)^2}. \tag{3.19}$$

The iteration method gives the following solution of system Eqs. (3.16), (3.17)

$$x_1^2 = \frac{-b+\sqrt{b^2-4ac}}{2a\gamma^2},\ x_2^2 = \frac{-b'+\sqrt{b'^2-4a'c'}}{2a'\beta^2} \tag{3.20}$$

where

$$a = 3a_1a_2t_2^2\beta^2, \tag{3.21}$$

$$b=-[a_1t_2^3\beta^2+a_2t_1(1-t_2\delta)^2], \tag{3.22}$$

$$c=\frac{(1-t_2\delta)^2}{\beta\gamma}d, \tag{3.23}$$

$$a'=3a_1a_2t_1^2\gamma^2, \tag{3.24}$$

$$b'=-[a_2t_1^3\gamma^2+a_2t_2(1-t_1\alpha)^2], \tag{3.25}$$

$$c'=\frac{(1-t_1\alpha)^2}{\beta\gamma}d, \tag{3.26}$$

$$d=t_1t_2\beta\gamma-(1-t_1\alpha)(1-t_2\delta). \tag{3.27}$$

When temperature approaches the ordering temperature from below magnetization x_1 and x_2 should turn to zero. One can see that this is carried out when the condition $d=0$ is fulfilled. Solution of this equation leads to the following expression for Curie temperature

$$T_C=\frac{1}{3}\{M_B+\sqrt{N_B+P_B}\}, \tag{3.28}$$

$$M_B=(1-x)^2S_1(S_1+1)(4I_1+2I_2)+x^2S_2(S_2+1)(4I_3+2I_4), \tag{3.29}$$

$$N_B=[(1-x)^2S_1(S_1+1)(4I_1+2I_2)-x^2S_2(S_2+1)(4I_3+2I_4)]^2, \tag{3.30}$$

$$P_B=4x^2(1-x)^2S_1(S_1+1)S_2(S_2+1)(4\widetilde{I}_5+2\widetilde{I}_6)^2. \tag{3.31}$$

One can easy see that magnetization tends to zero at approaching T_C according to the law

$$x_1^2\approx\frac{1}{\gamma^2(T_C)b(T_C)}\left(\frac{\partial c}{\partial T}\right)_{T_C}(T-T_C). \tag{3.32}$$

A - *Structure*

At antiferromagnetic ordering of A – type we have (see Figure 1.2)

$$x_3=x_1, x_5=x_7=-x_1, x_4=x_2, x_6=x_8=-x_2. \tag{3.33}$$

The iteration method analogous to that for ferromagnetic B -ordering leads to the following expression for Néel temperature

$$T_N^A = \frac{1}{3}\{M_A + \sqrt{N_A + P_A}\}, \tag{3.34}$$

where

$$M_A = (1-x)^2 S_1(S_1+1)(4I_1 - 2I_2) + x^2 S_2(S_2+1)(4I_3 - 2I_4), \tag{3.35}$$

$$N_A = [(1-x)^2 S_1(S_1+1)(4I_1 - 2I_2) - x^2 S_2(S_2+1)(4I_3 - 2I_4)]^2, \tag{3.36}$$

$$P_A = 4x^2(1-x)^2 S_1(S_1+1)S_2(S_2+1)(4\tilde{I}_5 - 2\tilde{I}_6)^2. \tag{3.37}$$

C *-structure*

As it can be seen from Figure 1.2, the following correlations between sub-lattices magnetizations take place in this case

$$x_3 = -x_1, x_5 = x_1, x_7 = -x_1, x_4 = -x_2, x_6 = x_2, x_8 = -x_2. \tag{3.38}$$

Then the Néel temperature has the form

$$T_N^C = \frac{1}{3}\{M_C + \sqrt{N_C + P_C}\}, \tag{3.39}$$

where

$$M_C = (1-x)^2 S_1(S_1+1)(-4I_1 + 2I_2) + x^2 S_2(S_2+1)(-4I_3 + 2I_4), \tag{3.40}$$

$$N_C = [(1-x)^2 S_1(S_1+1)(4I_1 - 2I_2) - x^2 S_2(S_2+1)(4I_3 - 2I_4)]^2, \tag{3.41}$$

$$P_C = 4x^2(1-x)^2 S_1(S_1+1)S_2(S_2+1)(4\tilde{I}_5 - 2\tilde{I}_6)^2. \tag{3.42}$$

G *-structure*

With the use of conditions (see Figure 1.2)

$$x_3 = -x_1, x_5 = -x_1, x_7 = x_1, x_4 = -x_2, x_6 = -x_2, x_8 = x_2, \tag{3.43}$$

we obtain the following expression for ordering temperature

$$T_N^G = \frac{1}{3}\{M_G + \sqrt{N_G + P_G}\}, \tag{3.44}$$

where

$$M_G = -(1-x)^2 S_1(S_1+1)(4I_1+2I_2) - x^2 S_2(S_2+1)(4I_3+2I_4), \tag{3.45}$$

$$N_G = [(1-x)^2 S_1(S_1+1)(4I_1+2I_2) - x^2 S_2(S_2+1)(4I_3+2I_4)]^2, \tag{3.46}$$

$$P_G = 4x^2(1-x)^2 S_1(S_1+1)S_2(S_2+1)(4\widetilde{I}_5+2\widetilde{I}_6)^2. \tag{3.47}$$

For all three collinear antiferromagnetic structures A, C and G the temperature dependence of separate sub-lattice magnetization near ordering temperature has the form

$$x_1 \approx \sqrt{T_N^i - T}, \; i = A, C, G. \tag{3.48}$$

3.2. The Wide Temperature Range

When we investigated the temperature dependence of magnetization near ordering temperature where magnetization tends to zero the square root in the expression of double exchange operator was expanded into series. If we are far from ordering temperature such an expansion is not righteous. The magnetization is expressed via Brillouin function only at Heisenberg form of the Hamiltonian. In our case magnetization should be calculated with the help of overall formula

$$\langle J_z \rangle = \frac{Sp(J_z \exp(-\widehat{H}/T))}{Sp(\exp(-\widehat{H}/T)}. \tag{3.49}$$

In the molecular field approximation the systems of equations for mean spin values of Mn^{3+} and Mn^{4+} ions, belonging to the first sub-lattice at different types of ordering have the following form ($i = B, A, C, G$):

$$x_1(i) = \frac{\sum_{m=-2}^{2} m \exp\left\{\frac{2(1-x)}{T}[K_i + L_i]\right\}}{\sum_{m=-2}^{2} \exp\left\{\frac{2(1-x)}{T}[K_i + L_i]\right\}}, \tag{3.50}$$

$$x_2(i)=\frac{\sum\limits_{m=-3/2}^{3/2} m\exp\left\{\dfrac{2x}{T}[R_i+Q_i]\right\}}{\sum\limits_{m=-3/2}^{3/2}\exp\left\{\dfrac{2x}{T}[R_i+Q_i]\right\}}, \tag{3.51}$$

$$K_B=m(1-x)(4I_1+2I_2)x_1+x(4I_5+2I_6)x_2, \tag{3.52}$$

$$L_B=x\sqrt{\frac{S_2+1}{2S_2+1}}(4B_1+2B_2)\sqrt{1+\eta x_2 m}, \tag{3.53}$$

$$R_B=m(1-x)(4I_5+2I_6)x_1+x(4I_3+2I_4)x_2, \tag{3.54}$$

$$Q_B=(1-x)\sqrt{\frac{S_2+1}{2S_2+1}}(4B_1+2B_2)\sqrt{1+\eta x_1 m}, \tag{3.55}$$

$$K_A=m(1-x)(4I_1-2I_2)x_1+x(4I_5-2I_6)x_2, \tag{3.56}$$

$$L_A=x\sqrt{\frac{S+1}{2S+1}}(4B_1\sqrt{1+\eta x_2 m}+2B_2\sqrt{1-\eta x_2 m}), \tag{3.57}$$

$$R_A=m(1-x)(4I_5-2I_6)x_1+x(4I_3-2I_4)x_2, \tag{3.58}$$

$$Q_A=(1-x)\sqrt{\frac{S+1}{2S+1}}(4B_1\sqrt{1+\eta x_1 m}+2B_2\sqrt{1-\eta x_1 m}), \tag{3.59}$$

$$K_C=-m(1-x)(4I_1-2I_2)x_1+x(4I_5-2I_6)x_2, \tag{3.60}$$

$$L_C=x\sqrt{\frac{S+1}{2S+1}}(4B_1\sqrt{1-\eta x_2 m}+2B_2\sqrt{1+\eta x_2 m}), \tag{3.61}$$

$$R_C=-m(1-x)(4I_5-2I_6)x_1+x(4I_3-2I_4)x_2, \tag{3.62}$$

$$Q_C=(1-x)\sqrt{\frac{S+1}{2S+1}}(4B_1\sqrt{1-\eta x_1 m}+B_2\sqrt{1+\eta x_1 m}), \tag{3.63}$$

$$K_G=-m(1-x)(4I_1+2I_2)x_1+x(4I_5+2I_6)x_2, \tag{3.64}$$

$$L_G = x\sqrt{\frac{S+1}{2S+1}}(4B_1+2B_2)\sqrt{1-\eta x_2 m}, \tag{3.65}$$

$$R_G = -m(1-x)(4I_5+2I_6)x_1 + x(4I_3+2I_4)x_2, \tag{3.66}$$

$$Q_G = (1-x)\sqrt{\frac{S+1}{2S+1}}(4B_1+2B_2)\sqrt{1-\eta x_1 m}; \tag{3.67}$$

$$\eta = \frac{2}{1+S(2S+3)}. \tag{3.68}$$

The systems of equations (3.50), (3.51) were solved numerically with the use of exchange parameters and transfer integrals values found in paper Part 1. At that for each type of ordering B, A, C or G some concentration was chosen from the corresponding interval. Figures 3.1-3.4 display the temperature dependences of mean values x_1 and x_2 of ions Mn^{3+} and Mn^{4+} spins, correspondingly. Figures 3.5-3.8 describe temperature dependences of contributions to magnetization on separate site from ions Mn^{3+}

$$\sigma_1 = (1-x)x_1 \tag{3.69}$$

and Mn^{4+}

$$\sigma_2 = xx_2. \tag{3.70}$$

In the same place on Figures 3.5-3.8 temperature dependence of the total magnetization of a separate site

$$\sigma = \sigma_1 + \sigma_2 \tag{3.71}$$

is presented for all investigated collinear configurations. It should be noted that for configurations B and C contributions to separate site magnetization from ions Mn^{3+} and Mn^{4+} have one and the same sign while for configurations A and G the signs are different.

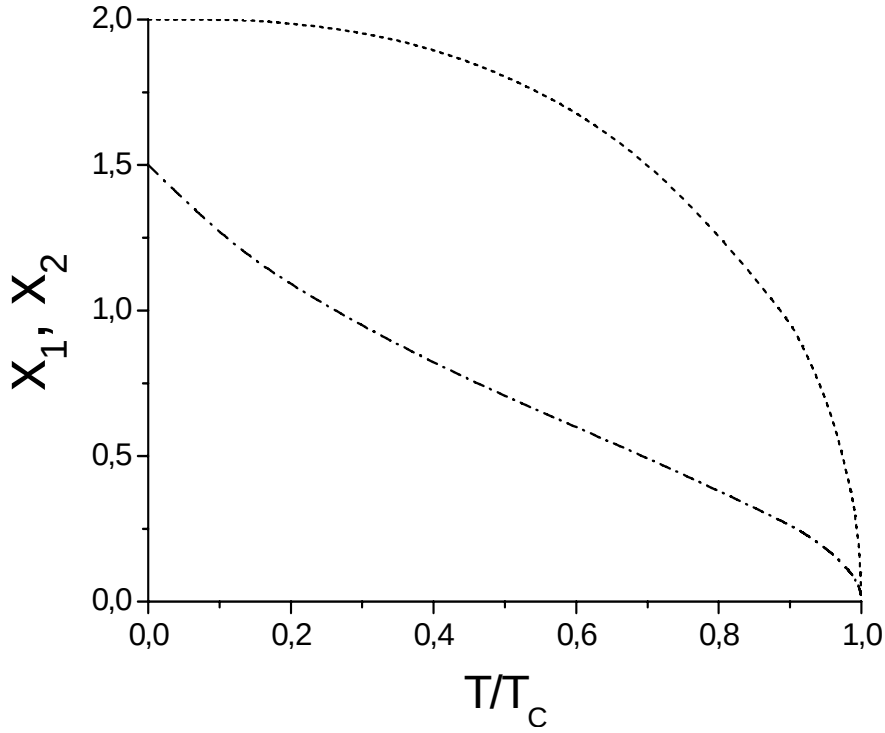

Figure 3.1. Temperature dependence of mean spin values for ions Mn^{3+} (short dashcurve) and Mn^{4+} (dash dot curve) at ferromagnetic ordering. The data are obtained with concentration $x = 0.3$, in this case $T_c = 55.9K$.

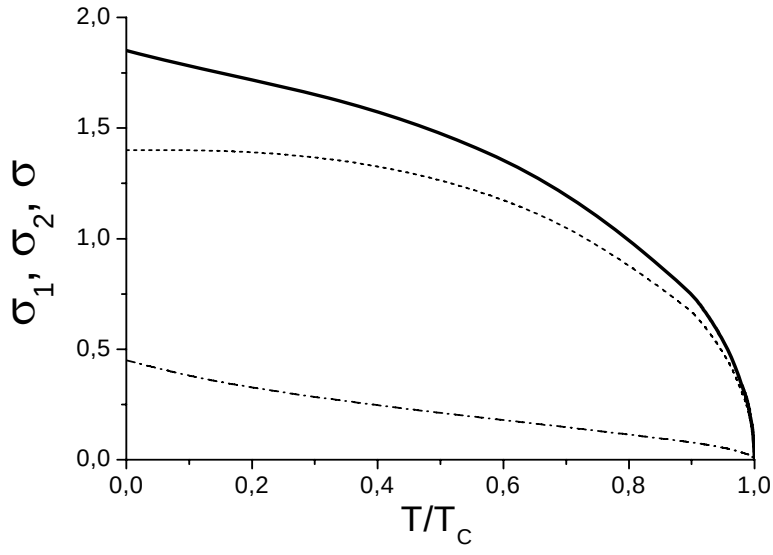

Figure 3.2. Temperature dependence of contributions to magnetization of a separate site from ions Mn^{3+} (short dash curve) and Mn^{4+} (dash dot curve) and the total magnetization of a separate site (solid curve) at ferromagnetic ordering.

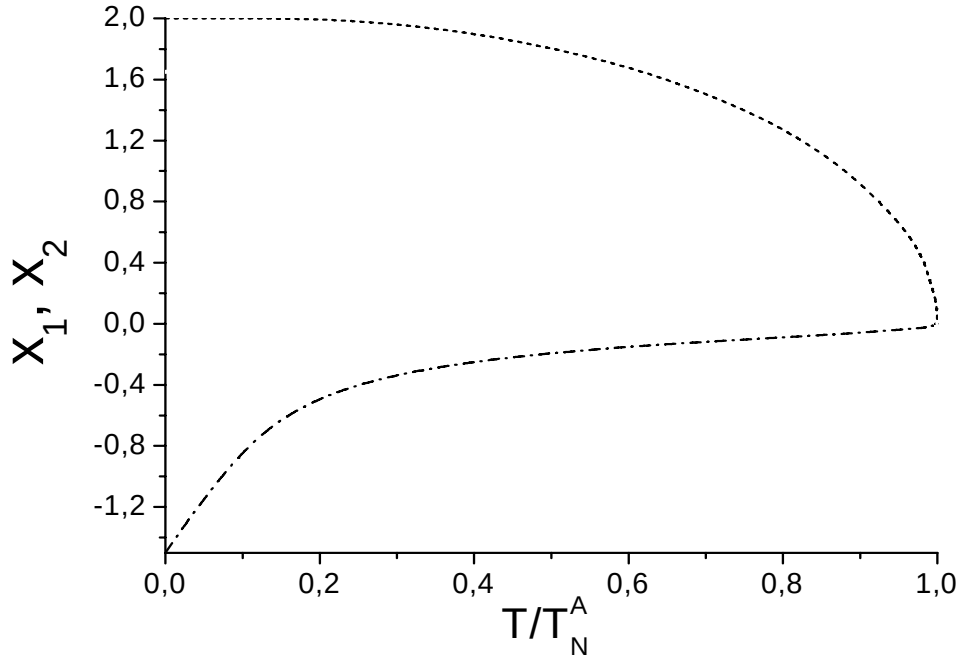

Figure 3.3. Temperature dependence of mean spin values for ions Mn^{3+} (short dashcurve) and Mn^{4+} (dash dot curve) at antiferromagnetic ordering of A-type ($x = 0.1, T_N^A = 168.7K$).

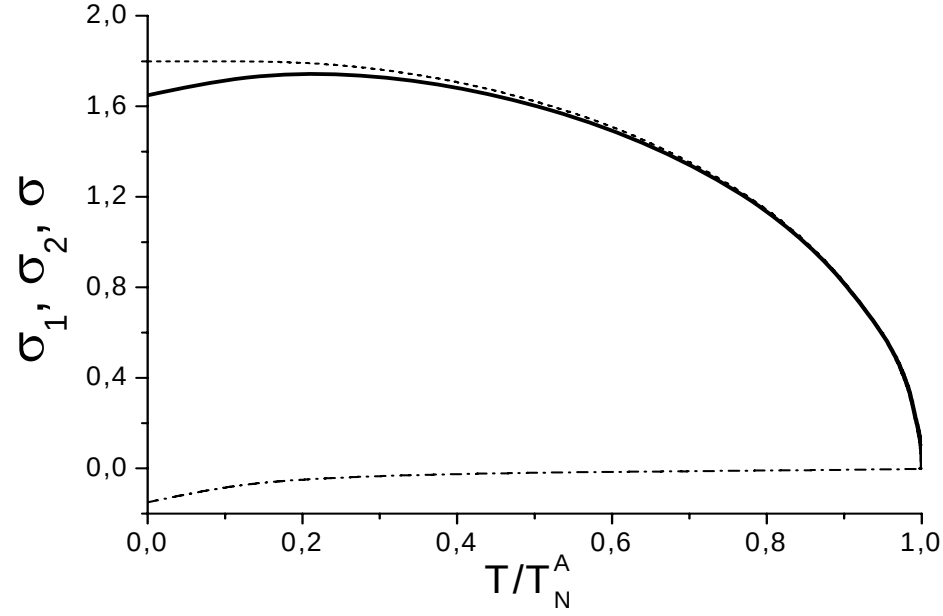

Figure 3.4. Temperature dependence of contributions to magnetization of a separate site from ions Mn^{3+} (short dash curve) and Mn^{4+} (dash dot curve) and the total magnetization of a separate site (solid curve) at antiferromagnetic ordering of A-type.

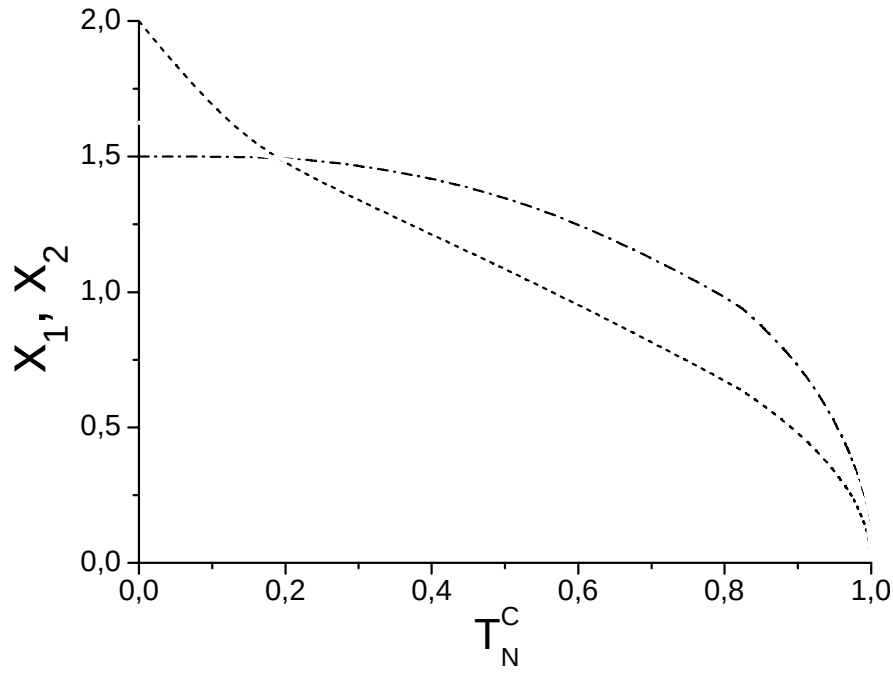

Figure 3.5. Temperature dependence of mean spin values for ions Mn^{3+} (short dashcurve) and Mn^{4+} (dash dot curve) at antiferromagnetic ordering of C-type ($x = 0.75, T_N^C = 37.2K$).

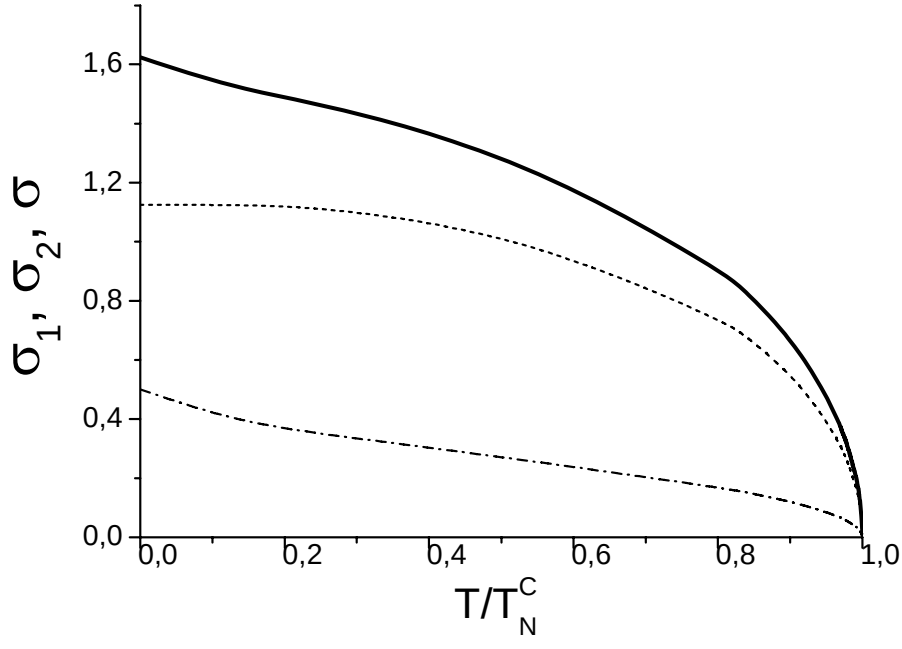

Figure 3.6. Temperature dependence of contributions to magnetization of a separate site from ions Mn^{3+} (short dash curve) and Mn^{4+} (dash dot curve) and the total magnetization of a separate site (solid curve) at antiferromagnetic ordering of C-type.

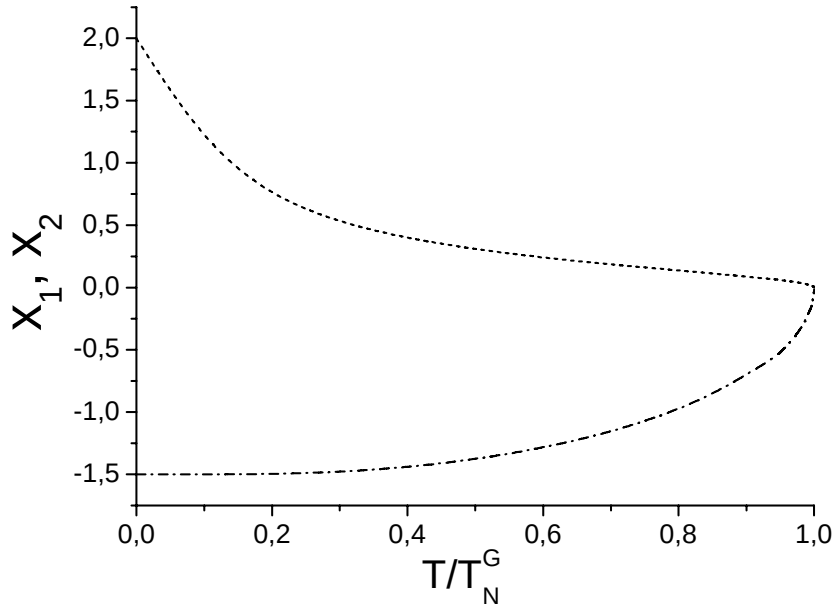

Figure 3.7. Temperature dependence of mean spin values for ions Mn^{3+} (short dashcurve) and Mn^{4+} (dash dot curve) at antiferromagnetic ordering of G-type ($x = 0.9, T_N^G = 106.5K$).

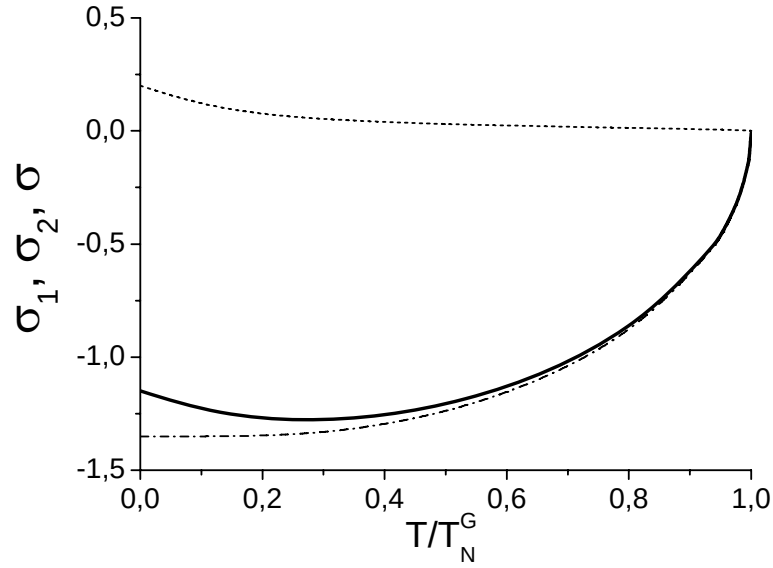

Figure 3.8. Temperature dependence of contributions to magnetization of a separate site from ions Mn^{3+} (short dash curve) and Mn^{4+} (dash dot curve) and the total magnetization of a separate site (solid curve) at antiferromagnetic ordering of G-type.

3.3. Some Notes

The magnetic properties of four collinear magnetic configurations of compound $La_{1-x}Ca_xMnO_3$ are investigated in molecular field approximation. Expressions for ordering temperatures are found. They have the form analogous to Néel temperature for ferrimagnets, and contain evident dependence upon concentration x of Mn^{4+} ions.

The analytical temperature dependences of spontaneous site magnetization were obtained at temperatures near the ordering temperature. For all collinear structures under investigation this dependence has the form

$$\sigma \approx \sqrt{T_{ord} - T}. \tag{3.72}$$

Temperature dependences of site magnetization are calculated in the whole temperature range from zero till ordering temperature. We used the results of papers [60, 61] in this Part.

CONCLUSION

Some problems of physics of lanthanum-calcium manganites were considered in this paper from theoretical point of view. In the frame of proposed model of spin alloy the system behavior was studied at different temperatures in the dependence of concentration heterovalent manganese ions.

In Part 1 at zero temperature the magnetic structures change one another with concentration variety and this process may be described as the pure concentration effect. No structural changes need for explanation of magnetic configuration transitions. But, of cause, it is not so in reality: with concentration variation both the crystallographic and electron structures change also. Therefore we called our object as a hypothetical compound. It seems that this is impossible just now to give the complete picture of magnetic transitions in the whole concentration range.

In Part 2 the spin-wave excitations were considered and in broad terms the concordance between theory and experiment was obtained. As to numerical values of interaction parameters then two difficulties are exist. First difficulty is the large spread of experimental data. Second difficulty is the shortcoming of theoretical treatment methods. Above used the mean square method they consider as incorrect approach. This method can not give the evidence of truth of some theory, but only gives the preference to certain set of parameter values rather then to any other. Therefore the good concordance between theory and experiment may turn out illusory. Nevertheless, after these, not very optimistic notes, say, that comparison theory and experiment must continue with attraction different theories and more sophisticated treatment methods. As to present paper we say, once more, that our results have rather quantitative not qualitative character.

In Part 3 the temperature dependences of spontaneous magnetization of sublattices were obtained. Not comparison with experiment was done, we hope to make it in future. The theoretical formulas have general character and obtained numerical values and graphical matter are given as peculiar examples. It is interesting is it possible to distinguish by some

measurements the contributions in general magnetization from three and four valence manganese ions.

In the conclusion must be said that present approach to the above considered problems is not unique; the different points of view, of cause, may exist.

ACKNOWLEDGMENTS

I thank L. P. Karpenko, L. V. Karpenko, E. A. Volkova, A. V. Kuznetsov, V.V. Dyakin, S. V. Naumov and L. D. Falkovskaya for help in the work.

The author is indebted to Department of Physical Science and Presidium of Ural Branch of the Russian Academy of Sciences, Program "The Physics of new materials and structures", the Russian Foundation for Basic Research (project N 07 02 000 68).

REFERENCES

[1] Jonker, G. H.; van Santen, J. H. *Physica 1950, 16, 337.*
[2] Jonker, G. H.; van Santen, J. H. *Physica 1950, 16, 599*.
[3] Zener, C. *Phys. Rev. 1951, 81, 440*.
[4] Zener, C. *Phys. Rev. 1951, 82, 403*.
[5] Wollan, E. O.; Koehler, W. C. *Phys. Rev. 1955, 100, 545*.
[6] Anderson, P.W.; Hasegawa, H. *Phys. Rev. 1955, 100, 675.*
[7] de Gennes, P.-G. *Phys. Rev. 1960, 118, 141*.
[8] Ramirez, A. P. *J. Phys.; Conds. Matter. 1997, 9, 81711.*
[9] Dagotto, E.; Yunoki, S.; Malvezzi, A. L.; Hu, J.; Capponi, S.; Poilblanc, D.; Furukawa, N. Phys. *Rev. B, 1998, 58, 6414.*
[10] Imada, M.; Fujimori, A.;Tokura, Y. *Rev. Mod. Phys. 1998, 70, 1039.*
[11] Moreo, A.;Yunoki, S.; Dagotto, E. *Science 1998, 283, 2034.*
[12] Coey, J.; Viret, M; von Molnar, S. *Adv. Phys. 1999, 48, 167.*
[13] Tokura, Y.; Tomioka, Y. *J. Magn. Magn. Matter. 1999, 200, 1*
[14] Ibarra, M. R.; De Teresa, J. M. *Mater. Sci. Forum 1999, 302-303, 125*.
[15] Loktev, V. M.; Pogorelov, Yu. G. *Fizika Nizkhih Temper. 2000, 26, 231*. (In Russian)
[16] Dagotto, E.; Hotta, T.; Moreo, A. *Phys. Rep. 2001, 344, 1.*
[17] Moreo, A. *Electron Spectrosc. Relat. Phenom. 2001, 117-118, 251.*
[18] Salamon, M. B.; Jaime, M. *Rev. Mod. Phys. 2001, 75, 583.*
[19] Kagan, M. Yu.; Kugel, K. I. *Usp. Fiz. Nauk 2001, 171 B, 577*. (In Russian)
[20] Dagotto, E. *Nanoscale Phase Separation and Colossal Magnetoresistance;* Springer: Berlin, 2002; p.p. 448.
[21] Haghiri-Gosnet, A.-M.; Renard, J.-P. *J. Phys. D: Appl. Phys. 2003, 36, R127*.
[22] Mathur, N.; Littlewood, P. *Phys. Today 2003, 56, 25.*
[23] Weisse, A; Fehske, H. *New J. Phys. 2004, 6, 158.*
[24] Dagotto, E. *New Journal of Physics 2005, 7, 67.*
[25] Ruderman, M. A.; Kittel, C. *Phys. Rev.1954, 96, 99.*

[26] Kasuya, T. *Progr. Theor. Phys.1956, 16, 45.*
[27] Yosida, K. *Phys. Rev. 1957, 106, 893.*
[28] Schubin, S. P.; Vonsovsky S. V. *Proc. Roy. Soc. 1934, A145, 159.*
[29] Vonsovsky, S. V. *Magnetism*; Nauka; Moscow, 1971, p.p. 805. (In Russian).
[30] Moussa, F.; Hennion, M.; Rodriguez-Carvajal, J.; Mouden, H.; Pinsard, L.; Revcolevschi, A. *Phys. Rev. B 1996, 54, 15149.*
[31] Hennion, M.; Moussa, F.; Rodriguez-Carvajal, J.; Pinsard, L.; Revcolevschi, A. *Phys. Rev. B 1997, 56, R497.*
[32] Hennion, M.; Moussa, F.; Bioteau, G.; Rodriguez-Carvajal, J.; Pinsard, L.; Revcolevchi, A. *Phys. Rev. Lett. 1998, 81, 1957.*
[33] Hennion, M.; Moussa, F.; Bioteau, G.; Rodriguez-Carvajal, J.; Pinsard, L.; Revcolevchi, A. *Phys. Rev B 2000, 61, 9513.*
[34] Bioteau, G.; Hennion, M.; Moussa, F.; Rodriguez-Carvajal, J.; Pinsard, L.; Revcolevschi, A.; Mukovskii, Y. M.; Shulyatev, D. *Phys. Rev. B 64, 2001, 104421.*
[35] Radaelli, P. G.; Cox, D. E.; Capogna, L.; Cheong, S.-W.; Marezio, M. *Phys. Rev. B 1999, 59, 14440.*
[36] Pissas, M.; Kallias, G.; Hofmann, M.; Többens, D. M. *Phys. Rev. B 2002, 65, 064413.*
[37] Pissas, M.; Kallias, G. *Phys. Rev. B 2003, 68, 134414.*
[38] Heffner, R. H.; Sonier, J. E.; Machlaughlin, D. E.; Nieuwenhuys, G. M.; Luke, G. M.; Uemura, Y. J.; William Ratcliff II; Cheong, S. W.; Balakrishnan, G. *Phys. Rev. B 2001 63, 094408.*
[39] Karpenko, B.V.; Falkovskaya, L. D.; Kuznetsov, A.V. (2005) Magnetic structure and double exchange in hypothetical compound $La_{1-x}Ca_xMnO_3$, cond-mat0509507.
[40] Karpenko, B.V.; Falkovskaya, L. D.; Kuznetsov, A.V. *The Physics of Metals and Metallography 2008, 105, 443.*
[41] Moussa, F.; Hennion, M.; Wang, F.; Kober, P.; Rodrigez-Carvajal, J.; Reutler, P.; Pinsard, L.; Revcolevcshi, A. *Phys. Rev. B 2003, 67, 214430-1.*
[42] Perring, F.G.; Aeplli, G.; Hayden, S. M.; Carter, S. A.; Remeika, J. P.; Cheong, S-W. *Phys. Rev. Lett. 1996, 77, 711.*
[43] Hwang, H. Y.; Dai, P.; Cheong, S. W.; Aeppli, G.; Tennant, D. A.; Mook, H. A. *Phys. Rev. Lett. 1998, 80, 1316.*
[44] Hennion, M.; Moussa, F. *New Journal of Physics 2005, 7, 84* .
[45] Ye, F.; Dai, P.; Fernandez-Baca, J. A.; Hao Sha; Lynn, J. W.; Kawano-Furukawa, H.; Tomioka, Y.; Tokura, Y.; Zhang, J. *Phys. Rev. Lett. 2006, 96, 047204-1.*
[46] Ye, F.; Dai, P.; Fernandez-Baca, J. A.; Adroja, D.T.; Perring, T. G.; Tokura, Y. *Phys. Rev. B 2007, 75, 144408-1.*
[47] Feiner, L. F.; Oleś, A. M. *Physica B 1999, 259-261, 796.*
[48] Oleś, A. M.; Feiner, L. F. *Phys. Rev. B 2002, 65, 052414-1.*
[49] Murakami, Y.; Hill, J. P.; Gibbs, D.; Blume, M.; Koyama, I.; Tanaka, M.; Kawata, H.; Arima, Y.; Tokura, Y.; Hirota, K.; Endoh, Y. *Phys. Rev. Lett. 1998, 81, 582.*
[50] Lines, M. E. *Phys. Rev. 1964, 133, A841.*
[51] Lines, M. E. *Phys. Rev. 1964, 135, A1336.*
[52] Karpenko, B. V.; Falkovskaya, L. D.; Dyakin, V. V.; Kaybitcheva, S. L. *Low-Dim. Struct. 2002, 7/8, 57.*

[53] Karpenko, B. V.; Falkovskaya, L. D.; Dyakin, V. V.; Kuznetsov, A. V.; Kaybitcheva, S. L. *Low-Dim. Struct. 2003, 5/6, 53.*

[54] Prado, F.; Zysler, R.; Morales, L.; Caneiro, A.; Tovar, M.; Causa, M. T. *J. Magn. Magn. Mater. 1999, 196-197, 481.*

[55] Causa, M. T.; Alejandro, G.; Zysler, R.; Prado, F.; Caneiro, A.; Tovar, M. *J. Magn. Magn. Mater. 1999, 196-197, 506.*

[56] Tovar, M.; Alejandro, G.; Butera, A.; Caneiro, A.; Causa, M.T.; Prado, F.; Sánchez, R. D. *Phys. Rev. B 1999,* 60, *10199.*

[57] Karpenko, B. V.; Falkovskaya, L. D.; Kuznetsov, A. V. *The Physics of Metals and Metallography 2008, 106, 136.*

[58] Karpenko, B. V.; Falkovskaya, L. D.; Kuznetsov, A. V. *Physics of the Solid State 2008, 50, 2102.*

[59] Karpenko, B. V.; Kuznetsov, A. V. (2008). The Exchange Parameters in Lanthanum Manganites, cond-mat arXiv:0805. 3006 v1.

[60] Karpenko, B. V.; Falkovskaya, L. D.; Kuznetsov, A. V. (2006). Magnetic Properties of Collinear Structures of Compound $La_{1-x}Ca_xMnO_3$, cond-mat/0604161.

[61] Karpenko, B. V.; Falkovskaya, L. D.; Kuznetsov, A. V. *Israel Journal of Chemistry 2007, 47, 397*.

In: Perovskites: Structure, Properties and Uses
Editor: Maxim Borowski, pp. 437-461
ISBN 978-1-61668-525-6

Chapter 10

CORRELATIONS BETWEEN THE STRUCTURE OF ORDERED SOLID SOLUTIONS AND PARAMETERS OF PAIR INTERACTIONS IN PEROVSKITES

A. Yu. Gufan[1] and K. Yu. Gufan[2]
[1]Institute of Physics, South Federal University, Rostov-on-Don, Russia
[2]Institute of Security Computing Devices and Automatics, Rostov-on-Don, Russia

ABSTRACT

In the chapter two approaches to the crystals ordered states description are used. The first is basing on the group theoretical considerations incorporated in theory with the help of Landau potential. The second way of ordering description consist of accounting different models of interatomic interactions. Our goal is to elucidate correlations between these two approaches. Complex oxides with composition $AB'_cB''_{1-c}O_3$ and perovskite like structure are considered as an example. Six supercells which may be realized as stable states in these solid solutions in accord with Landau theory are analyzed in the framework of both approaches. The potential of interatomic coupling includes van der Waals energy and terms following from pseudopotential model. The sum of interatomic energy in twelve coordination spheres was accounted to get correlation between the parameters of Landau potential and coefficients of interatomic energy and to define the domain of different ordering state stability in the space of phenomenological parameters. In particular it is shown that under certain conditions the type of ordering in a surface area may differ from the type of ordering in a bulk of crystal. Using a new approach to X-ray diffraction pattern interpretation there was established definite correlations between the parameters of pair interactions potential and the peculiarities of ordered states which may be defined from the experiment.

1. INTRODUCTION

The physical properties of multi-component oxides with the perovskite structures (OPS) are strongly correlated with the cationic composition. The magnetoresistive effect exists in almost all manganates containing rare-earth elements similar to $La_{2/3}Ca_{1/3}MnO_{3-\delta}$ [[1] the high-T_c conductivity occurs in many kinds of cuprates, containing *Ba* and rare-earth element *(R)* or Yttrium similar to $R_{1/3}Ba_{2/3}CuO_{3-y}$ [2],[3]; the relaxor properties exists in many Pb-based, complex OPS similar to $PbMg_{1/3}Nb_{2/3}O_3$, *etc*.

The cationic composition determines the specific properties of the structure. Usually, the structure of multi-component OPS is described by comparison with the structure of parent phase. The OPS parent phase of ABO_3 compound is characterized by O_h^1-symmetry. The structure of parent phase is determined by the distribution of *A,B* and *O* ions in vertexes of the system of regular points (SRP) of O_h^1-symmetric unit cell by the following way: A-ions are located in 1(*b*) ($\frac{1}{2},\frac{1}{2},\frac{1}{2}$) SRP, B-ions are in 1(*a*) ($0,0,0$) SRP and oxygen *O* occupies 3(*d*) SRP. The composition of the multi-component OPS is $(A'_{x1}A''_{x2}A''_{x3}...)(B'_{y1}B''_{y2}B''_{y3}...)O_3$, where $A^{(i)}$ and $B^{(i)}$ ions are distributed, regularly or randomly, in 1(b) and 1(a) SRP respectively. In complex OPS, the order of the cationic distribution in a crystal is strongly correlated with the crystal's composition. For example, the structures of all OPS similar to $R^{3+}_{1/3}Ba^{2+}_{2/3}CuO_{3-\gamma}$ are marked by the following ordered distribution of *R* and *Ba* cations along the axis of 4-fold parent phase symmetry [[4] in A-block: $\ldots \mathrm{R,Ba,Ba,R,Ba,Ba}\ldots.$ The structure of Ba-based OPS, that show anomaly high transparency in the range of millimeter-waves (for instance, $BaMg_{1/3}Nb_{2/3}O_3$ or $BaZr_{1/3}Ta_{2/3}O_3$ [[5]) is characterized by triple parent phase period caused by the ordered distribution of cations along the axis of 3-fold parent phase O_h^1.-symmetry in 1 (a) SRP (in B-sublattice), too. In the Pb-based relaxors featured by giant electrostriction such as $PbB'_{1/3}B''_{2/3}O_3$, the parent phase period is doubled because of the ordered distribution of the cations along the axis of 3-fold symmetry in B-sublattice [6].

The diversity of the observed types of the ordered cationic distribution inside crystal lattice put a question about the characteristics of structural elements of complex OPS, the combination of which determines a particular type of the order in the cationic distribution. In other words, it is interesting to build a sufficiently founded mathematical model of interactions between structural elements in crystals similar to $A(B'_xB''_{1-x})O_3$ and to clear (elucidate) conditions on the model parameters determining the type of the order of the cations distribution inside of crystal.

In this chapter, the model of the effective ion pair interaction spreads on not less than 11 coordinate spheres has been taken as a base model of interactions between structural components. Regardless of the criticism of the model, the usage of approximation of effective pair interactions has many advantages that become conclusive during the choice of the proper

model of interactions. First of all, this model gives possibility to conduct the numeric and analytical researches simultaneously and, also provides us with an ability to obtain some parameters of the model on the base of "the first principles". Moreover, the numeric parameters of the model have clear physical meaning and can be compared with real features of the studied objects independently from the experiment conditions.

These arguments, mainly practical, in favor of using the approximation of effective pair interactions, can not let us disregard very substantial arguments against the model. So, in the next section of this chapter, the results obtained by using the model of effective pair interactions for the interpretation of data received from X-ray diffraction pattern of $PbFe_{1/2}Nb_{1/2}O_3$ sample are given as an additional confirmation of usefulness of the model in case of a perovskite-like structure. Although the application of the model has to be legitimated during further discussion, the obtained result is of independent interest.

2. Interpretation of X-ray Diffraction Patterns of Complex Oxides with a Perovskite-type Structure

2.1. Theoretical Aspects

The primitive cell of the ideal perovskite ABO_3 structure is cubic. It is characterized by the following positions of ions in the arbitrarily chosen first unit cell: A, B and O ions occupy, respectively, the positions $1(a)\,(0,0,0)$, $1(b)\,(a/2, a/2, a/2)$ and $3(c)\,[(0, a/2/a/2), (a/2, 0, a/2), (a/2, a/2, 0)]$. A ions are generally have a large ionic radius, ($Pb^{2+}, Ba^{2+}, Ca^{2+}$...), whereas B ions ($Ti^{4+}, Mg^{2+}, Nb^{5+}$ etc) generally have a small ionic radius. In an perfect crystal of the ABO_3 composition , the static electric field induced by all ions at any site belonging to the regular system of points $1(a)$ is zero due to the symmetrical arrangement of the occupied regular systems of points $1(b)$ and $3(c)$. Such compensation occurs at any pair interactions between ions if these interactions depend only on distance.

If ions of two types, B' and B'', are distributed (regularly and irregularly) over the system of regular points $1(b)$, there will necessarily be an uncompensated electric field at some (or all) positions belonging to the regular system of points $1(a)$. The potential energy minimum determining the average position of *A* ions cannot be located at positions with an uncompensated field. Thus, in solid solutions of oxides with perovskite structure, A ions are spontaneously shifted from $1(a)$ positions. The shift of A ions in turn leads to the shift of other ions. Since shifts of B', B'' and O ions are secondary, this process is referred to as relaxation of the structure. In view of partial (or complete) randomness of the distribution of B' and B'' ions over the actual lattice sites, X-ray diffraction patterns of crystals of solid solutions (and compounds within the homogeneity range in the phase diagram) differ from the X-ray diffraction patterns of perfect crystals [[7]-[13]. In particular, an X-ray diffraction

pattern contains information about the degree and type of order in the distribution of $B^{/}$ and $B^{//}$, ions, the values and anisotropy of mean static and dynamic (thermal) shifts of $A, B^{/}, B^{//}, O$ ions, and the electron-density distribution in the unit cell. The question is on the basis of what models one can obtain reliable information about the above-mentioned specific features of an actual structure.

Let us describe some class of models used to interpret X-ray diffraction patterns of lead containing solid solutions of perovskites of the $PbB^{/}_{x}B^{//}_{1-x}O_3$ composition, where $B^{/}$ and $B^{//}$ ions are generally several times lighter than Pb (atomic weight 207,2) ions:: Mg (24), Nb (93), Zn (65,4), Sc (44) etc. It is well known that the scattering factor (amplitude) of an ion is approximately proportional to its atomic weight (more strictly, to the total number of electrons localized at the ion). This circumstance makes it possible to develop a model for interpreting X-ray diffraction patterns by the method of successive approximations [[7]-[13]].

The zero-order approximation [[7]-[13]] is based on the assumption that all atoms reliably occupy all sites which are allowed for them in the ideal perovskite structure and the scattering factor f of the ions located in positions ($1b$), is calculated for a mean ion. If $B^{/}$ and $B^{//}$ atoms are irregularly distributed over the $1(b)$ positions, $f(X) = f(B^{/}) \cdot c + f(B^{//}) \cdot (1-c)$. If the distribution of $B^{/}$ and $B^{//}$ ″atoms is ordered as in compounds (as for example in daltonides [[14]]) or partially ordered as in ordering solid solutions, X-ray diffraction patterns are interpreted using a unit cell of lower symmetry, whose positions are occupied by Y atoms with the scattering factor $f(Y) = P_1 f(B^{/}) + P_2 f(B^{//}),$ where P_1, $P_2 = 1 - P_1$ – are the occupation probabilities for $B^{/}$ and $B^{//}$ atoms. The fitting parameters used to fit the X-ray diffraction pattern calculated within the zero-order approximation model to experimental patterns, along with the tentative structure, are the Debye-Waller factors W. The factors W are proportional to the mean square shift of each ion (Pb, X, O) from its equilibrium position. In the calculation formulas for scattering intensity, they enter as factors at the scattering amplitudes of ions. The scattering amplitude modified by the factor W is $f^{/}_{\alpha} = f_{\alpha} \exp(-(W_{\alpha} / kT))$. Here α - is the type of an atom ($\alpha = Pb, O, X$). Within the zero-order approximation, the factors W_{α} are assumed to be spherically symmetric: $W_{\alpha} \sim (< x^2_{\alpha} > + < y^2_{\alpha} > + < z^2_{\alpha} >)$, where $< x_{\alpha} >$ - is the mean-square shift of an ion α along the x axis, etc. When the ideal perovskite structure is considered and the mean-X atom approximation is used to calculate f, the assumption about the isotropic Debye-Waller factor is valid only for oxygen atoms having tetragonal environment. The mean-square shift of an α atom from the equilibrium position: $< \vec{r}^{\,2}_{\alpha} > = < x^2_{\alpha} > + < y^2_{\alpha} > + < z^2_{\alpha} >$, includes both dynamic components due to thermal atomic vibrations with meansquare amplitudes proportional to $k_{Б}T$, and static components $< \delta r^2_{st} >$, due to the random

distribution of $B^{/}$ and $B^{//}$ ions over the regular system of points $1(b)$ in the ideal perovskite structure: $<\delta\ \ r^2>=<\delta\ \ r_{st}^2>+<\delta\ \ r_d^2>$.

Generally, the model in which all lead atoms in the solid solution are statically shifted from their equilibrium positions in the ideal structure is considered in the first-order approximation [10],[13] . In each unit cell, lead atoms are shifted in the same directions and at the same distance $<r_\alpha>$. In the first-order approximation models, shifts in asymmetric directions are sometimes chosen [[8]]. In this case, the model acquires three' additional fitting parameters: $\delta x_{Pb}, \delta y_{Pb}, \delta z_{Pb}$.

The models assuming that Pb ions are shifted with equal probabilities in several nonequivalent directions should also be assigned to the first-order approximation models. If we do not assume that shifts in nonequivalent directions are equiprobable, such models also include additional phenomenological parameters related only to Pb ions: shifting probabilities in a specified direction and the shift values.

The next-level models allow for some relaxations of the structure, i.e., take into account shifts of X or ($B^{/}$ and $B^{//}$) and O [7]-[13]. In these models, it is assumed that the system of unit cells of a crystal is divided into two or more subsystems. A specific model is put into correspondence with each subsystem and the concentrations of cells belonging to a particular subsystem are used as an additional fitting parameter [8],[12].

Thus, in the approach of current use, refinement of the X-ray diffraction pattern interpretation results in an increase in the number and variety of fitting parameters in the theoretical model of a structure studied. Besides that, most of these parameters are introduced ad hoc and have an unclear physical meaning outside the context of the interpretation of diffraction patterns.

However, as will be shown below, the zero-order approximation model has a potentiality of direct analytical calculation of a larger part of phenomenological (fitting) model parameters of the next approximations. Calculation is performed on the basis of theoretical probabilistic analysis of the chemical compositions of unit cells of a solid solution crystal, which are possible in principle. Consideration of this fact should simplify and refine the theory of X-ray diffraction patterns.

For example, the model of a perfect crystal suggests that all positions allowed for B atoms, are occupied by $B^{/}$ and $B^{//}$ with only one ($B^{/}$ or $B^{//}$) atom per position. Therefore, the distribution of $B^{/}$ and $B^{//}$ atoms over the $1(b)$ position obeys a binomial law. In more complex oxides $(A_{c1}^{/}A_{c2}^{//}...A_{1-c1-c2-...}^{n})(B_{c3}^{/}B_{c4}^{//}...B_{1-c1-c2-...}^{n})O_3$ the Fermi statistics is valid for independent distribution of A and B atoms. Note that vacancies in solid solutions can be considered as the third clement of A or B types.

Let us assume that all $B^{/}$ and $B^{//}$ atoms are randomly distributed over the sites belonging to the regular system of points $1(b)$ of the ideal perovskite structure. In this case, 22 structural versions of the inveronment of Pb ions are possible. They include: (i) eight versions in which 0, 1, 2, and 3 $B^{/}$ ions and 8, 7, 6, and 5 $B^{//}$ ions are arranged in

geometrically different ways around the lead ion; (ii) eight versions with interchanged positions of $B^{/}$ and $B^{//}$ ions; and (iii) six geometrically distinguishable positions of four $B^{/}$ and four $B^{//}$ ions. If only interaction with the nearest neighbors is taken into account, all 14 geometrically different environments of Pb ion form nine types of crystal field of different symmetry at $1(b)$ positions: $O_h, Td, D_{3d}, D_{2h}, C_{3v}, C_{4v}, C_{2v}, C_s, C_2$ (Figure 1). If the crystal field has any of the $C_{3v}, C_{4v}, C_{2v}, C_s, C_2$ types of symmetry, the Pb, ion will be necessarily shifted from its position in the ideal perovskite lattice toward the symmetry axis of the four above-mentioned point groups. If the field symmetry at the $1(b)$ position is C_s, the Pb, ion can be generally shifted in an arbitrary direction in one of the 12 planes of the $[1,1,0]$ family of the ideal cubic cell. However, if the interaction forces between lattice ions are central and pair, the situation is simplified. Let us consider a unit cell with seven sites occupied by $B^{/}$ atoms and one site occupied by $B^{//}$. The forces acting on the Pb ion from the $B^{/}$ ions located at the ends of one of the body diagonals of the cube balance each other. Therefore, the Pb ion can be shifted only along the body diagonal connecting $B^{/}$ and $B^{//}$ ions. Let us denote the corresponding shift as u. Obviously, the ion Pb will be shifted by the same value u and in the same direction (along the threefold symmetry axis) in the cell where seven sites are occupied by $B^{//}$ and one site is occupied by $B^{/}$. Let us now consider a unit cell with two sites in the $1(b)$ position, occupied by $B^{/}$ and six sites occupied by $B^{//}$ ions. There may be three geometrically different versions of arrangement of $B^{/}$. If $B^{/}$ ions occupy the lattice sites located along the same body diagonal of the unit cell, the field at the Pb ion has the D_{3d} symmetry and, therefore, the Pb ion will not be shifted from the 1(a) position. If $B^{/}$ ions are located in the lattice sites connected by the same edge of the unit cell, the symmetry of the crystal field induced by $B^{/}$ and $B^{//}$ ions will be C_{2v} at the center of the unit cell, and Pb ion should be shifted along the twofold axis of the (110) type. The value of this shift can easily be calculated from geometric considerations, $\nabla = u(2\sqrt{2}/3)$. All other shifts of Pb ions for all 256 possible geometries of arrangement of $B^{/}$ and $B^{//}$ ions in the ideal perovskite lattice are calculated similarly using the fitting parameter of the theory.

For a partially ordered crystal, the number of fitting parameters increases as a result of consideration of the degree and type of order. However, these additional parameters can be determined and/or calculated in interpretation of the· results of independent experiments [[15]. Moreover, the dependence of the probability distribution of shifts of Pb ions on the degree of order in the distribution of $B^{/}$ and $B^{//}$ ions and the type of ordered distribution of $B^{/}$ and $B^{//}$, ions (calculated, for example, in [[16]), makes it possible, minimizing the factor of incompatibility of theoretical and experimental X-ray diffraction patterns (R-factor), to independently establish the crystal symmetry in the ordered state and the degree of order.

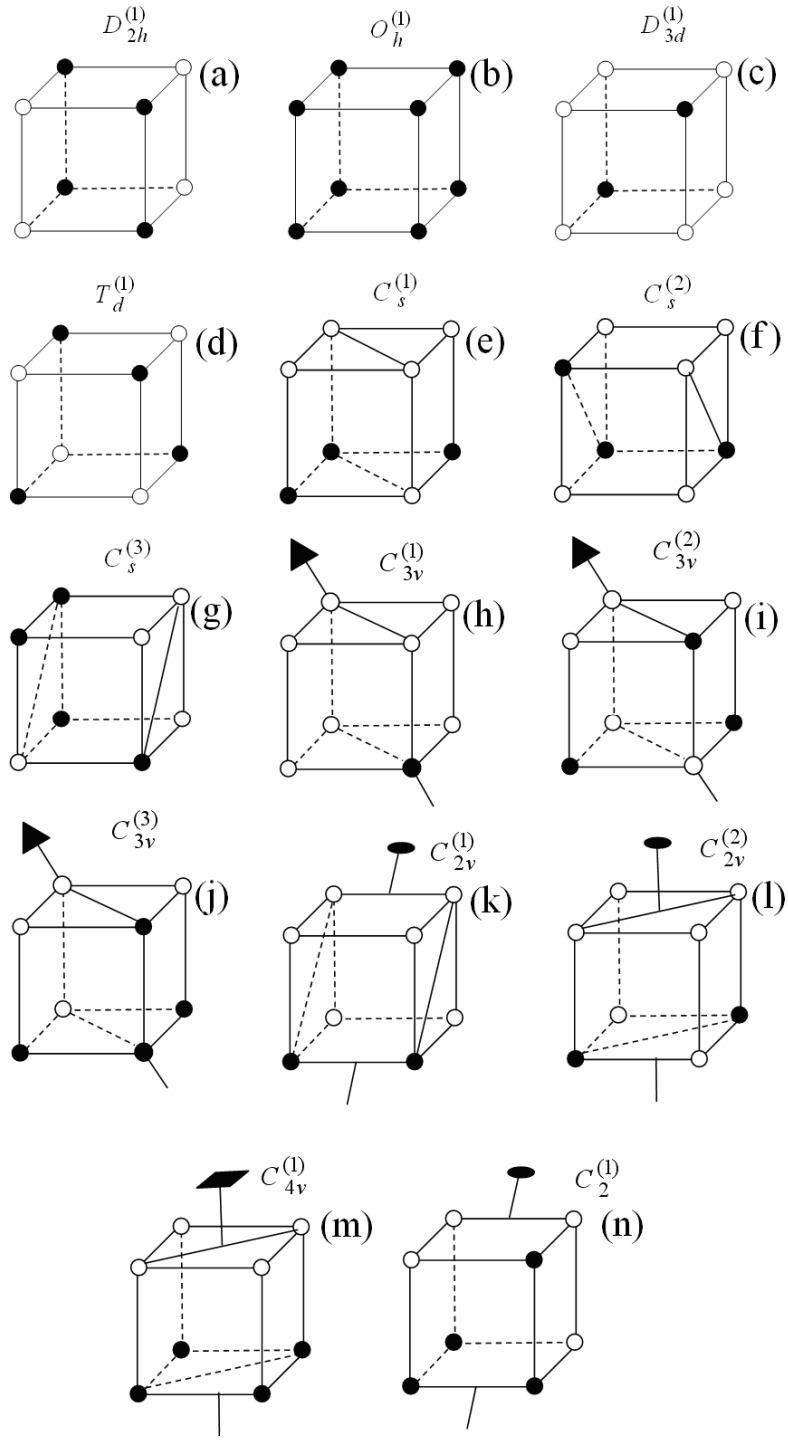

Figure 1. All possible types of geometrically different nearest environments of A-ion in $AB_x^{/}B_{1-x}^{//}O_3$. Solid and empty circles denotes $B^{/}$ and $B^{//}$ ions.

In what follows we present some evident results of calculation of the probabilities of implementing particular mean shifts, obtained within the model based on a binomial distribution of $B^{/}$ and $B^{//}$ ions over $1(b)$ positions.

Let us consider a disordered $PbB^{/}_{c}B^{//}_{1-c}O_3$ solution and try to determine (i) the probability of existing of a cell in which the Pb ion is shifted along one of 12 equivalent directions of $[1,1,0]$ type and (ii) the value of this shift, averaged over the crystal.

Such a shift of Pb ions can be implemented only when the nearest environment of the Pb ion includes 2, 4, or 6 $B^{//}$ ions located at ideal $1(b)$ positions. Therefore, the probability of shift of Pb ions in the above-mentioned direction is $P_{(110)} = (c^2(1-c)^2(c^6-(1-c)^6))/(c^2-(1-c)^2)$. In these cases, the crystal-field symmetries at the center of the cubic unit cell are different: C_{2v}, C_3 or. However, in the approximation of central pair forces of interatomic interactions, Pb ions will be always shifted in the $[1,1,0]$ direction; their mean shift in this direction is $P \cdot (2\sqrt{2}u_0)/\sqrt{3}$.

The results obtained for a disordered crystal are shown in Figure 2 which demonstrates the probabilities of shifts of Pb ions along the $[1,1,1]$, $[1,1,0]$, $[0,1,0]$ directions. To establish the relationship with the conventional models I [7]-[13], the dependences of the crystal averaged shifts of lead ions along the x, y, z axes on the concentration of $B^{/}$ are shown in Figure 3. Note that within the calculation scheme proposed here the static mean-square shifts are no more the fitting parameter of the theory and they are calculated with the same accuracy as if all shifts of lead ions would be identical and uniformly distributed over the crystal: $< x^2 > + < y^2 > + < z^2 >= 8u_0(c-c^2)$.

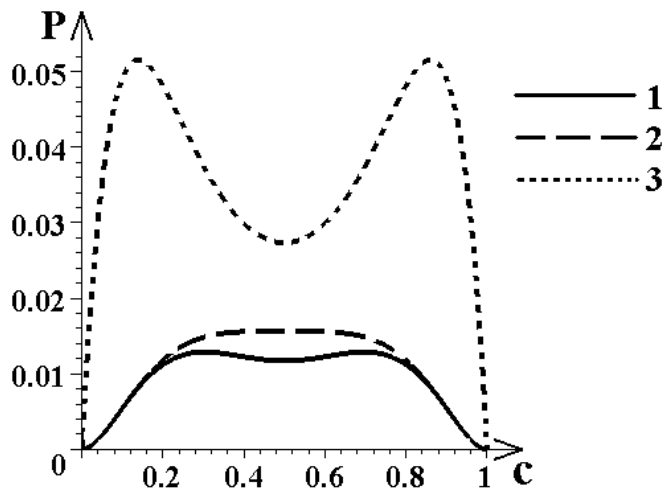

Figure 2. Probabilities of shifts of Pb ions along the $[1,1,1]$ (1), $[1,1,0]$ (2), $[0,1,0]$ (3) directions.

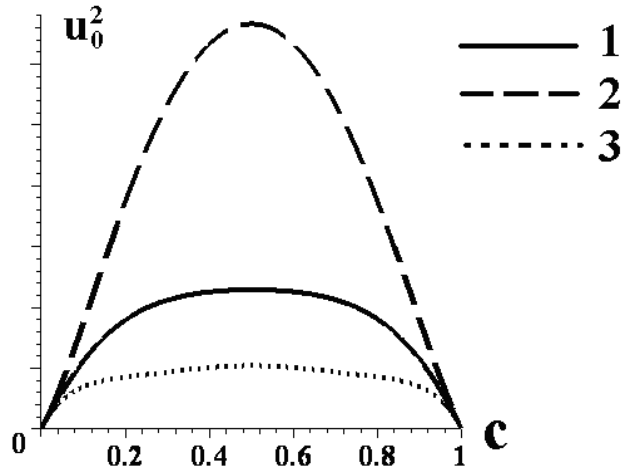

Figure 3. Dependences of the crystalaveraged shifts of lead ions along the x (1), y (2), z (3) axes on the concentration of $B^{/}$ ions.

If the distribution of $B^{/}$ and $B^{//}$ ions over the system of points $1(b)$ is more ordered, calculation of the probabilities of implementing particular shifts of lead ions or crystal-averaged shifts becomes more cumbersome. For brevity, we will present only the results for one of possible types of ordering of $B^{/}$ and $B^{//}$ ions. Let us consider the ordered state in which $1(b)$ sites of ideal perovskite are split into two nonequivalent sublattices and, thus, the volume of the perovskite primitive cell is larger by a factor of two. For clearness, we will use below a Bravais cell whose volume exceeds that of an ideal perovskite cell by a factor of eight. The model considered here neglects spontaneous strains and the Bravais cell is assumed to be cubic. The periods of the lattice composed of extended unit cells are $\vec{d}_1(2a,0,0), \vec{d}_2(0,2a,0), \vec{d}_3(0,0,2a)$. The eight $1(b)$ positions belonging to the extended Bravais cell have the coordinates:

$$\begin{aligned} &1.[0,0,0] \quad 2.[a,0,0] \quad 3.[0,a,0] \quad 4.[a,a,0] \\ &5.[0,0,a] \quad 6.[a,0,a] \quad 7.[0,a,a] \quad 8.[a,a,0] \end{aligned} \tag{2.1}$$

We consider the ordering at which the probabilities of occupying these positions by $B^{/}$ ions are determined by the relations:

$$P_1 = P_8 = c + 3\eta, \quad P_2 = P_3 = P_4 = P_5 = P = c - \eta \tag{2.2}$$

Here, the parameter η characterizes the degree of order in the distribution of $B^{/}$ ions over positions (2.1).

It is possible to calculate both the probabilities of occurring cells with different directions of shifts of Pb ions and all mean parameters used to interpret X-ray diffraction patterns. For example, the dependences of mean-square shifts of Pb ions along the x, y, z axes on the ion concentration and degree of order of ion distribution in a crystal are fairly cumbersome:

$$< y^2 >= 8 * u_0^2(-3c\eta^7 + (50/3 + 14c)\eta^6 + (33 - 58c - 25c^2)\eta^5 + (18 - 76c + 68c^2 + 20c^3)\eta^4 + (8/3 - 16c + 38c^2 - 76/3c^3 - 5c^4)\eta^3 + (-3 - 2c^4 - 2c^5 - 12c^2 + 12c^3 + 4c)\eta^2 + (-2c^5 + c^6 + c^4)\eta - 20/3c^3 + 8/3c^6 + 10c^4 + 1/3c - 8c^5 + 5/3c^2 \quad (2.3)$$

$$< z^2 >= 8 * u_0^2(-36\eta^8 + (-99 + 192c)\eta^7 + (-400c^2 - 334/3 + 414c)\eta^6 + (384c^3 - 63 + 326c - 601c^2)\eta^5 + (92c - 14 - 120c^4 - 220c^2 + 260c^3)\eta^4 + (-64c^5 - 16c + 155c^4 - 460/3c^3 + 70c^2 + 8/3)\eta^3 + (190c^4 + 48c^6 + 52c^2 - 146c^5 + 1 - 132c^3 - 12c)\eta^2 + (-2c^5 + c^6 + c^4)\eta + 28/3c^3 + 16c^7 - 22c^4 - 4c^8 + 32c^5 - 7/3c^2 - 88/3c^6 + 1/3c \quad (2.4)$$

$$< x^2 > + < y^2 > + < z^2 >= 8u_0[-9\eta^7 + (-6 + 42c)\eta^6 + (-75c^2 + 3 + 18c)\eta^5 - 12c(1 - 5c^2 + c)\eta^4 + + (18 - 15c^2 - 12c)c^2\eta^3 + (-6c^5 - 12c^3 + 18c^4 - 3)\eta^2 + 3c^4(c - 1)^2\eta + c - c^2] \quad (2.5)$$

Expressions (2.3)-(2.5) are pictorially illustrated in Figure 4a (dependences of x, y and z on η at $c = 0.5$ Figure 4b (dependences x, y, z on c at $\eta = 0.1$) and Figure 4c (dependences of x, y and z on c at $\eta = 0.2$). In addition, bearing in mind the possibility of applying the results obtained here to description of X-ray diffraction patterns of the $PbB'_{1/2}B''_{1/2}O_3$ and $PbB'_{1/3}B''_{2/3}O_3$ compounds, we present the mean-square shifts x, y, z and mean-square static shifts, calculated for $c = 1/2$ and $c = 1/3$ and two val1les of η, allowable at a given concentration:

	η=0,1	η=0,125		η=0,1	η=0,125
$<x^2>$ (c=1/2)	0,439	0,423	$<x^2>$ (c=1/3)	0,406	0,384
$<y^2>$ (c=1/2)	1,136	1,023	$<y^2>$ (c=1/3)	0,952	0,844
$<z^2>$ (c=1/2)	0,193	0,183	$<z^2>$ (c=1/3)	0,181	0,176
$<r^2>$ (c=1/2)	1,767	1,630	$<r^2>$ (c=1/3)	1,539	1,404

Thus, the theoretical probabilistic structural model makes it possible to express the probabilities of the distributions of shifts of A ions of the distributions of shifts of A ions in the crystal lattice, both in magnitudes and directions, in terms of only one positional fitting parameter and calculate the contribution of these spontaneous shifts to the anisotropic factor W. Within these models, consideration of the anisotropy of the factor W does not lead to an increase in the number of fitting parameters of the theory.

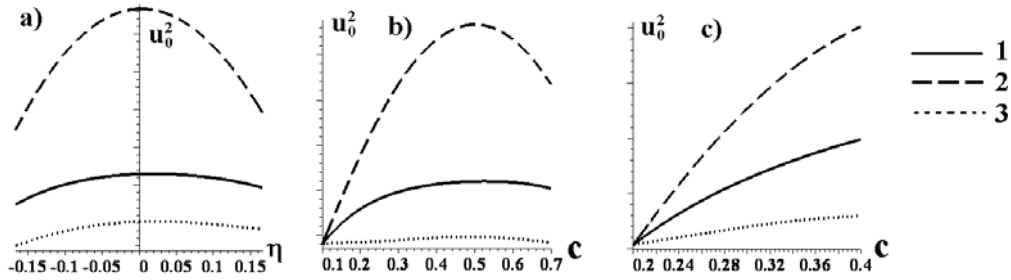

Figure 4. Illustration of expressions (2.3)-(2.5). Dependences of $< x^2 >$ (1), $< y^2 >$ (2) and $< z^2 >$ (3) on η at $c = 0.5$ (a), on c at $\eta = 0.1$ (b) and on c at $\eta = 0.2$ (c).

2.2. Interpretation of $PbFe_{1/2}Nb_{1/2}O_3$ X-ray Diffraction Pattern

The model presented above with a single phenomenological parameter u_0 is not seen founded enough. To make it more precise it is possible to apply following consideration. It is evident, that free volume in unit cell open for shifting of ion A in it, depends in some way on nominal radius of B' and B'' ions, and on the first approximation is proportional to the number of ions with less radius, which were placed in the given unit cell. Thereby it is reasonable to introduce a correction to the shifting value of *A* ion that will be proportional to concentration of B'' ions in its nearest surrounding. Thus, on Figure 1(f) Bravais parallelepiped will be characterized by shifting projection $\Delta r(C_s^{(2)}) = u_0 + 3/8v_0$. If ions B' will be substituted by B'' and vice versa, then projection $\Delta r(C_{3v}^{(1)})$ on reference axis will be equal to $u_0 - 5/8v_0$. Taking into account this correction, it is possible to evaluate the width of Bragg reflexes component associated with random distribution of B' and B'' ions according to common rules. While evaluating the complete intensity of reflexes, we considered ions thermal vibrations in isotropic approximation.

Intensity of 870 X-ray reflexes from PFN crystal annealed at 160^0C, measured on diffractometer CAD-4 using MoK_α-emission and graphite monochromator was used as experimental base to define of u_0 and v_0 values. Within the limits of measurement error, a unit cell appears to be a cube with edge length equal to 4.009±0.001Å, i.e. it contains one PFN formula unit. Set of 870 experiment modules of structure amplitude was split into 59 groups; inside each several group modules of structure amplitude should have equal value according to symmetry of paraelectric phase $G_0 = O_h^1$.

Lines $R = const$ that are presented at Figure 5, were calculated with step $\Delta R = 0.02$ and alteration of u_0 from 0.00 up to 0.40; and v_0 from -0.40 up to 0.40. We found two main ravines, in one of which (the primary) at $0.0 \le u_0 \le 0.2$ the smallest values of R are

concentrated. At Figure 6 there is the "tail" of primary ravine [17], where value of R-factor is higher than in its center.

As a result of minimization of R-factor the following values of positional parameters (u_0 and v_0) and thermal parameters were calculated (recall that while making interpretation of X-ray diffraction pattern, thermal parameters are understood as values $8\pi < u^2 >$, where $< u^2 >$ - is a mean-square amplitude of thermal oscillation of atoms):

u_0	v_0	B_{Pb}	B_{Nb}	B_{Fe}	B_O	R %
0.0326	0.0001	0.568	0.730	0.781	1.42	2.45

Deducted value of R-factor keep pace with the best results of adapting with use of traditional multiparametric models.

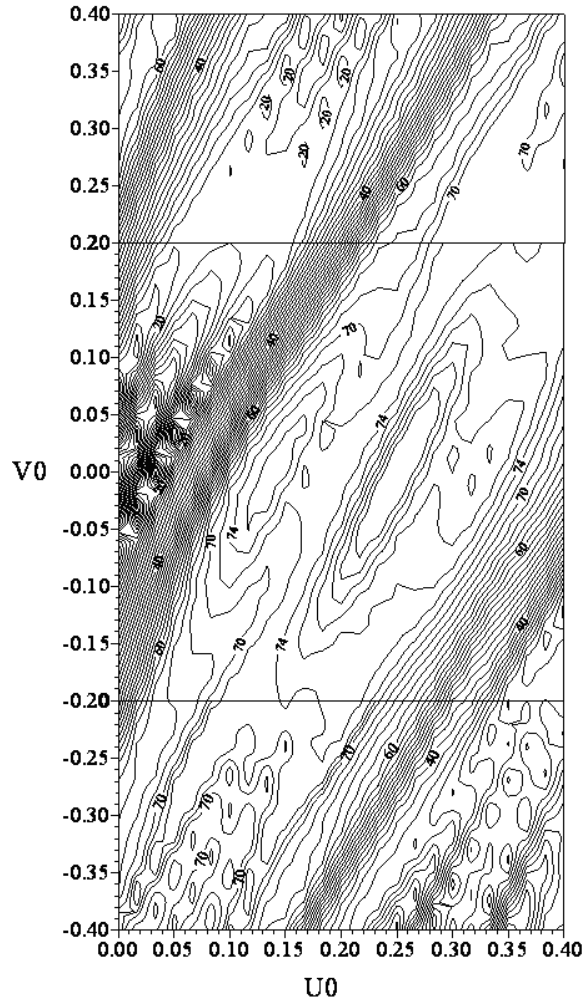

Figure 5. Constant R-factor lines in (u_0, v_0) - space with step $\Delta R = 0.02$.

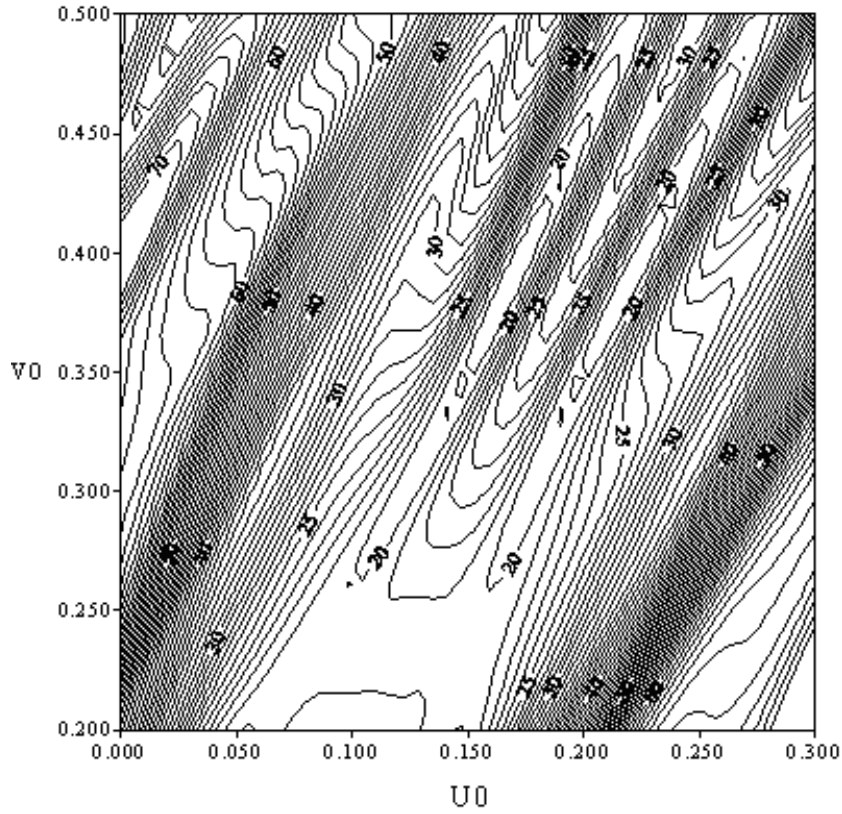

Figure 6. The "tail" of primary ravine in (u_0, v_0) - space.

Small value of v_0 parameter and, what is more important, clearly visible at Figure 5-6 highly correlating values of v_0 and u_0 under conditions of constant R-factor allows supposing that the correction v_0 doesn't contribute anything to the model. Thus, the model, based on an assumption of pair-wise interaction of closest neighbors, allows us to describe an average local structure of the object investigated equally to experiment.

3. THEORY OF ORDERING IN COMPLEX OPS

3.1. General Aspects

Discussions on Theory and numerical modeling of ordering in complex oxides with perovskite structure (and determination of ordering type) are commonly encountered in the literature. In [[19], the state of Pb, Zr, Ti and O ions in was calculated in the one-electron approximation. Both all possible electrostatic interactions (up to the quadrupole–quadrupole one) and short-range repulsive forces were taken into account in the effective pair interaction energy. Then, the minimum energy for nine ordered structures was calculated in this maximally complete model of interactions by successive decreasing of the energy of clusters

$16\times16\times16a_0^3$ and $18\times18\times18a_0^3$ in size (hereinafter, a_0 is the unit-cell parameter of the parent phase). It was predicted in [19] that the structure with a quadruple period along one of the four-fold axes must have the minimum energy. Purely coulomb interactions between point ions were taken into account in [[20] . The charge of the ions was assumed to be equal to their maximum valence, and a cluster $6\times6\times6a_0^3$ in size was considered. As a result, the stability of stoichiometrically ordered structures, characteristic of heterovalent ordering cations, was justified. However, the model proposed in [[20] made it impossible to explain why $PbMg_{1/3}Nb_{2/3}O_3$ and $BaMg_{1/3}Nb_{2/3}O_3$ are characterized by different ordered structures. The other studies in this line of research [[21],[22] have similar drawbacks.

In what follows, we used a phenomenological approach to solve the problem of the most stable ordered structure. As in all studies on the ordering in solid solutions known to us [[19]-[22], we will restrict ourselves to the approximation of effective pair interactions whose form is not specified in deriving the general relations. Within this approximation, we will calculate the coefficients in the Landau potential ($\Phi^{(i)}$), which describes the ordering in terms of the pair interaction energies of ions located at different distances.

It should be noted that in the approximation of effective pair interactions the ordered structure formed at the highest temperature ($T=T_{ord}$), remains stable in the entire temperature range from $T=T_{ord}$ to $T=0$ [[23] , which makes all calculations much easier. Thus, our problem is reduced to the calculation of the dependence of the coefficient in the Landau potential for the squared order parameter on the effective pair interactions. It is this coefficient that determines the temperature of the loss of stability of the high-temperature phase with respect to the stabilization of the order in the 1 arrangement of cations in the RPS O_h^1.

3.1.1. Conditions for the Stabilization of Ordered State Observed in $PbMg_{1/3}Nb_{2/3}O_3$

The ordering of cations of different valence, which occurs in lead-containing relaxors of the $Pb(B_{1/3}^{/+2}B_{2/3}^{//+5})O_3$ type is characterized by the alternation of $B^{/}$ and $B^{//}$ ions according to the scheme $1:1$ ($...B^{/}B^{//}B^{/}B^{//}...$) along the three-fold symmetry axis of the parent phase. In terms of the Landau theory, such ordering is characterized by the one-arm star vector $k_{13}=(b_1+b_2+b_3)/2$ [[25] and the one-component order parameter denoted by R [[26]. The ordering described by R, leads to the partition of the *B*- sublattice of perovskite into two equivalent sublattices (1 and 2). The energy of effective pair interactions between $B^{/}$ and $B^{//}$ ions with allowance for the partition into sublattices, can be written as:

$$E_2=\{V_{B^{/}1B^{/}1}(P_{B^{/}1}^2+P_{B^{/}2}^2)+V_{B^{//}1B^{//}2}(P_{B^{//}1}^2+P_{B^{//}2}^2)+V_{B^{1}1B^{/}2}P_{B^{/}1}P_{B^{/}2}+V_{B^{//}1}V_{B^{//}2}P_{B^{//}1}P_{B^{//}1}P_{B^{//}2}+$$
$$+V_{B^{1}1B^{//}1}(P_{B^{/}1}P_{B^{//}1}+P_{B^{/}2}P_{B^{//}2})+V_{B^{/}1B^{//}2}(P_{B^{/}1}P_{B^{//}2}+P_{B^{/}2}P_{B^{//}1})\}\frac{N}{2} \qquad (3.1)$$

where N is the number of sites in the RPS 1(a). Each separate term in (3.1), for example, $V_{B'1B'2}P_{B'1}P_{B'2}$, is a double sum (over all sites of sublattices 1 and 2 and the coordination spheres of each site [[24]):

$$V_{B'1B'2}P_{B'1}P_{B'2} \equiv \frac{4}{N^2}\sum_{i\in 1,j\in 2}\sum_{r_{1i}=r_{2j}} V_{B'1i,B''2j}(|\,r_{1i}-r_{2j}\,|)P_{B'1i}P_{B''2j} \tag{3.2}$$

of effective pair interaction energies $V_{B'1i,B''2j}\left(\left|r_{1i}-r_{2j}\right|\right)$ - of B' and B'' ions, located, respectively, in sites $1i$ and $2j$, which belong, respectively, to sublattices 1 and 2. Here $P_{B'1i}$ - is the probability of occupation of site *i*, belonging to the first sublattice, by B' ions. The approximation used in (3.1) assumes for all probabilities that $\forall i,j,k,l: P_{B'1i}=P_{B'1l}, P_{B''2j}=P_{B''2k}$. This circumstance allows us to introduce the concept of a probability for a B' (or B'') ion to be located at any site of sublattice 1 or 2: $P_{B'1}, P_{B'2}, P_{B''1}, P_{B''2}$. It is also assumed in (3.2) that the energy of pair interactions between ions $V_{B'1i,B''2j}\left(\left|r_{1i}-r_{2j}\right|\right)$ depends only on the distance between them. Thus, $V_{B'1,B'2}$ are averaged and normalized per atom sums of the energies of effective pair interactions of all *B* ions', located in sublattice 1, with all B'' ions located in sublattice 2. Generalization of this consideration to all other terms in (3.1) is obvious.

The interaction energy of B' and B'' in (3.2) atoms in (3.2) is given in terms of local (generalized) coordinates of the state of the crystal $P_{B'1i}, P_{B''2j}\ldots$. In (3.1), the generalized coordinates $P_{B'1}, P_{B''1}$ averaged over sublattices 1 and 2 are collective variables. The generalized coordinates $P_{B'1}, P_{B''1}$ can be related to the symmetric coordinates; i.e., the Landau order parameters R [[24],[28] and Frenkel order parameter (x) [[24],[26],[30]:

$$P_{B''2i}=1-P_{B'1i};\quad P_{B''2j}=1-P_{B'1j}; \tag{3.3a}$$

$$P_{B''1}=1-P_{B'1};\quad P_{B''2}=1-P_{B'1};P_{B'1}\equiv P_1;P_{B'2}\equiv P_2; \tag{3.3b}$$

$$x=(P_1+P_2)/\sqrt{2};\quad R=(P_1-P_2)/\sqrt{2} \tag{3.3c}$$

In the homogeneous state $x=\sqrt{2}c$. However, the interaction energy of B' and B'' ions may lead to the decomposition of oxides with perovskite structure into two phases [[24],[26],[27]. In the case of the decomposition, the order parameter x determines both the

concentration of $B^{/}$ ions in each phase and the fractions of averaged perovskite cells belonging to the new phases [[21],[29]. Substituting designations (3.3*a*) into (3.1) and (3.2) we can introduce into consideration the ordering energies of $B^{/}$ and $B^{//}$ ions at each coordination sphere:

$$u_{kk'ij} = V_{B'kiB'k'j}\left(\left|r_i - r_j\right|\right) + V_{B''kiB''k'j}\left(\left|r_i - r_j\right|\right) - 2V_{B'kiB''k'j}\left(\left|r_i - r_j\right|\right) \tag{3.4}$$

where $k, k^{/}$ are the numbers of sublattices and the value of $\left|r_i - r_j\right|$ determines the number of the coordination sphere. The local ordering energies (3.4) are aver- aged according to designations (3.2) and yield the effective ordering energies $u(R)$. With $u(R)$, the quadratic part of the Landau potential takes the form:

$$\Phi_2^{(1)}(k_{13}) = \mu_2 x^2 + a_{1R}R^2 = K_1(P_1^2 + P_2^2) + K_2 P_1 P_2 \tag{3.5}$$

With allowance for the structures of the parent phase and the ordered state, μ_2 and a_{1R} can be written as:

$$\mu_2 = 3u(1) + 6u(\sqrt{2}) + 4u(\sqrt{3}) + 3u(2) + 12u(\sqrt{5}) + 12u(\sqrt{6}) + ... + 4u(2\sqrt{3}) + ... \tag{3.6}$$

$$a_{1R} = -3u(1) + 6u(\sqrt{2}) - 4u(\sqrt{3}) + 3u(2) - 12u(\sqrt{5}) + 12u(\sqrt{6}) + ... + 4u(2\sqrt{3}) + ... \tag{3.7}$$

In (3.6) and (3.7) the distance between ions is expressed in terms of the edge lengths a_0 of the parent phase unit cells. According to (3.5), it follows from the Landau theory that, at $T \approx 0, \mu_2 < 0$, $a_{1R} > 0$ a complex oxide decomposes into two phases of different composition. If $\mu_2 > 0$, $a_{1R} < 0$, the ordering of the $1:1$ type (observed in $PbMg_{1/3}Nb_{2/3}O_3$) occurs in complex oxides with perovskite structure.

3.1.2. Conditions for the Stabilization of Ordered State Observed in $Ba(Mg_{1/3}Nb_{2/3})O_3$

$Ba(B'^{+2}_{1/3}B''^{+5}_{2/3})O_3$ The ordering of the described by the order parameter whose translational characteristics coincide with those of $\cos\left[2\pi(b_1 + b_2 + b_3)r\right]/3$ [5]. The ordered structure is characterized by the presence of identical packets consisting of three planes. One of the packet planes contains predominantly (with the probability P_1) $B^{/}$ ions and the other two planes (with equal probabilities $P_2 = P_3$) contain predominantly $B^{//}$ ions. It is convenient to represent the Landau potential describing such ordering as a function of the two components of the effective order parameter ($\lambda_1 \sim \cos\left[2\pi(b_1 + b_2 + b_3)r\right]/3; \lambda_2 \sim \sin\left[2\pi(b_1 + b_2 + b_3)r\right]/3$) and x.

Repeating the calculations of the previous section, we obtain the part of the Landau potential quadratic in the components λ_1, λ_2 in the form:

$$\Phi_2^{(2)}k_9) = \mu_2^{/}\xi^2 + a_{1\lambda}(\lambda_1^2 + \lambda_2^2) = Q_1(P_1^2 + P_2^2 + P_3^2) + Q_2(P_1\,P_2\, + P_2\,P_3\, + P_3\,P_1\,) \tag{3.8}$$

Here, the quantity $\xi \equiv (P_1 + P_2 + P_3)/\sqrt{3}$ plays the same role of the nonequilibrium concentration of $B^{/}$ ions as x in (3.5), accordingly $\mu_2^{/} = \mu_2(u_i(r))$ (3.6). The relation between the generalized state coordinates P_1, P_2, P_3 averaged over each sublattice and the components of the effective order parameter λ_1 and λ_2 is given by the expressions:

$$\lambda_1\, = (2P_1 - P_2 - P_3)/\sqrt{6}; \qquad \lambda_2 = (P_2 - P_3)/\sqrt{2}; \tag{3.9}$$

The ordering in $Ba(Mg_{1/3}Nb_{2/3})O_3$ occurs when $\lambda_2 = P_2 - P_3 = 0$. On the basis of (3.8) and (3.9), we obtain:

$$a_{1\lambda} = Q_1 - \frac{1}{2}Q_2 = -3u(1) + 3u(\sqrt{2}) - u(\sqrt{3}) - 3u(2) + 6u(\sqrt{5}) + ... - 0.5u(2\sqrt{3}) + ... \tag{3.10}$$

3.1.3. Conditions for the Stabilization of Ordered State Observed in $Y_{1/3}Ba_{2/3}CuO_3$

In the copper-containing oxides with perovskite structure of the $R_{1/3}Ba_{2/3}CuO_3$ type, the arrangement of the planes occupied by rare-earth R and Ba ions is of the $1:2$ type:...*RBaRBaRBa*.... These planes are perpendicular to the four-fold axis of the parent phase. The ordered [1] $R_{1/3}Ba_{2/3}CuO_3$ state is described by one component of the six-component order parameter [[32]:

$$\Delta_1 = \Delta_2 = ... = \Delta_5 = 0, \quad \Delta_6 \equiv \Delta \cong \Delta_0(T)\cos(2\pi)b_1 r/3 \tag{3.11}$$

The quadratic part of the effective Landau potential, dependent on

[1] Real phase transitions to the state of equiprobable distribution of R and Ba ions over the parent phase cell in $R_{1/3}Ba_{2/3}CuO_3$ compounds have not been observed. Nevertheless, different models describing various properties of $YBa_2Cu_3O_{7-y}$ on the basis of the concepts about the parent phase in the form of an ideal perovskite have been multiply considered [[31],[32]]. In the general case, the model of a parent phase or a virtual crystal does not imply necessary realization of real phase transitions.

$$\rho = (P_1 + P_2 + P_3)/\sqrt{3}; \quad \Delta_5 = (P_2 - P_3)/\sqrt{2}; \quad \Delta_6 = (2P_1 - P_2 - P_3)/\sqrt{6} \quad (3.12)$$

takes the form:

$$\Phi_2^{(3)} = \mu_2^{//}\rho^2 + a_{1\Delta}(\Delta_5^2 + \Delta_6^2) \quad (3.13)$$

at $\mu_2^{//} = \mu_2(6)$ and

$$a_{1\Delta} = [3u(1) - 4u(\sqrt{3}) + 3u(2) + 12u(\sqrt{6}) + ... - 2u(2\sqrt{3) + ...}]/2 \quad (3.14)$$

The condition for the stabilization of the order observed in $Y_{1/3}Ba_{2/3}CuO_3$ is expressed by the inequality $a_{1\Delta} < 0$.

3.1.4. Conditions for the Stabilization of the Suggested Order in Arrangement of Cations in A-sublattice in $Ca_{1/3}La_{2/3}MnO_3$

The unit cell parameters of $Ca_{1/3}La_{2/3}MnO_3$ in the ordered state [[1] suggest that the stable order is reached as a result of several transitions of different physical nature. The structure of $Ca_{1/3}La_{2/3}MnO_3$ can be used to establish two order parameters, which, even in the first-order approximation, determine the difference of all real structures of $A_{1/3}^{/2+}A_{2/3}^{//3+}MnO_3$ compounds from the ideal perovskite structure. One of these order parameters is determined by the three-arm vector star $k_{11}^{(1)} = (b_2 + b_3)/2$, and the other order parameter is determined by the three-arm vector star $k_{10}^{(1)} = b_1/2$. In both cases, the symmetry of the order parameter is described by the group $L = C48\alpha$ [[24], [33]]. The part of the Landau potential (which describes both types of ordering), quadratic in the components of the order parameter, has the form:

$$\Phi_2^{(4)} = \mu_2^{///}x^2 + a_{1x}(X_1^2 + X_2^2 + X_3^2) + a_{1M}(M_1^2 + M_2^2 + M_3^2) \quad (3.15)$$

Here $\mu_2^{///} = \mu_2$ (3.6), X_i – are the components of the order parameter describing the doubling of the parent-phase period along the four-fold axes, and the translational characteristics M_i are determined by the rays of the star $k_{10}^{(1)}$ [[24] . Calculation analogous to the previous one leads to the expressions:

$$a_{1x} = u(1) - 2u(\sqrt{2}) - 4u(\sqrt{3}) + 3u(2) + 4u(\sqrt{5}) + ... + 4u(2\sqrt{3}) + ... \quad (3.16)$$

$$a_{1M} = -u(1) - 2u(\sqrt{2}) + 4u(\sqrt{3}) + 3u(2) - 4u(\sqrt{5}) + ... + 4u(2\sqrt{3}) + ... \quad (3.17)$$

The conditions for the stabilization of each considered type of order in the arrangement of cations at low temperatures follow from (3.16) and (3.17).

4. CONSIDERATION OF RESULTS

4.1. Pair Interactions and Coordinate Spheres

To achieve actual results on the base of (3.6, 3.7, 3.10, 3.14, 3.16, 3.17) first of all it is necessary to solve the question of choosing the type of model potential of pair interactions.

The interaction between two non-bonded particles – called the van der Waals potential – is expressed as a function of the distance between the particles. The common form of this function is the following:

$$U_{VDW}(r) = D_{VDW}\left[e^{-Br} - \frac{C}{r}\right] \tag{4.1}$$

where D_{WDV}, B, C are phenomenological parameters. There are other functions, which are traditionally taken as approximations to the van der Waals potential. The most frequently used are the Lennard-Jones, the Rydberg and the Morse potentials:

$$U_{LJ}(r) = D_{LJ}\left[\left(\frac{R}{r}\right)^{12} - 2\left(\frac{R}{r}\right)^{6}\right] \tag{4.2}$$

$$U_{R} = -D_{R}\left[1 + \alpha_{R}(r-R)\right]e^{-\alpha_{R}(r-R)} \tag{4.3}$$

$$U_{M}(r) = D_{M}\left[1 - e^{-\alpha_{M}(r-R)}\right]^{2} \tag{4.4}$$

Here D_i, α_i are phenomenological parameters, and R is the distance between the particles, corresponding to the minimum energy of their interaction. Such potentials, mostly because of their simplicity, are widely used in different calculations, e.g. in such computer-intensive applications, as in [[34]-[42].

As all these functions approximate the energy of the same interaction, in main aspects the differences between them are nonessential. The explicit relationships between some generalizations of these functions are demonstrated in the papers [[43],[44]. To consider general problems which are observed in this chapter it is enough to confine ourselves to investigation of one representative of this class of pair interactions potentials. As a representative it is convenient to choose the (1) potential without the D_{VDW} multiplier, that does not play any role in the comparison of the Landau potential coefficients.

Another way of taking into account the particles interaction is the pseudopotential method, that as its known [[45]] may be reduced to the approximation of the effective pair interactions. As an approximation we chose the following sum:

$$U_{PP}(r) = -\frac{1}{r^6} + \frac{A\cos(qr)}{(qr)^3} \tag{4.5}$$

The first summand here is stipulated by the interaction of fluctuations of atom dipole moments. And the second summand takes the form predicted in the pseudopotential's approximation [[45]].

The second important problem which must be solved to proceed to the computations is limitation of the accounting coordinate spheres number. There are two functions expressing the energy of state – Hamiltonian and Landau potential. In the second order respect to generalized coordinates these functions can be written as

$$H = \sum_{k \geq i \geq 0}^{n} \alpha_{ik} P_i P_k \tag{4.6}$$

$$\Phi = \sum_{j=0}^{m} \beta_j \eta_j^2 \tag{4.7}$$

where P_i is probability of occupation of sublattice i by appointed ion, η_j are the Landau order parameters (symmetric coordinates). These two forms of energy are equivalent. There are linear relationships between symmetric coordinates and probabilities of sublattices occupation which leads to the linear relationships between coefficients α_{ik} and β_j. So the numbers of α_{ik} and β_j must be equal. It is easy to see that to fulfill this condition it is necessary and sufficient to take into account all pair interactions up to the interaction between two nearest ions situated in equivalent positions. In our case (with the possibility of tripling the lattice period) it means that we must take into account 11 coordinate spheres.

4.2. ORDERING CONDITIONS IN A BULK CRYSTAL

The Figure 7(a,b) displays the areas in the space of potentials (4.1) and (4.5) parameters, corresponding to the different types of ordering. The figures 7(a,b) were based on calculations that were made formally, without accounting the realistic restrictions on the parameters' values. So in fact only the segments of the phase diagrams shown on these figures have the physical meaning.

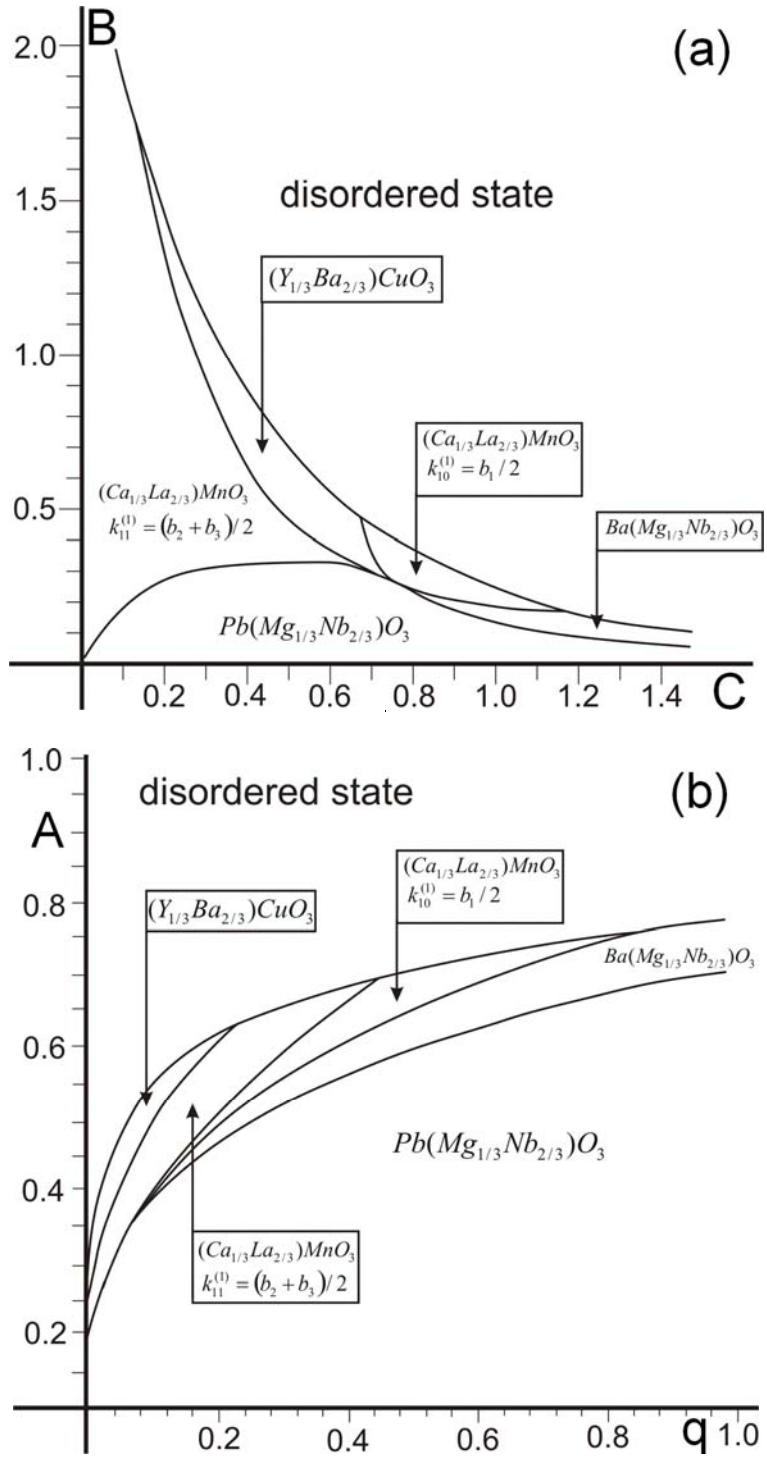

Figure 7. Phase diagrams of bulk sample of OPS in space of pair interaction potentials parameters: (a) – van der Waals potential (4.1), (b) – pseudopotential approximation (4.5).

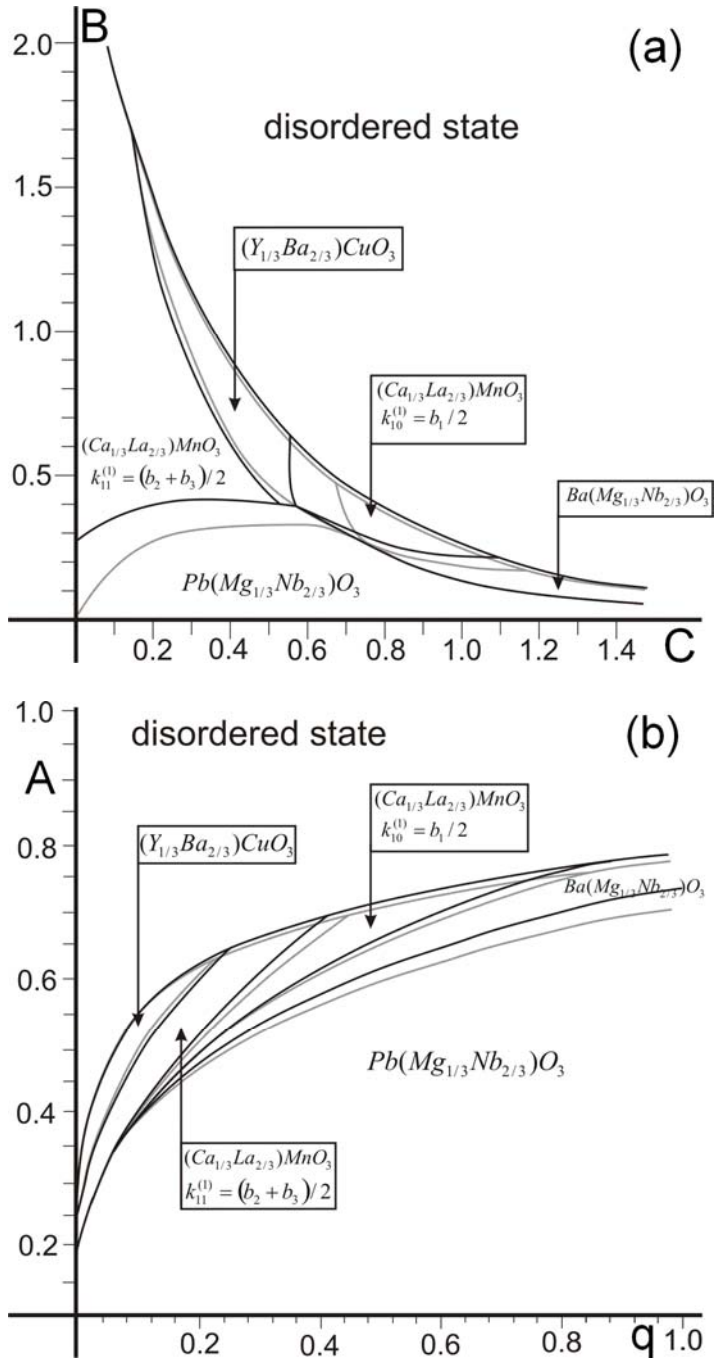

Figure 8. Phase diagrams of near-surface layer of OPS in space of pair interaction potentials parameters: (a) – van der Waals potential (4.1), (b) – pseudopotential approximation (4.5). Grey lines shows borders between phases in bulk sample.

Phenomenological parameters of the potential can vary with the external conditions. For example, obviously, with the increase of the external pressure the distances between the particles, corresponding to the minimum potential energy (R parameter in (2)-(4) or $-2W\left(-\frac{\sqrt{BC}}{2}\right)/B$ for the potential (4.1), where W(x) is the Lambert W function) are usually decreased. Without going into details of definite type of parameters of model potentials of the pair interactions dependence on external conditions, let us keep in mind the fact that this dependence can be determined. This means that it is possible to construct thermodynamic paths, corresponding to the defined variations of the external conditions on the phase diagrams in Figure 7(a,b). The conditions of ordering type variations can also be established. When comparing the Figure 7(a) and (b) it is seen, that in the Figure 7(b) there is a border line between two areas corresponding to the two phases of $Ca_{1/3}La_{2/3}MnO_3$ while there is no such line in the Figure 7(a). The fact that such variation of the ordering occurs on the experimental phase diagram is a strong argument in favor of a better match reality of the pseudopotential approximation in comparison with the model potentials (4.1)-(4.4).

4.3. ORDERING IN A NEAR-SURFACE LAYER OF A CRYSTAL

The effect of variation of the conditions of phase transition in the near-surface layer of a crystal relating to the conditions of phase transition in a bulk crystal is well known. For the first time such effect was estimated for magnetic phase transitions [[46], and later – for structural phase transitions [[47]. Similar effect is observed also for the transitions like ordering in a near-surface layer [[48].

The expressions for the coefficients of the Landau potential in terms of the energies of pair interactions (3.6, 4.7, 4.10, 4.14, 4.16, 4.17) are valid only for the description of ordering in a bulk sample. For the positions of the SRP, located near the crystal surface, coordination spheres of radius $r > h$, where h is the depth of the position relating to the crystal surface, situated partially outside the crystal boundaries, and total energy of interaction between the ion, located in the considering position, and the ions, located on the coordination sphere of such radius, will differ from the similar total energy for the position, located at depth $H > r$. To describe the ordering of cations in a near-surface layer correctly it is necessary to take this difference into account in a course of total interaction energies calculation, corresponding to several of the initial coordination spheres. Figure 8(a,b) shows the areas of spaces of the potentials' coefficients (4.1) and (4.5), where the type of ordering in a near-surface area of a crystal should differ from the one in a bulk sample. In Figure 8(a,b) there are also border lines of areas, corresponding to the different types of ordering in a bulk crystal. Among others, on the Figure 8(a,b) it is seen, that some types of ordering display high stability relating to near-surfaces effects, while others tend to the strong narrowing of the area in the space of model potentials' parameters, in which they are energetically favorable in near-surface layer.

REFERENCES

[1] Salamon M.B. *Reviews of Modern Phys*. 2001, vol.73. p.583.

[2] Bednorz G., Müller K. A., *Z. Phys. B*, 1986, vol. 64, p.189.

[3] Drake A., Abell J. S., Sutton S. D., *J. Less. Comm. Met*., 1990, 164-165, 187.

[4] Burns Gerald, Dacol F.N. *Solid State Communications.* 1983. vol.48. no. 10. P.853.

[5] Davies P.K., Tong J., Negas.T. *Jorn. Of Am.Ceram.Soc*. 1977. vol.80.no7. P.1727.

[6] Yan Y., Pennycook, Xu Z., Viehland D., *Applied Physics Letters*.1998, vol.72. no.24. p.3145.

[7] Kolesova R. V., Kolesov V. V., Kupriyanov M. F., Lavrova O. A.*Bulletin of the Russian Academy of Sciences - Physics*. vol.64 no.6,pp. 883-885.

[8] Kolesova R., Kolesov V., Kupriyanov M., Skulski R. *Phase Transitions*, 1999, vol .68. P.621.

[9] Kupriyanov M., Kogan V., *Ferroelectrics*. 1991. vol.124. p.213.

[10] Lebedinskaya A.R., Kupriyanov M.F., Skulski R., *Material Science and Engineering* , 2001. vol. 83, p.119.

[11] Vakhrushev S., Zhukov S., Fetisov G., Chernyshov V., *J.Phys. Condens.Matter.* 1994. vol.6. p.4021.

[12] Vakhrushev S., Nabereznov A., Sina S.K., Feng Y.P., Egami T. *J. Phys. Chem. Solids*. 1996. vol.57. no10. P.1517.

[13] Bonneau P., Garnier P., Calvarin G. *J.of Solid State Chemistry*. 1991. vol.91. p.350.

[14] Bokij G.B., *Proc. Nat. Inst. Sci. India* Part A 24 (1958), pp 142-150, available online: http://www.new.dli.ernet.in/rawdataupload/upload/insa/INSA_1/20005ac9_142.pdf

[15] Jona F., Shirane G., *Ferroelectric Crystals*; Pergamon Press: Oxford and London, 1962.

[16] K. Yu. Gufan *, Physics of the Solid State*, vol. 47, no. 3, pp. 459–465.

[17] M. Gelfand, Vul E. B., Ginzburg S.L., Fedorov Yu. G., *The Ravine Method in the Problems of the X-Ray Structural Analysis* [in. Russian]; Nauka: Moscow, 1966.

[18] Yan Y., Pennycook, Xu Z., Viehland D.*Applied Physics Letters,*1998.vol.72. no.24. p.3145.

[19] V.I.Zinenko, S.N.Safronova, *Physics of the Solid State*, 2004, vol.46, no.7, p.1291.

[20] Bellaiche L., Vanderbilt D., *Phys.Rev.Lett.*1998. vol.81. no.6. p.1318.

[21] Burton B.P., Cockayne E. *Phys.Rev.B*.1999. vol.60. no18. P.R12542.

[22] Burton B.P. *Phys.Rev.B.* 1999 . vol.59. no9 . P.6087.

[23] Smart J. S., *Effective Field Theories of Magnetism*; Saunders: Philadelphia, 1966.

[24] Gufan Yu. M., *Structural Phase Transitions* [in Russian], Nauka: Moscow, 1982.

[25] Kovalev O. V., *Irreducible and Induced Representations and Corepresentations of the Fedorov Groups* [in Russian], Nauka: Moscow, 1986.

[26] Bouckaert L.P., Smoluchowski R., Wigner E., *Phys. Rev.* 1936, vol. 50. p. 58.

[27] Gufan A.Yu., Klimova E.N., Prus Yu.V., Stryukov M.B., *Bulletin of the Russian Academy of Science: Physics*, 2001, vol.65 no.6, pp.850-854.

[28] Landau L.D., Lifshitz E.M., *Statistical Physics, 3ed*, Pergamon Press: Oxford and London, 1980.

[29] Gufan A Yu. *Bulletin of the Russian Academy of Science: Physics*, 2005, vol.68 no.5, pp.734-739.
[30] Frenkel Ya. I., *Introduction to the Theory of Metals* [in Russian], 3d. ed. Fizmatgiz: Moscow, 1958.
[31] Tolédano P., Dmitriev V., *Reconstructive Phase Transitions*, World Scientific: Singapore, 1996.
[32] Gufan Yu M, *JETP Lett*., 1968, no. 8, p.167.
[33] Stokes H. T., Hatch D. M. *Isotropy Subgrpoups of the 230 crystallographic space groups*. World Scientific: Singapore, 1988.
[34] Lifson S., Haggler A. T., Dauber P., *J. Amer. Chem. Soc*. 1979, vol. 101, p. 5111.
[35] Brooks R., Bruccoleri R. E., Olafson B. D., States D. J., Swaminathan S., Karplus M., *J. Comput. Chem*. 1983, vol. 4, p. 187.
[36] van Gunsterenm W. F. , Berendsen H. J. C., *Groningen Molecular Simulation (GROMOS) library manual*, 1987.
[37] Clark M., Cramer R. D. III, van Opdenbosch N., *J. Comput. Chem,* 1989, vol. 10, p. 982.
[38] Mayo S. L., Olafson B. D., Goddard W. A. III, *J. Phys. Chem*, 1990, vol. 94, p. 8897.
[39] Allured V. S., Kelly C. M., Landis C. R., *J. Amer. Chem. Soc.* 1991, vol.113, p. 9493.
[40] Rappe K., Casewit C. J., Colwell K. S., Goddard W. A. III, Skiff W. M., *J. Amer. Chem. Soc.* 1992, vol. 114, p. 10024.
[41] Nemethy G., Gibsen K.D., Palmer K. A., Yoon C.N., Paterlini G., Zagari A., Rumsey S., Sheraga H. A., *J. Phys. Chem*., 1992, vol. 96, p.6472.
[42] Cornell W. D., Cieplak P., Bayly C. I., Gould I.R., Merz K. M. Jr., Ferguson D. M., Spellmeyer D. C., Fox T., Caldwell J.W., Kollman P. A., *J. Amer. Chem. Soc.* 1995, vol. 117, p.5179.
[43] Lim T. C., (2003) *Zeitschrift fuer Naturforschung, A: Physical Sciences*, 2003, vol. 58 no. 11, p. 615.
[44] Lim T. C., *Acta Chim. Slov*. 2005, vol. 52, 149–152.
[45] Mott N.F., *MetalInsulator Transitions*; Taylor and Francis Ltd.: London, 1974.
[46] Mills D. L., *Phys. Rev. B* 1971, no. 3, p. 3885.
[47] Binder K., Hohenberg P. C., *Phys. Rev. B* 1974, no. 9, 2194.
[48] Dosch H., *Critical Phenomena at Surfaces and Interfaces*, Springer Tracts in Modern Physics Vol. 126, Springer-Verlag: Berlin, 1992.

In: Perovskites: Structure, Properties and Uses
Editor: Maxim Borowski, pp. 463-479
ISBN 978-1-61668-525-6

Chapter 11

ABX_3-TYPE OXIDES AND HALIDES: THEIR STRUCTURE AND PHYSICAL PROPERTIES

A. S. Verma**[*] and V. K. Jindal
Department of Physics, Panjab University Chandigarh, 160014, India

ABSTRACT

The term `perovskite` is used to denote a category of inorganic crystalline solids with the general formula ABX_3, where A and B are cations and X (oxides or halides) is an anion. The perovskite structure occupies a prominent place under all the known ternary systems of composition ABX_3. This is due not only to its wide occurrence, but also to a series of interesting and useful properties associated with this structural type. Crystallographic behaviour of perovskites is of great interest because most structures are close to an ideal cubic structure, however, frequently they are slightly distorted resulting in structures with lower symmetry such as orthorhombic, tetragonal, rhombohedral, trigonal systems and so on. These lattice distortions and structure changes are governed by temperature, pressure, chemical composition, and in some cases, electric field. As a rule, with rising temperature, perovskites tend to undergo a series of transitions to progressively higher symmetry, culminating in the cubic structure where experimentally accessible. They are widely investigated, not only because of interest in their crystal structural behaviour, but perovskites also exhibit a variety of interesting electronic, electromechanical and conductive properties, which are the basis for many existing and potential applications. Such properties are often symmetry dependent. In this chapter, a summary of the scientific work performed on the ABX_3 (X = Oxides and Halides) system during the last few years is presented.

[*] Corresponding author: e-mail: ajay_phy@rediffmail.com, Mob: +91 9412884655, Phone: +91 565 2423417

1. INTRODUCTION

The ternary nature appears at first to be clearly defined by the chemical composition. It is therefore more meaningful to speak of ternary structures (i.e. an anion and two significantly different cation sites within the structure) than it is to speak of ternay phases in the purely chemical sense (i.e. containing three different elements). Ternary structure is not comparable with ternary phase. For ceramists, other materials scientists and earth scientists the "ternary" structural families hold a specify the significance. To the best of our knowledge, most of the solid earth is made up of a material with a ternary structure. In modern technology we are concerned with large quantities of refractories, or with ferroelectric devices or computer-memory cores. In this chapter we hope especially to be able to point out the interrelationships between the various structral types, the transitions from one structure to another, and physical properties. The rational design of advanced materials assumes an understanding of the correlation between basic crystal chemistry and simple structure-property relationships.

Implicit in such a relationship is an understanding of the connection between chemical composition and crystal structure in solid-state materials. Properties such as electronegativity, radii, valence electron count, and principal quantum number can help establish a link between composition, structure, and properties for different classes of materials. Establishing such a link, however, is particularly difficult due to the large number of parameters which affect structures including the charge and coordination preferences of metals, the existence of energetically close-lying structure types, and synthetic parameters, e.g., pressure and temperature. The use of high-pressure or low-temperature synthesis complicates the problem through the introduction of kinetic considerations and the possibility of metastable phases. Numerous attempts have been made to correlate structural stability with chemical or physical variables derived from atomic properties of the constituent elements; however, for different classes of materials, different atomic properties must be used to achieve good corre1ation [1-6].

Although several predictive methods exist for ionic compounds [2,4-7], each has noticeable shortcomings. Very few systems allow the study of the relationship between structural changes and physical properties in such a clear way as ABX_3 perovskites (X = oxide and halide) [4-10]. In this review, we present past approaches that have been used for predicting composition-structure relationships for ABX_3 compounds.

Synthesis

Several methods have been described for the preparation of perovskite-type oxides. Many of them are analyzed in detail in several references [11, 12] and for this reason only a brief account on this aspect will be given here. Practically all the standard methods known for the synthesis of solid materials [13] can be applied to the preparation of perovskite-type oxides. The classical route is the reaction between intimate mixtures of the constituent binary oxides or their precursors (nitrates, carbonates, etc) in the solid state at high temperatures. These reactions are slow as a result of large diffusion distances, and repeated grinding and heating are required in order to obtain pure and fine powders. In some cases, special precautions must be taken. For example, compounds containing Pb (II) in the A-site of the perovskite structure

are often difficult to obtain due to the volatility of lead oxide. This problem can be overcome by heating the reactants in a lead oxide atmosphere, by using an excess of lead oxide or by working at relatively low temperatures in the primary reaction phase before the final high temperature treatment. In some cases, other structural types can be stabilized in the intermediate reaction stages, which sometimes are difficult to transform later into the desired perovskite phase.

Other useful methods are the so-called "precursors-techniques" in which usually the carbonates of the metals were coprecipitated in adequate proportions and subsequently decomposed by heating [14]. This method allows obtaining a better and more homogeneous starting mixture and, usually, a lowering of the final reaction temperature. Similar procedures involve the coprecipitation of oxalates or citrates and other similar materials, a technique that recently has been often used for the synthesis of the new high T_c, superconducting oxides [15]. Other procedures often used in the last years are the "Sol-Gel" methods [16-18] in which the hydrolysis of certain chemical species under controlled conditions is used to generate the necessary precursors for the synthesis of the oxide materials. The most common systems are metallic alkoxides, which are very useful because of their ability to form homogeneous solutions in a variety of solvents and in the presence of other alkoxides or metallic derivatives. These solutions are then transformed into gels which by desiccation or heat treatment produce glass or ceramic materials. Among non-alkoxide precursors, nitrates, carboxylates, acetylacetonates, chlorides and other inorganic species are appropriate to be used in Sol-Gel preparations.

Structure

The ABX_3 general group special attention has been paid to those compounds with the ideal cubic perovskite structures or with structures which are slightly distorted from the former, either by cation displacements, tilting of BX_6 octahedra or distortion in the shape of the X_6 group which surrounds the B cation. More recent attention has been paid to the group formed by compounds with hexagonal-close-packed structures which are closely related with the cubic ones [19]. The ideal perovskite (ABO_3) structure (Figure 1) has a cubic unit cell of side about 3.9 Å, space group *Pm3m* and contains one formula unit. The B ions have an octahedral oxygen coordination and the A ions have 12-fold coordination. The oxygen ions are linked to six cations (4A + 2B). If the unit cell is chosen with a B ion at the body centre, then the oxygen ions occupy the face centers and the A ions occupy the comers of the unit cell. When A ion is assigned the body centre position, the oxygen ions are at the middle of the edges and B ions at the comers of the unit cell. The structure can be visualized in several ways [20]. The most useful approach is to consider that it is based on that of ReO_3 with comer sharing octahedra arranged along the cube axis with the A ions occupying the interstices. The structure can also be viewed as a body-centered cubic (b.c.c.) arrangement of the A and B cations (as in CsCI) with the oxygen ions added at the centers of the edges. It can also be considered as a face-centered close-packed AO_3 array, as in the ordered Cu_3Au structure, with B ions occupying the octahedral hole in the centre of the unit cell (Figure 2).

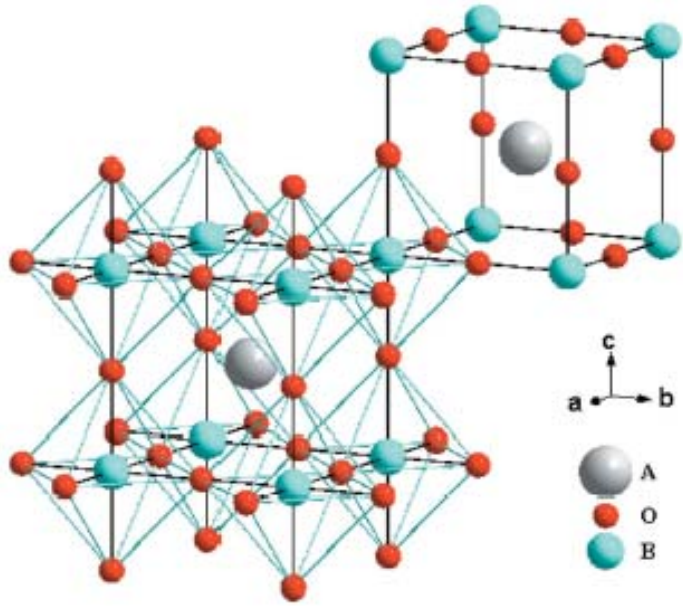

Figure 1.

In the ideal structure, where the atoms are just touching one another, the B-X distance is equal to a/2 whereas the A-X distance is $\sqrt{2}(a/2)$ (a = cubic unit cell length) and the following relation between the ionic radii holds:

$$(r_A + r_X) = \sqrt{2}\,(r_B + r_X)$$

Notwithstanding, it was found that the cubic perovskite structure, or slightly distorted variants of it, was still retained in ABX_3 compounds even where this relation is not exactly obeyed. As a measure of the deviation form ideality Goldschmidt [21], introduced a "tolerance factor" t, defined as,

$$t = (r_A + r_X) / \sqrt{2}\,(r_B + r_X)$$

That is applicable at room temperature to the empirical ionic radii.

For an ideal perovskite, t is unity; however, the perovskite structure is also found for lower t-values ($0.75 < t \leq 1$). In such cases, the structure distorts to tetragonal, rhombohedral or other lower symmetries. Indeed, many perovskite oxides are polymorphs. In ideal perovskite structure, the atoms are in the following positions; A; 000, B; ½ ½ ½ X; ½ ½ 0, ½ 0 ½, 0 ½ ½. Moreover, the above given geometric relations are not a sufficient condition for the stabilization of the perovskite lattice, since the A and B cations must, in themselves, be stable in twelvefold and sixfold coordination respectively. This latter condition sets lower limits for the cationic radii. In oxide systems these limits are $r_A > 0.90$ Å and $r_B > 0.51$ Å [19].

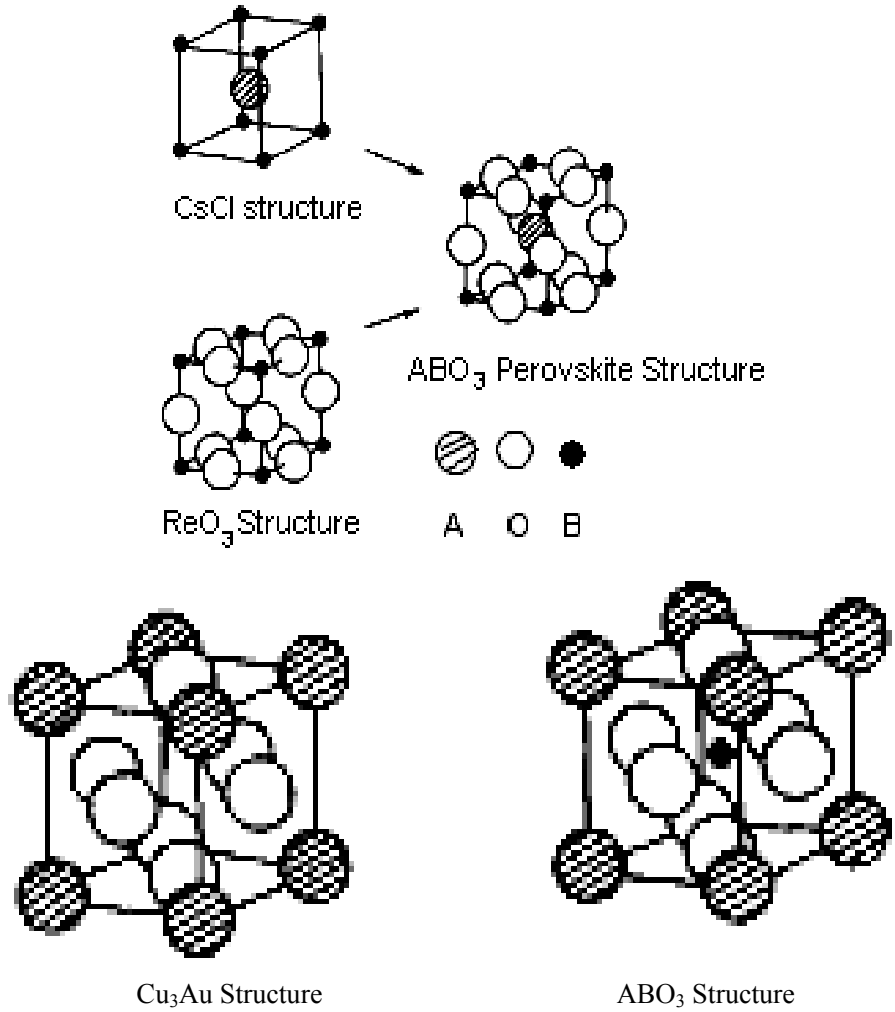

Figure 2. Perovskite structure and its relationship to CsCl, ReO_3 and Cu_3Au structures.

The concept of oxide and halide analogue compounds was first introduced by Goldschmidt [21], on the basis of a number of crystal chemical considerations: (a) the similarity in ionic radii of O^{-2} and F^-; (b) the applicability of the rigid ion model to compounds containing the O^{-2} and F^- ions, which have relatively low polarizabilities resulting in their ionic radii being almost independent of coordination number; and (c) the correspondence of the crystal structures of oxide and halide compounds in which the cations are also of comparable ionic radii. Notable examples of this modeling concept are LiF-MgO (rocksalt structure) CaF_2 – ThO_2 (flurite structure), MgF_2 – TiO_2 (rutile structure). Goldschmidt [21], also suggested that because of their lower ionic charge fluorides should be "weakened" models of their oxide analogues and thus be characterized by lower melting temperature, lower hardness and lower refractive index.

Some oxide and halide materials that adopt this ideal structure are $BaPbO_3$, $CaZrO_3$, $PbHfO_3$, $SrSnO_3$, $CdTiO_3$, $PbSnO_3$, $KMgF_3$, $KMnCl_3$, $CsPbBr_3$, $CsSnI_3$ etc. [22, 23]. Besides chalcogenides and halogenides, there are a few examples of perovskite hydrides (X=H). In

the case of A and B being a monovalent alkali metal (M) and a divalent alkaline earth metal, respectively, the ternary metal hydrides have a saline bonding character. Such hydrides are of interest for hydrogen storage at high temperature. There are five reported hydrides with the ideal *Pm3m* perovskite structure: $CsCaH_3$, $RbCaH_3$, $KMgH_3$, $BaLiH_3$, and $SrLiH_3$ [24-26]. The letter is sometimes referred to as inverse perovskites since the singly charged M cation occupies the octahedral voids. Additionally, it has been proposed that the light metal hydride $LiBeH_3$ adopts the cubic perovskite structure and displays high-temperature superconductivity [27]. It is interesting to remark that many compounds present the ideal cubic structure only at high temperature.

As the most important components in the Earth's mantle, ABO_3 (orthorhombic) perovskites have been intensively studied [7,8-10]. The understanding of the mechanisms that lead to the stabilization of the various perovskite structures has been a long-standing problem in material science. Due to the frequent occurrence of perovskites, and also to the great variety of properties presented by these systems, the accurate and transparent description of the driving forces toward the high or low symmetry crystal structures is of general interest [28]. The orthorhombic structures are derived from the ideal cubic structure via the titling and distortion of the BO_6 octahedra [5]. The degree of distortion of these perovskites can be correlated to the tilting of BO_6 octahedra, and even where a structural transition is not observed the tilt angle decreases as the temperature increases. The octahedral tilting, originating from finite rotations of the BO_6 octahedra, is realized by preserving the central symmetry of the B cation, while the A cation "prefers" off-center displacements. A number of workers have used such changes to infer the presence of thermally induced phase transitions. From the crystal chemistry point of view, the two different perovskites of ABO_3 compounds have very similar local structures, in which each B atom is octahedrally co-ordinated by O atoms, as shown in Figure 3 [2, 29-34]. Orthorhombic perovskite is basically built up from the corresponding cubic perovskite.

The rare earth ortho-ferrites $RFeO_3$ (R is a rare earth element) have a distorted perovskite crystal structure [35]. All the Fe^{+3} ions are crystallographically equivalent and lie in an octahedral oxygen environment. Each iron ion is surrounded by six Fe^{+3} ions and the Fe–O–Fe bond angle is close to 180° [36]. This results in a strong negative indirect Fe^{+3}–O–Fe^{+3} exchange interaction, which causes the formation of two magnetic sublattices whose moments are almost anti-parallel. The small angle between the moments of these sub-lattices produces a small ferromagnetic moment [37, 38]. The rhombic ortho-ferrites $RFeO_3$ (space group *Pbnm*) are usually attributed to the perovskite-like structures obtained as a result of all the possible distortions of the cubic $CaTiO_3$ perovskite lattice (space group *Pm3m*) on replacing the Ca cations by R and Ti by Fe. These distortions can change the crystal symmetry. A transition from the cubic perovskite structure to a rhombic structure in the rare earth ortho-ferrites has been established experimentally [39, 40]. RMO_3 compounds with M = Cr, Sc, V, Ga, and Al also have this type of structure [41-45]. It is interesting to note that the deformation which develops for the rhombic distortions has almost no effect on the oxygen octahedron surrounding the iron ions, while the coordination polyhedron of the R^{+3} cations is significantly distorted. The average inter-atomic Fe–O and O–O distances are essentially constant for the entire rare earth series $RFeO_3$, at 2.011 and 2.844 Å, respectively [39]. As R is changed, only the mutual positions of the oxygen octahedral change and this leads to a change in the angle of the Fe–O–Fe valence bond. The deviation from cubic symmetry increases as the R^{+3} ionic radius decreases; it is smallest in $LaFeO_3$ and greatest in $LuFeO_3$.

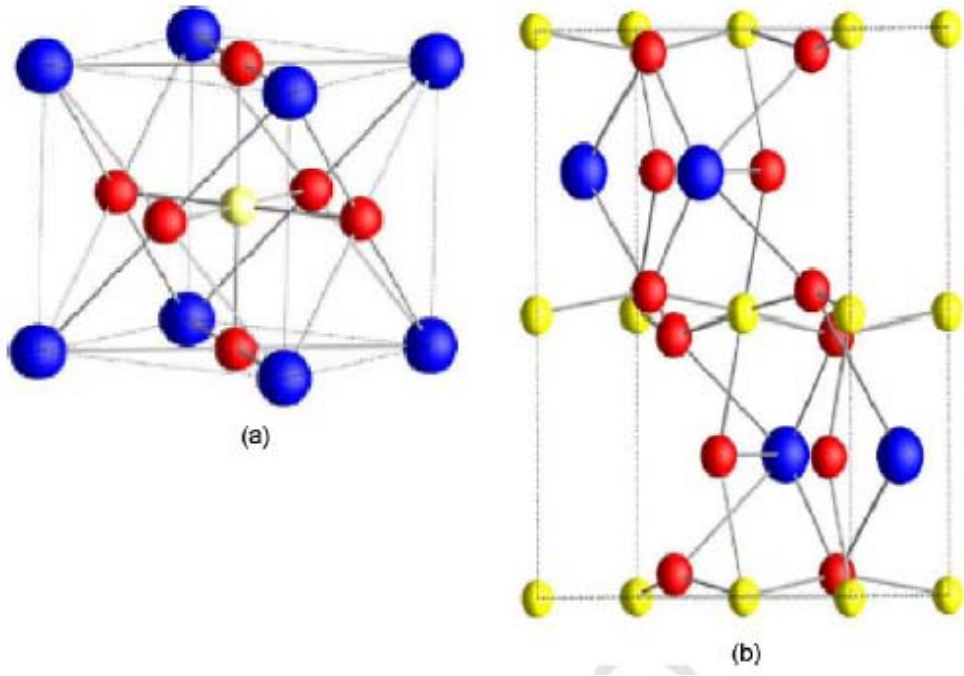

Figure 3. Schematic structures of cubic perovskite (a), orthorhombic perovskite (b) of ABO_3 compounds large filled blue circles represent A, small yellow B and small red O atoms.

In several materials the cubic cell may have a small deformation to rhombohedral symmetry. This deformation does not enlarge the unit cell. It is possible to index it on a unit cell containing either one or two formula units with rhombohedral angles $\alpha \sim 90^o$ or $\alpha \sim 60^o$ respectively. However, the anions are generally displaced as requires the larger unit cell with $\alpha \sim 60^o$.

The best known example of a tetragonal perovskite is probably the room temperature form of the ferroelectric $BaTiO_3$, with a = 3.994 Å, c = 4.038 Å and Z = 1. In this case the TiO_6-octahedra are somewhat distorted (one Ti-O bond at 1.86 Å, four at 2.00 Å and one longer at 2.17 Å). Barium is coordinated by four oxygens at 2.80 Å, four at 2.83 Å and four more at 2.88 Å. In the isotypic $PbTiO_3$, the TiO_6-polyhedra are more distorted than in $BaTiO_3$, a fact which can surely be related to the greater polarizing power of Pb (II), which has often been discussed in relation to other structural and bonding problems in systems containing this cation [46]. A number of other tetragonal perovskites ($PbHfO_3$, $SrPbO_3$, $SrZrO_3$, $AgTaO_3$, $KCoF_3$ etc.) are isotypic with $BaTiO_3$ and possess uni-molecular cells. The fact that most of them are tetragonal only at high temperatures makes accurate crystallographic studies very difficult. In some cases, more complex tetragonal unit cells have been found; also superstructure reflections can be observed in some tetragonal perovskite, pointing to multiple cells or to cells of lower symmetries [47]. $KCuF_3$ has a tetragonal superstructure with $a = \sqrt{}a'$, $c \sim 2a'$ and Z = 4 (a' = pseudocubic cell-length) due to a shift of the fluoride ions, caused by the Jahn-Teller effect. As expected, the CuF_6-octahedra are elongated, with two significantly longer Cu-F distances [48].

As stated in the preceding paragraphs, a great number of perovskite-like materials present several polymorphic modifications. Some of them are very important in relation to their

physical properties and applications. For example, in $BaTiO_3$ and $KNbO_3$ the following transformations are observed with increasing temperatures:

rhombohedral Φ orthorhombic Φ tetragonal Φ cubic

and the three lower temperature forms are ferroelectric. It should be noted that these phase changes reversible and all the polymorphic forms possess a pseudo-cubic unit cell with a'~4 Å. Obviously, these polymorphic changes further complicate the crystal chemistry of this type of material [47, 48].

2. MODELS FOR THE ANALYSIS OF PROPERTIES OF PEROVSKITES (ABX_3)

2.1. Structural Properties

First, Mooser and Perason [49] applied a two-dimension graphic to study the stability of different compounds, the two factors they used were the difference of electronegativity between the cation and the anion and the average principle quantum number. They succeeded to discriminate the crystal structures of AB-type compounds, of AX_2-type halides, and the metallic or non-metallic ternary fluorides ABX_3. Similar methods were called the structural map technology, and more parameters were used to draw the graphic. Muller and Roy [50] proposed to plot ''structural map'', which took the ionic radius of A and B as coordinates to study the distribution of different structures for many ternary structural families. Furthermore, the schematic distribution map of different crystal structure for $A^{+1}B^{+2}X_3$, $A^{+2}B^{+4}X_3$ and $A^{+3}B^{+3}X_3$ systems separately, were given by the same method [50, 51]. However, the criterion for perovskite formability was not discussed, possibly due to the lack of accurate data of crystal structure of some ABX_3 compounds at that time. The ionic radius is the most important ionic parameter that dominates the crystal structure of ionic compound. The ideal cubic structure form may be seen as a network of BX_6 octahedra, where all the octahedra are corner sharing. The *A* ions occupy the cubo-octahedral holes in between the octahedra. Many derivatives of the ideal structure are found and the distortion of the structure from cubic is often considered to be determined by the relative sizes of the different ions of the compound. The much used tolerance factor (t) is defined as

$$t = r_A + r_X / \sqrt{2}\,(r_B + r_X) \tag{1}$$

where r_A, r_B and r_X are the ionic radii of A, B and X_3 respectively. $t = 1$ corresponds to an ideal perovskite, while a $t < 1$ indicates tilting or rotation of the BX_6 octahedra. A $t > 1$ indicates preference for hexagonal perovskite structures, where the octahedra at least to some extent share faces. The face-sharing octahedra then form chains along the hexagonal *c* axis, bound to each other by *A*-X bonds. The face sharing octahedra give relatively short *B*-*B* distances, thus increasing the electrostatic repulsion between the *B*-site cations. Hexagonal stacking and face sharing is therefore introduced in stages with increasing size of the *A* cation. Alkaline-earth-metal manganese oxides show this importance of size well [52]. $CaMnO_3$

forms an orthorhombic derivative of the cubic structure with slightly tilted octahedra [53]. At high temperatures $SrMnO_3$ takes a cubic perovskite structure with corner-sharing octahedra only [54]. At low temperatures, on the other hand, $SrMnO_3$ forms a four-layer hexagonal structure with both face-sharing and corner-sharing octahedra corresponding to hexagonal and cubic stacking, respectively. $BaMnO_3$ forms a hexagonal structure with face sharing of octahedra only. The stabilization of the hexagonal structures at low temperatures has long been ascribed to the formation of metal-metal interactions across the shared face [55]. However, the Mn-Mn *d*-orbital overlap has recently been shown to be minimal [52, 56] Instead covalent interactions between manganese and oxygen atoms are indicated. Both the relative sizes of the cations and the covalency of the Mn-O bonds appear to be important for stabilizing the hexagonal structures of $SrMnO_3$ and $BaMnO_3$ at low temperatures [52, 56]. Tolerance factor (t) has been widely accepted as a criterion for the formation of the perovskite structure, many researchers have used it to discuss the cubic perovskites stability, and therefore, it is an important factor for the stability of cubic perovskites, so tolerance factor (t) constructs one axe of the structure map. Another important octahedron factor (r_B/r_O) [57] is as important as the tolerance factor to form cubic perovskites, so octahedron factor constructs another axe of the two-dimension structure map. Which are shown in figure 4.

According to Goldschmidt's point, t values of cubic perovskites are in the range of 0.8–0.9. From Figure 4, it is indicated that t values of cubic perovskites, except $BaMoO_3$, are in the range of 0.857–1.032, which is wider than Goldschmidt's range. However, t = 0.857–1.032 is a necessary but not a sufficient condition for the formation of the cubic perovskite structure. The 85 systems, the t values of which are in the range (0.857–1.032), can not form cubic perovskite structure [1]. The correct knowledge of lattice constants of unknown compounds is necessary for analyzing the structure and properties of materials. This helps in the selection of an appropriate material in many industries related problems [58]. Some empirical models were established that can predict lattice constant of perovskites from selected atomic properties of their constituent elements.

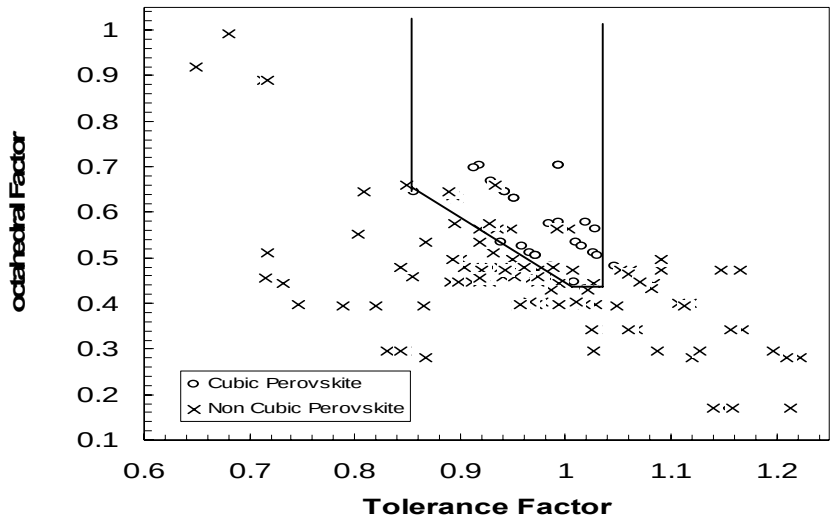

Figure 4. Classification of cubic (ABO_3) perovskite oxides [1].

Recently, the methodology developed by Jiang et al. [59], which allows one to predict the lattice constant of cubic perovskites by using the known ionic radii of the cations and anion. According to him the lattice constant may be determine by the following relation,

$$a\ (\text{in Å}) = 1.8836(r_B + r_X) + 1.4898\ r_A + \sqrt{}\ r_X\ 2(r_B + r_X)\ 1.2062 \quad (2)$$

where r_A, r_B and r_X are the ionic radii of A, B and X_3 (X =O, F, Cl, Br and I), respectively.

According to Ye et al. [60], the lattice constant of the ideal perovskite oxides (ABO_3) can be linearly correlated to some atomic parameters as,

$$a = 0.3166r_A + 1.422r_B - 0.1708X_A + 0.0562X_B - 0.0066(Z_B - Z_A) + 2.706 \quad (3)$$

where r_A, r_B, X_A, X_B, Z_A and Z_B are the ionic radii, electronegativity and valence number of ion A and B, respectively.

Equation (3), depends on the number of valence electrons and ionic charge also depends on the number of valence electrons, which changes when a metal forms a compound. Furthermore, perovskite oxide solids can be defined in different systems like as $A^{1+}B^{5+}O_3$, $A^{2+}B^{4+}O_3$ and $A^{3+}B^{3+}O_3$. Recently [9,10], the authors have presented alternative explanation for lattice constants of orthorhombic and cubic perovskites in terms of valence electrons and ionic charges. The lattice constants of cubic perovskite solids exhibit a linear relationship when plotted against average ionic radii r_{av} (Å), but fall on different straight lines according to the valence electron product of the compounds, which are presented in Figure 5. To obtain better agreement between experimental and theoretical data for cubic perovskite type compounds, relations (1) and (2) have been extended to [9],

$$\text{Lattice constant (a in Å)} = K\ (V_1V_2V_3)^S\ r_{av} \quad (4)$$

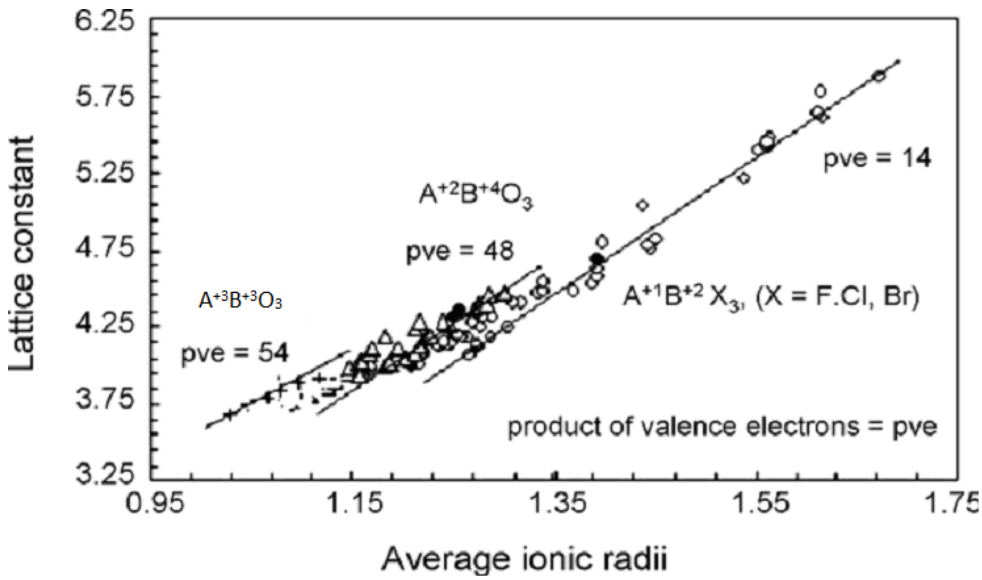

Figure 5.

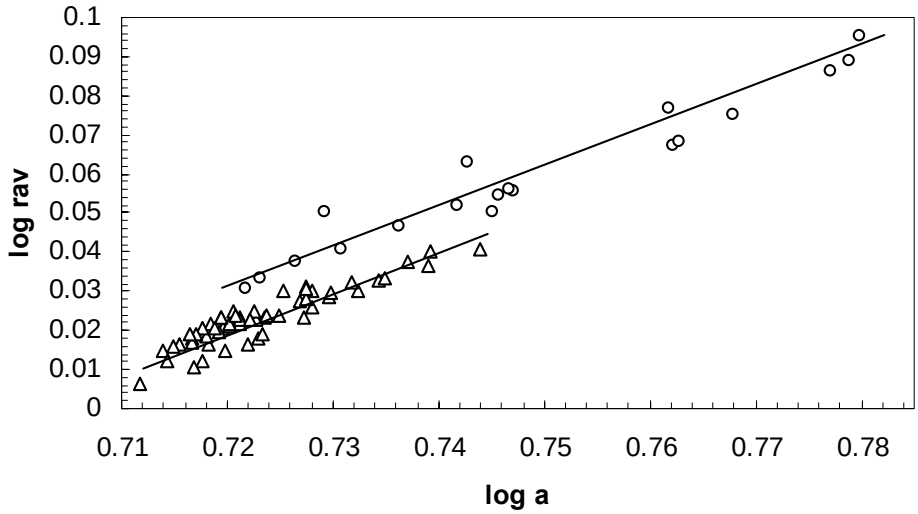

Figure 6. Plot of log a (lattice constant in Å) against log r_{av} (average ionic radii in Å) for $A^{+2}B^{+4}O_3$ and $A^{+3}B^{+3}O_3$ orthorhombic perovskites and $A^{+2}B^{+4}O_3$ and $A^{+3}B^{+3}O_3$ are represented by o and Δ respectively.

Where V_1, V_2 and V_3 are the valence electron on the A, B and X_3 respectively, K and S are constants, r_{av} is the average ionic radii of ABX_3 in Å and it can be calculated by $r_{av} = (r_A + r_B + r_X) / 3$.

The lattice constants of orthorhombic perovskite solids exhibit a linear relationship when plotted against average ionic radii r_{av} (Å), but fall on different straight lines according to the ionic charge product of the compounds, which are presented in Figs. 6–8. The lattice constant of orthorhombic perovskite-type crystal structure compounds can be evaluated using their ionic charge by following relations [10],

$$\text{lattice constant (a in Å)} = 4(Z_1Z_2Z_3)^{0.054}\, r_{av} \tag{5a}$$

$$\text{lattice constant (b in Å)} = 4(Z_1Z_2Z_3)^{0.055}\, r_{av} \tag{5b}$$

$$\text{lattice constant (c in Å)} = 6(Z_1Z_2Z_3)^{0.040}\, r_{av} \tag{5c}$$

where Z_1, Z_2 and Z_3 are the ionic charge on the A, B and O_3 respectively, r_{av} is the average ionic radii of ABO_3 in Å. The correct ionic radii (r_a, r_b and r_o) are taken from Shanon's work [47] and other Ref. [58]. The main advantage of Equations (4) and (5a)–(5c) are the simplicity of the formula, which does not require any experimental data expect the ionic radii of orthorhombic perovskite solids and the evaluated values are in close agreement with the experimental and theoretical data as compared to the values reported by previous researchers so far. The presented method is quite reasonable and can give us a useful guide in calculating and predicting of the more complex class of cubic and orthorhombic perovskite solids.

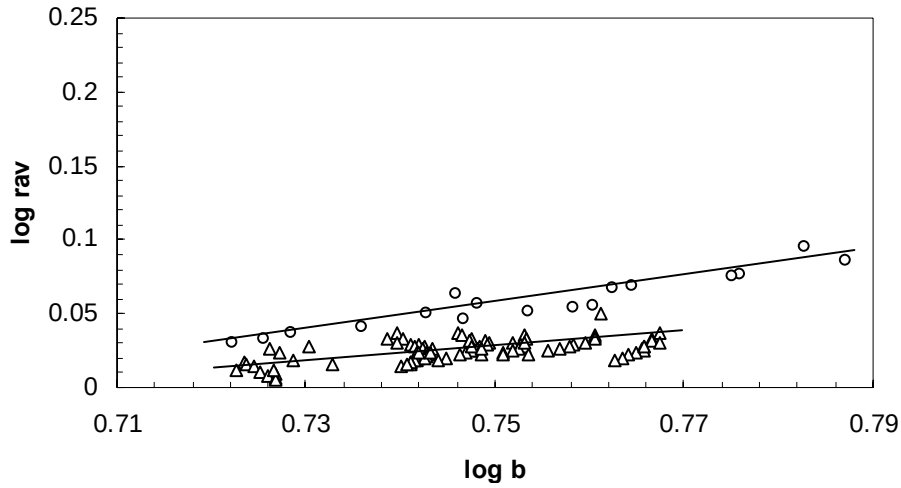

Figure 7. Plot of log b (lattice constant in Å) against log r_{av} (average ionic radii in Å) for $A^{+2}B^{+4}O_3$ and $A^{+3}B^{+3}O_3$ orthorhombic perovskites and $A^{+2}B^{+4}O_3$ and $A^{+3}B^{+3}O_3$ are represented by o and Δ respectively.

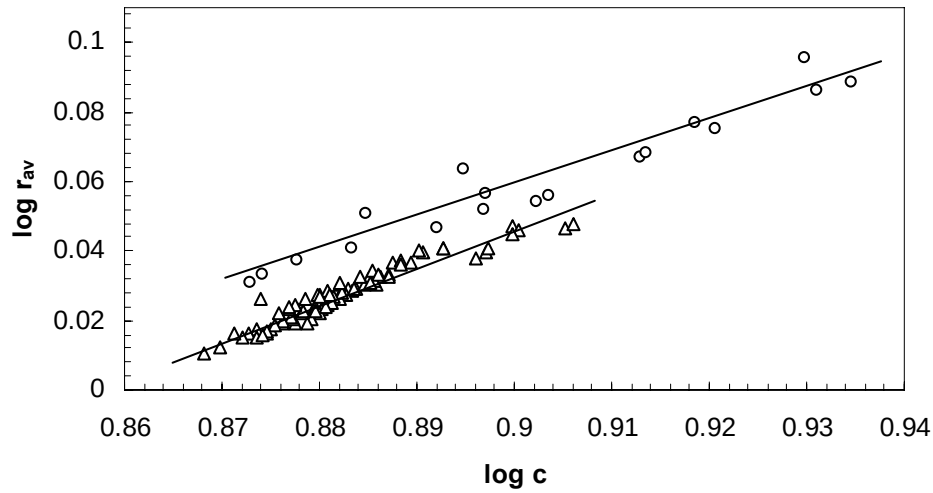

Figure 8. Plot of log c (lattice constant in Å) against log r_{av} (average ionic radii in Å) for $A^{+2}B^{+4}O_3$ and $A^{+3}B^{+3}O_3$ orthorhombic perovskites and $A^{+2}B^{+4}O_3$ and $A^{+3}B^{+3}O_3$ are represented by o and Δ respectively.

2.2. Mechanical Properties

Yamanaka et al [63] have studied mechanical properties of alkaline-earth perovskites. According to him, the elastic moduli and Debye temperature of $BaUO_3$, $BaZrO_3$, $BaCeO_3$, $BaMoO_3$, $SrTiO_3$, $SrZrO_3$ and $SrCeO_3$ are corrected to the values for 100% of the theoretical density by using a finite element method, while those of $SrMoO_3$, $SrHfO_3$ and $SrRuO_3$ are not corrected. It has found that $BaZrO_3$ and $SrZrO_3$ show the highest Young's modulus in Ba and Sr series perovskites, respectively. It is known that the Debye temperature (θ_D) can be related

to the melting temperature (T_m in K), the molar mass (M), and the molar volume (V_m) by the Lindemann relationship [64]. This relationships were re-examined for the perovskites, and the ratio of θ_D to $q^{5/6}(T_m/(MV_m^{2/3}))^{1/2}$ was evaluated to be 1.60 [65-68], where q is the number of atoms in the chemical formula.

2.3. Miscellaneous Properties and Applications

The measurement of electronic, optical and thermal properties has often been used to characterize perovskite materials [69-71] and also to identify phase transitions [11,72-74] M. Akaogi et al. [70], results shows that the recovered run products from conditions of 21.2-25.7 GPa and 1,673-2,073 K contained lithium niobate-structured phase. Based on the study by Leinenweber et al. [75], concluded that the phase was the quench product of $MgGeO_3$ orthorhombic perovskite stable at high pressure. According to M. Rousseau [74], E. P. R. experiment clearly indicates that an order-disorder local behaviour occurs in $SrTiO_3$ near T_c [76]; in the same way, ^{87}Rb NMR study in $RbCaF_3$ seems to indicate a local symmetry lowering far above T_c. In this context, $RbCaF_3$ with its large tilt angles in one of the most suitable compound for testing the validity of this description; to this purpose NMR spin-lattice relaxation time measurements are being carried out. Eglitis et al [69], quantum chemical INDO calculations have given additional evidence for the existence of electron polarons in $BaToO_3$ crystals which are expected to be stable at low temperatures. These calculations for a series of perovskite materials-$SrTiO_3$, $BaTiO_3$, $KNbO_3$ and $KTaO_3$- give a strong support to the green luminescence in these crystals as a result of the recombination of the electrons and holes forming the charge transfer vibronic exciton rather than due to the electron transitions in a MeO_6 complex.

Luana et al [77], have presented a systematic analysis of the topological properties of the electronic density in a family of ionic crystals: the halide perovskites AMX_3. AIM (atoms in molecules) theory provides a rigorous quantum-mechanical foundation to key concepts of the chemical structure, such as which bonds do exist, how the shape of an atom is and what is its charge, or how the properties of a functional group change form compound to compound. Although it has been extensively applied to a number of organic gas-phase molecules, not many studies have been published concerning solid-state systems [78-84] and Victor Luana et al [77] also studied formation of antiperovskites. Antiprovskites, MAX_3 have the same structure as perovskites, exvept that M^{2+} and A^+ exchange their position. A^+ ions are octahedrally coordinated by the anions and the A-X bonds will dominate. The only antiperovskites that is simultaneously more stable than the perovskite and $MX^{2+}AX$ are $CaLiF_3$, $SrLiF_3$ and $BaLiF_3$. Even more, the perovskite structure should be unstable in the three compounds. $BaLiF_3$ is the only antiperovskite experimentally observed among the AMX_3 compounds [85-87]

Applications

An especially important field of application is their use as hosts for laser systems. The perovskite structure appears as appropriate for this purpose because it contains a large A site suitable for the incorporation of Nd (III) and Sm (III), which are some of the most popular laser ions. And, on the other hand, the smaller B sites can receive the small Cr (III) ion which

is also frequently used in such systems. Many perovskite oxides present high electrical resistivities, which make them useful as dielectric materials. However, another group of materials such as $LaVO_3$, $LaTiO_3$, $SrMoO_3$, which contain B-ions in an oxidation state lower than their most stable one or which contain B-ions in two different oxidation states, are fairly good conductors or semiconductors. The best-known metallic conductors are probably the tungsten bronzes with the cubic-perovskite structure [4, 8, 11]. Perovskites abound both in nature and in the laboratory, and their wide compositional range renders a variety of useful properties such that perovskites are encountered in applications as disparate as electroceramics, superconductors, refractories, catalysts, magnetoresistrors, and proton conductors. The design of such advanced materials requires an understanding of the relationship between chemical composition and crystal structure.

Some perovskite-oxides can be used as oxygen sensors. These types of sensors utilize electrical conductivity changes due to oxygen adsorption. The conductivity is proportional to oxygen partial pressure. Among these materials, $SrTiO_3$ showed a high sensitivity to oxygen. On the other hand, $SrSnO_3$ appears as promising for use as a combustion monitoring-sensor [61]. Finally, it is interesting to remember that perovskite materials are probably the predominant minerals in the earth's lower mantle. Among these important geological perovskites, two phases seem to be the most important ones, namely (Mg, Fe)SiO_3 and $CaSiO_3$. Both materials adopt the perovskite structure at pressures of several hundred thousand atmospheres. Studies carried out on upper mantle silicate minerals, such as pyroxenes, spinels, garnets and olivines, show that at the high pressures and temperatures of the deep interior of the earth, these silicates are transformed, combining with some other minerals, to form rocks that are dominated by perovkite-like silicates [62].

CONCLUDING REMARKS

Generally ABO_3 oxides are electronic conductors. Ionic conduction is not favored because of the close-packed nature of the perovskite structure. However, it has recently been found that substitution in some ABO_3 oxides can lead to ionic conduction. Thus partial substitution by aluminium in $CaTiO_3$ gives rise to ionic conductivity close to that observed in oxides with the fluorite structure [88]. Substitution by lower valence ions of fixed valency at the B site in these ABO_3 oxides creates oxygen vacancies for charge neutrality. This increase in the oxygen ion mobility and oxygen ionic conduction is observed. Quantum chemical methods are a very efficient tool for the study of optical properties of advanced perovskite materials.

ACKNOWLEDGMENTS

One of the authors (Dr. Ajay Singh Verma, PH/08/0049) is thankful to the University Grant Commission New Delhi, India for supporting this research under the scheme of U.G.C. Dr. D. S. Kothari Post Doctoral Fellowship.

REFERENCES

[1] A. Kumar, A. S. Verma and S. R. Bhardwaj, *Open Applied Physics Journal,* 1, 11, (2008).

[2] Liu Liang, Lu Wencong and Chen Nianyi, *J. Phys. Chem. Solids,* 65, 855, (2004).

[3] A. B. A. Schippers, V. Brandwijk and E. W. Gorter, *J. Solid State Chemistry,* 6, 479, (1973).

[4] R. Ubic, J. Am. Ceram. Soc, 90, 3326, (2007).

[5] R. P. Liferovich and R. G. Mitchell, *J. Solid State Chemistry,* 177, 2188, (2004).

[6] S. Yamanaka, K. Kurosaki, T. Maekawa, T. Matsuda, S. Kobayashi and M. Uno, *J. Nuclear Materials,* 344, 61, (2005).

[7] L. Chonghe, T. Yihao, Z. Yingzhi, W. Chunmei and W. Ping, *J. Phys. Chem. Solids,* 64, 2147, (2003).

[8] R. Ubic and G. Subodh, *J. Alloys and Compounds,* (2009), doi:10.1016/ j.jallcom.2009.08.139.

[9] A. S. Verma and V. K. Jindal, *J. Alloys and Compounds,* 485, 514, (2009).

[10] A. Kumar and A. S. Verma, *J. Alloys and Compounds,* 480, 650, (2009).

[11] F.S.Galasso, *Structure, Properties and Preparation of Perovskite-Type Compounds,* Pergamon Press, Oxford, (1969).

[12] P.Courty and C.Marcilly, in *Preparation of Catalysts* (B. Delmon, P.A. Jacobs and G.Poncelet,Eds.), Elsevier,Amsterdam, (1976).

[13] A.K.Cheetham and P.Day, *Solid State Chemistry.Techniques,* Oxford University Press, Oxford, (1987).

[14] J.M.Longo, H.S.Horowitz and L.R.Clavenna, in Solid State Chemistry (S.L.Holt, J.B.Milstein and M.Robbins,Eds.), *Adv.Chem. Series 186, American Chemical Sot.*, Washington DC, (1980).

[15] M.Kanimoto and T.Ozawa, *Thermochim. Acta* 148, 219 (1989).

[16] R.Roy*, Science* 238, 1664 (1987).

[17] L.G.Hubert-Pfalzgraf, *New J. Chem.* 11, 663 (1987).

[18] M. Guglielmi and G.Carturan, *J.Non-Cryst.Solids* 100, 16 (1988).

[19] J. B. Goodenough and J. M. Longo, in H. H. Landolt and R. Bornstein (Eds.) *Zahlenwerte und Funktionen aus Naturwissenschaften und Technik,* New Series, Group III, Vol. 4 (part a) (1970).

[20] F. Galasso, *Structure and Properties of Inorganic Solids,* Pergamon, New York, (1970).

[21] V. M. Goldschmidt, *Skrifter Norske Videnskaps-Akad.* Oslo. I Mathemat. Naturwiss. Klasse No 8, (1926).

[22] O Fukunaga and T. Fujita, *J. Solid State Chemistry,* 8, 331, (1973).

[23] C. Li, X. Lu, W. Ding, L. Feng, Y. Gao and Z. Guo, *Acta Crystallographica,* B64, 702, (2008).

[24] H. H. Park, M. Pezat, B. Darriet, *Rev. Chim. Min.,* 23, 323, (1986), C.R.Acad. Sc. 306, 963, (1988).

[25] R. Schuhmacher, A. Weiss, *J. Less-Common Met.* 163, 179, (1990).

[26] C.E.Messer, J. C. Eastman, R. G. Mers, A. J. Maeland, *Inorg. Chem.* 3, 776, (1964).

[27] A. W. Overhauser*, Phys. Rev*. B, 35, 411, (1987).

[28] I. Kuzmanovski and S. Alcksovska, *Chemometrics and Intelligent Laboratory Systems,* 67, 167, (2003).
[29] H. Horiuchi, T. Shishido, A. Saitow, M. Tanaka and S. Hosoya, *Materials Science and Engg.* A, 312, 237, (2001).
[30] P. Wu and C. Li, *Computer Coupling Phase Diagrams Thermochemistry,* 27, 201, (2003).
[31] S. Sasaki, J. D. Bass Prewitt and W. A. Schulze, *Acta Crystal.* C43, 1668, (1987).
[32] S. Sasaki, C. T. Prewitt and R. C. Liebermann, *Am. Miner.* 68, 1189, (1983).
[33] S. K. Saxena, L. S. Dubrovinsky, P. Lazor, Y. Cerenius, P. Haggkvist, M. Hanfland, J. Z. Hu, *Science,* 274, 1357, (1996).
[34] R. A. Oganow, J. P. Brodholt and G. D. Price, Phys. *Earth Planet Interiors,* 122, 277 (2000).
[35] S. Geller, *J. Chem. Phys.* 24, 1236 (1956).
[36] W. C. Koehler and E. O. Wollan, *J. Phys. Chem. Solids* 2, 100 (1957).
[37] V. E. Naısh and E. A. Turov, *Fiz. Met. Metalloved.* 11, 161, 321 (1961).
[38] V. E. Naısh and E. A. Turov, *Fiz. Met. Metalloved.* 9, 10 (1960).
[39] M. Marezio, J. P. Remeika, and P. D. Dernier, Acta Crystallogr., Sect. B: *Struct. Crystallogr. Cryst. Chem*. 26, 2008 (1970).
[40] P. Coppens and V. Eibschutz, *Acta Crystallogr.* 19, 524 (1965).
[41] S. Geller and E. A. Wood, *Acta Crystallogr.* 9, 563 (1956).
[42] S. Geller and V. B. Bala, *Acta Crystallogr.* 9, 1019 (1956).
[43] S. Geller, *Acta Crystallogr.* 10, 243 (1957).
[44] S. Geller, Acta Crystallogr. 10, 248 (1957).
[45] M. A. Gilleo, *Acta Crystallogr.* 10, 161 (1957).
[46] E. J. Baran and P. J. Aymonino, *An Asoc. Quim. Argent,* 56, 11, (1968).
[47] R. D. Shannon, *Acta Crystallogr.* A32, 751, (1976).
[48] A. Okazaki and Y. Suemune, *J. Phys. Soc. Japan.* 16, 176, (1961)
[49] E. Mooser, W.B. Pearson, *Acta Cryst.* 12, 1015, (1959).
[50] O. Muller, R. Roy, *The Major Ternary Structural Families,* Springer, New York, 1974.
[51] A. S. Bhalla, R. Y. Guo, R. Roy, *Mater. Res. Innovations,* 4, 3, (2000).
[52] R. Sondena, S. Stolen, P. Ravindran, T. Grande, and N. L. Allan, *Phys. Rev.* B 75, 184105, (2007).
[53] F. F. Fava, P. D'Arco, R. Orlando, and R. Dovesi, *J. Phys.: Condens. Matter* 9, 489, (1997).
[54] Y. Syono, S. I. Akimoto, and K. Kohn, *J. Phys. Soc. Jpn*. 26, 993, (1969).
[55] R. H. Mitchell, *Perovskites: Modern and Ancient* (Almaz Press, Thunder Bay, Canada, (2002).
[56] R. Sondena, P. Ravindran, S. Stolen, T. Grande, and M. Hanfland, *Phys. Rev.* B 74, 144102 (2006).
[57] Z.L. Wang, Z.C. Kang, *Functional and Smart Materials: Structural Evolution and Structure Analysis,* Plenum Press, New York, 1998.
[58] R. L, Moreira and A. Dias, *J. Phys. Chem. Solids,* 68, 1617, (2007).
[59] L. Q. Jiang, J. K. Guo, H. B. Liu, M. Zhu, X. Zhou, P. Wu, and C. H. Li, *J. Phys. Chem. Solids,* 67, 1531, (2006).
[60] C. Z. Ye, J. Yang, L. X. Yao, N. Y. Chen, *Chinese Sci. Bull.,* 47, 725, (2002).

[61] Y. Shimizu, Y. Fukuyama, T. Narikiyo, H. Arai and T. Seiyama, *Chem. Letters* 377, (1985).
[62] R. M. Hazen, *Scient. Amer.* 258, 75, (1988).
[63] S. Yamanaka, K. Kurosaki, T. Maekawa, T. Matsuda, S. Kobayashi and M. Uno, *J. Nuclear Materials,* 344, 61, (2005).
[64] F. A. Lindemann, *Physikalische Zeitschrift,* 14, 609, (1910).
[65] The Chemical Society of Japan ed., Kikan Kagaku Sousetsu, *Perovskite-Related Compounds,* No. 32, p. 37, (1997).
[66] Y. Hanajiri, T. Sato, T. Matsui, *Netsu Sokutei,* 26, 92, (1992).
[67] E. R. Naimon, *Phys. Rev. B*, 9, 737, (1974).
[68] A. Bartolotta, G. Carini, G. D'Angelo, A. Fontana, F. Rossi, G. Tripodo, *J. Non-Cryst. Solids,* 245, 9, (1999).
[69] R. I. Eglitis, E. A. Kotomin, G. Borstel, S. E. Kapphan and V. S. Vikhnin, *Computational Materials Science* 27, 81, (2003).
[70] M. Akaogi, H. Kojitani, H. Yusa, R. Yamamoto, M. Kido and K. Koyama, *Phys. Chem. Minerals*, 32, 603, (2005).
[71] T. Nakamura, *J. Solid State Chemistry,* 38, 229, (1981).
[72] W. J. Merz, *Phys. Rev.* 76, 1221, (1949).
[73] H. El-Mallah, B. E. Watts and B. Wanklyn, *Phase Transit,* 9, 235, (1987).
[74] M. Rousseau, *Journal DE Physique Letters,* 40, L439, (1979).
[75] K. Leinenweber, Y. Wang, T. Yagi and H. Yusa, *Am. Mineral,* 79, 197, (1994).
[76] A. D. Bruce, K. A. Muller and W. Berlinger, *Phys. Rev. Lett.* 42, 185, (1979).
[77] V. Luana, A. Costales and A. Martin Pendas, *Phys. Rev*. B, 55, 4285, (1997).
[78] P. Zou and R. Bader, *Acta Crystallogr.* A50, 714, (1994).
[79] V. Tsirelson, P. Zou, T. Tang and R. Bader, *Acta Crystallogr.* A51, 143, (1995).
[80] M. Eberhart, M. Donovan, J. MacLaren and D. Clougherty, *Prog. Surf. Sci.* 36, 1, (1991).
[81] M. Eberhart, M. Donovan and R. Uutlaw, *Phys. Rev.* B, 46, 12744, (1992).
[82] M. Eberhart, J. MacLaren and D. Clougherty, *J. Mater. Res.,* 8, 438, (1993).
[83] C. Mei, K. Edgecombe, V. Smith and A. Heilingerbrunner, *Int. J. Quantum Chem.* 48, 287, (1993).
[84] G. Grosch, B. Freytag, K. Range and U. Rosler, *J. Chem. Phys.,* 101, 6782, (1994).
[85] S. Baldochi, V. Mazzocchi, C. Parcente and S. Morato, *Materials Research Bulletin,* 29, 1321, (1994).
[86] A. Boumriche, J. Gesland, A. Bulou, M. Rousseau, *J. Fourquct and B. Hennion, Solid State Commun.* 91, 125, (1994).
[87] M. Duarte, M. Vieira and S. Baldochi*, Mater. Sci. Eng.* B, 25, 133, (1994).
[88] K. W. Browall, O. Muller and R. H. Doreonous, *Mater. Res. Bull.,* 11, 1475 (1976).

Reviewed by Prof. B. K. Sarkar. Department of physics, VIT University, Vellore, Tamil Nadu 632014, India.

In: Perovskites: Structure, Properties and Uses
Editor: Maxim Borowski, pp. 481-499
ISBN 978-1-61668-525-6

Chapter 12

FERROELECTRIC $PbTiO_3$: FROM A SINGLE-DOMAIN STATE TO COMPOSITE COMPONENTS

V. Yu. Topolov**[*] and A. V. Krivoruchko
Department of Physics, Southern Federal University, 5 Zorge Street,
344090 Rostov-on-Don, Russia

ABSTRACT

Regular ferroelectric lead titanate ($PbTiO_3$) is one of the well-known perovskite-type compounds with physical properties studied intensively in the last decades. Of specific interest is $PbTiO_3$ as an element of a hierarchical chain 'single-domain single crystal – polydomain single crystal – poled ceramic – composite', and the last element, composite, can be based on other elements of the aforementioned chain. In this chapter examples of modern piezo-active composites based on either $PbTiO_3$ or $PbTiO_3$-type solid solutions are considered. These composites are regarded as matrix ones with 0–3 and 1–3 connectivity patterns and with a regular distribution of inclusions. To characterize the effective electromechanical properties of the composite, two methods are applied. The effective properties of the 0–3 composite with spheroidal inclusions and of the 1–3 composite with circular cylindric inclusions are predicted by means of the effective field method. The effective properties of the 1–3 composite with inclusions in the form of rectangular parallelepiped are determined within the framework of the matrix method. In both the methods, an electromechanical interaction between components is taken into account. The role of the $PbTiO_3$-containing component is emphasized in connection with the large piezoelectric anisotropy and considerable piezoelectric sensitivity of the composite in certain volume-fraction ranges.

[*] E-mail: vutopolov@sfedu.ru, kolandr@yandex.ru

INTRODUCTION

In the last decades, advanced functional materials based on lead titanate ($PbTiO_3$) are intensively studied for a variety of reasons. First, $PbTiO_3$ is the regular ferroelectric perovskite-type oxide [1–3] that undergoes the first-order phase transition near T_C = 765 K [4]. Features of physical properties, crystal and domain structures of $PbTiO_3$ single crystal (SC), and its behavior in the phase-transition region are subjects of experimental and theoretical studies providing new information on the ferroelectric state. Second, full sets of elastic, piezoelectric and dielectric constants (i.e., electromechanical constants) are known for single-domain [4, 5] and polydomain [6] SCs of $PbTiO_3$ at room temperature. At the same time, no full sets of electromechanical constants were experimentally determined on ferroelectric ceramic (FC) samples of $PbTiO_3$. Third, $PbTiO_3$ is the important component of the perovskite-type ferroelectric solid solutions, such as $Pb(Zr_{1-x}Ti_x)O_3$, $(Pb_{1-x}La_x)(Zr_{1-y}Ti_y)O_3$, $(Pb_{1-x}Ca_x)TiO_3$ (widespread FCs with important piezoelectric and other properties) [1, 2, 7] and $(1 - x)Pb(A_{1/3}Nb_{2/3})O_3 - xPbTiO_3$ (highly piezo-active SCs with so-called domain engineered structures), where A = Mg or Zn [8–10]. These and other $PbTiO_3$-based solid solutions are of interest due to remarkable piezoelectric, optical, dielectric, and other properties. Fourth, FCs of modified $PbTiO_3$, $(Pb_{1-x}Ca_x)TiO_3$ etc. and relaxor-ferroelectric SCs of $(1 - x)Pb(A_{1/3}Nb_{2/3})O_3 - xPbTiO_3$ are used as components of modern piezo-active composites [11–16] with 0–3, 1–3, 3–3 and other connectivity patterns. The piezoelectric anisotropy, activity, sensitivity, electromechanical coupling factors, and other parameters of there composites [12–16] are of value for sensor, actuator, hydrophone, and transducer applications. Fifth, electromechanical properties of materials based on $PbTiO_3$ were analysed within the framework on the hierarchical chain 'single-domain SC – polydomain SC – poled FC' [17–19]. A subsequent element of the chain, the composite based on $PbTiO_3$ (either SC or FC, including modified compositions), is of an independent interest due to various interrelations [16, 20–22] between the properties and microgeometry of components.

In the present chapter we discuss examples of performance of modern $PbTiO_3$-based composites and important interrelations between the electromechanical properties of the elements in the aforementioned hierarchical chain. Our aim is to show the role of the $PbTiO_3$-based components in forming the anisotropic piezoelectric response, considerable piezoelectric sensitivity and non-monotonic volume-fraction dependence of the effective properties of the piezo-active composites. Below we consider the FC / polymer and SC / FC matrix composites with α–3 connectivity (α = 0 or 1).

0–3 FERROELECTRIC CERAMIC / POLYMER COMPOSITE AND ITS PERFORMANCE

Modelling of Effective Electromechanical Properties

The 0–3 $PbTiO_3$-type FC/epoxy resin composite is an example of the piezo-active material prepared by electric-field structuring [11]. The microstructure and anisotropic electromechanical properties of this composite are attained due to use of dielectrophoresis for the structural modification. At means that a dispersion of FC particles embedded in a liquid

polymer or pre-polymer is exposed to a moderate as field that promotes the formation of chain-like structures in a polymer matrix. After a sodification of the polymer medium, these structures remain stable of the composite sample [11].

An analysis of the composite microstructure suggests that this material is characterized by 0–3 connectivity (in terms introduced by Newnham et al. [20]), and the shape of the FC inclusions therein approaches the spheroidal shape.

To predict the effective electromechanical properties of the 0–3 composite with the spheroidal inclusions, different averaging methods are applied [15, 16, 23–25]. Our current study is carried out within the framework of the model [15] that has first been applied to the 0–3 composite based on the $(Pb_{1-x}Ca_x)TiO_3$ FC with the large piezoelectric anisotropy. In this model the shape of each inclusion (Figure 1, component 1) is described by the equation

$$(x_1 / a_1)^2 + (x_2 / a_1)^2 + (x_3 / a_3)^2 = 1 \tag{1}$$

relative to the axes of the rectangular coordinate system ($X_1X_2X_3$), where the semi-axes of the spheroid are $a_1 = a_2$ and a_3. A remanent polarization vector of each inclusion is $\boldsymbol{P}_r^{(1)} \uparrow\uparrow OX_3$, and the OX_3 axis is the poling axis of the composite. We consider a regular distribution of the spheroidal inclusions occupy sites of a simple tetragonal lattice with unit-cell vectors parallel to the OX_j axes. It is assumed that the electrical conductivities $\gamma^{(1)}$ of FC and $\gamma^{(2)}$ of polymer are linked with an inequality $\gamma^{(2)} \geq \gamma^{(1)}$ and that surface charges caused by the ferroelectric polarization fully screened by free carriers coming to interfaces in the composite sample. The components of the composite are characterized by sets of elastic moduli $c_{ab}^{(n),E}$ measured at electric field E = const, piezoelectric coefficients $e_{ij}^{(n)}$ and dielectric permittivities $\varepsilon_{pp}^{(n),\xi}$ measured at mechanical strain ξ = const, where n = 1 and 2. The effective electromechanical properties determined in the long-wavelength limit depend on the volume fraction m of FC and the aspect ratio $\rho = a_1 / a_3$ where a_j are the semi-axes of the FC inclusion (Figure 1).

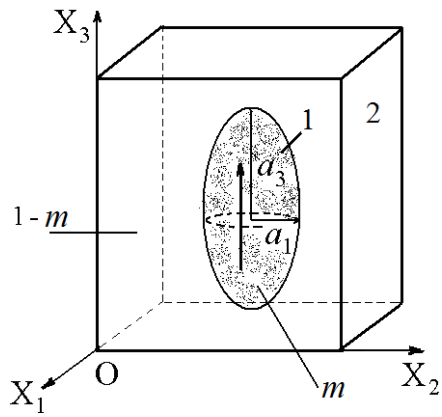

Figure 1. Schematic of the 0–3 composite with spheroidal inclusions. The polarization vector of the inclusion is denoted by an arrow therein. $X_1X_2X_3$ is the rectangular coordinate system, a_i are semiaxes of the spheroid, m is the volume fraction of component 1, and $1 - m$ is the volume fraction of component 2.

The calculation procedure is based on the effective field method (EFM), i.e., the Mori – Tanaka method [26] generalized for heterogeneous piezoelectric media [16, 23]. The EFM based on Eshelby's concept of spheroidal inclusions [27, 28] is a variant of the self-consistent scheme for the calculation of effective constants of the piezoactive composites. Following the EFM, we take into account the electromechanical interaction between the piezo-active inclusions in the matrix and related coupled effects. The effective electromechanical properties of the 0–3 composite are represented in the matrix form as

$$\| C^* \| = \| C^*(m, \rho) \| = \begin{pmatrix} \| c^{*E} \| & \| e^* \|^t \\ \| e^* \| & - \| \varepsilon^{*\xi} \| \end{pmatrix} \quad (2)$$

where the superscript "t" denotes the transposition. It should be noted that the matrices $\| c^{*E} \|$ (6 × 6), $\| e^* \|$ (3 × 6) and $\| \varepsilon^{*\xi} \|$ (3 × 3) from Eq. (2) correspond to ∞mm symmetry of the 0–3 composite. The effective electromechanical properties from Eq. (2) are determined by means of the EFM, and the matrix of these properties is written [16] as

$$\| C^* \| = \| C^{(2)} \| + m (\| C^{(1)} \| - \| C^{(2)} \|) \{ \| K \| + (1-m) \| S \| \| C^{(2)} \|^{-1} (\| C^{(1)} \| - \| C^{(2)} \|) \}^{-1}, \quad (3)$$

where matrices of the electromechanical properties of the components $\| C^{(1)} \|$ and $\| C^{(2)} \|$ have the form similar to that shown Eq. (2), $\| K \|$ is identity matrix, and $\| S \|$ is the matrix that comprises components of the electroelastic Eshelby tensor [28]. C omponents of the Eshelby tensor depend on elements of $\| C^{(2)} \|$ and the aspect ratio ρ of the inclusion. The effective piezoelectric coefficients d_{ij}^*, g_{ij}^* and h_{ij}^* are determined using the effective constants from Eq. (3) in accordance with formulae [29]

$$d_{ij}^* = e_{if}^* \, s_{fj}^{*E} = \varepsilon_{pi}^{*\sigma} \, g_{pj}^* \text{ and } e_{ij}^* = \varepsilon_{pi}^{*\xi} \, h_{pj}^* . \quad (4)$$

In Eqs. (4), $\varepsilon_{pi}^{*\sigma} = \varepsilon_{pi}^{*\xi} + e_{pf}^* \, d_{if}^*$ is dielectric permittivity measured at mechanical stress σ = const.

Effective Electromechanical Properties: Volume-fraction and Aspect-ratio Dependences

As is known from various experimental data (Figure 2), important features of the $PbTiO_3$-type FCs are three positive piezoelectric coefficients $e_{ij}^{(1)}$ (ij = 15, 31 and 33) and the large anisotropy of the piezoelectric coefficients $d_{3j}^{(1)}$, i.e., $d_{33}^{(1)} / | d_{31}^{(1)} | >> 1$. At the first stage of calculations, the full sets of room-temperature experimental electromechanical constants of FC I (see data I from Figure 2) and epoxy [32] are used.

FCs	$c_{11}^{(n),E}$	$c_{12}^{(n),E}$	$c_{13}^{(n),E}$	$c_{33}^{(n),E}$	$c_{44}^{(n),E}$	$e_{31}^{(n)}$	$e_{33}^{(n)}$	$e_{15}^{(n)}$	$\varepsilon_{11}^{(n),\xi} / \varepsilon_0$	$\varepsilon_{33}^{(n),\xi} / \varepsilon_0$
$(Pb_{0.9625}La_{0.025})(Ti_{0.99}Mn_{0.01})O_3$ (I)	14.33	3.220	2.413	13.16	5.587	0.4584	6.499	5.923	210	140
$(Pb_{0.9625}La_{0.025})(Ti_{0.99}Mn_{0.01})O_3$ (II)	15.8	4.20	4.55	15.2	6.32	1.32	6.80	3.35	203	133
$(Pb_{0.85}Nd_{0.10})(Ti_{0.99}Mn_{0.01})O_3$ (III)	17.5	5.49	5.65	16.5	6.26	1.80	8.83	5.41	265	193
$(Pb_{0.855}Nd_{0.11})(Ti_{0.94}Mn_{0.02}In_{0.04})O_3$ (IV)	17.3	5.31	5.68	16.6	6.09	2.00	8.81	4.84	270	198
Modified $PbTiO_3$ (V)	14.2	3.53	2.59	13.0	5.26	0.247	6.90	3.58	213	147

Figure 2. Room-temperature experimental values of elastic moduli $c_{ab}^{(n),E}$ (in 10^{10} Pa), piezoelectric coefficients $e_{ij}^{(n)}$ (in C / m^2) and relative dielectric permittivities $\varepsilon_{33}^{*\xi} / \varepsilon_0$ of FCs I [30], II – IV [31] and V [2]. FCs I and II with equal chemical formulae are distinguished by processing conditions.

Results on the calculated effective parameters of the 0–3 composite studied are shown in Figure 3. To avoid differences between electromechanical constants of the $PbTiO_3$-type FC used in experimental work [11] and constants of FC I from Figure 2, we consider normalized dielectric permittivity $\beta_\varepsilon = \varepsilon_{33}^{*\sigma} / \varepsilon_{33}^{(1),\sigma}$ and normalized piezoelectric coefficients $\beta_d = d_{33}^* / d_{33}^{(1)}$ and $\beta_g = g_{33}^* / g_{33}^{(1)}$. Good agreement between the experimental [11] and calculated volume-fraction dependences of β_ε is observed in the aspect-ratio range $\rho = 0.13 - 0.19$ (see Figure 3. a). It means that the structured 0–3 composite can be regarded as an aggregate of prolate inclusions in a matrix so that the semi-axes of the inclusions are linked by $a_3 / a_1 \approx 5 - 7$. The similar microstructure of the 0–3 composite is observed in experimental work [11]. The volume-fraction dependence of β_ε for the unstructured 0–3 composite can be approximated by pieces of curves calculated for $\rho \approx 0.32 - 0.50$ (Figure 3, b).

As follows from our analysis of the piezoelectric response of the composite studied, among the piezoelectric coefficients d_{3j}^*, e_{3j}^*, g_{3j}^*, and h_{3j}^* (j = 1 and 3) from Eqs. (4), g_{31}^* and g_{33}^* are most sensitive to changes in the m and ρ values. For example, in the aspect-ratio range $\rho = 0.01 - 0.20$, one can reach $\max\beta_g \approx 3 - 10$ and $\min g_{31}^* / g_{31}^{(1)} \approx 9 - 40$. A difference between the aforementioned ratios is concerned with the influence of the system of the prolate FC inclusions on forming the anisotropic piezoelectric response of the composite. Due to this system, the volume-fraction dependence of β_d and β_g (Figure 3, c and d) resembles behaviour of the piezoelectric coefficients d_{33}^* and g_{33}^*, respectively, in the 1–3 $PbTiO_3$-type FC / polymer composite [33] with the regularly-distributed FC rods. An advantage of the 0–3 composite based on the $PbTiO_3$-type FC consists in the relatively large $\max\beta_g$ values that are attained near the volume fraction $m = 0.1$ at various aspect ratios ρ (Figure 3, d). It is concerned with a favourable balance of elastic moduli $c_{ab}^{(n),E}$ of components and relatively low dielectric permittivity $\varepsilon_{33}^{*\sigma}$ at $0 < m \leq 0.1$. Eqs. (4) suggest that $\varepsilon_{33}^{*\sigma}$ considerably influences g_{33}^* and β_g of the composite. Examples of behaviour of two factors of the piezoelectric anisotropy, d_{33}^* / d_{31}^* and $e_{33}^* / e_{31}^* = (2 d_{31}^* c_{13}^{*E} + d_{33}^* c_{33}^{*E}) / [d_{31}^* (c_{11}^{*E} + c_{12}^{*E}) + d_{33}^* c_{13}^{*E}]$, is shown in Figure 3, e and f, respectively. It is seen that the ratio of e_{33}^* / e_{31}^* is varied in the wider range, and this behaviour is apparently concerned with an active influence

of elastic properties of the FC and polymer components on the piezoelectric coefficients e^*_{3j} and with the presence of the prolate FC inclusions aligned on the poling direction OX_3 (Figure 1).

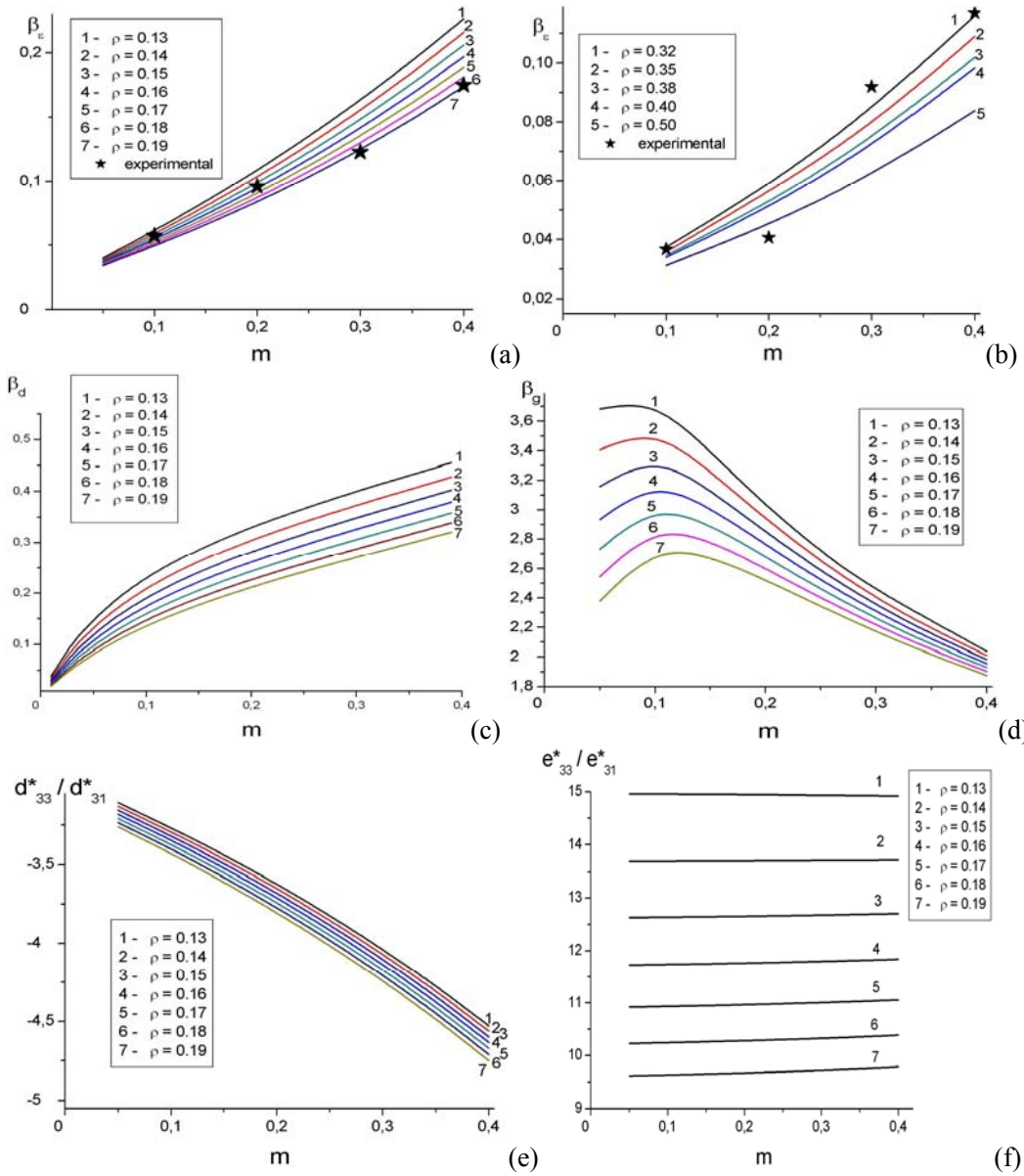

Figure 3. Volume-fraction dependence of normalized dielectric permittivity β_ε (a and b), normalized piezoelectric coefficients β_d (c) and β_d (d), and factors of the piezoelectric anisotropy $d^*_{33}/\ d^*_{31}$ (e) and $e^*_{33}\ /\ e^*_{31}$ (f) of the 0–3 $PbTiO_3$-based FC / epoxy composite. Graphs (a) and (b) correspond to the structured composite and unstructured composite, respectively. Experimental points are from dielectric measurements [11].

At the second stage of calculations, we compare the normalized parameters β_ε, β_d and β_g that are evaluated using the full sets of electromechanical constants of FC from Figure 2. Examples of the volume-fraction dependence of these parameters in the composite with the prolate spheroidal inclusions are shown in Figure 4. The composites based on different FC compositions with the large piezoelectric anisotropy have the similar performance. Values of $\max \beta_g$ are expected at volume fractions $0.05 < m < 0.10$, i.e., in the range where the influence of dielectric permittivity of polymer remains strong. In this connection, we mention that dielectric properties of the FC and polymer components along the OX_3 axis are interrelated by a ratio $\varepsilon_{33}^{(1),\sigma} / \varepsilon_{33}^{(2)} \sim 10$.

Transition to 1–3 Connectivity

Now we consider a transition from 0–3 connectivity to 1–3 one. In case of the 1–3 composite, we assume that $\rho = 0$ and the composite contains the infinitely long FC rods being parallel to the poling axis OX_3. They have the shape of a circular cylinder with a fixed radius and are aligned on the axis OX_3 of the rectangular co-ordinate system ($X_1X_2X_3$). Centres of sections of these cylinders constitute a square lattice in the (X_1OX_2) plane, i.e., square patterns in the arrangement of the FC rods are considered. The EFM is also applied for calculating the effective electromechanical properties of the 1–3 composite. Moreover, it should be added that the transition from 0–3 to 1–3 means continuous changes [28] in elements of the $\| S \|$ matrix from Eq. (3). As a consequence, we see a monotonic variation of the effective properties of the composite (Figure 5). To determine its effective properties, we used the full sets of electromechanical constants of $(Pb_{0.75}Ca_{0.25})TiO_3$ FC [15] with the large piezoelectric anisotropy and elastic and dielectric constants of piezo-passive araldite [15].

As follows from Figure 5, the decrease of the effective parameters Φ_{33}^* ($\Phi = e, d, g, h, \varepsilon^\xi$, and ε^σ) of the 0–3 composite as compared to Φ_{33}^* of the 1–3 composite at m = const is caused by a discrete distribution of the piezo-active component along the OX_3 axis and by a lowering of the piezoelectric activity. This lowering is concerned with an increase of the depoling field in the FC inclusions of the 0–3 composite. A slight increase of e_{31}^* and a decrease of $|d_{31}^*|$ as the aspect ratio increases at m = const is observed in the presence of the FC component with that the large anisotropy of the piezoelectric coefficients $d_{3j}^{(1)}$ and with the moderate anisotropy of the piezoelectric coefficients $e_{3j}^{(1)} > 0$. The more pronounced increase of h_{31}^* as compared to e_{31}^* at m = const is accounted for by the influence of the dielectric permittivity $\varepsilon_{33}^{*\xi}$ of the composite in accordance with Eqs. (4).

ρ	Normalized parameter	FC	m						
			0.01	0.05	0.1	0.15	0.20	0.30	0.40
0.05	β_e	I	0.0264	0.0548	0.0922	0.131	0.171	0.255	0.343
		II	0.0276	0.0564	0.0943	0.134	0.174	0.258	0.347
		III	0.0200	0.0481	0.0807	0.117	0.154	0.233	0.318
		IV	0.0202	0.0463	0.0808	0.117	0.154	0.233	0.318
		V	0.0249	0.0527	0.0895	0.128	0.167	0.250	0.338
	β_d	I	0.123	0.382	0.523	0.601	0.652	0.721	0.771
		II	0.128	0.393	0.535	0.612	0.663	0.731	0.780
		III	0.118	0.359	0.487	0.558	0.605	0.672	0.723
		IV	0.119	0.361	0.490	0.56	0.608	0.675	0.726
		V	0.120	0.374	0.513	0.59	0.641	0.710	0.761
	β_g	I	4.65	6.97	5.67	4.58	3.81	2.83	2.25
		II	4.63	6.97	5.68	4.59	3.81	2.83	2.25
		III	5.89	7.78	6.04	4.78	3.93	2.89	2.28
		IV	5.86	7.78	6.04	4.78	3.93	2.89	2.28
		V	4.81	7.10	5.73	4.62	3.83	2.84	2.25
0.10	β_e	I	0.0245	0.0441	0.0701	0.0977	0.127	0.191	0.263
		II	0.0257	0.0458	0.0724	0.101	0.131	0.195	0.268
		III	0.0178	0.0342	0.0561	0.0796	0.105	0.16	0.224
		IV	0.0180	0.0345	0.0565	0.0801	0.105	0.161	0.225
		V	0.0230	0.0418	0.0670	0.0937	0.122	0.184	0.255
	β_d	I	0.0573	0.205	0.307	0.373	0.421	0.495	0.557
		II	0.0598	0.213	0.318	0.384	0.433	0.508	0.569
		III	0.0491	0.174	0.260	0.315	0.357	0.423	0.482
		IV	0.0497	0.176	0.263	0.318	0.360	0.427	0.485
		V	0.0552	0.198	0.297	0.36	0.407	0.48	0.541
	β_g	I	2.34	4.66	4.39	3.81	3.32	2.59	2.12
		II	2.33	4.66	4.39	3.82	3.32	2.60	2.12
		III	2.76	5.10	4.63	3.97	3.42	2.64	2.15
		IV	2.75	5.09	4.63	3.97	3.42	2.64	2.15
		V	2.41	4.74	4.43	3.84	3.33	2.60	2.12
0.20	β_e	I	0.0223	0.0331	0.0476	0.0633	0.0804	0.119	0.167
		II	0.0235	0.0347	0.0497	0.066	0.0837	0.124	0.172
		III	0.0159	0.0242	0.0354	0.0476	0.0610	0.092	0.130
		IV	0.0161	0.0244	0.0357	0.0481	0.0616	0.0928	0.131
		V	0.0209	0.0311	0.0449	0.0598	0.0761	0.113	0.159
	β_d	I	0.0174	0.0735	0.124	0.164	0.137	0.254	0.308
		II	0.0183	0.0769	0.130	0.171	0.205	0.264	0.190
		III	0.0135	0.0569	0.0962	0.127	0.153	0.199	0.244
		IV	0.0137	0.0577	0.0975	0.129	0.155	0.201	0.247
		V	0.0166	0.0697	0.118	0.155	0.187	0.242	0.294
	β_g	I	0.782	2.22	2.61	2.58	2.45	2.13	1.85
		II	0.779	2.22	2.61	2.59	2.48	2.13	1.83
		III	0.853	2.35	2.72	2.67	2.51	2.16	1.87
		IV	0.852	2.35	2.72	2.67	2.51	2.16	1.87
		V	0.794	2.24	2.63	2.60	2.46	2.13	1.85

Figure 4. Volume-fraction dependence of normalized parameters β_e, β_d and β_g of the 0–3 composite "$PbTiO_3$-type FC / epoxy". Electromechanical constants of FCs I – V were taken from experimental data in Figure 2.

$\rho = 0$ (1–3 connectivity)					
Φ^*	$m = 0.1$	$m = 0.2$	$m = 0.3$	$m = 0.4$	$m = 0.5$
$10^2 e_{31}^*$	0.960	2.14	3.63	5.56	8.17
e_{33}^*	0.459	0.919	1.38	1.84	2.31
d_{31}^*	-6.73	-6.65	-5.99	-5.19	-4.35
d_{33}^*	22.0	25.0	26.1	26.8	27.2
g_{31}^*	-38.4	-21.1	-13.1	-8.69	-5.89
g_{33}^*	126	79.3	57.3	44.9	36.9
$10^2 h_{31}^*$	5.82	7.31	8.63	10.1	12.1
h_{33}^*	2.78	3.14	3.28	3.36	3.42
$\varepsilon_{33}^{*\xi} / \varepsilon_0$	18.6	33.1	47.5	61.9	76.4
$\varepsilon_{33}^{*\sigma} / \varepsilon_0$	19.8	35.6	51.5	67.5	83.4
$\rho = 0.01$ (0–3 connectivity)					
Φ^*	$m = 0.1$	$m = 0.2$	$m = 0.3$	$m = 0.4$	$m = 0.5$
$10^2 e_{31}^*$	0.972	2.16	3.66	5.61	8.23
e_{33}^*	0.440	0.885	1.34	1.79	2.26
d_{31}^*	-6.58	-6.54	-5.90	-5.12	-4.30
d_{33}^*	21.5	24.6	25.8	26.5	26.9
g_{31}^*	-38.0	-21.0	-13.1	-8.66	-5.88
g_{33}^*	124	78.7	57.1	44.8	36.8
$10^2 h_{31}^*$	5.94	7.45	8.78	10.3	12.2
h_{33}^*	2.69	3.05	3.20	3.29	3.36
$\varepsilon_{33}^{*\xi} / \varepsilon_0$	18.5	32.8	47.2	61.6	76.0
$\varepsilon_{33}^{*\sigma} / \varepsilon_0$	19.6	35.2	51.0	66.8	82.7
$\rho = 0.05$ (0–3 connectivity)					
Φ^*	$m = 0.1$	$m = 0.2$	$m = 0.3$	$m = 0.4$	$m = 0.5$
$10^2 e_{31}^*$	0.999	2.24	3.80	5.83	8.56
e_{33}^*	0.263	0.556	0.884	1.25	1.67
d_{31}^*	-4.85	-5.14	-4.82	-4.31	-3.72
d_{33}^*	16.2	19.7	21.5	22.7	23.8
g_{31}^*	-32.4	-19.1	-12.3	-8.24	-5.64
g_{33}^*	108	73.3	54.7	43.5	36.1
$10^2 h_{31}^*$	6.86	8.67	10.1	11.8	13.8
h_{33}^*	1.80	2.15	2.36	2.53	2.69
$\varepsilon_{33}^{*\xi} / \varepsilon_0$	16.5	29.2	42.3	55.8	70.1
$\varepsilon_{33}^{*\sigma} / \varepsilon_0$	16.9	30.4	44.4	59.0	74.5

Figure 5. Volume-fraction dependence of the piezoelectric coefficients e_{3j}^* (in C / m^2), d_{3j}^* (in pC / N), g_{3j}^* (in mV·m / N), and h_{3j}^* (in GV / m) and dielectric permittivities $\varepsilon_{33}^{*\xi} / \varepsilon_0$ and $\varepsilon_{33}^{*\sigma} / \varepsilon_0$ of the $(Pb_{0.75}Ca_{0.25})TiO_3$ FC / araldite composite at $0 \le \rho \le 0.05$ (reprinted from Topolov et al. [33], with permission from IOP Publishing).

	m = 0.1		m = 0.2		m = 0.3	
Φ^*	EFM	FEM	EFM	FEM	EFM	FEM
$10^2 e_{31}^*$	0.960	0.960	2.14	2.14	3.63	3.63
e_{33}^*	0.459	0.459	0.919	0.919	1.38	1.38
d_{31}^*	-6.73	-6.73	-6.65	-6.65	-5.99	-5.99
d_{33}^*	22.0	22.0	25.0	25.0	26.1	26.1
g_{31}^*	-38.4	-38.4	-21.1	-21.1	-13.1	-13.1
g_{33}^*	126	126	79.3	79.1	57.3	57.3
$10^2 h_{31}^*$	5.82	5.82	7.31	7.31	8.63	8.63
h_{33}^*	2.78	2.78	3.14	3.14	3.28	3.28
$\varepsilon_{33}^{*\xi} / \varepsilon_0$	18.6	18.7	33.1	33.1	47.5	47.5
$\varepsilon_{33}^{*\sigma} / \varepsilon_0$	19.8	19.8	35.6	35.7	51.5	51.6

	m = 0.4		m = 0.5		m = 0.6	
Φ^*	EFM	FEM	EFM	FEM	EFM	FEM
$10^2 e_{31}^*$	5.56	5.59	8.17	8.31	11.9	12.6
e_{33}^*	1.84	1.84	2.31	2.31	2.78	2.78
d_{31}^*	-5.19	-5.18	-4.35	-4.30	-3.51	-3.38
d_{33}^*	26.8	26.8	27.2	27.2	27.4	27.4
g_{31}^*	-8.69	-8.67	-5.89	-5.83	-3.99	-3.84
g_{33}^*	44.9	44.8	36.9	36.8	31.2	31.2
$10^2 h_{31}^*$	10.1	10.2	12.1	12.3	14.8	15.7
h_{33}^*	3.36	3.36	3.42	3.42	3.46	3.46
$\varepsilon_{33}^{*\xi} / \varepsilon_0$	61.9	62.0	76.4	76.4	90.8	90.8
$\varepsilon_{33}^{*\sigma} / \varepsilon_0$	67.5	67.5	83.4	83.4	99.3	99.3

Figure 6. Volume-fraction dependence of the piezoelectric coefficients e_{3j}^* (in C / m^2), d_{3j}^* (in pC / N), g_{3j}^* (in mV·m / N), and h_{3j}^* (in GV / m), dielectric permittivities $\varepsilon_{33}^{*\xi} / \varepsilon_0$ and $\varepsilon_{33}^{*\sigma} / \varepsilon_0$, and elastic moduli c_{ab}^{*E} (in GPa) which have been calculated for the 1–3 $(Pb_{0.75}Ca_{0.25})TiO_3$ FC / araldite composite by means of the EFM and finite element metod (reprinted from Topolov et al. [33], with permission from IOP Publishing).

Below we compare data on the effective parameters (Figure 6) calculated using two different methods, the EFM and the finite elemet method [33]. In general, the good agreement between the calculated values of the effective parameters (e.g., piezoelectric coefficients e_{3j}^*, d_{3j}^*, g_{3j}^*, and h_{3j}^*, dielectric permittivities $\varepsilon_{33}^{*\xi} / \varepsilon_0$ and $\varepsilon_{33}^{*\sigma} / \varepsilon_0$) is attained. The difference between the the effective parameters Φ_{33}^* of the 1–3 composite does not exceed 1 % in the volume-fraction range of $0.1 \le m \le 0.6$. At the largest volume fraction of FC $m = 0.6$ (Figure 6), a difference between values of the piezoelectric coefficient e_{31}^* evaluated using different methods equals about 6 %. The same difference takes place for the piezoelectric coefficient h_{31}^* evaluated using different methods.

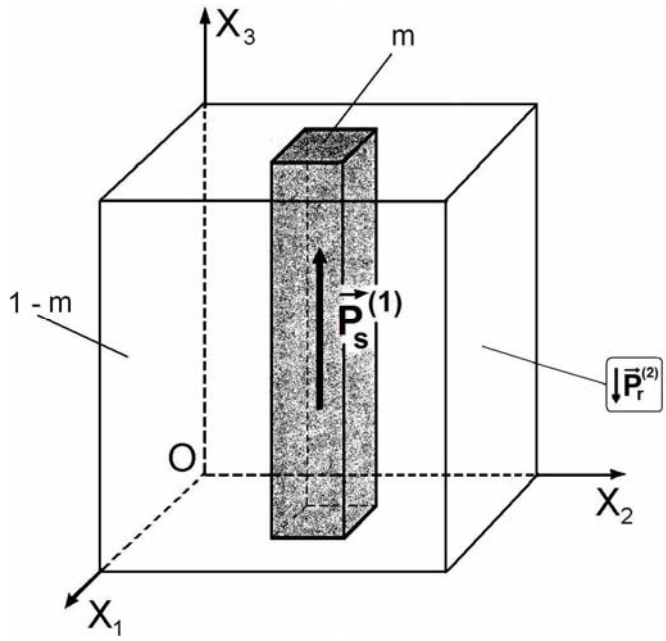

Figure 7. Schematic of the 1–3 SC / polymer composite with planar microgeometry. ($X_1X_2X_3$) is the rectangular co-ordinate system. m and $1 - m$ are volume fractions of SC and polymer, respectively. $\boldsymbol{P}_s^{(1)}$ and $\boldsymbol{P}_r^{(2)}$ are the spontaneous polarisation vector of SC and the remanent polarization vector of polymer, respectively.

1–3 Ferroelectric Single Crystal / Ferroelectric Polymer Composite and its Peformance

Effective Electromechanical Properties and Components

The ferroelectric SC / polymer composite with 1–3 connectivity is the novel piezo-active material that has attracted attention in the last decade due to efforts to improve the performace of the composite by using the relaxor-ferroelectric component with the very high piezoelectric activity [12–14, 16]. In this section we consider the 1–3 composite (Figure 7) containing SC rods in the form of rectangular parallelepipeds. The SC rods have a square base and are characterized by a square arrangement in the (X_1OX_2) plane. The rods (either single-domain or polydomain in the whole composite sample) are poled along the OX_3 axis, and the spontaneous polarisation vector $\boldsymbol{P}_s^{(1)} \uparrow\uparrow OX_3$ in each rod. The main crystallographic axes X, Y and Z of SC are parallel to the following perovskite unit-cell directions: $X \parallel [001]$, $Y \parallel [010]$ and $Z \parallel [001]$. The composite comprises one of the following groups of the SC rods poled along the [001] direction of the perovskite unit cell:

(i) single-domain $PbTiO_3$,
(ii) $(1 - x)Pb(Mg_{1/3}Nb_{2/3})O_3 - xPbTiO_3$ with domain engineered structure (four 71° domain types that are separated by the (100) and (010) domain walls) [3, 34] and compositions near the morphotropic phase boundary, or

(iii) polydomain $PbTiO_3$ with equal volume fractions of two types of 90° domains that are regularly distributed and separated by stressfree (001) domain walls [6]. The spontaneous polarization vectors of these domain types are $\boldsymbol{P_s'}(-P_s/\sqrt{2}\,;\,0;\,P_s/\sqrt{2}\,)$ and $\boldsymbol{P_s''}(P_s/\sqrt{2}\,;\,0;\,P_s/\sqrt{2}\,)$ in the co-ordinate system $(X_1X_2X_3)$ shown in Figure 7.

It is assumed that the composite matrix is made of polyvinylidene fluoride (PVDF). This ferroelectric polymer can be poled so that its remanent polarisation vector $\boldsymbol{P_r^{(2)}} \uparrow\downarrow OX_3$, and in this case the piezoelectric coefficients $d_{ij}^{(2)}$ of polymer obey condition $\operatorname{sgn} d_{31}^{(2)} = -\operatorname{sgn} d_{33}^{(2)} = -\operatorname{sgn} d_{15}^{(2)} < 0$. For the SC component (i) or (ii), the analogous condition $\operatorname{sgn} d_{31}^{(1)} = -\operatorname{sgn} d_{33}^{(1)} = -\operatorname{sgn} d_{15}^{(1)} < 0$ is also true [4–6, 12]. Conditions for the antiparallel orientation of the $\boldsymbol{P_s^{(1)}}$ and $\boldsymbol{P_r^{(2)}}$ vectors (Figure 7) can be satisfied on poling the composite sample in an electric field $\boldsymbol{E} \parallel OX_3$ due to the significant difference between the coercive fields [1–4, 35] of SC and polymer. In case of the composite based on single-domain $PbTiO_3$ SC, a bias electric field $\boldsymbol{E_b} \parallel OX_3$ is applied to stabilize the single-domain state with $\boldsymbol{P_s^{(1)}} \uparrow\uparrow OX_3$ in each SC rod.

The determination of the effective electromechanical properties of the 1–3 composite with planar interfaces (Figure 7) is carried out using a matrix approach [16]. An averaging procedure within the framework of this approach leads to averaging of the electromechanical constants of the SC rods and the polymer matrix in the OX_1 and OX_2 directions, in which the periodical structure of the composite is observed. In our calculations, the full sets of elastic compliances $s_{ij}^{(n),E}$ (measured at E = const), piezoelectric coefficients $d_{kl}^{(n)}$ and dielectric permittivities $\varepsilon_{ff}^{(n),\sigma}$ (measured at mechanical stress σ = const) of both components are used. The electromechanical properties are averaged by taking into account boundary conditions [16] for the electric and mechanical fields. These boundary conditions at the interface x_1 = const (Figure 7) mean the continuity of normal components of mechanical stress σ_{1v} (v = 1, 2 and 3), tangential components of mechanical strain ξ_{22}, ξ_{23} and ξ_{33}, normal component of electric displacement D_1, and tangential components of electric field E_2 and E_3. At the interface x_2 = const (Figure 7), the continuity of σ_{2v} (v = 1, 2 and 3), ξ_{11}, ξ_{13}, ξ_{33}, D_2, E_1, and E_3 is required. The matrix of the effective electromechanical properties of the composite [16] is given by

$$\| C^* \| = [\| C_1 \| \cdot \| M \| m + \| C_2 \| (1-m)]\,[\| M \| m + \| I \| (1-m)]^{-1} \tag{5}$$

In Eq. (5), $\| C_n \|$ are matrices of electromechanical constants of SC (n = 1) and polymer (n = 2), and these matrices are represented in the following form:

$$\| C_n \| = \begin{pmatrix} \| s^{(n),E} \| & \| d^{(n)} \|^t \\ \| d^{(n)} \| & \| \varepsilon^{(n),\sigma} \| \end{pmatrix}.$$

The matrix $\| M \|$ from Eq. (5) is related to the aforementioned boundary conditions at interfaces x_i = const (i = 1 and 2), and $\| I \|$ is the identity matrix. The effective

electromechanical properties determined on the basis of Eq. (5) are regarded as homogenised properties in the longwave approximation, when the wavelength of an external acoustic field is much longer than the size of the rod in the composite sample. We neglected a concentration of mechanical stress near the edge of the rod because of the small area of this concentration [36] in comparison to the area of the square section of the rod in the (X_1OX_2) plane. Our recent results [37] on the effective parameters calculated for the similar 1–3 SC / polymer composite by using the matrix method and the finite element method suggest that the good agreement between the parameters is observed in the whole volume-fraction range.

SCs	$s_{11}^{(n),E}$	$s_{12}^{(n),E}$	$s_{13}^{(n),E}$	$s_{22}^{(n),E}$	$s_{23}^{(n),E}$	$s_{33}^{(n),E}$
Single-domain $PbTiO_3$	6.70	-2.00	-5.79	6.70	-5.79	28.8
$0.67Pb(Mg_{1/3}Nb_{2/3})O_3 - 0.33PbTiO_3$	69.0	-11.1	-55.7	69.0	-55.7	119.6
$0.70Pb(Mg_{1/3}Nb_{2/3})O_3 - 0.30PbTiO_3$	52.0	-18.9	-31.1	52.0	-31.1	67.7
Polydomain $PbTiO_3$	9.28	-3.90	2.68	6.70	-3.90	9.28
PVDF at $P_r^{(2)} \uparrow\downarrow OX_3$	333	-148	-87.5	333	-87.5	299
	$s_{44}^{(n),E}$	$s_{55}^{(n),E}$	$s_{66}^{(n),E}$	$d_{31}^{(n)}$	$d_{32}^{(n)}$	$d_{33}^{(n)}$
Single-domain $PbTiO_3$	13.2	13.2	7.60	-26.9	-26.9	143
$0.67Pb(Mg_{1/3}Nb_{2/3})O_3 - 0.33PbTiO_3$	14.5	14.5	15.2	-1330	-1330	2820
$0.70Pb(Mg_{1/3}Nb_{2/3})O_3 - 0.30PbTiO_3$	14.0	14.0	15.2	-921	-921	1981
Polydomain $PbTiO_3$	9.65	25.2	10.4	20.7	-19.0	61.4
PVDF at $P_r^{(2)} \uparrow\downarrow OX_3$	$1.90 \cdot 10^4$	$1.90 \cdot 10^4$	943	-10.4	-10.4	33.6
	$d_{15}^{(n)}$	$d_{24}^{(n)}$	$\varepsilon_{11}^{(n),\sigma} / \varepsilon_0$	$\varepsilon_{22}^{(n),\sigma} / \varepsilon_0$	$\varepsilon_{33}^{(n),\sigma} / \varepsilon_0$	
Single-domain $PbTiO_3$	57.5	57.5	140	140	125	
$0.67Pb(Mg_{1/3}Nb_{2/3})O_3 - 0.33PbTiO_3$	146	146	1600	1600	8200	
$0.70Pb(Mg_{1/3}Nb_{2/3})O_3 - 0.30PbTiO_3$	190	190	3600	3600	7800	
Polydomain $PbTiO_3$	62.6	29.7	81.9	122	133	
PVDF at $P_r^{(2)} \uparrow\downarrow OX_3$	38	38	7.51	7.51	8.43	

Figure 8. Room-temperature elastic compliances elastic compliances $s_{ij}^{(n),E}$ (in 10^{-12} Pa^{-1}), piezoelectric coefficients $d_{kl}^{(n)}$ (in pC / N) and relative dielectric permittivities $\varepsilon_{ff}^{(n),\sigma}$ of $(1-x)Pb(Mg_{1/3}Nb_{2/3})O_3 - xPbTiO_3$ SCs: $x = 1$, single-domain and polydomain [6], $x = 0.33$ and 0.30, with domain engineered structure [38, 39]. The full set of electromechanical constants of polydomain $PbTiO_3$ SC has been determined [6] for case of motionless domain walls separating the 90° domains.

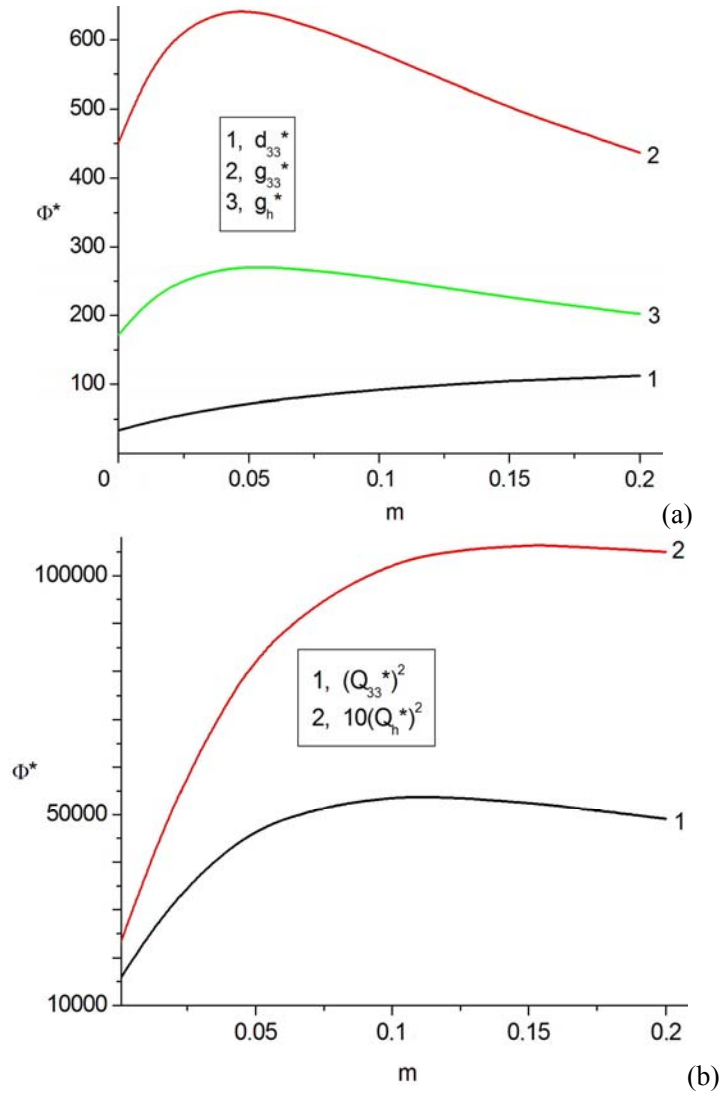

Figure 9. Volume-fraction dependence of effective parameters calculated for the 1–3 single-domain $PbTiO_3$ SC / PVDF composite with planar microgeometry: a, piezoelectric coefficients d_{33}^* (in pC / N), g_{33}^* and g_h^* (in mV·m / N) and b, squared figures of merit $(Q_{33}^*)^2$ and $(Q_h^*)^2$ (in 10^{-15} Pa^{-1}).

Maxima of Effective Parameters

Now we consider volume-fraction behaviour of the effective piezoelectric coefficient g_{33}^* and its hydrostatic analog $g_h^* = \sum_{k=1}^{3}\sum_{l=1}^{3} g_{kl}^*$. Based on d_{kl}^* being calculated within the framework of $\| C^* \|$ from Eq. (5) and g_{kl}^* being calculated using Eq. (4), we study the volume-fraction dependence of squared figure of merit $(Q_{33}^*)^2 = d_{33}^* g_{33}^* = (d_{33}^*)^2 / \varepsilon_{33}^{*\sigma}$ and

its hydrostatic analog $(Q_h^*)^2 = d_h^* g_h^* = (d_h^*)^2 / \varepsilon_{33}^{*\sigma}$. The parameters g_{33}^* and $(Q_{33}^*)^2$ are important for sensor applications, the parameters g_h^* and $(Q_h^*)^2$ are of value for hydrophone and other hydroacoustic applications. The parameters $(Q_{33}^*)^2$ and $(Q_h^*)^2$ are used to describe the sensor signal-to-noise ratio of the piezoelectric element [16]. Figure 8 contains the full sets of electromechanical constants of components of the studied 1–3 composites.

It is seen that g_{33}^*, g_h^*, $(Q_{33}^*)^2$, and $(Q_h^*)^2$ of the 1–3 composite have maxima at volume fractions $0.045 < m < 0.20$ (Figure 9), i.e., in the range where the piezoelectric coefficient d_{33}^* increases intensively (see curve 1 in Figure 9, a) and dielectric permittivity $\varepsilon_{33}^{*\sigma}$ remains relatively low. Volume fractions $m \approx 0.05$ and more are attainable when manufacturing the 1–3 composite, and this circumstance is to be taken into consideration for further applications. Of particular interest is the piezoelectric coefficient g_{33}^*: the value of $\max g_{33}^* = 641$ mV·m / N at $m \approx 0.045 – 0.050$ (see curve 2 in Figure 9, a) remains larger than, for example, $\max g_{33}^*$ found for the 1–3 $(1 – x)Pb(Mg_{1/3}Nb_{2/3})O_3 – xPbTiO_3$ SC / araldite composite (x = 0.30, 0.33 and 0.42) [40]. The presence of piezopassive araldite instead of piezo-active PVDF with approximately equal stiffness leads to decreasing the piezoelectric sensitivity of the 1–3 composite, even if it is based on the highly piezo-active SC component.

Figure 10 contains data on maxima of the aforementioned effective parameters of the related composites. Contrary to the composite based on single-domain $PbTiO_3$ SC, $\max g_{33}^*$ and $\max g_h^*$ of these composite are lower than those shown in Figure 9, a, and these maxima are attained at small volume fractions $m < 0.02$. In our opinion, such a performance is accounted for by a less-favourable balance of elastic constants of components (x = 0.33 and 0.30) or by a relatively low piezoelectric activity of polydomain $PbTiO_3$ along the poling axis OX_3. As follows from data in Figure 8, the piezoelectric coefficient $d_{33}^{(1)}$ of polydomain $PbTiO_3$ is about 1.8 times more than $d_{33}^{(2)}$ of PVDF, and this factor may promote the low piezoelectric sensitivity of the composite.

x	$\max g_{33}^*$, mV·m/N	$\max g_k^*$, mV·m/N	$\max (Q_{33}^*)^2$, 10^{-15} Pa^{-1}	$\max (Q_k^*)^2$, 10^{-15} Pa^{-1}
0, poly-domain	476 (m = 0.011)	189 (m = 0.015)	21100 (m = 0.029)	3640 (m = 0.049)
0.30	523 (m = 0.006)	206 (m = 0.006)	141000 (m = 0.103)	19300 (m = 0.070)
0.33	614 (m = 0.011)	241 (m = 0.011)	186000 (m = 0.053)	23600 (m = 0.085)

Figure 10. Maximum values of effective parameters Φ^* of the 1–3 $(1 – x)Pb(Mg_{1/3}Nb_{2/3})O_3 – xPbTiO_3$ SC / PVDF composite with planar microgeometry shown in Figure 7. In parentheses there are values of the SC volume fraction m that corresponds to $\max \Phi^*$.

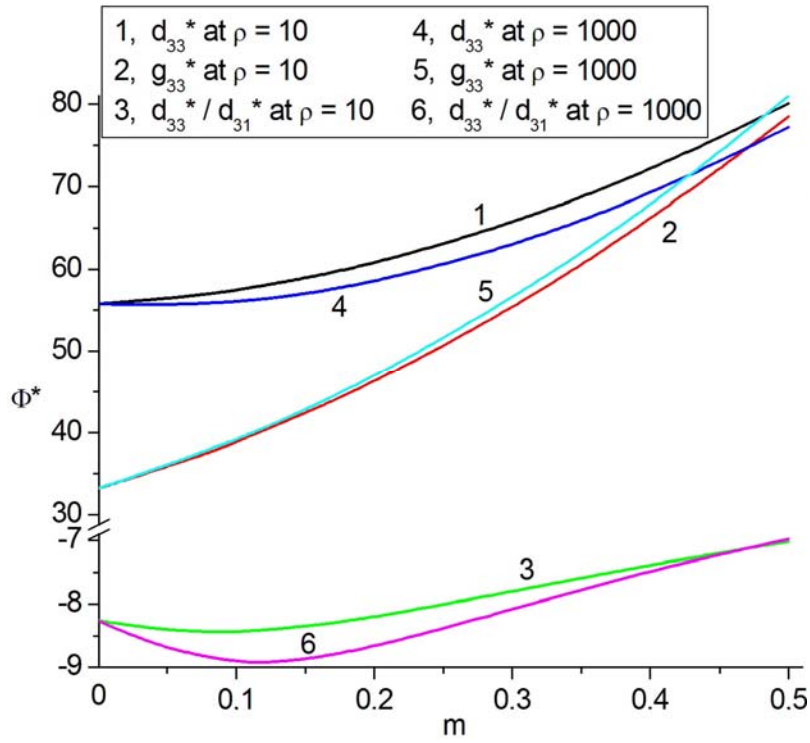

Figure 11. Volume-fraction dependence of effective piezoelectric coefficients d_{33}^* (in pC / N), g_{33}^* (in mV·m / N) and anisotropy d_{33}^* / d_{31}^* which have been calculated for the 0–3 single-domain $PbTiO_3$ SC / FC V composite with oblate spheroidal inclusions.

0–3 Ferroelectric Single Crystal / Ferroelectric Ceramic Composite and its Performance

The ferroelectric SC / FC composite is the novel piezo-active material that has attracted attention after research [41]. Smotrakov et al. [41] prepared samples of the ferroelectric SC / FC composite based on the perovskite-type solid solution of $(Pb_{1-x}Ca_x)TiO_3$ with $x \approx 0.24$ and studied microstructure of this composite. The 0–3 $0.71Pb(Ni_{1/3}Nb_{2/3})O_3–0.29PbTiO_3$ SC / $0.5Pb(Ni_{1/3}Nb_{2/3})O_3–0.15PbZrO_3–0.35PbTiO_3$ FC composite with perovskite-type relaxor-ferroelectric components and the regular arrangement of the SC inclusions was prepared and studied by Takahashi et al. [42]. First attempts to predict the effective electromechanical properties of the SC / FC composite were made on the basis of models of the 0–3 composite [21, 22] with isolated inclusions being either single-domain or polydomain. Examples of the performance of the 0–3 composite with the relaxor-ferroelectric SC inclusions surrounded by the FC matrix were described in paper [43]. In this section we consider an example of the 0–3 single-domain $PbTiO_3$ SC / FC V composite and its piezoelectric performance.

It is assumed that the 0–3 composite comprises the system of oblate spheroidal FC inclusions and they are distributed regularly in the FC matrix. The inclusions are single-

domain with the spontaneous polarisation vector $\boldsymbol{P}_s^{(1)} \uparrow\uparrow OX_3$, and the crystallographic axes of each inclusion are oriented along the co-ordinate axes shown in Figure 1. The FC medium surrounding the inclusions has the remanent polarization $\boldsymbol{P}_r^{(2)} \uparrow\uparrow OX_3$. To determine the effective electromechanical properties and other parameters of the composite, we apply the EFM (see Eq. (3)) and use the full sets of electromechanical constants of single-domain $PbTiO_3$ [6] and FC V [2] (see also data in Figs. 2 and 8). Now the volume fractions of SC (component 1 in terms of Figure 1) and FC (component 2 in terms of Figure 2) equal m and $1 - m$, respectively.

The studied 0–3 $PbTiO_3$-based composite exhibits the considerable stability of the piezoelectric properties with respect to changes in the aspect ratio ρ. For example, changes in ρ from 10 to 10^3 do not lead to appreciable changes in the piezoelectric coefficients of the composite $d_{3j}^*(m)$, $g_{3j}^*(m)$ and in the piezoelectric anisotropy $d_{33}^*(m) / d_{31}^*(m) = g_{33}^*(m) / g_{31}^*(m)$ (Figure 11). It can be accounted for by the presence of FC with the large piezoelectric anisotropy and by comparable values of electromechanical constants of the SC and FC components in the composite. Values of the piezoelectric coefficients d_{33}^* and g_{33}^* (see curves 1, 2, 4, and 5 in Figure 11) are comparable to those predicted in earlier papers [21, 22] for the related SC / FC composites.

CONCLUSION

This chapter has been devoted to the piezoelectric performance of modern composites based on perovskite ferroelectric $PbTiO_3$ or its solid solutions. Modelling and effective-property predictions have been carried out for the matrix α–3 composites with structures shown in Figs. 1 and 7. It should be noted that elements of the hierarchical chain 'single-domain SC of $PbTiO_3$ – polydomain SC of $PbTiO_3$ – poled FC of modified $PbTiO_3$' are attractive as components of the composites with the large piezoelectric anisotropy ($d_{33}^* / |d_{31}^*| >> 1$ and/or $e_{33}^* / |e_{31}^*| >> 1$), high piezoelectric sensitivity ($g_{33}^* \sim 10^2$ mV·m / N and $(Q_{33}^*)^2 \sim 10^{-11}$ Pa^{-1}), and considerable hydrostatic parameters ($g_h^* \sim 10^2$ mV·m / N and $(Q_h^*)^2 \sim 10^{-11}$ Pa^{-1}). This performance is attainable due to favourable relations between the electromechanical properties of the components and to the presence of the system of the prolate FC inclusions or long SC rods oriented along the poling axis. Contrary to this, the system of the oblate SC inclusions does not promote high piezoelectric sensitivity, as follows from data on the 0–3 single-domain $PbTiO_3$ SC / $PbTiO_3$-type FC composite.

The results discussed in this chapter can promote the selection of the proper SC and FC components for novel composites with high piezoelectric sensitivity, large piezoelectric anisotropy, considerable hydrostatic response, and other remarkable effective parameters. It is believed that the development of high-performance composites will be attractive for modern piezotechnical applications (sensors, hydrophones, transducers, etc.).

ACKNOWLEDGMENTS

The authors would like to thank Prof. Dr. A.V. Turik, Prof. Dr. A. E. Panich, Prof. Dr. I. A. Parinov, Dr. V.V. Eremkin, and Dr. V.G. Smotrakov (Southern Federal University, Russia), Prof. Dr. L.N. Korotkov (Voronezh State Technical University, Russia), Prof. Dr. R. Stevens and Dr. C.R. Bowen (University of Bath, UK), and Prof. Dr. P. Bisegna (University of Rome "Tor Vergata", Italy) for their continued interest in the research problems. This work was partially supported by the administration of the Southern Federal University (Project No. 11.1.09f on basic research), and the support is gratefully acknowledged.

REFERENCES

[1] Smolensky, G. A.; Bokov, V. A.; Isupov V. A.; Krainik, N. N.; Pasynkov, R. Ye.; Sokolov, A. I.; Yushin, N. K. *Physics of Ferroelectric Phenomena*; Nauka: Leningrad, 1985; 396 p (in Russian).

[2] Xu, Y. *Ferroelectric Materials and Their Applications*; North-Holland: Amsterdam, London, New York, NY, Toronto, 1991; 391 p.

[3] Cross, L. E. In *Piezoelectricity. Evolution and Future of a Technology;* Heywang. W.; Lubitz, K.;Wersing, W.; Eds.; *Springer Series in Materials Science* 114; Springer: Berlin, Heidelberg, 2008; pp 131–156.

[4] Fesenko, E. G.; Gavrilyatchenko, V. G.; Semenchev, A. F. *Domain Structure of Multiaxial Ferroelectric Crystals*; Rostov University Press: Rostov-on-Don, 1990; 192 p.

[5] Gavrilyatchenko, V.; Semenchev, A.; Fesenko, E. *Ferroelectrics* 1994, *158*, 31–35.

[6] Turik, A. V.; Topolov, V. Yu.; Aleshin, V. I. *J. Phys. D: Appl. Phys*. 2000, *33*, 738–743.

[7] Haertling, G. *J. Am. Ceram. Soc*. 1999, *82*, 797–818.

[8] Damjanovic, D. In *Piezoelectric and Acoustic Materials for Transducer Applications*; Safari, A.; Akdoğan, E. K.; Eds.; Springer: New York, NY, 2008; pp 59–79.

[9] Noheda, B. *Curr. Opinion i. Solid State a. Mater. Sci.* 2002, *6*, 27–34.

[10] Davis, M. *J. Electroceram*. 2007, *19*, 23–45.

[11] Wilson, S. A.; Maistros, G. M.; Whatmore, R. W. *J. Phys. D: Appl. Phys*. 2005, *38*, 175–182.

[12] Ritter, T.; Geng, X.; Shung, K. K.; Lopath, P. D.; Park, S.-E.; Shrout, T. R. *IEEE Trans. Ultrason., Ferroelec., a. Freq. Contr.* 2000, *47*, 792–800.

[13] Ren, K.; Liu, Y.; Geng, X.; Hofmann, H. F.; Zhang, Q. M. *IEEE Trans. Ultrason., Ferroelec., a. Freq. Contr.* 2006, *53*, 631–638.

[14] Wang, F.; He, C.; Tang, Y. *Mater. Chem. Phys*. 2007, *105*, 273–277.

[15] Glushanin, S. V.; Topolov, V. Yu.; Krivoruchko, A. V. *Mater. Chem. Phys*. 2006, *97*, 357–364.

[16] Topolov, V. Yu.; Bowen, C. R. *Electromechanical Properties in Composites Based on Ferroelectrics*; Springer: London, 2009; 202 p

[17] Topolov, V. Yu.; Bondarenko, E. I.; Turik, A. V.; Chernobabov, A. I. *Ferroelectrics* 1994, *152*, 237–242.
[18] Turik, A. V.; Topolov, V. Yu. *J. Phys. D: Appl. Phys*. 1997, *30*, 1541–1549.
[19] Topolov, V. Yu.; Turik, A. V.; Chernobabov, A. I. *Crystallogr. Repts* 1994, *39*, 805–809.
[20] Newnham, R. E.; Skinner, D. P.; Cross, L. E. *Mater. Res. Bull.* 1978, *13*, 525–536.
[21] Topolov, V. Yu.; Glushanin, S. V. *Tech. Phys. Lett.* 2002, *28,* 279–282.
[22] Glushanin, S. V.; Topolov, V. Yu., Turik, A. V. *Crystallogr. Repts.* 2003*, 48,* 491–499.
[23] Dunn, M. L.; Taya, M. *Internat. J. Solids Struct.* 1993, *30*, 161–175.
[24] Levin, V. M.; Rakovskaja, M. I.; Kreher, W. S. *Internat. J. Solids Struct*. 1999, *36*, 2683–2705.
[25] Fakri, N.; Azrar, L.; El Bakkali, L. *Internat. J. Solids Struct*. 2003, *40*, 361–384.
[26] Mori, T.; Tanaka, K. *Acta Metall*. 1973, *21*, 571–574.
[27] Eshelby, J. D. *Proc. Roy. Soc. (London)* 1957, *A241*, 376–396.
[28] Huang, J. H.; Yu, S. *Compos. Engin*. 1994, *4*, 1169–1182.
[29] Ikeda, T. *Fundamentals of Piezoelectricity*; Oxford University Press: Oxford, New York, NY, Toronto, 1990; p 17.
[30] Ikegami, S.; Ueda, I.; Nagata, T. *J. Acoust. Soc. Am*. 1971, *50*, 1060–1066.
[31] Nagatsuma, K.; Ito, Y.; Jyomura, S.; Takeuchi, H.; Ashida, S. In *Ferroelectricity and Related Phenomena. V. 4: Piezoelectricity*; Taylor, G. W.; Ed.; Gordon and Breach Sci. Publ.: New York, NY, London, Paris, Montreux, Tokyo, 1985; pp 167–176.
[32] Cao, W.; Zhang, Q. M.; Cross, L. E. *IEEE Trans. Ultrason., Ferroelec., a. Freq. Contr*. 1993, *40*, 103–109.
[33] Topolov, V. Yu.; Bisegna, P.; Krivoruchko, A. V. *J. Phys. D: Appl. Phys*. 2008, *41*, 035406–8 p.
[34] Yin, J.; Jiang, B.; Cao, W. *IEEE Trans. Ultrason., Ferroelec., a. Freq. Contr.* 2000, *47*, 285–291.
[35] Sessler, G. M. *J. Acoust. Soc. Am*. 1981, *70*, 1596–1608.
[36] Kar-Gupta, R.; Venkatesh, T.A. *J. Appl. Phys*. 2008, *104*, 024105–17 p.
[37] Topolov, V. Yu.; Krivoruchko, A. V.; Bisegna, P.; Bowen, C. R. *Ferroelectrics* 2008, *376*, 140–152.
[38] Zhang, R.; Jiang, B.; Cao, W. *J. Appl. Phys*. 2001, *90*, 3471–3475.
[39] Cao, H.; Schmidt, V. H.; Zhang, R.; Cao, W.; Luo, H. *J. Appl. Phys*. 2004, *96*, 549–554.
[40] Bezus, S.V.; Topolov, V.Yu.; Bowen, C.R. *J. Phys. D: Appl. Phys*. 2006, *39*, 1919–1925.
[41] Smotrakov, V. G.; Eremkin, V. V.; Aleshin, V. A.; Tsikhotsky, E. S. *Izv. RAN. Ser. Fiz*. 2000, *64*, 1220–1223 (in Russian).
[42] Takahashi, H.; Tukamoto, S.; Qiu, J.; Tani, J.; Sukigara, T. *Jpn. J. Appl. Phys. Pt. 1* 2003, *42*, 6055–6058.
[43] Topolov, V. Yu.; Kamlah, M. *J. Phys. D: Appl. Phys*. 2004, *37*, 1576–1585.

In: Perovskites: Structure, Properties and Uses
Editor: Maxim Borowski, pp. 501-254
ISBN 978-1-61668-525-6

Chapter 13

DOUBLE PEROVSKITES WITH STRUCTURE-DISORDERED OXYGEN SUBLATTICE AS HIGH-TEMPERATURE PROTON CONDUCTORS

I. Animitsa*
The Ural State University, av. Lenin 51, Ekaterinburg 620083, Russia

INTRODUCTION

Materials with high proton or oxide ion conductivity are widely studied for their potential application as electrolytes in fuel cells, electrolysers, batteries, sensors, etc. [1-5]. *Acceptor doped* perovskite-type oxides $ABO_{3-\delta}$ where A is Sr, Ba and B is Ce, Zr are well-known high temperature proton conductors in wet atmosphere. It was found that the main factor responsible for the appearance of protons in the structure was the presence of oxygen vacancies. Upon hydration by equilibration with water vapor the oxygen vacancies may be filled by oxygen from water and, in accordance with dissociative mechanism of water dissolution, the hydroxide ions are formed. In this case the dissolution of water may be written [6]:

$$H_2O_{(g)} + O_o + V_o \Leftrightarrow 2OH_o \quad (1)$$

In late 1990s it was shown that the proton transport can be also realized in perovskite-related compounds with *structural oxygen vacancies*. The niobates and tantalates of alkaline-earth metals of a general formula $A_4(B_2B'_2)O_{11}[V_{\boldsymbol{O}}^{\boldsymbol{S}}]_1$ are an examples of such structures. These phases can uptake a significant quantity of water and show a dominant proton transport below 500-600°C. In this work we summarized a principal relationships of the proton transfer and hydration processes for this novel class of high-temperature proton conductors.

* E-mail: irina.animitsa@usu.ru

STRUCTURE

Because of the high tolerance of the perovskite structure ABO_3, both A- and B-sublattices can adopt cations with different oxidation state and size, therefore numerous members of this family may form a various types of superstructures.

The structure of double perovskites is characterized by alternate nonequidimensional octahedrons containing cations in different oxidation states; at that the B-sublattice is partitioned into two sublattices (B and B′) and the edges are doubled as compared with the initial perovskite structure. For example, the elpasolite structure (named after the mineral $K_2[NaAlF_6]$) with general composition $A_2BB'O_6$ has predominantly ordered arrangement of cations in the B-sublattice (the ratio 1:1 provides the *staggered* ordering of a small $[BO_6]$ and big $[B'O_6]$ octahedra , Figure 1); when A and B′ are identical atoms we come to the cryolite structure $A_2(AB)O_6$. The cryolite structure (named after the mineral $Na_2[NaAlF_6]$) may be considered as an ordered perovskite too. A statistical distribution of two sorts of B-cations leads to the perovskite structure. The idealized cryolite/ elpasolite structure is the cubic system in space group *Fm3m* and contains four formula units per unit cell. In this structure the 8c crystallographic sites are occupied by larger cations (A-sublattice), B and B′-ions occupy two crystallographically nonequivalent positions: 4a and 4b. Oxygen anions (or F^-) occupy 24e sites.

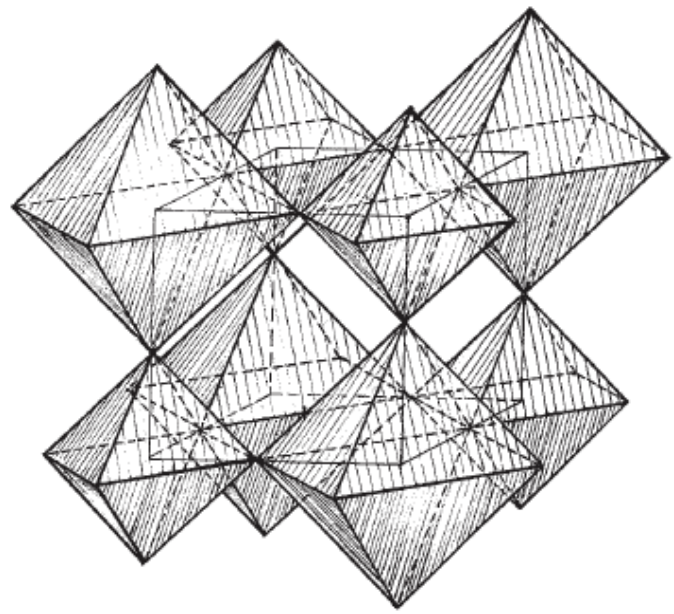

Figure 1. The structure of double perovskite (elpasolite/ cryolite).

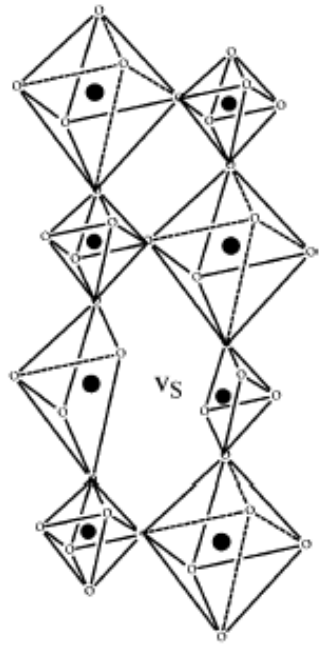

Figure 2. Hypothetical perovskite-related structure with structural oxygen vacancies [7].

At a proper combinations of oxidation states of atoms in B-sublattices (for the given A-cation) an *oxygen deficient* structures can be exist. The most oxygen-deficient composition (among double perovskites) corresponds to the general formula $A_2BB'O_{5.5}$ or $A_4B_2B'_2O_{11}$, where if A is nominally +2 cation, then B and B′ cations may have the charge combinations (1 + 6), (2 + 5) and (3 + 4). In general, such ordered perovskites (cryolite/ elpasolite) have a twice cubic perovskite unit cell, implying that oxygen vacancies are random. Thus, 22 oxygen atoms are distributed over 24e sites, i.e. 8.33% of oxygen sites remains unoccupied (Figure 2. [7]). These oxygen vacancies are inherent defects of the structure and do not require charge compensation. When the oxygen vacancies are formed, the metal atoms are shifted and simultaneously the coordination number of metal is lowered. The octahedrons are transformed to tetrahedrons or tetrahedral pyramids; therefore, the formation of such phases is possible when the atoms in the B-sublattice can have different coordination with respect to oxygen. A typical members of this family are $Me_6^{+2}M_2^{+5}O_{11}$, where Me^{+2} -represents an alkaline-earth metal and M^{+5}-niobium or tantalum.

The niobates and tantalates are the most widely studied as oxide-ion and proton conductors. The examples are $Sr_6Nb_2O_{11}$ [8, 20], $Sr_6Ta_2O_{11}$ [9-13], $Ba_4Ca_2Nb_2O_{11}$ [14-19] , $Ba_4Ca_2Ta_2O_{11}$ [21]. The homogeneity regions are described too: $Sr_{6-2x}Nb_{2+2x}O_{11+3x}$ [8,], $Sr_{6-2x}Ta_{2+2x}O_{11+3x}$ ($0 \le x \le 0.33$) [9-10], $(Ba_{1-y}Ca_y)_6Nb_2O_{11}$ ($0.23 \le y \le 0.47$) [16-18] . The homogeneity range of $Sr_{6-2x}Nb_{2+2x}O_{11+3x}$ is markedly dependent on the temperature, and the composition $Sr_6Nb_2O_{11}$ does not include in homogeneity range below 800°C (two-phase region with SrO-impurity) [22]. Other compositions are stable in wide range of the temperatures, pO_2 and pH_2O.

Such structure can provide predominant oxygen ion transport at high temperatures and proton transport at low temperatures and in wet atmospheres. The presence of coordination-unsaturated polyhedrons makes possible the water dissociative insertion from gas phase.

Upon hydration (by equilibration with water vapor) the oxygen vacancies may be filled by the oxygen from the water molecule. When the oxygen vacancies are completely occupied, the achievement of the theoretically possible hydration limit (50 mol % H_2O per formula unit $A_4B_2B_2'O_{11}$) becomes possible.

Other structural analogues with two octahedral sublattices are also known. For example, for charge combination of B-cations (1+6). The structure of the compositions $A_4^{+2}(B^{+1}B^{+6})_2O_{11}$ (A^{+2}=Sr, Ba, B^{+1}=Li, Na, B^{+6}=Mo, W) was described in [23,24].

WATER INCORPORATION IN OXYGEN-DEFICIENT NIOBATES AND TANTALATES OF ALKALINE-EARTH METALS

The presence of oxygen–hydrogen groups in the solids can be detected by thermogravimetry method. Upon heating these groups are decomposed and evacuated from the complex oxide as a water molecules. Therefore, the number of moles of water per one formula unit of the compound can be estimated. The notation of the total composition as $ABO_3 \cdot nH_2O$ is formal, but convenient for comparing.

The phases $Sr_6Nb_2O_{11}$, $Sr_6Ta_2O_{11}$, $Ba_4Ca_2Nb_2O_{11}$, $Ba_4Ca_2Ta_2O_{11}$ as well as solid solutions $Sr_{6-2x}Nb_{2+2x}O_{11+3x}$ (I), $Sr_{6-2x}Ta_{2+2x}O_{11+3x}$ (II), $(Ba_{1-x}Ca_x)_6Nb_2O_{11}$ (III) have been studied. In the systems (I) and (II) within of their homogeneity range the oxygen vacancies concentration changes, while in the system (III) the oxygen deficiency level does not change: it remains maximally high for the given cation-charge combinations. It follows from the thermogravimetry data that during the heating–cooling treatment in wet oxygen or argon (pH_2O = 0.02 atm) the samples of the composition $Sr_{6-2x}Nb_{2+2x}O_{11+3x}$, $Sr_{6-2x}Ta_{2+2x}O_{11+3x}$, and $(Ba_{1-x}Ca_x)_6Nb_2O_{11}$ show a reversible mass change. Thus observed effects were explained by the removal (during the heating) or insertion (during the cooling) of water in the structure and corroborated by thermal desorption and mass-spectrometry measurements. Figure 3. demonstrates thermogravimetry data for solid solution $Sr_{6-2x}Ta_{2+2x}O_{11+3x}$ [9,10]. Water is removed in two stages, that reflects the presence of nonequivalent oxygen–hydrogen groups. The correlation between water uptake and the number of vacant oxygen sites was established (Figure 4) : the water uptake in the composition range $Sr_{6-2x}Ta_{2+2x}O_{11+3x}$ increases with increasing oxygen vacancy concentration, and the highest reversible water uptake, close to the theoretical hydration limit, was found for the composition $Sr_6Ta_2O_{11}$ [10]. Similar trend was observed for solid solution $Sr_{6-2x}Nb_{2+2x}O_{11+3x}$ [8]. The general view of TG-curves for other compositions, such as $Ba_4Ca_2Nb_2O_{11}$ [16], $Ba_4Ca_2Ta_2O_{11}$ [21], is the same.

So, the phases with nominally high contents of vacant oxygen sites and the same high proton concentration are more interesting for detailed studies.

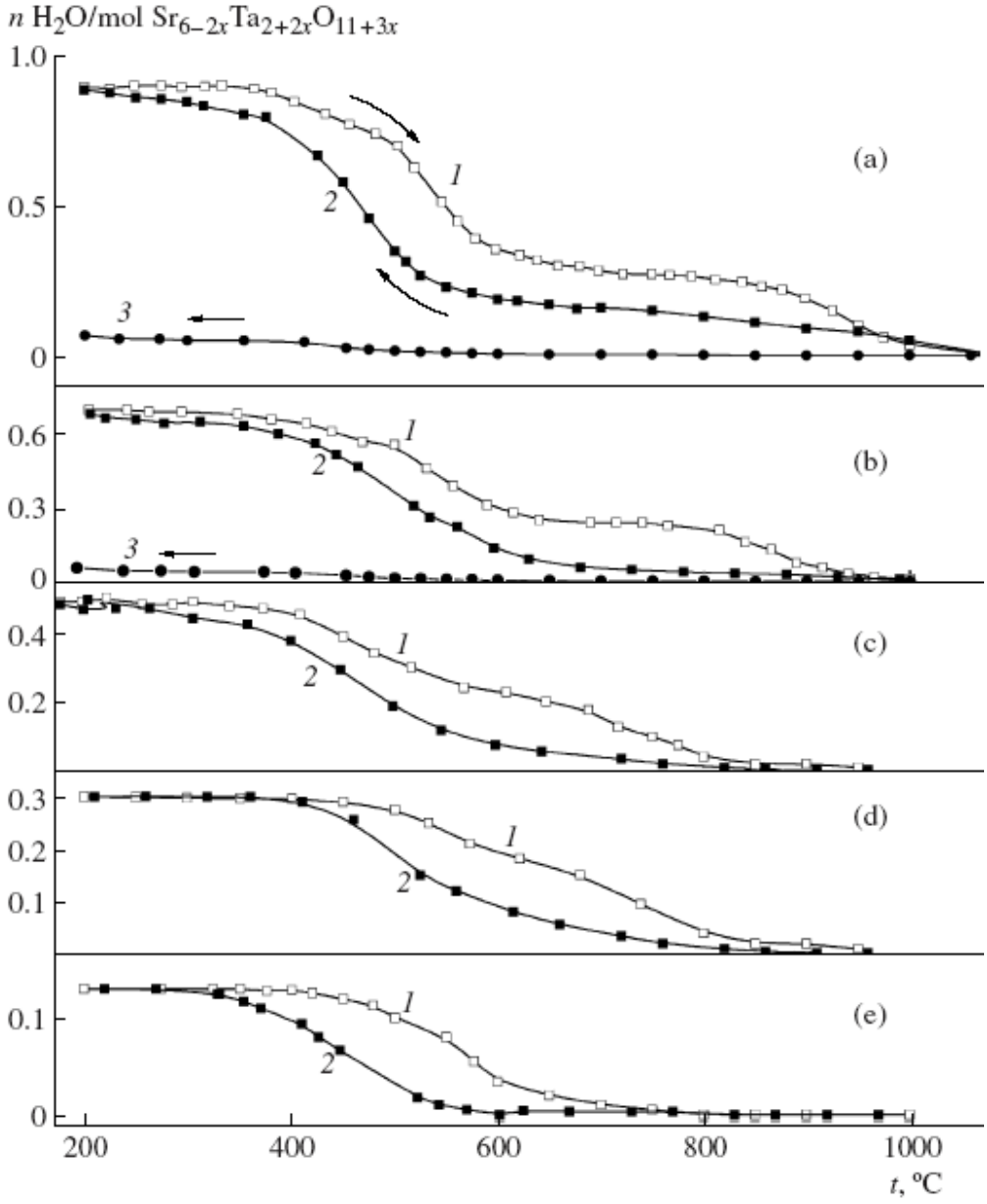

Figure 3. Thermogravimetric data for solid solution $Sr_{6-2x}Ta_{2+2x}O_{11+3x}$: (a) x= 0 , (b) x= 0.04, (c) x= 0.10, (d) x=0.15, (e) x=0.23; (*1*) heating, (*2*) cooling in wet atmosphere ($pH_2O = 2 \cdot 10^{-2}$ atm), (*3*) cooling in dry atmosphere ($pH_2O = 3 \cdot 10^{-5}$ atm) after the first stage of heating [10].

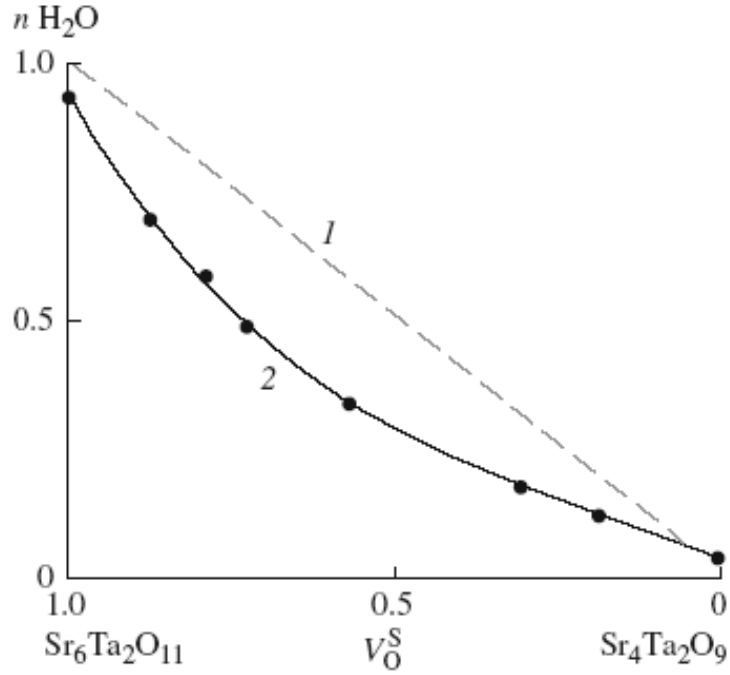

Figure 4. Dependence of water uptake vs. oxygen vacancies concentration in $Sr_{6-2x}Ta_{2+2x}O_{11+3x}$ (200°C, $pH_2O = 2 \cdot 10^{-2}$atm), (1) theoretical and (2) experimental dependencies [10].

The measurement of some properties at constant temperature as a function of pH_2O gives a better understanding of the behaviour of proton incorporation. In terms of quasichemical formalism, the process of water insertion can be represented by the following equation:

$$V_o^{\times} + H_2O + 2O_o^{\times} \Leftrightarrow O_{V_o}^{''} + 2(OH)_o^{\bullet} \qquad (2)$$

where $V_o^{\times}$ – is the oxygen structural vacancy, $O_o^{\times}$ – is the oxygen in its regular position, $O_{Vo}^{''}$ – is the oxygen in the position of the oxygen structural vacancy, and $(OH)_o^{\bullet}$ – is the hydroxo-group in the oxygen sublattice. In terms of the quasichemical approach the oxygen structural vacancies can be formally interpreted as ionized defects because the exchange between the lattice oxygen and the oxygen structural vacancies exists*:* $V_o^{\times} + O_o^{\times} \Leftrightarrow O_{Vo}^{''} + V_o^{\bullet\bullet}$. By applying the active mass law to equation (2) and bearing in mind the electroneutrality $[OH^{\bullet}_{O}] = 2[O^{''}_{Vo}]$, it was found that the proton concentration is proportional to $pH_2O^{1/3}$ [11]. Therefore, the dependence of $\log C_H = f(\log pH_2O)$ must be linear with a slope of 1/3, where C_H is the bulk concentration of protons. Thus, the apparent 1/3 slope in the double logarithmic plot of C_H vs pH_2O may represent dominance of protons. If oxygen vacancies dominate, for minority concentrations of protons it was obtained the commonly observed $[OH^{\bullet}_{O}] \sim K p(H_2O)^{1/2}$ dependency. When all vacancies are filled up, the uptake of water and concentration of protons will have to saturate and become independent of $p(H_2O)$. The description of the defect concentrations vs. pH_2O was given in work [18] too.

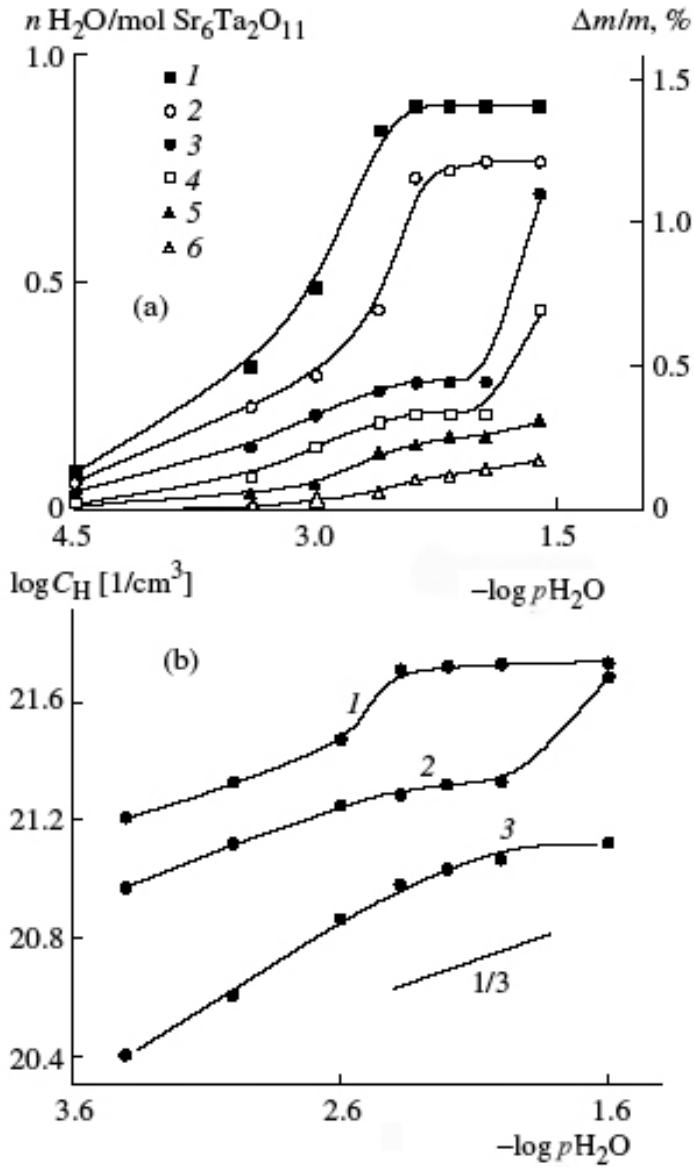

Figure 5. Dependence of (a) relative mass change and water uptake and (b) proton concentration in $Sr_6Ta_2O_{11}$ vs. the water vapor pressure at temperature (°C) of: (a) (*1*) 300, (*2*) 400, (*3*) 450, (*4*) 475, (*5*) 500, (*6*) 550; (b) (*1*) 400, (*2*) 450, (*3*) 500 [12, 19].

Figure 5. shows the dependences of the water uptake and proton concentration vs. the water vapor pressure for composition $Sr_6Ta_2O_{11}$ [12, 19]. The general view of the dependencies agrees well with the expected one: over a certain range, the proton concentration is proportional to $p(H_2O)^{1/3}$. However, at a high pH_2O values, that is, when proton concentrations are significant, the dependences show a sharp increase. This behaviour reflects a change in crystal structure as a result of water incorporation. The plateau on the thermogravimetry curves corresponds to approximately complete filling of the oxygen

vacancies by the oxygen from water molecules, and the concentration of protons will have to saturate and become independent of pH_2O.

X-ray diffraction measurements confirm that incorporation of H_2O up to ~0.50 mol H_2O per formula units $Sr_6Ta_2O_{11}$ takes place without change of the crystal structure, which could be described under the cubic space group *Fm3m* with a cell parameters of approximately 8.32 Å. Further incorporation of water leads to structure transformation to the orthorhombic space group *Fmmm*. The temperature of phase transition increases with increasing pH_2O. It is around 475–450°C at the humidity of surrounding atmosphere (pH_2O=0.02 atm) [12].

This phase transition is induced by pH_2O (T = const) and temperature (pH_2O= const) and can be observed as a jump on gravimetry curves vs. pH_2O or T. At 200°C, the most hydrated phases correspond to the compositions $Sr_6Ta_2O_{11}\cdot 0.96H_2O$ (close to the theoretical value of 1.0). The hydrated sample with the composition approaching the limiting one $Sr_6Ta_2O_{10}(OH)_2$ had the following crystal lattice parameters: a = 0.8223(6) nm, b = 0.8317(2) nm, and c = 0.8365(9) nm; $\alpha = \beta = \gamma = 90°$ [12].

A fragment of $Sr_6Ta_2O_{11}$– $Sr_6Ta_2O_{11}\cdot H_2O$ phase diagram is proposed (wet conditions pH_2O=0.02 atm), Figure 6. [12, 25]. The results may be summarized as follows.

(i) At temperatures higher than 1000°C, ‘‘dry’’ double oxide $Sr_6Ta_2O_{11}$ with cubic structure exists.
(ii) Over the temperature range of 500–1000 °C, intercalation of water with formation of a solid solution $Sr_6Ta_2O_{11}\cdot mH_2O$ takes place. The quantity of intercalated water depends on the temperature and reaches $m \approx 0.5$ mol (the line *di* in the diagram corresponds to equilibrium of solid solution of $Sr_6Ta_2O_{11}\cdot mH_2O$ with water vapor). This process occurs without serious structure reconstruction and, evidently, such dissolution may be described in the frame of commonly used quasi-chemical approach, where water is regarded as an impurity.
(iii) Further water incorporation at T≤500 °C results in change in crystal structure and formation of a new hydrated compound —the hydroxo-phase $Sr_6Ta_2O_{10-n}(OH)_{2n}$ ($n \leq 1$) with orthorhombic symmetry. The quantity of intercalated water increases when the temperature decreases and it indicates that this compound has a homogeneity range. In the phase diagram the peritectoid line *ic* corresponds to the compound decomposition, where three phases are in equilibrium: two solids and water vapor. The point *c* is the peritectic point in which one solid phase transforms into another.

However, by contrast to this, the hydration of the nominal composition $Sr_6Nb_2O_{11}$ (not included in homogeneity range of $Sr_{6-2x}Nb_{2+2x}O_{11+3x}$) is accompanied by the formation of the secondary phase $Sr(OH)_2$ [20].

For solid solution $(Ba_{1-y}Ca_y)_6Nb_2O_{11}$ the thermogravimetric studies carried out in wet argon or oxygen atmosphere showed that the water uptake is nearly the same: 0.85–0.95 mole, which approached the theoretical hydration limit [16,17]. The thermogravimetric measurements confirm that the dependences $\log C_H = f(\log pH_2O)$ are linear, with a slope of 1/3 (Figure 7. represents limited ranges of the dependences without phase transformations [16]).

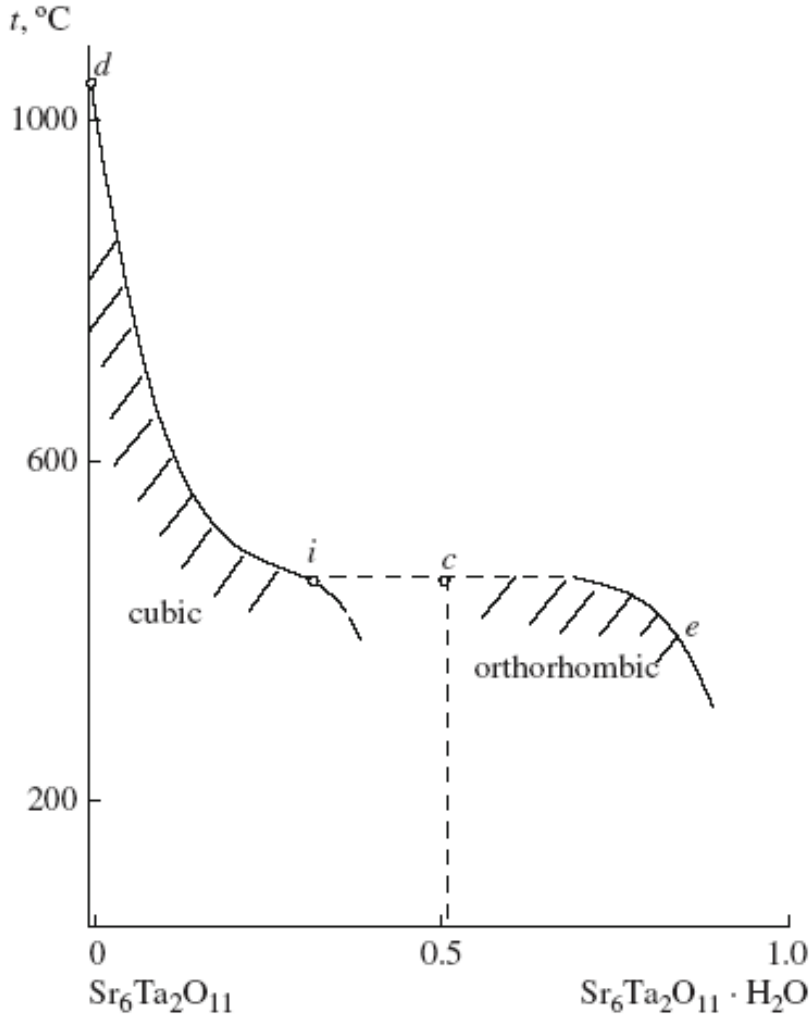

Figure 6. Quasibinary phase diagram of $Sr_6Ta_2O_{11}$ –$Sr_6Ta_2O_{11}{\cdot}H_2O$, pH_2O = 0.02 atm [12].

It was shown by X-ray diffraction analysis that in the row of solid solution $(Ba_{1-x}Ca_x)_6Nb_2O_{11}$ only one composition $Ba_4Ca_2Nb_2O_{11}$ (x= 0.33) changed its initial cubic symmetry upon hydration. During the process of water incorporation the compound $Ba_4Ca_2Nb_2O_{11}$ undergoes structural changes due to formation of a hydroxo-phase of approximate composition $Ba_4Ca_2Nb_2O_{10}(OH)_2$ with a lower, monoclinic symmetry (the space group $C2/m$) [14, 16]. The composition $Ba_4Ca_2Nb_2O_{11}$ is characterized by equal number (1:1) of calcium and niobium cations in the B-sublattice. Under such chequer-wise alternation of the large and small octahedrons, the crystal lattice energy appears being lower than for the phases without long range ordering in the cation sublattice. Obviously, any displacement of the cations in the 1:1 ordered phases, e.g., during the water insertion, results in macroscopically evident lattice distortion that is detected by the X-ray diffraction analysis.

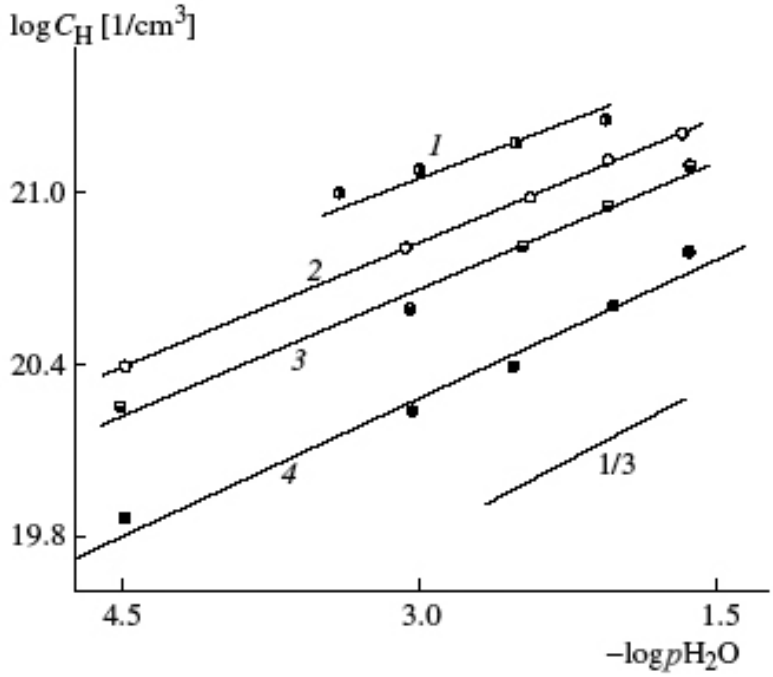

Figure 7. Dependence of proton concentration in a $Ba_4Ca_2Nb_2O_{11}$ on the water vapor pressure at a temperature (°C) of: (*1*) 300, (*2*) 350, (*3*) 400, (*4*) 500 [16].

STATES OF H^+-CONTAINING SPECIES IN HYDRATED NIOBATES AND TANTALATES OF ALKALINE-EARTH METALS WITH A PEROVSKITE-RELATED STRUCTURE

The oxygen–hydrogen groups can be identified by using the IR-spectroscopy and proton magnetic resonance (^{1}H NMR) methods. Generally, OH_n- groups can exist in solid inorganic materials as OH^-, H_2O or H_3O^+ groups.

IR-spectra of hydrated niobates and tantalates of alkaline-earth metals confirm the presence of the oxygen–hydrogen groups: the IR spectra for all studied phases contain a broad band at ~3500 cm^{-1} (absorption at 2800–3700 cm^{-1} should be assigned to stretching vibrations of oxygen-hydrogen groups).

However, in the stretching vibration region it is impossible to separate the bands related to vibrations in different types of the oxygen–hydrogen groups. Therefore, of interest is the studying of deformation vibrations. It is known that the frequency of deformation vibrations of isolated water molecule equals 1595 cm^{-1}. Association of the H_2O molecules (in particular, for reason of hydrogen bonds) results in the shift of the band to region 1600–1680 cm^{-1}. The hydroxonium ion H_3O^+ absorbs at higher frequencies (1680–1800 cm^{-1}); the hydroxo- group OH^- (δ MOH) absorbs below 1500 cm^{-1}. The number of components in the spectrum, as a rule, corresponds to the number of different types of the oxygen–hydrogen groups.

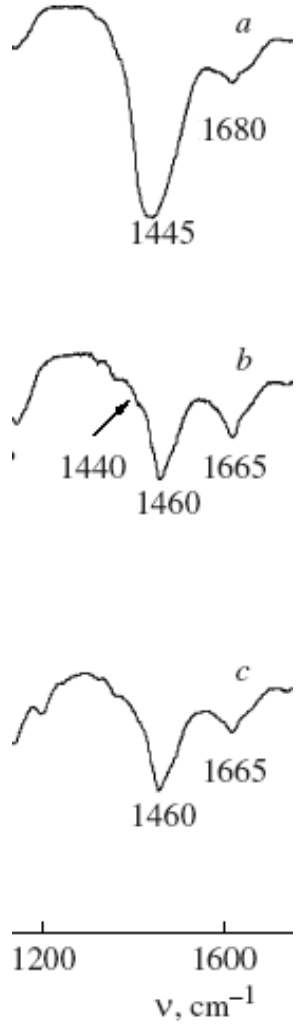

Figure 8. IR-spectra of hydrated niobates and tantalates of alkaline-earth metals: (*a*) $Ba_4Ca_2Nb_2O_{11}$, (*b*) $Sr_{5.92}Ta_{2.08}O_{11.12}$, (*c*) $Sr_6Ta_2O_{11}$ [7].

Figure 8. shows IR-spectra of hydrated niobates and tantalates of alkaline-earth metals. In all spectra we can distinguish a very intense band at ~1450 cm^{-1}, which can be related to the OH^- group vibrations, moreover, this band is a superposition of several contributions. It was shown [7, 13] that the IR band at ~1450 cm^{-1} can be correlated with the water uptake and is not observed for compounds without water uptake. The band at ~1650 cm^{-1} disappears after heating at 100°C and this indicates that this band corresponds to absorbed water.

To identify the OH_n -groups, the wide-line ^{1}H-NMR method was used too (the samples were hydrated down to 200 °C in order to eliminate the presence of absorbed water). Figure 9. presents ^{1}H-NMR spectra recorded at -150 °C for some samples. The spectra were complex and represented a superposition of several components caused by the presence of different oxygen–hydrogen groups [13]. Three components may be distinguished in a general case.

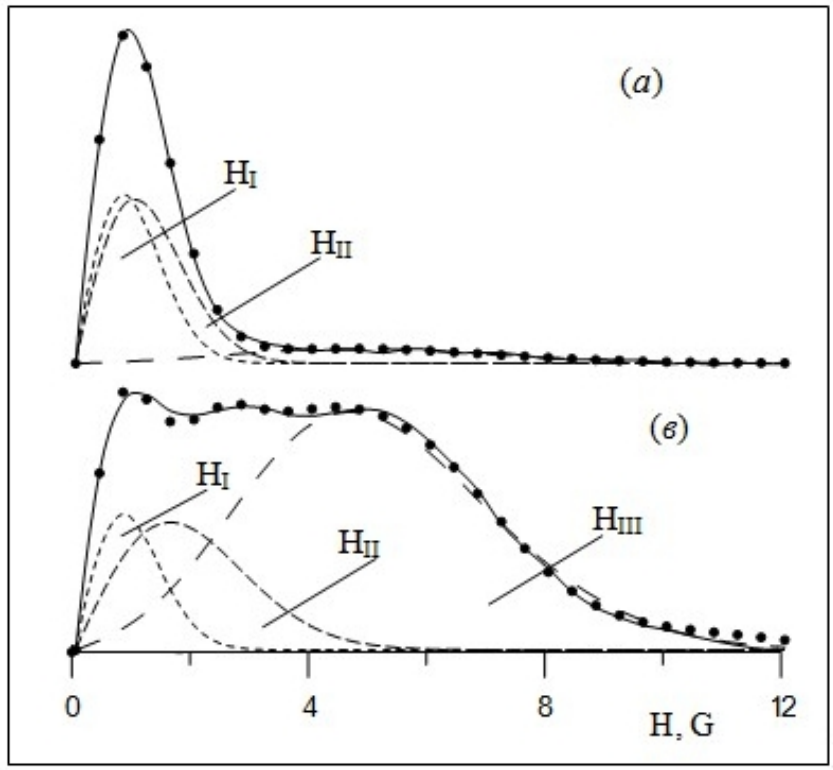

Figure 9. ^{1}H NMR-spectra for hydrated samples with the composition: (*a)* $Sr_6Ta_2O_{11}$, (*b*) $Ba_4Ca_2Nb_2O_{11}$ (–150°C). Points: experimental spectrum, line: model spectrum [13].

(i) The narrow signal (defined as H_I) can be described as a Gaussian with a broadening parameter ΔH_I = 0.4–0.8 G. It represents isolated OH^- groups with an inter-proton distance $R_{H–H}$ = 3.0–3.5 Å .

(ii) The Gaussian line with the parameter Δ H_{II} = 1.5–2.0 G (H_{II}) is due to closely spaced OH^- groups. The distance between the protons is $R_{H–H}$ = 2.2–2.4 Å. They are connected probably with the same metal atom and belong to the same edge of an octahedron, for example:

$$M\begin{matrix}\mathbf{OH}\\ \mathbf{OH}\end{matrix}$$

(iii) A broad signal at ΔH_{III} =4.5–5.5 G (defined as H_{III}) is modeled as a two-spin system (when the interaction of two nearest neighbors dominates). However, it cannot be related to water molecules. The distance between protons was estimated at 2.0 Å, which is much larger than the normal distance between water protons in crystals of 1.52–1.65 Å. This signal may be caused by the appearance of close-spaced OH^- groups in a structural element of the coordination-unsaturated polyhedrons, shown in Figure 10 [13]. Probably, such strong interaction of protons in OH^- groups reflects an intermediate state HO…HO → O … H…OH.

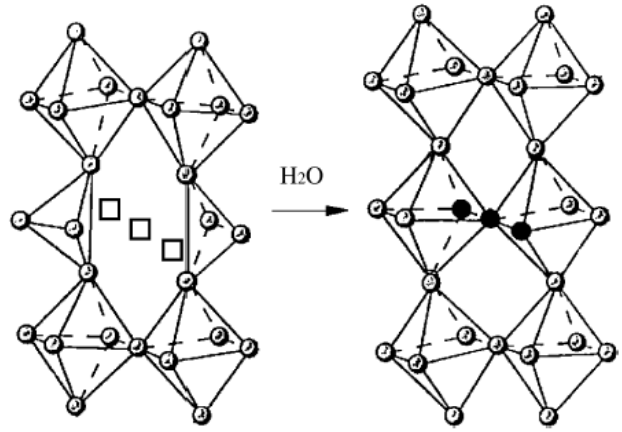

Figure 10. Scheme of formation of close-spaced OH^- groups. (□) oxygen vacancy; (●) hydroxyl [13].

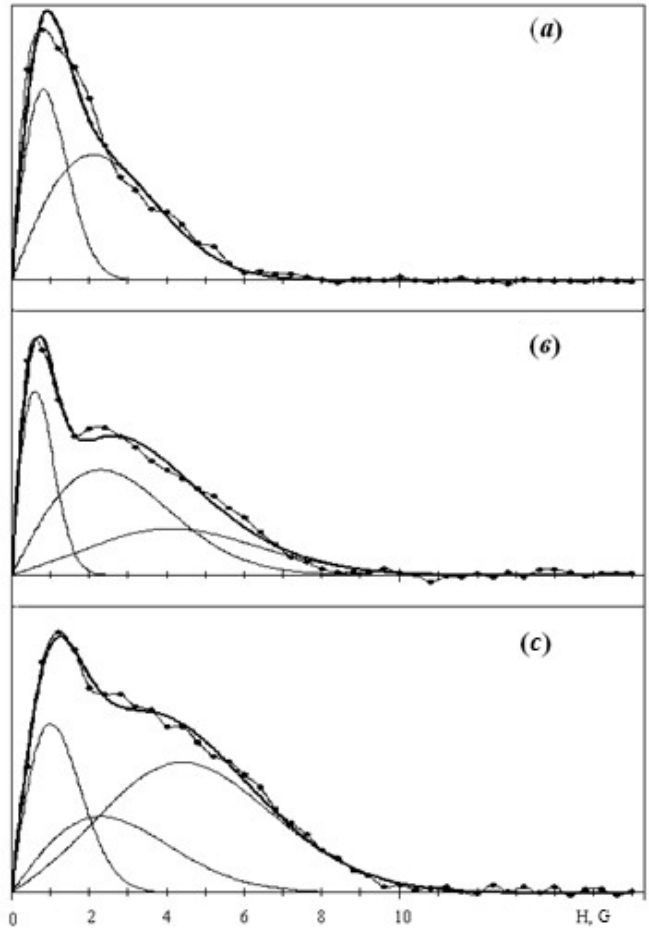

Figure 11. ^{1}H-NMR spectra recorded at -150 ^{o}C for $Ba_4Ca_2Nb_2O_{11}$ with different water uptake. (a) $Ba_4Ca_2Nb_2O_{11}\cdot 0.15H_2O$; (b) $Ba_4Ca_2Nb_2O_{11}\cdot 0.25H_2O$; (c) $Ba_4Ca_2Nb_2O_{11}\cdot 0.80H_2O$ [13].

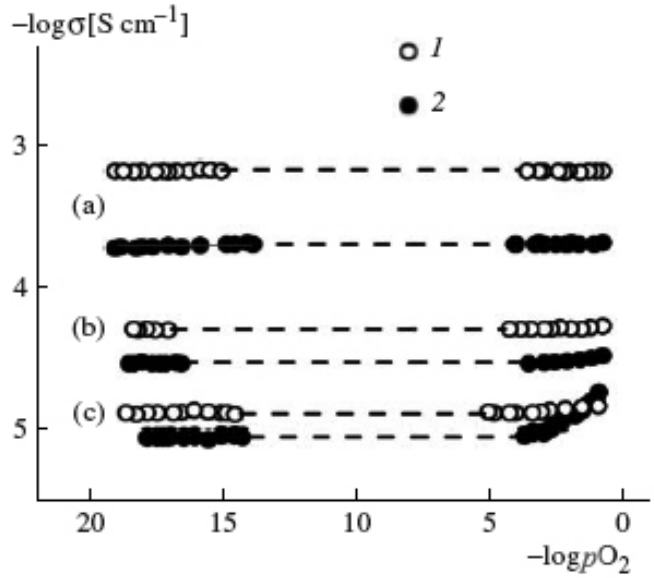

Figure 12. Dependence of total conductivity of solid solutions $Sr_{6-2x}Ta_{2+2x}O_{11+3x}$ vs. the oxygen partial pressure in (***1***) wet atmosphere ($pH_2O = 2 \cdot 10^{-2}$ atm) and (***2***) dry atmosphere ($pH_2O = 3 \cdot 10^{-5}$ atm) at (a) $x = 0$, (b) $x = 0.15$, (c) $x = 0.23$, $T = 600$°C [19].

An ^{1}H-NMR analysis of partially hydrated sample $Ba_4Ca_2Nb_2O_{11}$ containing 0.15 and 0.25 mol water was performed in order to determine the distribution of proton sites depending on the concentration of intercalated water (Figure 11., [13]). Separation of the NMR spectra into components allows to estimate the quantitative ratios of protons in each component of a spectrum. The results are given in Table 1. The following conclusions may be drawn:

- the fraction of protons in isolated OH^- groups (the H_I line) was a maximum in $Sr_6Ta_2O_{11}$;
- in the niobates (independently of the nature of alkaline-earth metals), most of the protons were present as closely spaced OH^- groups (the H_{II} line) and protons, which were defined as H_{III}.
- the fraction of protons of the H_{III} component diminishes with decreasing degree of hydration, i.e. the larger the degree of hydration, the more probable the appearance of closely spaced OH^- groups.

The difference between tantalates and niobates is due probably to different coordination tendencies of Ta and Nb. Since all phases have an oxygen vacancies, the structure must contain polyhedra with coordination number less than 6. Ta^{+5} favors a square–pyramidal coordination [TaO_5] rather than a tetrahedral coordination, whereas a tetrahedral coordination for Nb^{+5} is more common. In the case of full hydration (i.e. if water molecules occupy all oxygen vacancies), an initial tetrahedron is restored to an octahedron in accordance with appearance of the structural element [$NbO_4(OH)_2$], in which two OH^- groups belonging to the same metal atom are formed. The formation of an octahedron from a pyramidal coordination is accompanied probably by appearance of [$TaO_5(OH)$], leading to formation of isolated OH^- groups.

Table 1. The ratios of protons in each component of ^{1}H NMR spectrum [13]

Composition	H_I	H_{II}	H_{III}
$Sr_6Ta_2O_{11}\cdot 1.0\ H_2O$	0.23	0.23	0.54
$Ba_4Ca_2Nb_2O_{11}\cdot 0.95H_2O$	0.01	0.17	0.82
$Ba_4Ca_2Nb_2O_{11}\cdot 0.80H_2O$	0.07	0.23	0.70
$Ba_4Ca_2Nb_2O_{11}\cdot 0.25H_2O$	0.10	0.50	0.40
$Ba_4Ca_2Nb_2O_{11}\cdot 0.15H_2O$	0.20	0.80	-

Comparing the TG and ^{1}H-NMR data, it is possible to propose a dehydration scheme, because, the ratio of crystallographically (and, consequently, energetically) nonequivalent protons changes with temperature. During heating the hydrated sample, the beginning of an intensive weight loss corresponds to removal most of closely spaced protons. This process takes place in a relatively narrow temperature interval and is reflected in TG curves as a well-resolved step. As the sample is heated further, the dehydration deals with the removal of relatively isolated hydroxyl groups. This dehydration process is characterized by a continuous decrease in the weight over a relatively wide temperature interval (up to 800 ^{o}C).

Electrical Properties

By the studying of the total conductivity of the solid solution $Sr_{6-2x}Ta_{2+2x}O_{11+3x}$ under the *varying oxygen partial pressure* pO_2 (wet and dry conditions) the general relationships were shown. Figure 12. demonstrates the evolution of the conductivity isotherms [19, 26]. For the compositions with high concentration of oxygen vacancies $0<x\leq 0.20$ (that is, with high conductivity) the effect of humidity is most pronounced over a wide rang of pO_2 . The total conductivity of these samples was found to be independent of the oxygen partial pressure for all investigated temperatures. This indicates that the electronic component of the conductivity is negligible. Some contribution of the p-type electronic conductivity was observed for compositions $x>0.20$ at high oxygen partial pressure (dry atmosphere), in this case the equation may be written:

$$V_o^{\times} + 1/2O_2 \Leftrightarrow 2h^{\bullet} + O''_{V_O} \tag{3}$$

In wet atmosphere the hole concentration decreases as a result of the shift of the equilibrium (3) to the left. The summary process that includes the equilibria (2) and (3) can be written as follows:

$$H_2O + 2h^{\bullet} + 2O_o^{\times} \Leftrightarrow 1/2O_2 + 2(OH)_o^{\bullet} \tag{4}$$

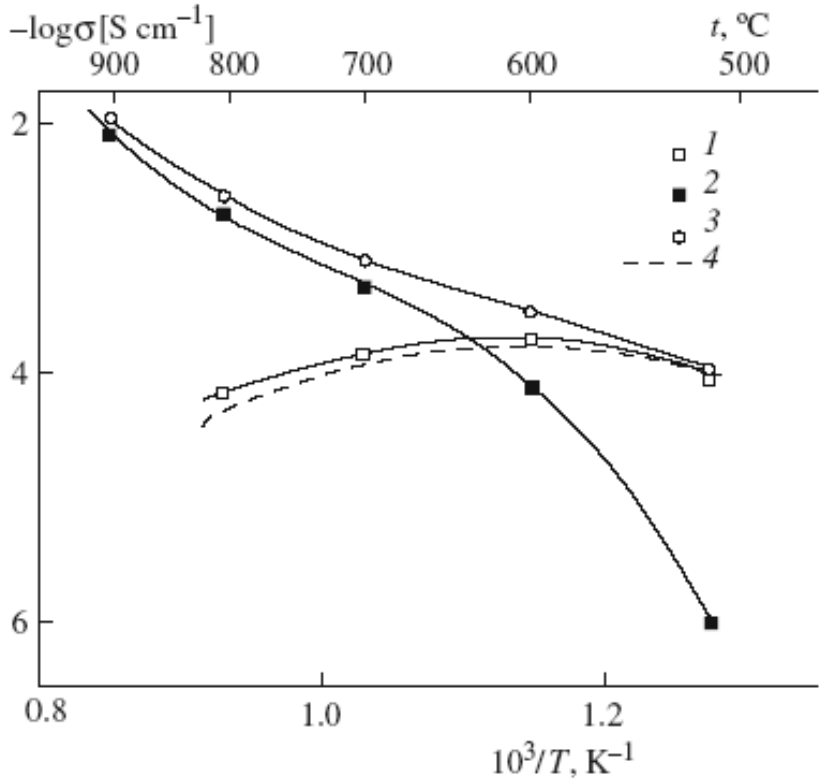

Figure 13. Temperature dependence of conductivity of $Sr_{5.92}Ta_{2.08}O_{11.12}$ in wet atmosphere ($pH_2O = 2 \cdot 10^{-2}$ atm). (*1*) proton , (*2*) oxygen-ion (estimated from EMF method) and (*3*) total conductivities. Curve (*4*) is the calculated value of the protonic conductivity, $\sigma_H = (\sigma_{ion})_{wet} - (\sigma_{ion})_{dry}$ [19].

Therefore, depending on the ratio of the hole and proton concentrations, the total conductivity can remain constant or even decrease at high pO_2 (air) and wet conditions.

The comparison of *temperature dependences* of the total conductivity in dry and wet atmospheres demonstrates the most typical situation: the conductivity in wet atmospheres is higher than in dry as a result of the contribution of proton conductivity in wet atmosphere ; the differences and, thus, the significance of protonic conduction, decrease with increasing temperature, and mainly disappear at temperatures above 800–900°C.

Figure 13. shows the partial conductivities obtained from the EMF-type transport number measurements for the composition $Sr_{5.92}Ta_{2.08}O_{11.12}$ ($x = 0.04$) from the homogeneity region of $Sr_{6-2x}Ta_{2+2x}O_{11+3x}$ [19]. The magnitude and temperature dependence of the partial proton conductivity confirm that for wet conditions protons become dominating defects and also dominate the conductivity below 550 C. The transition from predominantly oxygen to proton conductivity is accompanied by an overall change in activation energy from 0.96 to 0.56 eV, the latter being a typical value for proton mobility in oxygen deficient perovskites [11, 19].

For the phases demonstrating a phase transition during water incorporation a local maximum on temperature dependences of conductivity is observed (Figure 14, 15) [11, 14].

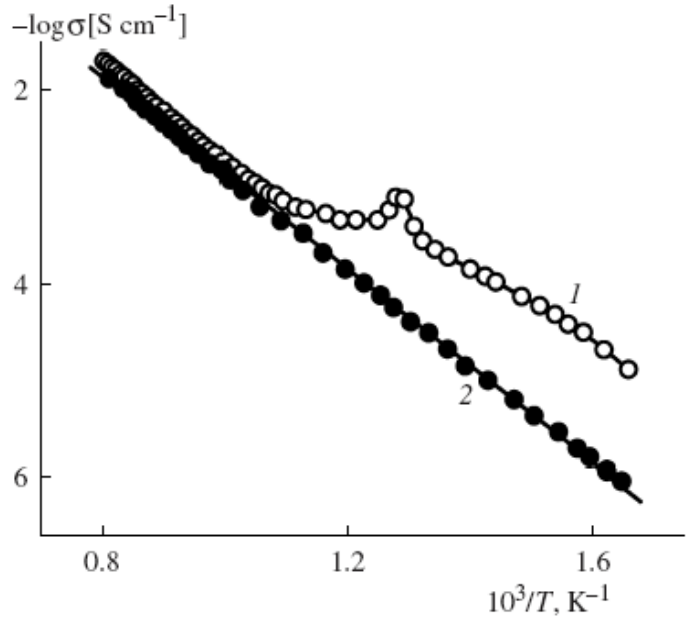

Figure 14. Temperature dependence of conductivity of $Sr_{5.92}Ta_{2.08}O_{11.12}$ in (*1*) wet atmosphere (pH_2O = $2 \cdot 10^{-2}$ atm) and (2) dry atmosphere (pH_2O =$3 \cdot 10^{-5}$ atm) [11].

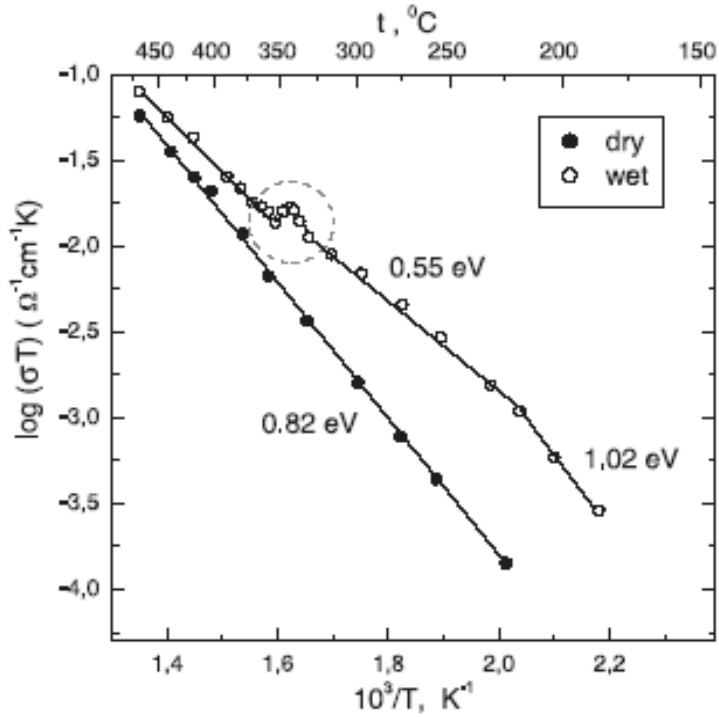

Figure 15. Temperature dependence of conductivity of single crystal $Ba_4Ca_2Nb_2O_{11}$ in wet (pH_2O = 2 $\cdot 10^{-2}$ atm) and dry atmospheres (pH_2O =$3 \cdot 10^{-5}$ atm) [14].

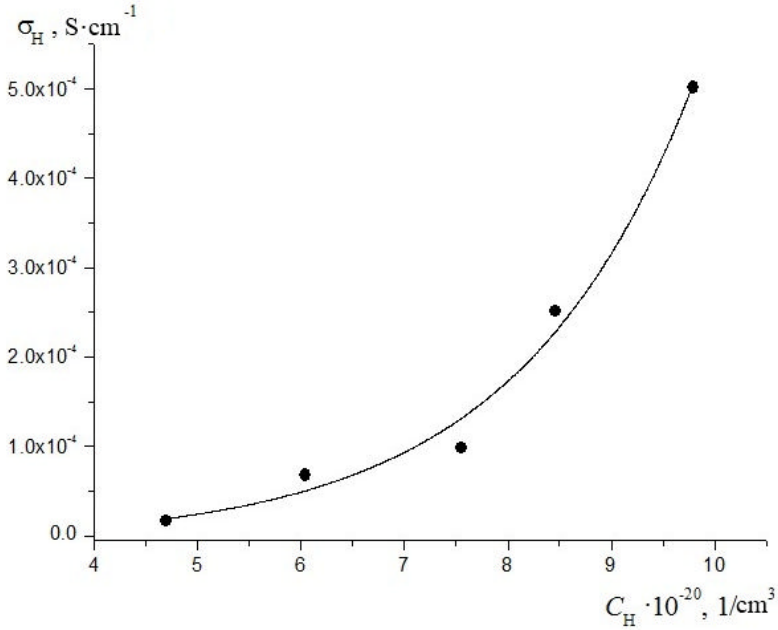

Figure 16. Dependence of proton conductivity vs. proton concentration in the solid solution $Sr_{6-2x}Ta_{2+2x}O_{11+3x}$ (T = 550°C) [26].

The proton conductivity of the solid solution $Sr_{6-2x}Ta_{2+2x}O_{11+3x}$ as a *function of their composition* was analyzed [26]. Figure 16. shows the dependence of the proton conductivity vs. the concentration of protons for a variety of x . It is seen that with the decreasing of the parameter $\boldsymbol{x}$, that is, with the increasing of the proton concentration, the value of proton conductivity increases monotonically. This result can be explained by the increase not only in the proton concentration but also in the proton mobility. Figure 17. shows the concentration dependence of the proton mobility [26], calculated in according with the relation:

$$\sigma_H = ZeC_H\mu_H, \tag{5}$$

where Ze is the charge, C_H is the proton bulk concentration, μ_H is the proton mobility.

The correlations between some experimental data are represented in Figure 18 [26]. The same tendency was observed for the solid solution $Sr_{6-2x}Nb_{2+2x}O_{11+3x}$ [8].

The effect of cationic sublattice on the value of proton conductivity was demonstrated by the example of the solid solution $(Ba_{1-y}Ca_y)_6Nb_2O_{11}$ with equal concentration of oxygen vacancies. With the decreasing of the parameter $\boldsymbol{y}$ (that is, with the increasing of BaO content) the oxygen-ion conductivity increased (Figure 19); the proton conductivity increased in the same way [19]. This effect can be explained by the increasing of the current carrier mobility. Because the cell parameter increases with the increasing of BaO content, the increase in the interatomic distance results in the decrease of the energy consumed in the oxygen ion migration, which leads to the increase in its mobility. The proton mobility also increases with the increasing of the oxygen ion mobility. Thus, the dynamics of the oxygen sublattice affects the proton conductivity.

The studies of the total conductivity *under the changing* pH_2O allowed revealing the principal trends (Figure 20 shows the typical dependences of $\sigma = f(pH_2O)$ for $Sr_6Ta_2O_{11}$ [11]). Similar plots were obtained for $(Ba_{1-y}Ca_y)_6Nb_2O_{11}$ [26]):

- At temperatures higher than 600°C the conductivity is almost independent on $p(H_2O)$. This indicates that protons are only present as minority defects and that proton conduction is insignificant.
- At lower temperatures (with the increasing of pH_2O) over a certain range of intermediate water vapour pressures, the conductivity is proportional to $p(H_2O)^{1/3}$.
- Increasing the water vapour pressure further, the conductivity shows a sharp increase near $p(H_2O) = 0.02$ atm in the temperature range 450-475 C. This behaviour agrees with the thermogravimetry data and reflects a change in crystal structure as a result of water incorporation. The breaking of monotonic character of the dependences is caused by the formation of hydroxo-phase.
- At low temperatures and high $p(H_2O)$, when all vacancies are filled up, the conductivity exhibits a weak dependence on water vapour pressure.

The recent investigation [27] demonstrates that the double perovskites are promising materials for electrochemical devices.

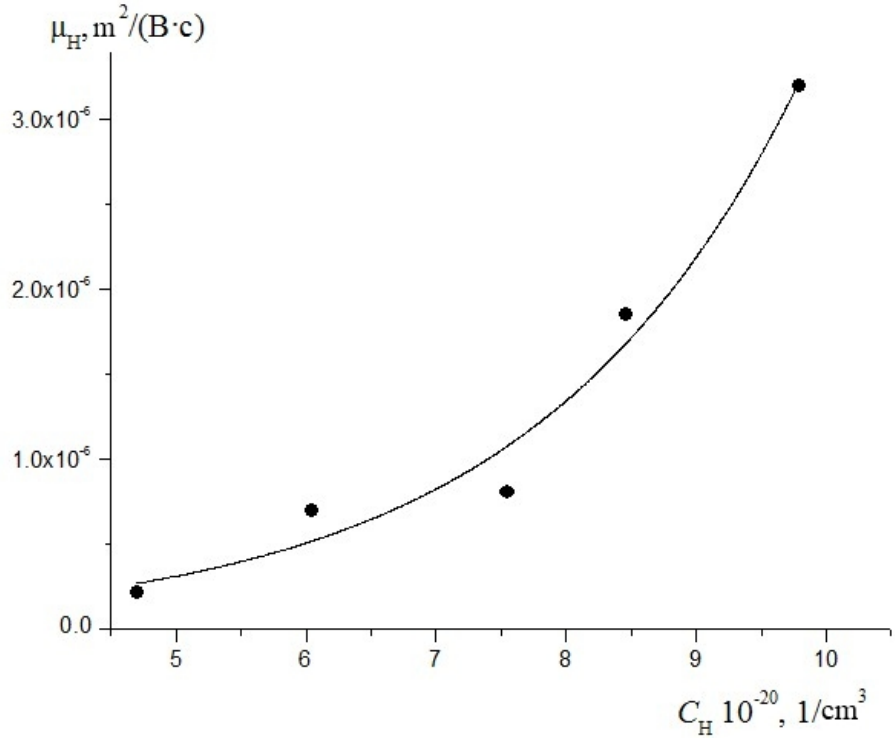

Figure 17. Dependence of proton mobility vs. proton concentration in the row of solid solution $Sr_{6-2x}Ta_{2+2x}O_{11+3x}$ (T = 550°C) [26].

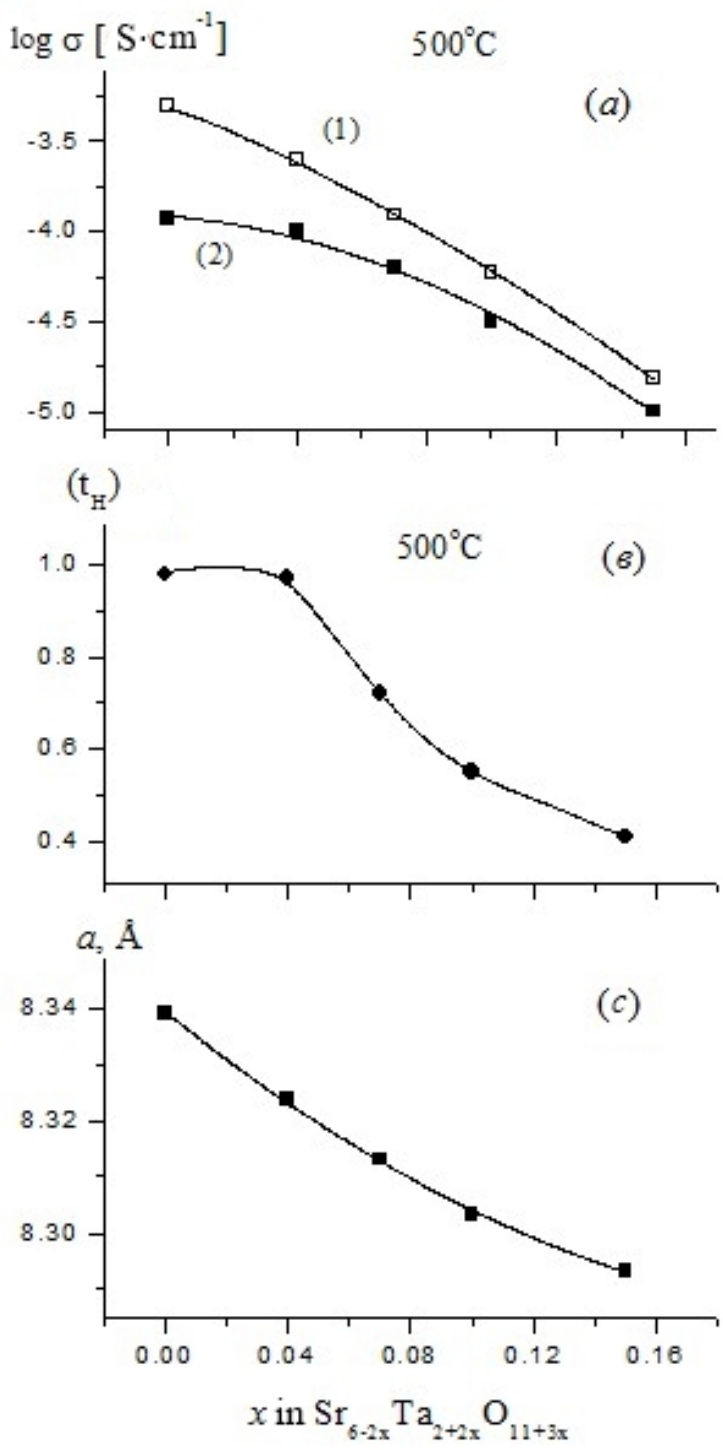

Figure 18. Concentration dependencies of (a) proton (1) and oxygen-ion (2) conductivities , (b) proton transport number, (c) unit cell in the row of solid solution $Sr_{6-2x}Ta_{2+2x}O_{11+3x}$ [26].

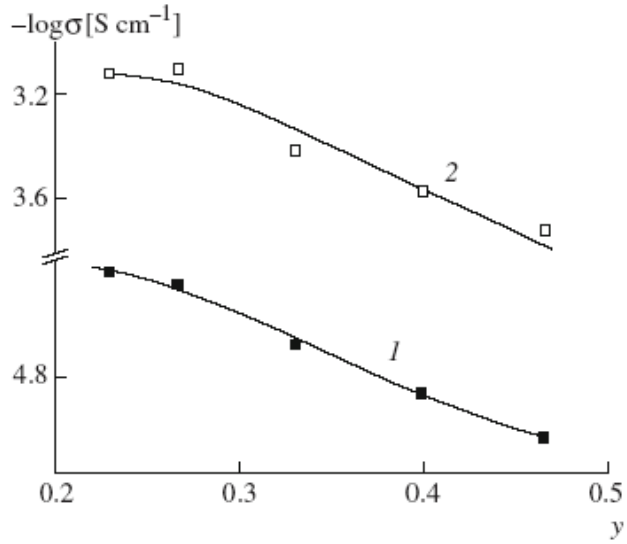

Figure 19. Dependence of (*1*) oxygen-ion conductivity and (*2*) proton conductivity on the composition of solid solution $(Ba_{1-y}Ca_y)_6Nb_2O_{11}$ (T = 400°C) [19].

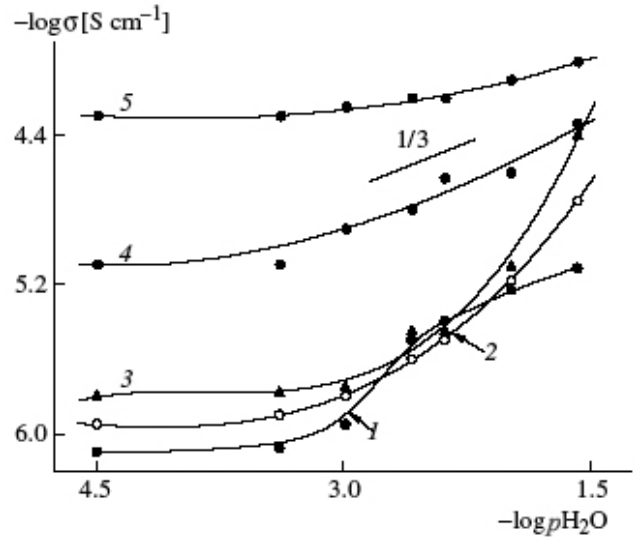

Figure 20. Dependences of total conductivity vs. partial water pressure for $Sr_6Ta_2O_{11}$. Temperature (°C): (*1*) 400, (*2*) 450, (*3*) 475, (*4*) 500, (*5*) 600, [11].

CONCLUSION

Data on the thermogravimetry, spectroscopy, and electrical properties as functions of T, $p(H_2O)$, $p(O_2)$ for niobates and tantalates of alkaline-earth metals with structure disordering of the oxygen sublattice are summarized. These phases reversibly incorporate of water and exhibit high-temperature proton transport.

Water uptake is close to the theoretical value expected from complete filling of oxygen vacancies by water. Incorporation of significant quantity of water leads to a phase transformation owing to formation of hydrated compositions close to $Me_6^{+2}M_2^{+5}O_{10-n}(OH)_{2n}$. The phase transformation is induced by both temperature and pH_2O changes. For the phases demonstrating a phase transition during water incorporation a local maximum on temperature dependences of conductivity and a jump on σ–pH_2O dependences are observed.

A wide-line ^1H NMR study indicates that the proton signal consists of three components, because protons were present in the form of energetically unequivalent OH^- – groups, namely (i) relatively isolated OH^- –groups, (ii) paired OH^- – groups located on one edge of an octahedron, and (iii) closely spaced OH^- –groups, which are ordered within some defect cluster. The niobates and tantalates have different ratios of those groups that may be explained by different coordination tendencies of niobium and tantalum and as a consequence a different arrangement of oxygen vacancies. The presence of different OH^- – groups determines staging of water removal.

It was shown that the mobility of protons depends on the dynamics of the oxygen sublattice: with the increasing of the lattice parameter and, as a consequence, the oxygen-ion conductivity, proton mobility increases.

REFERENCES

[1] Iwahara H., Asakura Y., Katahira K., Tanaka M. *Solid State Ionics* 168 (2004) 299.

[2] Sundmacher K., Rihko-Struckmann L.K., Galvita V. Solid electrolyte membrane reactors: Status and trends//*Catalysis Today* 104 (2005) 185–199.

[3] Athanassioua C., Pekridisc G., Kaklidisc N., Kalimeric K., Vartzokac S., Marnellosb G. Hydrogen production in solid electrolyte membrane reactors (SEMRs) //*International Journal of Hydrogen Energy* 32 (2007) 38 – 54.

[4] Guangyao Meng , Guilin Ma, Qianli Ma , Ranran Peng , Xingqin Liu. Ceramic membrane fuel cells based on solid proton electrolytes//*Solid State Ionics* 178 (2007) 697–703.

[5] Marques F.M.B., Kharton V.V., Naumovich E.N., Shaula A.L., Kovalevsky A.V., Yaremchenko A.A. Oxygen ion conductors for fuel cells and membranes: selected developments// *Solid State Ionics* 177 (2006) 1697–1703.

[6] Norby T. Korean *J. Ceram.* 1998. V. 4. P. 128.

[7] Colomban Ph., Romain F., Neiman A., Animitsa I. Double perovskites with oxygen structural vacancies: Raman spectra, conductivity and water uptake.// *Solid State Ionics.* 2001. V.145/1-4, p.339-347.

[8] Glöckner R., Neiman A., Larring Y., Norby T. Protons in $Sr_3(Sr_{1+x}Nb_{2-x})O_{9-3x/2}$ perovskite // *Solid State Ionics*, 1999. V.125. P.369-376.

[9] Animitsa I., Neiman A, Sharafutdinov A, Nochrin S. Strontium tantalates with perovskite-related structure.// *Solid State Ionics*. 2000. V.136-137, p.265-271.

[10] Animitsa I. E., Neiman A. Ya., Sharafutdinov A. R., Kazakova M. G. Strontium Tantalates with Perovskite Structure: Their Conductivity and High-Temperature Interaction with Water// *Russian Journal of Electrochemistry*, Vol. 37, No. 3, 2001, pp. 266–272.

[11] Animitsa I., Norby T., Marion S., Glockner R., Neiman A. Incorporation of water in strontium tantalates with perovskite-related structure.// *Solid State Ionics*. 2001. V.145/1-4, p.357-364.

[12] Animitsa I., Neiman A., Titova S., Kochetova N., Isaeva E., Sharafutdinov, Timofeeva N., Colomban Ph. Phase relations during water incorporation in the oxygen and proton conductor $Sr_6Ta_2O_{11}$// *Solid State Ionics*. 2003. V.156, 95-102.

[13] Animitsa I., Denisova T., Neiman A., Nepryahin A., Kochetova N., Zhuravlev N., Colomban Ph. States of H^+-Containing Species and Proton Migration Forms in Hydrated Niobates and Tantalates of Alkaline-Earth Metals with a Perovskite-Related Structure// *Solid State Ionics*. 2003. V.62-163, 73-81.

[14] Animitsa I., Neiman A., Kochetova N., Melekh B., Sharafutdinov A. Proton and oxygen-ion conductivity of $Ba_4Ca_2\ Nb_2O_{11}$// *Solid State Ionics*. 2003. V. 162-163, 63-71.

[15] Animitsa I., Neiman A., Kochetova N., Korona D., Sharafutdinov A. Chemical diffusion of water in the double perovskites $Ba_4Ca_2Nb_2O_{11}$ and $Sr_6Ta_2O_{11}$ // *Solid State Ionics*. 2006. V.177. P.2363-2368.

[16] Kochetova N. A., Animitsa I. E., Neiman A. Ya. The Synthesis and Properties of Solid Solutions Based on $Ba_4Ca_2Nb_2O_{11}$// *Russian Journal of Physical Chemistry* A, 2009, Vol. 83, No. 2, P. 203–208.

[17] Ashok A., Kochetova N., Norby T., Olsen A. Structural study of the perovskite system $Ba_{6-y}Ca_yNb_2O_{11}$ hydrated to proton conducting $Ba_{6-y}Ca_yNb_2O_{10}(OH)_2$//*Solid State Ionics* 179 (2008) 1858–1866.

[18] Korona D. V., Neiman A. Ya., Animitsa I. E., Sharafutdinov A. R. Effect of Humidity on Conductivity of $Ba_4Ca_2Nb_2O_{11}$ Phase and Solid Solutions Based on This Phase//*Russian Journal of Electrochemistry*, 2009, Vol. 45, No. 5. P. 586–592.

[19] Animitsa I.E. High-Temperature Proton Conductors with Structure-Disordered Oxygen Sublattice// *Russian Journal of Electrochemistry*, 2009, Vol. 45, No. 6. P. 668–676.

[20] Jalarvo N., Haavik C., Kongshaug C., Norby P., Norby T. Conductivity and water uptake of $Sr_4(Sr_2Nb_2)O_{11}\cdot nH_2O$ and $Sr_4(Sr2Ta_2)O_{11}\cdot nH_2O$// Solid State Ionics (2009).

[21] Baliteau S., Mauvy F., Fourcade S., Grenier J.C. Investigation on double perovskite $Ba_4Ca_2Ta_2O_{11}$// *Solid State Sciences* 11 (2009) 1572–1575.

[22] Spitsyn, V.I., Ippolitova, E.A., Kovba, L.M., et al., *Zh. Neorg. Khim*., 1982, vol. 27, p. 827.

[23] Hikichi Y., Suzuki S. *Preparation of cubic perovskites* $A(B_{2/5}W_{3/5})O_3$ (A=Ba or Sr, B=Na or Li). // Journal of the American Ceramic Society. 1987. V.70. N 5. P. 99-100.

[24] Hoffmann R., Hoppe R. Ein neuer perowskit mit Lucken im Anionenteil: $Ba_4[Na_2W_2O_{11}]$. // *Z.anorg.allg.chem*. 1989. V.575. P.154-164.

[25] Schober T. Phase diagrams in the proton conductor systems $Sr_6Ta_2O_{11}\times nH_2O$ and $Sr_{5.92}Ta_{2.08}O_{11.12}\times nH_2O$// Solid State Ionics, V. 177. Issues 5-6. 2006. P. 471-474. 26. Kochetova N.A., Animitsa I. E., Neiman A. Ya. Electrical properties of solid solutions based on strontium tantalate with perovskite related structure // *Russian Journal of Electrochemistry*. 2010, Vol. 46, No. 2.

[26] Bhella S. S., Thangadurai V. Synthesis and characterization of carbon dioxide and boiling water stable proton conducting double perovskite-type metal oxides // *Journal of Power Sources* 186 (2009) 311–319.

In: Perovskites: Structure, Properties and Uses
Editor: Maxim Borowski, pp. 525-537
ISBN 978-1-61668-525-6

Chapter 14

SHORT- AND LONG-RANGE FERROMAGNETIC ORDERS IN $La_{1-X}PB_XMnO_3$: CRITICAL BEHAVIOR STUDY

The-Long Phan* *and Seong-Cho Yu*
BK-21 Physics Program and Department of Physics, Chungbuk National University, Cheongju 361-763, South Korea

ABSTRACT

We have studied the influence of Pb-doping on critical behavior of polycrystalline manganites of $La_{1-x}Pb_xMnO_3$ (x = 0.1, 0.2 and 0.3) around their ferromagnetic-paramagnetic phase transition temperature (T_C) by means of analyzing isothermal magnetization data M-H. According to the critical criterion proposed by Banerjee, it was found that all three samples undergo the second-order phase transition as showing a positive slope of isotherm plots of H/M versus M^2. The critical parameters were determined by the modified Arrott method, used the Arrott-Noakes equation of state $M^{1/\beta}$ versus $(H/M)^{1/\gamma}$ and the asymptotic relations in the critical region. The obtained results reveal that with increasing the Pb-doping concentration in $La_{1-x}Pb_xMnO_3$, the T_C value increases from 162.0 K (for x = 0.1) to about 346.3 K (for x = 0.3). Concurrently, there is a remarkable variation in their critical exponents: β = 0.498, γ = 1.456 and δ = 3.92 for x = 0.1; β = 0.499, γ = 1.241 and δ = 3.49 for x = 0.2; and β = 0.502, γ = 1.063 and δ = 3.12 for x = 0.3. Having compared to the critical parameters expected from the theoretical models of mean-field theory, 3D-Ising model, and 3D-Heisenberg model, we have found an existence of the short-range ferromagnetic order in the samples with x = 0.1 and 0.2, and the long-range ferromagnetic order in the x = 0.3 sample. Under such circumstances, magnetic interaction mechanisms between Mn^{3+}-Mn^{4+} in the samples would be changed, particularly in the paramagnetic region.

* Corresponding author: Email: ptlong2512@yahoo.com; Phone: +82-43-261-2269 ; Fax: +82-43-275-6416

1. INTRODUCTION

Recently, the discovery of magnetoresistance and magnetocaloric phenomena in hole-doped perovskite-type manganites of $Ln_{1-x}A_xMnO_3$ (Ln = La, Pr, Nd; A = Ca, Sr, Ba, Pb etc.) around their ferromagnetic (FM) to paramagnetic (PM) phase transition temperature (T_C) has attracted interest in the community of solid-state physics [1-9]. Among these manganite compounds, the systems of $La_{1-x}Ca_xMnO_3$, $La_{1-x}Sr_xMnO_3$, and $La_{1-x}Pb_xMnO_3$ with x = 0.1 - 0.4 have received intensive attention as showing colossal magnetoresistance (CMR) and large magnetocaloric (MC) effects around room temperature [4, 5, 10]. This could lead to development of some manganites-based electronic devices, such as magnetic sensitive sensors, reading/recording heads, and cooling systems (magnetic refrigerators).

Basically, the CMR effect in perovskite manganites has been explained by means of the mechanism of double-exchange interaction taking place between Mn^{3+} and Mn^{4+} ions, which was supposed by Zener [11]. In some cases, however, this model only is not enough to explain fully the magneto-transport properties observed by experimental physicists, particularly for the material system $La_{1-x}Ca_xMnO_3$. The addition of the polaron effect (known as the Jahn-Teller effect) caused by strong electron-phonon interactions is necessary [12]. With such opinions, the magnetic and magneto-transport properties of perovskite manganites are definitely dependent on both the length bond ⟨Mn-O⟩ and ⟨Mn-O-Mn⟩ angle bond. As a matter of fact, these parameters are influenced strongly by concentration and the radius of divalent ions substituted into the A site (i.e., Ca, Sr, Ba, or Pb). Their presence in manganite compounds $Ln_{1-x}A_xMnO_3$ would lead to a lattice distortion (where the angle bond ⟨Mn-O-Mn⟩ is smaller than 180^o, and the length bond ⟨Mn-O⟩ becomes longer or shorter than its primitive value), and to the change in the concentration ratio of Mn^{3+}/Mn^{4+}. This is a key point that it could be exploited to control the magnetic, electrical and magneto-transport properties of perovskite manganites as expected. Notably, the possibility of utilizing perovskite manganites in electronic devices is currently still limited, probably since their physical behaviours are unstable and very sensitive to oxygen-concentration change [13]. This feature makes perovskite manganites become interesting in the field of fundamental research rather than the application aspect. The improvement of weaknesses in these materials is thus necessary, and currently an issue of interest.

To better understand the CMR and MC effects, it is necessary to understand the nature of the FM-PM phase transition and interaction mechanism taking place between Mn ions in the manganite host lattice in the vicinity of T_C. Besides the study of magneto-transport behaviors, one of the most effective approaches is to consider the critical exponents β, γ, and δ, which are associated with the spontaneous magnetization $M_s(T,0)$, initial magnetic susceptibility $\chi_0(T)$, and the critical isotherm $M(T_C,H)$, respectively. Based on these critical parameters in comparison with those predicted by the mean-field theory, 3D Ising and 3D Heisenberg models [14], one can figure out the magnetic-interaction type (or interaction mechanism) existing in a material, i.e long- and/or short-range ferromagnetic interactions. In this chapter, we present a careful study of critical behavior of polycrystalline perovskite manganites of $La_{1-x}Pb_xMnO_3$ (x = 0.1, 0.2 and 0.3) prepared by conventional solid-state reaction. We shall point out that the increase of Pb-doping concentration in $La_{1-x}Pb_xMnO_3$ influences remarkably their critical parameters of T_C, β, γ, and δ. For example, T_C increases from about 162.0 K (for x = 0.1) to about 346.3 K (for x = 0.3), and the exponents obtained is β = 0.498,

$\gamma = 1.456$ and $\delta = 3.92$ for $x = 0.1$; $\beta = 0.499$, $\gamma = 1.241$ and $\delta = 3.49$ for $x = 0.2$; and $\beta = 0.502$, $\gamma = 1.063$ and $\delta = 3.12$ for $x = 0.3$. Having compared to those expected by the theoretical models, we have found an existence of the short-range ferromagnetic order in the samples with $x = 0.1$ and 0.2, and the long-range ferromagnetic order in the $x = 0.3$ sample. This is due to an increase in Mn^{4+} concentration in $La_{1-x}Pb_xMnO_3$ as increasing the Pb-doping concentration, in which magnetic interaction mechanisms between Mn^{3+} and Mn^{4+} would be changed.

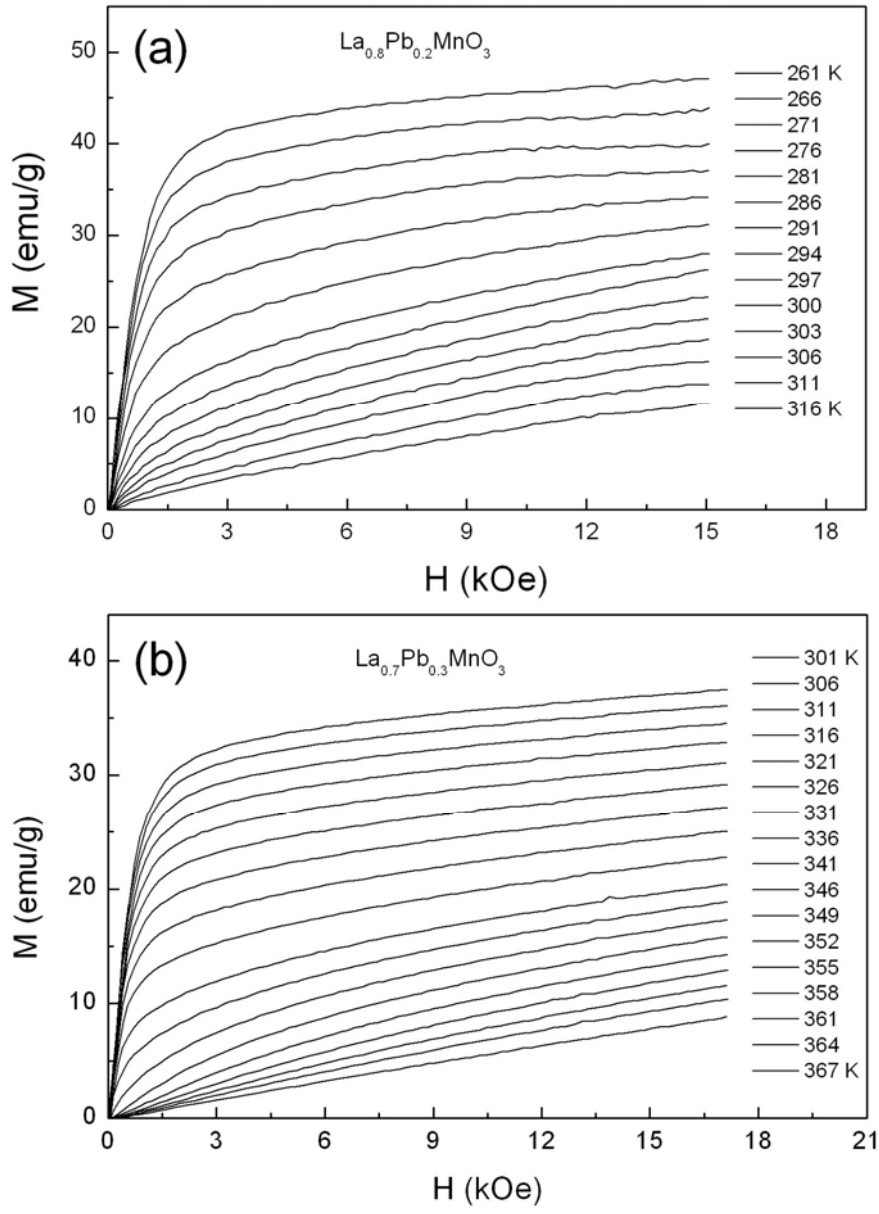

Figure 1. Field dependences of magnetization for (a) $La_{0.8}Pb_{0.2}MnO_3$, and (b) $La_{0.7}Pb_{0.3}MnO_3$ measured at various temperatures.

2. EXPERIMENT

Three polycrystalline samples of $La_{1-x}Pb_xMnO_3$ (x = 0.1, 0.2 and 0.3) were prepared by the conventional solid-state reaction method. The precursors of commercial powders La_2O_3, PbO and $MnCO_3$ (99.9 % in purity) combined with stoichiometrical quantities were well mixed, ground and pressed into pellets. These pellets were then pre-sintered at 900 °C for 15 hrs. After several times of intermediate grinding and pressing, they were sintered at 920 °C for 15 hrs in air. The cooling was carried out slowly to room temperature. It should be noticed that these pellets were annealed at a quite low temperature comparing to other perovskite manganites (usually at temperatures 1100 -1300 ^oC), because of the presence of PbO (its melting point is about 830 ^oC). The single phase in an orthorhombic structure of the final products was confirmed by an X-ray diffractometer [10, 15]. The dependence of magnetization on the magnetic field, *M-H*, at various temperatures were performed on a vibrating sample magnetometer (VSM) with the applied field up to 17 kOe. An incremental temperature (ΔT) for each *M-H* measurement is 3 K near T_C, and 5 K for the other regions.

3. RESULTS AND DISCUSSION

Figure 1 shows representatively the *M-H* data for $La_{1-x}Pb_xMnO_3$ (x = 0.2 and 0.3) measured at different temperatures in the vicinity of T_C. It appears that the *M-H* curves versus temperature separate into two characteristic regions. In the first region $T < T_C$, magnetization increases nonlinearly with increasing the magnetic field, and does not reach to a saturation value. Meanwhile, in the second region $T > T_C$, the field dependence of magnetization is linear. These features seem popular and could be found in most perovskite manganites in the ferromagnetic and paramagnetic regimes [1, 5, 16], excepting for the system $La_{1-x}Ca_xMnO_3$ where its magnetic phase transition is usually accompanied with structural changes, and thus its *M-H* curves become anomalous, see Refs. [3, 4, 7]. This could explain why the MC effect in $La_{1-x}Ca_xMnO_3$ ($x \approx 0.3$) becomes largest among perovskite manganite compounds [8].

To assess the nature of magnetic phase transition in the samples, we firstly pay attention to the free energy G near the critical temperature, which can be expressed in terms of the order parameter M (magnetization) as follows [9]

$$G(T, M) = G_0 + aM^2 + bM^4 - MH\,, \tag{1}$$

where a and b are temperature-dependent parameters. From the equilibrium condition of energy minimization, $\partial G / \partial H = 0$, it is easily deduced the magnetic equation of state (corresponding to the mean-field theory) [14]

$$H / M = 2a + 4bM^2\,. \tag{2}$$

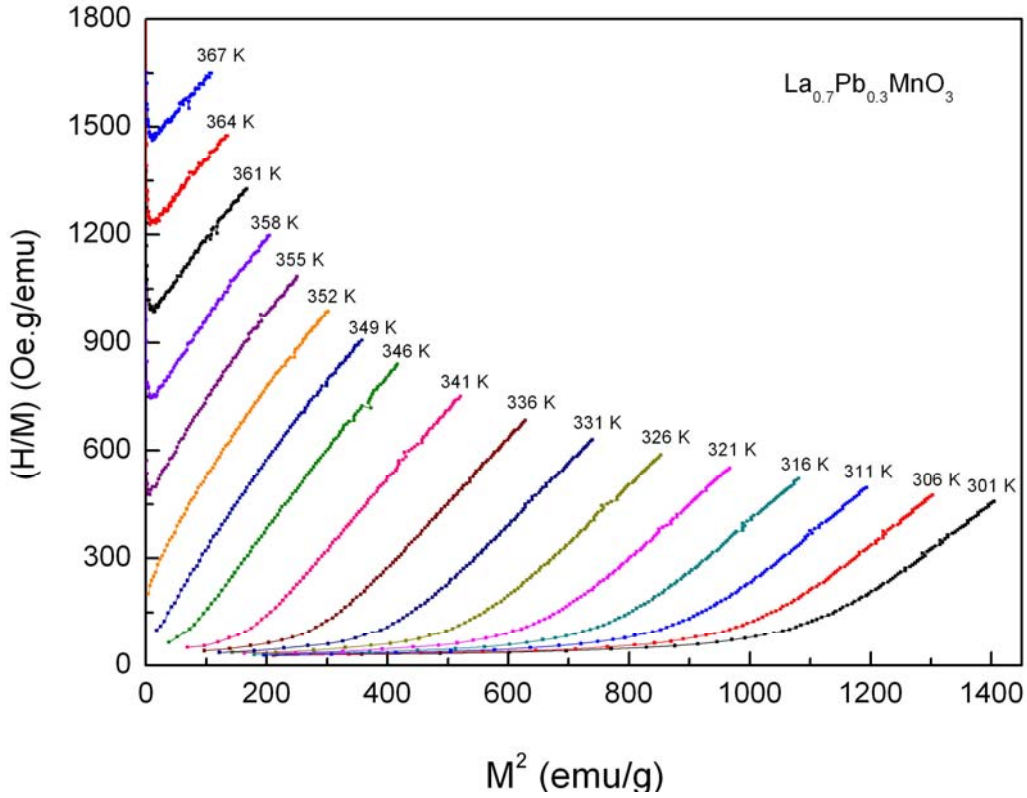

Figure 2. The Arrott plots of M^2 versus H/M for the sample $La_{0.7}Pb_{0.3}MnO_3$.

With this equation, the representation curves of H/M versus M^2 should be straight lines, and the intercept of these straight lines on the H/M axis gives the order of magnetic transition. The straight lines with a positive slope indicates for the second-order transition, and with a negative slope indicates for the first-order transition, known as the Banerjee criterion [17]. It could be generalized Eq. (2) to the form of $(H/M)^{1/\gamma} = (T-T_C)/T_1 + (M/M_1)^{1/\beta}$, the so-called Arrott-Noakes equation of state [18]. The representation of $(H/M)^{1/\gamma}$ versus $M^{1/\beta}$ is then known as the modified Arrott plots. In the case of the mean-field theory, the values β and γ are 0.5 and 1.0, respectively, which leads to the regular Arrott plots [19]. Concerning our work, Figure 2 shows the performance of H/M versus M^2 for a representative sample of $La_{0.7}Pb_{0.3}MnO_3$. One can see clearly that the plots of H/M versus M^2 give a positive slope, similar to those of $La_{0.7}Sr_{0.3}MnO_3$ reported by Mira et al. [4]. This feature was also met in the other samples with $x = 0.1$ and 0.2, not shown here. It means that a second-order transition exists in our samples. Concerning the first-order transition, it can be found in compositions $La_{0.7}Ca_{0.3}MnO_3$ and $La_{1.2}Sr_{1.8}Mn_2O_7$ [4, 20].

Mathematically, around the critical temperature the second-order transition could be described by a set of power functions through the exponents β, γ, and δ, which are obtained basing on the following asymptotic relations [21]

$$M_s(T)=\lim_{H\to 0}(M)=M_0(-\varepsilon)^{\beta}\ \varepsilon<0, \tag{3}$$

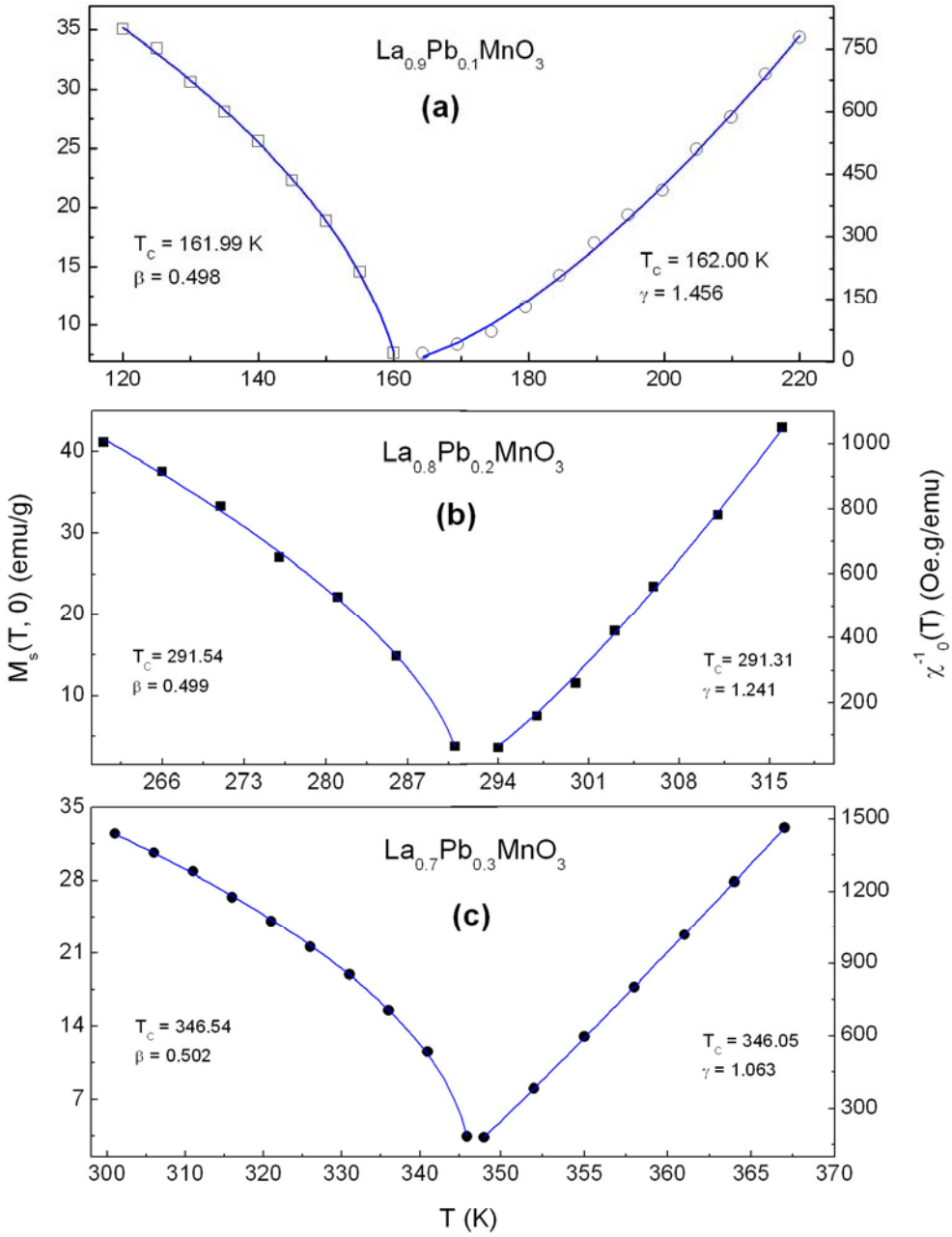

Figure 3. Temperature dependences of spontaneous magnetization, $M_s(T)$, and the inverse initial magnetic susceptibility, $\chi_0^{-1}(T)$, for the samples (a) $La_{0.9}Pb_{0.1}MnO_3$, (b) $La_{0.8}Pb_{0.2}MnO_3$ and (c) $La_{0.7}Pb_{0.3}MnO_3$ are fitted to the power laws of Eqs. (3 and 4). respectively.

$$\chi_0^{-1}(T)=\lim_{H\to 0}(H/M)=(h_0/M_0)\varepsilon^{\gamma}\ \varepsilon>0, \tag{4}$$

$$M=DH^{1/\delta},\ \varepsilon=0, \tag{5}$$

where M_0, h_0, and D are the critical amplitudes, and $\varepsilon = (T-T_C)/T_C$ is the reduced temperature. According to scaling theory [5, 21], on the other hand, the critical exponents could be also obtained via the magnetic equation of state in the critical region written as

$$M(H,\varepsilon) = |\varepsilon|^{\beta} f_{\pm}(H/|\varepsilon|^{\beta+\gamma}), \quad (6)$$

in which scaling functions of f_+ and f_- represent for variations in the temperature regions of $T>T_C$ and $T<T_C$, respectively. This relation implies that $M/|\varepsilon|^{\beta}$ as a function of $H/|\varepsilon|^{\beta+\gamma}$ falls on two different branches, one for temperatures $T>T_C$ and the other for $T<T_C$ corresponding to the paramagnetic and ferromagnetic regions, respectively. Accordingly, the critical exponents β and γ determined from Eqs. (3 and 4) must be in agreement with the descriptions of Eq. (6).

Table 1. The critical parameters (T_C, β, γ, and δ) obtained for $La_{1-x}Pb_xMnO_3$ are compared to those expected by theoretical models (Mean-field theory, 3D Heisenberg model, 3D Ising model, and Tricritical mean-field theory) and perovskite manganites (and cobaltites)

Material	β	γ	δ	T_C (K)	Ref.
$La_{0.9}Pb_{0.1}MnO_3$	0.498	1.456	3.92	162.0	This work
$La_{0.8}Pb_{0.2}MnO_3$	0.499	1.241	3.49	291.42	This work
$La_{0.7}Pb_{0.3}MnO_3$	0.502	1.063	3.12	346.29	This work
Mean-field theory	0.5	1.0	3.0		[14]
3D Heisenberg model	0.365	1.336	4.80		[14]
3D Ising model	0.325	1.241	4.82		[14]
Tricritical mean-field theory	0.25	1.0	5.0		[21]
$La_{0.8}Sr_{0.2}MnO_3$	0.50	1.08	3.13	315	[5]
$La_{0.8}Sr_{0.2}CoO_3$	0.46	1.39	4.02	198.5	[23]
$La_{0.75}Sr_{0.25}CoO_3$	0.46	1.39	4.02	222.3	[23]
$La_{0.7}Sr_{0.3}CoO_3$	0.43	1.43	4.38	223.4	[23]
$LaMnO_{3.14}$	0.415	1.47	NA	141.0	[22]
La_2NiMnO_6	0.408	1.295	4.174	271.1	[16]
$Nd_{0.6}Pb_{0.4}MnO_3$	0.374	1.329	4.54	156.5	[26]
$La_{0.7}Sr_{0.3}MnO_3$	0.37	1.22	4.25	354	[1]
$La_{0.875}Sr_{0.125}MnO_3$	0.37	1.38	4.72	186.1	[6]
$La_{0.67}Ba_{0.33}MnO_3$	0.365	1.22	NA	306.1	[24]
$La_{0.8}Ca_{0.2}MnO_3$	0.36	1.45	5.03	174.0	[2]
$Pr_{0.77}Pb_{0.23}MnO_3$	0.344	1.352	4.69	167.0	[25]
$La_{0.5}Sr_{0.5}CoO_3$	0.321	1.351	4.39	223.2	[27]
$La_{0.6}Ca_{0.4}MnO_3$	0.25	1.03	5.0	255.5	[3]
$La_{0.9}Te_{0.1}MnO_3$	0.201	1.27	7.14	239.5	[9]
$La_{0.7}Ca_{0.3}MnO_3$	0.14	0.81	1.22	222.2	[1]

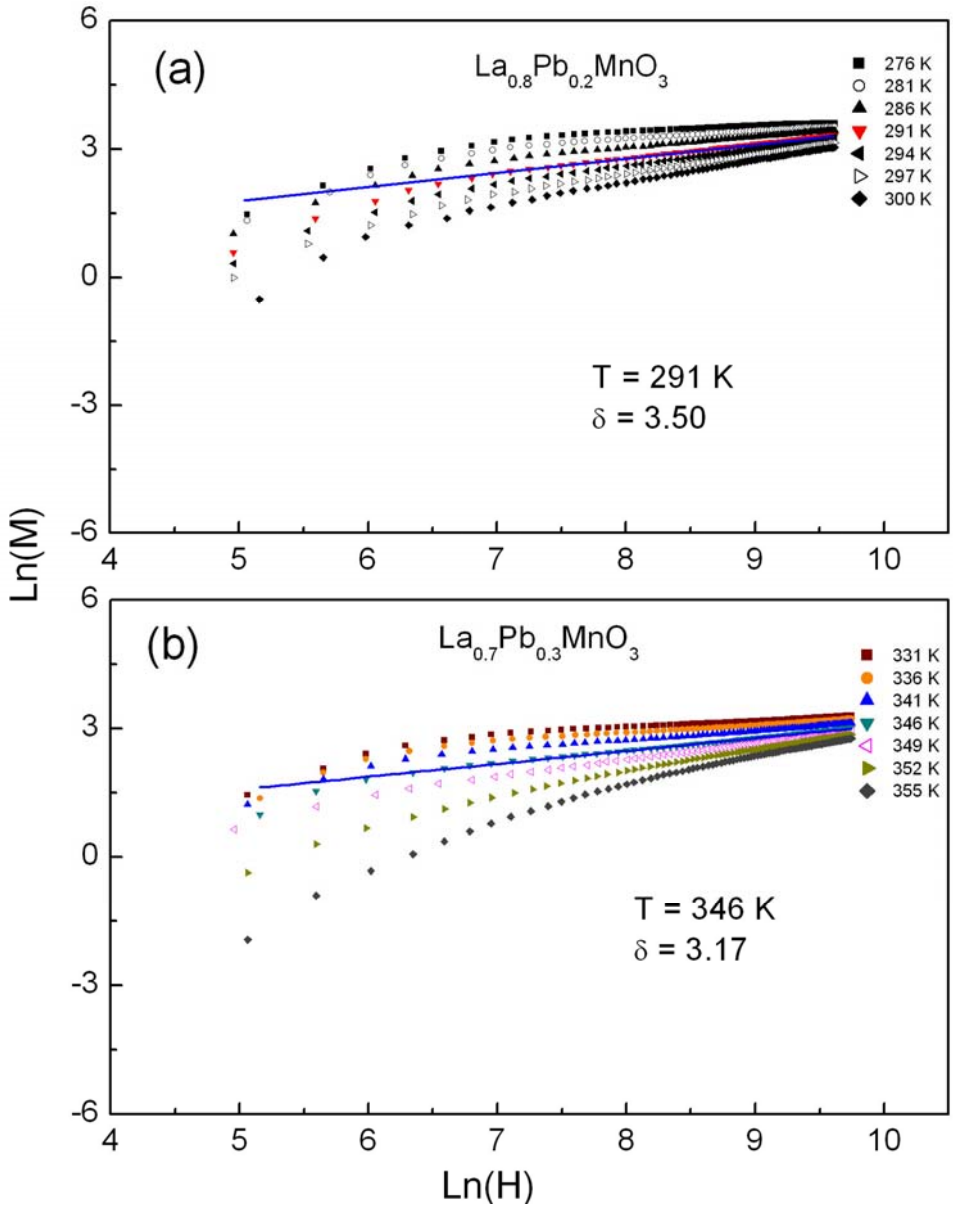

Figure 4. The plot of ln(M) versus ln(H) in the vicinity of T_C for (a) $La_{0.8}Pb_{0.2}MnO_3$, and (b) $La_{0.7}Pb_{0.3}MnO_3$. The solid lines are fitting curves of the isotherm to Eq. (5) at $T \approx T_C$.

Experimentally, to obtain these parameters, we followed the modified Arrott plots [18]. Firstly, $M_s(T,0)$ and $\chi_0^{-1}(T)$ data were determined by plotting $M^{1/\beta}$ versus $(H/M)^{1/\gamma}$ from trial exponents with $\beta = 0.365$ and $\gamma = 1.336$ (not shown); they are the exponents of the 3D Heisenberg model [14]. The linear extrapolation from the part of high fields of the curves to the intercepts with the axes $M^{1/\beta}$ and $(H/M)^{1/\gamma}$ would introduce the values of $M_s(T)$ and $\chi_0^{-1}(T)$, respectively. These values for three samples around T_C are shown in Figure 3. It should be noticed that if using the set of other trial exponents (for example, the exponents of the mean-field theory or 3D Ising model), the steps would be also carried out similarly to lead to $M_s(T)$

and $\chi_0^{-1}(T)$ values close to those obtained by the previous trial exponents. With $M_s(T)$ and $\chi_0^{-1}(T)$ data obtained, when fitting the $M_s(T)$ data of the samples to Eq. (3), we determined the parameters T_C = 161.99 K and β = 0.498 for $La_{0.9}Pb_{0.1}MnO_3$, T_C = 191.54 K and β = 0.499 for $La_{0.8}Pb_{0.2}MnO_3$, and T_C = 346.54 K and β = 0.502 for $La_{0.7}Pb_{0.3}MnO_3$. Meanwhile, the fitting of the $\chi_0^{-1}(T)$ data to Eq. (4) gave the results of T_C = 162.00 K and γ = 1.456 for $La_{0.9}Pb_{0.1}MnO_3$, T_C = 191.31 K and γ = 1.241 for $La_{0.8}Pb_{0.2}MnO_3$, and T_C = 346.05 K and γ = 1.063 for $La_{0.8}Pb_{0.2}MnO_3$, see Figure 3. Here, the T_C values determined by the above ways are quite close to each other. Having used the Widom scaling relation of $\delta = 1+\gamma/\beta$ [21], it was deduced δ to be 3.92, 3.49, and 3.12 for $La_{0.9}Pb_{0.1}MnO_3$, $La_{0.8}Pb_{0.2}MnO_3$, and $La_{0.7}Pb_{0.3}MnO_3$, respectively. On the other hand, if considering the *M-H* curves at temperatures in the vicinity of T_C and fitting the critical isotherm $M(T_C,H)$ data to Eq. (5), we could also obtained the values δ of the x = 0.1, 0.2 and 0.3 samples to be 3.90, 3.17 and 3.33, respectively, as shown representatively in Figure 4 for the x = 0.2 and 0.3 samples. One can see that these values are in good accordance with those determined from the Widom law. All the critical parameters obtained for the samples are shown in Table 1. For the following performance and discussion, we shall use average values of T_C taken from those obtained by fitting the $M_s(T)$ and $\chi_0^{-1}(T)$ data for the samples, as displayed in Table 1.

With the critical parameters of T_C, β and γ, we have performed the scaling plots of $\ln(M/|\varepsilon|^{\beta})$ versus $\ln(H/|\varepsilon|^{\beta+\gamma})$ for the samples at temperatures around their phase transition T_C. The results of this performance reveal that the *M-H* data fall on two branches, one for temperatures $T<T_C$ and the other for $T>T_C$, as can be seen in Figure 5. This is in good agreement with the descriptions of Eq. (6) as detailed above, revealing the reliability of the critical parameters obtained in our case when using the modified Arrott plots. The successful determination of the critical parameters based on the critical equations, i.e., Eqs. (3-5), proves an existence of the second-order phase transition in our samples of $La_{1-x}Pb_xMnO_3$ (x = 0.1-0.3), in accordance with the preliminary judgment based on the Banerjee criterion.

From the results displayed above, one can see that with increasing the Pb-doping concentration in $La_{1-x}Pb_xMnO_3$, T_C increases from about 162.0 K (for x = 0.1) to 346.3 K (for x = 0.3), see Table 1. This can be explained by means of changes in their structural parameters, particularly the average length bond ⟨Mn-O⟩ and angle bond ⟨Mn-O-Mn⟩. Chau et al. [15] found that ⟨Mn-O⟩ was decreased with increasing the Pb-doping concentration, which is 1.968, 1.966 and 1.962 Å for x = 0.1, 0.2 and 0.3, respectively. And, ⟨Mn-O-Mn⟩ was slightly increased from 162° (for x = 0.1) to 166° (for x = 0.3). Under such circumstances, the magnetic structure of the x = 0.2 and 0.3 samples becomes more stable than that of the x = 0.1 sample versus the thermal energy [10]. As a result, T_C increases with increasing the Pb concentration in $La_{1-x}Pb_xMnO_3$. However, the Pd doping does not much influence the exponent $\beta \approx 0.5$ of three samples. This proves magnetic interaction of our samples in the ferromagnetic regime can be described by the mean-field theory with β = 0.5 [12]. Having reviewed earlier reports on perovskite manganites and cobaltites as well, there was only one compound of $La_{0.8}Sr_{0.2}MnO_3$ having β = 0.50 [5], which is very close to our material system. Most perovskite compounds have β = 0.408 - 0.46 [16, 22, 23] lying between the mean-field theory and 3D Heidenberg model, or β = 0.344 - 0.374 [1, 2, 6, 24-26] that is very close to the value of the 3D Heidenberg model (β = 0.365), see Table 1. Few other compounds [3, 9, 27] displayed in Table 1 have β close to the 3D Ising theory (β = 0.325) or tricritical mean-field

theory ($\beta = 0.25$). For $La_{0.7}Ca_{0.3}MnO_3$, which usually exhibits the first-order transition, the using of the asymptotic relation of Eq. (1) for fitting would give $\beta = 0.14$ that is not close to any above models [1].

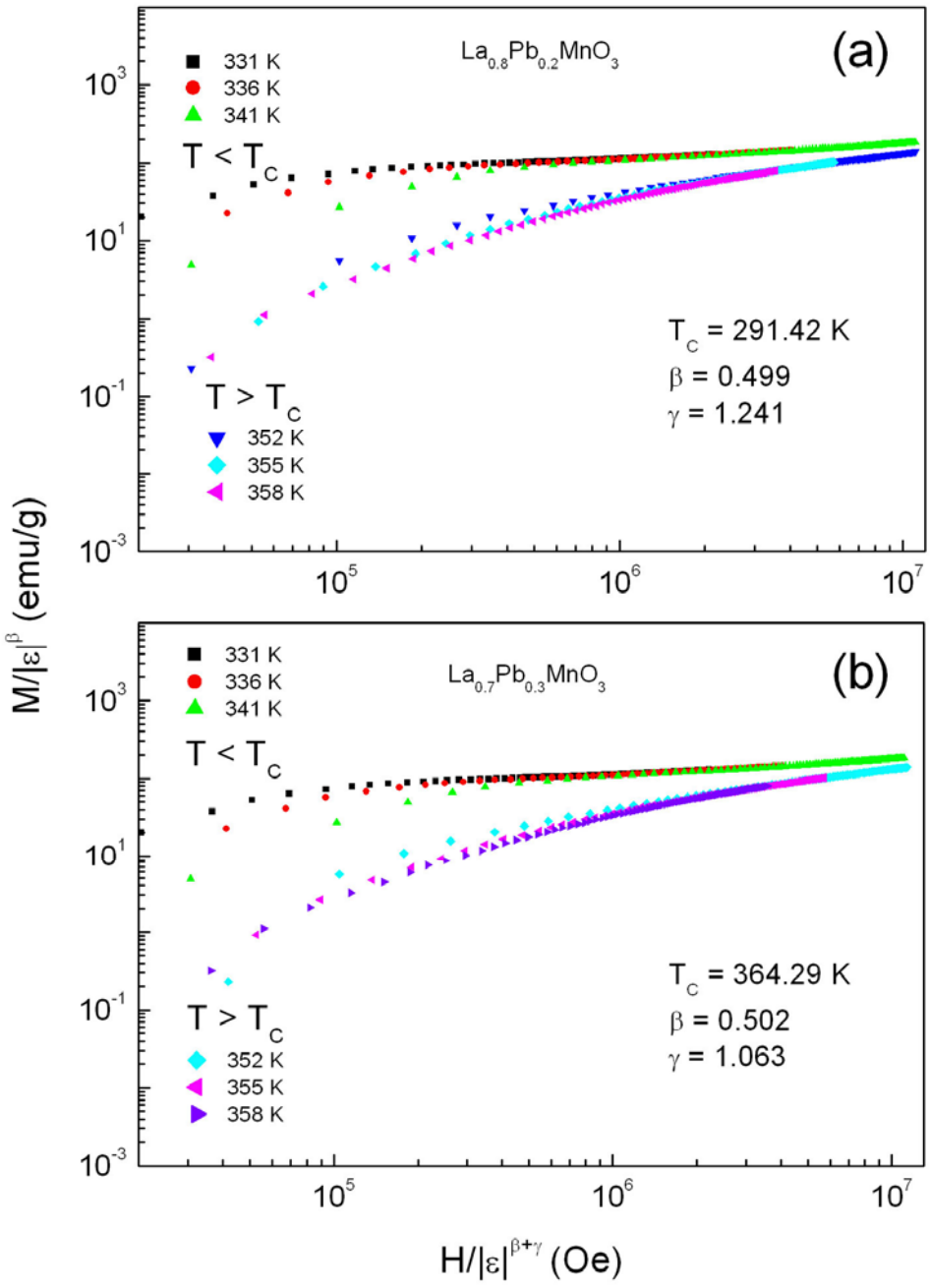

Figure 5. Scaling plots of $\ln(M/|\varepsilon|^{\beta})$ versus $\ln(H/|\varepsilon|^{\beta+\gamma})$ below and above T_C for (a) $La_{0.8}Pb_{0.2}MnO_3$, and (b) $La_{0.7}Pb_{0.3}MnO_3$ using the critical exponents listed in Table 1.

Regarding the mean-field theory, its main idea is to consider all magnetic interactions in a multi-body system as an effective interaction of one body system [21]. This can happen when our samples exhibit the long-range ferromagnetic order. However, to give the better conclusion of what type of magnetic order existing in our samples, it is necessary to take into account for the exponent γ characteristic for the paramagnetic region. As shown in Table 1, the x = 0.1 and 0.2 samples have γ = 1.456 and 1.241, respectively, while that of the x = 0.3 sample is 1.063. The γ values of two former samples are close to that of the 3D Ising model (γ = 1.241) with a short-range ferromagnetic order. This means that ferromagnetic interactions between Mn^{3+} and Mn^{4+} ions still persist in $La_{0.9}Pb_{0.1}MnO_3$ and $La_{0.8}Pb_{0.2}MnO_3$ at temperatures above T_C, which could be from ferromagnetic clusters, as observed by electron spin resonance [28]. However, a similar result is absent in $La_{0.7}Pb_{0.3}MnO_3$, where γ = 1.063 is very close to that of the mean-field theory with γ = 1.0 (see Table 1). Together with the above β data, it is made sure that the long-range ferromagnetic order is responsible for the magnetic phase transition in $La_{0.7}Pb_{0.3}MnO_3$, similar to the case of $La_{0.8}Sr_{0.2}MnO_3$ [5]. Meanwhile, the other compositions $La_{0.9}Pb_{0.1}MnO_3$ and $La_{0.8}Pb_{0.2}MnO_3$ exhibit the short-range ferromagnetic order, meaning an existence of a ferromagnetic phase above their T_C. Clearly, with increasing the Pb concentration in $La_{1-x}Pb_xMnO_3$, besides an enhancement in the phase-transition temperature T_C, the ferromagnetic interaction also varies from the short-to-long range interaction, with a threshold value of x = 0.3. This variation is characterized by the set of the critical exponents for each compound. The reason for the changes in the ferromagnetic orders can be explained as follows: it has been known that the antiferromagnetic Mn^{3+}-Mn^{3+} superexchange interaction plays an important role in the parent compound $LaMnO_3$. The Pb substitution for La leads to an appearance of Mn^{4+}, and thus introduces the ferromagnetic double-exchange interaction between Mn^{4+} and Mn^{3+} ions. At a low Pb-doping concentration with x = 0.1, the ferromagnetic Mn^{3+}-Mn^{4+} interaction could exist in ferromagnetic clusters surrounded by an antiferromagnetic host lattice due to the dominant interactions of Mn^{3+}-Mn^{3+} and Mn^{4+}-Mn^{4+}. Here, a compound exhibits the feature of ferromagnetic clusters would be considered as a short-range ferromagnetic order. With increasing the Pb-doping concentration to x = 0.2, the area of these ferromagnetic clusters would be enlarged, which competes with the antiferromagnetic phase. However, this ferromagnetic phase is not strong enough to be representative of the whole the x = 0.2 compound. As a result, the γ exponent of the x = 0.2 sample still stays round the γ value of the 3D Ising model with the short-range ferromagnetic interaction. If further doping Pb into $La_{1-x}Pb_xMnO_3$ with x = 0.3, this introduces more Mn^{3+} concentration and enhance the ferromagnetic Mn^{3+}-Mn^{4+} interaction that dilutes strongly the antiferromagnetic interactions existing in $La_{0.7}Pb_{0.3}MnO_3$. In this case, the ferromagnetic clusters could coalesce to form a uniform ferromagnetic phase dominant in the whole compound $La_{0.7}Pb_{0.3}MnO_3$. Consequently, its critical exponents β and γ are close to those expected by the mean-field theory, and the compound exhibits the long-range ferromagnetic order.

4. CONCLUSION

We studied in detail the influence of Pb-doping on critical behavior of $La_{1-x}Pb_xMnO_3$ (x = 0.1, 0.2 and 0.3) in the vicinity of their T_C, based on analyzing *M-H* data. It was revealed that both samples exhibited the second-order phase transition, where the critical parameters were determined according to the modified Arrott method. Basically, the increase of the Pb-doping concentration in $La_{1-x}Pb_xMnO_3$ led to the enhancement in T_C, and also caused the remarkable change in the critical exponents β, γ and δ of the samples. We found that the short-range ferromagnetic order existing in the x = 0.1 and 0.2 samples, while the long-range ferromagnetic order is present in the x = 0.3 sample.

ACKNOWLEDGMENTS

Authors would like to thank Dr. S. G. Min for performance of magnetic measurements. This work was supported by the research grant of the Chungbuk National University in 2009.

REFERENCES

[1] Ghosh, K.; Lobb, C. J.; Greene, R. L.; Karabashev, S. G.; Shulyatev, D. A.; Arsenov, A. A., and Mukovskii, Y. *Phys. Rev. Lett.* 1998, *vol 81*, pp 4740-4743.

[2] Hong, C. S.; Kim, W. S., and Hur, N. H. *Phys. Rev. B* 2001, *vol 63*, pp 092504.

[3] Kim, D.; Revaz, B.; Zink, B. L.; Hellman, F.; Rhyne, J. J., and Mitchell, J. F. *Phys. Rev. Lett.* 2002, *vol 89*, pp 227202.

[4] Mira, J.; Rivsa, J.; Rivadulla, F.; Vazquez, C. V., and Quintela, M. A. L. *Phys. Rev. B* 1999, *vol 60*, pp 2998-3001.

[5] Mohan, C. V.; Seeger, M.; Kronmuller, H.; Murugaraj, P., and Maier, J. *J. Magn. Magn. Mater.* 1998, *vol 183*, pp 348-355.

[6] Nair, S.; Banerjee, A.; Narlikar, A. V.; Prabhakaran, D., and Boothroyd, A. T. *arXiv:cond-mat/0305598v1 [cond-mat.str-el]* 2003.

[7] Shin, H. S.; Lee, J. E.; Nam, Y. S.; Ju, H. L., and Park, C. W. *Solid State Commun.* 2001, *vol 118*, pp 377-380.

[8] Yang, J.; Lee, Y. P., and Li, Y. *J. Appl. Phys.* 2007, *vol 102*, pp 0333913.

[9] Yang, J.; Lee, Y. P., and Li, Y. *Phys. Rev. B* 2007, *vol 76*, pp 054442.

[10] Phan, T. L.; Min, S. G.; Phan, M. H.; Ha, N. D.; Chau, N., and Yu, S. C. *Phys. Stat. Sol. (b)* 2007, *vol 244*, pp 1109 - 1117.

[11] Zener, C. *Phys. Rev. B* 1951, *vol 82*, pp 403-405.

[12] Millis, A. J.; Shraiman, B. I., and Mueller, R. *Phys. Rev. Lett.* 1996, *vol 77*, pp 175.

[13] Souza, J. A.; Neumeier, J. J.; Bollinger, R. K.; Mcguire, B.; Dos Santos, C. A. M., and Terashita, H. *Phys. Rev. B* 2007, *vol 76*, pp 024407.

[14] Stanley, H. E. *Introduction to phase transitions and critical phenomena*; Oxford University Press, London, 197.

[15] Chau, N.; Nhat, H. N.; Luong, N. H.; Minh, D. L.; Tho, N. D., and Chau, N. N. *Physica B* 2003, *vol 327*, pp 270-278.
[16] Luo, X.; Sun, Y. P.; Wang, B.; Zhu, X. B.; Song, W. H.; Yang, Z. R., and Dai, J. M. *Solid State Commun.* 2009, *vol 149*, pp 810-813.
[17] Banerjee, S. K. *Phys. Lett.* 1964, *vol 12*, pp 16-19.
[18] Arrott, A. and Noakes, J. E. *Phys. Rev. Lett.* 1967, *vol 19*, pp 786-789.
[19] Arrott, A. *Phys. Rev.* 1957, *vol 108*, pp 1394-1396.
[20] Potter, C. D.; Swiatek, M.; Bader, S. D.; Argyriou, D. N.; Mitchell, J. F.; Miller, D. J.; Hinks, D. G., and Jorgensen, J. D. *Phys. Rev. B* 1998, *vol 57*, pp 72-75.
[21] Huang, K. *Statistical Mechanics*; Wiley, New York, 1987, 2nd Edition.
[22] Freitas, R. S.; Haetinger, C.; Pureur, P.; Alonso, J. A., and Ghivelder, L. *J. Magn. Magn. Mater.* 2001, *vol 226-230*, pp 569-571.
[23] Mira, J.; Rivas, J.; Vazquez, M.; Beneytez, J. M. G.; Arcas, J.; Sanchez, R. D., and Rodriguez, M. A. S. *Phys. Rev. B* 1999, *vol 59*, pp 123-126.
[24] Moutis, N.; Panagiotopoulos, I.; Pissas, M., and Niarchos, D. *Phys. Rev. B* 1999, *vol 59*, pp 1129 - 1133.
[25] Padmanabhan, B.; Bhat, H. L.; Elizabeth, S.; Röszler, S.; Röszler, U. K.; Dörr, K., and Müller, K. H. *Phys. Rev. B* 2007, *vol 75*, pp 024419.
[26] Sahana, M.; Rossler, U. K.; Ghosh, N.; Elizabeth, S.; Bhat, H. L.; Dorr, K.; Eckert, D.; Wolf, M., and Muller, K. H. *Phys. Rev. B* 2003, *vol 68*, pp 144408.
[27] Mukherjee, S.; Raychaudhuri, P., and Nigam, A. K. *Phys. Rev. B* 2000, *vol 61*, pp 8651-8653.
[28] Phan, T. L.; Min, S. G.; Yu, S. C., and Oh, S. K. *J. Magn. Magn. Mater.* 2006, *vol 304*, pp e778-e780.

In: Perovskites: Structure, Properties and Uses
Editor: Maxim Borowski, pp. 539-557
ISBN 978-1-61668-525-6

Chapter 15

REDDISH CERAMIC PIGMENTS WITH PEROVSKITE STRUCTURE

C. P. Piña
División de Estudios de Posgrado, Facultad de Química, México, D. F.

ABSTRACT

In the past (1980), the ceramic pigments, 51 pigments in all, were classified into 14 structures of industrial interest and these were classified into black, white and colored pigments. These structures are oxides, materials used in ceramic as pigments because of their greater stability in oxygen-containing ceramic systems. However, thanks to modern and more refined methods of scientific investigation, new structures, new pigments, new synthetic methods and new applications were also included. Among these we have the development of new red ceramic pigments as perovskite structure of formula $A^{3+}B^{3+}O_3$ as ferrites $LnFeO_3$ and chromium aluminates $LnAl_{1-x}Cr_xO_3$ (Ln, lanthanide). These lanthanides aluminates ceramic pigments have been synthesized by different methods and characterization studies were realized by X ray diffraction, SEM, UV-VIS spectra, etc. The properties and uses of these lanthanides are appropriate as ceramic pigments; nevertheless, new possibilities for these pigments are its use for luminescent coatings in a diversity of devices or lasers.

1. INTRODUCTION

Perovskite materials have many interesting and spectacular properties such as high temperature superconductors, magneto resistance, ferroelectricity, charge ordering, spin dependent transport, high thermo power, optical properties, etc. As well as their applications in catalyst electrodes in certain types of fuel cells, memory devices, etc.

In the case of optical properties, nowadays the use of perovskites materials is very important in ceramic pigments overcoat in the reddish range. The reddish pigments must have suitable properties of high thermal stability at high temperature and chemical stability but are

restricted to zircon structure of hematite or cadmium sulfoselenide and malayaite (type sphene). In the last years ceramic pigments of cerianite solid solutions and ferrites of lanthanides type perovskites have been synthesized. Moreover in the case of ferrites, type perovskites $LnFeO_3$ (Ln= La, Ho, Nd, Er and Sm) show a reddish dark color mainly in the presence of iron in the chemical formula and these ferrites are mostly used for their magnetic properties.

In the reddish perovskite $LnAlO_3$ (Ln = lanthanides) lattice the color is obtained substituting Al^{3+} for Cr^{3+} into AlO_6 octahedral of perovskite lattice forming solid solutions resulting in an orthorhombic or rhombohedra distortion. These pigments are very interesting because adequate tinting strength and purity of color can be obtained. These materials are oxides showing greater stability in oxygen containing ceramic systems and are resistant to high temperature and corrosive environment in the firing process. The specific properties of inorganic pigments result from an interplay of solid state properties, particle size and particle shape.

2. CERAMIC PIGMENTS CLASSIFICATION

Most of the materials used in ceramic as pigments are oxides because of their great stability in oxygen-containing ceramic systems. In the past, ceramic pigments have been classified as colorants into: black, white and colored pigments because pigments depend for its color and its ability to reflect or absorb light. There are classifications on the majority of oxide materials, which can be used as inorganic pigments according to their color. Black color pigments absorb all wavelengths of visible range, white color pigments show no absorption in the visible range and colored pigments absorb certain wavelengths of visible light. In the electromagnetic spectrum the visible light is placed between the infrared and ultraviolet in the range of 400 to 700 nm. [1, 2]

The oxides pigments were classified in 1982 by the Dry Color Manufacturers Association DCMA system based in a structural approach. These structures are classified in 14 categories and each category has a number of determined pigments, 51 in total, and each pigment has a classification number. Perovskite structure is not included in this classification.

The structures must have several principles, such as the nearest neighbor cation-anion distances determine the lattice energy of an ionic solid material at room temperature. The preferred coordination polyhedral of the anions surrounding each cation in ionic solid phases is determined usually by the radio of the ionic size of the cation to that of the anion. The structures of any combination of cations and anions are subject to the rules of electrostatic neutrality, meaning that the ions replacing each other must have the same charge and must be fairly similar in size, with a difference of a maximum of 15% in the radii of the ionic elements. This allows a wide range of cation substitution, in particular the case of transition elements or lanthanides; this may be done if the ionic sizes of the substituted ions are similar. In this way the color obtained can vary. Each structure can take doped elements, may be incorporated by the host crystal lattice and in this way alter the color or other physical properties of the pigment without changing its structure [2-5]

Among the reddish pigments included in the DCMA classification we can find:

Category III. Corundum-Hematite Structure, ½(Al_2O_3-Fe_2O_3)

This category contains 4 pigments: chrome alumina pink corundum $CrAlO_3$ (3-03-5 DCMA number), manganese alumina pink corundum $MnAlO_3$ (3-04-5 DMCA number), Hematite α-Fe_2O_3, Cr_2O_3 and Mn_2O_3 have the same corundum structure Al_2O_3 with approximately hexagonal close packed array of oxygen in which Al^{3+} ions occupy two thirds of the octahedral holes. The structure is complex because there is a sharing of vertices, edges and each octahedron FeO_6, CrO_6, MnO_6 or AlO_6, shares a face with another in the layer above or below. All these pigments have the same ABO_3 perovskite stochiometry with radium size 0.6 Å < $r_A \cong r_B$ < 0.9 Å. When corundum (Al_2O_3) has 0.1% of chrome oxide is a ruby natural gemstone. [2, 5]

Category XI. Rutile Cassiterite $TiSnO_4$

ABO_4 stoichiometry, contains 12 pigments Chrome tin orchid cassiterite (11-23-5 DCMA number). It is prepared with equimolecular quantities of titanium and TiO_2 and SnO_2 chromium doped and heated at high temperatures. [2, 4-6]

Category XII. Sphene: $CaSnSiO_5$

In this category there is one pigment only: tin pink sphene chromium doped $CaSnSiO_5$ (12-25-5 DCMA number). It is used as ceramic pigment, was prepared with calcium oxide, tin oxide and silica doped with chromium oxide at 1200°C for 24 hours on the formation of malayaite or calcium tin silicate $CaSnSiO_5$. The color of this pigment depends on the ratio of the concentration of chromium oxide to that of tin oxide. Generally when the ratio is 1:15 the resulting color is purple, 1:17-20, is red or maroon, and 1:25 is pink. The valences of Cr doped in sphene type ($CaTiSiO_5$-$CaSnSiO_5$), were directly related to the color of the pigments and were dependent on the Ti/Sn ratio in the mother crystals. In $CaSnSiO_5$, Cr^{4+} is detected causing a reddish purple color in 2mol% Cr doped. When it is Cr^{3+}, the color changes to red brown and finally to brown.[2, 6-9]

Category XIII. Spinel Structure AB_2O_4

Contains 19 pigments Chrome alumina pink spinel $CrAl_2O_4$, (13-32-5 DCMA number). The color is explained by the ligand field theory of the ion oxygen tetrahedral of the spinel lattice. This ligand field splits the originally equivalent d levels of the ion chromium and allows transitions between the split energy levels as a result of light absorption in the visible range. When there are transition elements in the structures as: V, Cr, Mn, Fe, Co, Ni, or Cu forming the structures or as doped the compounds have color.

The synthesis of spinel structure is realized by solid state with the oxides of Al^{3+} and Cr^{3+} at 1200°C for 48 hours. [2, 3-5]

Category XIV. Zircon Pink and Coral Colors ABO_4

Contains 3 pigments. The zircon, orthosilicate of zirconium contains SiO^{4-} ions, the cations of Zr^{4+}, occupying interstices which are surrounded by a number of eight O^{2-} ions number appropriate to their size. The iron zircon pink $ZrSiO_4$-Fe, (14-44-5 DCMA number), was patented in 1961 and made with zirconium oxide, silica, iron oxide and used a mixture of sodium fluoride, sodium chloride and sodium nitrate as a mineralize. The calcinations temperature was realized at 880-1000°C. This pigment has been studied by several authors but the formation of iron zircon pink pigment synthesized by ceramic method with 2% weight LiF as a mineralize indicates the formation of a substitution solid solution with about 1.5 mol% irons. In this compound the shades extend from coral to pink. The iron zircon pinks are more difficult to control and develop than other zircon colors, vanadium zircon blue, (14-42-2 DCMA number) and praseodymium zircon yellow (14-42-4 DCMA number). [2, 6-12, 14]

Encapsulation in Zircon $ZrSiO_4$

The last red pigment based on zircon lattice was the inclusion of red cadmium sulfoselenide Cd (S Se) crystals. The cadmium sulfoselenide pigments are not of an oxide system but orange, red and dark red colors are obtained. The shades result from varying the ratio of the concentration of cadmium sulfide to that of cadmium selenide. Due to the fact that these pigments cannot be used in higher temperature applications its pigments are incorporated in a zircon lattice during manufacture, imparting stability of zircon to the pigment. That means the pigment is encapsulated. [13]

Hematite α- Fe_2O_3

It is important to indicate that between natural inorganic pigments, hematite α- Fe_2O_3 red is included. In ancient times the chemical analysis of caves paintings indicates that hematite among the iron oxides, was used as pigment. This explains the use of these and other minerals to create cave paintings, decoration of ceramic objects for the preservation of the history of human existence. [2, 14]

3. LANTHANIDES

3.1. Perovskite Structure

The perovskite structure is any material with the same type of crystal structure as $CaTiO_3$. It was discovered in the Ural mountain of Russia by Gustav Rose in 1839 and is named after the Russian mineralogist, L. A. Perovski (1792-1856).

Perovskites oxides[1] have the general formula ABO_3. This structure is reported as pigment [15] but is not included in the DCMA system. Their idealized structure is cubic, it is found in only a limited number of compounds. Each A of the formula, corresponds to an ion of large size and is 12-coordinated by oxygen and each B of the formula corresponds to an ion of small size and is 6-coordinated by oxygen. Each oxygen is linked to four A ions and two B ions. The large A ions are comparable in size with oxygen ions forming a close packing array and B small ions have a radius appropriate to octahedral coordination. See figure.

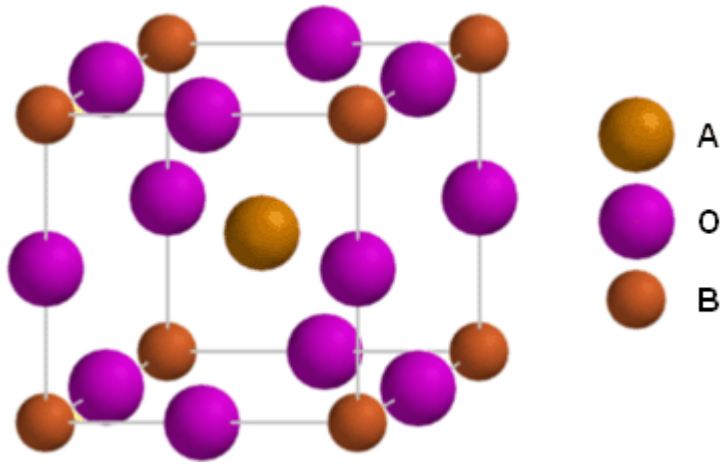

Ideally, there is a relationship between the radii of the ions. That is:

(1) $r_A + r_O = \mathbf{t} \cdot \sqrt{2} \cdot (r_B + r_O)$

(2) $\mathbf{t} = r_A + r_O / \sqrt{2} \cdot (r_B + r_O)$

There are a few cases of the cubic ideal structure: **t** is a Goldschmidt tolerance factor and in the cubic ideal perovskite must be 1, but the approximated limits are 0.7 – 1.0. For oxides the radii of the A and B ions must lie within the ranges 1.0-1.4Å and 0.45-0.75Å, In the lanthanides the radii trivalent found in the range from Cerium 1.07Å to Samarium1.00Å. The rest of radii trivalent lanthanides are in the range from Europium 0.98 Å to Lutetium 0.85 Å, all radii comparable in size with calcium ion radii 1.00Å, thus the lanthanides correspond to A ion of large size. In aluminates and ferrites the Al^{3+} and Fe^{3+} ions are of small size, corresponding to B ion, having 0.51Å and 0.64Å, respectively. This means that in the perovskites oxides A and B ions are between the indicated ranges according to the tolerance factor.

The most common perovskites have distortions derived from small displacements of the atoms. In perovskites structures there are distortions in orthorhombic and rhombohedra (Hex) symmetries; in particular there are rare distorted symmetries in the tetragonal, monoclinic and triclinic perovskite structures. In addition the number of these structures is very large and

[1] There are perovskite structures of: halides, hydrides, carbides, nitrides.

some compounds show polymorphism capable of existing in two or more forms with different crystal structures. [3-5]

It is important to remark that among oxides of perovskite structure, A and B ions besides having appropriate radii must confer electrical neutrality, that means that pairs of cations must have 1^+ and 5^+ ($KNbO_3$), 2^+ and 4^+ ($CaCeO_3$) and 3^+ and 3^+ ($LaFeO_3$) oxidation states. The last oxides correspond to lanthanides aluminates and lanthanides ferrites.

In some cases the perovskite structure is more complicated due to the fact that some of the unoccupied A sites or to the fact that there are non-stoichiometry ($ABO_{3-\delta}$). [16]

The perovskite structure is also found in a number of oxides in which A and or B sites are not all occupied by atoms of the same kind; vg. $AA'BO_3$ ($K_{0.5}La_{0.5}TiO_3$), $ABB'O_3$ ($SrGa_{05}Nb_{0.5}O_3$), $AA'BB'O_3$ $(BaK)(TiNb)O_3$. These compounds are called mixed oxides.

There have been reported double perovskite lanthanides structure $2(ABO_3)$ or ($A_2B_2O_6$) and $A_2BB'O_6$ in which two kinds of ions are found in B sites in alternating octahedral Ba_2LnSbO_6 and Sr_2LnSbO_6 (Ln = Ho, Dy, Gd). [17] Other oxides consisting of a single cation in different oxidation states are classified as complex oxides.

Due to the diversity of this complex oxides resulting from a thorough selection of the A and B ions, their fractions, ionic sizes, valences, spin states and orbital ordering, as well as the oxygen content and vacancy ordering, the distortions of the ideal cubic symmetry. These compounds show a large number of different properties: electronic, magnetic, ferroelectric, thermoelectric, optics mixed conducting. The best known examples are triple perovskites as the spectacular 123 high temperature superconducting cuprates as $LnBa_2Cu_3O_{7-\delta}$. These present Cu ions with different oxidation states and oxygen vacancies. [16, 18, 26]

3.2. Optical Properties

3.2.1. Reddish Perovskites

Colorants may be pigments or dyes, a colored pigment is opaque and insoluble a dye is colored and transparent and often soluble. Pigments are solid particles with solid state properties resulting from structure, chemical composition, the color, stability as heat, light and insolubility in solvents and binders, etc. For their chemical composition the pigments may be divided in two categories, organic and inorganic. In ceramic usually concerning to inorganic pigments. The particle size, distribution and shape including the hue and the light scattering are very important. If a pigment is red, it reflects radiation of 630-700 nm and absorbs the rest.

The need to developed ceramic pigments with great stability resulted in a thorough research during the 1960s. Some lanthanides ferrites were reported for their magnetic properties and not as pigments [19], for this reason the zircon have gained increasing acceptance in the industry for their resistance under high temperatures and corrosive atmosphere during firing. The zircon ($Zr\ Si\ O_4$) was discovered and patented in 1948 as ceramic pigment. In the case of red zircon iron there is a solid solution formation. [10]

A number of new high temperature pigments used in ceramic has led the search for the perovskite pigments of lanthanides. This system has been first developed in 1984-1986 in the red perovskite pigments lanthanides and recently in 2000 red, reddish and pink color

pigments with perovskite structure of $LnAlO_3$ (Ln= lanthanide) chromium doped have been reported. [20]

Chromium doped yttrium aluminates perovskite type have been reported. In 2006s red perovskite ceramic pigments have been developed efficiently in different ceramic applications. [21]

In 2005 and 2008 lanthanides ferrites perovskite structure $LnFeO_3$ (Ln = La, Ho) were synthesized by precursor and ceramic methods and reported as reddish ceramic pigments. [22, 23]

In 2000s Jansen and Letschert demonstrated that solid solutions of the perovskites of oxy-nitrides: $CaTaO_2N$ and $LaTaON_2$ constitute promising pigments in the yellow-red range without toxic metals. [25]

The preparation of these perovskites system was oriented in the study of other optical properties such as: red photoluminescence emitted by crystalline $NdAlO_3$ or photoluminescence of homogeneous dispersion of $NdAlO_3$ nanocrystals in an Al_2O_3 matrix synthesized by sol gel process. Fast ultraviolet emission was observed in $NdAlO_3$ and $SmAlO_3$ and strong photoluminescence was observed in $LaAlO_3$ and $YAlO_3$ crystals in visible and ultraviolet wavelength regions. [26-28]

The combination of luminescence and electrical conductivity in perovskite oxides make them promising materials for optical, electronic and structural application, for novel optoelectronic devices, window materials and a variety of lamps, for solid state lasers with fiber optics. In communication silica fluoride doped Eu^{3+} up to date is very important commercially and has been exploited. $NdAlO_3$ films are useful insulating dielectric for microelectronic applications. Superconductor's layers grow by sputtering over neodymium aluminates layers, they are also used for the substrates for the epitaxial growth of various perovskite type films such as ferroelectrics, piezoelectric and magneto resistance oxides. Other perovskites were synthesized as catalysts precursors and are being incorporated into automobile catalytic converters. The perovskite $GdAlO_3$ is a material for the neutron absorption and control rod applications [26, 28, 29, 32]

3.2.2. Fluorite Structure

The fluorite structure of the red pigment of praseodymium doped cerianite CeO_2 was known in 1960, the cerianite fluorite structure was patented in France and published in the years 1900-2000 as cerianite doped with Pr^{4+} as red ceramic pigment. [30]

Recently, in 2001 cerianite doped with lanthanides has been reported because of the low toxicity red pigments, as well as Pr with Tb, Eu, Pr-Mo (reddish color), Pr-Fe, (orange color) average size of 300nm and also doped with chromium or indium. [10]

Cerianite doped Pr is synthesized at high temperatures 1300-1500° C for 15-48 hours to obtain the red color but when it is applied on ceramic the color disappears. [31]

In 1971 rare earths were used in fluorescent lamps. Red-Y_2O_3-Eu^{+3}, blue-$BaMg_2Al_{16}O_{27}$-Eu^{2+}, green-(Ce-Tb)$MgAl_{11}O_{19}$ are deposited on lamps walls as fine particles. The research on photoluminescence materials doped lanthanides is actually an area of great demand.

4. METHODS USED IN PEROVSKITE SYNTHESIS

The scientific interest on the pigments used in the ceramic industry overcoat in reddish ceramic pigments has developed a series of possibilities in new systems of preparation of $LnFeO_3$ and $LnAlO_3$ perovskite lanthanides systems with a large and spectacular application. The selected synthesis depends on the knowledge of: reactivity of solids, crystalline chemistry and the necessary tools as reactants, material laboratory, equipment and the objective in the preparation of known compounds with specific properties, unknown or new compounds.

4.1. Conventional Method

In solid state chemistry the conventional method is denominated ceramic method where solids are mixed continuously, in general oxides. These were submitted afterwards to various thermal processes, generally at high temperatures in ranges 800°C, 1000°C, 1300°C, 1400°C, 1500°C. The iron zircon pink was patented in 1961 and made with zirconium oxide, silica, iron oxide and a mixture of sodium fluoride, sodium chloride and sodium nitrate was used as a mineralize. The calcinations temperature was realized at 880-1000°C. The iron zircon pinks are more difficult to control and develop than other zircon colors. The iron zircon pigments provide pink and coral colors. This pigment has been studied by several authors but the formation of iron zircon pink pigment synthesized by the ceramic method with 2% weight LiF as a mineralize, indicate the formation of substitution solid solution with about 1.5mol% iron. [3, 3b, 4, 8] without to forget: tri perovskites (superconductors 123) [18], layered perovskites with titanium and lanthanides [4].

Nowadays lanthanum ferrites and chromium doped lanthanide aluminates with perovskite structure are used as ceramic pigments because they have colorimetric properties, high thermal stability, fine particle size and chemical resistance. Also, the ferrites have interesting magnetic properties and the aluminates are materials having photoluminescence properties.

4.2. Precursor Method

This method has been realized for synthesis of perovskite solids. Precursor compounds with anions as oxalates, acetates, cyanides, nitrates, hydroxides have been employed as precursors for the perovskite synthesis. Examples are: $LaCoO_3$ from $LaCo(CN)_6.5H_2O$ and $LaNiO_3$ and $NdNiO_3$ from tri hydroxide of lanthanide in both examples can be a substitution of cations (lanthanides or transition elements), $LnFeO_3$, (Ln = Er, Sm, Nd). Sometimes in this method, it is necessary to find a suitable precursor compound for the synthesis of the desired composition because it is limited by the stoichiometric ratio of cations in the precursor and in the final oxide. [32, 33, 44]

4.3. Co Precipitation Method

This method is a precipitation together with two or more different compounds. For the preparation of perovskites, co precipitation as hydroxides, carbonates, oxalates, citric acid have been used. The precipitating agents were KOH, NH_4OH for hydroxides, K_2CO_3, NH_4CO_3 for carbonates, oxalic acid $H_2C_2O_4$ or ammonium oxalate $(NH_4)_2C_2O_4$ for the co-precipitation of oxalates. The carbonates and oxalates required higher temperatures than the hydroxides. The presence of alkaline ions could contaminate the product and must be eliminated. The presence of ion ammonium could form ammonium complexes with transition ions. Citric acid was employed for preparing $LaCrO_3$, $LnAlO_3$ (Ln = Y, La Sm) and $LaMO_3$ (M = V, Cr, Mn, Fe, Co Ni)

4.4. Sol Gel Synthesis

This method is useful in the preparation of perovskite type oxides and other complex oxides as they allow to obtain pure phase products and to control their stoichiometry. Neodymium aluminates $NdAlO_3$ and gadolinium strontium aluminates $Gd_{1-X}Sr_XAlO_3$ were synthesized [26, 27, 34-36]

4.5. Ion Exchange Method

Reported by proton exchange of $LiNbO_3$ to give $HNdO_3$ where a structural transformation of the rhombohedra $LiNbO_3$ structure to the cubic $HNdO_3$ structure occurs. [37]

4.6. Spray and Freeze Method

Procedure of spray and freeze techniques for the preparation of Cr-doped sphene pigments from an aqueous solution of precursors salts followed by calcinations. Chromium doped $CaSnSiO_5$ pigments, developed pink hues. In Cr-doped $CaTiSiO_5$ have brown colorations due to the combination of Cr (III) and Cr (IV) cations dissolved in the sphene matrix. [38]

4.7. Alkali Flux Method

This method is employed for the synthesis of solids using alkaline compounds as solid fluxes or in aqueous alkali solutions. Perovskites of $K_xBa_{1-x}BiO_3$ and spinels of lanthanides have been synthesized.

4.8. Nano Explosion Synthesis

This method was used for the preparation of nanoparticles with high surface energy and chemical activity. In this procedure sol gel process, coprecipitation, micellar nanoreactor, hydrothermal synthesis, sonochemically and/or microwave and combustion synthesis have been included [39]

4.9. Combustion Synthesis

This method was used for the preparation of $NdAlO_3$. When the sample is irradiated by unfocused ultraviolet pulsed laser light red light visible is emitted. [27]

5. Study of Ferrites and Chromium Doped Aluminates Reddish Ceramic Pigments with Perovskite Structure

The advances in most synthesis of lanthanides new solids have been realized for the ceramic method and the precursor method; for this reason these methods remain very important for solid state chemistry. Examples of studies realized using these methods are ferrites and lanthanides aluminates perovskites presented here below.

1. Synthesis

1.1. Ceramic Method of Ferrites: $LnFeO_3$ (Ln = La, Ho)

The raw materials used in the synthesis of $LnFeO_3$ (Ln = La, Ho) were Ln_2O_3 oxides Aldrich and Fe_2O_3 Baker R.A. This ferrites were prepared mixing the starting materials in stoichiometric relations 1:1 in an agate mortar, after were fired in an electric furnace at 900°C, 950°C by 20h each one and 1000°C, in the case of lanthanum ferrite by 24h and in the case of holmium ferrite by 30h. $LnFeO_3$ (Ln = Nd, Sm, Er) were synthesized by the precursor method. (See forward: Precursor method)

1.2. Precursor Method of Ferrites: $LnFeO_3$ (Ln = Nd, Sm, Er)

The $LnFeO_3$ (Ln = Nd, Sm, Er) were synthesized using Ln $(NO_3)_3.H_2On$, Rhone Poulenc. They were heated to dryness in a stove at 110°C; once dried they were weighed and dissolved in deionized water and gauged to 100ml. Aliquots of each one were taken and the stoichiometric amounts of $FeCl_3.6H_2O$ R.A. Baker, were added in a 1:1 ratio each of them. These samples were put in a platinum crucible and heated to complete dryness in an electric plate. The dry samples were fired in an electric furnace at 800°C, 1000°C and finally at 1300°C for 12 hours, every time with intermittent grinding in an agate mortar in each of the thermal processes.

1.3. Ceramic Method of Chromium Doped Lanthanide Aluminates: Ln $Al_{0.93}Cr_{0.07}O_3$ (Ln = Nd, Dy, Ho, Er)

The raw materials used in the synthesis of Ln $Al_{0.93}Cr_{0.07}O_3$ (Ln = Nd**,** Dy, Ho, Er) were: Nd_2O_3 and Er_2O_3, Rhone Poulenc, Dy_2O_3 and Ho_2O_3 Apl. Eng. Materials Inc., $Al(NO_3)_3.9H_2O$ E. Merck, Cr_2O_3 J.T.Baker and LiF Aldrich

The lanthanides perovskites have been prepared by mixing the starting materials in relations according to the chemical formula $LnAl_{0.93}Cr_{0.07}O_3$ and 5% LiF as mineralize, in an agate mortar. These samples were put in the platinum crucibles and heated to complete dryness in an electric plate, afterwards were fired in an electric furnace at 900°C, 1000°C by 24 h each one and at 1300°C for 48 h with grinding intermitting.

2. Characterization

The characterization of ferrites and aluminates was carried out by X-ray diffraction powders in a Siemens D5000 diffractometer using Cu, Kα radiation (λ = 1.5406Å) and a Ni filter in a 5° (2θ) 85° range. Details of the microstructure and morphology were done by a (SEM) scanning electron microscope JEOL model JSM-5900LV. Energy Dispersive X-ray Analysis (EDX) shows the microanalysis of the elements in the samples. The UV-Vis spectra were realized in a Cary-5000 spectrophotometer.

3. Results and Discussion

The examination of X-ray diffractograms shows that the perovskites structure $LnFeO_3$ (Ln = La, Nd, Sm, Ho, Er) and $LnAl_{0.93}Cr_{0.07}O_3$ (Ln = Nd, Dy, Ho and Er) have orthorhombic symmetry and the space group is *Pbnm,* which is a distorted perovskite where each iron remains essentially octahedral. Different opinion is that perovskites with larger tolerance factors have rhombohedra phases (Pr, Nd). In this work this occurs only in $NdAl_{0.93}Cr_{0.07}O_3$ with rhombohedra (Hex) symmetry but non in neodymium ferrite and praseodymium aluminates. The incorporation of the different lanthanides is related to the lanthanide contraction, decrease of the ionic radium and the tolerance factor; lanthanides with smaller tolerance factors have orthorhombic phases, this changes the symmetry lattice and the distortion increases. See Figures 1a, 1b.

The results from the observation of SEM micrographs reveal that the morphology of the pigments with agglomerates: such as flakes, in the case of holmium ferrite, the particles are approximately from 0.5 μm to 1.0 μm in size. Neodymium, samarium and erbium ferrites are agglomerates like globules of approximately 1.0 μm, and in the case of erbium ferrite approximately 2.0 μm. See Figure 2a.

The chromium doped lanthanide aluminates micrographs of Pr, Nd**,** Dy, Ho, and Er by SEM show the same type of agglomerates like globules of 1.0 μm, to 2.0 μm in size. The particle size, particle shape and particle morphology are very near between ferrites and aluminates and the materials are appropriate as pigments used in ceramic materials. See figure 2b.

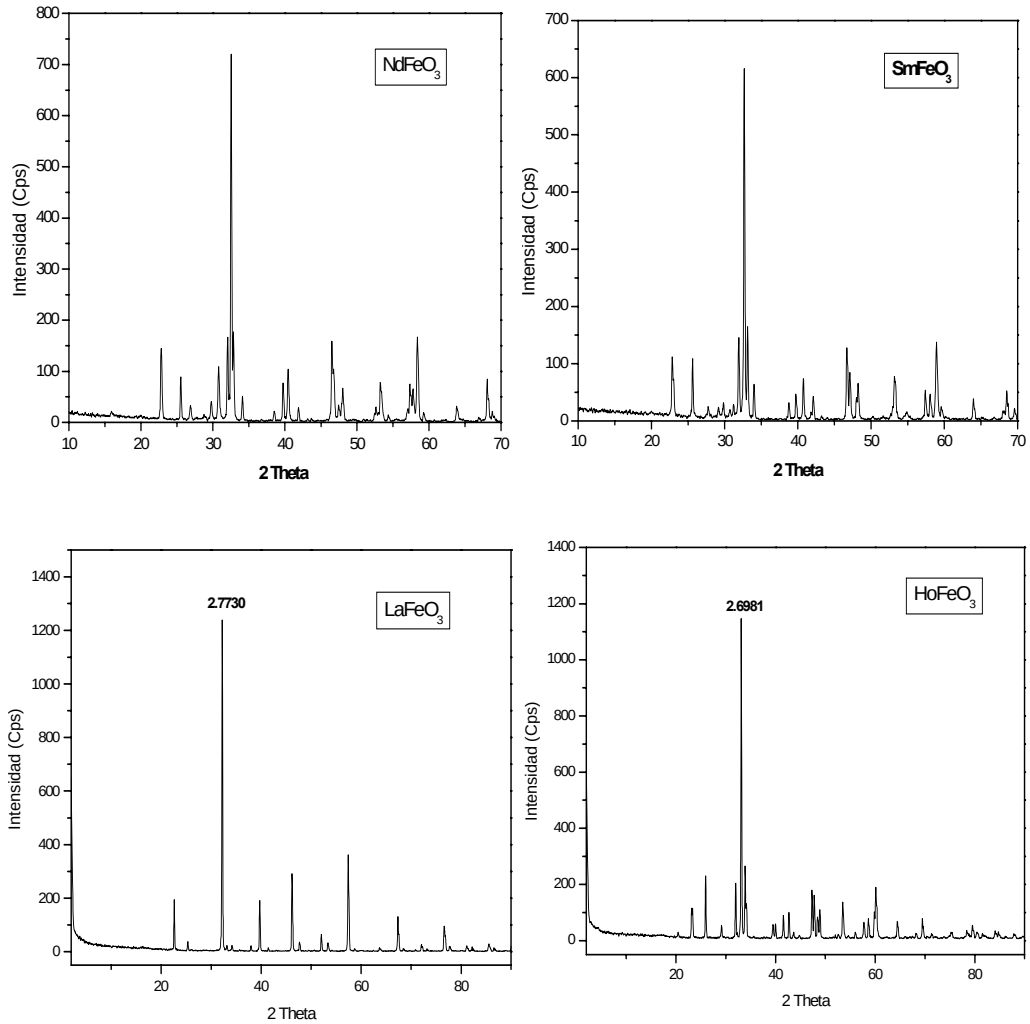

Figure 1a. X-ray diffraction patterns of $LnFeO_3$ (Ln= Nd, Sm, La, Ho)

All SEM micrographs have the same morphology and similar particle sizes in the range of 1-2 μm.

The reddish pigments with perovskite structure of type doped chromium lanthanides aluminates $LnAl_{1-X}Cr_XO_3$ is when Al^{3+} is substituted by Cr^{3+} occupying octahedral sites in the structure forming solid solution, because Cr^{3+} radium is 12.3% in size bigger than the size of Al^{3+}, (0.63Å) and (0.51Å) respectively. This makes that the Cr-O distance decreases and the Al-O distance and the perovskite distortion increase.

The UV-VIS of chromium doped lanthanide aluminates of Pr, Nd**,** Dy, Ho, and Er show that octahedral absorption in the visible range Cr^{+3} present two absorption bands due to the $^4A_{2g} \rightarrow {}^4T_{1g}$ in blue range and $^4A_{2g} \rightarrow {}^4T_{2g}$ in yellow range transitions. Absorption bands are displaced towards higher energies thus the two transitions forms a broad absorption green band region and consequently there is red reflection. See Figure 3b.

The reddish color variation, in the case of ferrites $LnFeO_3$ (Ln = La, Nd, Sm, Ho, Er)), is very dark in Pr, in Nd is a bright red color, in the rest is only reddish. See figure 3a.

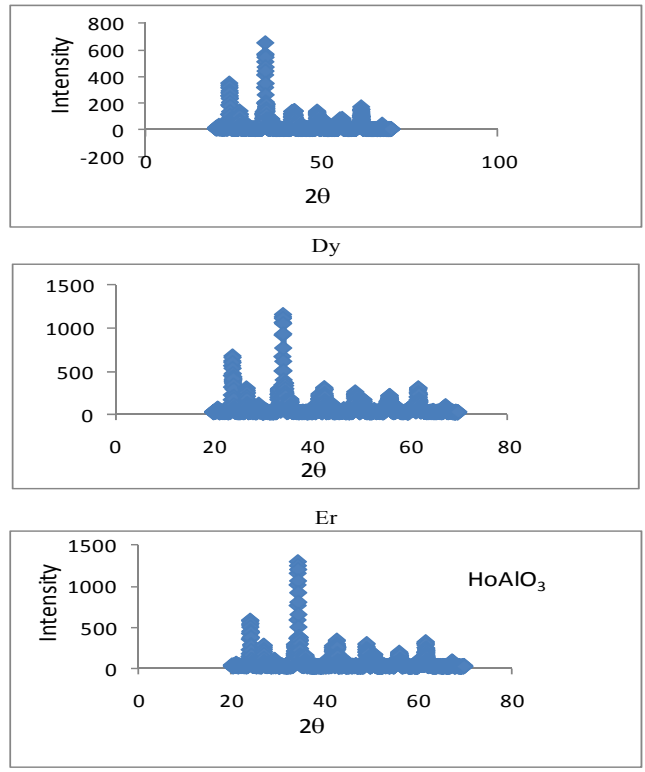

Figure 1b. X-ray diffraction patterns of $LnAl_{0.93}Cr_{0.07}O_3$ (Ln= Dy, Er, Ho)

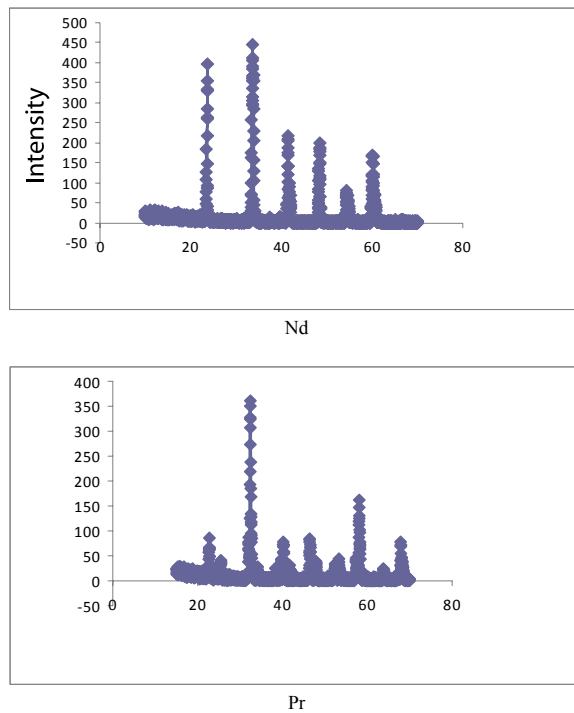

Figure 1b. X-ray diffraction patterns of Ln $Al_{0.93}Cr_{0.07}O_3$ (Ln = Nd, Pr)

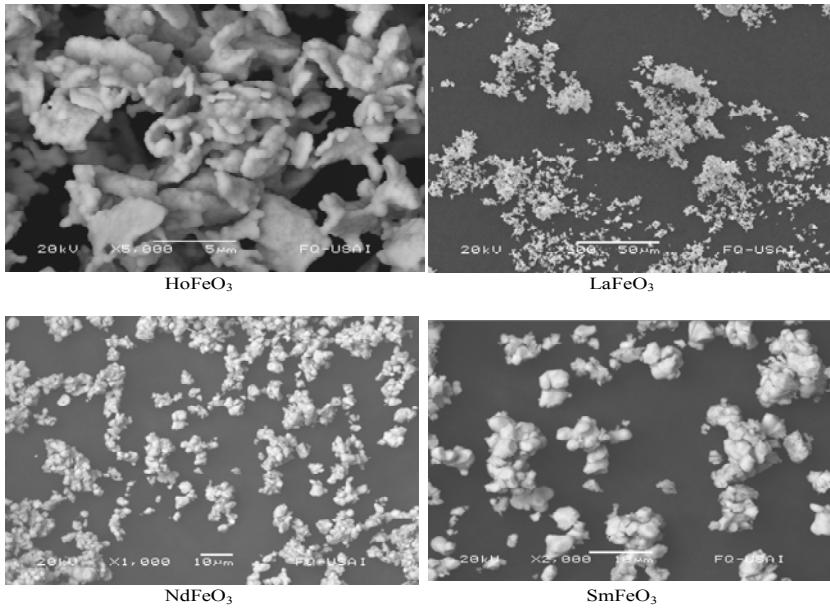

$HoFeO_3$ $LaFeO_3$

$NdFeO_3$ $SmFeO_3$

Figure 2a. Microstructures of $LnFeO_3$ (Ln = Ho, La, Nd, Pr, Sm).

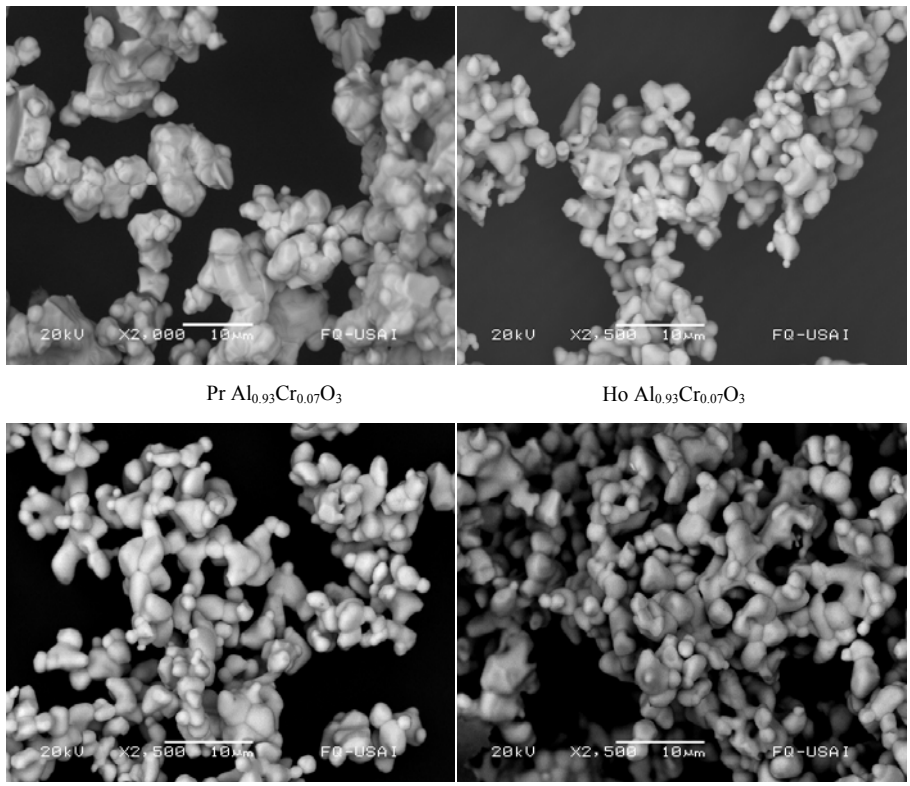

Pr $Al_{0.93}Cr_{0.07}O_3$ Ho $Al_{0.93}Cr_{0.07}O_3$

Dy $Al_{0.93}Cr_{0.07}O_3$ Er $Al_{0.93}Cr_{0.07}O_3$

Figure 2b. Microstructure of $LnAl_{0.93}Cr_{0.07}O_3$ (Ln = Pr, Ho, Dy, Er)

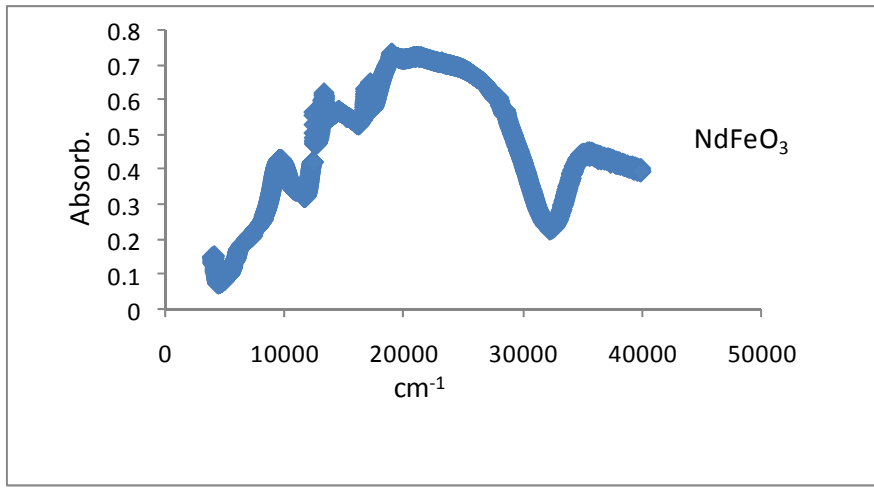

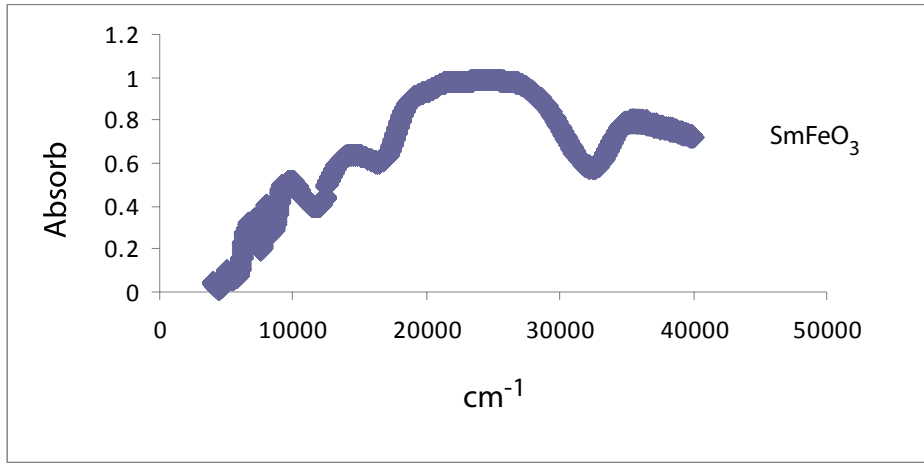

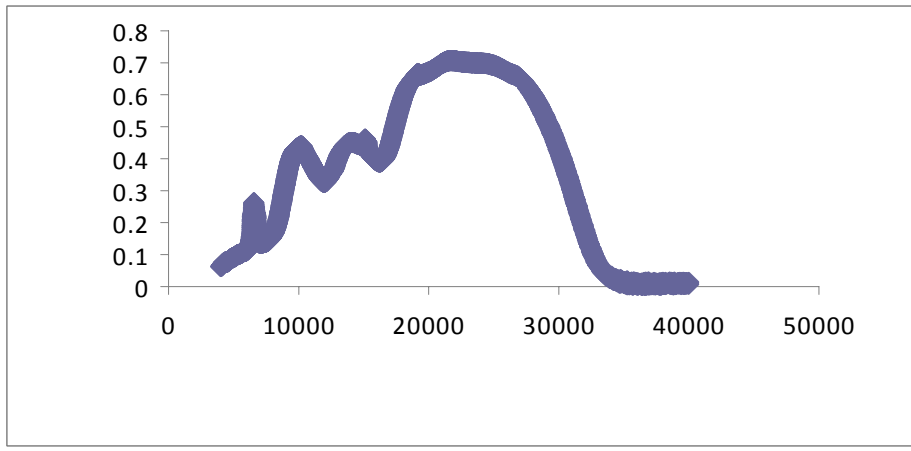

Figure 3a. UV-VIS of $LnFeO_3$ (Ln = Nd, Sm, Er)

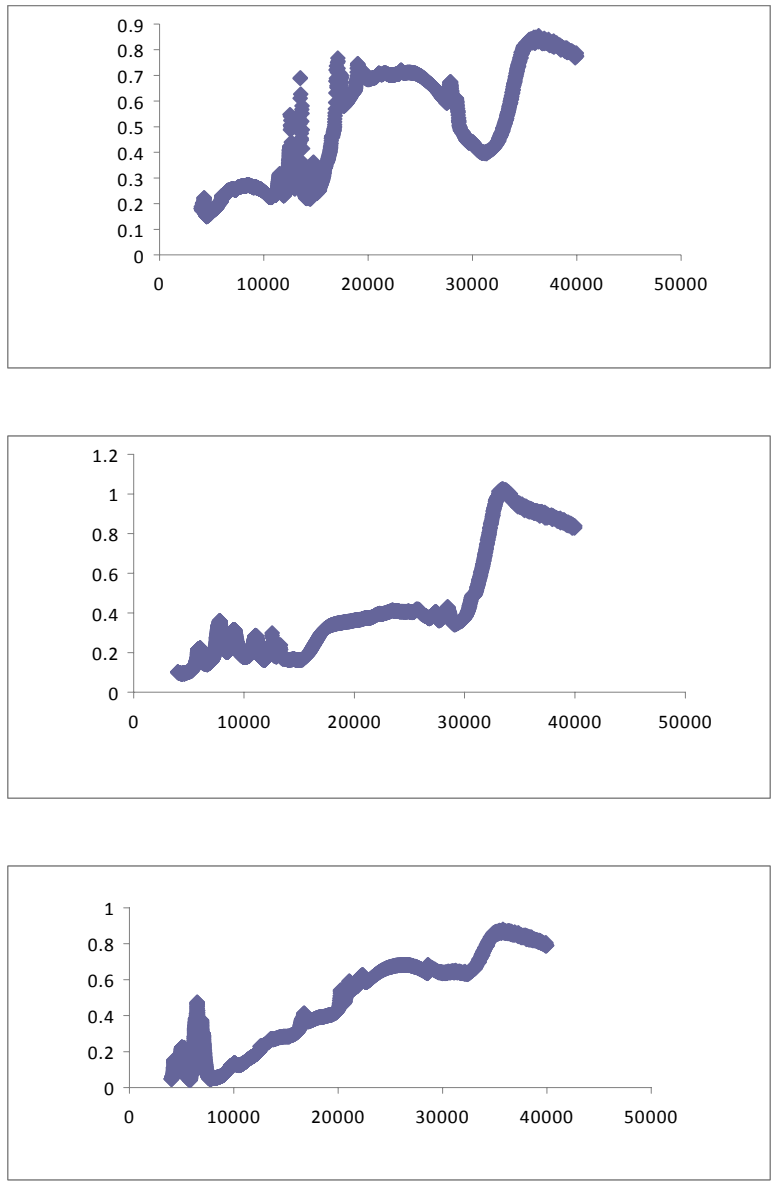

Figure 3b.UV-VIS of $LnAl_{0.93}Cr_{0.07}O_3$ (Ln = Nd, Ho, Dy)

In the chromium doped lanthanide aluminates Ln $Al_{0.93}Cr_{0.07}O_3$ (Ln = Nd**,** Dy, Ho, Er), the reddish color variation is red in Nd, pink shades lighter in color from Dy to Er.

That means that the development of the red color is related to different phenomena, between this: the change of the Cr-O distance of the crystal field, the symmetry that increases from orthorhombic phase (Er) to rhombohedra (Nd) and the lanthanides ions types revealed their influence associated to the variation of the color shades. [39, 40, 41, 42, 43]

Figures 4a, 4b, shows energy dispersive X-ray spectrum of the ferrites and aluminates of lanthanides compounds to confirm the assumptions made from the X-ray diffraction powder results.

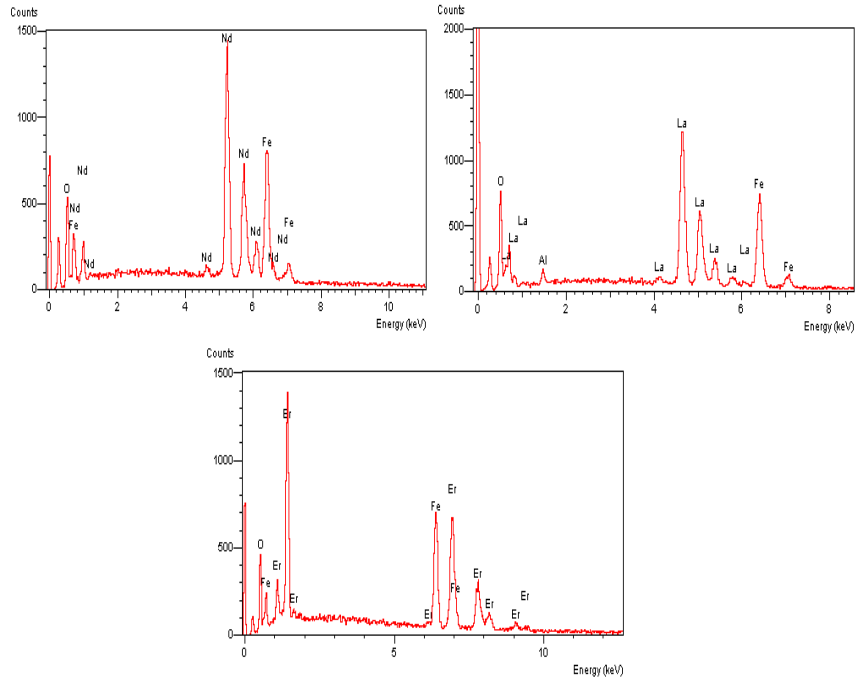

Figure 4a. EDX of $LnFeO_3$ (Ln = Nd, La, Er).

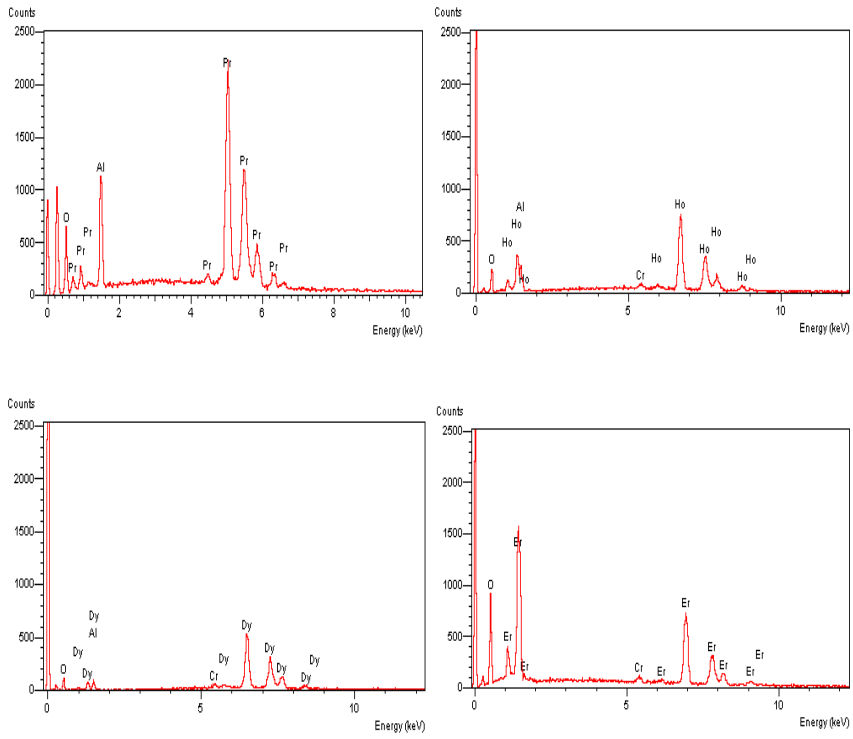

Figure 4b. E DX of $LnAl_{0.93}Cr_{0.07}O_3$ (Ln = Pr, Ho, Dy, Er)

REFERENCES

[1] Streatfield, G. R. *Trans.Br.Ceram.Soc.*1990, *89*, No.5, 177-180.

[2] Burgyan, A.; Eppler, R.A. *Am. Ceram. Soc. Bulletin*. 1983, *62*, No.9, 1001-1003.

[3] Evans, R. C. *An Introduction to Crystal Chemistry*, Cambridge, Univ. Press, London N. W., 1966, 1676-170

[4] West, A. R. *Solid State Chemistry*, John Wiley & Sons, Chichester, 1985.

[5] Wells, Wells, *Structural Inorganic Chemistry*. Oxford University Press *1975*, London, 483, 484, 486.

[6] 6. Eppler, R. A. *J. of the Am. Ceram. Soc*. 1976, No. 9-10, 455.

[7] Masahiro, K.; Hidero, U.; Minoru, T., *J. of the Ceram. Soc. Soc. of Japan* 200, *108,* No. 1257, 478-481

[8] Harriet, G. F. *J. of Chem. Educ*. 1981, *58* No. 4, 291-294.

[9] Kato, M.; Unuma H.; and Takahashi, M., *Jour. of the Ceramic Soc. of Japan,* 2000, *108*, No.1257, 478-481.

[10] Eppler R. A. *J. of the Am. Ceram. Soc. 53,* No. 8.

[11] Eppler R. A. *Am. Ceram. Soc. Bull*. 1977, *56*, No. 2, 213-2118.

[12] Carreto, E.; Piña, C.; Arriola, H.; Barahona, C.; Nava, N.; Castaño, V. *J. of Radioanal. and Nucl. Chem.* 2001, *250* No. 3, 453-458.

[13] Rincón, J.Ma.; Carda, J.; Alarcón, J., Nuevos productos y tecnologías de esmaltes y pigmentos cerámicos, Faenza, Editrice Ibérica, S. L.Madrid, 1992, 171-180.

[14] García, A.; Llusar, M.; Sorlí, S.; Calbo, J.; Ten A, M. A.; Monrós G., *Tour. of the European Ceramic Sopc*. 2003, 23, 11, 1829-1838.

[15] Piña, P. C., Pigmentos cerámicos, *Cuadernos de Posgrado 5, Química Inorgánica II*, 1982, 107-124.

[16] Dabrowski, B.; Kolesnik, S.; Chmaissem, O.; Suescun, L.; Mais, J., *Acta Phys. Polonica A*. 2007, *111* No.1, 15-24.

[17] Karunadasa, H. ; Huang, Q.; Ueland, B.G.; Schiffer, P.; Cava, R.J.*PNAS* 2003, *100* No.14, 8097-8102.

[18] Bednorz, J. G. and Muller, K. A. *ZPhys B. Condens. Matter*, 1986, *64*, 189.

[19] Eibschütz, M.; Shtrikman, S. Treces, D., *Physical Review* 1967, *156*, No.2, 562-577.

[20] Kato, M.; Takahashi, M., 2004, *J. of Material Science Letters* 2004, *20* No.5, 413-414.

[21] Matteucci, F.; Lepri, N.; Dondi, M.; Cruciani, G.; Baldi, G. Boschi, A. O.,*Advances in applies ceramics* 2006, *105* No.2, 99-106.

[22] Cunha, M.; Melo, D.; *Martinelli, A.; Melo. M.; Ma*ia, I; *Cun*ha, S., *Dyes Pigm. Elsevier* 2005, *65*, 11-14.

[23] Piña, P.; Buentello, H.; Arriola, H.; Nava E., *Hyperfine Interact* 2008, *185*, 173-177.

[24] Dohnalova, Z.; Sulcova, P.; Trojan, M. *J. of Thermal Analysis and Calorimetry*. 2008, *91*, No. 2, 559-563.

[25] Jansen, M.; Letschert, H.P., *Nature* 2000, 404, 980-082.

[26] Mathur, S.; Veith, M.; Shen, H.; Hufner, S.; Jilavi M.H., *Chem Mater*. 2002, *14* (2), 568-582.

[27] Maciel, G.; Rakov, N.; Zanon, R.A.; Fellows, C.E.; Guimaraes, R.B.; Rodríguez, J.J., *Chemical Physical Letters* 2008, *465* (4-6), 258-260.

[28] Yutaka, K.; Akio, Y.; Elichi, H.; Tsuyoshi, K.; Yoshinori, T.; Yoshihiro, T.,Hirofumi, K., Proceedings *Inorganic Optical Materials II* 2000, *4102*, 144-151.
[29] Rauch, W.; Benher, H.; Gieres, G.; Sipos, B.; Seeboeck, R. J.; Kerner, R.; Soelkner, G.; Gornik, E., *Applied Phys. Letters* 1992, *60* No.26, 3304-3306.
[30] Kalarical, J.; Cheruvathoor, P.; Balachandran, U.; Ramasami T., *Solar energy Mat. and solar cells*, 2008, *92* No.11, 1462-1467.
[31] García, A.; Llusar, M.; Calbo, J.; Tena, M.A., Monros, G., *Green Chemistry* 2001, *3*, 238-242.
[32] Goldwasser, M.; Rivas, M.; Pietri, E. ; Pérez-Zurita, M.; Cubeiro, M.; Gingembre L.; Leclercq, L.; Leclercq, G., *Applied Catalysis* 2003, *255*, No.1, 45-57
[33] Lepe, F. J.; Fernández, J.U.; Mestres, L.; Martínez M.L., *Journal of Powders Sources* 2005, *151*, 74-78.
[34] Feldhoff A.; Arnold, M.; Martynczuk, J.; Gesing, Th. M.; Wang, H., et al. *Solid State Sciences* 2008, *10*, 689-701.
[35] Chinie, A.M.; Stefan, A.; Georgescu, S., *Romanian Reports in Physic* 2005, *57*, No.3, 412-417.
[36] Cizauskaite, S.; Reichlova, V.; Nenartaviciene, G.; Beganskiene, A.; Pinkas, J.; Kareiva, A., et al. *Materials Science Poland* 2007, *25*, No. 3, 755- 7--.
[37] Rice, C.; Jackel, J. L., *Jour. of Solid State Chemistry* 1982, *41*, 308-314..
[38] Stoyanova, T. L.; Matteucci, F.; Costa, A.; Dondi, M.; Carda, J. *Powder Technology* 2009, 193 No.1, 1-5.
[39] Valsykiv, O.; Sakka, Y., Skorokhod V.V. *J. of the European Ceram. Soc*. 2006, *04*, 157 19.
[40] Pavlov, R.; Blasco, B.; Cordoncillo, E.; Escribano, P.; Carda, J. B., *Boletín de la Sociedad Española de Cerámica y Vidrio* 2000, *39*, No. 5, 609-616.
[41] Cruciani, G.; Matteucci, F.; Dondi, M.; Baldi, G.; Barzanti A., *Zeitschrift fur Kristallographie* 2005, *220* No.11, 930-937
[42] Matteucci, F.; Dondi, M; Cruciani, G; Baldi, G.; Barzanti, A., *Engineering Materials* 2004, 264-268.
[43] Dalziel, J. *Journal of the Chemical Society* 1959, 1993-1998.
[44] Bucko, M.; Stobierska, E.; Lis, J.; Gubernat, A. *Materialy Ceramiczne* 2008, *60*(1), 20-27.

INDEX

A

B

C

D

E

F

G

H

I

J

K

L

M

N

O

P

Q

R

S

T

U

V

W

X

Y

Z